Selected High Impact Journals

Dr. Huang Gang

Institute of Atmospheric physics,
Chinese Academy of Sciences

全文目录

第一部分　作者简介

第二部分　文章选编

黄刚，男，理学博士，中国科学院特聘核心研究员（二级），中国科学院大学岗位教授，LASG 国家重点实验室季风与海气团队负责人，中国科学院大气物理所大气科学人工智能研究中心主任，博士生导师，国家杰出青年基金获得者(2014)且优秀结题，国家中青年科技创新领军人才（2016），国家万人计划领军人才（2017），国务院政府特殊津贴获得者。研究生师从于气象泰斗叶笃正院士，1999 年 9 月获得中国科学院大气物理研究所博士学位。担任中国气象学会动力气象委员会委员，大气科学常务编委，气象学报、气候与环境研究以及中国科学数据编委；同时担任 SCI 刊物 Scientific Report，PeerJ, Frontiers in Earth Science，AAS 的编委以及 Advances in Meteorolog，Sustainability, Atmosphere 的客座编委；担任 The Innovation Geoscience 编委和 Geosciences （Climate）主编，担任 Nature 子刊（NCC，NC，NPJ，Communications Earth & Environmen）以及 SB，NSR，JC，BAMS 等 56 种 SCI 刊物审稿工作；CNC-WCRP（中国气候研究委员会）委员以及中国科学院大学、南京信息工程大学、河海大学、成都信息工程大学等兼职教授以及博士或硕士生导师；也是香港中文大学研究生课程特邀授课教授等。曾获国家气象局“十三五”以来气象科技优秀成果（排名第一）中国气象局 2023 年度科技成果评价良好等级（排名第一）以及 2019 年度中国气象学会大气科学基础研究成果奖一等奖（排名第一），2017 年度广东省科学技术一等奖（排名第二），“学笃风正”优秀博士论文和科研论文奖,涂长望青年科技奖,全国优秀气象科技工作者,中国科学院“朱李月华”优秀教师奖（2012,2020），2012、2013 和 2018 年度中科院优秀研究生指导教师奖以及 2023 学院级优秀课程（主讲教授）,并荣获 2013 年度赵九章优秀中青年科学奖以及 2014 年度卢嘉锡优秀导师奖等系列奖励。指导的博士获 2012、2013、2018 年度中科院优秀博士论文奖及其他青年奖项。截止到目前共发表 293 文章（包括 210 篇 SCI，69 篇 CSCD，14 篇书的章节），SCI 影响因子合计 1361.6；其中包括 Top 期刊（影响因子大于 9）30 篇（PNAS1 篇，Nature Climate Change 3 篇，Science Advances2 篇，Nature Geoscience3 篇，Nature Communications4 篇，Annual Review of Earth and Planetary Sciences1 篇，NPJ3 篇等）。SCI 总引 10264 次，Google 学术引用 12538 次，H 指数 54，入选全球顶尖前 10 万科学家排名，美国斯坦福大学发布了"2020-2024 全球前 2%顶尖科学家榜单"，“气候变化研究领域全球最具影响力的 1000 位科学家名单”“全球顶尖前 10 万科学家排名（2022-2023）”“Research.com 环境领域 Best Scientists in China for 2023-2024”以及 ESI 全球地球科学领域科学家排名前 1%高引用科学家目录，并且拥有 4 项计算机软著（3 项第一完成人）和 1 项发明专利（第一完成人）。

个人主页：http://hg.lasg.ac.cn email：hg@mail.iap.ac.cn

主要研究领域：气候动力学、季风动力学、海气相互作用、全球变暖动力学，人工智能与大气科学

Selected Impact Articles by Huang Gang

Table of Contents

1. **Huang, G.***, Y. Wang*, Y-G Ham, B. Mu, W. Tao and C. Xie. 2024:Toward a learnable climate model under the artificial intelligence era. Advances in Atmospheric Sciences，41(7), 1281−1288, https://doi.org/10.1007/s00376-024-3305-9 **(SCI)** (IF=6.6,2023)
2. Yao，M.,H. Tang*,**G. Huang*** and R. Wu，2024，Interdecadal shifts of ENSO influences on Spring Central Asian precipitation，npj Climate and Atmospheric Science, 7,194(2024), https://doi.org/10.1038/s41612-024-00742-x **(SCI)** (IF=9.45,2022)
3. Qu, X. and **G. Huang***, 2023: The primary factors influencing the cooling effect of carbon dioxide removal, NPJ climate and atmospheric science , 6, 215 (2023). https://doi.org/10.1038/s41612-023-00547-4 **(SCI)** (IF=9.45,2022)
4. Wang，L.*, **G. Huang***, W. Chen and T. Wang，2023:Super Drought under Global Warming: Concept, Monitoring Index and Validation, Bulletin of the American Meteorological Society (BAMS), 104(5),E943–E969, https://doi.org/10.1175/BAMS-D-22-0182.1 **(SCI)** (IF=9.12,2022)
5. Zhang, S., X. Qu*, **G. Huang*** and P. Hu,2023: Asymmetric Response of South Asian Summer Monsoon Rainfall in a Carbon Dioxide Removal Scenario, NPJ climate and atmospheric science，(2023) 6:10 , https://doi.org/10.1038/s41612 -023-00338-x **(SCI)** (IF=9.45,2022)
6. Gan, R., Q. Liu*, **G. Huang***, K. Hu and X. Li, 2023：Synchronized effects of greenhouse warming and internal variability have increased the frequency of extreme and central Pacific El Niño since 1980, Nature Communications，14, 394 (2023), https://doi.org/10.1038/s41467-023-36053-7 **(SCI)** (IF=17.69,2022)
7. Yang, K., W. Cai*,**G. Huang***, K. Hu, B. Ng and G. Wang,2022: Increased variability of western Pacific subtropical high under

greenhouse warming,Vol.119, No.23,e2120335119, Proceedings of the National Academy of Sciences , https://doi.org/10.1073/pnas.2120335119**(SCI)** (IF=12,78,2022)

8. **Huang, G***, Z. Xu, X. Qu, J. Cao, S. Long, K. Yang, H. Hou, Y. Wang and X. Ma, 2022: Critical climate issues towards carbon neutrality targets, Fundamental Research2(3):396-400， https://doi.org/10.1016/j.fmre.2022.02.011 **(ESCI)**
9. Wang S. **G. Huang***, T. Dai* and K. Hu, 2022: The First 5-year Clean Air Action Did Increase the Blue Days in winter over Beijing-Tianjin-Hebei, Science Bulletin, 67(8):774-776, https://doi.org/10.1016/j.scib.2022.01.009 **(SCI)** (IF=20.58,2022)
10. Lin,J., #*, C. Zhou, #, L. Chen, #, **G. Huang,*** , J.F. Lamarque, J. Nie, J. Yang, K. Hu, P. Liu, J. Wang and Y. Hu，2022： Comparable sulfate climate impacts by consumption of developed and developing countries despite large emission differences， Nature Geosciences, 15,184-189(2022), https://doi.org/10.1038/s41561-022-00898-2 **(SCI)** (IF=21.53,2022)
11. Ma,X., **G. Huang*** and J. Cao,2021: The significant roles of anthropogenic aerosols on surface temperature under carbon neutrality, Science Bulletin, 67(5)470-473, https://doi.org/10.1016/j.scib.2021.10.022 **(SCI)** (IF=20.58,2022)
12. Hu, K.*, **G. Huang***, P. Huang, K. Yu, and S-P. Xie,2021: Intensification of El Niño-induced atmospheric anomalies under greenhouse warming, Nature Geoscience, 14, 377-382 (2021), https://doi.org/10.1038/s41561-021-00730-3 **(SCI)** (IF=21.53,2022)
13. Ma, X., W. Liu, R. Allen, **G. Huang*** and X. Li, 2020: Dependence of regional ocean heat uptake on anthropogenic warming scenarios, Science Advances, 6(45):eabc0303,https://doi.org/10.1126/sciadv.abc0303 **(SCI)** (IF=14.96,2022)
14. Yao, S., J. Luo*, **G. Huang*** and P. Wang, 2017: Distinct global warming rates tied to multiple ocean surface temperature changes,

Nature Climate Change, 7, 486–491, https://doi.org/10.1038/NCLIMATE3304 **(SCI)** (IF=28.66,2022)

15. **Huang, G.*** and G. Wen, 2013: Spatial and temporal variations of light rain events over China and the mid-high latitudes of the Northern Hemisphere. Chinese Science Bulletin, 2013, 58(12):1402-1411,https://doi.org/10.1007/s11434-012-5593-1 **(SCI)**
16. **Huang, G.***, K. Hu and S.-P. Xie, 2010: Strengthening of tropical Indian Ocean teleconnection to the Northwest Pacific since the mid-1970s: An atmospheric GCM study. Journal of climate, 23(19):5294–5304, https://doi.org/10.1175/2010JCLI35 77.1 **(SCI)** (IF=5,38,2022)
17. **Huang, G.***, Y. Liu, and R. Huang, 2011: The interannual variability of summer rainfall in the arid and semi-arid region in northern China and its association with the northern hemisphere circumglobal teleconnection. Advances in Atmospheric Sciences, 28(2), 257-268, https://doi.org/10.1007/s00376-010-9225-x **(SCI)** (IF=3.9,2022)
18. **Huang, G.***, X. Qu, and K. Hu, 2011: The Impact of tropical Indian Ocean SST on South Asian High in Boreal Summer. Advances in Atmospheric Sciences, 28(2), 421-432, https://doi.org/10.1007/s00376-010-9224-y **(SCI)** (IF=3.9,2022)
19. **Huang, G.***, 2004: An Index Measuring the Interannual Variation of the East Asian Summer Monsoon-The EAP Index. Advances in Atmospheric Sciences, 21(1):41-52. https://doi.org/10.1007/BF02915679 **(SCI)** (IF=3.9,2022)
20. Wang, Z.-B., Q.-H. Ding*, R. Wu, T. Ballinger, B. Guan, D. Bozkurt, D. Nash, I. Baxter, D. Topál, Z. Li, **G. Huang**, W. Chen, S.-F. Chen, X. Cao, and Z. Chen, 2024: Role of atmospheric rivers in shaping long term Arctic moisture variability. Nature Communications,15, 5505 (2024). https://doi.org/10.1038/s41467-024-49857-y **(SCI)** (IF=17.69,2022)
21. Zhou, S., P. Huang*, L. Wang, K. Hu and **G. Huang**, 2024: Robust changes in global subtropical circulation under greenhouse warming,

Nature Communications， 15, 96 (2024), https://doi.org/10.1038/s41467-023-44244-5 **(SCI)** (IF=17.69,2022)

22. Liu, F. , C. Gao* , J. Chai , A. Robock , B. Wang* , J. Li , X. Zhang , **G. Huang** and W. Dong, 2022:Tropical volcanism enhanced the East Asian summer monsoon during the last millennium, Nature Communications, 13, 3429 (2022)， https://doi.org/10.1038/s41467-022-31108-7 **(SCI)** (IF=17.69,2022)
23. Yang ,Y., L. Wu*, Y. Guo, W. Cai*, **G. Huang**, X. Li, T. Geng, Z. J, S. Li and S.-P Xie, 2021: Greenhouse warming intensifies north tropical Atlantic climate variability, Science Advances， Vol. 7, No. 35, eabg9690, https://doi.org/10.1126/sciadv.abg9690 **(SCI)** (IF=14.96,2022)
24. Cai, W.*, K. Yang, L. Wu,*, **G. Huang**, A. Santoso, B. Ng, G. Wang and T. Yamagata, 2021: Opposite response of strong and moderate positive Indian Ocean Dipole to greenhouse warming，Nature Climate Change,11:27-32(2021),https://doi.org/10.1038/s41558-020-00943-1 **(SCI)** (IF=28.66,2022)
25. Ma, J.*, R. Chadwick, K. Seo, C. Dong, **G. Huang**, G. R. Foltz and J. H. Jiang,2018: Responses of the tropical atmospheric circulation to climate change and connection to the hydrological cycle, Annual Review of Earth and Planetary Sciences, 46: 549-580, https://doi.org/10.1146/annurev-earth-082517-010102 **(SCI)** (IF=16.3,2022)
26. Huang, P., S.-P. Xie, K. Hu, **G. Huang** and R. Huang, 2013: Patterns of the seasonal response of tropical rainfall to global warming. Nature Geoscience, 6(5) :357-361, https://doi.org/10.1038 /NGEO1792 **(SCI)** (IF=21.53,2022)
27. Li, J., S.-P. Xie, E. R. Cook, **G. Huang**, R. D'Arrigo, F. Liu, J. Ma and X. Zheng, 2011: Interdecadal modulation of El Niño amplitude during the past millennium. Nature Climate Change,1:114–118, https://doi.org/10.1038/NCLIMATE1086 **(SCI)** (IF=28.66,2022)
28. Xie, S.-P., K. Hu, J. Hafner, H. Tokinaga, Y. Du, **G. Huang**, and T.

Sampe, 2009: Indian Ocean Capacitor Effect on Indo–Western Pacific Climate during the Summer following El Nino. Journal of Climate, 22:730–747.https://doi.org/10.1175/2008JCLI2544.1 **(SCI)** (IF=5,38,2022)

ADVANCES IN ATMOSPHERIC SCIENCES, VOL. 41, JULY 2024, 1281–1288

• **Perspectives** •

Toward a Learnable Climate Model in the Artificial Intelligence Era※

Gang HUANG*[1,2,3], Ya WANG*[1], Yoo-Geun HAM[4], Bin MU[5], Weichen TAO[1], and Chaoyang XIE[1]

[1]*State key Laboratory of Numerical Modeling for Atmospheric Sciences and Geophysical Fluid Dynamics, Institute of Atmospheric Physics, Chinese Academy of Sciences, Beijing* 100029, *China*

[2]*Laboratory for Regional Oceanography and Numerical Modeling, Qingdao National Laboratory for Marine Science and Technology, Qingdao* 266237, *China*

[3]*University of Chinese Academy of Sciences, Beijing* 100049, *China*

[4]*Department of Environmental Planning, Graduate School of Environmental Studies, Seoul National University, Seoul* 08826, *South Korea*

[5]*School of Software Engineering, Tongji University, Shanghai* 200092, *China*

(Received 26 November 2023; revised 12 March 2024; accepted 18 March 2024)

ABSTRACT

Artificial intelligence (AI) models have significantly impacted various areas of the atmospheric sciences, reshaping our approach to climate-related challenges. Amid this AI-driven transformation, the foundational role of physics in climate science has occasionally been overlooked. Our perspective suggests that the future of climate modeling involves a synergistic partnership between AI and physics, rather than an "either/or" scenario. Scrutinizing controversies around current physical inconsistencies in large AI models, we stress the critical need for detailed dynamic diagnostics and physical constraints. Furthermore, we provide illustrative examples to guide future assessments and constraints for AI models. Regarding AI integration with numerical models, we argue that offline AI parameterization schemes may fall short of achieving global optimality, emphasizing the importance of constructing online schemes. Additionally, we highlight the significance of fostering a community culture and propose the OCR (Open, Comparable, Reproducible) principles. Through a better community culture and a deep integration of physics and AI, we contend that developing a learnable climate model, balancing AI and physics, is an achievable goal.

Key words: artificial intelligence, deep learning, learnable climate model

Citation: Huang, G., Y. Wang, Y.-G. Ham, B. Mu, W. C. Tao, and C. Y. Xie, 2024: Toward a learnable climate model in the artificial intelligence era. *Adv. Atmos. Sci.*, **41**(7), 1281−1288, https://doi.org/10.1007/s00376-024-3305-9.

1. Artificial intelligence's ascent in climate science

We are in a revolutionary era where artificial intelligence (AI), especially large AI models (Table 1), is redefining how we understand and address climate-related challenges. AI models have swept through most areas of the atmospheric sciences, including but not limited to weather forecasting (Table 1; Pathak et al., 2022; Bi et al., 2023; Chen et al., 2023a; Chen et al., 2023b; Lam et al., 2023), subseasonal and seasonal predictions (Ham et al., 2019, 2021; Pan et al., 2020; Kim et al., 2021; Mu et al., 2021; Ravuri et al., 2021; Ling et al., 2022; Fan et al., 2023; Hess et al., 2022; Zhang et al., 2023; Zhou and Zhang, 2023), extreme weather and climate prediction (e.g., Li et al., 2023), parameterization schemes (Rasp et al., 2018; Han et al., 2020), correction of model simulations (e.g., Pan et al., 2020), and climate detection and attribution (Labe and Barnes, 2021, 2022; Diffenbaugh and Barnes, 2023; Ham et al., 2023; Labe et al., 2023). With its ability to integrate and comprehend data from diverse sources such as satellites, weather stations, and ocean buoys, AI has delivered breakthrough advancements in numerous areas. Its strengths lie in enhancing the overall understanding of atmospheric systems, handling the complexity and nonlinearity of atmospheric dynamics, and offering rapid computational speeds.

While AI blazes forward, the role of physics, often described as the bedrock of climate science, has sometimes been overshadowed. Physical laws and climate theories provide the fundamental principles underpinning our understanding of climate systems. They form the basis of dynamical cli-

※ This paper is a contribution to the special issue on AI Applications in Atmospheric and Oceanic Science: Pioneering the Future.

* Corresponding authors: Gang HUANG, Ya WANG
Emails: hg@mail.iap.ac.cn, wangya@mail.iap.ac.cn

© Institute of Atmospheric Physics/Chinese Academy of Sciences, and Science Press 2024

Table 1. Details of large AI weather models.

Model	Forecast Duration	Spatial Resolution	Accuracy (Z500 ACC>0.6)	Forecast Variables	Computational Requirements	Train. Data	Algorithm	Institutions	Initial Release Date	Journal Publication Date and Name	Number of Parameters
GraphCast	10 days	0.25°×0.25°, 6 h	9–10 days	5 surface variables (including precipitation) + 6 atmospheric variables	21 days; 32 TPU v4	ERA5 39yr	GNN	Google DeepMind	2022.12.24, arXiv	2023.11.14, Science	36.7 Million
Pangu-Weather	1 hour–7days	0.25°×0.25°, 1 h	7 days	4 surface variables (excluding precipitation) + 5 atmospheric variables	16 days; 192 V100 GPUs	ERA5 39yr	Transformer	Huawei Cloud	2022.11.3, arXiv	2023.7.5, Nature	256 Million
FourCastNet	3 days	0.25°×0.25°, 6 h	~7 days	5 surface variables (including precipitation) + 4 atmospheric variables	4 A100 GPUs	ERA5 40yr	Adaptive Fourier Neural Operators	Nvidia	2022.2.22, arXiv	N/A	N/A
FuXi	15 days	0.25°×0.25°, 6 h	10–11 days	5 surface variables (including precipitation) + 5 atmospheric variables	~30 hours(pre-training)+2 days(fine-tune); 8 A100 GPUs	ERA5 39yr	U-Transformer	Fudan University	2023.6.22, arXiv	2023.11.16, npj Climate and Atmospheric Science	4.5 Billion
FengWu	10.75 days	0.25°×0.25°, 6 h	10–11 days	4 surface variables (excluding precipitation) + 5 atmospheric variables	17 days; 32 A100 GPUs	ERA5 39yr	Transformer	Shanghai Artificial Intelligence Lab	2023.4.6, arXiv	N/A	N/A
SwinVRNN	5 days	5.625°×5.625°, 6 h	N/A	4 surface variables (including precipitation) + 5 atmospheric variables	8 Tesla V100 GPUs	ERA5 40yr	Swin Transformer	Alibaba Group	2022.5.26, arXiv	N/A	N/A

mate models, offering a comprehensible framework for climate predictions and climate simulations. These models are interpretable, and they have proved their mettle for nearly one hundred years (Bauer et al., 2015). However, in the AI era, interpretability often takes a back seat. AI models are often recognized as "black boxes", which generate predictions and simulations without transparently explaining their involved physical processes. This opaqueness poses huge challenges when it comes to validating AI models and building trust in their generated results. Additionally, AI models lacking physical constraints often face issues such as poor generalization capabilities. This can lead to results that are inconsistent with physical properties and highly unstable, particularly in the context of extreme events.

So, where do we go from here? The answer lies in the symbiotic relationship between AI and physics. AI brings unparalleled computational power and the ability to recognize complex patterns, while physics offers transparency, interpretability, and a solid foundation for scientific understanding. The future of climate modeling is not an "either/or" scenario, and is a partnership between these two realms, leveraging AI's computational prowess and the laws of physics' grounding to create a learnable climate model with good interpretability.

2. Physics for AI modeling: limitations and solutions

Recently emerged large AI weather models have begun to rival or surpass traditional numerical weather predictions. This naturally raises the question of whether these AI models adhere to the principles of meteorological and climate theories. Climate theories derived from various mathematical physics equations, like quasi-geostrophic theory and quasi-steady Rossby waves, serve as the foundational structure for climate research (Hoskins and Karoly, 1981; Held et al., 2002; Held, 2019). Some might envisage a scenario where, if an AI model is complex enough, with multiple layers and variables, it might closely replicate observational data, learning and following the implied conservation laws and climate theories present in the observations. (Hakim and Masanam (2023) conducted a crucial analysis on this issue, applying perturbations to Pangu-Weather, and observed that introducing a tropical heat source in the model reproduces the Matsuno –Gill response (Matsuno, 1966; Gill, 1980) in the tropics and the associated extratropical Rossby wave train. This qualitative finding suggests that AI models seem to possess the capability to learn fundamental physical laws and atmospheric dynamics. However, the actual situation is more intricate. Quantitative analyses indicate persistent challenges, such as issues in geostrophic wind balance and the rotational and divergent wind components, despite the abundance of data and high complexity in models like Pangu and Graphcast Weather (Bonavita, 2023; Kochkov et al., 2024).

These assessment conclusions may appear contradictory but are, in fact, reflective of different degrees of evaluation perspectives. Hakim and Masanam (2023) indicated that AI models can qualitatively reproduce certain dynamic modes based on climatic dynamics. Considering that these responses are inherently embedded in the data at the weather and climate scale, learning and qualitatively reproducing such modes are reasonable. On the other hand, quantitative evaluations by Bonavita (2023) and Kochkov et al. (2024) revealed significant disparities in aspects like geostrophic wind and divergent wind compared to traditional models. The absence of these factors in the inputs and outputs of the AI model, coupled with the relatively small magnitude of the divergent winds, makes it relatively natural for such errors to occur.

While these evaluations pertain to weather models, considering the lower complexity, data volume, and parameter quantity in climate models compared to weather models, similar issues need to be addressed in the evaluation and optimization processes of AI climate models. This emphasizes the importance of dynamic diagnostic and physical constraints to AI climate models. First and foremost, a meticulous examination of climate dynamics is essential for analyzing and comprehending the performance of AI models. Current evaluation methods primarily focus on first-order and second-order statistics, but good performance in these statistics does not mean a model is good at reproducing the crucial features of targeted dynamical climate variability, such as ENSO's seasonal phase-locking and asymmetry (Jin, 1996; Wallace et al., 1998; McPhaden et al., 2006). Consequently, there is an imperative need to reevaluate AI simulations, giving prominence not only to fundamental statistics but also to dynamic modes and physical processes. A case in point is the research conducted by Wang et al. (2024), who revealed that generative models can rectify not only climatological sea surface temperature (SST) biases but also markedly mitigate the prevalent excessive westward bias in ENSO SST anomalies, which is a common issue in climate models and has a considerable impact on the ENSO decay and the East Asian climate (Li and Xie, 2012, 2014; Tao et al., 2018, 2019; Jiang et al., 2021). Due to the complexity of the climate system, evaluating climate simulations could be a challenging task. Numerical climate model evaluations have largely relied on the Coupled Model Intercomparison Project (CMIP), allowing scientists from various research domains to thoroughly assess these models based on their climate physics knowledge. To enhance the evaluation of AI simulations, it is imperative to establish a similar comparative project, such as the AI Model Intercomparison Project (AI-MIP). This initiative should construct and release unified dynamic diagnostic tools of varying complexities and benchmarks to facilitate comprehensive assessments. AI-MIP mandates the construction of AI models on a unified and open dataset, and the evaluation and comparison of these models based on standardized metrics. Through AI-MIP, we expect to significantly reduce the costs of data acquisition, model comparison, and learning. Individuals will be able to easily compare their models with state-of-the-art models, accelerat-

ing progress in the field.

Furthermore, it is imperative to apply physical constraints informed by climate dynamics to refine AI models. Basic physical knowledge plays a crucial role in providing physical constraints to AI models (Mohan et al., 2019; Beucler et al., 2020). PINNs (Physics-Informed Neural Networks) are a groundbreaking approach where deep-learning (DL) models are informed by physical laws, integrating differential equations directly into the learning process (Raissi et al., 2019). Besides, conservation laws such as energy conservation, mass conservation, and momentum conservation, have always been essential for model development and climate diagnostics.

These constraints can be categorized as soft constraints and hard constraints. Soft constraints do not explicitly impose specific network changes but provide some representations of physical linkages, and physical equations or mathematical constraints. They may encompass connections between different regions, such as teleconnections, or interactions between different variables. One popular soft constraint uses existing physical equations to constrain the loss function (Beucler et al., 2021). Moreover, Mu et al. (2021) offered an example where a graph neural network (GNN) was designed to predict ENSO. They employed a graph structure to represent various physical variables, particularly the coupling relationships between SST and clouds. This method can be understood as a feature fusion, improving the nonlinear combination of different variables/features to better identify critical processes influencing ENSO development. Another example comes from Chen et al. (2024) who designed a GNN for precipitation prediction considering the constraints of the omega equation and moisture equation. By using this physics-constrained network, the prediction of heavy rainfall was significantly improved, and the whole prediction results were also better than those of the other DL models without constraints. Meanwhile, a hard constraint usually modifies the neural network, ensuring an expected constraint during learning and inference (González-Abad et al., 2023; Harder et al., 2024). For instance, when downscaling T_{min} (minimum temperature) and T_{mean} (mean temperature) in González-Abad et al. (2023), the activation function for T_{min} was configured as ReLU, whereas the activation function for T_{mean}/T_{min} was set as (1 + ReLU). This specific configuration guarantees that the results consistently adhere to the *a priori* relationship where T_{mean} is greater than T_{min}. Besides, there are also studies that have extended convolutional networks to accommodate a wider variety of symmetries, such as rotations, reflections, and more extensive gauge symmetry transformations (Bronstein et al., 2017; Cohen et al., 2019). This enhancement enables convolutional networks to more effectively recognize and process data patterns exhibiting these symmetries, helping models more accurately capture complex patterns and dynamics in atmospheric phenomena, thereby improving the precision and reliability of weather forecasting and climate modeling.

3. AI for numerical modeling: limitations and solutions

In the previous discussion, we emphasize the importance of dynamic diagnostics and physical constraints for AI climate models. It is essential to understand how AI can affect the field of numerical climate models. AI applications within numerical models are already underway, with a prominent example being the use of AI to construct parameterization schemes, enhancing the performance of numerical models (e.g., Rasp et al., 2018; Han et al., 2020; Zhu et al., 2022; Wang and Tan, 2023). The Fortran Torch Adaptor (Mu et al., 2023) is an adapter designed to bridge Fortran and Torch, enabling researchers to load Torch model parameters and perform forward propagation within a Fortran environment, which facilitates the coupling of AI models with numerical models.

However, challenges persist in current AI parameterization schemes. Firstly, most AI parameterization schemes are currently offline. These offline parameterization schemes, when coupled with models for long-term integration, may lead to instability, resulting in model crashes, and potentially give rise to various issues such as climate drift. Secondly, a DL optimization of a specific parameter in isolation for a given parameterization scheme aims to achieve the optimum value for that parameter. In reality, climate models have numerous parameters, and optimizing one parameter may only represent a local optimum for the entire model.

A potential solution to address these issues could involve the development of online parameterization schemes. Such a system could potentially compute losses by comparing numerical model output to observations and optimizing AI weights that are coupled to numerical models using back-propagation. Is it possible to develop this AI-driven parameterization scheme that is updated online to correct the results of the numerical model (Chen et al., 2023c)? A similar approach has been adopted in the field of hydrology, known as “differentiable models”, which couple DL parameterization schemes with hydrological models, optimizing DL parameterizations based on hydrological model outputs (Shen et al., 2023). Even though attempts have been made to determine a few model parameters to reduce the difference between the observed and simulated results through the online parameter estimation (Han et al., 2014; Wu et al., 2016), implementing such an approach, especially within complex climate or coupled models, is still considered challenging. Recently, a groundbreaking development occurred with Google’s neural general circulation model (NGCM; Kochkov et al., 2024). It represents an online AI–physics hybrid GCM, exhibiting superior performance compared to current mainstream models and demonstrating excellent adherence to physical conservation laws. This pioneering work has the potential to catalyze the application of similar paradigms in climate modeling. Despite this advancement, constructing comparable climate models remains challenging. While the NGCM employs an embedding approach to

create AMIP-like experiments, there are substantial differences from climate simulations. In contrast to weather models, finding corresponding observations for climate model simulations is challenging due to the presence of internal variability, making it difficult to calculate errors for iterative optimization as demonstrated by the NGCM.

4. Infrastructure for the climate community

Earlier, we addressed the primary challenges faced by the integration of AI and climate studies, along with proposed potential solutions. We emphasize the crucial role of detailed dynamic diagnostics and physical constraints for AI models, along with the importance of developing online parameterization schemes for climate models. However, resolving these issues heavily relies on community culture and robust leadership. Currently, the climate-AI community lacks unified benchmarks and baselines, resulting in significant redundant efforts and making model comparisons exceptionally challenging. The principles of unified benchmarks and baselines are crucial for the advancement of the climate AI community. Wisdom can be gleaned from distant sources. Relevant experiences can be drawn from the computer science community to inform our approach.

The rapid development of the AI era is propelled by the explosion of computational power and the open nature of DL communities. For the continued advancement of climate models in the AI era, a similar condition is required, especially within the climate community, that is an open and collaborative infrastructure. It is essential to foster progress in the climate field, creating an environment where innovative models and ideas can be shared and developed collectively. We can summarize this requirement as the "Open, Comparable, Reproducible" (OCR) principle (Fig. 1).

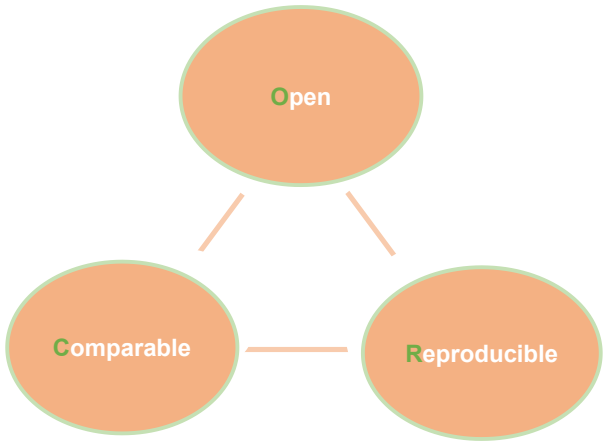

Fig. 1. The OCR principles.

- "Open" emphasizes open-source code and open datasets of AI climate modeling.
- "Comparable" signifies the creation of unified evaluation metrics. It involves integrating climate model evaluation frameworks to conduct thorough assessments involving climate dynamic assessments and the establishment of uniform datasets, task sets, and baselines.
- "Reproducible" denotes that the results published in research papers should be reproducible.

The OCR principles have a nuanced interplay and mutual influence. "Open" serves as the foundational bedrock for the subsequent principles to materialize. "Comparable" and "Reproducible" complement each other symbiotically. The "Reproducible" part of AI model results is crucial for comparing different model outputs. This, in turn, increases scientists' awareness and emphasis on model reproducibility, creating a harmonious framework that propels scientific research toward more reliable and enduring progress.

The OCR principles hold significant potential for expediting the application of AI in climate science, particularly in cli-

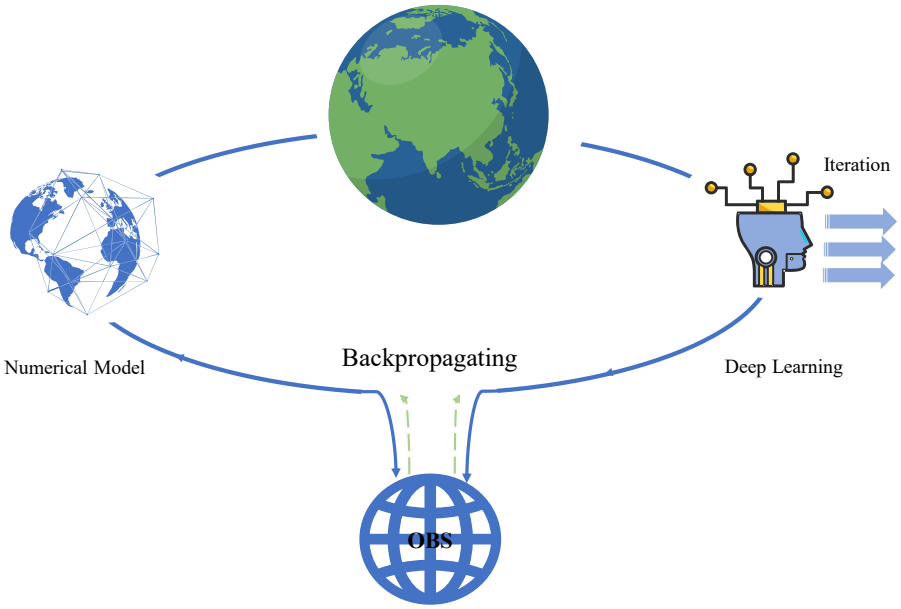

Fig. 2. Schematic of the balanced AI–physics model.

mate prediction and modeling. Regarding the latter, the success of CMIP has already demonstrated how an open-data comparison project can substantially advance the field. In accordance with the OCR principles, an AI-MIP can be established, which would greatly facilitate the evaluation, iteration, and optimization of AI models. Simultaneously, this initiative would promote the development of numerical modeling and AI–physics hybrid modeling.

5. Toward a balanced AI–physics climate model

Looking ahead, more comprehensive dynamic diagnostics and physical constraints can further enhance the performance of AI climate models. This progress will also stimulate the development of AI parameterization schemes. Considering the development of AI (especially unsupervised learning; physics-constrained AI) and numerical climate models, there is optimism that the challenge of discrepancies between climate model outputs and observations could be addressed. A balance between AI and numerical climate modeling may be attainable. This balance could involve using numerical methods to resolve solvable processes while employing online AI solutions to address critical parameterization schemes. As this hybrid approach advances, it becomes increasingly challenging to classify a model as purely numerical or AI-based. Ultimately, it evolves into a balanced AI–physics climate model (Fig. 2). Through the incorporation of AI-based parameterization schemes, such a model can be iteratively optimized, transforming into a learnable climate model. Furthermore, since it includes explicit computations of physical quantities and obeys physical equations, this model exhibits a high level of interpretability, guaranteeing direct climate diagnostic analyses.

Acknowledgements. This work was supported by the National Natural Science Foundation of China (Grant Nos. 42141019 and 42261144687) and STEP (Grant No. 2019QZKK0102). Yoo-Geun HAM was supported by the Korea Environmental Industry & Technology Institute (KEITI) through the "Project for developing an observation-based GHG emissions geospatial information map", funded by the Korea Ministry of Environment (MOE) (Grant No. RS-2023-00232066). Ya WANG would like to thank Prof. Baoxiang PAN for sharing related papers and useful discussions.

REFERENCES

Bauer, P., A. Thorpe, and G. Brunet, 2015: The quiet revolution of numerical weather prediction. *Nature*, **525**(7567), 47–55, https://doi.org/10.1038/nature14956.

Beucler, T., M. Pritchard, P. Gentine, and S. Rasp, 2020: Towards physically-consistent, data-driven models of convection. *2020 IEEE International Geoscience and Remote Sensing Symposium*, Waikoloa, HI, USA, IEEE, 3987–3990, https://doi.org/10.1109/IGARSS39084.2020.9324569.

Beucler, T., M. Pritchard, S. Rasp, J. Ott, P. Baldi, and P. Gentine, 2021: Enforcing analytic constraints in neural networks emulating physical systems. *Physical Review Letters*, **126**(9), 098302, https://doi.org/10.1103/PhysRevLett.126.098302.

Bi, K. F., L. X. Xie, H. H. Zhang, X. Chen, X. T. Gu, and Q. Tian, 2023: Accurate medium-range global weather forecasting with 3D neural networks. *Nature*, **619**(7970), 533–538, https://doi.org/10.1038/s41586-023-06185-3.

Bonavita, M., 2023: On some limitations of data-driven weather forecasting models. arXiv preprint arXiv: 2309.08473, https://doi.org/10.48550/arXiv.2309.08473.

Bronstein, M. M., J. Bruna, Y. LeCun, A. Szlam, and P. Vandergheynst, 2017: Geometric deep learning: Going beyond Euclidean data. *IEEE Signal Processing Magazine*, **34**, 18–42, https://doi.org/10.1109/MSP.2017.2693418.

Chen, L., X. H. Zhong, F. Zhang, Y. Cheng, Y. H. Xu, Y. Qi, and H. Li, 2023a: FuXi: A cascade machine learning forecasting system for 15-day global weather forecast. arXiv preprint arXiv: 2306.12873, https://doi.org/10.48550/arXiv.2306.12873.

Chen, K. and Coauthors., 2023b: Fengwu: Pushing the skillful global medium-range weather forecast beyond 10 days lead. arXiv preprint arXiv:2304.02948, https://doi.org/10.48550/arXiv.2304.02948.

Chen, M., and Coauthors, 2023c: Iterative integration of deep learning in hybrid Earth surface system modelling. *Nature Reviews Earth & Environment*, **4**, 568–581, https://doi.org/10.1038/s43017-023-00452-7.

Chen, Y. T., Y. Wang, G. Huang, and Q. Tian, 2024: Coupling physical factors for precipitation forecast in China with graph neural network. *Geophys. Res. Lett.*, **51**, e2023GL106676, https://doi.org/10.1029/2023GL106676.

Cohen, T. S., M. Weiler, B. Kicanaoglu, and M. Welling, 2019: Gauge equivariant convolutional networks and the icosahedral CNN. *Proceedings of the 36th International Conference on Machine Learning*, https://doi.org/10.48550/arXiv.1902.04615.

Diffenbaugh, N. S., and E. A. Barnes, 2023: Data-driven predictions of the time remaining until critical global warming thresholds are reached. *Proceedings of the National Academy of Sciences of the United States of America*, **120**(6), e2207183120, https://doi.org/10.1073/pnas.2207183120.

Fan, P. Y., J. Yang, Z. P. Zhang, N. H. Zang, Y. F. Li, and G. L. Feng, 2023: Summer precipitation prediction in eastern China based on machine learning. *Climate Dyn.*, **60**(9–10), 2645–2663, https://doi.org/10.1007/s00382-022-06464-1.

Gill, A. E., 1980: Some simple solutions for heat-induced tropical circulation. *Quart. J. Roy. Meteor. Soc.*, **106**(449), 447–462, https://doi.org/10.1002/qj.49710644905.

González-Abad, J., Á. Hernández-García, P. Harder, D. Rolnick, and J. M. Gutiérrez, 2023: Multi-variable hard physical constraints for climate model downscaling. arXiv preprint arXiv: 2308.01868, https://doi.org/10.48550/arXiv.2308.01868.

Hakim, G. J., and S. Masanam, 2023: Dynamical tests of a deep-learning weather prediction model. arXiv preprint arXiv:2309.10867, https://doi.org/10.48550/arXiv.2309.10867.

Ham, Y. G., J. H. Kim, and J. J. Luo, 2019: Deep learning for multi-year ENSO forecasts. *Nature*, **573**(7775), 568–572, https://doi.org/10.1038/s41586-019-1559-7.

Ham, Y. G., J. H. Kim, E. S. Kim, and K. W. On, 2021: Unified

deep learning model for El Niño/Southern Oscillation forecasts by incorporating seasonality in climate data. *Science Bulletin*, **66**(13), 1358–1366, https://doi.org/10.1016/j.scib.2021.03.009.

Ham, Y.-G., J.-H. Kim, S.-K. Min, D. Kim, T. M. Li, A. Timmermann, and M. F. Stuecker, 2023: Anthropogenic fingerprints in daily precipitation revealed by deep learning. *Nature*, **622**(7982), 301–307, https://doi.org/10.1038/s41586-023-06474-x.

Han, G. J., X. F. Zhang, S. Zhang, X. R. Wu, and Z. Liu, 2014: Mitigation of coupled model biases induced by dynamical core misfitting through parameter optimization: Simulation with a simple pycnocline prediction model. *Nonlinear Processes in Geophysics*, **21**, 357–366, https://doi.org/10.5194/npg-21-357-2014.

Han, Y. L., G. J. Zhang, X. M. Huang, and Y. Wang, 2020: A moist physics parameterization based on deep learning. *Journal of Advances in Modeling Earth Systems*, **12**(9), e2020MS002076, https://doi.org/10.1029/2020MS002076.

Harder, P., Q. D. Yang, V. Ramesh, P. Sattigeri, A. Hernandez-Garcia, C. Watson, D. Szwarcman, and D. Rolnick, 2024: Generating physically-consistent high-resolution climate data with hard-constrained neural networks. arXiv preprint arXiv: 2208.05424, https://doi.org/10.48550/arXiv.2208.05424.

Held, I., 2019: 100 years of progress in understanding the general circulation of the atmosphere. *Meteor. Monogr.*, **59**, 6.1–6.23, https://doi.org/10.1175/AMSMONOGRAPHS-D-18-0017.1.

Held, I. M., M. F. Ting, and H. L. Wang, 2002: Northern winter stationary waves: Theory and modeling. *J. Climate*, **15**(16), 2125–2144, https://doi.org/10.1175/1520-0442(2002)015<2125:NWSWTA>2.0.CO;2.

Hess, P., M. Drüke, S. Petri, F. M. Strnad, and N. Boers, 2022: Physically constrained generative adversarial networks for improving precipitation fields from Earth system models. *Nature Machine Intelligence*, **4**(10), 828–839, https://doi.org/10.1038/s42256-022-00540-1.

Hoskins, B. J., and D. J. Karoly, 1981: The steady linear response of a spherical atmosphere to thermal and orographic forcing. *J. Atmos. Sci.*, **38**(6), 1179–1196, https://doi.org/10.1175/1520-0469(1981)038<1179:TSLROA>2.0.CO;2.

Jiang, W. P., P. Huang, G. Huang, and J. Ying, 2021: Origins of the excessive westward extension of ENSO SST simulated in CMIP5 and CMIP6 models. *J. Climate*, **34**(8), 2839–2851, https://doi.org/10.1175/JCLI-D-20-0551.1.

Jin, F. F., 1996: Tropical ocean-atmosphere interaction, the Pacific cold tongue, and the El Niño-Southern Oscillation. *Science*, **274**(5284), 76–78, https://doi.org/10.1126/science.274.5284.76.

Kim, H., Y. G. Ham, Y. S. Joo, and S. W. Son, 2021: Deep learning for bias correction of MJO prediction. *Nature Communications*, **12**, 3087, https://doi.org/10.1038/s41467-021-23406-3.

Kochkov, D., and Coauthors, 2024: Neural general circulation models for weather and climate. arXiv preprint arXiv: 2311.07222, https://doi.org/10.48550/arXiv.2311.07222.

Labe, Z. M., and E. A. Barnes, 2021: Detecting climate signals using explainable AI with single-forcing large ensembles. *Journal of Advances in Modeling Earth Systems*, **13**(6), e2021MS002464, https://doi.org/10.1029/2021MS002464.

Labe, Z. M., and E. A. Barnes, 2022: Comparison of climate model large ensembles with observations in the arctic using simple neural networks. *Earth and Space Science*, **9**(7), e2022EA002348, https://doi.org/10.1029/2022EA002348.

Labe, Z. M., E. A. Barnes, and J. W. Hurrell, 2023: Identifying the regional emergence of climate patterns in the ARISE-SAI-1.5 simulations. *Environmental Research Letters*, **18**(4), 044031, https://doi.org/10.1088/1748-9326/acc81a.

Lam, R., and Coauthors, 2023: Learning skillful medium-range global weather forecasting. *Science*, **382**, 1416–1421, https://doi.org/10.1126/science.adi2336.

Li, G., and S. P. Xie, 2012: Origins of tropical-wide SST biases in CMIP multi-model ensembles. *Geophys. Res. Lett.*, **39**, L22703, https://doi.org/10.1029/2012GL053777.

Li, G., and S. P. Xie, 2014: Tropical biases in CMIP5 multimodel ensemble: The excessive equatorial pacific cold tongue and double ITCZ problems. *J. Climate*, **27**(4), 1765–1780, https://doi.org/10.1175/JCLI-D-13-00337.1.

Li, P. Y., Y. Yu, D. N. Huang, Z. H. Wang, and A. Sharma, 2023: Regional heatwave prediction using graph neural network and weather station data. *Geophys. Res. Lett.*, **50**(7), e2023GL103405, https://doi.org/10.1029/2023GL103405.

Ling, F. H., J. J. Luo, Y. Li, T. Tang, L. Bai, W. L. Ouyang, and T. Yamagata, 2022: Multi-task machine learning improves multi-seasonal prediction of the Indian Ocean Dipole. *Nature Communications*, **13**(1), 7681, https://doi.org/10.1038/s41467-022-35412-0.

Matsuno, T., 1966: Quasi-geostrophic motions in the equatorial area. *J. Meteor. Soc. Japan*, **44**(1), 25–43, https://doi.org/10.2151/jmsj1965.44.1_25.

McPhaden, M. J., S. E. Zebiak, and M. H. Glantz, 2006: ENSO as an integrating concept in earth science. *Science*, **314**(5806), 1740–1745, https://doi.org/10.1126/science.1132588.

Mohan, A. T., N. Lubbers, D. Livescu, and M. Chertkov, 2019: Embedding hard physical constraints in convolutional neural networks for 3D turbulence. *ICLR 2020 Workshop on Integration of Deep Neural Models and Differential Equations*.

Mu, B., B. Qin, and S. J. Yuan, 2021: ENSO-ASC 1.0.0: ENSO deep learning forecast model with a multivariate air-sea coupler. *Geoscientific Model Development*, **14**(11), 6977–6999, https://doi.org/10.5194/gmd-14-6977-2021.

Mu, B., L. Chen, S. J. Yuan, and B. Qin, 2023: A radiative transfer deep learning model coupled into WRF with a generic Fortran torch adaptor. *Frontiers in Earth Science*, **11**, 1149566, https://doi.org/10.3389/feart.2023.1149566.

Pan, B. X., G. J. Anderson, A. Goncalves, D. D. Lucas, C. J. W. Bonfils, and J. Lee, 2022: Improving seasonal forecast using probabilistic deep learning. mproving seasonal forecast using probabilistic deep learning. Journal of Advances in Modeling Earth Systems , 14, e2021MS002766. https://doi.org/10.1029/2021MS002766.

Pathak, Jaideep, and Coauthors, 2022: Fourcastnet: A global data-driven high-resolution weather model using adaptive Fourier neural operators. arXiv preprint arXiv:2202.11214 (2022), https://doi.org/10.48550/arXiv.2202.11214.

Raissi, M., P. Perdikaris, and G. E. Karniadakis, 2019: Physics-informed neural networks: A deep learning framework for solving forward and inverse problems involving nonlinear partial differential equations. *J. Comput. Phys.*, **378**, 686–707, https://doi.org/10.1016/j.jcp.2018.10.045.

Rasp, S., M. S. Pritchard, and P. Gentine, 2018: Deep learning to represent subgrid processes in climate models. *Proceedings of the National Academy of Sciences of the United States of*

America, **115**(39), 9684–9689, https://doi.org/10.1073/pnas.1810286115.

Ravuri, S., and Coauthors, 2021: Skilful precipitation nowcasting using deep generative models of radar. *Nature*, **597**(7878), 672–677, https://doi.org/10.1038/s41586-021-03854-z.

Shen, C. P., and Coauthors, 2023: Differentiable modelling to unify machine learning and physical models for geosciences. *Nature Reviews Earth & Environment*, **4**(8), 552–567, https://doi.org/10.1038/s43017-023-00450-9.

Tao, W. C., G. Huang, R. G. Wu, K. M. Hu, P. F. Wang, and H. N. Gong, 2018: Origins of biases in CMIP5 models simulating northwest Pacific summertime atmospheric circulation anomalies during the decaying phase of ENSO. *J. Climate*, **31**(14), 5707–5729, https://doi.org/10.1175/JCLI-D-17-0289.1.

Tao, W. C., G. Huang, P. F. Wang, Y. Liu, G. H. Wen, and D. H. Dong, 2019: Dominant modes of CMIP3/5 models simulating northwest Pacific circulation anomalies during post-ENSO summer and their SST dependence. *Theor. Appl. Climatol.*, **138**(3–4), 1809–1820, https://doi.org/10.1007/s00704-019-02936-3.

Wallace, J. M., E. M. Rasmusson, T. P. Mitchell, V. E. Kousky, E. S. Sarachik, and H. von Storch, 1998: On the structure and evolution of ENSO-related climate variability in the tropical Pacific: Lessons from TOGA. *J. Geophys. Res.: Oceans*, **103**(C7), 14 241–14 259, https://doi.org/10.1029/97JC02905.

Wang, L.-Y., and Z.-M. Tan, 2023: Deep learning parameterization of the tropical cyclone boundary layer. *Journal of Advances in Modeling Earth Systems*, **15**, e2022MS003034, https://doi.org/10.1029/2022MS003034.

Wang, Y., and Coauthors, 2024: Correcting climate model sea surface temperature simulations with generative adversarial networks: Climatology, interannual variability, and extremes. *Adv. Atmos. Sci.*, https://doi.org/10.1007/s00376-024-3288-6. (in press)

Wu, X. R., G. J. Han, S. Q. Zhang, and Z. Y. Liu, 2016: A study of the impact of parameter optimization on ENSO predictability with an intermediate coupled model. *Climate Dyn.*, **46**, 711–727, https://doi.org/10.1007/s00382-015-2608-z.

Zhang, Y. C., M. S. Long, K. Y. Chen, L. X. Xing, R. H. Jin, M. I. Jordan, and J. M. Wang, 2023: Skilful nowcasting of extreme precipitation with NowcastNet. *Nature*, **619**(7970), 526–532, https://doi.org/10.1038/s41586-023-06184-4.

Zhou, L., and R. H. Zhang, 2023: A self-attention–based neural network for three-dimensional multivariate modeling and its skillful ENSO predictions. *Science Advances*, **9**(10), eadf2827, https://doi.org/10.1126/sciadv.adf2827.

Zhu, Y. C., R. H. Zhang, J. N. Moum, F. Wang, X. F. Li, and D. L. Li, 2022: Physics-informed deep-learning parameterization of ocean vertical mixing improves climate simulations. *National Science Review*, **9**(8), nwac044, https://doi.org/10.1093/nsr/nwac044.

npj | climate and atmospheric science

Article

Published in partnership with CECCR at King Abdulaziz University

https://doi.org/10.1038/s41612-024-00742-x

Interdecadal shifts of ENSO influences on Spring Central Asian precipitation

Check for updates

Mengyuan Yao[1,2,3], Haosu Tang[1,4] ✉, Gang Huang[1,2,3] ✉ & Renguang Wu[5]

Spring Central Asian precipitation (SCAP) holds significant implications for local agriculture and ecosystems, with its variability mainly modulated by El Niño–Southern Oscillation (ENSO). The ENSO–SCAP relationship has experienced pronounced interdecadal shifts, though mechanisms remain elusive. Based on observations and climate model simulations, these shifts may result from transitions in ENSO-induced meridional circulation and Rossby wave trains triggered by North Atlantic (NA) sea surface temperature (SST) anomalies. During high (low) correlation periods, ENSO induces strong (weak) vertical motion anomalies over Central Asia, while NA SST anomalies exert a weak (strong) counteracting effect, modulated by the Pacific decadal oscillation (PDO). In the positive (negative) phase of PDO, a slow (fast) decaying ENSO triggers a strong (weak) NA horseshoe-like SST anomaly in the post-ENSO spring, affecting the ENSO–SCAP relationship. Our study identifies a strengthening trend in the ENSO–SCAP relationship since the 2000s, indicating improved predictability for SCAP in recent decades.

Central Asia (CA), recognized as one of the largest semi-arid to arid regions in the world, includes Kazakhstan, Uzbekistan, Turkmenistan, Kyrgyzstan, and Tajikistan. This region features a typical continental climate and hosts a fragile ecosystem, particularly susceptible to changes in local precipitation. The primary rainy season in CA, especially in southern CA, is spring[1,2]. The Spring Central Asian precipitation (SCAP) variability serves as a crucial indicator for local agricultural production, water sources, ecosystems, and economic activities. El Niño–Southern Oscillation (ENSO) is the dominant source of interannual variability in tropical ocean–atmosphere interactions. It exerts far-reaching impacts on global weather and climate via atmospheric teleconnections, and is a vital signal for seasonal forecasting and climate prediction worldwide[3–5]. Numerous studies have demonstrated that ENSO exerts a significant impact on the precipitation variability in CA[6], and spring precipitation over more than half of CA shows a positive correlation with El Niño in the preceding winter[7]. On the one hand, El Niño favors above-normal precipitation in CA as it enhances southwesterly water vapor flux from the Arabian Sea and tropical Africa, along with more northeasterly water vapor flux from Russia[1,8]. This mechanism is confirmed by an atmospheric general circulation model experiment forced by observed sea surface temperatures (SST)[1,6,8,9]. ENSO is also suggested to explain the large fluctuations of sea level pressure over the Caspian Sea[10], which is an important moisture transport source for CA. On the other hand, El Niño could lead to upper-level divergence anomalies over CA through large-scale convergence and divergence. This can induce anomalous updrafts, resulting in increased precipitation in the region[11,12]. To sum up, El Niño (La Niña) typically leads to increased (decreased) precipitation over CA through enhanced (weakened) moisture transportation and intensified updrafts (downdrafts), though the spatial pattern of precipitation anomalies exhibits seasonal variations during different phases of ENSO[13].

Changes in ENSO characteristics, such as flavors and intensity, contribute to diverse precipitation responses over CA. Previous studies have revealed that precipitation anomalies associated with cold-tongue El Niño mainly fall along the hills and Pamir Plateau, whereas those linked to warm-pool El Niño are concentrated around the mountains and the Aral area during the El Niño decaying spring[8]. Notably, the latter type of El Niño exerts a stronger influence on precipitation anomalies in CA. Regarding the varying intensity of El Niño events, stronger El Niño events normally lead to persisting above-normal precipitation over CA from the developing winter to decaying summer, whereas precipitation anomalies are less obvious in weaker El Niño events[13].

Previous studies have indicated that North Atlantic (NA) SST anomalies play a crucial role in influencing Eurasian climate anomalies, serving as a source for predicting Eurasian climate variability. The positive phase of the NA horseshoe-like SST anomaly pattern could excite an atmospheric quasi-barotropic Rossby wave train extending from NA through Eurasia to downstream East Asia, leading to reduced

[1]State Key Laboratory of Numerical Modeling for Atmospheric Sciences and Geophysical Fluid Dynamics (LASG), Institute of Atmospheric Physics, Chinese Academy of Sciences, Beijing, China. [2]Laboratory for Regional Oceanography and Numerical Modeling, Qingdao National Laboratory for Marine Science and Technology, Qingdao, China. [3]University of Chinese Academy of Sciences, Beijing, China. [4]Department of Geography, University of Sheffield, Sheffield, UK. [5]School of Earth Sciences, Zhejiang University, Hangzhou, China. ✉e-mail: tanghaosu@mail.iap.ac.cn; hg@mail.iap.ac.cn

rainfall east of the Caspian Sea and across CA[14,15]. Besides, summer extreme precipitation in eastern CA shows a close correlation with NA SST anomalies as well[16]. It is worth mentioning that the horseshoe-like SST anomaly pattern over NA is tightly associated with the North Atlantic Oscillation (NAO), which strongly influences the precipitation over CA through upper-tropospheric westerly jets[17–19]. Numerous researches have demonstrated that ENSO could induce the NA horseshoe-like SST anomaly pattern during its decaying spring. This is primarily attributed to surface heat flux anomalies resulting from the so-called atmospheric bridge (or teleconnection) induced by ENSO[20,21]. It has also been pointed out that the positive phase of NA SST anomalies is more pronounced during spring in slow-decaying El Niño events compared to fast-decaying ones. This discrepancy can largely be attributed to differences in lower-level wind anomalies and the associated surface heat flux anomalies[4]. Thus, NA SST anomalies may act as an important bridge in the cross-seasonal impacts of ENSO on precipitation anomalies over CA.

Studies have been conducted in exploring the impacts of ENSO on SCAP, and emerging evidence implies that the relationship between ENSO and SCAP may not be consistently stable[1,22]. However, the underlying mechanisms of interdecadal shifts remain a knowledge gap to date. In this study, we aim to investigate the plausible causes of interdecadal variations of the relationship between wintertime ENSO and subsequent SCAP. Given that relatively short observational records may constrain our understanding of interdecadal shifts, we also take advantage of climate model simulations from phase 6 of the Coupled Model Intercomparison Project (CMIP6). These simulations provide an extensive set of samples to verify the mechanisms driving interdecadal changes in the observations. By leveraging multiple observations and a subset of CMIP6 models capable of capturing interdecadal modulations, we discern the roles of Pacific and NA SST anomalies on the SCAP. We propose that the ENSO–SCAP relationship may be influenced by ENSO-induced large-scale meridional divergence and convergence, and zonal Rossby wave trains triggered by NA SST anomalies. Idealized model simulations are also performed to validate the dynamic mechanisms.

Results

Interdecadal shifts of ENSO–SCAP relationship

Figure 1 depicts the regression and 19-year sliding correlation of precipitation over CA from the El Niño developing winter to decaying summer with normalized DJF(0) Niño3.4 index in the observations during 1891–2020. Seasonal precipitation features homogeneous wet anomalies across the whole of CA. From DJF(0) to JJA(1), the highest correlation persists in the southern and eastern parts of CA, while the lower correlation is sustained in the northern part. Precipitation anomalies also exhibit distinct seasonal differences, with wet anomalies intensifying and expanding to central CA from DJF(0) to MAM(1) and then weakening in JJA(1). Notably, precipitation anomalies are obviously larger during the El Niño decaying spring than in other seasons (Fig. 1a–c). The 19-year sliding correlations indicate pronounced interdecadal shifts, sharply declining in the 1930s and then gradually strengthening until the 1960s. Moreover, there is an increasing trend after the 2000s for DJF(0) and MAM(1). Hereafter, we focus on interdecadal shifts of ENSO influences on SCAP, given that spring is the major growing season for arid CA and precipitation variability during spring may hold the utmost significance. We further define the high correlation (HC) period and low correlation (LC) period based on the 19-year sliding correlation. Thus, the periods 1951–1969 and 1920–1938 are selected as the HC and LC periods in the observations, respectively. To ensure the reliability of our conclusions, we also calculate sliding correlations of SCAP with normalized DJF(0) Niño3.4 index using two additional window lengths and two other precipitation datasets. The results remain robust (Supplementary Fig. 1).

The regression and 19-year sliding correlation of SCAP with normalized DJF(0) Niño3.4 index in 45 CMIP6 models during 1891–2014 are shown in Supplementary Figs. 2 and 3, respectively. Most CMIP6 models could capture the unstable ENSO–SCAP relationship except for ACCESS-CM2, CESM2-WACCM, FGOALS-g3 and MIROC-ES2L (Supplementary Fig. 3). To investigate the

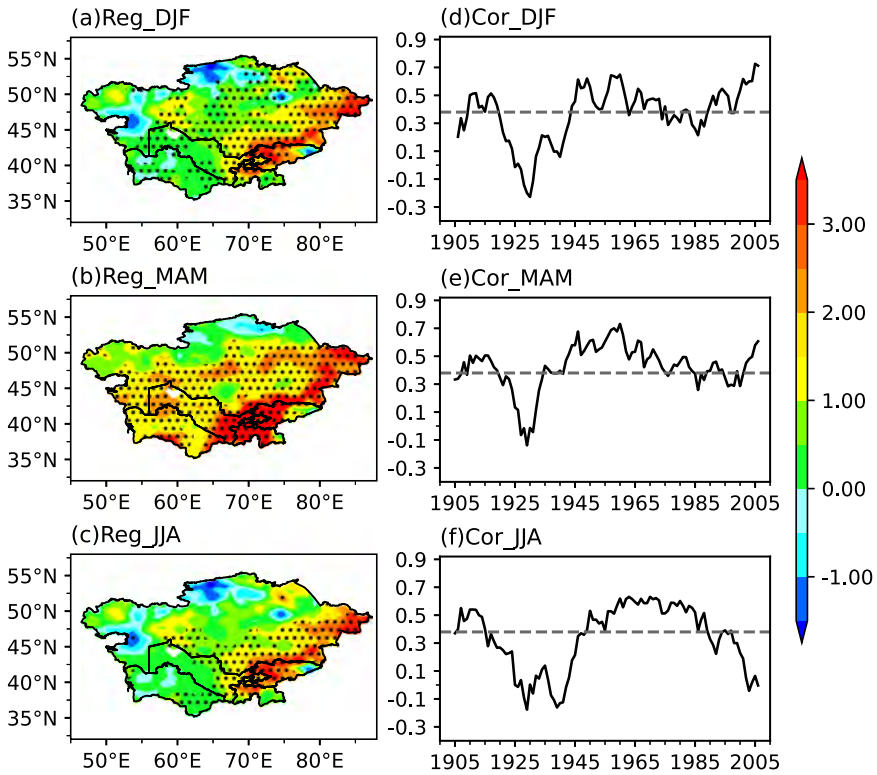

Fig. 1 | Response of different seasonal precipitation (unit: mm/day) to El Niño in observation. **a** Regression and **d** 19-year sliding correlation of the DJF(0) precipitation (based on GPCC) with the normalized DJF(0) Niño3.4 index in the observation for the period 1891–2020. **b**, **e** and **c**, **f** Same as (**a**, **d**), but for MAM(1) and JJA(1), respectively. The dots and dashed lines denote the 90% confidence level.

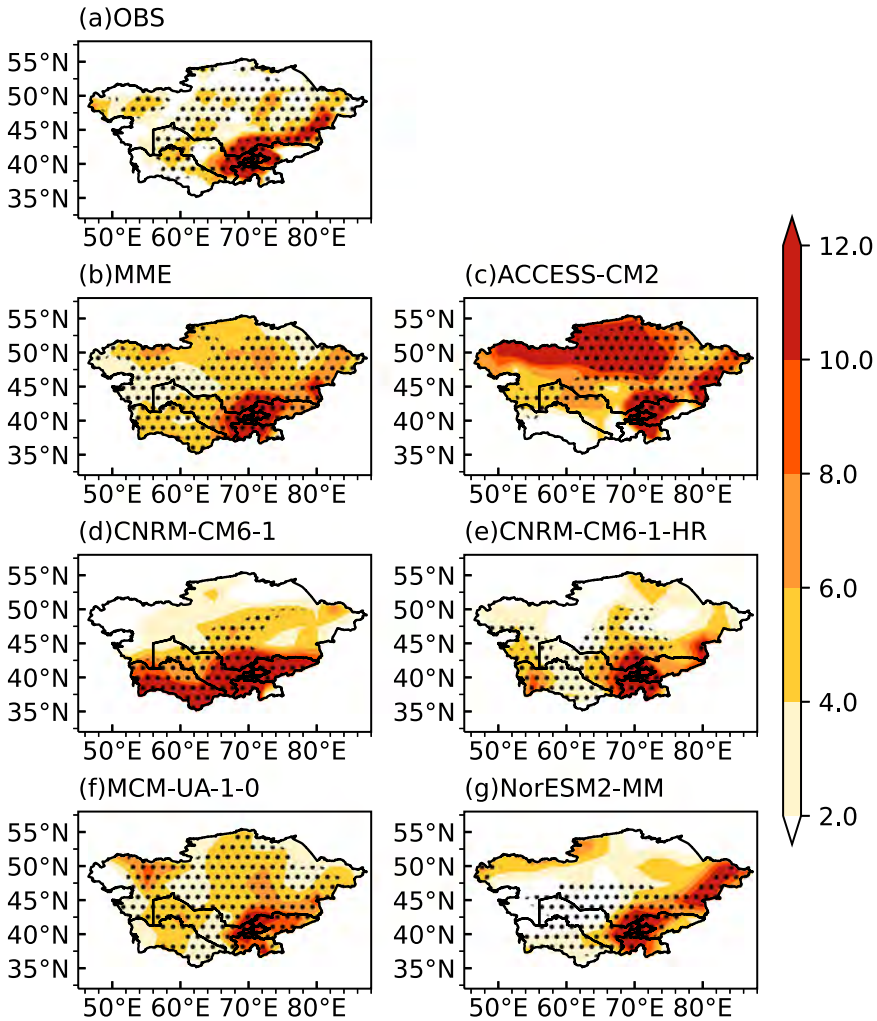

Fig. 2 | Response of precipitation (unit: mm/day) to El Niño in observation and selected models. Regression of MAM(1) precipitation over CA with normalized DJF(0) Niño3.4 index for HC minus LC differences in **a** observation, **b** MME and **c**–**g** five selected models from CMIP6. From here on, MME is derived from five selected models. The dots denote the 90% confidence level in the observation and 80% consistency in models in the HC period.

physical mechanisms of the interdecadal variations, high-skill models are further selected. The criteria for selecting proper models involve ensuring a degree of fidelity in simulating the ENSO-related anomalous precipitation pattern over CA and the capability to reproduce the differences between HC and LC periods. Based on (a) the spatial correlation of ENSO-related precipitation anomalies over CA in each model with the observation during the whole period, (b) the spatial correlation during the HC period, and (c) the maximum minus minimum value of 19-year sliding correlation, five models are finally selected and the detailed results are listed in Supplementary Table 2. They are CNRM-CM6-1-HR, HadGEM3-GC31-LL, HadGEM3-GC31-MM, SAM0-UNICON, and UKESM1-0-LL, in which the spatial correlations with the observations are above 0.56 and 0.33 for the whole and HC period, respectively. And the difference in correlation values between HC and LC periods exceeds 0.77. Here, the definition of HC and LC periods in each model aligns with that in the observations. Note that lowering thresholds and incorporating additional models do not alter the conclusions of this study, as the results from CMIP6 models are mainly used for verification (figures not shown).

Can the selected five models accurately reproduce the spatial pattern of ENSO-induced precipitation anomalies over CA in MAM(1)? Figure 2 illustrates the difference in ENSO-induced SCAP anomalies between HC and LC periods. In the observations, enhanced precipitation tends to occur during the HC period, with the most significant positive values centered over southern and eastern CA. Despite slight differences in magnitude and location, the results from the multi-model ensemble mean (MME) and five single models closely resemble the observed pattern. In other words, the models selected based on the above criteria can well capture the interdecadal changes in the relationship between ENSO and SCAP.

Potential mechanisms modulating the ENSO–SCAP relationship

Based on the observations and five models selected in the previous section, we explore the underlying mechanism for the interdecadal variations of the ENSO–SCAP relationship in this section.

Previous studies have suggested that ENSO influences the hydroclimate of CA through restructuring winds and moisture sources. Figure 3 shows the regression of MAM(1) vertically integrated moisture transportation and divergence with normalized DJF(0) Niño3.4 index in the observations and CMIP6 MME. During the HC period, notable cyclonic circulation anomalies are located over CA, with anomalous westerlies along the southern periphery favoring water vapor transport from the Atlantic and Mediterranean Sea in both observations and MME (Fig. 3a, c). As a result, moisture convergence anomalies are observed across nearly the entire region of CA, favoring above-normal local precipitation. In contrast, cyclonic circulation anomalies shift towards the west of CA during the observed LC period, while an anomalous anticyclonic circulation appears in northern CA (Fig. 3b). The northward moisture transport anomalies in southern CA carry moisture from the Indian Ocean to the region, although local moisture convergence anomalies are weaker compared to those in the HC period. Previous studies have found that during El Niño events, the weakened Pacific Walker circulation suppresses convection and precipitation over the Indo-western Pacific warm pool. This suppression induces a westward-propagating baroclinic Rossby wave train, leading to

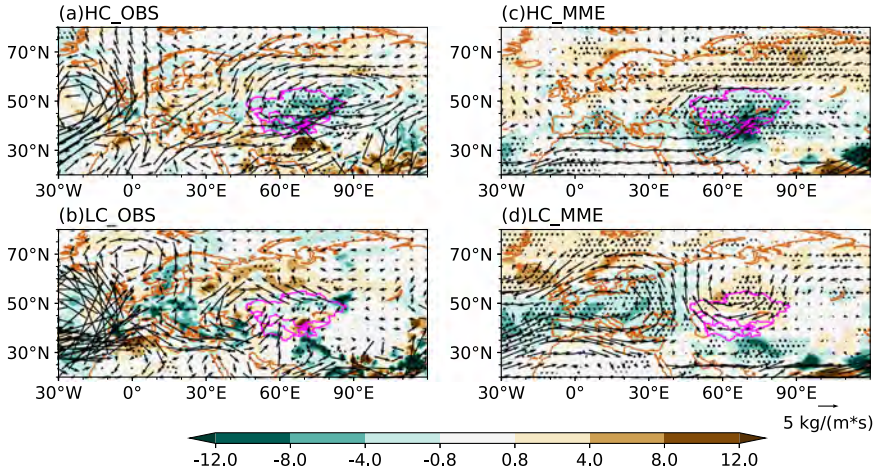

Fig. 3 | Response of vertically integrated moisture transportation and its divergence to El Niño. Regression of MAM(1) vertically integrated moisture transportation (vectors; unit: kg/(m s)) and its divergence (colors; unit: 10^{-6} kg/s) with normalized DJF(0) Niño3.4 index for **a** HC period and **b** LC period in the observation. Green (brown) shadings denote moisture convergence (divergence) anomalies. **c**, **d** Same as (**a**, **b**), but for MME.

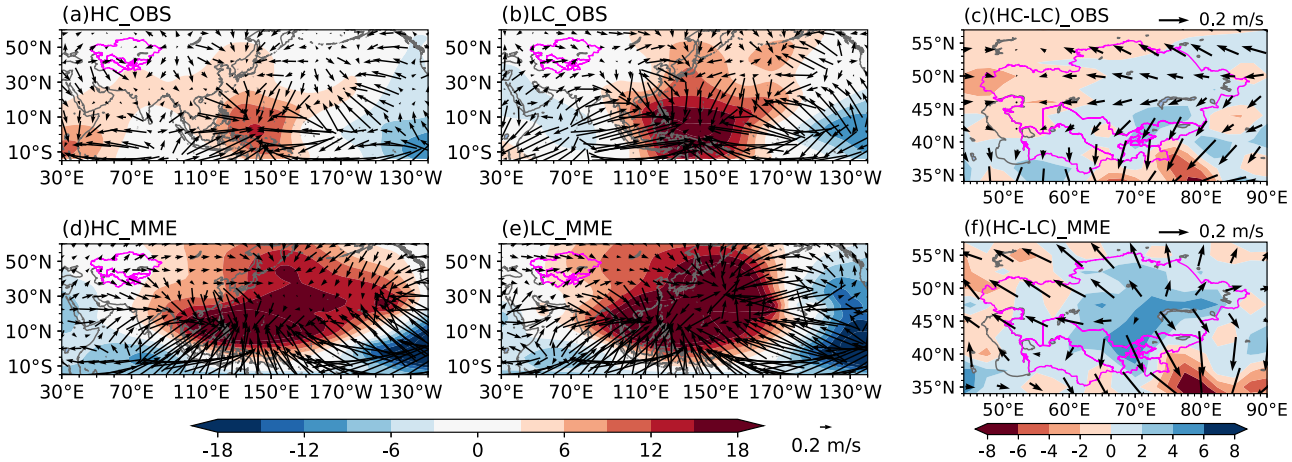

Fig. 4 | Response of 200-hPa velocity potential and divergent winds to El Niño. Regression of MAM(1) 200-hPa velocity potential (colors; 10^6 m^2/s) and divergent winds (vectors; m/s) with normalized DJF(0) Niño3.4 index for **a** HC period and **b** LC period in the observation. **c** Same as (**a**), but for divergence (colors; 10^{-7}/s) and divergent winds (vectors; m/s) for HC minus LC differences. **d**–**f** Same as **a**–**c**, but for MME.

anticyclonic/high-pressure anomalies over the Indian Ocean and extending to southern CA. This process can explain enhanced southwesterly water vapor flux from the Indian Ocean to southern CA[9,22–24]. MME results during the LC period display stronger anticyclonic circulation anomalies covering nearly the entire CA. This leads to easterly anomalies over northern CA, creating unfavorable conditions for water vapor transport from the oceans to reach the region (Fig. 3d). Consequently, moisture divergence anomalies occur, favoring below-normal precipitation across CA.

To further understand the ENSO-induced dynamic conditions over CA during the HC and LC periods, the regressions of MAM(1) 200-hPa velocity potentials and divergent winds against normalized DJF(0) Niño3.4 index in the observations and CMIP6 MME are shown in Fig. 4. The red (blue) colors indicate El Niño-induced upper-level convergence (divergence) anomalies. Notably, persistent upper-level convergence anomalies are evident over the western Pacific, while the anomalous upper-level divergence generally prevails over the eastern Pacific. Previous studies have indicated that ENSO could influence mid-latitude weather and climate via large-scale meridional convergence and divergence[13,25,26]. During the HC period, CA is dominated by El Niño-induced upper-level divergence anomalies, which are conducive to anomalous ascent and increased precipitation across the region (Fig. 4a, d). Compared to the HC period, the upper-level divergence and divergent wind anomalies are weaker in the LC period in both observations and MME (Fig. 4c, f). Thus, both El Niño-induced anomalous moisture transportation and ascending motion through large-scale convergence and divergence are stronger in the HC period compared to the LC period, which may account for the increased SCAP during the former period.

To further explore the potential mechanisms underlying the unstable relationship between ENSO and SCAP, the regressions of MAM(1) SST anomalies with normalized DJF(0) Niño3.4 index are examined for the HC and LC periods in the observations and CMIP6 MME (Fig. 5). A horseshoe-like SST anomaly pattern is salient in NA, characterized by cold SST anomalies near the east coast of the United States and warm SST anomalies in the NA subpolar gyre zone and tropical NA. Moreover, the horseshoe-like SST anomaly pattern is significantly stronger during the LC period than the HC period in both observations and MME (Fig. 5c, f). Compared to the observations, the difference in SST anomalies between the HC and LC periods over the tropical Atlantic is weaker in CMIP6 MME. Here, we construct an NA dipole SST index (NAI) to assess the impact of an NA horseshoe-like SST anomaly pattern on the SCAP. This index is defined as the difference between area-weighted regional mean SST anomalies over northeastern NA (blue box; 35°N–55°N, 20°W–40°W) and southwestern NA (red box; 30–50°N, 50–80°W). The regions are selected based on the anomalous SST difference between the HC and LC periods (Fig. 5c, f). The correlation between DJF(0) Niño3.4 index and MAM(1) NAI is insignificant during the

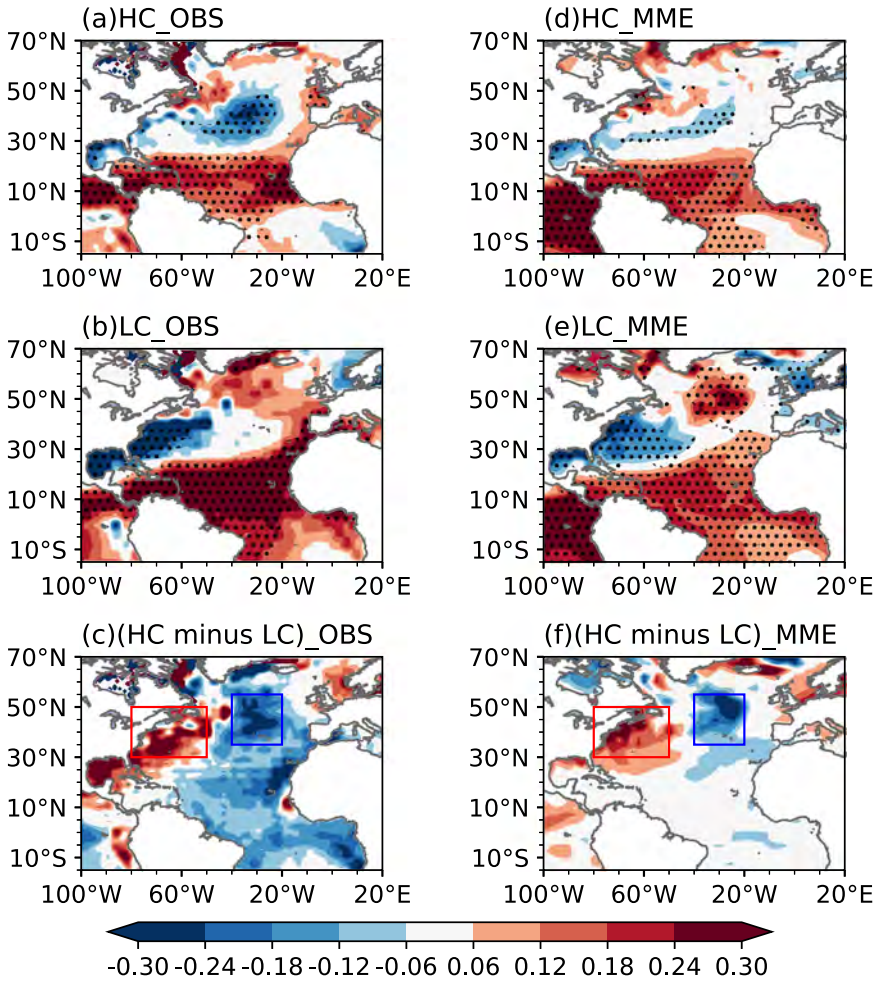

Fig. 5 | Response of Atlantic SST (unit: K) to El Niño. Regression of MAM(1) SST with normalized DJF(0) Niño3.4 index for **a** HC period, **b** LC period and **c** HC minus LC differences in the observation. **d**–**f** Same as **a**–**c**, but for MME. The dots denote the 90% confidence level in the observation and 80% consistency in models. The blue and red boxes denote the area of NA dipole SST index (40°W–20°W, 35°N–55°N) and (50°W–80°W, 30°N–50°N), respectively.

whole period in both observation and selected CMIP6 models, with correlation coefficients of 0.05 and 0.04 for the observation and CMIP6 MME, respectively.

Figure 6 illustrates the regression of MAM(1) 200-hPa geopotential height with normalized NAI and the corresponding wave activity flux in the observations and CMIP6 MME. The positive phase of the NA horseshoe-like SST anomaly pattern could trigger quasi-barotropic high-pressure anomalies across CA as part of the Eurasian Rossby wave train, thereby leading to decreased local precipitation (Supplementary Fig. 4). Figure 7 shows the 19-year sliding correlation of MAM(1) precipitation over CA and NAI against normalized DJF(0) Niño3.4 index in the observations and five selected models. In the observations, the sliding correlation between ENSO and NAI shows an upward trend before the 1930s and then gradually declines until the 1960s. Additionally, a decreasing trend is observed after the 1980s. The relationship between ENSO and NAI generally aligns well with the opposite evolution of the ENSO–SCAP relationship. Similar conclusions could be obtained in high-skill CMIP6 models as well. The 102-yr negative correlations between ENSO–NAI and ENSO–SCAP time series in the observations and simulations of each selected model can be further validated through a 99% significance test except for HadGEM3-GC31-MM. How to understand the dynamic processes behind the negative correlations? The results indicate that a stronger positive (negative) phase of the NA SST anomaly pattern corresponds to a weaker (stronger) relationship between El Niño and SCAP. During periods when the positive phase of the NA SST anomaly pattern is strong, it leads to an anticyclone occupying CA, suppressing local precipitation. This counteracts the direct wetting impacts of El Niño on SCAP, thereby resulting in a diminished ENSO–SCAP relationship. Conversely, the negative phase of the NA SST anomaly pattern induces an anomalous cyclone located over CA, intensifying the wetting impacts caused by El Niño. This finally leads to an enhanced ENSO–SCAP relationship.

To validate whether the NA dipole SST anomalies could trigger the Eurasian teleconnection pattern, we further conducted three sets of linear baroclinic model (LBM) experiments. They are driven by positive vorticity forcing in northeastern NA, negative vorticity forcing in southwestern NA, and their sum, respectively, along with climatological mean flow during the boreal spring (Fig. 8a, c, and d). The prescribed vorticity source exhibits a cosine elliptical pattern, with its peak set at the 0.25 sigma level. Similar to the observations, the 200-hPa geopotential height and wind responses manifest an atmospheric Rossby wave-like structure. Notably, among three sets of experiments, two prominent centers of anticyclonic circulation anomalies are consistently observed. One is located over North America, around 70°N, and the other is over CA. Additionally, two centers of cyclonic circulation anomalies are evident over the subtropical NA and northern Europe (Fig. 8b, d, and f).

Fast and slow decaying ENSO

Why is the positive phase of the NA SST anomaly pattern stronger in the LC period compared to the HC period? Previous studies have suggested that the surface heat flux anomalies play a dominant role in the formation of the NA horseshoe-like SST anomaly pattern[4,27–29]. Figure 9 illustrates the regression of JFM(1) latent heat flux and 850-hPa wind with normalized DJF(0) Niño3.4 index in the observations and CMIP6 MME. Here, JFM(1) represents the cross-seasonal months between DJF(0) and MAM(1), which helps in understanding the persistent impacts of anomalous latent heat flux in NA SST anomalies. Compared with the HC period, the anomalous latent

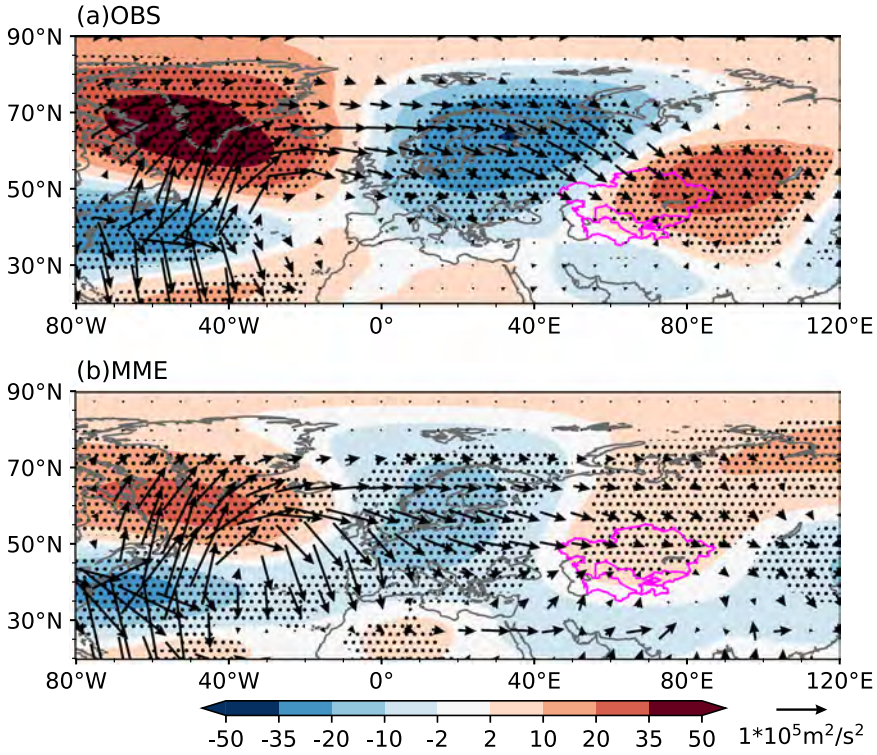

Fig. 6 | Response of 200-hPa geopotential height to North Atlantic SST anomalies. Regression of MAM(1) 200-hPa geopotential height (colors; m) with normalized MAM(1) NAI and the corresponding wave activity flux (vectors; m^2/s^2) in the observation (**a**) and MME (**b**). The dots denote the 90% confidence level in the observation and 80% consistency in models.

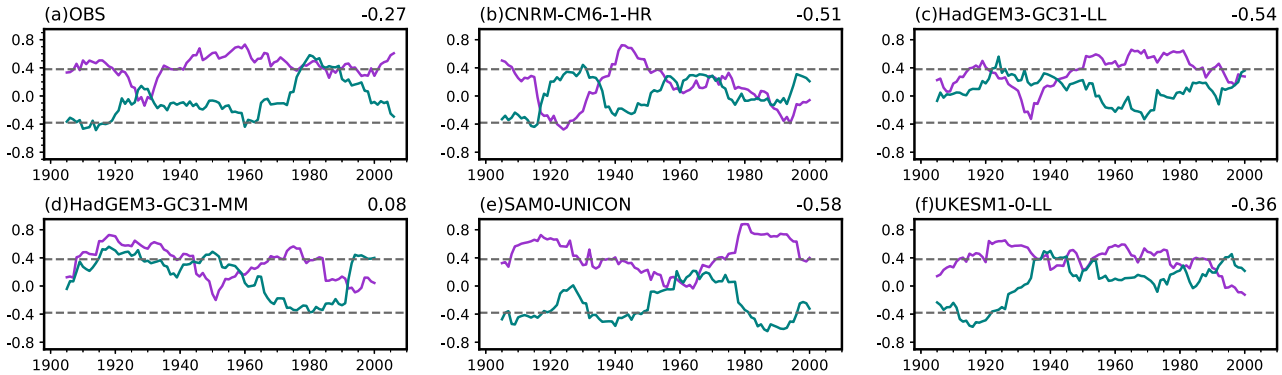

Fig. 7 | Interdecadal relationship of ENSO with SCAP and North Atlantic SST anomalies. The 19-year sliding correlation of MAM(1) precipitation (purple lines; mm/day) over CA and NAI (green lines; K) with normalized DJF(0) Niño3.4 index. **a** Is for observation and **b**–**f** is for five selected models. The numbers at the upper right present the 102-year correlation of the two lines. The gray dashed lines denote the 90% confidence levels of 19-year samples.

heat flux patterns over NA are more pronounced in the LC period. The difference in latent heat flux anomalies between the HC and LC periods could be further attributed to the varying lower-level wind anomalies[4]. Due to the intensified anomalous cyclonic circulation in the mid-latitude NA in the LC period, the stronger southwesterly (northeasterly) anomalies induce a reduction (enhancement) in wind speed and decrease (increase) positive latent heat flux anomalies in the tropical (subtropical) NA. Consequently, it leads to warmer (colder) SST in the tropical (subtropical) NA through wind–evaporation–SST feedback during the LC period compared with the HC period[30,31].

Previous studies have indicated that the lower-level wind anomalies over NA in MAM(1) are closely related to ENSO in the tropical eastern Pacific[20,21]. Therefore, we hypothesize that ENSO may manifest differently in distinct epochs, leading to varying lower-level wind anomalies over NA. We first examine the regressions of DJF(0) SST with normalized DJF(0) Niño3.4 index in the observations and CMIP6 MME (Supplementary Fig. 5). No significant spatial pattern transitions of ENSO are observed between the HC and LC periods. In the meantime, the observed and MME autocorrelations of the Niño3.4 index with its DJF (0) values display a distinct difference in the ENSO cycle, with observed and MME decaying rates of −0.40 (−0.25) and −0.23 (−0.16) in the HC (LC) period, respectively (Fig. 10a, b). Here, the decaying rate is calculated as the difference between MAM(1) and DJF(0) Niño3.4 index. These quantitative results indicate that the decaying pace of ENSO in the HC period may be faster than that in the LC period. These results are consistent with previous studies, which suggested that the NA horseshoe-like SST anomaly pattern in MAM(1) is stronger and more persistent during the slow than fast decaying ENSO events[4,32]. The ENSO amplitude is further examined to explore whether it is a potential modulator of the

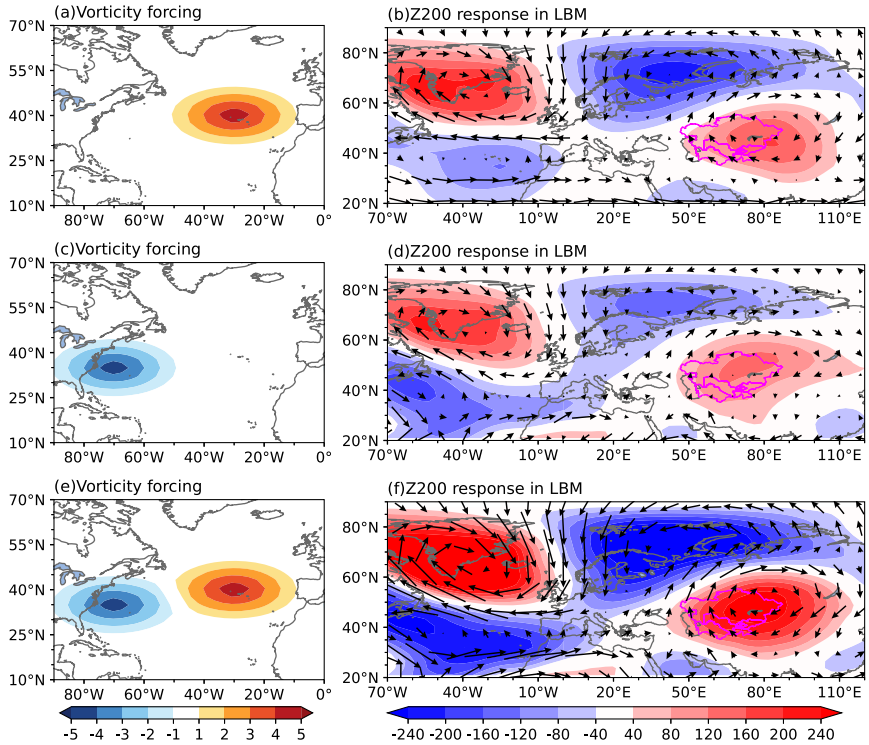

Fig. 8 | Response of upper-level circulation to vorticity forcing in LBM. a Horizontal distribution of imposed atmospheric positive vorticity forcing (colors; 10^{-5} s^{-1} d^{-1}) in the North Atlantic. **b** The 200-hPa geopotential height (colors; m) and wind (vectors; m/s) anomalies in response to the vorticity forcing. **c** and **d** same as **a**, **b**, but for negative vorticity forcing. **e** is sum of **a**, **c** and **f** is sum of **b**, **d**.

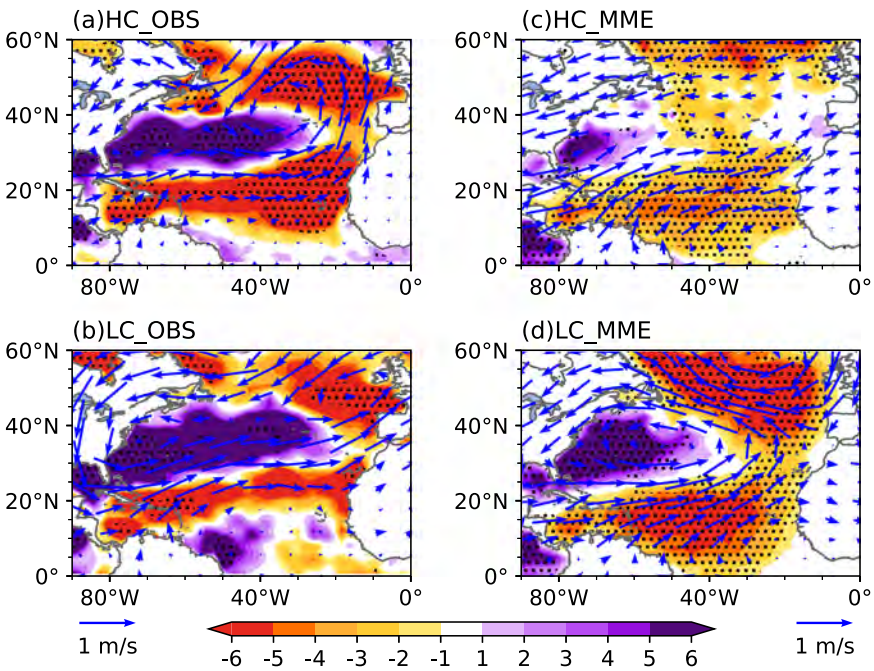

Fig. 9 | Response of latent heat flux and 850-hPa wind to El Niño. Regression of JFM(1) latent heat flux (colors; W/m^2) and 850-hPa wind (vectors; m/s) with normalized DJF(0) Niño3.4 index for **a** HC period and **b** LC period in the observation. **c**, **d** Same as **a**, **b**, but for MME. The dots denote the 90% confidence level in the observation and 80% consistency in models.

ENSO–SCAP relationship. Although stronger ENSO events appear to occur during the observational HC period, there is a lack of consistency among selected CMIP models (Fig. 10c). Furthermore, the 19-year sliding standard deviation of DJF(0) Niño3.4 index, verified across three SST datasets, indicates that the lowest amplitudes of ENSO occur around the 1930s and 1950s, which do not correspond very well with the evolution of ENSO–SCAP (Figs. 1e, 10d). Therefore, the ENSO amplitude may play an important role in the ENSO–SCAP relationship during certain epochs, but it cannot fully explain the historical interdecadal shifts in this relationship. In conclusion, two distinct types of ENSO decay rates, namely fast and slow decaying ENSO, might be important factors modulating the interdecadal shifts of ENSO–SCAP by influencing the magnitude and phase of the NA SST anomaly pattern.

Driver of ENSO decaying pace

What factors contribute to the variation in the decaying pace of ENSO across different epochs? Previous studies have suggested that the evolution of ENSO may be associated with the decadal variability of the climate system. Figure 11 shows the time series of the

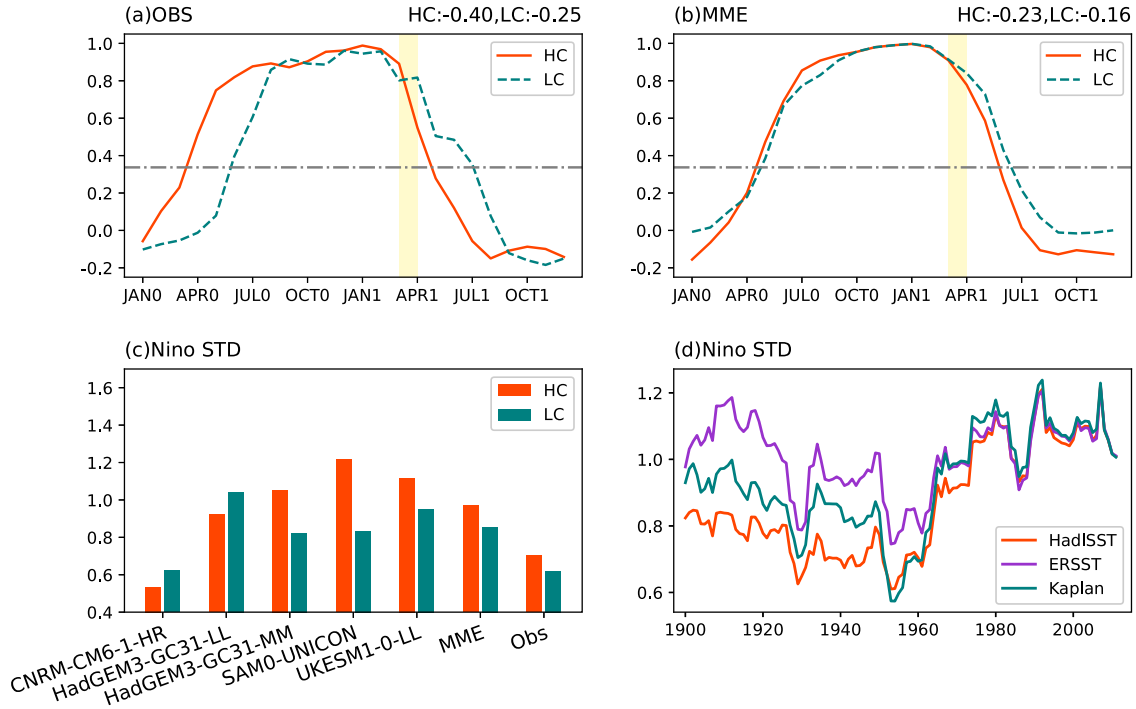

Fig. 10 | Interdecadal variations of ENSO characteristics in observation and selected models. a Observed and **b** MME autocorrelation of Niño3.4 index with its DJF(0) values in the HC and LC period. The gray lines denote the 90% confidence level. The light yellow bar indicates the MAM(1) period. The numbers in the upper right corner of panels **a**, **b** are calculated by the seasonal average difference of Niño3.4 index between MAM(1) and DJF(0). **c** Standard deviation of DJF(0) Niño3.4 index in the HC and LC period for five models, MME, and the observation. **d** The 19-year sliding standard deviation of the Niño3.4 index from HadISST, ERSST and Kaplan SST datasets.

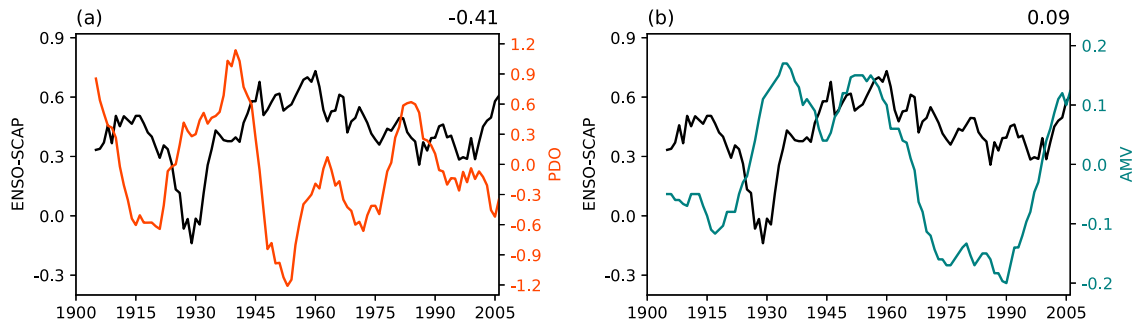

Fig. 11 | Interdecadal shifts in the ENSO–SCAP relationship and its linkage with PDO and AMV. 19-year sliding correlation of the MAM(1) precipitation with the DJF(0) normalized Niño3.4 index (**a**, **b**; black line), 10-year low-pass filtered DJF(0) PDO (**a**; orange line) and AMV (**b**; green line) index in the observation.

ENSO–SCAP relationship, Pacific Decadal Oscillation (PDO) index, and Atlantic Multidecadal Variability (AMV) index in the observations. The results indicate a relatively strong (weak) correlation between PDO (AMV) and ENSO–SCAP, with a correlation coefficient of −0.41 (0.09). To explore the reasons behind the generally strong negative correlation between PDO and ENSO–SCAP, we select El Niño cases during the positive and negative phases of PDO from observations and conduct composite analyses of El Niño-related SST anomalies from DJF(0) to JJA(1). It is found that the positive phase of PDO could lead to slower El Niño decay compared to its negative phase (Supplementary Fig. 6). Regarding the mechanisms, previous research suggests that the positive phase of PDO can enhance trade winds in the tropical Pacific and promote eastward wind convergence. The mean-state changes in tropical winds can induce an eastward displacement of El Niño-related equatorial westerly anomalies, resulting in a prolonged El Niño lifetime[33]. As a result, the phase of PDO could modulate the decaying pace of ENSO across different epochs. From this perspective, the strengthening ENSO–SCAP relationship after the 2000s may be attributed to the negative PDO phase in the recent decade, as this cold phase will favor faster El Niño decay and weaken the positive phase of the NA SST anomaly pattern.

Discussion

The present study investigates interdecadal shifts in the relationship between previous winter ENSO and subsequent SCAP based on observations and CMIP6 simulations. The observed ENSO–SCAP relationship displays pronounced interdecadal shifts, with a sharp decline in the 1930s followed by gradual strengthening around the 1960s. Furthermore, there is an increasing trend after the 2000s.

Two factors may contribute to the interdecadal shifts in the ENSO–SCAP relationship, which is summarized by a schematic diagram in Fig. 12. One factor is changes in the meridional pathway, i.e., large-scale convergence and divergence, through which Pacific SST anomalies influence moisture and dynamical conditions over CA. During warm ENSO events, persistent anomalous upper-level divergence generally prevails over the

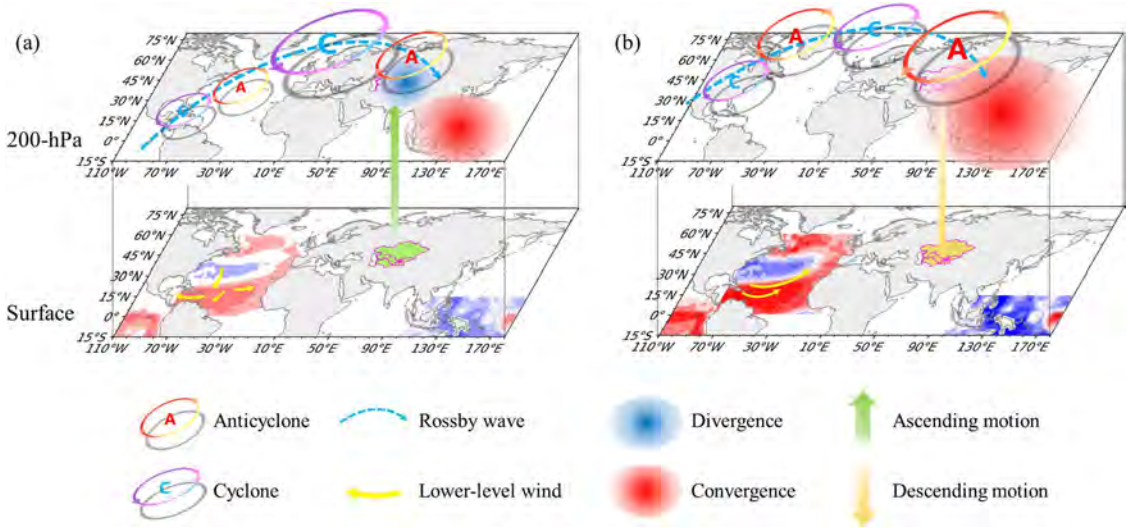

Fig. 12 | Schematic diagram illustrating underlying mechanisms of interdecadal shifts in the ENSO–SCAP relationship. The diagram includes decaying SST anomalies over the tropical Pacific, the NA SST anomaly pattern, precipitation anomalies over CA and the 200-hPa Rossby wave train induced by the NA SST anomaly pattern. **a** is for fast-decaying ENSO epochs and **b** is for slow-decaying ENSO epochs. Red (blue) shadings indicate positive (negative) SST anomalies at the surface and upper-level convergence (divergence) anomalies at 200-hPa, respectively. The blue dashed curve indicates the Rossby wave train path, and the size of the circles along the curve represents the amplitude of the circulation. The letter A (C) indicates atmospheric anticyclone (cyclone) anomalies. Surface yellow arrows over NA indicate lower-level wind anomalies. Green (brown) shadings and vertical arrows over CA denote above (below) normal precipitation and anomalous ascending (descending) anomalies, respectively.

central-eastern Pacific, while upper-level convergence anomalies emerge over the western Pacific. The large-scale upper-level convergence over the western Pacific further induces upper-level divergence in CA, resulting in anomalous vertical motion and increased local precipitation. The stronger upper-level divergence over CA during the HC period could induce a more robust ascending motion, further contributing to increased precipitation compared to the LC period. The other factor is the changes in the zonal Rossby wave train triggered by NA horseshoe-like SST anomalies. The MAM(1) cold SST anomalies are seen in the middle NA, and warm SST anomalies exist in the NA subpolar gyre zone and tropical NA, which is more pronounced during the LC period than the HC period. This NA SST anomaly pattern plays an opposing role compared to the wetting impacts of El Niño on SCAP, thereby disrupting the ENSO–SCAP relationship. The disruption caused by the NA SST anomaly pattern is more pronounced during the LC period than the HC period, resulting in a stronger ENSO–SCAP relationship in the latter period. We verify the dynamical processes induced by the NA SST anomaly pattern using the LBM. The results align well with our proposed mechanisms, with almost identical Eurasian Rossby wave trains as in the observations.

During the LC period, the stronger anomalous southwesterlies (northeasterlies) in the tropical (subtropical) NA aid in decreasing (increasing) latent heat flux anomalies, heating (cooling) the local SST and resulting in a more pronounced horseshoe-like SST anomaly pattern. Interestingly, the decaying pace of ENSO may modulate the interdecadal shifts of the NA horseshoe-like SST anomaly pattern, which can be further traced back to the phase of PDO. During the positive PDO phase, a slow decaying ENSO triggers a robust NA horseshoe-like SST anomaly pattern during MAM(1), counteracting the impact of ENSO on SCAP. In contrast, during the negative PDO phase, this counteracting effect is weakened, resulting in a more robust ENSO–SCAP relationship.

The findings of this study address important issues concerning the unstable ENSO–SCAP relationship and underlying mechanisms. Moreover, we identify a strengthening tendency in the ENSO–SCAP relationship after the 2000s, which indicates enhanced predictability for SCAP during recent decades. In this sense, this research may offer valuable information for regional stakeholders engaged in seasonal forecasting and climate prediction in arid CA. It should be noted that the NA horseshoe-like SST anomaly pattern is one of the pathways that may interfere with ENSO's impact on SCAP. Further research might be necessary to explore additional potential influence factors. Moreover, the factors modulating the decaying pace of ENSO are complex and cannot be solely attributed to PDO. Various influences and mechanisms involved are still unclear and call for future investigations to gain a comprehensive understanding. Furthermore, future efforts are preferred to examine how the ENSO–SCAP relationship will respond to greenhouse warming though projections driven by historical and future radiative forcing imply a slower decay of El Niño in the 21st century[34].

Methods

Data

Three datasets of monthly precipitation and three datasets of monthly SST have been used to ensure the reliability of results in the present study. The monthly precipitation datasets include Global Precipitation Climatology Centre (GPCC) monthly product version 2022[35], the Climatic Research Unit (CRU) high-resolution gridded datasets version 4.04[36], and the University of Delaware (Udel) Air Temperature & Precipitation version v4.01[37]. In terms of SST datasets, they are sourced from Hadley Centre Sea Ice and SST dataset (HadISST)[38], Extended Reconstructed Sea Surface Temperature (ERSST) v5[39], and Kaplan Extended SST V2[40]. Global atmospheric circulation data are derived from the NOAA-CIRES-DOE Twentieth Century Reanalysis (20CR) project, Version V2[41]. Outputs from the historical experiments of 45 CMIP6 climate models (more details in Supplementary Table 1) are also used. Here, we examine the first ensemble member (normally "r1i1p1f1") of each model's historical simulations, which involve running climate models to replicate past climate conditions from 1850 to 2014. These simulations can provide an extensive set of samples to understand the factors driving historical climate variability. Prior to analysis, all the observations and model simulations are bilinearly interpolated onto 2.5° × 2.5° grids in a horizontal manner for uniformity.

Interdecadal shifts

Throughout this study, we focus on the interdecadal shifts of ENSO–SCAP relationship. The 11-year sliding average has been moved from raw data before correlation and regression analysis to remove decadal and longer timescale variations. For a 19-year time series, correlations of 0.39 and 0.46 reach the 90% and 95% confidence levels, respectively, based on the two-sided Student's *t*-test.

ENSO index

To extract the year-to-year variations of ENSO and monitor the ENSO–SCAP relationship, we define the DJF(0) Niño3.4 index as the areal average of preceding December to following February seasonal mean SST anomalies in the NINO3.4 regions (170°W–120°W, 5°S–5°N). Here, the numbers in parentheses denote ENSO developing (0) and decaying (1) years. The regression of climate anomalies against DJF(0) Niño3.4 index is considered indicative of ENSO-induced climate anomalies. Since the regression analysis is linear, it can demonstrate climate anomalies induced by both El Niño and La Niña events. For simplicity, we primarily show the climate anomalies over CA during post-El Niño springs in the main text.

NA dipole SST index

Considering the potential influence of NA SST anomalies on the ENSO–SCAP relationship, we establish the NA dipole SST index (NAI) for the period MAM(1). This index is computed as the difference between the area-weighted averaged SST anomalies over northeastern region (35°N–55°N, 20°W–40°W) and southwestern region (30°N–50°N, 50°W–80°W), as delineated by the blue and red boxes in Fig. 5c and f, respectively.

Wave-activity fluxes

The horizontal wave-activity fluxes are defined as[42]

$$W = \frac{1}{2|\vec{V}|}\begin{cases} \bar{U}\left(\psi_x'^2 - \psi'\psi'_{xx}\right) + \bar{V}\left(\psi'_x\psi'_y - \psi'\psi'_{xy}\right) \\ \bar{U}\left(\psi'_x\psi'_y - \psi'\psi'_{xy}\right) + \bar{V}\left(\psi_y'^2 - \psi'\psi'_{yy}\right) \end{cases} \quad (1)$$

where $\vec{V}$ represents the horizontal wind velocity vector, U and V denote the zonal and meridional wind velocity, respectively. ψ symbolizes the stream function. The primes and overbars signify the regressed anomalies onto the normalized DJF(0) Niño3.4 index and climatological mean-state quantities, respectively.

PDO index

The Pacific decadal oscillation (PDO) is obtained by the leading pattern via empirical orthogonal function analysis of SST anomalies in the North Pacific basin (poleward of 20°N). The SST anomalies are obtained by removing both the climatological annual cycle and the global-mean SST anomaly from the data at each grid point.

AMV index

The Atlantic multidecadal variability (AMV) index is defined as detrended 10-year low-pass filtered DJF(0) mean area-averaged SST anomalies over the North Atlantic basin (0°–65°N, 80°W–0°).

Numerical simulation

In the present study, we employ the dry version of the linear baroclinic model (LBM) to investigate how the atmosphere responds to the vorticity perturbation induced by Atlantic SST anomalies[43]. The LBM is a model made up of atmospheric primitive equations linearized at a given state. The model has a horizontal resolution of T42 and a vertical resolution of 20σ. We set a maximum e-folding decay time of 6 h for horizontal diffusion to maintain model stability. For different levels of σ, we apply Rayleigh friction and Newtonian damping timescales ranging from 1 to 30 day^{-1}. Vertical diffusion across all layers is fixed at 1000 day^{-1}. We run the model for 50 days to reach a stable state and use the average of the last 30 days as results.

Data availability

All the data that support the findings in the present study are available for open access. The monthly precipitation datasets, including GPCC, CRU, and Udel are accessed from https://opendata.dwd.de/climate_environment/GPCC, https://crudata.uea.ac.uk/cru/data/hrg/cru_ts_4.07 and https://downloads.psl.noaa.gov/Datasets/udel.airt.precip, respectively. The HadISST, ERSST, and Kaplan SST datasets are from https://www.metoffice.gov.uk/hadobs/hadisst, https://www1.ncdc.noaa.gov/pub/data/cmb/ersst/v5/netcdf and https://psl.noaa.gov/data/gridded/data.kaplan_sst.html, respectively. Global atmospheric circulation dataset is derived from https://psl.noaa.gov/thredds/catalog/Datasets/20thC_ReanV2/Monthlies/gaussian/monolevel/catalog.html. In addition, CMIP6 model outputs are from https://aims2.llnl.gov/search/cmip6.

Code availability

All the codes for analyses and diagnostics are available from the corresponding authors upon reasonable request.

Received: 26 March 2024; Accepted: 11 August 2024;
Published online: 23 August 2024

References

1. Chen, X., Wang, S., Hu, Z., Zhou, Q. & Hu, Q. Spatiotemporal characteristics of seasonal precipitation and their relationships with ENSO in Central Asia during 1901–2013. *J. Geogr. Sci.* **28**, 1341–1368 (2018).
2. Chen, F., Huang, W., Jin, L., Chen, J. & Wang, J. Spatiotemporal precipitation variations in the arid Central Asia in the context of global warming. *Sci. China Earth Sci.* **54**, 1812–1821 (2011).
3. Hu, K. et al. Interdecadal variations in ENSO influences on Northwest Pacific–East Asian early summertime climate simulated in CMIP5 models. *J. Clim.* **27**, 5982–5998 (2014).
4. Wu, R., Lin, M. & Sun, H. Impacts of different types of El Niño and La Niña on northern tropical Atlantic sea surface temperature. *Clim. Dyn.* **54**, 4147–4167 (2020).
5. Yao, J. et al. Intensification of extreme precipitation in arid Central Asia. *J. Hydrol.* **598**, 125760 (2021).
6. Hu, Z.-Y. et al. Variations and changes of annual precipitation in Central Asia over the last century. *Int. J. Climatol.* **37**, 157–170 (2017).
7. de Beurs, K. M., Henebry, G. M., Owsley, B. C. & Sokolik, I. N. Large scale climate oscillation impacts on temperature, precipitation and land surface phenology in Central Asia. *Environ. Res. Lett.* **13**, 065018 (2018).
8. Feng, F., Zhao, Y., Huang, A., Li, Y. & Zhou, X. Different seasonal precipitation anomaly patterns in Central Asia associated with two types of El Niño during 1891–2016. *Front. Earth Sci.* **10**, 771362 (2022).
9. Mariotti & Annarita How ENSO impacts precipitation in southwest central Asia. *Geophys. Res. Lett.* **34**, 370–381 (2007).
10. Arpe, K. et al. Connection between Caspian Sea level variability and ENSO. *Geophys. Res. Lett.* **27**, 2693–2696 (2000).
11. Hurrell, J. W. Influence of variations in extratropical wintertime teleconnections on Northern Hemisphere temperature. *Geophys. Res. Lett.* **23**, 665–668 (1996).
12. Zhang, X., He, M., Bai, M. & Ge, Q. Meteorological drought and its large-scale climate patterns in each season in Central Asia from 1901 to 2015. *Clim. Change* **166**, 41 (2021).
13. Chen, Z., Wu, R., Zhao, Y. & Wang, Z. Different responses of Central Asian precipitation to strong and weak El Niño events. *J. Clim.* **35**, 1497–1514 (2022).
14. Wu, R. et al. Northeast China summer temperature and North Atlantic SST. *J. Geophys. Res. Atmos.* **116**, D16116 (2011).
15. Chen, S., Wu, R., Chen, W., Hu, K. & Yu, B. Structure and dynamics of a springtime atmospheric wave train over the North Atlantic and Eurasia. *Clim. Dyn.* **54**, 5111–5126 (2020).
16. Ma, Q. et al. How do multiscale interactions affect extreme precipitation in eastern Central Asia? *J. Clim.* **34**, 7475–7491 (2021).
17. Umirbekov, A., Peña-Guerrero, M. D. & Müller, D. Regionalization of climate teleconnections across Central Asian mountains improves the predictability of seasonal precipitation. *Environ. Res. Lett.* **17**, 055002 (2022).

18. Vicente-Serrano, S. M. et al. The Westerly Index as complementary indicator of the North Atlantic oscillation in explaining drought variability across Europe. *Clim. Dyn.* **47**, 845–863 (2016).
19. Xu, G. et al. Regional drought shifts (1710–2010) in East Central Asia and linkages with atmospheric circulation recorded in tree-ring $\delta^{18}O$. *Clim. Dyn.* **52**, 713–727 (2019).
20. Alexander, M. A. et al. The Atmospheric Bridge: the influence of ENSO teleconnections on air–sea interaction over the global oceans. *J. Clim.* **15**, 2205–2231 (2002).
21. Klein, S. A., Soden, B. J. & Lau, N.-C. Remote sea surface temperature variations during ENSO: evidence for a tropical atmospheric bridge. *J. Clim.* **12**, 917–932 (1999).
22. Rana, S., McGregor, J. & Renwick, J. Dominant modes of winter precipitation variability over Central Southwest Asia and inter-decadal change in the ENSO teleconnection. *Clim. Dyn.* **53**, 5689–5707 (2019).
23. Hoell, A. et al. The forcing of monthly precipitation variability over Southwest Asia during the Boreal Cold Season. *J. Clim.* **28**, 7038–7056 (2015).
24. Hoell, A., Barlow, M. & Saini, R. Intraseasonal and seasonal-to-interannual Indian Ocean convection and hemispheric teleconnections. *J. Clim.* **26**, 8850–8867 (2013).
25. Zhang, Y. & Wu, R. Asian meteorological droughts on three time scales and different roles of sea surface temperature and soil moisture. *Int. J. Climatol.* **41**, 6047–6064 (2021).
26. Zhang, J. et al. Influences of tropical Pacific and North Atlantic SST anomalies on summer drought over Asia. *Clim. Dyn.* **61**, 5827–5844 (2023).
27. Huang, B. & Shukla, J. Ocean–atmosphere interactions in the tropical and subtropical Atlantic Ocean. *J. Clim.* **18**, 1652–1672 (2005).
28. Enfield, D. B. & Mayer, D. A. Tropical Atlantic sea surface temperature variability and its relation to El Niño–Southern Oscillation. *J. Geophys. Res. Oceans* **102**, 929–945 (1997).
29. Curtis, S. & Hastenrath, S. Forcing of anomalous sea surface temperature evolution in the tropical Atlantic during Pacific warm events. *J. Geophys. Res. Oceans* **100**, 15835–15847 (1995).
30. Xie, S. The shape of continents, air–sea interaction, and the rising branch of the Hadley circulation (2004).
31. Xie, S. A dynamic ocean–atmosphere model of the tropical Atlantic decadal variability. *J. Clim.* **12**, 64–70 (1999).
32. Lee, S. K., Enfield, D. B. & Wang, C. Why do some El Niños have no impact on tropical North Atlantic SST?. *Geophys. Res. Lett.* **35**, L16705 (2008).
33. Feng, J., Wang, L. & Chen, W. How does the East Asian summer monsoon behave in the decaying phase of El Niño during different PDO phases? *J. Clim.* **27**, 2682–2698 (2014).
34. Lopez, H., Lee, S.-K., Kim, D., Wittenberg, A. T. & Yeh, S.-W. Projections of faster onset and slower decay of El Niño in the 21st century. *Nat. Commun.* **13**, 1915 (2022).
35. Schneider, U., Hänsel, S., Finger, P., Rustemeier, E. & Ziese, M. *GPCC Full Data Monthly Product Version 2022 at 0.5°: Monthly Land–surface Precipitation from Rain-gauges Built on GTS-based and Historical Data* [Data set] (Global Precipitation Climatology Centre (GPCC), 2022).
36. Harris, I., Osborn, T. J., Jones, P. & Lister, D. Version 4 of the CRU TS monthly high-resolution gridded multivariate climate dataset. *Sci. Data* **7**, 109 (2020).
37. Matsuura, K. & Willmott, C. *Terrestrial Air Temperature: 1900–2008 Gridded Monthly Time Series (Version 4.01)* (Department of Geography Center, University of Delaware, 2015).
38. Rayner, N. et al. Global analyses of sea surface temperature, sea ice, and night marine air temperature since the late nineteenth century. *J. Geophys. Res. Atmos.* **108**, 4407 (2003).
39. Huang, B. et al. Extended reconstructed sea surface temperature, version 5 (ERSSTv5): upgrades, validations, and intercomparisons. *J. Clim.* **30**, 8179–8205 (2017).
40. Kaplan, A. et al. Analyses of global sea surface temperature 1856–1991. *J. Geophys. Res. Oceans* **103**, 18567–18589 (1998).
41. Schneider, D. P., Deser, C., Fasullo, J. & Trenberth, K. E. Climate data guide spurs discovery and understanding. *EOS Trans. Am. Geophys. Union* **94**, 121–122 (2013).
42. Takaya, K. & Nakamura, H. A formulation of a phase-independent wave-activity flux for stationary and migratory quasigeostrophic eddies on a zonally varying basic flow. *J. Atmos. Sci.* **58**, 608–627 (2001).
43. Watanabe, M. & Kimoto, M. Atmosphere–ocean thermal coupling in the North Atlantic: a positive feedback. *Q J. R. Meteorol. Soc.* **126**, 3343–3369 (2000).

Acknowledgements

We thank the anonymous reviewers for their constructive comments and suggestions, which significantly enhances the quality of the manuscript. We acknowledge the World Climate Research Program (WCRP)'s Working Group on Coupled Modeling, and we extend our gratitude to the climate modeling groups worldwide (listed in Supplementary Table 1) for their efforts in producing and making their model outputs publicly available. This work was funded by the National Natural Science Foundation of China (42141019 and 42261144687).

Author contributions

M.Y.: Investigation, data curation, formal analysis, drafting the manuscript, writing review, and editing. H.T.: Conceptualization, methodology, formal analysis, writing review, and editing. G.H.: Supervision, funding acquisition, project administration, writing review, and editing. R.W.: Formal analysis, writing review, and editing. All authors have read and approved the final manuscript.

Competing interests

The authors declare no competing interests.

Additional information

Supplementary information The online version contains supplementary material available at https://doi.org/10.1038/s41612-024-00742-x.

Correspondence and requests for materials should be addressed to Haosu Tang or Gang Huang.

Reprints and permissions information is available at http://www.nature.com/reprints

Publisher's note Springer Nature remains neutral with regard to jurisdictional claims in published maps and institutional affiliations.

Open Access This article is licensed under a Creative Commons Attribution-NonCommercial-NoDerivatives 4.0 International License, which permits any non-commercial use, sharing, distribution and reproduction in any medium or format, as long as you give appropriate credit to the original author(s) and the source, provide a link to the Creative Commons licence, and indicate if you modified the licensed material. You do not have permission under this licence to share adapted material derived from this article or parts of it. The images or other third party material in this article are included in the article's Creative Commons licence, unless indicated otherwise in a credit line to the material. If material is not included in the article's Creative Commons licence and your intended use is not permitted by statutory regulation or exceeds the permitted use, you will need to obtain permission directly from the copyright holder. To view a copy of this licence, visit http://creativecommons.org/licenses/by-nc-nd/4.0/.

© The Author(s) 2024

npj | climate and atmospheric science

www.nature.com/npjclimatsci

ARTICLE OPEN

Check for updates

The primary factors influencing the cooling effect of carbon dioxide removal

Xia Qu[1,2] and Gang Huang[1,3,4]✉

Carbon dioxide removal (CDR) is a crucial approach in achieving the goals set by the Paris Climate Agreement. However, understanding the cooling effect (CE) of CDR and its primary controlling factors has been challenging due to the limited number of models conducting the CDR simulation. To address this, we employed an energy balance model (EBM), which effectively captures or reproduces the global mean surface air temperature change to CO_2 forcing. The outputs of the EBM revealed that even with the same CDR rate, the CE diverse significantly ($\sigma = 0.7K$). Two main factors significantly affect the CE of CDR. The primary factor is the coefficient of the vertical heat exchange in the ocean [contributes to $\sigma(CE) = 0.7K$], which governs the heat uptake and release of the deep ocean. It directly impacts the heat absorbed by the Earth's surface and influences the magnitudes of the transient climate responses. The second factor is the estimation of effective radiative forcing (ERF) resulting from changes in CO_2 concentration [contributes to $\sigma(CE) = 0.6K$]. This estimation is directly associated with the amplitude of the CO_2 radiative forcing and the responses of relevant energy processes, thereby influencing the temperature change. Regarding the timing of the CE emergence, the influences of processes within the EBM are quite small. Therefore, an accurate estimation of the vertical heat exchange in the ocean and ERF may favor designation of a better pathway to achieve the temperature goals outlined in the Paris Climate Agreement.

npj Climate and Atmospheric Science (2023)6:215 ; https://doi.org/10.1038/s41612-023-00547-4

INTRODUCTION

The global mean surface air temperature change (ΔT) is an important metric of climate change. The ΔT brings about vast consequences, such as changes in the hydrological cycle[1–5], clouds[6–8], radiative fluxes[3,6,8,9], sea levels[10,11], sea ice[11–13], carbon emissions[6,14], as well as regional climate[15,16]. To mitigate climate change, the United Nations Framework Convention on Climate Change proposed the Paris Climate Agreement to limit the global temperature increase below 2 °C and pursued efforts to limit it to 1.5 °C. According to estimations, the achievement of the goals in this century requires CDR[17–21]. It may interest us how the CE of CDR is implicated in the reversal of climate change; it is tightly associated with the stress regarding the realization of temperature goals.

If CDR is applied after the increase in CO_2 concentration, the ΔT exhibits hysteresis: it continues to rise for several years and then decreases; it cannot return to zero when the CO_2 concentration recovers to an unperturbed level[4,11,14,22,23]. To date, it has been reported that the CDR rate, equilibrium climate sensitivity (ECS) and ocean heat uptake may alter the hysteresis of the ΔT[14]. However, it is still unclear which factors are relatively important to the CE of CDR.

Most of the literature on the impacts of CDR is based on simulations of complex models, such as coupled general circulation models (CGCMs) and Earth system models (ESMs). Due to the great computational expense, investigations on CDR are mainly based on a single or few models[6,10,11,14,24]. This, to some extent, has hindered the understanding of the effects of some climatic properties on the behavior of the ΔT under CDR. For example, it is difficult to modulate the parameters associated with ocean processes. Recently, the Carbon Dioxide Removal Model Intercomparison Project (CDRMIP)[17] has been sponsored as a contribution to Coupled Model Intercomparison Project phase 6 (CMIP6)[25]. Within the project, although 8 models are used to conduct *1pctCO2-cdr* simulations (in which the CO_2 concentration declines) and the climatic properties of the models differ, it is still inadequate to discuss the effect of one climatic property while isolating the others.

The forcing and response energy budget framework may expand the understanding. To seek a straightforward understanding of the ΔT, the Intergovernmental Panel on Climate Change (IPCC) proposed the forcing and response energy budget framework[26–28]. It is expressed as follows:

$$\Delta N = F - \lambda \Delta T \quad (1)$$

where ΔN is the net incoming radiative flux at the top of the atmosphere (TOA), F is the ERF and λ is the climate feedback parameter (net radiative flux feedback to the TOA per ΔT). Conventionally, if the CO_2 concentration is 2 times the preindustrial level and the climate reaches equilibrium, the $\triangle T$ equates to the ECS (but for convenience, the present analysis uses 4 times the preindustrial concentration). To evaluate the transient response, the IPCC further introduced a two-layer EBM[28–32], which is an accredited tool in the translation of ECS to transient climate response[28]. Because of its small computational cost, the framework provides an opportunity to expand the understanding of the effects of each climatic property while isolating the effects of others.

RESULTS

Reproducibility of the EBM

Based on the outputs of 45 models in CMIP6, the EBM parameters were calibrated. Then, each CMIP6 model was applied to yield a

[1]State Key Laboratory of Numerical Modeling for Atmospheric Sciences and Geophysical Fluid Dynamics, Institute of Atmospheric Physics, Chinese Academy of Sciences, 100029 Beijing, China. [2]Center for Monsoon System Research, Institute of Atmospheric Physics, Chinese Academy of Sciences, 100029 Beijing, China. [3]Laboratory for Regional Oceanography and Numerical Modeling, Qingdao National Laboratory for Marine Science and Technology, 266237 Qingdao, China. [4]University of Chinese Academy of Sciences, 100049 Beijing, China. ✉email: hg@mail.iap.ac.cn

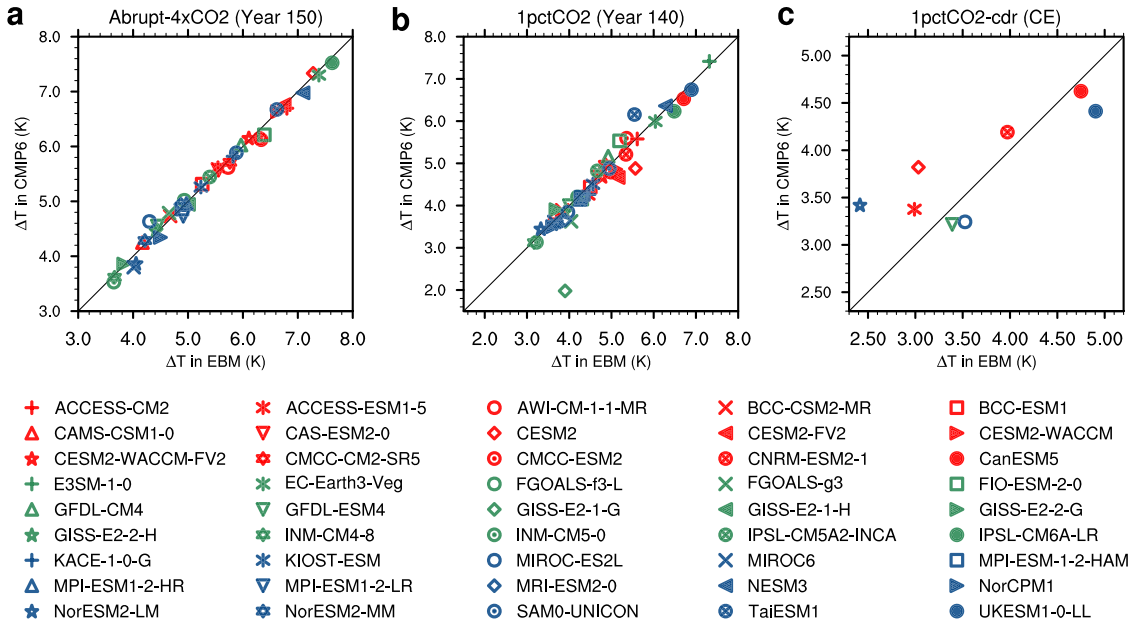

Fig. 1 The reproducibility of the Δ*T* in EBMs. The scatterplot of the Δ*T* (unit: K) in EBM (*x* axis) and CMIP6 (*y* axis). In (**a**), the results are the Δ*T* in year 150 in *Abrupt-4×CO2* simulations. In (**b**), the results are the change in year *140* in *1pctCO2* simulations. In (**c**), the results are the CE of CDR in *1pctCO2-cdr* simulations; the CE is defined as the Δ*T* differences between the ends of *1pctCO2* simulations and *1pctCO2-cdr* simulations.

surrogate EBM. The parameters are calibrated based on data from year 1–150 of *Abrupt 4×CO2* simulation and year 1–140 of *1pctCO2* simulation; the results of EBMs in year 141–280 are predictions. The EBM captures the Δ*T* evolutions under CO_2 forcing well.

In the *Abrupt 4×CO2* simulation, the Δ*T* in CMIP6 models are all captured by their surrogate EBMs. In the simulation, the CO_2 concentration abruptly quadruples relative to the preindustrial level and is then held fixed. The Δ*T* in both the CMIP6 and EBM results rises dramatically and then increases at a slower rate (Supplementary Fig. 1); if compared individually, the two kinds of results are nearly identical. Taken the Δ*T* in year 150 for example, the individual results in the CMIP6 and EBM is well coincident (Fig. 1a).

In the *1pctCO2* simulation, most of the surrogate EBMs captures the Δ*T* evolution in CMIP6 results. The Δ*T* evolution of both the CMIP6 models and their surrogate EBMs displays the same ramp-up feature and nearly all the surrogate EBMs fit the Δ*T* evolution of their CMIP6 models well (Supplementary Fig. 2). When the increase in the CO_2 concentration ceases in year 140 (Fig. 2a), the Δ*T* in most CMIP6 models and their surrogate EBMs are nearly identical (Fig. 1b). The exception is CESM2, GISS-E2-1-G and KACE-1-0-G (Fig. 1b and Supplementary Fig. 2). For CESM2, the mismatch in temperature in year 140 is possibly because the model may not fulfil our conditions of the ERF-CO_2 relationship (Eq. 6). GISS-E2-1-G displays an unusual plateau in the Δ*T* after 82 years (Supplementary Fig. 2). In KACE-1-0-G, the initial global mean surface air temperature is ~1 K cooler than the end of preindustrial simulation; it does not satisfy the protocol that *1pctCO2* simulation initiates from the end of *preindustrial* simulation[25]. So GISS-E2-1-G and KACE-1-0-G are excluded in the subsequent analysis.

For the *1pctCO2-cdr* simulation, only 8 models are available. Since the *1pctCO2-cdr* simulation is the extension of the *1pctCO2* simulation, the CE of CDR is defined as the temperature difference between the end of *1pctCO2* simulation (year 140 in Fig. 2a) and that of *1pctCO2-cdr* simulation (the year 280 in Fig. 2a). Considering the interference of climatic internal variability, six surrogate EBMs (ACCESS-ESM1-5, CNRM-ESM2-1, CanESM5, GFDL-ESM4, MIROC-ES2L and UKESM1-0-LL) reasonably reproduce the CE, all with errors and less than their climatic internal variability (Fig. 1c and Supplementary Fig. 2 and Supplementary Table 2 in Supplementary Information). Two surrogate EBMs (CESM2 and NorESM2-LM) underestimate the CE (Fig. 1c and Supplementary Table 2). For CESM2, similar to the situation in the *1pctCO2* simulation, the difference in CE is possibly due to a mismatch of the ERF-CO_2 relationship. For NorESM2-LM, the Δ*T* evolution during years 141–280 is nearly symmetric to that during years 1–140, which is an "unusual" behavior which does not match the Δ*T* behavior when the CO_2 concentration drops as described in previous literature[4,6,11,14,22,23,33]. Despite the "unusual" behaviors and climatic internal variabilities, the surrogate EBMs are able to reproduce the CE in CMIP6 models under the application of CDR.

As the EBM contains the simplified energetic processes associated with the Δ*T*, its good reproducibility in the aforementioned scenarios instills confidence its ability to study the effects of climatic properties on the CE of CDR. Together with the low computational cost of the EBM, the present analysis conducted 391 EBM simulation ensembles (see "Methods" section for more information) with varying climatic properties, greatly augmenting the sample size to supplement *1pctCO2-cdr* simulations, which only comprise 8 available models.

The CE of CDR

Under CDR conditions, the Δ*T* is affected by the accumulation of the ERF if the CO_2 concentration increases before the CDR is applied. Considering this, the EBMs are driven by the idealized evolution of CO_2 concentration below: during years 1–140, it increases 1% per year; during 141–280, the pathway mirrors that of years 1–140 (Fig. 2a). This favors the acquisition of data with a high signal-to-noise ratio. The evolution of the Δ*T* discussed in the following is based on the outputs of EBMs under such a pathway.

As changes in parameters affect the CE of CDR, the present analysis conducted *single parameter sensitive* simulations to investigate the effects of the parameters in the EBM (see "Methods"). The evolution of the Δ*T* is displayed in Fig. 2. Overall, the Δ*T* increases with the CO_2 concentration from year 1 to 140; it decreases as the CO_2 concentration declines from year 141 to 280; when the CO_2 concentration recovers to preindustrial level, the Δ*T* cannot fall back to 0. The Δ*T* varies as the parameters alter.

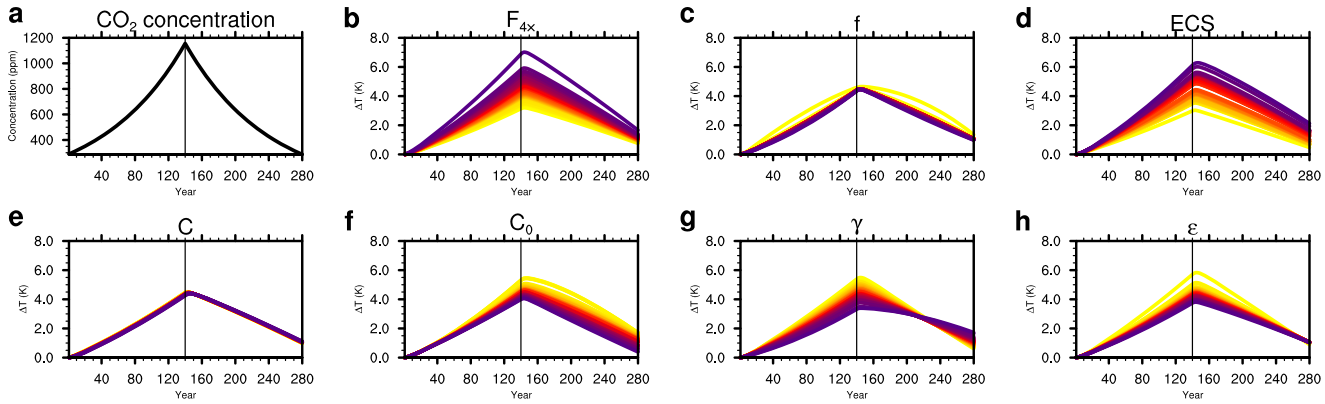

Fig. 2 The evolution of atmospheric CO_2 concentration and ΔT. The evolved CO_2 concentration (**a**; unit: ppm) is the forcing of the *single parameter sensitive* and *reconstructed* simulations. The time serials of ΔT (units: K) are the results of single parameter sensitive simulations. **b**–**h** demonstrates the results of the set of EBM simulations in which one parameter (indicated above each panel) was varied while the other parameters were set as multimodel averages; the colors of the curves from light to dark represent the varied parameters from small to large. The *x*-axis denotes the year.

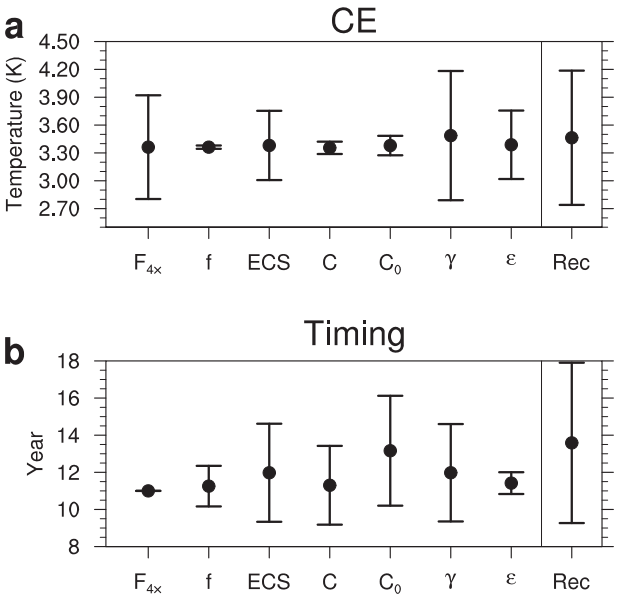

Fig. 3 The average and diversity of the CE features resulting from individual and all parameters. The error plots of the features of the ΔT under CDR scenarios in EBMs. For each of the 7 leftmost parameters on the *x*-axis, the corresponding box represents the span of the ΔT feature in the *single parameter sensitive* simulations; "Rec" represents the results of the *reconstructed* simulations. The dots are averaged results; the top and bottom lines of the error bars indicate the ±1 intermodel standard deviation, respectively. The features include the CE of CDR (**a**; unit: K) and the lag when cooling emerges after year 140 (**b**).

The averages and diversities of CDR CE in *the single parameter sensitive* simulation, as well as the *reconstructed* simulations, are displayed in Fig. 3a. In *the reconstructed* results, the averaged CE of CDR is 3.5 K with a standard deviation of 0.7 K.

The leading factor affecting the CE is the coefficient of the vertical heat exchange in the ocean (parameter γ). The sole change in γ leads to a CE of CDR with an average of 3.5 K and a standard deviation of 0.7 K, which is almost identical to the reconstructed results (Fig. 3a). This parameter means that under the same temperature difference between the Earth's surface and the deep ocean, a higher parameter yields higher heat exchange between the two. For instance, if the Earth's surface is warmer than the deep ocean, more heat is loss from the former to latter, resulting in smaller temperature gap between the two layers and smaller temperature response of the Earth's surface; if the Earth's surface is cooling and the deep ocean is warmer than it, it receives more heat from the deep ocean, also leading to a smaller temperature gap between the two layers and a less cooling rate of the Earth's surface.

Inferred from the magnitudes of the net energy gained by the Earth's surface ($Cd(\Delta T)/dt$; Figs 4g and 5a, b), before year 200, Eqs. (4) and (6) in "Methods" can be expressed as:

$$F - \lambda\Delta T - \varepsilon H \approx 0 \quad (2)$$

This equation indicates that the ERF is approximately balanced by heat transfer from the Earth's surface to the deep ocean and radiation feedback to the TOA.

When the CO_2 concentration increases, the Earth's surface receives energy due to CO_2 forcing, resulting in warming (Fig. 4a, d). Since the deep ocean has a much larger heat capacity than the Earth's surface (Supplementary Table 1), the surface warms faster than the deep ocean (Fig. 4c). A portion of the injected energy flows into the deep ocean (Fig. 4f), through advection, diffusion and mixing[34]; while the rest primarily feedbacks to the TOA (Fig. 4e). If only γ varies, a higher γ value leads to more heat being transferred from the Earth's surface to the deep ocean (higher εH), resulting in a lower efficiency of ERF in the warming of the Earth's surface (Fig. 5a). This is accompanied by a larger-warmed deep ocean, a less-warmed Earth's surface and a smaller temperature difference between the two layers. Consequently, the $\triangle T$ in year 140 is smaller (Fig. 4a, b, f).

After year 140 but before the temperature gap between the Earth's surface and the deep ocean disappears, higher γ values lead to slower decrease in the ΔT. During this period, although the ERF is decreasing, it is still the primary forcing (Fig. 5b). Similar to the period from years 1–140, the injected energy is partially transferred to the deep ocean and partially returned to the TOA. With higher γ values, more energy is transferred to the deep ocean, resulting in lower efficiency in driving changes in the ΔT (Eqs. 2 and 3 and Fig. 5b); consequently, when the ERF declines, the ΔT drops at a slower pace (Fig. 4a, d). Furthermore, if γ is higher, the rate of the ΔT decrease must be slower to maintain a consistent relationship between net energy budget and the ΔT change (refer to Supplementary Discussion in Supplementary Information).

As year 280 approaches, the CO_2 forcing is nearly vanished, and the warmed Earth surface emits outgoing radiative fluxes, contributing to a cooling to itself (Fig. 4a, e, d). Since the deep ocean is warmer than the Earth's surface, it provides heat to the surface (Fig. 4c, f). As the derivative of $Cd(\Delta T)/dt$ is small in this

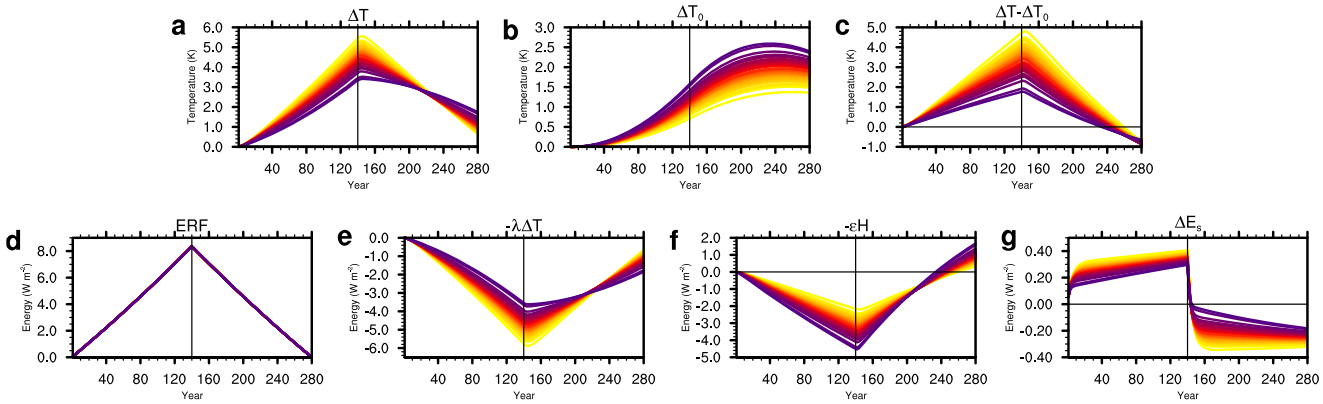

Fig. 4 The evolution of temperature and energy fluxes when the coefficient of vertical heat exchange in the ocean changes. The time serials in EBMs when the coefficient of vertical heat exchange in the ocean (γ) varies: ΔT (**a**; unit: K), temperature change in the deep ocean (**b**; unit: K), changes in temperature differences between the Earth's surface and the deep ocean (**c**; unit: K), ERF (**d**; unit: W m^{-2}), energy feedback ($-\lambda\Delta T$; **e**; unit: W m^{-2}), energy loss of the Earth's surface to the deep ocean ($-\varepsilon H$; **f**; unit: W m^{-2}), and net energy gained by the Earth's surface (the sum of (**c**–**e**); **g**; unit: W m^{-2}). The colors of the curves from light to dark represent γ from small to large. The results are the output of the *single parameter sensitive* simulations in which γ was varied and the other parameters were fixed.

period (Fig. 5d), the derivative of both sides of Eq. (4) against t yields:

$$F' - \lambda\Delta T' - \varepsilon H' \approx 0 \quad (3)$$

That means that the rate of the decline ERF is balanced by the rates of climate feedback and energy loss from Earth's surface to deep ocean.

Higher γ values tend to result in more dramatic changes in the heat exchange between the deep ocean and the Earth's surface; when approaching 280, it leads to a higher $-\varepsilon H'$ (Fig. 5d). According to Eq. (3) and with F' being fixed in all ensembles (Fig. 5d), the $\Delta T'$ must be higher to maintain the balance of F', $-\lambda\Delta T'$ and $-\varepsilon H'$. Given that the $\Delta T'$ is negative, its magnitude must be small and the ΔT need to decrease at a slower rate (Fig. 4a).

Based on the above results, it is evident that higher coefficient of the vertical exchange in the ocean results in a slower decrease in ΔT in period of year 141-200 and years approaching 280, indicating a lower CE of CDR. Conversely, a lower γ value corresponds to a higher CE (Fig. 4a). This finding aligns with Ehlert and Zickfeld[10], suggesting that enhanced vertical mixing results in a lower CE. The out-of-phase relationship of the ΔT between year 140 and 280 is not observed in other *single parameter sensitive* simulations (Fig. 2), further supporting the notion that the coefficient of the vertical heat exchange in the ocean to be the primary factor influencing the CE of CDR.

Simply speaking, the deep ocean acts as a "reservoir" of heat, wherein an increase in the CO_2 concentration coupled with a higher γ leads to a faster injection of heat into the "reservoir". This results in a less-warmed Earth's surface and a larger amount of heat being restored by the deep ocean. Conversely, when the CO_2 concentration is close to vanishing, the "reservoir" releases heat to prevent excessive cooling of the Earth's surface.

The estimation of ERF due to CO_2 concentration change ($F_{4\times}$) plays a secondary role in the CE variability. In *the single parameter sensitive* simulation, the sole change in $F_{4\times}$ yielded output with an averaged CE of CDR of 3.4 K and standard deviation of 0.6 K (Fig. 3a). In this set of simulations, the timings of the processes, such as the peak of the ΔT (year 144) and the transition of the deep ocean from heat uptake to heat release (year 245-246), do not change; the response amplitudes of the associated processes simply scale with $F_{4\times}$ (Fig. 6). Higher $F_{4\times}$ leads to stronger ERF, hence the higher temperature response of the earth surface and deep ocean, larger temperature gap between the earth surface and deep ocean, stronger vertical heat exchange in the ocean, more intensified energy gained by the Earth's surface when the CO_2 concentration increases, as well as more intensified energy lost by the earth surface when the CO_2 concentration decreases (Fig. 6). Thus, higher $F_{4\times}$ induces a relatively higher CE of CDR (Fig. 4a).

The individual contributions of the remaining parameters are much smaller (Fig. 3a), and therefore, their roles are not discussed here.

The timing of CE emergence

Another important aspect related to the CE of CDR is the timing of the CE emergence (TOCEE). Previous studies have generally agreed that if CDR is applied, the ΔT may peak several years after the maximum CO_2 concentration[1,6,14,23,24]. This implies that the CE of CDR does not immediately emerge upon the initiation of CDR. In this context, we defined the TOCEE the first year after 140 when the ΔT is lower than that in year 140. In the *Reconstruct* simulations, the mean TOCEE is 13.6 years. If one is interested in the CE during a period shorter than the entire CDR process, it is crucial to understand this TOCEE: before the TOCEE, the CE is less than zero, indicating a warming effect; only after TOCEE, the CE is positive. The relationship between CE and CO_2 concentration is not strictly linear.

However, the influences of the parameters on the TOCEE are minor. In the *Reconstruct* simulations, the TOCEE exhibits relatively small diversity, with a standard deviation of 4.3 years (Fig. 3b). The *single parameter sensitive* simulations, it is evident that the primary factor affecting TOCEE is the heat capacity of the deep ocean (C_0), accounting for a standard deviation of 3.0 years. The diversity in TOCEE is also influenced by the ECS, the coefficient of vertical heat exchange in the ocean (γ) and the heat capacity of the Earth's surface (C), with standard deviations of 2.6, 2.6 and 2.1 years, respectively. Considering the limited diversity in the TOCEE, the role of the parameters is not extensively discussed in present analysis.

DISCUSSION

The EMB results indicates that even under the same CDR pathway (reducing CO_2 concentration by 1% per year for 140 years to pre-industrial level), the CE of CDR varies. Two factors primarily affect the CE: the primary one is the coefficient of the vertical heat exchange in the ocean and the second one is the estimation of ERF to changes in CO_2 concentration. Additionally, it is worth noting that the CE does not manifest immediately after the application of CDR; typically, it emerges approximately 14.3 years later.

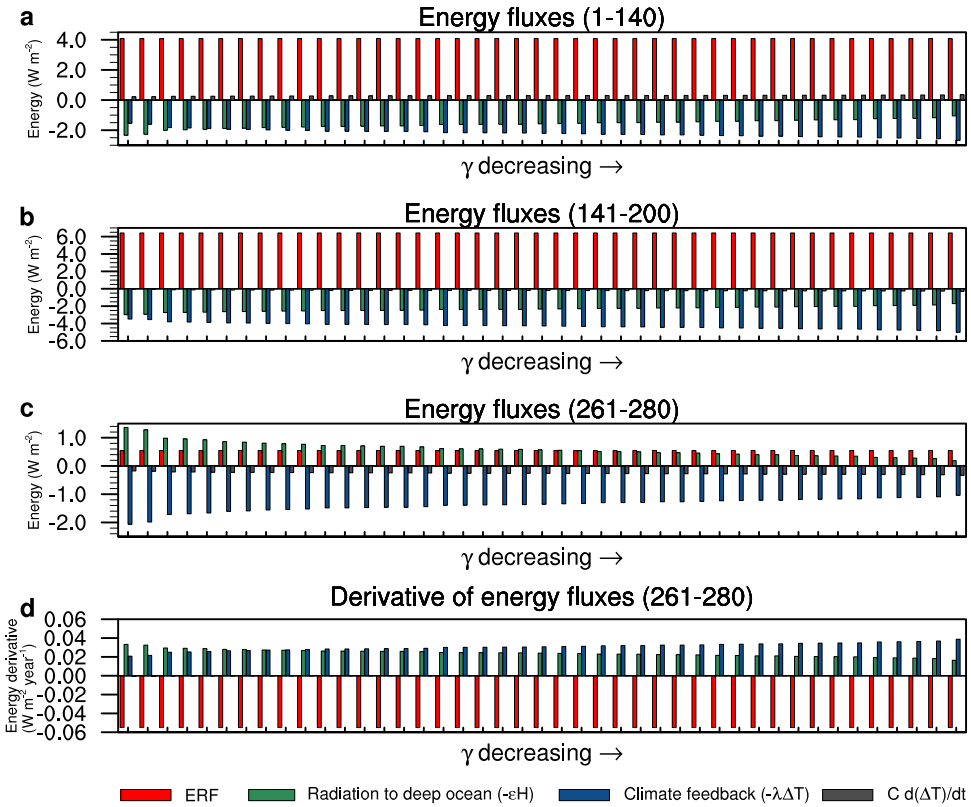

Fig. 5 The energy fluxes during three periods and the derivative of the fluxes during one period when the coefficient of vertical heat exchange in the ocean changes. The averaged radiation fluxes in *Single parameter sensitive* simulations during three periods: **a** year 1–140, **b** year 141–200 and **c** year 261–280. **d** is the derivative of the fluxes during year 261–280. Red, blue, green and gray bars are ERF, radiation to deep ocean ($-\varepsilon H$), climate feedback ($-\lambda\Delta T$) and $Cd(\Delta T)/dt$, respectively. The values from left to right in x-axis mean the γ is from large to small. Positive and negative mean the Earth's surface receiving and losing energy, respectively. The units of (**a**–**c**) are W m^{-2}, the one of (**d**) is W m^{-2} year^{-1}.

One implication of the findings concerns the coefficient of vertical heat exchange in the ocean. The question is how to define the depth of the boundary of the two layers. According to the estimation method in Geoffroy, et al.[29] and the mean heat capacities of the Earth's surface and deep ocean in Supplementary Table 1 in the Supplementary Information, the depth of the upper ocean is approximately 93 m, which roughly matches the previous estimation of the mixed-layer depth[35]. Thus, if we accurately estimate the vertical heat exchange coefficient between the mixed layer and the layer below, there is a potential to make a more precise projection of the CE of CDR.

The second implication concerns the estimation of ERF. Despite substantial effort and progresses made in understanding the relationship between ERF and changes in atmospheric CO_2 concentration[26,28,36,37], the ERF estimation still significantly affects the CE of CDR. To minimize the uncertainty in CE projection, a more accurate estimation of ERF is also required.

The third implication concerns the representativeness of model outputs in the CDRMIP. If the outputs of 8 models in the CDRMIP are used instead of outputs of the 43 CMIP6 models, the relative contributions to the CE diversity vary due to differences in the diversities of the parameters. Among the models participating in CDRMIP, owing to the larger standard deviation of ε (0.36; 0.24 in CMIP6 models; see Supplementary Table 3 in Supplementary Information) and smaller standard deviation of γ (0.18 W m^{-2} K^{-1}; 0.33 W m^{-2} K^{-1} in the CMIP6 models), ε contributes the most to the diversity of CE, followed by γ (Supplementary Fig. 3 in Supplementary Information). Therefore, when discussing the CE diversity among the models, due to the inadequate sampling, the current 8 models in the CDRMIP cannot fully represent the feature exhibited by the 43 CMIP6 models.

In addition, one may concern the effect of the Atlantic meridional overturning circulation (AMOC) on the vertical heat exchange in the ocean. This concern arises from the following findings: (1) In response to changes in CO_2 concentration, the AMOC may undergo a similar variation with slightly differences in phase[38]; (2) The AMOC is an important heat conveyor in the redistribution of global energy[39]. The relationship between the AMOC strength and the vertical heat exchange in the ocean appears contradictory. Some studies displayed that a stronger AMOC tends to delay global warming[40,41], as it leads to a more vigorous vertical heat exchange in the ocean. On the other hand, a stronger decline in the AMOC may lead to less global warming[42–44], suggesting that a weaker mean AMOC is associated with enhanced ocean heat uptake and intensified vertical heat exchange. This contradiction is reconciled by the explanation, proposed by He et al.[45], that the base climate ocean circulation, including the AMOC, is more influential, as it establishes the basic state for transient climate responses. This reconfirms that the fixed coefficient of vertical heat exchange in the EBM is able to grasp the majority of changes in global temperature. However, it is essential to keep in mind that the coefficient of vertical heat transport in ocean is not constant. Compared with varying vertical heat transport, present simplification may lead to slight differences in ocean heat uptake, as well as the global climate response.

METHODS

CMIP6 dataset

The parameter calibration of the EBM and the performance evaluation are based on CMIP6 simulations[25], including (1) *preindustrial control simulation*: the CO_2 concentration in the CGCMs or ESMs is held constant (284.7 ppm). The minimum

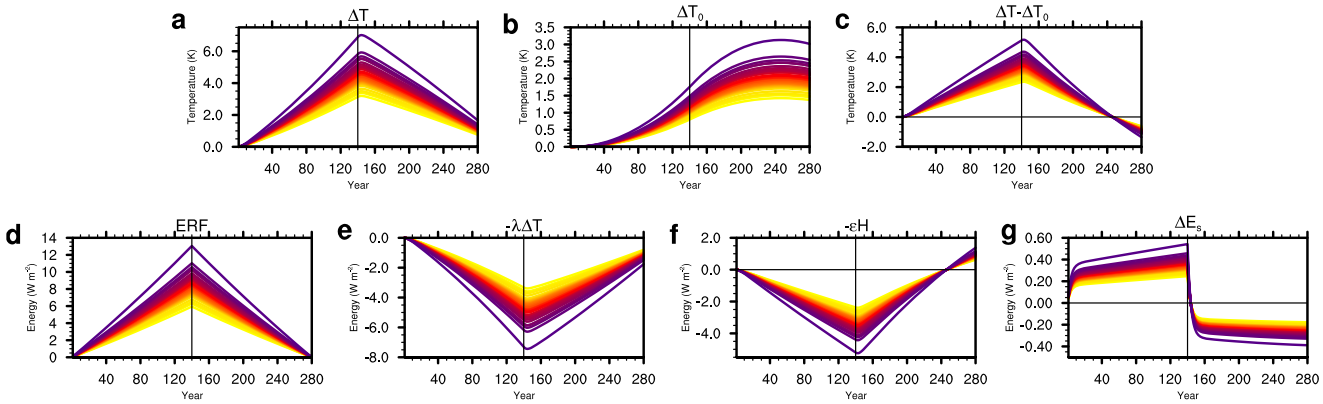

Fig. 6 The evolution of temperature and energy fluxes when the estimation of ERF varies. The time serials of energy processes and temperature change when $F_{4\times}$ varies: the time series of the ΔT (**a**; unit: K), temperature change in the deep ocean (**b**; unit: K), changes in temperature differences between the earth surface and the deep ocean (**c**; unit: K), ERF (**d**; unit: W m^{-2}), energy feedback ($-\lambda\Delta T$; **e**; unit: W m^{-2}), energy loss of the earth surface to the deep ocean ($-\varepsilon H$; **f**; unit: W m^{-2}) and net energy gained by the earth surface (the sum of (**c**–**e**); **g**; unit: W m^{-2}). The colors of the curves from light to dark represent the $F_{4\times}$ from small to large. The results are the output of the *single parameter sensitive* simulations in which $F_{4\times}$ was varied and the other parameters were fixed.

number of simulation years is 500. (2) *Abrupt 4×CO2 simulation*: the CO_2 concentration in the CGCMs and ESMs is abruptly quadrupled relative to the preindustrial level and then held constant. The simulation is initiated from the end of the preindustrial control simulation. The minimum number of simulation years is 150. (3) *1pctCO2 simulation*: starting from the preindustrial level, the CO_2 concentration in the CGCMs and ESMs is increased 1% per year until it quadruples at year 140. Then, it is held constant for 10 years. The simulation is initiated from the end of the preindustrial control simulation. Only the outputs of the first 140 years are used in the present analysis. (4) *1pctCO2-cdr simulation*: starting from the level at the 140th year of the *1pctCO2* simulation, the CO_2 concentration in the CGCMs and ESMs is decreased 1% per year until it recovers to the preindustrial level. Then, it is held constant[17]. The simulation is initiated from the 140th year of the *1pctCO2* simulation. The minimum number of simulation years is 140. Only the outputs of the first 140 years are used in the present analysis.

Forty-five models are used in the present analysis and are listed in Supplementary Table 1 in the Supplementary Information. The outputs of the *preindustrial control*, *Abrupt 4×CO2* and *1pctCO2-cdr* simulations are all available. Only eight models (ACCESS-ESM1-5, CESM2, CNRM-ESM2-1, CanESM5, GFDL-ESM4, MIROC-ES2L, NorESM2-LM and UKESM1-0-LL) conducted the *1pctCO2-cdr* simulation and they were used in present analysis.

EBM and parameter calibration

The present analysis employed a two-layer EBM[29–31] to analyze the effects of climatic properties on the ΔT evolution under a CDR pathway. The model splits the climate system into two layers: (1) the Earth's surface, including the atmosphere, the land surface, and the upper ocean, and (2) the deep ocean. It includes some key climatic processes, such as climate feedback, heat transfer between the two layers, the heat capacity of the climate system, and the efficacy of deep-ocean heat uptake. The equations of the EBM are

$$C\frac{d(\Delta T)}{dt} = F - \lambda\Delta T - \varepsilon H \tag{4}$$

$$C_0\frac{d(\Delta T_0)}{dt} = H \tag{5}$$

$$H = \gamma(\Delta T - \Delta T_0) \tag{6}$$

In Eqs. (4)–(6), ΔT_0 is the temperature change in the deep ocean; F, λ, ε, γ, C, C_0 and H are the ERF, climate feedback parameter, efficacy factor of ocean heat uptake, heat exchange coefficient between the two layers, heat capacity of the upper layer, heat capacity of the deep ocean and energy obtained by deep ocean, respectively. εH is the heat loss to deep ocean from the Earth's surface. The equivalent climate feedback is $\lambda + (\varepsilon - 1)H/\Delta T$, serving a varying parameter of climate feedback.

The parameters are calibrated based on *abrupt 4×CO2 simulations* in CMIP6 using the method in Geoffroy et al.[30]. Each model underwent 50 iterations to generation the parameters:

(1) For first iteration, we set $\varepsilon = 1$. The value of F, ECS and λ are obtained by performing a linear regression of ΔN and ΔT, which are CMIP6 outputs, following Eq. (1). To calibrate C, C_0 and γ, we introduce four parameters τ_f, τ_s, a_f and a_s. Using the following equation:

$$\ln\left(1 - \frac{\Delta T}{\mathrm{ECS}}\right) \approx \ln a_s - \frac{t}{\tau_s} \tag{7}$$

where the t is time. The linear regression of the left-hand side against right-hand side over the period 30–150 yields a_s and τ_s. Then, using:

$$a_f = 1 - a_s \tag{8}$$

we can determine a_f. Using the averaging of first 10 years of *abrupt 4×CO2* simulations and following:

$$\tau_f = \frac{t}{\ln a_f - \ln\left(1 - \frac{\Delta T}{\mathrm{ECS}} - a_s e^{-\frac{t}{\tau_s}}\right)} \tag{9}$$

we can calculate τ_f. To avoid division by 0, NorESM2-LM and NorESM2-MM utilized the first 4 and 7 years, respectively. C, C_0 and γ can be calculated as follows:

$$C = \frac{\lambda}{\frac{a_f}{\tau_f} + \frac{a_s}{\tau_s}} \tag{10}$$

$$C_0 = \frac{\tau_s(\tau_f a_f + \tau_s a_s) - C}{\varepsilon} \tag{11}$$

$$\gamma = \frac{C_0}{\tau_f a_s + \tau_s a_f} \tag{12}$$

Then, we can obtain the εH

(2) For iteration i ($i \geq 2$), the calculation process may be slightly different. By adding Eqs. (4) to (5), we can obtain:

$$\Delta N = F - \lambda \Delta T - (\varepsilon - 1)H \tag{13}$$

The multi-linear regression of ΔN against ΔT and H provided the F, ECS, λ and ε. The value of H is derived from iteration (i−1). The other steps remain the same as the first iteration.

Finally, 50 iterations yield the specific values of these parameters, listed in Supplementary Table 1 of the Supplementary Information.

The ERF, F, is a function of the CO_2 concentration (CO2) and satisfies[32]

$$F(\mathrm{CO2}) = F_{4\times}\left\{(1-f)\frac{\ln(\mathrm{CO2})}{\ln(4\times \mathrm{CO2_0})} + f\left[\frac{\ln(\mathrm{CO2})}{\ln(4\times \mathrm{CO2_0})}\right]^2\right\} \tag{14}$$

In Eq. (14), f is the fraction of nonlog-linearity of the ERF. $F_{4\times}$ represents the ERF when the CO_2 concentration is 4 times the preindustrial level. $CO2_0$ is the CO_2 concentration during the preindustrial period. f is calibrated based on *1pctCO2* simulation using the method described in Geoffroy and Saint-Martin[31]. To evaluate f, we define:

$$x = \log_4\left[\frac{\mathrm{CO2}}{\mathrm{CO2_0}}\right] - 1 \tag{15}$$

$$y = \frac{1}{\log_4\left[\frac{\mathrm{CO2}}{\mathrm{CO2_0}}\right]}\frac{\Delta N + \lambda \Delta T + (\varepsilon - 1)H}{F_{4\times}} - 1 \tag{16}$$

then, f is calculated as:

$$f = \frac{\sum_t xy}{\sum_t x^2} \tag{17}$$

Year 35-140 of *1pctCO2* simulation is utilized to minimize the influence of noise. The calculation of f uses iteration. In the first iteration, the H is set to zero; For iteration i ($i \geq 2$), the H is determined based on the results of the iteration (*i-1*). 50 iterations yield the f.

In Geoffroy and Saint-Martin[31], there is another option in which f is assigned as 0.09. For each model, we used the EBM to reproduce the ΔT in the *1pctCO2* simulation based on the calibrated f and assigned f. If the root mean square error relative to that of the CMIP6 result was lower, the corresponding f was adopted; otherwise, the assigned f was used. The parameter f is listed in Supplementary Table 1 in Supplementary Information.

EBM Simulations

To study the effects of the parameters, the present analysis conducted the following simulations: (1) *Single parameter sensitive* simulation: To investigate the effects of the parameters in the Eqs. (4)–(6) on the evolution of the ΔT, we changed one parameter according to the calibrated parameters of the CMIP6 models and set the other parameters as the mean of the CMIP6 models (The parameters are listed in Supplementary Table 1 in Supplementary Information; the parameters of GISS-E2-1-G and KACE-1-0-G are not used due to incorrect setup). The EBM (Eqs. (4)–(6)) is forced by the CO_2 concentration pathway, that is, during years 1–140, it uses the same concentration as that in the *1pctCO2* simulation; during years 141–280, it uses the same concentration as that in the *1pctCO2-cdr* simulation (see Fig. 2a). The total ensemble number is 301. (2) *Reconstructed* simulation: This simulation was designed to evaluate the performance of the EBM and determine the importance of the parameters. For each CMIP6 model, the surrogate EBM uses its corresponding parameters in Supplementary Table 1 in Supplementary Information. The EBM is forced by the CO_2 concentration pathway, as in *the single parameter sensitive* simulation. The total ensemble is 45. (3) *Abrupt 4×CO2 reconstructed* simulation: This simulation was designed to evaluate the reproducibility of the EBM for the *Abrupt 4×CO2* simulation in CMIP6. For each CMIP6 model, the surrogate EBM uses its corresponding parameters in Supplementary Table 1 in Supplementary Information. The EBM is forced by the CO_2 concentration, as in the *Abrupt 4×CO2 simulation* in CMIP6. The total ensemble is 45.

DATA AVAILABILITY

The CMIP6 outputs are available online at https://esgf-node.llnl.gov/projects/cmip6/.

Received: 23 August 2023; Accepted: 6 December 2023;
Published online: 20 December 2023

REFERENCES

1. Cao, L., Bala, G. & Caldeira, K. Why is there a short-term increase in global precipitation in response to diminished CO2 forcing? *Geophys. Res. Lett.* **38**, L06703 (2011).
2. Chou, C., Neelin, J. D., Chen, C.-A. & Tu, J.-Y. Evaluating the "rich-get-richer" mechanism in tropical precipitation change under global warming. *J. Clim.* **22**, 1982–2005 (2009).
3. Held, I. M. & Soden, B. J. Robust responses of the hydrological cycle to global warming. *J. Clim.* **19**, 5686–5699 (2006).
4. Yeh, S.-W., Song, S.-Y., Allan, R. P., An, S.-I. & Shin, J. Contrasting response of hydrological cycle over land and ocean to a changing CO2 pathway. *npj Clim. Atmos. Sci.* **4**, 53 (2021).
5. Andrews, T., Forster, P. M., Boucher, O., Bellouin, N. & Jones, A. Precipitation, radiative forcing and global temperature change. *Geophys. Res. Lett.* **37**, L14701 (2010).
6. Boucher, O. et al. Reversibility in an Earth System model in response to CO2 concentration changes. *Environ. Res. Lett.* **7**, 024013 (2012).
7. Hartmann, D. L. & Larson, K. An important constraint on tropical cloud - climate feedback. *Geophys. Res. Lett.* **29**, 1951 (2002).
8. Kamae, Y., Ogura, T., Watanabe, M., Xie, S. P. & Ueda, H. Robust cloud feedback over tropical land in a warming climate. *J. Geophys. Res. Atmos.* **121**, 2593–2609 (2016).
9. Qu, X. & Huang, G. CO2-induced heat source changes over the Tibetan Plateau in boreal summer-Part II: The effects of CO2 direct radiation and uniform sea surface warming. *Clim. Dyn.* **55**, 1631–1647 (2020).
10. Ehlert, D. & Zickfeld, K. Irreversible ocean thermal expansion under carbon dioxide removal. *Earth Syst. Dyn.* **9**, 197–210 (2018).
11. Wu, P., Ridley, J., Pardaens, A., Levine, R. & Lowe, J. The reversibility of CO2 induced climate change. *Clim. Dyn.* **45**, 745–754 (2015).
12. Dai, A. G., Luo, D. H., Song, M. R. & Liu, J. P. Arctic amplification is caused by sea-ice loss under increasing CO2. *Nat. Commun.* **10**, 121 (2019).
13. Pattyn, F. et al. The Greenland and Antarctic ice sheets under 1.5 degrees C global warming. *Nat. Clim. Chang.* **8**, 1053–1061 (2018).
14. Jeltsch-Thommes, A., Stocker, T. F. & Joos, F. Hysteresis of the Earth system under positive and negative CO2 emissions. *Environ. Res. Lett.* **15**, 124026 (2020).
15. Sun, M.-A. et al. Reversibility of the hydrological response in East Asia from CO_2-derived climate change based on CMIP6 simulation. *Atmosphere* **12**, 72 (2021).
16. Zhang, S. Q., Qu, X., Huang, G. & Hu, P. Asymmetric response of South Asian summer monsoon rainfall in a carbon dioxide removal scenario. *npj Clim. Atmos. Sci.* **6**, 10 (2023).
17. Keller, D. P. et al. The Carbon Dioxide Removal Model Intercomparison Project (CDRMIP): rationale and experimental protocol for CMIP6. *Geosci. Model Dev.* **11**, 1133–1160 (2018).
18. Rogelj, J. et al. Scenarios towards limiting global mean temperature increase below 1.5 degrees C. *Nat. Clim. Chang.* **8**, 325 (2018).
19. Sanderson, B. M., O'Neill, B. C. & Tebaldi, C. What would it take to achieve the Paris temperature targets? *Geophys. Res. Lett.* **43**, 7133–7142 (2016).
20. Sanderson, B. M. et al. Community climate simulations to assess avoided impacts in 1.5 and 2 degrees C futures. *Earth Syst. Dyn.* **8**, 827–847 (2017).
21. Xu, Y. & Ramanathan, V. Well below 2 degrees C: mitigation strategies for avoiding dangerous to catastrophic climate changes. *Proc. Natl Acad. Sci. USA* **114**, 10315–10323 (2017).
22. Kim, S. K. et al. Widespread irreversible changes in surface temperature and precipitation in response to CO2 forcing. *Nat. Clim. Chang.* **12**, 834 (2022).
23. Chadwick, R., Wu, P. L., Good, P. & Andrews, T. Asymmetries in tropical rainfall and circulation patterns in idealised CO_2 removal experiments. *Clim. Dyn.* **40**, 295–316 (2013).

24. Wu, P., Wood, R., Ridley, J. & Lowe, J. Temporary acceleration of the hydrological cycle in response to a CO_2 rampdown. *Geophys. Res. Lett.* **37**, L12705 (2010).
25. Eyring, V. et al. Overview of the Coupled Model Intercomparison Project Phase 6 (CMIP6) experimental design and organization. *Geosci. Model Dev.* **9**, 1937–1958 (2016).
26. Andrews, T., Gregory, J. M., Webb, M. J. & Taylor, K. E. Forcing, feedbacks and climate sensitivity in CMIP5 coupled atmosphere-ocean climate models. *Geophys. Res. Lett.* **39**, L09712 (2012).
27. Gregory, J. M. et al. A new method for diagnosing radiative forcing and climate sensitivity. *Geophys. Res. Lett.* **31**, L03205 (2004).
28. IPCC. *Climate Change 2021: The Physical Science Basis. Contribution of Working Group I to the Sixth Assessment Report of the Intergovernmental Panel on Climate Change* (eds Masson-Delmotte, V. et al.) 2391 (IPCC, 2021).
29. Geoffroy, O. et al. Transient climate response in a two-layer energy-balance model. Part I: Analytical solution and parameter calibration using CMIP5 AOGCM experiments. *J. Clim.* **26**, 1841–1857 (2013).
30. Geoffroy, O. et al. Transient climate response in a two-layer energy-balance model. Part II: Representation of the efficacy of deep-ocean heat uptake and validation for CMIP5 AOGCMs. *J. Clim.* **26**, 1859–1876 (2013).
31. Geoffroy, O. & Saint-Martin, D. Equilibrium- and transient-state dependencies of climate sensitivity: are they important for climate projections? *J. Clim.* **33**, 1863–1879 (2020).
32. Gregory, J. M., Andrews, T. & Good, P. The inconstancy of the transient climate response parameter under increasing CO2. *Philos. Trans. R. Soc. A* **373**, 20140417 (2015).
33. Held, I. M. et al. Probing the fast and slow components of global warming by returning abruptly to preindustrial forcing. *J. Clim.* **23**, 2418–2427 (2010).
34. Gregory, J. M. Vertical heat transports in the ocean and their effect on time-dependent climate change. *Clim. Dyn.* **16**, 501–515 (2000).
35. Sallee, J.-B. et al. Summertime increases in upper-ocean stratification and mixed-layer depth. *Nature* **591**, 592 (2021).
36. Andrews, T. & Forster, P. M. The transient response of global-mean precipitation to increasing carbon dioxide levels. *Environ. Res. Lett.* **5**, 025212 (2010).
37. Gregory, J. M. & Forster, P. M. Transient climate response estimated from radiative forcing and observed temperature change. *J. Geophys. Res. Atmos.* **113**, D23105 (2008).
38. Schwinger, J., Asaadi, A., Goris, N. & Lee, H. Possibility for strong northern hemisphere high-latitude cooling under negative emissions. *Nat. Commun.* **13**, 1095 (2022).
39. Buckley, M. W. & Marshall, J. Observations, inferences, and mechanisms of the Atlantic meridional overturning circulation: a review. *Rev. Geophys.* **54**, 5–63 (2016).
40. Hu, A. et al. Role of AMOC in transient climate response to greenhouse gas forcing in two coupled models. *J. Clim.* **33**, 5845–5859 (2020).
41. Kostov, Y., Armour, K. C. & Marshall, J. Impact of the Atlantic meridional overturning circulation on ocean heat storage and transient climate change. *Geophys. Res. Lett.* **41**, 2108–2116 (2014).
42. Drijfhout, S. Competition between global warming and an abrupt collapse of the AMOC in Earth's energy imbalance. *Sci. Rep.* **5**, 14877 (2015).
43. Caesar, L., Rahmstorf, S. & Feulner, G. On the relationship between Atlantic meridional overturning circulation slowdown and global surface warming. *Environ. Res. Lett.* **15**, 024003 (2020).
44. Bellomo, K., Angeloni, M., Corti, S. & von Hardenberg, J. Future climate change shaped by inter-model differences in Atlantic meridional overturning circulation response. *Nat. Commun.* **12**, 3659 (2021).
45. He, J., Winton, M., Vecchi, G., Jia, L. & Rugenstein, M. Transient climate sensitivity depends on base climate ocean circulation. *J. Clim.* **30**, 1493–1504 (2017).

ACKNOWLEDGEMENTS

We acknowledge the World Climate Research Program, which, through its Working Group on Coupled Modelling, coordinated and promoted CMIP6. We thank the climate modeling groups for producing and making available their model output, the Earth System Grid Federation (ESGF) for archiving the data and providing access, and the multiple funding agencies who support CMIP6 and ESGF. The study was supported by the National Natural Science Foundation of China (42141019, 42175055).

AUTHOR CONTRIBUTIONS

X.Q. and G.H. conceived the study; X.Q. performed the analysis, wrote and revised the paper; G.H. revised the paper. Both authors discussed and commented on the paper.

COMPETING INTERESTS

The authors declare no competing interests.

ADDITIONAL INFORMATION

Supplementary information The online version contains supplementary material available at https://doi.org/10.1038/s41612-023-00547-4.

Correspondence and requests for materials should be addressed to Gang Huang.

Reprints and permission information is available at http://www.nature.com/reprints

Publisher's note Springer Nature remains neutral with regard to jurisdictional claims in published maps and institutional affiliations.

Open Access This article is licensed under a Creative Commons Attribution 4.0 International License, which permits use, sharing, adaptation, distribution and reproduction in any medium or format, as long as you give appropriate credit to the original author(s) and the source, provide a link to the Creative Commons license, and indicate if changes were made. The images or other third party material in this article are included in the article's Creative Commons license, unless indicated otherwise in a credit line to the material. If material is not included in the article's Creative Commons license and your intended use is not permitted by statutory regulation or exceeds the permitted use, you will need to obtain permission directly from the copyright holder. To view a copy of this license, visit http://creativecommons.org/licenses/by/4.0/.

© The Author(s) 2023

BAMS Article

Super Drought under Global Warming

Concept, Monitoring Index, and Validation

Lin Wang, Gang Huang, Wen Chen, and Ting Wang

ABSTRACT: Recent decades have witnessed growing frequency and severity of catastrophic droughts in many regions of the world. Despite lots of studies having been dedicated to extreme drought investigation, the fundamental question that has long been ignored is, What is extreme drought? The answer is much more complex than it first appears, because a critical issue in the study of drought is the multiscalar nature. To address the challenge, this study establishes the theoretical basis of the super drought concept, which refers to the simultaneous occurrence of extreme droughts at multiple time scales. The physical significance of super drought represents compound dry extremes in all parts of water resources or equivalently a grand loss in total water storage, which is identified as the essential determinant distinguishing high-impact droughts from those causing mild damage. To have a quantitative representation, a novel monitoring index called comprehensive multiscalar index (CMI) is developed based on the vine copula framework. It turns out that CMI is a plausible measure to determine the overall rarity of multiscalar drought and recognize super drought. Furthermore, the worldwide skill of CMI and super drought identification are testified against Gravity Recovery and Climate Experiment (GRACE) total water storage. Compared to traditional indices that lack comprehensive treatment of drought, CMI performs better in capturing the variation of overall water availability and enables the accurate detection of real water scarcity, with gross improvements in correlation and root-mean-square error scores exceeding the 10^{-3} significance level. To facilitate end users and policy-makers, near-real-time monitoring and a historical data repository are available through the public website superdrought.com.

KEYWORDS: Drought; Extreme events; Water resources; Indices; Climate; Hydrology

https://doi.org/10.1175/BAMS-D-22-0182.1
Corresponding authors: Lin Wang, linwang@mail.iap.ac.cn and wang_lin@mail.iap.ac.cn; Gang Huang, hg@mail.iap.ac.cn
Supplemental material: https://doi.org/10.1175/BAMS-D-22-0182.2

In final form 26 February 2023
©2023 American Meteorological Society
For information regarding reuse of this content and general copyright information, consult the AMS Copyright Policy.

Unauthenticated | Downloaded 05/11/23 02:29 PM UTC

AFFILIATIONS: L. Wang—CAS Key Laboratory of Regional Climate-Environment for Temperate East Asia, Institute of Atmospheric Physics, Chinese Academy of Sciences, Beijing, China; **Huang**—State Key Laboratory of Numerical Modeling for Atmospheric Sciences and Geophysical Fluid Dynamics, Institute of Atmospheric Physics, Chinese Academy of Sciences, Beijing, China; **Chen**—Department of Atmospheric Science, Yunnan University, Kunming, China; **T. Wang**—Carbon Neutrality Research Center, Institute of Atmospheric Physics, Chinese Academy of Sciences, Beijing, China

Drought is one of the most damaging hazards worldwide, due to its prolonged and extensive impacts on agriculture, ecosystems, economy, and human society (Dai 2011; Ault 2020; AghaKouchak et al. 2021; Van Loon et al. 2016). In total, it is recorded that 1.4 billion people were affected by droughts in the period 2000–19 (UNDRR 2020). Under global warming, though the long-term trends in drought frequency and severity on a global scale remain an element of debate (Dai 2013; Sheffield et al. 2012; Huang et al. 2016; Berg and McColl 2021; Trenberth et al. 2014), drought conditions have unprecedentedly worsened in many regions of the world (Fu and Feng 2014; Sherwood and Fu 2014; He et al. 2020; Huang et al. 2017; Guan et al. 2019). The hotspots frequently struck by extreme drought events are southwestern North America (Williams et al. 2022), Southwest and southern China (Wang et al. 2015; Zhang et al. 2020; Wang et al. 2021), the transitional climate zone in East Asia (L. Wang et al. 2022), Europe (Naumann et al. 2021), the Amazonia (Lewis et al. 2011), Africa (Pascale et al. 2020), and Australia (Peterson et al. 2021). Future projection highlights significant drying tendency in most of the Americas, the Mediterranean region, southern Africa, and Australia (Zhao and Dai 2017, 2022; Qi et al. 2022; Spinoni et al. 2020). Recently, the United Nations warned that we are standing at a crossroads, as land is drying up, fertile grounds are turning to dust, and drought is prevailing (UNCCD 2022).

Facing the growing frequency of extreme drought events globally, much effort has been expended on the exploration and explanation of this area (J. Wang et al. 2022). However, the fundamental question that has long been ignored is, What is the extreme status of drought? It seems simple, as the event is typically defined as extreme if the observed value is above or below a certain percentile (Klein Tank et al. 2009). It has been noted that other synonyms, similar in meaning to "extreme," may be used interchangeably, such as "severe," and "exceptional." Generally, the traditional drought index possesses percentile-based extreme-value categorization that is applied to a one-dimensional time series. Taking the standardized precipitation index (SPI)/standardized precipitation evaporation index (SPEI) for example, the severe and extreme drought are initially defined as the time-scale-specific sequences less than –1.5 and –2, respectively corresponding to the 6.7th and 2.3rd percentiles. By doing so, most previous studies naturally imported the way to extract extreme events. Hence, this key issue receives little attention and has not been critically examined, as the task seems particularly simple and effortless. Unfortunately, the definition of extreme drought is much more complex than it first appears, because a critical issue in the study of drought, unlike heatwaves or heavy precipitation, is its multiscalar nature. Specifically, the multiscalar nature of drought refers to that the response of usable water resources, including soil moisture, groundwater, snowpack, river discharges, and reservoir storages to water shortage varies markedly and with different time scales (Beguería et al. 2010;

Unauthenticated | Downloaded 05/11/23 02:29 PM UTC

Hayes et al. 2011). It implies that the categorization of extreme drought would only make sense in reference to a particular time scale. As such, it is common to find extreme drought conditions recorded in one system (e.g., low river flows), whereas other systems in the same region (e.g., crops) have normal or even humid conditions (Vicente-Serrano et al. 2011, 2012). This makes it hard to define extreme drought event, since different water resources component can be heterogeneous within a region. To account multiscalar nature, Wang et al. (2016) prompted integrated treatment of drought and sparked the early form of super drought concept, whose task is to judge whether SPEI at multiple time scales are all below −1.5. However, such a concept and related indicator are indeed qualitative and far less effective in assessing the magnitude and patterns, and only have been achieved at specific regional scale. Motivated by this gap, the objective of the present research is establishing the theoretical basis of super drought and developing a quantitative index, as well as replicating the success on a global scale. In the next paragraph, we review a variety of quantitative ways devoted to combining multiple drought indices (Hao and Singh 2015) although not targeted toward super drought detection.

Linear combination is a natural choice to combine different drought variables or indices to integrate drought information, e.g., Mo and Lettenmaier (2014), Hao et al. (2016), Xia et al. (2014), Zhang et al. (2017), Keyantash and Dracup (2004), Rajsekhar et al. (2015), and Waseem et al. (2015). Although linear combination is generally easy to implement, it fails to characterize the covariability of drought-related variables, which may interact in a complex manner (Hao and Singh 2015). Copula is an effective way to solve the complicated and nonlinear relationship among multiple variables (Hofert et al. 2018). The first attempt of application of copula in constructing probability-based overall water deficit index was made by Kao and Govindaraju (2010). They developed the joint deficit index via empirical copula to join accumulated precipitation or streamflow with temporal scales varying from 1 to 12 months, in order to capture both short- and medium-term droughts. The similar copula framework is utilized by Hao and AghaKouchak (2013), Ma et al. (2014, 2015), Yang et al. (2018), Shah and Mishra (2020), and others.

Based on the above review, the copula technique is increasingly popular in modeling a joint drought index. While copula-based joint index modeling made substantial progress in the past decade, creating a comprehensive copula-based framework dealing with super drought detection is still far from complete. First, copula is a general tool, so it is paramount to identify how best to tailor it to super drought quantification. Second, in order to be well suited for the high-dimensional feature space of drought, we implement the advanced vine copula theory instead of classic copula to evade the curse of dimensionality. Third, the properties and true validation of the established joint index have not been well documented. This study will give a comprehensive perspective to achieve the goals for understanding the superiority of the novel index and the super drought concept. Last, unlike most of previous works conducted at regional scales, this study provides global-scale modeling and verification so as to guarantee a universally applicable concept and index.

In this study, we build a theoretical basis for super drought and propose a novel framework based on vine copula and the associated monitoring index. This paper is structured as follows. The second section introduces the data sources. The third section describes the background and motivation to develop the concept of super drought. The fourth section is the core part of this study, which details the procedure and specific settings to build the monitoring index called the comprehensive multiscalar index (CMI). The properties of CMI and associated super drought are interpreted in the fifth section. The sixth section is conducted to validate the performance of CMI and super drought recognition. Finally, the discussion and conclusions are made in the seventh and eighth sections, respectively.

Unauthenticated | Downloaded 05/11/23 02:29 PM UTC

Data

CRU precipitation and potential evapotranspiration. Monthly precipitation and potential evaporation (PET; units: mm) are obtained from the latest version TS4.05 of Climatic Research Unit (CRU; Harris et al. 2020). PET data are estimated by the Penman–Monteith parameterization scheme (Allen et al. 1994). CRU TS4.05 data are month-by-month variations over the period 1901–2020, provided on a 0.5° × 0.5° horizontal grid extending over the global land. In the "Validation of CMI" section, the worldwide skill of CMI will be testified against GRACE data, which is the only option to use at a global scale. Therefore, to match the true resolution of GRACE, the high-resolution CRU data are transformed to 3° resolution through conservative regridding. It should be mentioned that upscaling to the coarse pixel scale is undertaken for validation purposes, but not intended for drought characteristics evaluation. Once the novel algorithm and index are established and justified, the original 0.5° data source is placed back to produce a high-resolution map and restore fine-scale features.

Given the relatively poor quality and low spatial density of in situ measurements in the earlier part of the twentieth century, a period of 60 years from 1961 onward is used. In addition, extra treatment is performed in regard to this drought study, as explained below. To account for the intrinsic multiscalar nature of drought, raw values are accumulated to multiple time scales up to 48 months. However, this aggregation procedure will result in data gaps at the beginning of the accumulated time series. For example, at the longest 48-month time scale, the first 47 months of the accumulated time series are not defined. To avoid the missing data problem, the CRU data are extended back from the start date January 1961 to the previous 47 months. After implementing accumulation, the months before January 1961 are discarded, so that the study period 1961–2020 is not altered with the advantage of no null values contained.

In addition, the global land-cover map V2.3 compiled by the European Space Agency are used to exclude desert areas.

SPEI. Prior to describe the concept of super drought and the newly developed index CMI, it is necessary to outline the broadly used SPEI (Vicente-Serrano et al. 2010). SPEI can be calculated on a range of time scales, over which water deficits accumulate is vital to separate different types of droughts. In this study, the SPEI were calculated with various lags including 3, 6, 12, 24, and 48 months recommended by McKee et al. (1993). SPEI values can be classified into four drought classes, namely, mild or near normal (0 to −0.99), moderate (−1.00 to −1.49), severe (−1.5 to −1.99), and extreme (−2 and below). The theoretical probabilities of SPEI less than −1.5 and −2 are 6.7% and 2.3%, respectively.

GRACE total terrestrial water storage. The total terrestrial water storage (TWS), expressed in terms of equivalent water thickness (unit: cm), is obtained from Gravity Recovery and Climate Experiment (GRACE) satellite observations (Tapley et al. 2019). GRACE detects the spatiotemporal variation of the global gravity field. After removing atmospheric masses, GRACE gravity changes correspond mainly to the variations in TWS, which is the sum of all above and below surface water storages, including canopy water, rivers and lakes, soil moisture, and groundwater.

In this study, we retrieve the latest GRACE mascon product release 06 (RL06) compiled by the Center for Space Research (Save et al. 2016). The product has undergone all the appropriate corrections, including C20 (degree-2, order 0) and C30 (degree-3, order 0) replacements, degree-1 correction and GIA (glacial isostatic adjustment) correction. For further details on the calibration strategy, see section S1 of the online supporting information (https://doi.org/10.1175/BAMS-D-22-0182.2). For the temporal dimension, the dataset spans from January 2002 to the present at monthly intervals. For the spatial dimension, the dataset is provided

Unauthenticated | Downloaded 05/11/23 02:29 PM UTC

with a spatial sampling of 0.5°. However, the native resolution of the GRACE mascon solution is actually 330 km, or equivalently a 3° spherical cap (Landerer and Cooley 2021). As such, the initial 0.5° × 0.5° spatial resolution is upscaled to 3° × 3° with the area conservative remapping method.

Motivation and concept of super drought

Problem overview and motivation. In the introduction section, we have explained in theoretical consideration why it is challenging to arrive at a definition of extreme drought. This section carries out real-world evaluation to assess the degree to which the multiscalar nature obscures the extreme drought definition.

We use the time series at the grid point (49.5°N, 13.5°E) to illustrate the common problem of defining extreme drought, as shown in Fig. 1. The grid point is arbitrarily selected as an example to highlight the discordance of drought conditions among different time scales. In fact, such a trait appears to be a common consequence of multiscalar drought, irrespective of geographic location and local climate characteristics, as evidenced by the global examination in Fig. 2. More cases to display the effect of time scales are shown in section S2 of the supporting information, including not only drought index but also direct measurements of drought on different water resource components.

It has become clear and visible how the dry and wet states act differently, and sometimes opposite, across different time scale. Further, we select three representative time nodes representing November 1982, August 2018, and October 2020, as marked in Fig. 1. The corresponding SPEI values at the five time scales are [–2, –1.4, –1.3, 0.073, 1.2], [–1.8, –2.1, –1.7, –1.6, –1.9], and [1.2, 0.62, –0.34, –1.3, –2.1] for the three cases.

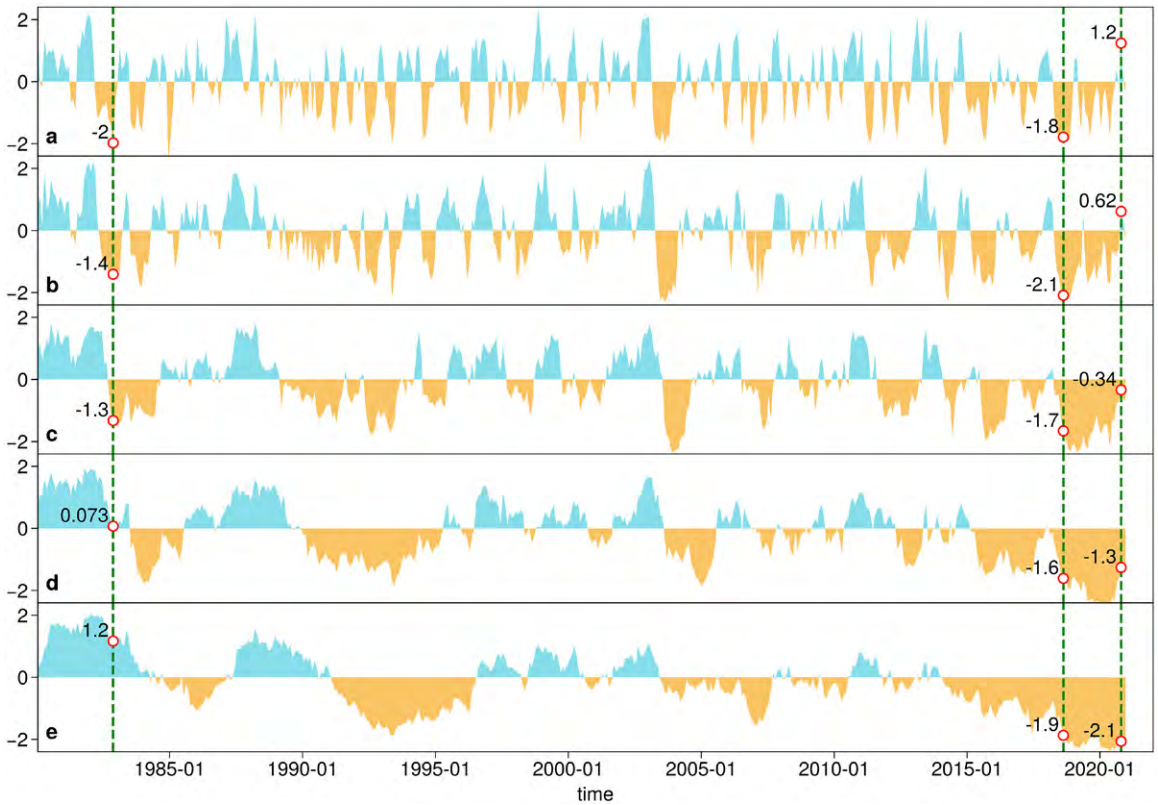

Fig. 1. Example of temporal evolution of SPEI at the grid point (49.5°N, 13.5°E) for time scales of (a) 3, (b) 6, (c) 12, (d) 24, and (e) 48 months from January 1980 to December 2020. The values in November 1982, August 2018, and October 2020 are marked with dashed lines. Note that the SPEI time series are calculated over the period of 1961–2020, but only the period since 1980 is reported here as an example.

Unauthenticated | Downloaded 05/11/23 02:29 PM UTC

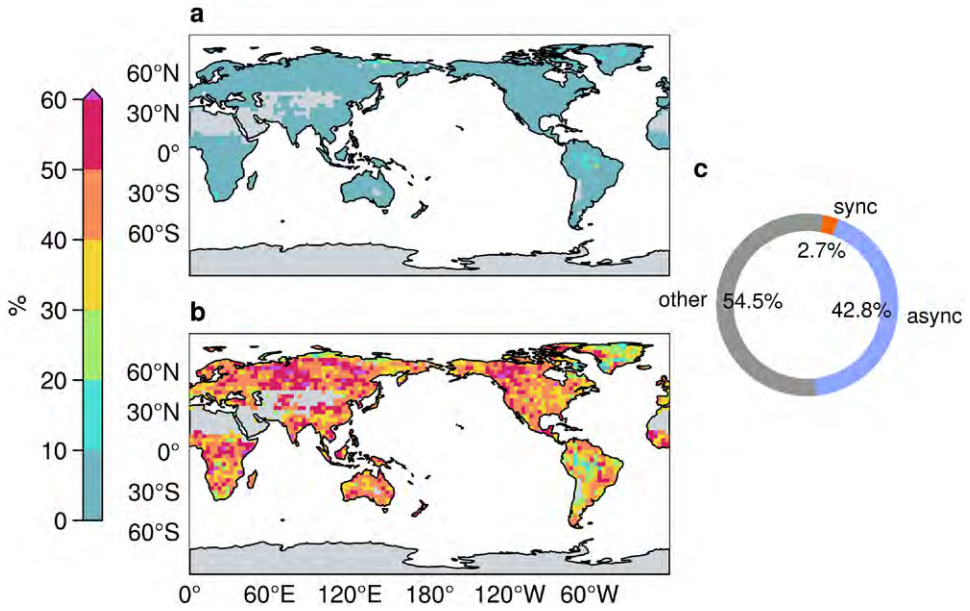

Fig. 2. Spatial patterns of the percent of (a) synchronous and (b) asynchronous occurrences of severe drought at multiple time scales, and (c) the corresponding donut chart summarizing the spatial data. Refer to the main text for the definition of synchronous and asynchronous as well as other groups.

For November 1982, the SPEI at 3-month time scale falls in the extreme drought category. However, it can only be concluded that the 3-month SPEI is affected by extreme drought, because the 24- and 48-month SPEI values are 0.073 and 1.2, respectively, indicative of a humid condition. October 2020 revealed a similar but reversed pattern of SPEI. Both cases illustrate that the dry and wet periods for different drought of hydrological components are not synchronous, and sometimes even opposite. On rare occasions, there exists the simultaneous occurrence of extreme droughts at multiple time scales. For example, August 2018 is the episode of concurrent severe dryness, as indicated by all SPEI values below −1.5.

We then calculate the percentage of synchronous and asynchronous occurrences over the globe. Denote by $\mathbf{W} = \{\mathbf{p}(p_1, p_2, p_3, p_4, p_5) | \exists p_j < -1.5\}$, the whole set that has at least one time-scale SPEI in the severe category, $\mathbf{S} = \{\mathbf{p}(p_1, p_2, p_3, p_4, p_5) | \mathbf{p} \in \mathbf{W}, \forall p_j < -1.5\}$, the subset of $\mathbf{W}$ that has all time-scale SPEI under the severe category, $\mathbf{A} = \{\mathbf{p}(p_1, p_2, p_3, p_4, p_5) | \mathbf{p} \in \mathbf{W}, \exists p_j > 0\}$, the subset of $\mathbf{W}$ that has at least one time-scale SPEI under humid conditions. The rest, not belonging to any of the above categories, will be allocated to the subset called "other," $\mathbf{O} = \mathbf{W} \backslash (\mathbf{A} \cup \mathbf{S})$, but it is clearly not our concern. Then, the percentages of occurrence assigned to subset $\mathbf{S}$ (synchronous) and $\mathbf{A}$ (asynchronous) are calculated in each grid cell and then summarized globally, as shown in Fig. 2.

Figure 2a shows that the percentage of synchronous droughts is less than 10%. The definite fraction of such events among the total events is estimated, globally averaged, to be 2.7% (Fig. 2c). To better reflect the spatial differentiation, Fig. 2a is duplicated but with a different color scheme, as shown in Fig. S2 in the supporting information. The result indicates that a very low rate of multiscalar severely drought turned out to coincide. However, the opposite phenomena, asynchronous events, as shown in Fig. 2b, exhibit much higher frequency, with uneven regional distribution ranging from 30% to 60%. On average, asynchronous events occur 42.8% of the time (Fig. 2c), which is far more often than the synchronous counterpart.

This testing goes further to examine the conditional probability that severe drought at one time scale will occur, given the presence of another time scale's event. As an example, we

Unauthenticated | Downloaded 05/11/23 02:29 PM UTC

take the 3- and 24-month time scales to represent meteorological and hydrological processes. With real-world assessment, the probability of severe meteorological drought is found to be 22% when hydrological drought has already occurred. Yet, in spite of increased likelihood relative to the theoretical one (6.7%), there is an equal chance (22%) that meteorological wet conditions occur. In this regard, a hydrological severely dry state cannot guarantee meteorological severely dry state, and vice versa. Therefore, conditional probability is also not adequate to express the likelihood with which multiple events co-occur.

In sum, the extreme drought and wet condition are much likely to coexist, rendering the distinction between extreme and nonextreme event difficult. As such, it is critical to establish a concept and criterion in what can be ranked as an extreme drought event.

Concept of super drought. We have known the fact that the phases and frequencies of dry–wet oscillations at different time scales all differ; at times they are opposite and at other times they coincide. It is conceivable that a devastating event appears when extreme phases of short- and long-term droughts coincide. Therefore, the concept of super drought referred to the simultaneous occurrence of extreme droughts at multiple time scales. In a physical sense, super drought can be regarded as compound water deficits in all parts of usable water resources, which is expected to reinforce the damage that would result from a single-time-scale event. The situation is clearly the case in August 2018 (Fig. 1). Conversely, if the extreme droughts at different time scales occur in isolation, the destructive effect of the droughts may not be as serious. For instance, the drought impact during October 2020 and November 1982 tended to be gentle, despite severe drought status at part of the time scales.

A schematic diagram Fig. 3 was constructed to better illustrate the super drought concept. The drought condition for the month of interest (labeled as n) depends not only on the event on the current month but also the preceding months ($n - 1$, $n - 2$, ...) up to a certain time scale. Time scale refers to the number of months extending through the end of the current month. Since droughts of different time scales have diverse impacts including meteorological,

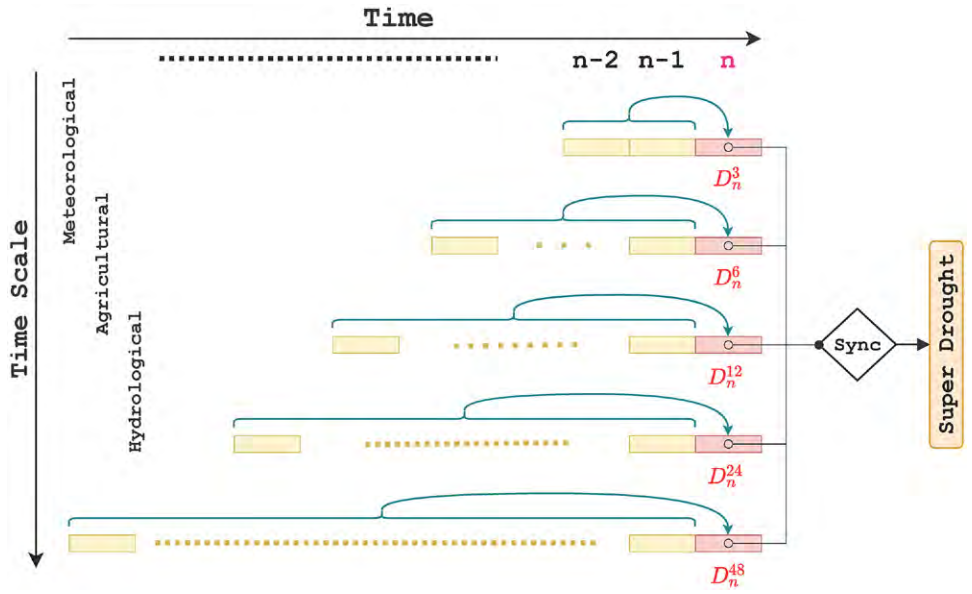

Fig. 3. Schematic diagram of the super drought concept. The rightward arrow on the top denotes the evolving time, while the time scale from short term to long term is represented by the downward arrow on the left. The month of interest is colored in a red block and the preceding months up to a certain time scale are colored in yellow blocks and dots. The number of dots signals the number of month blocks omitted. Six illustrative time scales involve 3, 6, 12, 24, and 48 months, with D_n^3, D_n^6, D_n^{12}, D_n^{24}, and D_n^{48} denoting the cumulative water balance at the corresponding time scale.

Unauthenticated | Downloaded 05/11/23 02:29 PM UTC

agricultural, and hydrological forms, the cumulative water deficit or surplus can be calculated across various months. The notation D_n^k is employed to denote the accumulated value starting from the current month n and adding the preceding $k-1$ months, where k corresponds to the desired time scale of the aggregation. For instance, the 6-month D_n^6 is constructed by the sum of the water status from 5 previous months to the current month. In this study, 3-, 6-, 12-, 24-, and 48-month windows are used to reflect short-term, medium-term, and long-term conditions. Here, it is important to note that the time scale does not measure drought length; rather, it serves as an aggregation scheme to quantify dry/wet state at one point in time. Specifically, D_n^k captures the influence of the climatic water balance conditions of the preceding $k-1$ months on the current month (n). As shown in Fig. 3, for the specific month n, it is possible to experience dry condition on one or more time scales and wet conditions at other time scales. This clearly poses a difficult situation to convey extreme drought events. Consequently, the super drought concept is designed to express the synchronous occurrence of extreme drought across multiple time scales.

At the same time, it is necessary to explain why we have chosen to use the terminology "super drought." In most previous studies, the terms "extreme drought," "exceptional drought," "massive drought," and "megadrought" are usually used. In comparison, the term "super drought" has no specific definition in scholarly literature, despite being used frequently in social media as a general description. In this study, we definitely coin the term "super drought" as simultaneous occurrence of extreme droughts at multiple time scales. The term "super drought" could be the ideal choice in the context. On the one hand, the word "super" means "beyond," "greater," or "on top of" (as in "superior"), referring to a higher level of destruction than each individual component. On the other hand, the word "super" also provides a sense of "superimposed," referring to the synthetic effect of each individual component.

As a summary, the physical significance of the super drought concept represents the combination of multiple stresses on water resources, or in other words the grand deficit in total usable water resources.

CMI and super drought detection based on vine copula

With the concept of super drought, how does one work out a quantitative index for determining the overall extremity? In this section, we employ vine copula theory to develop a novel index called CMI in ways that are tailored to super drought detection. Meanwhile, it is necessary to spare a little space to explain the background for adopting "comprehensive multiscalar index" as the novel index name. Our previous study (Wang et al. 2016) sparked the early form of super drought concept and proposed a qualitative indicator called comprehensive multiscalar indicator. In that work, the term "indicator" expresses a qualitative judgment, which is claimed to be either true or false. One objective of the current study is to develop a quantitative index for super drought characterization, which greatly improves and extends the previous approach. In this sense, "comprehensive multiscalar index" becomes the natural choice and thus can be regarded as the quantitative version of "comprehensive multiscalar indicator," which helps to maintain coherence and standardization of terms that are being used across a series of studies.

Copula and vine copula theory to measure the overall water deficit from multiscalar drought. First, we introduce the copula and vine copula theory, with emphasis on integrating multiscalar aspects of drought. The copula model was first introduced by Sklar (1959), and a more recent copula theory can be found in Nelsen (2007). In short, a copula is a multivariate cumulative distribution function where the marginal probability distribution of each variable is uniform. Assuming dry–wet status at two distinct time scales as random

Unauthenticated | Downloaded 05/11/23 02:29 PM UTC

variables X and Y, respectively, the two-dimensional joint cumulative distribution can be expressed as

$$\mathbb{P}\left(X \le x, Y \le y\right) = C\left[F\left(x\right), G\left(y\right)\right], \tag{1}$$

where C is the copula, and $F(x)$ and $G(y)$ are the marginal cumulative distributions that are uniform. The comma inside the parentheses stands for two conditions being simultaneously true. The principle can be readily extended to more than two variables, that is,

$$\mathbb{P}\left(X_1, X_2, ..., X_d\right) = C\left[F_1\left(X_1\right), F_2\left(X_2\right), ..., F_d\left(X_d\right)\right].$$

An example given in Eq. (1) based on the normal copula with linear correlation of 0.5 is displayed in Fig. 4. In this graph, the marginals describe the respective characteristics, while the copula contours evaluate the joint behavior. We define the percentile range from 0 to 1 spanning the range from wet to dry conditions. The three points representing the three combinations of X and Y with different marginal percentiles are marked in Fig. 4, namely, P1(0.9, 0.3), P2(0.3, 0.9), and P3(0.9, 0.9). Considering dry extreme is defined as the upper 90th percentile of the distribution. P1 corresponds to the condition in which X shows extreme drought, while Y does not, and P2 refers to the opposite case. However, they possess the same composite effect with the copula value being 0.29, suggesting overall normal to wet conditions. In contrast, P3 features that both X and Y are under extreme drought, resulting in compound dry stresses with joint risk abruptly soaring to 0.83. It indicates that if both X and Y exceed a threshold (P3), it will lead to a more severe drought than one agent working alone (P1 or P2). In addition, section S4.1 of the supporting information is presented to explain why nonexceedance copula $\mathbb{P}\left(X \le x, Y \le y\right)$ should be used instead of exceedance copula $\mathbb{P}\left(X > x, Y > y\right)$.

In conclusion, copula is capable of computing a probability-based overall water deficit. In addition, it is worth noting here that the Kendall rather the copula value is eventually used to measure the joint probability, but it does not change the basic principle. To keep the integrity of this study, the definition and significance of Kendall measure will be presented in the "Specific settings tailored to super drought monitoring" section.

With the above knowledge, it seems natural to extend the bivariate copula to high dimension for overall multiscalar drought characterization, which is a multidimensional rather than two-dimensional problem. But unfortunately, the direct extension of copula to high orders suffers from the "curse of dimensionality" (Kao and Govindaraju 2008). Even worse, although the catalogue of bivariate parametric copula families is large, this is not the case for dimensions larger than 2. To address the issues, vine copula, introduced by Joe (1996), is developed to

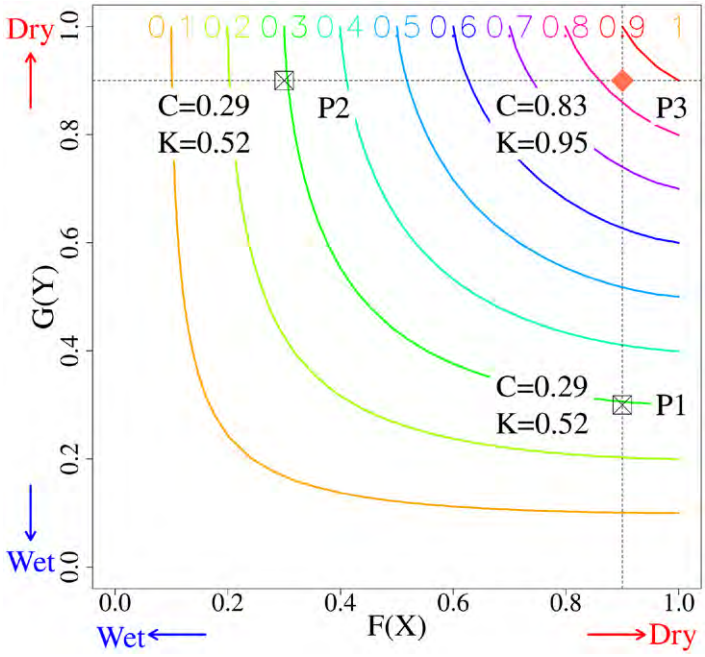

Fig. 4. The bivariate normal copula with linear correlation $\rho = 0.5$. The overlaid points at P1(0.9, 0.3), P2(0.3, 0.9), and P3(0.9, 0.9) show the copula value (*C*) and Kendall measure value (*K*).

Unauthenticated | Downloaded 05/11/23 02:29 PM UTC

decompose high-dimensional copula into a cascade of bivariate copulas. The mathematical form of the decomposition can be written as (Aas et al. 2009)

$$\begin{aligned} f\left(x_1,\ldots,x_d\right) &= f\left(x_d\right)\cdot f\left(x_{d-1}\middle|x_d\right)\cdot f\left(x_{d-2}\middle|x_{d-1},x_d\right)\ldots\cdot f\left(x_1\middle|x_2,\ldots x_d\right) \\ f\left(x\middle|\boldsymbol{\upsilon}\right) &= c_{x\upsilon_j|\boldsymbol{\upsilon}_{-j}}\left\{F\left(x\middle|\boldsymbol{\upsilon}_{-j}\right),F\left(\upsilon_j\middle|\boldsymbol{\upsilon}_{-j}\right)\right\}\cdot f\left(x\middle|\boldsymbol{\upsilon}_{-j}\right), \end{aligned} \tag{2}$$

where $c_{x\upsilon_j|\boldsymbol{\upsilon}_{-j}}$ is the copula density, υ_j is an arbitrary component of $\boldsymbol{\upsilon}$, and $\boldsymbol{\upsilon}_{-j}$ denotes the vector $\boldsymbol{\upsilon}$ excluding υ_j. Obviously, the same multivariate density can be expressed by a large number of different vine copulas with different tree structures and orderings of variables. The detailed theory is available in Kurowicka and Joe (2011) and Czado (2019). Thereby, vine copula provides an adaptable and manageable way to construct the joint distribution of multiscalar droughts. All candidate bivariate copula families to build vine are listed in Table 1.

Procedure to construct the novel CMI based on vine copula. In this part, we create a novel and systematic framework based on vine copula to probabilistically integrate multicomponent metrics of drought into an integrated metric CMI. There are three main stages to construct CMI and detect super drought.

Step 1: Data preparation and preprocess
Step 2: Vine copula construction and goodness-of-fit test
Step 3: CMI derivation and super drought detection

A sequential flowchart is elaborated in Fig. 5. Note that this process is carried out for each calendar month of each grid cell. The vine copula construction is implemented in the exemplary grid cell (49.5°N, 13.5°E) as a case study to give a clear perception of the methodology, which is documented in section S3 of the supporting information.

Step 1: Data preparation and preprocess. Based on precipitation and PET, water balance accumulated at various time scales is formulated as

$$D_n^k = \sum_{i=0}^{k-1}\left(\mathrm{PET}_{n-i} - P_{n-i}\right), \quad n \geq k, \tag{3}$$

Table 1. Candidate bivariate copula families.

Type	Name (abbreviation)	Rotations (°)	No. of parameters
—	Independence (I)	—	0
Elliptical	Normal/Gaussian (N)	—	1
	Student *t* (t)	—	2
Archimedean	Clayton (C)	90, 180,[a] 270	1
	Gumbel (G)	90, 180, 270	1
	Frank (F)	—	1
	Joe (J)	90, 180, 270	1
	Clayton–Gumbel (BB1)	90, 180, 270	2
	Joe–Gumbel (BB6)	90, 180, 270	2
	Joe–Clayton (BB7)	90, 180, 270	2
	Joe–Frank (BB8)	90, 180, 270	2

[a]A copula rotated by 180° is often called a survival copula.

Unauthenticated | Downloaded 05/11/23 02:29 PM UTC

where k is the time scale and n is the month. Note that the water balance defined here is the opposite of the traditional definition, which will be explained in the "Specific settings tailored to super drought monitoring" section. In this study, five time scales (k = 3, 6, 12, 24, 48) recommended by McKee et al. (1993) are used. The reason will be explained in the "Specific settings tailored to super drought monitoring" section.

Combing with the fact that copula is defined as distribution function whose marginal distributions are uniform in the interval [0, 1], the conversion of marginal uniformity is achieved by using the empirical probability integral transform (PIT):

$$\begin{aligned} &\mathbf{x}_j = \left(x_{1j}, x_{2j}, \ldots, x_{nj}\right)^{\mathrm{T}} \rightarrow \mathbf{u}_j = \left(u_{1j}, u_{2j}, \ldots, u_{nj}\right)^{\mathrm{T}}, \quad j \in \{1, \ldots, d\} \\ &u_{ij} = r_{ij} \big/ \left(n+1\right), \quad i \in \{1, \ldots, n\}, \forall_j \end{aligned} \tag{4}$$

where r_{ij} denotes the rank of x_{ij} among all x_{kj}, $k \in \{1, \ldots, n\}$. In the copula literature, values obtained by the PIT are called pseudo-observations.

Step 2: Vine copula construction and goodness-of-fit test. At the core of the methodology lies modeling of vine copula, which consist of a tree-based hierarchy of conditional bivariate copulas. This study implements the flexible tree structure known as regular vine (R-Vine), which is a powerful graphical tool to characterize complex dependence among multiple variables (Bedford and Cooke 2002). Formally, fitting an R-Vine copula specification to pseudo-observations requires the following three tasks: (i) selection of the R-Vine structure, that is, choosing and connecting the most dependent pairs in the tree; (ii) choice of a bivariate copula family for each pair and estimation of the corresponding parameters; and (iii) a goodness-of-fit test.

We first proceed to select the appropriate R-Vine structure, which requires correlation between studied signatures. Rank correlation coefficients defined by the empirical Kendall's τ between all pairwise variables are

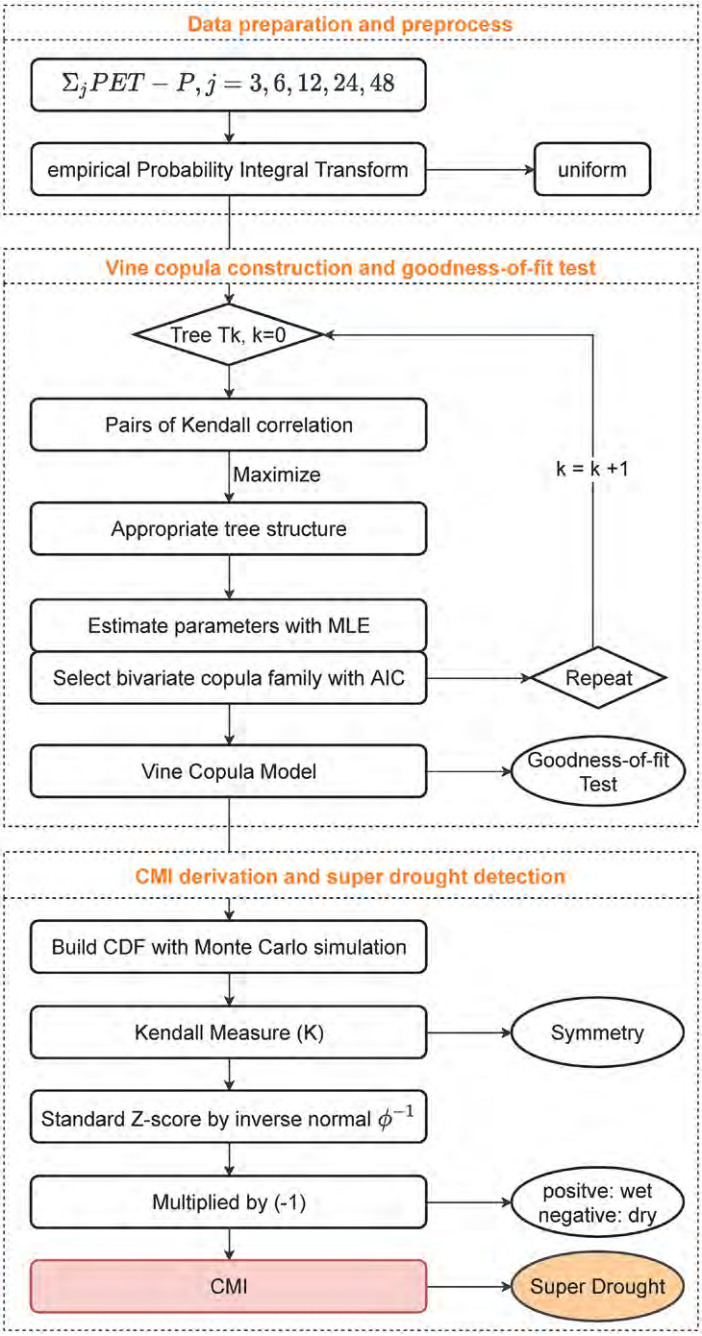

Fig. 5. Flowchart of CMI construction and super drought detection based on vine copula.

Unauthenticated | Downloaded 05/11/23 02:29 PM UTC

computed, so as to recognize the spanning tree that maximizes the sum of absolute empirical Kendall's τ. The Kendall's τ coefficient of X and Y is written as

$$\tau_{XY} \in [-1,1] = \mathbb{P}\left[\left(X_1 - X_2\right)\left(Y_1 - Y_2\right) > 0\right] - \mathbb{P}\left[\left(X_1 - X_2\right)\left(Y_1 - Y_2\right) < 0\right], \tag{5}$$

where (X_1, Y_1) and (X_2, Y_2) are two independent and identically distributed copies of (X, Y).

Having selected the appropriate order of the variables, in what follows, identifying the bivariate copula type and the corresponding parameters that best fit the observations is the most crucial part. To this end, all candidate copula models listed in Table 1 are fitted to the same data with parameters determined based on maximum likelihood estimation (MLE), and then the Akaike information criterion (AIC) is computed for each model. In symbols, the parameter estimation and AIC (Akaike 1998) are defined as

$$\begin{aligned} \hat{\boldsymbol{\theta}} &= \arg\max_{\boldsymbol{\theta}} \sum_{i=1}^{n} \ln\left[c\left(u_{i1}, u_{i2} \middle| \boldsymbol{\theta}\right)\right] \\ \mathrm{AIC} &= -2\sum_{i=1}^{n} \ln\left[c\left(u_{i1}, u_{i2}\right) \middle| \hat{\boldsymbol{\theta}}\right] + 2k, \end{aligned} \tag{6}$$

where $\{(u_{i1}, u_{i2}), i = 1, \ldots, n\}$ are pseudo-observations, c is the copula density, and k is the number of parameters in the model. The lower the AIC values, the better the model. As such, we select the best-fit copula family, which has the lowest AIC value.

The ultimate result of the case study is shown in Fig. 6, portraying the tree sequence together with copula family and parameters. Under the above procedure, vine copula is trained to observations independently for each grid cell and each calendar month.

After fitting the vine copula to samples, it is imperative to test the effectiveness of the proposed model. The goodness-of-fit (GOF) test is intended to test the validity of the null hypothesis $H_0 : C \in \mathcal{C}_0 = \{C_{\boldsymbol{\theta}} : \boldsymbol{\theta} \in \Theta\}$ against $H_1 : C \notin \mathcal{C}_0$, where C denotes the vine copula distribution function and $\mathcal{C}_0$ is class of parametric vine copula with Θ being the parameter space. There are different GOF tests proposed, as reviewed in Schepsmeier (2015). Here we use Rosenblatt's transform test, which projects the multivariate problem to a univariate problem and then applies a univariate test. The algorithm is provided in the section S4.2 of the supporting information.

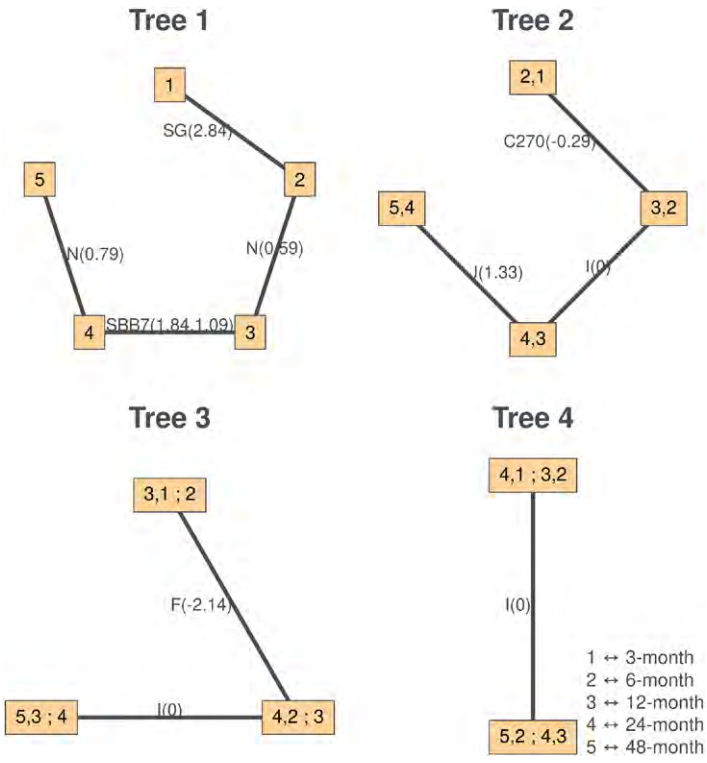

Fig. 6. Tree sequence for the estimated vine structure for the case study. Each edge in the vine graph is associate with the best-fit copula family and fitted parameters in brackets, where SG is survival Gumbel, N is normal, SBB7 is survival Joe–Clayton, C270 is rotated Clayton (270°), J is Joe, F is Frank, and I is independence. Labels 1, 2, 3, 4, and 5 represent the 3-, 6-, 12-, 24-, and 48-month time scales, respectively.

The result of GOF test is shown in Fig. 7, which depict the p value of the test. Choosing a threshold of 0.1, a large p value and hence failure to reject the null hypothesis is a good result. The spatial

Unauthenticated | Downloaded 05/11/23 02:29 PM UTC

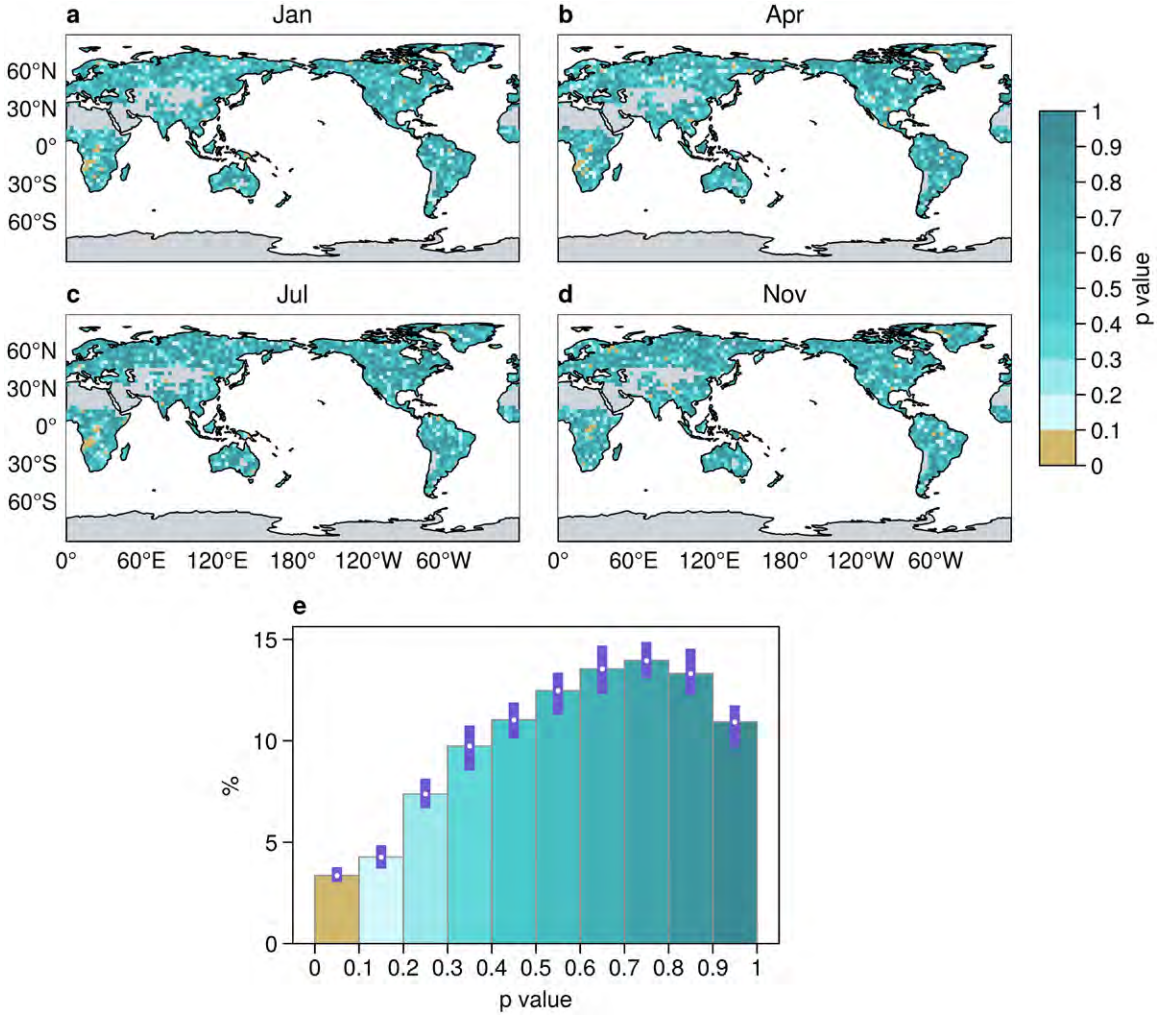

Fig. 7. The *p* values for the goodness-of-fit test for vine copula based on the Rosenblatt's transform, described in (a)–(d) the spatial patterns for January, April, July, and November, respectively, and (e) a histogram over all grid points and calendar months. The error bars in (e) represent the 5%–95% confidence interval across all calendar months.

patterns (Figs. 7a–d) demonstrate considerable confidence in the potential of vine copula for robust fitting over almost all corners of the global land, irrespective of climatic zone and the calendar month. Only for very few areas does the fitted vine copula model fail to match the observations. Further, a histogram is drawn to show the frequency distribution of p values. As seen from Fig. 7e, the p values are well above 0.4, as the percentage oscillates between 73% and 78%. The rejection rates of null hypothesis only account for less than 4%. In addition, the short error bar length shows little dependence of the performance on the seasonality. In conclusion, the vine copula is highly appropriate for modeling the joint distribution of multiscalar drought.

Step 3: CMI derivation and super drought detection. Although the vine copula model is built, it is copula density function (c) rather than copula distribution function (C) that has been established. However, there is no easy way to derive the analytic expression of C, which involves a $(d-2)$-dimensional integral. To get rid of the difficulty, a Monte Carlo simulation is carried out to numerically construct C given by its density c. In application, 50,000 Monte Carlo samples are used to guarantee the estimator of the target C is precise enough.

With the distribution function C, it seems likely that the final standardized score can be readily obtained by taking the inverse normal distribution function, as used in SPEI. Unlike univariate cases, however, it is necessary to make a transformation from copula

Unauthenticated | Downloaded 05/11/23 02:29 PM UTC

measure to Kendall measure via Kendall function (Nelsen et al. 2003). The reason will be further detailed in the "Specific settings tailored to super drought monitoring" section. Kendall function is designed to describe the distribution functions of copula values in the whole measure space:

$$K(q) = \mathbb{P}\left[C_{U_1,\ldots,U_d}(U_1,\ldots,U_d) \le q\right], \quad q \in (0,1). \tag{7}$$

In the final step, the standardized score can be computed based on the Kendall measure by taking the inverse normal Φ^{-1}. In addition, reminding the input logic to calculate CMI is PET minus precipitation, so we reverse the sign of the standardized score to conform to the traditional paradigm in the drought index community. The final CMI is defined as

$$\mathrm{CMI} = (-1)\cdot\Phi^{-1}(K). \tag{8}$$

Such a standardization algorithm makes the CMI follow a standardized normal distribution. Compared to SPEI, the proposed CMI incorporates the overall drought conditions reflected from multiscalar components. The negative CMI indicates joint dry status, while positive CMI represents an overall wet condition. A CMI near zero refers to overall normal condition. Based on CMI, we can set −1.5, −2, or other values as the threshold for identifying super drought events.

Specific settings tailored to super drought monitoring. Although the vine copula model provides a universal structure to model the multidimensional distribution, we need to tailor it to the specific requirements of super drought configuration and CMI establishment with a focus on concordant extreme events. The four key settings for the goal include (i) input logic of water balance definition, (ii) optimal selection of time scales, (iii) vine layout, and (iv) Kendall measure. Here, we only report the major conclusion, while further details are provided in section S4.3 of the supporting information.

As regards the input logic [setting (i)], the choice between PET–P or P–PET does matter in copula-based modeling which involves nonlinearity. Although P–PET is always the traditional choice in defining water balance, it is identified that PET–P could better highlight overlapping drought, known as super drought, compared to nonoverlapping type. Therefore, we reverse the traditional order of the water balance definition to yield PET–P as the input logic to the copula model. Selection of appropriate time scales that the copula model joins [setting (ii)] is one of the important topics to consider. We confirm that including the time scales of 3, 6, 12, 24, and 48 months is adequate for allowing an accurate detection in a very reduced computation time. In our question of multiscalar drought, the D-vine structure characterized by one path that goes through all the nodes [setting (iii)] is especially appropriate to be selected for the temporal-scale ordering of variables. The D-vine layout for five-dimensional drought is graphically depicted in Fig. 8a. Moreover, Fig. 8b suggests that more than three-quarters of training instances belong to D-vine. In sum, we can predetermine D-vine trees, which can reduce time complexity as the order of the nodes has been fixed. As a key step prior to determining the final standardized score, the Kendall function [setting (iv)] is implemented to convert the copula measure to the Kendall measure. In brief, the Kendall function is designed to describe the distribution functions of copula values in the whole measure space, as the same copula values are assumed to have the same impact. Figures 9a and 9b give geometrical interpretations of the copula measure and the Kendall measure. It can be seen that the copula measure represents the rectangular region starting from the origin, while the Kendall measure is depicted as the region bounded by the isolines of constant copula values. On the one hand, the theoretical significance of the Kendall measure is because the critical

Unauthenticated | Downloaded 05/11/23 02:29 PM UTC

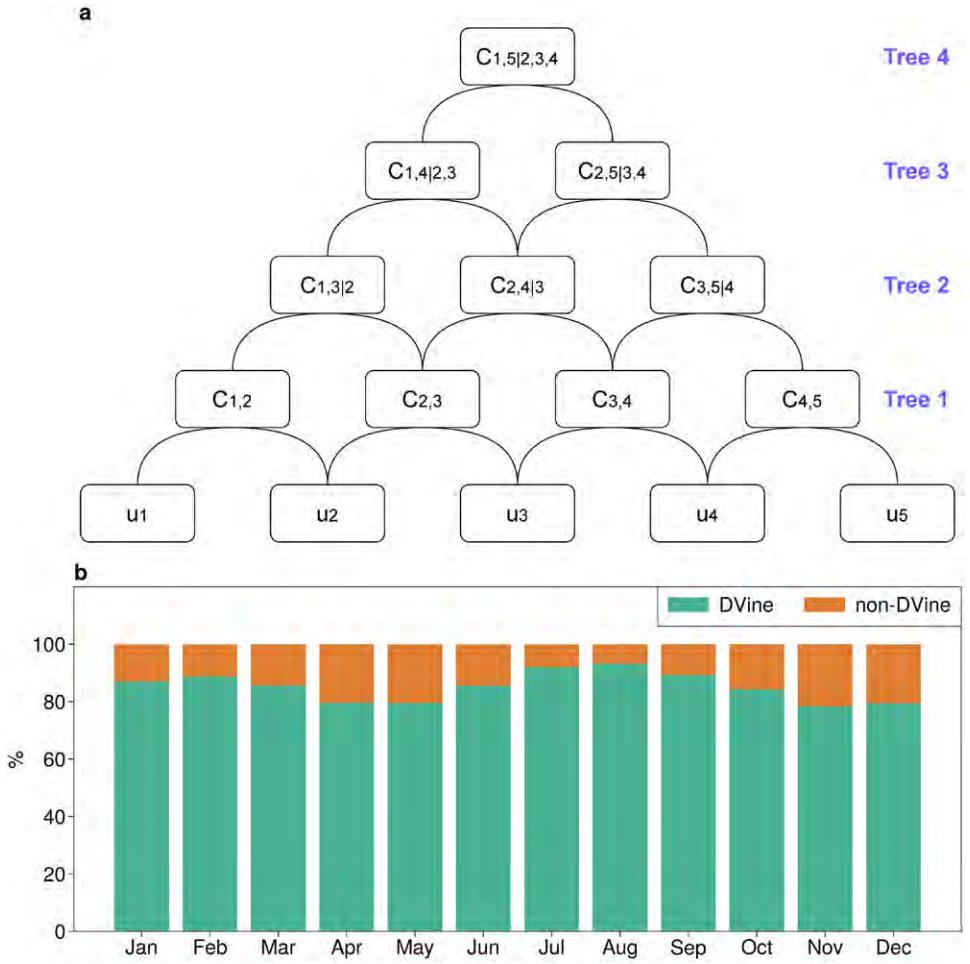

Fig. 8. (a) The structure of D-Vine in five dimensions. (b) The percentages of best-fit copulas falling in D-vine (green) and non-D-vine (orange) representation.

layer separating safe from dangerous events is unique for every design return period. More importantly in a practical sense, on the other hand, the Kendall measure is found to yield a complete symmetric index with a mean of zero, granting a fair chance of dry and wet events, as shown in the upper inset of Fig. 9b. In contrast, the indices created by copula measure contain a larger portion of negative than positive scores (upper inset of Fig. 9a), that is, 75%

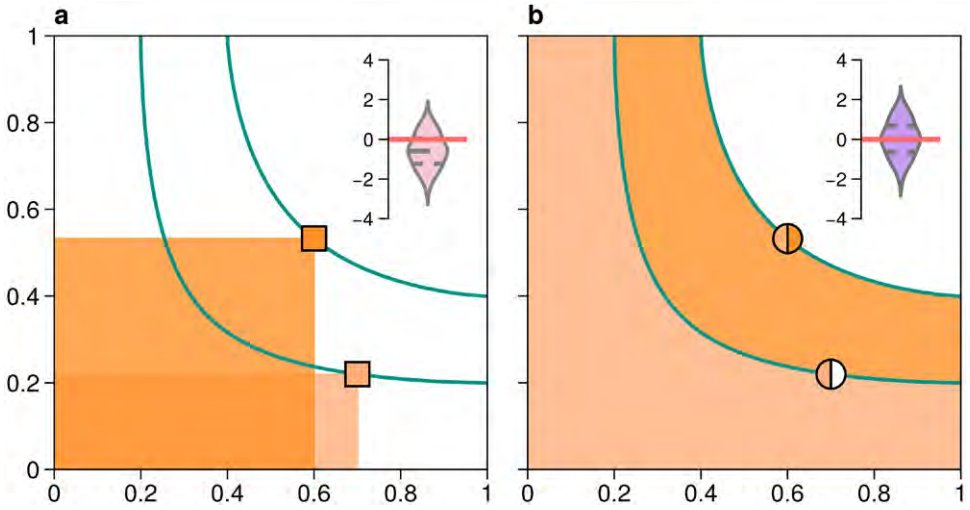

Fig. 9. Geometrical illustration of (a) copula measure and (b) Kendall measure, with the upper-right inset in each panel showing the frequency distribution of normalized scores expressed as a violin plot with the dashed horizontal lines representing the 25th, 50th, and 75th quantiles.

Unauthenticated | Downloaded 05/11/23 02:29 PM UTC

versus 25%. In short, we recommend using the Kendall measure to follow the general rule of drought index formulation.

The detailed descriptions pertaining to each specific setting are shown in section S4.3 in the supporting information.

Interpretation of CMI and super drought recognition

In this section, we demonstrate the properties of CMI and super drought recognition. Figure 10a affords a straightforward illustration of joining multiscalar dry–wet states based on CMI at May 2016. Further, we will assess again the three cases as marked in Fig. 1 to better demonstrate the powerful ability of CMI, as illustrated in Fig. 10b. In August 2018, the SPEI values at the five time scales are [−1.8, −2.1, −1.7, −1.6, −1.9], and the composite effect as denoted by the CMI value is −2.2, implying the emergence of super drought. At first glance, the result seems bewildering in its magnitude, as the maximum and mean magnitude of input

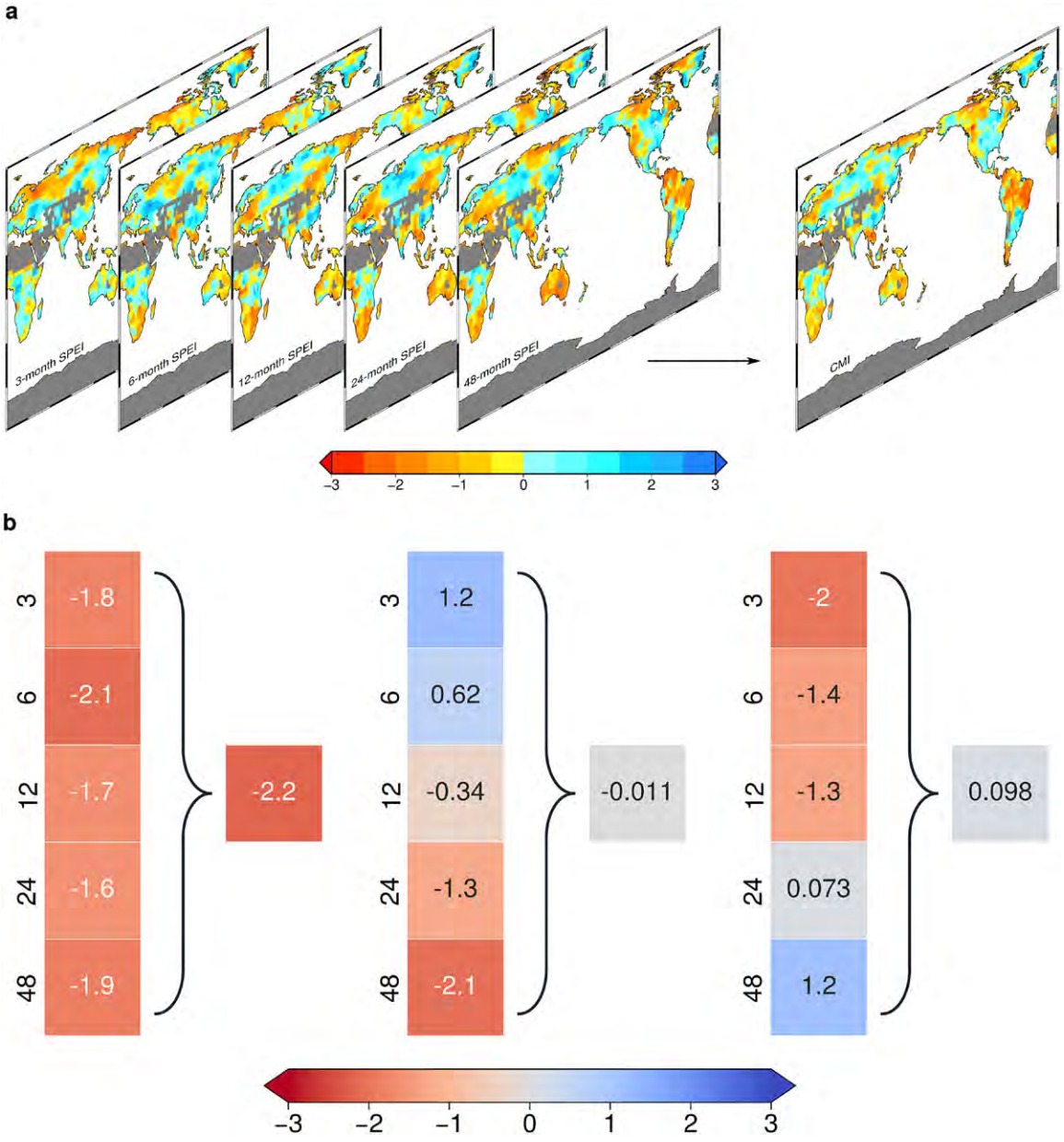

Fig. 10. Examples of joining multiscalar dry–wet states based on the proposed vine copula framework, in terms of spatial pattern on a globe in (a) May 2016 and (b) three representative samples. The three samples are collected in August 2018, October 2020, and November 1982 at the grid point 49.5°N, 13.5°E, which are marked in Fig. 1.

Unauthenticated | Downloaded 05/11/23 02:29 PM UTC

signals are −2.1 and −1.82 ([−1.8−2.1 − 1.7 − 1.6 − 1.9]/5 = −1.82), respectively. It has to be pointed out that the resultant value of −2.2 reflects the probability of drought combination risk under the whole measure space. In this way, the above result is expected as the joint likelihood of multidimensional drought peaks is even more rare. As a result, the coincidence probability must be extremely low and the joint score tends to be more negative than each component. The other two cases of October 2020 and November 1982 feature coexisting of dry and wet conditions. The resultant CMI is found to be near zero, representing overall normal condition. This is plausible because the positive and negative anomalies tend to cancel out.

In summary, the advantage of CMI is that it comprehensively explores the whole measure space and optimally determines how unusual the multidimensional observation is. In contrast, the linear combination perspective does not make use of the whole measure space and is thus not able to provide information accurately. As indicated by all above cases, the CMI value is significantly distinct from the mean value of the components. This affirms that the composite behavior is normally not a linear average of the individual behaviors.

Next, it is interesting to explore the relation between CMI and multiscalar SPEI when super drought occurs. Since multiscalar SPEI being high-dimensional is very hard to process, principal component analysis (PCA) is employed to reduce the dimensionality by extracting the most important feature. To guarantee the robustness, prefiltering process and method of PCA are applied to observations over all points on a globe rather than on an individual grid cell. The first two rows of Fig. 11 report the eigenvector and the frequency histogram of PC scores over the first principal axis. Each panel, from left to right, corresponds to the precondition CMI < −1.5, CMI < −2, and CMI < −2.5. These thresholds are referred to as CMI critical values. As indicated by the variance contribution, the first leading mode accounts for more than 90% of total variance, so the one-dimensional representation is a very good approximation to the original SPEIs in five-dimensional space. As shown by the eigenvector, it can be seen that all loadings have the same sign and similar magnitude, meaning in-phase variation pattern along the time-scale dimension. Owing to the overall coherent variability, we scale the eigenvector components to quasi-unit vector by a scaling factor and then multiply the PC score by the same factor. This rescaling does not alter the result, but has the strength of making the PC score be directly interpreted as the original SPEIs. Based on the histograms, we define the SPEI critical value that marks the 90th percentile.

With the above preparation, Fig. 11g illustrates the one-to-one relation between CMI critical values and SPEI critical values. For example, we see that CMI < −1.5 corresponds to SPEIs < −1.14, CMI < −2 to SPEIs < −1.57, and CMI < −2.5 to SPEIs < −1.64. Since the general rule is established through global-scale assessment, it is to a large extent appropriate in all situations and local significant exceptions to the rule would be in the minority. Figure 11g tells us two things. On the one hand, compared to SPEI critical values' profile, CMI critical values have a profile significantly shifted toward lower values. This shift again supports the view that simultaneous concurrence of extreme values can result in larger impact. On the other hand, there is a nonlinear interrelation between CMI and SPEI. When SPEIs become more negative, a small decrease in SPEIs leads to a large decrease in CMI. This means that adding extra pressure to individual drought type can cause the overall drought stress to deteriorate faster.

Validation of CMI

Aiming for integrated drought characterization and super drought detection, the validation of the proposed CMI is of vital importance. Ideally, the validating measurement should detect the same target as CMI, that is, stands out to capture drought features from an integrated perspective; meanwhile, global coverage is also required. Considering the above two aspects together, GRACE TWS available on a global scale is adopted as benchmark to test the worldwide skill of CMI and super drought identification. The reason is that up to now GRACE has had

Unauthenticated | Downloaded 05/11/23 02:29 PM UTC

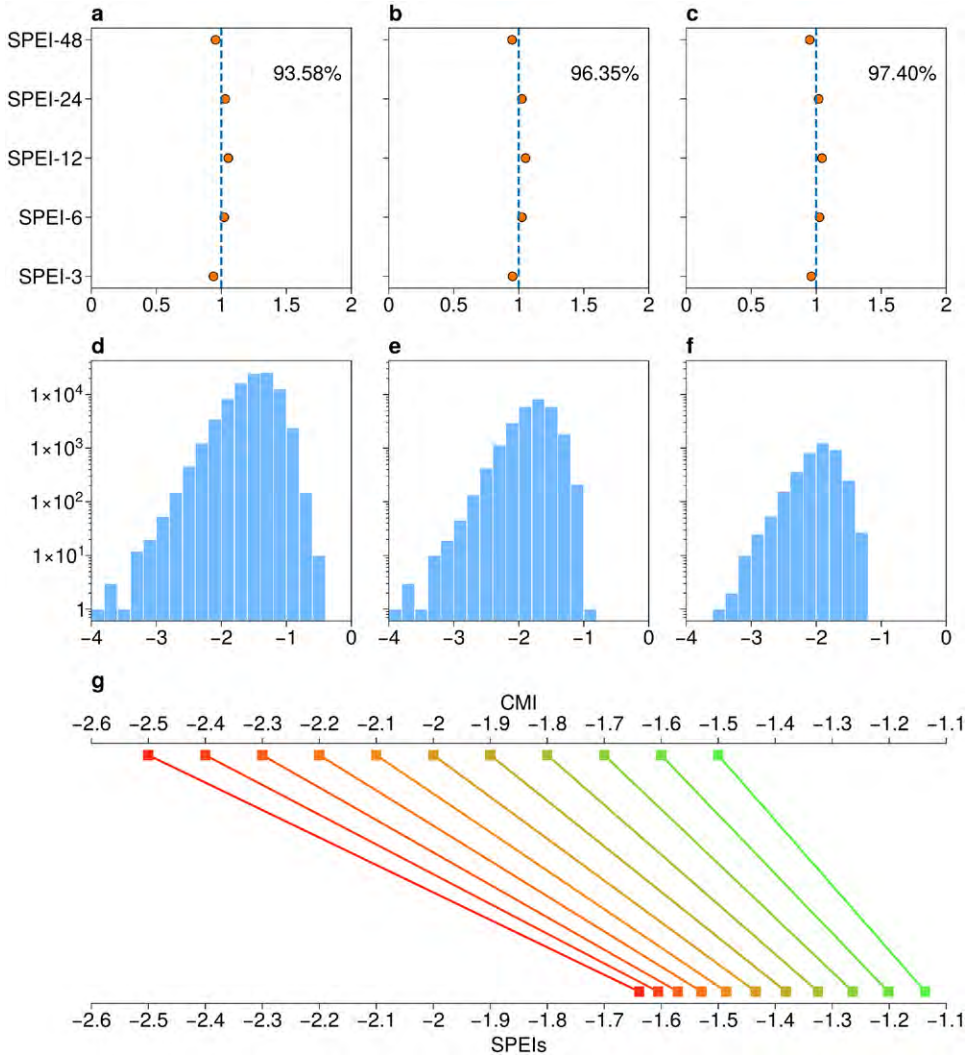

Fig. 11. (a)–(c) The eigenvectors and (d)–(f) the frequency histograms of PC scores over the first principal axis computed from SPEI at 3-, 6-, 12-, 24-, and 48-month time scales when CMI is less than (left) –1.5, (center) –2, and (right) –2.5. The explained variance of the first PC is labeled in the upper-right corner in (a)–(c). (g) Relation between CMI critical values and SPEI critical values, which are designated in the main text.

the unique ability to sense vertically integrated water storage and thus to comprehensively reflect changes in all of the available water (Deng et al. 2021), so that GRACE TWS is the only and best option for validating CMI. Nevertheless, this does not exclude the use of many other validating indicators (e.g., vegetation, soil moisture, actual records) in other specific aims. In this section, we conduct both a detailed case study and a global-scale assessment. In addition, a special focus is on investigating the ability of CMI to capture extreme events.

Case illustration. The central European drought (45°–50°N, 5°–20°E) in the summer of 2003 is used as a case study to demonstrate the merit of CMI as well as the significance of the super drought concept. Figure 12 portrays the dry–wet changes from the beginning of 2002 to the end of 2004 from multiple perspectives.

Figure 12b shows that central Europe experienced prolonged below-average rainfall from February to September 2003. When inspecting the conditions in March, the SPEI-3 is found to decrease to –1.68 and is accordingly allocated to the severe class (Fig. 12c), which was triggered by the consecutive precipitation deficit initiated in February. Similarly, most striking in Fig. 12a is that the 3-month water balance jumped from a low percentile score of 9.8% in January to an extremely high percentile score of 96.7% in March. However, Fig. 12a shows

Unauthenticated | Downloaded 05/11/23 02:29 PM UTC

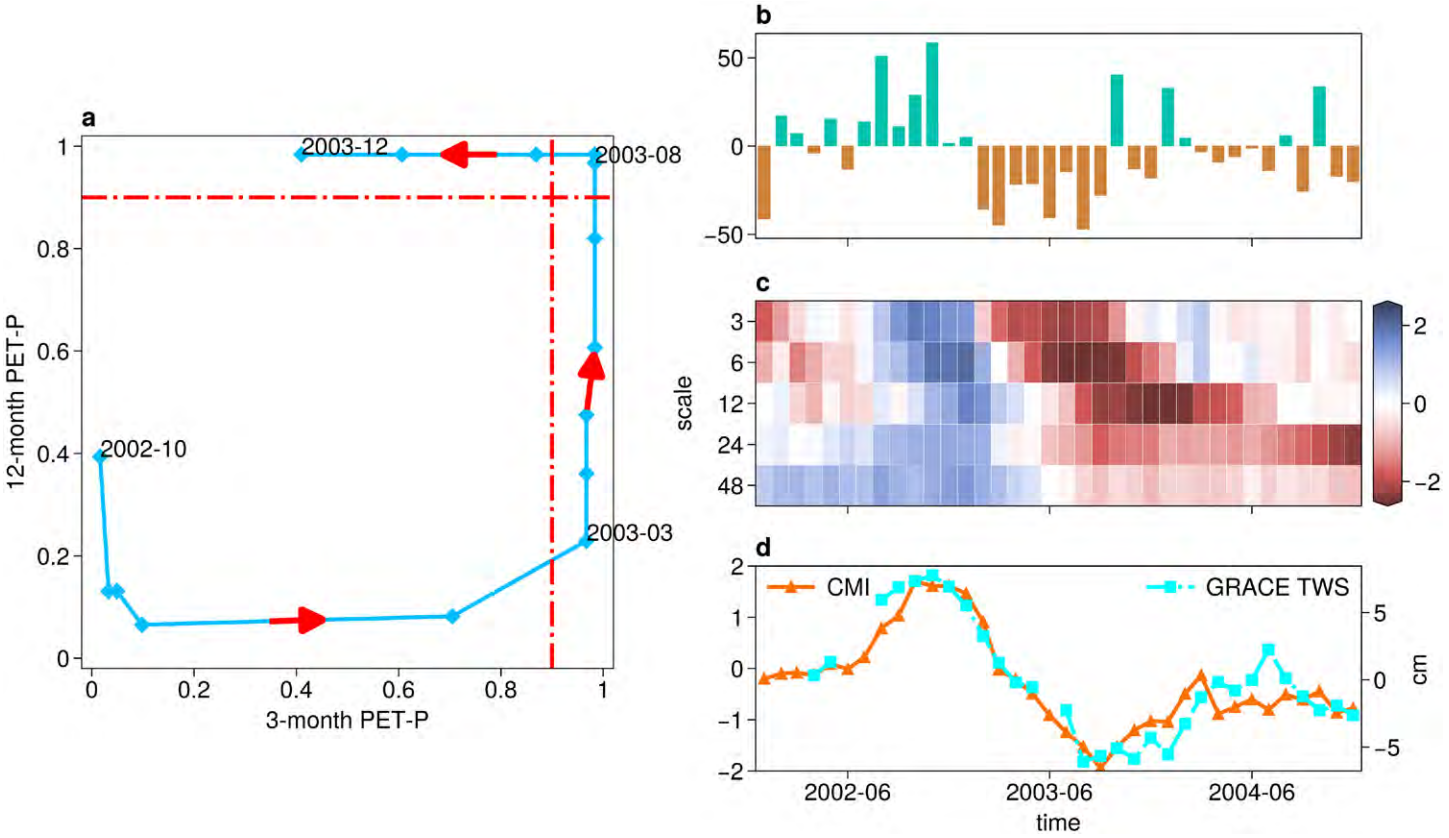

Fig. 12. (a) The track of dry–wet evolution from October 2002 to December 2003 depending upon the percentiles of 3-month (*x* axis) and 12-month (*y* axis) scale PET – P. Values around 0.5 are normal conditions, values above 0.5 indicate dry to exceptional drought conditions, and values below 0.5 represent wet to exceptional wet conditions. (b) Temporal evolution of precipitation anomalies, (c) SPEI at the time scales of 3, 6, 12, 24, and 48 months, and (d) CMI and GRACE TWS during January 2002–December 2004. The domain for the analysis is over central Europe (45°–50°N, 5°–20°E).

that the 12-month water balance exhibits a smoother temporal signal and remains on the lower end of the percentile score. Besides, considering time scales greater than 12 months, positive SPEI values between 0.26 and 0.95, indicative of humid conditions, are observed in March (Fig. 12c). This can be attributed to the fact that the long-term water balance has "memory" and the spring of 2003 was preceded by generous precipitation (Fig. 12b), which played a key role in suppressing long-term drought. As a consequence, it is no surprise to find TWS characterized by near-normal status (Fig. 12d). Meanwhile, the proposed CMI also has a value close to zero, confirming a good agreement with TWS. In conclusion, with the concept of super drought and CMI, it turns out no overall water deficits occurred in March 2003, despite the presence of short-term extreme drought.

From March 2003 onward, a continued series of short-term dry events (Fig. 12b) frequently hit central Europe, which is crucial to invoking long-term drought. As shown in Fig. 12c, negative SPEI values propagate from short to long scales with a time lag of several months. As March progressed to August and September, the 12-month water balance reached the highest percentile score of 0.98, falling in extremely dry conditions (Fig. 12a). Further, it can be seen in the top-right corner of Fig. 12a that the extreme phases of short-term and long-term drought coincided in August and September. In other words, concurrent extremes of drought at multiple time scales resulted in super drought, with CMI showing a minimum value equal to −1.94 as the lowest annual drought level (Fig. 12d). The presence of such a super drought event is corroborated by the measure of TWS, which declined to the concordant lowest value at −6 cm. In short, the essential feature behind the European drought in the late summer of 2003 is super drought.

After the summer of 2003, the long-term drought remained continuously in an extremely dry category (Fig. 12c). However, the super drought ended thanks to the recovery of short-term

Unauthenticated | Downloaded 05/11/23 02:29 PM UTC

drought in response to short-lived ample precipitation (Fig. 12b). As shown in Fig. 12a, the short-scale water balance returned to normal conditions toward the end of 2013, despite lingering hydrological drought. Thereby, no super drought showed up after the summer of 2003 due to the disappearance of drought overlap, preventing drought tensions from being far worse.

The above analysis has explained the formation mechanism of super drought by exploring the whole process of regional mean drought evolution. To gain deeper insights into what makes the intrinsic difference between high-impact droughts and those causing mild damage, the spatial comparison between the drought status of March and August 2003 is presented in Fig. 13. Notice that the original high resolution of 0.5° is adopted to facilitate spatial analysis at regional scale. In March 2003, it is apparent that substantial negative precipitation departures covered broad areas of the central Europe and short-term 3-month SPEI fell in the severe to extreme dry categories, which bears a great resemblance to the pattern in August 2003. However, why was devastating drought not perceived in March 2003? Neither precipitation anomalies nor traditional drought indices are able to explain this issue, owing to a lack of a comprehensive treatment of drought. By depending

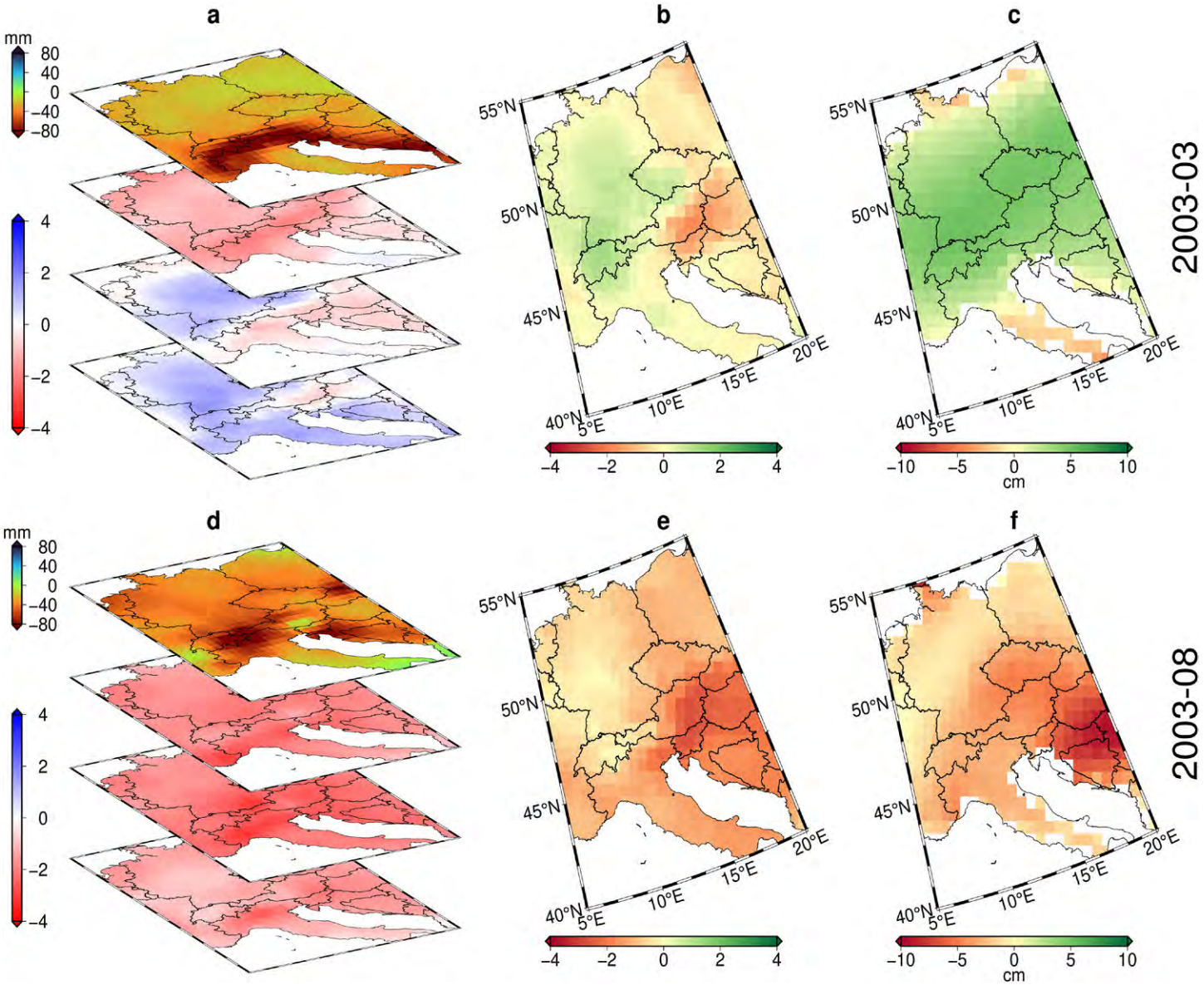

Fig. 13. Spatial comparison between the drought status of (a)–(c) March and (d)–(f) August 2003 over central Europe. The drought metrics analyzed are based on (a),(d) precipitation, SPEI-3, SPEI-6, and SPEI-12 (arranged in a stack from top to bottom), (b),(e) CMI, and (c),(f) GRACE TWS.

Unauthenticated | Downloaded 05/11/23 02:29 PM UTC

on the super drought concept and the CMI index developed, it can be easily interpreted as an absence of concurrent extremes at multiple time scales, because normal to wet conditions were noticed at medium to long time scales. As a consequence, it is not surprising to find CMI characterized by overall normal to wet conditions (Fig. 13b), which agrees well with the observed positive water thickness measured by GRACE (Fig. 13c). Therefore, the case in March 2003 suggests that individually occurring drought in a certain component leads to relatively moderate stress and that CMI successfully avoids false alarm, while traditional practices fail to achieve. Turning to the case in August 2003, it can be seen that extreme droughts at multiple time scales coincided (Fig. 13d), which is expected to yield more severe damage and widespread disruption to human society than events occurring in isolation. This is responsible for the substantial deficit of total water storage, as shown in Fig. 13f. Perfectly consistent with GRACE TWS observations, the CMI has good capability to reproduce the drought pattern with the most intense being located in the southeast sector (Fig. 13e). In sum, the comparison between the cases in March and August 2003 make it clear that the essential feature behind devastating drought is not that precipitation is deficient, soil moisture is drying out, or lake/reservoir water levels are depleted, but a combination of multiple drought extremes or equivalently grand loss in the total water storage.

The above case study illustrates the necessity and physical significance of the super drought concept, which is useful to improve the understanding of overall drought extremity. Meanwhile, the proposed CMI performs well to monitor super drought events as well as to exclude inconsequential ones and thus avoid false alarms.

Global-scale assessment. The global-scale performance of CMI in reproducing TWS is evaluated and compared against that of SPEI using correlation coefficient (CC), effective p value, and root-mean-square error (RMSE). The evaluation is made by a pixel-level comparison and boxplot summary of the skill scores computed globally, as depicted in Fig. 14.

First examined are the CC and associated p-value metrics, both of which describe the strength of the association. On the one hand, the correlation pattern (Fig. 14a) indicates a worldwide better ability of CMI than SPEI to capture TWS variability, with 0.1 higher CC on average. Particularly, the improvements in skill are more pronounced in the Eurasian continent, mainland Southeast Asian region, central-south North America, and Australia. On the other hand, the p-value pattern confirms the higher significance of the correlation between CMI and TWS, as reflected in Fig. 14c. Further, the boxplot (Fig. 14b) summarizing correlation coefficients indicates that although the correspondence between SPEI and TWS is good, the CMI offers higher skill. This is also true for the p-value score, because the median p value tested for CMI–TWS connection is 1.6×10^{-4}, about one order of magnitude smaller than that of SPEI. Most important, the annotations on top of the boxes highlight that the improvement in the simulation of TWS after applying CMI is statistically significant at the level of no less than 10^{-3}.

Next, the evaluation is further performed by calculating RMSE, which is relevant for evaluating the skill in reproducing the amplitude. Figure 14e clearly shows CMI generates fewer errors globally, with 58% of grid cells harboring RMSE of less than 1. The boxplot in Fig. 14f again proves that CMI causes the least deviation from TWS, as evidenced by the RMSE reduction ranging from 0.04 to 0.15 compared to SPEI. Meanwhile, the comparison of boxes supports that the capacity of CMI for reducing RMSE is statistically significant at 10^{-4} level.

In addition, in light of landmark role of self-calibrating PDSI (sc-PDSI) in the development of drought indices, section S6 in the supporting information compares the performance of CMI and sc-PDSI in estimating the overall drought condition. As a result, CMI exhibits a better fit with GRACE TWS measurement than sc-PDSI.

Unauthenticated | Downloaded 05/11/23 02:29 PM UTC

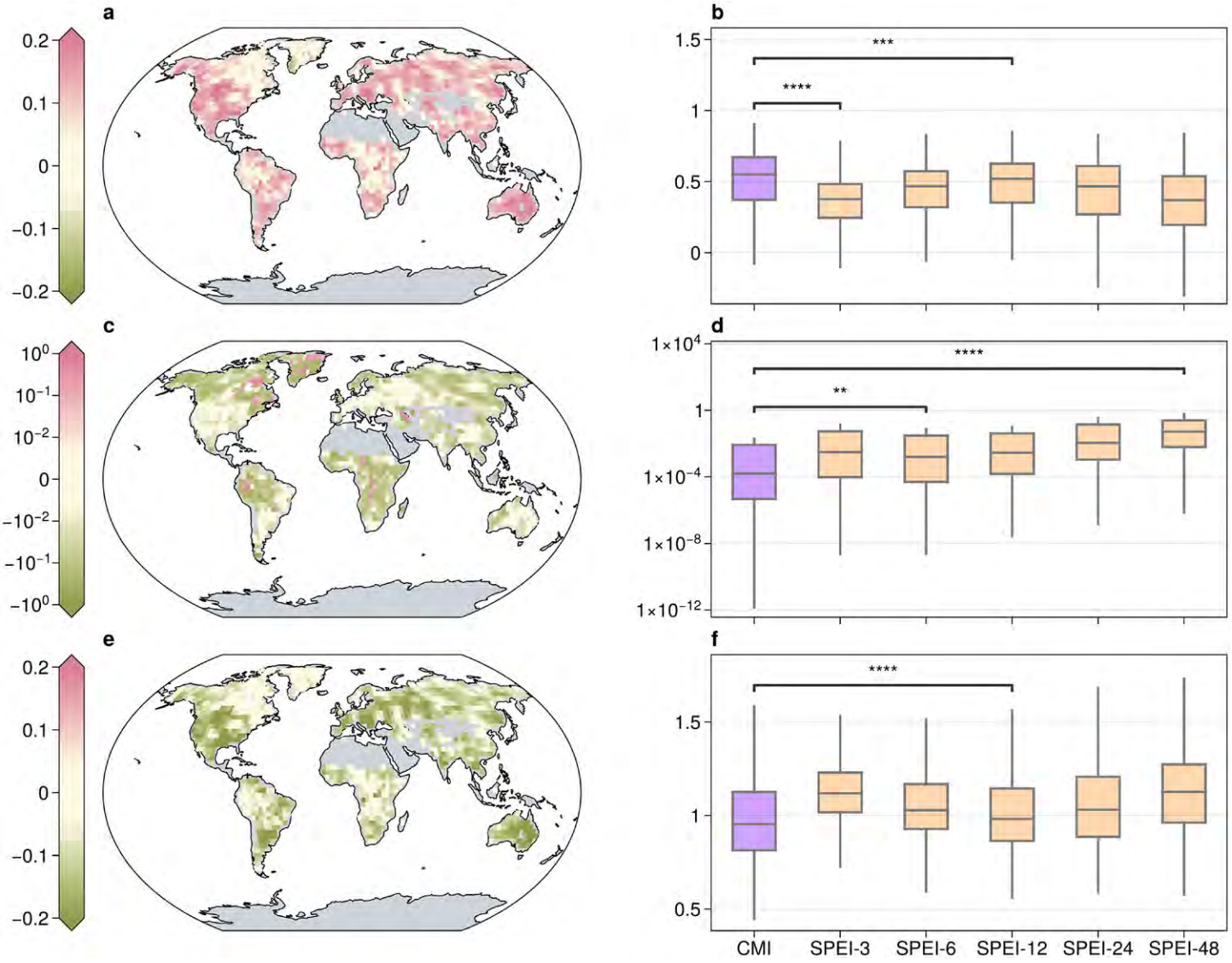

Fig. 14. (a),(c),(e) Spatial patterns of difference in skill metrics of CMI and SPEI against GRACE TWS. A symmetric logarithmic color scale is used for (c) with the scaling being linear between [-10^{-2}, 10^{-2}] and logarithmic otherwise. (b),(d),(f) Boxplot comparisons of the skill metrics for CMI and SPEI. The skills are measured by (a),(b) correlation coefficient, (c),(d) *p* value, and (e),(f) RMSE, with the higher value of correlation coefficient and the lower value of *p* value and RMSE referring to better performance. The boxplot includes median, the lower and upper quartiles, and the lower and upper fences (Q1 − 1.5 × IQR and Q3 + 1.5 × IQR, where Q1, Q3, and IQR denote the 25th percentile, 75th percentile, and interquartile range, respectively). In addition, the asterisks on top describe distributions with a statistically different mean based on one-tailed *T* test. Two (**), three (***), and four (****) asterisks mean that the CMI outperforms SPEI with significance levels of 10^{-2}, 10^{-3}, and 10^{-4}, respectively.

In conclusion, the overall water deficit–surplus represented by CMI has higher skill than that represented by SPEI. Of course, this is not meant to make a judgment on which index is intrinsically better. Instead, each index offers specific features and functionalities, and the suitability needs to be decided by the context. This research establishes the CMI metric as better for describing the overall extremity of multiscalar drought and recognizing super drought, while SPEI is most relevant for identifying characteristics of different drought types.

Extremity assessment. Subsequently, we also evaluate to what extent the CMI-based super drought detection exhibits better skill to represent extreme TWS events. To this end, histograms of TWS are compared between the two kinds of cases: the synchronous and asynchronous occurrences of drought at multiple time scales. The synchronous event is indeed super drought, defined as CMI < −2.14 approximately corresponding to SPEIs < −1.5, while

Unauthenticated | Downloaded 05/11/23 02:29 PM UTC

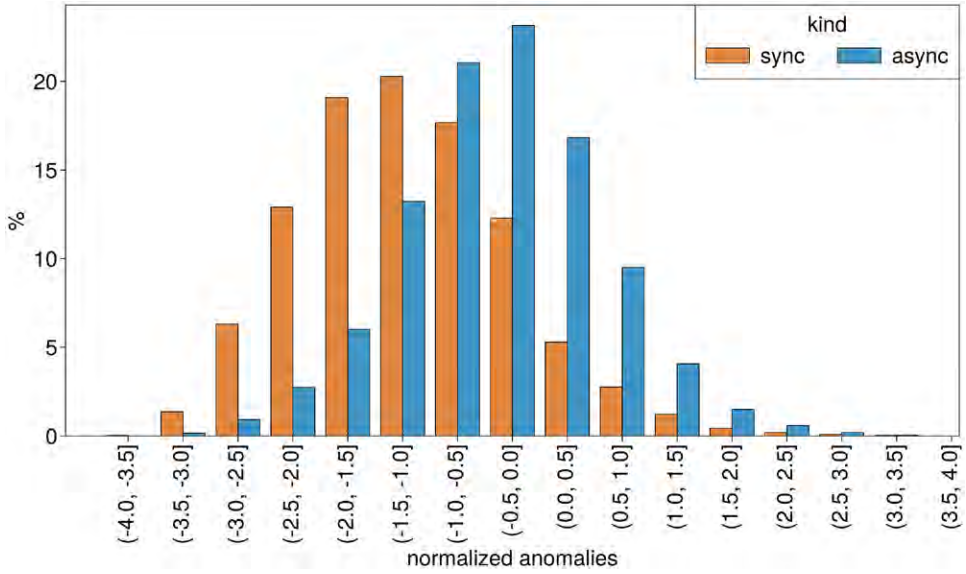

Fig. 15. A bin-to-bin comparison of frequency distribution (%) of normalized TWS anomalies between synchronous (orange bars) and asynchronous (blue bars) drought events. The definition for the synchronicity of drought events across multiple time scales can be found in the main text. Note that the synchronous event is indeed a super drought.

the asynchronous event is designated as severe drought (SPEI < −1.5) and humid status (SPEI > 0) coexisting. The result is visualized as a bin-to-bin histogram comparison of normalized TWS anomalies, as shown in Fig. 15.

The blue bars indicate that an asynchronous event yields a much weaker preference of positive or negative TWS and the percent contribution of TWS values less than one standard deviation is merely 23%. In the presence of super drought, in contrast, the frequency distribution of TWS is heavily skewed toward more negative values, with 90% and 60% of the values falling below 0 and −1 standard deviation, respectively.

In summary, the CMI-based super drought enables accurate estimation of the real water scarcity, which cannot be achieved by single time-scale fingerprint.

Discussion

In this section, we remark on some important issues, with detailed explanations reported in the supporting information.

Despite being driven by meteorological data, CMI does achieve the goal to quantitatively integrate multiple drought variables including agricultural and hydrological types. Furthermore, the proposed framework to calculate CMI is general enough to be used for various kinds of data sources other than meteorological data. The details are presented in section S5 of the supporting information. In addition, we have proven that the proposed CMI metric is not very sensitive to the influence of individual component behavior and does reflect the coexposure to multiple drought stresses. Refer to section S4.4 in the supporting information for details.

A special concern is that the proposed algorithm and parameter settings have been perceived as complex and numerically demanding. In section S4.5 of the supporting information, we highlight that the workflow is automated in merely three stages and has the outstanding advantage due to it being totally free from parameter settings. Meanwhile, the computing burden primarily exerted by the Monte Carlo simulation can be greatly alleviated by parallel programming.

Finally, it is noteworthy that the novel framework to calculate CMI does not consider asymmetry and nonstationarity in the modeling. The former one describes unequal impacts posed

Unauthenticated | Downloaded 05/11/23 02:29 PM UTC

by drought at different time scales. Section S4.6 in the supporting information suggests a feasible solution for how to incorporate asymmetric weights, which is inspired by portfolio value at risk theory (Byun and Song 2021). However, an absence of priori asymmetric information constitutes a major obstacle for application. The latter one is an important issue to be considered if the probable values for a certain period are typically outside the range of calibration in which the vine copula model is trained. However, the nonstationarity does not severely impact the validity of a vine copula fitting model in the historical 1961–2020 period (see section S4.7 in the supporting information for details). Moreover, (WMO (2012)) recommended that climatology length of 50–60 years is optimal and preferred to promote parameter stability in drought modeling. Although not currently accounted for, the nonstationarity must be coupled with future scenario projection, which is marked by a considerable degree of shifts in the underlying probability distribution. The basic idea to introduce nonstationarity is to express the fitting parameters as a function of time, which is usually called dynamic copula in financial science (Cherubini et al. 2012). We decide to develop the nonstationary version of CMI in the course of work evaluating the future scenario of super drought.

Conclusions

Monitoring and assessing extreme drought remain a profound challenge primarily owing to the multiscalar nature of drought. To overcome this challenge, the current study establishes the theoretical basis of the super drought concept, which refers to the simultaneous occurrence of extreme droughts at multiple time scales. The physical significance of super drought represents a combination of extreme dry states in multiple components of water resources or equivalently substantial deficits of total water storage, which is identified as the intrinsic difference compared to inconsequential ones with less impact. To have a quantitative representation, this study develops a complete framework based on vine copula and an associated novel monitoring index, CMI, in ways that are tailored to the needs of super drought detection. Furthermore, we interpret the properties of CMI and evaluate its performance against GRACE TWS at the global scale. The results demonstrate that CMI is a plausible metric to combine different forms of drought probabilistically and can better reflect overall rarity of water storage and recognize super drought.

The important issue to emphasize is that CMI is developed to describe the overall extremity of multiscalar drought and recognize super drought, but definitely it is not a universal solution that will be suitable for every specific application. Different drought indices offer specific features and functionalities. For this reason, CMI is not meant to replace other classic drought indices (WMO 2016). In addition to the novel concept and framework, accurate data sources are of equal importance to improve drought monitoring ability.

The current research is the first in a two-part series and constitutes a key prerequisite for advanced research and successful application. In the follow-up study, CMI will be used to explore super drought changes under global warming, including frequency–duration–area analysis, compilation of an event inventory, and driving mechanisms.

Finally, we create and manage a website (superdrought.com) to publish the CMI dataset and display near-real-time monitoring of global super drought. This web interface provides an operational assessment for overall drought risk, which not only benefits scientific end users for ease of use but decision-makers for drought preparedness and mitigation.

Acknowledgments. We thank the editor and the three anonymous referees for their valuable comments that helped to improve the manuscript. This work was supported by the National Natural Science Foundation of China Grants 42175041, 42230605, and 41831175, the International Partnership

Unauthenticated | Downloaded 05/11/23 02:29 PM UTC

Program of Chinese Academy of Sciences for Future Network (060GJHZ2022104FN), and the Second Tibetan Plateau Scientific Expedition and Research Program (2019QZKK0102).

Data availability statement. The CMI dataset generated in this study is available at superdrought.com. The CRU TS4.05 precipitation and PET data used to calculate CMI can be accessed online through https://data.ceda.ac.uk/badc/cru/data/cru_ts/cru_ts_4.05. The GRACE data used for validation can be downloaded from www2.csr.utexas.edu/grace/. The GlobCover land-cover data to exclude desert area can be downloaded from http://due.esrin.esa.int/page_globcover.php.

Unauthenticated | Downloaded 05/11/23 02:29 PM UTC

References

Aas, K., C. Czado, A. Frigessi, and H. Bakken, 2009: Pair-copula constructions of multiple dependence. *Insur. Math. Econ.*, **44**, 182–198, https://doi.org/10.1016/j.insmatheco.2007.02.001.

AghaKouchak, A., and Coauthors, 2021: Anthropogenic drought: Definition, challenges, and opportunities. *Rev. Geophys.*, **59**, e2019RG000683, https://doi.org/10.1029/2019RG000683.

Akaike, H., 1998: Information theory and an extension of the maximum likelihood principle. *Selected Papers of Hirotugu Akaike*, H. Akaike et al., Eds., Springer, 199–213.

Allen, R. G., M. Smith, L. S. Pereira, and A. Perrier, 1994: An update for the calculation of reference evapotranspiration. *ICID Bull.*, **43**, 35–92.

Ault, T. R., 2020: On the essentials of drought in a changing climate. *Science*, **368**, 256–260, https://doi.org/10.1126/science.aaz5492.

Bedford, T., and R. M. Cooke, 2002: Vines—A new graphical model for dependent random variables. *Ann. Stat.*, **30**, 1031–1068, https://doi.org/10.1214/aos/1031689016.

Beguería, S., S. M. Vicente-Serrano, and M. Angulo-Martínez, 2010: A multiscalar global drought dataset: The SPEIbase: A new gridded product for the analysis of drought variability and impacts. *Bull. Amer. Meteor. Soc.*, **91**, 1351–1356, https://doi.org/10.1175/2010BAMS2988.1.

Berg, A., and K. A. McColl, 2021: No projected global drylands expansion under greenhouse warming. *Nat. Climate Change*, **11**, 331–337, https://doi.org/10.1038/s41558-021-01007-8.

Byun, K., and S. Song, 2021: Value at risk of portfolios using copulas. *Commun. Stat. Appl. Methods*, **28**, 59–79, https://doi.org/10.29220/CSAM.2021.28.1.059.

Cherubini, U., F. Gobbi, S. Mulinacci, and S. Romagnoli, 2012: *Dynamic Copula Methods in Finance.* John Wiley and Sons, 288 pp.

Czado, C., 2019: *Analyzing Dependent Data with Vine Copulas: A Practical Guide with R.* Springer, 242 pp.

Dai, A., 2011: Drought under global warming: A review. *Wiley Interdiscip. Rev.: Climate Change*, **2**, 45–65, https://doi.org/10.1002/wcc.81.

——, 2013: Increasing drought under global warming in observations and models. *Nat. Climate Change*, **3**, 52–58, https://doi.org/10.1038/nclimate1633.

Deng, S., S. Liu, and X. Mo, 2021: Assessment and attribution of China's droughts using an integrated drought index derived from GRACE and GRACE-FO data. *J. Hydrol.*, **603**, 127170, https://doi.org/10.1016/j.jhydrol.2021.127170.

Fu, Q., and S. Feng, 2014: Responses of terrestrial aridity to global warming. *J. Geophys. Res. Atmos.*, **119**, 7863–7875, https://doi.org/10.1002/2014JD021608.

Guan, X. J., J. Ma, R. Huang, L. Huang, and Z. M. A. Zhang, 2019: Impact of oceans on climate change in drylands. *Sci. China Earth Sci.*, **62**, 891–908, https://doi.org/10.1007/s11430-018-9317-8.

Hao, Z., and A. AghaKouchak, 2013: Multivariate standardized drought index: A parametric multi-index model. *Adv. Water Resour.*, **57**, 12–18, https://doi.org/10.1016/j.advwatres.2013.03.009.

——, and V. P. Singh, 2015: Drought characterization from a multivariate perspective: A review. *J. Hydrol.*, **527**, 668–678, https://doi.org/10.1016/j.jhydrol.2015.05.031.

——, F. Hao, and V. P. Singh, 2016: A general framework for multivariate multi-index drought prediction based on multivariate ensemble streamflow prediction (MESP). *J. Hydrol.*, **539**, 1–10, https://doi.org/10.1016/j.jhydrol.2016.04.074.

Harris, I., T. J. Osborn, P. Jones, and D. Lister, 2020: Version 4 of the CRU TS monthly high-resolution gridded multivariate climate dataset. *Sci. Data*, **7**, 109, https://doi.org/10.1038/s41597-020-0453-3.

Hayes, M., M. Svoboda, N. Wall, and M. Widhalm, 2011: The Lincoln declaration on drought indices: Universal meteorological drought index recommended. *Bull. Amer. Meteor. Soc.*, **92**, 485–488, https://doi.org/10.1175/2010BAMS3103.1.

He, X., M. Pan, Z. Wei, E. F. Wood, and J. Sheffield, 2020: A global drought and flood catalogue from 1950 to 2016. *Bull. Amer. Meteor. Soc.*, **101**, E508–E535, https://doi.org/10.1175/BAMS-D-18-0269.1.

Hofert, M., I. Kojadinovic, M. Machler, and J. Yan, 2018: *Elements of Copula Modeling with R.* Springer International, 267 pp.

Huang, J., H. Yu, X. Guan, G. Wang, and R. Guo, 2016: Accelerated dryland expansion under climate change. *Nat. Climate Change*, **6**, 166–171, https://doi.org/10.1038/nclimate2837.

——, and Coauthors, 2017: Dryland climate change: Recent progress and challenges. *Rev. Geophys.*, **55**, 719–778, https://doi.org/10.1002/2016RG000550.

Joe, H., 1996: Families of m-variate distributions with given margins and $m(m-1)/2$ bivariate dependence parameters. *Distributions with Fixed Marginals and Related Topics, Lecture Notes Monogr.*, Vol. 28, Institute of Mathematical Statistics, 120–141.

Kao, S.-C., and R. S. Govindaraju, 2008: Trivariate statistical analysis of extreme rainfall events via the Plackett family of copulas. *Water Resour. Res.*, **44**, W02415, https://doi.org/10.1029/2007WR006261.

——, and ——, 2010: A copula-based joint deficit index for droughts. *J. Hydrol.*, **380**, 121–134, https://doi.org/10.1016/j.jhydrol.2009.10.029.

Keyantash, J. A., and J. A. Dracup, 2004: An aggregate drought index: Assessing drought severity based on fluctuations in the hydrologic cycle and surface water storage. *Water Resour. Res.*, **40**, W09304, https://doi.org/10.1029/2003WR002610.

Klein Tank, A. M. G., F. W. Zwiers, and X. Zhang, 2009: Guidelines on analysis of extremes in a changing climate in support of informed decisions for adaptation. WMO Rep. WMO/TD-1500, 56 pp., https://library.wmo.int/index.php?lvl=notice_display&id=138#.ZCrDBXZByUk.

Kurowicka, D., and H. Joe, Eds., 2011: *Dependence Modeling: Vine Copula Handbook.* World Scientific, 360 pp.

Landerer, F. W., and S. S. Cooley, 2021: GRACE D-103133 Gravity Recovery and Climate Experiment level-3 data product user handbook. NASA Jet Propulsion Laboratory Doc., 62 pp.

Lewis, S. L., P. M. Brando, O. L. Phillips, G. M. F. van der Heijden, and D. Nepstad, 2011: The 2010 Amazon drought. *Science*, **331**, 554, https://doi.org/10.1126/science.1200807.

Ma, M., L. Ren, V. P. Singh, X. Yang, F. Yuan, and S. Jiang, 2014: New variants of the Palmer drought scheme capable of integrated utility. *J. Hydrol.*, **519**, 1108–1119, https://doi.org/10.1016/j.jhydrol.2014.08.041.

——, ——, ——, X. Tu, S. Jiang, and Y. Liu, 2015: Evaluation and application of the SPDI-JDI for droughts in Texas, USA. *J. Hydrol.*, **521**, 34–45, https://doi.org/10.1016/j.jhydrol.2014.11.074.

McKee, T. B., N. J. Doesken, and J. Kleist, 1993: The relationship of drought frequency and duration to time scales. Preprints, *Eighth Conf. on Applied Climatology*, Anaheim, CA, Amer. Meteor. Soc., 179–184.

Mo, K. C., and D. P. Lettenmaier, 2014: Objective drought classification using multiple land surface models. *J. Hydrometeor.*, **15**, 990–1010, https://doi.org/10.1175/JHM-D-13-071.1.

Naumann, G., C. Cammalleri, L. Mentaschi, and L. Feyen, 2021: Increased economic drought impacts in Europe with anthropogenic warming. *Nat. Climate Change*, **11**, 485–491, https://doi.org/10.1038/s41558-021-01044-3.

Nelsen, R. B., 2007: *An Introduction to Copulas.* Springer Science and Business Media, 269 pp.

——, J. J. Quesada-Molina, J. A. Rodríguez-Lallena, and M. Úbeda-Flores, 2003: Kendall distribution functions. *Stat. Probab. Lett.*, **65**, 263–268, https://doi.org/10.1016/j.spl.2003.08.002.

Pascale, S., S. B. Kapnick, T. L. Delworth, and W. F. Cooke, 2020: Increasing risk of another Cape Town "day zero" drought in the 21st century. *Proc. Natl. Acad. Sci. USA*, **117**, 29 495–29 503, https://doi.org/10.1073/pnas.2009144117.

Peterson, T. J., M. Saft, M. C. Peel, and A. John, 2021: Watersheds may not recover from drought. *Science*, **372**, 745–749, https://doi.org/10.1126/science.abd5085.

Qi, Y., H. Yu, Q. Fu, Q. Chen, J. Ran, and Z. Yang, 2022: Future changes in drought frequency due to changes in the mean and shape of the PDSI probability

Unauthenticated | Downloaded 05/11/23 02:29 PM UTC

density function under RCP4.5 scenario. *Front. Earth Sci.*, **10**, 857885, https://doi.org/10.3389/feart.2022.857885.

Rajsekhar, D., V. P. Singh, and A. K. Mishra, 2015: Multivariate drought index: An information theory based approach for integrated drought assessment. *J. Hydrol.*, **526**, 164–182, https://doi.org/10.1016/j.jhydrol.2014.11.031.

Save, H., S. Bettadpur, and B. D. Tapley, 2016: High-resolution CSR GRACE RL05 mascons. *J. Geophys. Res. Solid Earth*, **121**, 7547–7569, https://doi.org/10.1002/2016JB013007.

Schepsmeier, U., 2015: Efficient information based goodness-of-fit tests for vine copula models with fixed margins: A comprehensive review. *J. Multivar. Anal.*, **138**, 34–52, https://doi.org/10.1016/j.jmva.2015.01.001.

Shah, D., and V. Mishra, 2020: Integrated drought index (IDI) for drought monitoring and assessment in India. *Water Resour. Res.*, **56**, e2019WR026284, https://doi.org/10.1029/2019WR026284.

Sheffield, J., E. F. Wood, and M. L. Roderick, 2012: Little change in global drought over the past 60 years. *Nature*, **491**, 435–438, https://doi.org/10.1038/nature11575.

Sherwood, S., and Q. Fu, 2014: Climate change. A drier future? *Science*, **343**, 737–739, https://doi.org/10.1126/science.1247620.

Sklar, A. 1959: Fonctions de répartition à n dimensions et leurs marges. *Publ. Inst. Stat. Univ. Paris*, **8**, 229–231.

Spinoni, J., and Coauthors, 2020: Future global meteorological drought hot spots: A study based on CORDEX data. *J. Climate*, **33**, 3635–3661, https://doi.org/10.1175/JCLI-D-19-0084.1.

Tapley, B. D., and Coauthors, 2019: Contributions of GRACE to understanding climate change. *Nat. Climate Change*, **9**, 358–369, https://doi.org/10.1038/s41558-019-0456-2.

Trenberth, K. E., A. Dai, G. van der Schrier, P. D. Jones, J. Barichivich, K. R. Briffa, and J. Sheffield, 2014: Global warming and changes in drought. *Nat. Climate Change*, **4**, 17–22, https://doi.org/10.1038/nclimate2067.

UNCCD, 2022: Drought in numbers 2022—Restoration for readiness and resilience. UNCCD Rep., 51 pp., https://reliefweb.int/report/world/drought-numbers-2022-restoration-readiness-and-resilience.

UNDRR, 2020: The human cost of disasters—An overview of the last 20 years 2000-2019. UNDRR Rep., 30 pp., www.undrr.org/publication/human-cost-disasters-overview-last-20-years-2000-2019#:~:text=In%20the%20period%202000%20to,over%20the%20previous%20twenty%20years.

Van Loon, A. F., and Coauthors, 2016: Drought in the Anthropocene. *Nat. Geosci.*, **9**, 89–91, https://doi.org/10.1038/ngeo2646.

Vicente-Serrano, S. M., S. Beguería, and J. I. López-Moreno, 2010: A multiscalar drought index sensitive to global warming: The standardized precipitation evapotranspiration index. *J. Climate*, **23**, 1696–1718, https://doi.org/10.1175/2009JCLI2909.1.

——, ——, and ——, 2011: Comment on "Characteristics and trends in various forms of the Palmer drought severity index (PDSI) during 1900–2008" by Aiguo Dai. *J. Geophys. Res.*, **116**, D19112, https://doi.org/10.1029/2011JD016410.

——, and Coauthors, 2012: Performance of drought indices for ecological, agricultural, and hydrological applications. *Earth Interact.*, **16**, https://doi.org/10.1175/2012EI000434.1.

Wang, J., Q. Zhang, L. Zhang, Y. Wang, P. Yue, Y. Hu, and P. Ye, 2022: The global pattern and development trends and directions on the drought monitoring research from 1983 to 2020 by using bibliometric analysis. *Bull. Amer. Meteor. Soc.*, **103**, E2081–E2107, https://doi.org/10.1175/BAMS-D-21-0324.1.

Wang, L., W. Chen, W. Zhou, and G. Huang, 2015: Drought in Southwest China: A review. *Atmos. Ocean. Sci. Lett.*, **8**, 339–344, https://doi.org/10.3878/AOSL20150043.

——, ——, ——, and ——, 2016: Understanding and detecting super-extreme droughts in Southwest China through an integrated approach and index. *Quart. J. Roy. Meteor. Soc.*, **142**, 529–535, https://doi.org/10.1002/qj.2593.

——, ——, Q. Fu, G. Huang, Q. Wang, C. Chotamonsak, and A. Limsakul, 2022: Super droughts over East Asia since 1960 under the impacts of global warming and decadal variability. *Int. J. Climatol.*, **42**, 4508–4521, https://doi.org/10.1002/joc.7483.

Wang, S., J. Huang, and X. Yuan, 2021: Attribution of 2019 extreme spring–early summer hot drought over Yunnan in Southwestern China [in "Explaining Extreme Events of 2019 from a Climate Perspective"]. *Bull. Amer. Meteor. Soc.*, **102** (1), S91–S96, https://doi.org/10.1175/BAMS-D-20-0121.1.

Waseem, M., M. Ajmal, and T.-W. Kim, 2015: Development of a new composite drought index for multivariate drought assessment. *J. Hydrol.*, **527**, 30–37, https://doi.org/10.1016/j.jhydrol.2015.04.044.

Williams, A. P., B. I. Cook, and J. E. Smerdon, 2022: Rapid intensification of the emerging southwestern North American megadrought in 2020–2021. *Nat. Climate Change*, **12**, 232–234, https://doi.org/10.1038/s41558-022-01290-z.

WMO, 2012: Standardized precipitation index user guide. WMO Doc. WMO-1090, 16 pp., https://library.wmo.int/index.php?lvl=notice_display&id=13682#.ZFD8b2BII2c.

——, 2016: Handbook of drought indicators and indices. WMO Doc. WMO-1173, 45 pp., https://community.wmo.int/en/bookstore/handbook-drought-indicators-and-indices.

Xia, Y., M. B. Ek, C. D. Peters-Lidard, D. Mocko, M. Svoboda, J. Sheffield, and E. F. Wood, 2014: Application of USDM statistics in NLDAS-2: Optimal blended NLDAS drought index over the continental United States. *J. Geophys. Res. Atmos.*, **119**, 2947–2965, https://doi.org/10.1002/2013JD020994.

Yang, J., J. Chang, Y. Wang, Y. Li, H. Hu, Y. Chen, Q. Huang, and J. Yao, 2018: Comprehensive drought characteristics analysis based on a nonlinear multivariate drought index. *J. Hydrol.*, **557**, 651–667, https://doi.org/10.1016/j.jhydrol.2017.12.055.

Zhang, C., H. Liu, Y. Song, Y. Liao, J. Duan, W. Cai, and S. Wang, 2017: *Grades of Meteorological Drought.* China Quality Inspection Press, 24 pp.

Zhang, L., T. Zhou, X. Chen, P. Wu, N. Christidis, and F. C. Lott, 2020: The late spring drought of 2018 in South China [in "Explaining Extreme Events of 2018 from a Climate Perspective"]. *Bull. Amer. Meteor. Soc.*, **101** (1), S59–S64, https://doi.org/10.1175/BAMS-D-19-0202.1.

Zhao, T., and A. Dai, 2017: Uncertainties in historical changes and future projections of drought. Part II: Model-simulated historical and future drought changes. *Climatic Change*, **144**, 535–548, https://doi.org/10.1007/s10584-016-1742-x.

——, and ——, 2022: CMIP6 model-projected hydroclimatic and drought changes and their causes in the twenty-first century. *J. Climate*, **35**, 897–921, https://doi.org/10.1175/JCLI-D-21-0442.1.

Unauthenticated | Downloaded 05/11/23 02:29 PM UTC

npj | climate and atmospheric science

www.nature.com/npjclimatsci

ARTICLE OPEN

Check for updates

Asymmetric response of South Asian summer monsoon rainfall in a carbon dioxide removal scenario

Suqin Zhang[1,2,3,4], Xia Qu[1,2,5]✉, Gang Huang[1,3,4]✉ and Peng Hu[5,6]

The reversibility of South Asian summer monsoon (SASM) precipitation under the CO_2 removal scenario is critical for climate mitigation and adaptation. In the idealized CO_2 ramp-up (from 284.7 to 1138.8 ppm) and symmetric ramp-down experiments, SASM precipitation is largely reversible while exhibiting strong asymmetry: it may overshoot the unperturbed level when CO_2 recovers. Such asymmetric response is mainly due to the enhanced El Niño-like and Indian Ocean dipole-like warming during the ramp-down period. The uneven sea surface warming weakens Walker circulation, with anomalous sinking over the SASM region. Meanwhile, the warming also affects the rainfall over the Maritime Continent and tropical western Indian Ocean. The suppressed rainfall over the Maritime Continent triggers the equatorial Rossby wave, which weakens the ascent over the SASM region; the increased rainfall over the tropical western Indian Ocean excites the equatorial Kelvin wave, which reduces moisture transport. Additionally, tropic-wide warming reduces the land-sea thermal contrast and weakens monsoonal circulation. Consequently, the combined effects of the weakened ascent and moisture transport lead to the overshooting of SASM rainfall. Our results suggest that symmetric CO_2 removal, although unlikely in the foreseeable future, may result in a risk of local drought over the SASM region.

npj Climate and Atmospheric Science (2023)6:10 ; https://doi.org/10.1038/s41612-023-00338-x

INTRODUCTION

The concentration of Carbon Dioxide (CO_2) in the atmosphere has been increasing since the Industrial Revolution. It exerts severe, widespread, and irreversible influences on climate and human society[1]. To avoid or lower these influences, the Paris Agreement proposed a strict target, i.e., holding the increase in the global average temperature to well below 2 °C above pre-industrial (PI) level and pursuing efforts to limit the temperature increase to 1.5 °C above PI. Such long-term temperature goals call for reaching the global peak of greenhouse gas emissions as soon as possible to achieve a climate-neutral world by the middle of the 21st century. Achieving this target requires Carbon Dioxide Removal (CDR) methods to decrease atmospheric CO_2 concentration in the future[1–6]. Due to its huge heat capacity, the ocean acts as heat storage which absorbs most of the redundant energy arising from the CO_2 concentration increases[1,7]. In particular, the response of the ocean is much slower, with a timescale of decades to millennia[8–10]. If CDR methods are applied, the excess heat accumulated in the ocean would affect the climate response during the CO_2 ramp-down period[11–13]. At present, the climate effect of CDR is still inconsistent and inadequately understood in the scientific community[14,15].

The South Asian summer monsoon (SASM), a crucial component of the global monsoon system, directly affects the lives of more than one billion people. Slight changes in SASM precipitation can cause tremendous socioeconomic impacts, including impacts on agricultural production, water resources, and basic human needs[16,17]. Hence, understanding the response of SASM precipitation to climate change is of great importance. Under a global warming scenario where the CO_2 concentration increases monotonically, SASM precipitation is projected to increase in nearly all models, despite a weakening of SASM circulation[18,19]. Previous studies have reported that enhanced atmospheric water vapor content and the larger moisture convergence into the SASM region[20–23] are responsible for the increased rainfall, which is consistent with the "wet-get-wetter" mechanism[24–26]. However, the positive contribution of the thermodynamic effect is partially offset by the dynamic effect due to the weakened circulation, which results in a lower increase in SASM precipitation than water vapor content[27,28]. The enhanced upper-tropospheric warming over the tropical Indian Ocean[29], as well as the mean advection of the stratification change mechanism[30], may all contribute to the weakened SASM circulation.

Under the CDR scenario, SASM precipitation displays an overshooting relative to that during the CO_2 ramp-up period[31], namely, SASM precipitation may fully recover and exhibit drought when the CO_2 concentration recovers. This is significantly different from that of the global hydrological cycle[12,13,32–35]. In the idealized experiment in which the CO_2 rise is followed by a symmetric decline, global precipitation continues to rise for decades after CO_2 peaks and cannot return to the initial level when CO_2 recovers. Such an asymmetric response of global precipitation originates mainly from the ocean, and precipitation on land is nearly symmetrical[11,36]. The response of rainfall at the regional scale has a similar response to global precipitation, including the Intertropical Convergence Zone (ITCZ)[37], East Asia[34], and the Korean Peninsula[35]. For example, the location of the ITCZ changes minimally during the CO_2 ramp-up period; in contrast, it shifts rapidly to the south during the CO_2 ramp-down period and resides in the south when the CO_2 concentration recovers to the initial level, leading to the asymmetric responses of the ITCZ-related precipitation[37].

[1]State Key Laboratory of Numerical Modeling for Atmospheric Sciences and Geophysical Fluid Dynamics, Institute of Atmospheric Physics, Chinese Academy of Sciences, Beijing, China. [2]Key Laboratory of Meteorological Disaster (KLME), Ministry of Education & Collaborative Innovation Center on Forecast and Evaluation of Meteorological Disasters (CIC-FEMD), Nanjing University of Information Science & Technology, Nanjing, China. [3]Laboratory for Regional Oceanography and Numerical Modeling, Qingdao National Laboratory for Marine Science and Technology, Qingdao, China. [4]University of Chinese Academy of Sciences, Beijing, China. [5]Center for Monsoon System Research, Institute of Atmospheric Physics, Chinese Academy of Sciences, Beijing, China. [6]Department of Atmospheric Sciences, Yunnan University, Kunming, China. ✉email: quxia@mail.iap.ac.cn; hg@mail.iap.ac.cn

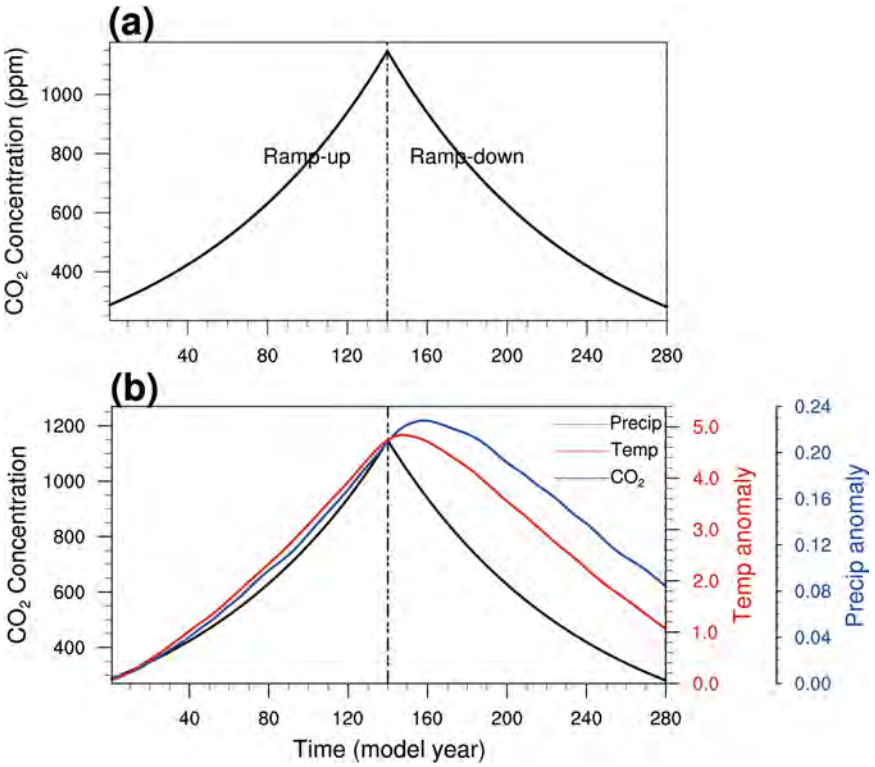

Fig. 1 The global mean surface temperature and precipitation changes in the idealized CO_2 ramp-up and ramp-down experiments. a The evolution of the atmospheric CO_2 concentration (unit: ppm) in CDR experiments. **b** The global mean surface temperature (GMST; unit: K) and precipitation (GMP; unit: mm day^{-1}) responses in CO_2 ramp-up and ramp-down experiments relative to the PI from the MME. Time series of the CO_2 concentration (black line; unit: ppm), annual GMST (red line), and GMP (blue line) anomalies. A 3-point (1/4,1/2,1/4) filter with 40 times is used to remove interannual variability. The vertical dashed line denotes Year 140 when CO_2 peaks.

Researchers have inferred that both the accumulated heat in the deep ocean during the CO_2 ramp-up period[11,13] and the rainfall sensitivity to CO_2 forcing through tropospheric adjustment processes[33] are responsible for such asymmetric responses. For the distinct response of SASM precipitation, the HadCM3 output suggested that it may result from the lag recovery of Pacific and Indian Ocean Sea Surface Temperature (SST)[31]. The weakened moisture flux convergence related to the southward ITCZ shift during the CO_2 ramp-down period compared to the ramp-up period also plays a role[38]. As a part of Coupled Model Intercomparison Project phase six (CMIP6), the Carbon Dioxide Removal Model Intercomparison Project (CDRMIP) was sponsored[15]. To date, eight models have participated in this project and have conducted CDR experiments (see "Methods"). The evolution of CO_2 concentration of these experiments is presented in Fig. 1a, which increases for 140 years and then gradually decreases to the initial level. It is a good opportunity to verify the robustness of the response of SASM precipitation under the CDR scenario. Moreover, there is the possibility of uncovering other process responsible for the asymmetric response. Therefore, this study aims to address the following two scientific questions: (a) How does SASM rainfall respond to CDR in multiple models? How is the inter-model consistency? (b) What major processes are responsible for this response?

RESULTS

Asymmetric response of temperature and rainfall

The global mean surface temperature (GMST) and precipitation (GMP) responses during the CO_2 ramp-up and ramp-down experiments from the Multi-Model Ensemble (MME) are presented in Fig. 1b. Both the GMST and GMP respond asymmetrically and show hysteresis concerning symmetric CO_2 forcing, which is consistent with previous studies[33,35,37]. The GMST and GMP increase consistently with CO_2 but continue to increase for about 10 and 20 years, respectively, after CO_2 peaks and show significant positive anomalies after CO_2 recovers. Such GMST and GMP hysteresis can be interpreted by the release of heat stored in the deep ocean[11,13,31]. The brief increase in GMP after CO_2 peaks is a consequence of rainfall sensitivity to CO_2 forcing through tropospheric adjustment processes[33].

However, compared to the GMP, SASM precipitation evolves quite differently. SASM precipitation is the area average of land rainfall over the domain (7.5–30.5°N, 73–90°E; see the red rectangles in Fig. 3). It increases during the CO_2 ramp-up period; after CO_2 peaks, it continues to increase for approximately a decade before diminishing rapidly; it overshoots an unperturbed level before CO_2 recovers to the PI (Fig. 2). We select two 40-year periods with the same CO_2 concentration to analyze the reversibility of SASM precipitation: year 21–60 in the CO_2 ramp-up period (hereafter RU) and year 220–259 in the CO_2 ramp-down period (hereafter RD; gray bands in Fig. 2). Precipitation increases consistently across the SASM region relative to the PI during the RU period (Fig. 3a), which agrees with the results under the global warming scenario[18,19,39]. During the RD period, precipitation over South Asia (SA) displays a "decreased-increased-decreased" tripolar response from southwest to northeast relative to the PI (Fig. 3b). Overall, despite the CO_2 concentration being the same in both periods, SA is significantly drier in the RD period than in the RU period (Fig. 3c). If we change the length of the two periods with equivalent CO_2 concentration levels to 30 years and 50 years, the asymmetric response of precipitation is still significant (Supplementary Fig. 1). Thus, the model simulations imply that if CDR is applied, SASM precipitation may gradually decline to a level below the unperturbed level when CO_2 recovers to the PI.

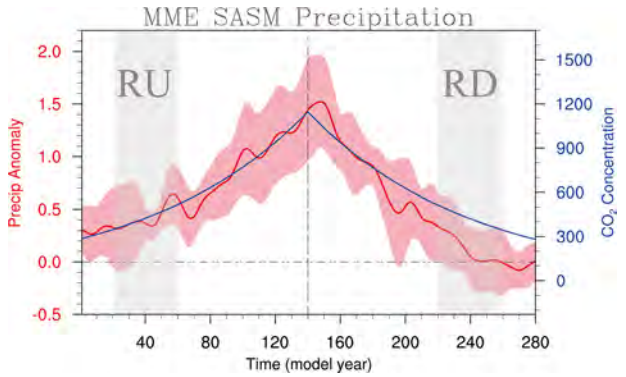

Fig. 2 The evolution of SASM precipitation in the idealized CO_2 ramp-up and ramp-down experiments. Time series of the CO_2 concentration (blue line; unit: ppm) and rainfall (red line; unit: mm day^{-1}) anomaly compared to PI. Pink shadings indicate the ensemble spread of the seven models. A 3-point (1/4,1/2,1/4) filter with 40 times is used to remove interannual variability. The vertical dotted line denotes the CO_2 peak year (Year 140). Two gray shadings in Year 21–60 (RU) and Year 220–259 (RD) indicate the two 40-year periods with the same average CO_2 concentration during the ramp-up and ramp-down periods.

Under global warming scenario, the precipitation change mainly comes from the contribution of the dynamic term related to the circulation and the thermodynamic term related to the moisture according to the moisture budget. To understand the asymmetric response of SASM precipitation, the simplified moisture budget equation is employed[40]:

$$\Delta P \sim -(\Delta\omega \cdot q + \Delta q \cdot \omega) \quad (1)$$

Where Δ represents the departure from the PI; P, ω and q are precipitation, pressure velocity at 500 hPa, and surface specific humidity, respectively. Horizontal moisture advection and quadratic (nonlinear processes) terms were omitted because they are insignificant compared with the thermodynamic and dynamic components in the tropics[25,40,41]. The sum of the thermodynamic and dynamic terms (Fig. 4c) resembles the contemporary precipitation distribution (Fig. 3c) with a small difference in magnitude, which indicates that the linear approximation of the moisture budget (Eq. 1) can well represent the total precipitation change. The thermodynamic component ($-\Delta q \cdot \omega$, Fig. 4a) shows increased precipitation over the region where ascent prevails climatologically. This can be explained by the "wet-get-wetter" mechanism. According to the Classius–Clapeyron equation, a higher GMST may lead to more water vapor in the atmosphere during the RD period than during the RU period (Fig. 1; Fig. 4d). Supposing that the ascent remained fixed, more water vapor may contribute to a wetter SA during the RD period (Fig. 4a). The results of the dynamic component ($-\Delta\omega \cdot q$, Fig. 4b) indicate that the weakening of the ascent (Fig. 4e) in SA leads to less precipitation during the RD period relative to the RU period, which is partly offset by the thermodynamic effect. Moreover, the spatial pattern of the dynamic component (Fig. 4b) resembles the contemporary precipitation change (Fig. 3c; Fig. 4c). This indicates that the asymmetric response of SASM precipitation is mainly the result of the dynamic component, which is dominated by changes in vertical motion.

Atmospheric circulation change and its driving mechanisms

We found that the asymmetric response of SASM precipitation mainly comes from the contribution of vertical circulation; therefore, the causes of change in vertical velocity are further explored. Figure 5 displays the difference in upper-level (200 hPa) velocity potential and divergence winds between the RU and RD periods. The large-scale circulation features a weakened Walker circulation. Over SA and MC, anomalous upper-level convergence favors local precipitation suppression (Fig. 3c). Divergence anomalies exist over the tropical central Pacific. The TWIO has increased rainfall (Fig. 3c) due to anomalous rising motion, and the delayed response of moisture (Fig. 4d) further strengthens such positive rainfall anomalies.

In the lower troposphere, an anomalous anticyclone is evident with its center in the northeastern part of SA during the RD period relative to the RU period (Fig. 6a). Via the effect of Ekman downwelling, the anomalous anticyclone contributes to a weakened ascent on the top of the planetary boundary layer, which also favors rainfall suppression over the SASM region. In addition, the anomalous easterlies (Fig. 6a) over southern SA hinder local southwesterly water vapor transport. Since the moisture is mainly confined in the lower troposphere, the pattern of the vertically integrated moisture flux (vectors in Fig. 6b) highly resembles the horizontal wind pattern at 850 hPa. The responses of atmospheric horizontal wind and vertical velocity over the SASM region are well coupled, which corresponds to the divergence of moisture flux suppressing rainfall (shadings in Fig. 6b).

What causes the asymmetric response of the SASM horizontal circulation? As shown in Fig. 3c, the decreased precipitation over the MC and the enhanced precipitation over the TWIO are hypothesized to be responsible. The suppressed precipitation over the MC induces an equatorial Rossby wave response with an anomalous anticyclone over SA[21,42]. The positive rainfall over the TWIO may induce an equatorial Kelvin wave response with easterly anomalies over southern SA. To test these hypotheses, we employed the LBM, which is widely used in studying tropical dynamics[43,44]. The climatology of the RU period is set as the model basic state since we focus on the asymmetric response between the RU and RD periods. The LBM is forced by (1) cooling over the MC (−10°S–0°, 90–130°E, Fig. 7a), with a maximum cooling rate of −2.67 K day^{-1}, and (2) heating over the TWIO (−10°S–10°N, 50–70°E, Fig. 7c), with a maximum heating rate of 2.67 K day^{-1}. The vertical profiles of atmospheric diabatic heating (cooling) follow the gamma distribution, and their maximum (minimum) is at $\sigma = 0.45$ (Fig. 7b, d).

The forced results of the LBM reproduced the key features of lower-level horizontal wind over SA well in the CMIP6 results (Fig. 7e). The cooling over the MC excites an equatorial Rossby wave response to its northwest. Over northeastern SA, a pronounced anomalous anticyclone occurs (Fig. 7a). The Rossby wave response is substantially stronger north than south of the equator due to the effects of monsoon easterly vertical shear mean flows[45,46]. The warming over the TWIO triggers an equatorial Kelvin wave response to its east. Easterly anomalies as part of the Kelvin wave response exist over southern SA (Fig. 7c). According to the theories of Matsuno[47] and Gill[48], in a resting basic state without mean flow, the Kelvin wave response is confined to the vicinity of the equator and shows remarkable symmetry with respect to the equator. However, because of the strong monsoon circulation, the low-level circulation shows a stronger response north of the equator, with a remarkable asymmetry[49]. Equatorial symmetry strengthens in the upper level (Supplementary Fig. 2). Therefore, the two numerical experiments support the hypothesis that the rainfall responses over the MC and TWIO induce weakened SASM circulation, including the anomalous anticyclone and easterly winds, which leads to drier condition over SA.

In addition to the forcings over the equatorial regions, the land–sea contrast may be responsible for the asymmetric responses of SASM precipitation during the two periods. Previous studies suggested that the land–sea thermal contrast plays a crucial role in SASM circulation changes[21,50]. Following their definitions, we use thicknesses between 200 and 500 hPa to represent the thermal conditions. The thickness anomalies center over the tropical western and central Indian Ocean (Fig. 8a). The stronger warming over the Indian Ocean leads to a weaker

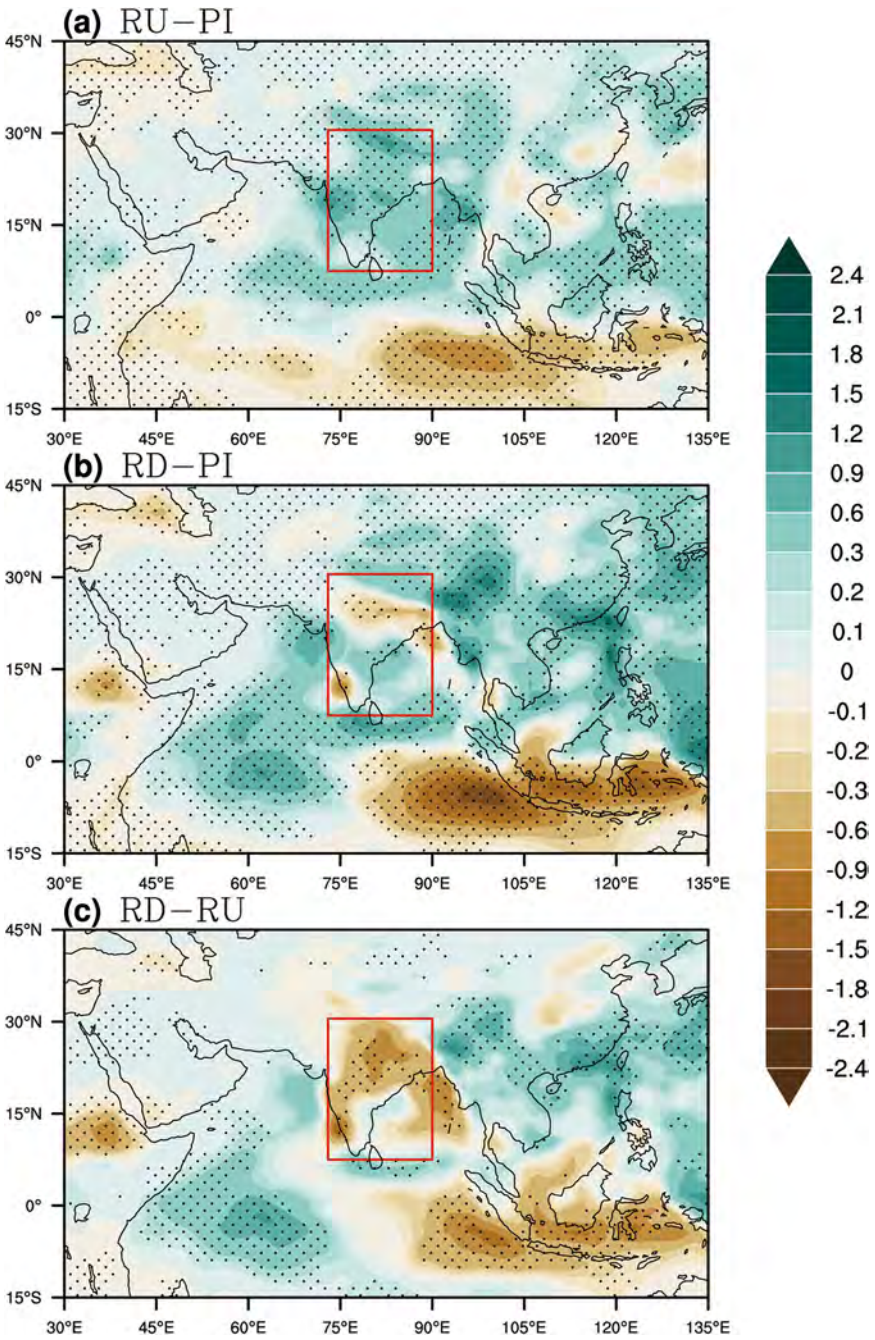

Fig. 3 The rainfall response (unit: mm day^{-1}) to the CO_2 forcing. The RU (**a**) and RD (**b**) periods rainfall anomalies compared to PI. **c** Difference in rainfall between the RU (20–60) and RD (220–259) periods. Black dots in (**a**, **b**) denotes the regions where more than 70% ensemble members agree with the sign of the MME. The regions denoted by the black dots in (**c**) indicate where the rainfall difference between the RU and RD periods are statistically significant at a 90% confidence level and more than 70% ensemble members agree with the sign of the MME. The red rectangles highlight the SASM region.

land–sea thermal contrast over the Indian Ocean and SA sector. We defined the land–sea thermal contrast index (TC_{upper}) as the difference of 200–500 hPa thickness between northern SA (20.5–40.5°N, 55–100°E; northern box in Fig. 8a) and the TWIO (10.5°S–10.5°N, 40–85°E; southern box in Fig. 8a). TC_{upper} decreases as the CO_2 concentration increases and shows noticeable inertia after CO_2 peaks (Fig. 8b). The inertia may be due to the strong warming over the TWIO during the RD period led by local enhanced latent heating (Fig. 3c). TC_{upper} during the RD period is markedly weaker than that in the RU period. The weaker land–sea thermal contrast decreases the baroclinicity in the troposphere and decreases the low-tropospheric westerly (Fig. 6a) and the upper-tropospheric easterly[51]. Finally, the weakened circulation leads to drier conditions over the SASM region during the RD period relative to the RU period.

The tropical SST response in the CO_2 ramp-up and ramp-down experiments

Under global warming scenario, the rainfall change over the Asian monsoon regions mainly consists of two components: the rapid adjustment associated with CO_2 radiative forcing and the slow

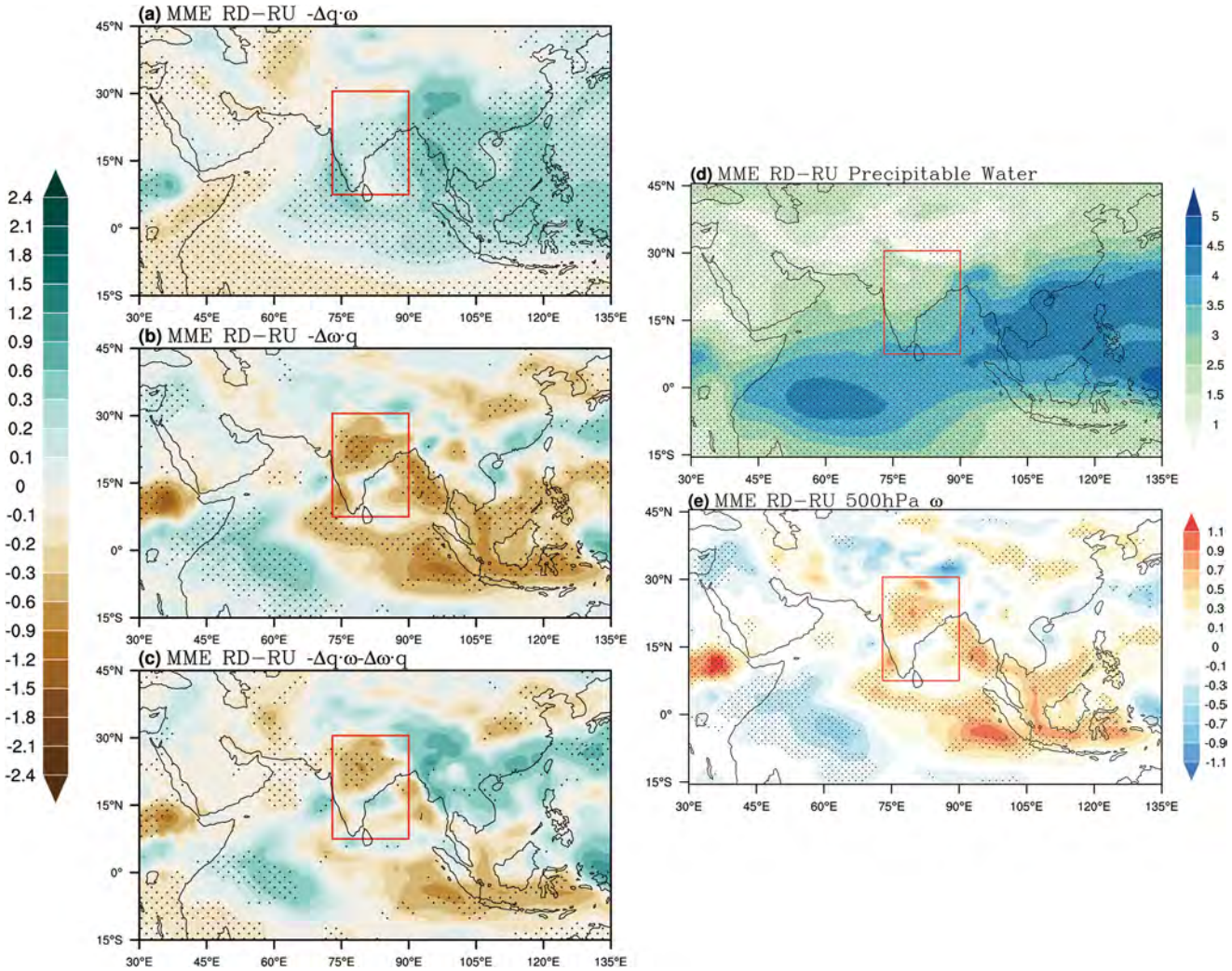

Fig. 4 The decomposition of the rainfall response. The difference in thermodynamic term (**a**), dynamic term (**b**), and both of them (**c**) between the RU and RD periods (unit: mm day^{-1}). **d**, **e** The same as in (**a**–**c**), but for the integration of specific humidity from the surface to 1 hPa (unit: kg m^{-2}) and pressure velocity at 500 hPa (unit: 10^{-2} Pa s^{-1}). The black dots denote the region in which at least 70% of models agree on the sign of the MME. The red rectangles highlight the SASM region.

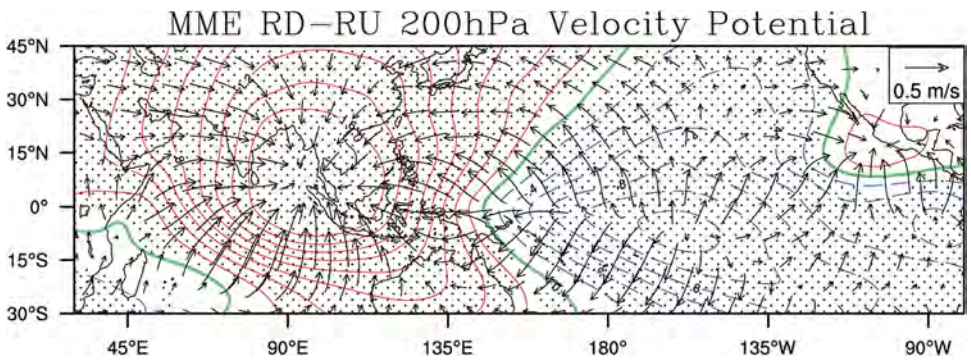

Fig. 5 The response of the velocity potential and divergence winds at 200 hPa. The difference in the velocity potential (color lines; unit: 10^6 m^2 s^{-1}) and divergence winds (vectors; unit: m s^{-1}) at 200 hPa between the RU and RD periods. The black dots denote the region in which at least 70% of models agree on the sign of the MME.

response associated with the SST changes[52,53]. The rapid adjustment has a timescale of less than one year and the slow response has a timescale of decades to millennia[1,8,54]. Under the scenario that the CO_2 concentration evolves symmetrically (1% CO_2 and 1%CO_2-CDR experiments), the rapid adjustment largely follows the evolution of the CO_2 concentration[10], making it difficult to produce the asymmetric response of SASM precipitation. In contrast, the contribution of the slow response lags the evolution of CO_2 concentration remarkably and dominates the total climate response during the CO_2 ramp-down period[10].

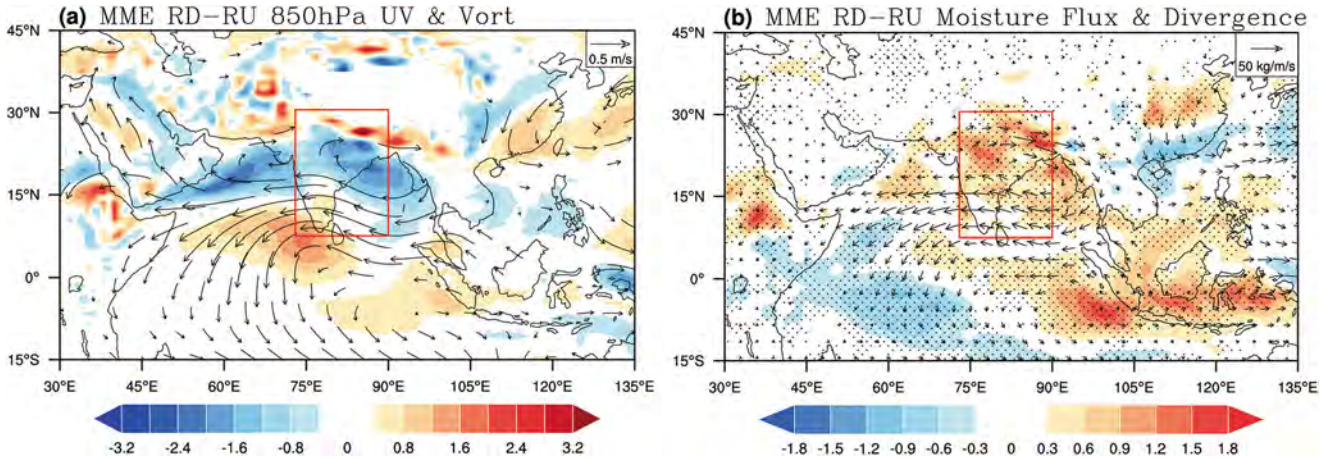

Fig. 6 The response of the low-level circulation and the moisture transport. a The difference in the pattern of the 850 hPa wind (vectors; unit: m s^{-1}) and vorticity (shadings; unit: 10^{-6} s^{-1}) between the RU and RD periods. **b** The same as in (**a**), but for vertically integrated moisture fluxes from the surface to 1 hPa (vectors; unit: 10^2 kg m^{-1} s^{-1}) and their divergence (shadings; unit: 10^{-5} kg m^{-2} s^{-1}). The black dots denote the region in which at least 70% of models agree on the sign of the MME. Vectors only exceeding 70% of model consistency are shown. The red rectangles highlight the SASM region.

In particular, the ocean continues to absorb heat after the CO_2 peaks[11,13]. Therefore, to understand the asymmetric response, it is necessary to analyze the SST response in the CO_2 ramp-up and ramp-down experiments.

The tropical Pacific and Indian Ocean SSTs all warmed (left panel in Fig. 9) and featured El Niño-like and Indian Ocean dipole (IOD)-like warming patterns (right panel in Fig. 9), respectively, in the RU and RD periods. Furthermore, the magnitude of SST warming over the tropics, as well as El Niño-like and IOD-like warming, is larger during the RD period than during the RU period (Fig. 9c, f). This indicates that the tropical SST displays an asymmetric response in the CO_2 ramp-up and ramp-down experiments, consistent with previous studies[12,55–57].

For the asymmetric response of El Niño-like warming in the tropical Pacific Ocean, the continued accumulation of heat in the ocean after the CO_2 peaks plays an important role[11,13]. During the RU period, the Walker circulation weakens due to temperature and precipitation constraints, accompanied by the decrease in upwelling intensity, which ultimately results in an El Niño-like warming in the tropical Pacific[25,26]. In addition, the upper ocean warms faster than the deep ocean (Fig. 10), resulting in a sharp increase in vertical temperature stratification; it transmits heat downward by thermal diffusion or other ocean dynamic processes, allowing the deep ocean to warm and accumulate heat. The faster warming in the upper ocean and the climatological upwelling contribute to a cooling in the central and eastern Pacific. But this effect is overwhelmed by the warming effect led by Walker circulation (its slowdown leads to anomalous westerlies and results in an anomalous warm horizontal advection)[34]. Thus, an El Niño-like warming occurs in the tropical Pacific. After the CO_2 peaks, the upper ocean continues to warm for about a decade and then begins to cool. In contrast, the deep ocean response is much slower, which continues to warm for about 70 years before it begins to cool. During the RD period, the deep ocean continues to warm and warms stronger than the upper (Fig. 10), which generally weakens the vertical temperature gradient and hence reduces the cooling effect led by the climatological upwelling in the central and eastern Pacific[58]. It contributes to an enhanced El Niño-like warming pattern during the RD period compared to the RU period.

The asymmetric response of the tropical SST affects the SASM rainfall via atmospheric circulation, showing drought in the RD period. During the RD period, the warmer SST (Fig. 9c) leads to more water vapor in the atmosphere (Fig. 4d) and a larger contribution of the thermodynamic component (Fig. 4a). Following an approximately moist adiabatic lapse rate, tropic-wide warming increases with height in the atmosphere[30,59,60], which leads to the enhanced warming center in the middle-to-upper troposphere over the Indian Ocean (Fig. 8a). Meanwhile, the enhanced El Niño-like and IOD-like warming patterns (Fig. 9f) cause the Walker circulation to weaken during the RD period (Fig. 5). Therefore, on the one hand, the decreased Walker circulation directly weakens the ascent in SA; on the other hand, it influences the rainfall in the MC and TWIO through anomalous convergence and divergence motion, thereby indirectly affecting SASM circulation. The contribution of the weakened circulation is stronger than the positive contribution of the thermodynamic component, which leads to the drier condition over the SASM region during the RD period compared to the RU period.

DISCUSSION

We investigated the response of SASM precipitation based on CO_2 ramp-up (1%CO_2) and ramp-down (1%CO2-CDR) experiments in CMIP6. The results show that if CDR is applied, SASM precipitation is largely reversible although it exhibits asymmetry about symmetric CO_2 forcing. Despite the CO_2 concentration being the same in the RU and RD periods, precipitation over the SASM region is significantly reduced during the RD period relative to the RU period. The diagnosis reveals that thermodynamic and dynamic components contribute oppositely: the thermodynamic effect favors the increased rainfall, while the dynamic effect favors the decreased rainfall. The asymmetric response of SASM precipitation in the CO_2 ramp-up and ramp-down experiments mainly originates from the dynamic effect (i.e., atmospheric circulation) rather than the thermodynamic effect (i.e., moisture change), which is different from that under the global warming scenario.

Subsequently, the possible mechanisms of anomalous atmospheric circulation are revealed. Figure 11 is a schematic diagram illustrating the key processes. Owning to the continued accumulation of heat in the ocean after the CO_2 peaks, which feedback to the surface ocean causing the asymmetric response of the SST[12,56,58]. Relative to the RU period, the tropical Pacific and Indian Ocean show stronger warming during the RD period, featuring an enhanced El Niño-like and IOD-like warming pattern, respectively. Following the moist adiabatic lapse rate, tropical-wide warming increases with height. The enhanced warming

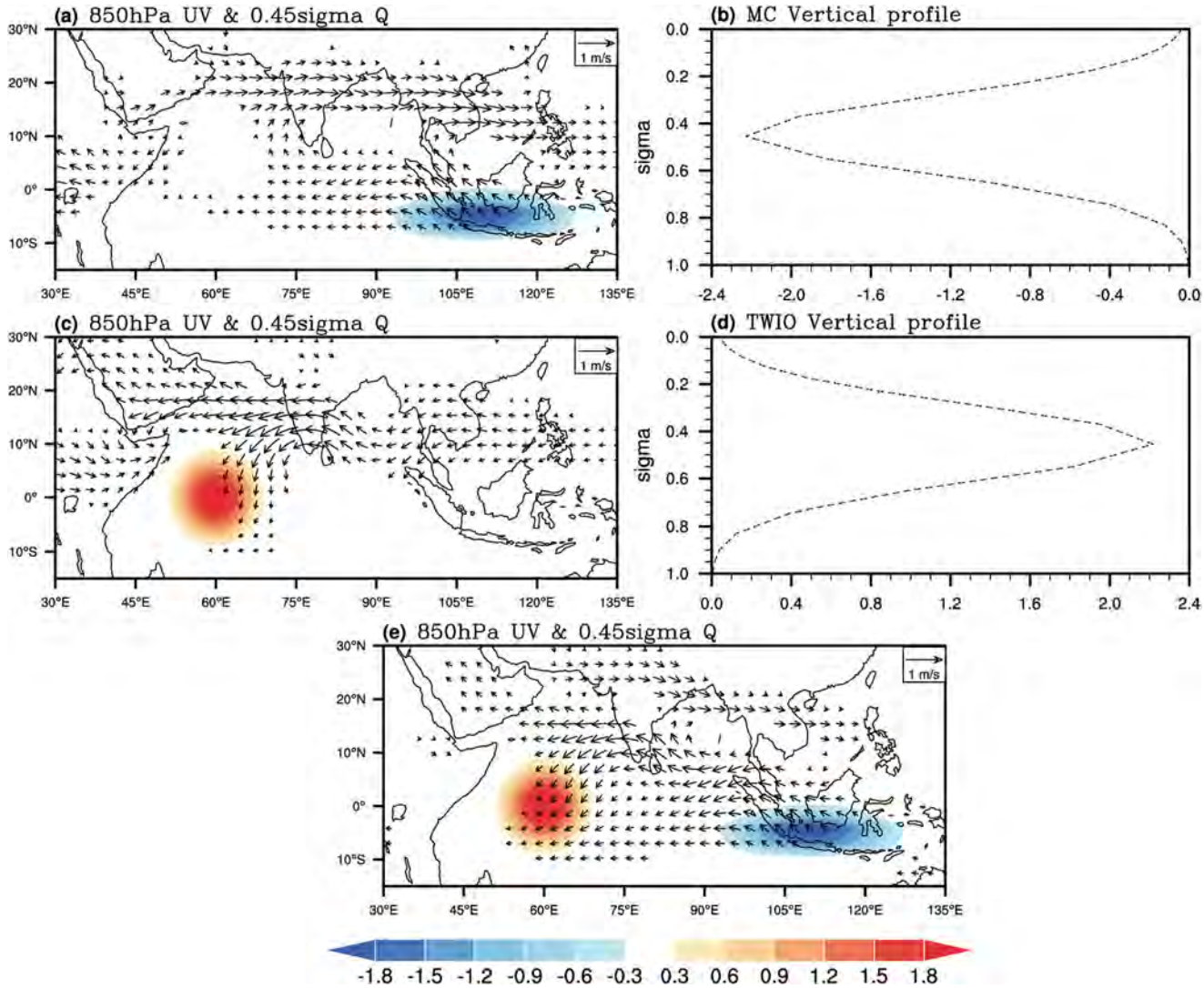

Fig. 7 The response of the LBM to the diabatic forcing. The response of the 850 hPa wind (vectors; unit: m s^{-1}) in the LBM, which is forced by the atmospheric diabatic heating (shadings; unit: K day^{-1}) over the MC (**a**), TWIO (**c**) and the sum of the two (**e**). **b**, **d** The vertical distribution of atmospheric diabatic heating over the TWIO and atmospheric diabatic cooling over the MC (unit: K day^{-1}). Wind speed changes less than 0.095 in (**a**), 0.075 in (**c**), and 0.085 in (**e**) are omitted.

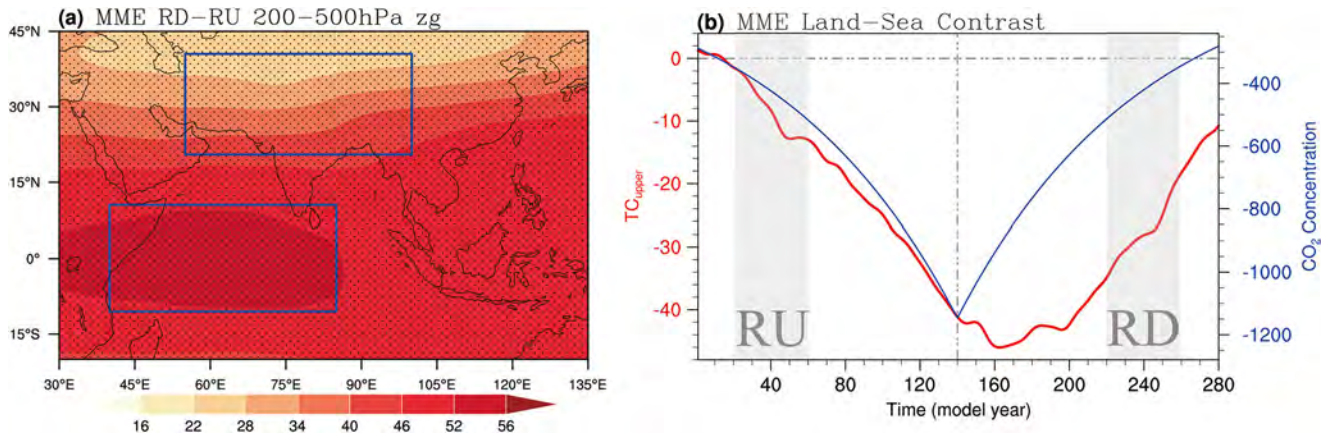

Fig. 8 The response of the thermal contrast. a The difference in 200–500 hPa thickness (shadings; unit: m) between the RU (21–60) and RD (220–259) periods. **b** Time series of the land–sea thermal contrast (TC_{upper}; red line; unit: m) and CO_2 concentration (blue line; unit: ppm). The 200–500 hPa thickness difference between the land (northern blue box in (**a**), 20.5°–40.5°N, 55°–100°E) and ocean (southern blue box in (**a**), −10.5°–10.5°N, 40°–85°E) is defined as the land–sea contrast index. A 3-point (1/4,1/2,1/4) filter with 40 times is performed on the land-sea contrast index. The atmospheric CO_2 concentration is multiplied by −1 to facilitate comparison.

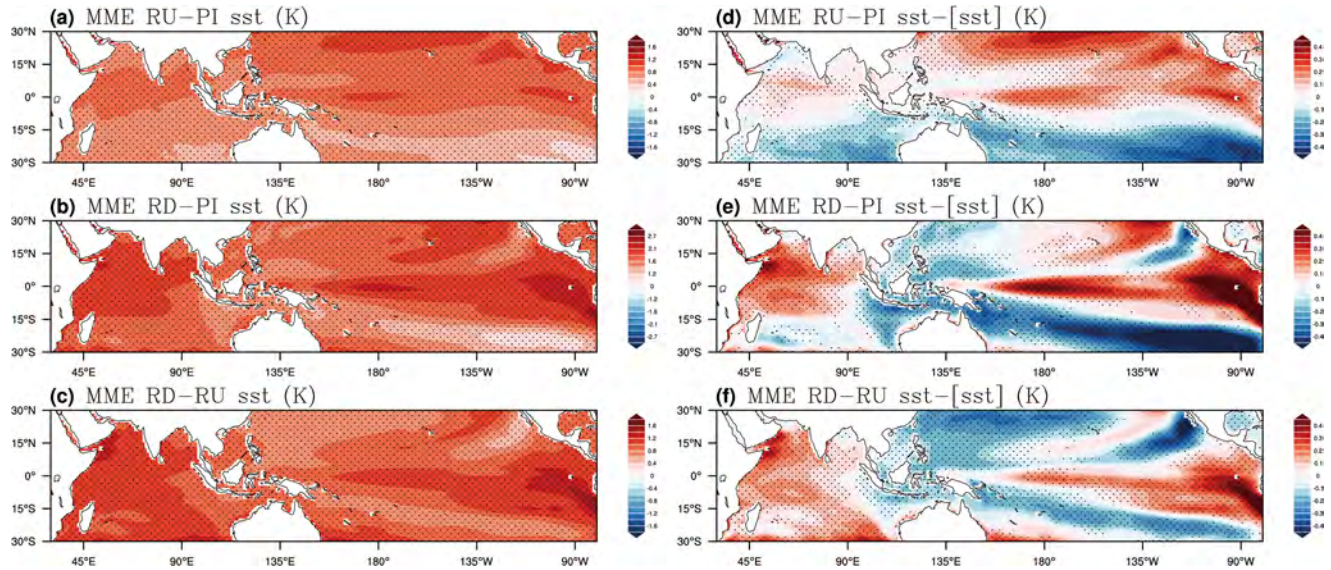

Fig. 9 The responses of SST (unit: K) in the CO_2 ramp-up and ramp-down experiments. a, **b** The SST anomalies during the RU (**a**) and RD (**b**) periods compared to PI, respectively. **c** The difference between the RU and RD periods. The right panel (**d**–**f**) is the same as the left panel, but with the tropical mean SST removed. The black dots denote the region in which at least 70% of models agree on the sign of the MME.

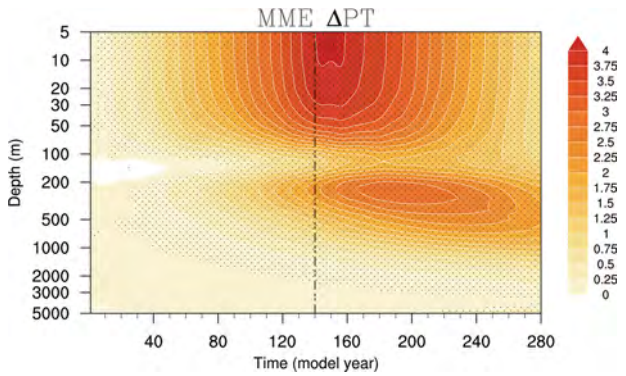

Fig. 10 The response of the oceanic potential temperature. Time evolution of tropical Pacific Ocean mean (−10.5°S–10.5°N, 180°–100°W) potential temperature change (Δ*PT*; unit: °C) profile in CO_2 ramp-up and ramp-down experiments at all depths, based on repeated application of 3-point (1/4, 1/2, 1/4) filter with 40 times. Δ*PT* is relative to the PI. The black dashed line indicates the CO_2 peak year (Year 140). Black dots indicate more than 70% ensemble members agree with the sign of the MME. Note that the vertical depth coordinate is logarithmic.

center over the Indian Ocean weakens the SA-Indian Ocean thermal and thus SASM circulation. The uneven enhanced warming leads to anomalous sinking, as well as decreased precipitation over the SASM region directly. Additionally, over the Pacific and Indian Ocean sectors, the weakened Walker circulation affects SASM circulation indirectly. It suppresses the rainfall over the MC and increases the rainfall over the TWIO. The suppressed precipitation over the MC triggers an equatorial Rossby wave response to generate an anomalous lower-level anticyclone, which weakens the ascent on the top of the planetary boundary layer, via the effect of Ekman downwelling. The increased rainfall over the TWIO triggers an equatorial Kelvin wave response to hinder water vapor transport to SA. The enhanced IOD-like warming pattern may reinforce the anomalous easterly over the tropical Indian Ocean and further weaken water vapor transport. The combination of the weakened ascent and water vapor transport caused by the enhanced uneven SST warming leads to the asymmetric response of SASM precipitation.

In the present study, our results are mainly based on the MME of seven models participating in the 1%CO_2 and 1%CO_2-CDR experiments. Compared to studies based on a single model, the MME analysis can partially exclude the model-dependent response and the role of internal variabilities in the climate system, indicating the robustness of the asymmetric response to SASM precipitation. This study systematically reveals the prominent dynamic processes (e.g., equatorial waves) in the formation of the asymmetric response of SASM precipitation. In particular, we highlight the role of atmospheric thermal forcings on SASM circulation induced by uneven tropical SST warming. These important thermal forcings, including rainfall anomalies over the MC and TWIO, have not been mentioned by previous studies concerning the asymmetric response of SASM precipitation. However, we cannot completely eliminate model dependence due to the limited number of models, which may disturb the response of SASM precipitation under the CDR scenario. The internal variabilities of the climate system, such as the Interdecadal Pacific Oscillation and Atlantic Multidecadal Oscillation, are associated with the SASM[61–63]. Despite this, it is necessary to understand the sources of model uncertainty and the effects of internal variabilities in future studies. In addition to this, the detailed processes leading to an enhanced IOD-like warming pattern during the RD period compared to the RU period remain to be understood. We infer that this may be related to the slow recovery of Walker circulation and the enhanced El Niño-like warming pattern during the RD period.

Although the scenario used in this study is idealized, it is useful for exploring the reversibility and hysteresis of the climate system, especially in providing insight into the CDR scenario. It is noteworthy that SASM precipitation overshoots the unperturbed level before the CO_2 concentration returns to PI. This indicates that the symmetric CDR may increase the risk of drought and may affect water management in the SASM region. This gives us a hint that one should consider the side effects of climate mitigation when making climate change policies.

METHODS

Observation and reanalysis datasets

The observational and reanalysis data used in the present study include (1) the Global Precipitation Climatology Project (GPCP)

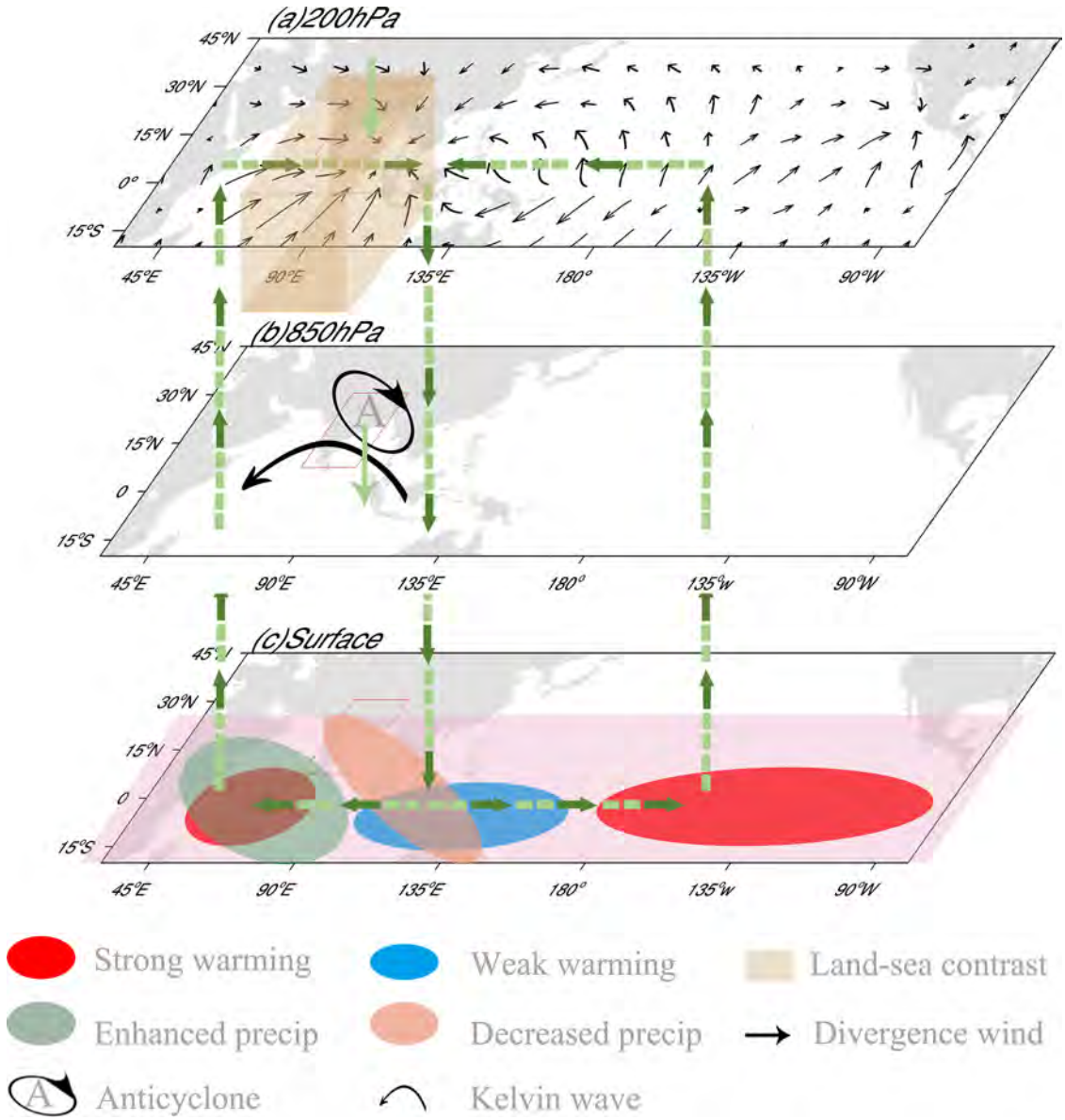

Fig. 11 Schematic diagram showing the key processes involved in the asymmetric response of SASM precipitation under the CDR scenario. The processes at the 200 hPa (**a**), 850 hPa (**b**), and surface (**c**), respectively.

monthly precipitation dataset[64]; (2) the National Centers for Environmental Prediction-Department of Energy (NCEP-DOE) reanalysis[65]; and (3) the Hadley Center Global Sea Surface Temperature (HadISST) dataset[66]. All the above datasets cover 1979–2014.

CMIP6 model datasets

The present study is mainly based on the monthly outputs of the following experiments (Supplementary Table 1) of CMIP6: (1) historical experiment, in which time-dependent observed anthropogenic and natural forcings are specified to reflect observational estimates valid for the historical period (i.e., 1850–2014)[67]; (2) pre-industrial control (piControl) experiment (global mean atmospheric CO_2 concentration of 284.7 ppm), started from initial conditions obtained from a spin-up with the same, which should ideally represent a near-equilibrium state of the climate system under imposed year 1850 conditions[67]; (3) 1%CO_2 experiment, in which the climate (including CO_2 concentration) initiates from the end of the piControl experiment and the CO_2 concentration gradually increases at a rate of 1% per year for 140 years until it quadruples (i.e., 1138.8 ppm; all other forcing is kept at that of the year 1850)[67], which is named the ramp-up period; and (4) 1%CO_2-CDR experiment, in which the climate (including CO_2 concentration) initiates from the end of the 1%CO_2 experiment and the evolution of CO_2 concentration is the mirror of that in the 1%CO_2 experiment (all other forcing is kept at that of the year 1850), which is named the ramp-down period[15]. The evolution of the CO_2 concentration in the 1%CO_2 and 1%CO_2-CDR experiments is displayed in Fig. 1a. The total time of these two experiments is 280 years (140 years for ramp-up and 140 years for ramp-down). Seven models (ACCESS-ESM1-5, CanESM5, CNRM-ESM2-1, GFDL-ESM4, MIROC-ES2L, NorESM1-LM, and UKESM1-0-LL) participated in the present study (Supplementary Table 2). CESM2 is excluded because the differences between ramp-down and ramp-up periods are exaggerated (Supplementary Fig. 3). If it is involved in the calculation, the MME is dominated by the results of CESM2. UKESM1-0-LL does not participate in vertical-velocity-associated calculations due to data unavailability.

To obtain the MME, the outputs are regridded to a common 1° × 1° grid. We consider the results to be robust when more than 70% of the models (5 out of 7) agree on the sign of the MME. For convenience, we defined the 1st year of the 1%CO_2 experiments as Year 1. To examine the reversibility of SASM precipitation, we select two periods during which the mean CO_2 concentration is identical: CO_2 ramp-up (year 21–60; RU) and ramp-down (year 220–259; RD) periods. It is reasonable to choose the periods at the beginning of the CO_2 ramp-up and the end of the CO_2 ramp-down. However, to increase the magnitude of the response signal, we shift these two periods to the middle by 20 years. A repeated application of the 3-point filter is used to remove interannual variability, and the results do not fundamentally change when the 21-year running mean is applied. The two-sided Student's *t-test* is used to evaluate the statistical significance of the difference. The climatology of the last 100 years in the piControl experiment is defined as the baseline (PI). The analysis focuses on the average boreal summer (June–August) because the precipitation over South Asia is mainly concentrated in summer[68].

Model evaluation

Before analyzing the response of SASM precipitation to CO_2 forcing, we examine the performance of models based on the CMIP6 MME. SASM precipitation and its associated variables are compared and examined (Supplementary Fig. 4). The CMIP6 MME can grasp the spatial distribution of variables, but with slight differences in magnitude. The spatial correlation coefficients of the individual models with reanalysis all exceed 0.71, and those of the CMIP6 MME all exceed 0.84 (Supplementary Fig. 5). Overall, the CMIP6 MME is capable of investigating the SASM response to CO_2 forcing.

The Linear Baroclinic Model

To investigate the effects of heat forcing on the atmosphere, the Linear Baroclinic Model (LBM) is employed. This model has 20 vertical levels based on the sigma coordinate system and a horizontal resolution of T42. The horizontal diffusion has an *e*-folding decay time of 6 h for the largest wavenumber. The Rayleigh friction and Newtonian damping have a time-scale of 1 day^{-1} for sigma levels below 0.9, 5 day^{-1} for sigma levels of 0.89, 15 day^{-1} for sigma levels of 0.83, 30 day^{-1} for sigma levels between 0.83 and 0.03, and 1 day^{-1} for sigma levels above 0.03. Further information on the model is given in Watanabe and Kimoto (2000)[69]. In the present study, the model is integrated for 36 days, and the average from 25 to 35 days is displayed.

DATA AVAILABILITY

The CMIP6 outputs are available online at https://esgf-node.llnl.gov/projects/cmip6/. The observational and reanalysis data that examine the performance of models are openly available at https://psl.noaa.gov/data/gridded/data.gpcp.html (GPCP), https://psl.noaa.gov/data/gridded/data.ncep.reanalysis2.pressure.html (NCEP-DOE) and https://www.metoffice.gov.uk/hadobs/hadisst/data/download.html (HadISST). The LBM is available online at https://ccsr.aori.u-tokyo.ac.jp/~lbm/sub/lbm_4.html.

Received: 21 June 2022; Accepted: 8 February 2023;
Published online: 20 February 2023

REFERENCES

1. IPCC. *Climate Change 2021: The Physical Science Basis. Contribution of Working Group I to the Sixth Assessment Report of the Intergovernmental Panel on Climate Change* (eds Masson-Delmotte, V. et al.) (Cambridge University Press, 2021).
2. Field, C. B. & Mach, K. J. Rightsizing carbon dioxide removal. *Science* **356**, 706–707 (2017).
3. Fuss, S. et al. Betting on negative emissions. *Nat. Clim. Change* **4**, 850–853 (2014).
4. Realmonte, G. et al. An inter-model assessment of the role of direct air capture in deep mitigation pathways. *Nat. Commun.* **10**, 3277 (2019).
5. Rogelj, J. et al. Scenarios towards limiting global mean temperature increase below 1.5 °C. *Nat. Clim. Change* **8**, 325–332 (2018).
6. Zickfeld, K., Azevedo, D., Mathesius, S. & Matthews, H. D. Asymmetry in the climate-carbon cycle response to positive and negative CO2 emissions. *Nat. Clim. Change* **11**, 613–617 (2021).
7. von Schuckmann, K. et al. An imperative to monitor Earth's energy imbalance. *Nat. Clim. Change* **6**, 138–144 (2016).
8. Zappa, G., Ceppi, P. & Shepherd, T. G. Time-evolving sea-surface warming patterns modulate the climate change response of subtropical precipitation over land. *Proc. Natl Acad. Sci. USA* **117**, 4539–4545 (2020).
9. Monerie, P.-A., Pohl, B. & Gaetani, M. The fast response of Sahel precipitation to climate change allows effective mitigation action. *npj Clim. Atmos. Sci.* **4**, 1–8 (2021).
10. Zhou, S., Huang, P., Xie, S.-P., Huang, G. & Wang, L. Varying contributions of fast and slow responses cause asymmetric tropical rainfall change between CO2 ramp-up and ramp-down. *Sci. Bull.* **67**, 1702–1711 (2022).
11. Yeh, S. W., Song, S. Y., Allan, R. P., An, S. I. & Shin, J. Contrasting response of hydrological cycle over land and ocean to a changing CO2 pathway. *npj Clim. Atmos. Sci.* **4**, 1–8 (2021).
12. Chadwick, R., Wu, P., Good, P. & Andrews, T. Asymmetries in tropical rainfall and circulation patterns in idealised CO_2 removal experiments. *Clim. Dyn.* **40**, 295–316 (2012).
13. Wu, P., Wood, R., Ridley, J. & Lowe, J. Temporary acceleration of the hydrological cycle in response to a CO2 rampdown. *Geophys. Res. Lett.* **37**, L12705 (2010).
14. Huang, G. et al. Critical climate issues toward carbon neutrality targets. *Fundam. Res.* **2**, 396–400 (2022).
15. Keller, D. P. et al. The Carbon Dioxide Removal Model Intercomparison Project (CDRMIP): rationale and experimental protocol for CMIP6. *Geosci. Model Dev.* **11**, 1133–1160 (2018).
16. Singh, D., Tsiang, M., Rajaratnam, B. & Diffenbaugh, N. S. Observed changes in extreme wet and dry spells during the South Asian summer monsoon season. *Nat. Clim. Change* **4**, 456–461 (2014).
17. Turner, A. G. & Annamalai, H. Climate change and the South Asian summer monsoon. *Nat. Clim. Change* **2**, 587–595 (2012).
18. Li, G., Xie, S. P., He, C. & Chen, Z. S. Western Pacific emergent constraint lowers projected increase in Indian summer monsoon rainfall. *Nat. Clim. Change* **7**, 708–712 (2017).
19. Rajesh, P. V. & Goswami, B. N. A new emergent constraint corrected projections of Indian summer monsoon rainfall. *Geophys. Res. Lett.* **49**, e2021GL096671 (2022).
20. Douville, H. & Royer, J.-F. Impact of CO_2 doubling on the Asian summer monsoon robust cersus model-dependent responses. *J. Meteorol. Soc. Jpn.* **78**, 421–439 (2000).
21. Li, Z. B., Sun, Y., Li, T., Chen, W. & Ding, Y. H. Projections of South Asian summer monsoon under Global Warming from 1.5 degrees to 5 degrees C. *J. Clim.* **34**, 7913–7926 (2021).
22. Maharana, P., Dimri, A. P. & Choudhary, A. Future changes in Indian summer monsoon characteristics under 1.5 and 2 °C specific warming levels. *Clim. Dyn.* **54**, 507–523 (2019).
23. Ueda, H., Iwai, A., Kuwako, K. & Hori, M. E. Impact of anthropogenic forcing on the Asian summer monsoon as simulated by eight GCMs. *Geophys. Res. Lett.* **33**, L06703 (2006).
24. Endo, H. & Kitoh, A. Thermodynamic and dynamic effects on regional monsoon rainfall changes in a warmer climate. *Geophys. Res. Lett.* **41**, 1704–1711 (2014).
25. Held, I. M. & Soden, B. J. Robust responses of the hydrological cycle to global warming. *J. Clim.* **19**, 5686–5699 (2006).
26. Vecchi, G. A. & Soden, B. J. Global warming and the weakening of the tropical circulation. *J. Clim.* **20**, 4316–4340 (2007).
27. Ma, J. & Yu, J.-Y. Paradox in South Asian summer monsoon circulation change: lower tropospheric strengthening and upper tropospheric weakening. *Geophys. Res. Lett.* **41**, 2934–2940 (2014).
28. Wang, B., Yim, S.-Y., Lee, J.-Y., Liu, J. & Ha, K.-J. Future change of Asian-Australian monsoon under RCP 4.5 anthropogenic warming scenario. *Clim. Dyn.* **42**, 83–100 (2013).
29. Sun, Y., Ding, Y. H. & Dai, A. G. Changing links between South Asian summer monsoon circulation and tropospheric land-sea thermal contrasts under a warming scenario. *Geophys. Res. Lett.* **37**, L02704 (2010).
30. Ma, J., Xie, S. P. & Kosaka, Y. Mechanisms for tropical tropospheric circulation change in response to global warming. *J. Clim.* **25**, 2979–2994 (2012).
31. Wu, P., Ridley, J., Pardaens, A., Levine, R. & Lowe, J. The reversibility of CO_2 induced climate change. *Clim. Dyn.* **45**, 745–754 (2014).
32. Abe, M., Shiogama, H., Yokohata, T., Emori, S. & Nozawa, T. Asymmetric impact of the physiological effect of carbon dioxide on hydrological responses to instantaneous negative and positive CO_2 forcing. *Clim. Dyn.* **45**, 2181–2192 (2015).
33. Cao, L., Bala, G. & Caldeira, K. Why is there a short-term increase in global precipitation in response to diminished CO2 forcing? *Geophys. Res. Lett.* **38**, L06703 (2011).

34. Song, S. Y. et al. Asymmetrical response of summer rainfall in East Asia to CO_2 forcing. *Sci. Bull.* **67**, 213–222 (2022).
35. Sun, M.-A. et al. Reversibility of the hydrological response in East Asia from CO_2-derived climate change based on CMIP6 simulation. *Atmosphere* **12**, 72 (2021).
36. Boucher, O. et al. Reversibility in an Earth System model in response to CO_2 concentration changes. *Environ. Res. Lett.* **7**, 024013 (2012).
37. Kug, J. S. et al. Hysteresis of the intertropical convergence zone to CO_2 forcing. *Nat. Clim. Change* **12**, 47–53 (2022).
38. Oh, H. et al. Contrasting hysteresis behaviors of Northern hemisphere land monsoon precipitation to CO_2 pathways. *Earth's Future* **10**, e2021EF002623 (2022).
39. Bhowmick, M., Mishra, S. K., Kravitz, B., Sahany, S. & Salunke, P. Response of the Indian summer monsoon to global warming, solar geoengineering and its termination. *Sci. Rep.* **11**, 9791 (2021).
40. Huang, P., Xie, S. P., Hu, K. M., Huang, G. & Huang, R. H. Patterns of the seasonal response of tropical rainfall to global warming. *Nat. Geosci.* **6**, 357–361 (2013).
41. Seager, R., Naik, N. & Vecchi, G. A. Thermodynamic and dynamic mechanisms for large-scale changes in the hydrological cycle in response to global warming. *J. Clim.* **23**, 4651–4668 (2010).
42. Wang, B., Wu, R. G. & Li, T. Atmosphere-warm ocean interaction and its impacts on Asian-Australian monsoon variation. *J. Clim.* **16**, 1195–1211 (2003).
43. Hu, K. M., Huang, G., Xie, S. P. & Long, S. M. Effect of the mean flow on the anomalous anticyclone over the Indo-Northwest Pacific in post-El Nino summers. *Clim. Dyn.* **53**, 5725–5741 (2019).
44. Hu, P. et al. Close linkage of the South China sea summer monsoon onset and extreme rainfall in May over Southeast Asia: role of the synoptic-scale systems. *J. Clim.* **35**, 4347–4362 (2022).
45. Wang, B. & Xie, X. Low-frequency equatorial waves in vertically sheared zonal flow. Part I: Stable waves. *J. Atmos. Sci.* **53**, 449–467 (1996).
46. Xie, X. & Wang, B. Low-frequency equatorial waves in vertically sheared zonal flow. Part II: Unstable waves. *J. Atmos. Sci.* **53**, 3589–3605 (1996).
47. Matsuno, T. Quasigeostrophic motions in the equatorial area. *J. Meteorol. Soc. Jpn.* **44**, 25–43 (1966).
48. Gill, A. E. Some simple solutions for heat-induced tropical circulation. *Q. J. R. Meteorol. Soc.* **106**, 447–462 (1980).
49. Xie, S. P. et al. Indian Ocean capacitor effect on Indo-Western Pacific climate during the summer following El Nino. *J. Clim.* **22**, 730–747 (2009).
50. Dai, A. G. et al. The relative roles of upper and lower tropospheric thermal contrasts and tropical influences in driving Asian summer monsoons. *J. Geophys. Res.: Atmos.* **118**, 7024–7045 (2013).
51. Luo, X. Q., Xu, J. J. & Li, K. Discrepancies oft upper troposphere summer thermal contrast between Tibetan Plateau and tropical Indian Ocean in multiple data. *Front. Environ. Sci.* **9**, 655521 (2021).
52. Endo, H., Kitoh, A. & Ueda, H. A unique feature of the Asian summer monsoon response to global warming: the role of different land-sea thermal contrast change between the lower and upper troposphere. *Sci. Online Lett. Atmos.* **14**, 57–63 (2018).
53. Li, X. Q. & Ting, M. F. Understanding the Asian summer monsoon response to greenhouse warming: the relative roles of direct radiative forcing and sea surface temperature change. *Clim. Dyn.* **49**, 2863–2880 (2017).
54. Bony, S. et al. Robust direct effect of carbon dioxide on tropical circulation and regional precipitation. *Nat. Geosci.* **6**, 447–451 (2013).
55. An, S.-I. et al. Intensity changes of Indian Ocean dipole mode in a carbon dioxide removal scenario. *npj Clim. Atmos. Sci.* **5**, 1–8 (2022).
56. Long, S.-M., Xie, S.-P., Zheng, X.-T. & Liu, Q. Fast and slow responses to global warming: sea surface temperature and precipitation patterns. *J. Clim.* **27**, 285–299 (2014).
57. Ohba, M., Tsutsui, J. & Nohara, D. Statistical parameterization expressing ENSO variability and reversibility in response to CO_2 concentration changes. *J. Clim.* **27**, 398–410 (2014).
58. Long, S. M. et al. Effects of ocean slow response under low warming targets. *J. Clim.* **33**, 477–496 (2020).
59. Chen, X. L. & Zhou, T. J. Distinct effects of global mean warming and regional sea surface warming pattern on projected uncertainty in the South Asian summer monsoon. *Geophys. Res. Lett.* **42**, 9433–9439 (2015).
60. Knutson, T. R. & Manabe, S. Mean response over the tropical Pacific to increased CO_2 in a coupled ocean-atmosphere model. *J. Clim.* **8**, 2181–2199 (1995).
61. Chinta, V., Chen, Z. S., Du, Y. & Chowdary, J. S. Influence of the interdecadal Pacific Oscillation on South Asian and East Asian summer monsoon rainfall in CMIP6 models. *Clim. Dyn.* **58**, 1791–1809 (2022).
62. Huang, X. et al. South Asian summer monsoon projections constrained by the interdecadal Pacific oscillation. *Sci. Adv.* **6**, eaay6546 (2020).
63. Sandeep, N. et al. On the weakening association between South Asian Monsoon and Atlantic Multidecadal Oscillation. *Clim. Dyn.* **59**, 2531–2547 (2022).
64. Adler, R. F. et al. The version-2 global precipitation climatology project (GPCP) monthly precipitation analysis (1979-present). *J. Hydrometeorol.* **4**, 1147–1167 (2003).
65. Kanamitsu, M. et al. NCEP-DOE AMIP-II reanalysis (R-2). *Bull. Am. Meteorol. Soc.* **83**, 1631–1643 (2002).
66. Rayner, N. A. et al. Global analyses of sea surface temperature, sea ice, and night marine air temperature since the late nineteenth century. *J. Geophys. Res.: Atmos.* **108**, 4407 (2003).
67. Eyring, V. et al. Overview of the Coupled Model Intercomparison Project Phase 6 (CMIP6) experimental design and organization. *Geosci. Model Dev.* **9**, 1937–1958 (2016).
68. Bollasina, M. A. HYDROLOGY Probing the monsoon pulse. *Nat. Clim. Change* **4**, 422–423 (2014).
69. Watanabe, M. & Kimoto, M. Atmosphere-ocean thermal coupling in the North Atlantic: a positive feedback. *Q. J. R. Meteorol. Soc.* **126**, 3343–3369 (2000).

ACKNOWLEDGEMENTS

We acknowledge the World Climate Research Program, which, through its Working Group on Coupled Modeling, coordinated and promoted CMIP6. We thank the climate modeling groups for producing and making available their model output, the Earth System Grid Federation (ESGF) for archiving the data and providing access, and the multiple funding agencies who support CMIP6 and ESGF. Suqin Zhang thanks Hongyu Hou of the Institute of Atmospheric Physics for helping to solve the LBM-related problems. The study was supported by the National Natural Science Foundation of China (NSFC; 42141019, 42175055, 41831175), the Second Tibetan Plateau Scientific Expedition and Research program (2019QZKK0102), and project of Key Laboratory of Meteorological Disaster, Ministry of Education & Collaborative Innovation Center on Forecast and Evaluation of Meteorological Disasters, Nanjing University of Information Science & Technology (KLME202111).

AUTHOR CONTRIBUTIONS

S.Z.: Investigation, data Curation, formal analysis, drafted the manuscript, writing review, and editing. X.Q.: Conceptualization, methodology, formal analysis, writing review, and editing. G.H.: Conceptualization, supervision, funding acquisition, project administration. P.H.: Methodology, formal analysis, writing review, and editing. All authors contributed to the discussion.

COMPETING INTERESTS

The authors declare no competing interests.

ADDITIONAL INFORMATION

Supplementary information The online version contains supplementary material available at https://doi.org/10.1038/s41612-023-00338-x.

Correspondence and requests for materials should be addressed to Xia Qu or Gang Huang.

Reprints and permission information is available at http://www.nature.com/reprints

Publisher's note Springer Nature remains neutral with regard to jurisdictional claims in published maps and institutional affiliations.

Open Access This article is licensed under a Creative Commons Attribution 4.0 International License, which permits use, sharing, adaptation, distribution and reproduction in any medium or format, as long as you give appropriate credit to the original author(s) and the source, provide a link to the Creative Commons license, and indicate if changes were made. The images or other third party material in this article are included in the article's Creative Commons license, unless indicated otherwise in a credit line to the material. If material is not included in the article's Creative Commons license and your intended use is not permitted by statutory regulation or exceeds the permitted use, you will need to obtain permission directly from the copyright holder. To view a copy of this license, visit http://creativecommons.org/licenses/by/4.0/.

© The Author(s) 2023

nature communications

Article

https://doi.org/10.1038/s41467-023-36053-7

Greenhouse warming and internal variability increase extreme and central Pacific El Niño frequency since 1980

Received: 7 June 2022

Accepted: 13 January 2023

Published online: 24 January 2023

Check for updates

Ruyu Gan[1,2,3], Qi Liu[4,5] ✉, Gang Huang[1,2,3] ✉, Kaiming Hu[1,6] & Xichen Li[7]

El Niño has been recorded to change its properties since the 1980s, characterized by more common extreme El Niño and Central Pacific (CP) El Niño events. However, it is still unclear whether such change is externally forced or part of the natural variability. Here, we find that the frequency of the extreme and CP El Niño events also increased during the period 1875–1905, when the anthropogenic CO2 concentration was relatively lower, but with a positive phase of the Atlantic Multidecadal Oscillation (AMO). Models and palaeoclimate proxies reveal that a positive AMO enhances the zonal sea surface temperature gradient in the CP, which strengthens zonal advective feedback, favoring extreme and CP El Niño development. Moreover, we estimate that internal variability contributed to ~65% of the increasingly extreme and CP El Niño events, while anthropogenic forcing has made our globe experience ~1 more extreme and ~2 more CP events over the past four decades.

El Niño, the warm phase of the most dominant interannual climate variability, has changed its behavior since the 1980s[1–4]. Extreme El Niño events have occurred frequently in the past 40 years, at a rate of one event per 13 years, usually causing reorganizations of atmospheric convection and inducing severe climatic disruptions around the globe, such as disastrous floods and droughts across the Pacific region[5–7]. At the same time, the Central Pacific (CP) El Niño[8–10] (also termed the Dateline El Niño[11], El Niño Modoki[12], or warm pool El Niño[13]), which is characterized by the peak ocean warming in the central equatorial Pacific, has become more common[13–16] and the canonical Eastern Pacific (EP) El Niño, which is characterized by the strongest sea surface temperature anomalies (SSTA) located in the far eastern equatorial Pacific, has become less frequent[8–10,12]. The movement of the sea surface temperature (SST) anomaly center shifts atmospheric circulation and convection, causing different climate impacts around the globe[9,11,14,17].

Several studies using climate models have projected that El Niño amplitude increases[7] and CP El Niño variability increases[14] under greenhouse warming and have suspected that the observed El Niño behavior changes could be a consequence of anthropogenic warming. With the buildup of greenhouse gases, the eastern equatorial Pacific warmed faster than the surrounding regions, and the thermocline in the equatorial Pacific flattened, facilitating more occurrences of extreme El Niño and CP El Niño events[7,14]. The enhanced response of atmospheric vapor to air temperature under greenhouse warming also increases the extreme El Niño[18]. Multiple palaeo-El Niño proxies also provide evidence for the impact of the climate change on the observed change in El Niño properties. These include enhanced El Niño variability during the late twentieth century relative to the preindustrial period[15,19–21] and more frequent CP events in recent decades relative to the preindustrial era[15,22]. In addition to anthropogenic forcing, natural

[1]State Key Laboratory of Numerical Modeling for Atmospheric Sciences and Geophysical Fluid Dynamics, Institute of Atmospheric Physics, Chinese Academy of Sciences, Beijing, China. [2]Laboratory for Regional Oceanography and Numerical Modeling, Qingdao National Laboratory for Marine Science and Technology, Qingdao 266237, China. [3]University of Chinese Academy of Sciences, Beijing 100049, China. [4]School of Atmospheric Sciences, Nanjing University, Nanjing 210023, China. [5]Joint International Research Laboratory of Atmospheric and Earth System Sciences, Nanjing University, Nanjing 210023, China. [6]Collaborative Innovation Center on Forecast and Evaluation of Meteorological Disasters (CIC-FEMD), Nanjing University of Information Science & Technology, Nanjing, China. [7]International Center for Climate and Environment Sciences, Institute of Atmospheric Physics, Chinese Academy of Sciences, Beijing, China. ✉e-mail: qiliu@nju.edu.cn; hg@mail.iap.ac.cn

variability also plays a role in the change in El Niño properties[23,24]. Preindustrial model simulations show that El Niño characteristics exhibit strong interdecadal and intercentennial modulation in the absence of external forcing[23]. Palaeo-El Niño reconstructions also show a wide range of El Niño variance over the past 7000 year[21] and find the El Niño variabilities in both the early 1900s and recent decades are relatively higher than preindustrial levels[25], highlighting the role of internal variability. Observations and preindustrial-control model simulations show that Atlantic Multidecadal Oscillation (AMO), a long-lived basin-wide warming or cooling in the Northern Atlantic that generally persists for 60–80 years, could modulate El Niño amplitude[26–28] and El Niño type[29,30].

It is still unclear whether the frequent occurrence of extreme El Niño events and CP El Niño events in the last 40 years is part of natural variability[23,24] or a consequence of global warming[1,7,14]. In order to investigate this, we can analyze past El Niño records to see whether there are other periods with frequent extreme El Niño and CP El Niño occurrences like the past 40 years, but without strong anthropogenic forcing. If this is the case, we can deduce that factors other than anthropogenic activity must play a role in the decadal transition of El Niño types. In this study, we examine multiple long-term instrumental SST datasets and apply cluster analysis to classify El Niño events. We show that there exists another extreme El Niño and CP El Niño epoch, around year 1900, with similar spatial and temporal evolution, dynamic processes, and climate impacts as those that occurred in the last 40 years. The results suggest a role of internal variability. Moreover, we found that both the two periods with increased extreme El Niño and CP El Niño events coincide with the positive phase of the AMO. Then, we investigate the influence of internal variability associated with the AMO on El Niño multidecadal modulation using outputs from the fifth and sixth phases of the Coupled Model Intercomparison Project (CMIP5 and CMIP6) and palaeoclimate proxies. Furthermore, we quantify the contribution of anthropogenic forcing and internal variability to the recently observed El Niño diversity based on a statistical model. Our results highlight that both internal variability associated with the AMO and anthropogenic forcing contribute to the changes in El Niño properties in recent decades.

Results

A period beyond the last four decades with frequent extreme and CP events

We applied a cluster analysis to the evolution from the onset to the development of 38 El Niño events for the period 1871 to 2017 using a "merged" SST dataset from HadISST1[31], Extended Reconstructed SST version 5 (ERSSTv5)[32], and Kaplan Extended SST[33] (see Methods). Based on the cluster analysis, El Niño events were classified into 4 physically meaningful clusters: (1) extreme, (2) EP, (3) CP, and (4) successive El Niño events (Fig. 1 and Supplementary Fig. 1). The four types of El Niño in this study are mutually exclusive. This categorization distinguishes extreme from moderate events, thus the "EP" in this study refers to "moderate EP". The four types of identified El Niño events are consistent with ref. [34] during the common period (1901–2017). We focus on the extreme, EP, and CP types of El Niño events in this study. It is intriguing that almost all extreme and CP events occurred in the two periods. One is the period from the 1980s to the present, in which ~8 CP and 3 extreme events exist, and the other is the period 1870s to the 1900s, among which 3 extreme and 3 CP events consecutively occur (Fig. 2a). In contrast, EP events mainly occurred in the 1900s–1930s and 1950s–1980s. The two increased extreme and CP event periods are also detectable from the HadISST1, ERSSTv5, and Kaplan SST datasets (Supplementary Fig. 2a–c). In the three datasets, the numbers of extreme El Niño events are 3, 2, and 2 during the period from the 1870s to the 1900s and 3, 3, and 3 during the period from the 1980s to the present, respectively. For CP El Niño, the number are 3, 3, and 3 during the period from 1870s to the 1900s and 7, 8, and 7 during the period from the 1980s to the present. The slight difference should arise from data uncertainty.

The extreme and CP El Niño events that occurred in the 1870s to 1900s were similar to those in the 1980s to present in both their spatiotemporal evolution of SSTA and dynamic processes. We compare the spatiotemporal evolution of extreme El Niño and CP El Niño events for the two periods using the "merged" SST dataset. The evolution of the extreme El Niño events in the two periods is similar: the warm SST anomaly starts to develop in the western Pacific (WP) during the preceding boreal winter and then propagates eastward with a rapid basin-wide development in the boreal spring. Later, a warm anomaly occurs in the far eastern Pacific during boreal spring and then propagates westward. The maximum intensity occurs around 120°W in December (Fig. 1a, b; Supplementary Fig. 3a). Strong westerly anomalies develop in the western Pacific in the preceding boreal winter and spring (Supplementary Fig. 4a, b). Coupled with pronounced westerly, convective, and warm SST anomalies near the dateline (180°E) (Supplementary Fig. 4e, f), these anomalies are conducive to initiating an eastward propagation of SST anomalies[35–37]. Moreover, we conducted an ocean mixed-layer heat budget analysis of the mixed-layer ocean temperature averaged over the central-eastern Pacific (5°S–5°N, 180°–80°W) region during the El Niño development phase. It shows that during the onset phase, the zonal advective feedbacks are dominant for the extreme events in these two periods (Fig. 1c), and this result is robust, with a total of 5 of 6 extreme events in these two periods (83.3%) supporting it (Supplementary Table 1).

The CP El Niño events in the two periods also show a similar evolution and feature initial warming in the western Pacific and eastward propagation from the western Pacific from early boreal summer to boreal winter (Fig. 1d, e, Supplementary Fig. 3c). The onset occurs around July with warm SST in the western Pacific and anomalous westerlies and convection in the west of the warm SST (Supplementary Fig. 4g, h). The zonal advective feedback is dominant in the CP El Niño events for both periods during the onset phase (Fig. 1f; 10 of 11 CP El Niño events in these two periods, or 90.9%, are dominated by zonal advective feedback[13]; Supplementary Table 1). The spatiotemporal evolution of EP El Niño events is different from those of extreme and CP El Niño events (Fig. 1g). The initial warm anomalies originate from the EP and then propagate westward. The thermocline feedback is dominant for EP events during the onset phase (Fig. 1h).

To further confirm the similarity of El Niño events that occurred in the 1870s to 1900s and in the 1980s to the present, we compare the climate impacts of El Niño events in the two periods. The composite of boreal winter air temperature anomaly patterns during extreme El Niño events in the period of 1875–1905 closely resembles those in the post-1980s (Supplementary Fig. 5a, b), with a high spatial correlation coefficient of 0.68 ($p < 0.001$). The boreal autumn air temperature anomaly patterns during CP El Niño events that occurred from 1875 to 1905 are also similar to those that occurred in the post-1980s (Supplementary Fig. 5d, e). Meanwhile, the extreme and CP El Niño events exert different impacts on global temperature to EP El Niño events (Supplementary Fig. 5c, f). Note that we compare boreal autumn rather than boreal winter because the temperature anomaly patterns show more prominent differences between CP and EP El Niño events in boreal autumn than in boreal winter[38].

The above results imply that the period of 1875 to 1905 is another extreme and CP El Niño event epoch. Here we use a 2-way table to test the statistical significance (see Methods). The result indicates that the regime shifts in the 1900s and 1980s are both significant at the 99% confidence level (Supplementary Table 2). It suggests that factors other than anthropogenic forcing must play a role in the decadal transition of El Niño types. This result is consistent with a model study showing that variations in El Niño behavior can occur on multidecadal and intercentennial timescales even with fixed climate forcing[23].

https://doi.org/10.1038/s41467-023-36053-7

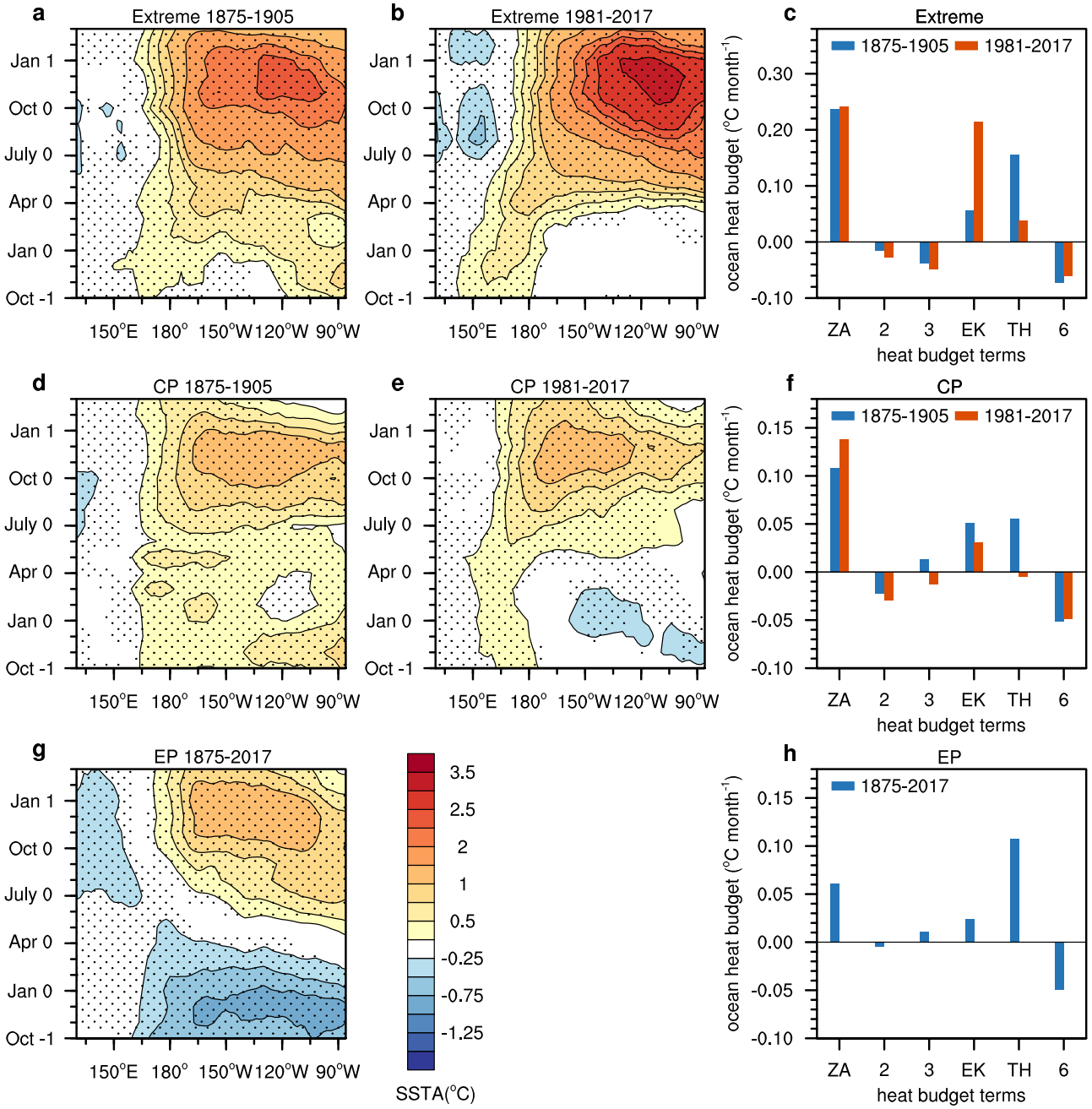

Fig. 1 | Composite evolution of the equatorial Pacific sea surface temperature (SST) anomalies and heat budget analysis in extreme and Central Pacific (CP) El Niño for two periods. a, **b** The evolution of equatorial Pacific averaged (5°S–5°N) sea surface temperature anomalies (SSTA) (shading units: °C) for extreme El Niño events during the period of (**a**) 1875–1905 and (**b**) 1981–2017. **d**, **e** Same as **a**, **b** but for CP El Niño events. **g** Same as **a** but for Eastern Pacific (EP) El Niño events during the period of 1875–2017. The stippling indicates the regions where the signal (group mean) is larger than the noise (one standard deviation from the group mean of each member). The group mean and standard deviation are calculated based on the events used in each panel. The anomalies are calculated referenced to the climatology of the full period and linearly detrended. **c**, **f** Comparison between the period of 1875–1905 and 1981–2017 in the ocean mixed-layer heat budget analysis of extreme El Niño (**c**) and CP El Niño (**f**) events during their respective onset phases (onset phases are defined as the month when the value of the Niño-3.4 index first exceeds 0.5 °C and the 2 months after that) over the central-eastern Pacific (5°S–5°N, 180°–80°W). **h** Same as **c** but for EP El Niño events during the period of 1875–2017. The terms $-u'\partial\bar{T}/\partial x$, $-\bar{w}\partial T'/\partial z$, and $-w'\partial\bar{T}/\partial z$ denote the zonal advective feedback (ZA), thermocline feedback (TH) and upwelling feedback (EK), respectively. The 6 terms from left to right are $-u'\partial\bar{T}/\partial x$ (bar 1 denoted by ZA), $-\bar{u}\partial T'/\partial x$ (bar 2), $-u'\partial T'/\partial x$ (bar 3), $-w'\partial\bar{T}/\partial z$ (bar 4 denoted by EK), $-\bar{w}\partial T'/\partial z$ (bar 5 denoted by TH), and $-w'\partial T'/\partial z$ (bar 6). The units in the ordinates are °C month^{-1}. The merged HadISST1, ERSST5 and Kaplan SST data from 1871 to 2017 was used. The heat budget is calculated based on the merged Simple Ocean Data Assimilation (SODA) and Global Ocean Data Assimilation System (GODAS) data.

To examine the sensitivity of the extreme and CP El Niño event epoch of 1875- 1905 to the traditional classification method, we categorized 38 El Niño into two broad types (EP and CP) based on the Niño method[13,14,39] (see Supplementary Discussion), and then we further divide the EP type El Niño events into moderate EP and extreme El Niño events by the criterion of DJF-averaged value of the normalized Niño3 index below or above a threshold value of 1.75 standard deviations (s.d.) (see Supplementary Fig. 2e and Supplementary Discussion). Based on the traditional classification method, we identified a total of 16 CP events and 8 extreme events, with 7 CP and 3 extreme events

https://doi.org/10.1038/s41467-023-36053-7

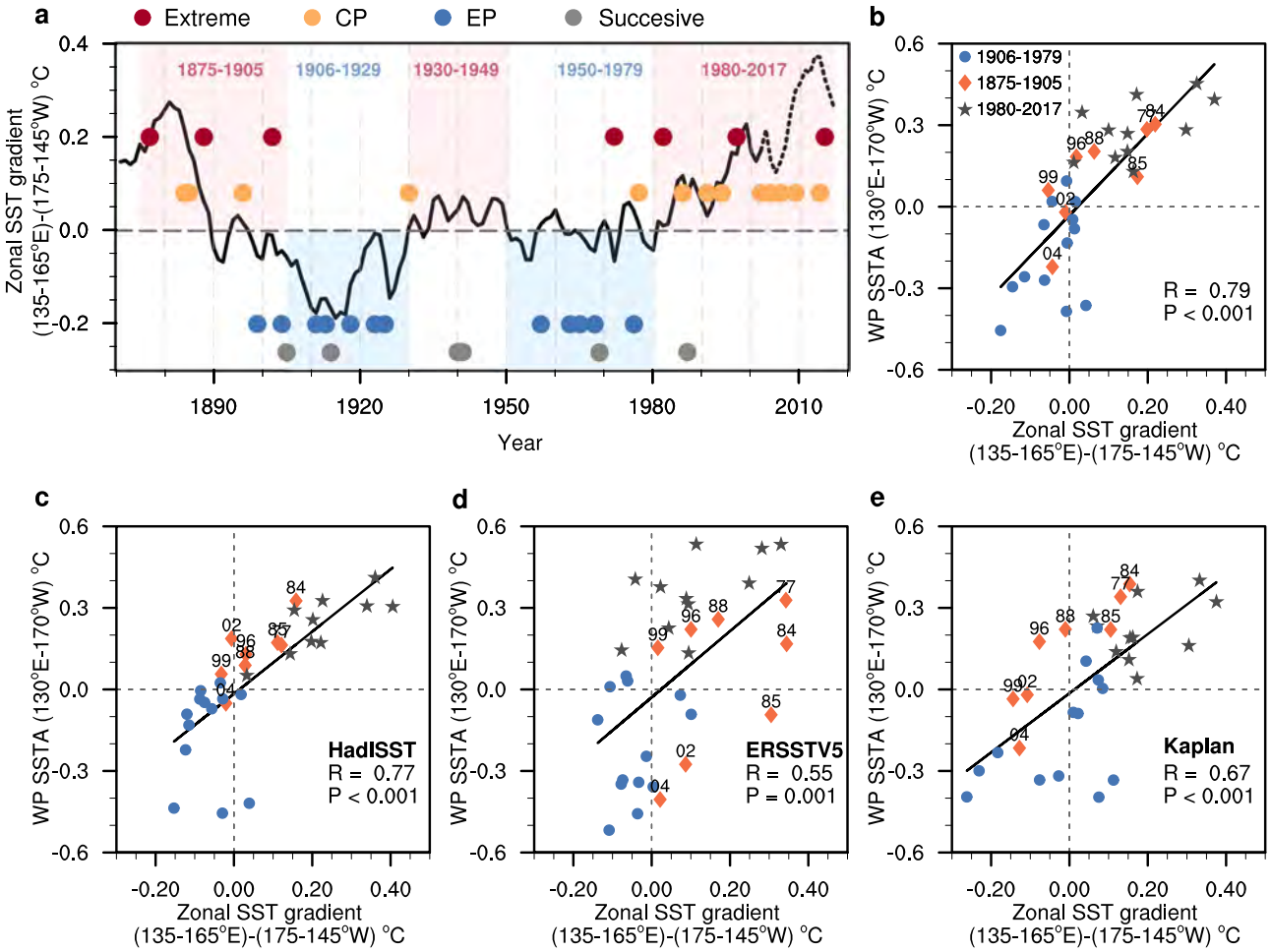

Fig. 2 | The changing El Niño types from 1871 to 2017 and their relationship with the mean state zonal sea surface temperature (SST) gradient. a The occurrence of different types of El Niño events. The 38 El Niño events are classified into extreme (red), Central Pacific (CP, orange), Eastern Pacific (EP, blue), and Successive (gray) events. The time series of the 31-year running mean, annual-mean zonal SST gradient [western Pacific SST (135–165°E) minus central Pacific SST (165–145°W)] for the observations from 1871–2017 (°C, relative to the mean of 1901–2010, black line). The positive (black line is greater than the 1901–2010 mean) and negative (black line is less than the 1901–2010 mean) phases of the zonal equatorial SST gradient are represented by light red and light blue shading, respectively. The dashed lines represent not full 31-year running. **b** The relationship between the mean-state zonal SST gradient and the western Pacific (WP) (130°E–170°W) sea surface temperature anomalies (SSTA) in merged SST during the El Niño onset phase from April (0) to August (0). The merged SST from 1871 to 2017 was used in **a**, **b**. **c**–**e** Similar to **b** but for HadISST (**c**), ERSSTV5 (**d**), and Kaplan (**e**). The black stars and orange diamonds in **b**–**e** represent the El Niño events that occurred from 1875 to 1905 (year 1877, 1884, 1885, 1896, 1899, 1902, 1904) and 1980 to 2017 (year 1982, 1986, 1991, 1994, 1994, 1997, 2002, 2004, 2006, 2009, 2014, 2015), respectively. Solid blue circles represent El Niño events that occurred from 1906 to 1979 (year 1911, 1913, 1918, 1923, 1925, 1930, 1957, 1963, 1965, 1968, 1972, 1976, 1977). The correlation (R) and the *P*-value of linear regression (black solid line) are also shown. The mean state is defined by the 31-year running mean.

existing in the period from the 1980s to the present and 3 extreme and 3 CP events consecutively occurring in the period 1870s to the 1900s. Thus, the period of 1875–1905, like the recent decades, characterized by increased extreme El Niño and CP El Niño events are still detectable when employing the traditional classification method.

Decadal variations in El Niño types modulated by the AMO

What has caused the observed decadal transition of El Niño types? Previous studies suggest a relationship between changes in El Niño types and those in the Pacific zonal temperature gradient[40,41]. Figure 2a shows the relationship between the Pacific zonal temperature gradient and El Niño types using the merged SST data. El Niño behavior is tightly connected with the variation in the zonal mean SST gradient (defined as the 31-year running mean of the difference between SSTA in the western Pacific [135°E–165°E] and SST in the eastern Pacific [175°W–145°W]) on a multidecadal time series: that is, the zonal gradient is stronger in the higher-frequency periods of extreme and CP El Niño events than in the higher-frequency period of EP El Niño events (Fig. 2a). Observation and model experiments suggest that the enhanced zonal SST gradient could provide a favorable condition for amplifying the zonal advective feedback, and the zonal advective feedback is a major dynamical feedback process, especially in the developing stage of El Niño initiated in the western Pacific[13,40,41]. The enhanced zonal advective feedback over the CP is conducive to triggering the development of El Niño over the western Pacific region[40,42]. We noted that both extreme and CP El Niño events are associated with an initial warm anomaly in the western Pacific, while EP El Niño events are not (Fig. 1; Supplementary Fig. 3). We measure the initial development of El Niño over the western Pacific by calculating the observed western Pacific (130°E–170°W) SSTA during the El Niño onset phase (April through August). The western Pacific SSTA of El Niño is closely related to the mean-state zonal SST gradient ($r = 0.79$, $P < 0.001$, Fig. 2b), indicating that extreme El Niño and CP El Niño events rather than EP El Niño events tend to occur during periods of strengthened mean-state zonal SST gradients. This result remains qualitatively unchanged if we use the HadISST1 ERSSTV5, and Kaplan SST datasets

separately (Fig. 2c-e). Our results suggest that zonal SST gradient change is a controlling factor in determining the decadal transition of El Niño types.

Figure 3a shows the correlation of the SST field with the zonal SST anomaly gradient in the merged SST dataset. Here, the signal induced by external forcing, including the change in greenhouse gases (GHGs), natural forcing (NAT), and anthropogenic aerosols (AA), has been removed in the SST field and the zonal SST anomaly gradient (Fig. 3a, see Estimates of the forced and internal components in Method). The spatial correlation field shows significant positive values over the western Pacific, suggesting that the equatorial zonal SST gradient is dominated by the western Pacific. Meanwhile, significant positive values are also found over the North Atlantic Ocean and the pattern resembles the AMO (Fig. 3a), suggesting that the zonal SST anomaly gradient is related to the AMO. This result is consistent with previous studies showing that the AMO could remotely affect the mean state of the Pacific[43–46]. Thus, the AMO seems to be a key candidate for leading to the multidecadal change in El Niño types.

We further analyzed the relationship between the AMO and El Niño diversity based on outputs from the fifth and sixth phases of the Coupled Model Intercomparison Project (CMIP5 and CMIP6). We use outputs from 20 CMIP5 and 23 CMIP6 pre-industrial control simulations over the last 300 years. The CMIP5 and CMIP6 models could reproduce the observed AMO characteristics, with similar spatial patterns in the North Atlantic Ocean (Supplementary Fig. 6). Due to the model's bias in simulating the evolution of El Niño, we use the El Niño onset phase (April to August) averaged western Pacific SSTA > 0 °C to roughly distinguish the extreme/CP from EP events. A total of 30 of 43 CMIP5 and CMIP6 models (70%) simulated an increased western Pacific SST for the AMO-positive state minus the AMO-negative state (Fig. 3b). The increased western Pacific SST enhances the zonal SST gradients, which is conducive to the development of El Niño in the Niño4 region[13,40]. Models that generate a larger increase in the western Pacific SST/zonal SST gradient for the AMO-positive state minus the AMO-negative state tend to simulate a larger increase in the frequency of extreme/CP El Niño events for the AMO-positive state minus the AMO-negative state ($r = 0.66$, $P < 0.001$). A total of 29 of 43 CMIP5 and CMIP6 models (67.4%) produce an increased occurrence of CP and extreme El Niño for the AMO-positive state minus the AMO-negative state.

We also use multicentury palaeoclimate reconstructions to examine the relationship between the AMO and the decadal modulation of the different types of El Niño events prior to the instrumental record. The palaeoclimate reconstructions include a 700-year (1300–2006) El Niño Niño3.4 index reconstruction[20], a 1200-year (800–2008) AMO index reconstruction[47], and a 400-year (1617–2008) record of CP El Niño events reconstructed from ENSO-sensitive proxy records[15]. To focus on the decadal modulation of different types of El Niño events, we count the occurrences of extreme El Niño events (defined by a Niño-3.4 index >1.2 s.d.) and CP Niño events (identified following the pioneering work of ref. [15]) over a 21-year sliding period. The 21-year sliding frequencies of extreme El Niño events and CP Niño events increased in the positive phase of the AMO (Fig. 3c) and they are statistically significant above the 95% confidence level according to a bootstrap test (see Methods).

How does AMO impact El Niño diversity? We examined the process using the 5 CMIP6 and 3 CMIP5 models, in which the western Pacific SST responses to the AMO are comparable to the observations (Supplementary Fig. 7a). The simulated spatial pattern of the Pacific response to the AMO among these models exhibits a common feature: annual mean anticyclonic flows over the Northwest Pacific (NWP), significant warm SSTA over the western Pacific and the subtropical North Pacific (SNP), and strong northward flows from the tropics towards the SNP (Supplementary Fig. 7). We find that these features of the Pacific response to AMO derived from CMIP5 and CMIP6 are consistent with those derived from the observations (Supplementary Fig. 8) and a suite of Atlantic Pacemaker experiments[45]. Such a spatial pattern of the Pacific response implies that the AMO could induce anomalous high pressure over SNP (Supplementary Fig. 8b), thereby causing SNP warming via wind–evaporation–SST feedback, and SNP warming could further develop warm SSTs in the western Pacific through SST–sea level pressure–cloud–longwave radiation positive feedback[45]. The zonal SSTA gradient over the central Pacific increases as the western Pacific SSTA increases (Supplementary Fig. 9b), which in turn leads to enhanced zonal advection feedback in the development of El Niño (Supplementary Fig. 9c). Thus, a positive AMO corresponds to a warm SSTA in the western Pacific, a large zonal SSTA gradient over the central Pacific, and an enhanced CP and extreme El Niño, vice versa. These results imply that the AMO could modulate the frequency of the three types of El Niño events, with more frequent extreme and CP events in the positive phase of the AMO.

Contribution of external forcing and internal variability

The zonal SST gradient is divided into the externally forced component and internal variability-related component in Fig. 4a (see Estimates of the forced and internal components in Method). The externally forced (EX) zonal SST gradient shows an upward trend (Fig. 4a). In response to external forcing, the eastern Pacific warms less than the western Pacific due to upwelling and the shallow thermocline, strengthening the zonal SST gradient via Bjerknes feedback[48,49]. The contribution of EX to the multidecadal equatorial zonal SST gradient variations increased over time and exceeded that of internal variability from 1981 to 2017 (Fig. 4b).

Although the contribution of EX to the multidecadal equatorial zonal SST gradient variations varies in 5 periods, there is a significant linear correlation between the mean zonal SST gradient and the percentages of occurrence ratio of different types of El Niño events to total El Niño events (Supplementary Fig. 10). We use a linear regression model to estimate the EX-induced and IV-induced occurrence of different types of El Niño events from 1981 to 2017 (see Methods). Note that the results of the linear regression for the sum of extreme and CP El Niño events (Supplementary Fig. 10a) are consistent with the model result (Fig. 3b), providing high confidence for the estimation. If both EX and IV are considered in the model, we use the observed zonal gradient in the last 40 years as a predictor in the linear regression model, which yields ~9.1 extreme and CP El Niño events (including ~2.7 extreme and ~6.3 CP El Niño events) and ~0 EP El Niño events in the last 40 years, which are close to the actual number of occurrences of El Niño events (Fig. 4c). If only IV was considered in the model, ~1.8 extreme and ~4.1 CP El Niño events are predicted, and the AMO accounts for 77.8% and 75.6% of IV-induced extreme and CP El Niño events, respectively. This result suggests that the extreme and CP El Niño event epochs still exist even without considering anthropogenic forcing. Moreover, anthropogenic forcing also plays a role in changing the El Niño diversity in the last 40 years. The linear regression model result shows that anthropogenic forcing-induced warming accounts for up to ~1 more extreme and ~2 more CP El Niño events from the 1980s to the present. Our result, that the recent changes in El Niño events were attributed to synchronized effects of greenhouse warming and internal variability, still holds when the traditional El Niño classification method is used (Supplementary Information gives a detailed analysis).

Discussion

In this study, we found an extreme El Niño and CP El Niño epoch from 1875 to 1905, with the El Niño events that occurred in this period showing similar spatiotemporal evolution, dynamic processes, and global climatic impacts to those that occurred after 1980, suggesting a role of internal variability. Then, we revealed that anthropogenic forcing and the internal variability associated with the AMO synchronously contributed to the increased frequency of extreme and CP events since

https://doi.org/10.1038/s41467-023-36053-7

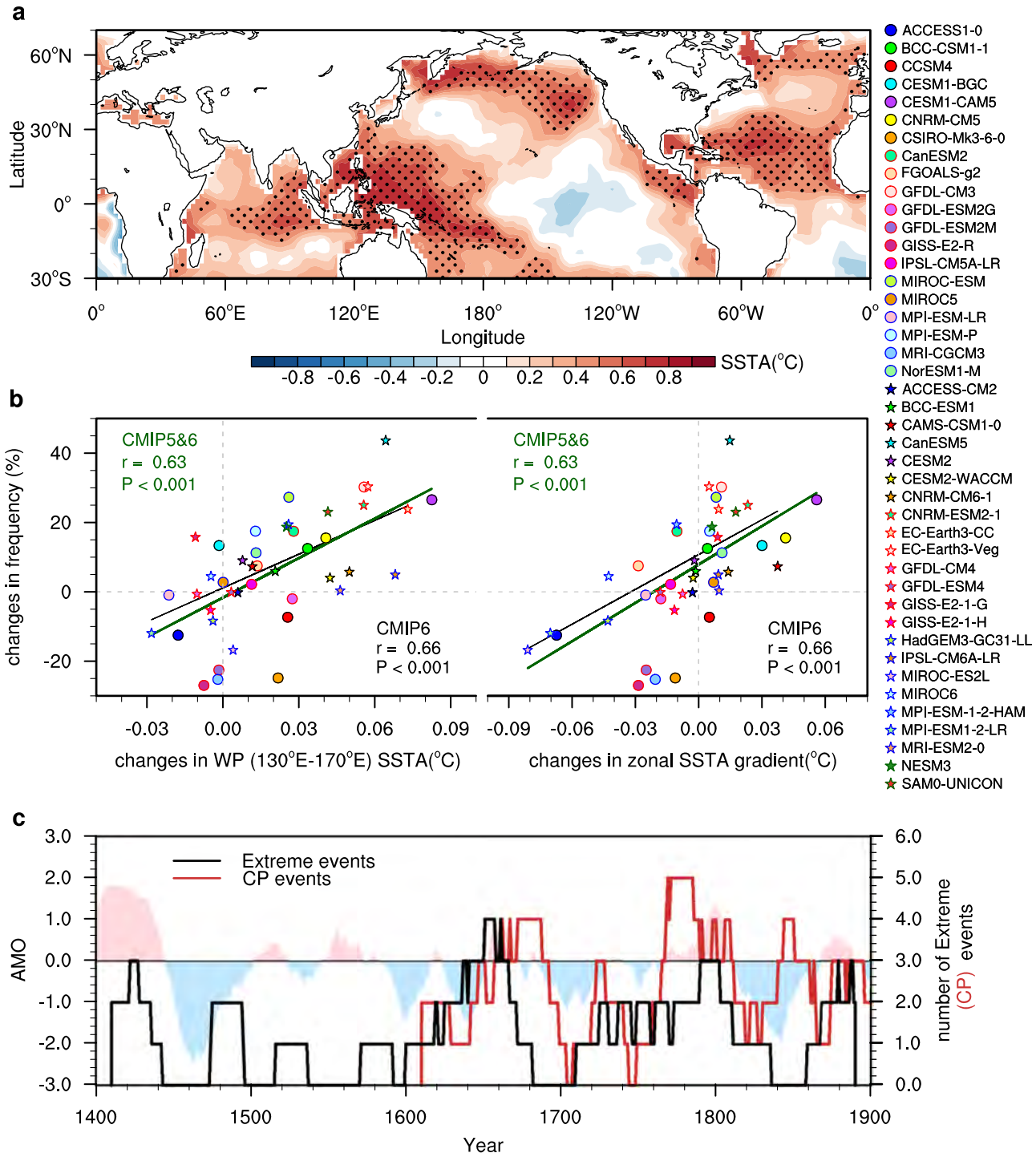

Fig. 3 | The relationship between the Atlantic Multidecadal Oscillation (AMO) and El Niño types. a The correlation between the internal variability (IV) induced zonal sea surface temperature (SST) anomaly gradient and the residual SST anomaly (SSTA) field. The black stippling indicates statistically significant correlations at the 0.05 level. The merged SST from 1871 to 2017 was used. **b** Inter-model relationship between the changes in the 21-year running mean western Pacific (WP) SSTA (130°E–170°E) /Zonal SST gradient [WP SST (155°E–175°W) minus central Pacific SST (115°W–145°W)] (x-axis, units: °C) and the frequency changes in the extreme/ Central Pacific (CP) El Niño events (*y*-axis, units: %) and for AMO positive state (AMO-positive state) minus AMO-negative state. Due to the model's bias in simulating the evolution of El Niño, we use the El Niño onset phase (April to August) averaged WP SSTA > 0 °C to roughly distinguish the extreme/CP from Eastern Pacific (EP) events. 20 CMIP5 and 23 CMIP6 pre-industrial control simulations were used. **c** The 21-year sliding frequency of extreme El Niño events (black solid line)/CP El Niño events (red solid line) in the reconstruction and the normalized 21-year running mean AMO reconstruction index[47]. The 21-year sliding frequency is defined by counting extreme/CP El Niño events during the 21 years. The CP El Niño events in the reconstruction are according to ref. [15]. The extreme El Niño events are defined by Niño-3.4 reconstruction index >1.2 standard deviations.

https://doi.org/10.1038/s41467-023-36053-7

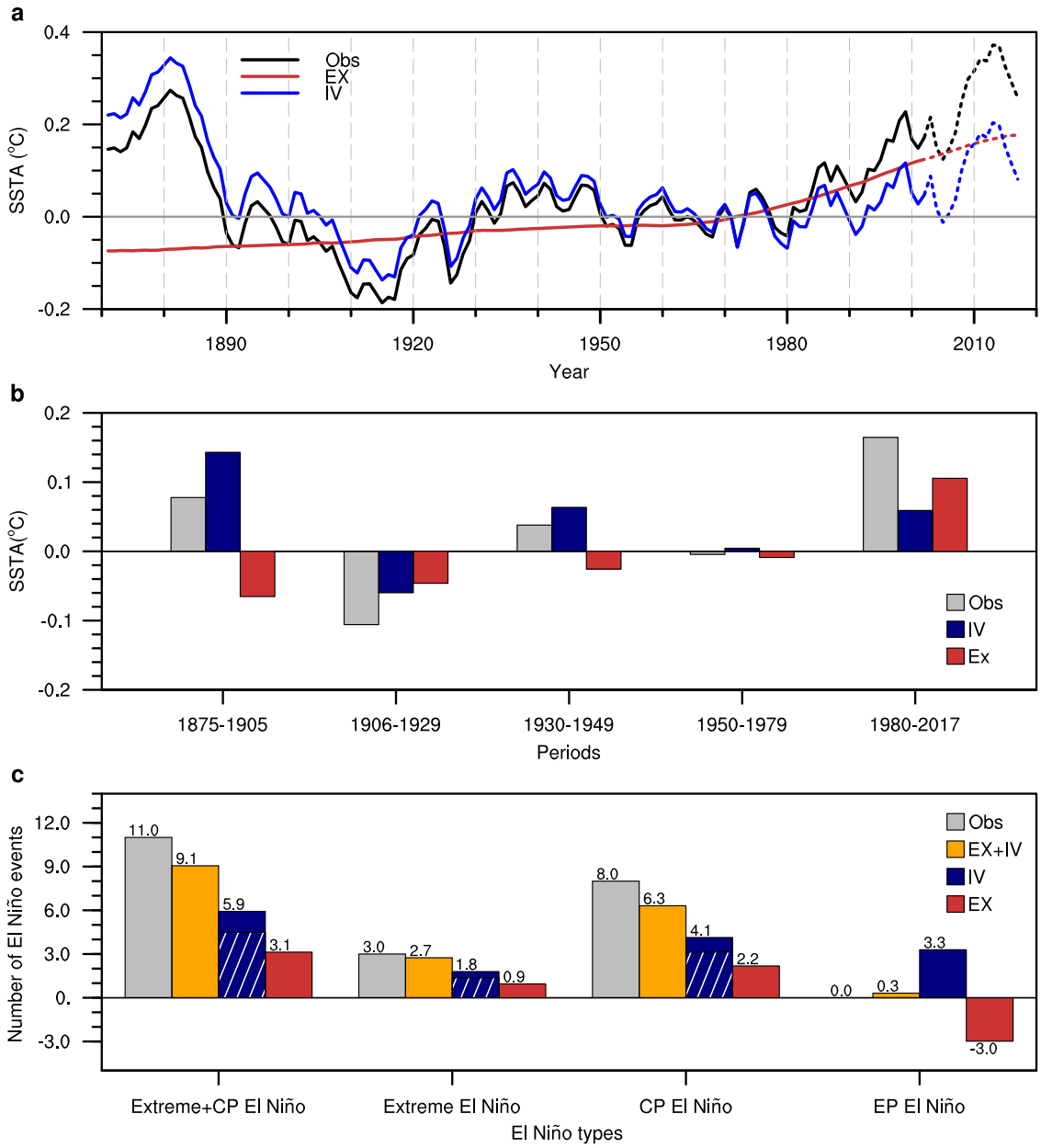

Fig. 4 | Contributions of external forcing and internal variability to the frequencies of extreme El Niño events and central Pacific El Niño events over the past four decades. a Time series of the 31-year running mean, annual-mean zonal sea surface temperature anomaly (SSTA) gradient [western Pacific SSTA (135–165°E) minus central Pacific SSTA (165–145°W)] for the observations from 1871–2017 (Obs, black line, the same as the black line in Fig. 2a, relative to the mean of 1901–2010), the estimated externally forced signal (EX, red) and internal variability (IV, dark blue) in the observations. The dashed lines represent not full 31-year running. **b** Time-averaged zonal equatorial SST anomalies (°C, relative to 1901–2010 mean) gradient from Obs (gray), IV (blue), and EX (red) for 5 different periods marked in Fig. 2a. The merged sea surface temperature (SST) from 1871 to 2017 was used. **c** Histograms for the estimated numbers of different types of El Niño events in 1981–2017 based on a linear regression model (see Methods and Supplementary Fig. 10). The orange, blue, and red bars denote the EX + IV-, IV-, and EX-induced numbers of different types of El Niño events, respectively. Slant hatching denotes the Atlantic Multidecadal Oscillation (AMO) induced numbers of different types of El Niño events.

1980 by modulating the background warming in the western Pacific and the associated zonal advective processes. Furthermore, the internal variability is estimated to contribute to the observed extreme and CP El Niño event epochs since 1980 by up to 65%, with AMO accounting for more than 3/4 of that. However, anthropogenic forcing can explain ~1 more extreme and ~2 more CP events in the last 40 years. Our findings highlight that both the external forcing and the internal variability of the AMO are important factors to be considered in projecting the diversity of El Niño events in a changing climate.

Future changes in El Niño are a crucial issue. Climate models project a tropical Pacific mean state change under global warming, which could not only exert a significant impact on tropical precipitation patterns[50,51] but also influence the ENSO characteristics[52,53]. As extreme El Niño and CP El Niño events tend to occur in periods of enhanced equatorial west-minus-east SST gradient, the projection of El Niño types should partly depend on the projection of this gradient in the Pacific.

Methods

Observation datasets

We analyze (a) the Hadley Center Sea Ice and SST dataset version 1 (HadISST1[31]) (b) the Extended Reconstructed Sea Surface Temperature

(ERSST) version 5 global SST monthly dataset[32] and (c) the Kaplan extended SST version 2 dataset[33] for 1871–2017. Data uncertainties exist prior to 1950 due to the sparse coverage of instrumental observations across the equatorial Pacific[54]. To reduce the uncertainty in the three SST datasets, we used a "merged monthly mean SST dataset (merged SST hereafter) following the pioneering work of ref. [34]". The merged SST is defined as the arithmetic mean of the three monthly mean SST datasets. In addition to the "merged" SST dataset, we also used the HadISST1, ERSSTV5, and Kaplan SST datasets to examine the sensitivity of the results to different instrumental datasets (Supplementary Fig. 2). Although slight differences still exist, our key conclusion is not sensitive to the SST products, and it also provides some confidence to our result.

The surface winds and atmospheric circulation fields are derived by merging the NOAA-CIRES Twentieth Century Reanalysis (20CRv2c)[55] from 1871 to 2012 and NCEP/DOE Reanalysis 2 data[56] from 1979 to 2018. To ensure temporal consistency, we use the differences in monthly climatology between 20CRv2c and NCEP/DOE2 data during the overlap period 1979–2012 to calibrate the mean state of NCEP/DOE. The ocean reanalysis dataset used is from SODA version 2.2.4 for 1871–2008[57] with a resolution of 0.5° × 0.5° and extended from 2009 to 2018 with the Global Ocean Data Assimilation System (GODAS) with a 1° × 1° grid[58]. We use the difference between GODAS and SODA2.2.4 during the overlay period 1980–2008 to calibrate the mean state of GODAS. The land air temperature used is the HadCRUT5[59] gridded monthly surface temperature datasets. The long-term ship-observed sea level pressure (SLP) and marine cloud cover were used from the International Comprehensive Ocean–Atmosphere Data Set (ICOADS) release 3[60]. The SLP field derived from the Hadley SLP (HadSLP2) dataset[61] was also used.

Reconstruction data

We also use multi-century palaeoclimate reconstructions to extend the observational record. The Niño-3.4 index and AMO index reconstructions used are from the NOAA/World Data Center for Paleoclimatology archive, including a 700-year (1300–2006) El Niño Niño-3.4 index reconstruction based on 2,222 tree-ring chronologies from both the tropics and mid-latitudes in both hemispheres[20] and a 1200-year (800–2008) Atlantic Multidecadal Variability/Oscillation (AMV/AMO) Reconstructions based on 46 annual resolved terrestrial proxy records[47]. A 21-year running mean is applied to the AMV/AMO reconstruction index. The first and last 100 years are cut-offs to minimize edge effects introduced by the spectral filter. The overlay period of 1401–1900 is used. We define extreme El Niño as when the Niño 3.4 index is greater than 1.2 standard deviations. In addition to the multi-century record of extreme El Niño events reconstructed from the Niño-3.4 reconstruction, we also use 400 years (1601–2008) of CP El Niño events reconstructed from 27 seasonally resolved coral records[15] to study the relationship between CP events and AMO. The period of 1601–1900 is used, and a total of 34 CP events are identified based on the pioneering work of ref. [12]: 1618, 1620, 1641, 1652, 1657, 1667, 1672, 1677, 1682, 1688, 1693, 1718, 1730, 1733, 1759, 1769, 1775, 1778, 1779, 1781, 1790, 1799, 1801, 1808, 1816, 1832, 1840, 1850, 1853, 1854, 1873, 1884, 1885, and 1895 years.

Model simulation data

We used all forcing (ALL) and single-forcing experiments forced separately by greenhouse gases (GHGs), natural forcing (NAT), and anthropogenic aerosols (AAs) from 27 CMIP6 models (Supplementary Table 3). We used the pre-industrial control runs from 23 CGCMs of CMIP6 and 20 CGCMs of CMIP5. The 23 CMIP6 models were ACCESS-CM2, BCC-ESM1, CAMS-CSM1-0, CanESM5, CESM2, CESM2-WACCM, CNRM-CM6-1, CNRM-ESM2-1, EC-Earth3-CC, EC-Earth3-Veg, GFDL-CM4, GFDL-ESM4, GISS-E2-1-G, GISS-E2-1-H, HadGEM3-GC31-LL, IPSL-CM6A-LR, MIROC-ES2L, MIROC6, MPI-ESM-1-2-HAM, MPI-ESM1-2-LR, MRI-ESM2-0, NESM3, and SAM0-UNICON. The 20 CMIP5 models were ACCESS1-0, BCC-CSM1-1, CCSM4, CESM1-BGC, CESM1-CAM5, CNRM-CM5, CSIRO-Mk3-6-0, CanESM2, FGOALS-g2, GFDL-CM3, GFDL-ESM2G, GFDL-ESM2M, GISS-E2-R, IPSL-CM5A-LR, MIROC-ESM, MIROC5, MPI-ESM-LR, MPI-ESM-P, MRI-CGCM3, and NorESM1-M. These models were usually used to understand the changing behavior of El Niño[62,63].

Definition of El Niño years

We define El Niño events based on SST anomalies averaged in the Niño-3.4 region (5°N–5°S, 120°W–170°W), here called the Niño-3.4 index. We denote the El Niño first developing year, the following year, and the year prior to El Niño as year 0, year 1, and year −1, respectively. We smooth the Niño-3.4 index with a 3-month running-mean filter. El Niño events are defined as occurring when the detrended October–February (ONDJF)-averaged Niño-3.4 index is greater than or equal to 0.6 °C. A total of 38 El Niño events are identified using the merged SST dataset from 1871 to 2017.

Cluster analysis

We used a nonlinear K-means cluster analysis focused on the spatio-temporal evolution of El Niño events from the onset to the mature phase (from Nov-1 to Oct 0), which is depicted by SST anomalies averaged between 5°S and 5°N. The data used in the cluster analysis were 3-month running mean SST anomalies based on the original SST data, and to focus on the onset phase to mature phase, only SSTAs greater than 0.3 °C were used for the K-means cluster analysis, which is different from the pioneering work of ref. [34].

In the K-means cluster analysis, we use the squared Euclidean distance to measure the similarity between each cluster member and the corresponding cluster pattern. The silhouette clustering evaluation criterion was used to evaluate the performance of the cluster analysis. A high silhouette value indicates that the member is well matched to its cluster and poorly matched to neighboring clusters. Through nonlinear K-means cluster analysis of the evolution of El Niño events, we obtained four types of El Niño events. Supplementary Fig. 1 shows the silhouette values for each El Niño event within each of the 4 clusters for the 1871–2017 period for the merged SST, HadISST1, ERSSTV5, and Kaplan SST datasets. Furthermore, we tested different SST datasets to identify the extreme and CP El Niño events, and they yielded similar results, indicating that the results are robust and not sensitive to the exact choice of dataset (see Supplementary Discussion). Our results are not sensitive to the classification method—for example, we find similar results if we used the traditional Niño method[13,14,39] to categorize El Niño events into EP and CP events and then extracted the extreme El Niño events (see Supplementary Fig. 2, Supplementary Fig. 10-11 and Supplementary Discussion).

Ocean mixed layer heat budget equation

To compare the dominant dynamic processes of extreme and CP types of El Niño between the two periods, we conduct an ocean mixed layer heat budget analysis. The heat budget is computed according to the following equation:

$$\frac{\partial T'}{\partial t} = \left\langle -u'\frac{\partial \bar{T}}{\partial x}\right\rangle + \left\langle -\bar{u}\frac{\partial T'}{\partial x}\right\rangle + \left\langle -u'\frac{\partial T'}{\partial x}\right\rangle + \left\langle -v'\frac{\partial \bar{T}}{\partial y}\right\rangle + \left\langle -\bar{v}\frac{\partial T'}{\partial y}\right\rangle + \left\langle -v'\frac{\partial T'}{\partial y}\right\rangle + \left\langle -w'\frac{\partial \bar{T}}{\partial z}\right\rangle + \left\langle -\bar{w}\frac{\partial T'}{\partial z}\right\rangle + \left\langle -w'\frac{\partial T'}{\partial z}\right\rangle + \frac{Q'_{net}}{\rho C_p H} + R \quad (1)$$

where T is the mixed layer temperature; u, v, and w represent the zonal, meridional, and vertical ocean currents, respectively; Q_{net} is the net surface heat flux comprised of shortwave, longwave, latent, and sensible heat fluxes; ρ (=10^3 kg m^{-3}) is the ocean water density; C_p (=4000 J kg^{-1} K^{-1}) is the specific heat of water; H is the climatological mixed layer depth as a constant 50 m; R represents the residual term; and the overbar and prime denote the climatological mean and

anomalies, respectively. The analysis result is not sensitive to the constant H we choose, such as H = 70 m. $-u'\partial\bar{T}/\partial x$, $-\bar{w}\partial T'/\partial z$, and $-w'\partial\bar{T}/\partial z$ denote the zonal advective feedback, thermocline feedback and upwelling feedback, respectively.

Contingent (2-way) table and Pearson's chi-square test

The contingency table, also known as a cross-tabulation or a two-way table, is usually used to present categorical data in terms of frequency counts. We use Pearson's chi-square test to examine independence between the row and column variables in the contingency table[64]. Pearson's chi-square test statistic follows an asymptotic chi-square distribution with (r−1)X(c−1) degrees of freedom when the row and column variables are independent. It is calculated as

$$\chi^2 = \sum_{i=1}^{r}\sum_{j=1}^{c}\frac{\left(O_{ij}-E_{ij}\right)^2}{E_{ij}} \quad (2)$$

where O_{ij} is the observed value shown in the contingency table and E_{ij} is the expected value. E_{ij} is calculated as $E_{ij} = \frac{N_i N_j}{N}$, $N_i = \sum_{j=1}^{c} O_{ij}$, and $N_j = \sum_{i=1}^{r} O_{ij}$. where r and c are the numbers of rows and columns in the contingency table, N_i is the row total and N_j is the column total.

Estimates of the forced and internal components

Many previous studies used the global-mean SST (GMSST) from the multi-model ensemble mean (MMM) simulation to represent the externally forced signal. It is a preferred way to define the forced signal, which has the same temporal evolution over all grid boxes because it is determined by the external forcing series[65]. This method is based on the principle that the internal variations among the ensemble runs are usually uncorrelated. Thus, after averaging over a large number of ensemble simulations, the uncorrelated internal variations among the ensemble runs were largely smoothed out[65]. To calculate the MMM, we averaged all the ensemble runs for each single-forcing simulation from all the models. The MMM was similar if we first average over the available ensemble runs for each model to derive the ensemble mean for each model and then average the ensemble mean over all the models with the same weight for each model. Then we calculate the GMSST time series, T_{GHG}, T_{NAT}, T_{AA} from the MMM of GHG, NAT and AA forcing, respectively. A combined index $aT_{GHG} + bT_{NAT} + cT_{AA}$ is constructed based on a multiple linear regression of the observed GMSST time series onto T_{GHG}, T_{NAT}, T_{AA}, where a,b,c are the regressed coefficients. We use the combined index to estimate the externally forced component of the observed GMSST. We removed changes associated with the externally forced component through linear regression from observed SSTs at each grid point. The residual SST fields primarily contain unforced internal variations[65].

Linear regression method

Since there is a good relationship between the background zonal SSTA gradient and the frequency of different types of El Niño occurrence, for example, frequent occurrence of extreme and CP El Niño events is observed in the period of 1875–1905, 1930–1949 and 1981–2017 coincide with the enhanced zonal SST gradient, while in the other period (from 1905 to 1930 and from 1950 to 1980), EP El Niño events are dominant with a weakened zonal SST gradient. Here, we attempt to estimate the relative contribution of EX- and IV-induced zonal gradients to the El Niño type changes in the last 40 years. We use the background zonal SSTA gradient as predictor X and the occurrence ratio of the sum of extreme and CP El Niño events to total El Niño events in one period as response variable Y

$$Y = \beta_0 + \beta_1 X \quad (3)$$

We used the merged SST dataset shown in Fig. 2a and the HadISST1, ERSSTv5, and Kaplan SST datasets shown in Supplementary Fig. 2, and for each dataset, we calculated the mean zonal SSTA gradient in five periods (1875–1905, 1906–1929, 1930–1949, 1950–1980, 1981–2017) and the occurrence ratio of the sum of extreme and CP El Niño events to total El Niño events in the five periods, so we obtained $N = 20$ and used them to calculate the intercept β_0 and slope β_1. Then, we calculate the IV-induced and IV + EX-induced mean zonal SSTA gradients from 1981 to 2017 and use them to estimate the IV-induced and IV + EX-induced occurrence ratio of the sum of extreme and CP El Niño events to total El Niño events. A total of 11 El Niño events occurred during the period 1981 to 2017, so we could further estimate the IV-induced and IV + EX-induced occurrence of the sum of extreme and CP El Niño events in this period. The difference between IV + EX-induced and IV-induced occurrence of total extreme and CP El Niño events in this period is used to estimate the EX-induced occurrence of total extreme and CP El Niño events. We also applied the above analysis to extreme, CP, and EP El Niño events.

Statistical analyses

Statistical significance tests were based on Student's t test with reduced degrees of freedom[66]. We calculate the effective degrees of freedom (EDF) using the following equation:

$$\frac{1}{N^*} \approx \frac{1}{N} + \frac{2}{N}\sum_{j=1}^{N}\frac{N-j}{N}\rho xx(j)\rho yy(j) \quad (4)$$

where N is the sample size, and $\rho xx(j)$ and $\rho yy(j)$ are the autocorrelations of the two sampled time series x and y at time lag j. Here, we follow ref. [67] and use the above equation but without the weighting function $(N - j)/N$.

We use a bootstrap test to examine whether the number of extreme El Niño/CP El Niño events is statistically different in the positive phase of AMO and negative phase of AMO. We use Monte Carlo bootstrapping to estimate the probability density function (PDF) of the number of the 21-year sliding frequencies of extreme El Niño events and the number of the 21-year sliding frequencies of CP El Niño during positive and negative phases of the AMO. The resampling procedure was repeated 10 000 times. The 2.5 and 97.5% rankings from the probability distribution function indicate the 95% confidence level. The number of extreme El Niño increased in positive phase of AMO compared to negative phase of AMO is statistically significant above the 95% confidence level if distributions of number of extreme El Niño during positive phase of AMO are well-distinguished from that during the negative phase of AMO.

Data availability

The data that support the findings of this study are freely available. Observational SST datasets can be acquired from: (1) https://www.metoffice.gov.uk/hadobs/hadisst/ for HadISST1, (2) https://psl.noaa.gov/data/gridded/index.html for ERSSTV5 and Kaplan SST. The surface wind and atmospheric circulation fields observations or reanalysis can be acquired from https://psl.noaa.gov/data/gridded/index.html. The ocean reanalysis dataset can be acquired from: (1) http://apdrc.soest.hawaii.edu/datadoc/soda_2.2.4.php for SODA2.2.4, (2) https://psl.noaa.gov/data/gridded/data.godas.html for GODAS. The HadCRUT5 is available at https://www.metoffice.gov.uk/hadobs/hadcrut5/. The HadSLP2 and ICOADS are available at https://psl.noaa.gov/data/gridded/index.html. CMIP5 and CMIP6 data can be acquired from https://esgf-node.llnl.gov/projects/esgf-llnl/. The reconstruction data can be acquired from http://www.ncdc.noaa.gov/paleo/.

Code availability

The source code for kmeans clustering used in this study are available at website: https://www.mathworks.com/help/stats/kmeans.html. The

data in this study is mainly analyzed with NCAR Command Language (NCL; v6.6.2, https://www.ncl.ucar.edu/), which is a public access software. Key codes can be accessed from https://doi.org/10.6084/m9.figshare.21546912.v5.

References

1. Fedorov, A. V. & Philander, S. G. Is El Niño changing? *Science* **288**, 1997–2002 (2000).
2. Ren, H.-L., Jin, F.-F., Stuecker, M. F. & Xie, R. ENSO regime change since the late 1970s as manifested by two types of ENSO. *J. Meteorol. Soc. Jpn II* **91**, 835–842 (2013).
3. Aiken, C. M., Santoso, A., McGregor, S. & England, M. H. Optimal forcing of ENSO either side of the 1970's climate shift and its implications for predictability. *Clim. Dyn.* **45**, 47–65 (2014).
4. An, S.-I. & Wang, B. Interdecadal change of the structure of the ENSO mode and its impact on the ENSO frequency. *J. Clim.* **13**, 2044–2055 (2000).
5. Philander, S. G. H. Meteorology—anomalous El-Niño of 1982–83. *Nature* **305**, 16–16 (1983).
6. Vos, R., Velasco, M., Edgar d. L. R. *Economic and Social Effects of El Niño in Ecuador, 1997–1998*. (IDB, 1999).
7. Cai, W. et al. Increasing frequency of extreme El Niño events due to greenhouse warming. *Nat. Clim. Change* **4**, 111–116 (2014).
8. Fu, C. & Fletcher, J. Two patterns of equatorial warming associated with El Niño. *Chin. Sci. Bull.* **30**, 1360–1364 (1985).
9. Fu, C., Diaz, H. F. & Fletcher, J. O. Characteristics of the response of sea-surface temperature in the central Pacific associated with warm episodes of the southern oscillation. *Mon. Weather Rev.* **114**, 1716–1738 (1986).
10. Kao, H.-Y. & Yu, J.-Y. Contrasting Eastern-pacific and central-pacific types of ENSO. *J. Clim.* **22**, 615–632 (2009).
11. Larkin, N. K. On the definition of El Niño and associated seasonal average U.S. weather anomalies. *Geophys. Res. Lett.* **32**, (2005).
12. Ashok, K., Behera, S. K., Rao, S. A., Weng, H., Yamagata, T. El Niño Modoki and its possible teleconnection. *J. Geophys Res.* https://doi.org/10.1029/2006JC003798 (2007).
13. Kug, J.-S., Jin, F.-F. & An, S.-I. Two types of El Niño events: cold tongue El Niño and warm pool El Niño. *J. Clim.* **22**, 1499–1515 (2009).
14. Yeh, S. W. et al. El Niño in a changing climate. *Nature* **461**, 511–514 (2009).
15. Freund, M. B. et al. Higher frequency of Central Pacific El Niño events in recent decades relative to past centuries. *Nat. Geosci.* **12**, 450–455 (2019).
16. Lee, T., McPhaden, M. J. Increasing intensity of El Niño in the central-equatorial Pacific. *Geophys Res. Lett.* https://doi.org/10.1029/2010GL044007 (2010).
17. Kim, H.-M., Webster, Peter, J. & Curry, J. A. Impact of shifting patterns of Pacific ocean warming on north Atlantic tropical cyclones. *Science* **325**, 77–80 (2009).
18. Hu, K., Huang, G., Huang, P., Kosaka, Y. & Xie, S.-P. Intensification of El Niño-induced atmospheric anomalies under greenhouse warming. *Nat. Geosci.* **14**, 377–382 (2021).
19. McGregor, H. V. et al. A weak El Nino/Southern oscillation with delayed seasonal growth around 4300 years ago. *Nat. Geosci.* **6**, 949–953 (2013).
20. Li, J. et al. El Niño modulations over the past seven centuries. *Nat. Clim. Change* **3**, 822–826 (2013).
21. Cobb, K. M. et al. Highly variable El Nino-Southern oscillation throughout the Holocene. *Science* **339**, 67–70 (2013).
22. Liu, Y. et al. Recent enhancement of central Pacific El Niño variability relative to last eight centuries. *Nat. Commun.* **8**, 15386 (2017).
23. Wittenberg AT. Are historical records sufficient to constrain ENSO simulations? *Geophys. Res. Lett.* https://doi.org/10.1029/2009GL038710 (2009).
24. Newman, M., Shin, S. I. & Alexander, M. A. Natural variation in ENSO flavors. *Geophys. Res. Lett.* **38**, L14705 (2011).
25. Grothe, P. R. et al. Enhanced El Nino-Southern oscillation variability in recent decades. *Geophys. Res. Lett.* **47**, e2019GL083906 (2020).
26. Gong, Y., Li, T. & Chen, L. Interdecadal modulation of ENSO amplitude by the Atlantic multi-decadal oscillation (AMO). *Clim. Dyn.* **55**, 2689–2702 (2020).
27. Zanchettin, D. et al. A decadally delayed response of the tropical Pacific to Atlantic multidecadal variability. *Geophys. Res. Lett.* **43**, 784–792 (2016).
28. Kang, I. S., No, H. H. & Kucharski, F. ENSO amplitude modulation associated with the mean SST changes in the tropical central pacific induced by Atlantic multidecadal oscillation. *J. Clim.* **27**, 7911–7920 (2014).
29. Yu, J. Y. et al. Linking emergence of the central Pacific El Niño to the Atlantic multidecadal oscillation. *J. Clim.* **28**, 651–662 (2015).
30. Wang, C. Three-ocean interactions and climate variability: a review and perspective. *Clim. Dyn.* **53**, 5119–5136 (2019).
31. Rayner, N. A. et al. Global analyses of sea surface temperature, sea ice, and night marine air temperature since the late nineteenth century. *J. Geophys. Res. Atmos.* https://doi.org/10.1029/2002JD002670 (2003).
32. Huang, B. et al. Extended reconstructed sea surface temperature, version 5 (ERSSTv5): upgrades, validations, and intercomparisons. *J. Clim.* **30**, 8179–8205 (2017).
33. Kaplan, A. et al. Analyses of global sea surface temperature 1856–1991. *J. Geophys Res. Oceans* **103**, 18567–18589 (1998).
34. Wang, B. et al. Historical change of El Nino properties sheds light on future changes of extreme El Niño. *Proc. Natl Acad. Sci. USA* https://doi.org/10.1073/pnas.19111301 (2019).
35. Fedorov, A. V., Hu, S., Lengaigne, M. & Guilyardi, E. The impact of westerly wind bursts and ocean initial state on the development, and diversity of El Niño events. *Clim. Dyn.* **44**, 1381–1401 (2014).
36. Chen, D. et al. Strong influence of westerly wind bursts on El Niño diversity. *Nat. Geosci.* **8**, 339–345 (2015).
37. Lengaigne, M. et al. Triggering of El Niño by westerly wind events in a coupled general circulation model. *Clim. Dyn.* **23**, 601–620 (2004).
38. Larkin, N. K. Global seasonal temperature and precipitation anomalies during El Niño autumn and winter. *Geophys. Res. Lett.* https://doi.org/10.1029/2005GL022860 (2005).
39. Ham, Y.-G. & Kug, J.-S. How well do current climate models simulate two types of El Niño? *Clim. Dyn.* **39**, 383–398 (2012).
40. Choi, J., An, S.-I., Kug, J.-S. & Yeh, S.-W. The role of mean state on changes in El Niño's flavor. *Clim. Dyn.* **37**, 1205–1215 (2010).
41. Xiang, B., Wang, B. & Li, T. A new paradigm for the predominance of standing Central Pacific warming after the late 1990s. *Clim. Dyn.* **41**, 327–340 (2013).
42. Fang, X.-H. & Mu, M. A three-region conceptual model for central Pacific El Niño including Zonal advective feedback. *J. Clim.* **31**, 4965–4979 (2018).
43. McGregor, S. et al. Recent Walker circulation strengthening and Pacific cooling amplified by Atlantic warming. *Nat. Clim. Change* **4**, 888–892 (2014).
44. Li, X., Xie, S.-P., Gille, S. T. & Yoo, C. Atlantic-induced pan-tropical climate change over the past three decades. *Nat. Clim. Change* **6**, 275–279 (2015).
45. Sun, C. et al. Western tropical Pacific multidecadal variability forced by the Atlantic multidecadal oscillation. *Nat. Commun.* **8**, 15998 (2017).
46. Levine, A. F. Z., McPhaden, M. J. & Frierson, D. M. W. The impact of the AMO on multidecadal ENSO variability. *Geophys Res. Lett.* **44**, 3877–3886 (2017).

47. Wang, J. et al. Internal and external forcing of multidecadal Atlantic climate variability over the past 1200 years. *Nat. Geosci.* **10**, 512–517 (2017).
48. Clement, A. C., Seager, R., Cane, M. A. & Zebiak, S. E. An ocean dynamical thermostat. *J. Clim.* **9**, 2190–2196 (1996).
49. Cane, M. A. et al. Twentieth-century sea surface temperature trends. *science* **275**, 957–960 (1997).
50. Huang, P., Xie, S.-P., Hu, K., Huang, G. & Huang, R. Patterns of the seasonal response of tropical rainfall to global warming. *Nat. Geosci.* **6**, 357–361 (2013).
51. Zhou, W., Xie, S.-P. & Yang, D. Enhanced equatorial warming causes deep-tropical contraction and subtropical monsoon shift. *Nat. Clim. Change* **9**, 834–839 (2019).
52. Callahan, C. W. et al. Robust decrease in El Nino/Southern oscillation amplitude under long-term warming. *Nat. Clim. Change* **11**, 752–757 (2021).
53. Cai, W. et al. Changing El Niño–Southern Oscillation in a warming climate. *Nat. Rev. Earth Environ.* **2**, 628–644 (2021).
54. Deser, C., Alexander, M. A., Xie, S. P. & Phillips, A. S. Sea surface temperature variability: patterns and mechanisms. *Ann. Rev. Mar. Sci.* **2**, 115–143 (2010).
55. Compo, G. P. et al. The twentieth century reanalysis project. *Q J. R. Meteorol. Soc.* **137**, 1–28 (2011).
56. Kanamitsu, M. et al. NCEP–DOE AMIP-II reanalysis (R-2). *Bull. Am. Meteor Soc.* **83**, 1631–1644 (2002).
57. Carton, J. A. & Giese, B. S. A reanalysis of ocean climate using Simple Ocean Data Assimilation (SODA). *Mon. Weather Rev.* **136**, 2999–3017 (2008).
58. Saha, S. et al. The NCEP climate forecast system. *J. Clim.* **19**, 3483–3517 (2006).
59. Morice, C. P. et al. An updated assessment of near-surface temperature change from 1850: the HadCRUT5 data set. *J. Geophys. Res. Atmos.* https://doi.org/10.1029/2019JD032361 (2021).
60. Freeman, E. et al. ICOADS Release 3.0: a major update to the historical marine climate record. *Int J. Climatol.* **37**, 2211–2232 (2017).
61. Allan, R. & Ansell, T. A new globally complete monthly historical gridded mean sea level pressure dataset (HadSLP2): 1850–2004. *J. Clim.* **19**, 5816–5842 (2006).
62. Stevenson, S. et al. Will there be a significant change to El Niño in the twenty-first century? *J. Clim.* **25**, 2129–2145 (2012).
63. Taschetto, A. S. et al. Cold tongue and warm pool ENSO events in CMIP5: mean state and future projections. *J. Clim.* **27**, 2861–2885 (2014).
64. Campbell, I. Chi-squared and Fisher-Irwin tests of two-by-two tables with small sample recommendations. *Stat. Med* **26**, 3661–3675 (2007).
65. Dai, A., Fyfe, J. C., Xie, S.-P. & Dai, X. Decadal modulation of global surface temperature by internal climate variability. *Nat. Clim. Change* **5**, 555–559 (2015).
66. Pyper, B. J. & Peterman, R. M. Comparison of methods to account for autocorrelation in correlation analyses of fish data. *Can. J. Fish. Aquat. Sci.* **55**, 2127–2140 (1998).
67. Zhao, W. & Khalil, M. A. K. The relationship between precipitation and temperature over the contiguous United States. *J. Clim.* **6**, 1232–1236 (1993).

Acknowledgements

The work was supported by the National Natural Science Foundation of China (42141019, 41831175, 41721004, 42175040), STEP (2019QZKK0102), Strategic Priority Research Program of Chinese Academy of Sciences (XDA20060500), the National Basic Research Program of China (2018YFA0605900, 2019YFA0606703). The work was also supported by the Youth Innovation Promotion Association of CAS (2021072), the Chinese Jiangsu Collaborative Innovation Center for Climate Change, the Frontiers Science Center for Critical Earth Material Cycling of Nanjing University, and High-Performance Computing Centers of Nanjing University.

Author contributions

Q.L. and G.H. designed the research, provided comments, and revised the manuscript. R.G. performed the analysis and drafted the manuscript. K.H. helped organize and revise the draft. X.L. gave comments and contributed to the discussion of the results. R.G., Q.L., G.H., K.H. and X.L. contributed to scientific interpretations and subsequent revisions.

Competing interests

The authors declare no competing interests.

Additional information

Supplementary information The online version contains supplementary material available at https://doi.org/10.1038/s41467-023-36053-7.

Correspondence and requests for materials should be addressed to Qi Liu or Gang Huang.

Peer review information *Nature Communications* thanks the anonymous reviewers for their contribution to the peer review of this work. Peer reviewer reports are available.

Reprints and permissions information is available at http://www.nature.com/reprints

Publisher's note Springer Nature remains neutral with regard to jurisdictional claims in published maps and institutional affiliations.

Open Access This article is licensed under a Creative Commons Attribution 4.0 International License, which permits use, sharing, adaptation, distribution and reproduction in any medium or format, as long as you give appropriate credit to the original author(s) and the source, provide a link to the Creative Commons license, and indicate if changes were made. The images or other third party material in this article are included in the article's Creative Commons license, unless indicated otherwise in a credit line to the material. If material is not included in the article's Creative Commons license and your intended use is not permitted by statutory regulation or exceeds the permitted use, you will need to obtain permission directly from the copyright holder. To view a copy of this license, visit http://creativecommons.org/licenses/by/4.0/.

© The Author(s) 2023

PNAS RESEARCH ARTICLE | EARTH, ATMOSPHERIC, AND PLANETARY SCIENCES OPEN ACCESS

Increased variability of the western Pacific subtropical high under greenhouse warming

Kai Yang[a], Wenju Cai[b,c,1], Gang Huang[a,d,e,1], Kaiming Hu[a], Benjamin Ng[c], and Guojian Wang[b,c]

Edited by John Wallace, University of Washington, Seattle, WA; received November 11, 2021; accepted April 4, 2022

An anomalous strengthening in western Pacific subtropical high (WPSH) increases moisture transport from the tropics to East Asia, inducing anomalous boreal summer monsoonal rainfall, causing extreme weather events in the densely populated region. Such positive WPSH anomalies can be induced by central Pacific (CP) cold sea-surface temperature (SST) anomalies of an incipient La Niña and warm anomalies in the Indian and/or the tropical Atlantic Ocean, both promoting anticyclonic anomalies over the northwestern Pacific region. How variability of the WPSH, its extremity, and the associated mechanisms might respond to greenhouse warming remains elusive. Using outputs from 32 of the latest climate models, here we show an increase in WPSH variability translating into a 73% increase in frequency of strong WPSH events under a business-as-usual emission scenario, supported by a strong intermodel consensus. Under greenhouse warming, response of tropical atmosphere convection to CP SST anomalies increases, as does the response of the northwestern Pacific anticyclonic circulation. Thus, climate extremes such as floods in the Yangtze River Valley of East China associated with WPSH variability are likely to be more frequent and more severe.

western Pacific subtropical high | East Asia flooding | climate extreme | climate change

Significance

The western Pacific subtropical high (WPSH) channels moisture from the tropics that underpins the East Asian summer climate. Interannual variability of the WPSH dominates climate extremes in the densely populated countries of East Asia. In 2020, an anomalously strong WPSH led to catastrophic floods with hundreds of deaths, 28,000 homes destroyed, and tens of billions in economic damage in China alone. How the frequency of such strong WPSH events will change is of great societal concern. Our finding of an increase in future WPSH variability, translating into an increased frequency of climate extreme as seen in the 2020 episode, highlights the increased risks for the billions of people in the densely populated East Asia with profound socioeconomic consequences.

The western Pacific subtropical high (WPSH) is an anticyclonic system hovering over the middle and lower troposphere of the northwestern Pacific, strongest in boreal summer (1, 2) (*SI Appendix*, Fig. S1*A*). The southerly winds in the west flank of the system transport moisture from the tropics to East Asia and collide with dry and cold flows from the north (2–4). These winds influence *meiyu* (*Baiu* in Japan and *Changma* in Korea) and an associated elongated rain belt that usually starts moving northward from southern China in May before its seasonal southward withdrawal in August, dominating variability of East Asian summer rainfall (3–6). The WPSH undergoes strong interannual variability (*SI Appendix*, Fig. S1*B*), exerting a severe impact on the boreal summer climate over the densely populated region of East Asia (2, 6–8).

A strong WPSH event occurs when the WPSH undergoes a westward intensification, influencing regional climate and leading to anomalous rainfall and inducing severe floods (4, 9). For example, during the 2020 strong WPSH event, floods in the Yangtze River Valley of East China caused hundreds of deaths, millions of hectares of crops destroyed, and tens of billions in economic damage (9, 10). Further back, in 1998, a strong WPSH contributed to river floods in East China that killed thousands and affected more than 200 million people (11).

Previous research examined observed WPSH variability, impact, and change over the period from 1979 to 2017 (12) or response of future climatological WPSH to greenhouse warming in models (13–17). There is an upward trend of the observed WPSH, which is expressed in a leading mode, but whether the WPSH variability above the trend has changed is not clear (12). Other studies found either a stronger or little changed mean WPSH under greenhouse warming (12–17). However, how WPSH variability that rides on the mean state, frequency of strong WPSH anomalies above the mean change, and associated mechanisms will change under future greenhouse warming remain largely unknown.

Multiple processes from ocean basins affect variability of the WPSH (5, 8, 18–22). One process is an atmospheric response to sea-surface temperature (SST) variability in the central Pacific (CP) (Niño4 region, 5°S-5°N, 160°E-150°W), where cool anomalies of an incipient La Niña develop in boreal summer (June, July, and August, JJA) (23); an incipient La Niña suppresses CP local convection, generating a westward propagated atmospheric Rossby wave that strengthens the WPSH (8, 24–29). An enhanced convection over the Maritime Continent associated with the La Niña strengthens the WPSH by modulating local Hadley circulation with increased anticyclonic circulation over the northwestern Pacific (30–32). Anomalous warming of the tropical North Atlantic is also

Author contributions: K.Y. and W.C. designed research; K.Y. performed research; K.H. contributed new reagents/analytic tools; B.N. and G.W. analyzed data; and K.Y., W.C., and G.H. wrote the paper.

The authors declare no competing interest.

This article is a PNAS Direct Submission.

Copyright © 2022 the Author(s). Published by PNAS. This open access article is distributed under Creative Commons Attribution-NonCommercial-NoDerivatives License 4.0 (CC BY-NC-ND).

[1]To whom correspondence may be addressed. Email: Wenju.Cai@csiro.au or hg@mail.iap.ac.cn.

This article contains supporting information online at http://www.pnas.org/lookup/suppl/doi:10.1073/pnas.2120335119/-/DCSupplemental.

Published May 31, 2022.

Downloaded from https://www.pnas.org by CSIRO Library Services on May 31, 2022 from IP address 140.253.235.29.

involved in driving positive WPSH anomalies by inducing CP cold SST anomalies and suppressed convection (33–35).

Another process involves the Indian Ocean, where boreal summer warming induced by a previous-year El Niño triggers warm Kelvin waves emanating into the tropical western Pacific, inducing an anomalous anticyclone at the low troposphere of the northwest Pacific (36, 37). Although the Indian Ocean mechanism can operate by itself with a residual warm condition of the decaying El Niño in the equatorial Pacific, it is in part incorporated in the impact of CP SST variability as the previous-year El Niño transitions to an incipient La Niña.

Because of the vast impact, how variability of the WPSH might change under greenhouse warming is an important issue. Assuming that greenhouse warming has an impact, one expects that observed WPSH variability of the past 42 y (1979 to 2020) should already be impacted. However, due to the short length of observational data and strong internal variability (38), whether change between the latter half (2000 to 2020) and former half (1979 to 1999) period has emerged out of internal variability is not clear. As such, we examine how WPSH variability might change under long-term further increasing greenhouse warming by comparing simulated WPSH variability between two 100-y periods of the 20th and 21st centuries. Over a longer period, impact of greenhouse warming is more detectable because the influence from internal variability is weaker and the climate change signal is larger (39, 40). Below we show that WPSH variability increases under long-term global warming, in turn suggesting that part of the observed change in WPSH variability is driven by greenhouse warming.

Observed WPSH Variability Associated with CP SST

To depict observed WPSH variability we use the circulation field from a reanalysis product (see *Reanalysis Datasets*). We apply an empirical orthogonal function (EOF) analysis (41) to the detrended JJA 850-hPa stream function anomalies referenced to the climatological average of the period 1979 to 2020, in the northwestern Pacific domain (10°N-40°N, 110°E-180°E). We use EOF analysis to identify and separate the main process dominating WPSH variability. The stream function is calculated based on winds (7, 42) and can capture the main characteristics of WPSH variability (30, 34) (see *Indices of WPSH*). We specifically avoid the commonly used geopotential height in the low or middle troposphere (18), as geopotential height is expected to increase with rising tropospheric temperatures under global warming (43–45).

The first two leading EOF patterns and principal component (PC) time series correspond to two components of WPSH variability (Fig. 1 *A* and *B*). EOF1 explains 77% of the total variance and features positive stream function anomalies over the whole northwestern Pacific with maximum anomalies around 20°N, 135°E. Its spatial pattern (Fig. 1*A*) captures main characteristics of a positively abnormal WPSH event, such as coherent high-pressure anomalies over the middle (500 hPa) and low (850 hPa) troposphere, an anomalous anticyclone anomaly at low troposphere, and positive rainfall anomalies in the Yangtze River Valley (*SI Appendix*, Fig. S2).

EOF2 explains 9.3% of the total variance. It is characterized by a southwest–northeast dipole pattern with positive anomalies over the northwest Pacific and negative anomalies to its northeast (Fig. 1*B*) and is associated with anomalous warming in the north Indian Ocean, preceded by a prior-year El Niño event with residual warm anomalies in the Pacific (36, 37) (*SI Appendix*, Fig. S3). Our depiction of WPSH variability above is similar to that in previous studies (8), but the order of the EOFs is different, due in part to the focused domain and data we used (see *Indices of WPSH*).

Time series of our PC1 compares well with other WPSH indices used in previous studies, for example based on areal average of 850-hPa eddy geopotential height over 15°N-25°N, 120°E-150°E (44) or areal average of stream function anomalies over the same domain (30, 34), where highest variability is seen (Fig. 1*C*). Correlation of the PC1 with the areal stream function anomalies average, or the areal eddy geopotential height average, is 0.95 or 0.80, respectively. All the three indices identify four strong positive WPSH events that occurred in 1995, 1998, 2010, and 2020, defined as when an index is larger than a threshold value of 1.5 SD over the 42 y of 1979 to 2020 (Fig. 1*C*) (see *Indices of WPSH*).

EOF2 reflects influence from the Indian Ocean warming, which is in part contributed by a previous-year El Niño, and shows a positive correlation with Niño4 (*SI Appendix*, Fig. S3). Large values of PC1 and PC2 appear in different years. PC2 contributes only to the 1995 and the 2020 strong WPSH events. As such, normalized PC1 is used to assess WPSH variability and identify strong WPSH events.

The PC1 varies coherently with SST variability in the Niño4 region, a positive index being associated with cold Niño4 anomalies, accompanied by anomalous warming over the Maritime Continent/South China Seas and in the tropical Atlantic (Fig. 1*D*; see *Indices of WPSH*). Warm tropical Atlantic anomalies usually peak in JJA and are conducive to an incipient La Niña (33, 46), via anomalous CP easterlies resulting from increased CP subsidence as the tropical Atlantic convection enhances (34, 35). The anomalous CP easterlies contribute to Niño4 cooling and hence to strengthening of the WPSH.

Focusing on the Pacific, the anomalous cooling in the Niño4 region suppresses local convection (*SI Appendix*, Fig. S4), strengthening the WPSH by generating a westward propagated atmospheric Rossby wave (8, 24–27). The positive SST anomalies and enhanced convection over the Maritime Continent associated with La Niña also strengthen the WPSH (*SI Appendix*, Fig. S4) by modulating local Hadley circulation with increased anticyclonic circulation over the northwestern Pacific (30, 31). In addition, easterly anomalies over the equatorial western Pacific associated with the WPSH in turn induce eastward propagating oceanic upwelling Kelvin waves, strengthening the CP cool anomalies, suggesting a positive feedback loop between the CP SST and the WPSH. These processes lead to a correlation coefficient of −0.73 between PC1 and the Niño4 SST, statistically significant above the 99% confidence level (Fig. 1*E*).

Increased WPSH Variability in Future Projection

We use outputs from 32 models participating in the Coupled Model Intercomparison Project phase 6 (CMIP6). These models are forced with historical forcing until 2014 and with Shared Socioeconomic Pathways (SSP) 5–8.5 (SSP5–8.5) emission scenario from 2015 onward to 2099 (47) (see *CMIP Models*). Monthly anomalies are calculated referenced to the climatological mean over the whole period and subsequently quadratically detrended. We apply EOF analysis on JJA stream function anomalies to obtain the WPSH variability pattern and index, as in the observations. Sharing a similar spatial pattern with observation,

Downloaded from https://www.pnas.org by CSIRO Library Services on May 31, 2022 from IP address 140.253.235.29.

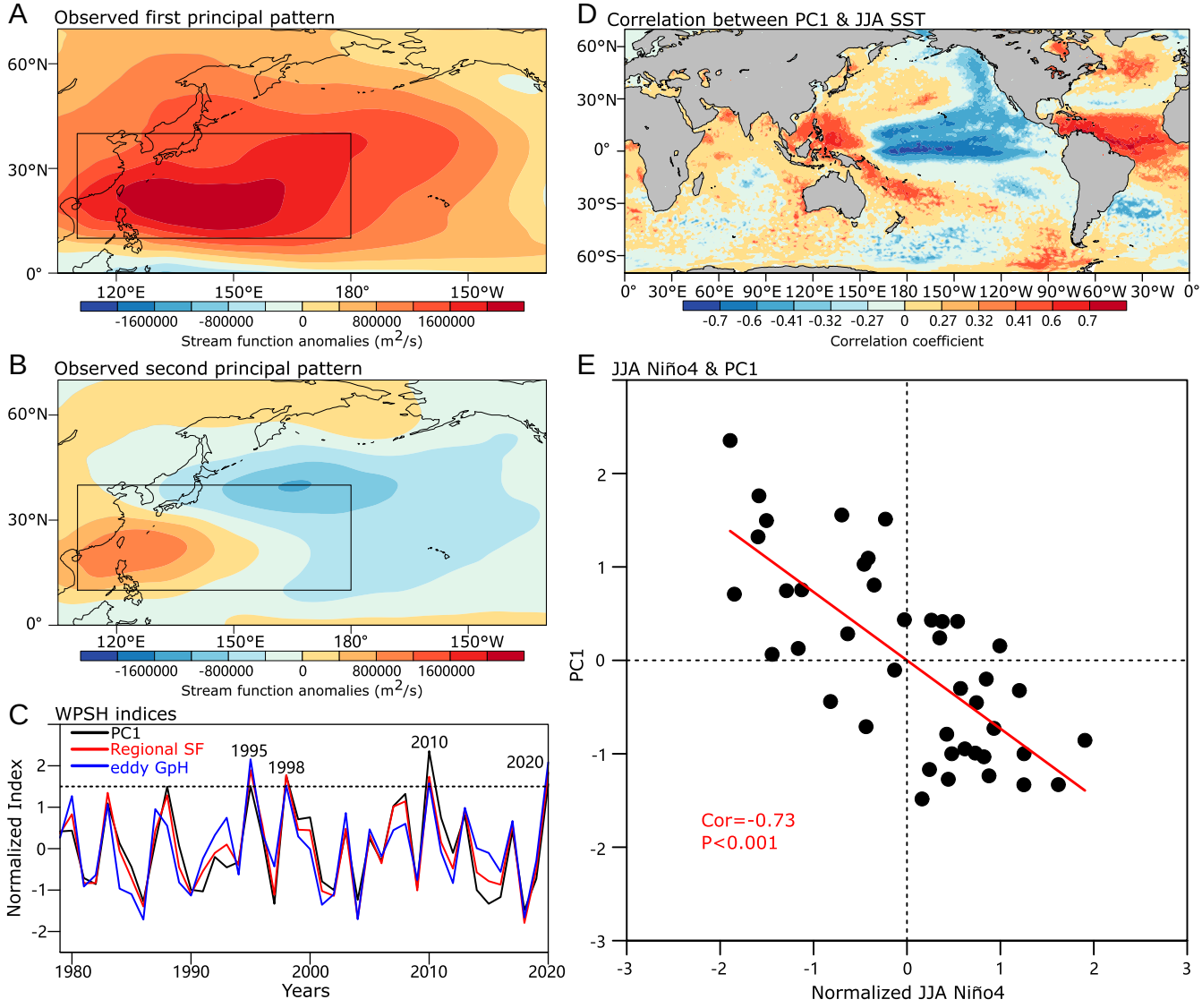

Fig. 1. Depiction of observed WPSH variability. (*A*) JJA averaged 850-hPa stream function anomalies (square meters per second) regressed onto the first PC (PC1) of EOF of JJA 850-hPa stream function anomalies over the northwest Pacific (10°N-40°N, 110°E-180°E) for the period of 1979 to 2020. EOF1 accounts for 77% of the total variance. (*B*) Same as *A*, but for PC2, which accounts for 9.3% of the total variance. The black box in *A* and *B* shows area of our EOF analysis. (*C*) Time series of normalized PC1 (black curve) and regional average of 850-hPa stream function anomalies (Regional SF, red curve) and 850-hPa eddy geopotential height over 15°N-25°N, 120°E-150°E (eddy GpH, blue curve). The black dashed line shows the 1.5 SD value. Years with an index larger than 1.5 SD are identified as 1995, 1998, 2010, and 2020. (*D*) Correlation of JJA SST anomalies with PC1. Correlation coefficients of ±0.27, ±0.32, and ±0.41 are statistically significant above the 90%, 95%, and 99% confidence levels, respectively. (*E*) Relationship between normalized JJA Niño4 and PC1, with a linear fit (red line) and corresponding correlation coefficient (Cor) and *P* value (P) shown. PC1 is principally influenced by Niño4 SST variability. The observed WPSH variability might be influenced by greenhouse warming, but we focus on changes in WPSH variability under future greenhouse warming.

the dominant EOF (EOF1) accounts for 60 to 83% of the total variance across the 32 models and on a multimodel mean basis explains 72% of the total variance (Fig. 2*A*). The second mode does not show an intermodel consensus in its response to greenhouse warming (further details are discussed in *Influence from SST beyond the Pacific Ocean*). Like in observations, we mainly focus on the variability change of PC1.

The PC1 is related to Niño4 SST variability, in particular to an incipient CP La Niña when the JJA Niño4 index is negative, accompanied by anomalous warming over the Maritime Continent/South China Sea region (Fig. 2*B*). In every model, a statistically significant (95%) correlation is produced between the PC1 and the Niño4 SST index, and the simulated correlation between the PC1 and the Niño4 index aggregated over all models is high and statistically significant (Fig. 2*C*), and this conclusion holds even if CP El Niño samples are excluded. In contrast to the observed, involvement of the tropical Atlantic is weak owing to a weaker tropical Atlantic influence on the Pacific (46, 48). Nevertheless, simulation of WPSH variability and its dynamics is reasonable.

We first compare simulated WPSH variability between the periods 2000 to 2020 and 1979 to 1999. The multimodel ensemble mean shows an increase of 4%, indicating a potential impact from greenhouse warming. However, only a total of 19 out of 32 (59%) models generate an increase (*SI Appendix*, Fig. S5). The intermodel consensus is low and does not exceed 68%, and the multimodel ensemble mean increase in not statistically significant, suggesting that any influence from greenhouse warming is yet to emerge out of internal variability. Despite this, below we show greenhouse warming during the past 42 y should have generated an increase in WPSH variability even though it is yet to emerge out of internal variability.

Downloaded from https://www.pnas.org by CSIRO Library Services on May 31, 2022 from IP address 140.253.235.29.

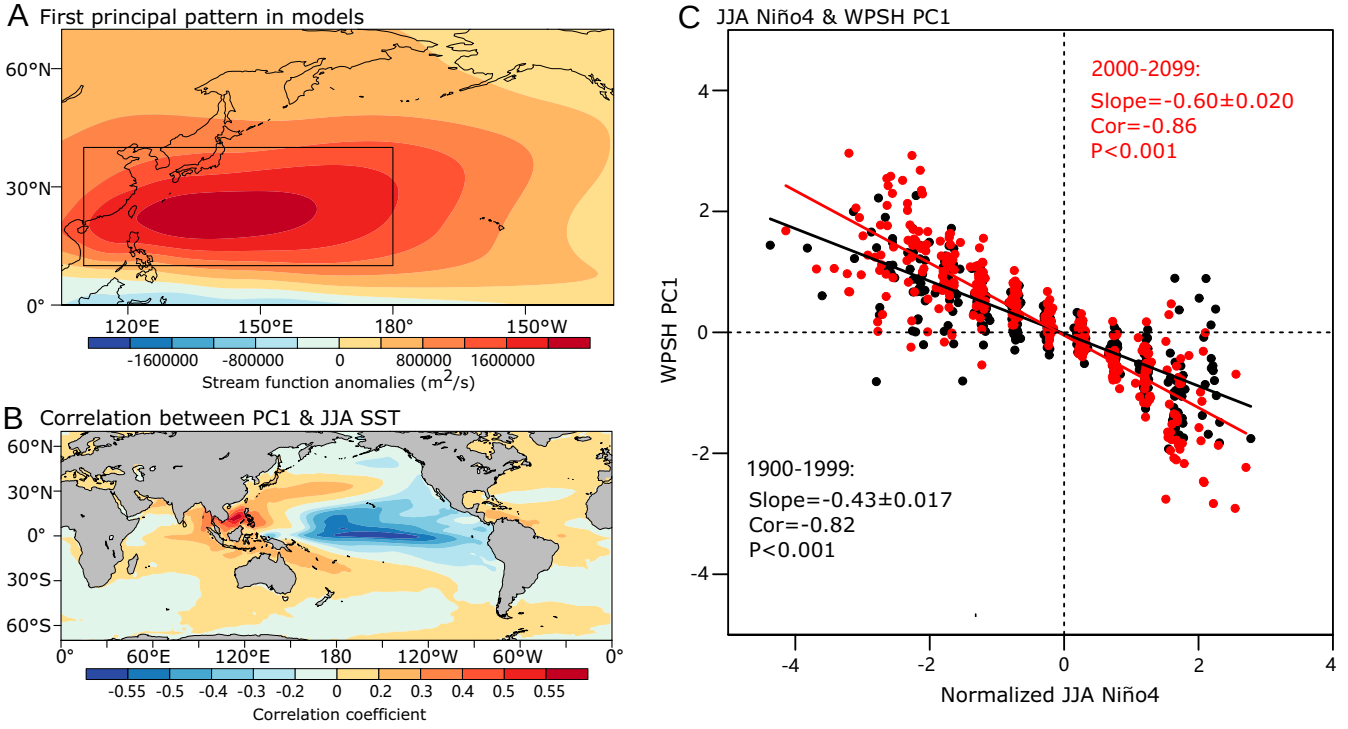

Fig. 2. WPSH variability and mechanism in CMIP6 models. (*A*) Multimodel average of JJA 850-hPa stream function anomaly (square meters per second) pattern obtained by regression onto modeled first PC (PC1) of EOF of JJA 850-hPa stream function anomalies over the northwest Pacific (10°N-40°N, 110°E-180°E) in the period of 1900 to 2099. (*B*) Multimodel average correlations of JJA SST anomalies with PC1. (*C*) Relationship between normalized Niño4 and PC1 aggregated over 32 CMIP6 models for the present-day (1900 to 1999) and future (2000 to 2099) climate, with a linear fit (solid line) and statistical properties shown, including the slope of the linear fit (Slope) and its SE, correlation coefficient (Cor) and *P* value (P). In each model, Niño4 and PC1 are averaged in bins of 0.5 intervals. The models reasonably simulate the observed WPSH variability and its relationship with Niño4 SST.

We compare variability of the PC1 between the 20th- (1900 to 1999) and 21st-century (2000 to 2099) climate. A total of 30 out of 32 models (94%) show an increase in PC1 variability from the 20th century to the future period (Fig. 3*A*). The strong intermodel consensus is supported by a multimodel ensemble mean increase of 16%, statistically significant above the 95% confidence level according to a bootstrap test (see *Statistical Test*). The increase in variability translates to an increased frequency of strong WPSH events, defined as when the PC1 is greater than 1.5 SD. A total of 27 out of the 32 (84%) models produce a higher frequency of strong WPSH events in 2000 to 2099. The multimodel ensemble mean frequency increases by 73%, from 4.5 events per century in the 20th century to 7.8 events per century in the 21st century (Fig. 3*B*). The conclusion of an increased frequency of the strong WPSH is not sensitive to the threshold used (*SI Appendix*, Fig. S6).

The increase in WPSH variability in response to greenhouse warming is further supported by results from CMIP5 models. We analyze 35 available CMIP5 models forced by historical emissions of greenhouse gases before 2005 and a Representative Concentration Pathway 8.5 (RCP8.5) (49) from 2006 to 2099, equivalent to the SSP5–8.5 emission scenario (see *CMIP Models*). An analysis identical to that conducted for CMIP6 models finds that 27 out of 35 CMIP5 models (77%) generate an increase in WPSH PC1 variability, translating into a multimodel ensemble mean increase of 11% in WPSH PC1 variability and 56% in occurrences of strong WPSH events (*SI Appendix*, Fig. S7).

An increased variability of PC1 and generally unchanged variability of PC2 result in an increased variability of WPSH in the future. The total variability of WPSH, defined as stream function anomalies averaged over 15°N-25°N, 120°E-150°E, shows an increase in the future climate supported by 84% of the models (27 out of the 32 models show an increase) (*SI Appendix*, Fig. S8 *A* and *B*). Models that generate a greater increase in WPSH stream function index variability systematically generate a greater increase in the detrended WPSH geopotential height index variability and WPSH zonal wind shear index variability (*SI Appendix*, Fig. S8*C*), suggesting that the long-term increase in the mean geopotential height associated with the rising tropospheric temperatures under global warming is accompanied by the increase in WPSH variability that rides on the long-term trend.

Thus, by comparing simulated 100-y-long WPSH variability between the 20th and 21st centuries we show that greenhouse warming leads to increased WPSH variability. It follows that greenhouse warming over the past 42 y should have contributed to the increase in WPSH variability over the period 1979 to 2020 discussed above.

Higher Sensitivity to CP SST in a Warming Climate

The increase in WPSH variability and in frequency of strong WPSH events underpinned by the strong intermodel consensus is despite the fact that only half of the models (16 out of 32, or 50%) produce an increase in JJA Niño4 SST variability, suggesting that the increase in WPSH variability is not due to a change in JJA Niño4 SST variability (*SI Appendix*, Fig. S9). Instead, the increase in WPSH variability results from an increased WPSH sensitivity to Niño4 SST under global warming.

We calculate the sensitivity by regressing the PC1 onto the Niño4 index separately for the 20th century and the 21st century to obtain the change between the two periods. To facilitate intermodel comparison, changes in WPSH variability and in

Downloaded from https://www.pnas.org by CSIRO Library Services on May 31, 2022 from IP address 140.253.235.29.

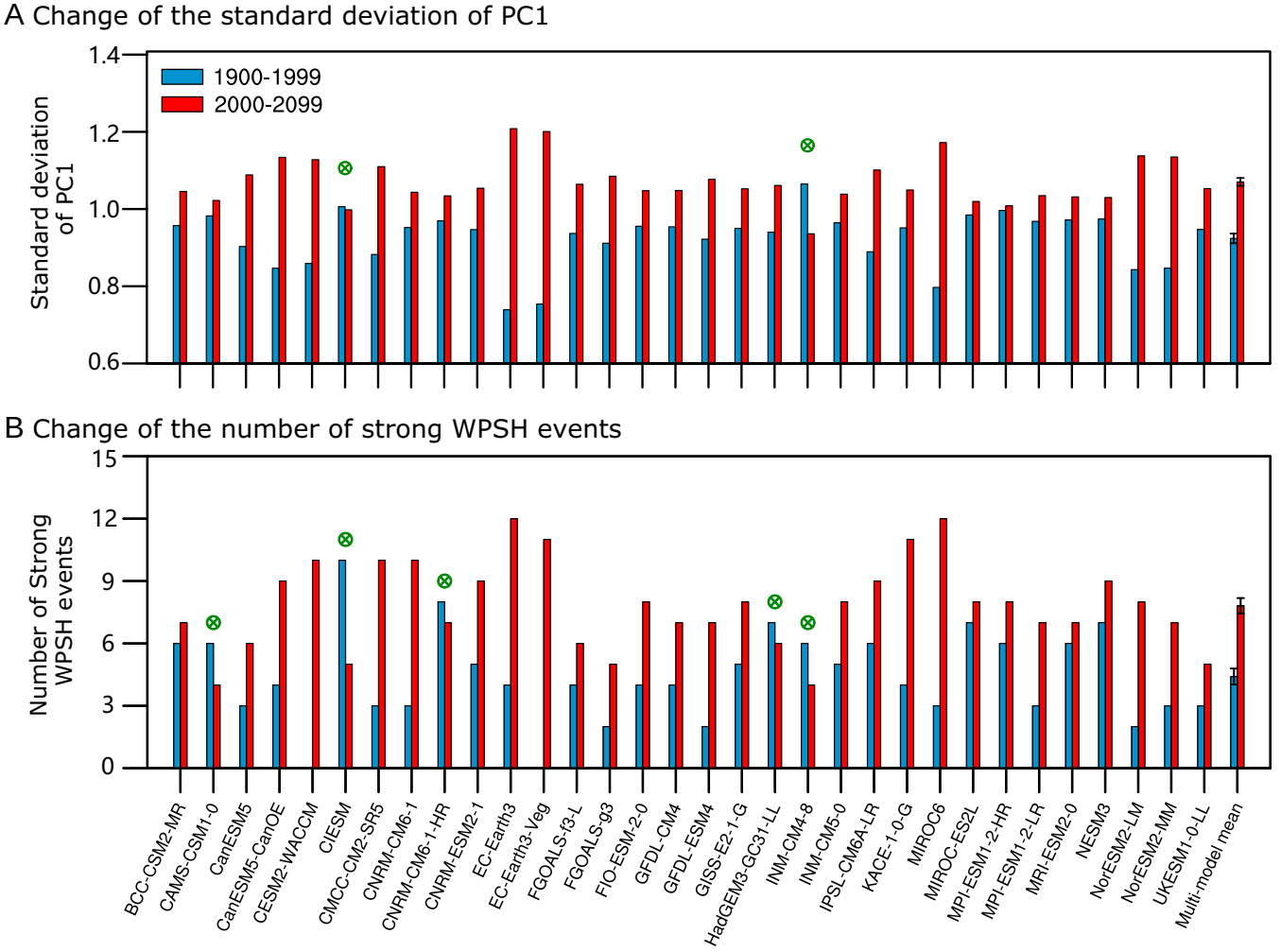

Fig. 3. Projected changes of WPSH variability and strong events. (*A*) A total of 30 out of the 32 CMIP6 models (94%) generate an increase in WPSH PC1 variability from the 20th-century (blue bars) to the 21st-century (red bars) climate. The multimodel mean of the increase is 16%, which is statistically significant above the 95% confidence level (see *Statistical Test*). (*B*) The increase in WPSH PC1 variability translates into a 73% increase in the frequency of strong WPSH events defined as when PC1 > 1.5 SD. The increased frequency is supported by a strong intermodel consensus, with 84% (27 out of the 32) models simulating an increase and is statistically significant (see *Statistical Test*). Models show a decrease are marked by green circles.

the sensitivity are both scaled by the corresponding rise in global mean temperature in each model. In most models, the sensitivity increases, and a greater increase in WPSH sensitivity is systematically associated with a greater increase in WPSH variability (Fig. 4*A*). An overall increased sensitivity of the WPSH to Niño4 is also seen among models (Fig. 2*C*).

Similarly, for each model, we calculate sensitivity of tropical atmosphere convection to Niño4 SST by regressing grid-point outgoing longwave radiation (OLR) anomalies at the top of the atmosphere to the Niño4 index in each period separately to obtain pattern of change in convective sensitivity, scaled by the corresponding global mean temperature rise. The multimodel ensemble mean over the 32 models shows an overall increase in convective sensitivity in the future period. In response to same-sized CP negative SST anomalies, the pattern of depressed convection in the central to eastern Pacific but enhanced convection in the western Pacific and the Maritime Continent, and vice versa, for CP positive SST anomalies is stronger in the 21st-century than in the 20th-century climate (Fig. 4*B*). Consequently, there is a commensurate increase in sensitivity of grid-point 850 hPa stream function anomalies to the Niño4 index, obtained similarly as for the grid-point OLR. The multimodel ensemble mean change in the circulation sensitivity features a stronger anomalous anticyclonic circulation response over the northwestern Pacific to the same Niño4 cooling in the 21st century than in the 20th century (Fig. 4*C*).

That the increased atmosphere convective sensitivity is systematically responsible for enhanced sensitivity of the northwest Pacific stream function is further illustrated in an intermodel relationship between changes in the convective sensitivity pattern and changes in the circulation sensitivity pattern. For each model, we obtain intensity of the convective sensitivity change, and of the circulation sensitivity change, by a pattern regression of an individual-model change pattern onto the ensemble-mean pattern. A greater change in the tropical Pacific convective sensitivity leads to a greater circulation sensitivity (Fig. 4*D*), and therefore a greater increase in WPSH variability.

Several factors are responsible for the increased convective sensitivity. These include a faster warming in the Maritime Continent than in the CP such that atmosphere convection is more likely to move to the Maritime Continent, generating greater convective anomalies (23), and a generally more sensitive atmosphere to the SST anomalies because of the Clausius–Clapeyron relationship, whereby saturation vapor pressure increases exponentially with the increasing temperature (50). As such, response of the tropical humidity and

Downloaded from https://www.pnas.org by CSIRO Library Services on May 31, 2022 from IP address 140.253.235.29.

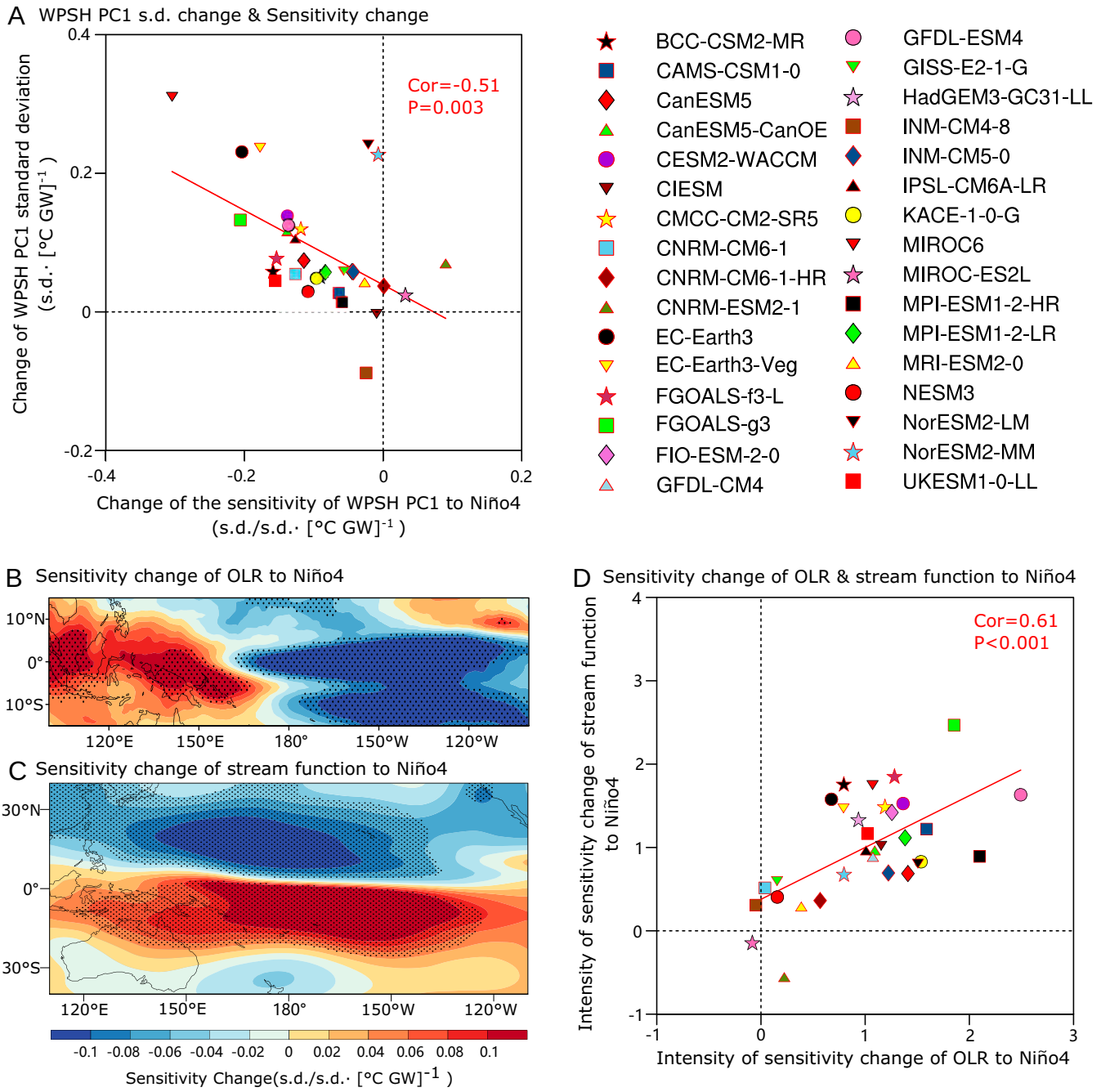

Fig. 4. Mechanisms for projected changes of WPSH. (*A*) Intermodel relationship between projected changes in WPSH PC1 variability and changes in sensitivity of WPSH to JJA Niño4 using 32 CMIP6 models, scaled by global warming rate in each model. A linear fit (red line) and statistical property are shown. The sensitivity is calculated as the regression coefficient of PC1 onto Niño4. JJA Niño4 has been normalized over the whole period first. (*B*) Multimodel average of projected change in sensitivity of JJA OLR to JJA Niño4 scaled by global warming rate in each model. Stippled areas indicate where the multimodel averaged change is statistically significant above the 95% confidence level according to a two-tailed Student's *t* test. (*C*) Same as *B* but for JJA stream function. The OLR and stream function anomalies in each grid have been normalized over the whole period in each model before calculating the sensitivity. (*D*) Intermodel relationship between intensity of the projected change in the OLR sensitivity pattern shown in *B* and in the stream function sensitivity pattern shown in *C*. The intensity is calculated by regressing the sensitivity change pattern scaled by global warming rate in each model onto the multimodel mean sensitivity change pattern in the domain of (10°S-10°N, 100°E-120°W) for OLR and (30°S-30°N, 110°E-120°W) for stream function. A linear fit and statistical properties are shown in red. An increased sensitivity of tropical convection to Niño4 in warming climate leads to an increased response of atmosphere circulation to Niño4 variability and hence strengthened WPSH variability.

associated gross moist instability to SST anomalies is larger in a warmer world of the 21st century than in the 20th century.

Impact from Internal Variability

To examine the possibility that the increase in WPSH variability is due to chances or internal variability, we make use of a set of 40-member simulation experiments with the Community Earth System Model Large Ensemble (CESM-LE) (39) (see *Large Ensemble Experiments*). These experiments are forced similarly to CMIP5 models, starting from 1920, and the only difference among them is a small perturbation in the initial condition resulting in different internal variability (51). We compare the change between the two 90-y periods: 1920 to 2009 and 2010 to 2099.

Downloaded from https://www.pnas.org by CSIRO Library Services on May 31, 2022 from IP address 140.253.235.29.

Without impact from greenhouse warming, there would be a 50 ± 18% chance of generating an increase or decrease in WPSH variability. However, like in CMIP5 or CMIP6 models, the set of experiments produce an increase in WPSH variability in 35 out of 40 (88%) experiments (*SI Appendix*, Fig. S10), with a statistically significant increase in the multiexperiment ensemble mean change. Further, the increase in WPSH variability similarly results from an enhanced sensitivity to Niño4 SST variability (*SI Appendix*, Fig. S11; see *Large Ensemble Experiments*).

We also apply outputs of an 1800-y preindustrial (PI)-control experiment using the CESM. The PI-control simulation, with no greenhouse warming forcing, is used to measure the impact of internal variability on the WPSH. We calculate 1,700 sets of 90-y SD of the WPSH index by constructing 1,700 sets of 90-y continuous time series of WPSH index with different starting year. We then rank the 1,700 values of 90-y SD of the WPSH index from the smallest to the largest (*SI Appendix*, Fig. S12) and identify the 95th percentile value to represent the upper bound of magnitude of WPSH variability associated with internal variability.

The 95th percentile value of the 90-y SD is 2.9×10^6 m^2/s, which is larger than the CESM-LE 40-experiment ensemble mean value (2.7×10^6 m^2/s) of the WPSH index SD during the period 1920 to 2009. Further, only 7 out of the total 40 experiments have an SD larger than 2.9×10^6 m^2/s (*SI Appendix*, Fig. S12). Thus, although greenhouse warming has already been proceeding in 1920 to 2009, its impact on WPSH variability has not emerged out of internal variability.

By contrast, the 40-experiment ensemble mean value of the WPSH index variability during 2010 to 2099 (future period defined in CESM-LE) is 3.2×10^6 m^2/s and is larger than the 95th percentile value of the 90-y SD (2.9×10^6 m^2/s) in the PI-control experiment. In addition, 36 out of the total 40 experiments have a WPSH variability larger than 2.9×10^6 m^2/s, indicating that the increased WPSH variability in the future is not due to internal variability but to greenhouse warming (*SI Appendix*, Fig. S12).

We further compare the magnitude of internal variability in different time length over which the statistics are calculated. The SD of the 1,700 values of 90-y SD of WPSH index is 1.8×10^5 m^2/s, while the SD of the 1,700 values of 40-y SD of WPSH index is 3.0×10^5 m^2/s (*SI Appendix*, Fig. S12*A*), supporting the notion that the impact of internal variability is smaller when the time length used to calculate statistics is longer.

In conclusion, the projected increases in WPSH variability and in frequency of strong WPSH events are despite a lack of intermodel consensus on changes in boreal summer SST variability in the central equatorial Pacific. Instead, the increase in WPSH variability is underpinned by a stronger sensitivity of the atmosphere convection to SST in the central equatorial Pacific under greenhouse warming. The higher convective sensitivity in turn generates a greater circulation response, giving rise to higher WPSH variability. The associated increase in the frequency of strong WPSH events means that climate extremes as seen in 1998 and 2020 are projected to occur more frequently (*SI Appendix*, Fig. S13) with severe impacts on lives of the densely populated East Asian countries.

Materials and Methods

Reanalysis Datasets. Monthly wind, stream function, SST, geopotential height, OLR, and precipitation data are from ERA5 (fifth generation of the European Centre for Medium-Range Weather Forecasts atmospheric reanalyses) datasets (52) for the period of 1979 to 2020 with a horizontal resolution of 0.25° × 0.25°. All anomalies are referenced to the climatology over the whole period and linearly detrended. We also use monthly stream function data from NCEP/NCAR (National Centers for Environmental Prediction/National Center for Atmospheric Research) reanalysis (53) and precipitation data from GPCP (Global Precipitation Climatology Project) Version 2.3 Combined Precipitation Data Set (54) over the same period and get similar results.

Indices of WPSH. Variability of the WPSH is conventionally described by geopotential height over the northwestern Pacific. However, geopotential height under greenhouse warming increases with temperature (44, 45). As such, we use stream function to represent the WPSH and apply EOF (41) analysis to the stream function field over the northwestern Pacific (10°N-40°N, 110°E-180°E). The WPSH index defined as regional average of stream function anomalies over the 15°N-25°N, 120°E-150°E is highly correlated with geopotential height anomalies averaged over the same domain and another zonal wind shear index, defined as the zonal wind anomalies difference between 5°N-15°N, 100°E-130°E, and 20°N-30°N, 110°E-140°E (36, 55, 56), with a correlation coefficient of 0.87 and 0.86, respectively. These three indices show a similar ability in depicting the East Asian summer climate.

The leading mode of the EOF based on ERA5 reanalysis explains 77% of the total variance. PC1, scaled to unity, is highly correlated with the regionally averaged stream function anomalies and eddy geopotential height (Fig. 1*C*) both averaged over the 15°N-25°N, 120°E-150°E. Eddy geopotential height is defined as geopotential height anomalies referenced to zonal mean geopotential height over 0 to 40°N and is constructed to remove the increase associated with global warming (44).

PC1 is highly correlated with JJA Niño4 with a correlation coefficient of −0.73 (Fig. 1*E*), while previous research (8, 36) documented that WPSH index defined based on geopotential height and zonal wind shear is not significantly correlated with the concurrent El Niño–Southern Oscillation (ENSO) index. The stream function index tends to have a higher correlation with CP SST than the other indices. The geopotential height index has a larger variance over the higher latitude than over the lower latitudes, whereas the stream function index has a larger loading over the tropical region and therefore is more linked to the CP SST. The distinct relationship of CP SST with the indices is mainly contributed by the nonstrong event years because the WPSH index based on stream function or geopotential height generally identifies the same strong events (Fig.1*C*). The more fundamental cause of the weak correlation is because PC1 is negatively correlated with Niño4, but PC2 is positively correlated with Niño4 at a correlation coefficient of 0.38 (see also Fig. 1 and *SI Appendix*, Fig. S3*B*), such that the total WPSH variability is weakly correlated with CP SST. This further demonstrates the need for a EOF analysis to separate the two parts of WPSH variability.

CMIP Models. We use monthly outputs from 32 climate models participating in CMIP6 (47) and 35 models participating in CMIP5 (49). These models are forced with historical anthropogenic and natural forcings before 2005 for CMIP5 and prior to 2014 for CMIP6 and future greenhouse gases under the RCP8.5 for CMIP5 and the equivalent updated scenario for CMIP6, the SSP5–8.5. Each model simulation covers a 200-y period of 1900 to 2099. To enable intermodel comparison, all data are regridded to a common resolution of 1° longitude by 1° latitude. Monthly anomalies are constructed from a climatological average over the full period 1900 to 2099 before they are quadratically detrended.

Influence from SST beyond the Pacific Ocean. EOF2 of JJA stream function over the northwestern Pacific is associated with a warm north Indian Ocean and a preceding eastern Pacific El Niño (*SI Appendix*, Fig. S3). An anomalous warming in the Indian Ocean occurs in the ensuing summer after an El Niño event matures. The warming causes an anomalous anticyclone at the low troposphere of the northwest Pacific by triggering warm Kelvin waves emanating into the tropical western Pacific, a process referred to as the Indian Ocean capacitor effect (36, 37). In observations PC2 only contributes to half of the strong WPSH events, i.e., 1995 and 2020 (*SI Appendix*, Fig. S3). EOF3 reflects the influence of local SST on WPSH through atmosphere–ocean feedback (8, 27), which explains 4% of the total variance and is not considered further in our analysis of model outputs.

CMIP models simulate a PC2 pattern similar to that in observations. Changes in variability of PC2 between the 20th century and future period show no

Downloaded from https://www.pnas.org by CSIRO Library Services on May 31, 2022 from IP address 140.253.235.29.

intermodel consensus, with 50% of the models showing an increase and the other 50% showing a decrease. The intensity of the anomalous anticyclone associated with a warm Indian Ocean and a preceding El Niño under global warming is influenced by several processes. Similar to the stronger response of EOF1 to the CP La Niña, the anomalous anticyclone induced by the warm Indian Ocean may be stronger under global warming due to the increased sensitivity of tropospheric temperature to SST anomalies (57). However, rainfall and latent heat anomalies over the Indian Ocean associated with SST anomalies are weaker because of an increase in static stability of the boundary layer in a warmer climate, unfavorable for formation of anomalous anticyclone over the northwest Pacific (58). In addition, a projected smaller SST gradient between the tropical Indian Ocean and the northwest Pacific also weakens the anomalous anticyclone associated with the preceding El Niño (59). Competition of these processes and intermodel differences in ENSO property, such as El Niño decaying pace (60), contribute to the intermodel divergence of the projected change in PC2 variability.

Statistical Test. We use a bootstrap test (61) to examine whether the increased WPSH variance is statistically significant. We randomly resample the 32 WPSH index SD values of the CMIP6 models in the 20th-century climate (1900 to 1999) to form 10,000 realizations of 32-sample mean SD. Each resampling process for a realization is independent and any of the 32 samples can be repeated. The same is carried out for the 21st-century climate (2000 to 2099). The multimodel ensemble mean increase in WPSH variability between the 20th-century and 21st-century climate is statistically significant above the 95% confidence level if the multimodel mean increase in WPSH index SD between the two centuries is greater than the sum of the SDs of the 10,000 interrealizations in the 20th-century and 21st-century climate.

Large Ensemble Experiments. We take 40 members of simulation experiments of the CESM-LE (39) to examine the role of internal variability. These experiments are subject to greenhouse warming that follows the CMIP5 design protocol (49) with historical emissions of greenhouse gases from 1850/1920 to 2005 and RCP8.5 forcing from 2006 to 2100. Ensemble member 1 was carried out from 1850, and the other members were created from perturbations of ensemble member 1 in 1920. The initial conditions are identical (end of 1919), except with an imposed infinitesimally small random perturbation to the atmospheric state at the level of machine round-off error (10^{-14} °C in air temperature) at the beginning of 1920. Therefore, any subsequent difference between model experiment members is due to internal variability (51).

Results from CESM-LE strengthen the conclusions and mechanisms in CMIP models. The multiexperiment mean EOF1 pattern is similar to those in observation and CMIP models (*SI Appendix*, Fig. S10 *A* and *B*). We compare changes between the initial 90 y (1920 to 2009) and last 90 y (2010 to 2099). Among the 40 experiments, 35 (88%) experiments show an increase in WPSH variability in the future. The multiexperiment increase is significant above the 95% confidence level according to the bootstrap test (*SI Appendix*, Fig. S10*C*). The interexperiment difference in the WPSH variability change is due to the internal variability, in which the change in Niño4 variability plays an important role (*SI Appendix*, Fig. S11*A*). Similar to CMIP6, the change in Niño4 variability under greenhouse warming shows no interexperiment consensus (*SI Appendix*, Fig. S11*A*), but an increased sensitivity of WPSH index to Niño4 leads to the increase in WPSH variability (*SI Appendix*, Fig. S11*B*).

Data Availability. All study data are included in the article and/or *SI Appendix*.

ACKNOWLEDGMENTS. This work is supported by the National Natural Science Foundation of China (42141019, 41831175, 91937302, and 42105032), the Strategic Priority Research Program of Chinese Academy of Sciences (XDB40000000 and XDA20060501), The Second Tibetan Plateau Scientific Expedition and Research (STEP) program (2019QZKK0102), and the China Postdoctoral Science Foundation (2018M640168). W.C., G.W., and B.N. are supported by the Center for Southern Hemisphere Oceans Research, a joint research Center for Southern Hemisphere Oceans Research between Qingdao National Laboratory for Marine Science and Technology and the Commonwealth Scientific and Industrial Research Organisation. We acknowledge the World Climate Research Programme's Working Group on Coupled Modelling, which is responsible for CMIP, and we thank the climate modeling groups for producing and making available their model output. For CMIP, the US Department of Energy's Program for Climate Model Diagnosis and Intercomparison provides coordinating support and led development of software infrastructure in partnership with the Global Organization for Earth System Science Portals. We are grateful to the reanalysis groups for making the datasets publicly available.

Author affiliations: [a]State Key Laboratory of Numerical Modeling for Atmospheric Sciences and Geophysical Fluid Dynamics, Institute of Atmospheric Physics, Chinese Academy of Sciences, Beijing 100029, China; [b]Key Laboratory of Physical Oceanography–Institute for Advanced Ocean Studies, Ocean University of China and Qingdao National Laboratory for Marine Science and Technology, Qingdao 266003, China; [c]Center for Southern Hemisphere Oceans Research, CSIRO Oceans and Atmosphere, Hobart, TAS 7004, Australia; [d]Laboratory for Regional Oceanography and Numerical Modeling, Qingdao National Laboratory for Marine Science and Technology, Qingdao 266237, China; and [e]University of Chinese Academy of Sciences, Beijing 100049, China

1. S. Y. Tao, L. X. Liu, A review of recent research on the East Asian summer monsoon in China. *Monsoon Meteorol.* **1987**, 60–92 (1987).
2. Y. Ding, C. L. C. Johnny, The East Asian summer monsoon: An overview. *Meteorol. Atmos. Phys.* **89**, 117–142 (2005).
3. R. Zhang, A. Sumi, M. Kimoto, A diagnostic study of the impact of El Niño on the precipitation in China. *Adv. Atmos. Sci.* **16**, 229–241 (1999).
4. C. P. Chang, Y. Zhang, T. Li, Interannual and interdecadal variations of the East Asian summer monsoon and tropical Pacific SSTs. Part I: Roles of the subtropical ridge. *J. Clim.* **13**, 4310–4325 (2000).
5. T. Zhou *et al.*, Why the Western Pacific subtropical high has extended westward since the late 1970s. *J. Clim.* **22**, 2199–2215 (2009).
6. T. Tomita, T. Yoshikane, T. Yasunari, Biennial and lower-frequency variability observed in the early summer climate in the Western North Pacific. *J. Clim.* **17**, 4254–4266 (2004).
7. E.-J. Lee, J.-G. Jhun, C.-K. Park, Remote connection of the Northeast Asian summer rainfall variation revealed by a newly defined monsoon index. *J. Clim.* **18**, 4381–4393 (2005).
8. B. Wang, B. Xiang, J.-Y. Lee, Subtropical high predictability establishes a promising way for monsoon and tropical storm predictions. *Proc. Natl. Acad. Sci. U.S.A.* **110**, 2718–2722 (2013).
9. Z.-Q. Zhou, S.-P. Xie, R. Zhang, Historic Yangtze flooding of 2020 tied to extreme Indian Ocean conditions. *Proc. Natl. Acad. Sci. U.S.A.* **118**, e2022255118 (2021).
10. Huaxia, China raises flood response to second-highest level. www.xinhuanet.com/english/2020-07/12/c_139207054.htm. *Xinhua News*, 12 July 2020. Accessed 12 February 2021.
11. S. N. Jonkman, Global perspectives on loss of human life caused by floods. *Nat. Hazards* **34**, 151–175 (2005).
12. W. Choi, K.-Y. Kim, Summertime variability of the western North Pacific subtropical high and its synoptic influences on the East Asian weather. *Sci. Rep.* **9**, 7865 (2019).
13. C. He, T. Zhou, Responses of the Western North Pacific subtropical high to global warming under RCP4.5 and RCP8.5 scenarios projected by 33 CMIP5 models: The dominance of Tropical Indian Ocean–Tropical Western Pacific SST Gradient. *J. Clim.* **28**, 365–380 (2015).
14. B. Preethi, M. Mujumdar, A. Prabhu, R. Kripalani, Variability and teleconnections of South and East Asian summer monsoons in present and future projections of CMIP5 climate models. *Asia-Pac. J. Atmospheric Sci.* **53**, 305–325 (2017).
15. A. Cherchi *et al.*, The response of subtropical highs to climate change. *Curr. Clim. Change Rep.* **4**, 371–382 (2018).
16. W. Li, L. Li, M. Ting, Y. Liu, Intensification of Northern Hemisphere subtropical highs in a warming climate. *Nat. Geosci.* **5**, 830–834 (2012).
17. X. Chen, T. Zhou, P. Wu, Z. Guo, M. Wang, Emergent constraints on future projections of the western North Pacific Subtropical High. *Nat. Commun.* **11**, 2802 (2020).
18. R. Lu, B. Dong, Westward extension of North Pacific subtropical high in summer. *J. Meteorol. Soc. Japan. Ser. II* **79**, 1229–1241 (2001).
19. H. Li, F. Xu, Y. Lin, The impact of SST on the zonal variability of the Western Pacific subtropical high in boreal summer. *J. Geophys. Res.: Atmos.* **125**, e2019JD031720 (2020).
20. S. Matsumura, T. Horinouchi, Pacific Ocean decadal forcing of long-term changes in the western Pacific subtropical high. *Sci. Rep.* **6**, 37765 (2016).
21. S. Matsumura, S. Sugimoto, T. Sato, Recent intensification of the Western Pacific subtropical high associated with the East Asian summer monsoon. *J. Clim.* **28**, 2873–2883 (2015).
22. K.-S. Yun, S.-W. Yeh, K.-J. Ha, Distinct impact of tropical SSTs on summer North Pacific high and western North Pacific subtropical high. *J. Geophys. Res. D Atmospheres* **118**, 4107–4116 (2013).
23. W. Cai *et al.*, Increased frequency of extreme La Niña events under greenhouse warming. *Nat. Clim. Chang.* **5**, 132–137 (2015).
24. Z. Chen, Z. Wen, R. Wu, X. Lin, J. Wang, Relative importance of tropical SST anomalies in maintaining the Western North Pacific anomalous anticyclone during El Niño to La Niña transition years. *Clim. Dyn.* **46**, 1027–1041 (2016).
25. T. Li *et al.*, Theories on formation of an anomalous anticyclone in western North Pacific during El Niño: A review. *J. Meteorol. Res.* **31**, 987–1006 (2017).
26. M. F. Stuecker, F.-F. Jin, A. Timmermann, S. McGregor, Combination mode dynamics of the anomalous Northwest Pacific anticyclone. *J. Clim.* **28**, 1093–1111 (2015).
27. B. Xiang, B. Wang, W. Yu, S. Xu, How can anomalous western North Pacific Subtropical High intensify in late summer? *Geophys. Res. Lett.* **40**, 2349–2354 (2013).
28. L. Fan, S.-I. Shin, Q. Liu, Z. Liu, Relative importance of tropical SST anomalies in forcing East Asian summer monsoon circulation. *Geophys. Res. Lett.* **40**, 2471–2477 (2013).
29. N.-C. Lau, M. Nath, ENSO modulation of the interannual and intraseasonal variability of the East Asian Monsoon–A model study. *J. Clim.* **19**, 4508–4530 (2006).
30. P.-H. Chung, C.-H. Sui, T. Li, Interannual relationships between the tropical sea surface temperature and summertime subtropical anticyclone over the western North Pacific. *J. Geophys. Res. D Atmospheres* **116**, D13111 (2011).

Downloaded from https://www.pnas.org by CSIRO Library Services on May 31, 2022 from IP address 140.253.235.29.

31. C.-H. Sui, P.-H. Chung, T. Li, Interannual and interdecadal variability of the summertime western North Pacific subtropical high. *Geophys. Res. Lett.* **34**, L11701 (2007).
32. B. Wu, T. Zhou, Oceanic origin of the interannual and interdecadal variability of the summertime western Pacific subtropical high. *Geophys. Res. Lett.* **35**, L13701 (2008).
33. Y.-G. Ham, J.-S. Kug, J.-Y. Park, F.-F. Jin, Sea surface temperature in the north tropical Atlantic as a trigger for El Niño/Southern Oscillation events. *Nat. Geosci.* **6**, 112–116 (2013).
34. C.-C. Hong, M.-Y. Lee, H.-H. Hsu, N.-H. Lin, B.-J. Tsuang, Tropical SST forcing on the anomalous WNP subtropical high during July–August 2010 and the record-high SST in the tropical Atlantic. *Clim. Dyn.* **45**, 633–650 (2015).
35. J. Zuo, W. Li, C. Sun, H.-C. Ren, Remote forcing of the northern tropical Atlantic SST anomalies on the western North Pacific anomalous anticyclone. *Clim. Dyn.* **52**, 2837–2853 (2019).
36. S.-P. Xie *et al.*, Indian ocean capacitor effect on Indo–Western pacific climate during the summer following El Niño. *J. Clim.* **22**, 730–747 (2009).
37. J. Yang, Q. Liu, S.-P. Xie, Z. Liu, L. Wu, Impact of the Indian Ocean SST basin mode on the Asian summer monsoon. *Geophys. Res. Lett.* **34**, L02708 (2007).
38. K. Hu, G. Huang, S.-P. Xie, Assessing the internal variability in multi-decadal trends of summer surface air temperature over East Asia with a large ensemble of GCM simulations. *Clim. Dyn.* **52**, 6229–6242 (2019).
39. J. E. Kay *et al.*, The Community Earth System Model (CESM) large ensemble project: A community resource for studying climate change in the presence of internal climate variability. *Bull. Am. Meteorol. Soc.* **96**, 1333–1349 (2015).
40. J. M. Wallace, C. Deser, B. V. Smoliak, A. S. Phillips, "Attribution of climate change in the presence of internal variability" in *Climate Change: Multidecadal and Beyond*, C.-P. Chang, M. Ghil, M. Latif, J. M. Wallace, Eds. (*World Scientific Series on Asia-Pacific Weather and Climate*, World Scientific, 2013), **vol. 6**, pp. 1–29.
41. E. N. Lorenz, "Empirical orthogonal functions and statistical weather prediction" (Statistical Forecast Project Report 1, Department of Meteorology, Massachusetts Institute of Technology, 1956).
42. B. Jia, J. Peng, S. Hu, G. Feng, Novel dynamical indices for the variations of the western Pacific subtropical high based on three-pattern decomposition of global atmospheric circulation in a warming climate. *Clim. Dyn.* **56**, 3473–3487 (2021).
43. Y. Huang, H. Wang, K. Fan, Y. Gao, The western Pacific subtropical high after the 1970s: Westward or eastward shift? *Clim. Dyn.* **44**, 2035–2047 (2015).
44. C. He *et al.*, Enhanced or weakened Western North Pacific subtropical high under global warming? *Sci. Rep.* **5**, 16771 (2015).
45. L. Wu, C. Wang, Has the Western Pacific subtropical high extended westward since the late 1970s? *J. Clim.* **28**, 5406–5413 (2015).
46. W. Cai *et al.*, Pantropical climate interactions. *Science* **363**, eaav4236 (2019).
47. V. Eyring *et al.*, Overview of the Coupled Model Intercomparison Project Phase 6 (CMIP6) experimental design and organization. *Geosci. Model Dev.* **9**, 1937–1958 (2016).
48. F. Jia *et al.*, Weakening Atlantic Niño-Pacific connection under greenhouse warming. *Sci. Adv.* **5**, eaax4111 (2019).
49. K. E. Taylor, R. J. Stouffer, G. A. Meehl, An Overview of CMIP5 and the experiment design. *Bull. Am. Meteorol. Soc.* **93**, 485–498 (2012).
50. K. Hu, G. Huang, P. Huang, Y. Kosaka, S.-P. Xie, Intensification of El Niño-induced atmospheric anomalies under greenhouse warming. *Nat. Geosci.* **14**, 377–382 (2021).
51. W. Cai *et al.*, Butterfly effect and a self-modulating El Niño response to global warming. *Nature* **585**, 68–73 (2020).
52. H. Hersbach, *et al.*, "ERA5 monthly averaged data on pressure levels from 1979 to present." Copernicus Climate Change Service (C3S) Climate Data Store (CDS). https://cds.climate.copernicus.eu/cdsapp#!/dataset/reanalysis-era5-pressure-levels-monthly-means?tab=overview. Accessed 3 January 2021.
53. E. Kalnay *et al.*, The NCEP/NCAR 40-year reanalysis project. *Bull. Am. Meteorol. Soc.* **77**, 437–472 (1996).
54. R. F. Adler *et al.*, The Version-2 Global Precipitation Climatology Project (GPCP) monthly precipitation analysis (1979–present). *J. Hydrometeorol.* **4**, 1147–1167 (2003).
55. B. Wang, Z. Fan, Choice of South Asian summer monsoon indices. *Bull. Am. Meteorol. Soc.* **80**, 629–638 (1999).
56. G. Huang, K. Hu, S.-P. Xie, Strengthening of tropical Indian Ocean teleconnection to the Northwest Pacific since the mid-1970s: An atmospheric GCM study. *J. Clim.* **23**, 5294–5304 (2010).
57. K. Hu *et al.*, Interdecadal variations in ENSO influences on Northwest Pacific–East Asian early summertime climate simulated in CMIP5 models. *J. Clim.* **27**, 5982–5998 (2014).
58. C. He, T. Zhou, T. Li, Weakened anomalous Western North Pacific anticyclone during an El Niño–decaying summer under a warmer climate: Dominant role of the weakened impact of the tropical Indian Ocean on the atmosphere. *J. Clim.* **32**, 213–230 (2019).
59. W. Jiang, G. Huang, P. Huang, K. Hu, Weakening of Northwest Pacific anticyclone anomalies during post–El Niño summers under global warming. *J. Clim.* **31**, 3539–3555 (2018).
60. M. Wu, T. Zhou, X. Chen, B. Wu, Intermodel uncertainty in the projection of the anomalous Western North Pacific anticyclone associated with El Niño under global warming. *Geophys. Res. Lett.* **47**, e2019GL086139 (2020).
61. P. C. Austin, J. V. Tu, Bootstrap methods for developing predictive models. *Am. Stat.* **58**, 131–137 (2004).

Downloaded from https://www.pnas.org by CSIRO Library Services on May 31, 2022 from IP address 140.253.235.29.

Fundamental Research 2 (2022) 396–400

Contents lists available at ScienceDirect

Fundamental Research

journal homepage: http://www.keaipublishing.com/en/journals/fundamental-research/

Perspective

Critical climate issues toward carbon neutrality targets

Gang Huang[a,b,c,*], Zhenhao Xu[a,c], Xia Qu[a], Junji Cao[d], Shangmin Long[e], Kai Yang[a], Hongyu Hou[a,c], Ya Wang[a,c], Xiaofan Ma[a]

[a] State Key Laboratory of Numerical Modeling for Atmospheric Sciences and Geophysical Fluid Dynamics, Institute of Atmospheric Physics, Chinese Academy of Sciences, Beijing 100029, China
[b] Laboratory for Regional Oceanography and NumericalModeling, Qingdao National Laboratory for Marine Science and Technology, Qingdao 266237, China
[c] College of Earth and Planetary Sciences, University of Chinese Academy of Sciences, Beijing 100049, China
[d] Institute of Atmospheric Physics, Chinese Academy of Sciences, Beijing 100029, China
[e] International Polar Environment Research Laboratory, College of Oceanography, Hohai University, Nanjing 210098, China

ARTICLE INFO

Article history:
Received 28 September 2021
Received in revised form 7 February 2022
Accepted 24 February 2022
Available online 10 March 2022

Keywords:
Carbon neutrality
Climate dynamics
Climate-carbon feedback
Diplomacy
Possible solutions
Future prospects

ABSTRACT

In 2020, China announced the "emission peak, carbon neutrality" policy, that is, China aims to have CO2 emissions peak before 2030 and achieve carbon neutrality before 2060. The scenario of carbon neutrality will be significantly distinguished from the scenario we experienced since the industrial revolution. However, instrumental data are unavailable in the future carbon-neutral scenario. Earth system models and climate dynamics theory are needed to comprehend and project the climate change. In this paper, we illustrate our perspective of the issues related to "emission peak, carbon neutrality", including climate dynamics, climate-carbon feedback, interaction between China and global climate and carbon emissions and solutions, etc. We highlight that climate change has profoundly affected human production and life. The frequent occurrence of extreme weather disasters in recent years, together with the impact of epidemics, make the future "carbon peak & carbon-neutral" scenario more complex. There is whopping uncertainty but also a massive challenge to the scientific community. Thus, carbon neutrality is closely related to domestic production and lives, and there is little time left for planning. We believe that we will make a breakthrough in climate dynamics in the context of carbon neutrality with our joint efforts, which will serve our country's carbon emission policy at different stages.

1. Introduction

On September 22, 2020, Chinese President Xi Jin-Ping solemnly announced that "China will scale up its Intended Nationally Determined Contributions by adopting more vigorous policies and measures, aiming to have CO_2 emissions peak before 2030 and achieve carbon neutrality before 2060" at the General Debate of the 74th Session of the United Nations General Assembly. The so-called carbon neutrality means a state of net-zero carbon dioxide emissions. This ritual commitment shows the responsibility of China as a global superpower to follow a "green, low-carbon, high-quality" development path. Our series of deployments to address climate change and carbon neutrality will have far-reaching impacts on the energy structure, industrial structure, and socioeconomic development of China and even the world. It will also have considerable effects on technological progress and global governance. The ultimate goal of carbon neutrality is to unify international countries to jointly achieve the temperature target of the Paris Agreement, i.e., to control the global average temperature rise within 2 ˚C and to strive for only 1.5 ˚C above preindustrial levels. Different from the traditional carbon emission scenarios [1], the Paris Agreement established the first scenario in which temperature is regarded as a target to constrain climate change, pushing a new direction of climate research. Achievement of the target would require a decrease in atmospheric CO_2 concentration [2,3]. However, the World Climate Research Programme (WCRP) stated in 2018 that "the scientific community lacks consensus on the climate effects of CO_2 removal" and launched the Carbon Dioxide Removal Model Comparison Program [4]; as of 2021, the data were still renewing, and relevant studies were few.

Climate change is closely related to human society. Current global warming, mainly caused by the massive emissions of greenhouse gases, especially carbon dioxide, has dramatically affected human production and life. Despite a continuous increase in CO_2 since the 20th century, the global average temperature has shown a stepwise increase, including warming in the early 20th century, cooling in the mid-20th century, rapid warming in the late 20th century, and a hiatus in the early 21st century [5–7], underpinned by the nonmonotonic evolution of surface temperature [8,9]. During the period of warming, global temperature change followed the familiar "temperature–CO_2" relationship, but dur-

* Corresponding author.
E-mail address: hg@mail.iap.ac.cn (G. Huang).

https://doi.org/10.1016/j.fmre.2022.02.011
2667-3258/© 2022 The Authors. Publishing Services by Elsevier B.V. on behalf of KeAi Communications Co. Ltd. This is an open access article under the CC BY-NC-ND license (http://creativecommons.org/licenses/by-nc-nd/4.0/)

ing the hiatus period, i.e., the early 21st century, the relationship was decoupled. This implies that the relationship between CO_2 concentration and surface temperature, which is of most concern to humans, is not linear and may involve complex dynamic feedbacks. Previous studies have suggested that the coupled and decoupled "temperature–CO_2" relationship can be due to the different time-scale responses of the climate system to anthropogenic activities, such as a slow response due to the large heat capacity of the ocean to anthropogenic radiative forcing [10–13]. On the other hand, the internal variability of the climate system, such as the cold phase of the Pacific Decadal Oscillation (PDO), may offset the warming effect of human activities [5,6]. In the future, under the scenario of "emission peak" and "carbon neutrality," our ultimate goal is to limit the rise of global surface temperature. Our control of carbon emissions will finally act on climate change. The management of CO_2 concentration is only a method, not the ultimate goal. Therefore, a scientific understanding of the "temperature–CO_2" relationship (especially around some key turning points) is essential for planning and coping with climate change in the coming decades.

2020 was an extraordinary year with worldwide climate extremes. The sudden epidemic of COVID-19 early in the year led to a severe reduction in our productivity. As a vast industrial country, the stagnation in productivity caused a significant decrease in CO_2 and aerosol emissions. With effective epidemic prevention measures, our productivity levels began to recover at the end of the year and were coming on strong in 2021, while the emissions in the rest of the world continued to decline. COVID-19 forced us to passively experience an emission reduction. Reductions in CO_2 or aerosols may cause an asynchronous response of the ocean and atmosphere in a short period, as the response of the ocean to radiative change is slower than that of the land and atmosphere, which may cause potential ecological, environmental, and engineering safety risks. Extreme weather tends to become more frequent under global warming; for example, the record-breaking Yangtze River floods in China triggered by the strong anomalous Mei-yu event in 2020; the dust storms in northern China and thunderstorms and windy weather in southern China in early 2021; the daily rainfall of more than 100 mm in South Xinjiang in June; and the once-in-a-thousand-year event in Zhengzhou on July 20, of which the hourly rainfall exceeded 200 mm. Beyond China, these extreme weather events include the wildfires in Australia and California in 2020, the snowstorm on the eastern coast of Canada, the heatwave in India and France, the extreme cold weather in Texas in February 2021 that led to widespread, long-term power outages, the extreme precipitation in Europe in spring, etc. These extreme events resulted in tremendous damage to the production and lives of human beings. Should these severe weather and climate disasters be attributed mainly to human activities or natural variability? The actual physical processes of the "emission peak and carbon neutrality" scenario may be more complex. A better comprehension of the changes in the proportion of the climate disaster process is of high scientific and application value for predicting the intensity, area, and duration of extreme weather and climate disasters under future scenarios.

The target of carbon neutrality is an integrated and extremely complex issue that is widely associated with climate, ecology, energy, environment, society, etc. It results from interactions of multiple systems, such as land, atmosphere, ocean, and cryosphere. At present, the climate impact of carbon neutrality is still unclear, and it may be related to planning a reasonable carbon emission path to realize the optimal layout of energy, industry, the ecological environment, and other fields to achieve carbon neutrality with relatively small socioeconomic costs. To date, there are several questions that still need to be answered. How will the regional climate over China and the global climate respond to the three critical stages of the carbon neutrality target (Fig. 1), i.e., from now to the "emission peak", from the "emission peak" to "carbon neutrality," and from "carbon neutrality" to the end of this century? What will be our stance on achieving an "emission peak"? Are there feedbacks from climate change on carbon emissions or uptakes in both directions? What are the possible feedbacks? How much uncertainty is there? To address these questions, it is essential to understand the relationship between atmospheric CO_2 and temperature, i.e., to address the climate under carbon neutrality, which is now a critical task.

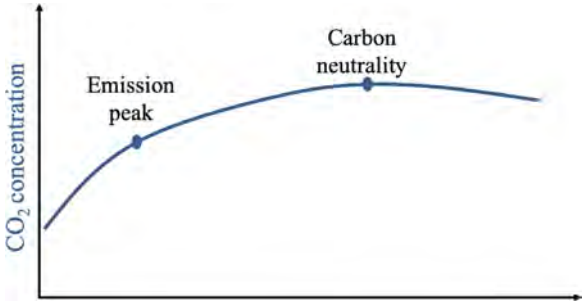

Fig. 1. Schematic diagram of the evolution of CO_2 concentration in a carbon-neutral background.

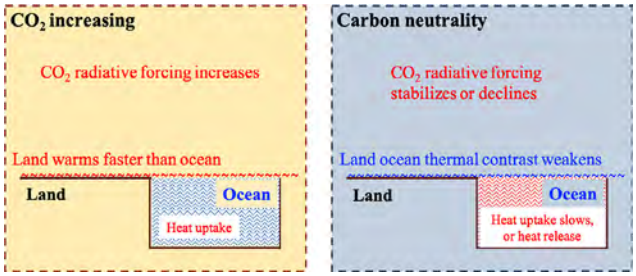

Fig. 2. Diagrams of climate-dynamical processes at different stages of atmospheric CO_2 concentration change. (a) During rising stages, CO_2 radiative forcing is the main driving force of the climate system. Due to the small heat capacity, land warms rapidly with the increasing of CO_2 radiative forcing; the ocean's response is slow owing to its large heat capacity. The thermal difference between land and ocean increases, which enhances monsoon circulation. (b) After carbon neutrality, CO_2 radiative forcing stabilizes or decreases, while the ocean is still slowly absorbing heat and warming. The land-ocean thermal contrast diminishes, weakening the monsoon circulation; if the CO_2 concentration decreases dramatically, the deep ocean will release heat upward to decelerate the cooling of the sea and land surface.

2. Understanding climate dynamics under carbon neutrality

During the historical period, researchers have conducted climate analysis with instrumental data, which, however, are unavailable in the future carbon-neutral scenario. Earth system models and climate dynamics theory are needed to comprehend and project climate change.

Under a carbon-neutral scenario, accurate prediction of climate–carbon feedbacks and the hazards of weather and climate highly depends on the precise projection of the future climate. The scenario of carbon neutrality will be significantly distinguished from the scenario we have experienced since the industrial revolution. Additionally, the corresponding climate dynamics are different from the well-known stages during which CO_2 is rising. Before neutrality, the CO_2 concentration will continue to increase, and radiative forcing during this period will be the leading factor in global warming, dominated by the rapid responses of the climate system (especially land and mixed-layer oceans). The heating effect due to the greenhouse gas (GHG) effect notably (approximately 90%) enters the ocean, which acts as a "heat reservoir" [1,14]. After carbon neutrality, GHGs will stabilize or decline. The slow responses of the climate system (the slow absorption or release of heat from the deep ocean) will gradually increase. The "heat reservoir" effect may resist the cooling effect led by the decline in CO_2 concentration or slowly warm the global surface when the CO_2 concentration stabilizes. Supposing that the CO_2 concentration decreases too rapidly, the ocean may even overwhelm GHGs and become the driver of global climate change, as shown in Fig. 2.

China features a typical monsoon climate. The thermal contrast between land and ocean plays an essential role in forming the East Asian monsoon [15]. Before carbon neutralization, the land warms more rapidly than the ocean, strengthening the thermal contrast and favoring the continued enhancement of the East Asian summer monsoon. After carbon neutralization, the ocean may still warm or cool slowly due to its thermal inertia, leading to a weaker thermal contrast and weakening the East Asian summer monsoon [16,17]. All of the above factors may have impacts on the climate in China.

Multiple studies have suggested that the El Niño–Southern Oscillation (ENSO) amplitude will strengthen, and extreme El Niño events will continue to increase during the carbon-neutral stage [18,19]. During extreme El Niño events (e.g., the 2015–2016 super El Niño event), the carbon emissions from the biosphere will increase due to high temperatures and droughts in the tropics [20]. The response in the oceans under global warming may alter the uptake and storage of CO_2, which can impact the realization of carbon neutrality. For example, the North Atlantic Ocean is one of the major global carbon sinks. Due to deep convection in the sinking branch of the AMOC, a large amount of carbon is sequestered in the deep North Atlantic; therefore, a weakening of the AMOC will reduce its carbon storage capacity [21], thus affecting the atmospheric carbon concentration. In addition, under the low-carbon emissions scenario, the North Atlantic Ocean would potentially gradually replace the Southern Ocean as the focus of global ocean heat uptake due to the weakening of the Atlantic Meridional Overturning Circulation (AMOC) [22]. Under the carbon neutrality goal, future anthropogenic aerosol emissions will continue to decrease. The subsequent warming effect will be superimposed on the cooling effect caused by CO_2 reduction, resulting in an increase in surface warming and a decrease in the rate of temperature decline, thus prolonging the time needed to achieve the Paris Agreement's low-temperature rise target [23]. Therefore, when designing specific pathways to achieve carbon neutrality, the critical climate impacts of anthropogenic aerosols need to be considered.

Although the scientific community has some preliminary understanding of the above processes, some difficulties appear in research:

(1) Uncertainty in atmospheric CO_2 concentrations in the future. The future pathway of CO_2 concentration is a result of net carbon emissions from countries all over the world. At present, although most countries have proposed related carbon neutral policies, there is still much uncertainty regarding the pathway of CO_2 emissions as well as its concentration. This increases the difficulty of climate prediction.

(2) Uncertainty of numerical simulation. The Earth system model is an ideal tool to carry out climate prediction in the carbon neutrality scenario. Many physical processes in the Earth system model are simplified, and the details of weather and climate processes are not fully described, which introduce simulation biases. Moreover, the lack of observation data and knowledge of some regional climate phenomena makes it difficult to judge whether the presentation in the Earth system model is reasonable. This uncertainty may affect other regional climate phenomena.

(3) The influence of internal climate variability. In addition to human activities, the climate is also influenced by internal climate variability. For example, during the first decade of the 21st century, atmospheric CO_2 continued to rise, but global temperature displayed a hiatus due to the cooling of the eastern Pacific Ocean [5]. Considering that in numerical simulation experiments, internal climate variability is stochastic, it is a challenge to force out the variability. This makes climate prediction more difficult.

In general, the scientific understanding of climate dynamics under carbon-neutral scenarios is insufficient. The impact of these dynamic processes on East Asia and the global climate is less understood. In addition, the precise quantification of the climate–carbon feedbacks under future climate relies on a deeper understanding of climate dynamics and a more accurate prediction of climate change under a carbon-neutral scenario. Therefore, we need to conduct independent research and systematically understand the climate dynamic processes under carbon neutrality scenarios, as well as their impacts on climate change in China and the globe. A deep understanding of these issues may enable us to accurately and scientifically project the risk of climate in China and the world under the influence of carbon-neutral policies, the climate conditions in critical areas of carbon sources and sinks, and the climate–carbon feedback before and after carbon neutrality. It provides scientific support to the rational layout of energy, industry, ecology, and the environment in China and makes carbon neutrality better and more stable.

3. Quantitative analyses of climate–carbon feedback

At present, while there has been some relevant research on carbon–climate feedback, there is still considerable uncertainty in the climate–carbon-cycle model results that still need to be further developed [24–26]. In the field of climatology, recent studies have primarily focused on one-way impacts, i.e., carbon emissions on climate change, while in fact, the carbon cycle and climate are interactive. The IPCC Fifth Assessment Report (IPCC AR5) concludes that there is positive feedback between the carbon cycle and climate: under the future scenario, global warming may weaken the carbon sink of ecosystems, leading to higher CO_2 concentrations in the atmosphere and further reinforcing global warming. The above understanding provides some implications: (1) If we ignore the weakening of the carbon sink under global warming, the timing of carbon neutrality achievement may be delayed. (2) If the atmospheric CO_2 concentration does not decrease enough after carbon neutrality, the global temperature may rise slowly and continue to weaken the global carbon sink. Therefore, all countries cannot evade the efforts to control carbon emissions.

However, there is uncertainty in understanding some key parameters in the climate–carbon feedback (e.g., feedback strength, critical thresholds, and spatial distribution), which significantly constrains the planning of carbon-emission reduction. Supposing that we do not have an accurate understanding of the climate–carbon feedback; then we may fail to achieve the optimal deployment of the development of energy, industry, ecological environment and other fields in China. It may bring additional socioeconomic losses. Therefore, there is an urgent need to conduct research on the carbon cycle and climate feedback. In addition, in recent years, the WCRP updated the "Grand Challenges" on climate research, in which carbon–climate feedback was listed as one of the seven challenges. This implies the importance of climate–carbon feedback.

4. Interaction between China/global climate and carbon emissions

CO_2 can mix in the atmosphere and affect the climate through changes in its concentration on a global scale. That is, the climate change of each country is not solely determined by the net carbon emissions within the territory of each country but depends on the net carbon emissions on Earth. Therefore, on the issue of climate change and carbon emissions, all countries on the worldwide scale are not isolated but are closely linked communities [1,27-29], as shown in Fig. 3.

China has developed a long-term plan to achieve carbon neutrality, which will significantly contribute to global climate mitigation and carbon reduction. Based on the understanding of carbon–climate feedbacks and climate dynamics under the "carbon neutrality" scenario, this makes it possible to estimate the contribution of China's carbon neutrality policy to global warming mitigation, climate disasters, and ecological carbon sinks. On the other hand, other countries might also influence the domestic carbon emissions in China. Imagine an extreme scenario under which our country achieves carbon neutrality while the net CO_2 emissions of other countries are positive. Then, the CO_2 concentration still rises, leading to a higher-than-expected temperature increase in our country, further weakening the (ecosystem) carbon sink and destroying

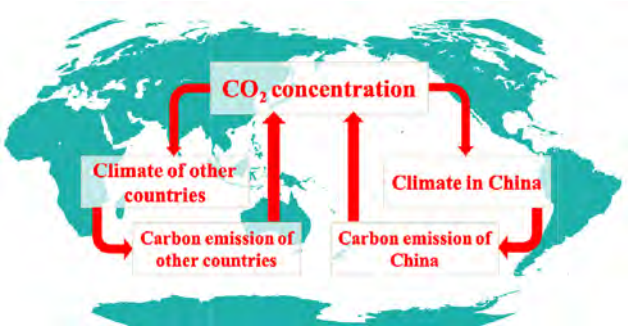

Fig. 3. Relationship between China and other countries in terms of net carbon emissions and climate.

the carbon-neutral state of China. Considering this, we can also rely on the further study of climate–carbon feedback and climate dynamics to assess the impact of carbon emissions from other countries on our carbon-neutral status. These two aspects are important issues to be considered in climate diplomacy.

Based on an in-depth understanding of the carbon–climate feedback and carbon-neutral climate dynamics, it is feasible to conduct a study on the interaction among China's carbon neutrality, global climate, and carbon emissions with the aid of sophisticated Earth system models. Conducting research in this area and quantifying the contribution of China's carbon neutral policies to global climate and carbon emissions helps increase China's discourse power in climate diplomacy. Moreover, assessing the impacts of carbon emissions of other countries on climate and carbon emissions in China and timely adjusting China's deployment in the fields of energy, industry, ecology, and the environment prudently favor the achievement of carbon-neutral goals.

5. Solutions to scientific problems associated with carbon neutrality

The major political plan of carbon neutrality gives rise to a series of scientific problems. Future human-induced GHG change is a physical problem and a complex problem involving politics, society, and the economy. Anthropogenic perturbations can result in impacts and consequences that threaten the security of the Earth system. Due to the complexity of the Earth system and the nature of nonlinear responses, changes in the relationship between humans and nature in the short term will inevitably cause significant uncertainty in the prediction of the future environment. Thus, it is worthwhile to start from the following three aspects.

(1) One solution is climate dynamic research and Earth system model development. The understanding of climate dynamics under carbon neutrality relies on the theoretical study of climate dynamics and Earth system models. The Earth system model is the only dynamic tool that we use to predict the future. Climate dynamics studies can be used to validate Earth system models and jointly contribute to accurate estimates of climate–carbon feedbacks together with models. With a proper understanding of carbon-neutral climate dynamics and the key quantitative indicators of the climate–carbon feedback, we can use them to assess the interactions between China and the globe on climate and carbon emissions.

(2) The second solution is to develop multidisciplinary theoretical research, emphasizing the interactions of multiple systems of the Earth, including the atmosphere–ocean, atmosphere–land, and other multilayer interactions, as well as the two-way feedback of climate and carbon. Carbon neutrality is not only a scientific issue but also a complex sociological topic. It is important to focus on the intersection of social sciences (e.g., economics and international relations) with climatology. Currently, the promotion of interdisciplinary research is an inevitable trend in the development of Earth sciences. The understanding of carbon neutrality is also accompanied by the rapid development of computer technology, which provides computing power for large numerical calculations.

(3) The third solution is to effectively gather human resources, extensively recruit outstanding scientists in related fields, and bring into research teamwork synergy. For example, we could build large-scale computer devices to provide strong support for large-scale scientific calculations and establish carbon-neutral research centers. In particular, attention and emphasis should be placed on institutional arrangements and national scientific policies to strengthen the scientific innovation of China. For example, funding for fundamental research should be strengthened, and young researchers, especially scholars who have recently received their doctoral degrees, should be given more opportunities to explore independently, and the evaluation mechanism should not be paper-centered but should be more varied.

6. Conclusion and prospects

In the process of energy change and carbon neutrality emerging globally, greenhouse gases such as CO_2 in the atmosphere will be influenced by significant anthropogenic perturbations. Although low-carbon emissions may slow atmospheric warming, the overall trend of climate warming will continue for a long time. Achieving carbon neutrality is likely to lead to changes in global and national weather hazard patterns and potentially decrease the uncertainty of climate variability and the occurrence of climate extremes, with important implications for global security. Therefore, the feedback and response of the Earth system to anthropogenic CO_2 emissions after carbon neutrality and its impacts will be scientific issues worthy of attention in the future. Carbon neutrality is closely related to domestic production and lives, and there is little time left for planning. This set of factors has given rise to key scientific questions that need to be addressed in the context of carbon neutrality, mainly including the following:

(1) Carbon-neutral climate dynamics research (understanding the key climate dynamic processes under carbon-neutral scenarios, including the fast and slow responses of the climate system, internal climate variability, and their impacts on our domestic and global climate).

(2) Two-way feedbacks between the regional and global climate–carbon feedback (to understand the spatial distributions of the crucial quantitative indicators, such as feedback coefficients and critical thresholds and climate–carbon feedbacks in China and worldwide).

(3) The contribution of China's carbon neutrality to global climate and carbon emissions (assessing the contribution of China's carbon neutrality policy to global warming mitigation, climate disasters, ecological carbon sinks, etc. and evaluating the impact of other countries' carbon emissions on China's carbon neutrality status and route).

In summary, climate change has profoundly affected human production and life. Carbon neutrality is not a purely scientific topic but a complex and comprehensive issue. Established policies and emission reduction pathways might be highly affected by unexpected events, such as the frequent occurrence of extreme weather disasters and outbreaks of epidemics in recent years, which make the "carbon peak and carbon-neutral" scenario face great uncertainty. There is enormous uncertainty but also a massive challenge to the scientific community. However, we should believe that we will make a breakthrough in climate issues in the context of carbon neutrality with our joint efforts, which will serve our country's carbon emission policy at different stages.

Declaration of Competing Interest

The authors declare that they have no conflicts of interest in this work.

Acknowledgments

This work was supported by the National Natural Science Foundation of China (Grants No. 42141019, 41831175, 91937302, and 41721004), Key Deployment Project of Centre for Ocean Mega-Research of Science, Chinese academy of science (Grant No. COMS2019Q03) and Strategic Priority Research Program of Chinese Academy of Sciences (Grant No. XDA20060501).

References

[1] IPCC, Climate Change 2013: The Physical Science Basis. Contribution of Working Group I to the Fifth Assessment Report of the Intergovernmental Panel on Climate Change, Cambridge University Press, Cambridge, United Kingdom and New York, USA, 2013, p. 1535. [Stocker, T.F., D. Qin, G.-K. Plattner, M. Tignor, S.K. Allen, J. Boschung, A. Nauels, Y. Xia, V. Bex and P.M. Midgley (eds.)].
[2] B.M. Sanderson, B.C. O'Neill, C. Tebaldi, What would it take to achieve the Paris temperature targets? Geophys. Res. Lett. 43 (2016) 7133–7142.
[3] B.M. Sanderson, Y. Xu, C. Tebaldi, et al., Community climate simulations to assess avoided impacts in 1.5 and 2 degrees C futures, Earth Sys. Dyna. 8 (3) (2017) 827–847.
[4] D.P. Keller, L. Andrew, S. Vivian, et al., The Carbon Dioxide Removal Model Intercomparison Project (CDRMIP): rationale and experimental protocol for CMIP6, Geosci. Model Dev. 11 (2018) 1133–1160.
[5] Y. Kosaka, S.-P. Xie, Recent global-warming hiatus tied to equatorial Pacific surface cooling, Nature 501 (2013) 403–407.
[6] Y. Kosaka, S.-P. Xie, The tropical pacific as a key pacemaker of the variable rates of global warming, Nat. Geosci. 9 (9) (2016) 669–673.
[7] S.-L. Yao, J.-J. Luo, G. Huang, et al., Distinct global warming rates tied to multiple ocean surface temperature changes, Nat. Clim.Change 7 (2017) 486–491.
[8] F. Ji, Z. Wu, J. Huang, et al., Evolution of land surface air temperature trend, Nat. Clim. Change 4 (6) (2014) 462–466.
[9] Z. Xu, F. Ji, B. Liu, et al., Long-term evolution of global sea surface temperature trend, Int. J. Climatol. 41 (9) (2021) 4494–4508.
[10] T. Andrews, P.M. Forster, O. Boucher, et al., Precipitation, radiative forcing and global temperature change, Geophys. Res. Lett. 37 (2010) L14701.
[11] G. Bala, K. Caldeira, R. Nemani, Fast versus slow response in climate change: implications for the global hydrological cycle, Climate Dyn 35 (2010) 423–434.
[12] I.M. Held, M. Winton, K. Takahashi, et al., Probing the fast and slow components of global warming by returning abruptly to preindustrial forcing, J. Climate 23 (2010) 2418–2427.
[13] S.M. Long, S.-P. Xie, X.-T. Zheng, et al., Fast and slow responses to global warming: sea surface temperature and precipitation patterns, J. Climate 27 (2014) 285–299.
[14] L. Cheng, J. Abraham, J. Zhu, et al., Record-setting ocean warmth continued in 2019, Adv. Atmos. Sci. 37 (2020) 137–142.
[15] B. Wang, Q. Ding, Global monsoon: dominant mode of annual variation in the tropics, Dyn. Atmos. Oceans 44 (3–4) (2008) 165–183.
[16] Y. Kamae, M. Watanabe, M. Kimoto, et al., Summertime land-sea thermal contrast and atmospheric circulation over East Asia in a warming climate-Part II: Importance of CO_2-induced continental warming, Climate Dyn 43 (2014) 2569–2583.
[17] X.Q. Li, M.F. Ting, Understanding the Asian summer monsoon response to greenhouse warming: the relative roles of direct radiative forcing and sea surface temperature change, Climate Dyn 49 (2017) 2863–2880.
[18] M. Ohba, J. Tsutsui, D. Nohara, Statistical Parameterization Expressing ENSO Variability and Reversibility in Response to CO2 Concentration Changes, J. Climate 27 (2014) 398–410.
[19] G.J. Wang, W. Cai, B. Gan, et al., Continued increase of extreme El Nino frequency long after 1.5 degrees C warming stabilization, Nat. Clim. Change 7 (2017) 568–572.
[20] J. Liu, K.W. Bowman, D.S. Schimel, et al., Contrasting carbon cycle responses of the tropical continents to the 2015–16 El Niño, Science 358 (2017) eaam5690.
[21] M. Srokosz, M. Baringer, H. Bryden, et al., Past, present, and future changes in the Atlantic meridional overturning circulation, Bull. Am. Meteorol. Soc. 93 (11) (2012) 1663–1676.
[22] X. Ma, W. Liu, R.J. Allen, et al., Dependence of regional ocean heat uptake on anthropogenic warming scenarios, Sci. Adv. 6 (2020) eabc0303.
[23] X. Ma, G. Huang, J. Cao, The significant roles of anthropogenic aerosols on the climate system under carbon neutrality, Sci. Bull. (2021) In Press.
[24] Y. Malhi, J.T. Roberts, R.A. Betts, et al., Climate change, deforestation, and the fate of the amazon, Science 319 (2008) 169–172.
[25] J.P. Dunne, J.G. John, A.J. Adcroft, et al., Gfdl's esm2 global coupled climate—carbon earth system models. Part I: physical formulation and baseline simulation characteristics, J. Climate 25 (19) (2012) 6646–6665.
[26] P.M. Cox, D. Pearson, B.B. Booth, et al., Sensitivity of tropical carbon to climate change constrained by carbon dioxide variability, Nature 494 (7437) (2013) 341–344.
[27] P.M. Cox, R.A. Betts, C.D. Jones, et al., Acceleration of global warming due to carbon-cycle feedbacks in a coupled climate model, Nature 408 (2000) 184–187.
[28] H.D. Matthews, A.J. Weaver, K.J. Meissner, Terrestrial carbon cycle dynamics under recent and future climate change, J. Climate 18 (2005) 1609–1628.
[29] N. Zeng, H.F. Qian, E. Munoz, et al., How strong is carbon cycle-climate feedback under global warming? Geophys. Res. Lett. 31 (20) (2004) 183–213.

Gang Huang received his Ph.D. degree from Institute of Atmospheric Physics, Chinese Academy of Sciences (CAS) in 1999. He is now a full professor in the State Key Laboratory of Numerical Modeling for Atmospheric Sciences and Geophysical Fluid Dynamics (LASG), Institute of Atmospheric Physics, CAS. His research interests focus on climate dynamics, especially, the mechanism of variability of atmosphere circulation and monsoon system in East Asia.

Science Bulletin 67 (2022) 774–776

Contents lists available at ScienceDirect

Science Bulletin

journal homepage: www.elsevier.com/locate/scib

News & Views

The first 5-year Clean Air Action did increase the blue days in winter over Beijing-Tianjin-Hebei

Su Wang [a,c], Gang Huang [a,b,c,*], Tie Dai [a,d,*], Kaiming Hu [a,e]

[a] State Key Laboratory of Numerical Modeling for Atmospheric Sciences and Geophysical Fluid Dynamics, Institute of Atmospheric Physics, Chinese Academy of Sciences, Beijing 100029, China
[b] Laboratory for Regional Oceanography and Numerical Modeling, Pilot National Laboratory for Marine Science and Technology (Qingdao), Qingdao 266237, China
[c] University of Chinese Academy of Sciences, Beijing 100049, China
[d] Collaborative Innovation Center on Forecast and Evaluation of Meteorological Disasters/Key Laboratory of Meteorological Disaster of Ministry of Education, Nanjing University of Information Science and Technology, Nanjing 210044, China
[e] Center for Monsoon System Research, Institute of Atmospheric Physics, Chinese Academy of Sciences, Beijing 100029, China

China has made great efforts to mitigate its long-standing environmental problem in recent years. In China, during the first 5-year Clean Air Action (2013–2017), remarkable reductions in primary pollutants such as SO_2 and fine particle matter ($PM_{2.5}$) have been achieved, especially in Beijing-Tianjin-Hebei (BTH) region [1,2]. After an explosive increase in concern for the Beijing Blue Events in 2015, the direct changes of blue days in China have received widespread attention [3,4]. However, less air pollution does not directly correspond to more blue skies. For example, days with high cloud cover or precipitation do not belong to blue days even though there is less air pollution. In addition, inconsistencies between dropping PM, unchanged low visibility events, and a remarkable increase of aerosol optical depth can be found even during the COVID-19 lockdown period [5–7]. Beyond that, unfavorable meteorological conditions counteract the effects of reduced emissions, resulting in frequent haze in the BTH region [8,9]. Therefore, emission reductions do not lead directly to more blue days.

Along with living standard enhancement, there is an advanced understanding that the blue day should be a day with blue sky and great air quality. Then a novel index named the Chinese Blue Days Index (CBDI) has been put forward to reveal the long-term spatiotemporal change of Chinese blue days [10]. However, the CBDI represents a national average level, which is inappropriate for BTH. In addition, earlier works that have focused on daily observational data are unable to rule out the effects of meteorology and air pollution.

In this study, to quantitatively distinguish the impact of aerosol on blue days from the meteorology, the effectiveness of the first 5-year Clean Air Action was assessed with using the Weather Research and Forecasting Model coupled with chemistry (WRF-Chem). Two sensitivity experiments were designed to investigate the effects of emission control strategies since 2013. The baseline experiment was the control simulation, which was conducted using anthropogenic emissions from 2017 and fully coupling aerosols and meteorology. The sensitivity experiment had the same configurations apart from anthropogenic emissions in 2012. Our experiments were conducted for two typical winters as the blue days in winter were the greatest concern. The first one is the last winter of the first 5-years Clean Air Action (i.e., Nov., Dec. 2017, and Jan. 2018), and the second one is the first winter after the first 5-years Clean Air Action (i.e., Nov. and Dec. 2018). Due to a lack of meteorological observations for model evaluation, our experiments did not include Jan. 2019. To focus on the BTH region, a triple nesting scheme was adopted (Fig. S1 online). Model configuration can be found in Table S1 (online). Detailed descriptions of the materials, methods, and model set are summarized in Supplementary materials.

The BTH blue days (BBDs) were firstly defined with three criteria following methods of Wang et al. [10]: no precipitation (Non-Prep), low cloud cover (LCC) $\leq$ 30%, and visibility $\leq$ 15 km at 14:00 BJT. The model performances were evaluated with *in situ* observations in BTH. The simulated temporal variations in visibility, LCC, and Non-Prep matched well with the observed ones, with correlation coefficient values higher than 0.88, 0.76, and 0.84 respectively (Fig. S2a–c online). Consequently, the simulated BBDs agreed well with the observed ones, with a correlation coefficient beyond 0.85 and a high accuracy beyond 80.23% (Fig. S2d online). These results indicated a good model performance. The spatial distributions of the simulated visibility, LCC, Non-Prep, and BBD showed patterns similar with the observed ones (Fig. S3 online). These results indicated the rationality of evaluating BBDs changes under different emission scenarios.

A widespread decline in anthropogenic emissions during 2013–2017 has been documented in many studies [1,11,12], while few have focused on the variations in winter. Based on the Multi-resolution Emission Inventory for China (MEIC v1.3; http://meicmodel.org) [13], the average emissions of primary aerosol species and trace gases during winter 2012 and 2017 in BTH are shown in Table S2 (online). Compared with 2012, the remarkable effectiveness of Clean Air Action can be detected for SO_2 and PM coarse

* Corresponding authors.
E-mail addresses: hg@mail.iap.ac.cn (G. Huang), daitie@mail.iap.ac.cn (T. Dai).

https://doi.org/10.1016/j.scib.2022.01.009
2095-9273/© 2022 Science China Press. Published by Elsevier B.V. and Science China Press. All rights reserved.

(coarse mode of particle matter, calculated by the difference between PM_{10} and $PM_{2.5}$), whose amplitudes were reduced by more than 50% in winter for BTH. In contrast, minor declines were detected for NO_x and NH_3, which were below −26% and −15% respectively. These results were consistent with earlier studies [11,12,14]. Nonetheless, the emissions of volatile organic compounds (VOCs) still increased beyond 12.66% and 16.84% in Beijing and Tianjin and displayed a weak reduction below −6.58% in Hebei. These indicated that more attentions should be paid to the VOCs, NO_x, and NH_3 emission controls in the future.

Accordingly, a noticeable cut-emission effect on blue days is manifested in Fig. 1a. There was a comprehensive increase in BBDs in BTH and surrounding areas compared with that using emission in 2012, which was closely related to the cut-aerosol distribution (Fig. S4a–f online). In comparison, southeastern Beijing (over 45%), southern Tianjin (over 65%), and Hebei (over 65%) showed the highest increasing rate, with a maximum exceeding 53 d at an increasing rate of 157.14%. We also noticed a mismatch between the most apparent emission reduction in Beijing and the most obvious BBDs increase in southern Hebei (Fig. S5a online). This may be caused by the variations of VOCs and the corresponding climate-aerosol feedback effect, which needs further study.

Furthermore, the major contributor to the increase of BBDs was detected. With fixed meteorology, the simulation suggested that reduction of emissions would lead to significantly higher visibility (Fig. 1b, passing the 95% confidence level). In addition, the most notable increase of visibility (over 46%) ran slightly from the northeast to southwest, which was consistent with the BBDs variations. Overall, the correlation coefficient between visibility and BBDs was beyond 0.93. It should be mentioned that winter is the "dry" season for BTH with low LCC and little precipitation, therefore the difference of LCC and Non_Prep between two MEIC emissions can not pass the 95% confidence level (Fig. S6 online) [15]. This demonstrated the dominant role of visibility and the minor effects of LCC and precipitation on BBD increase. Meanwhile, it emphasized the significance of emission control in increasing BBDs in recent years.

The variations in regional hourly average BBDs and visibility under different emissions in BTH are plotted in Fig. 1c. Clearly, emission controls contribute to greater visibility, with a mean increment of 2.57 km. Meanwhile, it helped to weaken visibility decline during serious pollution episodes (in blue bars in Fig. 1c). Additionally, it was emphasized that emission reduction brings into a better-than-better effect, meaning that control measures

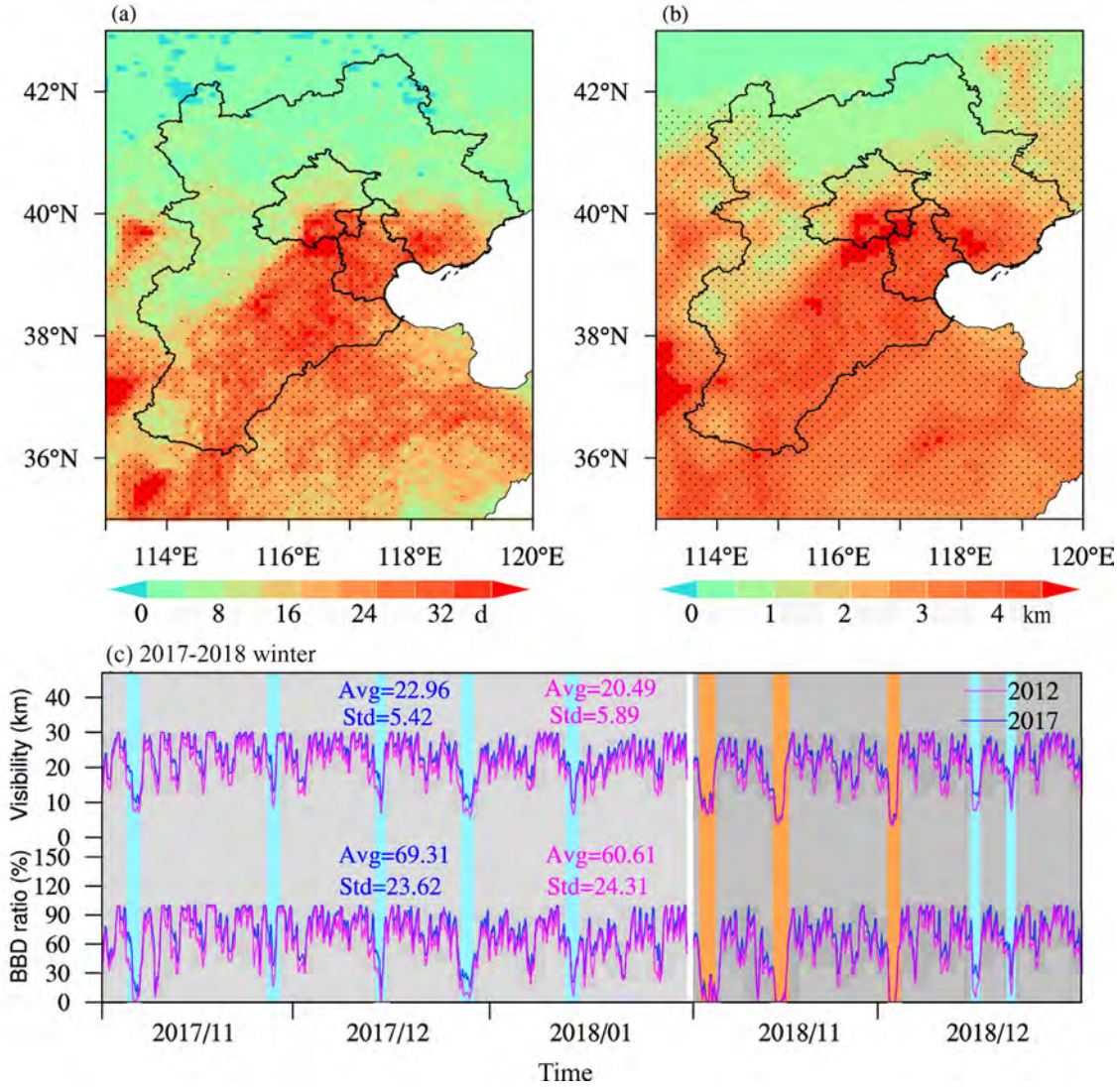

Fig. 1. Spatial distributions of differences of simulated total blue days (Sum_BBD, unit: d) (a), and average visibility (unit: km) (b) under different MEIC (2017 and 2012) during winter 2017 and winter 2018 over BTH. The black dots mean the changes pass the 95% confidence level by *t*-test. (c) The time series of the regional hourly average BBDs occurrence rates (BBD ration) over BTH. The blue bars represent the serious pollution episodes have been improved by emission control measures, and the orange bars mean the opposite.

improved visibility during relatively higher-visibility days efficiently, such as Nov. 16–21, 2017, and Dec. 30–31, 2017. By reducing the amplitude of oscillation at an hourly scale, lower standard deviations can be detected for visibility. Following the variations of visibility, the emission controls seemed to be effective to improve most of the extreme pollution events and favored a bluer-than-bluer mechanism during relatively bluer days on the regional scale in the same period. We also noticed that the extreme pollution episodes in Nov. 2018 and early Dec. 2018 seemed to refute strict emission measures (in orange bars in Fig. 1c). This suggests that the unfavorable influence of meteorology may have played a more important role for regional non-blue days in BTH on that days.

On average, the regional average BBDs occurrence rates over the 16 sites rose from 54% to 65%, which was consistent with the regional mean results (from 60% to 69%). Regionally, those control measures remarkably increased the Beijing blue days from 22.32 days/month (d/m) in 2012 to 25.73 d/m in 2018, from 12.4 to 17.67 d/m in Tianjin, and 18.91 to 22.01 d/m in Hebei, respectively. Overall, a regional mean BBDs increase beyond 2.79 d/m was revealed. It was also notable that the emission-cut measures lead to a weaker correlation coefficient between visibility and BBDs in BTH. The correlation coefficients decrease from 0.97/0.93/0.93 to 0.94/0.92/0.91 in Beijing/Tianjin/Hebei, respectively. This meant that the dominant role of visibility on BBDs may have been diminished with its improvement, which needs further study.

The impacts of Clean Air Action since 2013 on the blue days in winter over BTH were explored in this study. Emission reduction led to significantly higher visibility and widespread increase of BBDs in BTH by an average of 2.79 d/m and a maximum exceeding 53 d. Although the unique emission controls may favor more extensive blue days and reduce extreme pollution episodes in China, more efforts should be implemented to increase more blue days effectively in the future, which would provide a reference to future policymaking from a new perspective. Further study should be conducted to qualify the positive feedback mechanism of emission-cut and blue days and the effects of the newest Blue Sky Protection Campaign Plan should be evaluated.

Conflict of interest

The authors declare that they have no conflict of interest.

Acknowledgments

This work was supported by the National Natural Science Foundation of China (42141019, 41831175, 91937302, 41721004, 41875133, 41590875, and 41605083), the Second Tibetan Plateau Scientific Expedition and Research (STEP) Program (2019QZKK0102), the Youth Innovation Promotion Association of Chinese Academy of Sciences (2020078), and the International Partnership Program of Chinese Academy of Sciences (134111KYSB20200006).

Appendix A. Supplementary materials

Supplementary materials to this article can be found online at https://doi.org/10.1016/j.scib.2022.01.009.

References

[1] Zhang Q, Zheng Y, Tong D, et al. Drivers of improved $PM_{2.5}$ air quality in China from 2013 to to 2017. Proc Natl Acad Sci USA 2019;116:24463–9.
[2] Ministry of Envirionmental Protection, the People's Republic of China. Report on the state of the ecology and environment in China 2017. 2018;1.
[3] Han Y, Li VOK, Lam JCK, et al. How blue is the sky? Estimating air qualities in Beijing during the blue sky day period (2008–2012) by Bayesian Multi-Task Lstm. Environ Sci Policy 2021;116:69–77.
[4] Li CD, Ma XW, Fu TB, et al. Does public concern over haze pollution matter? Evidence from Beijing-Tianjin-Hebei region, China. Sci Total Environ 2021;755:8.
[5] Zou J, Liu Z, Hu B, et al. Aerosol chemical compositions in the North China Plain and the impact on the visibility in Beijing and Tianjin. Atmos Res 2018;201:235–46.
[6] Liu J, Ren C, Huang X, et al. Increased aerosol extinction efficiency hinders visibility improvement in eastern China. Geophys Res Lett 2020;47:20.
[7] Nichol JE, Bilal M, Ali MA, et al. Air pollution scenario over China during COVID-19. Remote Sens 2020;12:2100.
[8] Huang X, Ding A, Wang Z, et al. Amplified transboundary transport of haze by aerosol–boundary layer interaction in China. Nat Geosci 2020;13:428–34.
[9] Sulaymon ID, Zhang Y, Hopke PK, et al. Persistent high $PM_{2.5}$ pollution driven by unfavorable meteorological conditions during the COVID-19 lockdown period in the Beijing-Tianjin-Hebei region. China Environ Res 2021;198:16.
[10] Wang S, Huang G, Lin J, et al. Chinese blue days: a novel index and spatio-temporal variations. Environ Res Lett 2019;14:074026.
[11] Fan H, Zhao C, Yang Y. A comprehensive analysis of the spatio-temporal variation of urban air pollution in China during 2014–2018. Atmos Environ 2020;220:117066.
[12] Zhang K, Zhao C, Fan H, et al. Toward understanding the differences of $PM_{2.5}$ characteristics among five China urban cities. Asia-Pac J Atmos Sci 2020;56:493–502.
[13] Li M, Liu H, Geng G, et al. Anthropogenic emission inventories in China: a review. Natl Sci Rev 2017;4:834–66.
[14] Ji D, Gao W, Maenhaut W, et al. Impact of air pollution control measures and regional transport on carbonaceous aerosols in fine particulate matter in urban Beijing, China: insights gained from long-term measurement. Atmos Chem Phys 2019;19:8569–90.
[15] Sun Y, Zhao C. Distinct impacts on precipitation by aerosol radiative effect over three different megacity regions of eastern China. Atmos Chem Phys 2021;21:16555–74.

Su Wang received the M.S. degree in environmental engineering in 2019 from the Institute of Atmospheric Physics, Chinese Academy of Sciences. Her research interest includes climate change, air quality numerical simulation, and the interaction between climate change and air pollution.

Gang Huang is a professor at Institute of Atmospheric Physics, Chinese Academy of Sciences. His research interest includes tropical atmosphere-ocean interaction, monsoon dynamics, climate change and climate variability, global warming dynamics, and climate modeling.

Tie Dai is an associate professor at Institute of Atmospheric Physics, Chinese Academy of Sciences. His research interest includes remote sensing, air quality numerical simulation, and data assimilation.

nature geoscience

ARTICLES

https://doi.org/10.1038/s41561-022-00898-2

Check for updates

Sulfur emissions from consumption by developed and developing countries produce comparable climate impacts

Jintai Lin[1,12] ✉, Chunjiang Zhou[2,3,4,12], Lulu Chen[1,12], Gang Huang[2,5,4] ✉, J.-F. Lamarque[6], Ji Nie[1], Jun Yang[1], Kaiming Hu[7,4], Peng Liu[1,8], Jingxu Wang[1,9], Yan Xia[10], Yang Yang[11] and Yongyun Hu[1]

Regional consumption activities supported by domestic production and international trade have led to substantial aerosol-related emissions worldwide. Here we quantify sulfur dioxide emissions associated with consumption by developed and developing countries and assess the resulting climate impacts using an Earth system model. We find that although the consumption-associated emissions of developed countries are 40% less than those of developing countries, they lead to similar impacts on global mean surface air temperature and precipitation. This is because the effective radiative forcing induced per emission is greater for developed countries, which we attribute to the emissions being located at higher northern latitudes and being more evenly distributed zonally. Emissions from developing countries have a greater impact on temperature and precipitation over the tropical monsoon regions of China and India. Our results demonstrate the importance of trade and emission region in determining how consumption translates into global climate impact.

Climate Action and Responsible Consumption and Production are two closely linked Sustainable Development Goals of the United Nations. Consumption activities affect the climate through greenhouse gases and aerosols associated with production to supply consumption. Raw materials extracted to meet global final consumption demands reached 92 billion metric tons in 2017 and will probably increase to 190 billion metric tons by 2060 without concerted action[1], and extraction, processing, use and disposal of these materials often lead to substantial emissions. Many emission pathways of 1.5 °C warming require shifts towards sustainable consumption[2]. As international trade allows consumption of any region to be supplied by production worldwide, this affects the magnitude and geographical pattern of consumption-associated emissions[3–5]. Understanding the climate response to consumption-associated emissions offers crucial information to support policymaking and international cooperation in climate change mitigation action from a consumption perspective.

For aerosols, which are short-lived, the spatial distribution of consumption-associated emissions determines the distribution of their atmospheric loadings and thus exerts spatially inhomogeneous forcing[6,7] to the nonlinear climate system. Emerging evidence has suggested strong nonlinearity in the climate response to the magnitude[8,9] and location[10–13] of aerosols. For example, a given amount of aerosol emissions released in Western Europe may cause 14 times as much global average cooling as when emitted in India[11]. These studies are based solely on idealized model experiments by scaling the emissions with an arbitrary factor or by putting the same amount of emissions to different locations. Many studies have analysed the climate impacts of aerosols associated with each region's own production activities and resulting (realistic) emissions[14–17]. The climate response to aerosols associated with the same region's consumption could differ substantially due to the large differences in the magnitude and spatial pattern of emissions and forcing. Yet this consumption-induced climate response has never been assessed explicitly. One recent study has estimated the direct radiative forcing of aerosols embedded in trade[6], but it does not quantify how such forcing affects temperature and precipitation.

In this article, we provide an assessment of the effects of aerosols from consumption of developed and developing countries on global temperature and precipitation. We quantify the climate response to sulfate aerosol forcing due to consumption-associated emissions of sulfur dioxide (SO_2) in 2014, the latest year for which all data and models are available. For this purpose, we combine an emission inventory[18], a multiregional input–output table[19] and the fully coupled Community Earth System Model version 2 (CESM2)[20] (Methods). Identification of developing (including emerging markets) and

[1]Laboratory for Climate and Ocean–Atmosphere Studies, Department of Atmospheric and Oceanic Sciences, School of Physics, Peking University, Beijing, China. [2]State Key Laboratory of Numerical Modeling for Atmospheric Sciences and Geophysical Fluid Dynamics (LASG), Institute of Atmospheric Physics, Chinese Academy of Sciences, Beijing, China. [3]School of Ecology and Environment, Inner Mongolia University, Hohhot, China. [4]University of Chinese Academy of Sciences, Beijing, China. [5]Laboratory for Regional Oceanography and Numerical Modeling, Qingdao National Laboratory for Marine Science and Technology, Qingdao, China. [6]Climate and Global Dynamics Laboratory, National Center for Atmospheric Research, Boulder, CO, USA. [7]Center for Monsoon System Research, Institute of Atmospheric Physics, Chinese Academy of Sciences, Beijing, China. [8]Frontiers Science Center for Deep Ocean Multispheres and Earth System, Key Lab of Submarine Geosciences and Prospecting Techniques, MOE and College of Marine Geosciences, Ocean University of China, Qingdao, China. [9]Key Laboratory of Physical Oceanography, Ocean University of China, Qingdao, China. [10]College of Global Change and Earth System Science, Beijing Normal University, Beijing, China. [11]Jiangsu Key Laboratory of Atmospheric Environment Monitoring and Pollution Control, Jiangsu Collaborative Innovation Center of Atmospheric Environment and Equipment Technology, School of Environmental Science and Engineering, Nanjing University of Information Science and Technology, Nanjing, China. [12]These authors contributed equally: Jintai Lin, Chunjiang Zhou, Lulu Chen. ✉e-mail: linjt@pku.edu.cn; hg@mail.iap.ac.cn

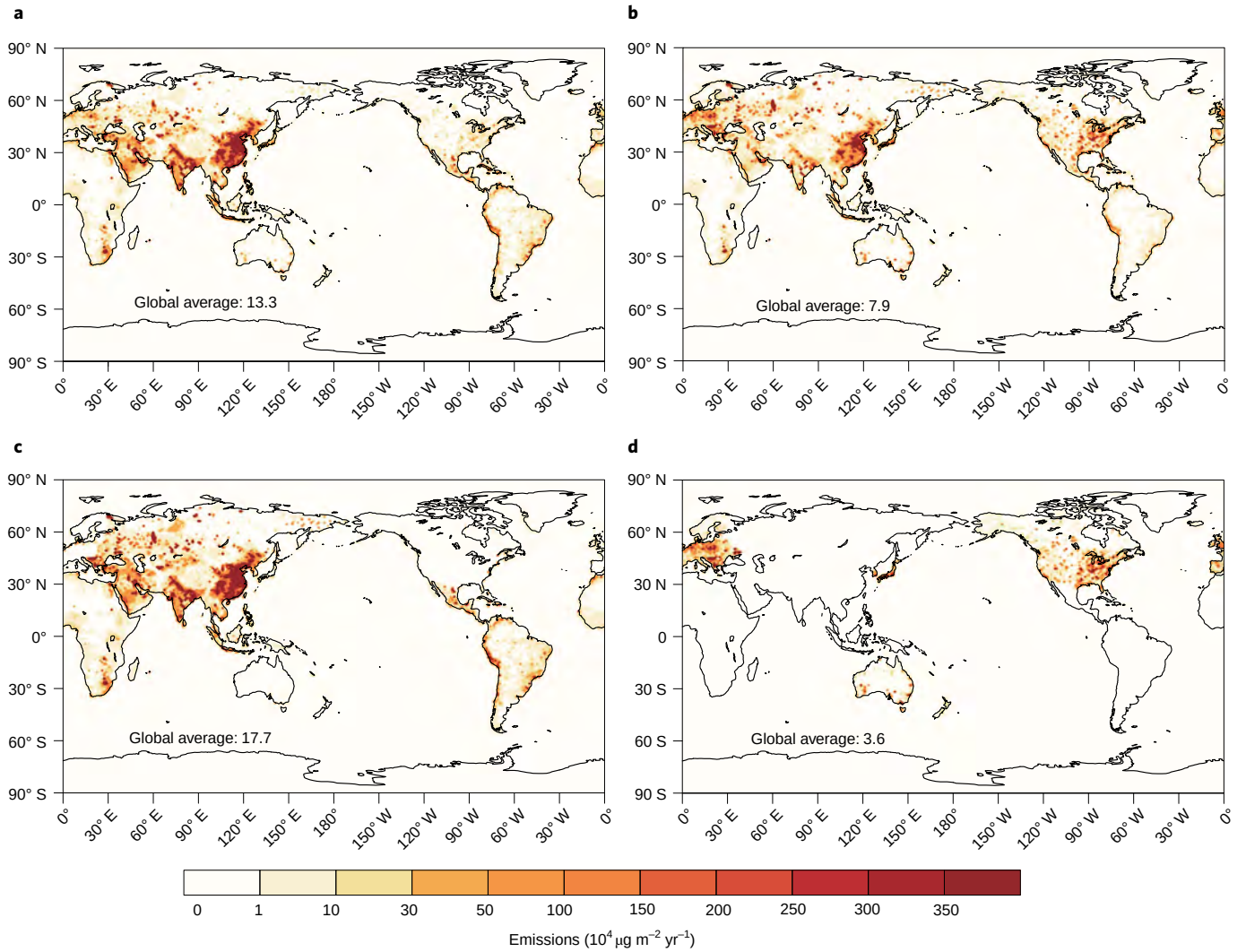

Fig. 1 | Contrasting consumption-based and production-based emissions. Anthropogenic SO_2 emissions associated with consumption and production activities of developing and developed countries in 2014. **a**, E_c of developing countries. **b**, E_c of developed countries. **c**, E_p of developing countries. **d**, E_p of developed countries. The E_c data are calculated in this study, and the E_p data are taken directly from the inventory. The global average is shown in each panel. Map outlines were generated using NCL scripts.

developed countries is based on International Monetary Fund[21]. Uncertainty estimates for global average results are represented by 2 s.d. (corresponding to 95% confidence interval (CI)), and a paired z test for statistical significance is used to account for autocorrelation[22]. Our results show unexpectedly similar effects of consumption by developed and developing countries on the global average near-surface air temperature and precipitation, despite the large difference in the magnitude of consumption-associated SO_2 emissions by a factor of 1.7.

Consumption-associated sulfur emissions and loadings

Figure 1 compares the production-based emissions (E_p) and consumption-based emissions (E_c) of SO_2 for both developed and developing countries. The E_c of a region denote worldwide emissions due to production of goods and services to supply consumption by that region. By contrast, the E_p are associated with production by that region to supply global consumption, as recorded in the inventory used here. The global total E_c of developing countries (67.7 Tg yr^{-1}) are about 1.7 times those of developed countries (39.9 Tg yr^{-1}). This is in contrast to the factor-of-five difference in global total E_p (89.7 versus 17.8 Tg yr^{-1}). The E_c exhibit much greater spatial coverage than do the E_p, especially for the emissions of developed countries (Fig. 1).

Figure 1 further shows that the E_c of developed countries that are released in developing countries are larger than the E_c of developing countries that are released in developed countries by a factor of 7. These differences are because developed countries are net importers of goods from developing countries and have much lower emission intensities than the latter[6,23]. Overall, the E_c of developing countries are more concentrated in Asia low and middle latitudes, whereas the E_c of developed countries more spread out over northern latitudes. These geographical characteristics are further depicted in the zonal average and meridional average emissions in Extended Data Fig. 1. The unique features of regional E_c in magnitude and spatial pattern warrant a detailed assessment of resulting climate impacts to supplement prevailing production-based studies.

Extended Data Fig. 2a,b shows the spatial distribution of sulfate aerosol column densities associated with consumption (S_c) by developed and developing countries. Sulfate is formed in the atmosphere from emitted SO_2 and lost through dry and wet deposition. The spatial pattern of S_c largely follows the E_c due to short atmospheric lifetimes of SO_2 and sulfate, although portions of sulfate

Table 1 | Climate response to E_c of SO_2

	Due to E_c of developing countries	Due to E_c of developed countries
E_c (SO_2 10^4 μg m^{-2} yr^{-1})	13.3	7.9
S_c (SO_4 μg m^{-2})	17.5 (±0.83)	9.1 (±0.89)
ΔAOD (10^{-2})	0.50 (±0.32)	0.32 (±0.36)
ERF (W m^{-2})	-0.48 (±0.64)	-0.42 (±0.64)
ΔT (K)	-0.18 (±0.11)	-0.20 (±0.09)
ΔP (mm d^{-1})	-0.019 (±0.019)	-0.017 (±0.017)

Included are the changes in global average annual mean S_c, AOD, ERF, 2 m air temperature (T) and precipitation (P). The values in brackets represent 2 s.d.

are transported from emission source regions to downwind areas[3]. The global average S_c of developing countries are 1.9 times the S_c of developed countries, consistent with the difference in E_c. The S_c of developing and developed countries are both large in the Northern Hemisphere (NH), but their regional patterns differ. The S_c of developing countries are concentrated over East and South Asia. By comparison, the S_c of developed countries are more evenly distributed in the zonal direction at northern latitudes, with high values over Eurasia and North America. The difference in spatial pattern is also evident for aerosol optical depth (AOD, Extended Data Fig. 2c,d).

Climate responses to sulfur emissions

The E_c of developing and developed countries reduce the global average annual mean 2 m air temperature by 0.18 ± 0.11 K and 0.20 ± 0.09 K, respectively (Table 1). The magnitudes of temperature reduction are both close to the magnitude of observed surface warming (~0.2 K) over the past decade[2]. The comparable temperature reductions are despite the global average E_c and S_c of developing countries being 1.7 and 1.9 times those of developed countries. The temperature reduction is most evident in the NH (Fig. 2a,b), by a hemispheric average of 0.23 K driven by the E_c of developing countries and by 0.25 K driven by the E_c of developed countries. The E_c of developed countries cause significant cooling at the NH extratropics (30°–90° N) with weak effects over tropical East and South Asia. By comparison, the E_c of developing countries cool East and South Asia but less so at higher latitudes of Eurasia (Fig. 2a). The zonal average results in Fig. 3a,b further show substantial cooling between 60° S and 60° N by the E_c of each region (by 0.10–0.40 K depending on the latitude). The temperature responses in the polar areas are much more uncertain (Fig. 3) due to natural variability[14,22], although the Arctic cooling induced by the E_c of developed countries are statistically significant at 68% CI.

The unexpectedly comparable cooling effects by the E_c of developing and developed countries are because the E_c of developed countries, although smaller in magnitude, have a stronger per-emission capability to induce forcing. To demonstrate this point, we calculate the effective radiative forcing (ERF) of E_c with additional Community Atmosphere Model version 6 (CAM6) simulations (Methods). The global mean ERFs due to the E_c of developing and developed countries are comparable (−0.48 ± 0.64 versus −0.42 ± 0.64 W m^{-2}), consistent with the similar temperature changes. The ERFs per emission of SO_2 for these two regions are −0.0071 ± 0.0094 and −0.011 ± 0.016 W m^{-2} (Tg yr^{-1})$^{-1}$, respectively, with the latter higher by about 50%.

Extended Data Fig. 3a,b further shows the horizontal distribution of ERF. The E_c of developed countries lead to significant negative ERF throughout the NH middle and high latitudes, whereas the E_c of developing countries result in the greatest ERF at the low and middle latitudes around China and India. The negative ERF caused by E_c of developing countries is statistically significant at 95% CI over South Asia, East Asia and the downwind northern Pacific, significant at 68% CI over the majority of the NH but insignificant over the contiguous United States (Extended Data Fig. 3a). The negative ERF by E_c of developed countries is statistically significant at 95% CI over parts of East Asia, the northern Pacific, northern Eurasia and North America and significant at 68% CI over many other NH areas (Extended Data Fig. 3b).

Decomposition of the ERF by using radiative kernels[24] shows major contributions from the direct radiative forcing of sulfate and fast adjustment of clouds, with minor effects from fast adjustments of other climate variables (Extended Data Table 1). The spatial distribution of sulfate direct radiative forcing (Extended Data Fig. 3c,d) follows those of S_c and AOD (Extended Data Fig. 2), with the global average sulfate forcing induced by the E_c of developing countries 2.5 times that of developed countries (−0.16 ± 0.031 versus −0.066 ± 0.026 W m^{-2}). The E_c of developing and developed countries exert similar global average radiative effects via fast cloud adjustment (−0.32 ± 0.70 versus −0.32 ± 0.72 W m^{-2}, Extended Data Table 1). The fast cloud adjustment corresponds to the overall increase in clouds coverage (statistically significant at 95% or 68% CI over large regions; Extended Data Fig. 4).

Extended Data Table 2 shows radiative kernel decomposition[24] for the top-of-atmosphere (TOA) net radiative flux resulting from E_c perturbation, as averaged over the past 110 years of fully coupled CESM2 simulations. Contributors to the net flux include ERF and the resulting responses of water vapour, surface albedo, temperature and clouds. The contributions of all non-ERF factors are in addition to the radiative effects of their fast adjustments presented in Extended Data Table 1. The 110-year average net fluxes due to the E_c of developing and developed countries are much smaller than the respective values of ERF. Over the 110 years, the net flux is varying but with no trends (Supplementary Fig. 3). The net flux is not zero because the response of deep ocean to ERF (which may take thousands of years) has not been fully realized; this is evident from the imbalance in surface energy flux over the oceans (Extended Data Fig. 3e,f).

Extended Data Table 2 shows that the ERF-induced reduction in surface temperature (in addition to the small fast adjustment) leads to a large positive radiative effect, whereas the corresponding reduction in water vapour leads to a negative radiative effect. The ERF-induced change in clouds (in addition to the fast adjustment) leads to a small radiative effect. The total radiative effect of clouds change induced by E_c of each region is negative (−0.23 ± 1.26 W m^{-2} for developing countries and −0.26 ± 1.43 W m^{-2} for developed countries), calculated as the sum of the respective values in Extended Data Tables 1 and 2. This is consistent with the overall enhancement in clouds coverage simulated by fully coupled CESM2 (statistically significant at 95% or 68% CI over vast areas; Extended Data Fig. 5).

In the Arctic areas, the E_c of developed countries lead to an increase in sea-ice coverage (Extended Data Fig. 6b) and a deepened polar vortex (as manifested in the geopotential height and wind field at 500 hPa, Extended Data Fig. 7b). The increase in sea ice coincides with the strong surface cooling there (Fig. 2b). The change in polar vortex is consistent with the widespread cooling over the northern middle and high latitudes (Fig. 2b). By comparison, the E_c of developing countries lead to weaker Arctic responses (Extended Data Figs. 6a and 7a) because the emissions are located at lower latitudes.

The E_c of developing and developed countries each result in warming along the coasts of Greenland. The temperature change is consistent with the reduction in sea-ice coverage (Extended Data Fig. 6a,b) and the increase in the surface (latent + sensible) heat flux to the atmosphere (Extended Data Fig. 6e,f). Correspondingly, the change in surface winds reduces the sea-ice drift to these locations (Extended Data Fig. 6c,d).

In the tropics, the Southern Hemisphere (SH) Hadley cell circulation strengthens and the NH Hadley cell weakens, and the associ-

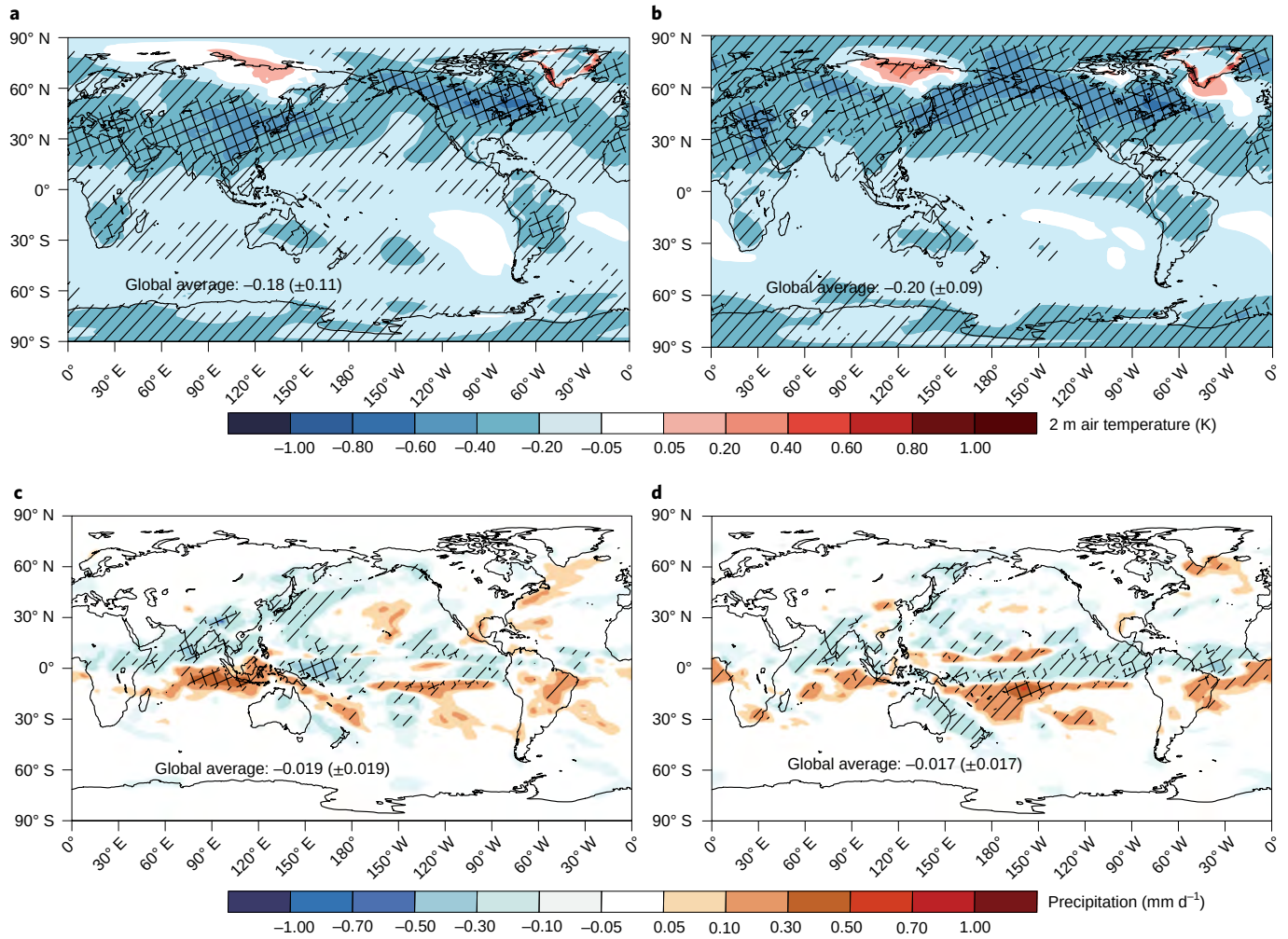

Fig. 2 | Climate response to consumption-based emissions. a, Changes in annual mean 2 m air temperature due to E_c of developing countries. **b**, Changes in annual mean 2 m air temperature due to E_c of developed countries. **c**, Changes in precipitation due to E_c of developing countries. **d**, Changes in precipitation due to E_c of developed countries. The grid cells with cross lines pass the paired *z* test at 95% CI, and those with diagonal lines pass the test at 68% CI. The global average is shown in each panel. Map outlines were generated using NCL scripts.

ated intertropical convergence zone shifts southwards, as manifested in the weakened rising in the NH tropics and enhanced rising in the SH tropics (Extended Data Fig. 8). These tropical responses are because the sulfate-induced cooling is stronger in the NH than in the SH, resulting in reduced hemispheric temperature asymmetry (because the NH is warmer than the SH climatologically) and less atmospheric cross-Equator energy transport to the SH by the Hadley cell[25,26]. The tropical circulation change is associated with weakened precipitation[27,28] in South and East Asian monsoon areas (Fig. 2c,d), which has a warming effect[29] that partly offsets the radiative cooling effect. Since the magnitude of ERF by developing countries is large in East and South Asia (Extended Data Fig. 3a), the sinking enhancement at 0–20° N is strong (Extended Data Fig. 8a). The ERF by developed countries occurs at higher latitudes and is zonally evener. The resulting effect on the Hadley cell is weaker in magnitude (Extended Data Fig. 8b versus 8a), as also reflected in the weaker change in meridional winds in tropical Asian monsoon areas at 850 hPa (Extended Data Fig. 7d versus 7c).

The E_c of developing and developed countries result in similar reductions in global average annual mean precipitation (-0.019 ± 0.019 versus -0.017 ± 0.017 mm d^{-1}, Fig. 2c,d) since the response of precipitation is strongly constrained by radiative energy balance[30]. The calculated changes in precipitation are statistically significant at 68% CI over the majority of tropical oceans. The precipitation changes are even statistically significant at 95% over parts of the tropical regions of China, India, the Indian Ocean and the western Pacific due to the E_c of developing countries (Fig. 2c) and over parts of the tropical Pacific due to the E_c of developed countries (Fig. 2d). The E_c of developing countries result in the greatest reduction (by up to 0.57 mm d^{-1}, statistically significant at 95% CI; Fig. 2c) over tropical Asian continental monsoon areas (India, IndoChina Peninsula and south China), whereas the E_c of developed countries do not cause such a strong reduction (Fig. 2c,d). The zonal average results also show the strongest precipitation changes in the tropics (by up to about ± 0.1 mm d^{-1}), with a reduction in the NH and an enhancement in the SH (Fig. 3c,d), consistent with the changes in the Hadley cell and intertropical convergence zone (Extended Data Fig. 8). The peak zonal average precipitation enhancement over the SH tropics is statistically significant at 68% CI.

A consumption-based perspective for climate action

For each region, there exist substantial differences between its E_c and E_p in the magnitude and geographical pattern. The climate response to emissions associated with regional consumption presented in this study is very different from that inferred from prevailing production-based studies. For example, applying the global

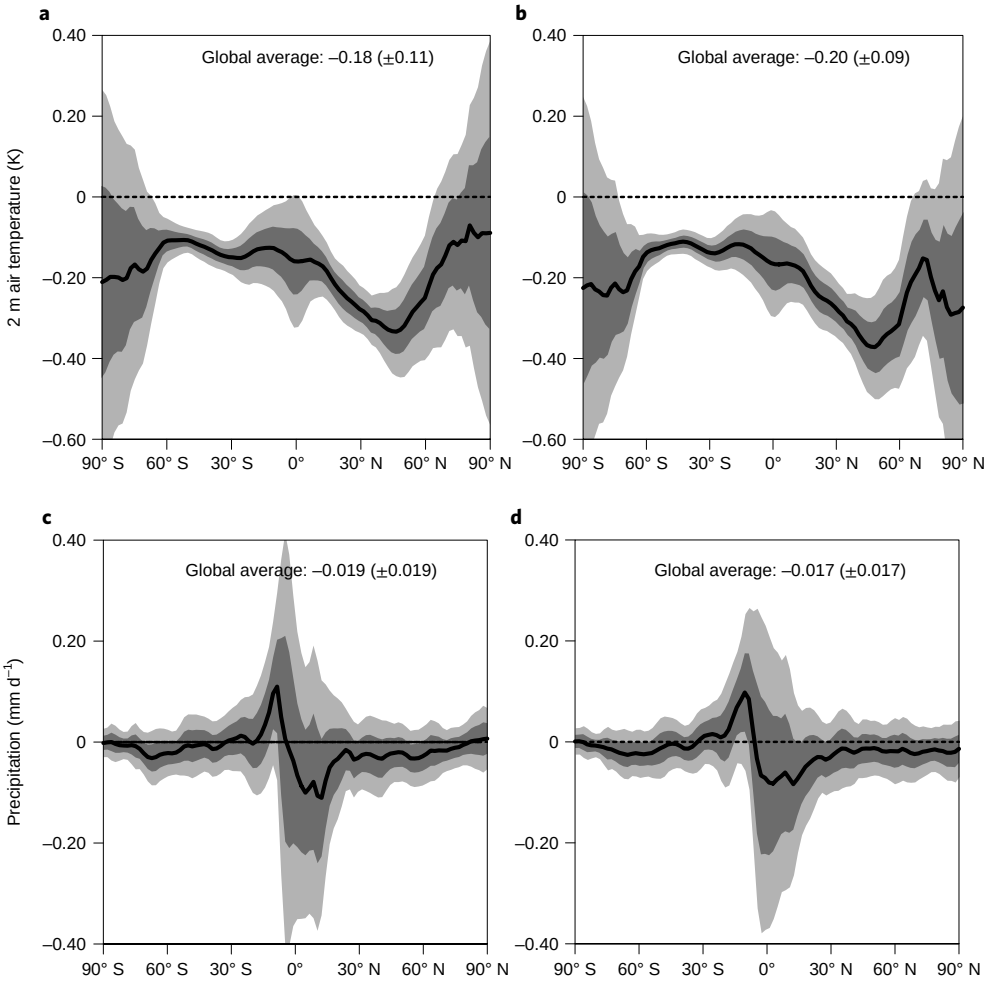

Fig. 3 | Zonal average climate response to consumption-based emissions. a, Changes in zonal average annual mean 2 m air temperature in response to E_c of developing countries. **b**, Changes in zonal average annual mean 2 m air temperature in response to E_c of developed countries. **c**, Changes in precipitation in response to E_c of developing countries. **d**, Changes in precipitation in response to E_c of developed countries. The light shading indicates 2 s.d. of the 110 yr time series, and the dark shading indicates 1 s.d. The global average value is shown in each panel.

average temperature change per unit of E_p suggested by ref. [9] would mean a factor-of-five difference in the temperature response to the E_p of developing and developed countries, in contrast to the comparable temperature effects by their E_c shown here. This suggests that a picture of the regional contribution to climate change drawn from both production and consumption perspectives will be more complete in supporting regional efforts to combat climate change.

Although the E_c of SO_2 by developing and developed countries differ by a factor of 1.7, they result in comparable changes in the global average surface air temperature and precipitation. This highlights the complex response of the nonlinear climate system to not only the magnitude but also the spatial pattern of aerosols. This finding is broadly consistent with previous E_p-based, idealized model simulations[8–13], although our results are based on realistic E_c emissions. For climate policy considerations and international negotiations, a climate change attribution assessment based on fully coupled model simulations driven by realistic, regionally detailed emissions is important. Such an assessment will also offer a reference to validate and correct results based on simplified metrics (for example, global average radiative forcing and global warming potential) in situations where these metrics are used to save computational resources and time.

Our study is based on emissions in a recent year. Along with the economic globalization and trade liberation, the world has experienced rapid changes in regional E_p and E_c. The E_p of developed countries have continued to decline for decades[18], but their E_c have declined at much weaker rates[3,31]. Over the recent few years, the E_p of China have been reduced substantially[32], whereas the E_p of many developing countries have continued to grow or changed little[33,34] (except for the temporary disruption by COVID-19), and the resulting changes in E_c remain unclear. Future changes in E_p and E_c will depend on the pathway of socioeconomic development and emission control. Many future scenarios assume transition in the energy–industrial sector at a scale not experienced in the past[2,35]. A few ongoing events such as the Sino-US trade war[23], Brexit and COVID-19 have disrupted the global trade, but the duration of these events and their direct and indirect emissions impacts are less clear. Also not clear are whether the world will embrace continuous globalization—regional rivalry is one of the few plausible shared socioeconomic pathways projected for this century[36]—and how this will affect the magnitude and distribution of regional E_c. These pose important questions of how the continuously changing E_c of each region have been affecting and will affect the climate system.

Our study is focused on the effect of sulfate. However, consumption activities also affect other aerosols (for example, black carbon) and greenhouse gases. Given the importance of responsible consumption to the success of climate change mitigation and environmental protection[1,2], it will be very beneficial to conduct a com-

prehensive assessment of the climate response to the whole suite of climate-relevant constituents associated with regional consumption. A multimodel assessment will help reduce the intrinsic uncertainty in model simulations. This, of which our sulfate study serves as the first step, will complement prevailing production-based analyses to help understand how human activities affect the climate system more thoroughly. As much of the E_c of any region are released in other regions, such a consumption-based assessment will also provide a basis for international cooperation to act towards sustainable consumption and climate change mitigation, which will have substantial co-benefits for public health[4].

Online content

Any methods, additional references, Nature Research reporting summaries, source data, extended data, supplementary information, acknowledgements, peer review information; details of author contributions and competing interests; and statements of data and code availability are available at https://doi.org/10.1038/s41561-022-00898-2.

Received: 15 July 2020; Accepted: 10 January 2022;
Published online: 17 February 2022

References

1. *The Sustainable Development Goals Report* (United Nations, 2019); https://unstats.un.org/sdgs/report/2019/
2. IPCC: Summary of Policymakers. In *Special Report on Global Warming of 1.5° C* (eds Masson-Delmotte, V. et al.) (WMO, 2018).
3. Lin, J.-T. et al. Retrieving tropospheric nitrogen dioxide from the ozone monitoring instrument: effects of aerosols, surface reflectance anisotropy, and vertical profile of nitrogen dioxide. *Atmos. Chem. Physics* **14**, 1441–1461 (2014).
4. Zhang, Q. et al. Transboundary health impacts of transported global air pollution and international trade. *Nature* **543**, 705–709 (2017).
5. Wiedmann, T. & Lenzen, M. Environmental and social footprints of international trade. *Nat. Geosci.* **11**, 314–321 (2018).
6. Lin, J. et al. Global climate forcing of aerosols embodied in international trade. *Nat. Geosci.* **9**, 790–794 (2016).
7. Wang, J.-X. et al. Socioeconomic and atmospheric factors affecting aerosol radiative forcing: production-based versus consumption-based perspective. *Atmos. Environ.* **200**, 197–207 (2019).
8. Yang, Y., Smith, S. J., Wang, H., Mills, C. M. & Rasch, P. J. Variability, timescales, and nonlinearity in climate responses to black carbon emissions. *Atmos. Chem. Physics* **19**, 2405–2420 (2019).
9. Lewinschal, A. et al. Local and remote temperature response of regional SO_2 emissions. *Atmos. Chem. Physics* **19**, 2385–2403 (2019).
10. Shindell, D. & Faluvegi, G. Climate response to regional radiative forcing during the twentieth century. *Nat. Geosci.* **2**, 294–300 (2009).
11. Persad, G. G. & Caldeira, K. Divergent global-scale temperature effects from identical aerosols emitted in different regions. *Nat. Commun.* **9**, 3289 (2018).
12. Sand, M., Berntsen, T. K., Ekman, A. M. L., Hansson, H.-C. & Lewinschal, A. Surface temperature response to regional black carbon emissions: do location and magnitude matter? *Atmos. Chem, Physics* **20**, 3079–3089 (2020).
13. Liu, L. et al. A PDRMIP multimodel study on the impacts of regional aerosol forcings on global and regional precipitation. *J. Clim.* **31**, 4429–4447 (2018).
14. Westervelt, D. M. et al. Multimodel precipitation responses to removal of US sulfur dioxide emissions. *J. Geophys. Res.* **122**, 5024–5038 (2017).
15. Acosta Navarro, J. C. et al. Amplification of Arctic warming by past air pollution reductions in Europe. *Nat. Geosci.* **9**, 277–281 (2016).
16. Li, B. et al. The contribution of China's emissions to global climate forcing. *Nature* **531**, 357–361 (2016).
17. Menon, S., Hansen, J., Nazarenko, L. & Luo, Y. Climate effects of black carbon aerosols in China and India. *Science* **297**, 2250–2253 (2002).
18. Hoesly, R. M. et al. Historical (1750–2014) anthropogenic emissions of reactive gases and aerosols from the Community Emissions Data System (CEDS). *Geosci. Model Dev.* **11**, 369–408 (2018).
19. *GTAP* Version 10 (Pre-Released Version) (Purdue Univ., 2019); https://www.gtap.agecon.purdue.edu/about/project.asp
20. Danabasoglu, G. et al. The Community Earth System Model Version 2 (CESM2). *J. Adv. Model. Earth Syst.* https://doi.org/10.1029/2019ms001916 (2020).
21. *World Economic Outlook* (IMF, 2011).
22. Conley, A. J. et al. Multimodel surface temperature responses to removal of US sulfur dioxide emissions. *J. Geophys. Res.* **123**, 2773–2796 (2018).
23. Lin, J. et al. Carbon and health implications of trade restrictions. *Nat. Commun.* **10**, 4947 (2019).
24. Huang, Y., Xia, Y. & Tan, X. On the pattern of CO_2 radiative forcing and poleward energy transport. *Geophys. Res. Atmos.* **122**, 10578–10593 (2017).
25. Kang, S. M., Held, I. M., Frierson, D. M. W. & Zhao, M. The response of the ITCZ to extratropical thermal forcing: idealized slab–ocean experiments with a GCM. *J. Clim.* **21**, 3521–3532 (2008).
26. Schneider, T., Bischoff, T. & Haug, G. H. Migrations and dynamics of the intertropical convergence zone. *Nature* **513**, 45–53 (2014).
27. Ganguly, D., Rasch, P. J., Wang, H. & Yoon, J.-H. Climate response of the South Asian monsoon system to anthropogenic aerosols. *J. Geophys. Res.* https://doi.org/10.1029/2012jd017508 (2012).
28. Song, F., Zhou, T. & Qian, Y. Responses of East Asian summer monsoon to natural and anthropogenic forcings in the 17 latest CMIP5 models. *Geophys. Res. Lett.* **41**, 596–603 (2014).
29. Mueller, B. & Seneviratne, S. I. Hot days induced by precipitation deficits at the global scale. *Proc. Natl Acad. Sci. USA* **109**, 12398–12403 (2012).
30. Held, I. M. & Soden, B. J. Robust responses of the hydrological cycle to global warming. *J. Clim.* **19**, 5686–5699 (2006).
31. Kanemoto, K., Moran, D., Lenzen, M. & Geschke, A. International trade undermines national emission reduction targets: new evidence from air pollution. *Glob. Environ. Change* **24**, 52–59 (2014).
32. Zheng, B. et al. Trends in China's anthropogenic emissions since 2010 as the consequence of clean air actions. *Atmos. Chem. Physics* **18**, 14095–14111 (2018).
33. McDuffie, E. E. et al. A global anthropogenic emission inventory of atmospheric pollutants from sector- and fuel-specific sources (1970–2017): an application of the Community Emissions Data System (CEDS). *Earth Syst. Sci. Data Discuss.* https://doi.org/10.5194/essd-2020-103 (2020).
34. Chen, L.-L. et al. Inequality in historical transboundary anthropogenic PM2.5 health impacts. *Sci. Bull.* https://doi.org/10.1016/j.scib.2021.11.007 (2021).
35. Shindell, D. & Smith, C. J. Climate and air-quality benefits of a realistic phase-out of fossil fuels. *Nature* **573**, 408–411 (2019).
36. Riahi, K. et al. The shared socioeconomic pathways and their energy, land use, and greenhouse gas emissions implications: an overview. *Glob. Environ. Change* **42**, 153–168 (2017).

Publisher's note Springer Nature remains neutral with regard to jurisdictional claims in published maps and institutional affiliations.

© The Author(s), under exclusive licence to Springer Nature Limited 2022

Methods

An interdisciplinary framework. Through an interdisciplinary framework, we employ sector-, region- and pollutant-specific anthropogenic emission data from the Community Emissions Data System (CEDS) inventory for the Coupled Model Intercomparison Project phase 6 (CMIP6) project[18], use the latest Global Trade Analysis Project (GTAP) multiregional input–output (MRIO) table (version 10 for 2014)[19] to estimate consumption-related emissions of SO_2, and run the fully coupled CESM2[20] to simulate the climate impacts of such sulfur emissions. The widely used[4,6,23] GTAP MRIO table offers quantitative information on the inter-sectoral and inter-regional economic linkage along the global supply chain and tracks worldwide production activities in support of consumption of each region. The MRIO table together with the CEDS CMIP6 emission inventory allows for an estimate of consumption-based emissions. Such emissions are then implemented into the fully coupled CESM2 for climate impact simulations, supplemented by additional atmosphere-only simulations.

The CESM2 Model. We use fully coupled CESM2 in this study. CESM2 is the most current-generation Earth system model developed by the National Center for Atmospheric Research and other institutions. CESM2 is built on many successes of its predecessor, CESM1.2, which is one of the best models in the CMIP5 set of model simulations according to a pattern distance metric of present-day precipitation and temperature[37,38]. CESM1.2 captures the spatial pattern of climatic surface temperature at a country scale in the meteorological reanalysis data, with a high correlation coefficient and a low normalized mean deviation[39]. CESM2 contains many updates to CEMS1.2 and results in an improved historical simulation, including a better representation of low-latitude precipitation and shortwave cloud forcing[20]. An overview of CESM2 can be found elsewhere[20].

CAM6 is the atmospheric component of CESM2. Inside CAM6, we choose a fully interactive aerosol scheme, the Modal Aerosol Model version 4 (MAM4)[40], following the CESM2 set-up for submission to CMIP6. The main difference between MAM4 and the MAM3 scheme used in CESM1.2 is the representation of carbonaceous aerosols[40]. SO_2 is oxidized by the hydroxyl radical, hydrogen peroxide and ozone to form sulfate (SO_4), and sulfate size distributions are simulated prognostically in three lognormal modes: Aitken, accumulation and coarse[41,42]. Both MAM4 and MAM3 provide aerosol simulations with reasonable agreement with observations[43,44]; and they have been used widely to simulate the effects of sulfate on global temperature, precipitation and local climate[11,14,22,45–51]. In this study, CAM6 is run at a horizontal resolution of 1.9°×2.5° with 32 vertical levels.

CESM2 includes an interactive land surface model (the Community Land Model version 5)[52] run at the same horizontal resolution as CAM6, with an extensive suite of new and updated processes and parameterizations to previous versions. The ocean component of CESM2 adopts the Parallel Ocean Program version 2 (POP2)[53] with several physics and numerical improvements[20] and is run at an equivalent resolution of 1°. CESM2 uses the Los Alamos sea-ice model version 5.1.2 (CICE5)[54] as its sea-ice component, and CICE5 shares the same horizontal grid with POP2.

Supplementary Fig. 1a describes the suite of model simulations in this study. We conduct three cases of fully coupled CESM2 simulations, including GLOBAL, Xdeveloping_CE and Xdeveloped_CE. The three cases differ only in anthropogenic SO_2 emissions, with global emissions in GLOBAL, removal of E_c of developing countries in Xdeveloping_CE and removal of E_c of developed countries in Xdeveloped_CE. The impacts of consumption by developing and developed countries are obtained by subtracting simulation results of Xdeveloping_CE and Xdeveloped_CE from GLOBAL, respectively.

Before running the three cases, we conduct an additional fully coupled simulation Pre_run for 300 years from an initial climate state in the year 2000. The GLOBAL case then starts from the climate state in the 300th year of the Pre_run and continues for an additional 407 years; Supplementary Fig. 2 shows that the climate has reached quasi-equilibrium state at this time. Xdeveloping_CE contains three ensemble members branched from the 201st, 211th and 265th years of GLOBAL, respectively. Xdeveloped_CE contains three ensemble members branched from the 201st, 235th and 247th years of GLOBAL, respectively. Each ensemble member of Xdeveloping_CE and X_developed_CE is run for 140 years, with the last 110 years used for analysis. Depending on the years of each ensemble member of Xdeveloping_CE and X_developed_CE, results from GLOBAL are paired temporally for comparison.

Each simulation outputs monthly mean values for temperature, precipitation and other variables. For Xdeveloping_CE or X_developed_CE, each of the three ensemble members provides a monthly time series of paired difference relative to GLOBAL, and the three resulting time series are averaged to obtain an ensemble mean time series. The 110 yr average and standard deviation for the ensemble mean time series are analysed. To correct for the model autocorrelation, we apply the paired z test[22] to the monthly time series and focus the analysis on areas where the climate response passes the significance test with respect to 95% or 68% CI.

Effective radiative forcing calculations. The ERF represents the change in the TOP net (shortwave + longwave) radiative flux due to emission perturbations and fast adjustments of the atmosphere and land surface, with sea surface temperature and sea ice unchanged.

To calculate the ERF, we conduct three additional simulations of CAM6 with specified sea surface temperature and sea ice, following ref. [22]. Here, the ERF is computed from individual simulations with SO_2 emissions identical to GLOBAL, Xdeveloping_CE or X_developed_CE. An all-emission CAM6 simulation is run for 199 years. Other simulations branch from the fifth year of the all-emission simulation and are run for 195 years. The last 190 years of all simulations are used to calculate the ERF.

Radiative kernel decomposition. We calculate the TOA radiative feedbacks using the radiative kernel method introduced by ref. [24], which has been widely used in decomposition of radiative effects for climate change analysis[55–61]. The radiative kernel, K_X, is pre-calculated by a partial perturbation method using the radiative transfer model RRTM[62] for temperature (T), water vapour (q) and surface albedo (a). Then, for non-cloud climate variables, the radiative feedback is computed as

$$\Delta_X R = K_X \Delta X$$

for $X = T$, q or a. The direct radiative forcing (G) from sulfate is calculated on the basis of CAM6 simulations, as determined by contrasting the TOA radiative flux (calculated at each time step but outputted every month) from CAM6 simulations with and without the E_c (GLOBAL versus Xdeveloping_CE or GLOBAL versus X_developed_CE). The cloud feedback is then obtained from the residual of the radiation budget

$$\Delta_{\mathrm{cld}} R = \Delta R - \mathrm{G} - K_T \Delta \mathrm{T} - K_q \Delta q - K_a \Delta a$$

where ΔR is the response of the net TOA radiative flux.

Emissions. In a globalized economy with regions and sectors inter-connected through trade, the difference between E_p and E_c lies in the attribution of emissions associated with production to supply consumption. For example, a cell phone sold in the United States may be assembled in China with steel produced in Japan and iron ore extracted in Australia, and all associated emissions are allocated to the United States from the consumption perspective (E_c) but to these individual countries from the production perspective (E_p).

Anthropogenic emissions of all species but SO_2 represent the year 2000, as taken from the CESM2 present-day simulations. Emissions of SO_2 for the year 2014 are obtained by combining the (production-based) CEDS CMIP6 inventory[18] and the latest version (v.10, for 2014) of the widely used[4,6,23] GTAP MRIO table[19].

The GTAP MRIO table is a result of an internationally collaborative effort to produce a regionally and sectorally harmonized, high-quality input–output database for global trade analysis. It has been widely used as a core dataset in general equilibrium models. The disaggregation details of regions and sectors in the GTAP v.10 table are compatible with those in CEDS, with sectoral and regional mapping established in previous work[23,63].

The calculation of SO_2 E_c follows our previous studies[4,6,23] and is briefly described here (see the flow chart in Supplementary Fig. 1b). We first obtain the worldwide E_p of SO_2 in 2014 from the CEDS CMIP6 emissions inventory, which specifies monthly emissions for 55 sectors on a 0.5°×0.5° horizontal grid. We also calculate the production and consumption (each in monetary quantity) in 57 sectors of 141 countries/regions on the basis of the GTAP v.10 MRIO table for 2014. Production of each country/region and sector is to supply direct and indirect consumption by all regions and sectors. GTAP provides quantitative information of the linkages between sectors and regions along the global supply chain. The mapping from 55 sectors in CEDS to 57 sectors in GTAP follows ref. [23] (see their supplementary data 6). We then calculate country- and sector-specific emission intensities (emission divided by monetary economic output) of SO_2 on the basis of the E_p and production data. We further calculate the E_c of individual countries/regions and sectors by multiplying the sectoral emission intensities with consumption-associated sectoral output. Within each country, the spatial and monthly distributions of E_c follow the distributions of the corresponding E_p. For example, the E_c of the United States that are released in China (due to Chinese production for US consumption) follow the spatial and monthly distributions of the E_p of China. For consumption activities not associated with monetary economic output such as residential use and private vehicle driving (and thus not shown in the GTAP MRIO table), emissions are taken from the CEDS CMIP6 dataset directly, following ref. [23].

Data availability

The GTAP data are available at https://www.gtap.agecon.purdue.edu/. The CEDS CMIP6 emissions are available at https://esgf-node.llnl.gov/search/input4mips/. Model results that support the findings of this study are available on Zenodo with the identifier https://doi.org/10.5281/zenodo.5722962. Raw model simulation results generated during this study are large in size and are available upon reasonable request. Source data are provided with this paper.

Code availability

The CESM is available at http://www.cesm.ucar.edu/models/cesm2/. The codes for kernel calculation are available at http://www.meteo.mcgill.ca/~huang/. Data

analysis and visualizations are created by the NCAR Command Language, which is freely available at https://doi.org/10.5065/D6WD3XH5. All computer codes generated during this study are available from the corresponding authors upon reasonable request.

References

37. Knutti, R., Masson, D. & Gettelman, A. Climate model genealogy: generation CMIP5 and how we got there. *Geophys. Res. Lett.* **40**, 1194–1199 (2013).
38. Gettelman, A. et al. High climate sensitivity in the Community Earth System Model version 2 (CESM2). *Geophys. Res. Lett.* **46**, 8329–8337 (2019).
39. Zheng, Y., Davis, S. J., Persad, G. G. & Caldeira, K. Climate effects of aerosols reduce economic inequality. *Nat. Clim. Change* **10**, 220–224 (2020).
40. Liu, X. et al. Description and evaluation of a new four-mode version of the Modal Aerosol Module (MAM4) within version 5.3 of the Community Atmosphere Model. *Geosci. Model Dev.* **9**, 505–522 (2016).
41. Liu, X. et al. Toward a minimal representation of aerosols in climate models: description and evaluation in the Community Atmosphere Model CAM5. *Geosci. Model Dev.* **5**, 709–739 (2012).
42. Emmons, L. K. et al. The chemistry mechanism in the Community Earth System Model version 2 (CESM2). *J. Adv. Model. Earth Syst.* https://doi.org/10.1029/2019ms001882 (2020).
43. Tilmes, S. et al. Description and evaluation of tropospheric chemistry and aerosols in the Community Earth System Model (CESM1.2). *Geosci. Model Dev.* **8**, 1395–1426 (2015).
44. Mills, M. J. et al. Global volcanic aerosol properties derived from emissions, 1990–2014, using CESM1(WACCM). *J. Geophys. Res. Atmos.* **121**, 2332–2348 (2016).
45. Kasoar, M. et al. Regional and global temperature response to anthropogenic SO_2 emissions from China in three climate models. *Atmos. Chem. Physics* **16**, 9785–9804 (2016).
46. Yang, Y., Wang, H., Smith, S. J., Easter, R. C. & Rasch, P. J. Sulfate aerosol in the Arctic: source attribution and radiative forcing. *J. Geophys. Res.* **123**, 1899–1918 (2018).
47. Westervelt, D. M. et al. Local and remote mean and extreme temperature response to regional aerosol emissions reductions. *Atmos. Chem. Physics* **20**, 3009–3027 (2020).
48. Undorf, S., Bollasina, M. A., Booth, B. B. B. & Hegerl, G. C. Contrasting the effects of the 1850–1975 increase in sulphate aerosols from North America and Europe on the Atlantic in the CESM. *Geophys. Res. Lett.* **45**, 11,930–911,940 (2018).
49. Jiang, Y., Yang, X.-Q. & Liu, X. Seasonality in anthropogenic aerosol effects on East Asian climate simulated with CAM5. *J. Geophys. Res. Atmos.* **120**, 10837–10861 (2015).
50. Zhao, A., Stevenson, D. S. & Bollasina, M. A. Climate forcing and response to greenhouse gases, aerosols, and ozone in CESM1. *J. Geophys. Res.* **124**, 13876–13894 (2019).
51. Zhou, C. et al. The impact of secondary inorganic aerosol emissions change on surface air temperature in the Northern Hemisphere. *Theor. Appl. Climatol.* https://doi.org/10.1007/s00704-020-03249-6 (2020).
52. Lawrence, D. M. et al. The Community Land Model version 5: description of new features, benchmarking, and impact of forcing uncertainty. *J. Adv. Model. Earth Syst.* **11**, 4245–4287 (2019).
53. Smith, R. et al. *The Parallel Ocean Program (POP) Reference Manual. Ocean Component of the Community Climate System Model (CCSM) and Community Earth System Model (CESM)* Technical Report LAUR–10–01853 (Los Alamos National Laboratory, 2010).
54. Hunke, E. C., Hebert, D. A. & Lecomte, O. Level-ice melt ponds in the Los Alamos sea ice model, CICE. *Ocean Model.* **71**, 26–42 (2015). 71.
55. Xia, Y. et al. Significant contribution of severe ozone loss to the Siberian-Arctic surface warming in spring 2020. *Geophys. Res. Lett.* **48**, e2021GL092509 (2021).
56. Xia, Y. et al. Stratospheric ozone-induced cloud radiative effects on Antarctic sea ice. *Adv. Atmos. Sci.* **37**, 505–514 (2020).
57. Xia, Y., Huang, Y. & Hu, Y. On the climate impacts of upper tropospheric and lower stratospheric ozone. *J. Geophys. Res. Atmos.* **123**, 730–739 (2018).
58. Zelinka, M. D. et al. Causes of higher climate sensitivity in CMIP6 models. *Geophys. Res. Lett.* **47**, e2019GL085782 (2020).
59. Sherwood, S. C. et al. An assessment of Earth's climate sensitivity using multiple lines of evidence. *Rev. Geophys.* **58**, e2019RG000678 (2020).
60. Harrop, B. E., Lu, J., Liu, F., Garuba, O. A. & Leung, L. R. Sensitivity of the ITCZ location to ocean forcing via q-flux Green's function experiments. *Geophys. Res. Lett.* **45**, 13116–13123 (2018).
61. Xia, Y. & Huang, Y. Differential radiative heating drives tropical atmospheric circulation weakening. *Geophys. Res. Lett.* **44**, 10592–10600 (2017).
62. Mlawer, E. J., Taubman, S. J., Brown, P. D., Iacono, M. J. & Clough, S. A. Radiative transfer for inhomogeneous atmospheres: RRTM, a validated correlated-k model for the longwave. *J. Geophys. Res. Atmos.* **102**, 16663–16682 (1997).
63. Du, M. et al. Winners and losers of the Sino–US trade war from economic and environmental perspectives. *Environ. Res. Lett.* https://doi.org/10.1088/1748-9326/aba3d5 (2020).

Acknowledgements

We thank M. Mills, H. Wang, X. Li and Z. Lu for help with model set-up at the beginning of the project and Y. Liu for discussion. This work is funded by the National Natural Foundation of China (42075175, 41831175, 41775115) and the Second Tibetan Plateau Scientific Expedition and Research (2019QZKK0604, 2019QZKK0102), the Key Deployment Project of Centre for Ocean Mega-Research of Science, the Chinese Academy of Sciences (COMS2019Q03) and the Strategic Priority Research Program of the Chinese Academy of Sciences (XDA20060501). Y.H. is supported by the National Natural Science Foundation (41888101). J.W. is supported by the Fundamental Research Funds for the Central Universities (202113005) and the Natural Science Foundation of Shandong Province (ZR2021QD119). P.L. is supported by the National Natural Science Foundation of China (42105043) and China Postdoctoral Science Foundation (2021M690142 and 2021T140629).

Author contributions

J.L. and G.H. conceived the study. J.L. and C.Z. designed the research. L.C. calculated the emissions. C.Z. conducted the CAM and CESM simulations. P.L., J.W. and Y.Y. contributed to the experiments. Y.X. conducted radiative kernel calculations. J.L., C.Z., G.H., J.-F.L., J.N., J.Y. and K.H. analysed the results. J.L. and C.Z. wrote the paper with comments from J.-F.L., J.N., J.Y., K.H. and Y.H.

Competing interests

The authors declare no competing interests.

Additional information

Extended data is available for this paper at https://doi.org/10.1038/s41561-022-00898-2.

Supplementary information The online version contains supplementary material available at https://doi.org/10.1038/s41561-022-00898-2.

Correspondence and requests for materials should be addressed to Jintai Lin or Gang Huang.

Peer review information *Nature Geoscience* thanks Geeta Persad, S. Ramachandran and Manfred Lenzen for their contribution to the peer review of this work. Primary Handling Editor: Tom Richardson, in collaboration with the *Nature Geoscience* team.

Reprints and permissions information is available at www.nature.com/reprints.

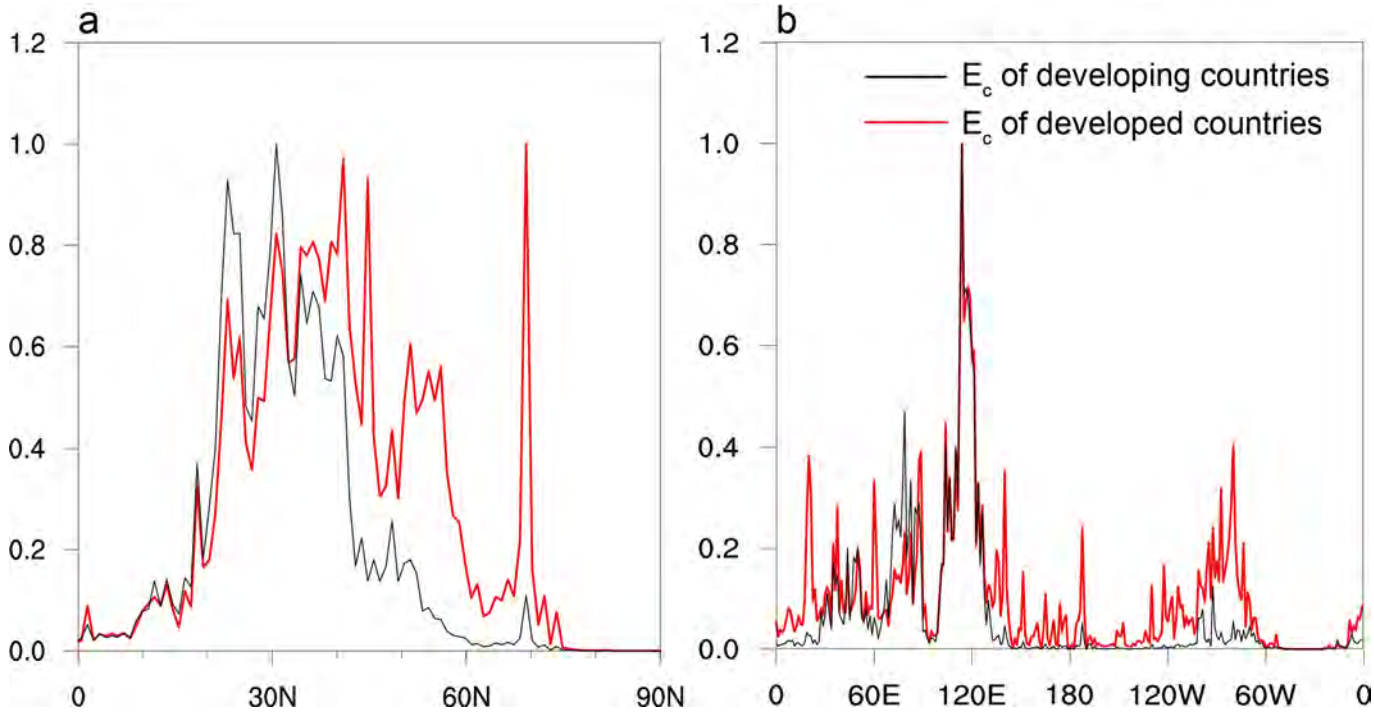

Extended Data Fig. 1 | Latitudinal and longitudinal variations of emissions in the Northern Hemisphere. Zonal average E_c (a) by developing and developed countries, and meridional average E_c (b). Emission values are averaged over land and then normalized relative to their min-max value.

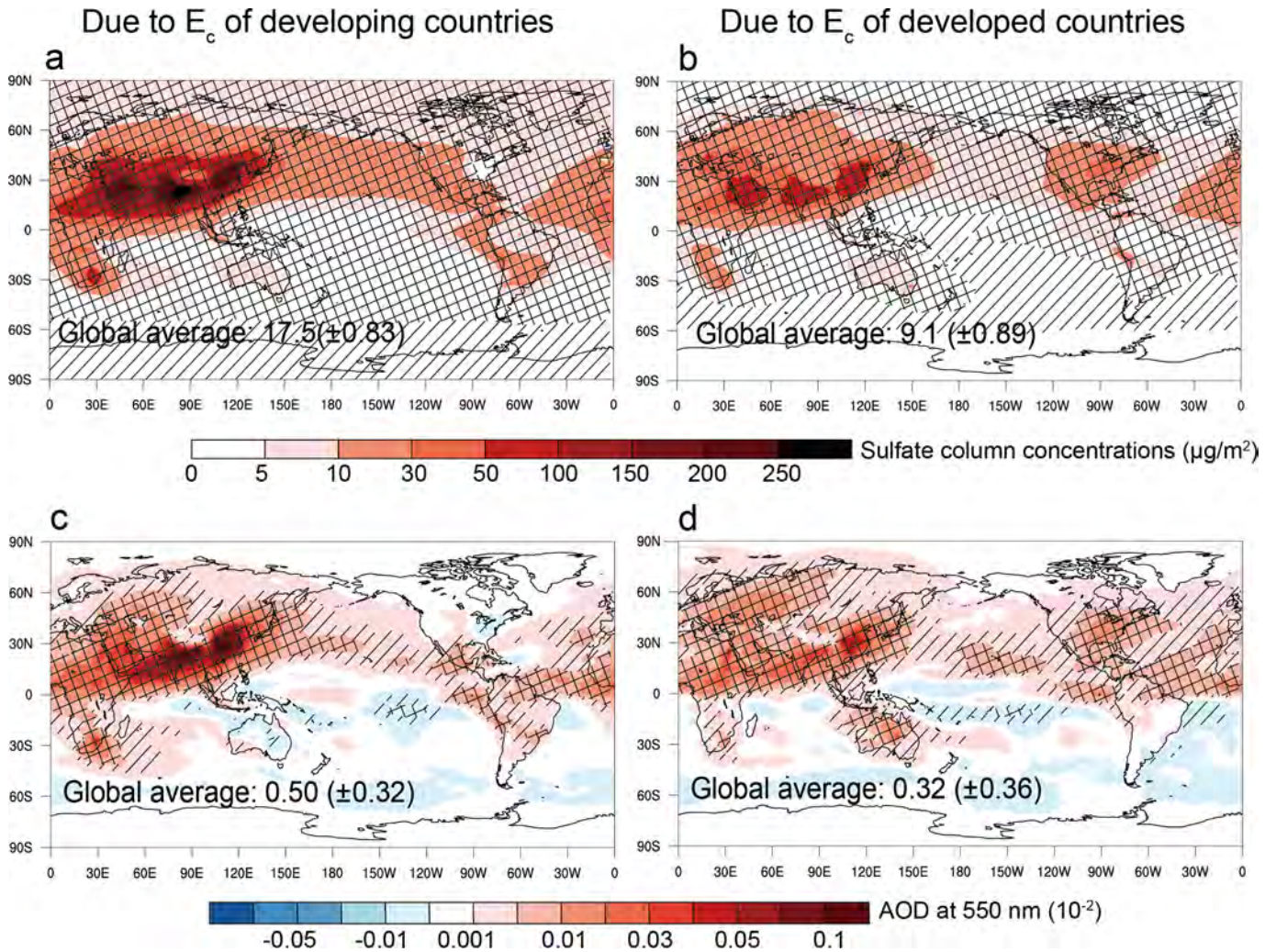

Extended Data Fig. 2 | Sulfate and AOD responses to consumption-based emissions. Changes in annual mean S_c (a, b) and AOD (c, d) due to E_c of developing and developed countries. AOD includes the effect of all aerosol compositions. The grid cells with cross lines pass the paired z-test at 95% CI and those with diagonal lines pass the test at 68% CI. The global average with 2 standard deviations is shown in each panel.

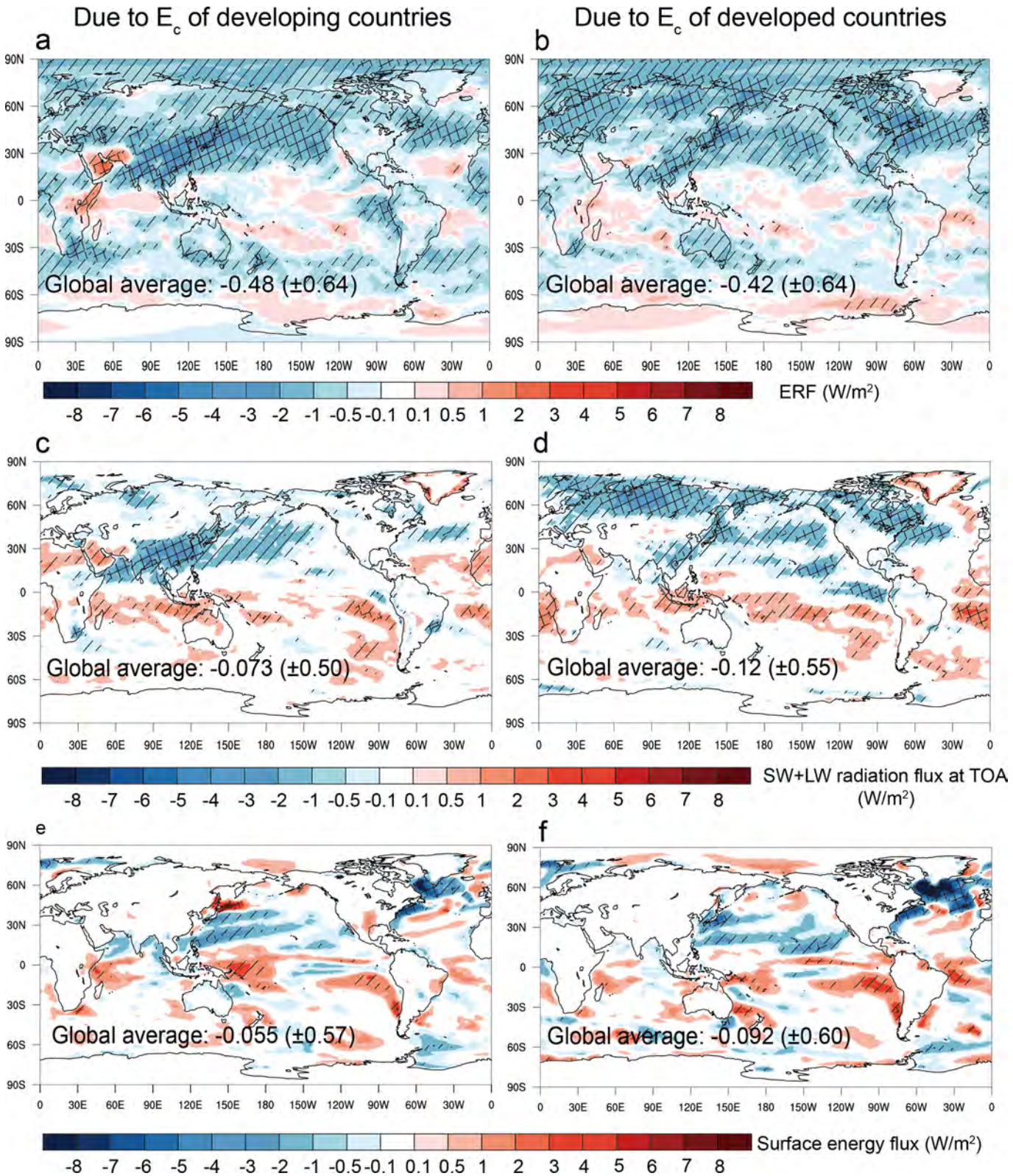

Extended Data Fig. 3 | Energy imbalance induced by consumption-based emissions. (a,b) Annual mean ERF due to E_c of developing and developed countries calculated based on CAM6 simulations. (c-f) Annual mean TOA net radiative flux (shortwave + longwave; c,d) and surface energy flux (shortwave + longwave + latent heat + sensible heat; e,f) due to E_c of developing and developed countries calculated based on fully coupled CESM2 simulations. The grid cells with cross lines pass the paired *z*-test at 95% CI and those with diagonal lines pass the test at 68% CI. The global average with 2 standard deviations is shown in each panel.

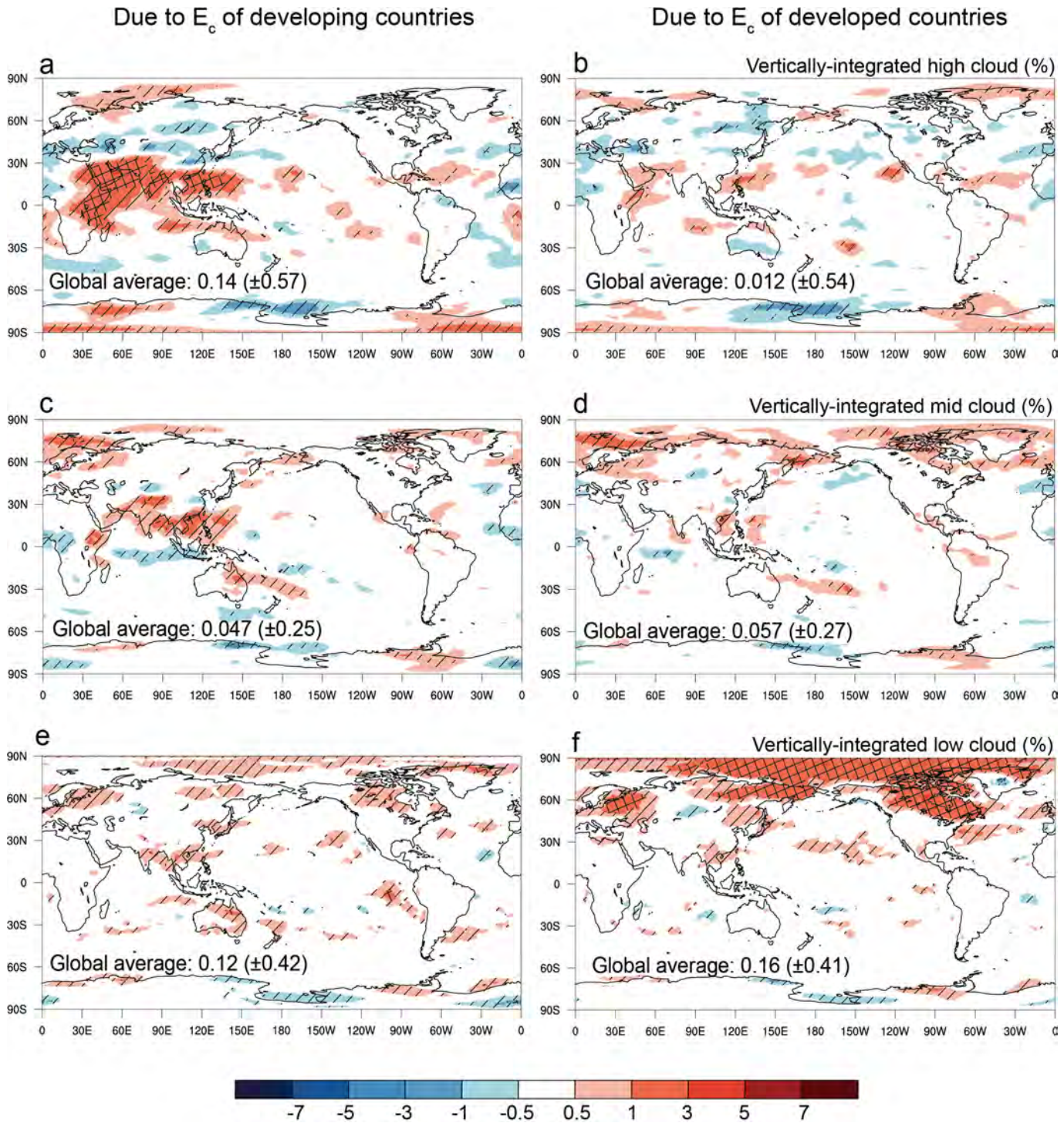

Extended Data Fig. 4 | Fast adjustment of cloud coverage induced by consumption-based emissions in CAM6 simulations. Changes in annual mean high clouds (cloud top pressure < 400 hPa), mid clouds (700–400 hPa) and low clouds (> 700 hPa) due to E_c of developing and developed countries. The grid cells with cross lines pass the paired z-test at 95% CI and those with diagonal lines pass the test at 68% CI. The global average with 2 standard deviations is shown in each panel.

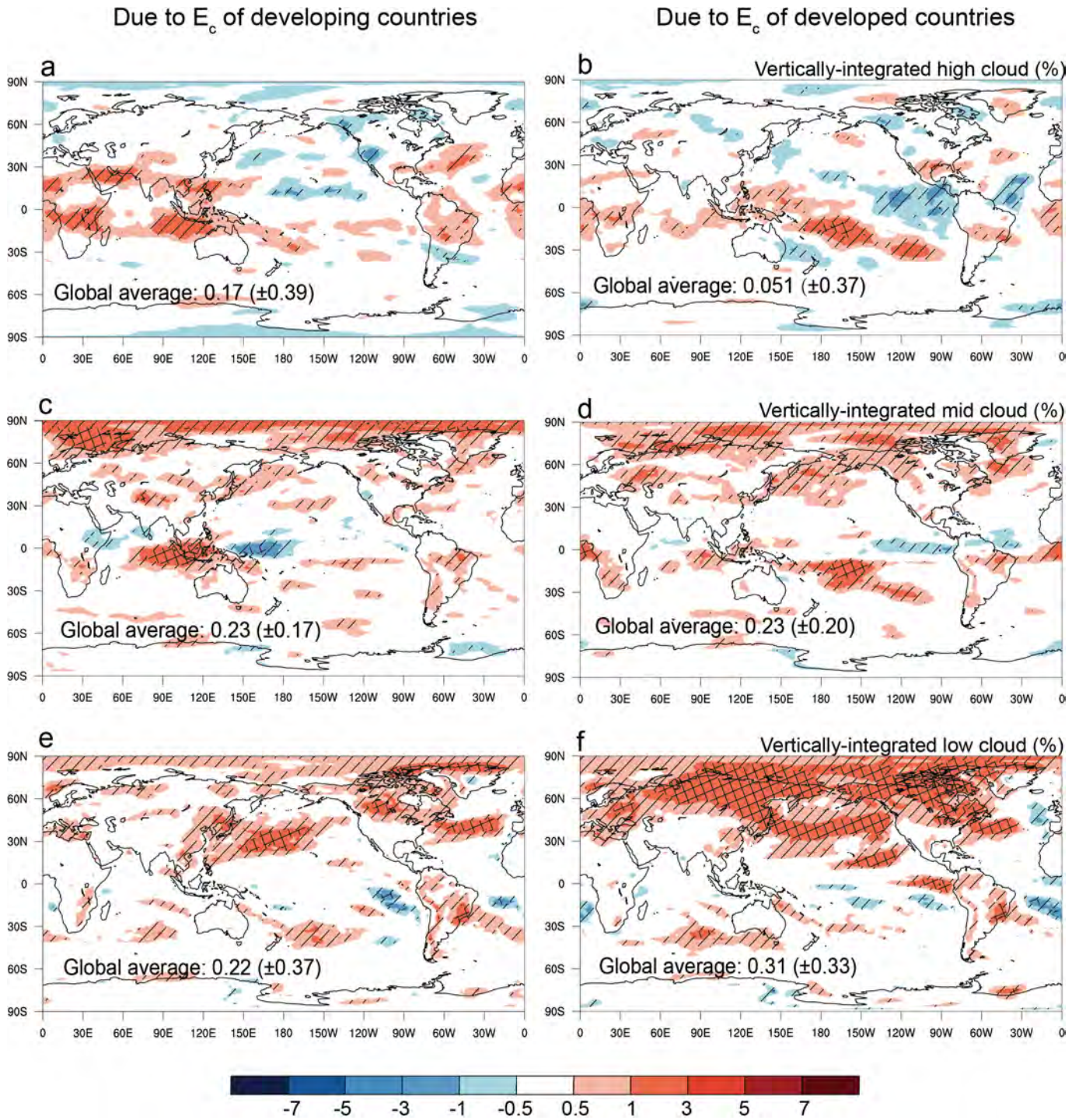

Extended Data Fig. 5 | Response of cloud coverage to consumption-based emissions in fully coupled CESM2 simulations. Changes in annual mean high clouds (cloud top pressure < 400 hPa), mid clouds (700–400 hPa) and low clouds (> 700 hPa) due to E_c of developing and developed countries. The grid cells with cross lines pass the paired z-test at 95% CI and those with diagonal lines pass the test at 68% CI. The global average with 2 standard deviations is shown in each panel.

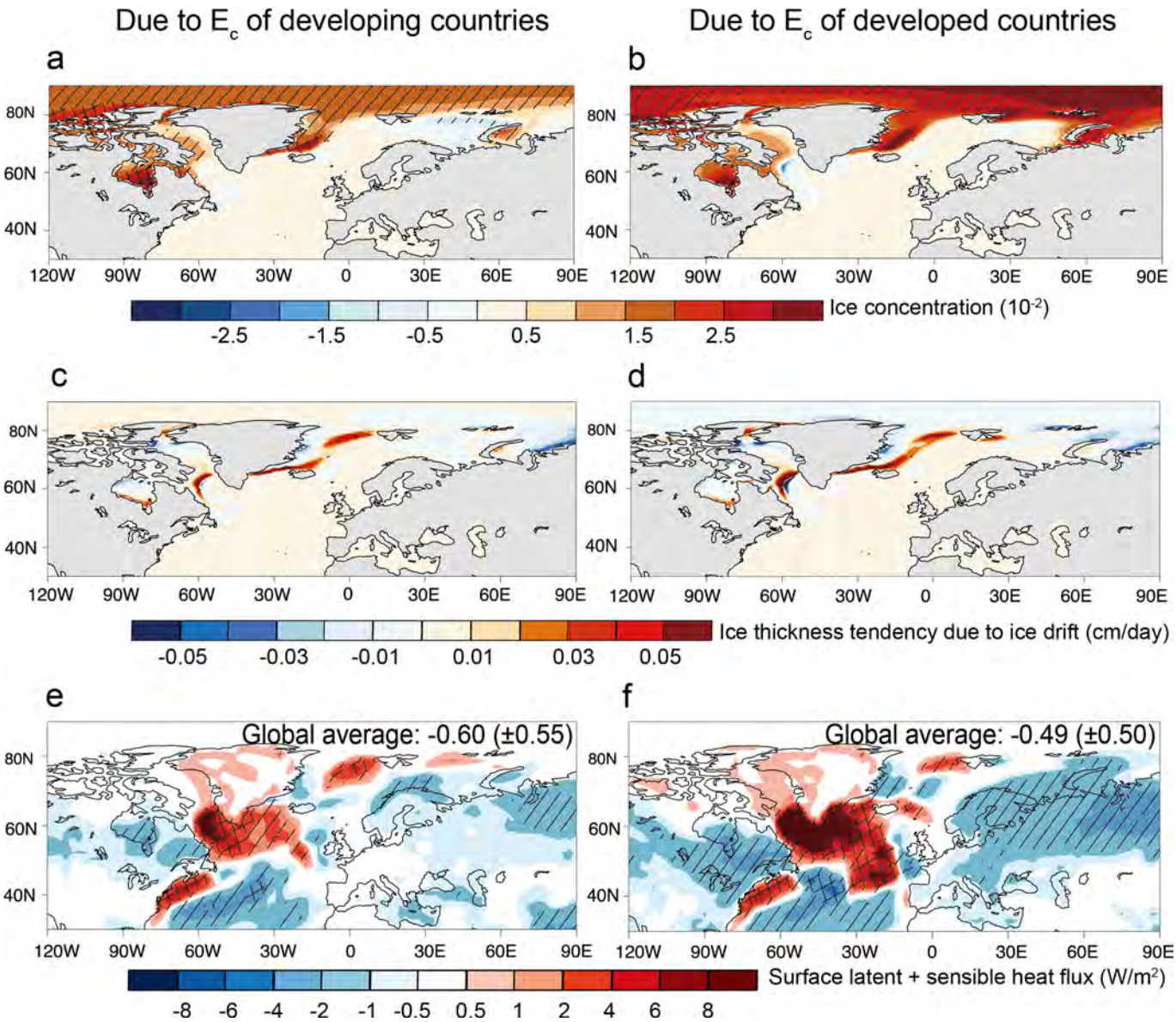

Extended Data Fig. 6 | Responses of sea ice and heat flux to consumption-based emissions. Changes in annual mean sea ice concentration (that is, fraction of the area covered by sea ice in each grid cell) (a, b), wind-driven sea ice drift (c, d) and surface heat flux (latent + sensible) (e, f) due to E_c of developing and developed countries. The grid cells with cross lines pass the paired z-test at 95% CI and those with diagonal lines pass the test at 68% CI. In e and f, the global average of surface heat flux with 2 standard deviations is shown for comparison.

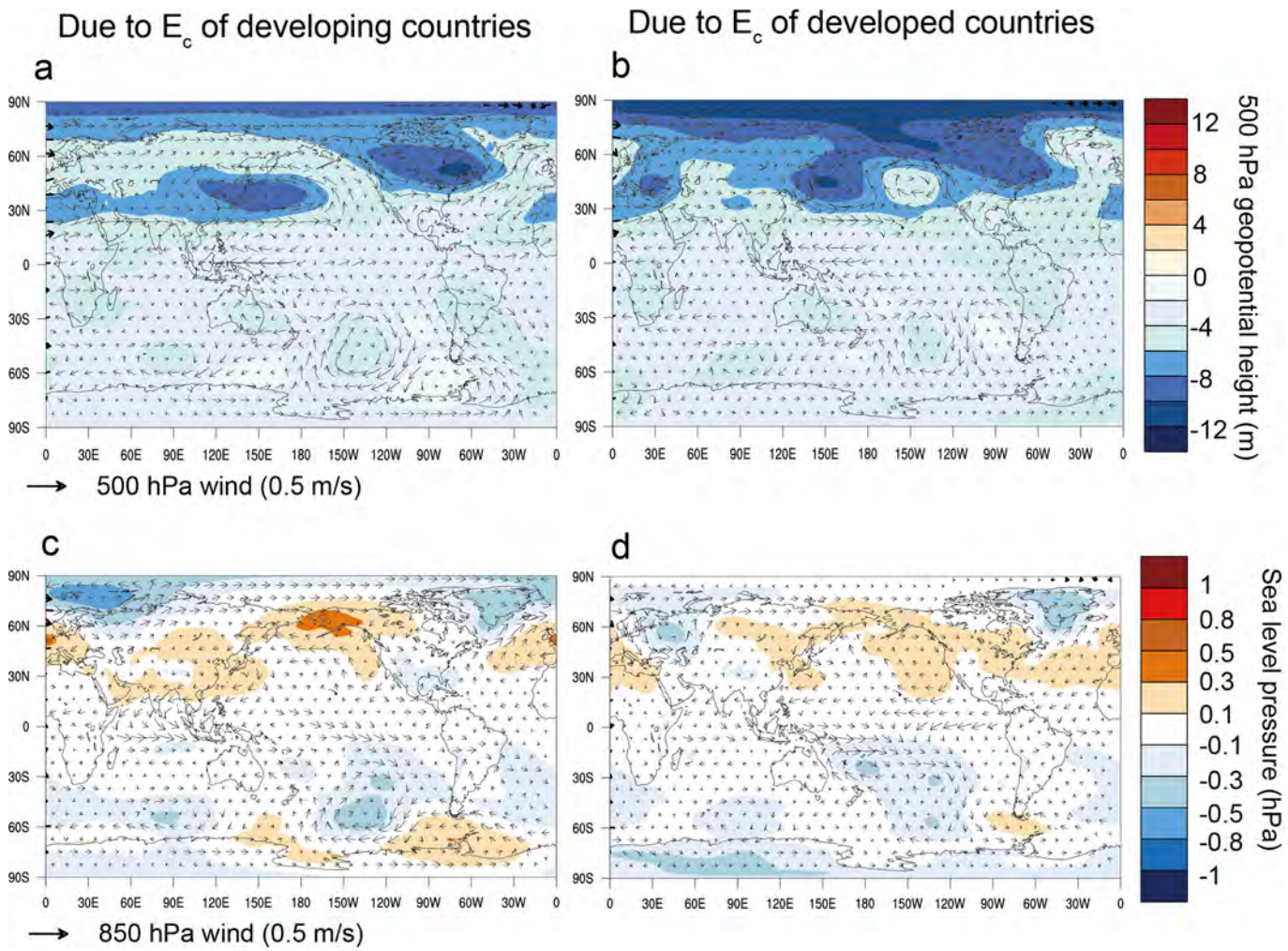

Extended Data Fig. 7 | Circulation response to consumption-based emissions. Changes in annual mean geopotential height (color, m) and winds (vector) at 500 hPa (a,b) and changes in annual mean sea-level pressure (color, hPa) and winds (vector) at 850 hPa (c,d) due to E_c of developing and developed countries.

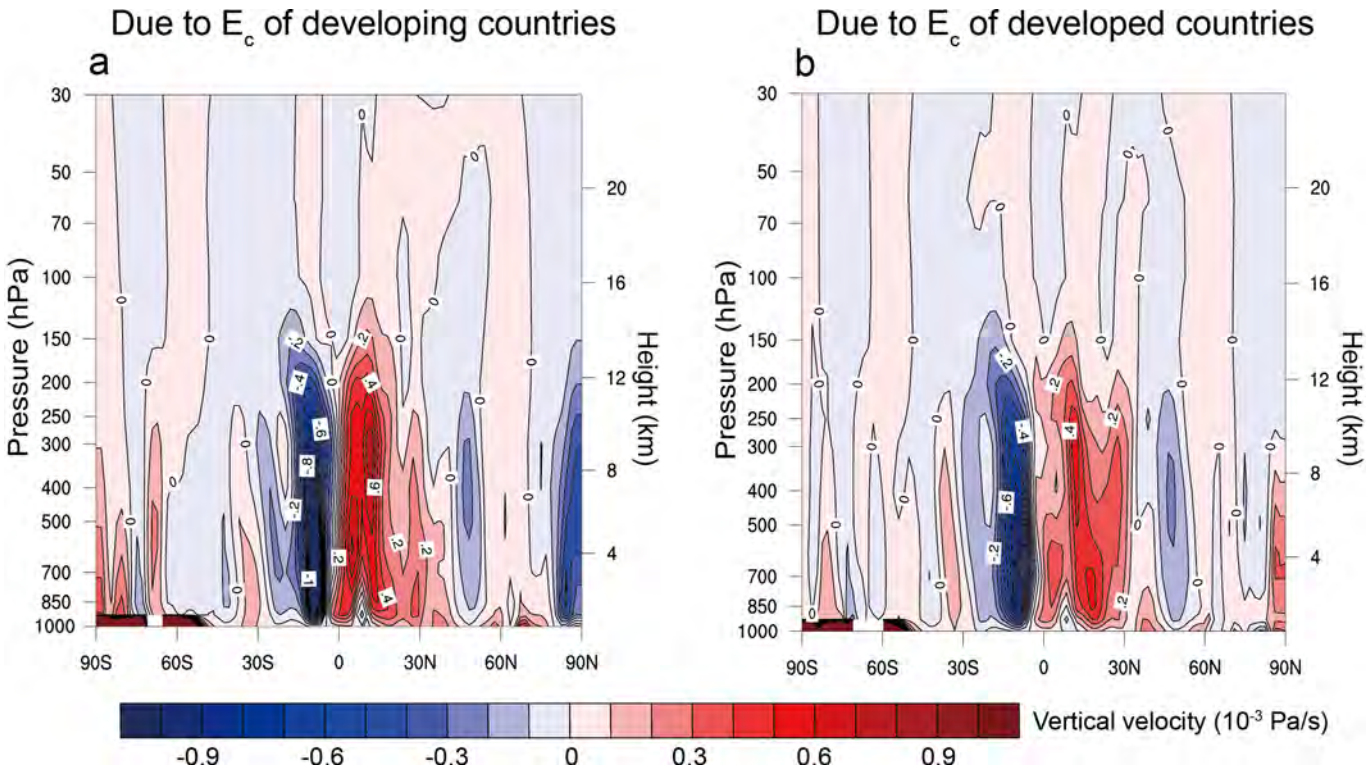

Extended Data Fig. 8 | Meridional circulation response to consumption-based emissions. Zonal average annual mean changes in vertical velocity ($\omega = dp/dt$) due to E_c of developing and developed countries. Negative values represent rising air.

Extended Data Table 1 | Radiative kernel decomposition of Ec induced ERF. Factors contributing to the annual mean ERF include aerosol direct radiative forcing and fast adjustments of water vapor, surface albedo, temperature and clouds. Units are in W/m2. The values in brackets represent 2 standard deviations

	Due to E_c of Developing countries	Due to E_c of Developed countries
ERF	-0.48 (±0.64)	-0.42 (±0.64)
Direct radiative forcing	-0.16 (±0.031)	-0.066 (±0.026)
H_2O	0.036 (±0.19)	0.010 (±0.19)
Albedo	-0.022 (±0.16)	-0.040 (±0.17)
Temperature	-0.019 (±0.39)	-0.007 (±0.41)
Cloud	-0.32 (±0.70)	-0.32 (±0.72)

Extended Data Table 2 | Radiative kernel decomposition of Ec induced TOA net radiation flux in the fully coupled simulations. Factors contributing to the annual mean net radiation flux include ERF and the responses of water vapor, surface albedo, temperature and clouds. The contributions of all non-ERF factors are in addition to the radiative effects of their fast adjustments presented in Extended Data Table 1. Units are in W/m2. The values in brackets represent 2 standard deviations

	Due to E_c of Developing countries	Due to E_c of Developed countries
TOA net radiation flux	-0.073 (±0.50)	-0.12 (±0.55)
ERF	-0.48 (±0.64)	-0.42 (±0.64)
H_2O	-0.26 (±0.94)	-0.32 (±1.20)
Albedo	-0.046 (±0.13)	-0.060 (±0.13)
Temperature	0.62 (±1.54)	0.61 (±1.91)
Cloud	0.090 (±1.05)	0.062 (±1.23)

Science Bulletin 67 (2022) 470–473

Contents lists available at ScienceDirect

Science Bulletin

journal homepage: www.elsevier.com/locate/scib

Short Communication

The significant roles of anthropogenic aerosols on surface temperature under carbon neutrality

Xiaofan Ma [a,c,d], Gang Huang [a,b,c,d,*], Junji Cao [c]

[a] State Key Laboratory of Numerical Modeling for Atmospheric Sciences and Geophysical Fluid Dynamics, Institute of Atmospheric Physics, Chinese Academy of Sciences, Beijing 100029, China
[b] Laboratory for Regional Oceanography and Numerical Modeling, Pilot National Laboratory for Marine Science and Technology (Qingdao), Qingdao 266237, China
[c] Institute of Atmospheric Physics, Chinese Academy of Sciences, Beijing 100029, China
[d] University of Chinese Academy of Sciences, Beijing 100049, China

ARTICLE INFO

Article history:
Received 10 June 2021
Received in revised form 15 September 2021
Accepted 17 September 2021
Available online 2 November 2021

© 2021 Science China Press. Published by Elsevier B.V. and Science China Press. All rights reserved.

A target of limiting global warming below 1.5 or 2 °C by 2100 relative to the preindustrial level was established in the *2015 Paris Agreement* to combat the climate crisis. The fast increase in human-induced CO_2 in the atmosphere has accelerated the warming during the past decades. To achieve the low-warming target, China has announced that it will endeavor to reach the carbon emission peak by 2030 and carbon neutrality by 2060 [1]. Many other regions or countries have also issued legislation or policies to accomplish carbon neutrality by the middle of this century such as the European Union, India, Canada, South Africa, etc. [2]. The achievement of the ambitious carbon neutrality in the future will require anthropogenic emissions to decrease quickly from now, which could lead to reductions in both CO_2 and aerosols [3]. However, the same trends in CO_2 and aerosols have the opposite radiative forcings. The cooling effect of declined CO_2 will be superimposed by the warming effect of declined aerosols. Meanwhile, aerosol changes could affect oceanic processes from the surface to the depth [4,5] and alter the regional pattern of surface temperature. Therefore, the roles of anthropogenic aerosols on surface temperature changes under carbon neutrality need further investigations.

In this study, we adopt an extensively applied climate model, the Community Earth System Model version 1 with the Community Atmospheric Model version 5 [6] (CESM1-CAM5; Supplementary materials), which could well simulate the observed warming over the 20th century [6]. This model contains aerosol direct and indirect effects with the inclusion of both the cloud albedo and cloud lifetime effects. The aerosol radiative forcing in CESM1-CAM5 is −1.5 W m^{-2} and within the uncertainty range at a 90% confidence level (−2.0 to −0.4 W m^{-2}) of models in the Coupled Model Intercomparison Project Phase 5 (CMIP5) [7]. We use simulations under the Representative Concentration Pathways 2.6 (RCP2.6), which is the only scenario near the low-warming target in CMIP5 future projections [3]. According to the released all-forcing simulations under RCP2.6 (rcp26), we conduct fixed-aerosol simulations (rcpFA26) over the 21st century in which anthropogenic aerosol emissions are fixed at the 2005 levels (Supplementary materials). The climate effects of the projected decrease in anthropogenic aerosols could be derived from the difference between these two simulations (rcp26-rcpFA26).

Under RCP2.6, the anthropogenic aerosols decrease since the beginning of the 21st century as shown by the change of aerosol optical depth (Fig. 1a), after a large reduction in anthropogenic emissions especially SO_2 [3]. However, CO_2 concentration increases before it starts to decrease after 2050 (Fig. 1a) due to the difficulties in carbon reduction technologies that could not be tackled. In rcp26, the increased CO_2 and decreased aerosols shall generate consistent warming effects and cause a large increase in global mean surface temperature before 2050 (0.031 °C a^{-1}; Fig. 1b, black). After 2050, despite the decline in CO_2, the decrease in anthropogenic aerosols will continue to produce a warming effect, which will enable the surface temperature to rise with a speed slower than that before 2050 (0.006 °C a^{-1}; Fig. 1b, black). However, in rcpFA26, the surface temperature is primarily driven by CO_2 and shows a slight cooling trend (−0.002 °C a^{-1}) after peaking at 2060 (Fig. 1b, green) without the extra warming from anthropogenic aerosols. The 10-year delay of temperature changes in response to CO_2 forcing is consistent with the previous studies [8]. The persistent net warming effect of anthropogenic aerosols

* Corresponding author.
E-mail address: hg@mail.iap.ac.cn (G. Huang).

https://doi.org/10.1016/j.scib.2021.10.022
2095-9273/© 2021 Science China Press. Published by Elsevier B.V. and Science China Press. All rights reserved.

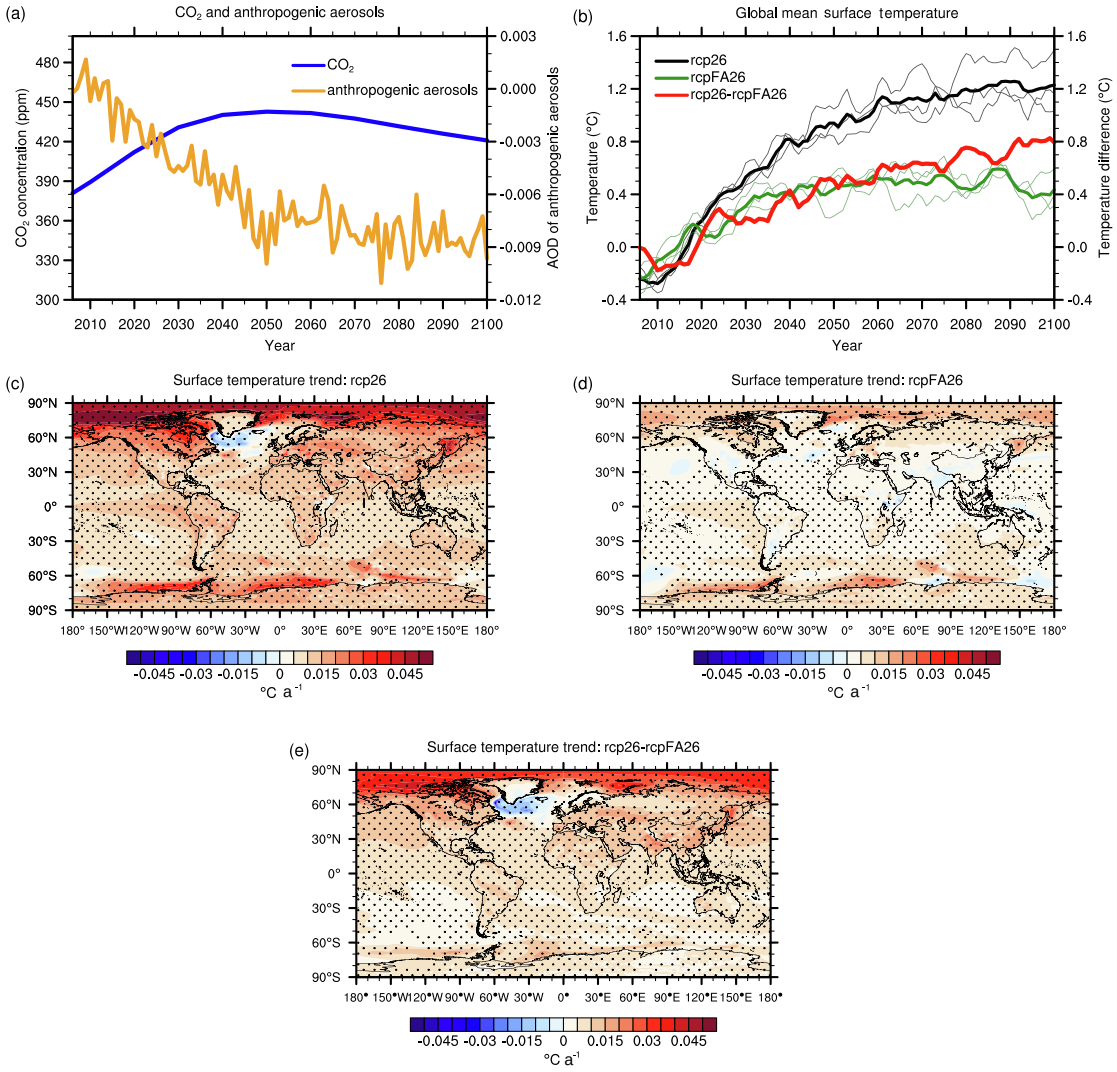

审图号：GS（2021）6643号

Fig. 1. Changes in atmospheric CO_2 and anthropogenic aerosols as well as the response of surface temperature under RCP2.6 in CESM1-CAM5. (a) CO_2 concentration (blue) and aerosol optical depth (AOD) at 500 nm of anthropogenic aerosols (orange) in the 21st century. (b) Time series of global mean surface temperature anomalies (relative to 2006–2025 mean) in rcp26 (black), rcpFA26 (green), and their difference rcp26-rcpFA26 (red). Thin lines denote the results in three ensemble members. Long-term trends of surface temperature over 2006–2100 in (c) rcp26, (d) rcpFA26, and (e) their difference rcp26-rcpFA26. Trends in (c–e) are the results of the ensemble mean. Stippling indicates where SST trends are statistically significant at the 95% confidence level based on the Student's *t*-test.

leads to an increase in the surface temperature throughout the entire century (0.010 °C a^{-1}) as demonstrated by the simulation difference rcp26-rcpFA26 (Fig. 1b, red). The long-term evolution in the time series of global mean surface temperature is consistent with the temperature trend over 2006–2100 in spatial maps (Fig. 1c–e). The aerosol forcing makes more contributions to the total changes in the surface temperature relative to other forcings (mainly CO_2). This is evident in the Northern Hemisphere, especially Asia, Europe, and North America, which are the major sources of aerosol emissions (Fig. S1 online). The surface temperature does not vary consistently over the globe. The greatest warming occurs over the Arctic (Fig. 1c). In the case of declining aerosols, the Arctic temperature amplification is primarily due to the strong positive feedback between sea-ice-albedo and temperature [9] as well as an increase in horizontal energy transported to the Arctic region [10]. In contrast, a significant surface cooling dominated by the anthropogenic aerosol effects appears in the subpolar North Atlantic (Fig. 1c, e). This distinctive cooling occurring in a warming environment has been referred to as the North Atlantic warming hole and is related to variations in deep ocean circulations in the Atlantic basin [11], which is mainly the Atlantic Meridional Overturning Circulation (AMOC).

Under the net effect of decreased anthropogenic aerosols, the long-term (2006–2100) surface cooling trend over the subpolar North Atlantic (Fig. 1e) mostly comes from the second half-century, as indicated by the times series of the regionally averaged (50°–70°N, 60°–10°W) sea surface temperature (SST) in rcp26-rcpFA26 (Fig. 2c, red). The decreasing anthropogenic aerosols trigger a weakening AMOC at the beginning of the century (Figs. 2a (red) and S2 online). The initial weakening of the AMOC is possibly related to changes in atmospheric circulation [4]. The decline of aerosols reduces sea level pressure gradient, weakens surface winds over the North Atlantic, reduces surface latent and sensible heat fluxes, and ultimately leads to a decrease in surface density flux [4]. In turn, the deep convection weakens and the AMOC slows down. The weakened AMOC induces a reduction in northward ocean heat transport in the Atlantic (Fig. 2b, red). Less heat is transported from the tropics to high latitudes. As time goes by, a large SST cooling trend over the subpolar North Atlantic will emerge after 2050 (Fig. 2c, red). The SST fluctuations in the first half-cen-

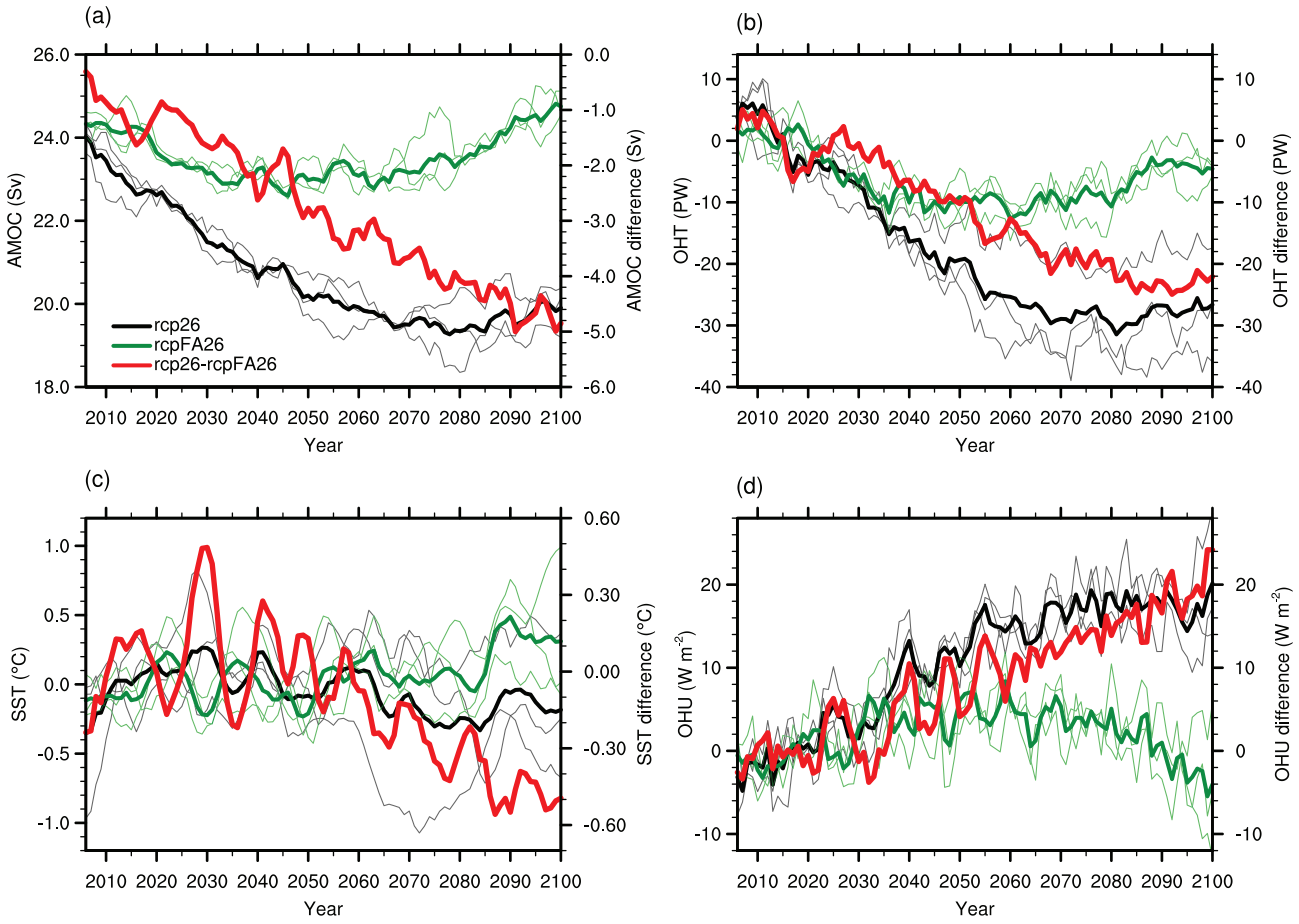

Fig. 2. Evolutions of oceanic processes in the Atlantic under RCP2.6 in CESM1-CAM5. Time series of (a) the AMOC index, (b) total ocean heat transport (OHT) anomalies in the Atlantic, (c) SST anomalies, and (d) ocean heat uptake (OHU) anomalies in the subpolar North Atlantic (50°–70°N, 60°–10°W) in rcp26 (black), rcpFA26 (green), and their difference rcp26-rcpFA26 (red; right *Y*-axis). Thin lines denote the results in three ensemble members. Thick lines denote the results of the ensemble mean. Anomalies are relative to the 2006–2025 mean.

tury might be associated with the competing roles between the direct warming effect of decreased aerosols and the AMOC-induced heat loss. In the second half of the century, the direct warming weakens as the aerosol reduction slows down (Fig. 1a) and the continuous weakening of the AMOC dominates the SST decline in the subpolar North Atlantic. The continuous AMOC weakening after 2050 under declining aerosols mainly results from a continuous increase of surface freshwater flux in the subpolar North Atlantic [5]. The surface freshwater flux increase is possibly controlled by a reduction in surface evaporation due to the cooling of local SST [5]. The SST decline further causes an increase in ocean heat uptake on the surface through the turbulent heat flux feedback [12] in the subpolar North Atlantic (Fig. 2d, red). The variations of ocean heat uptake in the first half of the century might be a comprehensive result of oscillating SST and direct warming effects of aerosols.

Comparing the evolutions in oceanic processes during the 21st century in rcp26 and rcpFA26 simulations (Fig. 2, black and green), we find that the extra warming effect of reduced anthropogenic aerosols in rcp26 causes a prolonged weakening in the AMOC strength (Fig. 2a, black). This subsequently leads to prolonged decreases in the Atlantic's poleward heat transport and subpolar North Atlantic SST, which in turn causes a prolonged increase in the local ocean heat uptake (Fig. 2b–d, black). However, these variables in rcpFA26 tend to recover in the second half-century, mainly following the CO_2 pathway (Fig. 2a–d, green). In addition to the reduced aerosol forcing, the North Atlantic warming hole could appear under increased CO_2 [13] via inducing a largely weakened AMOC. The warming hole in rcpFA26 is not obvious (Fig. 1d) due to the recovery of the AMOC (Fig. 2a) dominated by CO_2 changes.

In summary, the concentrations of CO_2 and aerosols in the atmosphere will decrease at the same time because anthropogenic emissions are significantly cut down to fulfill the carbon neutrality and low-warming target. The extra warming effect produced by the reduction in anthropogenic aerosols synchronizes with the cooling effect induced by CO_2 decrease. Thus, the reduced aerosols will allow global surface temperature to keep rising for an unexpected long period rather than gradually decline as the CO_2 decreases. In the 21st century, compared with the consistent long-term warming trends elsewhere, there is a long-term cooling trend of surface temperature in the subpolar North Atlantic, which leads to a large increase in local ocean heat uptake. This is primarily related to a weakening in the AMOC and a decrease in northward ocean heat transports throughout the century under the forcing of declining aerosols, which causes a substantial cooling in SST over the subpolar North Atlantic in the last decades of the century.

The response in oceans to changes in aerosol forcing could last long (e.g., decades or centuries) due to the slow adjustments of oceanic processes. In addition to modulating long-term climate change, changes in oceans could also affect the uptake and storage of atmospheric CO_2, which would influence carbon neutrality [1] over a long period. The North Atlantic is a major atmospheric CO_2 sink because the deep convection branch of the AMOC [14] leads to the deep storage of carbon, thus a weakened AMOC would

result in increased carbon concentration in the atmosphere. Beyond the CESM1 simulations under RCP2.6 scenario, the latest CESM2 model and the updated low-emission scenario SSP1-2.6 in the framework of CMIP6 could be applied in the next step of the study. One caveat in this study is the potential model dependence of the aerosol-induced climate responses. The current climate models differ in aerosol schemes [7], deep convection sites [15], parameterization, etc. The findings from the CESM model need to be compared with those in other climate models.

Our study indicates that future decreases in anthropogenic aerosols could amplify the warming maximum and slow down the cooling rate due to CO_2 reduction, thereby extending the time required to reach the low-warming target. Despite the 1.5 °C/2 °C temperature goal set in the *Paris Agreement*, the zero-emission pathways in practice are subject to various possibilities. The specific future emissions are different among countries due to their different policies [2]. The carbon emission peak and emission reduction rate could be distinct from those under RCP2.6. Hence, future climate change under carbon neutrality could have some biases against that projected under RCP2.6. Nevertheless, the significant roles played by anthropogenic aerosols on the spatiotemporal evolution of surface temperature need to be considered in designing the specific pathway of carbon neutrality.

Conflict of interest

The authors declare that they have no conflict of interest.

Acknowledgments

This work was supported by the National Natural Science Foundation of China (41831175, 91937302, and 41721004), the Key Deployment Project of Centre for Ocean Mega-Research of Science, Chinese Academy of Sciences (COMS2019Q03), and the Second Tibetan Plateau Scientific Expedition and Research Program (2019QZKK0102). We thank the National Center for Atmospheric Research for publishing the code of the CESM1-CAM5 model. We thank the two anonymous reviewers for their suggestions that greatly improve this manuscript. Maps in this article were reviewed by Ministry of Natural Resources of the People's Republic of China (GS(2021)6643).

Author contributions

Gang Huang and Xiaofan Ma conceived the research. Xiaofan Ma performed model simulations, prepared figures, and led the writing of the manuscript. Junji Cao contributed to the discussion and explanation of the results.

Appendix A. Supplementary materials

Supplementary materials to this article can be found online at https://doi.org/10.1016/j.scib.2021.10.022.

References

[1] Cai Z, Cheng L, Li T, et al. Key scientific and technical issues in Earth system science towards achieving carbon neutrality in China. Bull Chin Acad Sci 2021;36:602–13.
[2] United Nations Environment Programme. Emissions gap report 2020. Nairobi; 2020.
[3] Stocker TF, Qin D, Plattner G-K, et al. Climate change 2013: the physical science basis. Contribution of Working Group I to the Fifth Assessment Report of the Intergovernmental Panel on Climate. Change. Cambridge: Cambridge University Press; 2013.
[4] Hassan T, Allen RJ, Liu W, et al. Anthropogenic aerosol forcing of the Atlantic meridional overturning circulation and the associated mechanisms in CMIP6 models. Atmos Chem Phys 2021;21:5821–46.
[5] Ma X, Liu W, Allen RJ, et al. Dependence of regional ocean heat uptake on anthropogenic warming scenarios. Sci Adv 2020;6:eabc0303.
[6] Hurrell JW, Holland MM, Gent PR, et al. The community earth system model: a framework for collaborative research. Bull Am Meteorol Soc 2013;94:1339–60.
[7] Bellouin N, Quaas J, Gryspeerdt E, et al. Bounding global aerosol radiative forcing of climate change. Rev Geophys 2020;58:e2019RG000660.
[8] Zickfeld K, MacDougall AH, Matthews HD. On the proportionality between global temperature change and cumulative CO_2 emissions during periods of net negative CO_2 emissions. Environ Res Lett 2016;11:055006.
[9] Screen JA, Simmonds I. The central role of diminishing sea ice in recent Arctic temperature amplification. Nature 2010;464:1334–7.
[10] Navarro JCA, Ekman AM, Pausata FS, et al. Future response of temperature and precipitation to reduced aerosol emissions as compared with increased greenhouse gas concentrations. J Clim 2017;30:939–54.
[11] Drijfhout S, Van Oldenborgh GJ, Cimatoribus A. Is a decline of AMOC causing the warming hole above the North Atlantic in observed and modeled warming patterns? J Clim 2012;25:8373–9.
[12] Hausmann U, Czaja A, Marshall J. Mechanisms controlling the SST air-sea heat flux feedback and its dependence on spatial scale. Clim Dyn 2017;48:1297–307.
[13] Winton M, Takahashi K, Held IM. Importance of ocean heat uptake efficacy to transient climate change. J Clim 2010;23:2333–44.
[14] Srokosz M, Baringer M, Bryden H, et al. Past, present, and future changes in the Atlantic meridional overturning circulation. Bull Am Meteorol Soc 2012;93:1663–76.
[15] Heuzé C. North Atlantic deep water formation and AMOC in CMIP5 models. Ocean Sci 2017;13:609–22.

Xiaofan Ma got her Ph.D. degree at Institute of Atmospheric Physics, Chinese Academy of Sciences. Her research interest includes climate change and climate variability, climate modeling, physical oceanography, with particular emphasis on the Atlantic Meridional Overturning Circulation.

Gang Huang is a professor of Institute of Atmospheric Physics, Chinese Academy of Sciences. His research interest includes tropical atmosphere-ocean interaction, monsoon dynamics, climate change and climate variability, global warming dynamics, and climate modeling.

nature geoscience

ARTICLES

https://doi.org/10.1038/s41561-021-00730-3

Check for updates

Intensification of El Niño-induced atmospheric anomalies under greenhouse warming

Kaiming Hu[1,2,3] ✉, Gang Huang[1,2,4] ✉, Ping Huang[1,3], Yu Kosaka[5] and Shang-Ping Xie[6]

The El Niño/Southern Oscillation (ENSO) has a profound influence on global climate and ecosystems. Determining how the ENSO responds to greenhouse warming is a crucial issue in climate science. Despite recent progress in understanding, the responses of important ENSO characteristics, such as air temperature and atmospheric circulation, are still unknown. Here, we use a suite of global climate model projections to show that greenhouse warming drives a robust intensification of ENSO-driven variability in boreal winter tropical upper tropospheric temperature and geopotential height, tropical humidity, subtropical jets and tropical Pacific rainfall. These robust changes are primarily due to the Clausius–Clapeyron relationship, whereby saturation vapour pressure increases nearly exponentially with increasing temperature. Therefore, the vapour response to temperature variability is larger under a warmer climate. As a result, under global warming, even if the ENSO's sea surface temperature remains unchanged, the response of tropical lower tropospheric humidity to the ENSO amplifies, which in turn results in major reorganization of atmospheric temperature, circulation and rainfall. These findings provide a novel theoretical constraint for ENSO changes and reduce uncertainty in the ENSO response to greenhouse warming.

The El Niño/Southern Oscillation (ENSO) arises from complex interactions between the atmosphere and ocean[1–5]. On a timescale of 2–7 years, the eastern equatorial Pacific varies between anomalously cold (La Niña) and warm (El Niño) conditions. These swings in sea surface temperature (SST) shift atmospheric convection in the tropical Pacific and cause tropical and extratropical climate anomalies by changing the Walker circulation and exciting atmospheric teleconnection such as the Pacific–North American pattern[6–9]. Furthermore, the ENSO-induced tropical tropospheric temperature anomalies spread from the Pacific to all longitudes[10–12], broadening climate variability around the globe[12–15].

Because of the climatic effects around the globe, how the ENSO and its impacts might change in response to greenhouse warming has been investigated extensively during the past 20 years[16–24]. Coupled general circulation models (CGCMs) disagree on ENSO changes in SST due to the complexity of air–sea feedbacks in the tropical Pacific Ocean[16,25,26]. Therefore, understanding and determining how the ENSO responds to greenhouse warming remains a great challenge. A robust change in ENSO-driven rainfall variability was identified in CGCM projections[27]. Most CGCMs project an intensification of El Niño-driven drying over the western Pacific Ocean and wetting over the central and eastern equatorial Pacific[18,27–29]. Associated with changes in rainfall variability, the ENSO-forced Pacific–North American teleconnection pattern shifts eastward[30–32] and ENSO-driven precipitation variability is projected to increase in many regions around the globe[33]. However, it remains unclear how other important ENSO characteristics, such as tropospheric temperature, humidity and atmospheric circulation, might change under greenhouse warming.

Tropical humidity and temperature variability

Based on output from 19 Coupled Model Intercomparison Project Phase 6 (CMIP6) models, we examined changes in the ENSO between 1% yr^{-1} [CO_2] increase experiments and pre-industrial control experiments. We compared climate in two periods: 400–449 model years in the pre-industrial control experiments (P_{ctrl}) and 100–149 model years in the 1% yr^{-1} [CO_2] experiments (P_{warm}). From P_{ctrl} to P_{warm}, the multi-model ensemble (MME) mean of December-to-February (DJF) climatological tropical-mean (10° S–10° N) SST increased by 3.7 K, with the maximum increase located in the equatorial eastern Pacific (Fig. 1a), in agreement with previous studies[34,35]. Figure 1b compares the standard deviations of the DJF Niño3.4 SST index between two periods in each model and the MME. Hereafter, the linear trends in Niño3.4 SST index, specific humidity, air temperature, wind and geopotential height have been removed to isolate interannual variability. A different method[36] to detrend the data produced almost the same results (Extended Data Fig. 1). Among the 19 models, 11 showed an increase while the other eight showed a decrease in the standard deviation of the Niño3.4 SST index from P_{ctrl} to P_{warm}, highlighting a lack of consensus in the projection of SST variability, consistent with previous studies[16]. Nevertheless, the ENSO-driven variability in DJF tropical-mean (10° S–10° N) surface air specific humidity (q'_{sfc}) showed a coherent increase in every model (Fig. 1c). Here, the prime denotes the regression coefficient against the DJF Niño3.4 SST index, representing anomalies in tropospheric specific humidity, air temperature, geopotential height and zonal wind shown afterward. The MME q'_{sfc} increased by 33 ± 19% from P_{ctrl} to P_{warm} (hereafter, the numbers indicate the MME mean ± one standard deviation range), which is equivalent to 8.9 ± 5.1% amplification per 1-K background warming in the tropics. The regression of DJF tropical-mean (10° S–10° N) 200-hPa temperature against the Niño3.4 SST index also increased robustly in every model from P_{ctrl} to P_{warm} (Fig. 1d), by as much as 49.6 ± 32.8% (or 13.4 ± 8.8% per 1-K background tropical warming), highlighting the dramatic strengthening of the upper

[1]State key Laboratory of Numerical Modeling for Atmospheric Sciences and Geophysical Fluid Dynamics, Institute of Atmospheric Physics, Chinese Academy of Sciences, Beijing, China. [2]Laboratory for Regional Oceanography and Numerical Modeling, Qingdao National Laboratory for Marine Science and Technology, Qingdao, China. [3]Center for Monsoon System Research, Institute of Atmospheric Physics, Chinese Academy of Sciences, Beijing, China. [4]University of Chinese Academy of Sciences, Beijing, China. [5]Research Center for Advanced Science and Technology, University of Tokyo, Tokyo, Japan. [6]Scripps Institution of Oceanography, University of California, San Diego, La Jolla, CA, USA. ✉e-mail: hkm@mail.iap.ac.cn; hg@mail.iap.ac.cn

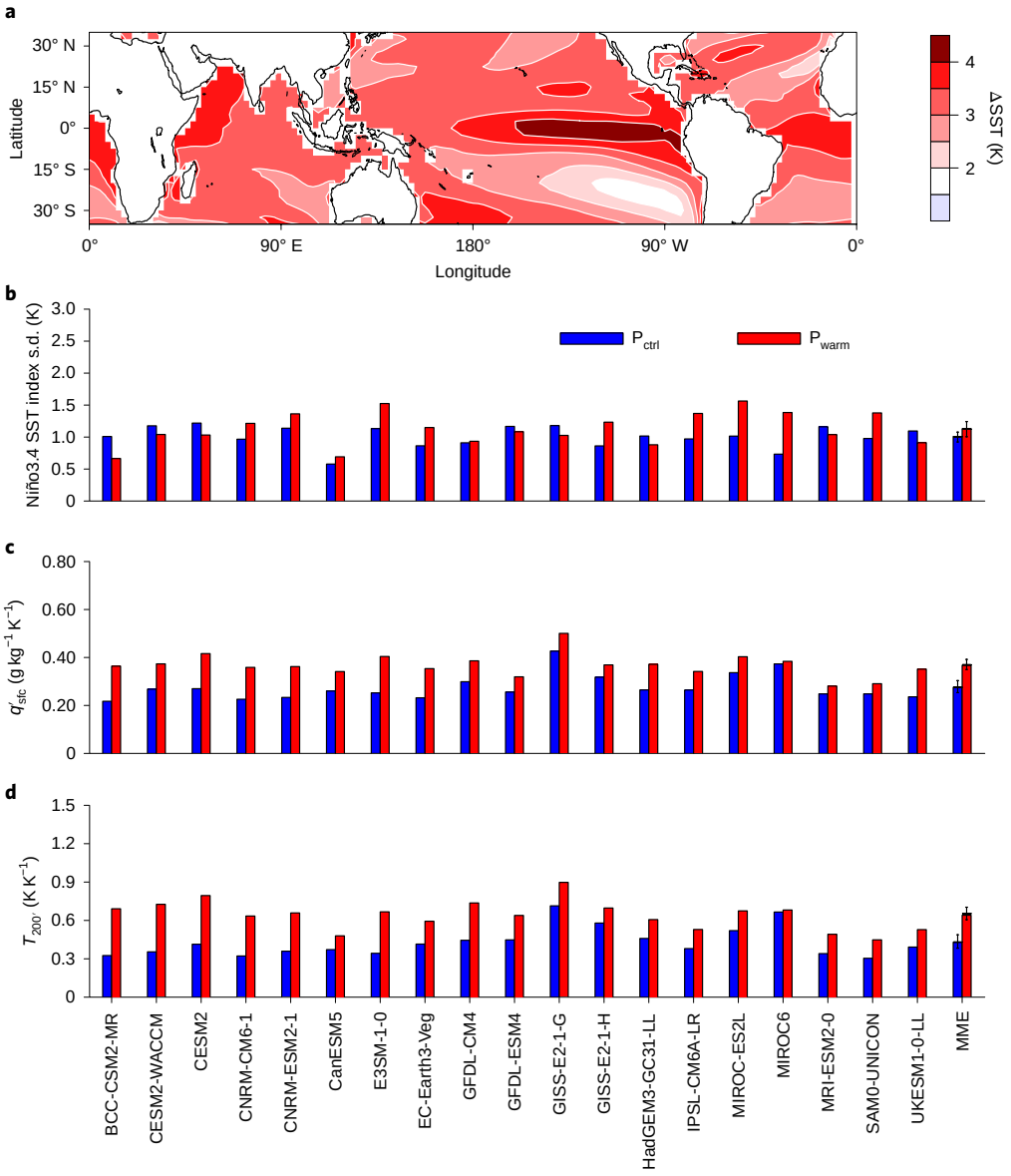

Fig. 1 | Projected changes of ENSO humidity and air temperature. a, Changes in MME mean boreal winter (DJF) climatological SST from P_{ctrl} to P_{warm}. **b**, Comparison of the standard deviation of the DJF Niño3.4 SST index over P_{ctrl} (blue) and P_{warm} (red) in each model and the MME. **c**,**d**, Comparison of DJF tropical-mean (10° S–10° N) ENSO-driven surface specific humidity (q'_{sfc}; **c**) and 200-hPa air temperature (T_{200}'; **d**) between P_{ctrl} (blue) and P_{warm} (red). Error bars in the MME mean correspond to the 95% confidence interval (see Methods).

tropospheric temperature response to the ENSO under greenhouse warming. The amplification of ENSO-driven variability in surface specific humidity and upper tropospheric temperature in the tropics was also robust across models in other scenario simulations for both CMIP5 and CMIP6 (Extended Data Figs. 2 and 3).

Why does ENSO variability amplify in tropical air humidity and tropospheric temperature under global warming? We start from the Clausius–Clapeyron expression for the saturation vapour pressure: $dq_s/dT = q_s/L(R_vT^2)$, where L is the latent heat of vaporization, R_v is the gas constant, q_s is the saturation vapour pressure and T is the air temperature. The relationship between q_s and T is nearly exponential and the value of dq_s/dT is approximately proportional to q_s[37,38]. Under global warming, q_s increases by ~7% for each 1-K increase in temperature[39], as does dq_s/dT. Since the tropical atmosphere tends to maintain a fixed tropospheric relative humidity as it warms[39], the increase of dq_s/dT means a strengthening response of vapour to air temperature variability. Thus, we can deduce that the ENSO drives a larger tropical lower tropospheric moisture anomaly in a warmer world, even if the SST variability remains unchanged.

CGCM projections agree well with the theoretical deduction. Figure 2a shows the percentage changes of DJF tropical-mean (10° S–10° N) surface dq_s/dT against the DJF tropical-mean surface air temperature increase ($\Delta\bar{T}$) in each model and the MME mean. The value of dq_s/dT was calculated as the regression of surface saturation vapour pressure against surface air temperature in each of the four periods (400–449 model years in the pre-industrial control runs and 0–49, 50–99 and 100–149 model years in the 1% yr^{-1} [CO_2] runs), which represent the reference and the three different warming stages. The linear fit has a slope of ~6.2% K^{-1}, which agrees well with the Clausius–Clapeyron scaling. The change in the response of DJF tropical surface specific humidity to air temperature (dq/dT) also generally obeys the Clausius–Clapeyron scaling, at a rate of

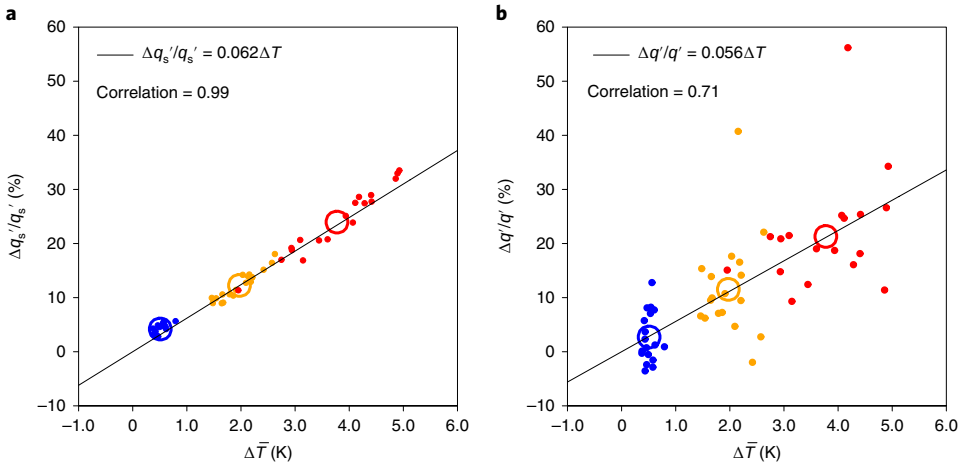

Fig. 2 | Projected changes in the tropical humidity response to air temperature under global warming. a, Percentage changes in DJF tropical-mean dq_s/dT (abbreviated as q_s') against the increase of tropical climatological surface temperature ($\Delta\bar{T}$) in each model (dots) and the MME (open circles) during three periods. The blue, orange and red colours denote the changes in the periods 0–49, 50–99 and 100–149 model years, respectively, in the 1% yr^{-1} [CO_2] runs from P_{ctrl}. The value of dq_s/dT was calculated as the regression of surface saturation vapour pressure onto surface air temperature in each period. **b**, As in **a**, but for surface-specific humidity.

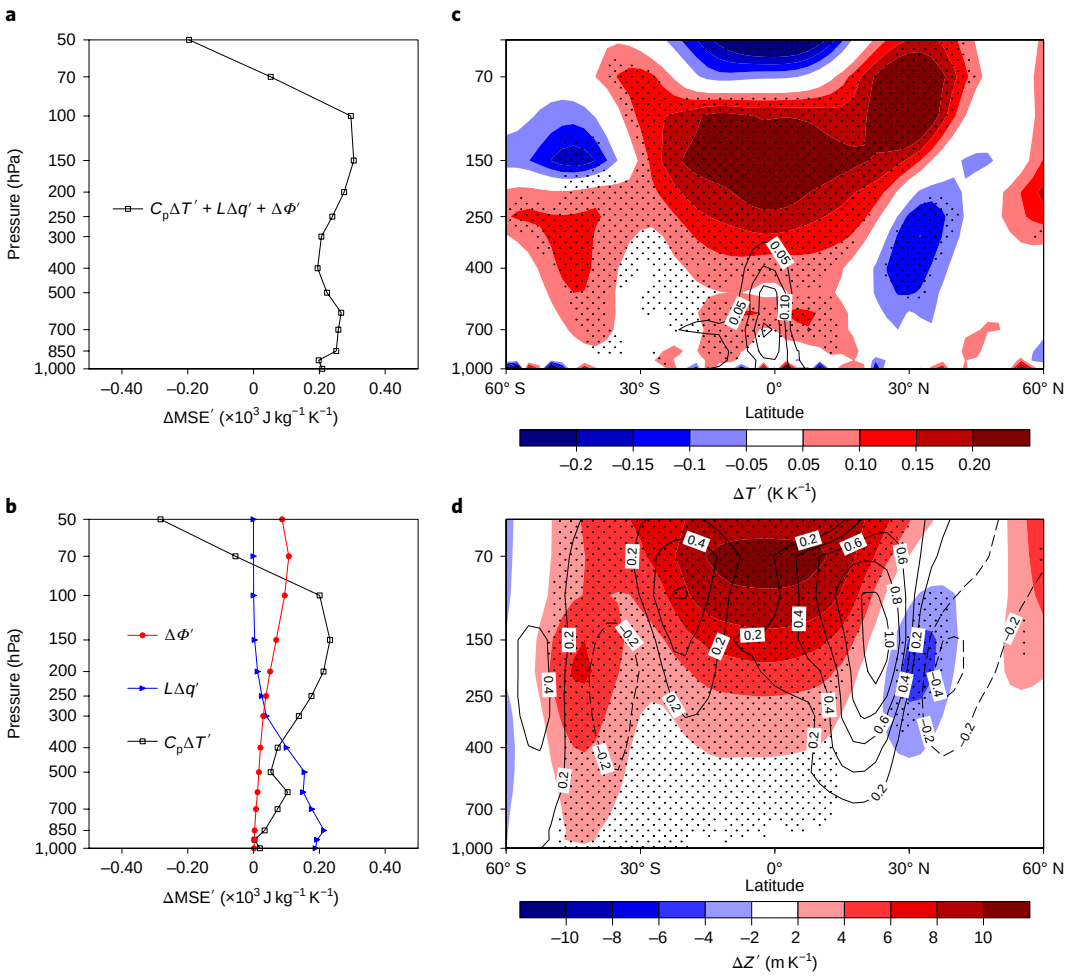

Fig. 3 | Vertical structure of the changes in ENSO humidity, temperature and circulation. a, Changes in DJF tropical-mean ENSO-driven moist static energy anomalies (ΔMSE′) in the MME. **b**, Components of the changes in moist static energy anomalies ($C_p\Delta T'$, $L\Delta q'$ and $\Delta\phi'$). **c**, Changes in DJF zonal-mean ENSO-driven specific humidity anomalies ($\Delta q'$; contours; at intervals of 0.05 g kg^{-1} K^{-1}) and air temperature anomalies ($\Delta T'$; colours). **d**, Changes in DJF zonal-mean ENSO-driven zonal wind anomalies ($\Delta U'$; black contours; at intervals of 0.2 m s^{-1} K^{-1}) and geopotential height anomalies ($\Delta Z'$; colours). In **c** and **d**, stippling indicates that more than 85% of models agree on the sign of the MME.

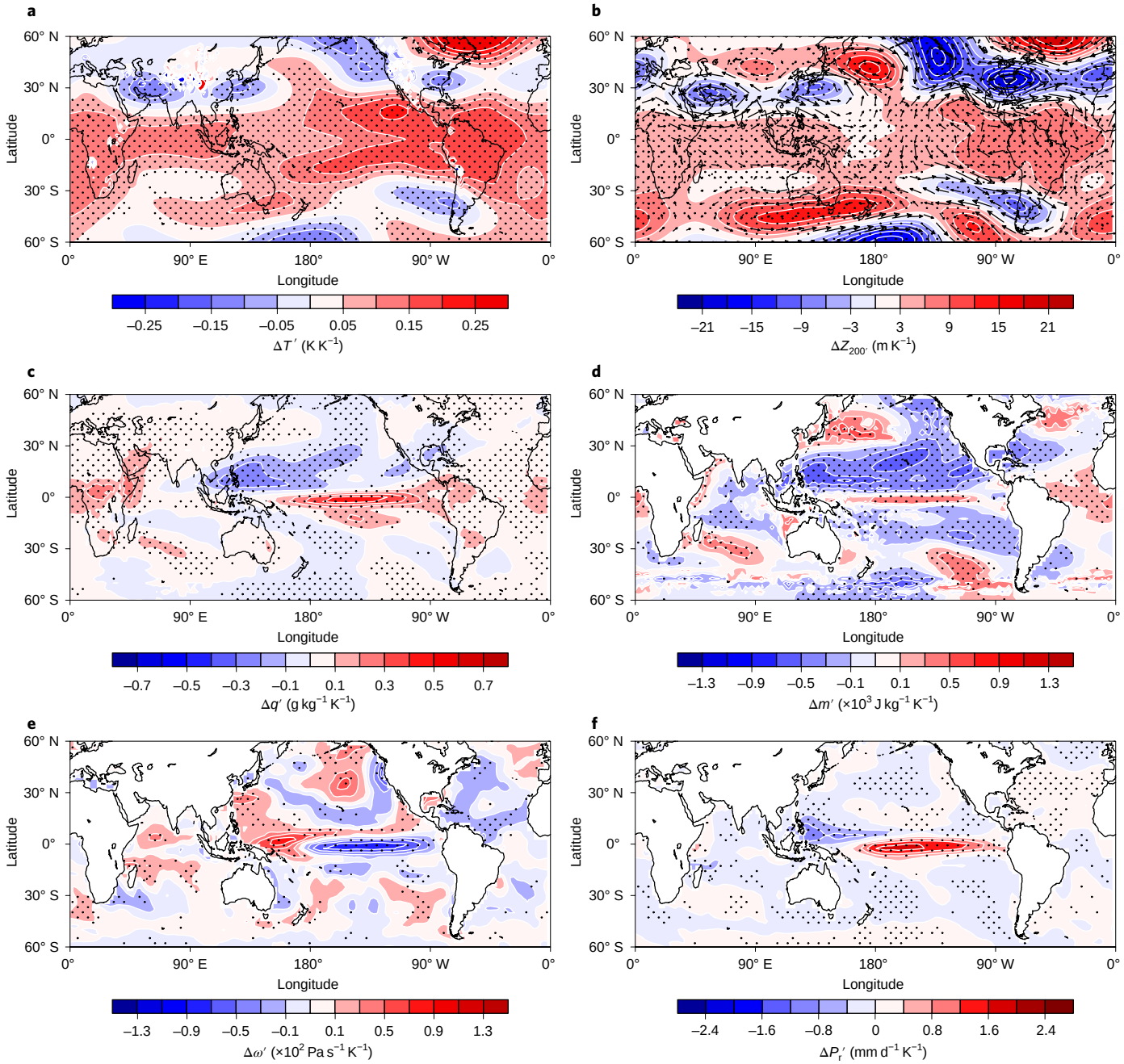

Fig. 4 | Mechanism for the changes in ENSO atmospheric circulation and precipitation. a, Changes in the ENSO-driven DJF vertically averaged (850–200 hPa) air temperature anomaly ($\Delta T'$). **b**, Changes in ENSO-driven DJF 200-hPa geopotential height ($\Delta Z_{200}'$; colours) and wind ($\Delta UV_{200}'$; vectors; arrows represent 3 m s^{-1} K^{-1}) anomalies. *UV*, zonal (*U*) and meridional (*V*) components of wind. **c**, Changes in ENSO-driven DJF low-level averaged (1,000–500 hPa) specific humidity anomalies ($\Delta q'$). **d**, Changes in ENSO-related DJF moist instability anomalies ($\Delta m'$). **e**, Changes in ENSO-driven DJF 500-hPa vertical pressure velocity anomalies ($\Delta\omega'$). **f**, Changes in ENSO-driven DJF rainfall anomalies ($\Delta P_r'$). Stippling indicates that more than 85% of models agree on the sign of the MME.

~5.6% per 1-K background warming (Fig. 2b). Compared with dq_s/dT, the relationship between dq/dT and $\Delta\bar{T}$ has some diversity, probably caused by uncertainty in the relative humidity change. Figure 3a shows the vertical profile of the change in El Niño-induced tropical-mean (10° S–10° N) moist static energy (MSE)[40] (see Methods) anomalies from P_{ctrl} to P_{warm} in the MME. In the troposphere, the El Niño-induced MSE anomaly increases almost uniformly in the vertical profile under global warming, due to moist adiabatic adjustment in convection[11,39]. Unlike MSE itself, the three components (see Methods) in the troposphere do not distribute uniformly in the vertical profile (Fig. 3b). The ENSO-induced humidity anomaly amplifies under global warming, obeying the Clausius–Clapeyron scaling, which is confined to the lower troposphere. To maintain moist adiabats in the tropics, ENSO-induced upper tropospheric temperature anomalies increase proportionally (Fig. 3b). Thus, the Clausius–Clapeyron-based mechanism can explain why ENSO-driven variability will amplify in tropical air humidity and at tropospheric temperature under global warming.

Atmospheric circulation variability

The enhanced response of tropical air temperature and humidity to the ENSO can result in a major reorganization of the atmospheric circulation. As shown in Fig. 3c, the change of zonal-mean specific humidity anomalies from P_{ctrl} to P_{warm} is mainly confined in the lower troposphere below 500 hPa, while the change of air temperature anomalies peaks at around 150 hPa. By hydrostatic balance, the El Niño-induced geopotential height anomaly strengthens in the upper tropical troposphere, with intensified westerly wind anomalies in the upper troposphere around 20° S and 20° N (Fig. 3d). Previous studies[12,15] showed that subtropical jets in both hemispheres strengthen on their equatorward flanks in El Niño events (Extended Data Fig. 4) and our results indicate that this response will amplify under global warming. We found that the El Niño-induced zonal-mean westerly wind anomalies in the upper troposphere around 20° N increase by ~61.7 ± 60% from P_{ctrl} to P_{warm}, or by 16.6 ± 16.2% for each 1-K background warming in the tropics.

Because of equatorial wave adjustments[13,37], the increase of ENSO-induced air temperature anomalies in the free troposphere spread horizontally in the entire tropics (Fig. 4a). Consequently, there are positive changes of El Niño-induced 200-hPa height anomalies within the tropics between 20° S and 20° N, and enhanced westerly wind anomalies along 20° S and 20° N due to the equatorward pressure gradient (Fig. 4b). Poleward of the tropical warming, there is a latitude belt of marked tropospheric cooling in the Northern Hemisphere, probably caused by the changes in the eddy-driven meridional circulation[12]. The cooling is prominent over the Asian continent and North America, which corresponds to robust 200-hPa low-pressure anomalies in these regions. Thus, the pressure gradient south of these regions is stronger than in other regions, and so are the westerly wind anomalies. Compared with the ENSO-induced air temperature and atmospheric circulation anomalies in the present real climate (Extended Data Fig. 5), the anomalies intensify in a warmer climate. Particularly, the westerly wind anomalies over subtropical North America (15° N–30° N, 130° W–30° W) increase from 1.9 ± 0.7 m s^{-1} K^{-1} for P_{ctrl} to 3.3 ± 0.5 m s^{-1} K^{-1} for P_{warm}, corresponding to a 19.2 ± 11.3% increase for each 1-K background tropical warming. This intensified circulation response makes the US west coast more susceptible to ENSO varibility[30–33].

Precipitation variability

The changes in ENSO-driven humidity anomalies are localized. In El Niño, SST and low-level tropospheric air temperature anomalies are positive in the tropical central-eastern Pacific but negative in the tropical Northwest Pacific. Hence, the background greenhouse warming will strengthen both the positive humidity anomalies over the central-eastern Pacific and negative humidity anomalies over the Northwest Pacific (Fig. 4c and Extended Data Fig. 6). The changes of ENSO-related gross moist instability[40] (see Methods) are primarily determined by the changes of ENSO-driven humidity anomalies, with increasing trends over the tropical central-eastern Pacific but decreasing trends in the Northwest Pacific (Fig. 4d). In the tropics, the increase of gross moist instability tends to lead to low-level convergence, and vice versa[40]. Indeed, the changes of ENSO-induced 500-hPa vertical velocity anomalies are spatially consistent with the change of gross moist instability in the tropics, with upwelling change over the equatorial central-eastern Pacific but downwelling change over the Northwest Pacific (Fig. 4e). Therefore, the enhanced response of humidity to air temperature can intensify both the El Niño-driven precipitation decrease over the Northwest Pacific and the increase over the central-eastern equatorial Pacific (Fig. 4f and Extended Data Fig. 6). This explanation does not require spatial variations in mean warming[18,27,29] or ENSO SST anomalies[41]. The relative contributions from the SST pattern effect need to be evaluated in future studies.

Year-to-year ENSO variability is controlled by complicated air–sea feedbacks and affected by the noise arising from internal variability. It proves difficult to determine how ENSO behaviours change under global warming[16,42–46]. Here, we find that the nonlinear response of saturation vapour pressure to temperature change (that is, the Clausius–Clapeyron relationship) causes robust changes in key characteristics of the ENSO under global warming. Specifically, the boreal winter response of tropical humidity, tropospheric upper temperature, the subtropical jet in both hemispheres and tropical Pacific rainfall to the ENSO intensify robustly across the models. As extreme weather often results from ENSO-induced anomalous atmospheric circulation and temperature[47–49], the intensification of ENSO-driven atmospheric variability offers a key step to project how ENSO-related extreme weather will change in the future, which deserves further studies.

This study shows that the Clausius–Clapeyron-based mechanism is an important constraint for ENSO projections. This mechanism is based on the change in the sensitivity of vapour response to temperature but not on the change in the mean-state vapour, as has been widely used in previous studies[39,50]. The response of tropospheric humidity to SST variability also intensifies elsewhere (for example, the tropical Indian Ocean and Atlantic; Extended Data Figs. 7 and 8) under greenhouse warming, suggesting that our method can be applied to projecting changes in other tropical modes.

Online content

Any methods, additional references, Nature Research reporting summaries, source data, extended data, supplementary information, acknowledgements, peer review information; details of author contributions and competing interests; and statements of data and code availability are available at https://doi.org/10.1038/s41561-021-00730-3.

Received: 29 June 2020; Accepted: 12 March 2021;
Published online: 15 April 2021

References

1. Jin, F.-F. Tropical ocean–atmosphere interaction, the Pacific Cold Tongue, and the El Niño–Southern Oscillation. *Science* **274**, 76–78 (1996).
2. Wallace, J. M. et al. The structure and evolution of ENSO-related climate variability in the tropical Pacific: lessons from TOGA. *J. Geophys. Res.* **103**, 14241–14259 (1998).
3. Neelin, J. D. et al. ENSO theory. *J. Geophys. Res.* **103**, 14261–14290 (1998).
4. McPhaden, M. J., Zebiak, S. E. & Glantz, M. H. ENSO as an integrating concept in Earth science. *Science* **314**, 1740–1745 (2006).
5. Deser, C., Alexander, M. A., Xie, S. P. & Phillips, A. S. Sea surface temperature variability: patterns and mechanisms. *Ann. Rev. Mar. Sci.* **2**, 115–143 (2010).
6. Horel, J. D. & Wallace, J. M. Planetary-scale atmospheric phenomena associated with the Southern Oscillation. *Mon. Weather Rev.* **109**, 813–829 (1981).
7. Trenberth, K. E. et al. Progress during TOGA in understanding and modeling global teleconnections associated with tropical sea surface temperatures. *J. Geophys. Res.* **103**, 14291–14324 (1998).
8. Gill, A. E. Some simple solutions for heat-induced tropical circulation. *Q. J. R. Meteorol. Soc.* **106**, 447–462 (1980).
9. Wang, B., Wu, R. G. & Fu, X. H. Pacific–East Asian teleconnection: how does ENSO affect East Asian climate? *J. Clim.* **13**, 1517–1536 (2000).
10. Chiang, J. C. H. & Sobel, A. H. Tropical tropospheric temperature variations caused by ENSO and their influence on the remote tropical climate. *J. Clim.* **15**, 2616–2631 (2002).
11. Su, H., Neelin, J. D. & Meyerson, J. E. Sensitivity of tropical tropospheric temperature to sea surface temperature forcing. *J. Clim.* **16**, 1283–1301 (2003).
12. Seager, R., Harnik, N. I., Kushnir, Y., Robinson, W. A. & Miller, J. Mechanisms of hemispherically symmetric climate variability. *J. Clim.* **16**, 2960–2978 (2003).
13. Neelin, J. D. & Su, H. Moist teleconnection mechanisms for the tropical South American and Atlantic sector. *J. Clim.* **18**, 3928–3950 (2005).
14. Xie, S.-P. et al. Indian ocean capacitor effect on Indo-Western Pacific climate during the summer following El Niño. *J. Clim.* **22**, 730–747 (2009).

15. Adames, Á. F. & Wallace, J. M. On the tropical atmospheric signature of El Niño. *J. Atmos. Sci.* **74**, 1923–1939 (2017).
16. Collins, M. et al. The impact of global warming on the tropical Pacific Ocean and El Niño. *Nat. Geosci.* **3**, 391–397 (2010).
17. Cai, W. J. et al. Increasing frequency of extreme El Niño events due to greenhouse warming. *Nat. Clim. Change* **4**, 111–116 (2014).
18. Cai, W. J. et al. ENSO and greenhouse warming. *Nat. Clim. Change* **5**, 849–859 (2015).
19. Cai, W. J. et al. Increased variability of eastern Pacific El Niño under greenhouse warming. *Nature* **564**, 201–206 (2018).
20. Yeh, S. W. et al. El Niño in a changing climate. *Nature* **461**, 511–514 (2009).
21. Yeh, S. W. et al. ENSO atmospheric teleconnections and their response to greenhouse gas forcing. *Rev. Geophys.* **56**, 185–206 (2018).
22. Fasullo, J. T., Otto-Bliesner, B. L. & Stevenson, S. ENSO's changing influence on temperature, precipitation, and wildfire in a warming climate. *Geophys. Res. Lett.* **45**, 9216–9225 (2018).
23. Perry, S. J., McGregor, S., Sen Gupta, A., England, M. H. & Maher, N. Projected late 21st century changes to the regional impacts of the El Niño–Southern Oscillation. *Clim. Dynam.* **54**, 395–412 (2020).
24. Wang, B. et al. Historical change of El Niño properties sheds light on future changes of extreme El Niño. *Proc. Natl Acad. Sci. USA* **116**, 22512–22517 (2019).
25. Watanabe, M. et al. Uncertainty in the ENSO amplitude change from the past to the future. *Geophys. Res. Lett.* **39**, L20703 (2012).
26. Kim, S. T. et al. Response of El Niño sea surface temperature variability to greenhouse warming. *Nat. Clim. Change* **4**, 786–790 (2014).
27. Power, S., Delage, F., Chung, C., Kociuba, G. & Keay, K. Robust twenty-first-century projections of El Niño and related precipitation variability. *Nature* **502**, 541–545 (2013).
28. Chung, C. T. Y., Power, S. B., Arblaster, J. M., Rashid, H. A. & Roff, G. L. Nonlinear precipitation response to El Niño and global warming in the Indo-Pacific. *Clim. Dynam.* **42**, 1837–1856 (2014).
29. Huang, P. & Xie, S. P. Mechanisms of change in ENSO-induced tropical Pacific rainfall variability in a warming climate. *Nat. Geosci.* **8**, 922–927 (2015).
30. Meehl, G. A. & Teng, H. Multi-model changes in El Niño teleconnections over North America in a future warmer climate. *Clim. Dynam.* **29**, 779–790 (2007).
31. Kug, J.-S., An, S.-I., Ham, Y.-G. & Kang, I.-S. Changes in El Niño and La Niña teleconnections over North Pacific–America in the global warming simulations. *Theor. Appl. Climatol.* **100**, 275–282 (2010).
32. Zhou, Z., Xie, S., Zheng, X., Liu, Q. & Wang, H. Global warming-induced changes in El Niño teleconnections over the North Pacific and North America. *J. Clim.* **27**, 9050–9064 (2014).
33. Power, S. B. & Delage, F. P. D. El Niño–Southern Oscillation and associated climatic conditions around the world during the latter half of the twenty-first century. *J. Clim.* **31**, 6189–6207 (2018).
34. McPhaden, M. J., Lee, T. & McClurg, D. El Niño and its relationship to changing background conditions in the tropical Pacific Ocean. *Geophys. Res. Lett.* **38**, L15709 (2011).
35. Ying, J., Huang, P., Lian, T. & Chen, D. K. Intermodel uncertainty in the change of ENSO's amplitude under global warming: role of the response of atmospheric circulation to SST anomalies. *J. Clim.* **32**, 369–383 (2019).
36. Frankcombe, L. M., England, M. H., Mann, M. E. & Steinman, B. A. Separating internal variability from the externally forced climate response. *J. Clim.* **28**, 8184–8202 (2015).
37. Xie, S. P. et al. Global warming pattern formation: sea surface temperature and rainfall. *J. Clim.* **23**, 966–986 (2010).
38. Hu, K. et al. Interdecadal variations in ENSO influences on Northwest Pacific–East Asian early summertime climate simulated in CMIP5 models. *J. Clim.* **27**, 5982–5998 (2014).
39. Held, I. M. & Soden, B. J. Robust responses of the hydrological cycle to global warming. *J. Clim.* **19**, 5686–5699 (2006).
40. Neelin, J. D. & Held, I. M. Modeling tropical convergence based on the moist static energy budget. *Mon. Weather Rev.* **115**, 3–12 (1987).
41. Yan, Z. et al. Eastward shift and extension of ENSO-induced tropical precipitation anomalies under global warming. *Sci. Adv.* **6**, eaax4177 (2020).
42. Liu, Z. Y. et al. Evolution and forcing mechanisms of El Niño over the past 21,000 years. *Nature* **515**, 550–553 (2014).
43. Stevenson, S., Capotondi, A., Fasullo, J. & Otto-Bliesner, B. Forced changes to twentieth century ENSO diversity in a last Millennium context. *Clim. Dynam.* **52**, 7359–7374 (2019).
44. Zheng, X. T., Hui, C. & Yeh, S. W. Response of ENSO amplitude to global warming in CESM large ensemble: uncertainty due to internal variability. *Clim. Dynam.* **50**, 4019–4035 (2018).
45. Wang, L., Chen, W. & Huang, R. Interdecadal modulation of PDO on the impact of ENSO on the East Asian winter monsoon. *Geophys. Res. Lett.* **35**, L20702 (2008).
46. Maher, N., Matei, D., Milinski, S. & Marotzke, J. ENSO change in climate projections: forced response or internal variability? *Geophys. Res. Lett.* **45**, 11390–11398 (2018).
47. Seager, R., Kushnir, Y., Nakamura, J., Ting, M. & Naik, N. Northern Hemisphere winter snow anomalies: ENSO, NAO and the winter of 2009/10. *Geophys. Res. Lett.* **37**, L14703 (2010).
48. Hu, K., Xie, S.-P. & Huang, G. Orographically anchored El Niño effect on summer rainfall in central China. *J. Clim.* **30**, 10037–10045 (2017).
49. Chen, W., Feng, J. & Wu, R. Roles of ENSO and PDO in the link of the East Asian winter monsoon to the following summer monsoon. *J. Clim.* **26**, 622–635 (2013).
50. Seager, R., Naik, N. & Vogel, L. Does global warming cause intensified interannual hydroclimate variability? *J. Clim.* **25**, 3355–3372 (2012).

Publisher's note Springer Nature remains neutral with regard to jurisdictional claims in published maps and institutional affiliations.

© The Author(s), under exclusive licence to Springer Nature Limited 2021

Methods

Datasets and index definition. We used the pre-industrial control runs and 1% yr^{-1} [CO_2] increase runs from 19 CGCMs of CMIP6. These were BCC-CSM2-MR, CESM2-WACCM, CESM2, CNRM-CM6-1, CNRM-ESM2-1, CanESM5, E3SM-1-0, EC-Earth3-Veg, GFDL-CM4, GFDL-ESM4, GISS-E2-1-G, GISS-E2-1-H, HadGEM3-GC31-LL, IPSL-CM6A-LR, MIROC-ES2L, MIROC6, MRI-ESM2-0, SAM0-UNICON and UKESM1-0-LL. To confirm the results, we performed two additional analyses. One was to analyse the changes from the historical scenario run (1950–1999) to the SSP585 run (2050–2099) in 30 CMIP6 models (Extended Data Fig. 3). The other was to analyse the changes from the historical scenario run (1950–1999) and the representative concentration pathway 8.5 run (2050–2099) in 18 CMIP5 models (Extended Data Fig. 2). The 30 CMIP6 models were ACCESS-CM2, ACCESS-ESM1-5, BCC-CSM2-MR, CESM2-WACCM, CESM2, CNRM-CM6-1-HR, CNRM-CM6-1, CNRM-ESM2-1, CanESM5-CanOE, GFDL-CM4, CanESM5, EC-Earth3-Veg, FGOALS-f3-L, FGOALS-g3, GFDL-CM4, GFDL-ESM4, GISS-E2-1-G, INM-CM4-8, INM-CM5-0, IPSL-CM6A-LR, KACE-1-0-G, MCM-UA-1-0, MIROC-ES2L, MIROC6, MPI-ESM1-2-HR, MPI-ESM1-2-LR, MRI-ESM2-0, NorESM2-LM, NorESM2-MM and UKESM1-0-LL. The 18 CMIP5 models were ACCESS1-0, BNU-ESM, CCSM4, CESM1-BGC, CNRM-CM5, CSIRO-Mk3-6-0, CanESM2, IPSL-CM5A-LR, IPSL-CM5A-MR, IPSL-CM5B-LR, MIROC-ESM-CHEM, MIROC-ESM, MIROC5, MRI-CGCM3, NorESM1-ME, NorESM1-M, bcc-csm1-1-m and bcc-csm1-1. More detailed online model documentations for the CMIP6 and CMIP5 models are available at https://pcmdi.llnl.gov/CMIP6/ and https://esgf-node.llnl.gov/search/cmip5/, respectively.

The MME is defined as the simple average of the 19 models. SST, precipitation, air temperature, geopotential height, winds, air specific humidity and vertical pressure velocity at 500 hPa were used. We constructed a DJF Niño3.4 SST index by averaging DJF SST anomalies in the domain of 5° S–5° N and 90°–150° W to indicate ENSO variations. ENSO-driven anomalies of specific humidity, air temperature, geopotential height, vertical pressure velocity and winds were calculated by regression on the DJF Niño3.4 SST index so that they represent variable anomalies per 1 K Niño3.4 SST index change. Before the regression analyses, the linear trend was removed. We also used a scaling method[36] to detrend the data and the result was almost the same as when applying a linear detrending method, indicating that the result is not sensitive to method choices (Extended Data Fig. 1).

For comparison, we calculated the observed ENSO-driven atmospheric anomalies based on the 2.5° latitude × 2.5° longitude daily National Centers for Environmental Prediction/Department of Energy version 2 Reanalysis[51] and Global Precipitation Climatology Project monthly precipitation datasets[52] and the 1° latitude × 1° longitude monthly Hadley Center SST[53] over 1979–2018. The results are shown in the Extended Data Figs. 4–6.

Moist static energy and moist instability analyses. MSE[40] is defined as $MSE = C_pT + \phi + Lq$, where L is the latent heat of condensation, C_p is the specific heat capacity, T is the air temperature, ϕ is the geopotential and q is the air specific humidity. Thus, the change of ENSO-driven MSE anomalies ($\Delta MSE'$) can be represented by $C_p\Delta T' + L\Delta q' + \Delta\phi'$. Here, $\Delta T'$, $\Delta q'$ and $\Delta\phi'$ denote the change of ENSO-driven anomalies of air temperature, specific humidity and geopotential, respectively. Since large-scale divergence tends to have a simple vertical structure in the tropics, with one sign in the lower troposphere and the opposite sign in the upper troposphere, for simplicity, we define gross moist instability (m) as the difference in moist static energy between the lower troposphere (1,000–500 hPa) and upper troposphere (500–200 hPa) following previous studies[13,37,40].

Statistical significance. We applied a 10,000-resampling bootstrap method to test whether the variance changes of the DJF Niño3.4 SST index, ENSO-related tropical-mean surface humidity and 200 hPa air temperature were statistically significant. For each of the three variables, its values in the 19 models were resampled randomly to construct 10,000 realizations of mean values. In this random resampling process, any model was allowed to be selected again. The 10,000 mean values were sorted in ascending order and the 250th and 9,750th values were set as the 2.5% lower confidence bound and the 97.5% upper confidence bound. Between the two bounds was the 95% confidence interval. In the observational analyses, the confidence level was based on a two-tailed Student's t-test.

Data availability

The CMIP6 data are available at https://pcmdi.llnl.gov/CMIP6/. The CMIP5 data are available at https://esgf-node.llnl.gov/search/cmip5/. The version 2 National Centers for Environmental Prediction/Department of Energy reanalysis and Global Precipitation Climatology Project precipitation data are from http://www.esrl.noaa.gov/psd/data/gridded/. Hadley Center SST data were provided by the Met Office Hadley Center (https://www.metoffice.gov.uk/hadobs/hadisst/).

Code availability

The code associated with this paper is available on request from K.H.

References

51. Kanamitsu, M. et al. NCEP-DOE AMIP-II reanalysis (R-2). *Bull. Am. Meteorol. Soc.* **83**, 1631–1643 (2002).
52. Adler, R. F. et al. The Version-2 Global Precipitation Climatology Project (GPCP) Monthly Precipitation Analysis (1979–present). *J. Hydrometeorol.* **4**, 1147–1167 (2003).
53. Rayner, N. A. et al. Global analyses of sea surface temperature, sea ice, and night marine air temperature since the late nineteenth century. *J. Gerophys. Res.* **108**, 4407 (2003).

Acknowledgements

The work was supported by the National Key Research and Development Program of China (fund number 2019YFA0606703), National Natural Science Foundation of China (41831175), Second Tibetan Plateau Scientific Expedition and Research (STEP) programme (grant number 2019QZKK0102), Strategic Priority Research Program of the Chinese Academy of Sciences (XDA20060500), National Natural Science Foundation of China (41775086, 41722504 and 91937302), Key Deployment Project of the Centre for Ocean Mega-Research of Science, Chinese Academy of Sciences (COMS2019Q03) and Youth Innovation Promotion Association of CAS. Y.K. was supported by the Japan Ministry of Education, Culture, Sports, Science and Technology (JPMXD0717935457) and Japan Society for the Promotion of Science (18H01278, 18H01281 and 19H05703). S.-P.X. was supported by the National Science Foundation (AGS 1934392).

Author contributions

K.H. and G.H. conceived the study, performed the analyses, built the mechanism and wrote the paper. P.H., Y.K. and S.-P.X. contributed to improving the paper and assisted in interpretation of the results.

Competing interests

The authors declare no competing interests.

Additional information

Extended data is available for this paper at https://doi.org/10.1038/s41561-021-00730-3.

Correspondence and requests for materials should be addressed to K.H. or G.H.

Peer review information Primary Handling Editor: Tom Richardson. *Nature Geoscience* thanks Tobias Bayr, Andrea Taschetto and the other, anonymous, reviewer(s) for their contribution to the peer review of this work.

Reprints and permissions information is available at www.nature.com/reprints.

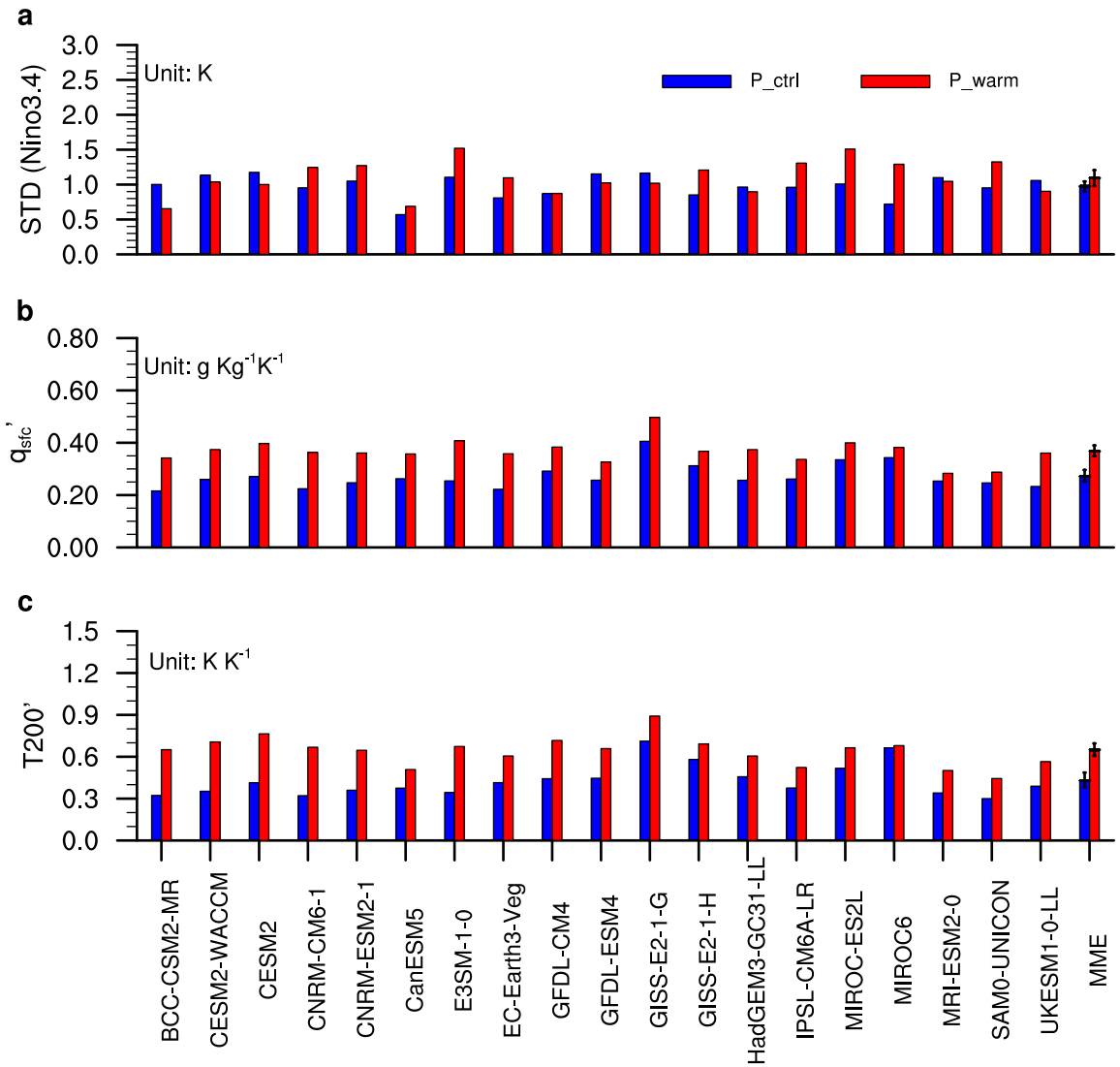

Extended Data Fig. 1 | Projected change in ENSO-driven variability in boreal winter tropical SST, humidity and air temperature. The analysis is the same as that in Fig. 1 except for applying a "scaling" method (see Method) for detrending data prior to regressions. The result is almost the same as that in Fig. 1, indicating the result is not sensitive to the selection of method for detrending.

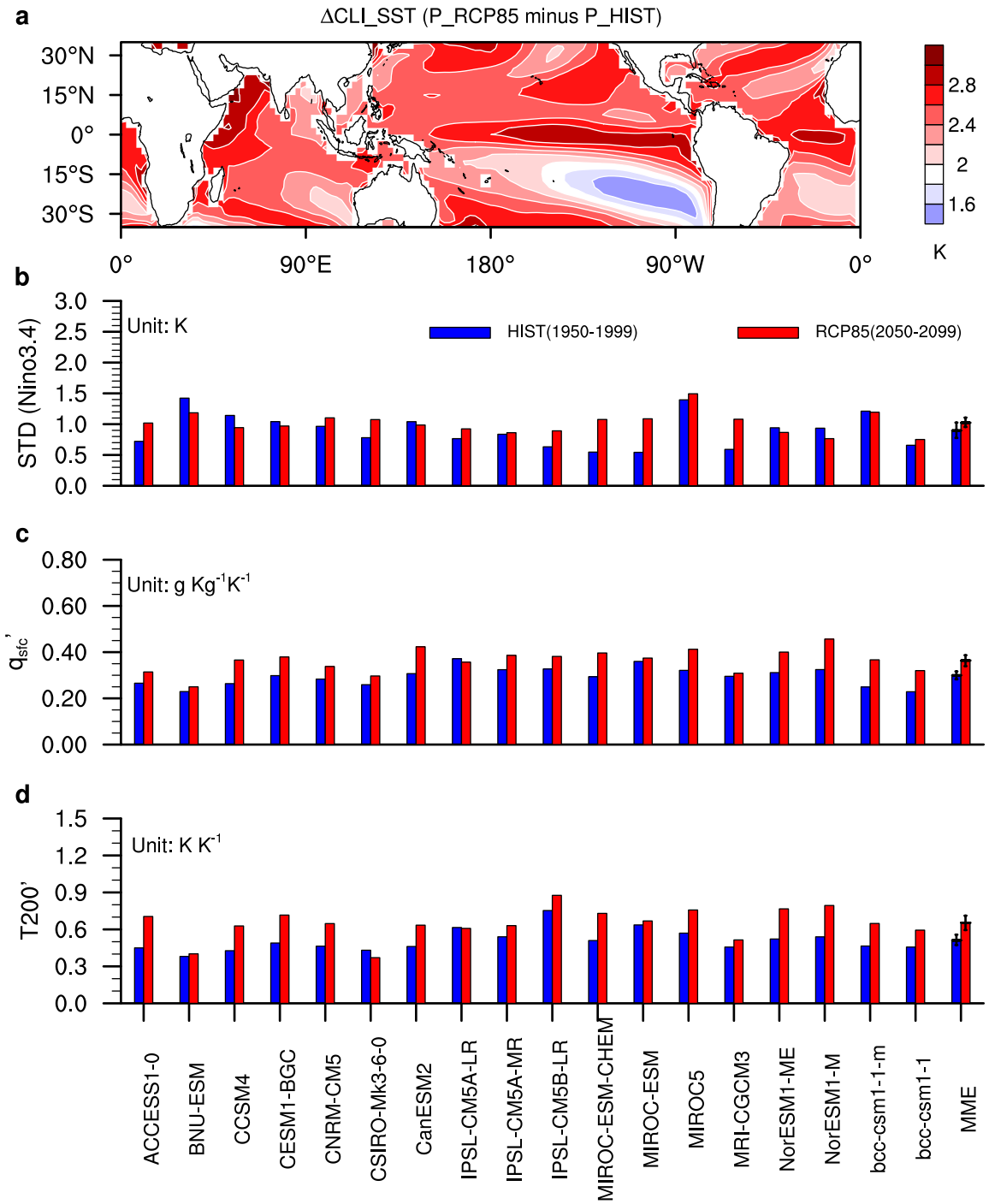

Extended Data Fig. 2 | Projected change in ENSO SST, humidity and air temperature in 18 CMIP5 models (see Methods) from 1950-1999 in historical experiments to 2050-2099 in RCP8.5 experiments. a, Changes in DJF climatological SST in the MME. **b**, Comparison of the standard deviation of DJF Niño 3.4 SST index over the two periods in each model and the MME. **c, d**, Comparison of DJF tropical mean (10°S-10°N) ENSO-driven surface specific humidity (q'_{sfc}; **c**) and 200-hPa air temperature (T'_{200}; **d**) between the two periods. Error bars in the MME mean correspond to the 95% confidence interval (see Methods). The MME q'_{sfc} and T'_{200} increases by 9.6±6.1% and 11.5±8.4% respectively for per 1K background warming in the tropics.

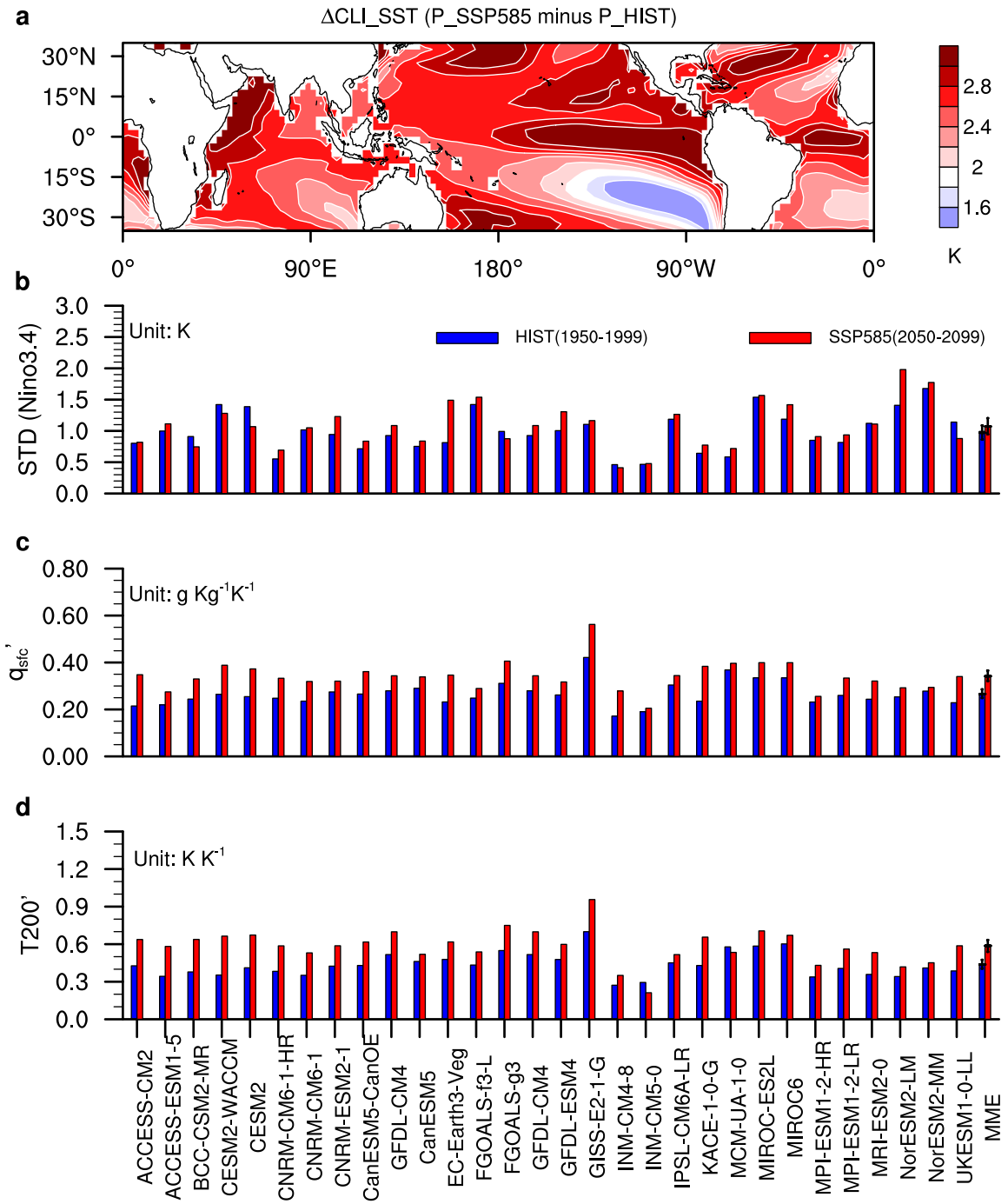

Extended Data Fig. 3 | Projected change in ENSO SST, humidity and air temperature in 30 CMIP6 models (see Methods) from 1950-1999 in historical experiments to 2050-2099 in SSP585 experiments. a, Changes in DJF climatological SST in the MME. **b**, Comparison of the standard deviation of DJF Niño 3.4 SST index over the two periods in each model and the MME. **c, d**, Comparison of DJF tropical mean (10°S-10°N) ENSO-driven surface specific humidity (q'_{sfc}; **c**) and 200-hPa air temperature (T'_{200}; **d**) between the two periods. Error bars in the MME mean correspond to the 95% confidence interval (see Methods). The MME q'_{sfc} and T'_{200} increases by 10.2±6.0% and 12.2±8.5% respectively for per 1 K background warming in the tropics.

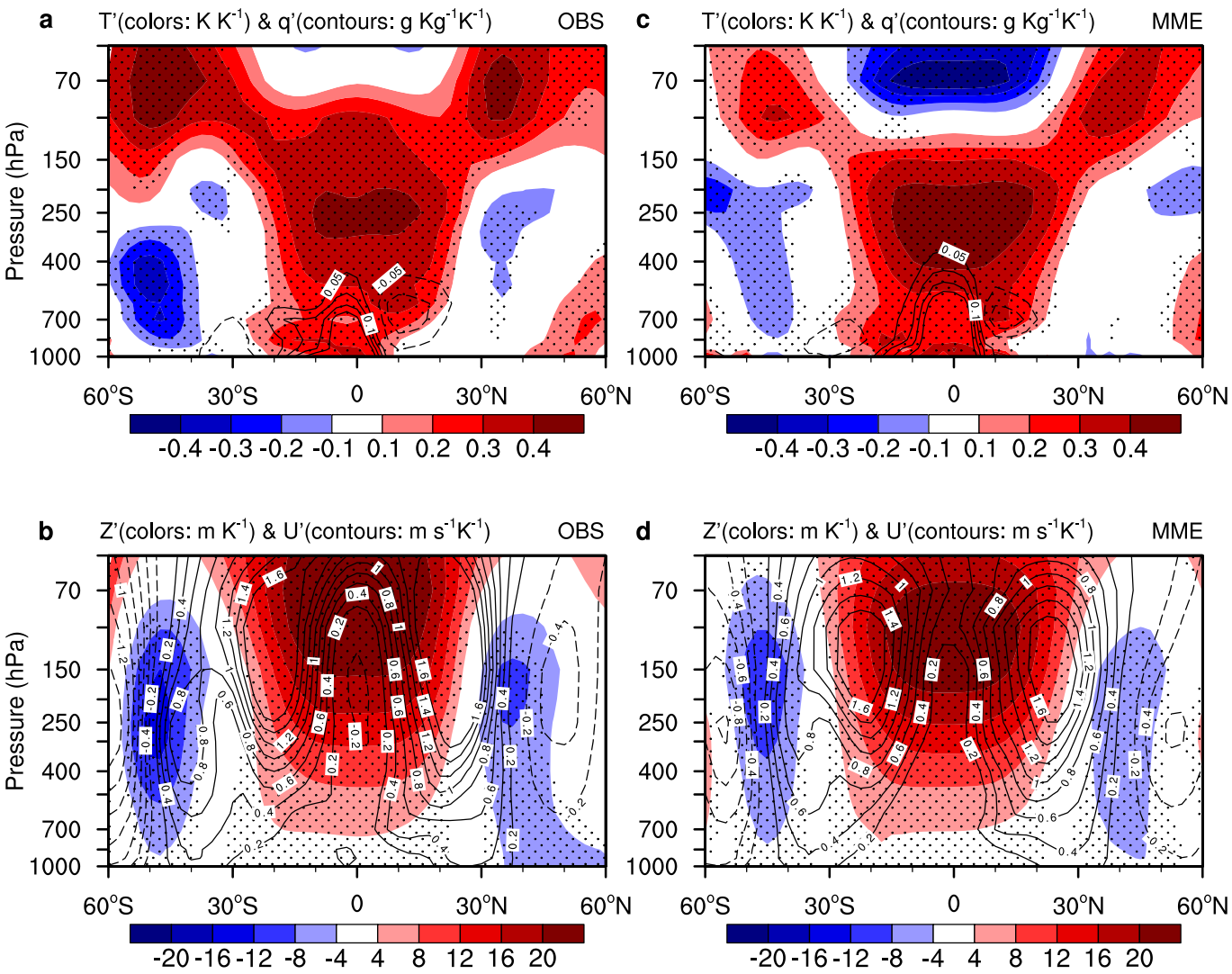

Extended Data Fig. 4 | Vertical structure of ENSO-driven anomalies of boreal winter air humidity, temperature and circulation. a, DJF zonally mean ENSO-driven specific humidity anomalies (q′; contours; at interval of 0.05 g kg^{-1} K^{-1}) and air temperature anomalies (T′; colors) during 1979-2018 in the observations. **b**, DJF zonally mean ENSO-driven zonal wind anomalies (U′; black contours; at interval of 0.2 m s^{-1} K^{-1}) and geopotential height anomalies (Z′; colors) during 1979-2018 in the observations. **c**-**d**, similar to **a** and **b** but for the MME during 400-449 model years in the PI control runs. Stippling in **a** and **b** denotes passing 95% confidence level based on a two-tailed Student's t test, and in **c** and **d** indicates that more than 85% of models agree on the sign of the MME.

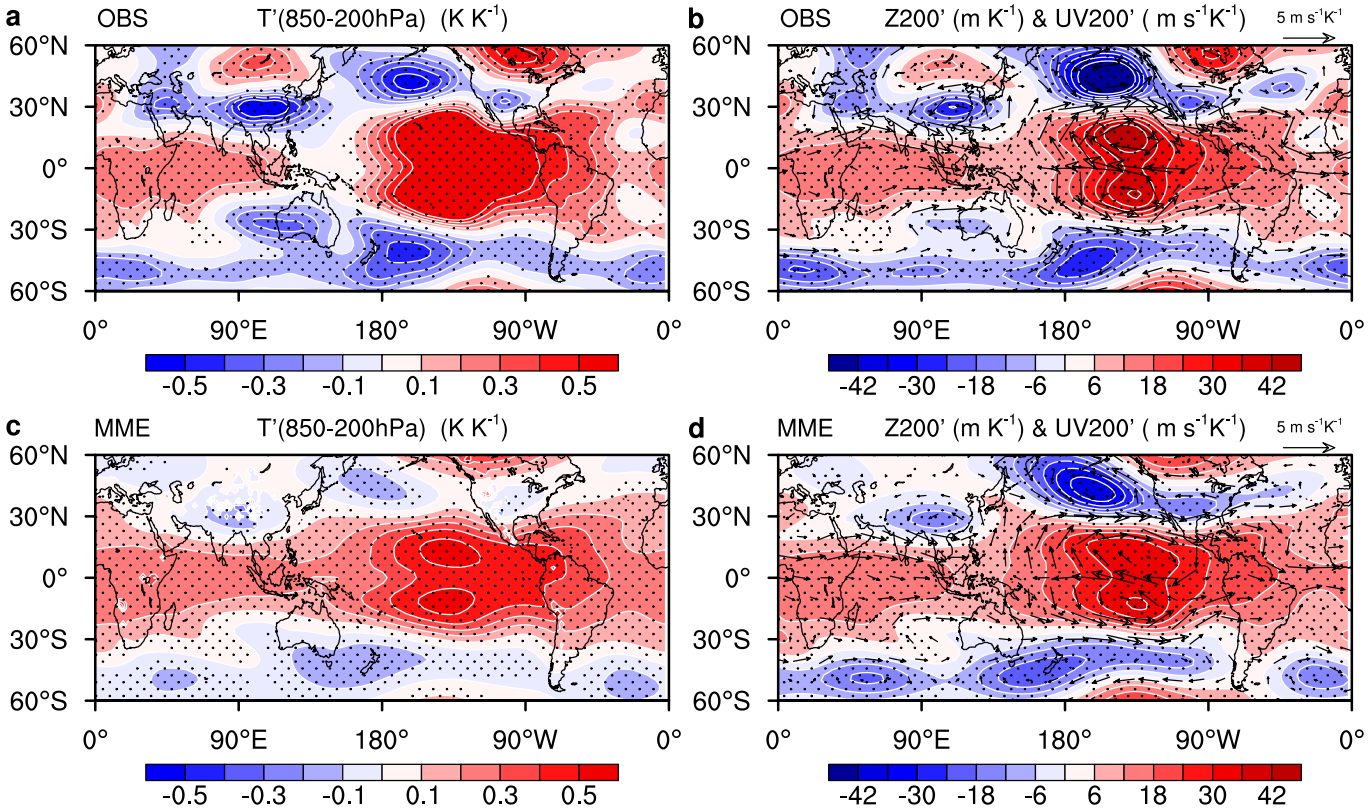

Extended Data Fig. 5 | ENSO-driven anomalies of boreal winter tropospheric air temperature, 200hPa geopotential height and circulation. a and **c**, Vertically averaged (850-200 hPa) ENSO-driven DJF air temperature anomalies (T′). **b** and **d**, 200-hPa ENSO-driven DJF geopotential height (Z200′; colors) and wind (UV200′; vectors) anomalies. Anomalies in **a** and **b** are derived from the observations during 1979-2018, while in **c** and **d** are from the MME during 400-449 model years in the PI control runs. Stippling in **a** and **b** denotes passing 95% confidence level based on a two-tailed Student's t test, and in **c** and **d** indicates that more than 85% of models agree on the sign of the MME.

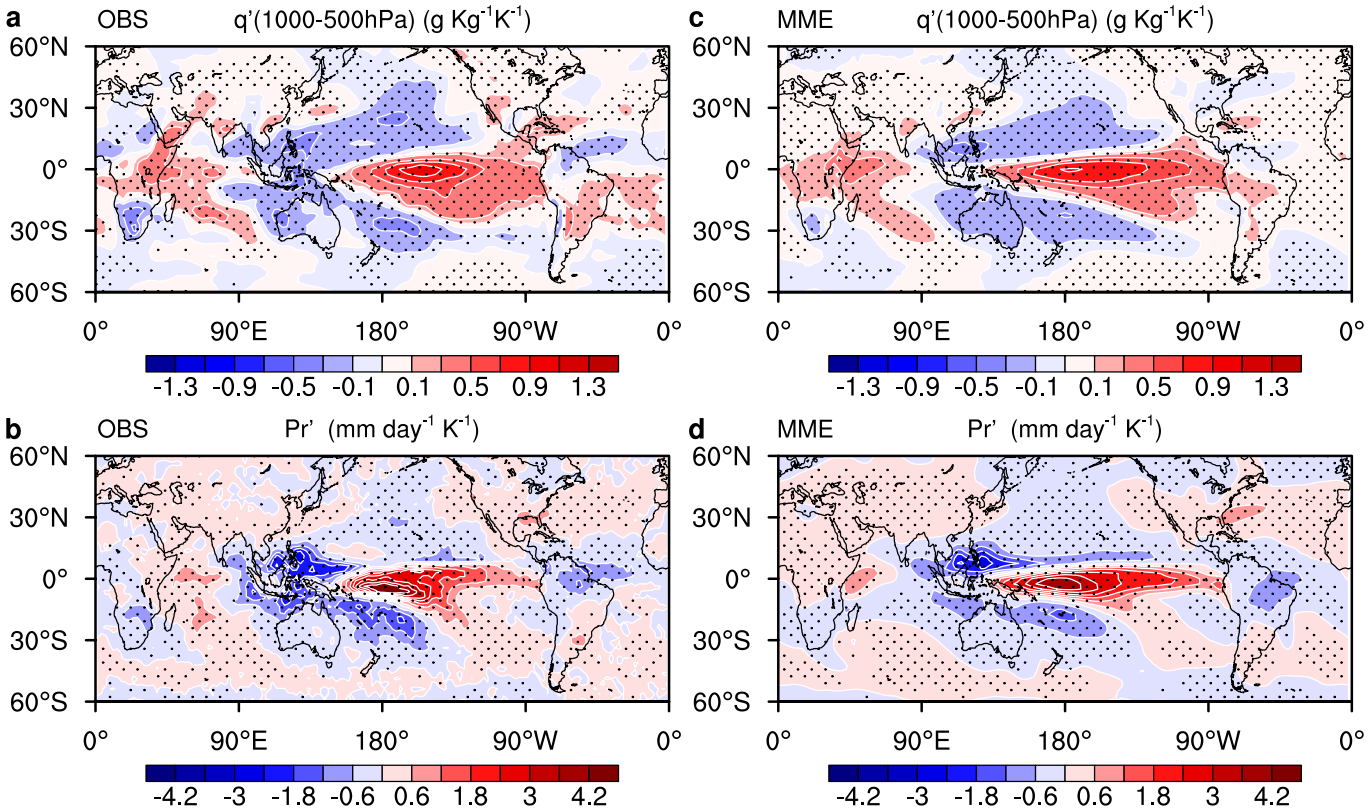

Extended Data Fig. 6 | ENSO-driven DJF anomalies in boreal winter specific humidity and rainfall. a and **c**, ENSO-driven DJF low-level 1000-500hPa vertically averaged specific humidity anomalies (q'). **b** and **d**, ENSO-driven DJF rainfall anomalies (Pr'). Anomalies in **a** and **b** are derived from the observations during 1979-2018, while in **c** and **d** are from the MME during 400-449 model years in the PI control runs. Stippling in **a** and **b** denotes passing 95% confidence level based on a two-tailed Student's t test, and in **c** and **d** indicates that more than 85% of models agree on the sign of the MME.

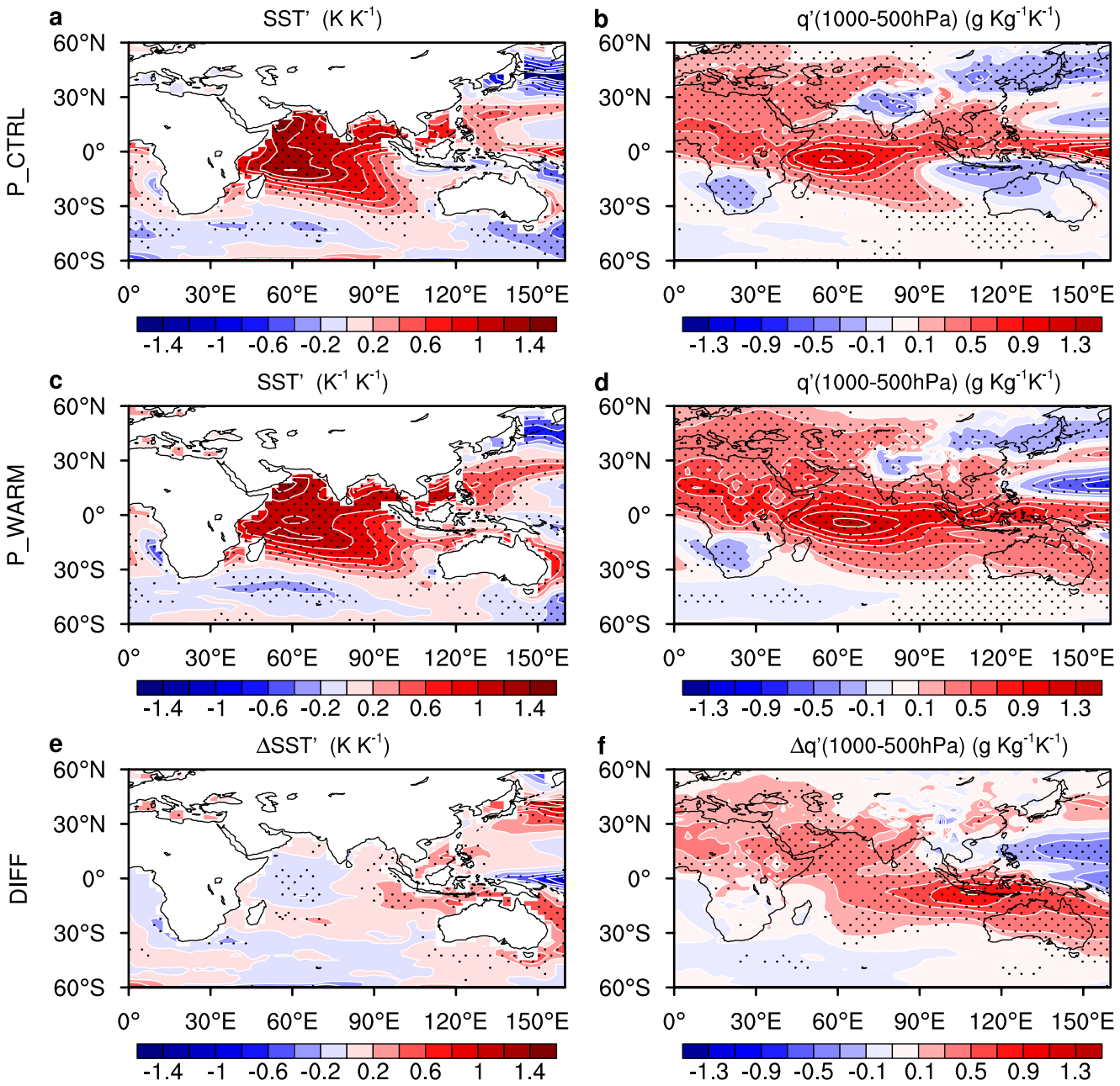

Extended Data Fig. 7 | Changes in the response of specific humidity to tropical Indian Ocean SST variability under global warming. a and **b**, The regression of June-to-August (JJA) mean SST **(a)** and 1000-500hPa vertically averaged specific humidity **(b)** onto a tropical Indian Ocean SST index in the period of P_ctrl. The tropical Indian Ocean SST index is defined as averaging JJA SST anomalies in the domain of 10°S-10°N, 40°E-100°E. **c** and **d**, Similar to **a** and **b** but for the period of P_warm. **e** and **f**, Differences between the two periods (P_warm- P_ctrl). Stippling indicates that more than 85% of models agree on the sign of the MME. The result shows that the response of specific humidity to tropical Indian Ocean SST variability strengthens under global warming.

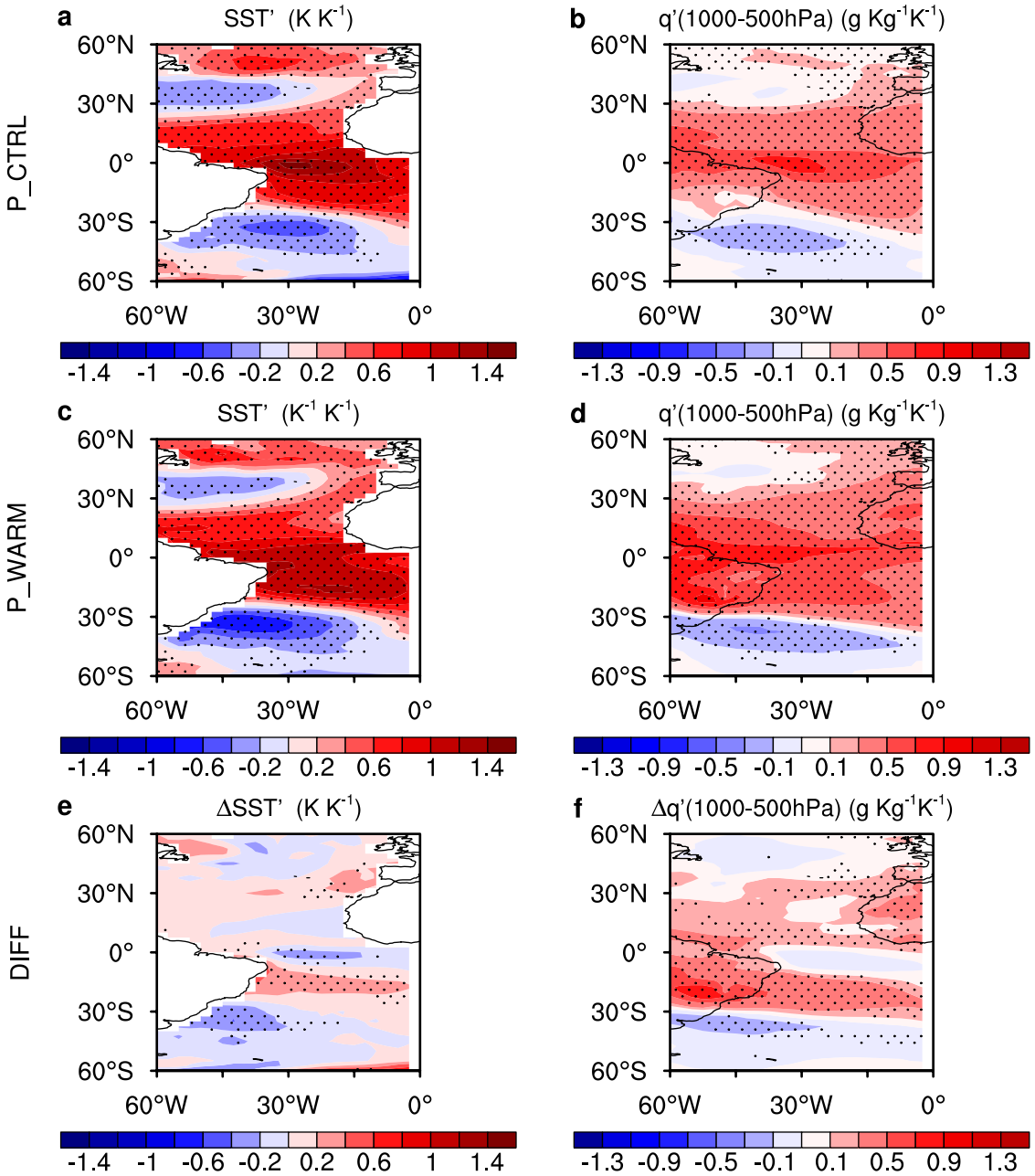

Extended Data Fig. 8 | Changes in the response of specific humidity to tropical Atlantic SST variability under global warming. a and **b**, The regression of JJA SST (**a**) and 1000-500hPa vertically averaged specific humidity (**b**) onto a tropical Atlantic SST index in the period of P_ctrl. The tropical Atlantic SST index is defined as averaging JJA SST anomalies in the domain of 10°S-10°N, 60°W-0°. **c** and **d**, Similar to **a** and **b** but for the period of P_warm. **c** and **d**, Differences between the two periods (P_warm- P_ctrl). Stippling indicates that more than 85% of models agree on the sign of the MME. The result shows that the response of specific humidity to tropical Atlantic SST variability strengthens under global warming.

OCEANOGRAPHY

Dependence of regional ocean heat uptake on anthropogenic warming scenarios

Xiaofan Ma[1,2,3], Wei Liu[2], Robert J. Allen[2], Gang Huang[1,3,4]*, Xichen Li[5]

Copyright © 2020 The Authors, some rights reserved; exclusive licensee American Association for the Advancement of Science. No claim to original U.S. Government Works. Distributed under a Creative Commons Attribution NonCommercial License 4.0 (CC BY-NC).

The North Atlantic and Southern Ocean exhibit enhanced ocean heat uptake (OHU) during recent decades while their future OHU changes are subject to great uncertainty. Here, we show that regional OHU patterns in these two basins are highly dependent on the trajectories of aerosols and greenhouse gases (GHGs) in future scenarios. During the 21st century, North Atlantic and Southern Ocean OHU exhibit similarly positive trends under a business-as-usual scenario but respectively positive and negative trends under a mitigation scenario. The opposite centurial OHU trends in the Southern Ocean can be attributed partially to distinct GHG trajectories under the two scenarios while the common positive centurial OHU trends in the North Atlantic are mainly due to aerosol effects. Under both scenarios, projected decline of anthropogenic aerosols potentially induces a weakening of the Atlantic Meridional Overturning Circulation and a divergence of meridional oceanic heat transport, which leads to enhanced OHU in the subpolar North Atlantic.

INTRODUCTION

Since the industrial era, Earth's energy imbalance has largely been caused by changes in greenhouse gases (GHGs) and aerosols due to human activities (*1*). Global oceans absorb 93% of the net energy (*1*) through air-sea heat flux or in the form of the so-called ocean heat uptake (OHU). Regional OHU change is of great importance for regional sea level change (*2*), transient climate sensitivity and related feedbacks (*3*, *4*), and meridional displacement of the intertropical convergence zone (*5*, *6*). Throughout the historical period (1850–2005), the broad Southern Ocean has accounted for a majority of global OHU while the North Atlantic has taken a relatively smaller share (*7*–*9*). This asymmetry of OHU and ocean heat distribution could be attributed largely to the concurrent increases in GHGs and aerosols during the past century (*10*–*12*) and also to the alterations of deep ocean circulations in these two basins (*13*–*21*). In the North Atlantic, the warming effect of increasing GHGs leads to a weakening of the Atlantic Meridional Overturning Circulation (AMOC) and an increase of OHU, while the cooling effect of increasing aerosols has opposite influences on the AMOC and OHU (*22*, *23*). As a result of the compensation between the effects of aerosols and GHGs, the North Atlantic has shown a relatively small OHU increase during the historical period. On the other hand, anthropogenic aerosols are mainly confined to the Northern Hemisphere (*24*), which is quite different from GHGs that are homogeneously distributed over the globe. Over the Southern Ocean, increasing GHGs have served as one key factor in determining the intensive deep-water upwellings and enhanced OHU (*19*), whereas aerosols have had minimal impacts in this region.

Future emissions of GHGs and aerosols in the 21st century will be different from those in the historical period, as quantified by the Coupled Model Intercomparison Project Phase 5 (CMIP5) Representative Concentration Pathways (RCPs) (*25*). For example, the RCP8.5 scenario is a business-as-usual scenario while the RCP2.6 scenario is a mitigation scenario close to the target of the 2015 Paris Agreement that limits global warming of 1.5°C above preindustrial levels by 2100 (*26*). Both scenarios feature large and similar reductions in anthropogenic aerosol emissions (e.g., ~80% reduction in SO_2 emission by 2100) (*25*) but include different changes in GHG concentrations. For example, atmospheric CO_2 concentration will peak around 2050 and then decrease under the RCP2.6 scenario but will continue to increase throughout the 21st century under the RCP8.5 scenario (*25*). Such different evolutions of aerosols and GHGs will lead to a large scenario-driven uncertainty in regional OHU, indicating that future regional OHU change under the RCP2.6 scenario could be notably different from that under the RCP8.5 scenario (*12*, *22*, *27*). Nevertheless, the characteristics and underlying mechanisms of this scenario-driven uncertainty in regional OHU remain unclear.

RESULTS

Scenario-driven uncertainty in regional OHU

To explore the scenario-driven uncertainty in regional OHU, we examine CMIP5 RCP2.6 and RCP8.5 simulations. We use the multimodel ensemble mean (MME) of 26 CMIP5 models (table S1 and Materials and Methods) to minimize the effects of internal variability and intermodel uncertainty. We examine the long-term trends (Materials and Methods) of regional OHU during the 21st century under both scenarios (Fig. 1). Under the RCP2.6 scenario, OHU exhibits generally opposite trends between hemispheres: a significant positive trend in the subpolar North Atlantic but a negative trend in the Southern Ocean during 2006–2100 (Fig. 1A). These OHU trend patterns are consistent with the time series of regionally averaged OHU (Fig. 1C). In the subpolar North Atlantic, the averaged OHU increases rapidly before 2050 (0.139 W m^{-2} $year^{-1}$, $P < 0.01$) and levels off or declines slightly after that, which corresponds to a positive trend of 0.045 W m^{-2} $year^{-1}$ ($P < 0.01$) during 2006–2100. On the other hand, in the Southern Ocean, the averaged OHU shows a very weak increase by the late 2030s (0.035 W m^{-2} $year^{-1}$, $P < 0.01$) but a large decrease afterward, which corresponds to a negative trend of −0.017 W m^{-2} $year^{-1}$ ($P < 0.01$) during 2006–2100. Note that Southern Ocean OHU begins to decrease one to two decades earlier

[1]State Key Laboratory of Numerical Modeling for Atmospheric Sciences and Geophysical Fluid Dynamics, Institute of Atmospheric Physics, Chinese Academy of Sciences, Beijing 100029, China. [2]Department of Earth Sciences and Planetary Sciences, University of California Riverside, Riverside, CA 92521, USA. [3]University of Chinese Academy of Sciences, Beijing 100049, China. [4]Laboratory for Regional Oceanography and Numerical Modeling, Qingdao National Laboratory for Marine Science and Technology, Qingdao 266237, China. [5]International Center for Climate and Environment Sciences, Institute of Atmospheric Physics, Chinese Academy of Sciences, Beijing 10029, China.
*Corresponding author. Email: hg@mail.iap.ac.cn

Downloaded from http://advances.sciencemag.org/ on November 6, 2020

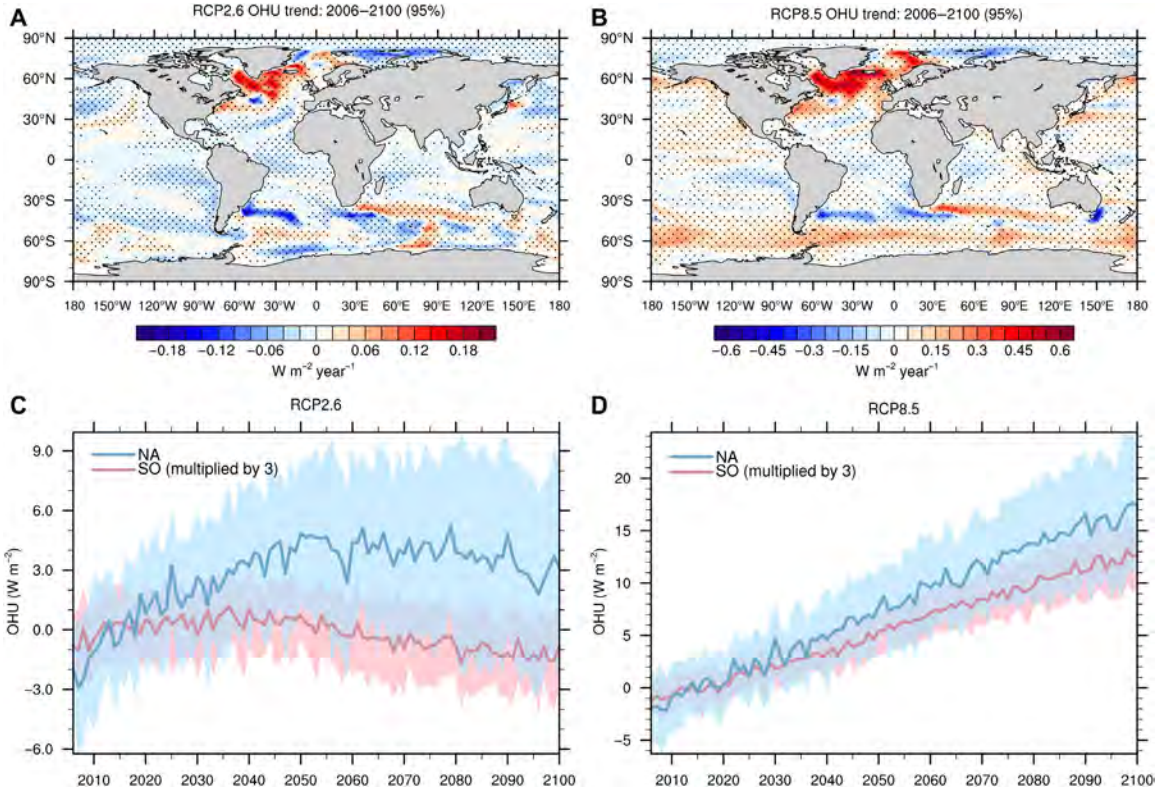

Fig. 1. CMIP5-simulated OHU changes under the RCP2.6 and RCP8.5 scenarios. Top row: CMIP5 MME OHU trends during 2006–2100 under the (**A**) RCP2.6 and (**B**) RCP8.5 scenarios. Stippling denotes where the OHU trends are statistically significant at the 95% confidence level based on the Student's *t* test. Positive (negative) values mean ocean gains (losses) heat. Bottom row: Annual mean OHU anomalies of CMIP5 model averaged over the North Atlantic (35°N to 70°N, 80°W to 10°W; MME, blue curve; model spread, blue shading) and averaged over the Southern Ocean (35°S to 70°S, 0° to 360°; MME, pink curve; model spread, pink shading) during 2006–2100 under the (**C**) RCP2.6 and (**D**) RCP8.5 scenarios. Anomalies are relative to the 2006–2025 mean. Model spread is represented by 1 SD of model results. Southern Ocean OHU anomalies are multiplied by a factor of 3 for a better illustration.

than the decline of CO_2 as projected under the RCP2.6 scenario, which might be associated with the stratospheric ozone recovery since the 2000s (*28*). In contrast, under the RCP8.5 scenario, OHU in both basins shows significant positive trends during 2006–2100, with the stronger one in the North Atlantic (Fig. 1B). For both basins, the regionally averaged OHU increases rapidly throughout the current century, with a larger trend in the North Atlantic (0.209 W m^{-2} $year^{-1}$, $P < 0.01$) relative to the Southern Ocean (0.154 W m^{-2} $year^{-1}$, $P < 0.01$) (Fig. 1D). Here, it merits attention that time series of regionally averaged OHU are not strictly linear in both the North Atlantic and Southern Ocean under both the RCP2.6 and RCP8.5 scenarios, which are largely due to complex trajectories of aerosols and GHGs. To explore the scenario-driven uncertainty in regional OHU, we resort to a common metric—the OHU trend during 2006–2100—to compare the primary regional OHU changes on a centurial time scale between the two scenarios. To summarize, the CMIP5 MME results suggest that regional OHU projections vary substantially between the mitigation and business-as-usual scenarios, which is potentially owing to the different trajectories of anthropogenic aerosols and GHGs between the two scenarios.

In addition, we investigate the relationship between aerosol radiative effect and regional OHU in CMIP5 models. In each model, the total aerosol radiative effect is estimated as aerosol effective radiative forcing (ERF) (Materials and Methods). We demonstrate the relationship between aerosol ERF and regional OHU trend during the 21st century among 15 of the 26 CMIP5 models according to the availability of model aerosol ERF (table S1) (*6*). Over the Southern Ocean, the correlation between aerosol ERF and OHU trend is not significant under both scenarios (Fig. 2, C and D), indicative of a potentially small influence of aerosols on the Southern Ocean OHU, while in the North Atlantic, a significant positive correlation between aerosol ERF and OHU trend is evident under either the RCP2.6 or the RCP8.5 scenario (Fig. 2, A and B), which means that models with stronger aerosol ERFs generally simulate larger centurial OHU trends in the North Atlantic. In addition, the correlation coefficient is larger under the RCP2.6 scenario than that under the RCP8.5 scenario. Under the RCP2.6 scenario, models with no aerosol indirect effects (Materials and Methods) show the smallest OHU trends, while models with both aerosol indirect effects (Materials and Methods) show the largest OHU trends (Fig. 2A). As such, our result confirms the importance of aerosol effects on the North Atlantic OHU, especially for the RCP2.6 scenario, although it might be partially affected by the implicit tuning of models over the historical period due to uncertainty in aerosol ERF and climate sensitivity (*29*, *30*).

Roles of anthropogenic aerosols and GHGs in modulating regional OHU

To further explore the roles of anthropogenic aerosols and GHGs in modulating regional OHU under the RCP2.6 and RCP8.5 scenarios, we choose a broadly used CMIP5 model—the Community Earth

Downloaded from http://advances.sciencemag.org/ on November 6, 2020

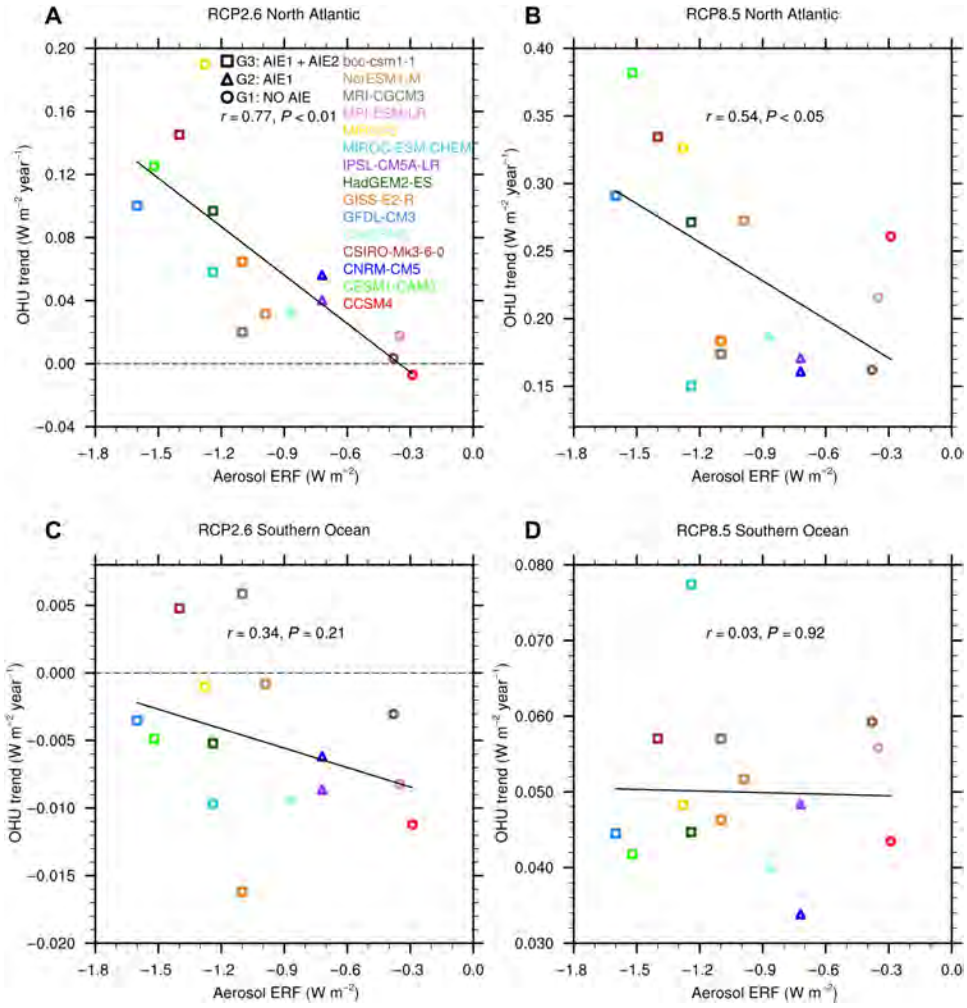

Fig. 2. Relationships between aerosol ERFs and regional OHU trends in CMIP5 models over the 21st century under the RCP2.6 and RCP8.5 scenarios. Top row: Aerosol ERFs of 2000 relative to 1850 and North Atlantic OHU trends of 2006–2100 under the (**A**) RCP2.6 and (**B**) RCP8.5 scenarios in CMIP5 models. Bottom row: As in the top row but for aerosol ERFs and Southern Ocean OHU trends (**C** and **D**). Models are denoted by different colors. Models with no aerosol indirect effects (G1: NO AIE) are denoted by circles. Models with only the first aerosol indirect effects, cloud albedo effects (G2: AIE1), are denoted by triangles. Models with both aerosol indirect effects, cloud albedo and cloud lifetime effects (G3: AIE1 + AIE2), are denoted by squares. Solid black line in each panel represents the linear regression line for the scatters. Correlation coefficient (*r*) between ERFs and OHU trends and *P* value are noted in each case. Notice the different scales in each panel.

System Model version 1 with the Community Atmosphere Model version 5 (CESM1-CAM5; Materials and Methods). CESM1-CAM5 includes both aerosol indirect effects and shows an aerosol ERF of −1.52 W m^{-2} in 2000 relative to 1850, which is strong (table S1) but still within the range of uncertainty estimates of CMIP5 models (for CMIP5 models, 90% confidence level of aerosol ERF corresponds to −2.0 to −0.4 W m^{-2}) (*31*). Given the importance of aerosols to North Atlantic OHU, CESM1-CAM5 projects a large OHU change in the North Atlantic at least partially due to its strong aerosol ERF (Fig. 2, A and B). Nevertheless, this model does well capture the characteristics of centennial OHU evolution patterns as in CMIP5 MME for both North Atlantic and Southern Ocean under both the RCP2.6 and RCP8.5 scenarios. Using CESM1-CAM5, we conduct parallel sensitivity experiments with fixed present-day anthropogenic aerosol emissions (rcpFA26 and rcpFA85 hereafter; Materials and Methods) based on the archived all-forcing CESM1-CAM5 simulations for the RCP2.6 and RCP8.5 scenarios (rcp26 and rcp85 hereafter; Materials and Methods). The difference between the two experiments in each pair (rcp26-rcpFA26 or rcp85-rcpFA85) then yields the net climate effect of future anthropogenic aerosols reduction under each scenario.

We find that major differences of regional OHU changes between rcp26 and rcpFA26 occur in the North Atlantic. OHU exhibits a much stronger positive centurial trend in the subpolar North Atlantic in rcp26 than that in rcpFA26 (Fig. 3, A and C). The regionally averaged OHU time series show that North Atlantic OHU in rcp26 increases throughout the century (0.126 W m^{-2} $year^{-1}$, $P < 0.01$) with a larger rate before 2050 (0.243 W m^{-2} $year^{-1}$, $P < 0.01$), while North Atlantic OHU in rcpFA26 increases before the 2040s and then declines until 2100 (Fig. 4A). On the other hand, OHU changes in the Southern Ocean are highly similar between the two simulations. In both rcp26 and rcpFA26, Southern Ocean OHU exhibits generally negative centurial trends during 2006–2100 (Fig. 3, A and C). The regionally averaged OHU time series depict that Southern Ocean OHU peaks around the 2030s and diminishes afterward (Fig. 4C).

Downloaded from http://advances.sciencemag.org/ on November 6, 2020

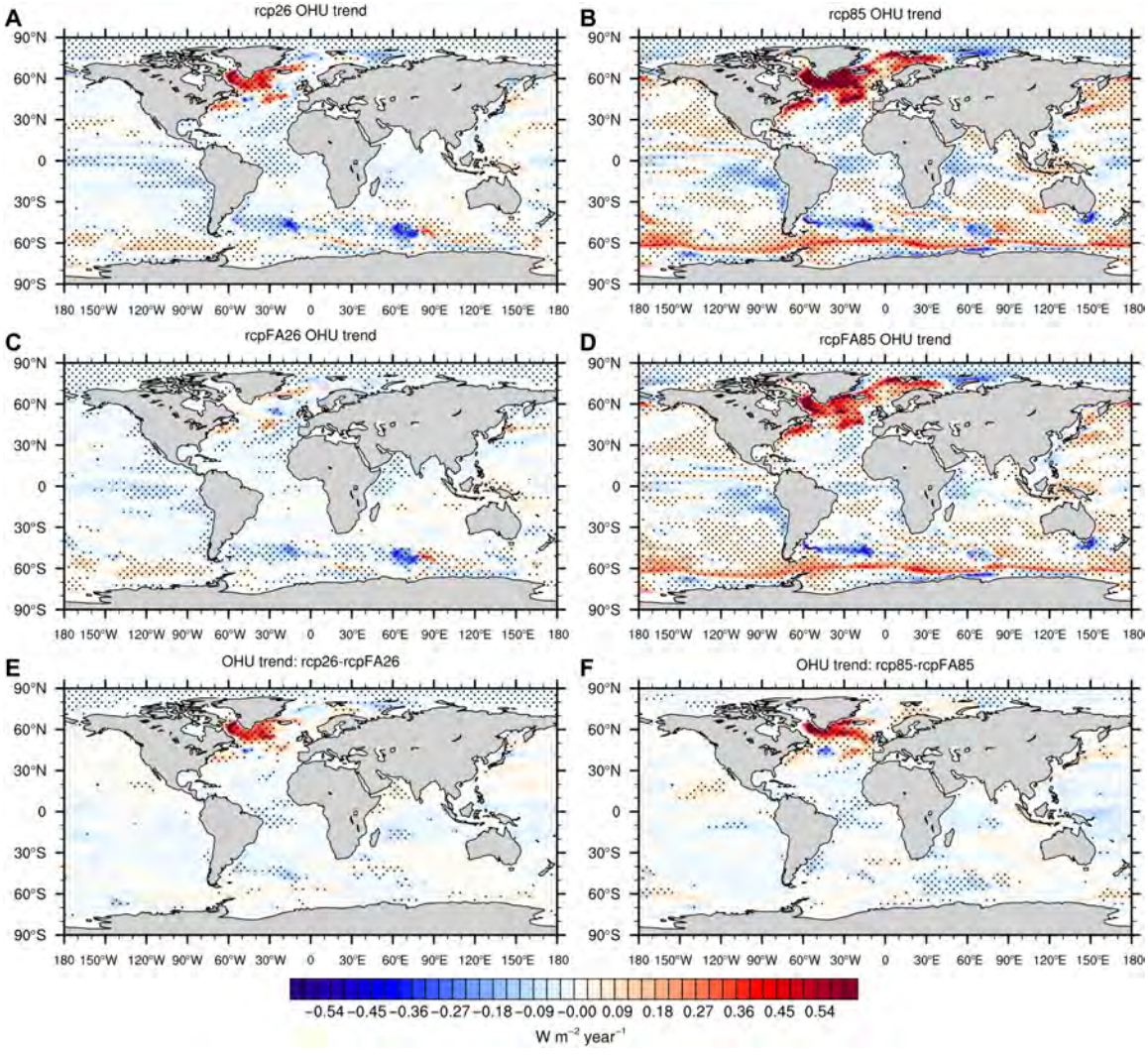

Fig. 3. CESM1-CAM5 OHU trends under the RCP2.6 and RCP8.5 scenarios and aerosol effects on OHU trends. Left column: OHU trends during 2006–2100 (**A**) in rcp26 and (**C**) rcpFA26 simulations with CESM1-CAM5 and (**E**) for their difference (rcp26-rcpFA26), which indicates aerosol effects. Right column: As in the left column but for (**B**) rcp85 and (**D**) rcpFA85 and (**F**) their difference. Stippling denotes where trends are statistically significant at the 95% confidence level based on the Student's *t* test. Positive (negative) values mean ocean gains (losses) heat.

The comparison between rcp26 and rcpFA26 suggests that the interhemispheric contrast of future OHU change is evident only when aerosol effects are included. This is because anthropogenic aerosols mainly concentrate in the Northern Hemisphere and are projected to decline under the RCP2.6 scenario (figs. S1 and S2; see Supplementary Materials), which produces an extra warming effect superimposed on the GHG effect. In the North Atlantic, OHU response is primarily attributed to the total effects of anthropogenic aerosols and GHGs. In rcp26, North Atlantic OHU increases at a larger rate before 2050 and then continues to increase until 2100 (Fig. 4A). This is consistent with the extra aerosol warming effect under the RCP2.6 scenario, as reflected by the aerosol evolution of large decrease before 2050 and continued reduction until 2100 (fig. S2). However, in rcpFA26, North Atlantic OHU decreases after 2050 (Fig. 4A), following the GHG evolution under the RCP2.6 scenario. Differences of North Atlantic OHU between rcp26 and rcpFA26 can be seen from the significant positive long-term trend during 2006–2100 within the subpolar North Atlantic in rcp26-rcpFA26 (Fig. 3E). Over the Southern Ocean, the OHU difference between rcp26 and rcpFA26 is not robust (Figs. 3E and 4C) primarily due to a minimal effect of anthropogenic aerosols.

We also compare rcp85 and rcpFA85 and find that the significant OHU differences due to aerosol effects again occur in the subpolar North Atlantic (Fig. 3F). As anthropogenic aerosols decline under the RCP8.5 scenario (fig. S2), North Atlantic OHU in rcpFA85 shows a smaller positive trend than that in rcp85 (Fig. 3, B and D), largely owing to the lack of aerosol-induced warming. Meanwhile, this difference can be seen from regional averaged OHU time series in which North Atlantic OHU increases at a smaller rate in rcpFA85 (0.241 W m^{-2} $year^{-1}$, $P < 0.01$) than rcp85 (0.379 W m^{-2} $year^{-1}$, $P < 0.01$) during 2006–2100 (Fig. 4B). Over the Southern Ocean, anthropogenic aerosol effects are minimal, while GHG effects are major. Southern Ocean OHU exhibits highly similar evolution patterns in both rcpFA85 and rcp85, featuring continuous increases during

Downloaded from http://advances.sciencemag.org/ on November 6, 2020

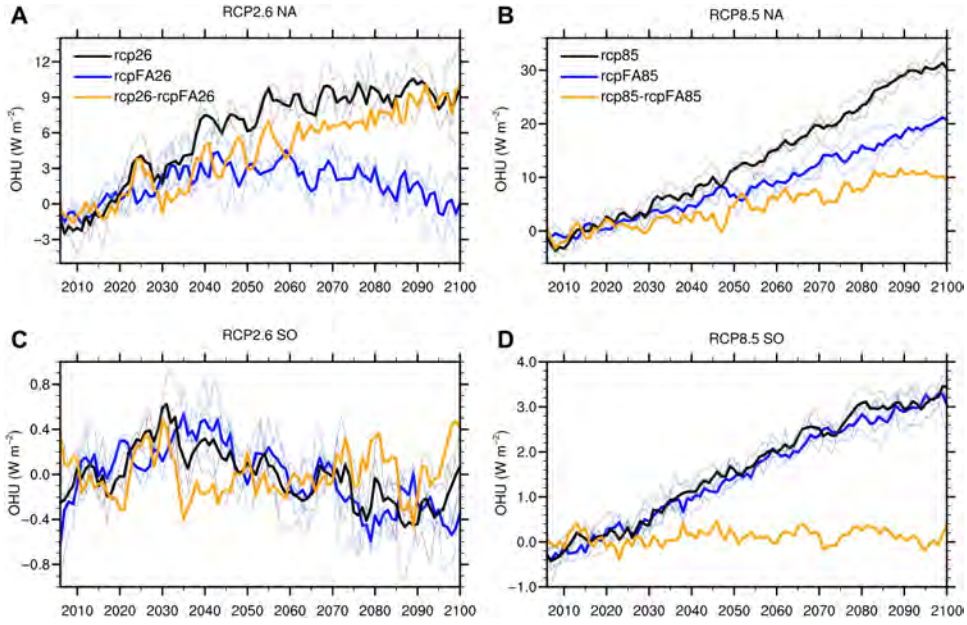

Fig. 4. CESM1-CAM5 regional OHU time series under the RCP2.6 and RCP8.5 scenarios. Top row: Annual mean OHU anomalies averaged over the North Atlantic (NA) (35°N to 70°N, 80°W to 10°W) during 2006–2100 under the (**A**) RCP2.6 and (**B**) RCP8.5 scenarios. Bottom row: As in the top row but for annual mean OHU anomalies averaged over the Southern Ocean (SO) (35°S to 70°S, 0° to 360°) (**C** and **D**). Thick black and blue curves indicate OHU anomalies in rcp and rcpFA simulations with CESM1-CAM5, which are calculated from the ensemble means of individual simulations. Thin black and blue curves denote OHU anomalies for three ensemble members in each of the rcp and rcpFA simulations. Orange lines denote the difference between the ensemble means of rcp and rcpFA simulations, which indicate aerosol effects. OHU anomalies are relative to the 2006–2025 mean and a 5-year running mean is applied. Notice the different scales in each panel.

2006–2100 (Fig. 4D; 0.041 and 0.042 W m^{-2} $year^{-1}$, respectively, both $P < 0.01$). To summarize, our results from CESM1-CAM5 experiments suggest that aerosol effects play an important role in the North Atlantic in future OHU changes under both the RCP2.6 and RCP8.5 scenarios. Projected decline of anthropogenic aerosols enhances OHU in the subpolar North Atlantic, resulting in positive long-term trends during 2006–2100 under both scenarios. Over the Southern Ocean, the effect of aerosols is minimal, while the effect of GHGs is major such that the projected OHU shows negative and positive long-term trends during 2006–2100 under the RCP2.6 and RCP8.5 scenarios, respectively.

Effect of aerosols on ocean heat storage via altering ocean circulation

We discover that the effect of aerosols not only acts on the OHU at Atlantic Ocean surface but also extends deep into the interior ocean and affects ocean heat storage (OHS) through altering ocean circulation and heat transport across the basin. Since 2006, the reduced anthropogenic aerosols trigger a weakened AMOC under both the RCP2.6 and RCP8.5 scenarios (fig. S3), which likely follows the mechanism as described in (*13*). Although the anthropogenic aerosol forcing turns steady after 2050 under the RCP2.6 scenario (fig. S2), the weakening of the AMOC continues, primarily owing to the subsequent ocean adjustments in the interior Atlantic Ocean (*32*). Here, we examine the difference between rcp26 and rcpFA26 simulations during three subperiods: 2006–2050, 2051–2075, and 2076–2100. When comparing the two post-2050 periods (2051–2075 and 2076–2100), we find that the continued AMOC slowdown induces a further cooling of sea surface temperatures (SSTs) in the subpolar North Atlantic (figs. S4B and S5, E and I). The enhanced SST cooling causes a further increase of North Atlantic OHU (Fig. 4A and fig. S4B) primarily via a turbulent heat flux feedback (*33*, *34*) and, meanwhile, a further reduction of evaporation to the south of Greenland (fig. S6, E and H). As a dominant factor, the intensified reduction of evaporation enlarges the surface freshwater input (fig. S6, D and G), acting to freshen the surface water to the south of Greenland. Although either surface cooling (fig. S5, E and I) or freshening (fig. S5, F and J) is present in this deep convection region, the haline effect dominates, which leads to a reduction of local sea surface density (fig. S5, G and K), a suppression of deep convection (fig. S5, H and L), and hence a further weakening of the AMOC (fig. S4B). As this loop continues, SST cooling and OHU increase persist in the subpolar North Atlantic after 2050. Under the RCP8.5 scenario, similar processes also operate (figs. S4, S7, and S8).

We further conduct an ocean heat budget analysis on the Atlantic (*18*, *20*, *21*, *35*, *36*) during 2006–2100 for either scenario using CESM1-CAM5 simulations, which incorporates OHU, OHS, meridional ocean heat transport (OHT), and diffusive processes into a dynamically consistent framework (Materials and Methods). From the difference of the 2006–2100 averages of rcp26 and rcpFA26, we find that the aerosol-driven AMOC change shows the maximum weakening at ~40°N, around the latitude of climatological AMOC maximum under the RCP2.6 scenario (Fig. 5E and fig. S3). This AMOC decline brings about a reduced northward OHT across the Atlantic primarily through its Eulerian-mean component (Fig. 5G). The magnitude of OHT reduction markedly diminishes poleward from ~40°N, leading to a meridional divergence of OHT in the subpolar North Atlantic (Fig. 5I). The OHT divergence acts to cool the whole column ocean waters in the subpolar North Atlantic (fig. S9A), which triggers more heat uptake from the atmosphere via ocean surface (Fig. 5, A and I) to

Downloaded from http://advances.sciencemag.org/ on November 6, 2020

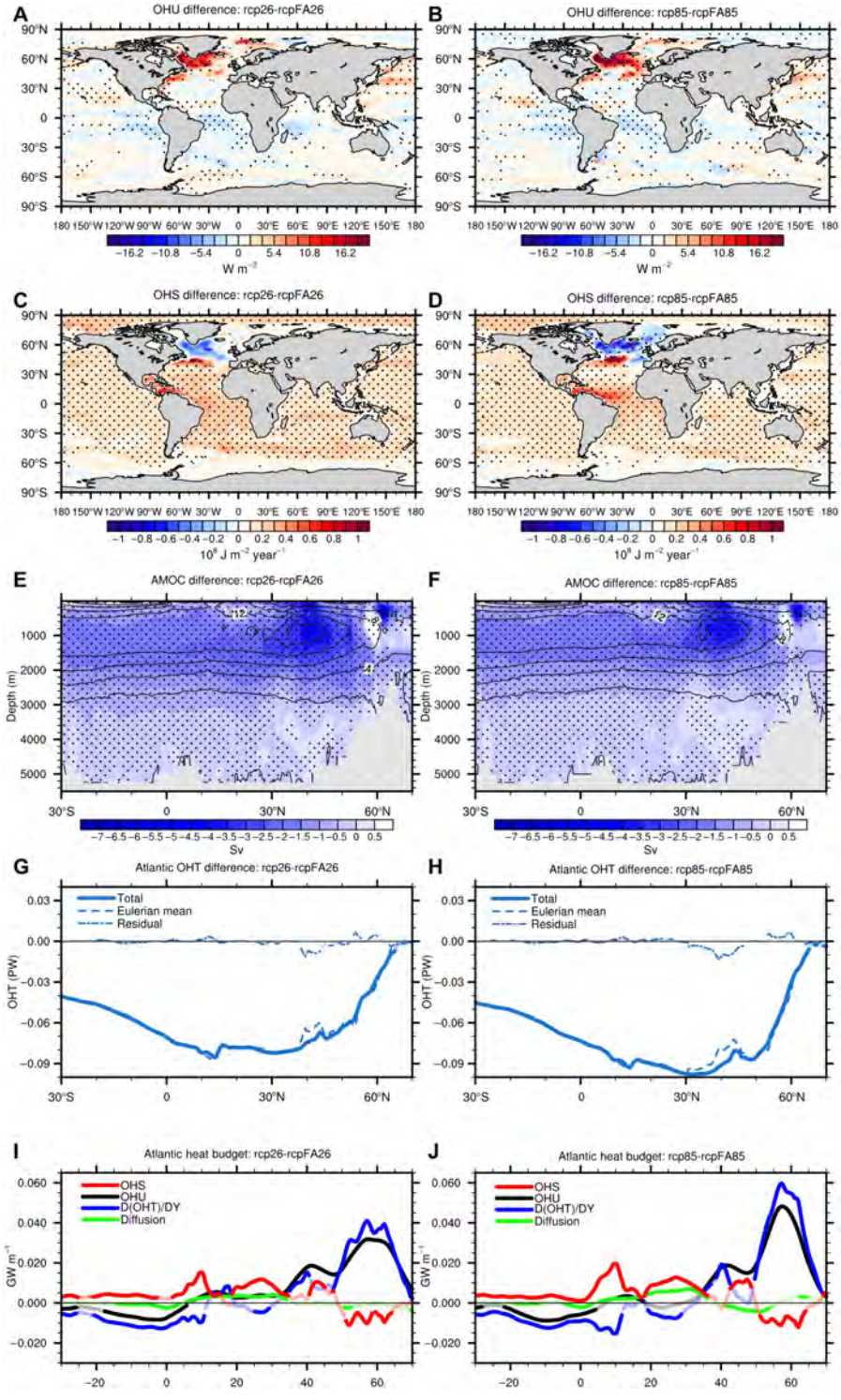

Fig. 5. CESM1-CAM5 aerosol effects on OHU and ocean heat redistribution under the RCP2.6 (left) and RCP8.5 (right) scenarios. Left column: Differences of annual mean (**A**) OHU (positive into the ocean); (**C**) OHS (positive values mean increases of heat in the ocean); (**E**) meridional overturning streamfunction in the Atlantic (negative values denote the weakening of meridional circulation); (**G**) OHT in the Atlantic (positive values denote anomalous northward heat transport): heat transport induced by total advection (solid), Eulerian-mean advection (dashed), and their residual (dotted; including eddy-induced advection and sub-mesoscale advection); (**I**) heat budget in the Atlantic: zonally integrated full-depth OHS (red), zonally integrated OHU (black), divergence of OHT induced by advections (blue), and zonally integrated full-depth heat change due to diffusive processes (green) during 2006–2100 under the RCP2.6 scenario. Right column: As in the left column but for the RCP8.5 scenario (**B**, **D**, **F**, **H**, and **J**). Stippling in the top six panels denotes where differences are statistically significant at the 95% confidence level based on the Student's *t* test. In the bottom four panels, dark colors (relative to light colors) denote where differences are statistically significant at the 95% confidence level based on the Student's *t* test. Contours in (E) and (F) denote the annual mean AMOC averaged over 2006–2100 under the RCP2.6 and RCP8.5 scenarios, respectively. Curves in (I) and (J) are derived after a 7.5° running mean.

Downloaded from http://advances.sciencemag.org/ on November 6, 2020

compensate for this dynamically induced cooling (*37*). Nevertheless, the compensation from enhanced OHU is incomplete, and meanwhile, a small amount of heat can escape from the subpolar region through diffusive processes. As a result, the storage of oceanic heat diminishes in the subpolar North Atlantic (Fig. 5, C and I). Here, note that in the subpolar North Atlantic, the diminished OHS represents a cooling tendency of full-depth ocean waters (fig. S9A) as consistent with the anomalous cooling of SSTs (fig. S10E).

Under the RCP8.5 scenario, the aerosol effect is similar to that under the RCP2.6 scenario. Enhanced OHU is evident over the subpolar North Atlantic (Fig. 5, B and J). The reduction of anthropogenic aerosols induces a weaker and shallower AMOC (Fig. 5F and fig. S3) and results in a redistribution of oceanic heat within the Atlantic. In particular, heat is moved from high-latitude ocean to low-latitude ocean such that OHS decreases in the former region but increases in the latter (Fig. 5D). The significantly decreased OHS in the subpolar North Atlantic is tied to the strong cooling of local full-depth ocean waters (fig. S9B), which is consistent with the cooling of local SSTs (fig. S10F).

DISCUSSION

Our study suggests that during the 21st century, the projected OHU shows respectively positive and negative trends in the North Atlantic and Southern Ocean under the RCP2.6 scenario but collectively positive trends within the two basins under the RCP8.5 scenario. Such large scenario-driven uncertainty in regional OHU projections is tightly related to different evolution patterns of anthropogenic aerosols and GHGs under both scenarios. In the RCP2.6 scenario, anthropogenic aerosol reduction potentially serves as a main factor contributing to the enhanced OHU in the North Atlantic, which is evident from the significant positive correlation between aerosol ERF and OHU trend among CMIP5 models. Over the Southern Ocean, the decreased OHU after the 2030s could be related to the projected GHG decline in the latter half of the century and stratospheric ozone recovery since the 2000s. In the RCP8.5 scenario, both anthropogenic aerosol reduction and GHG increase contribute to the OHU increase in the North Atlantic. Over the Southern Ocean, the rising GHGs promote the OHU increase throughout the 21st century given that the strong GHG effect in this scenario likely overwhelms the effect of ozone recovery. Under both the RCP2.6 and RCP8.5 scenarios, aerosol effects induce an enhanced OHU but diminished storage of oceanic heat in the subpolar North Atlantic. This is due to an aerosol-induced AMOC slowdown, which engenders a redistribution of oceanic heat from high latitudes to low latitudes.

Besides aerosol changes, other forcings such as GHG changes can also induce hemispheric contrast of SSTs and hence OHU. One example is the SST warming minimum or the so-called North Atlantic warming hole (*38*) developed to the south of Greenland under increasing CO_2 (*3*, *39*), which is suggested to be associated with an AMOC slowdown. A similar feature can be found under the RCP8.5 scenario when GHG forcing is exclusively considered (fig. S10D). This GHG-driven warming minimum, however, exhibits a smaller magnitude than that in the full SST response to the total RCP8.5 forcing. This is because the strong SST cooling driven by future anthropogenic aerosol reduction reinforces the warming minimum to the south of Greenland, making the warming hole more evident in the full SST response (fig. S10). Moreover, beyond the RCPs used in CMIP5, multiple shared socioeconomic pathway scenarios have been introduced to current CMIP6 models, which span much broader aerosol emission pathways (*40*). Improved understanding of how anthropogenic emissions affect OHU and ocean circulations under different scenarios is necessary to reduce the uncertainty of climate projections.

MATERIALS AND METHODS

Datasets

Model results from the CMIP5 of the Intergovernmental Panel on Climate Change (*41*) are used to examine OHU trends and its evolution in the North Atlantic and Southern Ocean over 2006–2100 (Fig. 1). Here, based on the availability of surface heat fluxes (SHFs) over 2006–2100, we use 26 CMIP5 models, in which 62 members of CMIP5 RCP2.6 simulation and 66 members of CMIP5 RCP8.5 simulation are analyzed (table S1). CO_2 concentrations in the RCP2.6 and RCP8.5 scenarios (*42*, *43*) are available from the RCP database website (http://tntcat.iiasa.ac.at:8787/RcpDb/dsd?Action=htmlpage&page=about).

Analysis methods

The CMIP5 MME provides an estimate of climate response to external forcing, as internal climate variability is averaged out. For each scenario, we first calculate the ensemble member mean for each model and then average the mean values from all the models to achieve the MME of CMIP5 models. This approach allows equal weighting for each model in the calculation of MME.

The least-square linear regression is used at each grid box to estimate the long-term trends over 2006–2100 for future scenarios. Long-term trends of the difference between "rcp" and "rcpFA" simulations for OHU (Fig. 3), aerosol optical depth (fig. S1), zonal-mean Atlantic Ocean temperature (fig. S9), and SSTs (fig. S10) are calculated to reveal the net anthropogenic aerosol effect. The statistical significance of trends is performed with the Student's *t* test. In Fig. 5, we take the difference between the 2006–2100 means in rcp and rcpFA simulations at each grid box to obtain the net anthropogenic aerosol effect and then calculate the significance for the difference based on the Student's *t* test.

Aerosol radiative effects

Aerosol radiative effects on climate include direct effects in which aerosols scatter and absorb shortwave radiation and indirect effects in which aerosols alter the cloud albedo (first) and cloud lifetime (second). The model representations of aerosol effects are used to further subdivide the CMIP5 models into three groups: those without aerosol indirect effects (NO AIE), those with only the first aerosol indirect effect (AIE1), and those with both aerosol indirect effects (AIE1 + AIE2) (table S1). For climate models, ERF is calculated from the top-of-the-atmosphere (TOA) flux differences between atmosphere-only simulations with identical SSTs but different atmospheric compositions (*44*), and aerosol ERF is calculated as the TOA flux difference between the atmosphere-only simulation with aerosol forcing and that without aerosol forcing. Models that include aerosol indirect effects generally have larger aerosol ERF than models that do not include aerosol indirect effects, and models with both aerosol indirect effects generally have larger aerosol ERF than those with only one aerosol indirect effect (Fig. 2).

The NCAR CESM1-CAM5 and the fixed-aerosol experiments

The CESM1-CAM5 coupled climate model (*45*) from the National Center for Atmospheric Research (NCAR) is used to investigate the

Downloaded from http://advances.sciencemag.org/ on November 6, 2020

responses of OHU and ocean heat redistribution to the projected decline of anthropogenic aerosols under the RCP2.6 and RCP8.5 scenarios. The atmosphere component is the CAM5. The ocean component is the Parallel Ocean Program version 2. The land component is the Community Land Model version 4. The sea ice component is the Community Ice Code version 4. We use the f09_g16 version, with ~1° horizontal resolution and 30 vertical levels in the atmosphere component and ~1° horizontal resolution and 60 vertical levels in the ocean component. In CESM1-CAM5, the total surface freshwater flux into the ocean is computed as a sum of precipitation (P) minus evaporation ($-E$), river runoff (R), freshwater fluxes due to sea ice melting (M), and brine rejection (Br) and other sources.

We use the archived rcp simulations (rcp26 and rcp85) with CESM1-CAM5. Each rcp simulation is composed of three ensemble members over 2006–2100 and is available from the CMIP5 archives. Using CESM1-CAM5, we perform the rcpFA experiments (rcpFA26 and rcpFA85) from 2006 to 2100 under the same RCP scenarios except that the emissions of anthropogenic aerosols and their precursors (including aerosols from biomass burning) are fixed at 2005 levels with a constant annual cycle. All the other forcings are identical as in rcp simulations. For both rcpFA26 and rcpFA85 simulations, we conduct three-member ensemble simulations. Each member starts from 2006 with the initial condition obtained from the archived CESM historical simulations. Unless otherwise specified, the results of CESM simulations presented in this study are based on the three-member ensemble means of individual simulations. In model simulations, the AMOC index is defined as the maximum of streamfunction below 500 m in the Atlantic.

Ocean heat budget analysis

OHU is defined as net downward SHF into the ocean, which is equal to the sum of net surface shortwave radiation flux, net surface longwave radiation flux, latent heat flux, sensible heat flux, and fluxes from other sources. OHS is defined as the tendency of ocean heat content (OHC) and denotes the rate of oceanic heat change for full-depth water column. OHT is defined as the transport of heat by advective processes, including Eulerian-mean, eddy-induced, and sub-mesoscale advective processes.

Along each latitude of the Atlantic, the full-depth ocean heat budget follows

$$\frac{\partial}{\partial t}\int_{X_W}^{X_E}\int_{-H}^{0}\rho_0 c_p\theta dz\,dx = \int_{X_W}^{X_E}(\mathrm{SHF})\,dx - \int_{X_W}^{X_E}\int_{-H}^{0}\rho_0 c_p\ \nabla\cdot(\mathbf{v}\theta)\,dz\,dx + \int_{X_W}^{X_E}\int_{-H}^{0}\rho_0 c_p D\,dz\,dx \quad (1)$$

$\rho_0 = 1026$ kg m^{-3} is seawater density, $c_p = 3996$ J K^{-1} kg^{-1} is the specific heat capacity of seawater, θ is the potential temperature of seawater, H is the depth of ocean bottom, and X_W and X_E denote the longitudes of the western and eastern boundaries of the Atlantic, respectively. ∇ denotes the three-dimensional gradient operator and $\mathbf{v} = \overline{\mathbf{v}} + \mathbf{v}^*$, where $\overline{\mathbf{v}}$ is Eulerian-mean velocity and $\mathbf{v}^*$ denotes the sum of eddy-induced and sub-mesoscale velocities. D denotes diffusive processes.

We then define OHS as

$$\mathrm{OHS} = \frac{\partial}{\partial t}\mathrm{OHC} = \frac{\partial}{\partial t}\int_{X_W}^{X_E}\int_{-H}^{0}\rho_0 c_p\theta\,dz\,dx \quad (2)$$

OHU as

$$\mathrm{OHU} = \int_{X_W}^{X_E}(\mathrm{SHF})\,dx \quad (3)$$

OHT as

$$\mathrm{OHT} = \int_{X_W}^{X_E}\int_{-H}^{0}\rho_0 c_p(\overline{\nabla}\theta + \mathrm{v}^*\theta)\,dz\,dx = \overline{\mathrm{OHT}} + \mathrm{OHT}^* \quad (4)$$

and integrated heat change due to diffusive processes as

$$\mathrm{Diff} = \int_{X_W}^{X_E}\int_{-H}^{0}\rho_0 c_p D\,dz\,dx \quad (5)$$

where $\overline{\mathrm{OHT}} = \int_{X_W}^{X_E}\int_{-H}^{0}\rho_0 c_p\overline{\nabla}\theta dz\,dx$ denotes the OHT by Eulerian-mean advection ($\overline{\nabla}$ is Eulerian-mean meridional velocity) and $\mathrm{OHT}^* = \int_{X_W}^{X_E}\int_{-H}^{0}\rho_0 c_p\mathrm{v}^*\theta dz\,dx$ denotes the OHT by eddy-induced and sub-mesoscale advection (v* is the sum of eddy-induced and sub-mesoscale meridional velocities). Hence, the heat budget (Eq. 1) can be written as

$$\mathrm{OHS} = \mathrm{OHU} - \frac{\partial}{\partial y}\mathrm{OHT} + \mathrm{Diff} \quad (6)$$

As can be seen from Eq. 6, OHS is determined by OHU, meridional gradient (divergence) of OHT, and heat change due to diffusive processes.

SUPPLEMENTARY MATERIALS

Supplementary material for this article is available at http://advances.sciencemag.org/cgi/content/full/6/45/eabc0303/DC1

REFERENCES AND NOTES

1. K. von Schuckmann, M. D. Palmer, K. E. Trenberth, A. Cazenave, D. Chambers, N. Champollion, J. Hansen, S. A. Josey, N. Loeb, P.-P. Mathieu, B. Meyssignac, M. Wild, An imperative to monitor Earth's energy imbalance. *Nat. Clim. Change* **6**, 138–144 (2016).
2. J. M. Gregory, J. A. Church, G. J. Boer, K. W. Dixon, G. M. Flato, D. R. Jackett, J. A. Lowe, S. P. O'Farrell, E. Roeckner, G. L. Russell, R. J. Stouffer, M. Winton, Comparison of results from several AOGCMs for global and regional sea-level change 1900–2100. *Clim. Dynam.* **18**, 225–240 (2001).
3. M. Winton, K. Takahashi, I. M. Held, Importance of ocean heat uptake efficacy to transient climate change. *J. Climate* **23**, 2333–2344 (2010).
4. B. E. J. Rose, K. C. Armour, D. S. Battisti, N. Feldl, D. D. B. Koll, The dependence of transient climate sensitivity and radiative feedbacks on the spatial pattern of ocean heat uptake. *Geophys. Res. Lett.* **41**, 1071–1078 (2014).
5. S. M. Kang, I. M. Held, D. M. W. Frierson, M. Zhao, The response of the ITCZ to extratropical thermal forcing: Idealized slab-ocean experiments with a GCM. *J. Climate* **21**, 3521–3532 (2008).
6. R. J. Allen, O. Ajoku, Future aerosol reductions and widening of the northern tropical belt. *J. Geophys. Res. Atmos.* **121**, 6765–6786 (2016).
7. S. Levitus, J. I. Antonov, T. P. Boyer, O. K. Baranova, H. E. Garcia, R. A. Locarnini, A. V. Mishonov, J. R. Reagan, D. Seidov, E. S. Yarosh, M. M. Zweng, World ocean heat content and thermosteric sea level change (0–2000 m), 1955–2010. *Geophys. Res. Lett.* **39**, L10603 (2012).
8. D. Roemmich, J. Church, J. Gilson, D. Monselesan, P. Sutton, S. Wijffels, Unabated planetary warming and its ocean structure since 2006. *Nat. Clim. Change* **5**, 240–245 (2015).
9. T. L. Frölicher, J. L. Sarmiento, D. J. Paynter, J. P. Dunne, J. P. Krasting, M. Winton, Dominance of the southern ocean in anthropogenic carbon and heat uptake in CMIP5 models. *J. Climate* **28**, 862–886 (2015).
10. R. A. F. Bilbao, J. M. Gregory, N. Bouttes, M. D. Palmer, P. Stott, Attribution of ocean temperature change to anthropogenic and natural forcings using the temporal, vertical and geographical structure. *Clim. Dynam.* **53**, 5389–5413 (2019).
11. D. Paynter, T. L. Frölicher, Sensitivity of radiative forcing, ocean heat uptake, and climate feedback to changes in anthropogenic greenhouse gases and aerosols. *J. Geophys. Res. Atmos.* **120**, 9837–9854 (2015).

Downloaded from http://advances.sciencemag.org/ on November 6, 2020

12. D. B. Irving, S. Wijffels, J. A. Church, Anthropogenic aerosols, greenhouse gases, and the uptake, transport, and storage of excess heat in the climate system. *Geophys. Res. Lett.* **46**, 4894–4903 (2019).
13. M. B. Menary, C. D. Roberts, M. D. Palmer, P. R. Halloran, L. Jackson, R. A. Wood, W. A. Müller, D. Matei, S.-K. Lee, Mechanisms of aerosol-forced AMOC variability in a state of the art climate model. *J. Geophys. Res. Oceans* **118**, 2087–2096 (2013).
14. J. M. Gregory, K. W. Dixon, R. J. Stouffer, A. J. Weaver, E. Driesschaert, M. Eby, T. Fichefet, H. Hasumi, A. Hu, J. H. Jungclaus, I. V. Kamenkovich, A. Levermann, M. Montoya, S. Murakami, S. Nawrath, A. Oka, A. P. Sokolov, R. B. Thorpe, A model intercomparison of changes in the Atlantic thermohaline circulation in response to increasing atmospheric CO_2 concentration. *Geophys. Res. Lett.* **32**, L12703 (2005).
15. A. J. Weaver, M. Eby, M. Kienast, O. A. Saenko, Response of the Atlantic meridional overturning circulation to increasing atmospheric CO_2: Sesnsitivity to mean climate state. *Geophys. Res. Lett.* **34**, L05708 (2007).
16. J. Marshall, J. R. Scott, K. C. Armour, J.-M. Campin, M. Kelley, A. Romanou, The ocean's role in the transient response of climate to abrupt greenhouse gas forcing. *Clim. Dynam.* **44**, 2287–2299 (2014).
17. M. Winton, S. M. Griffies, B. L. Samuels, J. L. Sarmiento, T. L. Frölicher, Connecting changing ocean circulation with changing climate. *J. Climate* **26**, 2268–2278 (2013).
18. C. He, Z. Liu, A. Hu, The transient response of atmospheric and oceanic heat transports to anthropogenic warming. *Nat. Clim. Change* **9**, 222–226 (2019).
19. K. C. Armour, J. Marshall, J. R. Scott, A. Donohoe, E. R. Newsom, Southern Ocean warming delayed by circumpolar upwelling and equatorward transport. *Nat. Geosci.* **9**, 549–554 (2016).
20. A. K. Morrison, S. M. Griffies, M. Winton, W. G. Anderson, J. L. Sarmiento, Mechanisms of southern ocean heat uptake and transport in a global eddying climate model. *J. Climate* **29**, 2059–2075 (2016).
21. W. Liu, J. Lu, S.-P. Xie, A. Fedorov, Southern Ocean heat uptake, redistribution, and storage in a warming climate: The role of meridional overturning circulation. *J. Climate* **31**, 4727–4743 (2018).
22. J.-R. Shi, S.-P. Xie, L. D. Talley, Evolving relative importance of the southern ocean and north atlantic in anthropogenic ocean heat uptake. *J. Climate* **31**, 7459–7479 (2018).
23. M. B. Stolpe, I. Medhaug, J. Sedláček, R. Knutti, Multidecadal variability in global surface temperatures related to the atlantic meridional overturning circulation. *J. Climate* **31**, 2889–2906 (2018).
24. O. Boucher, D. Randall, P. Artaxo, C. Bretherton, G. Feingold, P. Forster, V.-M. Kerminen, Y. Kondo, H. Liao, U. Lohmann, P. Rasch, S. K. Satheesh, S. Sherwood, B. Stevens, X. Y. Zhang, Clouds and Aerosols, in *Climate Change 2013: The Physical Science Basis. Contribution of Working Group I to the Fifth Assessment Report of the Intergovernmental Panel on Climate Change*, T. F. Stocker, D. Qin, G.-K. Plattner, M. Tignor, S. K. Allen, J. Boschung, A. Nauels, Y. Xia, V. Bex, P. M. Midgley, Eds. (Cambridge Univ. Press, 2013).
25. D. P. van Vuuren, J. Edmonds, M. Kainuma, K. Riahi, A. Thomson, K. Hibbard, G. C. Hurtt, T. Kram, V. Krey, J.-F. Lamarque, T. Masui, M. Meinshausen, N. Nakicenovic, S. J. Smith, S. K. Rose, The representative concentration pathways: An overview. *Clim. Change* **109**, 5 (2011).
26. IPCC, Summary for Policymakers, in *Global warming of 1.5°C. An IPCC Special Report on the Impacts of Global Warming of 1.5°C Above Pre-industrial Levels and Related Global Greenhouse Gas Emission Pathways, in The Context of Strengthening the Global Response to the Threat of Climate Change, Sustainable Development, and Efforts to Eradicate Poverty*, V. Masson-Delmotte, P. Zhai, H. O. Pörtner, D. Roberts, J. Skea, P. R. Shukla, A. Pirani, W. Moufouma-Okia, C. P. an, R. Pidcock, S. Connors, J. B. R. Matthews, Y. Chen, X. Zhou, M. I. Gomis, E. Lonnoy, T. Maycock, M. Tignor, T. Waterfield, Eds. (World Meteorological Organization, 2018), 32 pp.
27. S.-M. Long, S.-P. Xie, Y. Du, Q. Liu, X.-T. Zheng, G. Huang, K.-M. Hu, J. Ying, Effects of ocean slow response under low warming targets. *J. Climate* **33**, 477–496 (2020).
28. K. L. Smith, L. M. Polvani, D. R. Marsh, Mitigation of 21st century Antarctic sea ice loss by stratospheric ozone recovery. *Geophys. Res. Lett.* **39**, L20701 (2012).
29. J. T. Kiehl, Twentieth century climate model response and climate sensitivity. *Geophys. Res. Lett.* **34**, –L22710 (2007).
30. R. Knutti, Why are climate models reproducing the observed global surface warming so well? *Geophys. Res. Lett.* **35**, L18704 (2008).
31. N. Bellouin, J. Quaas, E. Gryspeerdt, S. Kinne, P. Stier, D. Watson-Parris, O. Boucher, K. S. Carslaw, M. Christensen, A.-L. Daniau, J.-L. Dufresne, G. Feingold, S. Fiedler, P. Forster, A. Gettelman, J. M. Haywood, U. Lohmann, F. Malavelle, T. Mauritsen, D. T. McCoy, G. Myhre, J. Mülmenstädt, D. Neubauer, A. Possner, M. Rugenstein, Y. Sato, M. Schulz, S. E. Schwartz, O. Sourdeval, T. Storelvmo, V. Toll, D. Winker, B. Stevens, Bounding global aerosol radiative forcing of climate change. *Rev. Geophys.* **58**, e2019RG000660 (2020).
32. M. Kawase, Establishment of deep ocean circulation driven by deep-water production. *J. Phys. Oceanogr.* **17**, 2294–2317 (1987).
33. U. Hausmann, A. Czaja, J. Marshall, Mechanisms controlling the SST air-sea heat flux feedback and its dependence on spatial scale. *Clim. Dynam.* **48**, 1297–1307 (2017).
34. W. Liu, A. V. Fedorov, Global impacts of Arctic sea ice loss mediated by the Atlantic meridional overturning circulation. *Geophys. Res. Lett.* **46**, 944–952 (2019).
35. M. A. Rugenstein, M. Winton, R. J. Stouffer, S. M. Griffies, R. Hallberg, Northern high-latitude heat budget decomposition and transient warming. *J. Climate* **26**, 609–621 (2013).
36. S. Hu, S.-P. Xie, W. Liu, Global pattern formation of net ocean surface heat flux response to greenhouse warming. *J. Climate* **33**, 7503–7522 (2020).
37. W. Liu, A. V. Fedorov, S.-P. Xie, S. Hu, Climate impacts of a weakened Atlantic Meridional Overturning Circulation in a warming climate. *Sci. Adv.* **6**, eaaz4876 (2020).
38. H. Kim, S.-I. An, On the subarctic North Atlantic cooling due to global warming. *Theor. Appl. Climatol.* **114**, 9–19 (2013).
39. C. Li, J.-S. von Storch, J. Marotzke, Deep-ocean heat uptake and equilibrium climate response. *Clim. Dynam.* **40**, 1071–1086 (2013).
40. V. Eyring, S. Bony, G. A. Meehl, C. A. Senior, B. Stevens, R. J. Stouffer, K. E. Taylor, Overview of the coupled model intercomparison project phase 6 (CMIP6) experimental design and organization. *Geosci. Model Dev.* **9**, 1937–1958 (2016).
41. K. E. Taylor, R. J. Stouffer, G. A. Meehl, An overview of CMIP5 and the experiment design. *Bull. Am. Meteorol. Soc.* **93**, 485–498 (2012).
42. D. P. van Vuuren, M. G. J. den Elzen, P. L. Lucas, B. Eickhout, B. J. Strengers, B. van Ruijven, S. Wonink, R. van Houdt, Stabilizing greenhouse gas concentrations at low levels: An assessment of reduction strategies and costs. *Clim. Change* **81**, 119–159 (2007).
43. K. Riahi, A. Grübler, N. Nakicenovic, Scenarios of long-term socio-economic and environmental development under climate stabilization. *Technol. Forecast. Soc. Change* **74**, 887–935 (2007).
44. P. M. Forster, T. Richardson, A. C. Maycock, C. J. Smith, B. H. Samset, G. Myhre, T. Andrews, R. Pincus, M. Schulz, Recommendations for diagnosing effective radiative forcing from climate models for CMIP6. *J. Geophys. Res. Atmos.* **121**, 12460–12475 (2016).
45. J. W. Hurrell, M. M. Holland, P. R. Gent, S. Ghan, J. E. Kay, P. J. Kushner, J.-F. Lamarque, W. G. Large, D. Lawrence, K. Lindsay, W. H. Lipscomb, M. C. Long, N. Mahowald, D. R. Marsh, R. B. Neale, P. Rasch, S. Vavrus, M. Vertenstein, D. Bader, W. D. Collins, J. J. Hack, J. Kiehl, S. Marshall, The community earth system model: A framework for collaborative research. *Bull. Am. Meteorol. Soc.* **94**, 1339–1360 (2013).

Acknowledgments: We thank the National Center for Atmospheric Research for providing the CESM1-CAM5 coupled general circulation model and the World Climate Research Programme's Working Group on Coupled Modelling for providing the CMIP5 multimodel datasets. **Funding:** X.M. and G.H. were supported by the National Natural Science Foundation of China (91937302, 41831175, 41676190, and 41721004), the Chinese Academy of Sciences (COMS2019Q03 and XDA20060501), the National Key R&D Program of China (2018YFA0605904). X.L. is supported by the National Natural Science Foundation of China (41676190 and 41976193). X.M. is supported by the China Scholarship Council. **Author contributions:** X.M. conceived the project, designed model experiments, performed model simulations, carried out the data analysis, and prepared all figures. R.J.A. helped to set up the model simulations. X.M. led the writing of the paper. W.L. and R.J.A. advised on interpretations of the results. All authors discussed the results and commented on the manuscript. **Competing interests:** The authors declare that they have no competing interests. **Data and materials availability:** All data needed to evaluate the conclusions in the paper are present in the paper and/or the Supplementary Materials. Additional data related to this paper may be requested from the authors. The CMIP5 data are publicly available at ESFG data portal (https://esgf-data.dkrz.de/search/esgf-dkrz/).

Submitted 7 April 2020
Accepted 21 September 2020
Published 6 November 2020
10.1126/sciadv.abc0303

Citation: X. Ma, W. Liu, R. J. Allen, G. Huang, X. Li, Dependence of regional ocean heat uptake on anthropogenic warming scenarios. *Sci. Adv.* **6**, eabc0303 (2020).

Downloaded from http://advances.sciencemag.org/ on November 6, 2020

ScienceAdvances

Dependence of regional ocean heat uptake on anthropogenic warming scenarios

Xiaofan Ma, Wei Liu, Robert J. Allen, Gang Huang and Xichen Li

Sci Adv **6** (45), eabc0303.
DOI: 10.1126/sciadv.abc0303

ARTICLE TOOLS http://advances.sciencemag.org/content/6/45/eabc0303

SUPPLEMENTARY MATERIALS http://advances.sciencemag.org/content/suppl/2020/11/02/6.45.eabc0303.DC1

REFERENCES This article cites 43 articles, 1 of which you can access for free
http://advances.sciencemag.org/content/6/45/eabc0303#BIBL

PERMISSIONS http://www.sciencemag.org/help/reprints-and-permissions

Use of this article is subject to the Terms of Service

Science Advances (ISSN 2375-2548) is published by the American Association for the Advancement of Science, 1200 New York Avenue NW, Washington, DC 20005. The title *Science Advances* is a registered trademark of AAAS.

Copyright © 2020 The Authors, some rights reserved; exclusive licensee American Association for the Advancement of Science. No claim to original U.S. Government Works. Distributed under a Creative Commons Attribution NonCommercial License 4.0 (CC BY-NC).

Downloaded from http://advances.sciencemag.org/ on November 6, 2020

LETTERS
PUBLISHED ONLINE: 12 JUNE 2017 | DOI: 10.1038/NCLIMATE3304
nature climate change

Distinct global warming rates tied to multiple ocean surface temperature changes

Shuai-Lei Yao[1,2], Jing-Jia Luo[3]*, Gang Huang[1,2,4]* and Pengfei Wang[1,5]

The globally averaged surface temperature has shown distinct multi-decadal fluctuations since 1900[1–4], characterized by two weak slowdowns in the mid-twentieth century and early twenty-first century and two strong accelerations in the early and late twentieth century. While the recent global warming (GW) hiatus has been particularly ascribed to the eastern Pacific cooling[5,6], causes of the cooling in the mid-twentieth century and distinct intensity differences between the slowdowns and accelerations remain unclear[7,8]. Here, our model experiments with multiple ocean sea surface temperature (SST) forcing reveal that, although the Pacific SSTs play essential roles in the GW rates, SST changes in other basins also exert vital influences. The mid-twentieth-century cooling results from the SST cooling in the tropical Pacific and Atlantic, which is partly offset by the Southern Ocean warming. During the recent hiatus, the tropical Pacific-induced strong cooling is largely compensated by warming effects of other oceans. In contrast, during the acceleration periods, ubiquitous SST warming across all the oceans acts jointly to exaggerate the GW. Multi-model simulations with separated radiative forcing suggest diverse causes of the SST changes in multiple oceans during the GW acceleration and slowdown periods. Our results highlight the importance of multiple oceans on the multi-decadal GW rates.

The Paris Climate Conference in December 2015 has agreed to pursue efforts to limit the global warming (GW) to no more than 1.5 °C above pre-industrial levels by 2100 (ref. 9). The observed annual-mean globally averaged surface temperature (GST) has already risen about 0.89 °C (0.69–1.08 °C, 90% confidence interval)[10] during the period 1900–2012 (Fig. 1 and Supplementary Table 1), leaving room for just another 0.5–0.6 °C warming relative to today for the rest of the twenty-first century. While the early twenty-first-century GW hiatus indicates that the relentlessly increasing greenhouse gases (GHGs) may not always boost the GST warming simultaneously[6], it is yet unclear whether the recent hiatus has surely ended and how strongly GW will resume in the next decades. In addition, it is found that the GW rate since 1900 has experienced a pronounced multi-decadal fluctuation, characterized by two accelerations in the early and late twentieth century and two slowdowns during the mid-twentieth century and the early twenty-first century[1,2] (Fig. 1). Correspondingly, the globally averaged land surface air temperature shows similar multi-decadal modulations. The distinctive multi-decadal fluctuation undoubtedly affects the estimation of centennial mean GW rate[11,12]. Improved understanding of these GW accelerations and slowdowns could help provide a better estimate of the future GW rate for the Paris Climate Agreement.

The estimated rates of the multi-decadal GW accelerations and slowdowns are subject to the time interval selection[13], which is often based on an arbitrary decision[14]. Here, the GW acceleration and slowdown periods are objectively determined according to three thresholds: a maximum magnitude of statistically significant trends in observed GST, relatively low uncertainty among different observations (represented by error bars in Supplementary Fig. 1), and a high percentage of global areas where the merged land air temperature and ocean surface temperature has a statistically significant trend (Supplementary Fig. 1 and Methods). Our approach identifies two periods with maximum accelerations of the GW during 1908–1945 and 1975–1998 and two periods with maximum slowdowns during 1940–1976 and 2001–2012 (Fig. 1).

It is found that observed GST trends during the two acceleration periods are statistically significant across four different observational data sets, whereas those during the two slowdown periods are less significant (Supplementary Table 1), especially for the early twenty-first-century slowdown. The latest slowdown does not show a consistently negative GW rate among the different observations and is statistically insignificant (Supplementary Table 1), probably owing to a relatively short period for the trend estimation. Despite this, the recent GW slowdown has received tremendous attention and has been examined extensively[5,6,8]. The magnitudes of the GW rates during the two slowdown periods are considerably smaller than those during the two acceleration periods. This difference has been explained as being due to the naturally occurring decadal/multi-decadal climate variability halting the steady GW rate attributed to the continuously increasing GHGs emissions[15]. For instance, the recent slowdown has been tied to the equatorial Pacific sea surface temperature (SST) cooling[5,6], which is underpinned by the large impacts of Interdecadal Pacific Oscillation (IPO) on the GST[16,17]. The IPO's impacts are similar but not identical to those exerted by El Niño[18].

Consistent with previous findings[5,6], SST warming (cooling) occurs in the tropical Pacific during the acceleration (slowdown) periods (Supplementary Fig. 2). The SST change differences between the slowdown and acceleration periods bear a close resemblance to the pattern of the cold phase of the IPO[19] or a La Niña-like decadal/multi-decadal variability[20]. This indicates the possible importance of internal climate variability in modulating GW[5,16]. However, notable differences in global SST changes exist among the acceleration and slowdown periods (Fig. 2). While the SST shows a similar warming in the tropical Pacific between the two acceleration periods (Fig. 2a,c), the equatorial central-eastern Pacific cooling during 2001–2012 is far stronger than that during 1940–1976 (Fig. 2b,d). Its magnitude is also greater than those

[1]State Key Laboratory of Numerical Modeling for Atmospheric Sciences and Geophysical Fluid Dynamics, Institute of Atmospheric Physics, Chinese Academy of Sciences, Beijing 100029, China. [2]University of Chinese Academy of Sciences, Beijing 100049, China. [3]Australian Bureau of Meteorology, Melbourne, Victoria 3008, Australia. [4]Laboratory for Regional Oceanography and Numerical Modeling, Qingdao National Laboratory for Marine Science and Technology, Qingdao 266237, China. [5]Center for Monsoon System Research, Institute of Atmospheric Physics, Chinese Academy of Sciences, Beijing 100029, China. *e-mail: J.luo@bom.gov.au; hg@mail.iap.ac.cn

© 2017 Macmillan Publishers Limited, part of Springer Nature. All rights reserved.

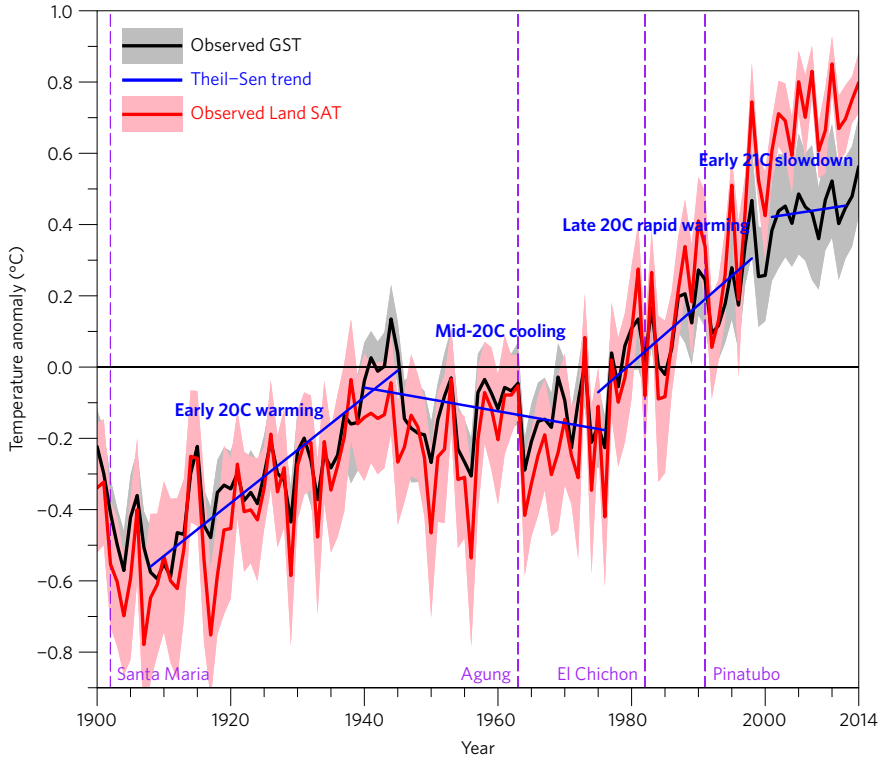

Figure 1 | Observed annual-mean globally averaged surface temperature (GST) and land surface air temperature (SAT) anomalies. Anomalies are relative to 1961–1990 climatology. The grey-shaded and pink-shaded areas represent one standard deviation of the differences among the observed GST and SAT, respectively. The solid blue lines indicate the Theil–Sen trend estimates for the early twentieth-century warming period (1908–1945), the mid-twentieth-century cooling period (1940–1976), the late twentieth-century rapid warming period (1975–1998) and the early twenty-first-century slowdown period (2001–2012), respectively. The vertical purple lines indicate the dates of major volcanic eruptions.

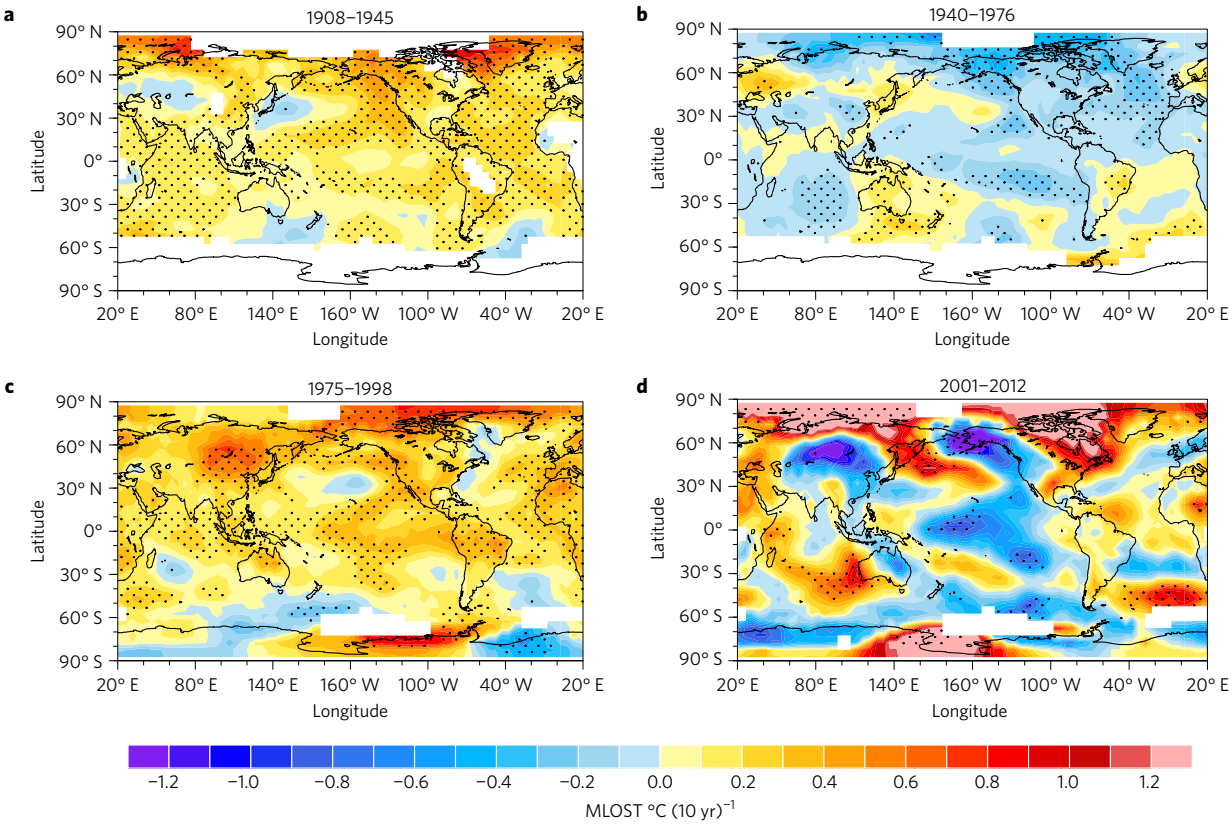

Figure 2 | Observed annual-mean merged land air temperature and ocean surface temperature (MLOST) trend patterns during the two acceleration and slowdown periods. a, 1908–1945. **b**, 1940–1976. **c**, 1975–1998. **d**, 2001–2012. The MLOST trends are estimated on the basis of the ensemble mean of four observations (Methods). White areas represent missing values. Stippling denotes 5% significance according to a two-sided Student's *t*-test.

© 2017 Macmillan Publishers Limited, part of Springer Nature. All rights reserved.

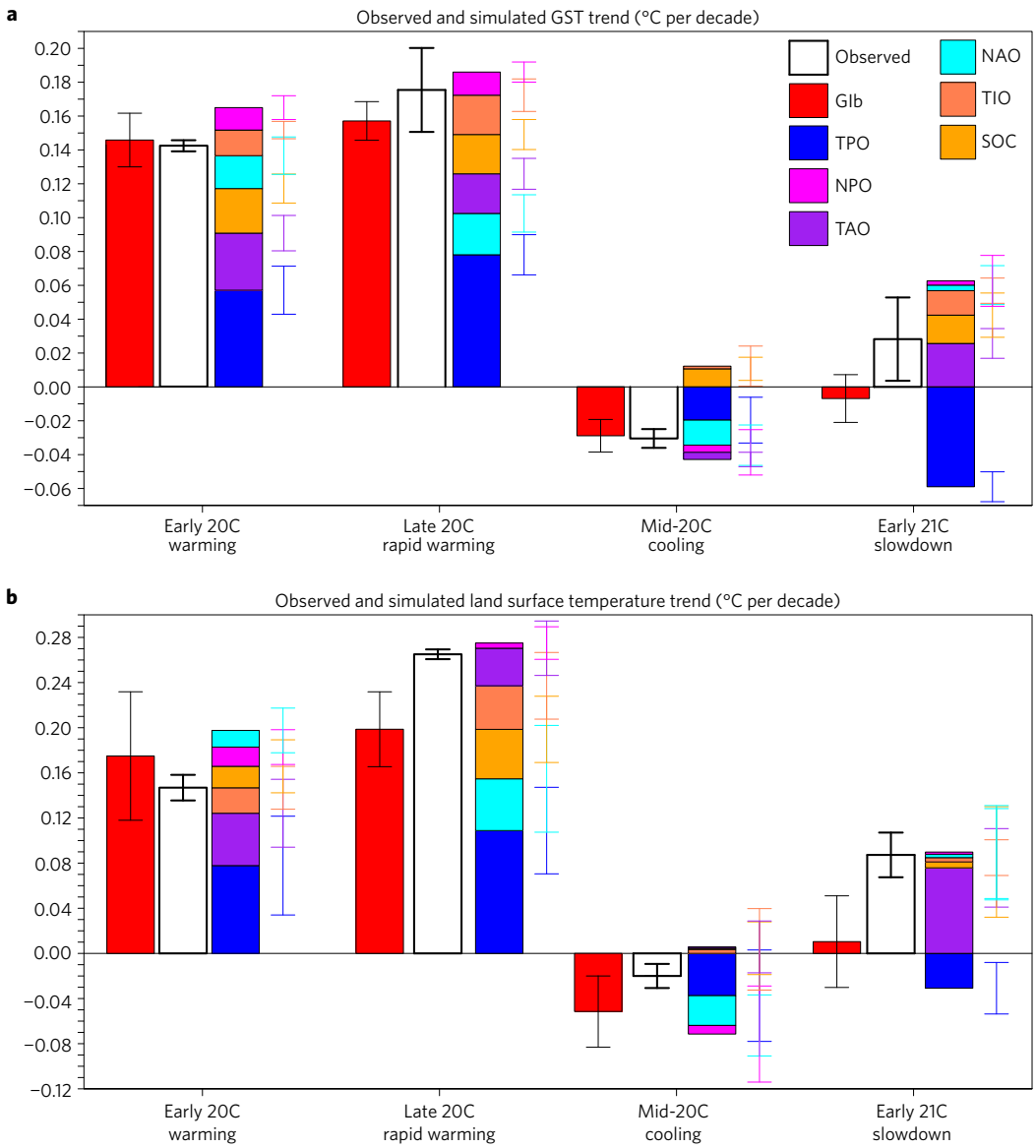

Figure 3 | Near-surface temperature trends during the two acceleration and two slowdown periods. a, Observed GST trends and simulated globally averaged near-surface air temperature trends. **b**, Observed and simulated land surface air temperature trends. The black empty bars indicate the observed ensemble mean GST and land surface air temperature of the four different data sources during each period. The simulated global near-surface air temperature trends include those forced by the global ocean (Glb), tropical Pacific Ocean (TPO), North Pacific Ocean (NPO), tropical Atlantic Ocean (TAO), North Atlantic Ocean (NAO), tropical Indian Ocean (TIO), and Southern Ocean (SOC). The model's simulations are based on six-member ensemble mean for each experiment (Methods). The order of the colour filled bars follows the order of the magnitudes of individual oceans' contributions. The error bars denote one standard deviation of the differences among the four observations (thick black bars) and across six members of each experiment (thin black bars for the global ocean forcing; and individual ocean forcings in colours indicated).

during the two acceleration periods. This is strongly at odds with the differences in GW rates between the slowdown and acceleration periods (compare Fig. 2 and Supplementary Table 1), although the amplified polar surface air temperature warming in the early twenty-first century (Fig. 2d) may partly offset the tropical Pacific-induced cooling effects[21].

A prominent feature during the two acceleration periods is that significant SST warming appears across almost the entire global ocean except patches of weak cooling in the extratropics (Fig. 2). Consistently, surface air temperature warming occurs over the majority parts of global continents (Fig. 2a,c). In contrast, SST cooling during the two slowdown periods does not extend to the entire global ocean (Fig. 2b,d). In particular, extensive warming appeared in the Atlantic, the Indian Ocean, and the extratropical Pacific during 2001–2012, opposite to the strong tropical Pacific cooling (Fig. 2d). Correspondingly, only limited areas of the global continents experienced significant cooling or warming during 2001–2012 (Fig. 2d). These results suggest that, while the tropical Pacific warming/cooling plays a major role, the SST changes in other basins may also have important influences on the GW rates[22–24].

As an attempt to quantify the relative contributions of individual ocean SST changes to the GW rates, we perform a set of atmospheric general circulation model experiments (Methods) in which the global SST trend during the two acceleration and slowdown periods is split into six regions, including the three tropical oceans that have predominant influences on the GST, and the North Atlantic, North Pacific and Southern Ocean (Supplementary Fig. 3). The simulations with the entire global SST trend forcing reproduce the

© 2017 Macmillan Publishers Limited, part of Springer Nature. All rights reserved.

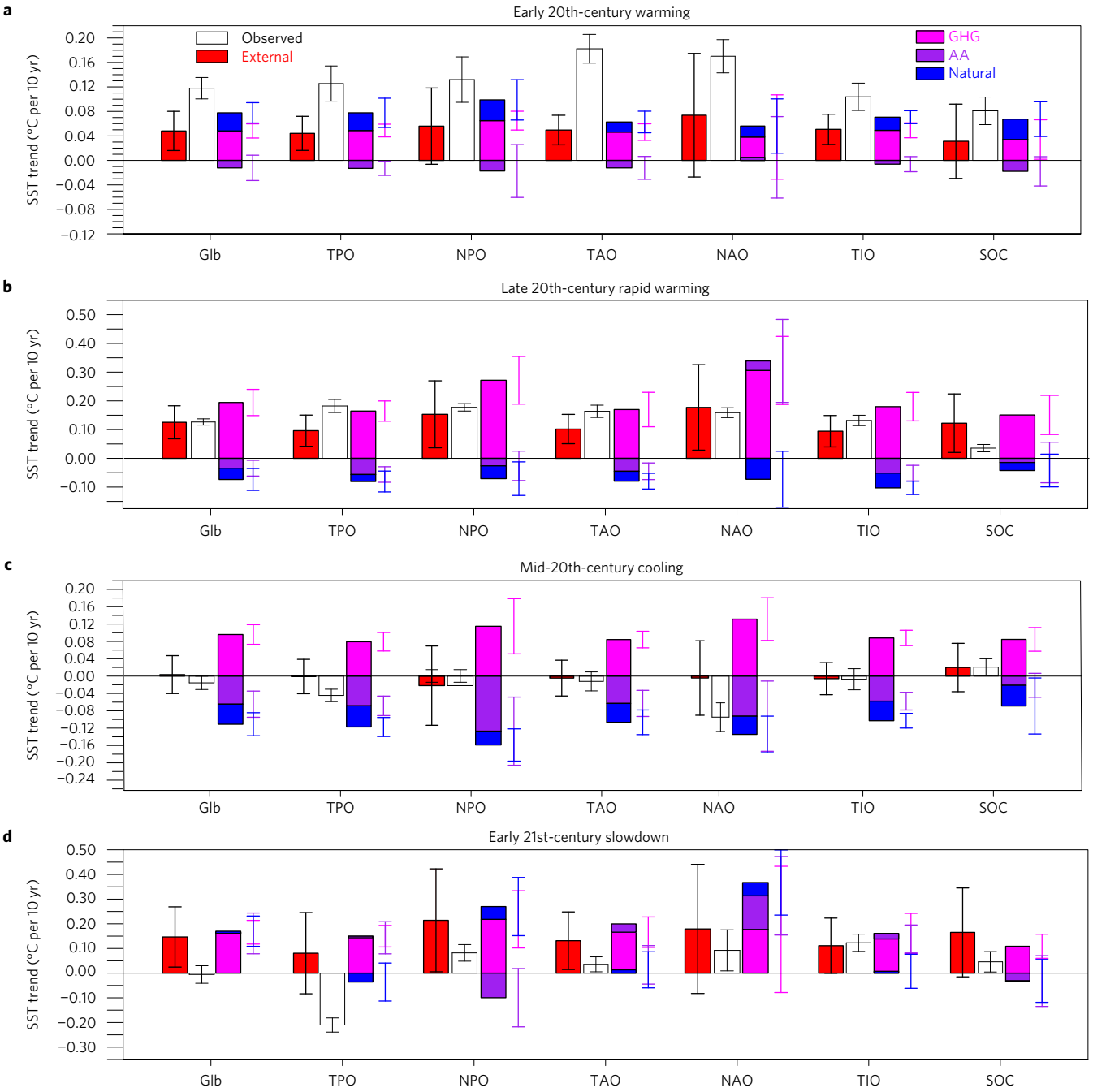

Figure 4 | Observed and CMIP5-simulated SST trends in the global ocean and six individual ocean basins. a–d, SST trends in the global ocean (Glb), tropical Pacific Ocean (TPO), North Pacific Ocean (NPO), tropical Atlantic Ocean (TAO), North Atlantic Ocean (NAO), tropical Indian Ocean (TIO) and Southern Ocean (SOC) from the observations, CMIP5 multi-model ensemble mean historical simulations (External, ideally represent the externally forced trends), multi-model ensemble mean simulation with greenhouse gas forcing only (GHG, Supplementary Table 2), with anthropogenic aerosol forcing only (AA), and with natural forcing only (Natural) for the early twentieth-century warming period (**a**), the late twentieth-century rapid warming period (**b**), the mid-twentieth-century cooling period (**c**) and the early twenty-first-century slowdown period (**d**). The error bars indicate one standard deviation of the differences among four observations (thick black bars) and across CMIP5 models (thin black bars for historical simulations; and individual radiative forcings in colours indicated).

observed GST and land SAT warming during the early and late twentieth century fairly well (Fig. 3a,b, red filled and black empty bars). The model also successfully reproduces the observed GST and land SAT cooling in the mid-twentieth century (Fig. 3a,b). The recent slowdown, however, is not well simulated. While the observations show a muted warming, the model produces a weak GST cooling and a weak land SAT warming; this may be partly because Arctic amplification[21] is not captured (Supplementary Fig. 4d) due to the fact that observed sea-ice changes are not prescribed in the model. Besides, model's GHGs concentrations are fixed for each period and therefore the large direct forcing effect is not simulated (Methods).

The simulated land SAT trends are weaker than the observed (Supplementary Fig. 4c,d), particularly for the late twentieth-century rapid warming and recent slowdown periods; this suggests a role of direct external forcing[25] (Supplementary Information and Supplementary Table 3). The estimated direct forcing effect has

© 2017 Macmillan Publishers Limited, part of Springer Nature. All rights reserved.

persistently increased since 1900, in accordance with the increased trend of CO_2. Despite model deficiencies (Supplementary Information) and possible impacts of internal variability[26,27], the spatial distributions of observed GW trends during the two acceleration and slowdown periods (compare Fig. 2 and Supplementary Fig. 4) are generally well reproduced by the model with the global SST trend forcing, with pattern correlation reaching approximately 0.74, 0.82, 0.57 and 0.46, respectively.

The summed contributions of the SST changes in the six basins to the GW rates during the four inter-decadal periods are close (albeit not equal) to those simulated with the global SST trend forcing (Fig. 3, see Supplementary Information for the nonlinear effect discussion). During the two accelerated warming periods in the early and late twentieth century, the tropical Pacific (occupying ~21.1% of global area) SST warming plays the largest role, accounting for approximately 34% (39%) and 42% (39%) of the total GST (land SAT) warming rates, respectively (Fig. 3a,b). In the early twentieth century, the tropical Atlantic (~8.5% of global area) SST warming plays the second largest role (explaining ~20% and ~23% of the total GST and land SAT warming rates, respectively). In addition, for the two accelerated warming periods, the total SST warming in the Southern Ocean (~22.5% of global surface), North Atlantic (~4.1% of global area), tropical Indian Ocean (~8.4% of global area) and North Pacific (~5.8% of global area) accounts for nearly half and ~45% of the summed GST rates, respectively. These four oceans also explain large portions of land SAT warming rates (totally ~38% and ~49% during the two accelerated warming periods, respectively) and produce extensive warming over the global lands (Supplementary Fig. 5 and Supplementary Information).

During the mid-twentieth century, the cooling in the tropical Pacific plays an important role in the GST cooling, which is nearly equal to the summed contributions of the SST cooling in the North Atlantic, tropical Atlantic and North Pacific (Fig. 3a). Similarly, the summed contribution of the North Atlantic and North Pacific SST cooling to the global land SAT cooling is as important as that of the tropical Pacific (Fig. 3b). In contrast, the SST warming in the Southern Ocean and tropical Indian Ocean acts to increase the GST and land SAT by ~30% and ~7%, respectively, which tends to partly offset the cooling effects of the other oceans (Supplementary Fig. 6 and Supplementary Information). The compensation effect among the different oceans is more striking during the recent slowdown period. The strong cooling in the tropical Pacific generates a GST (land SAT) cooling of approximately −0.059 °C (−0.031 °C) per decade, consistent with the previous finding[5,6]. However, the induced GST and land SAT cooling is completely offset or overwhelmed by the summed warming effects of the tropical Atlantic and Indian Ocean, Southern Ocean, North Pacific and North Atlantic (Fig. 3 and Supplementary Fig. 7 and Supplementary Information).

In summary, our results reveal distinct impacts of individual basin's SST changes on the GW rates between the acceleration and slowdown periods. In the acceleration cases, the SST warming in all the oceans acts jointly to generate strong GW rates. In contrast, in the slowdown cases, the GST cooling induced by the tropical Pacific cooling is reduced or negated by the warming effects in the other oceans, leading to weak GW rates.

Thus, it is the SST changes in multiple oceans, not merely those in the tropical Pacific, that are crucial to determine the GW rates. On the basis of the Coupled Model Intercomparison Project Phase 5 (CMIP5) simulations with various radiative forcing (Methods), we explore possible causes of observed SST changes in individual oceans during the acceleration and slowdown periods. The observed SST warming in the global ocean and individual basins in the early twentieth century is partly reproduced by the multi-model historical simulations due to increased GHGs and natural forcing (Fig. 4a). Note that the difference between the observed and model simulations could be caused by internal variability[28] and errors in models[29] and historical forcings. In contrast, the late twentieth-century SST warming in the global ocean and most of the individual oceans is largely simulated in response to increased GHGs (Fig. 4b), which is partly offset by the cooling effects of anthropogenic aerosols and natural forcing.

In agreement with previous studies[30], our results suggest that increased anthropogenic aerosols during the mid-twentieth-century cooling period induce large cooling in global ocean and individual oceans, which overwhelms the warming effects of increased GHGs (Fig. 4c). However, large discrepancy is seen between the observed and multi-model historical simulations in the tropical Pacific and North Atlantic, which bears a resemblance to the observed SST trend pattern in the mid-twentieth century (Supplementary Fig. 8e). The discrepancy between the observations and multi-model historical simulations becomes more apparent in the tropical Pacific during the recent slowdown period (Fig. 4d and Supplementary Fig. 8g), suggesting that internal variability and/or model errors[29] may play an important role. The external radiative forcing produces generally uniform warming across the global ocean, largely accounting for the basin-wide average SST warming in the other oceans (Fig. 4d and Supplementary Fig. 8h).

The results imply that the SST changes in global and regional oceans during the two accelerations and slowdowns are driven by complicated and distinct mechanisms, which cannot be solely explained by modelled response to external radiative forcing. Improved understanding and projection of the distinct SST changes in multiple oceans between the multi-decadal GW acceleration and slowdown periods could help achieve a more accurate estimate of the future GW rate to better meet the GW target of the Paris Conference, compared with that based on increasing GHG emissions alone and/or a single-ocean SST change alone.

Methods

Methods, including statements of data availability and any associated accession codes and references, are available in the online version of this paper.

Received 12 September 2016; accepted 27 April 2017; published online 12 June 2017

References

1. Kosaka, Y. & Xie, S.-P. The tropical Pacific as a key pacemaker of the variable rates of global warming. *Nat. Geosci.* **9,** 669–673 (2016).
2. Meehl, G. A., Hu, A., Santer, B. D. & Xie, S.-P. Contribution of the Interdecadal Pacific Oscillation to twentieth-century global surface temperature trends. *Nat. Clim. Change* **6,** 1005–1008 (2016).
3. Knutson, T. R., Zhang, R. & Horowitz, L. W. Prospects for a prolonged slowdown in global warming in the early 21st century. *Nat. Commun.* **7,** 13676 (2016).
4. IPCC: Summary for Policymakers. In *Climate Change 2013: The Physical Science Basis* (eds Stocker, T. F. *et al.*) (Cambridge Univ. Press, 2013).
5. Meehl, G. A., Arblaster, J. M., Fasullo, J. T., Hu, A. & Trenberth, K. E. Model-based evidence of deep-ocean heat uptake during surface-temperature hiatus periods. *Nat. Clim. Change* **1,** 360–364 (2011).
6. Kosaka, Y. & Xie, S.-P. Recent global-warming hiatus tied to equatorial Pacific surface cooling. *Nature* **501,** 403–407 (2013).
7. Clement, A. & DiNezio, P. The tropical Pacific ocean—back in the driver's seat? *Science* **343,** 976–978 (2014).
8. Fyfe, J. C. *et al*. Making sense of the early-2000s warming slowdown. *Nat. Clim. Change* **6,** 224–228 (2016).
9. Hulme, M. 1.5 °C and climate research after the Paris Agreement. *Nat. Clim. Change* **6,** 222–224 (2016).
10. Hartmann, D. *et al*. in *Climate Change 2013: The Physical Science Basis* (eds Stocker, T. F. *et al*.) 159–254 (IPCC, Cambridge Univ. Press, 2013).
11. Dai, A., Fyfe, J. C., Xie, S.-P. & Dai, X. Decadal modulation of global surface temperature by internal climate variability. *Nat. Clim. Change* **5,** 555–559 (2015).
12. Watanabe, M. *et al*. Contribution of natural decadal variability to global warming acceleration and hiatus. *Nat. Clim. Change* **4,** 893–897 (2014).

© 2017 Macmillan Publishers Limited, part of Springer Nature. All rights reserved.

13. Santer, B. *et al*. Separating signal and noise in atmospheric temperature changes: the importance of timescale. *J. Geophys. Res.* **116,** D22105 (2011).
14. Karl, T. R. *et al*. Possible artifacts of data biases in the recent global surface warming hiatus. *Science* **348,** 1469–1472 (2015).
15. Bindoff, N. L. *et al*. in *Climate Change 2013: The Physical Science Basis* (eds Stocker, T. F. *et al*.) 867–952 (IPCC, Cambridge Univ. Press, 2013).
16. Meehl, G. A., Hu, A., Arblaster, J. M., Fasullo, J. & Trenberth, K. E. Externally forced and internally generated decadal climate variability associated with the interdecadal Pacific oscillation. *J. Clim.* **26,** 7298–7310 (2013).
17. Trenberth, K. E., Fasullo, J. T., Branstator, G. & Phillips, A. S. Seasonal aspects of the recent pause in surface warming. *Nat. Clim. Change* **4,** 911–916 (2014).
18. Pan, Y. H. & Oort, A. H. Global climate variations connected with sea surface temperature anomalies in the eastern equatorial Pacific Ocean for the 1958–73 period. *Mon. Weath. Rev.* **111,** 1244–1258 (1983).
19. Power, S., Casey, T., Folland, C., Colman, A. & Mehta, V. Inter-decadal modulation of the impact of ENSO on Australia. *Clim. Dynam.* **15,** 319–324 (1999).
20. Luo, J.-J. & Yamagata, T. Long-term El Niño–Southern Oscillation (ENSO)-like variation with special emphasis on the South Pacific. *J. Geophys. Res.* **106,** 22211–22227 (2001).
21. Cowtan, K. & Way, R. G. Coverage bias in the HadCRUT4 temperature series and its impact on recent temperature trends. *Q. J. R. Meteorol. Soc.* **140,** 1935–1944 (2014).
22. Chen, X. & Tung, K.-K. Varying planetary heat sink led to global-warming slowdown and acceleration. *Science* **345,** 897–903 (2014).
23. Drijfhout, S. *et al*. Surface warming hiatus caused by increased heat uptake across multiple ocean basins. *Geophys. Res. Lett.* **41,** 7868–7874 (2014).
24. Keenlyside, N. S. & Ba, J. Prospects for decadal climate prediction. *WIREs Clim. Change* **1,** 627–635 (2010).
25. Booth, B. B., Dunstone, N. J., Halloran, P. R., Andrews, T. & Bellouin, N. Aerosols implicated as a prime driver of twentieth-century North Atlantic climate variability. *Nature* **484,** 228–232 (2012).
26. Swart, N. C., Fyfe, J. C., Hawkins, E., Kay, J. E. & Jahn, A. Influence of internal variability on Arctic sea-ice trends. *Nat. Clim. Change* **5,** 86–89 (2015).
27. Screen, J. A. & Francis, J. A. Contribution of sea-ice loss to Arctic amplification is regulated by Pacific Ocean decadal variability. *Nat. Clim. Change* **6,** 856–860 (2016).
28. Tett, S. F. *et al*. Estimation of natural and anthropogenic contributions to twentieth century temperature change. *J. Geophys. Res.* http://doi.org/10.1029/2000JD000028 (2002).
29. Luo, J.-J., Wang, G. & Dommenget, D. May common model biases reduce CMIP5's ability to simulate the recent Pacific La Niña-like cooling? *Clim. Dynam.* http://dx.doi.org/10.1007/s00382-017-3688-8 (2017).
30. Wilcox, L. J., Highwood, E. J. & Dunstone, N. J. The influence of anthropogenic aerosol on multi-decadal variations of historical global climate. *Environ. Res. Lett.* **8,** 024033 (2013).

Acknowledgements

This work was supported by the National Natural Science Foundation of China (41425019 and 41661144016), and the Public Science and Technology Research Funds Projects of Ocean (201505013). P.W. was supported by the National Natural Science Foundation of China (41375112). We thank the Max Plank Institute for Meteorology for providing the ECHAM5 atmospheric general circulation model, the World Climate Research Programme's Working Group on Coupled Modeling for providing the CMIP multi-model data sets, S.-P. Xie, C. Chung and P. Reid for their helpful comments and/or discussions.

Author contributions

S.-L.Y., J.-J.L. and G.H. conceived the research; J.-J.L. and S.-L.Y. designed the model experiments; S.-L.Y. and P.W. performed numerical simulations; S.-L.Y. performed the data analysis; J.-J.L. and S.-L.Y. wrote the paper; J.-J.L. and G.H. supervised this study.

Additional information

Supplementary information is available in the online version of the paper. Reprints and permissions information is available online at www.nature.com/reprints. Publisher's note: Springer Nature remains neutral with regard to jurisdictional claims in published maps and institutional affiliations. Correspondence and requests for materials should be addressed to J.-J.L. or G.H.

Competing financial interests

The authors declare no competing financial interests.

© 2017 Macmillan Publishers Limited, part of Springer Nature. All rights reserved.

Methods

Data sets. We use the Hadley Centre-Climate Research Unit merged land air temperature and ocean surface temperature (MLOST) version 4.4.0.0 median (HadCRUT4)[31] and global land near-surface air temperature (SAT) version 4.4.0.0 (CRUTEM4)[32], the National Aeronautics and Space Administration Goddard Institute for Space Studies (NASA GISS) GISTEMP[33] with 1,200 km smoothing and global mean land SAT, the National Oceanic and Atmospheric Administration National Climatic Data Center (NOAA NCDC) MLOST version 4.0.0 (ref. 34) and the Global Historical Climatology Network land SAT version 3.3.0, the International Surface Temperature Initiative (ISTI) databank[14] MLOST time series and gridded data sets and land SAT time series for the period 1900–2014. We use monthly mean Centennial In Situ Observation-Based Estimates of the Variability of Sea Surface Temperature (COBE-SST) and version 2 (COBE-SST2)[35], corrected Extended Reconstructed Sea Surface Temperature version 4 (ERSST v4)[14], and merged Hadley-Optimal-Interpolation sea surface temperature and sea-ice concentration data sets[36] for the period 1900–2012. To reduce observational uncertainty, the ensemble mean of the observed MLOST, land SAT and SST from the four different data sets is employed in this study.

We also analyse the multi-model ensemble mean SST provided by the Coupled Model Intercomparison Project[37] (CMIP5) of the Intergovernmental Panel on Climate Change. 128 members of 42 models' historical simulations that are extended from 2006 to 2012 on the basis of RCP4.5 scenario runs, 35 members of 9 models' greenhouse gas (GHG) forcing simulations, 38 members of 10 models' natural forcing simulations, and 21 members of 5 models' anthropogenic aerosol forcing simulations for the period 1900–2012 (Supplementary Table 2) are analysed to investigate causes of the observed SST changes in multiple ocean basins (Fig. 4 and Supplementary Fig. 8). To reduce model uncertainty, we calculate the multi-model ensemble mean of each scenario experiment using the same weight for each model.

Analysis methods. We adopt an optimal piecewise linear regression to fit the trends with increasing time intervals of observed GST and MLOST. On the basis of the following three thresholds: a maximum magnitude of GST trends above 95% confidence level, relatively low observational uncertainty, and a high percentage of grid boxes that show statistical significant trends above 95% confidence level, we detect two robust accelerated warming periods in the early twentieth century (1908–1945) and the late twentieth century (1975–1998), and two global warming (GW) slowdown periods in the mid-twentieth century (1940–1976) and the early twenty-first century (2001–2012) (Supplementary Fig. 1). Note that some of the time windows are slightly overlapped, representing an uncertainty in defining the periods of GW accelerations and slowdowns. Removing the overlapped time intervals among these periods gives similar results. The least-square linear regression and Theil–Sen slope[38] methods are used to estimate the observed GST trends, with the statistical significance being performed with the Student's *t*-test and Mann–Kendall test (Supplementary Table 1). The observed SST and MLOST trends are computed at each grid box where the data availability covers more than 80% of the years during individual GW acceleration and slowdown periods.

AGCM sensitivity experiments. The Max Plank Institute for Meteorology atmospheric general circulation model[39] (AGCM, ECHAM5.4.1) is used to examine the response of globally averaged surface temperature (GST) to the observed SST trend forcing in the global ocean and individual oceans. Given the important impacts of the tropical SST on the GST, we first split the tropical oceans into the tropical Pacific Ocean (TPO), tropical Atlantic Ocean (TAO), and tropical Indian Ocean (TIO). The extratropical regions are then separated into the North Pacific Ocean (NPO), North Atlantic Ocean (NAO) and Southern Ocean (SOC) (Supplementary Fig. 3). We adopt ECHAM5 T63L31, which has a horizontal resolution of ~209 km and 31 vertical layers[39]. In the model sensitivity runs, we prescribe the observed SST trends in the global ocean and six different basins separately with carbon dioxide (CO_2) concentration being fixed to the level at the centre year of the period during 1908–1945, 1975–1998, 1940–1976 and 2001–2012, respectively. An additional model sensitivity experiment, in which the observed CO_2 trend during 1958–2012 is prescribed but the global SST forcing is fixed with the climatological monthly mean of 1981–2010, produces a GW rate of ~0.028 °C per decade and a land SAT warming rate of ~0.07 °C per decade that accounts for ~22% and ~32% of the observed GW rate of ~0.13 °C per decade and observed land SAT warming rate of ~ 0.22 °C per decade averaged during 1958–2012, respectively. To avoid potential instability, a linear buffer zone with a width of five latitudes and longitudes is applied to prescribe the observed SST trends in individual basins (for example, in the tropical Pacific Ocean, the linear buffer zone extends from 30° N to 35° N, 35° S to 30° S, and 115° E to 120° E). For each of the model experiments that are integrated for 30 model years, we perform six-member ensemble simulations in which the same SST and CO_2 forcing is prescribed but their initial conditions are different and provided by an additional model run with climatological SST forcing. Results shown are based on the six-member ensemble mean of individual model experiments. Note that the global mean results are similar if model outputs in areas where the observations are missing during the GW acceleration and slowdown periods are excluded in the model's calculations.

Data availability. The data that support the findings of this study are available from the corresponding authors on request. The model outputs from the ECHAM5 sensitivity experiments are available to readers on request. Other model data are available from the CMIP5 data portal (http://cmip-pcmdi.llnl.gov/cmip5/data_portal.html). Sources for the observed data sets are: HadCRUT4 (ref. 31) and CRUTEM4 (ref. 32) (accessed on 1 October 2015): http://www.metoffice.gov.uk/hadobs/index.html; GISTEMP[33] (accessed on 1 October 2015): https://data.giss.nasa.gov/gistemp; NOAA NCDC[34] (accessed on 30 August 2015): https://www.ncdc.noaa.gov/data-access/marineocean-data/mlost; ISTI[14] (accessed on 15 July 2015): http://www.surfacetemperatures.org; COBE-SST and COBE-SST2 (ref. 35) (accessed on 10 August 2015): https://climatedataguide.ucar.edu/climate-data/sst-data-cobe-centennial-situ-observation-based-estimates; ERSST v4 (ref. 14) (accessed on 10 August 2015): https://www.ncdc.noaa.gov/data-access/marineocean-data/extended-reconstructed-sea-surface-temperature-ersst-v4; Hurrell SST[36] (accessed on 15 August 2015): https://cdp.ucar.edu/security/loginout.htm.

References

31. Morice, C. P., Kennedy, J. J., Rayner, N. A. & Jones, P. D. Quantifying uncertainties in global and regional temperature change using an ensemble of observational estimates: the HadCRUT4 data set. *J. Geophys. Res.* **117,** D08101 (2012).
32. Jones, P. *et al*. Hemispheric and large-scale land-surface air temperature variations: an extensive revision and an update to 2010. *J. Geophys. Res.* **117,** D05127 (2012).
33. Hansen, J., Ruedy, R., Sato, M. & Lo, K. Global surface temperature change. *Rev. Geophys.* **48,** RG4004 (2010).
34. Vose, R. S. *et al*. NOAA's merged land-ocean surface temperature analysis. *Bull. Am. Meteorol. Soc.* **93,** 1677–1685 (2012).
35. Hirahara, S., Ishii, M. & Fukuda, Y. Centennial-scale sea surface temperature analysis and its uncertainty. *J. Clim.* **27,** 57–75 (2014).
36. Hurrell, J. W., Hack, J. J., Shea, D., Caron, J. M. & Rosinski, J. A new sea surface temperature and sea ice boundary dataset for the Community Atmosphere Model. *J. Clim.* **21,** 5145–5153 (2008).
37. Taylor, K. E., Stouffer, R. J. & Meehl, G. A. An overview of CMIP5 and the experiment design. *Bull. Am. Meteorol. Soc.* **93,** 485–498 (2012).
38. Sen, P. K. Estimates of the regression coefficient based on Kendall's tau. *J. Am. Stat. Assoc.* **63,** 1379–1389 (1968).
39. Roeckner, E. *et al*. *The atmospheric general circulation model ECHAM 5. PART I: model description* Report 349 (Max-Planck-Institut für Meteorologie, 2003).

© 2017 Macmillan Publishers Limited, part of Springer Nature. All rights reserved.

Article

Chinese Science Bulletin

SPECIAL ISSUE: Extreme Climate in China

April 2013 Vol.58 No.12: 1402–1411
doi: 10.1007/s11434-012-5593-1

Spatial and temporal variations of light rain events over China and the mid-high latitudes of the Northern Hemisphere

HUANG Gang[1*] & WEN GuanHuan[2,3]

[1] *Key Laboratory of Regional Climate-Environment for East Asia, Institute of Atmospheric Physics, Chinese Academy of Sciences, Beijing 100029, China;*
[2] *Center for Monsoon System Research, Institute of Atmospheric Physics, Chinese Academy of Sciences, Beijing 100190, China;*
[3] *Graduate University of Chinese Academy of Sciences, Beijing 100049, China*

Received August 28, 2012; accepted November 2, 2012; published online January 11, 2013

Based on observed daily precipitation data, monthly gridded radiosonde upper air temperature and sea surface temperature data from the UK Met Office Hadley Centre, monthly surface air temperature from the Climatic Research Unit at the University of East Anglia and the NCEP/NCAR monthly reanalysis data, this study investigates the spatial and temporal variations of light rain events over China and the mid-high latitudes of the Northern Hemisphere during 1961–2010, and discusses the relationship between the change of light rain events and atmospheric stability, sea surface temperature and atmospheric circulation. The light rain events over East China display a decreasing trend of 3.0%/10 a in summer and winter half years. Over Northwest China, an increasing trend of 4.1%/10 a is found in winter half years, but there is no trend in summer half years. Using empirical orthogonal function (EOF) analysis, it is found that the first two principal components of light rain events over the mid-high latitudes of the Northern Hemisphere show long time scale variations in summer and winter half years. The first EOF modes (EOF1s) for summer and winter half years both depict a long-term increase in light rain events over North America and Southern Europe as well as Northwest China (except in summer half years), and a long-term decrease over most of the Eurasia (Central Europe, Eastern Europe, North Asia and East China). The second EOF mode (EOF2) for summer half year shows that light rain events increase over North America, Southern Europe and South China, but decrease over Eurasia north of 45°N from 1961 to early 1980s, while the trends reverse from late 1980s to 2010. The second EOF mode (EOF2) for winter half years indicates that light rain events increase over North America and South and North China, but decrease over Eurasia north of 40°N from 1961 to early 1980s, while the trends reverse from late 1980s to 2009. Correlation analysis and linear regression analysis suggest that EOF1s may be related to the change in atmospheric static stability associated with global warming, and EOF2s are possibly linked to the AMO.

light rain, the mid-high latitudes of the Northern Hemisphere, EOF, atmospheric stability, global warming

Citation: Huang G, Wen G H. Spatial and temporal variations of light rain events over China and the mid-high latitudes of the Northern Hemisphere. Chin Sci Bull, 2013, 58: 1402–1411, doi: 10.1007/s11434-012-5593-1

In recent decades, the global precipitation characteristic has changed significantly, following the continuous rise in the global temperature. In general, there have been increases in land precipitation at high latitudes, and deceases at the tropics and subtropics [1,2]. Precipitation in China as a whole has increased slightly since 1960s, with strong regional and seasonal differences [3–6]. Regionally, precipitation increased in Northwest China, but decreased in North China; seasonally, precipitation increased in winter and summer, but decreased in spring and autumn; precipitation extreme events increased in Northwest China and South China, but decreased in North China. Previous studies [7–12] mainly focused on the precipitation amount and extreme precipitation events, with little attention to the precipitation frequency, especially the light rain frequency. Trenberth [13] indicated that the characteristics of precipitation are just as vital as the total amount, and they are more apt to change as climate changes. Additionally, light rain events account for

*Corresponding author (email: hg@mail.iap.ac.cn)

© The Author(s) 2013. This article is published with open access at Springerlink.com

a large part of the precipitation events, while the proportion of extreme precipitation events is quite small [14,15]. Moreover, light rain soaks into the soil and benefit plants, while the heavy rain may cause local flooding and runoff, leaving soil much drier at the end [1,13]. Previous studies primarily investigated the long-term change of light rain in China. The results of Qian et al. [16] and Fu et al. [17] showed that the summer and annual light rain events (< 1 mm/d) in East China decreased, and the change might be associated with global warming. However, the study of Qian et al. [18] suggested that the light rain decrease in East China be a result of air pollution. Furthermore, Liu et al. [19] found that precipitation events of 0.1–0.3 mm/d decreased in whole China, and indicated that the reduction might be related with the decrease in solar radiation and cloud.

The changes of light rain events over large spatial region have not been well documented, although the decrease in light rain events in East China has been found. Therefore, this study is expected to analyze the spatial and temporal variations of light rain events over the Northern Hemisphere. Although Qian et al. [20] has investigated the long-term change of light rain over North America, Europe and Asia using Global Summary of Day (GSOD) dataset, the results have some uncertainties due to errors and a number of missing values in the dataset that consists of real-time data from Global Telecommunication System (GTS) [21,22]. This study investigates the spatial and temporal variations of light rain events over China and the mid-high latitudes of the Northern Hemisphere based on daily rain gauge precipitation data with quality control, and then discusses the probable causes of these changes.

1 Data and methods

1.1 Data

Data for this study consist of daily rain gauge precipitation dataset, monthly gridded radiosonde upper air temperature dataset [23] and sea surface temperature dataset [24] from the UK Met Office Hadley Centre (Hadley), monthly surface air temperature dataset [25] from the Climatic Research Unit at the University of East Anglia (CRU) and the NCEP/NCAR monthly reanalysis dataset [26].

Daily rain gauge precipitation data includes Global Historical Climatology Network-Daily (GHCN-Daily) station precipitation dataset [21] from the National Climate Data Center (NCDC), European station precipitation dataset [27] from European Climate Assessment and Dataset (ECA&D) project and Chinese station precipitation dataset from China Meteorological Administration (CMA). We replace the precipitation data over China and Europe in GHCN-Daily dataset with those from CMA and ECA&D project, since the GHCN-Daily dataset contain fewer stations in China especially in western China and more missing values in China and Europe especially for some stations in China after late 1990s and for some European stations after 2000.

Monthly gridded radiosonde upper air temperature dataset has a horizontal resolution of 10°×5°, 9 levels from 850 to 30 hPa, which is available starting in January 1958. Monthly sea surface temperature dataset has a horizontal resolution of 1°×1° and is available from January 1870 forward. Monthly surface air temperature has a horizontal resolution of 5°×5°, available from January 1850 forward. The NCEP/NCAR monthly reanalysis dataset includes sea level pressure and air temperature on pressure levels (17 pressure levels from 1000 to 10 hPa), with a horizontal resolution of 2.5°×2.5° and covering the period of January 1948 to present.

1.2 Data quality control

In order to ensure the reliability of the results, the daily precipitation dataset is quality controlled. NCDC has applied a set of quality assurance procedures to GHCN-Daily dataset to detect duplicate data, climatological outliers and various inconsistencies. A detail description was documented by Durre et al. [28]. We remove the data errors failing in quality checks and retain the valid data. ECA&D project has also checked the European station daily precipitation dataset and detected data errors including climatological outliers and negative values. We only use the data passing quality tests. Since the daily precipitation dataset from CMA hasn't been quality controlled by CMA, we detect the climatological outliers, negative values and world record exceedances referring to the quality checks applied to GHCN-Daily [28], and retain the valid data.

In this study, the year with no missing value is classified as usable. A station with no less than 40 usable years during 1961–2010 is accepted in this analysis. As a result, we select 3033 stations over the Northern Hemisphere, with 1135 stations from GHCN-Daily, 1276 stations from ECA&D and 622 stations from CMA. The locations of these stations are shown in Figure 1. Since most of the stations locate over the mid-high latitudes of the Northern Hemisphere with a small number of exception at low latitudes (0°–30°N), the stations at low latitudes have not been excluded in this study.

1.3 Methods

CMA defines light rain as that with daily precipitation less than 10 mm. The 10 mm/d was also selected as the threshold for light rain in Qian et al.'s [18] and Qian et al.'s [20] investigations of the changes of light rain events over East China and North America, Europe and Asia. According to this definition, almost all the stations' light rain events in climatological mean account for more than 50% of precipitation events over the mid-high latitudes of the North Hemisphere, with 50%–80% at mid latitudes and more than 90% at high latitudes and Northwest China (figure not shown). Therefore, a fixed threshold to define light rain may not be

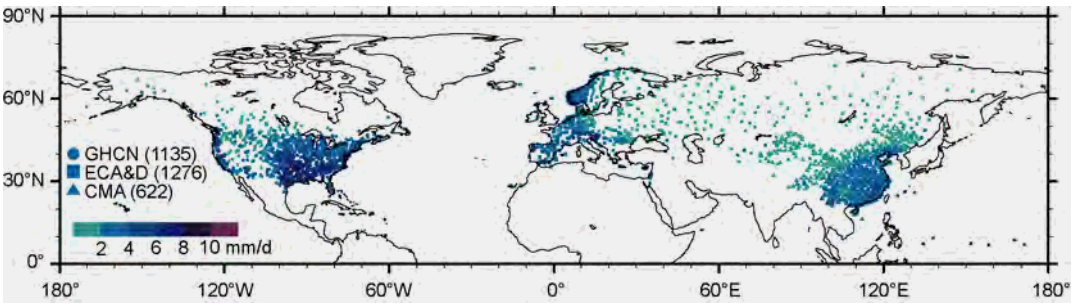

Figure 1 The locations of 3033 precipitation stations and the thresholds for light rain events (the 50th percentile, mm/d). Circles, squares and triangles denote stations from GHCN-Daily, ECA&D, CMA, respectively.

appropriate. Considering regional differences in precipitation, we use percentile threshold to define light rain. The 50th percentile, which is the smallest percentage (47% actually) of precipitation days of less than 10 mm/d accounting for all the precipitation days in all stations, is chosen to be the threshold for light rain. Here, we want to point out that similar results are obtained when the analysis is based on the 30th or 40th percentile. For a station, if the daily precipitation is less than the threshold, then the precipitation event on that day is regarded as a light rain event. We refer to the method of Bonsal et al. [29] and Zhai et al. [30] to calculate the 50th percentile value. Daily precipitation during 1961–1990 is first ranked in ascending order x_1, x_2,$\cdots$, x_m, $\cdots$, x_n. The probability P that a random value is less than or equal to the rank of that value x_m is estimated by the equation of $p=(m-0.31)/(n+0.38)$, in which m is the sequence number of x_m. The 50th percentile value is the x_m when m makes p equal 50%. The thresholds for light rain event of every station are shown in Figure 1, ranging from 6–12 mm/d in Southeast United States, 2–6 mm/d in Southeast China and less than 2 mm/d over most of the mid-high latitudes of the Northern Hemisphere.

Considering the seasonal differences of climate background, this study divides a year into summer half year and winter half year, and analyzes the changes of light rain events in summer and winter half years respectively. Same as the study of Zhai et al. [6], summer half year is from April to September and winter half years is from October to March in the next year.

Linear regression is used to analyze the long-term trends in light rain events over China. Empirical orthogonal function (EOF) analysis is employed to obtain the first two dominant EOF modes and principal components of the light rain events over the mid-high latitudes of the Northern Hemisphere. Like the method of Wu et al. [31], the EOF modes and principal component, are multiplied by the square root of the eigenvalues and the reciprocal of the square root of eigenvalues, respectively. Linear regression and correlation analysis are applied to the investigations of the relationship between the change of light rain events and atmospheric stability, sea surface temperature and atmospheric circulation. The Student's *t*-test is used to examine the significance of the linear regression and correlation.

2 Results and discussion

2.1 Long-term trends in light rain events over China

Previous studies [16–18] mainly focused on the decrease in light rain events over East China, while the change in the rest of China was less studied. Moreover, fixed threshold was often used to define light rain. In this analysis, the changes of light rain events in summer and winter half years based on percentile thresholds are investigated over whole China.

Figure 2(a) shows the long-term trends in light rain events of 622 stations over China for summer half years during 1961–2010. Decreasing trends in light rain events are obvious in East China (east of 100°E). Although more stations in Northwest China (west of 100°E, north of 30°N) have upward trends, most of the trends are not statistically significant. The regionally averaged light rain events in East China has a decreasing trend of 0.9 d/10a or equivalently 3.0%/10 a (Figure 2(b)), which exceeds the 99% confidence level; while there is no significant tendency in regionally averaged light rain events over Northwest China (Figure 2(c)).

Figure 2(d) is the same as Figure 2(a) but for the winter half years during 1961–2009. The light rain events for winter half years in East China primarily exhibit decreasing trends, although the trends for some stations over northern China are not statistically significant and a small number of stations in Northeast China show increasing trends. However, the light rain events for most of the stations in Northwest China have increasing trends. The trend in regionally averaged light rain events in East China is −0.8 d/10 a corresponding to −3.0%/10 a (Figure 2(e)), and that in Northwest China is 0.6 d/10 a or 4.1%/10 a, which both exceed the 99% confidence level (Figure 2(f)).

2.2 Spatial and temporal variations of light rain events over the mid-high latitudes of the Northern Hemisphere

The EOF analysis is applied to the light rain days of 3303

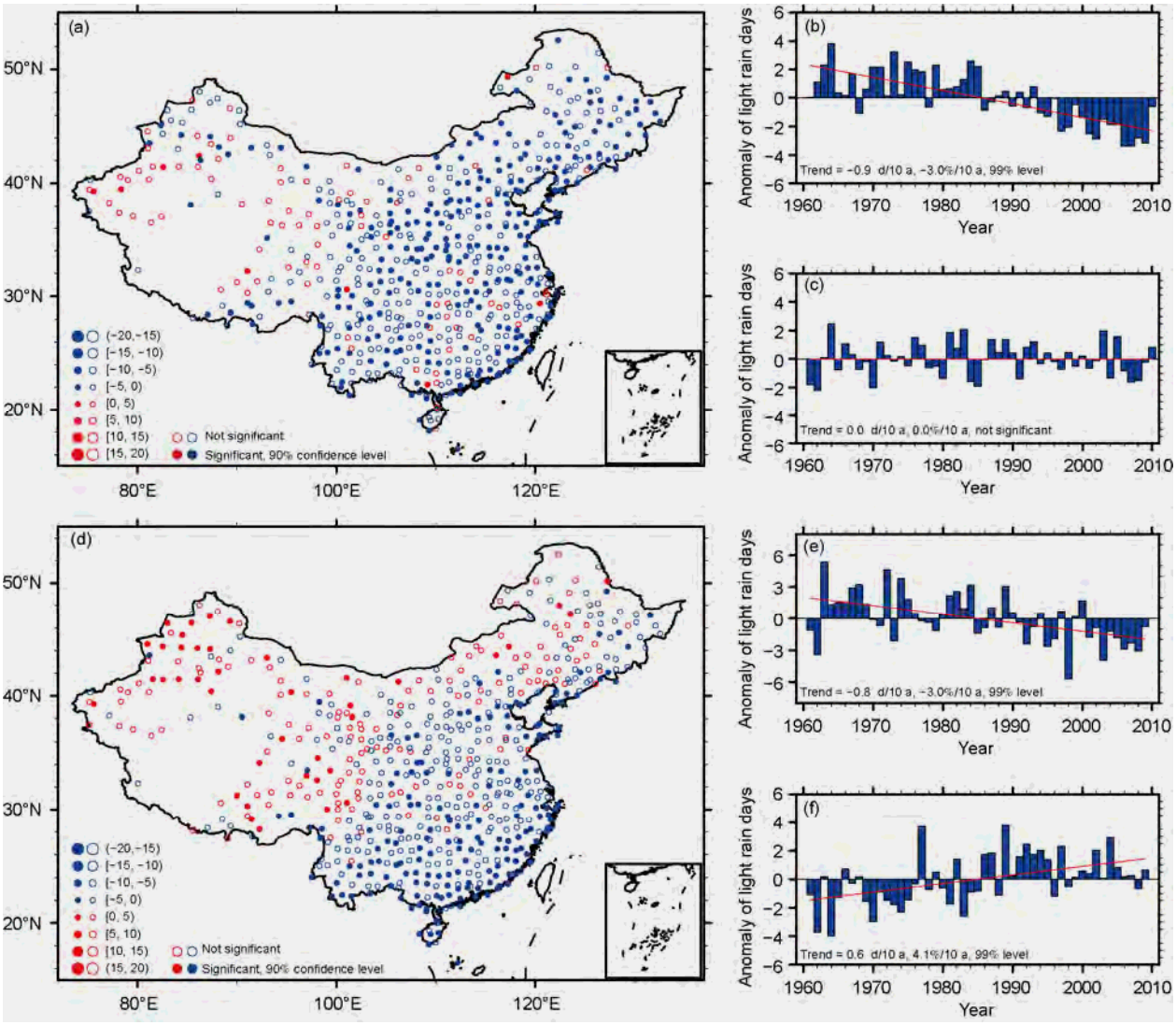

Figure 2 Trends (d/10 a) in light rain days of 622 stations over China (a) and light rain day anomalies (d) averaged over East China (east of 100°E) (b) and Northwest China (c) in summer half years during 1961–2010. (d), (e) and (f) are the same as (a), (b) and (c), respectively, but for winter half years.

stations over the mid-high latitudes of the Northern Hemisphere in summer and winter half years during 1961–2009 respectively. The first two EOF modes and the corresponding principal components for summer and winter half years, which explain about 10.2% and 5.2% of the total variances for summer half years and 10.3% and 6.5% for winter half years, are shown in Figure 3.

The first two principal components (PCs) for summer half years indicate slow variations of light rain events (Figure 3(c)). PC1 represents the long-term trends during 1961–2010 and, PC2 depicts the two opposite trends during 1961 to early 1980s and during late 1980s to 2010. The first EOF mode (EOF1, Figure 3(a)) for summer half years is characterized by a positive anomaly covering North America, Southern Europe and a negative anomaly covering most of the Eurasia including Central and Eastern Europe, North Asia (east of the Urals, about east of 60°E) and East China. As mentioned above, the corresponding principal component (PC1) represents the long-term trends in recent 50 years. Therefore, the EOF1 and PC1 indicate that the light rain events in summer half years increase over North America and Southern Europe during 1961–2010, but decrease over most of the Eurasia (Central and Eastern Europe, North Asia and East China), especially in East China. The second EOF mode (EOF2, Figure 3(b)) for summer half years is characterized by a negative anomaly in North America, Southern Europe and South China and a positive anomaly over Eurasia north of 45°N. The second principal component (PC2) depicts a decreasing trend from 1961 to early 1980s and an increasing trend from late 1980s to 2010. Hence, the EOF2 and PC2 reveal that the light rain events in summer half years increase in North America, Southern Europe and South China during 1961 to early 1980s, but decrease over Eurasia north of 45°N; the trends reverse in these areas during late 1980s to 2010.

The leading two principal components of light rain events

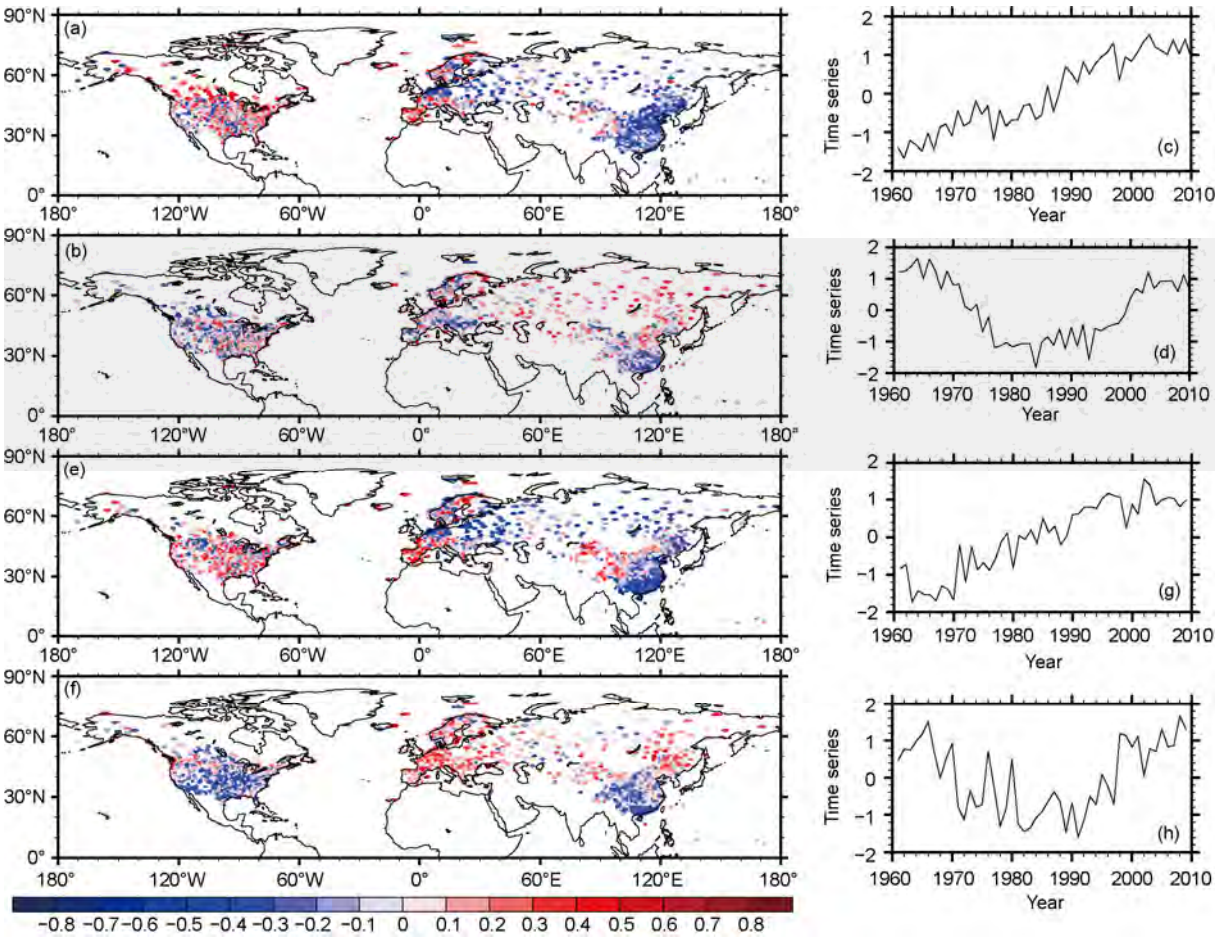

Figure 3 The first EOF mode (a) and the second EOF mode (b) of light rain days over the mid-high latitudes of the North Hemisphere and the first principal components (c) and the second principal components (d) for summer half years during 1961–2010. (e), (f), (g) and (h) are the same as in (a), (b), (c) and (d), respectively, but for winter half years.

in winter half years are similar to those for summer half years respectively, with PC1 (Figure 3(g)) depicting long-term change and PC2 (Figure 3(h)) describing opposite trends during periods of 1961 to early 1980s and late 1980s to 2009. The first EOF mode (EOF1, Figure 3(e)) for winter half years is also similar to that for summer half years except for Northwest China where the long-term change of light rain events is significant. The EOF1 for winter half years is characterized by a positive anomaly covering North America, Southern Europe and Northwest China and a negative anomaly covering most of the Eurasia (Central and Eastern Europe, North Asia and East China). This indicates that the light rain events in winter half years increase over North America, Southern Europe and Northwest China during 1961–2010, but decrease over most of Eurasia (Central and Eastern Europe, North Asia and East China). The second EOF mode (EOF2, Figure 3(f)) for winter half years is analogous to that for summer half years except for Southern Europe, where the change for winter half years is contrary to summer half years. The EOF2 for winter half years shows a negative anomaly in North America, South and North China and a positive anomaly over Eurasia north of 40°N. This implies that the light rain events in winter half years increase in North America, South and North China during 1961 to early 1980s, and decrease over Eurasia north of 40°N; the trends reverse in these areas during late 1980s to 2009.

2.3 Discussion

Precipitation events are generally accompanying upward motions. The vertical motion is usually associated with the atmospheric stratification, in other words, it is associated with the vertical distribution of atmospheric temperature and humidity. Unstable atmospheric stratification favors upward motion and heavy precipitation, while stable atmospheric stratification suppresses the upward motion and is unfavorable for intense precipitation [32]. Thus the change of atmospheric static stability may influence the change of light rain events. While the atmospheric stability strengthens, the upward motion abates so that the precipitation intensity decreases and light rain events increase. When the atmospheric stability weakens, the upward motion strengthens so that the precipitation intensity increases and

light rain events decrease. As mentioned above, the first principal component of light rain events in both summer and winter half years represent the long-term trend during 1961–2010. This section mainly investigates the relationship between the trend of light rain events and the atmospheric stability over the mid-high latitudes of the Northern Hemisphere.

Figure 4(a) and (b) shows the trend of lower troposphere temperature difference between lower and upper level in summer half years during 1961–2010, based on reanalysis air temperature from the NCEP/NCAR and upper radiosonde temperature from Hadley Centre, surface air temperature from CRU, respectively. The result from NCEP/NCAR reanalysis air temperature (Figure 4(a)) indicates that the temperature difference between 1000 and 700 hPa decrease over the mid latitudes of North America in recent 50 years, where the temperature difference between surface air temperature from CRU and radiosonde temperature at 700 hPa from Hadley Center (Figure 4(b)) also shows a decreasing trend. Thus, both datasets imply that the atmospheric stability strengthens over the mid latitudes of North America. As mentioned above, the light rain events for summer half years increase over North America. The air temperature differences between lower level and upper level decrease and the atmospheric stability weakens over Central and Eastern Europe, North Asia and East China (Figure 4(a), (b)), where the light rain events decrease. The air temperature differences in winter half years from reanalysis data (Figure 4(d)) and from CRU data and Hadley Centre radiosonde data (Figure 4(e)) have decreasing trends over the mid latitudes of North America and Southern Europe (not shown in Figure 4(d) for statistical significance). This indicates that the atmospheric stability strengthens. The air temperature differences in winter half years have increasing trends over Central and Eastern Europe, North Asia and East China (except for South China in reanalysis data) based on CRU and Hadley Centre data (Figure 4(e)) and the NCEP/NCAR reanalysis data (Figure 4(d)). This corresponds to the light rain events decrease over Central and Eastern Europe, North Asia and East China. The reanalysis data (Figure 4(d)) show that the temperature differences between lower and upper level in winter half years decrease and the atmospheric stability strengthens over South and Northwest China, while the observed data (Figure 4(e)) indicate that the atmospheric stability weakens over South and Northwest China. The contrary results from different data make it difficult to verify the association between the change of light rain events and atmospheric stability over South and Northwest China. From the above analysis, in most of the areas light rain events increase when atmospheric stability strengthens and light rain events decrease when atmospheric stability weakens. However, there are still some exceptions. For example, the air temperature difference between surface and 700 hPa in summer half years based on observed data increase and atmospheric stability weakens over Southern Europe (Figure 4(b)), but the light

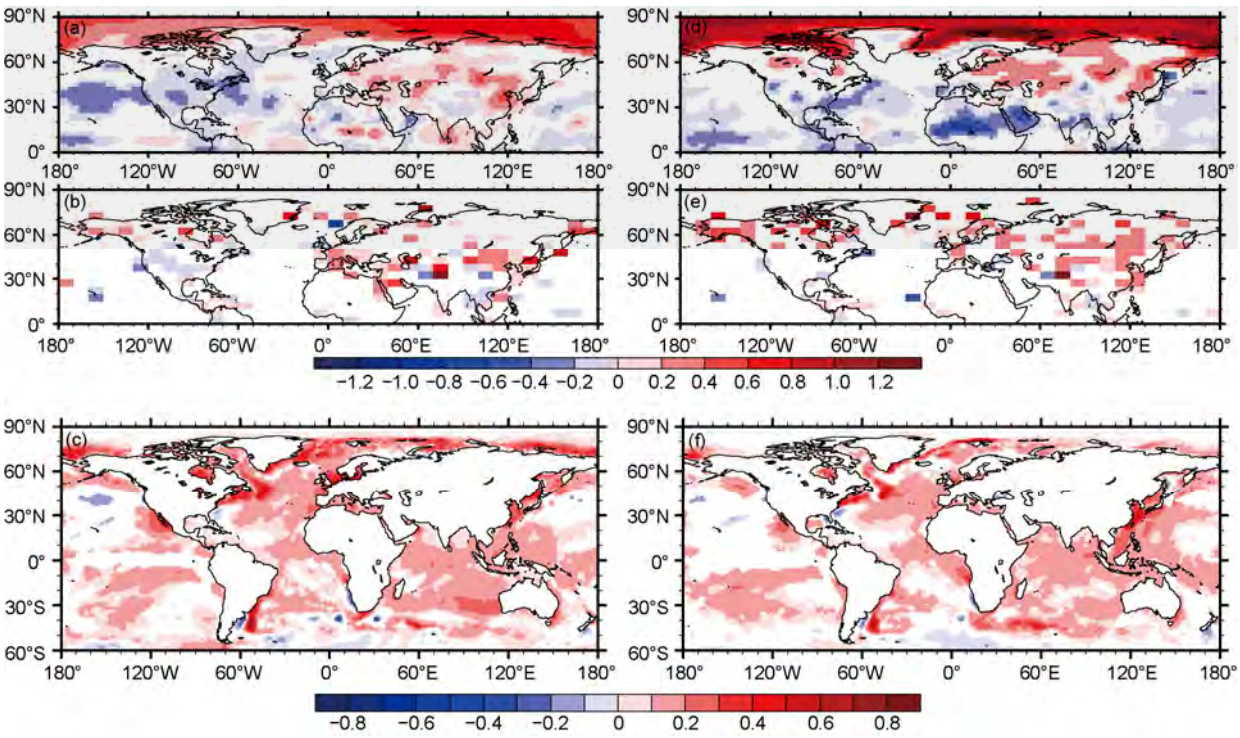

Figure 4 Trends (°C/10 a) in air temperature difference between 1000 and 700 hPa based on NCEP/NCAR Reanalysis air temperature (a) and between surface and 700 hPa based on surface air temperature from CRU and radiosonde upper air temperature from Hadley Centre (b), and trends (K/10 a) in global sea surface temperature (c) in summer half years during 1961–2010. (d), (e) and (f) are the same as in (a), (b) and (c), respectively, but for winter half years. Shaded areas denote 90% confidence level.

rain events increase. So the change may be influenced by other factors. This study primarily discusses the probable causes for the change of light rain events on large spatial scale, and the local factors are not our concern in this study. The cause for the change of precipitation pattern on local scale may be complicated. We will investigate the local cause in the near future.

The trends in sea surface temperature for summer and winter half years are shown in Figure 4(c) and Figure 4(f), respectively. A number of studies [2,33–35] have pointed out that the Earth surface (sea and land surface) and troposphere temperatures continuously increase. Following the increase in sea surface temperature, the evaporation increases and more water vapor would be in the atmosphere. The latent heat from more water vapor condensation makes the upper air become warmer. Meanwhile, the Earth surface warming makes the surface air temperature increase. However, the magnitudes of warming of lower and upper air are different in different area. So the atmospheric stability changes, which induce the change in light rain events.

In addition, the present analysis indicates an increase in light rain events for summer and winter half years over North America and Southern Europe, which is different from the result of Qian et al. [20] who showed that the light rain events decrease over North America and Europe (including Southern Europe). Their results may be associated with too high threshold for light rain event and too much missing values (less than 10% of annual days, which is 36 d/a) in the used data.

A number of studies [36–42] have revealed the connection between the precipitation or extreme precipitation events and sea surface temperature and atmospheric circulation. In order to investigate the relationship between the second EOF mode of light rain events and sea surface temperature and atmospheric circulation, we calculate respectively the correlation coefficient between the PC2 of the light rain events in summer and winter half years and global sea surface temperature (SST) and sea level pressure (SLP), which are shown in Figure 5. It can be seen from Figure 5(a) and (c) that high correlation between PC2 and SST are mainly located in North Atlantic and North Pacific in summer and winter half years. North Atlantic sea surface temperature has multidecadal variation, which is known as Atlantic Multidecadal Oscillation (AMO). The AMO can impact the climate of North America, Europe and Asia [43–46]. We calculate the correlation coefficient between AMO index [47] and PC2 for summer and winter half years. The coefficients are 0.56 and 0.76, respectively, exceeding the 99% confidence level (correlation coefficient of 0.36).

The observation and simulation results of previous studies [45,46,48] showed that during the AMO warm phase, the summer rainfall and river flows decrease in North America, while summer precipitation increase in Europe, which implies that there are negative correlation between the AMO and summer precipitation in North America and positive correlation in Europe. The AMO was changing from warm phase to cold phase during 1961 to early 1980s and from cold phase to warm phase after late 1980s (figure not shown), which is similar to the change of PC2. As mentioned above, the second EOF mode of light rain events in summer half years indicates that light rain events increase over North America and decrease over Europe (except for Southern Europe) during 1961 to early 1980s, while the trends reverse after late 1980s. Therefore, there are negative

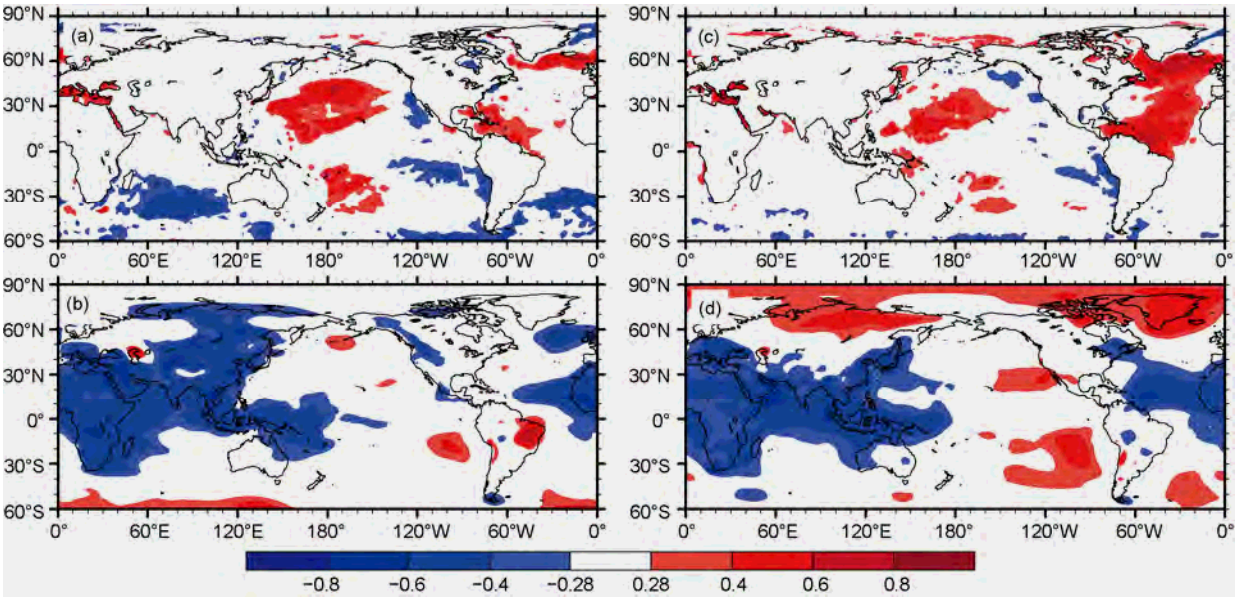

Figure 5 Correlation coefficient between the second principal component of the light rain days and sea surface temperature (a) and sea level pressure (b) in summer half years during 1961–2010. (c) and (d) are the same as in (a) and (b), respectively, but for winter half years. Shaded areas denote 95% confidence level.

correlation between the AMO and the second EOF mode of light rain events in summer half years over North America and positive correlation over most of Europe. Sutton et al. [45] found that there are two low-pressure anomaly centers over North Atlantic during the AMO warm phase, one located to the southwest of United States, the other being to the west of Europe, and indicated that the two anomaly centers were associated with the precipitation change over North America and Europe. It can be seen from the pattern of the correlation between PC2 and sea level pressure (Figure 5(b)) that there are two significant correlative regions over North Atlantic, with the northern one corresponding to the anomaly center to the west of Europe, and the southern one located in the North Atlantic to the southwest of United States, to the southeast of the anomaly center. Thus, the AMO is probably linked to the second EOF mode of light rain events for summer half years over North America and Europe. The AMO influences the change of precipitation and precipitation days, and the change of light rain events probably keeps in line with the change of precipitation and precipitation days. Therefore, the second EOF mode of light rain events displays opposite trends in two periods. However, whether the change of light rain events is accordance with precipitation and precipitation days or not should be investigated further. Using observed precipitation data, Li et al. [44] and Wang et al. [43] found that during the AMO warm phase, the autumn and winter precipitation decrease in South China. The result indicates that there is negative correlation between the AMO and autumn and winter precipitation in South China, which is in accordance with the fact that South China is covering negative anomaly in EOF2 for winter half years. However, the mechanism how AMO influences the East Asian climate is not clear, and should be studied onward [49]. Although no research revealed the connection between the AMO and autumn and winter precipitation over North America and Europe, Knight et al.'s model results [48] showed that the AMO was directly related to autumn and winter precipitation over Europe, in agreement with the fact that Europe is covering positive anomaly in EOF2 for winter half years. Their results also indicated that the AMO was negatively correlated with the autumn and winter sea level pressure, which is similar to the pattern of correlation between PC2 and sea surface pressure in winter half years (Figure 5(d)). Thus, the AMO is possibly associated with the second mode of light rain events in winter half years. It should be noted that the AMO is a multidecadal oscillation with a cycle of 65–80 years [49], but the temporal period in this study is only 50 years, which is less than a cycle of the AMO. Therefore, longer precipitation data is needed to verify the association between the AMO and the second EOF mode of light rain events.

The North Pacific sea surface temperature decreased during 1961 to early 1980s, and increased after late 1980s (figure not shown). Thus PC2 of light rain events in summer and winter half years is positively correlated with the North Pacific sea surface temperature. Nevertheless, we have not found the probable connection between the North Pacific sea surface temperature and the second EOF mode of light rain events. Aleutian low weakens during North Pacific warm phase and strengthens during cold phase [50]. Nevertheless, there is no significant correlation between PC2 for summer and winter half years and Aleutian low (Figure 5(b), (d)). In addition, the precipitation in coastal Southeast China increases during warm phase and decreases during cold phase [51,52]. The positive correlation disagrees with the negative anomaly in coastal Southeast China in EOF2 (Figure 3(b),(f)). Thus, it could not be determined that the change of light rain events is in accordance with the change of precipitation and precipitation days.

3 Summary

This study investigates the long-term trend in light rain events over China in summer and winter half years during 1961–2010 based on daily precipitation data of 622 stations. The results show that the light rain events over East China in summer and winter half years decrease significantly by 0.9 d/10 a and 0.8 d/10 a corresponding to 3%/10 a respectively, while those in Northwest China increase by 0.6 d/10 a corresponding to 4.1%/10 a in winter half years, but display no trend in summer half years.

In order to study the change of light rain events on large spatial scale, this investigation uses EOF analysis to obtain the first two EOF modes and corresponding principal components of light rain events in summer and winter half years, based on station daily precipitation data over the mid-high latitudes of the Northern Hemisphere. The first two principal components (PCs) for summer and winter half years are characterized by long time scale changes, with PC1 for summer and winter half years both representing long-term trend during 1961 to 2010 and PC2 for summer and winter half years both standing for opposite trends during periods of 1961 to early 1980s and late 1980s to 2010. The first EOF modes (EOF1) for summer and winter half years both primarily depict that the light rain events increase over North America and Southern Europe and decrease over most of Eurasia (including Central and Eastern Europe, North Asia and East China) during 1961–2010. The EOF1 for winter half years also shows that the light rain events increase in Northwest China. The second EOF mode (EOF2) for summer half years reveals that the light rain events increase over North America, Southern Europe and South China during 1961 to early 1980s, and decrease over Eurasia north of 45°N, while the trends reverse after late 1980s. The second EOF mode (EOF2) for winter half years indicates that the light rain events increase over North America, South and North China during 1961 to early 1980s, and decrease over Eurasia north of 40°N, while the trends reverse after late 1980s.

This study discusses the probable cause for the change of light rain events. The relationship between the pattern of the trend in atmospheric stability and the trend in light rain events depicted in EOF1 indicate that in most areas the light rain events increase when atmospheric stability strengthens, and decrease when atmospheric stability weakens. The long-term change of atmospheric stability is a probable cause for the long-term change of light rain events. The change of atmospheric stability is possibly related to different vertical warming of troposphere associated with global warming. The second EOF modes may be linked to the AMO. Nevertheless, the influencing mechanism is not clear, and needs to be investigated further.

This work was supported by the National Basic Research Program of China (*2012CB955604 and 2011CB309704*), *the Strategic Priority Research Program of the Chinese Academy of Sciences* (*XDA05090402*), *and the National Natural Science Foundation of China* (*41275083*). *The authors would like to thank Prof. Wu Renguang and two anonymous reviewers as well as editors for their useful comments.*

1 Trenberth K E. Changes in precipitation with climate change. Clim Res, 2011, 47: 123–138
2 Trenberth K E, Jones P D, Ambenje P, et al. Observations: Surface and atmospheric climate change. In: Solomon S, Qin D, Manning M, et al., eds. Climate Change 2007: The Physical Science Basis. Cambridge, United Kingdom and New York: Cambridge University Press, 2007. 235–336
3 Ma Z G, Fu C B. Some evidences of drying trend over North China from 1951 to 2004. Chin Sci Bull, 2006, 51: 2913–2925
4 Liu B H, Xu M, Henderson M, et al. Observed trends of precipitation amount, frequency, and intensity in China, 1960–2000. J Geophys Res, 2005, 110: D08103
5 Wang Y Q, Zhou L. Observed trends in extreme precipitation events in China during 1961–2001 and the associated changes in large-scale circulation. Geophys Res Lett, 2005, 32: L17708
6 Zhai P M, Zhang X B, Wan H, et al. Trends in total precipitation and frequency of daily precipitation extremes over China. J Clim, 2005, 18: 1096–1108
7 Li J, Dong W J, Yan Z W. Changes of climate extremes of temperature and precipitation in summer in eastern China associated with changes in atmospheric circulation in East Asia during 1960–2008. Chin Sci Bull, 2012, 57: 1856–1861
8 Chen F H, Huang W, Jin L Y, et al. Spatiotemporal precipitation variations in the arid Central Asia in the context of global warming. Sci China Earth Sci, 2011, 54: 1812–1821
9 Zolina O, Simmer C, Belyaev K, et al. Improving estimates of heavy and extreme precipitation using daily records from European rain gauges. J Hydrometeor, 2009, 10: 701–716
10 Alexander L V, Zhang X, Peterson T C, et al. Global observed changes in daily climate extremes of temperature and precipitation. J Geophys Res, 2006, 111: D05109
11 Easterling D R, Evans J L, Groisman P Y, et al. Observed variability and trends in extreme climate events: A brief review. Bull Am Meteorol Soc, 2000, 81: 417–425
12 Karl T R, Knight R W. Secular trends of precipitation amount, frequency, and intensity in the United States. Bull Am Meteorol Soc, 1998, 79: 231–241
13 Trenberth K E, Dai A, Rasmussen R M, et al. The changing character of precipitation. Bull Am Meteorol Soc, 2003, 84: 1205–1217
14 Michaels P J, Knappenberger P C, Frauenfeld O W, et al. Trends in precipitation on the wettest days of the year across the contiguous USA. Int J Climatol, 2004, 24: 1873–1882
15 Groisman P Y, Karl T R, Easterling D R, et al. Changes in the probability of heavy precipitation: Important indicators of climatic change. Clim Change, 1999, 42: 243–283
16 Qian W H, Fu J K, Yan Z W. Decrease of light rain events in summer associated with a warming environment in China during 1961–2005. Geophys Res Lett, 2007, 34: L11705
17 Fu J L, Qian W H, Lin X, et al. Trends in graded precipitation in China from 1961 to 2000. Adv Atmos Sci, 2008, 25: 267–278
18 Qian Y, Gong D Y, Fan J W, et al. Heavy pollution suppresses light rain in China: Observations and modeling. J Geophys Res, 2009, 114: D00K02
19 Liu B, Xu M, Henderson M. Where have all the showers gone? Regional declines in light precipitation events in China, 1960–2000. Int J Climatol, 2010, 31: 1177–1191
20 Qian Y, Gong D Y, Leung R. Light rain events change over North America, Europe, and Asia for 1973–2009. Atmos Sci Lett, 2010, 11: 301–306
21 Menne M J, Durre I, Vose R S, et al. An overview of the global historical climatology network-daily database. J Atmos Oceanic Technol, 2012, 29: 897–910
22 Yatagai A, Arakawa O, Kamiguchi K, et al. A 44-year daily gridded precipitation dataset for Asia based on a dense network of rain gauges. SOLA, 2009, 5: 137–140
23 Thorne P W, Parker D E, Tett S F B, et al. Revisiting radiosonde upper air temperatures from 1958 to 2002. J Geophys Res, 2005, 110: D18105
24 Rayner N A, Parker D E, Horton E B, et al. Global analyses of sea surface temperature, sea ice, and night marine air temperature since the late nineteenth century. J Geophys Res, 2003, 108: 4407
25 Jones P D, Lister D H, Osborn T J, et al. Hemispheric and large-scale land surface air temperature variations: An extensive revision and an update to 2010. J Geophys Res, 2012, 117: D05127
26 Kalnay E, Kanamitsu M, Kistler R, et al. The NCEP/NCAR 40-year reanalysis project. Bull Am Meteorol Soc, 1996, 77: 437–471
27 Klein Tank A M G, Wijngaard J B, Können G P, et al. Daily dataset of 20th-century surface air temperature and precipitation series for the European climate assessment. Int J Climatol, 2002, 22: 1441–1453
28 Durre I, Menne M J, Gleason B E, et al. Comprehensive automated quality assurance of daily surface observations. J Appl Meteor Climatol, 2010, 49: 1615–1633
29 Bonsal B R, Zhang X, Vincent L A, et al. Characteristics of daily and extreme temperatures over Canada. J Clim, 2001, 14: 1959–1976
30 Zhai P M, Pan X H. Change in extreme temperature and precipitation over northern China during the second half of the 20th century (in Chinese). Acta Geograph Sin, 2003, 58: 1–10
31 Wu H B, Wu L. Methods for Diagnosis and Forecasting Climate Variability (in Chinese). Beijing: Meteorological Press, 2005. 15–33
32 Chen Y S, Jiang R B. Meteorology (in Chinese). Beijing: Meteorological Press, 1989. 206–207
33 Hansen J, Sato M, Ruedy R, et al. Global temperature change. Proc Natl Acad Sci USA, 2006, 103: 14288–14293
34 Mears C A, Wentz F J. The effect of diurnal correction on satellite-derived lower tropospheric temperature. Science, 2005, 309: 1548–1551
35 Vinnikov K Y, Grody N C. Global warming trend of mean tropospheric temperature observed by satellites. Science, 2003, 302: 269–272
36 Zhou B T. Linkage between winter sea surface temperature east of Australia and summer precipitation in the Yangtze River valley and a possible physical mechanism. Chin Sci Bull, 2011, 56: 1821–1827
37 Yang F L, Lau K M. Trend and variability of China precipitation in spring and summer: Linkage to sea-surface temperatures. Int J Climatol, 2004, 24: 1625–1644
38 Lau K M, Lee J Y, Kim K M, et al. The North pacific as a regulator of summertime climate over Eurasia and North America. J Clim, 2004, 17: 819–833
39 Zhang Y L, Ding Y G. The teleconnection between summer extreme precipitation over East China and North Pacific SST (in Chinese). J

Nanjing Inst Meteorol, 2004, 35: 244–252
40 Ye H. Characteristics of winter precipitation variation over northern Central Eurasia and their connections to sea surface temperatures over the Atlantic and Pacific oceans. J Clim, 2001, 14: 3140–3155
41 Higgins R W, Schemm J K E, Shi W, et al. Extreme precipitation events in the western United States related to tropical forcing. J Clim, 2000, 13: 793–820
42 Ting M, Wang H. Summertime US precipitation variability and its relation to Pacific sea surface temperature. J Clim, 1997, 10: 1853–1873
43 Wang Y, Li S, Luo D. Seasonal response of Asian monsoonal climate to the Atlantic multidecadal oscillation. J Geophys Res, 2009, 114: D02112
44 Li S, Bates G. Influence of the Atlantic multidecadal oscillation on the winter climate of East China. Adv Atmos Sci, 2007, 24: 126–135
45 Sutton R T, Hodson D L R. Atlantic ocean forcing of North American and European summer climate. Science, 2005, 309: 115–118
46 Enfield D B, Mestas, Nuñez A M, et al. The Atlantic multidecadal oscillation and its relation to rainfall and river flows in the continental U.S. Geophys Res Lett, 2001, 28: 2077–2080
47 Trenberth K E, Shea D J. Atlantic hurricanes and natural variability in 2005. Geophys Res Lett, 2006, 33: L12704
48 Knight J R, Folland C K, Scaife A A. Climate impacts of the Atlantic multidecadal oscillation. Geophys Res Lett, 2006, 33: L17706
49 Li S L, Wang Y M, Gao Y Q. A review of the researches on the Atlantic Multidecadal Oscillation (AMO) and its climate influence (in Chinese). Trans Atmos Sci, 2009, 23: 458–465
50 Latif M, Barnett T P. Decadal climate variability over the North Pacific and North America: Dynamics and predictability. J Clim, 1996, 9: 2407–2423
51 Wu B Y, Zhang R H. Interdecadal shift in the wester North Pacific summer SST anomally in the late 1980s. Chin Sci Bull, 2007, 52: 2559–2564
52 Li C Y, Zhu J H, Sun Z B. The study interdecadal climate variation (in Chinese). Clim Environ Res, 2002, 7: 209–219

Open Access This article is distributed under the terms of the Creative Commons Attribution License which permits any use, distribution, and reproduction in any medium, provided the original author(s) and source are credited.

Strengthening of Tropical Indian Ocean Teleconnection to the Northwest Pacific since the Mid-1970s: An Atmospheric GCM Study*

GANG HUANG

LASG, Institute of Atmospheric Physics, Chinese Academy of Sciences, Beijing, China

KAIMING HU

LASG, Institute of Atmospheric Physics, and Graduate University of the Chinese Academy of Sciences, Beijing, China

SHANG-PING XIE

International Pacific Research Center, and Department of Meteorology, University of Hawaii at Manoa, Honolulu, Hawaii

(Manuscript received 15 December 2009, in final form 21 April 2010)

ABSTRACT

The correlation of northwest (NW) Pacific climate anomalies during summer with El Niño–Southern Oscillation (ENSO) in the preceding winter strengthens in the mid-1970s and remains high. This study investigates the hypothesis that the tropical Indian Ocean (TIO) response to ENSO is key to this interdecadal change, using a 21-member ensemble simulation with the Community Atmosphere Model, version 3 (CAM3) forced by the observed history of sea surface temperature (SST) for 1950–2000. In the model hindcast, the TIO influence on the summer NW Pacific strengthens in the mid-1970s, and the strengthened TIO teleconnection coincides with an intensification of summer SST variability over the TIO. This result is corroborated by the fact the model's skills in simulating NW Pacific climate anomalies during summer increase after the 1970s shift.

During late spring to early summer, El Niño–induced TIO warming decays rapidly for the epoch prior to the 1970s shift but grows and persists through summer for the epoch occurring after it. This difference in the evolution of the TIO warming determines the strength of the TIO teleconnection to the NW Pacific in the subsequent summer. An antisymmetric wind pattern develops in spring across the equator over the TIO, and the associated northeasterly anomalies aid the summer warming over the north Indian Ocean by opposing the prevailing southwest monsoon. In the model, this antisymmetric spring wind pattern is well developed after but absent before the 1970s shift.

1. Introduction

The northwest Pacific (NWP) summer monsoon is an important component of the Northern Hemisphere summer monsoon (Murakami and Matsumoto 1994; Ueda and Yasunari 1996; Ueda et al. 2009; Wu and Wang 2000). Year-to-year variations of the NWP monsoon significantly affect the occurrence of the flooding–drought events over East Asia (Huang and Wu 1989; Chang et al. 2000) via the Pacific–Japan teleconnection pattern (Nitta 1987; Kosaka and Nakamura 2006; Arai and Kimoto 2008). Interannual variability in the NWP summer monsoon is correlated with El Niño–Southern Oscillation (ENSO) in the preceding winter (Wang et al. 2003). In the summer following El Niño, rainfall decreases over the subtropical NWP with an anomalous anticyclone near the surface. In East Asia, summer rainfall tends to be excessive.

ENSO-induced SST anomalies persist through summer over the tropical Indian Ocean (TIO; Du et al. 2009). They have been implicated as anchoring summer climate anomalies over the NWP and East Asia via the so-called capacitor effect (Yang et al. 2007; Li et al. 2008). Xie et al. (2009) show that atmospheric Kelvin waves are

* International Pacific Research Center Publication Number 704 and School of Ocean and Earth Science and Technology Publication Number 7093.

Corresponding author address: Gang Huang, LASG, IAP, CAS, P.O. Box 9804, Beijing 100029, China.
E-mail: hg@mail.iap.ac.cn

DOI: 10.1175/2010JCLI3577.1

© 2010 American Meteorological Society

the key bridge between the TIO and subtropical NWP. El Niño–induced TIO swarming force a Matsuno (1966)–Gill (1980) pattern in tropospheric temperature. The warm tropospheric Kelvin wave propagates into the western Pacific, inducing Ekman divergence in the subtropical NWP to suppress convection and develop an anticyclonic circulation near the surface. Recent forecast experiments using a coupled general circulation model (GCM) confirm this TIO teleconnection to the NWP (Chowdary et al. 2010).

The correlation between the NWP monsoon and ENSO has apparently strengthened since the mid-1970s, possibly related to the enhanced ENSO variance (Wang et al. 2008). An observational study by Xie et al. (2010) suggests that this interdecadal change originates in changes in the TIO teleconnection to the NWP. The El Niño–induced TIO warming takes place during epochs both before and after the mid-1970s shift, but it persists into summer only after the mid-1970s. Accordingly, the tropospheric Kelvin wave it forces strengthens substantially in the postshift epoch.

The earlier-mentioned observational studies suggest a strengthening of the TIO teleconnection to the NWP, which seems to explain the apparent increase in correlation of NWP summer monsoon variability with ENSO two seasons in advance. Given that TIO SST anomalies are an important source of summer climate predictability over the NWP and East Asia (Chowdary et al. 2010), it is important to investigate the cause of the interdecadal change in the TIO teleconnection. While increased ENSO activity (Wang et al. 2008) and enhanced TIO SST variability (Xie et al. 2010) are a plausible cause, alternative explanations cannot be ruled out from observations alone. For example, improvements in observations and their assimilation into reanalysis products reduce sampling errors and may lead to an apparent increase in correlation, or chaotic variability in the atmosphere can also cause apparent variations in correlation.

The present study examines the cause of the apparent strengthening of the TIO teleconnection to the summer NWP based on a 21-member ensemble simulation using an atmospheric general circulation model (AGCM) forced by observed SST for 1950–2000. The AGCM ensemble simulation reproduces the interdecadal change similar to observations. We then proceed to examine interdecadal change in TIO SST response to ENSO and its subsequent influence on the NWP. The enhanced persistence of TIO SST anomalies since the mid-1970s is related to a change in wind pattern in the preceding season.

The rest of the paper is organized as follow. Section 2 describes the data and numerical simulation. Section 3 reviews observational evidence for the interdecadal change in the TIO teleconnection. Sections 4 and 5 diagnose the model output, examining the interdecadal change during boreal summer and spring, respectively. Section 6 is a summary.

2. Data and model

We use the Met Office Hadley Centre Sea Ice and SST (HadISST) dataset (Rayner et al. 2003) and the National Centers for Environmental Prediction (NCEP) atmospheric reanalysis (Kalnay et al. 1996), originally on 1° and 2.5° grids, respectively. Our study focuses on interannual variability. Except in the wavelet analysis, a linear trend has been subtracted from raw anomalies to remove decadal and longer variations.

SST anomalies averaged over the region of 10°S–20°N, 40°–100°E are used as an index for TIO SST variations, and the meridional difference of 850-hPa zonal wind anomalies between a southern region (5°–15°N, 100°–130°E) and a northern region (20°–30°N, 110°–140°E) is used as an index for the NWP summer anticyclone, following the NWP summer monsoon index by Wang et al. (2001), but with the sign reversed. Both indices are defined for boreal summer [June–August (JJA)]. Hereafter, seasons refer to those for the Northern Hemisphere.

We use the Community Atmosphere Model, version 3 (CAM3) at T42 resolution (equivalent to 2.8° latitude × 2.8° longitude) in the horizontal and 23 sigma levels in the vertical. Details of the models are provided in Collins et al. (2006). A 21-member ensemble of CAM3 simulations are performed with HadISST observations as surface boundary conditions for a 51-yr period of 1950–2000. Each member simulation differs only in the initial conditions.

3. Observed interdecadal change in TIO teleconnection

This section presents results from an observational analysis to be compared with the AGCM hindcast. Figure 1 shows the correlation in 15-yr sliding windows between JJA TIO SST and NWP anticyclone indices (solid line). The correlation is weak (−0.4 to 0.1) and insignificant for the first half of the record and rises dramatically in the mid-1970s. It peaks above 0.8 in 1980 and somewhat decreases afterward but stays above the 95% significance level for the past three decades. The strengthening in the mid-1970s of this TIO teleconnection to the NWP is the focus of this study. A weakening is also seen in the WNP anticyclone–TIO SST relationship in the mid-1990s, which may be related to the decadal change in the East Asian summer monsoon as studied by Kwon et al. (2005).

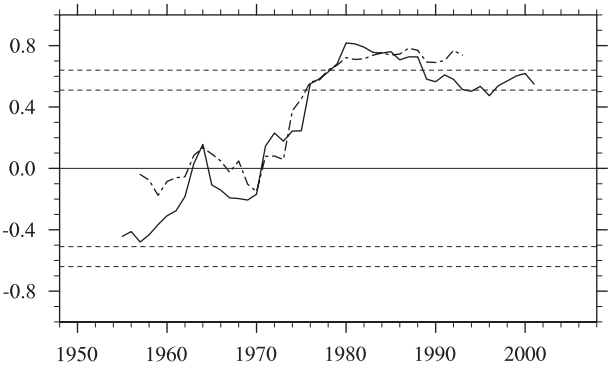

FIG. 1. The 15-yr sliding correlation between the NWP anticyclone and JJA TIO SST indices of observation (solid line), and for the NWP anticyclone index between observations and the ensemble-mean simulation (dot–dash line). Horizontal black dash lines denote 95% and 99% confidence levels.

To document the interdecadal change, we partition the data into preshift (PRE) and postshift (POST) periods of 1953–76 and 1977–2000, respectively. Figure 2 compares the correlations of SST, 850-hPa wind velocity, and tropospheric (850–200-hPa mean) temperature with the NWP anticyclone index between the PRE and POST epochs. During the POST epoch, positive SST correlation is found over the north TIO through the South China Sea. In response to the TIO warming, troposphere temperature displays a Matsuno–Gill pattern with the maximum correlation over the eastern TIO. A Kelvin wave wedge penetrates the western Pacific along the equator, with a pronounced anticyclonic circulation on its northern flank. These results are consistent with the Kelvin wave–induced Ekman divergence mechanism of Xie et al. (2009) for the NWP anticyclone. During the PRE epoch, SST correlation with the NWP anticyclone is weak, except over small patches off Sumatra, in the South China Sea and NWP. SST correlation features an east–west contrast in the TIO, with negative values in the western TIO and westerly wind anomalies on the equator. Consistent with weak SST anomalies, there is no significant tropospheric temperature correlation over the TIO. The NWP anticyclone correlation with the concurrent summer Niño-3.4 SST index is low, -0.41 and -0.11 for the PRE and POST epochs, respectively. These results support that the TIO influence on the NWP anticyclone is weak prior to the mid-1970s and strengthens afterward.

Figure 3 show wavelet spectra of summer TIO SST and NWP anticyclone indices. In a frequency band of approximately four years, TIO SST variability experienced a prominent increase in the late 1970s (Fig. 3a). There is a concurrent increase in NWP anticyclone variability in the same frequency band (Fig. 3b). Moreover, both TIO SST and NWP anticyclone variability displays a concurrent shift in dominant frequency from 4 to 3 yr in the 1990s. All this suggests TIO SST and its teleconnection as the cause of intensified variability in the NWP anticyclone. This hypothesis is consistent with the earlier-mentioned correlation analysis and will be tested with the CAM hindcast.

4. Summer interdecadal change in model

We first evaluate model skills by performing the empirical orthogonal function (EOF) analysis for ensemble-mean variability in JJA 850-hPa wind velocity over the NWP. Figure 4 compares the leading EOF modes with observations. In observations, the first mode explains 28% of the total variance, featuring an anticyclone associated with positive sea level pressure (SLP) anomalies over the subtropical NWP (Fig. 4, upper left). The second mode explains 16% of the variance, featuring westerly anomalies along the equator with zonal SLP gradient. There is a weak subtropical anticyclone over East Asia and the NWP (Fig. 4, lower left). Correlation analysis with eastern Pacific SST indicates that the second EOF (EOF-2) represents anomalies during the summer when El Niño develops [JJA(0)] and EOF-1 represents the summer after El Niño decays [JJA(1)]. Here the numerals in parentheses denote the El Niño developing (0) and decay (1) years. The first principal component (PC-1) is highly correlated with the NWP anticyclone index at $r = 0.92$.

The model ensemble-mean simulation captures the salient features of observed EOFs with the following differences: 1) the model EOF-1 explains a much larger fraction of variance possibly because of weaker noise than in observations; 2) the anticyclone in the model EOF-1 is shifted by 5° northward; and 3) in the model EOF-2, the subtropical anticyclone is confined to East Asia and the off-equatorial low-pressure belt to the south is more pronounced.

Figure 5 shows the 15-yr sliding correlation for PCs between observations and the ensemble mean. While the PC-2 correlation remains nearly constant and above the 95% significance level throughout, the model's skills in PC-1 displays a pronounced interdecadal change in the late 1970s, low and insignificant before the shift but rising rapidly afterward to values as high as 0.7. The ensemble-mean AGCM simulation helps isolate the SST-forced variability (Rowell et al. 1995; Lu et al. 2006). The high correlation for the NWP EOF-1 mode between observations and the ensemble-mean simulation during the POST epoch (Fig. 5) indicates that the year-to-year variations in the NWP summer monsoon are forced by SST anomalies, while the low correlation suggests that the SST forcing is weak during the PRE

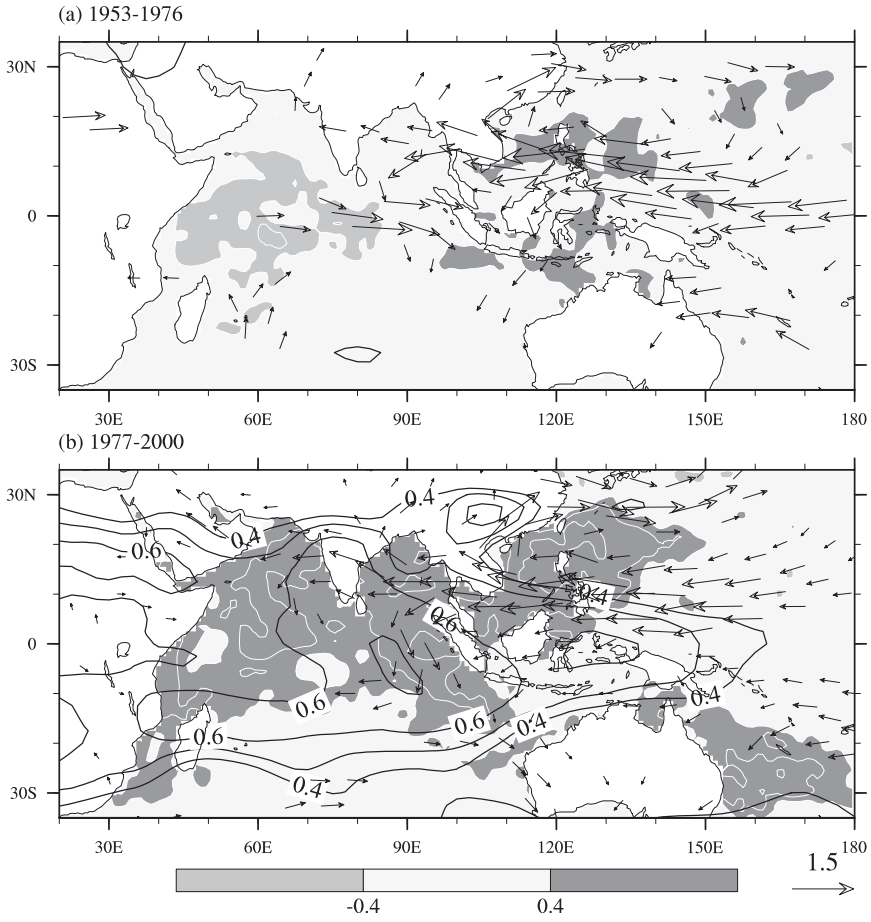

FIG. 2. Correlation with the NWP anticyclone index in observation during (a) 1953–76 and (b) 1977–2000: JJA SST (gray shade and white contours at intervals of 0.2) and tropospheric temperature (vertical average from 850 to 200 hPa; contours $r \geq 0.4$). Wind vectors (m s^{-1}, pass the 95% confidence level) show the regression of 850-hPa wind with the NWP anticyclone index.

epoch. Thus, it is possible that changes in SST patterns cause this interdecadal change.

Indeed, the model simulates the late 1970s' increase in interannual variability of the NWP anticyclone (Fig. 3c), even the shift of the dominant frequency from 4–5 to 3 yr. The concurrent increase in TIO SST variability suggests it as the cause of enhanced NWP anticyclone variability. NWP anticyclone variability may be due to internal variability or forced by SST anomalies (Lu et al. 2006). Ensemble AGCM simulations capture only SST-forced variability, which appears to dominate the NWP anticyclone after the mid-1970s. Figure 5 shows that the rise of the model's skills in simulating NWP climate anomalies coincides with the increase in observed correlation between TIO SST and NWP anticyclone variability (Fig. 2).

TIO teleconnection

The rest of the section examines the TIO teleconnection to the NWP. Figure 6 compares the correlation between the TIO SST and NWP anticyclone in 21 simulations with CAM3. A total of 12 members out of 21 show the correlation exceeding the 95% confidence level during the POST epoch, but none passes the 95% confidence level during the PRE epoch. Moreover, the correlation coefficients are higher during the POST epoch than the PRE epoch in every member of the simulations, illustrating the strengthened TIO teleconnection after the mid-1970s.

Figure 7 compares summer correlations of ensemble-mean precipitation, tropospheric temperature, and 850-hPa wind with TIO SST between the PRE and POST epochs. Consistent with observations during the POST epoch, a TIO warming forces a Matsuno–Gill pattern in tropospheric temperature, with a warm Kelvin wave propagating into the western Pacific along the equator and Rossby wavelike off-equatorial maxima over the western TIO and Africa. Precipitation increases over the TIO except over the Bay of Bengal. A low-level anticyclone

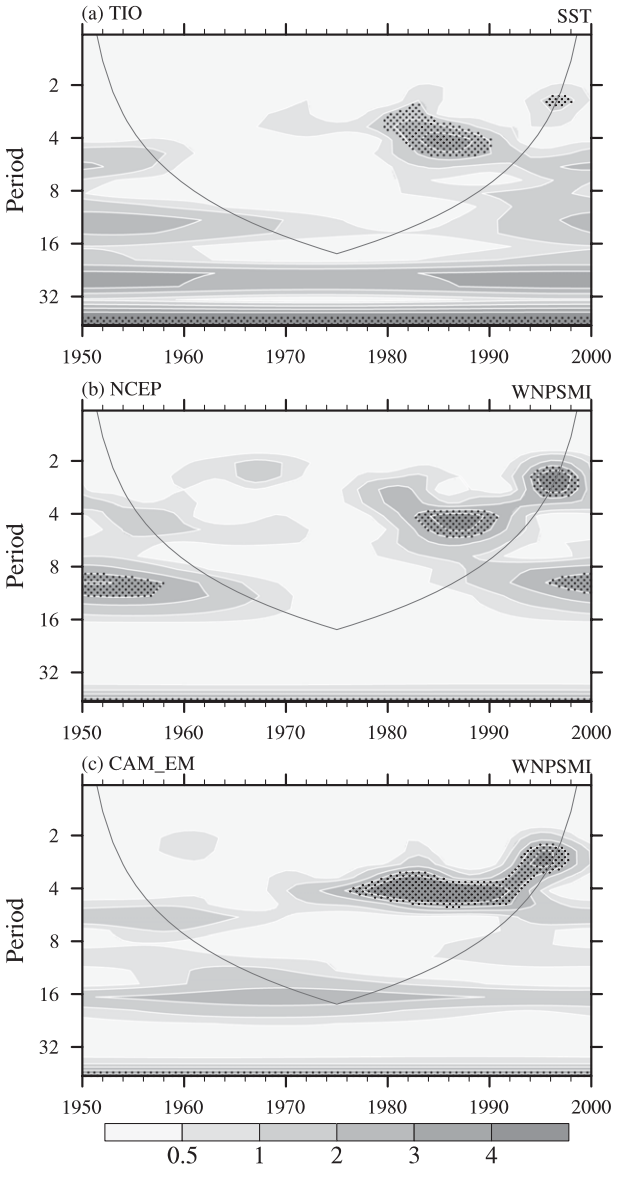

FIG. 3. Wavelet spectra of the standard deviation of the (a) JJA TIO SST index, (b) observations NWP anticyclone index, and (c) ensemble-mean NWP anticyclone index. All shaded regions denote 95% confidence levels.

appears on the northern flank of the tropospheric Kelvin wave from the Bay of Bengal to the subtropical WNP, where precipitation shows a tendency to decrease. During the PRE epoch, by contrast, the Matsuno–Gill pattern weakens over the TIO, without the development of the warm Kelvin wave in the equatorial western Pacific and anticyclonic anomalies over the NWP. Over the central Pacific, a pair of warm anomaly maxima develops in tropospheric temperature on either side of the equator. The cause of these off-equatorial maxima in tropospheric warming needs further investigation.

These results from the model hindcast indicate that the increase in TIO SST variability strengthens its influence on NWP climate. They support the notion that the warm tropospheric Kelvin wave is a key element of this teleconnection.

5. Antisymmetric wind pattern in spring and early summer

What caused the increase in TIO SST variability in summer after the mid-1970s? Previous studies show that El Niño induces TIO warming through atmospheric bridge (Alexander et al. 2002; Schott et al. 2009). Ocean Rossby waves are important over the southwest TIO (Xie et al. 2002; Huang and Kinter 2002), and surface heat flux adjustments dominate the rest of the TIO (Klein et al. 1999; Lau and Nath 2003).

Figure 8 shows the observed correlations with the December–February (0) [DJF(0)] Niño-3.4 SST index of SST and 850-hPa wind velocity averaged zonally over the TIO (40°–100°E). El Niño–induced SST warming persists long over the TIO, with the correlation staying above 0.6 through JJA(1) during the POST epoch but falling below this level before June(1) in the PRE epoch. During the POST epoch, an equatorially antisymmetric wind pattern develops in March and persists through June (Kawamura et al. 2001; Wu et al. 2008). Over the North Indian Ocean (NIO), the associated easterly wind anomalies act to warm SST after the onset of the southwest monsoon by reducing the prevailing winds and surface evaporation (Du et al. 2009). Over the NIO, the easterly wind anomalies during May–July explain the peculiar SST warming that grows after El Niño has already dissipated. During the PRE epoch, the antisymmetric wind pattern does not appear in spring, and wind anomalies are weak afterward over the NIO, where SST anomalies decay rapidly (Fig. 10a).

The model reproduces observed wind anomalies quite well for the POST epoch (Fig. 9b), including the antisymmetric wind pattern during March–May(1) [spring; MAM(1)]. In both observations and the model, easterly anomalies appear in a broad equatorial band during January–March and then gradually move northward and persist over the NIO through June and July. The easterly anomalies during May–July sustain the NIO warming, and their successful simulation in our AGCM hindcast indicate that they are forced by SST anomalies—most likely those over the southwest TIO (Du et al. 2009). Indeed, positive precipitation anomalies are found over the southwest TIO during both MAM(1) (Fig. 10b) and JJA(1) (Fig. 7b). The zonal-mean wind anomalies in the model do not correlate very well with observations for the PRE epoch (Fig. 9a)—the model winds are even westerly over the NIO during JJA(1).

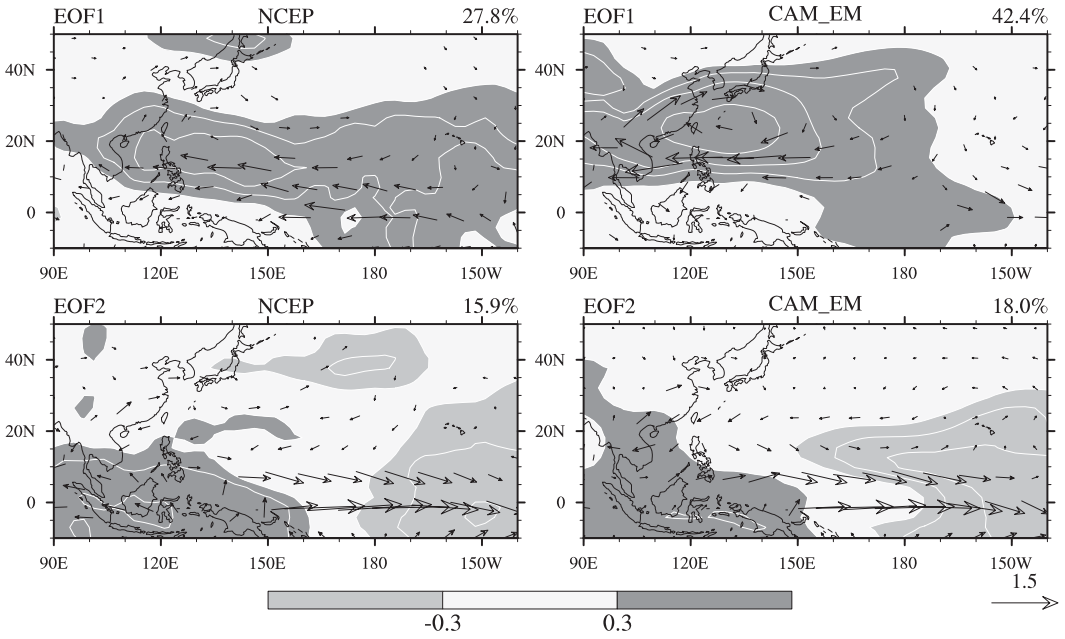

FIG. 4. Correlation of 850-hPa wind vectors and sea surface pressure in JJA with the leading PCs of 850-hPa wind velocity in (left) observations and (right) the ensemble-mean simulation: (top) EOF-1 and (bottom) EOF-2. The domain for EOF analysis covers the NWP (5°–50°N, 90°–180°E).

Figure 10 compares the leading EOF mode for MAM 850-hPa wind velocity and associated precipitation anomalies between the PRE and POST epochs in the model. As in summer, the model skills in MAM wind simulation are low before but high after the 1970s shift (the PC-1 correlation between the hindcast and observations changes from −0.1 to 0.68). During the POST epoch, EOF-1 explains a large fraction (42%) of the total variance, featuring an antisymmetric wind pattern with anomalous northeasterlies over the NIO. The associated precipitation anomalies are rough out of phase north and south of the equator, consistent with the result of Wu et al. (2008) that the leading precipitation EOF for spring is antisymmetric about the equator. The reduced rainfall north of the equator is accompanied by anticyclonic circulation, with easterlies over the NIO. A blob of positive rainfall anomalies is found over the southwest TIO, accompanied by cyclonic circulation. Over the southwest TIO, the slow propagation of downwelling ocean Rossby waves induces SST warming and intensifies atmospheric convection, thereby forcing the antisymmetric wind pattern across the equator (Xie et al. 2002; Annamalai et al. 2005; Du et al. 2009).

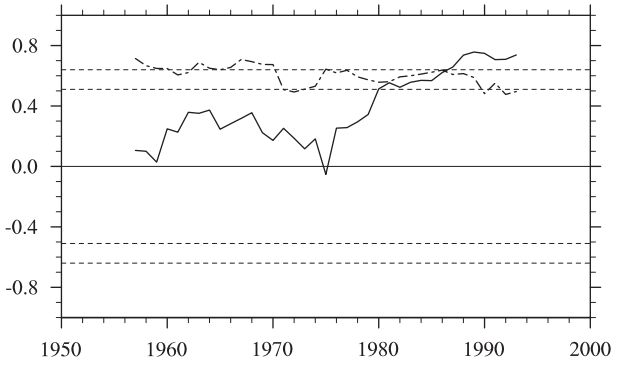

FIG. 5. Correlation between observations and the ensemble-mean simulation in 15-yr sliding windows for the first (solid line) and second (dash) PCs of JJA 850-hPa wind over the NWP. Horizontal black dash lines denote 95% and 99% confidence levels based on *t* test.

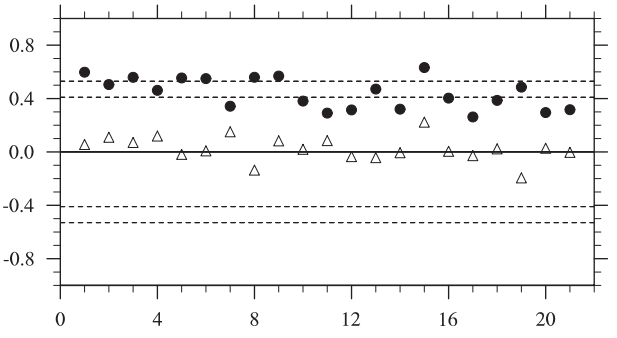

FIG. 6. Correlation coefficients between the JJA TIO SST and NWP anticyclone indices in the 21-member simulations during 1977–2000 (black circles) and 1953–76 (triangles). Horizontal dash lines denote 95% and 99% confidence levels.

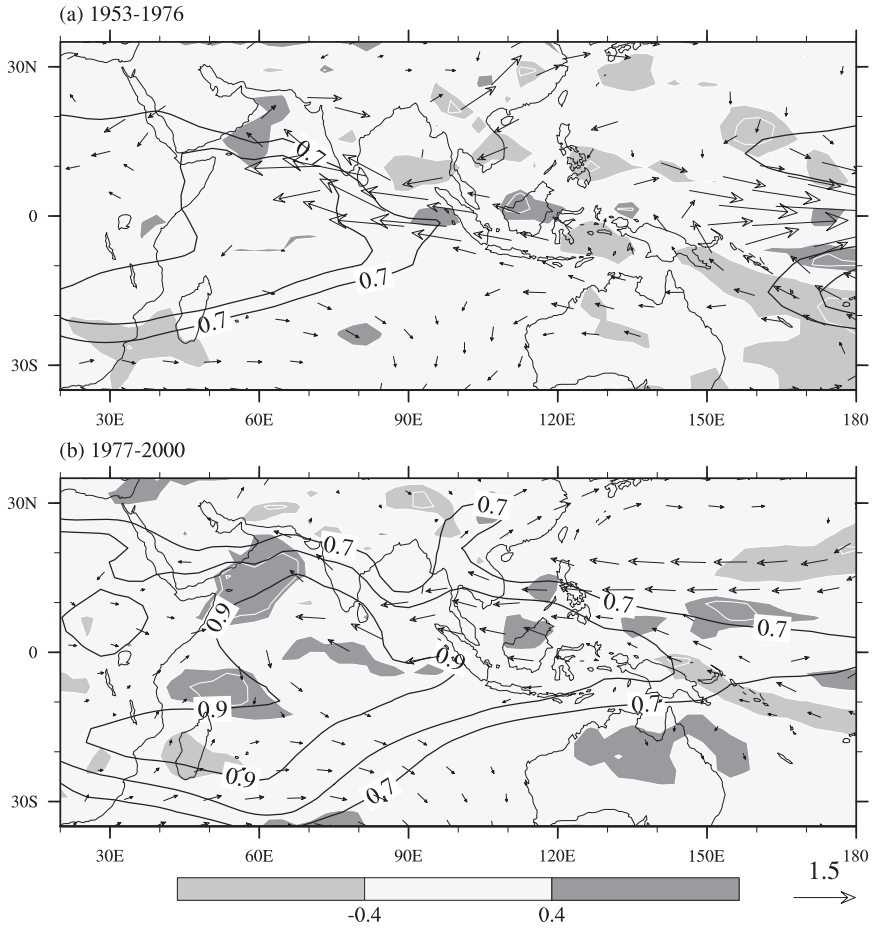

FIG. 7. As in Fig. 2, but for correlation with the JJA TIO index and ensemble-mean precipitation (gray shade and white contours at intervals of 0.2).

For the PRE epoch, EOF-1 explains a smaller fraction (33%) of variance and features easterly wind anomalies centered on the equator (Fig. 10a). The wind anomalies are consistent with a slowdown of the Walker circulation and resemble the wind pattern forced by remnant SST anomalies of a decaying El Niño (Annamalai et al. 2005). Precipitation anomalies are weak over the southwest TIO, consistent with the notion that they anchor the antisymmetric wind pattern across the equator.

Figure 11 shows the evolution of SST correlation with the model PC-1 for ensemble-mean MAM wind, to identify the SST forcing. From December to May, SST warming takes place over the entire TIO for the PRE epoch but is weak over the NIO for the POST epoch. Wu et al. (2008) suggest that the meridional SST gradient is important for the antisymmetric wind pattern, in line with wind–evaporation–SST (WES) feedback (Xie and Philander 1994). The TIO warming decays rapidly from June onward for the PRE epoch but persists through JJA for the POST epoch.

The TIO wind EOF-1 pattern for MAM is associated with Pacific SST anomalies indicative of El Niño. The evolution of Pacific SST correlation, however, is very different between the PRE and POST epochs. El Niño decays earlier during the PRE than the POST epoch. During the POST epoch, the slower decay of El Niño applies teleconnective forcing longer on the TIO, making the southwest TIO warming stronger and persist longer (Xie et al. 2010). The stronger SST forcing over the southwest TIO helps induce and persist the antisymmetric wind pattern, causing the NIO to warm during May–July. Positive SST anomalies over the southwest TIO have another effect of delaying the onset of the Indian summer monsoon, which may help sustain the NIO warming with increased solar radiation and reduced wind (Joseph et al. 1994; Annamalai et al. 2005).

For the POST epoch, we note a well-organized band of negative SST correlation over the subtropical NWP from December to May, conducive to forming a surface anticyclone (Wang et al. 2003). The NWP anticyclone

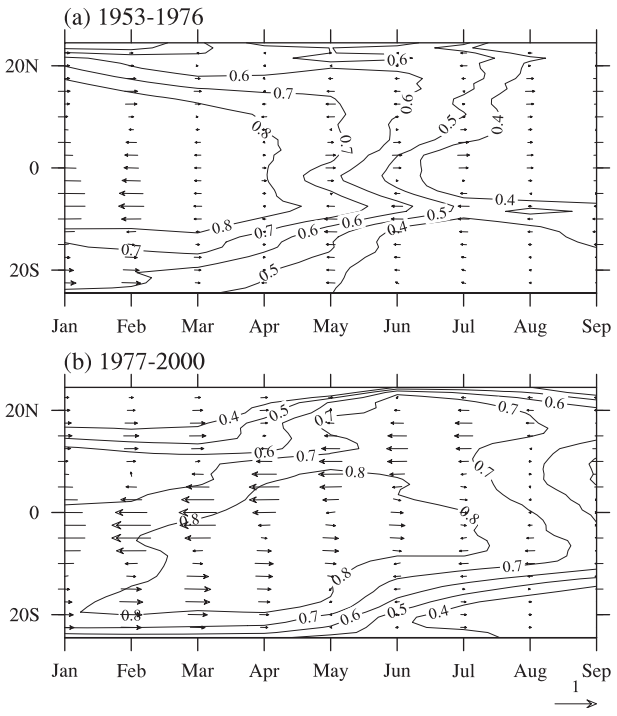

FIG. 8. Observed correlation (contours) between zonal-mean TIO SST (40°–100°E) and the DJF Niño-3.4 index, and regression (vector) of zonal-mean 850-hPa wind upon the Niño-3.4 index during (a) 1953–76 and (b) 1977–2000, as a function of calendar month and latitude.

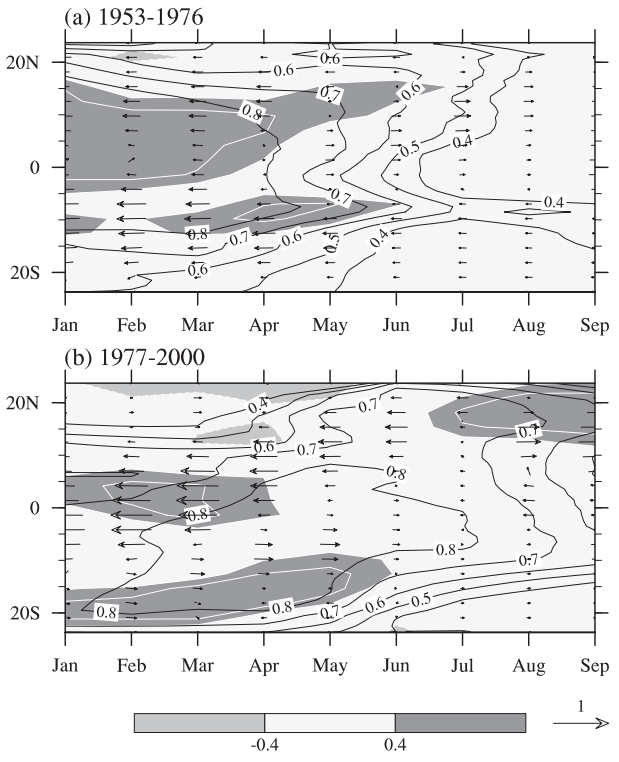

FIG. 9. As in Fig. 8, but for the ensemble-mean simulation. Superimposed is the correlation between zonal-mean (40°–100°E) precipitation (gray shade and white contours at intervals of 0.2) and the Niño-3.4 index.

may propagate westward into the NIO as an atmospheric Rossby wave, helping to suppress atmospheric convection there (Kawamura et al. 2001). This suggests that the NWP cooling may serve as a remote forcing for the antisymmetric wind pattern over the TIO.

6. Summary and discussion

The present study has investigated interdecadal change in the relationship between TIO SST and the NWP summer anticyclone using both observations and AGCM simulations. Observations show that the NWP anticyclone is negatively correlated with summer TIO SST after the mid-1970s, but the relationship is weak for the period of 1958–76. A 21-member ensemble AGCM hindcast reproduces this interdecadal change. Together, our observational and model results show that the TIO teleconnection to the NWP strengthens after the mid-1970s, most likely as a result of enhanced variability in summer TIO SST.

Our AGCM hindcast confirms that the interannual TIO warming excites a warm tropospheric Kelvin wave and that this Kelvin wave is instrumental in inducing summer climate anomalies over the subtropical NWP, including suppressed convection and an anomalous surface anticyclone. The model captures the pronounced Kelvin wave response of the troposphere to the El Niño–induced TIO warming for the POST epoch, but the Kelvin wave response is weak for the PRE epoch, explaining weak correlation between TIO SST and NWP climate anomalies. The strong (weak) TIO teleconnection coincides with high (low) SST variability over the summer TIO on one hand and with the period when the model skills are high (low) in simulating NWP circulation anomalies on the other.

An antisymmetric wind pattern develops in spring and persists through June, likely anchored by the positive SST and precipitation anomalies in the southwest TIO. With northeasterlies north of the equator opposing the mean southwest monsoon, this wind pattern is instrumental in the summer peak of the NIO warming (Du et al. 2009). This antisymmetric spring wind pattern is captured for the POST epoch but absent in the PRE epoch in the model. The SST correlation analysis suggests that stronger meridional SST gradients during the POST epoch rather than the PRE epoch contributes to the formation of this wind pattern, and so does the slower decay of El Niño SST anomalies in the Pacific.

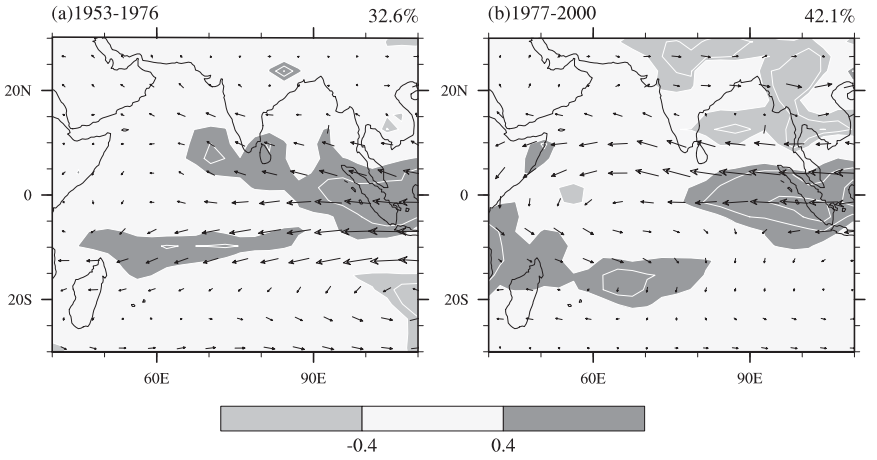

FIG. 10. First EOF modes of MAM 850-hPa wind velocity (vectors) over the TIO during (a) 1953–76 and (b) 1977–2000, with MAM precipitation correlation superimposed (gray shades and white contours at intervals of 0.2). The results are based on the ensemble-mean simulation.

Our AGCM hindcast prescribes observed SST, but SST anomalies could be interactive with wind anomalies. For example, the easterly wind anomalies and SST warming over the NIO may interact with each other: The NIO warming induced the NWP anticyclone and easterly anomalies over the Bay of Bengal–South China Sea as simulated in our hindcast (Fig. 7b) as these wind anomalies cause the ocean to warm (Du et al. 2009).

Results from our AGCM hindcast show that the interdecadal strengthening of both the antisymmetric spring wind pattern over the TIO and summer TIO teleconnection is due to changes in the pattern and magnitude of TIO SST anomalies. Such changes in TIO SST anomalies, in turn, appear to trace back to those in ENSO in the Pacific. TIO SST anomalies are interactive with the atmosphere and with Pacific SST via atmospheric bridge [see Schott et al. (2009) for a recent review]. The interdecadal change in ENSO and its interaction with the TIO needs to be studied from a coupled ocean–atmospheric perspective.

Two strong El Niño events happened after the mid-1970s: 1982/83 and 1997/98. We have computed the correlation coefficient between the TIO SST and NWP summer anticyclone indices during 1977–2000 by excluding the years of 1983 and 1998. The correlation coefficients drop to 0.49 and 0.41 for observations and the

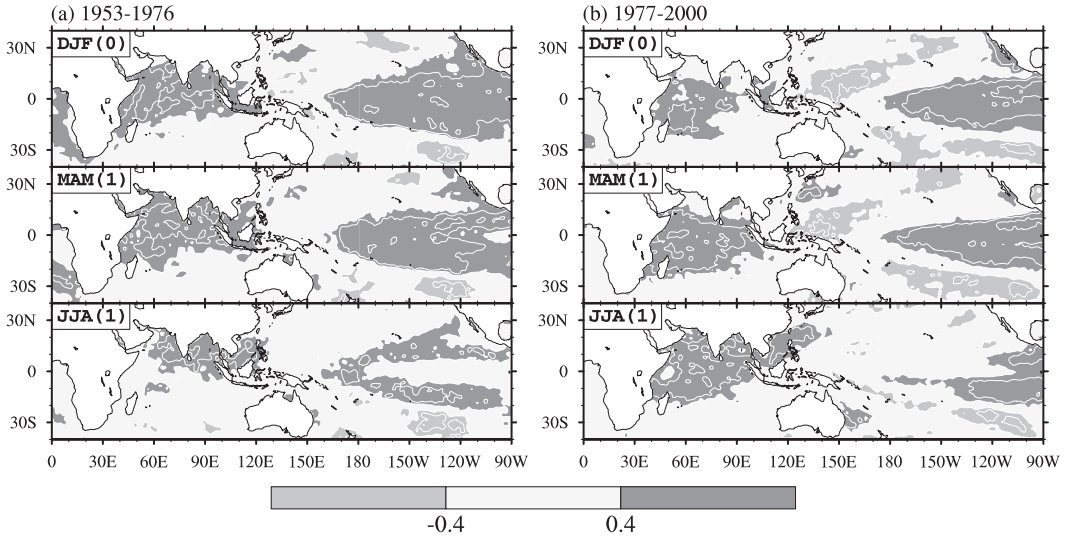

FIG. 11. Correlation of SST (gray shades and white contours at intervals of 0.2) with the first PC of MAM 850-hPa wind over the TIO from DJF to JJA during (a) 1953–76 and (b) 1977–2000.

model ensemble mean, respectively. They are lower than using the original time series (0.63 and 0.55 for observations and the simulation, respectively) but are still much higher than the correlation for the PRE epoch (Fig. 2). Thus, individual El Niño events can influence the relationship between the NWP summer monsoon and the Indian Ocean to some extent, but the sharp interdecadal change remains without the 1982/83 and 1997/98 events. The result does illustrate, however, the need to study low-frequency variations in ENSO properties.

Acknowledgments. The authors are grateful to Prof. Ronghui Huang and Dr. Renguang Wu for their insightful comments that led to a significant improvement of the manuscript. GH and KH are jointly supported by the National Key Technology R&D Program 2008BAK50B02 and the Natural Science Foundation of China under Grants 40890155, 40775051, and U0733002, and Project KZCX2-YW-220 CAS. S.-P. Xie is supported by the U.S. National Science Foundation and the Japan Agency for Marine-Earth Science and Technology.

REFERENCES

Alexander, M. A., I. Bladé, M. Newman, J. R. Lanzante, N.-C. Lau, and J. D. Scott, 2002: The atmospheric bridge: The influence of ENSO teleconnections on air–sea interaction over the global oceans. *J. Climate,* **15,** 2205–2231.

Annamalai, H., P. Liu, and S.-P. Xie, 2005: Southwest Indian Ocean SST variability: Its local effect and remote influence on Asian monsoons. *J. Climate,* **18,** 4150–4167.

Arai, M., and M. Kimoto, 2008: Simulated interannual variation in summertime atmospheric circulation associated with the East Asian monsoon. *Climate Dyn.,* **31,** 435–447.

Chang, C.-P., Y. Zhang, and T. Li, 2000: Interannual and interdecadal variations of the East Asian summer monsoon and tropical Pacific SSTs. Part I: Roles of the subtropical ridge. *J. Climate,* **13,** 4310–4325.

Chowdary, J. S., S.-P. Xie, J.-J. Luo, J. Hafner, S. Behera, Y. Masumoto, and T. Yamagata, 2010: Predictability of Northwest Pacific climate during summer and the role of the tropical Indian Ocean. *Climate Dyn.,* doi:10.1007/s00382-009-0686-5, in press.

Collins, W. D., and Coauthors, 2006: The Community Climate System Model version 3 (CCSM3). *J. Climate,* **19,** 2122–2143.

Du, Y., S.-P. Xie, G. Huang, and K. Hu, 2009: Role of air–sea interaction in the long persistence of El Niño–induced north Indian Ocean warming. *J. Climate,* **22,** 2023–2038.

Gill, A. E., 1980: Some simple solutions for heat-induced tropical circulation. *Quart. J. Roy. Meteor. Soc.,* **106,** 447–462.

Huang, B., and J. L. Kinter III, 2002: Interannual variability in the tropical Indian Ocean. *J. Geophys. Res.,* **107,** 3319, doi:10.1029/2001JC001278.

Huang, R., and Y. Wu, 1989: The influence of ENSO on the summer climate change in China and its mechanism. *Adv. Atmos. Sci.,* **6,** 21–32.

Joseph, P. V., J. K. Eischeid, and R. J. Pyle, 1994: Interannual variability of the onset of the Indian summer monsoon and its association with atmospheric features, El Niño, and sea surface temperature anomalies. *J. Climate,* **7,** 81–105.

Kalnay, E., and Coauthors, 1996: The NCEP/NCAR 40-Year Reanalysis Project. *Bull. Amer. Meteor. Soc.,* **77,** 437–471.

Kawamura, R., T. Matsuura, and S. Iizuka, 2001: Role of equatorially asymmetric sea surface temperature anomalies in the Indian Ocean in the Asian summer monsoon and El Nino-Southern Oscillation coupling. *J. Geophys. Res.,* **106,** 4681–4693.

Klein, S. A., B. J. Soden, and N.-C. Lau, 1999: Remote sea surface temperature variations during ENSO: Evidence for a tropical atmospheric bridge. *J. Climate,* **12,** 917–932.

Kosaka, Y., and H. Nakamura, 2006: Structure and dynamics of the summertime Pacific Japan teleconnection pattern. *Quart. J. Roy. Meteor. Soc.,* **132,** 2009–2030.

Kwon, M., J.-G. Jhun, B. Wang, S.-I. An, and J.-S. Kug, 2005: Decadal change in relationship between east Asian and WNP summer monsoons. *Geophys. Res. Lett.,* **32,** L16709, doi:10.1029/2005GL023026.

Lau, N.-C., and M. J. Nath, 2003: Atmosphere–ocean variations in the Indo-Pacific sector during ENSO episodes. *J. Climate,* **16,** 3–20.

Li, S., J. Lu, G. Huang, and K. Hu, 2008: Tropical Indian Ocean Basin warming and East Asian summer monsoon: A multiple AGCM study. *J. Climate,* **21,** 6080–6088.

Lu, R. Y., Y. Li, and B. W. Dong, 2006: External and internal summer atmospheric variability in the western North Pacific and East Asia. *J. Meteor. Soc. Japan,* **84,** 447–462.

Matsuno, T., 1966: Quasi-geostrophic motions in the equatorial area. *J. Meteor. Soc. Japan,* **44,** 25–43.

Murakami, T., and J. Matsumoto, 1994: Summer monsoon over the Asian continent and western North Pacific. *J. Meteor. Soc. Japan,* **72,** 719–745.

Nitta, T., 1987: Convective activities in the tropical western Pacific and their impact on the Northern Hemisphere summer circulation. *J. Meteor. Soc. Japan,* **65,** 373–390.

Rayner, N. A., D. E. Parker, E. B. Horton, C. K. Folland, L. V. Alexander, D. P. Rowell, E. C. Kent, and A. Kaplan, 2003: Global analyses of sea surface temperature, sea ice, and night marine air temperature since the late nineteenth century. *J. Geophys. Res.,* **108,** 4407, doi:10.1029/2002JD002670.

Rowell, D. P., C. K. Folland, K. Maskell, and N. M. Ward, 1995: Variability of summer rainfall over tropical north Africa (1906 92): Observations and modelling. *Quart. J. Roy. Meteor. Soc.,* **121,** 669–704.

Schott, F. A., S.-P. Xie, and J. P. McCreary Jr., 2009: Indian Ocean circulation and climate variability. *Rev. Geophys.,* **47,** RG1002, doi:10.1029/2007RG000245.

Ueda, H., and T. Yasunari, 1996: Maturing Process of the Summer Monsoon over the Western North Pacific—A Coupled Ocean/Atmosphere System. *J. Meteor. Soc. Japan,* **74,** 493–508.

——, M. Ohba, and S.-P. Xie, 2009: Important factors for the development of the Asian–Northwest Pacific summer monsoon. *J. Climate,* **22,** 649–669.

Wang, B., R. Wu, and K.-M. Lau, 2001: Interannual variability of the Asian summer monsoon: Contrasts between the Indian and the western North Pacific–East Asian monsoons. *J. Climate,* **14,** 4073–4090.

——, ——, and T. Li, 2003: Atmosphere–warm ocean interaction and its impacts on Asian–Australian monsoon variation. *J. Climate,* **16,** 1195–1211.

——, J. Yang, T. Zhou, and B. Wang, 2008: Interdecadal changes in the major modes of Asian–Australian monsoon variability: Strengthening relationship with ENSO since the late 1970s. *J. Climate,* **21,** 1771–1789.

Wu, R., and B. Wang, 2000: Interannual variability of summer monsoon onset over the western North Pacific and the underlying processes. *J. Climate,* **13,** 2483–2501.

——, B. P. Kirtman, and V. Krishnamurthy, 2008: An asymmetric mode of tropical Indian Ocean rainfall variability in boreal spring. *J. Geophys. Res.,* **113,** D05104, doi:10.1029/2007JD009316.

Xie, S.-P., and S. G. H. Philander, 1994: A coupled ocean-atmosphere model of relevance to the ITCZ in the eastern Pacific. *Tellus,* **46A,** 340–350.

——, H. Annamalai, F. A. Schott, and J. P. McCreary Jr., 2002: Structure and mechanisms of South Indian Ocean climate variability. *J. Climate,* **15,** 864–878.

——, K. Hu, J. Hafner, H. Tokinaga, Y. Du, G. Huang, and T. Sampe, 2009: Indian Ocean capacitor effect on Indo-western Pacific climate during the summer following El Niño. *J. Climate,* **22,** 730–747.

——, Y. Du, G. Huang, X.-T. Zheng, H. Tokinaga, K. Hu, and Q. Liu, 2010: Decadal shift in El Nino influences on Indo–western Pacific and East Asian climate in the 1970s. *J. Climate,* **23,** 3352–3368.

Yang, J., Q. Liu, S.-P. Xie, Z. Liu, and L. Wu, 2007: Impact of the Indian Ocean SST basin mode on the Asian summer monsoon. *Geophys. Res. Lett.,* **34,** L02708, doi:10.1029/2006GL028571.

ADVANCES IN ATMOSPHERIC SCIENCES, VOL. 28, NO. 2, 2011, 257–268

The Interannual Variability of Summer Rainfall in the Arid and Semiarid Regions of Northern China and Its Association with the Northern Hemisphere Circumglobal Teleconnection

HUANG Gang*[1,2] (黄 刚), LIU Yong[2,3] (刘 永), and HUANG Ronghui[2] (黄荣辉)

[1] *Key Laboratory of Regional Climate-Environment Research for Temperate East Asia, Institute of Atmospheric Physics, Chinese Academy of Sciences, Beijing* 100029

[2] *State Key Laboratory of Numerical Modeling for Atmospheric Sciences and Geophysical Fluid Dynamics, Center for Monsoon System Research, Institute of Atmospheric Physics, Chinese Academy of Sciences, Beijing* 100083

[3] *Graduate University of Chinese Academy of Sciences, Beijing* 100049

(Received 17 December 2009; revised 8 May 2010)

ABSTRACT

Using the latest daily observational rainfall datasets for the period 1961–2008, the present study investigates the interannual variability of June–September (JJAS) mean rainfall in northern China. The regional characteristics of JJAS mean rainfall are revealed by a rotated empirical orthogonal function (REOF) analysis. The analysis identifies three regions of large interannual variability of JJAS rainfall: North China (NC), Northeast China (NEC), and the Taklimakan Desert in Northwest China (TDNWC). Summer rainfall over NC is shown to have displayed a remarkable dry period from the late 1990s; while over NEC, decadal-scale variation with a significant decreasing trend in the last two decades is found, and over TDNWC, evidence of large interannual variability is revealed. Results also show that the interannual variability of JJAS rainfall in northern China is closely associated with the Northern Hemisphere circumglobal teleconnection (CGT). Correlation coefficients between the CGT index and regional-averaged JJAS mean rainfall over NC and NEC were calculated, revealing values of up to 0.50 and 0.53, respectively, both of which exceeded the 99% confidence level.

Key words: rotated empirical orthogonal function analysis, arid, semiarid, interannual variability, circumglobal teleconnection

Citation: Huang, G., Y. Liu, and R. H. Huang, 2011: The interannual variability of summer rainfall in the arid and semiarid regions of northern China and its association with the northern hemisphere circumglobal teleconnection. *Adv. Atmos. Sci.*, **28**(2), 257–268, doi: 10.1007/s00376-010-9225-x.

1. Introduction

The arid and semi-arid regions (ASAR) of China, mainly located in the north, cover nearly half of the land area (e.g. Chen et al., 2009). The annual rainfall in these regions is almost less than 400 mm. The amount of rainfall in most parts of ASAR, during the rainy months of June, July, August, September (JJAS), accounts for more than 70% of annual rainfall (Fig. 1). Rainfall is an essential component of the water balance. Its anomalies have crucial effects on industry and agriculture, as well as the lives of people, particularly for ASAR in China. Previous studies have shown signs of severe desertification and persistent drought in the semiarid region of northern China in recent decades (Wang and Li, 1990; Yatagai and Yasunari, 1994; Huang et al., 1999; Huang, 2006). The local and remote effects of the land surface processes and land degradation over ASAR in northern China have also been discussed in observational and numer-

*Corresponding author: HUANG Gang, hg@mail.iap.ac.cn

© China National Committee for International Association of Meteorology and Atmospheric Sciences (IAMAS), Institute of Atmospheric Physics (IAP) and Science Press and Springer-Verlag Berlin Heidelberg 2011

ical studies (e.g. Xue, 1996; Zhang et al., 2005; Zhou and Huang, 2006). These studies have indicated that variations in land-surface sensible flux and land degradation can cause local and remote rainfall anomalies. In turn, rainfall anomalies will affect land surface processes and cause changes to the environment. Therefore, identifying the long-term and interannual variability of rainfall and understanding the underlying mechanisms are of great importance to the future development of the economy, not only in ASAR, but also for other parts of the East Asian monsoon region. Much effort has been applied in studying summer rainfall variability in northern China during recent decades. Such work can generally be divided into two aspects, based on the domain of interest: persistent drought in North China, and the climate variations of ASAR in Northwest China.

For the first aspect, many previous studies have indicated there exists a decadal shift and a significant decreasing trend in summer precipitation over North China since the mid-1970s (Wang and Li, 1990; Chen et al., 1992; Yatagai and Yasunari, 1994; Yatagai and Yasunari, 1995; Nitta and Hu, 1996; Huang et al., 1999; Li et al., 2002; Gong et al., 2004; Xu et al., 2005; Ding et al., 2008; Huang et al., 2008). Wang and Li (1990) documented a possible link between precipitation fluctuations over the semiarid region of northern China and the summer monsoon, the western Pacific subtropical high, and ENSO. Huang et al. (2008) put forward a schematic model for how the interdecadal variations of the East Asian Climate system cause the persistent drought in North China, which is associated with ENSO, the subtropical High, mid-latitude wave train activity, Tibetan Plateau snow, and land surface processes. They proposed that the East Asian monsoon system was a coupling system of atmosphere, ocean, and land, and that the drought in North China (NC) was affected by the variability of East Asian monsoon climate subsystems, as well as their interaction between each other.

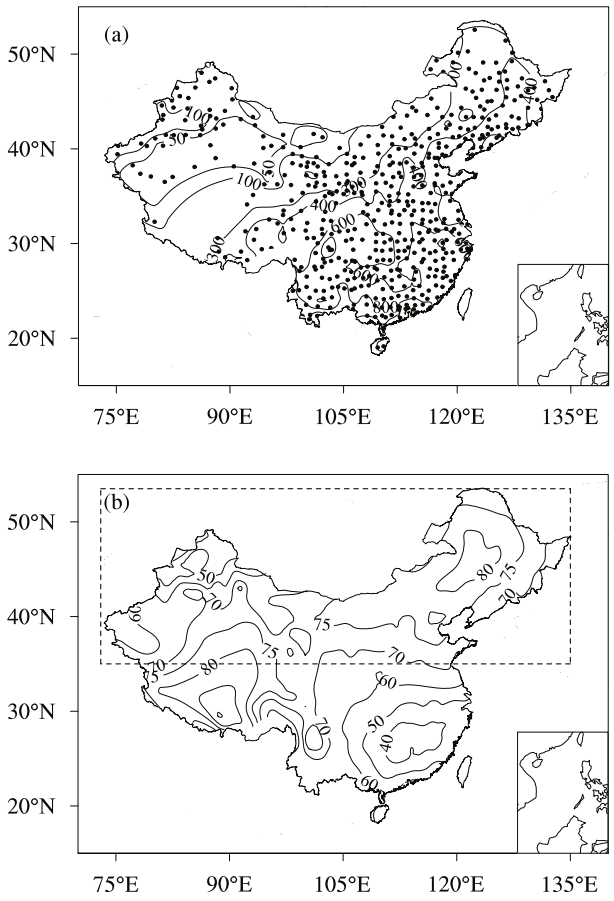

Fig. 1. (a) Geographical distribution of mean JJAS total precipitation (mm) and (b) the ratio (%) of JJAS mean rainfall to annual mean rainfall in China for the period 1961–2008. Dots in (a) denote the 552 weather stations. The dashed rectangular area represents the domain covered in the study.

For the second aspect, many observational studies have revealed that summer rainfall in Northwest China (NWC) shows an increasing trend since the 1960s, with a remarkable shift in the mid-1970s (Yatagai and Yasunari, 1994, 1995; Gong et al., 2004; Endo et al., 2005; Ma and Fu, 2006; Shi et al., 2007; Yang and Zhang, 2008; Zhou and Huang, 2009). These studies have also indicated that summer rainfall change in NWC exhibits regional characteristics, with a stage of relative increase in western parts of NWC, but a stage of drought in eastern parts, and that the intensity of the increasing trend of summer rainfall is greater in northern Xinjiang than in southern Xinjiang. Yang and Zhang (2008) analyzed the relationships between summer rainfall in Xinjiang and the Asian subtropical westerly jet stream (ASWJS). They revealed that the summer rainfall anomaly in Xinjiang had a notable correlation to the position of the ASWJS, as well as quasi-stationary wave activity. Zhou and Huang (2009) investigated the possible cause of interdecadal variability in summer rainfall in NWC and pointed out that an increase in near-surface temperature after 1978 enhanced convective instability, which in turn contributed to a strengthening of ascent and an increase in summer rainfall in NWC during the period 1978–2000.

ASAR has a large span in the east–west direction. The rainfall anomaly pattern in this region may mirror large-scale characteristics of atmospheric circulation and indicate internal connections between different parts. However, most previous work has focused on decadal-scale rainfall variability and on one part

of ASAR only. Few studies have addressed climatic variations over ASAR as a whole, which may provide essential information for understanding the nature of desertification in northern China. Therefore, one of the aims of the present paper is to investigate the interannual variability and regional characteristics of JJAS mean precipitation, and the associated atmospheric circulation, across the whole of ASAR.

The influence of atmospheric teleconnnection on boreal summer climate has been studied extensively. For example, a study by Nitta and Hu (1996) indicated that the Pacific–Japan (PJ) and Eurasia teleconnection patterns (EU) play very important roles in the variation of coupled patterns of summer rainfall and temperature in China, especially along the middle-lower reaches of the Yangtze River. More recent studies have suggested that the EU teleconnection is a bridge connecting the Indian summer monsoon (ISM) and the East Asian summer monsoon (EASM) (e.g. Wang et al., 2001; Wu and Wang, 2002). Lu et al. (2002) indentified a teleconnection pattern in July emerging from North Africa to East Asia along the westerly jet in the middle latitudes. They suggested that the teleconnection is a possible linkage of the EASM to the Indian monsoon, and even to subtropical heating anomalies over the Atlantic. Ding and Wang (2005) revealed a recurrent CGT pattern in the summertime mid-latitude circulation in the Northern Hemisphere. The CGT, actually a combination of the ISM–EASM teleconnection, the Silk-Road, and the Tokyo–Chicago express, is accompanied by significant rainfall and surface temperatures in the continental regions of Western Europe, European Russia, India, East Asia, and North America. ASAR is mainly located between 35°N and 55°N, which is on the path of the CGT. As revealed in this paper, the dominant mode of the JJAS mean rainfall in ASAR is closely associated with the CGT, which may suggest a new way to understand drought in northern China.

The remainder of the text is organized as follows. The datasets and methodology used are described in section 2. Section 3 presents the spatial and temporal variations of JJAS mean rainfall in northern China. In section 4, the relationship between the upper-level circumglobal teleconnection and JJAS rainfall in China is examined. A discussion is provided in section 5. And finally, conclusions are summarized in section 6.

2. Data and methods

2.1 *Datasets*

Two major datasets were used in this study. The first comprised daily observational rainfall data from 828 weather stations, and was provided by the National Meteorological Information Center of China, spanning the period 1951–2008. To achieve temporal continuity in terms of coverage from each station, we chose 552 stations (dots in Fig. 1a) from the complete data archive, as well as a slightly shorter period spanning 1961–2008 for this study. The second dataset comprised monthly atmospheric data for the period 1961–2008 from the National Centers for Environmental Prediction-National Center for Atmospheric Research (NCEP-NCAR) reanalysis (Kalnay et al., 1996), on a horizontal resolution of 2.5°×2.5°. The variables used in this study included winds and height at the 200, 500, 700, and 850 hPa levels.

2.2 *Methods*

As already mentioned, the present study concerns the area of northern China; however, more specifically, this covers the domain (35°–55°N, 73°–136°E), which includes a total of 273 weather stations (area denoted by the dashed rectangle in Fig. 1b). The rotated empirical orthogonal function (REOF) method of analysis was applied to reveal the regional characteristics of interannual variations in JJAS mean precipitation over the domain concerned. Firstly, the station datasets were normalized and long-term trends removed. Then, a correlation matrix of the rainfall data was used to compute the eigenvalues and eigenvectors of EOFs. After that, the first three EOFs were rotated orthogonally from the six leading modes of EOFs. Regression and correlation analysis were also used, in order to study the relationship between the interannual variation of JJAS rainfall in northern China and general atmospheric circulations.

3. Spatial and temporal variations of JJAS mean rainfall in northern China

3.1 *Long-term trend of JJAS mean rainfall in northern China* (1961–2008)

This study employed a relative variation ratio (RVR) to indicate the extent of change in JJAS mean rainfall during the period 1961–2008 in northern China. The RVR was obtained by dividing the linear trend of JJAS mean rainfall of one station by the JJAS mean rainfall of that station. The distribution of RVR in China is displayed in Fig. 2. A notable west–east contrast, with rainfall increasing in most parts of NWC, but decreasing in NC, Northeast China (NEC), can be observed. Furthermore, the largest positive and negative centers exist in North Xinjiang, and NC, respectively. These results are consistent with previous studies.

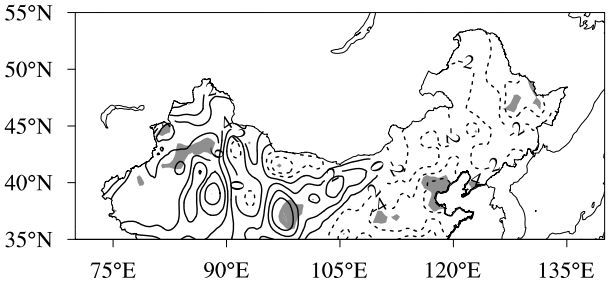

Fig. 2. RVR (%) of JJAS mean rainfall in northern China over the period 1961–2008 [units: mm (10 yr)$^{-1}$]. Shading indicates regions with trend anomalies beyond the 90% confidence level.

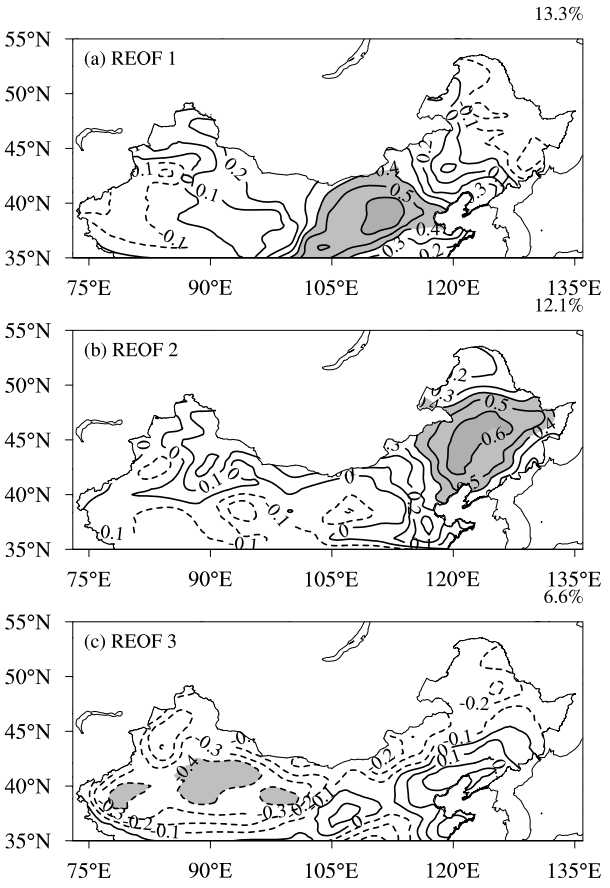

Fig. 3. Spatial modes of the first three REOFs of JJAS mean rainfall anomalies in northern China (contour interval: 0.1). Shaded areas indicate regions with values beyond 0.4 and less than −0.4. The contribution of each mode to the total variance is displayed in the upper right of each panel.

3.2 *Spatial and temporal variation of JJAS mean rainfall in northern China* (1961–2008)

To investigate the interannual variation in JJAS mean precipitation in northern China, REOF analysis, a widely used diagnostic tool in climatology, was applied. It retains the advantages but avoids the spatial limitations of EOF analysis, and can reveal efficiently the regionality of climatic factors (e.g. Richman, 1986; Murata, 1990; Yatagai and Yasunari, 1995; Li et al., 2002). The spatial patterns of the first three leading REOFs of the JJAS mean rainfall in northern China are shown in Fig. 3. The three modes account for 13.3%, 12.1%, and 6.6% of the total variance, respectively. The first two REOF modes feature a quasi-zonal tripole-like distribution with an anomalous center over the horseshoe-shaped arc region and adjacent region in between. The pattern in Xinjiang Province shows an opposing north–south distribution, which agrees with Yang and Zhang (2008). The third mode displays a consistent anomalous pattern in most

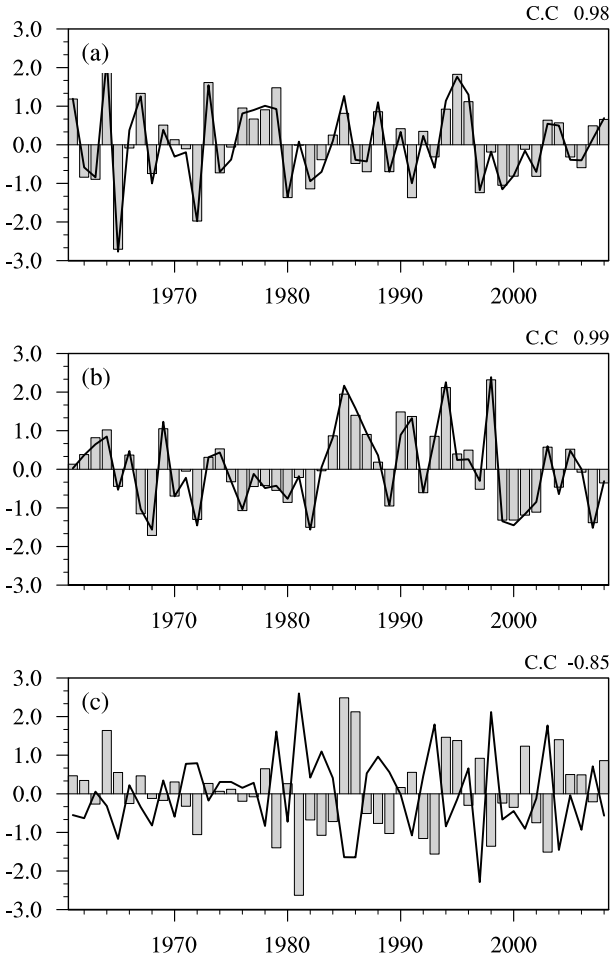

Fig. 4. Normalized time coefficients of each REOF mode [histograms: (a) for REOF1, (b) REOF2, and (c) REOF3] and the normalized series of regional mean JJAS rainfall for each relevant region [solid lines: (a) for NC, (b) NEC, and (c) TDNWC]. And the correlation coefficient (C.C) between the two time series in each subpanel is also added in its upper right.

parts of northern China, especially in NWC.

The spatial distribution in Fig. 3 designates the correlation coefficients of JJAS mean rainfall anomalies at each station with the time series corresponding to the REOF modes. The shaded areas, with values beyond 0.4 or less than −0.4, denote the correlation coefficients exceeding the 99% confidence level. So, three regions (shaded in Fig. 3) associated with the three dominant modes can be deduced: most parts of NC, NEC, and the Taklimakan Desert region in northwest China (TDNWC), with 76, 67, and 28 weather stations in each region, respectively.

The corresponding time coefficient of each principle component (PC) to the three REOF modes (histogram) and the JJAS mean rainfall anomalies over the regions of NC, NEC, and TDNWC (solid lines) are depicted in Fig. 4. It is obvious that the three PCs match well with the regional averaged JJAS mean rainfall anomaly of the associated region. The correlation coefficients between the three pairs of time series are 0.99, 0.98, and −0.86, respectively, all beyond the 99% confidence level based on Pearson's r statistical significance test. Thus, the three PCs characterize JJAS mean rainfall variability of the corresponding region. Furthermore, by combing the power spectrum of each PC (Fig. 5), each of their features of variability can be obtained. PC1 exhibits a 3- and 9-year periodic variation, showing a remarkable relatively dry period from the mid-1990s to the present day. PC2 shows decadal-scale variation and a distinct decreasing trend in the last two decades, with dry periods from the late 1960s to the early 1980s, and from the late 1990s to the present day, and with wet periods between. Meanwhile, there is no significant frequency based on the spectral analysis, as shown by Fig. 5b. For the third PC, the spectral analysis result reveals large interannual variability, with 4–5- and 9-year periods of variation (Fig. 5c).

4. The relationship between the CGT and interannual variations of JJAS mean rainfall in northern China

The CGT is a geographically phase-locked recurrent teleconnection pattern during boreal summer from July to September, having its path within the westerly jet stream from the Northeast Atlantic through Eurasia, the North Pacific, to North America, and having three center cells primarily in East Asia, mainly in northern China (Ding and Wang, 2005). Interestingly, the interannual variability of JJAS mean rainfall in northern China shows a clear quasi-zonal wave-like distribution in the first two REOFs, with the center over a horseshoe-shaped arc region, where the transition area of ASAR is located. It is conceivable that the first two leading REOFs may have a potential connection with the CGT. This section investigates this relationship.

4.1 *The CGT patterns associated with the first two leading modes of JJAS mean rainfall in northern China*

To begin with, the atmospheric circulation anomalies corresponding to the first two dominant modes of the REOFs are explored using the regression method. Figure 6 shows the regressed patterns of JJAS mean height at the 200 hPa and 700 hPa levels with respect to the first two time coefficients mentioned above. The

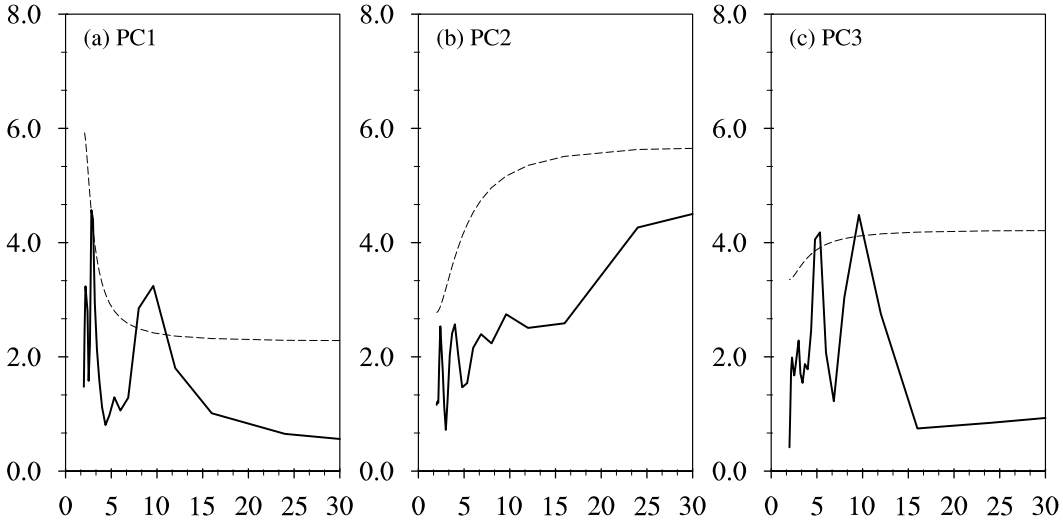

Fig. 5. The power spectrum (solid line) for the principle component (PC) of the three REOFs, and the dotted thin lines represent the power spectrum at the 95% confidence level.

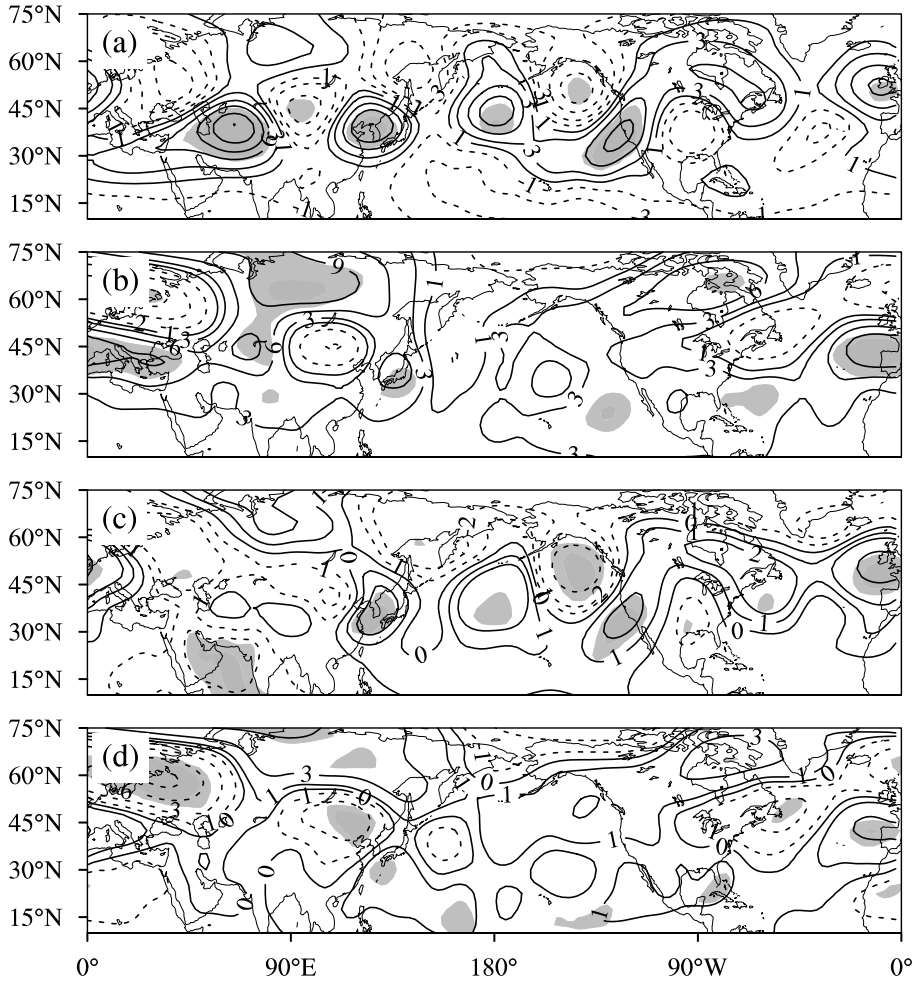

Fig. 6. Anomalies of regressed geopotential height at 200 hPa (a, b) and 700 hPa (c, d). (a, c) against PC1; (b, d) against PC2. Shading represents regions with height anomalies beyond the 95% confidence level.

most prominent feature in Fig. 6a, which is related to PC1 regressed onto the height at 200 hPa, is a wave train structure from the Northeast Atlantic through Eurasia, the North Pacific, to North America, with positive anomalous centers over the Northeast Atlantic, central Asia, Northeast Asia, the central-north Pacific, and western North America, with negative centers between. The largest positive center is found over central Asia in the domain (35°–40°N, 60°–70°E).

The regressed height pattern at the 200 hPa level against PC2 is shown in Fig. 6b. A similar wave train structure emerges, although not as clear and strong as that in Fig. 6a, especially over the North Pacific and North America. The positions of the anomalous centers move a little eastward compared to those in Fig. 6a. In addition, a NAO-like (North Atlantic Oscillation) pattern presents along the coastline of Western Europe from North Africa to the North Atlantic, suggesting influence from the high latitudes.

The atmospheric circulation at the 500 hPa level related to the two REOF modes exhibits a good similarity to that at the 200 hPa level (Figs. 6a, b), having anomalous centers over the same locations, but the amplitude of the anomalies increases with height (figures not shown).

The regressed geopotential height anomalies at 700 hPa corresponding to the two REOFs modes are shown in Figs. 6c and d. The regressed low-level height anomalies exhibit wave train patterns similar to those shown in Figs. 6a and b, though with weaker intensity and a tilted baroclinic structure over the northwest part of India where there is an anomalous ridge at 200 hPa and an enhanced cyclonic anomaly over the Arabian Peninsula and adjacent sea at 700 hPa. The regressed wind fields against the two REOF modes match the height anomalies well (figure not shown).

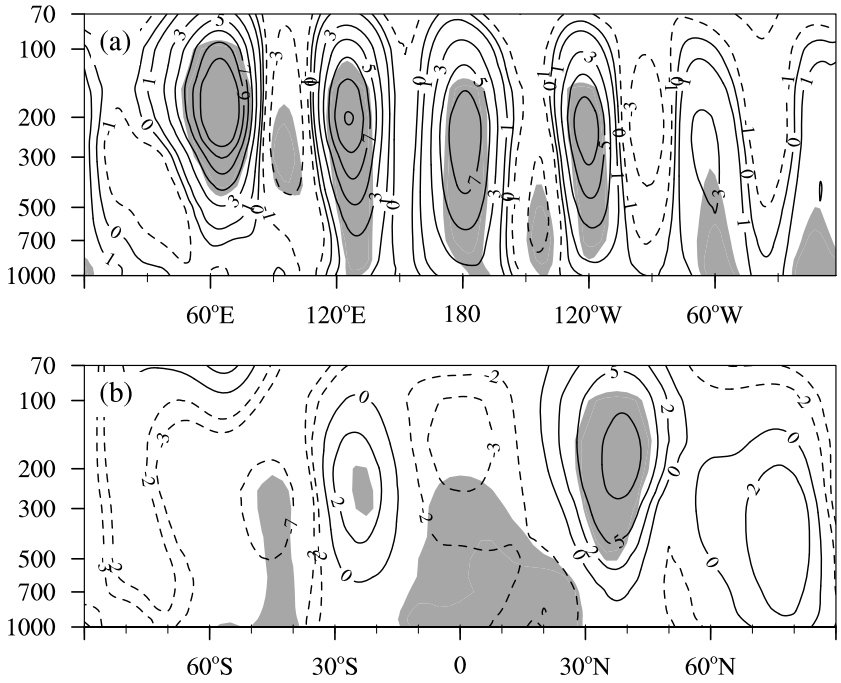

Fig. 7. (a) Height–longitude cross-section anomalies of PC1 regressed onto height averaged within 30°–50°N. (b) Height–latitude cross-section anomalies of PC1 regressed onto height averaged within 60°–70°E. Shaded reveals the regions with height anomalies exceed the 90% confidence level.

The vertical structure of the wave train pattern can also be examined. Figure 7a illustrates the height–longitude cross section anomalies of PC1 regressed onto height averaged within 30°–50°N. Evidently, a wave train structure emerges along the westerly jet from near 60°E, passing over Eurasia to North America. This wave-like pattern shows a vertically quasi-barotropic structure for nearly all the wave train centers, except for a tilted baroclinic pattern over the northwest part of India. Also, it has a wavenumber-6 structure, with an intense region of positive/negative anomalous centers confined to 30°–50°N within a waveguide associated with the westerly jet stream extending from Eurasia to North America. Furthermore, it is evident that the maximum anomalous center for each cell is at about the 200 hPa level, with the largest one occurring around 65°E. These features demonstrate a geographically fixed global-scale teleconnection pattern, strikingly similar to the CGT revealed in Ding and Wang (2005). Moreover, the regressed patterns at 200 hPa are identical to the two scenarios of the CGT proposed by Ding and Wang (2005) [see Fig.15 in Ding and Wang (2005)], respectively. These similarities can be clearly seen in Fig. 8.

Figure 8 displays the meridional wind anomalies associated with the first two PCs. The pattern corresponding to PC1, as shown in Fig. 8a, exhibits an apparent wave-like structure propagating within the westerly jet stream from the Northeast Atlantic, through Eurasia and the North Pacific, to eastern America, and for the regressed pattern against PC2 shown in Fig. 8b, a notable teleconnection pattern emerges over the Eurasian continent from Northern Europe to East Asia. Additionally, a distinct discrepancy is observed over the Arctic region in which the magnitude of anomalies regressed against PC1 are much weaker than those against PC2. This implies that the strong anomalous activity over the Arctic area, or from high latitudes, may affect the wave-like anomaly pattern. The features revealed in Fig. 8 matches well with Ding and Wang (2005).

4.2 *JJAS rainfall anomalies in China associated with CGT patterns*

The results thus far have indicated that the interannual variability of JJAS mean rainfall in northern China shows a considerable correlation with the CGT pattern. Here, following Ding and Wang (2005), the correlation distributions between them are examined. First, two indices, CGTI-1 and CGTI-2, are defined to represent the two scenarios of CGT variability, respectively.

For the first scenario, we employ the definition by Ding and Wang (2005), which is defined as the norma-

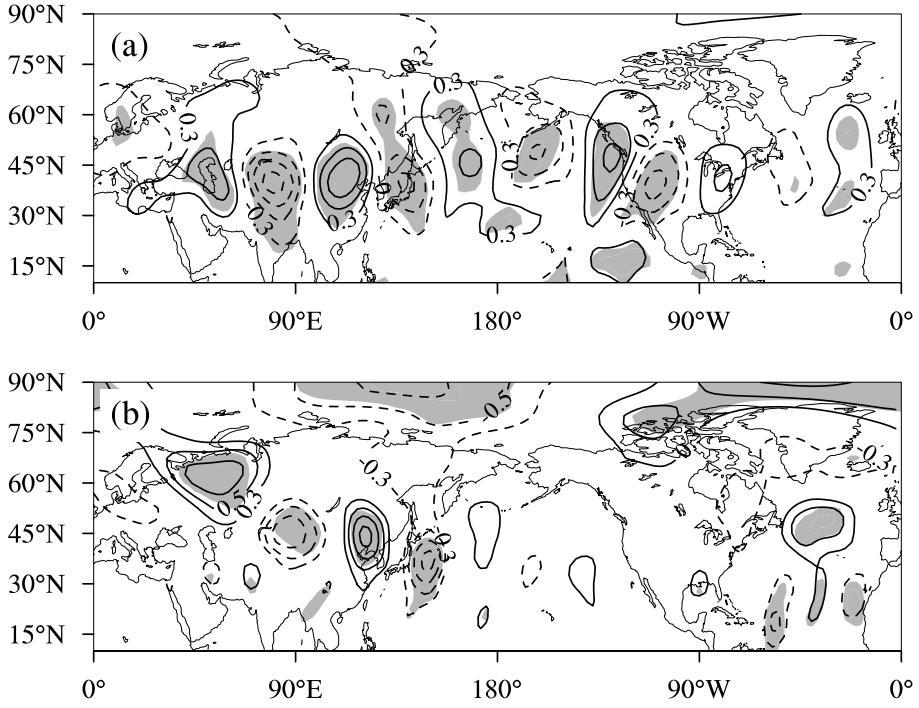

Fig. 8. Anomalies of JJAS mean meridional wind at 200 hPa regressed against PC1 (a) and PC2 (b). Shallow area indicates the region with wind anomalies beyond the 95% confidence level.

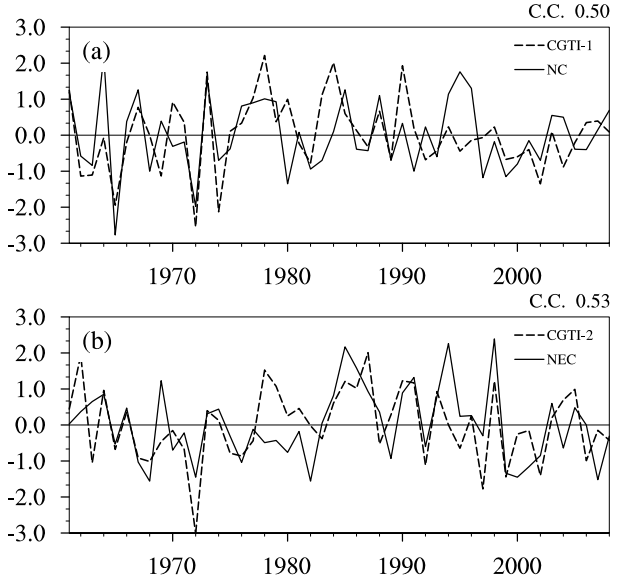

Fig. 9. Normalized time series of CGTI 1-2 (dashed lines) and regional mean JJAS rainfall in NC and NEC (solid lines). And the correlation coefficient (C.C) between each pair of time series is also added in the upper right of each panel.

zlied time series of the interannual variability of the 200 hPa height averaged over the reference area (35°–40°N, 60°–70°E), and denote it as CGTI-1. CGTI-2, corresponding to the second scenario, is defined using the difference between the normalized time series of regionally-averaged height at 200 hPa over the two areas, (40°–50°N, 20°–10°W) and (60°–65°N, 15°–25°E). The regressed height anomalies at 200 hPa against the two indices resemble those in Fig. 6 (figures not shown).

Figure 9 displays the two indices and the normalized time series of regionally-averaged JJAS mean rainfall in NC and NEC. The correlation coefficients between the two pairs of time series are 0.50 and 0.53, respectively, both beyond the 99% confidence level. The correlation coefficients of the JJAS mean rainfall and the two CGTIs are displayed in Fig. 10, the patterns of which resemble the spatial modes of the first two REOFs (Figs. 3a, b), with significant anomalies located in northern China, especially NC, NEC, and western part of Xinjiang Province. The composite atmospheric circulations related to the CGTIs are also performed. Figure 11 shows the positive-minus-negative CGTI composite wind anomalies at 850 hPa (vector) and vertical velocities at 500 hPa (contour), the cases of which are chosen from the lower and upper bounds, respectively, with a 0.5 standard deviation of the CGTIs. The composite results show that, corresponding to each scenario, an anomalous southerly

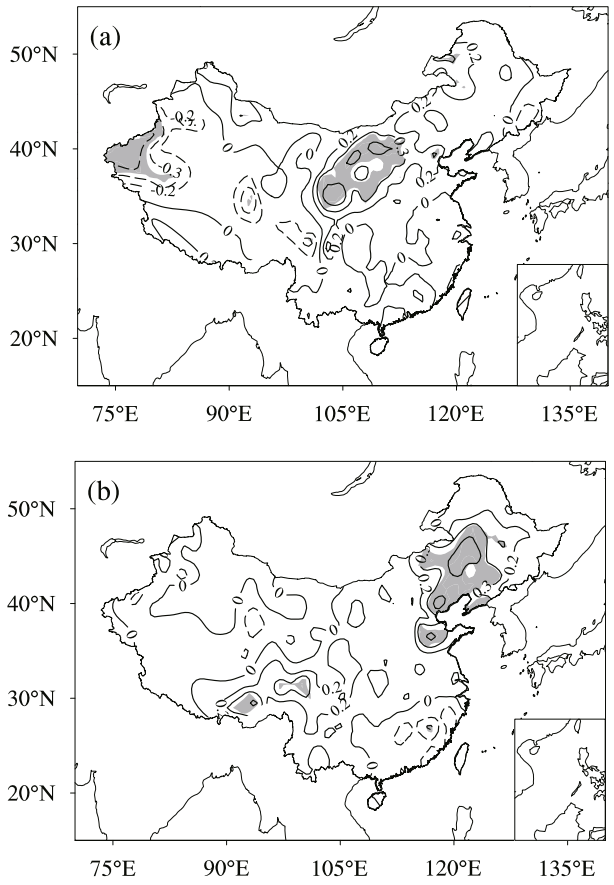

Fig. 10. Correlation coefficients between CGTI and the JJAS mean rainfall in China: (a) CGTI-1; (b) CGTI-2. Shaded area illustrates the region of rainfall anomalies beyond the 95% confidence level.

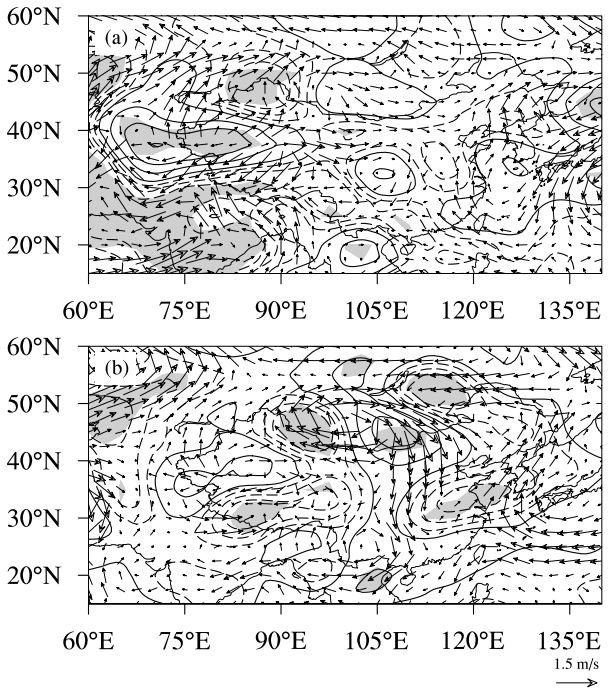

Fig. 11. Composite anomalies of winds (vectors, arrow with scale at bottom right of the panels) at 850 hPa and vertical velocity (contour) at 500 hPa associated with the two CGTIs: (a) CGTI-1; (b) CGTI-2. Shading denotes the region with vertical velocity anomalies beyond the 95% confidence level.

over Eastern China with abundant moisture flows to northern China converges with the cold air from high latitudes and triggers anomalous ascending motion over NC/NEC, all of which are most favorable for the occurrence of rainfall, and thus positive rainfall anomalies are found over the two regions. Meanwhile, both the two CGTIs and the rainfall anomalies in NC/NEC are in a below-normal phase during recent decades. As to why this happens requires further study.

5. Discussion

Previous studies have already revealed that there are teleconnection patterns and stationary Rossby waves propagating eastward within the Asian jet in boreal summer (e.g. Ambrizzi et al., 1995; Rodwell and Hoskins, 1996; Krishnan and Sugi, 2001; Lu et al., 2002; Wu and Wang, 2002; Enomoto et al., 2003; Enomoto, 2004; Ding and Wang, 2005; Sato and Takahashi, 2006) and these features can be achieved by a few variables, such as geopotential height, streamfuction, and meridional wind. The formation mechanism of the wave-like pattern on the jet has also been discussed (Rodwell and Hoskins, 1996; Enomoto et al., 2003; Ding and Wang, 2005; Sato and Takahashi, 2006; Shi and Lu, 2010). Rodwell and Hoskins (1996) revealed that the diabatic heating associated with the Indian monsoon resulted in diabatic cooling and downward motion over the Eurasian continent and Mediterranean Sea. A study by Enomoto et al. (2003) indicated that heating from the Indian monsoon and the related diabatic forcing over the continent would excite a quasi-stationary disturbance on the jet, triggering a barotropic structure propagating within the westerly jet. Sato and Takahashi (2006) reported that a Rossby wave packet propagated eastward from the Middle East, passing over East Asia, and reaching North America. They showed that the anomaly pattern was strengthened through kinetic energy conversion near the entrance of the Asian jet over the Middle East, and that the interaction between the anomaly pattern and the basic field contributed to the appearance of the anomalous wave-like pattern.

Most of the studies mentioned above discuss the teleconnection pattern on the monthly or submonthly

timescale. On the seasonal scale, the features of the teleonnection also, to some extent, reveal the possible relationship between the teleconnection and associated factors mentioned above, such as the westerly jet (shown in Fig. 7a) and the heating from the ISM. Figure 7a shows a clear wave train pattern propogating eastward along the westerly jet, which plays the role of the waveguide confining the wave train to within the domain 30°–50°N. Furthermore, interestingly, the teleconnection pattern exhibits an evident baroclinic structure around 65°E, with a maximum center at about 200 hPa. Thus the vertical structure around 65°E is investigated. Figure 7b depicts the height–latitude cross section of geopotential height anomalies (averaged within the domain 50°–70°E) regressed against PC1. A barotropic teleconnecton pattern appears with out-of-phase anomalies between the tropics and extratropics, especially in the Northern Hemisphere. This structure can also be seen in Fig. 11a, where the vertical velocity anomalies at 500 hPa show an "ascent–descent–ascent" pattern around 65°E. Furthermore, we can determine that the meridional teleconnection pattern may be closely related to the low level activity over the Indian Continent/Ocean, where significant height anomalies are apparent. This meridional teleconnection pattern resembles the low-frequency waveguide (or a biweekly oscillation) at 200 hPa near 60°E, mentioned in Liu and Yu (1993). These authors documented that the wave source of this waveguide was located around 10°–25°N, and the perturbation propagated polarward from the wave source to affect the westerlies of the Southern and Northern Hemispheres. This indicates that the waveguide near 60°E may be a bridge connecting the tropics and extratropics. Wang et al. (2005) proposed a mechanism for how the tropical activity affected the extratropical atmosphere. They indicated that a forcing embedded in the deep tropical easterlies may excite a Rossby wave response in the extratropical westerlies and the southerly flow component in the basic state played a role of a conveyor, transferring a Rossby wave source northward. The study by Wang et al. (2005) also showed that the southerly conveyor determined the location of the effective Rossby wave source and that the extratopical response is relatively insensitive to the location of the tropical forcing, provided that the tropical response can reach the southerly conveyor. A stronger southerly flow favors a stronger extratropical response, and the spatial structure of the extratropical response is determined by the extratropical westerly basic flows. This result agrees well with Sato and Takahashi (2006), that the appearance of the Rossby wave on the westerly jet is clearly phase-dependent, and may be dominanted by the internal dynamics of interaction between the anomaly pattern and the basic flows. This implies that the anomalous convectivity over the Indian Ocean, or diabatic heating from the ISM, exicites a Rossby wave response in the extratropical westerly by triggering the anomalous southerly in the tropics, thus affecting the wavelike pattern on the jet. However, these results were achieved based on a simple barotropical model or statistical analysis, and the real atmosphere is much more complicated. The impact of tropical acitivity on the wavelike pattern on the jet is still affirmative.

6. Conclusions

Using the latest daily observation rainfall data sets for the period 1961–2008, the trend and interannual variations of JJAS mean rainfall in northern China have been studied. Atmospheric circulation anomalies associated with the interannual variation of summer rainfall have also been explored. The major findings are summarized as follows.

Firstly, the RVR of the JJAS rainfall in northern China over the period 1961–2008 shows a "west–increase–east–decrease" pattern, with considerable anomalies over Xinjiang Province and North China. Secondly, the spatial and temporal structures of the interannual variation of JJAS mean rainfall in northern China were revealed by REOF analysis. The first two dominant modes showed a quasi-zonal tripole-like pattern, with the centers over the transition areas of ASAR in northern China. Three regional divisions were identified by the REOF analysis: NC, NEC, and TDNWC. Results indicated that the variation frequency of the summer rainfall anomaly varies between regions. Summer rainfall over NC revealed two dominant variation frequencies and a remarkable dry period from the late 1990s. Over NEC, decadal-scale variation and a decreasing trend in the last two decades was found, but with no significant frequency variation. TDNWC exhibited large interannual variability.

This study has also demonstrated that interannual variations of JJAS mean rainfall in northern China are well related to the upper-level CGT in boreal summer, especially in NC and NEC. The significant summer rainfall anomalies related to the CGT were found to be closely connected with the locations of the action centers of the CGT. There are three center cells of the CGT primarily over East Asia, mainly in northern China, which affect moisture transportation and ascending motion over these regions. Results showed that a positive CGTI will excite a southerly anomaly, bringing more moisture to northern China; meanwhile, upper-level divergence favors low-level convergence and ascending motion over

NC/NEC. As such, positive rainfall anomalies tend to be found in NC/NEC. The correlation coefficients of the regional averaged JJAS mean rainfall over NC and NEC with the CGTI were up to 0.50 and 0.53, respectively, both beyond the 99% confidence level.

The CGT pattern reveals a geographically phase-locked structure during boreal summer from July to September (Ding and Wang, 2005) and is accompanied by significant climate anomalies along its path. This is confirmed by the present study. The closely in-phase relationship between the rainfall anomalies in NC/NEC and the teleconnection patterns provides us with a new way to understand the persistent drought in NC and the decreasing rainfall in NEC. Finally, what contributes to the long-term negative phase of CGTI, and whether the wavelike pattern is the dominant factor contributing to the long-term decrease in northern China, which remain unclear and require further investigation.

Acknowledgements. The authors are grateful to Dr. Shang-Ping XIE, Dr. WU Renguang, and the two anonymous reviewers for their insightful comments that led to a significant improvement of the manuscript. This work was supported by the CAS Innovation Key Program (Grant No. KZCX2-YW-BR-14), National Basic Research Program of China (2011CB309704), Special Scientific Research Project for Public Interest (Grant No. GYHY201006021), and the National Natural Science Foundation of China (Grant Nos. 40890155, 40775051, U0733002).

REFERENCES

Ambrizzi, T., B. Hoskins, and H. Hsu, 1995: Rossby wave propagation and teleconnection patterns in the austral winter. *J. Atmos. Sci*, **52**, 3661–3672.

Chen, L., M. Dong, and Y. Shao, 1992: The characteristics of interannual variations on the East Asian monsoon. *J. Meteor. Soc. Japan*, **70**, 397–421.

Chen, W., D. Zhu, H. Liu, and S. Sun, 2009: Land-air interaction over arid/semi-arid areas in China and its impact on the east Asian summer monsoon. Part I: Calibration of the land surface model (BATS) using multicriteria methods. *Adv. Atmos. Sci.*, **26**, 1088–1098, doi: 10.1007/s00376-009-8187-3.

Ding, Q., and B. Wang, 2005: Circumglobal teleconnection in the Northern Hemisphere summer. *J. Climate*, **18**, 3483–3505.

Ding, Y., Z. Wang, and Y. Sun, 2008: Inter-decadal variation of the summer precipitation in East China and its association with decreasing Asian summer monsoon. Part I: Observed evidences. *Int. J. Climatol*, **28**, 1139–1161.

Endo, N., B. Ailikun, and T. Yasunari, 2005: Trends in precipitation amounts and the number of rainy days and heavy rainfall events during summer in China from 1961 to 2000. *J. Meteor. Soc. Japan*, **83**, 621–631.

Enomoto, T., 2004: Interannual variability of the Bonin high associated with the propagation of rossby waves along the Asian jet. *J. Meteor. Soc. Japan*, **82**, 1019–1034.

Enomoto, T., B. Hoskins, and Y. Matsuda, 2003: The formation mechanism of the Bonin high in August. *Quart. J. Roy. Meteor. Soc*, **129**, 157–178.

Gong, D., P. Shi, and J. Wang, 2004: Daily precipitation changes in the semi-arid region over northern China. *Journal of Arid Environments*, **59**, 771–784.

Huang, G., 2006: Global climate change phenomenon associated with the droughts in North China. *Climatic and Environmental Research*, **11**, 270–279. (in Chinese)

Huang, R. H., Y. H. Xu, and L. T. Zhou, 1999: The interdecadal variation of summer precipitations in China and the drought trend in North China. *Plateau Meteorology*, **18**, 465–476. (in Chinese)

Huang, R. H., L. Gu, J. L. Chen, and G. Huang, 2008: Recent progresses in studies of the temporal-spatial variations of the east asian monsoon system and their impacts on climate anomalies in China. *Chinese J. Atmos. Sci.*, **32**, 691–719. (in Chinese)

Kalnay, E., and Coauthors, 1996: The NCEP/NCAR 40-year reanalysis project. *Bull. Amer. Meteor. Soc.*, **77**, 437–471.

Krishnan, R., and M. Sugi, 2001: Baiu rainfall variability and associated monsoon teleconnections. *J. Meteor. Soc. Japan*, **79**, 851–860.

Li, X., Y. Zhu, and W. Qian, 2002: Spatiotemporal variations of summer rainfall over eastern China during 1880–1999. *Adv. Atmos. Sci.*, **19**, 1055–1068.

Liu, Z., and S. Yu, 1993: The upper tropospheric low-frequency waveguides in summer. *Journal of Tropical Meteorology*, **9**, 142–149. (in Chinese)

Lu, R., J. Oh, and B. Kim, 2002: A teleconnection pattern in upper-level meridional wind over the North African and Eurasian continent in summer. *Tellus A*, **54**, 44–55.

Ma, Z., and C. Fu, 2006: Some evidences of drying trend over North China from1951 to 2004. *Chinese Science Bulletin*, **51**, 2913–2925.

Murata, A., 1990: Regionality and periodicity observed in rainfall variations of the Baiu season over Japan. *Int. J. Climatol.*, **10**, 627–646.

Nitta, T., and Z. Hu, 1996: Summer climate variability in China and its association with 500 hPa height and tropical convection. *J. Meteor. Soc. Japan*, **74**, 425–445.

Richman, M., 1986: Rotation of principal components. *Int. J. Climatol.*, **6**, 293–335.

Rodwell, M., and B. Hoskins, 1996: Monsoons and the dynamics of deserts. *Quart. J. Roy. Meteor. Soc*, **122**, 1385–1404.

Sato, N., and M. Takahashi, 2006: Dynamical processes related to the appearance of quasi-stationary waves

on the subtropical jet in the midsummer northern hemisphere. *J. Climate*, **19**, 1531–1544.

Shi, S. F., and R. Y. Lu, 2010: Teleconnection patterns along the Asian jet associated with different combinations of convetion oscillation over the Indian continent and western North Pacific during summer. *Atmos. Oceanic Sci. Lett.*, **3**, 14–18.

Shi, Y., Y. Shen, E. Kang, D. Li, Y. Ding, G. Zhang, and R. Hu, 2007: Recent and future climate change in northwest China. *Climatic Change*, **80**, 379–393.

Wang, B., R. Wu, and K. Lau, 2001: Interannual variability of the Asian summer monsoon: Contrasts between the Indian and the western North Pacific-East Asian monsoons. *J. Climate*, **14**, 4073–4090.

Wang, W., and K. Li, 1990: Precipitation fluctuation over semiarid region in northern China and the relationship with El Niño/Southern Oscillation. *J. Climate*, **3**, 769–783.

Wang, Z., C. Chang, B. Wang, and F. Jin, 2005: Teleconnections from Tropics to northern extratropics through a southerly conveyor. *J. Atmos. Sci*, **62**, 4057-4070.

Wu, R., and B. Wang, 2002: A contrast of the east Asian summer monsoon-ENSO relationship between 1962–77 and 1978–93. *J. Climate*, **15**, 3266–3279.

Xu, G., X. Yang, and X. Sun, 2005: Interdecadal and interannual variation characteristics of rainfall in North China and its relation with the northern hemisphere atmospheric circulations. *Chinese Journal Geophysics*, **48**, 511–518. (in Chinese)

Xue, Y., 1996: The impact of desertification in the Mongolian and the inner Mongolian grassland on the regional climate. *J. Climate*, **9**, 2173–2189.

Yang, L., and Q. Zhang, 2008: Interannual variation of summer precipitation in Xinjiang and Asian subtropical westerly jet stream. *Journal of Applied Meteorological Science*, **19**, 171–179. (in Chinese)

Yatagai, A., and T. Yasunari, 1994: Trends and decadal-scale fluctuations of surface air temperature and precipitation over China and Mongolia during the recent 40 year period(1951–1990). *J. Meteor. Soc. Japan*, **72**, 937–957.

Yatagai, A., and T. Yasunari, 1995: Interranual variations of summer precipitation in the arid/semi-arid regions in China and Mongolia: Their regionality and relation to the Asian summer monsoon: Special edition on HEIFE. I. *J. Meteor. Soc. Japan*, **73**, 909–923.

Zhang, J., W. Dong, and C. Fu, 2005: Impact of land surface degradation in northern China and southern Mongolia on regional climate. *Chinese Science Bulletin*, **50**, 75–81.

Zhou, L., and R. Huang, 2009: Interdecadal variability of summer rainfall in Northwest China and its possible causes. *Int. J. Climatol.*, **30**, 549–557.

Zhou, L. T., and R. H. Huang, 2006: Characteristics of interdecadal variability of the difference between surface temperature and surface air temperature in spring in arid and semi-arid region of Northwest China and its impact on summer precipitation in North China. *Climatic and Environmental Research*, **11**, 1–13. (in Chinese)

ADVANCES IN ATMOSPHERIC SCIENCES, VOL. 28, NO. 2, 2011, 421–432

The Impact of the Tropical Indian Ocean on South Asian High in Boreal Summer

HUANG Gang*[1] (黄 刚), QU Xia[2,3] (屈 侠), and HU Kaiming[2,3] (胡开明)

[1]*Key Laboratory of Regional Climate-Environment Research for Temperate East Asia, Institute of Atmospheric Physics, Chinese Academy of Sciences, Beijing* 100029

[2]*State Key Laboratory of Numerical Modeling for Atmospheric Sciences and Geophysical Fluid Dynamics, Center for Monsoon System Research, Institute of Atmospheric Physics, Chinese Academy of Sciences, Beijing* 100083

[3]*Graduate University of Chinese Academy of Sciences, Beijing* 100049

(Received 16 December 2009; revised 24 February 2010)

ABSTRACT

The tropical Indian Ocean (TIO) is warmer than normal during the summer when or after the El Niño decays. The present study investigates the impact of TIO SST on the South Asian High (SAH) in summer. When the TIO is warmer, the SAH strengthens and its center shifts southward. It is found that the variations in the SAH cannot be accounted for by the precipitation anomaly. A possible mechanism is proposed to explain the connection between the TIO and SAH: warmer SST in the TIO changes the equivalent potential temperature (EPT) in the atmospheric boundary layer (ABL), alters the temperature profile of the moist atmosphere, warms the troposphere, which produces significant positive height anomaly over South Asia and modifies the SAH.

An atmospheric general circulation model, ECHAM5, which has a reasonable prediction skill in the TIO and South Asia, was selected to test the effects of TIO SST on the SAH. The experiment with idealized heating over the TIO reproduced the response of the SAH to TIO warming. The results suggest that the TIO-induced EPT change in the ABL can account for the variations in the SAH.

Key words: tropical Indian Ocean, South Asia High, equivalent potential temperature

Citation: Huang, G., X. Qu, and K. M. Hu, 2011: The impact of the tropical Indian Ocean on the South Asian High in boreal summer. *Adv. Atmos. Sci.*, **28**(2), 421–432, doi: 10.1007/s00376-010-9224-y.

1. Introduction

The ENSO is a major mode of air–sea interaction on interannual timescale with profound influences on global climate. The tropical Indian Ocean (TIO) gradually warms when El Niño is in its developing phase, and the warming reaches a maximum nearly one season after the NINO3.4 SST anomaly has peaked (Klein et al., 1999; Lau and Nath, 2000; Alexander et al., 2002; Lau and Nath, 2003). The warm anomaly still exists during the summer after the peak of El Niño (Du et al., 2009). Klein et al. (1999) pointed out that changes in evaporation and cloud cover induced by the El Niño account for the warm anomaly over most parts of the Indian Ocean during the ENSO decaying phase; while the warm anomaly over the southwest Indian Ocean could not be explained by the above changes. Previous research (Masumoto and Meyers, 1998; Yu et al., 2005) revealed that, when the ENSO matures, changes in the Walker circulation generate an anticyclonic wind anomaly over the TIO, which forces downwelling Rossby waves in the southeast Indian Ocean. The Rossby waves propagate westward, arrive in the southwest Indian Ocean several months later, deepen the thermocline ridge and warm the SST (Huang and Kinter, 2002; Xie et al., 2002). Thus, ocean dynam-

*Corresponding author: HUANG Gang, hg@mail.iap.ac.cn

© China National Committee for International Association of Meteorology and Atmospheric Sciences (IAMAS), Institute of Atmospheric Physics (IAP) and Science Press and Springer-Verlag Berlin Heidelberg 2011

ics may play an important role in the warming in the southwest Indian Ocean.

The warming of the TIO in response to El Niño has influences on the climate locally and remotely after El Niño decays. This phenomenon is called the "capacitor effect" (Annamalai et al., 2005; Yang et al., 2007; Yang and Liu, 2008; Xie et al., 2009). In the years when there is basin-wide warming in the TIO, anticyclonic wind anomaly occurs over the western North Pacific, rainfall over Yangtze River is above normal and the South Asian High (SAH) strengthens in the summer (Yang et al., 2007). The Fast Ocean-Atmosphere Model and five Atmospheric General Circulation Models (AGCMs) have reproduced the phenomena (Yang et al., 2007; Li et al., 2008). Analysis by Xie et al. (2009) showed that a Kelvin wave anomaly induced by warming in TIO is key to the generation of an anticyclone anomaly over the western North Pacific. Earli er studies (Wang et al., 2000, 2003) suggested a role played by local air-sea interaction in the maintenance of the western North Pacific anomalous anticyclone in early summer.

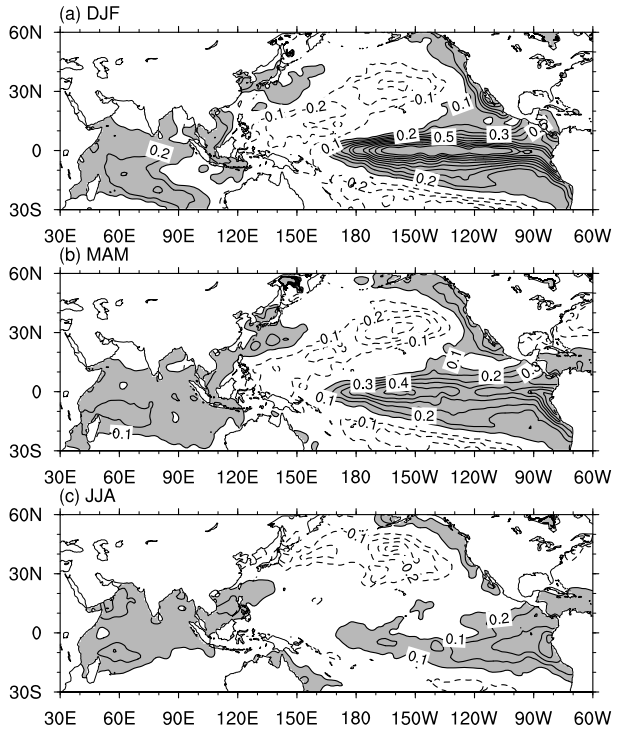

Fig. 1. Regression of SST against N(0)D(0)J NINO3.4 SST index from 1979–2007, (a), (b) and (c) are the results of D(0)JF, MAM and JJA, respectively. Negative values are shown in dash contours. Shading indicates values larger than 0.1; and the interval of white contours is 0.1 K, the unit is K. For the sake of clarity, spatial 9-point smoothing is performed and the zero contour is omitted.

Figures 1 and 2 demonstrate the regression of SST and 200-hPa velocity potential, respectively, on the NINO3.4 SST index from November(0) to January (N(0)D(0)J). The numeral "0" denote the preceding year. In the winter when El Niño peaks and the following spring, SST is warmer than normal in the equatorial eastern Pacific (EEP) and the 200-hPa velocity potential shows an upper-level anomalous divergence. Though there is a warming in the TIO, the 200-hPa velocity potential suggests a weak anomalous divergence or convergence over the TIO. This indicates that during these two seasons, the EEP SST has a major impact on circulation over the tropical Indo-Pacific Ocean and that TIO SST does not have a large impact on circulation or it just responds to the atmosphere passively. During the summer following El Niño, the warm anomaly over the EEP is weaker than that in N(0)D(0)J and March to May (MAM), and the intensity of the warm anomaly over the TIO is approximately equal to that in N(0)D(0)J and MAM. The 200-hPa velocity potential in summer shows an anomalous divergence over the TIO and no significant anomaly over the EEP, indicating an active role of the TIO SST on local and surrounding circulation in sum-

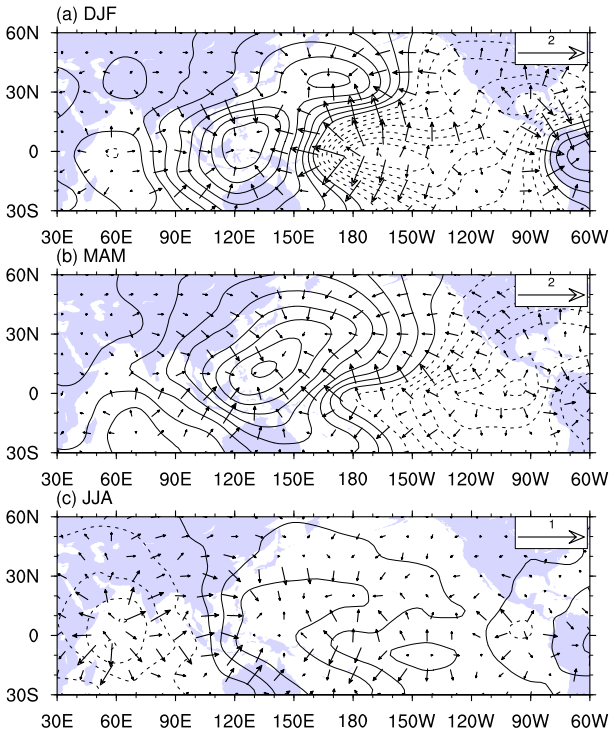

Fig. 2. As in Fig. 1, except for the results of 200-hPa velocity potential (contours) and divergent wind component (vectors), the contour interval is 2.5×10^5 m^2 s^{-1}. Solid and dashed lines represent positive and negative values, respectively.

mer, in agreement with Wu et al. (2009). The regression of SST and 200-hPa velocity potential in the preceding winter, spring, and summer, on the TIO SST in summer shows similar results. The present study focuses on the impacts of the TIO SST in summer.

The SAH is a high pressure system located in the upper troposphere over the Tibetan Plateau and its surrounding area in summer. It is a result of the elevated heating of the Tibetan Plateau to the atmosphere (Flohn, 1960) and has been recognized to be the strongest and steadiest system in the upper troposphere (Mason and Anderson, 1963). The variations of the SAH are tightly linked to precipitation and circulation over Asia. Tao and Zhu (1964) reported that longitudinal displacement of the SAH leads that of a 500-hPa subtropical anticyclone over the Western Pacific for a few days and is a good index for short- to medium-range weather forecasts in Asia. In the summer, when the SAH shifts eastward, significant positive rainfall anomalies occur in southern Japan, over the Korea Peninsula, and in the Yangtze River-Yellow River Valley of China and the Tibetan Plateau. As the SAH shifts westward, the rainfall over these areas tends to be below average (Zhang et al., 2002). Zhang and Wu (2001) pointed out there is a good relationship between the strength of the SAH and rainfall over the Yangtze River valley in summer. The variation of the summer SAH can modulate climate downstream. A strengthened SAH emanates anomalous wave energy downstream along the westerly jet stream, leading to the occurrence of an intensified subtropical high over the extratropical North Pacific (Zhao et al., 2009). Also, the summer SAH is linked to global circulation and precipitation. A strengthened SAH is accompanied by a strengthened and westward Western Pacific subtropical high, weakened mid-Pacific trough and strengthened Mexican high. Furthermore, rainfall tends to increase over South Asia, Central America, Australia and Central Africa, and decrease over the Pacific and Mediterranean (Zhang et al., 2005). In addition, the easterly and westerly jets residing on the south and north sides of the SAH form a transport barrier of some chemicals, such as water vapor and ozone (Dethof et al., 1999; Randel and Park, 2006). Meanwhile, because of upward transportation in the center of SAH, some chemicals such as carbon monoxide are transported to the upper troposphere and trapped there (Park et al., 2004; Li et al., 2005).

Because of the large heat content of water, warm oceans heat the atmosphere and exert deep influence on circulation. The TIO and SAH are adjacent in geographical position, and change in thermal regime over the TIO may affect the variability of the SAH. The Indian Ocean basin-wide mode strengthens the summer SAH probably through the Matsunuo-Gill response forced by condensational heating associated with increased precipitation over the TIO (Yang et al., 2007; Yang and Liu, 2008; Li et al., 2008).

In addition to changes in its strength, the SAH also varies in its latitudinal and longitudinal locations (Zhang et al., 2000, 2002). Although there have been studies on the relationship between the TIO SST and SAH strength, the impact of the TIO SST on the displacements of the SAH is not clear. At the same time, former studies on the effects of the TIO SST on the SAH do not clearly address the influencing mechanism. Our present analysis will show that precipitation over the TIO is not significantly correlated with TIO SST. The influence mechanism is therefore still not well understood, an issue that will be discuss further, below.

The paper is organized as follows. Section 2 describes data, the method and AGCM experiments. Section 3 analyses the effects of TIO SST on SAH variations and the possible influencing mechanism. Section 4 uses simulations to validate the relationship and influencing mechanism proposed in section 3. Section 5 presents a discussion and summary of the findings.

2. Data and method

2.1 *Observational data*

This study used the Hadley Center Global Sea Surface Temperature (HadISST) dataset (Rayner et al., 2006), the Center for Climate Prediction (CPC) Merged Analysis of Precipitation (CMAP; Xie and Arkin, 1997), and the National Centers for Environmental Prediction–National Center for Atmosphere Research (NCEP–NCAR) atmospheric reanalysis dataset (Kalnay et al., 1996). The horizontal grid resolutions of these datasets are $1^\circ\times1^\circ$, $2.5^\circ\times2.5^\circ$, and $2.5^\circ\times2.5^\circ$, respectively. In order to be consistent with the period covered by the CMAP dataset which starts from 1979, and considering that there is interdecadal change in the influence of TIO SST during the late 1970s (Xie et al., 2010), the analysis and discussion in this paper will focus on the period 1979–2007.

Another focuses of the study is on the interannual variability of the TIO and SAH. For this purpose, three-month mean data were obtained and used in order to remove intraseasonal variability. Further, decadal and longer variations, which are significant over the TIO and surrounding areas (Du and Xie, 2008), were removed.

Correlation, regression and composite analysis were used to examine the relationship between the two variables. The statistical significance of a composite difference was assessed using the Student's t test. All

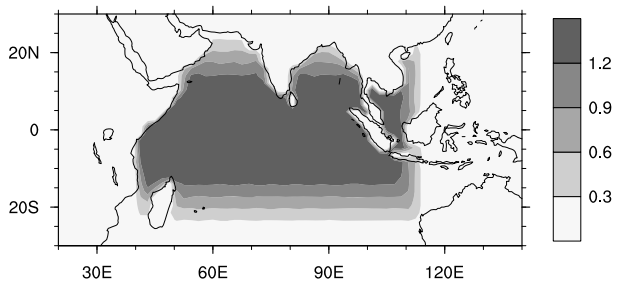

Fig. 3. Idealized SSTA imposed on climatological SST in ECHAM5.

significances referred to in this paper are at the 95% confidence level, unless otherwise stated. Finally, summer, in the context of this study, refers to the period from June to August.

2.2 *AGCM experiment*

The AGCM was ECHAM5, the latest Hamburg version of the European Center for Medium-Range Weather Forecast model, with a resolution of T63L19 (Roeckner et al., 2003).

Two experiments were designed. The first used prescribed SST and sea-ice from 1957–1999 to drive ECHAM5 (hereafter, AMIP2). The results of this experiment will be used to examine the ability of the AGCM with respect to SAH and climate over the TIO and the surrounding regions. In order to be consistent with the period of observational analysis, a dataset with covering the period 1979–1999 was selected. In the second experiment, referred to as the TIO sensitivity experiment (TIOSE), the AGCM was driven by an idealized SST anomaly in the TIO superposed on the model's climatological monthly SST. The SST anomaly is maximum along the equator and gradually decreases to 0 at 30°N and 30°S (Fig. 3). The SST anomaly increases linearly at a rate of 0.2 K yr^{-1} from 0 to 2.2 K. Five simulations were performed with different initial conditions. In the discussion, the ensemble mean is analyzed to remove the uncertainties induced by the initial conditions and internal variability.

3. observations

3.1 *Relationship between TIO SST and the SAH*

Figure 4a illustrates normalized June–August (JJA) TIO (40°–100°N, 20°S–20°E) SST time series. Seven warm cases (1983, 1987, 1988, 1991, 1998, 2003, and 2007) and nine cold cases (1981, 1984, 1985, 1989, 1994, 1996, 1999, 2000, and 2004) were chosen when the JJA TIO SST index exceeded 0.5 and −0.5 standard deviation, respectively.

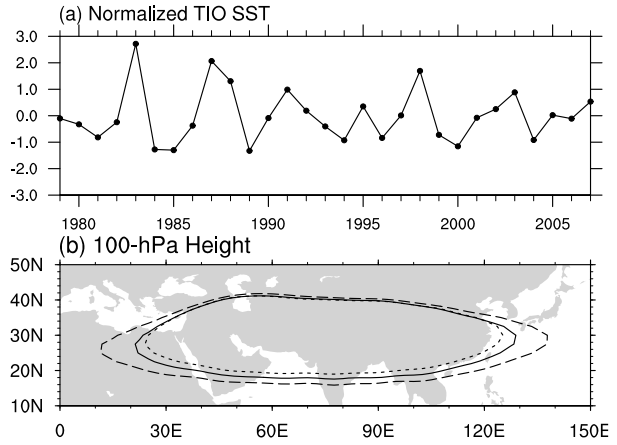

Fig. 4. (a) Normalized TIO (20°S–20°N, 40°–100°E) SST in June–August from 1979–2007. (b) Contour lines for 100-hPa 16720 gpm geopotential height when TIO SST is warm (dashed line), cold (dotted line) and climatological (solid line) in JJA.

Figure 4b shows contour lines for 16720 gpm of 100-hPa geopotential height when TIO SST represents warm cases (dashed contour line), cold cases (dotted contour line) and climatology (solid contour line). When the TIO is warmer (or colder) than normal, the SAH strengthens (or weakens) and moves southward (or northward). As TIO SST moves from cold to warm, the center of the SAH shifts southward, its southern boundary moves southward, the eastern and western boundaries respectively shifts eastward and westward, while almost no movement is found in the northern boundary. The definition of the SAH indices follow those in Zhang et al. (2000) and Zhou et al. (2006). The center of the SAH is the grid where the geopotential height is the largest and is expressed by its latitude and longitude. The area of the SAH is the total number of the points where the geopotential height is no less than 16600 m in the region (10°S–50°N, 30°W–180°E). The SAH intensity is the sum of differences between 16600 m and the geopotential height at each point where the geopotential height is no less than 16600 m in that region. The correlation coefficients between the TIO SST and SAH indices (including strengthening index, area index, center latitude and center longitude), are 0.63, 0.53, −0.43 and −0.08, respectively. Among the four correlation coefficients, the first two reach the 99% confidence level and the third reaches the 95% significance level. Thus when the TIO is warmer, not only does the SAH strengthen, but its center and main body also shift southward. However, at the interannual timescale, no direct relationship could be found between TIO SST and zonal displacement of the SAH in boreal summer.

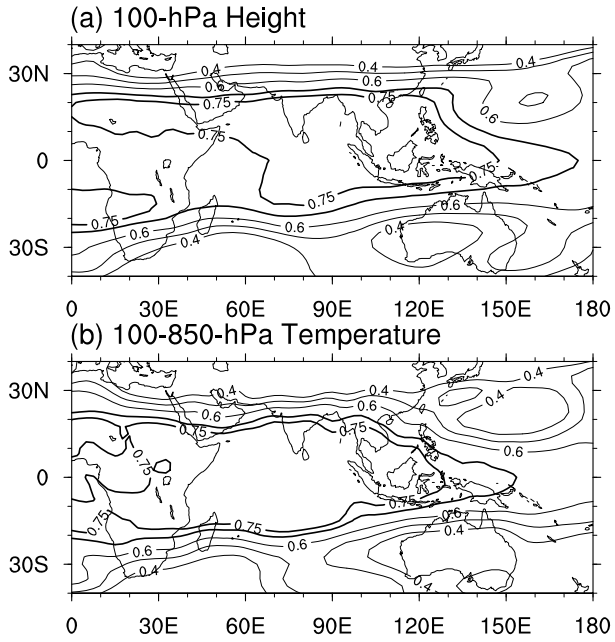

Fig. 5. Correlation with JJA TIO SST index: (a) 100-hPa geopotential height, (b) tropospheric temperature. The value 0.4, 0.5, 0.6, 0.65, 0.7 and 0.75 are shown in contours, and the value 0.7 and 0.75 are shown in thick contours.

3.2 *Possible mechanism of impact*

Figure 5 shows the correlation distribution of 100-hPa geopotential height (hereafter H100) and tropospheric temperature (100–850-hPa temperature; hereafter TT) with TIO SST. In the H100 field (Fig. 5a), a significant positive anomaly is situated in the tropical and subtropical region over the TIO and surrounding areas. The height anomaly over the domain (15°–30°N, 30°–120°E), south of the SAH's climatological location, is the key area for the strengthening and southward displacement of the SAH in boreal summer. As anomalies of H100 are closely related to the variation in 100–850-hPa temperature, TT field was analyzed. In the TT field (Fig. 5b), to the west of the Indian Ocean, two maximums reside off the equator over tropical Africa; to the east, the maximum lies along the equator over the maritime continents. The TT anomaly over the Indian Ocean and the surrounding regions exhibits a Matsunuo-Gill pattern in response to local heating (thick contours in Fig. 5b), indicating an active area of the TIO on the atmosphere.

Previous studies (Yang et al., 2007; Yang and Liu, 2008) on the impacts of the TIO on the SAH have suggested that condensational heating associated with precipitation anomalies plays an important role in the effects of the TIO on the SAH. However, the correlation results between TIO SST and precipitation do

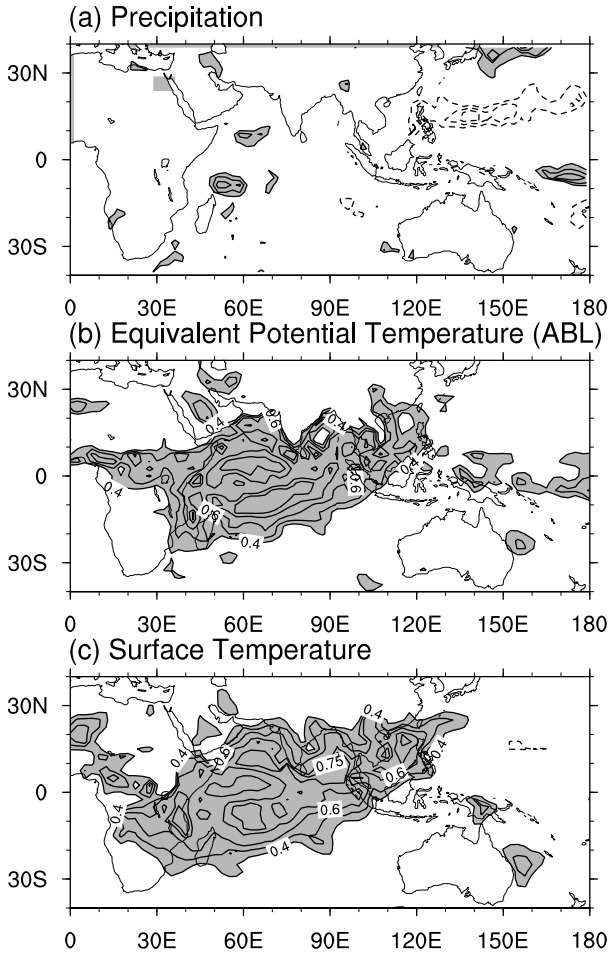

Fig. 6. Correlation with JJA TIO SST index: (a) precipitation; (b) EPT in 1000-hPa and (c) surface temperature. Shading indicates values larger than 0.4. The value −0.75, −0.7, −0.6, −0.5, −0.4, 0.4, 0.5, 0.6, 0.65, 0.7 and 0.75 are shown in contours; negative values are shown in dash contours.

not exhibit large scale anomalous rainfall, and significant precipitation anomalies only locate over the southwest Indian Ocean and south Arabian Sea (Fig. 6a). The weak correlation between TIO SST and precipitation in boreal summer has also been pointed out by Xie et al. (2009). For convenience, the area average of H100 in summer over the domain (15°–30°N, 30°–120°E), which is the key area for the strengthening and southward displacement of the SAH, is defined as an index, named SAHSE; also, the area mean of precipitation over the domain (20°S–20°N, 40°–100°E) is defined as an index, named PTIO. The correlation coefficient between SAHSE and PTIO is 0.25, not reaching the 90% significance level. Thus, the correlation analysis indicates that condensational heating associated with local precipitation over the Indian Ocean does not play the key role in the response of the H100.

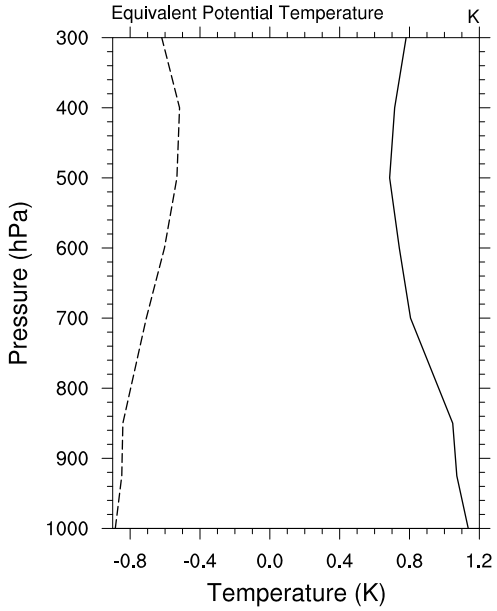

Fig. 7. Anomalous EPT (K) profile over the TIO when the TIO is warm (solid line) and cold (dash line).

In order to better understand the tropospheric warming over the TIO when the TIO is warm, the theory of moist adjustment is introduced. In the tropical wet atmosphere, the temperature profile follows approximately a moist-adiabatic profile which can be determined by moist static energy (MSE) or equivalent potential temperature (EPT) in the atmospheric boundary layer (ABL; Emanuel et al., 1994, 1997; Su and Neelin, 2003). It was pointed out by Xie et al. (2009) that the TIO warms the atmospheric column through modifying the EPT or MSE in the ABL. Figure 7 shows the anomalous EPT profiles when the TIO is warm and cold in boreal summer. As the specific humidity dataset in the NCEP-NCAR reanalysis is limited up to 300 hPa, the EPT profile was calculated between that level and 1000 hPa. Unlike the latent heat profile with a prominent peak at one level, the EPT profile shows an approximate uniform warm (or cold) profile from lower to upper level, further indicating that precipitation-induced latent heat may not play the key role. Correlation of EPT1000 with TIO SST shows a large-scale significant positive anomaly over the TIO (Fig. 6b). The correlation coefficient between the area average of EPT1000 over the domain (20°S–20°N, 40°–100°E) and SAHSE is 0.75, far exceeding that between PTIO and SAHSE. The correlation coefficient reveals that TIO-SST-induced EPT change in the ABL is a more important manner through which TIO SST effects tropospheric warming.

In brief, in boreal summer, the warming of the TIO induces EPT variation in the ABL, modulates the temperature profile of the atmosphere above it, heats the atmospheric column, elevates H100 with a significant positive H100 anomaly to the south of the SAH's climatological location, strengthens the SAH and leads to a southward shift of its center.

Besides the direct influence of the TIO on the SAH, some indirect processes, such as TIO-SST-anomaly-induced anomalous conditions on land and the thermal contrast between land and ocean, may also contribute to variation in the SAH. When the TIO is warm in boreal summer, precipitation increases over the north of the Bay of Bengal (Fig. 6a), in accordance with the simulation results of Yang and Liu (2008). The associated condensational heating contributes to tropospheric warming over the area and forces an anomalous anticyclone in the upper troposphere over the SAH's climatological position. These processes are favorable for the strengthening and southward displacement of the SAH. As the TIO warms, warm anomalies in surface temperature are found in the southwest of the Indian Peninsula, east of the Indian and north of the Indo-China Peninsula (Fig. 6c). It can be inferred that the consequent sensible heat anomaly may also contribute to tropospheric warming. Moreover, TIO warming may reduce the thermal contrast between the Indian Ocean and the continent of Asia, thus height difference over the two regions is reduced and a positive height anomaly occurs over the TIO region. This may also cause a strengthening and southward displacement of the SAH.

4. Model results

AGCM experiments were designed to test the hypothesis that TIO SST affects the strength and latitudinal displacement of the SAH in summer. For convenience, NCEP and CMAP results are referred to as "observation", though the NCEP reanalysis is obviously not observational data.

4.1 *Prediction ability of ECHAM5*

In the observation, summer mean precipitation in climatology locates mainly in the equatorial Indian Ocean, east Arabian Sea, Indian Peninsula and the Bay of Bengal, with a maximum over the equatorial southeast Indian Ocean, west of the Indian Peninsula and northeast of the Bay of Bengal (Fig. 8a). For the summer mean TT field, a ridge exists from northern Madagascar to the Somali Peninsula and two maximums exist over the Iran and Tibet Plateaus (Fig. 8a). In H100, a large-scale high system, the SAH, locates over Iran and Tibet Plateaus, with its center above the Tibet Plateau (Fig. 9a).

In ECHAM5, the large-scale characteristics of cli-

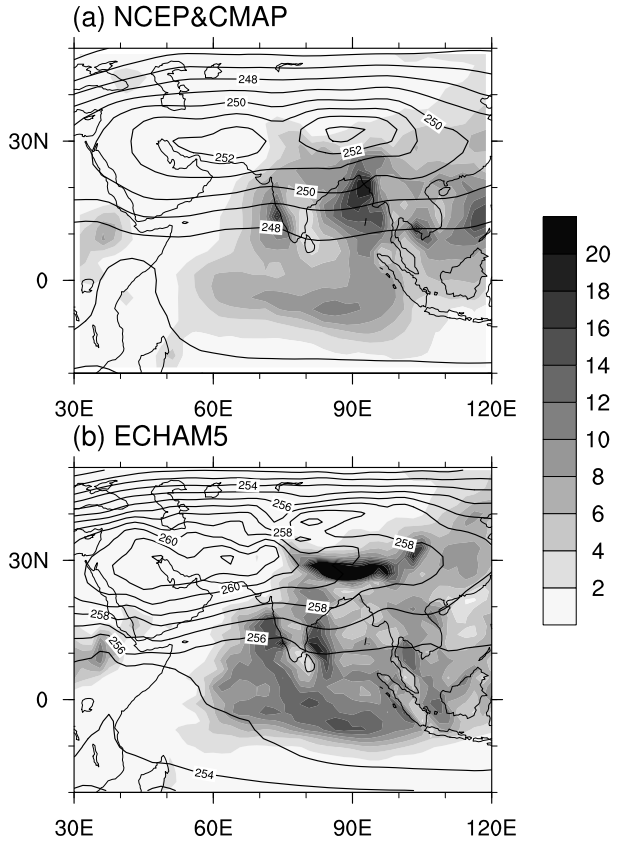

Fig. 8. Climatology of tropospheric temperature (contours) and precipitation (shaded) in JJA, (a) results of NCEP and CMAP; (b) results of ECHAM5. The units of tropospheric temperature and precipitation are K and mm d^{-1}, respectively.

matological precipitation in summer are consistent with those in observation, with large-scale precipitation along the equatorial south Indian Ocean, Arabian Sea and the Bay of Bengal; ECHAM5 also captures well the maximums in the equatorial southeast Indian Ocean and west Indian Peninsula, but fails to capture the maximum in the northeast of the Bay of Bengal (Fig. 8b). In ECHAM5, the TT ridge in the observation is reproduced well and there is also a maximum over 30°N. Although, the maximum shifts westward compared to the observation, and locates over the Iran Plateau (Fig. 8b). The value of simulated H100 is larger than that of the observation, and the SAH is reproduced but shifts westward relative to the observation (Fig. 9b). Therefore ECHAM5 can simulate tropospheric temperature, precipitation and geopotential height near the Indian Ocean well, and the climatology of the SAH is reproduced quite well. It is reasonable to discuss the impact of TIO SST on the strengthening and latitudinal variations of the SAH by using ECHAM5.

Owing to the difference of H100 value between ECHAM5 and the observation, 16860-gpm contour is adopted to characterize the SAH in simulation. Figure 10a illustrates the contour lines for 16860-gpm of 100-hPa geopotential height when JJA TIO SST is warm, cold and climatological. As the TIO warms (or cools), the SAH strengthens (or weakens) and shifts slightly southward (or northward), consistent with observed results.

4.2 *The TIO sensitivity experiment*

In order to investigate the effect of TIO SST alone and exclude the influences of SST over other oceans, TIOSE was analyzed. Figure 10b illustrates contour lines for 16860 gpm of 100-hPa geopotential height when the SSTA imposed on the TIO is 0–1 K and 1–2 K mean. Compared to the results of 0–1 K mean, the SAH strengthens and expands southward when the TIO SSTA is 1–2 K mean, with more significant movement in the southern boundary than that in the northern boundary. The SAH indices in this experiment were defined according to the definition in Zhang et al. (2000) and Zhou et al. (2006), except that the characteristic contour is 16 860 gpm. The scatter plots of SAH intensity (Fig. 11a), area (Fig. 11b) and center latitude (Fig. 11c) in TIOSE show good linear relation with SSTAs imposed on the TIO (the linear regression of all three reach the 99.9% significance level), while the linear relationship between center longitude and SSTA is poor (Fig. 11d). The results are well in accordance with the relationship between the TIO and SAH variation in the observation.

Figure 12 shows the differences in H100, TT, precipitation and EPT1000 between 1–2 K SSTA mean and 0–1 K SSTA mean. The H100 field (Fig. 12a) shows a significant positive height anomaly extending northward to 40°N. The height anomaly decreases from tropics to the mid latitude, leading to more significant movement in the SAH's southern boundary than in its northern boundary, as well as the southward displacement of its center. The response of TT shows two maximums off the equator, one to the west of the Indian Ocean and the other along the equator (Fig. 13b), which features a Matsuno-Gill type response. EPT1000 shows a large-scale significant positive anomaly over the TIO, also in good accordance with the observation (Fig. 12d). The results of H100, TT and EPT1000 support the notion that the TIO warms the troposphere through modulating EPT or MSE in the ABL, strengthens the SAH and makes it expand southward.

Compared to observations, the simulated precipitation is different, with a significant positive precipitation anomaly over the east Indian Ocean, and a

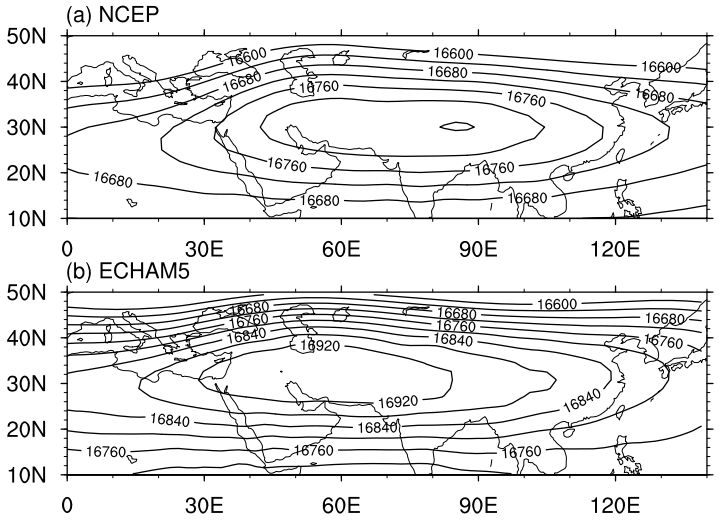

Fig. 9. Climatology of 100-hPa geopotential height (m) in JJA: (a) NCEP, (b) ECHAM5.

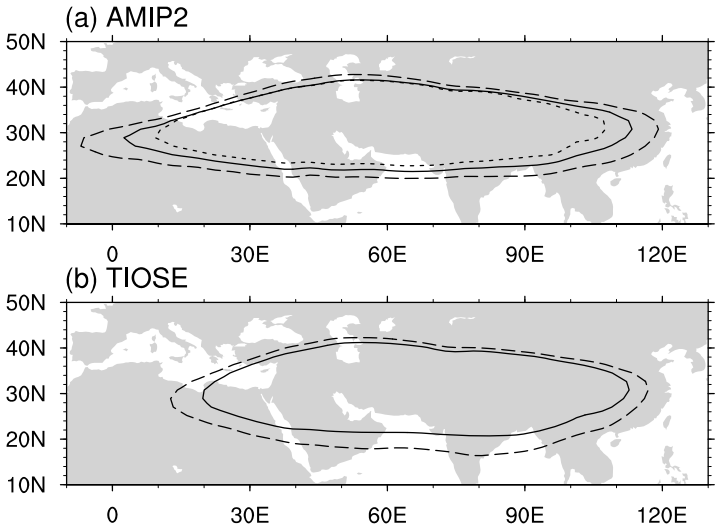

Fig. 10. (a) As Fig. 5, except for 16 860 gpm contour lines in AMIP2 run of ECHAM5. (b) Contour lines for 16 860 gpm of 100-hPa geopotential height when summer TIO SSTA is 0–1 K (solid contour lines) and 1–2 K (dashed contour lines).

negative anomaly over central North Africa from 10°–20°N, Tanzania, the Bay of Bengal and the maritime continents (Fig. 12c). Although the precipitation response over the Bay of Bengal in TIOSE is opposite to that in observations, the SAH strengthens and shifts southward in both TIOSE and the observations. So compared to the effects of precipitation over the Bay of Bengal, another process may be more important to the response of the SAH.

Su and Neelin (2003) pointed out that assuming remote SST is fixed, as local SST increases, moisture in atmospheric boundary adjusts quickly, the temperature profile of the atmosphere changes, convective available potential energy increases, and convective precipitation occurs, making the actual temperature profile close to a moist-adiabatic profile, meaning the atmosphere tends to be stable. Convection acts as a key factor in modulating actual temperature close to a moist-adiabatic profile. Thus there is a good relationship between precipitation and SSTAs under these condition. However, in the observation, when the TIO is warm in summer, a SSTA also exists over other oceans (Fig. 1). Provided the TIO SSTA is fixed, SSTAs outside the Indian Ocean may affect the

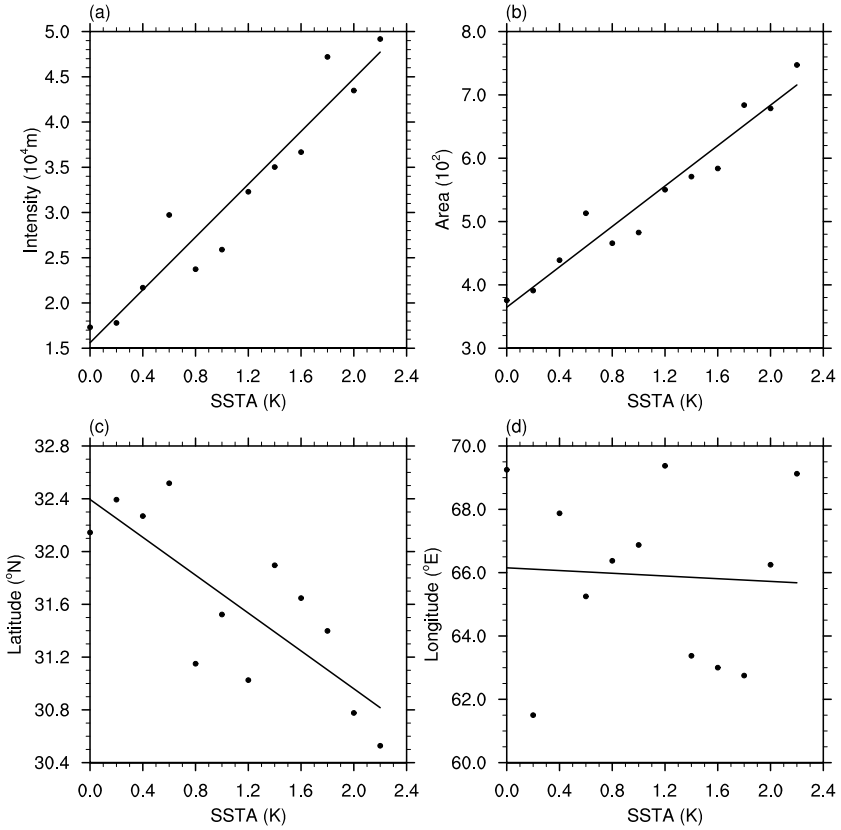

Fig. 11. Scatter plots of SAH (a) intensity ($\times 10^4$ m), (b) area ($\times 10^2$), (c) center latitude (°N) and (d) center longitude (°E) in JJA with respect to SSTA in TIOSE. Linear lines in the four plots are the linear fit lines.

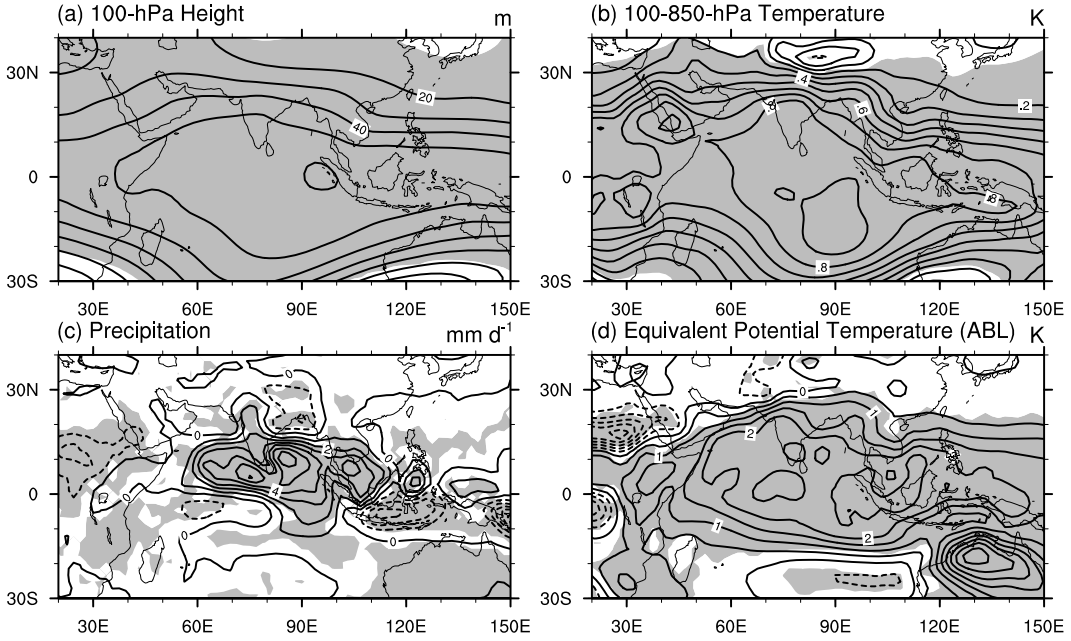

Fig. 12. Differences between 1–2 K mean and 0–1 K mean in TIOSE: (a) 100-hPa geopotential height (m); (b) tropospheric temperature (K); (c) precipitation (mm d^{-1}) and (d) EPT at 1000-hPa (K). Shading indicates the values reaching the 95% significance level. For the sake of clarity, spatial 9-point smoothing is performed.

atmosphere over the Indian Ocean, tending to make it warmer or colder. As the TIO SSTA is fixed, an anomalous EPT in the ABL over the TIO varies very little. From the changes in the vertical temperature profile, the atmosphere over the TIO tends to be more stable or unstable than normal and decreased or increased precipitation occurs to modulate the atmosphere to a neutral state. If the heating of the Indian Ocean is taken into consideration, a warm (or cold) TIO makes the actual temperature profile get close to a moisture-adiabatic profile through increased (or decreased) convective heating. Due to the combined effects of SSTAs over the TIO and outside the TIO, precipitation over the TIO is not significant. Thus the impacts of other oceans on TT over the TIO may account for the insignificant precipitation when the TIO is warm and it is not difficult to understand that precipitation does not necessarily correlate well to local SST. Despite that, the mechansim that the TIO warms the troposphere through modulating EPT or MSE in the ABL and affects the SAH can be applied to explain the results in both TIOSE and the observation. The heat budget of the troposphere over the TIO is still not understood and needs further investigation.

5. Discussion and summary

The effects of TIO SSTA on variations of the SAH and the possible underlying mechanism have been investigated. In the summer when the ENSO decays, the SST and circulation anomalies indicate that TIO SST directly or indirectly plays an active role in circulation changes over the TIO, with an active role by the eastern Pacific not being obvious. This phenomenon is not obvious in spring, nor the preceding winter. Thus the impact of TIO SST in summer was the focus of this study.

Compared to cold cases, when the TIO warms in summer, the main body of the SAH becomes larger, the SAH intensifies and its center shifts southward. A significant correlation can be found between TIO SST and the indices (intensity, area and center latitude) of the SAH, while the relationship between TIO SST and the SAH center longitude is poor. When the TIO warms, the whole troposphere over the TIO is heated with a Matsunuo-Gill response in the troposphere. No significant large-scale precipitation anomaly can be found over the TIO, indicating that precipitation does not act as a key factor in forcing the Matsunuo-Gill response. Emanual et al. (1994, 1997) and Su and Neelin (2003) pointed out that, the temperature in the tropical atmosphere follows approximately a moist-adiabatic profile which is determined by EPT or MSE in the ABL. TIO SST modulates tropospheric temperature through changing the EPT or MSE in the ABL, forcing the Matsunuo-Gill response. As the TIO warms, because of the spread of tropospheric warming and the Rossby wave response over the northern Indian Ocean, a positive height anomaly occurs in the south of the SAH's climatological location in summer, making the SAH intensify and its center move southward.

AGCM ECHAM5, with a resolution of T63L19, was used to test the effects of TIO SST on variations in the SAH. The model experiment indicated that, as the summer TIO SSTA increases, the SAH strengthens and its center shifts southward significantly. When the TIO warms, a significant tropospheric warm anomaly locates over tropics and subtropics, featuring a Matsuno-Gill type response over the TIO, consistent with the observation. However, the precipitation response to the TIO SSTA is different to that in the observation. By using the theory proposed by Su and Neelin (2003) and analyzing the results obtained in the present study, it can be inferred that when the TIO is warm, SST in other oceans may make a positive or negative contribution to precipitation over the TIO. Thus precipitation over the TIO is not all determined by local SST and the influences of SSTs in other oceans may account for the insignificant precipitation over the TIO in the observation. Although simulated precipitation was different from observed precipitation, the simulation results can still be explained by the mechanism that the TIO warms the troposphere through the modulation of the temperature profile and has impact on the SAH.

The simulations have shown that TIO warming contributes to the strengthening and southward displacement of the SAH in summer. However, the correlation coefficient between the SAH center latitude and simultaneous NINO3.4 index is -0.45, a little higher than that between TIO SST and the SAH center latitude. Therefore, besides the influence of the TIO, a simultaneous influence of eastern Pacific SST may also contribute to the latitudinal movement of the SAH in summer. How the former affects the latter also need further study.

Acknowledgements. The authors are grateful to Prof. HUANG Ronghui, Prof. Shang-Ping Xie, Dr. WU Renguang and two anonymous reviewers for their insightful comments which undoubtedly led to significant improvement in the manuscript. This work was supported by the National Key Technology R&D Program 2008BAK50B02, CAS Innovation Key Program (Grant No. KZCX2-YW-BR-14), National Basic Research Program of China (2011CB309704), Special Scientific Research Project for Public Interest (Grant No. GYHY201006021), and the

National Natural Science Foundation of China (Grant Nos. 40890155, 40775051, U0733002).

REFERENCES

Alexander, M. A., I. Bladé, M. Newman, J. R. Lanzante, N. C. Lau, and J. D. Scott, 2002: The atmospheric bridge: The influence of ENSO teleconnections on air–sea interaction over the global oceans. *J. Climate*, **15**, 2205–2231.

Annamalai, H., P. Liu, and S.-P. Xie, 2005: Southwest Indian Ocean SST variability: Its local effect and remote influence on Asian monsoons. *J. Climate*, **18**, 4150–4167.

Dethof, A., A. O'Neill, J. M. Slingo, and H. G. J. Smit, 1999: A mechanism for moistening the lower stratosphere involving the Asian summer monsoon. *Quart. J. Roy. Meteor. Soc.*, **125**, 1079–1106.

Du, Y., and S. P. Xie, 2008: Role of atmospheric adjustments in the tropical Indian Ocean warming during the 20th century in climate models. *Geophys. Res. Lett.*, **35**, L08712, doi: 10.1029/2008GL033631.

Du, Y., S. P. Xie, G. Huang, and K. Hu, 2009: Role of air–sea interaction in the long persistence of El Niño–induced North Indian Ocean warming. *J. Climate*, **22**, 2023–2038.

Emanuel, K. A., J. D. Neelin, and C. S. Bretherton, 1994: On large-scale circulations in convecting atmospheres. *Quart. J. Roy. Meteor. Soc.*, **120**, 1111–1143.

Emanuel, K. A., J. D. Neelin, and C. S. Bretherton, 1997: Reply to comments by Bjorn Stevens, David A. Randall, Xin Lin and Michael T. Montgomery on "On large-scale circulations in convecting atmospheres". *Quart. J. Roy. Meteor. Soc.*, **123**, 1779–1782.

Flohn, H., 1960: Recent investigations on the mechanism of the "Summer Monsoon" of Southern and Eastern Asia. *Proc. Symp. Monsoon of the World*, New Delhi, Hind Union Press, 75–88.

Huang, B., and J. L. Kinter, 2002: Interannual variability in the tropical Indian Ocean. *J. Geophys. Res.*, **107**, 3199, doi: 10.1029/2001JC001278.

Kalnay, E., and Coauthors, 1996: The NCEP/NCAR 40-Year Reanalysis Project. *Bull. Amer. Meteor. Soc.*, **77**, 437–471.

Klein, S. A., B. J. Soden, and N. C. Lau, 1999: Remote sea surface temperature variations during ENSO: Evidence for a tropical atmospheric bridge. *J. Climate*, **12**, 917–932.

Lau, N. C., and M. J. Nath, 2000: Impact of ENSO on the variability of the Asian–Australian monsoons as simulated in GCM experiments. *J. Climate*, **13**, 4287–4309.

Lau, N. C., and M. J. Nath, 2003: Atmosphere-Ocean variations in the Indo-Pacific sector during ENSO episodes. *J. Climate*, **16**, 3–20.

Li, Q., and Coauthors, 2005: Convective outflow of South Asian pollution: A global CTM simulation compared with EOS MLS observations. *Geophys. Res. Lett.*, **32**, L14826, doi: 10.1029/2005GL022762.

Li, S., J. Lu, G. Huang, and K. Hu, 2008: Tropical Indian Ocean basin warming and East Asian summer monsoon: A multiple AGCM study. *J. Climate*, **21**, 6080–6088.

Mason, R. B., and C. E. Anderson, 1963: The development and decay of the 100-MB. Summertime anticyclone over Southern Asia. *Mon. Wea. Rev.*, **91**, 3–12.

Masumoto, Y., and G. Meyers, 1998: Forced Rossby waves in the southern tropical Indian Ocean. *J. Geophys. Res.*, **103**, 27589–27602.

Park, M., W. J. Randel, D. E. Kinnison, R. R. Garcia, and W. Choi, 2004: Seasonal variation of methane, water vapor, and nitrogen oxides near the tropopause: Satellite observations and model simulations. *J. Geophys. Res*, **109**, D03302, doi: 10.1029/2003JD003706.

Randel, W. J., and M. Park, 2006: Deep convective influence on the Asian summer monsoon anticyclone and associated tracer variability observed with Atmospheric Infrared Sounder (AIRS). *J. Geophys. Res.*, **111**, D12314, doi: 10.1029/2005JD006490.

Rayner, N. A., P. Brohan, D. E. Parker, C. K. Folland, J. J. Kennedy, M. Vanicek, T. J. Ansell, and S. F. B. Tett, 2006: Improved analyses of changes and uncertainties in sea surface temperature measured in situ since the mid-nineteenth century: The HadSST2 dataset. *J. Climate*, **19**, 446–469.

Roeckner, E., and Coauthors, 2003: The atmospheric general circulation model ECHAM5: Part 1: Model description. Max-Planck-Institut für Meteorologie Rep. 349, 140pp.

Su, H., and J. D. Neelin, 2003: The scatter in tropical average precipitation anomalies. *J. Climate*, **16**, 3966–3977.

Tao, S., and F. Zhu, 1964: The variation of 100mb circulation over South Asia in summer and its association with march and withdraw of West Pacific Subtropical High. *Acta Meteorological Sinica*, **34**, 385–395. (in Chinese)

Wang, B., R. Wu, and X. Fu, 2000: Pacific–East Asian teleconnection: How does ENSO affect East Asian climate? *J. Climate*, **13**, 1517–1536.

Wang, B., R. Wu, and T. Li, 2003: Atmosphere-warm ocean interaction and its impacts on Asian-Australian monsoon variation. *J. Climate*, **16**, 1195–1211.

Wu, B., T. Zhou, and T. Li, 2009: Seasonally evolving dominant interannual variability modes of East Asian climate. *J. Climate*, **22**, 2992–3005.

Xie, P., and P. A. Arkin, 1997: Global precipitation: A 17-year monthly analysis based on gauge observations, satellite estimates, and numerical model outputs. *Bull. Amer. Meteor. Soc.*, **78**, 2539–2558.

Xie, S.-P., H. Annamalai, F. A. Schott, and J. P. McCreary, 2002: Structure and mechanisms of South Indian Ocean climate variability. *J. Climate*, **15**, 864–878.

Xie, S.-P., K. Hu, J. Hafner, H. Tokinaga, Y. Du, G.

Huang, and T. Sampe, 2009: Indian Ocean capacitor effect on Indo–Western Pacific climate during the Summer following El Niño. *J. Climate*, **22**, 730–747.

Xie, S.-P., Y. Du, G. Huang, X.-T. Zheng, H. Tokinaga, K. Hu, and Q. Liu, 2010: Decadal shift in El Niño influences on Indo-western Pacific and East Asian climate in the 1970s. *J. Climate*, **23**, 3352–3368.

Yang, J., Q. Liu, S. P. Xie, Z. Liu, and L. Wu, 2007: Impact of the Indian Ocean SST basin mode on the Asian summer monsoon. *Geophys. Res. Lett.*, **34**, L02708, doi: 10.1029/2006GL028571.

Yang, J., and Q. Liu, 2008: The "charge/discharge" role of the basin-wide mode of the Indian Ocean SST anomaly-influence on the South Asian High in summer. *Acta Oceanologica Sinica*, **30**, 12–19. (in Chinese)

Yu, W., B. Xiang, L. Liu, and N. Liu, 2005: Understanding the origins of interannual thermocline variations in the tropical Indian Ocean. *Geophys. Res. Lett.*, **32**, L24706, doi: 10.1029/2005GL024327.

Zhang, P., S. Yang, and V. E. Kousky, 2005: South Asian High and Asian-Pacific-American Climate Teleconnection. *Adv. Atmos. Sci.*, **22**, 915–923.

Zhang, Q., Y. Qian, and X. Zhang, 2000: Interannual and Interdecadal variations of the South Asia High. *Chinese J. Atmos. Sci.*, **24**, 67–78. (in Chinese)

Zhang, Q., and G. Wu, 2001: The large area flood and drought over Yangtze river valley and its relation to the South Asia High. *Acta Meteorologica Sinica*, **59**, 569–577. (in Chinese)

Zhang, Q., G. Wu, and Y. Qian, 2002: The bimodality of the 100 hPa South Asia high and its relationship to the climate anomaly over East Asia in summer. *J. Meteor. Soc. Japan*, **80**, 733–744.

Zhao, P., X. Zhang, Y. Li, and J. Chen, 2009: Remotely modulated tropical-North Pacific ocean–atmosphere interactions by the South Asian high. *Atmos. Res.*, **94**, 45–60.

Zhou, N., Y. Yu, and Y. Qian, 2006: Simulation of the 100-hPa South Asian High and precipitation over East Asia with IPCC coupled GCMS. *Adv. Atmos. Sci.*, **23**, 375–390.

An Index Measuring the Interannual Variation of the East Asian Summer Monsoon—The EAP Index

HUANG Gang* (黄 刚)

RCE-TEA and LASG, Institute of Atmospheric Physics, Chinese Academy of Sciences, Beijing 100029

(Received 18 February 2003; revised 10 June 2003)

ABSTRACT

Based on the EAP (East Asia/Pacific) teleconnection in the summer circulation anomalies over the Northern Hemisphere, an index measuring the strength of the East Asian summer monsoon, i.e., the so-called EAP index, is defined in this paper. From the analyses of observed data, it is clearly shown that the EAP index defined in this study can well describe the interannual variability of summer rainfall and surface air temperature in East Asia, especially in the Yangtze River valley and the Huaihe River valley, Korea, and Japan. Moreover, this index can also reflect the interannual variability of the East Asian summer monsoon system including the monsoon horizontal circulation and the vertical-meridional circulation cell over East Asia. From the composite analyses of climate and monsoon circulation anomalies for high EAP index and for low EAP index, respectively, it is well demonstrated that the EAP index proposed in this study can well measure the strength of the East Asian summer monsoon.

Key words: East Asia/Pacific index, East Asian summer monsoon, interannual variability

1. Introduction

As well known, the interannual variability of the East Asian summer monsoon is very obvious and causes severe droughts and floods in East Asia, especially in the eastern part of China (see Tao and Chen, 1985; Ding, 1994; Ye et al., 1996; Huang et al., 1998; Huang and Zhou, 2002). Therefore, the interannual variability of the East Asian summer monsoon (EASM) is an important issue for Chinese meteorologists. Through the efforts of more than sixty years, Chinese meteorologists have achieved many advances in the studies on the EASM. Tao and Chen (1987) made a systematical review on these advances.

Recently, many scholars have made many efforts to study the interannual variability of EASM and its causes. Nitta (1987, 1996), Huang and Li (1987, 1988), Kurihara (1989), and Huang and Sun (1992) pointed out the significant effect of the thermal state in the tropical western Pacific and the convective activities around the Philippines on the interannual variability of EASM. Nitta (1987), and Huang and Li (1987) showed that there is an obvious teleconnection pattern in the summer circulation anomalies over the Northern Hemisphere, which has been called the PJ (Pacific-Japan) pattern and the EAP (East Asia/Pacific) pattern teleconnection by Nitta (1987), and Huang and Li (1987), respectively.

In order to describe the interannual variability of EASM, a monsoon index measuring the strength of EASM is necessary. Up to now, there are two kinds of definitions of the Asian monsoon index. One is defined from the thermodynamical elements. For example, Tao and Chen (1987), and Murakami and Matsumoto (1994) defined the monsoon index with the strength of monsoon rainfall and OLR, respectively. The other is defined from the dynamical elements, i.e., wind field. Webster and Yang (1992), and Zeng et al. (1994) defined the monsoon index from the difference of the zonal winds between the high level and lower level atmosphere over the Asian monsoon region, while Zhang and Peng (2003) defined the East Asian summer monsoon index with the difference of the zonal winds between the middle latitudes and low latitudes over East Asia. There are some advantages and disadvantages in these definitions. The former may be easily influenced by local thermodynamical conditions, but the latter may be only suitable for the South Asian monsoon. Since the EASM has the feature of a subtropical monsoon and a meridional component (see Huang et

*E-mail: hg@mail.iap.ac.cn

al., 1998), it may be not suitable to define an index only with the zonal component of the wind field over the regions of EASM. Therefore, how to define a monsoon index measuring the strength of the EASM is still necessary for the study of the interannual variations of EASM.

Guo (1983) and Shi et al. (1996) defined the index measuring the interannual variations of EASM with the difference of sea-level pressure between the North Pacific and Eurasian continent, which is also an element related with the dynamics. As described above, the observational and theoretical studies have shown that the interannual variation of EASM is greatly influenced by the EAP teleconnection pattern suggested by Nitta (1987) and Huang and Li (1987), respectively. This teleconnection pattern has been widely used in the seasonal prediction of climate anomalies in China. Thus, based on this teleconnection shown in Figure 1 (from Huang and Li, 1987), the NCEP/NCAR reanalysis data of height fields at 500 hPa are used to defined an index measuring the strength of the EASM. And the observed data of monthly precipitation in China, Korea, and Japan are further used to study the interannual variations of EASM in this paper.

2. Definition of the EAP index measuring the interannual variation of EASM.

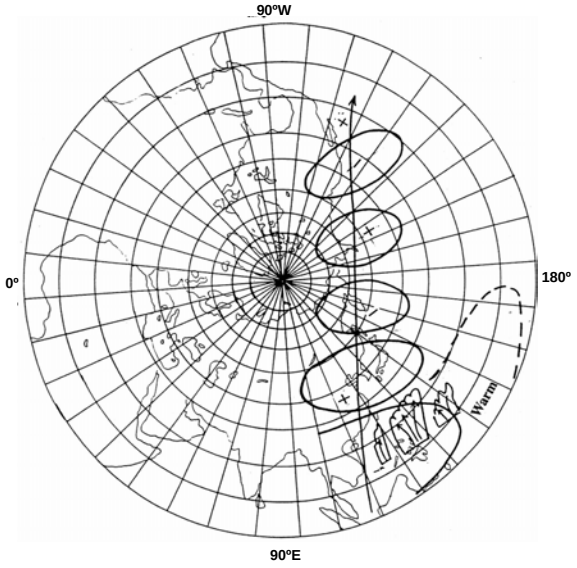

Fig. 1. The schematic map of the EAP teleconnection pattern (from Huang and Li, 1987). The "+" and "–" in the figure denote the positive and negative height anomalies at 500 hPa, respectively.

Fig.1

EASM, an index of EASM is defined based on this pattern. This index is simply called the EAP index, i.e., $I_{\rm EAP}$. The definition of $I_{\rm EAP}$ is as follows:

$$I_{\rm EAP} = -0.25Z'_{\rm s}(60^\circ{\rm N}, 125^\circ{\rm E}) + 0.50Z'_{\rm s}(40^\circ{\rm N}, 125^\circ{\rm E}) - 0.25Z'_{\rm s}(20^\circ{\rm N}, 125^\circ{\rm E}) \,, \quad (1)$$

where $Z'_{\rm s}{=}Z\sin 45^\circ / \sin\varphi$ is the standardized seasonal-mean 500-hPa height anomaly at a grid point with the latitude φ, and $Z'{=}Z-\bar{Z}$ is the summer seasonal-mean 500-hPa height anomaly at the grid point.

Figure 2 shows the interannual variation of $I_{\rm EAP}$ calculated using Formula (1) with the NCAR/NCEP reanalysis data of the 500-hPa height fields from 1951 to 2000.

The results of Nitta (1987), Huang and Li (1987), Kurihara (1989), and Huang and Sun (1992), show that the convective activities are strong around the Philippines in the warming state of the West Pacific warm pool; in this case, the western Pacific subtropical high shifts northward, and the summer monsoon rainfall may be below normal in the Yangtze River and Huaihe River valley of China, and in South Korea and Japan. Then the $Z'_{\rm s}$ at the grid point of (40°N, 125°E) is positive, and $Z'_{\rm s}$ at the grid point of (60°N, 125°E) and (20°N, 125°E) are both negative. Thus, $I_{\rm EAP}$ will be positive. Therefore, if the EAP index shown in Fig. 2 is positive, the East Asian summer monsoon rainfall may be weak in the Yangtze River and Huaihe River valley of China, and in South Korea and Japan. On the other hand, in the cooling state of the West Pacific warm pool, the convective activities are weak around the Philippines. Then the western Pacific subtropical high shifts southward, and the summer monsoon rainfall may be above normal in the Yangtze River and Huaihe River valley of China, and in South Korea and Japan. In this case, the $I_{\rm EAP}$ shown in Fig. 2 is negative. Therefore, if the index is negative, the East Asian summer monsoon rainfall may be strong in the Yangtze River and Huaihe River valley of China, and in South Korea and Japan.

3. Relationship between the EAP index and the summer monsoon rainfall in East Asia

Ramage (1971) pointed out that monsoon exhibits not only wind reversal, but also the seasonal precipitation criterion. Therefore, a good monsoon index should indicate well the variation of precipitation in the monsoon region. In order to investigate whether the EAP index can well describe the interannual variations of EASM or not, the point correlations between the summer monsoon rainfall anomalies in China and

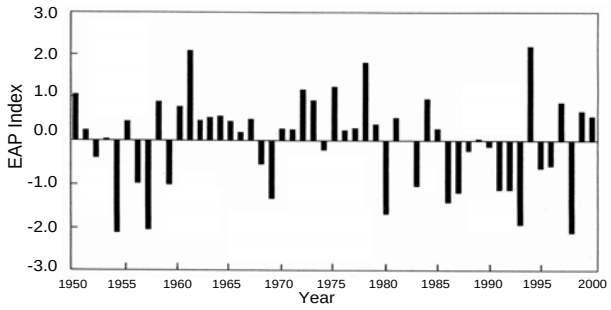

Fig. 2. Interannual variation of I_{EAP} calculated by using Formula (1) with the observed data of the 500-hPa height fields from 1951 to 2000.

the EAP index are calculated by using the observed data of summer (June–August) monthly precipitation at 160 observational stations in China from 1951 to 1996. Figure 3 presents the distribution of the correlation coefficients between the summer rainfall anomalies in China and the EAP index. It may be clearly seen from the figure that there are large negative correlations in the Yangtze River valley and the Huaihe River valley. This means that in a summer with positive EAP index the summer rainfall is below normal. For example, in the summers of 1961, 1978, and 1994, the EAP index was larger than or equal to 1, and correspondingly, severe droughts occurred in this region. However, in a summer with negative EAP index such as in 1954, 1957, 1980, 1987, 1996, and 1998, the EAP index was smaller than or equal to –1, and serious floods were caused in this region.

This negative correlation between the EAP index and summer rainfall anomalies in the Yangtze River valley and the Huaihe River valley is also seen from the interannual variations of the normalized summer rainfall anomalies in the (29°–33°N, 114°–125°E) region of the Yangtze River and Huaihe River valley and the EAP index shown in Fig. 4. It shows that there is a good out of phase relationship between the summer rainfall in the Yangtze River and Huaihe River valley and the EAP index. The maximum correlation coefficience between them can reach 0.58, which greatly exceeds the confidence level of 95%. This indicates that the EAP index can well reflect the summer monsoon rainfall anomalies in the Yangtze River valley and the Huaihe River valley.

The EAP index can reflect the interannual variation of summer monsoon rainfall in South Korea. Figure 5 shows the normalized summer rainfall anomalies in South Korea and indicates a negative correlation between the summer rainfall anomaly in South Korea and the EAP index. The maximum negative correlation coefficient can reach –0.37, which is significant at the confidence level of 95%.

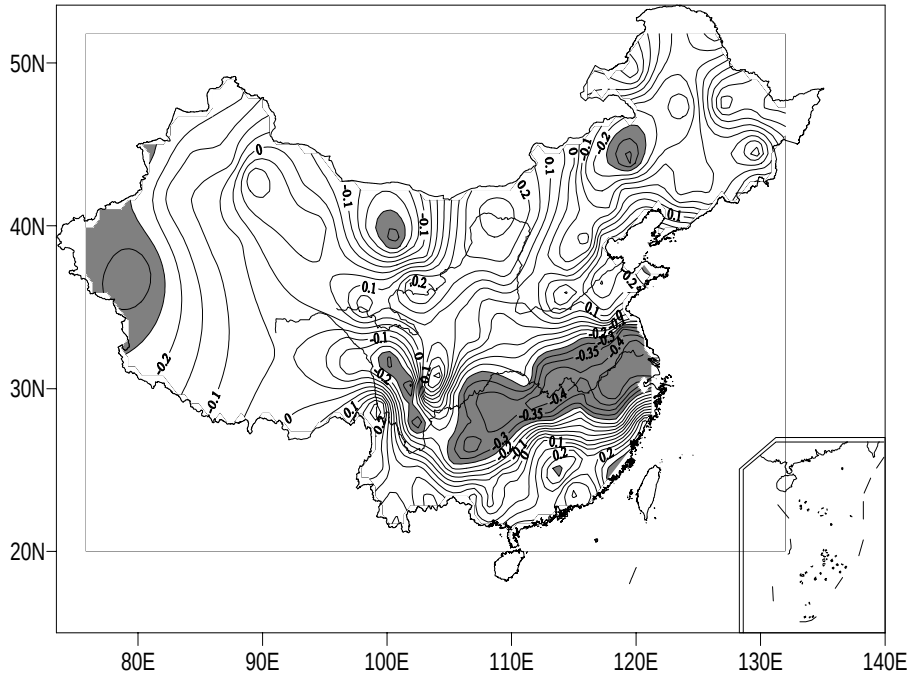

Fig. 3. Distribution of the correlation coefficients between the summer (June–August) rainfall anomalies in China and the EAP index from 1951 to 1996. The shaded areas indicate where the confidence level is over 95%.

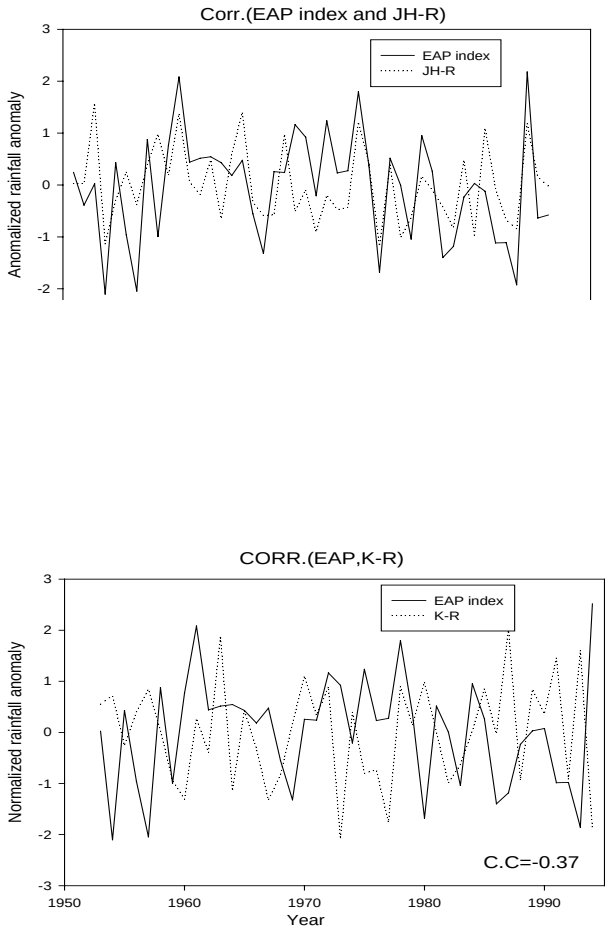

Fig. 5. Same as Fig. 4 but for the normalized summer monsoon rainfall anomalies in South Korea (dashed line).

We also calculate the correlation coefficients between the summer monsoon rainfall in East Asia and the EAP index, the summer monsoon index (SM index) suggested by Guo (1983), and the Webster-Yang index (WY index) proposed by Webster and Yang (1992), respectively, by using the Xie-Arkin precipitation data for 1979 to 1998.

Figures 6a–c are the distributions of the correlation coefficients between the summer monsoon rainfall anomalies in East Asia and the SM index, WY index, and EAP index, respectively. Comparing Fig. 6c with Figs. 6a and 6b, it may be clearly seen that the correlation between the summer monsoon rainfall anomalies in East Asia and the EAP index proposed in this study is larger than the other correlations, especially in the positive correlation region of the lower reaches of the Huaihe River, and South Korea and Japan, and in the negative correlation region of the southeastern coast of China and around the Philippines. Thus we can conclude that the EAP index defined in this study can better describe the interannual variations of the East Asian summer monsoon.

4. Relationship between the EAP index and the summer surface air temperature in East Asia

Generally, the interannual variability of summer surface air temperature has an out of phase relationship with the variability of summer rainfall in the East Asian monsoon region. Therefore, it is also possible that there is a close relationship between the summer surface air temperature anomalies and the EAP index. Figure 7 is the distribution of the correlation coefficients between the summer surface air temperature anomalies in China and the EAP index. It may be seen from the figure that there are large positive correlations in the Yangtze River valley, the Huaihe River valley, North China, and Northeast China. The maximum correlation coefficient reaches 0.6 in Northeast China and the Korean Peninsula, which greatly exceeds the confidence level of 95%. That is to say, in a summer with high EAP index, the summer surface air temperature may be high and a hot summer may occur in these regions. For example, in the summers of 1961, 1978, and 1994, drought and hot summers occurred in the middle and lower reaches of the Yangtze River and the Huaihe River valley. Our results suggest that the EAP index proposed in this study can describe the interannual variations of summer surface air temperature not only in the Yangtze River valley and the Huaihe River valley, but also in North China and Northeast China.

Table 1. The correlation coefficients among the summer rainfall (YH-R) and surface air temperature anomalies (YH-T) in the Yangtze River valley and the Huaihe River valley, and the summer rainfall (K-R) and surface air temperature anomalies (K-T) in South Korea, and the EAP index for 42 summers.

Parameters	I_{EAP}	YH-R	YH-T	K-R	K-T
I_{EAP}	1.00				
YH-R	–0.59	1.00			
YH-T	0.54	–0.68	1.00		
K-R	–0.37	0.33	–0.25	1.00	
K-T	0.77	–0.56	0.66	–0.50	1.00

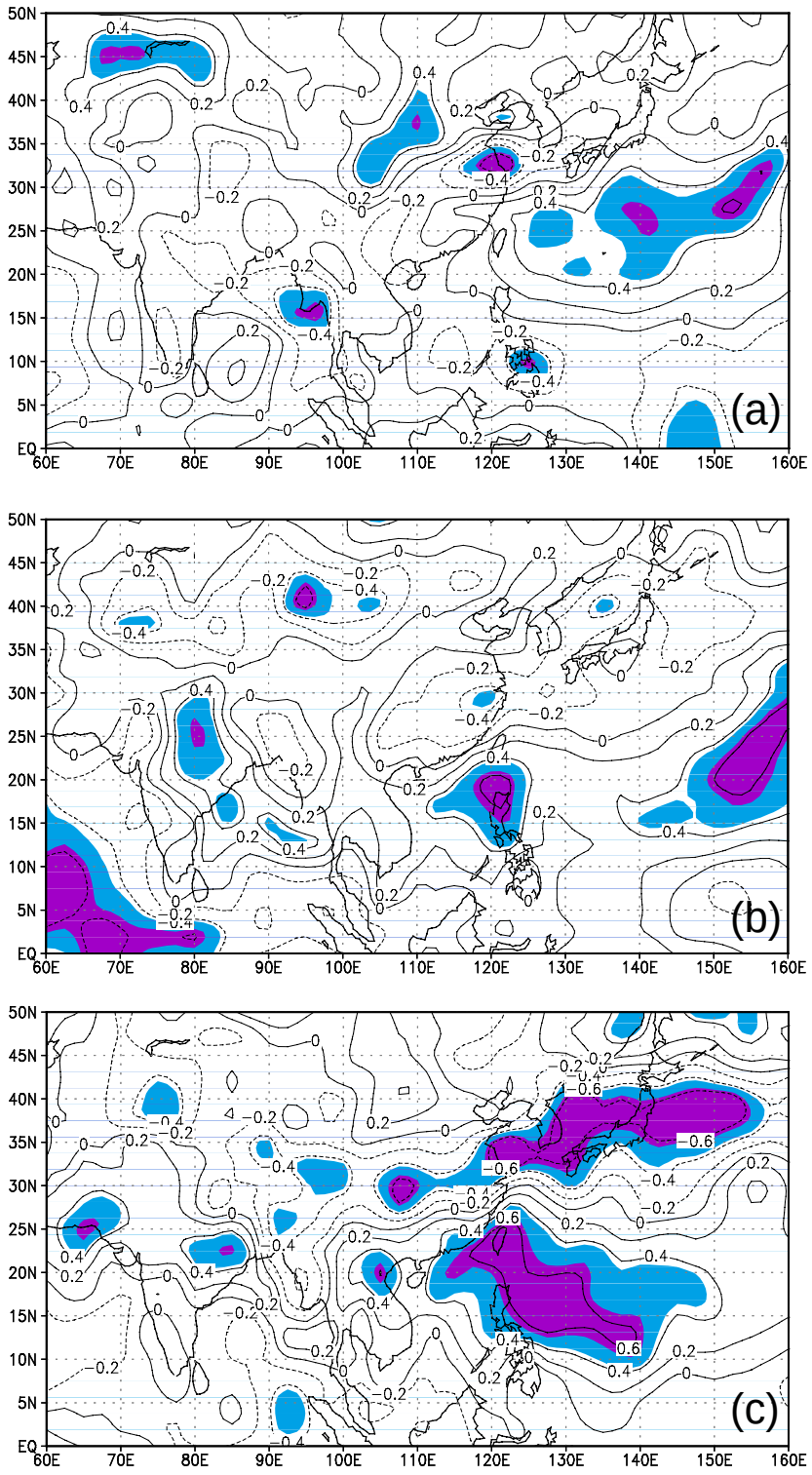

Fig. 6. Distribution of the correlation coefficients between the summer (June–August) rainfall anomalies in China with (a) the SM index, (b) the WY index, and (c) the EAP index. The shaded areas in the figure denote where the confidence level is over 95%.

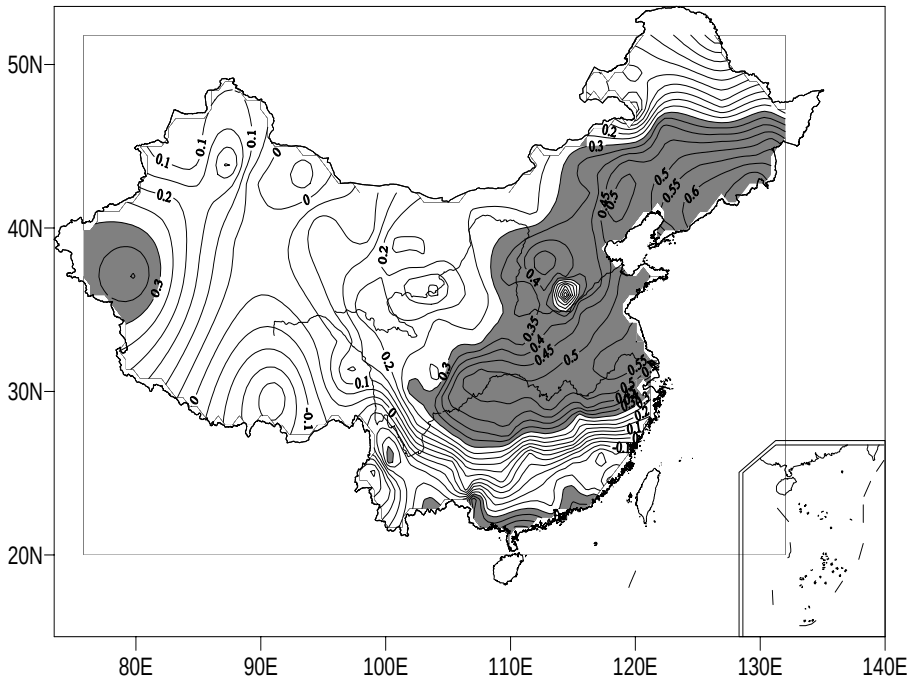

Fig. 7. Distribution of the correlation coefficients between the summer surface air temperature anomalies in China and the EAP index. The shaded areas denote where the confidence level is over 95%.

Similarly, the EAP index can also describe the interannual variations of summer surface air temperature anomalies in South Korea (figures not shown). Table 1 shows that the correlation between the summer surface air temperature anomalies in Korea and the EAP index is significant with a correlation coefficient of 0.77, which exceeds the confidence level of 99%.

From the above results and the correlation coefficients shown in Table 1, it is clearly seen that the EAP index based on the EAP teleconnection pattern can well describe not only the interannual variations of summer rainfall, but also the interannual variations of summer surface air temperature anomalies in the East Asian summer monsoon region, especially in the Yangtze River valley and the Huaihe River valley of China, and in South Korea and Japan. Therefore, the interannual variation of the EAP index defined in this study can be used to denote the interannual variability of monsoon climate in East Asia.

5. Relationship between the EAP index and the East Asian summer monsoon circulation

As mentioned above, there is a close relationship between the EAP index and the interannual variations of summer rainfall and surface air temperature in East Asia. But what causes the close relationship between the EAP index and the interannual variability of monsoon climate in East Asia? This may be due to the fact that the EAP index can well indicate the interannual variability of the East Asian summer monsoon circulation. In order to demonstrate this, the composite anomalous distributions of the 500-hPa height fields, the wind fields and their meridional component at 700 hPa over East Asia for the summers with high EAP index, (i.e., $I_{\rm EAP} \geqslant 1$), namely, 1961, 1978, and 1994 and for the summers with low EAP index, ($I_{\rm EAP} \leqslant -1$), namely, 1954, 1957, 1980, 1987, 1996, and 1998, are respectively analyzed.

Figures 8a and 8b indicate the composite distributions of the 500-hPa height anomaly fields over East Asia for the summers with $I_{\rm EAP} \geqslant 1$ and for the summers with $I_{\rm EAP} \leqslant -1$, respectively. Comparing Fig. 8a with Fig. 8b, it may be seen that the composite anomaly pattern of summer monsoon circulations for the summers with high EAP index is opposite to those for the summers with low EAP index. In a summer with high EAP index, as shown in Fig. 8a, the western Pacific subtropical high shifts northward. The positive 500-hPa height anomaly area is located over the Huaihe River valley, North China and the southern part of Northeast China, the Korean Peninsula and Japan, and the negative 500-hPa height anomaly areas are located over South China and eastern Siberia. Therefore, in a summer with high EAP index, the

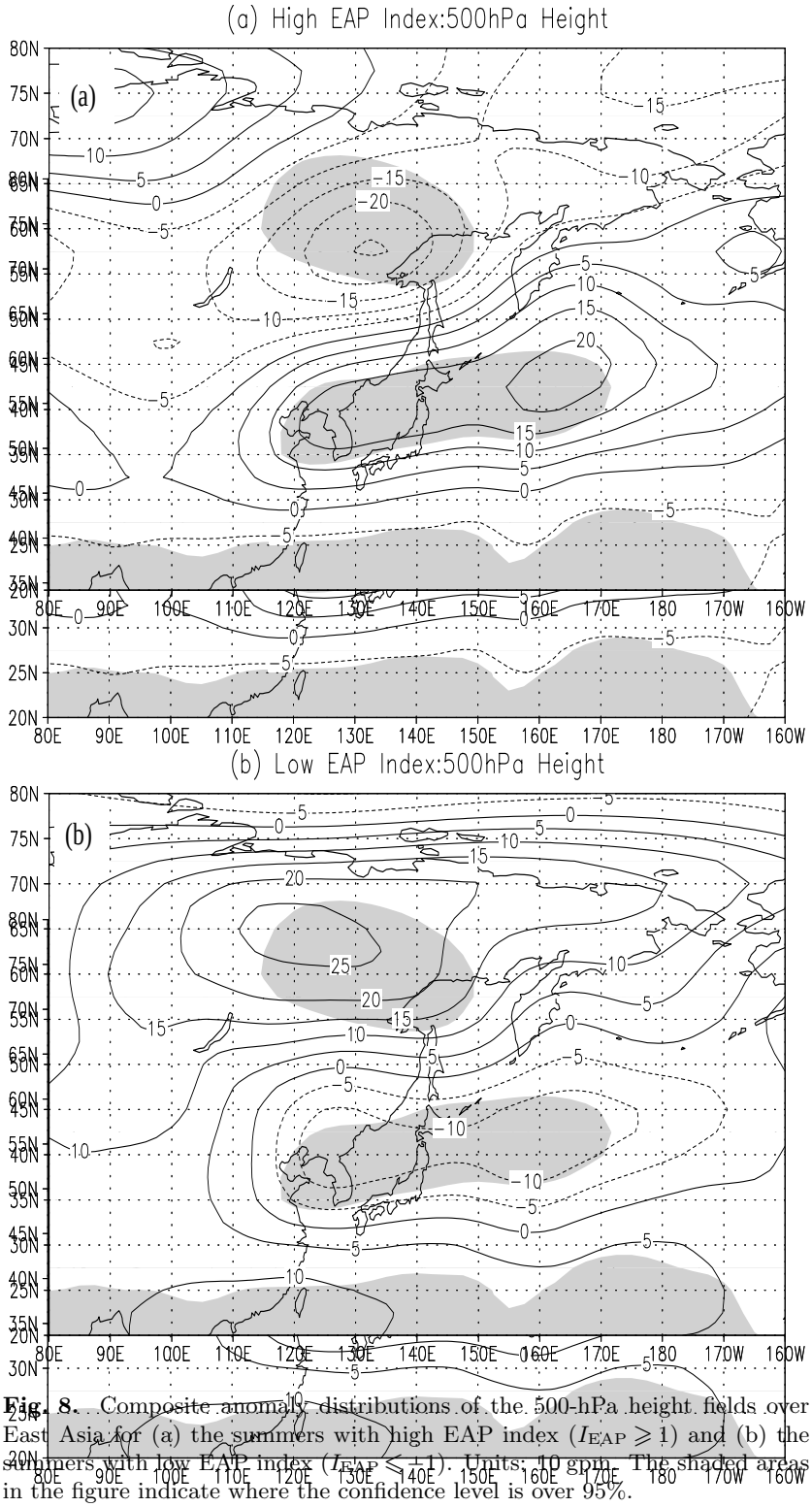

Fig. 8. Composite anomaly distributions of the 500-hPa height fields over East Asia for (a) the summers with high EAP index ($I_{\mathrm{EAP}} \geqslant 1$) and (b) the summers with low EAP index ($I_{\mathrm{EAP}} \leqslant -1$). Units: 10 gpm. The shaded areas in the figure indicate where the confidence level is over 95%.

summer surface air temperature is high and the summer monsoon rainfall is less in the middle and lower reaches of the Yangtze River and the Huaihe River valley, Korea, and Japan. In contrast, in a summer with low EAP index, as shown in Fig. 8b, the western Pacific subtropical high shifts southward. The negative 500-hPa height anomaly area is located over the Huaihe River valley, North China and Northeast China, the Korean Peninsula and Japan, and the positive 500-hPa height anomaly areas are located over South China and eastern Siberia. Therefore, in a summer with low EAP index, the summer surface air temperature is normal or below normal, and the summer monsoon rainfall is strong in the middle and lower reaches of the Yangtze River and the Huaihe River valley, Korea, and Japan.

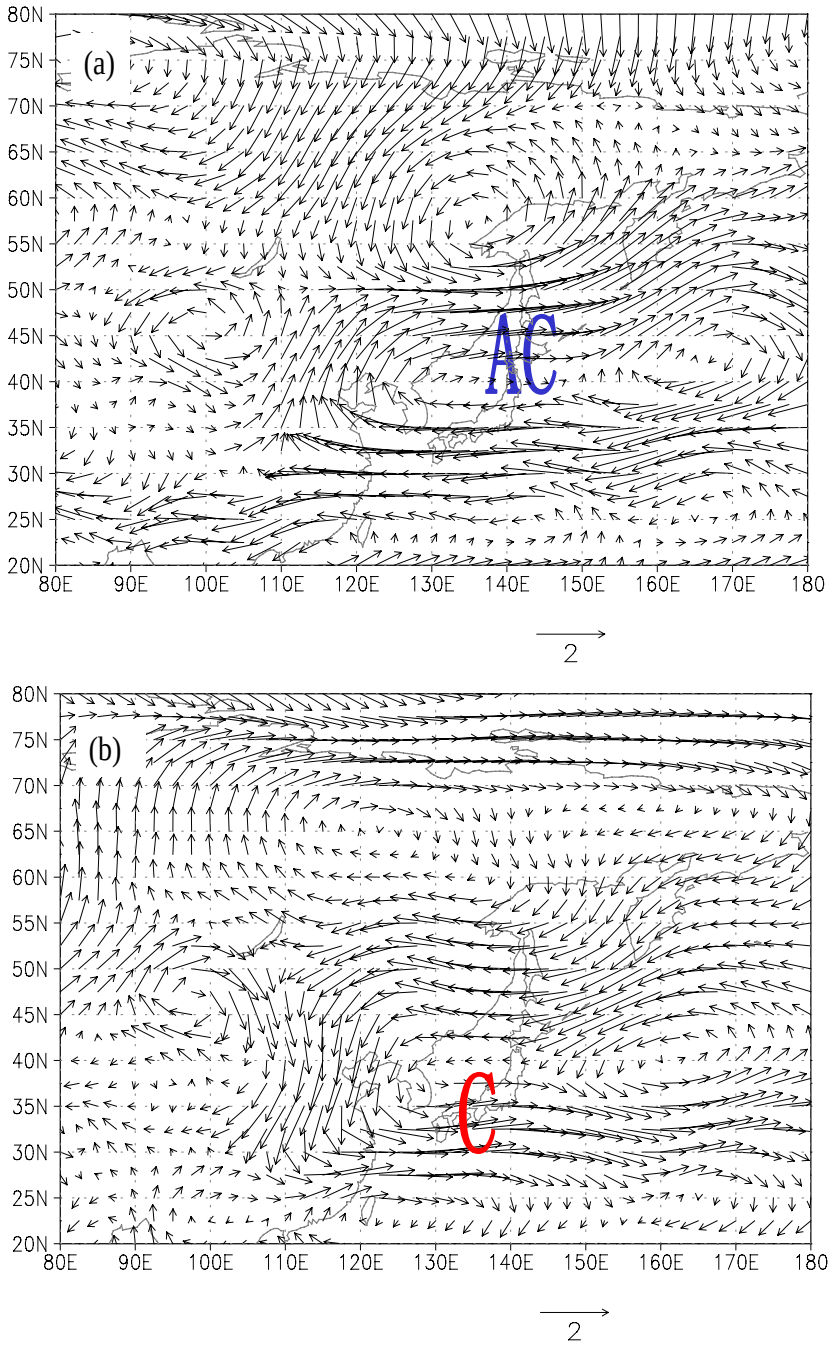

Fig. 9. Same as Fig. 8 but for the horizontal wind anomaly distribution at 700 hPa.

Generally, the monsoon flow is most obvious at 700 hPa over East Asia. Thus, the composite anomaly distributions of the wind fields at 700 hPa over East Asia for the summers with high EAP index ($I_{\mathrm{EAP}} \geqslant 1$), namely, 1961, 1978, and 1994, and for the summers with low EAP index ($I_{\mathrm{EAP}} \leqslant -1$), namely, 1954, 1957, 1980, 1987, 1996, and 1998, are respectively analyzed (see Fig. 9). As shown in Fig. 9a, in a summer with high EAP index, the strong anomalous anticyclonic circulation is located over the Huaihe River valley, North China, and Northeast China, and the anomalous cyclonic circulation is located over South China and eastern Siberia. In contrast, in a summer with low EAP index, as shown in Fig. 9b, the anomalous cyc-

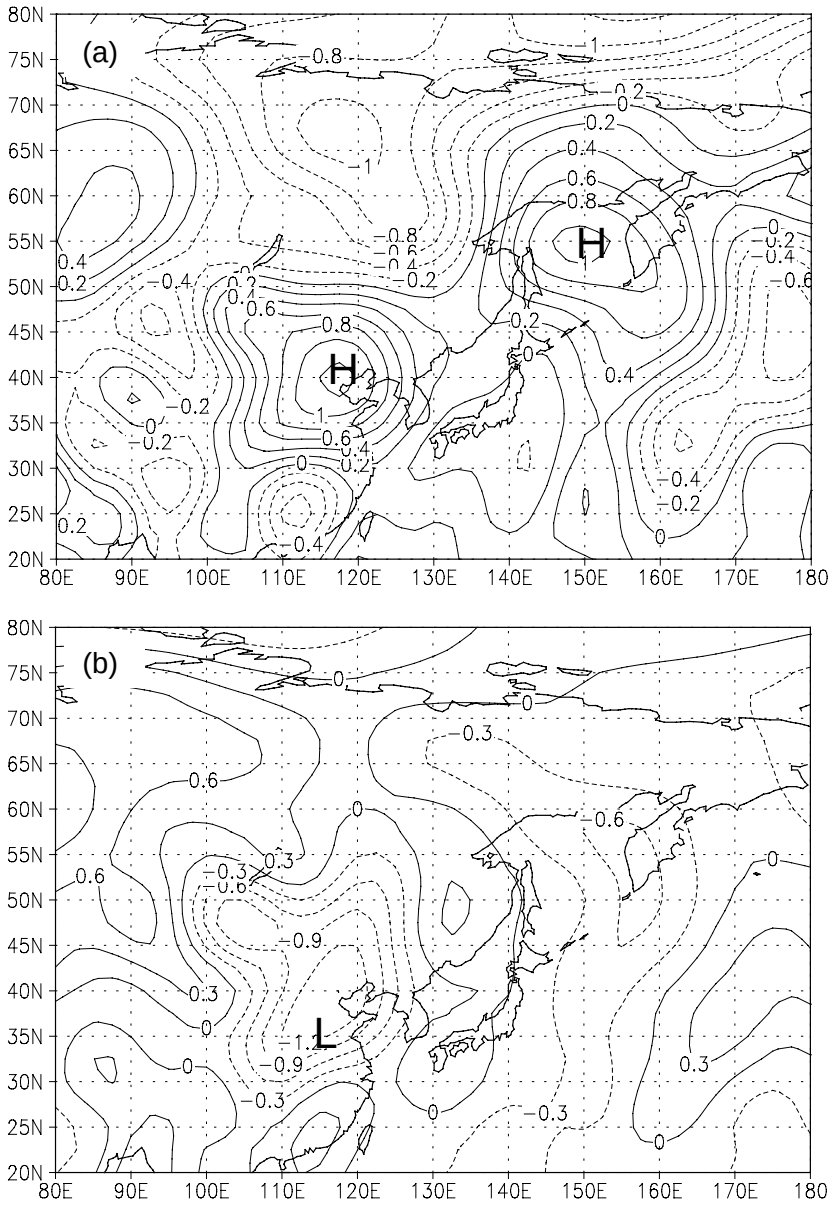

Fig. 10. Same as Fig. 8 but for the meridional wind anomalies at 700 hPa. Units: m s^{-1}.

lonic circulation is located over the Huaihe River valley, North China and Northeast China, the Korean Peninsula, and Japan, and the anomalous anticyclonic circulations are located over South China and eastern Siberia. Therefore, the anomaly circulation pattern shown in Fig. 9a is opposite to that shown in Fig. 9b. These patterns are similar to the distributions of the 500-hPa height anomaly field shown in Fig. 8.

From the above analyses, it is clear that the EAP index can well describe the interannual variability of summer monsoon circulation over East Asia.

An important characteristic of the summer monsoon flow over East Asia is its large meridional component. Huang et al. (1998) pointed out that the meridional component of water vapor transport associated with the East Asian summer monsoon is dominant. The convergence of water vapor transport, which can cause rainfall, is closely associated with the meridional transport of water vapor from south to north by monsoon flow. Therefore, the composite distributions of the meridional component of the wind fields at 700 hPa over East Asia for the summers with high EAP index and for the summers with low EAP index are also analyzed and shown in Figs. 10a and 10b, respec-

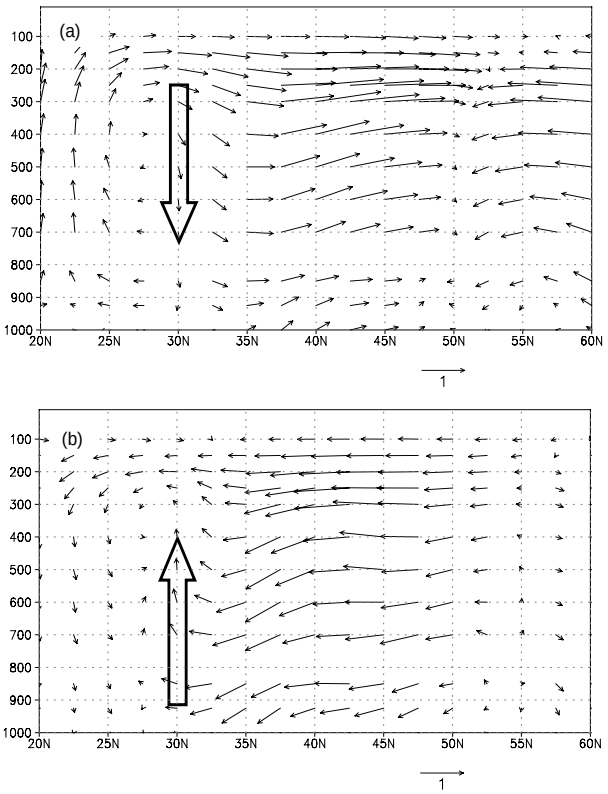

Fig. 11. Same as Fig. 8 but for the vertical-meridional circulation anomalies averaged between 110°–125°E.

tively. Comparing Fig. 10a with Fig. 10b, the anomalous meridional component of the wind fields at 700 hPa for the summers with high EAP index is different from that for the summers with low EAP index. In a summer with high EAP index, the positive meridional wind anomalies appear over the Huaihe River valley, North China, and the Korean Peninsula, i.e., the strong southerly winds of the monsoon flow over these regions. However, in a summer with low EAP index, the negative meridional wind anomalies appear over the Huaihe River valley, North China, and the Korean Peninsula, as shown in Fig. 10b. This indicates that in a summer with low EAP index, the southerly monsoon flow is weak over these regions.

6. Relationship between the EAP index and the vertical-meridional circulation over East Asia

Tao and Chen (1987) pointed out that the mean vertical-meridional circulation over the East Asian summer monsoon region is different from that over the Indian monsoon region. In East Asia there is no high mountain barriers and the flow can frequently penetrate from the mid-latitudes into the subtropical region of East Asia. In the climatological mean state, the convective activities are strong over the monsoon trough (or ITCZ) located at about 15°N. The outflow in the upper troposphere caused by the convective activities can be directed equatorward and northward from 15°N. Another ascending flow can be caused by the strong convective activities over the mei-yu front in the Yangtze River valley and the Baiu front in Japan. Thus the northward flow from the monsoon trough converges with the southward outflow due to the strong convective activities over the mei-yu front. This convergence can form a strong descending flow, which contributes to the formation of the western Pacific subtropical high.

Here the results show that the vertical-meridional circulation over the East Asian summer monsoon region in a summer with high EAP index is very different from that in a summer with low EAP index. Figures 11a and 11b are the composite anomaly distributions of vertical-meridional circulation averaged along 110°–125°E for the summers with $I_{\mathrm{EAP}} \geqslant 1$ and for the summers with $I_{\mathrm{EAP}} \leqslant -1$, respectively. Comparing Fig. 11a with Fig. 11b, it may be found that the vertical-meridional circulation in a summer with high EAP index is opposite to that in a summer with low EAP index. As shown in Fig. 11a, the positive anomaly distribution of vertical-meridional circulation, i.e., the Hadley cell-like circulation, is located over the region from South China to the Yangtze River valley. And there are strong southerly wind anomalies not only in the lower troposphere but also in the upper troposphere over the area to the north of 30°N. In this case, there is strong descending anomaly flow at 30°N. This means that the ascending flow is not strong over the mei-yu front in China and the Baiu front in Japan. Thus, the monsoon rainfall and the convective activities are not strong in these regions. However, there are strong southerly wind anomalies over the Yellow River valley, North China, and North Korea, which may cause strong rainfall. In a summer with low EAP index, as shown in Fig. 11b, the anomaly distribution of vertical-meridional circulation exhibits an anti-Hadley cell-like circulation, or a monsoon cell-like circulation, over the region from South China to the Yangtze River valley. There are strong northerly wind anomalies in both the lower and upper troposphere over the area to the north of 30°N. In this case, there is a strong ascending anomaly flow at 30°N, indicating a strong ascending flow over the mei-yu front in China and the Baiu front in Japan. The monsoon rainfall and the convective activities are strong in these regions. However, the southerly winds are weak over the Yellow River valley, North China, and North Korea. And the monsoon rainfall is weak in North China and North Korea in this case.

Therefore, our results also show that the EAP index proposed in this study can describe well the interannual variability of vertical-meridional circulation over East Asia.

7. Conclusion and discussion

Based on the EAP (East Asia/Pacific) teleconnection pattern in the summer atmospheric circulation anomalies over the Northern Hemisphere suggested by Nitta (1987), and Huang and Li (1987, 1988), respectively, an index measuring the strength of the East Asian summer monsoon is defined in this paper. This index is called the EAP index. The composite analyses of observed data clearly show that the EAP index can well describe not only the interannual variations of summer rainfall and surface air temperature in the Yangtze River valley and the Huaihe River valley, the Korean Peninsula, and Japan, but also the interannual variability of the East Asian summer monsoon system including the horizontal monsoon circulation and the vertical-meridional circulation cell over East Asia.

With the NCEP/NCAR reanalysis data and summer rainfall and surface air temperature data from the observational stations of China and Korea, it is shown that in a summer with high EAP index, the monsoon rainfall is weak in the Yangtze River valley and the Huaihe River valley, South Korea, and Japan. And the surface air temperature is also high in the Huaihe River valley, North China and Northeast China, and North Korea. In this case, the anticyclonic anomaly circulation is located over the Yangtze River valley and the Huaihe River valley, Korea, and Japan. The southerly monsoon flow is strong over East Asia. A positive vertical-meridional anomaly circulation cell is located over the area from South China to the Yangtze River valley, and there is a descending anomaly flow at about 30°N. However, in a summer with low EAP index, the monsoon rainfall is strong in the Yangtze River valley and the Huaihe River valley, South Korea, and Japan. The surface air temperature is low in the Huaihe River valley, North China and Northwest China, and North Korea. In this case, the cyclonic anomaly circulation is located over the Yangtze River valley and the Huaihe River valley, Korea, and Japan. The southerly monsoon flow is weak over East Asia. A reverse vertical-meridional anomaly circulation cell is located over the area from South China to the Yangtze River valley, and there is an ascending anomaly flow at about 30°N.

The analyses of observed data show that the EAP index can well denote the interannual variations of summer monsoon climate in East Asia because the index can well describe the East Asian summer monsoon circulation system. However, our study is preliminary. Further research is needed to improve the definition of this index so that it can be more suitable for measuring the interannual variations of the East Asian summer monsoon.

Acknowledgments. The author is grateful to Prof. Ye Duzheng (i.e., Yeh, T. C.) for his detailed supervision and Dr. Lu Riyu and Dr. Chen Jilong for their help. This study was supported jointly by the National Key Basic Research Development Program (Grant No. G1999043403), the Knowledge Innovation Project of the Chinese Academy of Sciences (CAS) (Grant No. KZCX3-SW-218), and the National Natural Science Foundation of China project for young scientists fund (No. 40305012) and the Western Project of the CAS (KZCX1-10-07).

REFERENCES

Ding, Y. H., 1994: Monsoon over China. Kluwer Academic Publishers, 420pp.

Guo Qiyun, 1983: The strength index of East Asian summer monsoon and its variation. *Chinese J. Geography. Soc.*, **38**, 207–217. (in Chinese)

Huang Ronghui, and Li Weijing, 1987: Influence of heat source anomaly over the tropical western Pacific on the subtropical high over East Asia. Proc. International Conference on the General Circulation of East Asia, Chengdu, China, April 10-15, 1987, 40-45.

Huang Ronghui, and Li Weijing, 1988: Influence of heat source anomaly over the western tropical Pacific on the subtropical high over East Asia during summer and its physical mechanism. *Chinese J. Atmos. Sci.*, Special Issue, 107–117. (in Chinese)

Huang Ronghui, and Sun Fengying, 1992: Impact of the tropical western Pacific on the East Asian summer monsoon. *J. Meteor. Soc. Japan*, **70**(1B), 243–256.

Huang Ronghui, Xu Yuhong, Wang Pengfei, and Zhou Liantong, 1998: The features of the catasfrophic flood over the Changjiang River basin during the summer of 1988 and cause exploration. *Climatic Environ. Res.*, **3**, 300–313. (in Chinese)

Huang Ronghui, Zhang Zhenzhou, and Huang Gang, 1998: characteristics of water vapor transport in East Asian monsoon region and its differences from that of South Asian monsoon region in summer. *Chinese J. Atmos. Sci.*, **22**, Special Issue, 368–379. (in Chinese)

Huang Ronghui, and Zhou Liantong, 2002: Research on the characteristics, formation mechanism and prediction of severe climate disasters in China. *J. Natural Disasters*, **11**, 1–9. (in Chinese)

Kurihara, K., 1989: A climatological study on the relationship between the Japanese summer weather and the subtropical high in the western northern Pacific. *Geophys. Mag.*, **43**, 45–104.

Murakami, T., and J. Matsumoto, 1994: Summer monsoon over the Asian continent and western North Pacific. *J. Meteor. Soc. Japan*, **72**, 745–791.

Nitta, Ts., 1987: Convective activities in the tropical western Pacific and their impact on the Northern Hemisphere summer circulation. *J. Meteor. Soc. Japan*, **64**, 373–390.

Nitta, Ts., and Z. Z. Hu, 1996: Summer climate variability in China and its association with 500 hPa height and tropical convections. *J. Meteor. Soc. Japan,* **74**, 425–445.

Ramage, C., 1971: *Monsoon Meteorology*, International Geophysics Series, 15, Academic Press, San Diego, California., 296pp.

Shi Neng, Zhu Qiangen, and Wu Bingui, 1996: The East Asian summer monsoon in relation to summer large-scale weather-climate anomaly in China for last 40 years. *Chinese J. Atmos. Sci.*, **20**, 385–394. (in Chinese)

Tao Shiyan, and Chen Longxun, 1985: The East Asian summer monsoon. Proc. of International Conference on Monsoon in the Far East, Tokyo. Nov. 5–8. 1985, 1-11.

Tao Shiyan, and Chen Longxun, 1987: A review of recent research on the East Asian summer monsoon in China. *Monsoon Meteorology*, C. P. Chang and T. N. Krishnamurti, Eds., Oxford University. Press, 60–92.

Webster, P. J., and S. Yang, 1992: Monsoon and ENSO: Selectively interactive system. *Quart. J. Roy. Meteor. Soc*, **118**, 877–926.

Ye Duzheng, and Huang Ronghui, 1996: *Research on the Regularity and Cause of Droughts and Floods in the Yellow River and the Yangtze River Valleys*, Shandong Press for Science and Technology, 384pp. (in Chinese)

Zeng Qingcun, Zhang Banglin, and Liang Youlin, 1994: East Asian summer monsoon-A case study. *Proceedings of the Indian National Science Academy. Indian Nat. Sci. Acad.*, **60**, 81-96.

Zhang Qingyun, and Peng Jingbei, 2003: Influence of the interannual and interdecadal variations of atmospheric circulation over East Asia on the landing typhoon in China. *Chinese J. Atmos. Sci.*, **27**, 97–106. (in Chinese)

nature communications

Article

https://doi.org/10.1038/s41467-024-49857-y

Role of atmospheric rivers in shaping long term Arctic moisture variability

Received: 31 October 2023

Accepted: 21 June 2024

Published online: 29 June 2024

Check for updates

Zhibiao Wang[1], Qinghua Ding[2] ✉, Renguang Wu[3], Thomas J. Ballinger[4] ✉, Bin Guan[5], Deniz Bozkurt[6,7,8], Deanna Nash[9], Ian Baxter[2], Dániel Topál[10,11], Zhe Li[2], Gang Huang[12], Wen Chen[13], Shangfeng Chen[1], Xi Cao[1] & Zhang Chen[14]

Atmospheric rivers (ARs) reaching high-latitudes in summer contribute to the majority of climatological poleward water vapor transport into the Arctic. This transport has exhibited long term changes over the past decades, which cannot be entirely explained by anthropogenic forcing according to ensemble model responses. Here, through observational analyses and model experiments in which winds are adjusted to match observations, we demonstrate that low-frequency, large-scale circulation changes in the Arctic play a decisive role in regulating AR activity and thus inducing the recent upsurge of this activity in the region. It is estimated that the trend in summertime AR activity may contribute to 36% of the increasing trend of atmospheric summer moisture over the entire Arctic since 1979 and account for over half of the humidity trends in certain areas experiencing significant recent warming, such as western Greenland, northern Europe, and eastern Siberia. This indicates that AR activity, mostly driven by strong synoptic weather systems often regarded as stochastic, may serve as a vital mechanism in regulating long term moisture variability in the Arctic.

Arctic surface air temperatures have shown a warming trend at a rate more than twice that of the global average in recent decades, attributed to various Arctic Amplification (AA) processes driven by both anthropogenic and natural climate forcing[1–9]. As constrained by the Clausius–Clapeyron (CC) relationship, Arctic atmospheric warming also leads to atmospheric moistening, resulting in higher specific humidity, greater cloud cover and cloud water content, and more precipitation across the Arctic[10–13]. This moisture increase has substantially altered the Arctic hydrological and cryospheric variability over the past few decades[14,15], owing to various moisture-related positive feedbacks connected to changing radiative properties of the atmosphere, clouds, and surface conditions.

This increase in moisture is prominent throughout the year, with the most significant rise occurring during the summer months

[1]Center for Monsoon System Research, Institute of Atmospheric Physics, Chinese Academy of Sciences, Beijing, China. [2]Department of Geography and Earth Research Institute, University of California, Santa Barbara, Santa Barbara, CA, USA. [3]School of Earth Sciences, Zhejiang University, Hangzhou, China. [4]International Arctic Research Center, University of Alaska Fairbanks, Fairbanks, AK, USA. [5]Joint Institute for Regional Earth System Science and Engineering, University of California, Los Angeles, Los Angeles, CA, USA. [6]Department of Meteorology, University of Valparaíso, Valparaíso, Chile. [7]Center for Climate and Resilience Research (CR)2, Santiago, Chile. [8]Center for Oceanographic Research COPAS COASTAL, University of Concepción, Concepción, Chile. [9]Center for Western Weather and Water Extremes, Scripps Institution of Oceanograph, University of California San Diego, La Jolla, CA, USA. [10]Earth and Climate Research, Earth and Life Institute, Université catholique de Louvain, Louvain-la-Neuve, Belgium. [11]Institute for Geological and Geochemical Research, HUN-REN Research Centre for Astronomy and Earth Sciences, MTA-Centre for Excellence, Budapest, Hungary. [12]State Key Laboratory of Numerical Modelling for Atmospheric Sciences and Geophysical Fluid Dynamics, Institute of Atmospheric Physics, Chinese Academy of Sciences, Beijing, China. [13]Department of Atmospheric Sciences, Yunnan University, Kunming, China. [14]School of Atmospheric Sciences, Chengdu University of Information Technology, Chengdu, China. ✉e-mail: qinghua@ucsb.edu; tjballinger@alaska.edu

(June–July–August, abbreviated as JJA)[16,17], which has been attributed to multiple sources triggered by global warming, including increased evaporation from local ocean and surrounding continents[18], enhanced sublimation of ice and snow within the Arctic[19,20], and intensified moisture transport from lower latitudes[15,16,21–27]. Climate models forced by historical anthropogenic emissions can replicate a warmer and more humid Arctic in summer, featuring a rather uniform rise in atmospheric temperature and specific humidity across most of the Arctic. Future climate projections suggest that this wetting trend will intensify under continued global warming scenarios, and bring about a number of cascading effects in the Arctic, such as a precipitation regime shift from snow to rain that will substantially change local ecosystems in the coming decades[28–31]. While these modeling studies highlight the dominance of the CC relationship in shaping Arctic temperature and specific humidity, it is evident that over recent decades summertime changes in these parameters are influenced by large-scale circulation variability, manifested as a long-term trend toward the local barotropic high-pressure anomaly situated over Greenland over the past four decades. This summertime circulation trend pattern is thought to have origins, in part, from internal climate variability and contribute to warming in the mid-to-lower troposphere of the Arctic, as well as the melting of sea ice and the Greenland ice sheet (GrIS) through adiabatic warming processes[32–37]. Thus, both anthropogenic forcing and internal variability should be factored in when considering the underlying mechanisms behind recent moisture trends in the Arctic.

While the CC equation governs the temperature–humidity relationship on a global scale, internal atmospheric circulation variability also plays a key role in the Arctic. Circulation variability regulates the distribution and transport of moisture across a wide range of timescales through its effects on weather systems including extratropical storms such as Arctic cyclones and atmospheric rivers (ARs). ARs are characterized by elongated, ribbon-like plumes of intense water vapor, driven by synoptic-scale cold-frontal systems, which normally move northeastward and persist for a few days in the extratropcis[12,38,39]. ARs typically form as a result of the interaction between a cold front, which transports a substantial amount of water vapor, and a warm front[40]. Thus, ARs represent a unique and intensely extreme phenomenon linked to the storm tracks[41,42], closely tied to extratropical cyclone and anticyclone activity[43].

Over the annual cycle, ARs contribute to more than 90% of poleward transport of water vapor into the Arctic and are observed across the Arctic for about 1–3 days per month throughout the year, with their highest occurrence from June to August (Supplementary Fig. 1a, which can be found in the Supplementary Information section). This is mainly due to the northward shift of the subtropical jet in these warmer months relative to the cold season, resulting in more ARs propagating into the Arctic[44–46] (Supplementary Fig. 1b, c). Thus, boreal summer stands out as a critical period during which ARs have a greater potential of altering moisture distribution in the Arctic and consequently impacting the local climate.

It is worth noting that AR frequency in the Arctic has increased in recent decades, particularly over western Greenland, where stronger ARs have contributed to significant melt over the GrIS' ablation zone[47]. These AR-related changes have complex origins, and their causes remain uncertain. Suggestions have been made that mid- and high-latitude AR characteristics (i.e., frequency, intensity, trajectory and duration) are sensitive to thermodynamic effects related to global warming[42,48–54] and/or anthropogenic and natural aerosol forcing[55–57]. Sufficient moisture and eddy kinetic energy are necessary conditions for the formation and activity of ARs. Under global warming, the available potential energy and atmospheric moisture are expected to increase, particularly in the Arctic, consequently increasing the occurrence of ARs there[58–60]. These AR changes could also be attributed to atmospheric internal variability[61–63]. It is unclear whether a combination of these mechanisms can fully account for the recent observed features of ARs and the moistening trend in the Arctic. A particularly unaddressed question is how global warming and the low-frequency circulation variability, both separately and in concert, have moistened the Arctic in the past decades through AR activity. This is an emerging topic of interest given the significant potential impacts of summertime ARs in destabilizing the GrIS in recent decades. For instance, extreme GrIS melt in the summer of 2012, which contributed 1.2 mm global mean sea level rise[64], was exacerbated by AR activity[65,66] connected with amplified JJA anticyclonic circulation over the region[67,68]. More recently, ARs prompted a mid-summer melt event in northeast Greenland in 2014 and a late summer melt event across much of the GrIS ablation area in 2021[69].

One hurdle in understanding the interplay between ARs and large-scale circulation change lies in the inability of models in capturing the observed circulation pattern in the Arctic over the past decades when they are forced by anthropogenic radiative forcing or observed boundary SST and sea ice forcing[70–72]. This poses a significant challenge toward precisely investigating the governing role of circulation on ARs. In this study, we overcome this challenge by employing a nudging approach in Community Earth System Model version 1 (CESM1)[73] to examine how ARs respond when observed wind trends are introduced into the model. We then compare these simulated AR changes against observations and AR responses to anthropogenic forcing in the same model. Through this approach, we aim to disentangle the relative roles and underlying mechanisms of anthropogenic forcing and large-scale circulation in regulating the moisture distribution in the Arctic via AR activity. Our goal is to develop physical and qualitative insights about the contribution of ARs to the Arctic moistening trends. We focus our analysis on the summer months (JJA) when the Pan-Arctic moistening trend is most notably positive and significant over the period (Fig. 1b and Supplementary Figs. 1a and 2).

Results

Concurrent changes in large-scale atmospheric circulation and AR characteristics

Shaped by the mean atmospheric circulation pattern (Supplementary Fig. 3c), the average frequency of summertime ARs in each grid point is about 3–4 days per month over western Greenland, northern Europe, from Scandinavia to western Russia and northward to the Barents Sea, and eastern Siberia (Supplementary Fig. 3a). Climatologically, specific humidity, circulation, and air temperature in summer exhibit a consistent pattern, with a minimum value centered at the pole surrounded by higher values in the subarctic (Supplementary Fig. 3b–d).

Over the past few decades, coinciding with the period of enhanced AA and rapid global warming, the frequency of JJA AR events reaching the Arctic exhibits an overall increase of 0.1 days month^{-1} decade^{-1} from 1979 to 2019. However, this increase is not uniform. AR frequency increases significantly over northern Canada extending to western Greenland, eastern Siberia, and small portions of the central Arctic and northern Europe, while the North Atlantic Ocean, western Alaska, and central Siberia witness weak negative trends (Fig. 1a). Patterns of long-term variations in AR frequency reveal notable similarities to the observed trends in large-scale JJA circulation (Fig. 1c). Upper-level geopotential heights significantly increase across western Greenland, northern Europe, and eastern Siberia, (highlighted in Supplementary Fig. 3e) but over the North Atlantic Ocean, Alaska, and central Siberia the increase is relatively small. In line with these atmospheric circulation trends, both specific humidity and temperature display pronounced rises over western Greenland, northern Europe, and eastern Siberia (Fig. 1b–d).

However, these observed changes are not fully captured by our best estimate of the climate response to anthropogenic forcing, as derived from ensemble means of historical simulations in the Coupled Model Intercomparison Project Phase 6 (CMIP6) and the CESM2 large ensemble. The ensemble mean model simulations show a slight

https://doi.org/10.1038/s41467-024-49857-y

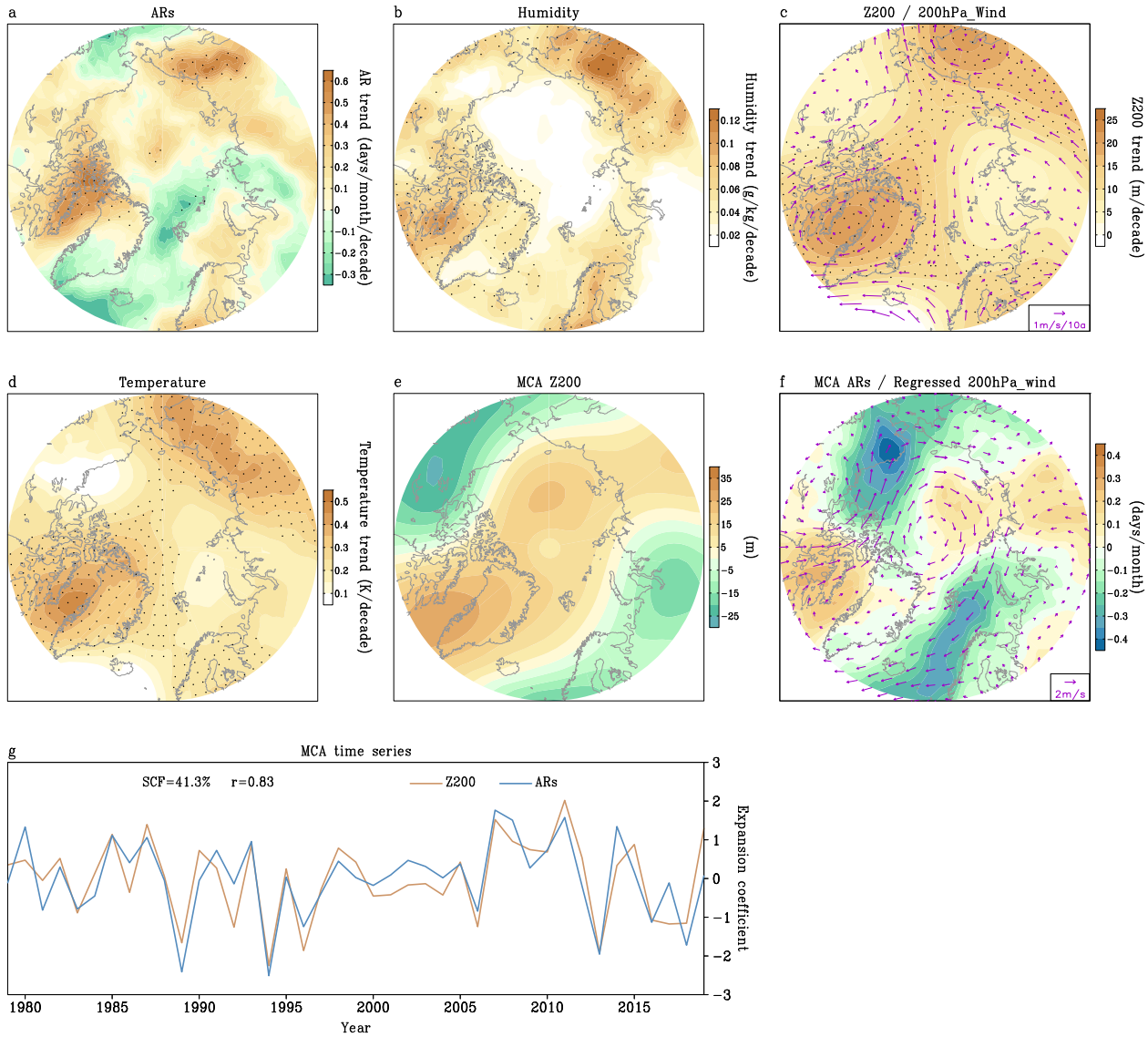

Fig. 1 | Relationships between summer atmospheric rivers (ARs) and atmospheric variables. a–d Linear trends of June–July–August (JJA) AR frequency (days/month/decade) (**a**), lower to middle tropospheric (surface to 500 hPa average) specific humidity (g/kg/decade) (**b**), 200 hPa geopotential height (Z200, shaded) (m/decade) and 200 hPa winds (200hPa_Wind, vectors) (m/s/decade) (**c**), and tropospheric (surface to 200 hPa average) air temperature (K/decade) (**d**) in the Arctic from 1979 to 2019. **e**, **f** Spatial pattern of the leading Maximum Covariance Analysis (MCA) mode of detrended summer Z200 (**e**, in m) and AR frequency (**f**, in days/month) over the period. **g** Standardized time series of the leading MCA mode of summer Z200 (orange line) and AR frequency (blue line). Black dots in (**a**–**d**) denote statistically significant trends at the 95% confidence level. The scale for the wind trend is shown at the bottom-right corner of (**c**). Wind anomalies (vectors, m/s) at 200 hPa in (**f**) are obtained by linear regression of anomalous JJA winds at 200 hPa against the standardized time series of the Z200 pattern in the leading MCA mode. The scale for wind anomalies is shown at the bottom-right corner of (**f**). "SCF" in (**g**) indicates the squared covariance fraction of the leading MCA mode. "r" in (**g**) indicates the correlation coefficient between the time series of Z200 and AR frequency patterns in the leading MCA mode.

change or nearly uniform rise of geopotential height (200 hPa), air temperature (surface to 200 hPa average), and specific humidity (surface to 500 hPa average) over Greenland and Eurasia, respectively, which strongly contrasts observational findings (Fig. 1 vs. Supplementary Fig. 4) and may signify the role of internal variability in shaping the patterns. It has been extensively discussed in earlier studies that this discrepancy is a common issue across most historical simulations, partially attributed to models' limitations in replicating the observed low-frequency variability of tropical–extratropical teleconnections[33,36,37,71,72,74,75]. In particular, the ensemble mean of JJA ARs displays only an increasing trend, with the highest values located over the Arctic Ocean close to the North Pacific, rather than primarily centered atop and around Greenland as observed (Supplementary Fig. 5a). This suggests that the storm track shift over the North Pacific close to the Bering Strait has a larger contribution to the increasing trend of ARs in the Arctic under the influence of AA in models.

A better understanding of these discrepancies between observations and the model response to external forcing is necessary to accurately assess the sensitivity of ARs to global warming and to account for other potential forcing factors. The above-described alignment between the observed trends in atmospheric circulation, temperature and specific humidity fields, and AR frequency suggests that large-scale circulation plays a key role in regulating poleward moisture transport through the circulation's control on ARs[76–78] (Fig. 1a, c). We assess these connections from a statistical perspective by employing maximum covariance analysis (MCA)[79] to objectively examine the primary coupled patterns among climatic variables. Figure 1e, f shows the spatial pattern of the leading MCA mode of

detrended JJA 200 hPa geopotential heights (Z200, m) and JJA frequency of ARs between 1979 and 2019. The leading MCA mode (MCA1) explains 41.3% of the squared covariance and its spatial pattern clearly exhibits a zonal wave number 2 structure along 70°N. Regarding the MCA1 pattern, the positive signals of Z200 and ARs are found over western Greenland and the Siberian Arctic, while negative loadings of the two variables are observed over western Europe/western Siberia and areas from western Canada to the Bering Strait. Apparently, these two patterns bear some resemblance to the long-term trends of ARs and circulation, respectively, particularly over Greenland. This resemblance suggests that the secular trends of Z200 and ARs over Greenland may be physically connected, as indicated by their interannual connections identified by MCA1.

MCA1-related 200 hPa wind anomalies demonstrate how JJA mean circulation anomalies shape ARs on interannual timescales. During the summer season, westerly winds prevail in the Arctic troposphere across the region in the climatology (Supplementary Fig. 3c, vectors). ARs are more frequent over the regions marked by strong southerly wind anomalies, while decreased AR frequency is seen over the regions dominated by anomalous JJA northerly or easterly flows (Fig. 1f, indicated by wind vectors). This suggests a strong governing forcing of anomalous seasonal mean flow on AR activities within the season on interannual timescales. In light of the strong impacts of seasonal mean circulation on ARs, if large-scale circulation also varies on low-frequency timescales in specific areas, ARs may respond to these changes and reflect long-term variability.

Moreover, we observe a consistent coupling pattern in the MCA mode between any two fields from Fig. 1, whether trends are removed or not (figures not shown). To further link the change of this MCA mode to other fields of the Arctic climate system, we correlate the time series of MCA1-ARs (or MCA1-Z200) with the detrended JJA low cloud, downward longwave radiation, surface air temperature, and sea ice. We obtain significant correlations among these variables, indicating the importance of the large-scale circulation trend in creating a warmer, cloudier, and more humid atmosphere, characterized by increased AR incursions into many areas over the past decades. This, in turn, amplifies downward longwave radiation and leads to accelerated Arctic sea ice and land ice melt (Supplementary Fig. 6).

Contribution of ARs to long-term changes in specific humidity

While ARs are statistically connected with large-scale atmospheric variables, such as geopotential height, specific humidity and temperature, in the Arctic on interannual and lower frequency timescales (see Fig. 1), it remains unclear how ARs are physically driven by these large-scale climate variables and potentially feedback on these fields. In this section, we use 6-hourly changes in specific humidity to examine how moisture changes in some regions are associated with 6-hourly AR propagation into the Arctic. This analysis will enable us to develop an approach to estimate the contribution of ARs to the increasing humidity observed over the past 41 years. We first focus our analysis on the western Greenland region, given that it has witnessed the most significant increases in AR frequency and lower tropospheric specific humidity. The year 2012 is particularly noteworthy as it marked the most extreme melt season of the GrIS and Pan-Arctic sea ice since 1979[64]. Therefore, our first examination centers on that year. An MCA analysis between daily AR frequency and specific humidity anomalies during JJA of 2012 is computed to understand their day-to-day connection (for more details, refer to the Methods section). Climatological seasonal cycles and interannual variability are removed from each grid cell to ensure that the identified MCA pattern primarily reflects the connection on shorter timescales.

The leading MCA mode, explaining 58.3% of the squared covariance, displays a large positive AR loading west of Greenland that is collocated with a widespread increase in specific humidity (Fig. 2a, b). The time series of the ARs and moisture modes closely covary throughout the season (Fig. 2d). In particular, in mid-July, a strong AR preceded a significant surge of atmospheric moisture over most of Greenland[65,66,80] and impacted Summit Station, where exceptional surface air temperatures reached 2.2 °C[81]. This moisture intrusion resulted in widespread ice sheet melt, a phenomenon not observed since 1889[80,82,83]. An MCA analysis for all summers (by connecting all summertime daily data together) from 1979 to 2019 over the region yields a similar coupling pattern (Supplementary Fig. 7a, b). Likewise, MCA for the regions over northern Europe and eastern Siberia exhibits a highly similar coupled mode and a close coherence in the temporal variations for individual summers from 1979 to 2019 (Supplementary Figs. 8 and 9). This highlights the consistent influence of ARs in driving specific humidity changes on synoptic timescales. To illustrate this effect across all summers, we make composites of specific humidity associated with the strongest ARs centered in three key regions (western Greenland, northern Europe, and eastern Siberia, Supplementary Fig. 3e). In each of these regional centers, specific humidity begins to increase approximately 1 day prior to the onset of ARs. Subsequently, following the occurrence of ARs, specific humidity experiences a rapid increase and peaks approximately 1 day after the AR onset, and then swiftly returns to values similar to those observed before the onset of ARs (Fig. 2c and Supplementary Fig. 10). We also create similar composites for areas near the North Pole and southwestern Alaska (Supplementary Fig. 3e), where long-term trends of ARs show a strong increase and decrease over the past four decades, respectively. A similar temporal progression of ARs and specific humidity changes is observed in all of these areas (Supplementary Fig. 11). This analysis suggests that specific humidity changes across most Arctic regions are partly determined by AR activity within the season. Possibly, changes in long-term trends of atmospheric moisture are also mirrored by long-term changes in Arctic AR frequency to some extent.

To quantify the impacts of ARs on moisture changes over the past four decades, we use a statistical method to differentiate AR impacts on the long-term changes of JJA-specific humidity in the Arctic (see "Methods"). As shown in Fig. 3a, the long-term trend of JJA-specific humidity unrelated to AR activity has only increased in some subarctic areas, especially in the North Atlantic. The difference between this trend pattern (Fig. 3a) and the original one (Fig. 1b) is empirically attributed to long-term impacts of ARs in summer (Fig. 3b). More specifically, the moisture trends related to and unrelated to ARs in the Arctic (north of 60°N) are 0.017 g kg^{-1} decade^{-1} and 0.03 g kg^{-1} decade^{-1}, respectively, indicating that the trend of ARs activity may contribute to 36% of the overall increase in atmospheric moisture across the Arctic since 1979. In addition, the impact of ARs is most pronounced in specific regions, including western Greenland, northern Europe, and eastern Siberia, where ARs account for 57.1%, 47.1%, and 67.8% of the corresponding increases in moisture over the period, respectively.

Role of circulation variability in shaping AR activity in CESM1

The CMIP6 and CESM2 model response to historical radiative forcing indicates that the observed AR changes cannot be fully explained by anthropogenic forcing (Supplementary Fig. 5). Based on the statistical connection of ARs and circulation revealed by the aforementioned MCA analysis, we hypothesize that the large-scale circulation may direct more ARs into the Arctic region in recent decades. To further assess the plausibility of this linkage, we conduct three sets of simulations using CESM1. The first one is a CMIP6-type simulation with CO_2 forcing set at constant values of the year 2000 (CO_2 = 370 ppm) (referred to as "CTL" hereafter). This run aids in understanding how ARs behave in a climate state without changes in any radiative forcing. In the second set, in order to evaluate how long-term trends of JJA circulation exert a forcing on ARs in the Arctic, 3-D wind anomalies from the surface to the top of the atmosphere derived from long-term

https://doi.org/10.1038/s41467-024-49857-y

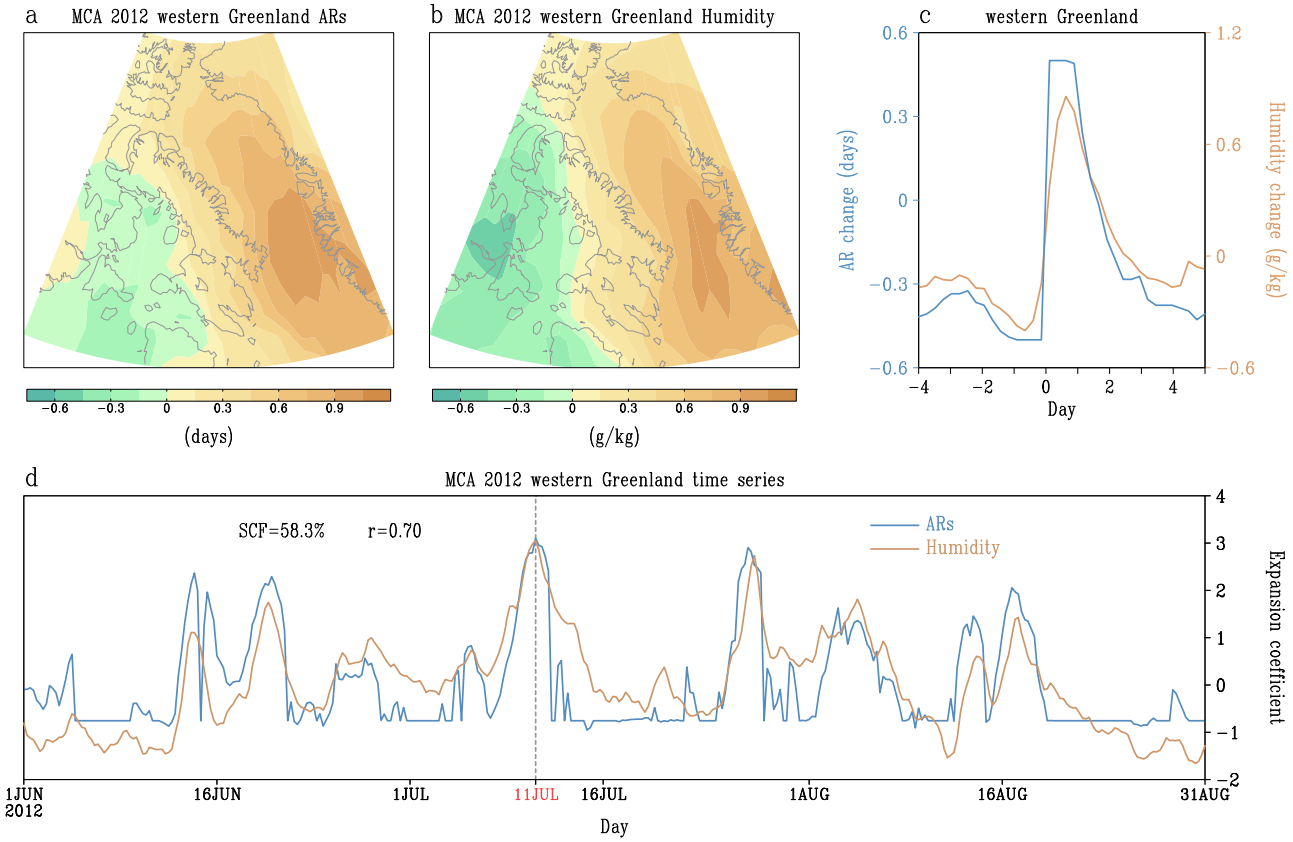

Fig. 2 | Connections between atmospheric rivers (ARs) and specific humidity on a day-to-day time scale. a, **b** Spatial pattern of the leading Maximum Covariance Analysis (MCA) mode of ARs (**a**, in days) and lower to middle tropospheric (surface to 500 hPa average) specific humidity (**b**, in g/kg) over western Greenland in summer 2012 (detrended and with climatological seasonal cycles removed). **c** Composite 6-hourly ARs (days) and lower to middle tropospheric specific humidity (g/kg) anomalies (from four days before to 5 days after the outbreak of ARs) within the western Greenland region from 1979 to 2019 (detrended and with climatological seasonal cycles removed). **d** Standardized time series of the leading MCA mode of ARs and lower to middle tropospheric specific humidity over western Greenland in summer 2012. "SCF" in (**d**) indicates the squared covariance fraction of the leading MCA mode. "r" in (**d**) indicates the correlation coefficient between the time series of the two patterns in the leading MCA mode. Numerous long horizontal blue lines in (**d**) indicate the absence of AR activity during the period. Both AR activity and humidity anomalies reached the maximum on July 11, which is marked in (**d**).

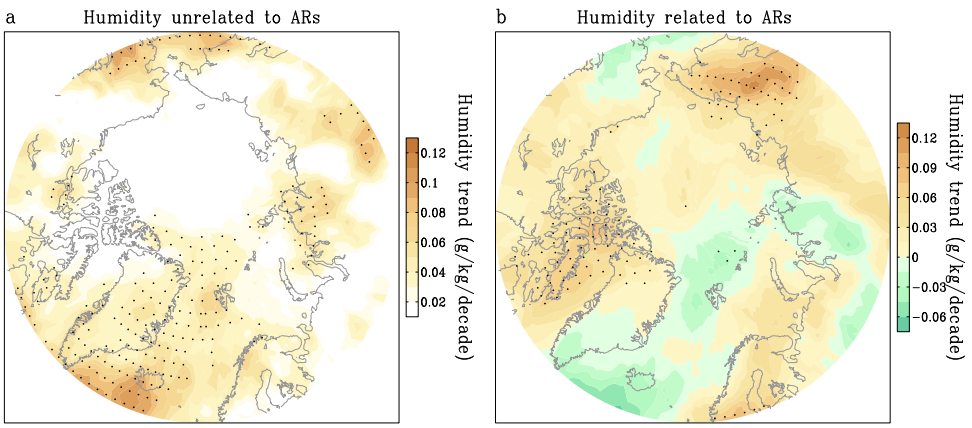

Fig. 3 | Contribution of atmospheric rivers (ARs) to observed trends of specific humidity. a, **b** Linear trends (g/kg/decade) of summer-specific humidity at lower to middle troposphere (surface to 500 hPa average) unrelated (**a**) and related (**b**) to the activity of ARs from 1979 to 2019. Black dots denote statistically significant trends at the 95% confidence level.

trends (m/s/decade) of JJA ERA5 circulation over the past 41 years (U and V) are added to the model during summer, only within the Arctic (north of 60°N) (see "Methods") (referred to as "WIN"). These anomalous 3-D winds (constant values in each grid cell over the 3 months) are incorporated in the model at each time step through the season, introducing seasonal mean wind anomalies without introducing any synoptic or intraseasonal variability in the wind fields. The goal of this design is to assess whether the model's response to these imposed wind trends can generate conditions conducive to ARs varying in a manner consistent with observations. The third set is the same as the second one except that anthropogenic forcing is imposed at the values of the year 2020 (CO_2 = 415 ppm) to include impacts of both

https://doi.org/10.1038/s41467-024-49857-y

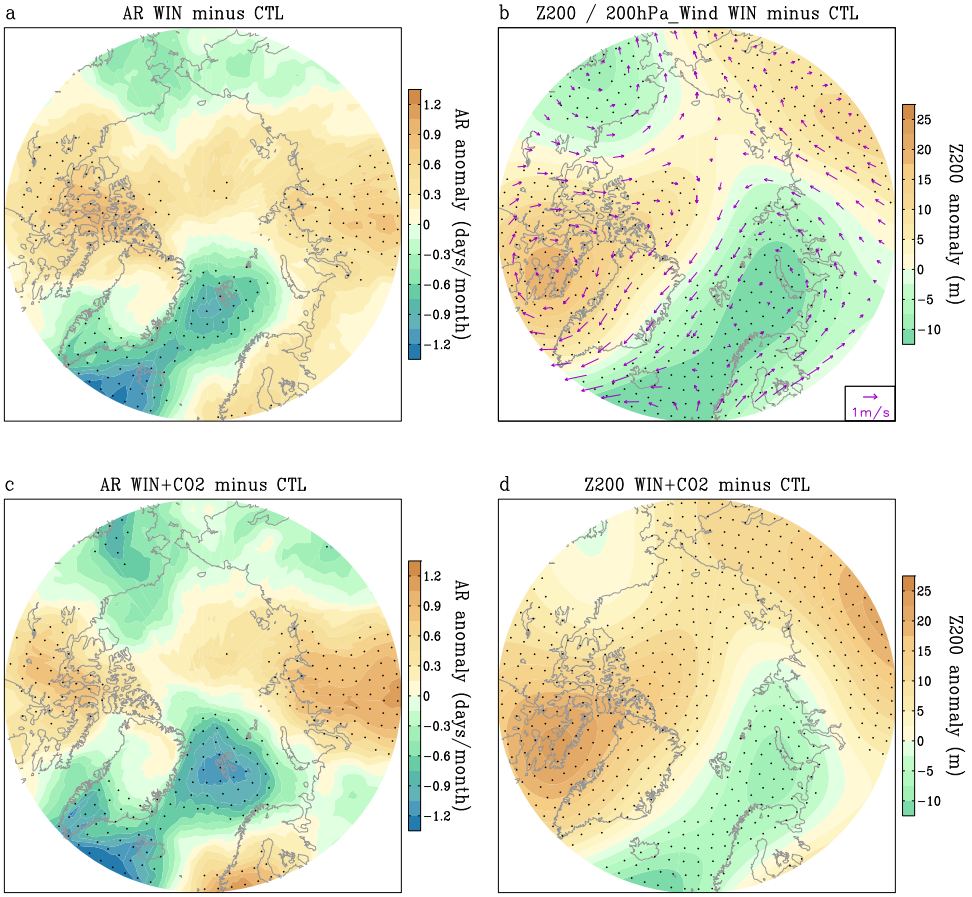

Fig. 4 | Simulated influences of large-scale circulation and anthropogenic forcing on Atmospheric River (AR) changes. a, **c** Differences of summer AR frequency (days/month) between the nudging run and the control run (WIN minus CTL) (**a**) and between the nudging+anthropogenic forcing run and the control run (WIN + CO_2 minus CTL) (**c**) based on the 40-year simulations. **b**, **d** Differences of summer geopotential height at 200 hPa (Z200) (m) between the nudging run and control run (**b**) and between the nudging+anthropogenic forcing run and the control run (**d**) based on the 40-year simulations. Wind anomalies (vectors, m/s) at 200 hPa in (**b**) are the differences of summer winds at 200 hPa between the nudging run and control run based on the 40-year simulations. The scale for winds is shown at the bottom-right corner of (**b**). Black dots denote statistically significant differences at the 95% confidence level for AR frequency in (**a**, **c**), and for Z200 in (**b**, **d**). WIN refers to the simulation with wind nudging used. CTL refers to the control run. WIN + CO_2 refers to the runs with both wind nudging and anthropogenic forcing imposed.

anthropogenic forcing and anomalous winds (referred to "WIN + CO_2"). The decadal change rate of CO_2 concentration from 2000 to 2020 ((415 ppm − 370 ppm) ÷ 2 decades ≈ 20 ppm/decade) is very similar to changes observed over the past four decades (~20 ppm/decade). This enables us to examine how anthropogenic forcing, along with the influence of the long-term wind trend pattern, regulated ARs from 1979 to 2019. Each set is continuously integrated for 40 years and the 40-year means of each set are used to estimate a relatively stable model response to the imposed forcing.

Figure 4a shows the difference of AR frequency between WIN and CTL simulations. It is clear that ARs occur more frequently over northwestern Greenland and the northern part of Eurasia, but less frequently in southern and eastern Greenland and the Bering Strait, similar to observations (Figs. 4a and 1a). The simulated ARs appear to be closely related to the large-scale circulation pattern. Southerly wind anomalies to the west of the high pressure over Greenland and central Siberia increase the frequency of ARs, while northerly wind anomalies to the east of the high pressure reduce AR activity (Fig. 4b, vectors). The positive AR response in northwestern Greenland and northern Europe is approximately 0.5 days per month, which is consistent with changes in observations (Figs. 4a and 1a). Around southern and eastern Greenland and the Bering Strait, the magnitude of the negative AR response is around −0.5 day per month (Fig. 4a). This implies that a wind field change in magnitude around 1 m/s can lead to significant JJA AR changes. The simulated patterns of ARs and Z200 are consistent with the observed covariability of ARs and Z200 detected by MCA (Figs. 1e, f and 4a, b).

The difference in AR frequency and circulation between WIN + CO_2 and CTL is similar to that between WIN and CTL (Fig. 4a–d), suggesting that anthropogenic forcing in this model has a minor effect on AR activity in the Arctic. Since the response of ARs to anthropogenic forcing may be model dependent, we cannot exclude the possibility that some observed AR signals are indeed a consequence of global warming effects over the past few decades.

Role of circulation variability in shaping AR activity using a fingerprint analysis

To further examine the impact of large-scale circulation on ARs we adapt a distinct approach, referred to as fingerprint analysis[63], based on the CESM2 large ensemble. In this approach, we use the AR and Z200 trends in the ensemble mean of 40 members to represent the forced response of the two fields to anthropogenic forcing, and the difference between each member with the ensemble mean as long-term trends due to internal variability. The ensemble mean of the ARs (Supplementary Fig. 5b) and Z200 trends (Supplementary Fig. 12) exhibit markedly different patterns from those in observations (Fig. 1a, c), echoing our findings derived from the CMIP6 result (Supplementary Fig. 5a), and reinforcing the notion that the observed AR

https://doi.org/10.1038/s41467-024-49857-y

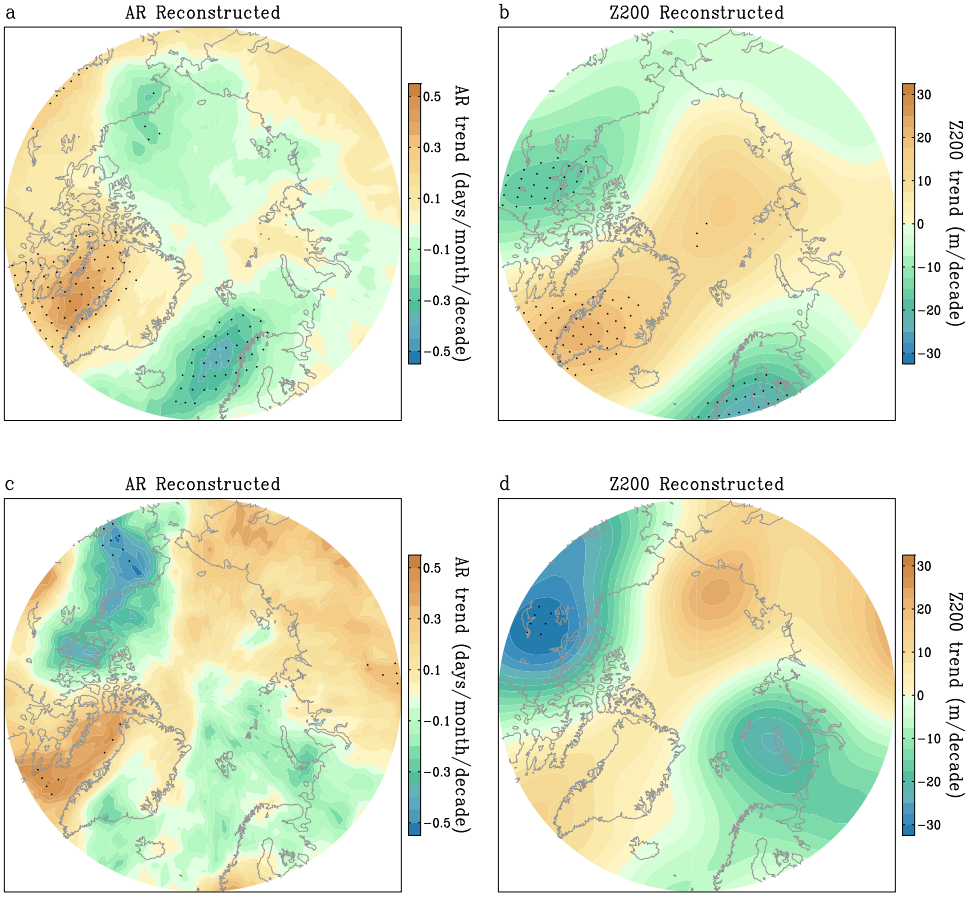

Fig. 5 | Reconstructed trends of atmospheric rivers (ARs) and geopotential height at 200 hPa (Z200) in the subgroups of CESM2-LEN. a, **c** Linear trends of summer AR frequency (days/month/decade) derived from the subgroup exhibiting strong increasing AR frequency trends over western Greenland (8 members) (**a**) and over both western Greenland and eastern Siberia (2 members) (**c**). **b**, **d** Linear trends in summer Z200 (m/decade) based on the subgroup with strong increasing AR frequency trends over western Greenland (**b**) and over both western Greenland and eastern Siberia (**d**). The 40 members from CESM2-LEN are used in this calculation (see "Methods"). Black dots denote statistically significant trends at the 95% confidence level.

and circulation trend patterns over the past decades cannot be fully explained by anthropogenic forcing.

To further understand how internal variability has contributed to the observed changes, we select a subset of 8 members from the 40-member ensemble, if their simulated AR frequency trends exhibit an increase (>80% percentile of simulated AR trends) over western Greenland. We then compare the large-scale circulation trend from this subgroup to examine whether the high-pressure pattern also emerges over Greenland, as observed. As we expect, the subgroup, possessing a better chance of replicating an increasing trend of ARs over western Greenland, also replicates the observed high-pressure trend over Greenland, indicating a strong constraint of large-scale JJA circulation trends on long-term changes of AR frequency over the region (Fig. 5a, b). Similar constraints of circulation on ARs are evident when focusing on northern Europe and eastern Siberia (Supplementary Fig. 13). Furthermore, two of the 40 members demonstrate an AR frequency increases trend in both western Greenland and eastern Siberia, and the corresponding large-scale circulation clearly exhibits a chain of high pressure in the above two areas as observed (Fig. 5c, d). This result suggests that long-term trends of large-scale circulation, particularly in forms similar to those observed, have a capacity to strongly modulate AR activity on low-frequency timescales. The establishment of this governing effect is attributed to a strong internal origin, as it is only discernible in a subset of the 40 members, rather than the ensemble means. This approach, emphasizing the internal variability of the model system, facilitates us to reasonably use model results to interpret observed features.

Our model experiments collectively support our initial hypothesis that the large-scale wind trend is able to apply a forcing to regulate changes of AR frequency, particularly over Greenland, northern Europe, and part of Eurasia. Over eastern Siberia, the wind-induced increase of AR frequency is shifted toward the interior of the continent in our nudging simulation results. However, the results obtained by the fingerprint method show that the large-scale circulation may still have some influences on ARs in that area (Supplementary Fig. 13c, d), indicating the need for further studies.

Discussion

ARs are mainly driven by the atmosphere's baroclinic instability of the mean state and exhibit highly variable behavior on shorter timescales, but demonstrate sensitivity to low-frequency changes in the background flow. Over the past few decades, the summer season Arctic AR frequency has exhibited a well-organized increase in various regions, significantly influencing their local climates. To understand the underlying causes of these long-term changes in AR frequency, we employ a combination of observational and numerical modeling approaches. Our findings illustrate that a significant portion of the long-term AR frequency changes can be attributed to a steering flow effect generated by the large-scale circulation trend patterns, particularly characterized by a zonal wave number 2 structure in the Arctic. This circulation trend pattern involves a sequence of high- and low-pressure centers encircling the Arctic Ocean and Greenland, inducing corresponding shifts in AR activity along the same latitudinal band. By applying a statistical reconstruction method, we estimate that these

long-term trends in AR frequency have contributed to approximately 36% of the overall Pan-Arctic increase in atmospheric moisture and over ~50% of the increase in specific humidity over western Greenland, northern Europe, and eastern Siberia.

While the response of ARs to anthropogenic forcing in most climate models does not precisely match the observed pattern, we cannot rule out the possibility of indirect influences of anthropogenic forcing through changes in large-scale circulation and other systems, or the potential limitations of current models in capturing the forced response of ARs in a warming world. More in-depth analyses are needed, especially in regions close to eastern Siberia, where recent large-scale circulation trends appear to be of less significance in explaining long-term AR trends.

In addition, the Northern Hemisphere midlatitude jets are predicted to weaken and shift poleward due to anthropogenic influences in the coming decades[84]. How ARs in the Arctic may respond to a weaker, poleward-shifted jet stream and whether the identified impact of large-scale circulation on ARs, as shown in this study, will persist in a warming world alongside a more meandering jet remain open questions.

The increase in water vapor is a known contributor to enhanced cloud cover and increased downward longwave radiation in the Arctic, further exacerbating surface warming and the reduction of sea ice and land ice. These processes, collectively known as the moisture feedback, may also induce changes in large-scale circulation in the Arctic and beyond. However, the specific role of ARs, which are highly responsive to large-scale circulation variability over a wide range of timescales, in high-latitude moisture feedbacks remains unclear. In particular, ARs, which can cause rapid and extreme moisture surges, may lead to significant Arctic melt events and initiate positive feedback loops. Future studies are essential to explore these potential new roles of ARs in AA as the Arctic continues to warm.

Methods

Reanalysis and observational data

We examine changes in Arctic atmospheric circulation (Z200), specific humidity (For brevity, in some parts of the text, we use "humidity" and "specific humidity" interchangeably.), temperature, cloud cover, and radiation over the period from 1979 to 2019 using 6-hourly and monthly reanalysis data from ERA5[85] and ERA-Interim[86]. Our results are consistent between the two reanalysis datasets. Therefore, in this work, we focus on the findings derived from ERA5. All variables are regridded to a 1.5° × 1.5° resolution. We primarily utilize monthly reanalysis data to calculate the trend (calculated by the least-square regression method) of variables in our study (or for MCA). However, when identifying AR variability, 6-hourly data is ideal due to the transient and extreme nature of ARs, where higher temporal resolution data can better capture their temporal characteristics. Unfortunately, only a few CMIP6 models provide daily data (U, V, and specific humidity over multiple representative vertical levels) for the public, and 6-hourly data for these variables are not available. Consequently, we employ a remedial approach using daily data to detect ARs for these models. Monthly sea ice concentrations are acquired from NSIDC[87] for the analysis of the impact of ARs on sea ice variations.

Large ensemble CESM2 simulations and CMIP6 experiments

We use 6-hourly data from 40 realizations of the CESM2 historical run[88] for the period spanning 1979-2014, each with slightly different initial atmospheric states. These 40-member CESM2 (CESM2-LEN) simulations are employed to explore the relationship between ARs and circulation and to assess how ARs respond to atmospheric internal variability. In addition, the multi-model ensemble mean of monthly output from the historical runs of 34 climate models archived in CMIP6[89] (Supplementary Table 1) is used to investigate the response of the atmosphere to historical anthropogenic forcing. We also incorporate daily data from the multi-model ensemble mean of 10 (as daily outputs needed for AR calculations are only accessible in these 10 members) climate models stored in CMIP6 historical runs (Supplementary Table 2) to calculate AR frequency and estimate the AR response to historical anthropogenic forcing. All of the CMIP6 model output mentioned above is focused on the period from 1979 to 2014. To facilitate comparison with the reanalysis data, we regrid all model datasets to a 1.5° × 1.5° resolution.

Nudging experiments with the CESM1

To examine the regulation of large-scale circulation on AR activity in the Arctic in the fully coupled CESM1[73], we incorporate long-term trend wind patterns (the 200 hPa winds pattern is shown in Fig. 1c) from ERA5 to constrain the Arctic (north of 60°N) circulation in the WIN (with wind nudging only) and WIN + CO_2 (with wind nudging and anthropogenic forcing) runs from the surface to the top of the atmosphere. The magnitude of these wind trends is those changes spanning over 10 years (per decade). In each model step from June 1 to August 31 for these two runs (WIN and WIN + CO_2), within the nudging region, additional wind tendency terms, equal to the observed long-term wind trends, are added on top of the model's tendencies of zonal and meridional winds at each grid point. Since we impose constant wind anomalies each summer, this method acts to numerically incorporate observed wind trends into the model without introducing artificial short term variability. The same method has been used in a number of previous studies[37,70,71], which indicates the reliability of this approach in replaying observed circulation changes in the model. In addition, CO_2 concentration is held constant in CTL and WIN at the year 2000 level (370 ppm). In the WIN + CO_2 run, CO_2 is held constant at the value of the year 2020 (415 ppm). Other radiative and anthropogenic forcing, such as solar constant, other types of greenhouse gases, ozone concentration, various aerosols, land-use/land cover conditions are exactly the same between the two runs.

AR detection

The ARs are defined via a detection algorithm based on integrated water vapor transport (IVT)[90]. In this algorithm, the 85th percentile of the climatological monthly IVT magnitude at each grid point is used as the threshold to identify ARs. IVT is calculated from ERA5 6-hourly wind and specific humidity fields integrated from 1000 to 300 hPa on 0.25° × 0.25° global grids. Additional criteria include the requirement that the length of the identified AR area should be greater than or equal to 2000 km and that the length-to-width ratio should be greater than or equal to 2. The ARs dataset is regridded to a 1.5° × 1.5° spatial resolution for analysis. This algorithm is recommended by the Atmospheric River Tracking Method Intercomparison Project (ARTMIP)[91], and has been extensively used in previous studies in detecting ARs in the Arctic and Antarctic[78,92–94]. In this study, ARs in the Arctic refer to all AR activity north of 60°N. Given that ARs represent transient and extreme moisture transport events, data with higher temporal resolution better describe their characteristics. Therefore, 6-hourly ERA5 reanalysis data are typically utilized to detect their signatures. We note that relatively few CMIP6 models (10 total) provide daily data as their highest temporal resolution data. As such, we only use this group to detect changes in ARs within the models. To study the year-to-year variability of ARs in the Arctic, a monthly mean AR field is created based on 6-hourly AR data. This field counts the number of AR activity in each grid point within each calendar month, with the value representing the monthly AR frequency (unit: days/month) in each grid point.

AR frequency and specific humidity composites

To assess the impact of daily ARs on Arctic water vapor changes, we focus on strong AR events that occurred since 1979. These strong ARs are defined based on their continuous activity at the central points of

three key regions (western Greenland, northern Europe, and eastern Siberia) for a minimum duration of 24 h. It is important to note that the water vapor (specific humidity) anomalies associated with ARs are found to last behind the end of ARs by approximately 1 day. To ensure that the selected AR cases were not influenced by the prior water vapor changes resulting from preceding AR activity, we apply a criterion that requires these selected ARs to have no other AR activity on the day before their occurrence. Using this approach, we identify a total of 97 cases of ARs in the central point of western Greenland, 90 cases in northern Europe, and 83 cases in eastern Siberia. We then conduct composite analyses to examine the specific humidity anomalies associated with the AR events. Specifically, we analyze the changes in specific humidity (after detrending and removing the climatological seasonal cycles) for 4 days preceding and 5 days following the onset of ARs.

Quantification of the contribution of ARs to specific humidity trends

We apply an AR removal method to isolate water vapor changes associated with 6-hourly AR activity. Initially, vertically integrated specific humidity fields for each summer (1979 to 2019) with 6-hourly resolution are generated. For each 6-hourly field from June 1st to August 31st, grid points with AR activity are determined by the "shape" of ARs as defined by the detection algorithm. When reconstructing the JJA seasonal mean humidity values in these grid points for any given summer, specific humidity values within these AR impact areas are excluded (with humidity over AR-shape grids set as zero). Conversely, averaging those 6-hourly grid points impacted by ARs (with humidity over non-AR grids set to zero) will form a JJA-specific humidity field related to ARs. This approach allowed us to reconstruct two JJA-specific humidity fields over the past 41 years, representing humidity variability unrelated to ARs and related to ARs, respectively.

Description of the MCA approach

Maximum Covariance Analysis (MCA), often referred to as Singular Value Decomposition (SVD) analysis, is a valuable statistical method utilized in meteorological and oceanographic research to capture coupled modes of covariability between two fields[79]. Typically, this method operates on two distinct 2-D fields, X(m,t) and Y(n,t), where m and n represent spatial points and t represents the temporal dimension. MCA aims to compute a SVD of X×Y′ (transpose matrix of Y), where each element in the matrix (X×Y′) represents the covariance of a pair of points from X and Y, respectively (one spatial point from X and one spatial point from Y). This enables MCA to identify the dominant coupling modes between variations in X and Y. Specifically, we use MCA to extract the dominant coupled modes between the AR frequency and atmospheric variables over the Arctic in summer.

Significance of correlation

The assumption for the statistical significance test of linear correlation is that the time series used to calculate the correlation consists of completely independent samples characterized by white-noise processes[95]. However, if the data contain strong autocorrelation (indicating some red-noise processes), this assumption may not hold well. To address this issue, it is necessary to consider the effect of effective sample size when assessing the significance of correlation by using conventional T test[96]. Accordingly, the statistical significance of the correlation coefficient is estimated by using an effective sample size N^*, which is given by:

$$N^* = N\frac{1 - r_1 r_2}{1 + r_1 r_2} \quad (1)$$

where N is the number of available time steps, r_1 and r_2 are lag-one autocorrelation coefficients of each variable[97].

Data availability

ECMWF ERA5 reanalysis product is available at https://www.ecmwf.int/en/forecasts/datasets. Simulated circulation, specific humidity, and temperature under anthropogenic forcing were obtained from CMIP6 and CESM2 archive at https://esgf.llnl.gov/ and IBS openDAP server. Sea Ice Concentrations from Nimbus-7 SMMR and DMSP SSM/I-SSMIS Passive Microwave Data, Version 2 are accessed from NSIDC at https://nsidc.org/data/nsidc-0051/versions/2. The AR data and CESM nudging experiment output are available from the corresponding authors upon request. The data used to make the plots for this paper can be accessed at https://zenodo.org/records/11159190.

Code availability

All code necessary for performing the reported analyses is available upon request from the corresponding authors.

References

1. Serreze, M. C. & Francis, J. A. The Arctic amplification debate. *Clim. Change* **76**, 241–264 (2006).
2. Graversen, R. G., Mauritsen, T., Tjernström, M., Källén, E. & Svensson, G. Vertical structure of recent Arctic warming. *Nature* **451**, 53–56 (2008).
3. Screen, J. A. & Simmonds, I. The central role of diminishing sea ice in recent Arctic temperature amplification. *Nature* **464**, 1334–1337 (2010).
4. Cohen, J. et al. Recent Arctic amplification and extreme mid-latitude weather. *Nat. Geosci.* **7**, 627–637 (2014).
5. Pithan, F. & Mauritsen, T. Arctic amplification dominated by temperature feedbacks in contemporary climate models. *Nat. Geosci.* **7**, 181–184 (2014).
6. Dai, A., Luo, D., Song, M. & Liu, J. Arctic amplification is caused by sea-ice loss under increasing CO_2. *Nat. Commun.* **10**, 1–13 (2019).
7. Fang, M., Li, X., Chen, H. W. & Chen, D. Arctic amplification modulated by Atlantic Multidecadal Oscillation and greenhouse forcing on multidecadal to century scales. *Nat. Commun.* **13**, 1865 (2022).
8. Rantanen, M. et al. The Arctic has warmed nearly four times faster than the globe since 1979. *Commun. Earth Environ.* **3**, 168 (2022).
9. Preece, J. R. et al. Summer atmospheric circulation over Greenland in response to Arctic amplification and diminished spring snow cover. *Nat. Commun.* **14**, 3759 (2023).
10. Held, I. M. & Soden, B. J. Robust responses of the hydrological cycle to global warming. *J. Clim.* **19**, 5686–5699 (2006).
11. Min, S. K., Zhang, X. & Zwiers, F. Human-induced Arctic moistening. *Science* **320**, 518–520 (2008).
12. Payne, A. E. et al. Responses and impacts of atmospheric rivers to climate change. *Nat. Rev. Earth Environ.* **1**, 143–157 (2020).
13. Boisvert, L. N., Webster, M. A., Parker, C. L. & Forbes, R. M. Rainy days in the Arctic. *J. Clim.* **36**, 6855–6878 (2023).
14. Bring, A. et al. Arctic terrestrial hydrology: a synthesis of processes, regional effects, and research challenges. *J. Geophys. Res. Biogeosci.* **121**, 621–649 (2016).
15. Vihma, T. et al. The atmospheric role in the Arctic water cycle: a review on processes, past and future changes, and their impacts. *J. Geophys. Res. Biogeosci.* **121**, 586–620 (2016).
16. Boisvert, L. N. & Stroeve, J. C. The Arctic is becoming warmer and wetter as revealed by the Atmospheric Infrared Sounder. *Geophys. Res. Lett.* **42**, 4439–4446 (2015).
17. Rinke, A. et al. Trends of vertically integrated water vapor over the Arctic during 1979–2016: consistent moistening all over? *J. Clim.* **32**, 6097–6116 (2019).
18. Bintanja, R. & Selten, F. M. Future increases in Arctic precipitation linked to local evaporation and sea-ice retreat. *Nature* **509**, 479–482 (2014).

19. Johnsen, S. J., Dansgaard, W. & White, J. W. C. The origin of Arctic precipitation under present and glacial conditions. *Tellus B: Chem. Phys. Meteorol.* **41**, 452–468 (1989).
20. Liston, G. E. & Sturm, M. The role of winter sublimation in the Arctic moisture budget. *Hydrol. Res.* **35**, 325–334 (2004).
21. Serreze, M. C., Barrett, A. P. & Stroeve, J. Recent changes in tropospheric water vapor over the Arctic as assessed from radiosondes and atmospheric reanalyses. *J. Geophys. Res. Atmos.* **117**, 1–21 (2012).
22. Liu, C. & Barnes, E. A. Extreme moisture transport into the Arctic linked to Rossby wave breaking. *J. Geophys. Res. Atmos.* **120**, 3774–3788 (2015).
23. Gimeno, L. et al. Atmospheric moisture transport and the decline in Arctic Sea ice. *Wiley Interdiscip. Rev. Clim. Change* **10**, e588 (2019).
24. Olonscheck, D., Mauritsen, T. & Notz, D. Arctic sea-ice variability is primarily driven by atmospheric temperature fluctuations. *Nat. Geosci.* **12**, 430–434 (2019).
25. Bintanja, R. et al. Strong future increases in Arctic precipitation variability linked to poleward moisture transport. *Sci. Adv.* **6**, eaax6869 (2020).
26. Bokuchava, D. D. & Semenov, V. A. Mechanisms of the early 20th century warming in the Arctic. *Earth Sci. Res.* **222**, 103820 (2021).
27. Choi, H. J., Min, S. K., Yeh, S. W., An, S. I. & Kim, B. M. Seasonally distinct contributions of greenhouse gases and anthropogenic aerosols to historical changes in Arctic moisture budget. *NPJ Clim. Atmos. Sci.* **6**, 189 (2023).
28. Bintanja, R. & Andry, O. Towards a rain-dominated Arctic. *Nat. Clim. Change* **7**, 263–267 (2017).
29. McCrystall, M. R., Stroeve, J., Serreze, M., Forbes, B. C. & Screen, J. A. New climate models reveal faster and larger increases in Arctic precipitation than previously projected. *Nat. Commun.* **12**, 1–12 (2021).
30. Dou, T. F., Pan, S. F., Bintanja, R. & Xiao, C. D. More frequent, intense, and extensive rainfall events in a strongly warming Arctic. *Earth's Future* **10**, e2021EF002378 (2022).
31. Parker, C. L., Mooney, P. A., Webster, M. A. & Boisvert, L. N. The influence of recent and future climate change on spring Arctic cyclones. *Nat. Commun.* **13**, 6514 (2022).
32. Fettweis, X. et al. Brief communication" Important role of the mid-tropospheric atmospheric circulation in the recent surface melt increase over the Greenland ice sheet". *Cryosphere* **7**, 241–248 (2013).
33. Ding, Q. et al. Influence of high-latitude atmospheric circulation changes on summertime Arctic sea ice. *Nat. Clim. Change* **7**, 289–295 (2017).
34. Hofer, S., Tedstone, A. J., Fettweis, X. & Bamber, J. L. Decreasing cloud cover drives the recent mass loss on the Greenland Ice Sheet. *Sci. Adv.* **3**, e1700584 (2017).
35. Tedesco, M. & Fettweis, X. Unprecedented atmospheric conditions (1948–2019) drive the 2019 exceptional melting season over the Greenland ice sheet. *Cryosphere* **14**, 1209–1223 (2020).
36. Topál, D. et al. Discrepancies between observations and climate models of large-scale wind-driven Greenland melt influence sea-level rise projections. *Nat. Commun.* **13**, 6833 (2022).
37. Topál, D. & Ding, Q. Atmospheric circulation-constrained model sensitivity recalibrates Arctic climate projections. *Nat. Clim. Change* **13**, 1–9 (2023).
38. Ralph, F. M., Neiman, P. J. & Wick, G. A. Satellite and CALJET aircraft observations of atmospheric rivers over the eastern North Pacific Ocean during the winter of 1997/98. *Mon. Weather Rev.* **132**, 1721–1745 (2004).
39. Ralph, F. M., Dettinger, M. D., Cairns, M. M., Galarneau, T. J. & Eylander, J. Defining "atmospheric river": how the glossary of meteorology helped resolve a debate. *Bull. Am. Meteorol. Soc.* **99**, 837–839 (2018).
40. Dacre, H. F., Clark, P. A., Martinez-Alvarado, O., Stringer, M. A. & Lavers, D. A. How do atmospheric rivers form? *Bull. Am. Meterol. Soc.* **96**, 1243–1255 (2015).
41. Lavers, D. A., Ralph, F. M., Richardson, D. S. & Pappenberger, F. Improved forecasts of atmospheric rivers through systematic reconnaissance, better modelling, and insights on conversion of rain to flooding. *Commun. Earth Environ.* **1**, 39 (2020).
42. Wang, S. et al. Extreme atmospheric rivers in a warming climate. *Nat. Commun.* **14**, 3219 (2023).
43. Blackmon, M. L. A climatological spectral study of the 500 mb geopotential height of the Northern Hemisphere. *J. Atmos. Sci.* **33**, 1607–1623 (1976).
44. Fu, Q., Johanson, C. M., Wallace, J. M. & Reichler, T. Enhanced mid-latitude tropospheric warming in satellite measurements. *Science* **312**, 1179–1179 (2006).
45. Hu, Y. & Fu, Q. Observed poleward expansion of the Hadley circulation since 1979. *Atmos. Chem. Phys.* **7**, 5229–5236 (2007).
46. Shields, C. A. & Kiehl, J. T. Atmospheric river landfall-latitude changes in future climate simulations. *Geophys. Res. Lett.* **43**, 8775–8782 (2016).
47. Mattingly, K. S., Mote, T. L. & Fettweis, X. Atmospheric river impacts on Greenland Ice Sheet surface mass balance. *J. Geophys. Res. Atmos.* **123**, 8538–8560 (2018).
48. Gao, Y. et al. Dynamical and thermodynamical modulations on future changes of landfalling atmospheric rivers over western North America. *Geophys. Res. Lett.* **42**, 7179–7186 (2015).
49. Warner, M. D., Mass, C. F. & Salathé, E. P. Changes in winter atmospheric rivers along the North American west coast in CMIP5 climate models. *J. Hydrometeorol.* **16**, 118–128 (2015).
50. Hagos, S. M., Leung, L. R., Yoon, J. H., Lu, J. & Gao, Y. A projection of changes in landfalling atmospheric river frequency and extreme precipitation over western North America from the Large Ensemble CESM simulations. *Geophys. Res. Lett.* **43**, 1357–1363 (2016).
51. Massoud, E. C., Espinoza, V., Guan, B. & Waliser, D. E. Global climate model ensemble approaches for future projections of atmospheric rivers. *Earth's Future* **7**, 1136–1151 (2019).
52. Gershunov, A. et al. Precipitation regime change in Western North America: the role of atmospheric rivers. *Sci. Rep.* **9**, 1–11 (2019).
53. Algarra, I. et al. Significant increase of global anomalous moisture uptake feeding landfalling atmospheric rivers. *Nat. Commun.* **11**, 5082 (2020).
54. Kamae, Y., Imada, Y., Kawase, H. & Mei, W. Atmospheric rivers bring more frequent and intense extreme rainfall events over East Asia under global warming. *Geophys. Res. Lett.* **48**, e2021GL096030 (2021).
55. Lavers, D. A. et al. Future changes in atmospheric rivers and their implications for winter flooding in Britain. *Environ. Res. Lett.* **8**, 034010 (2013).
56. Best, J. Anthropogenic stresses on the world's big rivers. *Nat. Geosci.* **12**, 7–21 (2019).
57. Baek, S. H. & Lora, J. M. Counterbalancing influences of aerosols and greenhouse gases on atmospheric rivers. *Nat. Clim. Change* **11**, 958–965 (2021).
58. Hwang, Y. T., & Frierson, D. M. Increasing atmospheric poleward energy transport with global warming. *Geophys. Res. Lett.* **37**, 1–5 (2010).
59. Sang, X., Yang, X. Q., Tao, L., Fang, J. & Sun, X. Decadal changes of wintertime poleward heat and moisture transport associated with the amplified Arctic warming. *Clim. Dyn.* **58**, 137–159 (2022).
60. Cardinale, C. J. & Rose, B. E. The increasing efficiency of the poleward energy transport into the Arctic in a warming climate. *Geophys. Res. Lett.* **50**, e2022GL100834 (2023).
61. Kamae, Y., Mei, W. & Xie, S. P. Ocean warming pattern effects on future changes in East Asian atmospheric rivers. *Environ. Res. Lett.* **14**, 054019 (2019).

62. Liu, X. et al. Ocean fronts and eddies force atmospheric rivers and heavy precipitation in western North America. *Nat. Commun.* **12**, 1268 (2021).
63. Li, C., Mei, W. & Kamae, Y. Variability and predictability of cold-season North Atlantic atmospheric river occurrence frequency in a set of high-resolution atmospheric simulations. *Clim. Dyn.* **58**, 2485–2500 (2022).
64. Van den Broeke, M. R. et al. On the recent contribution of the Greenland ice sheet to sea level change. *Cryosphere* **10**, 1933–1946 (2016).
65. Neff, W., Compo, G. P., Martin Ralph, F. & Shupe, M. D. Continental heat anomalies and the extreme melting of the Greenland ice surface in 2012 and 1889. *J. Geophys. Res. Atmos.* **119**, 6520–6536 (2014).
66. Bonne, J. L. et al. The summer 2012 Greenland heat wave: In situ and remote sensing observations of water vapor isotopic composition during an atmospheric river event. *J. Geophys. Res. Atmos.* **120**, 2970–2989 (2015).
67. Barrett, B. S., Henderson, G. R., McDonnell, E., Henry, M. & Mote, T. Extreme Greenland blocking and high-latitude moisture transport. *Atmos. Sci. Lett.* **21**, e1002 (2020).
68. Hanna, E. et al. Greenland surface air temperature changes from 1981 to 2019 and implications for ice-sheet melt and mass-balance change. *Int. J. Climatol.* **41**, E1336–E1352 (2021).
69. Mattingly, K. S. et al. Increasing extreme melt in northeast Greenland linked to foehn winds and atmospheric rivers. *Nat. Commun.* **14**, 1743 (2023).
70. Ding, Q., Schweiger, A. & Baxter, I. Nudging observed winds in the Arctic to quantify associated sea ice loss from 1979 to 2020. *J. Clim.* **35**, 6797–6813 (2022).
71. Roach, L. A. & Blanchard-Wrigglesworth, E. Observed winds crucial for September Arctic sea ice loss. *Geophys. Res. Lett.* **49**, e2022GL097884 (2022).
72. Feng, X. et al. Comprehensive representation of tropical–extratropical teleconnections obstructed by tropical Pacific convection biases in CMIP6. *J. Clim.* **36**, 7041–7059 (2023).
73. Hurrell, J. W. et al. The community earth system model: a framework for collaborative research. *Bull. Am. Meteorol. Soc.* **94**, 1339–1360 (2013).
74. Athanase, M. et al. Impact of the atmospheric circulation on the Arctic snow cover and ice thickness variability. EGU General Assembly, Vienna (2022).
75. Li, Z., Ding, Q., Steele, M. & Schweiger, A. Recent upper Arctic Ocean warming expedited by summertime atmospheric processes. *Nat. Commun.* **13**, 362 (2022).
76. Baggett, C., Lee, S. & Feldstein, S. An investigation of the presence of atmospheric rivers over the North Pacific during planetary-scale wave life cycles and their role in Arctic warming. *J. Atmos. Sci.* **73**, 4329–4347 (2016).
77. Nash, D., Waliser, D., Guan, B., Ye, H. & Ralph, F. M. The role of atmospheric rivers in extratropical and polar hydroclimate. *J. Geophys. Res. Atmos.* **123**, 6804–6821 (2018).
78. Lee, S. H., Polvani, L. M. & Guan, B. Modulation of atmospheric rivers by the Arctic stratospheric polar vortex. *Geophys. Res. Lett.* **49**, e2022GL100381 (2022).
79. Bretherton, C. S., Smith, C. & Wallace, J. M. An intercomparison of methods for finding coupled patterns in climate data. *J. Clim.* **5**, 541–560 (1992).
80. Nghiem, S. V. et al. The extreme melt across the Greenland ice sheet in 2012. *Geophys. Res. Lett.* **39**, 1–6 (2012).
81. Hanna, E. et al. Atmospheric and oceanic climate forcing of the exceptional Greenland ice sheet surface melt in summer 2012. *Int. J. Climatol.* **34**, 1022–1037 (2014).
82. Mattingly, K. S. et al. Strong summer atmospheric rivers trigger Greenland Ice Sheet melt through spatially varying surface energy balance and cloud regimes. *J. Clim.* **33**, 6809–6832 (2020).
83. Ding, Q. et al. Fingerprints of internal drivers of Arctic sea ice loss in observations and model simulations. *Nat. Geosci.* **12**, 28–33 (2019).
84. Coumou, D., Di Capua, G., Vavrus, S., Wang, L. & Wang, S. The influence of Arctic amplification on mid-latitude summer circulation. *Nat. Commun.* **9**, 2959 (2018).
85. Hersbach, H. et al. The ERA5 global reanalysis. *Q. J. R. Meteorol. Soc.* **146**, 1999–2049 (2020).
86. Dee, D. P. et al. The ERA-Interim reanalysis: configuration and performance of the data assimilation system. *Q. J. R. Meteorol. Soc.* **137**, 553–597 (2011).
87. DiGirolamo, N., Parkinson, C. L., Cavalieri, D. J., Gloersen, P. & Zwally, H. J. Sea Ice Concentrations from Nimbus-7 SMMR and DMSP SSM/I-SSMIS Passive Microwave Data, Version 2 [Data Set]. Boulder, Colorado USA. NASA National Snow and Ice Data Center Distributed Active Archive Center. https://doi.org/10.5067/MPYG15WAA4WX (2022).
88. Kay, J. E. et al. The Community Earth System Model (CESM) large ensemble project: a community resource for studying climate change in the presence of internal climate variability. *Bull. Am. Meteorol. Soc.* **96**, 1333–1349 (2015).
89. Eyring, V. et al. Overview of the Coupled Model Intercomparison Project Phase 6 (CMIP6) experimental design and organization. *Geosci. Model Dev.* **9**, 1937–1958 (2016).
90. Zhu, Y. & Newell, R. E. A proposed algorithm for moisture fluxes from atmospheric rivers. *Mon. Weather Rev.* **126**, 725–735 (1998).
91. Shields, C. A. et al. Defining uncertainties through comparison of atmospheric river tracking methods. *Bull. Am. Meteorol. Soc.* **100**, ES93–ES96 (2019).
92. Zhang, P. et al. More frequent atmospheric rivers slow the seasonal recovery of Arctic sea ice. *Nat. Clim. Change* **13**, 266–273 (2023).
93. Lauer, M. et al. Influence of atmospheric rivers and associated weather systems on precipitation in the Arctic. *EGUsphere* **2023**, 1–32 (2023).
94. Ma, W., Chen, G., Peings, Y. & Alviz, N. Atmospheric river response to Arctic sea ice loss in the Polar Amplification Model Intercomparison Project. *Geophys. Res. Lett.* **48**, e2021GL094883 (2021).
95. Wilks, D. S. *Statistical Methods in the Atmospheric Sciences,* Vol. 100 (Academic Press, 2011).
96. Bretherton, C. S., Widmann, M., Dymnikov, V. P., Wallace, J. M. & Bladé, I. The effective number of spatial degrees of freedom of a time-varying field. *J. Clim.* **12**, 1990–2009 (1999).
97. Wallace, J. M., Smith, C. & Bretherton, C. S. Singular value decomposition of wintertime sea surface temperature and 500-mb height anomalies. *J. Clim.* **5**, 561–576 (1992).

Acknowledgements

This study is supported by NSF Arctic System Science awards OPP 2246601 and OPP 2246600, and Climate Variability & Predictability (NA23OAR4310273) programs as part of NOAA's Climate Program Office. Z.W. acknowledges support from the National Natural Science Foundation of China Grants 42105028, the China Postdoctoral Science Foundation 2020T130640, the Natural Science Foundation of Hunan Province of China 2024JJ6101, and the Open Grants of the State Key Laboratory of Severe Weather 2022LASW-B23. G.H. acknowledges support from the National Natural Science Foundation of China 42141019 and 41831175. R.W. received support from the National Natural Science Foundation of China Grants 41721004.

Author contributions

Q.D. and T.B. conceived the study. Z.W. analyzed the data and created the figures. Q.D. and Z.W. led analyses, interpreted results, and wrote the paper. Q.D. created the nudging simulations and designed the fingerprint analysis. T.B. and R.W. provided insightful comments. G.H., W.C., B.G., S.C., X.C., Z.C., D.B., D.N., I.B., D.T., and Z.L. contributed to discussions and provided comments.

Competing interests
The authors declare no competing interests.

Additional information
Supplementary information The online version contains supplementary material available at https://doi.org/10.1038/s41467-024-49857-y.

Correspondence and requests for materials should be addressed to Qinghua Ding or Thomas J. Ballinger.

Peer review information *Nature Communications* thanks the anonymous reviewers for their contribution to the peer review of this work. A peer review file is available.

Reprints and permissions information is available at http://www.nature.com/reprints

Publisher's note Springer Nature remains neutral with regard to jurisdictional claims in published maps and institutional affiliations.

Open Access This article is licensed under a Creative Commons Attribution 4.0 International License, which permits use, sharing, adaptation, distribution and reproduction in any medium or format, as long as you give appropriate credit to the original author(s) and the source, provide a link to the Creative Commons licence, and indicate if changes were made. The images or other third party material in this article are included in the article's Creative Commons licence, unless indicated otherwise in a credit line to the material. If material is not included in the article's Creative Commons licence and your intended use is not permitted by statutory regulation or exceeds the permitted use, you will need to obtain permission directly from the copyright holder. To view a copy of this licence, visit http://creativecommons.org/licenses/by/4.0/.

© The Author(s) 2024

nature communications

Article

https://doi.org/10.1038/s41467-023-44244-5

Robust changes in global subtropical circulation under greenhouse warming

Received: 11 April 2023

Accepted: 5 December 2023

Published online: 02 January 2024

Check for updates

Shijie Zhou[1], Ping Huang[1,2] ✉, Lin Wang[1,2] ✉, Kaiming Hu[1,2], Gang Huang[2,3] & Peng Hu[4]

The lower tropospheric subtropical circulation (SC) is characterized by monsoons and subtropical highs, playing an important role in global teleconnections and climate variability. The SC changes in a warmer climate are influenced by complex and region-specific mechanisms, resulting in uneven projections worldwide. Here, we present a method to quantify the overall intensity change in global SC, revealing a robust weakening across CMIP6 models. The weakening is primarily caused by global-mean surface warming, and partly counteracted by the direct CO_2 effect. The direct CO_2 effect is apparent in the transient response but is eventually dominated by the surface warming effect in a slow response. The distinct response timescales to global-mean warming and direct CO_2 radiative forcing can well explain the time-varying SC changes in other CO_2 emission scenarios. The declined SC implies a contracted monsoon range and drying at its boundary with arid regions under CO_2-induced global warming.

The subtropical circulation (SC) in the lower troposphere consists of subtropical highs over the oceans and monsoons[1]. The proportion of subtropical highs and monsoons varies seasonally, following the seasonal variation in the descending branches of the Hadley cell and the land–sea thermal contrast[2–5]. The SC connects the trade winds with the midlatitude westerlies and transports the tropical moisture poleward via the western flank of the subtropical high[6–9], playing an important role in global energy and moisture transport. Changes in intensity and location of the SC can impact the tropical cyclone tracks[10], modulate the distribution and variability of rainfall over East Asia, North and South America, and South Africa[11–14], and bring extreme events such as droughts and heatwaves[15,16].

Projection of the SC changes under greenhouse warming has been widely studied[17–22]. When the divergent SC is projected to weaken due to a weakened tropical overturning circulation under global warming[23–26], the change in the dominant rotational component of SC remains inconclusive[19,20,22,27–29]. The projection for the rotational SC represented by 850 hPa streamfunction (hereafter referred to as SC) is crucially dependent on the location and season (Fig. 1 and Supplementary Fig. S1). The SC changes are distinct during the boreal summer and winter in the Northern Hemisphere, whereas the seasonal variation of the SC changes in the Southern Hemisphere is relatively weak. The typical seasonal SC changes include the slightly weakened Australian summer monsoon (Fig. 1a), the slightly strengthened East Asian summer monsoon, and the robust westward shifted North Atlantic subtropical high in JJA (Fig. 1b). On closer inspection, the SC change projection even depends on the chosen domain and metrics sensitively. The domain-average low-level streamfunction in the center of the subtropical high increases under global warming[20,29]. The eddy streamfunction in an extended domain exhibits an insignificant change in the North Pacific subtropical high[22], but several studies selecting variable-dependent polygonal domains project a weakened North Pacific subtropical high[19,28]. Furthermore, the responses of SC to global warming often exhibit a mixture of varying intensity and shifting location, such as the intensified and westward shifting North Atlantic subtropical high in boreal summer (Fig. 1b)[19,22]. Considering the center

[1]Center for Monsoon System Research, Institute of Atmospheric Physics, Chinese Academy of Sciences, 100029 Beijing, China. [2]State Key Laboratory of Numerical Modeling for Atmospheric Sciences and Geophysical Fluid Dynamics, Institute of Atmospheric Physics, Chinese Academy of Sciences, 100029 Beijing, China. [3]Laboratory for Regional Oceanography and Numerical Modeling, Qingdao National Laboratory for Marine Science and Technology, 266237 Qingdao, China. [4]Department of Atmospheric Sciences, Yunnan University, 650500 Kunming, China. ✉e-mail: huangping@mail.iap.ac.cn; wanglin@mail.iap.ac.cn

https://doi.org/10.1038/s41467-023-44244-5

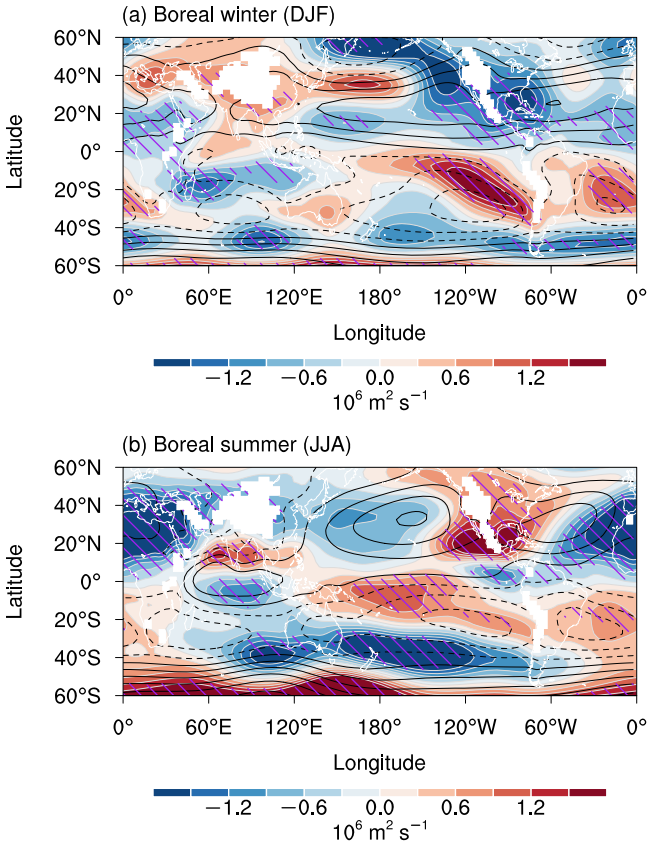

Fig. 1 | Seasonal changes in subtropical circulation under greenhouse warming. **a**, **b** Changes in the 850 hPa streamfunction (shading) in the Shared Socioeconomic Pathway 5-8.5 (SSP5-8.5) experiment relative to the historical experiment during **a** the boreal winter (December–February; DJF) and **b** the boreal summer (June–August; JJA). The contours in **a** and **b** represent the climatology of the 850 hPa streamfunction in the historical experiment (interval: 5×10^6 m^2 s^{-1}). Hatching indicates that the change is robust (see the "Methods" section for the details of the criteria).

and intensity of background SC seasonally vary, we cannot choose a domain that is suitable for all seasons and distinguish the changes in intensity and location. Due to the mixture of these factors, we did not obtain a robust projection on global SC changes.

The uncertainty of SC changes is also associated with the multiplicity of the influencing factors, including the direct CO_2 radiative forcing[17,30–32], sea surface temperature (SST) warming[28,30,33], and increased atmospheric stability[34]. The direct CO_2 effect can induce enhanced land–sea thermal contrast[34] with an intensification of the Asian and northern African monsoons in boreal summer[31,32,35]. The SST warming comprises two components: a uniform component and a patterned component. The uniform component is closely linked to the magnitude of global-mean surface warming, which weakens the tropical overturning circulation[23,24,36] and increases low-level water vapor with further intensification of the hydrological cycle[24,37,38]. By contrast, the patterned SST warming can induce a shift in tropical convection and circulation[39–41]. These mechanisms can result in specific local circulation changes[27], but the delicate offset of different physical processes differs among the climate models participating in Phase 6 and 5 of the Coupled Model Intercomparison Project (CMIP6 and CMIP5)[19,22,28,42], leading to uncertain projections of the global SC changes.

Here, we present a method to extract intensity change in global SC independent of the domain and season selection. A robust weakening of global SC is projected under the Shared Socioeconomic Pathway (SSP) 5-8.5 scenario by the end of the 21st century in 34 CMIP6 models and in the abrupt-4×CO2 experiments forced by an abrupt quadrupling of the pre-industrial CO_2 level in 32 CMIP6 models. The robustness of the weakening is verified by the single-model initial-condition large ensemble (SMILE)[43] and the 'Database for Policy Decision Making for Future Climate Change' (d4PDF) simulations[44], which consider the uncertainties from internal variability and SST warming pattern, respectively. We clarify that the robust weakening of global SC is dominated by global-mean surface warming and partly counteracted by the direct CO_2 effect on different timescales, confirmed by the third Phase of the Cloud Feedback Model Intercomparison Project (CFMIP-3) in CMIP6[45]. This unified mechanism highlights the dependence of projected SC changes on simulation scenarios, thus providing an explanation for prior uncertainties in projections.

Results

Robust weakening in the subtropical circulation

The overall intensity change of SC is defined by the projection of global (10°–45°S, 10°–45°N) SC changes onto the SC climatology (see the "Methods" section for details). Figure 2 shows the intensity change in global SC in several sets of experiments, including the SSP5-8.5, abrupt-4×CO2, CFMIP-3, SMILEs, and the d4PDF (see the "Methods" section for details). The multiple experiments illustrate the impacts of different mechanisms. The intensity changes in SSP5-8.5 (black dots in Fig. 2) and abrupt-4×CO2 (orange dots in Fig. 2) show a weakened SC in most models and both hemispheres (Supplementary Figs. S2 and S3), although the degree shows a large inter-model spread. The inter-model correlation coefficient between the intensity change in global SC and global-mean surface warming among the models is −0.43 ($P < 0.02$) in SSP5-8.5 and −0.55 ($P < 0.002$) in abrupt-4×CO2, suggesting that the degree of weakened global SC is related to the degree of global warming. The weakening is more apparent in the abrupt-4×CO2 experiments (orange dots in Fig. 2) and in both hemispheres, with a stronger global-mean surface warming than SSP5-8.5.

We also confirm the earlier conclusion of a decline in the divergent SC resulting from the weakening of the tropical overturning circulation[23–26]. As shown in Supplementary Fig. S4, the divergent component of SC, represented by the velocity potential at 850 hPa, demonstrates a more robust decrease in the SSP5-8.5 scenario, aligning with previous findings[23–26].

As the internal variability could greatly influence the regional SC changes[27], we analyze the SMILEs of five models, CESM1-CAM5, CanESM2, CSIRO-Mk3-6-0, GFDL-CM3, and MPI-ESM, and confirm a limited role of internal variability to the weakened SC (gray hollow markers in Fig. 2). An apparent exception projecting a strengthened global SC is MPI-ESM (Fig. 2), including the 100 members of MPI-ESM in the SMILEs, and the related versions of MPI-ESM in the SSP5-8.5 (MPI-ESM1-2-HR and MPI-ESM1-2-LR) and abrupt-4×CO2 (MPI-ESM-1-2-HAM, MPI-ESM1-2-HR, and MPI-ESM1-2-LR) from the CMIP6. Even though, the results of MPI-ESM-related models follow the negative correlation between global SC change and global-mean surface warming, reflecting the enhanced SC could be related to the lower warming in the models.

The uncertainty from patterned SST warming is also evaluated by the simulations from d4PDF, which are six atmosphere-only experiments forced by 4-K patterned warming scaled from six representative SST warming patterns (Supplementary Fig. S5) extracted from the CMIP5 models (purple markers in Fig. 2). The spread of the intensity changes in the six d4PDF experiments does not exceed the inter-model spread of SSP5-8.5 and abrupt-4×CO2 experiments, also exhibiting a robust weakening of global SC. We contrast two extreme results in the six d4PDF experiments: one involving slight intensification and the other a considerable weakening (Fig. 2), particularly in the Southern Hemisphere (Supplementary Figs. S2 and S3). These results are associated with HFB_4K_MI (Supplementary Fig. S5d) and HFB_4K_MR

https://doi.org/10.1038/s41467-023-44244-5

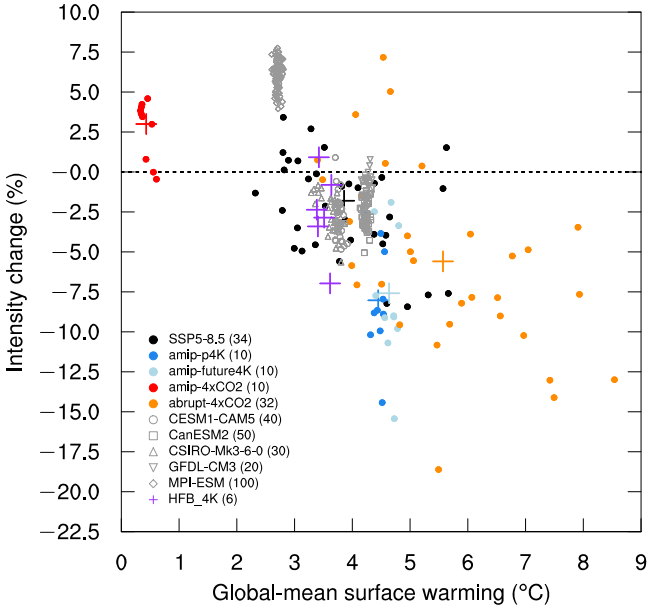

Fig. 2 | Intensity changes in the global subtropical circulation with respect to global-mean surface warming in several sets of experiments. The intensity changes in the global subtropical circulation in Shared Socioeconomic Pathway 5-8.5 (SSP5-8.5) runs (years 2070–2099; black dots; 34 models) relative to historical runs (years 1979–2008), in amip-p4K (years 1979–2008; blue dots; 10 models) relative to amip experiment (years 1979–2008), in amip-future4K (light-blue dots) relative to amip experiment, in amip-4×CO2 (red dots) relative to amip experiment, in abrupt-4×CO2 (years 121–150; orange dots) relative to piControl experiment (second 100 years), in SMILEs (single-model initial-condition large ensembles) from CESM1-CAM5 (years 2070–2099 relative to years 1979–2008; gray hollow circles; 40 ensembles), in SMILEs from CanESM2 (gray hollow squares; 50 ensembles), in SMILEs from CSIRO-Mk3-6-0 (gray hollow triangles; 30 ensembles), in SMILEs from GFDL-CM3 (gray hollow inverted triangles; 20 ensembles), in SMILEs from MPI-ESM (gray hollow rhombuses; 100 ensembles) and in six HFB-4K experiments (purple crosses) relative to HPB experiment from the Database for Policy Decision Making for Future Climate Change (d4PDF). For the changes in each model expressed as dots, the cross with the same color represents their multi-model mean.

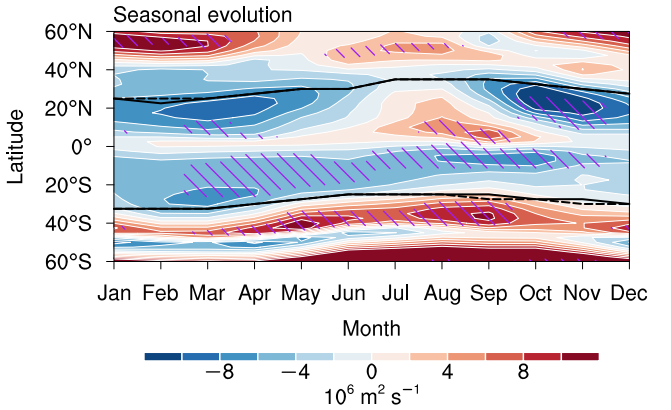

Fig. 3 | Seasonal and latitudinal intensity changes in the 850 hPa streamfunction (shading) in the Shared Socioeconomic Pathway 5-8.5 (SSP5-8.5) experiment relative to the historical experiment. The black solid (dashed) curves indicate the center of the subtropical circulation in each hemisphere in the historical (SSP5-8.5) experiment (see the "Methods" section for details). Hatching indicates that the change is robust (see the "Methods" section for the details of the criteria).

(Supplementary Fig. S5f), respectively. In HFB_4K_MI, a rare cooling occurs over the Southern Ocean, enhancing the meridional temperature gradient and strengthening westerlies[46]. Additionally, there is a relatively weak El Niño-like warming in the tropical Pacific, resulting in a weaker westerly change over the equatorial western Pacific. Both these features in HFB_4K_MI contribute to strengthening the Southern Hemisphere SC.

The role of the three primary processes in CO_2 increase, the uniform SST warming, the patterned SST warming, and the direct CO_2 radiative forcing[22,30], are investigated using a set of atmosphere-only experiments from CFMIP-3[45], including amip, amip-p4K, amip-future4K, and amip-4×CO2. Uniform (blue dots in Fig. 2) and patterned (light-blue dots in Fig. 2) SST warming both significantly weaken the global SC. By contrast, the direct CO_2 effect strengthens the global SC confirmed by the amip-4×CO2 experiment (red dots in Fig. 2), opposite to the effect of SST warming. On a global scale, the diminishing influence of SST warming overcomes the enhancement of the direct CO_2 effect, leading to a robust weakening, although these two mechanisms are comparable in some regions[22].

The effects of SST warming and direct CO_2 radiative forcing have distinct temporal features. The direct CO_2 effect is a rapid process with timescales from weeks to months[22,34], whereas the SST warming associated with its impact is almost proportional to the relatively slow global-mean surface warming. The opposite roles of SST warming and direct CO_2 effect with distinct temporal features can explain the more robust decrease in abrupt-4×CO2 than in SSP5-8.5 experiments (Fig. 2). There is persistent new CO_2 emission in SSP5-8.5[47] but not in abrupt-4×CO2, resulting in more transient response in SSP5-8.5 during the years 2070–2099 than in abrupt-4×CO2 during the years 121–150. Given that the warming of the transient response to a CO_2 emission is weaker compared to the response nearing equilibrium, the role of uniform SST warming is underrated in SSP5-8.5 relative to the response nearing equilibrium in abrupt-4×CO2. This process could be the reason for the absence of a robust change obtained in many previous studies utilizing SSP5-8.5 experiments.

Seasonal variation of the changes in the subtropical circulation

As SC and the associated processes are seasonally and latitudinally varying[1], we further investigate the seasonal and latitudinal SC change by projecting the SC onto the climatological SC latitude-by-latitude and month-by-month (see the "Methods" section for details). Figure 3 shows the seasonal and latitudinal intensity changes in SC of the multi-model mean of CMIP6 models. The center of the climatological SC is shown as a reference for the SC changes (see the "Methods" section for details; Supplementary Fig. S6). The Northern Hemisphere SC is weakened around the equatorward flank of the climatological SC center throughout the year, except in JJA (Fig. 3). The Southern Hemisphere SC is weakened mainly on the equatorward flank of the climatological center but strengthened on the poleward flank (Fig. 3), resembling a poleward shift.

The weakened SC is not robust in all months and latitudes (see the definition of robustness in the "Methods" section), implying a more intricate mechanism underlying these changes in SC. In the amip-p4K simulation, uniform SST warming results in a robust weakening of global SC throughout the year (Fig. 4a and Supplementary Fig. S7). This weakening shifts seasonally with the climatological SC center and occurs primarily on its equatorward flank in a few months, possibly linked to the more pronounced circulation weakening in the tropics than in the extratropics[23]. The impact of the patterned SST warming (Supplementary Fig. S8) on the SC with the impact from uniform SST warming removed (Fig. 4b) is relatively weak compared to the uniform SST warming (Fig. 4a), but it enhances the poleward flank of the SC in the Southern Hemisphere during the austral summer (Fig. 4b and Supplementary Fig. S9). This enhancement is associated with the southeasterly wind changes over the southeastern Pacific (Supplementary Fig. S8), which is modulated by a stronger west-minus-east gradient during the austral summer around 20°S–40°S of the prescribed-SST change pattern (Supplementary Fig. S8)[48]. The results in the d4PDF

https://doi.org/10.1038/s41467-023-44244-5

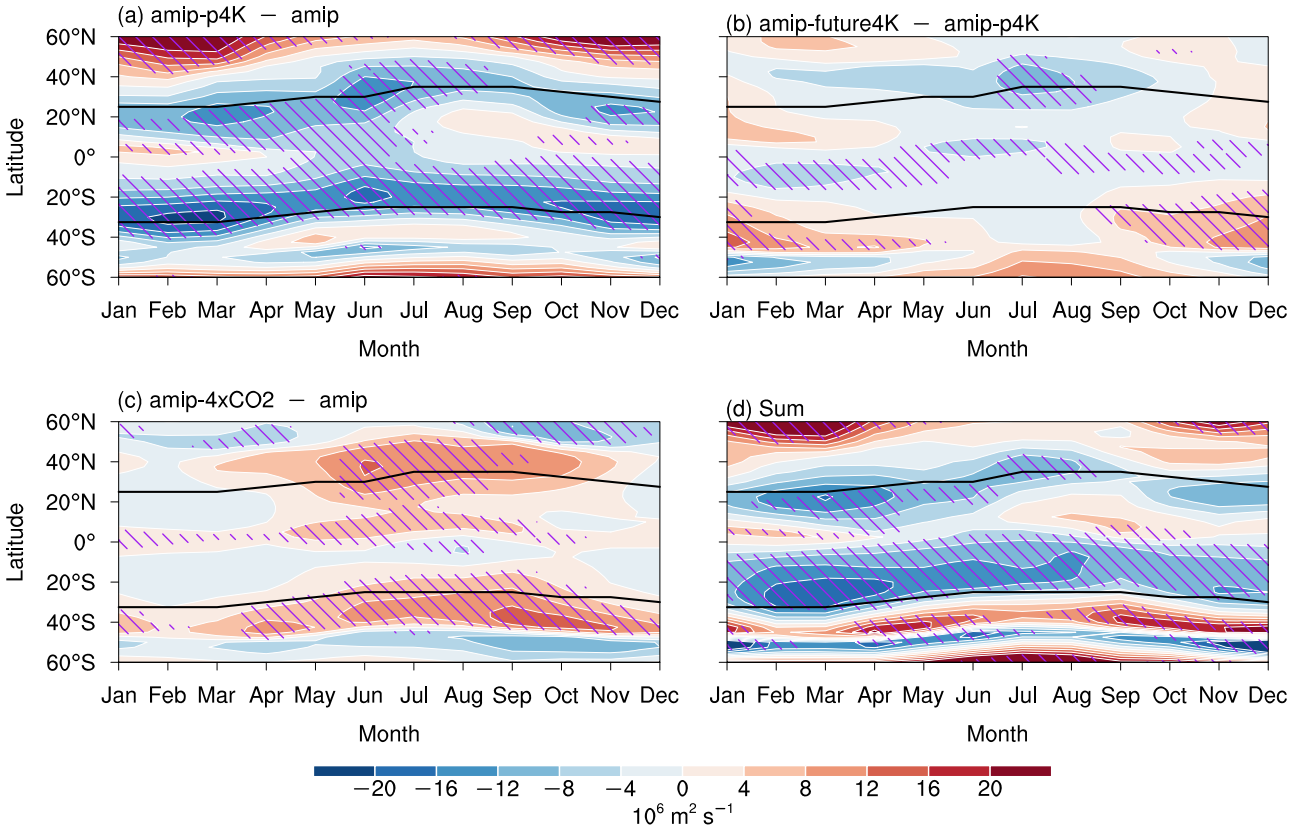

Fig. 4 | Seasonal and latitudinal intensity changes in the global subtropical circulation in the atmosphere-only experiments. a–**c** Seasonal and latitudinal intensity changes in 850 hPa streamfunction under **a** uniform sea surface temperature (SST) warming, **b** patterned SST warming, and **c** direct CO_2 radiative forcing. The black curves indicate the center of the subtropical circulation in each hemisphere. **d** Sum of (**a**–**c**). Hatching indicates that the change is robust (see the "Methods" section for the details of the criteria).

simulations with six different SST change patterns (Supplementary Fig. S10) are consistent with those in SSP5-8.5 (Fig. 3), also suggesting a weak influence of the uncertainty in the SST change pattern.

By contrast, direct CO_2 radiative forcing strengthens the global SC, especially during the boreal summer monsoon season (June–September; Fig. 4c and Supplementary Fig. S11). Strengthening of the SC is stronger on the poleward flank of the climatological SC center because of the superposition of the poleward shift in the midlatitude jet (Supplementary Fig. S12). Direct CO_2 radiative forcing can induce stratospheric cooling and a poleward shift of midlatitude jet throughout the year[46,49], favoring the strengthening of the SC in both hemispheres. However, its impact is located around the midlatitude jets, exactly the poleward boundary of the climatological SC in both hemispheres (Fig. 4c and Supplementary Fig. S12), indicating the poleward shift in the midlatitude jet could not be the major factor enhancing SC, especially during the boreal summer.

The combined impact of the uniform and patterned SST warming, and direct CO_2 radiative forcing (Fig. 4d) closely resembles the SC changes in the SSP5-8.5 runs (Fig. 3). Some minor discrepancies between Figs. 3 and 4d still appear in Northern Hemisphere during the boreal autumn, implying a relatively weak role of the atmosphere–ocean coupled process that is neglected in the atmosphere-only experiments. Compared with the SC changes in the SSP5-8.5 runs (Fig. 3), the weakening of SC is more robust in most months and latitudes in the Southern Hemisphere (Fig. 4d), which should be associated with the stronger warming in the +4-K amip experiments than the SSP5-8.5 runs (Fig. 2).

The weakened SC under uniform SST warming is robust throughout the subtropics (Fig. 5a), whereas the SC is strengthened in June–September under direct CO_2 radiative forcing (Fig. 5b), except over the Atlantic Ocean. The low-level SC weakening under uniform SST warming is spatially homogeneous throughout the subtropics, which is consistent with the decreased vertical velocity in the mid-level troposphere (Fig. 5c)[23] and reflects the mechanism of the Sverdrup balance connected with the weakened tropical circulation[1]. The degree of weakening in low-level SC is weaker than that in mid-level circulation and is close to that in the Hadley cell[50], given that the low-level SC is closely related to the descending branch of the Hadley cell. The major contribution to the slowdown in the tropical overturning circulation is from the Walker circulation, but not the Hadley cell[23,24,50]. The direct CO_2 effect mainly strengthens the SC in the boreal summer monsoon season, most apparent in the low level, by enhancing the land–sea thermal contrast[22].

The land–sea thermal contrast (Supplementary Fig. S13) could induce tropical diabatic heating and then influence the SC in both hemispheres through stationary barotropic Rossby waves[33,51,52]. The process is verified by a linear baroclinic model (LBM; see the "Methods" section for details). According to the boreal summer changes in rainfall under direct CO_2 effect (Fig. 5d), we select six regions with idealized heating and cooling to force the LBM in the respective experiment (Supplementary Figs. S14 and S15). The steady responses to the heating and cooling show that the diabatic heating in North Africa and cooling in the northeastern Pacific contribute most to the strengthened SC (Fig. 5b and Supplementary Fig. S16). The tropical responses are close to a Matsuno–Gill pattern[53] dependent on the location of forcing.

Timescales of responses

The distinct temporal features of SST warming and direct CO_2 effect cause their relative contributions to vary across different emission

https://doi.org/10.1038/s41467-023-44244-5

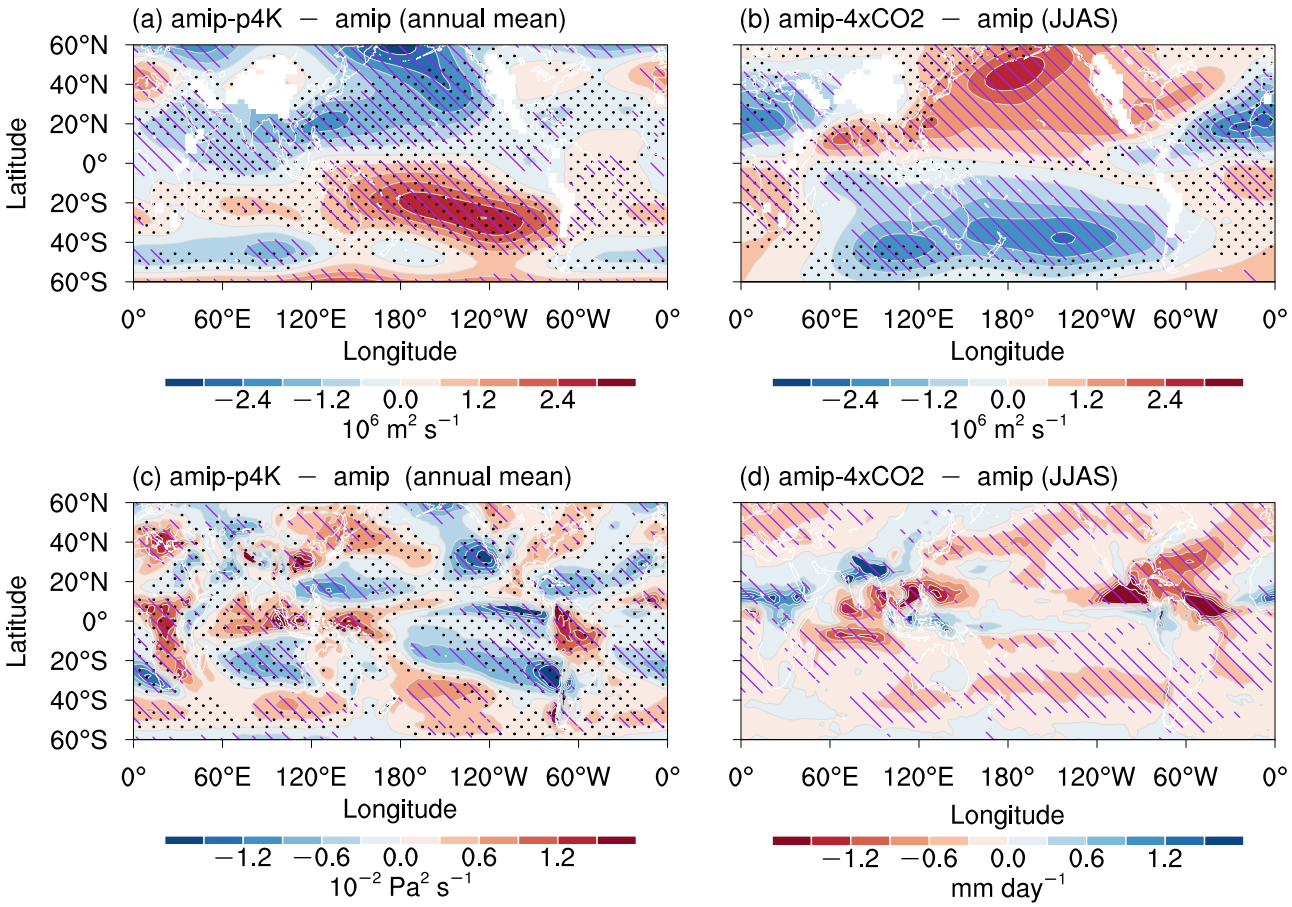

Fig. 5 | Changes in the low-level subtropical and the mid-level vertical circulation in the atmosphere-only experiments. a, **c** Annual changes in **a** 850 hPa streamfunction and **c** 500 hPa vertical pressure velocity under uniform sea surface temperature (SST) warming. **b** The same as **a** but for the boreal summer (June–September; JJAS) changes under direct CO_2 radiative forcing. **d** Boreal summer changes in rainfall under direct CO_2 radiative forcing. Hatching indicates that the change is robust (see the "Methods" section for the details of the criteria). Stippling in **a**–**c** indicates that the changes and their corresponding climatologies are opposite in sign, which is equivalent to local weakening.

scenarios. This property is used to verify their combined role by explaining the time-varying SC in the abrupt-4×CO2 simulation. In abrupt-4×CO2 (Fig. 6a), the direct CO_2 effect—the enhanced land–sea thermal contrast—reaches its peak in the first year strengthening SC. Then the weakening of SC is increasingly robust in the low-level SC, along with the increase of slow SST warming overcoming the direct CO_2 effect. The rate of weakening in the low-level SC at the end of the abrupt-4×CO2 experiment is about −1.14% (with a 5–95% range of −2.90% to 0.21%), per 1 K global surface warming.

The enhanced SC by the direct CO_2 effect appears in all latitudes and seasons in the first year of the abrupt-4×CO2 experiment (Fig. 6b). The Northern Hemisphere SC changes are slightly shifted from the boreal summer to spring and early summer. One possible reason is that the change in a single year is susceptible to internal variability, while another possibility is that the annual global-mean surface warming is around 1 K in the first year, indicating that the influence of SST warming has already occurred. However, the response in the Southern Hemisphere (Fig. 6b) closely resembles that in the atmosphere-only model (Fig. 4c), confirming the direct CO_2 effect on the SC in the coupled model. As greenhouse warming continues, the SC changes during years 21–30 in the abrupt-4×CO2 experiment (Fig. 6c) resemble those at the end of the SSP5-8.5 scenario (Fig. 3). In years 141–150 of the abrupt-4×CO2 experiment, the Southern Hemisphere SC is clearly weakened throughout the year, and the Northern Hemisphere SC is also weakened, except in August–September (Fig. 6d). Overall, the combined roles of SST warming and direct CO_2 radiative forcing in the low-level SC changes shown here explain well the time-varying SC changes in the abrupt-4×CO2 simulations.

Discussion

The present study reveals a robust weakening in global lower-tropospheric SC under greenhouse warming, based on a metric projecting the SC changes onto the SC climatology. The weakening of global SC is robust in the SSP5-8.5 and abrupt-4×CO2 simulations participating in CMIP6. The SC weakening is increasingly evident with the rise in global-mean surface temperature. The uncertainties from internal variability and future SST warming pattern do not apparently influence this conclusion, verified by the SMILE and d4PDF simulations. The robust weakening of SC is mainly induced by global-mean surface warming and partly counteracted by the direct CO_2 effect. Uniform SST warming tends to weaken the global SC throughout the year, mainly on the equatorward flank of the climatological SC center, whereas direct CO_2 forcing strengthens the global SC on the poleward flank during the boreal summer monsoon season. The combined mechanisms in which the effect of SST warming and direct CO_2 radiative forcing have different temporal features explain well the time-varying SC changes in the abrupt-4×CO2 experiment. The global SC weakening finally emerges in most models, when the slow effect of SST warming overcomes the fast effect of direct CO_2 radiative forcing.

The decrease in global SC is associated with a weakening global monsoon circulation under CO_2-induced global warming, suggesting a contracted monsoon range and drying at its boundary with arid

https://doi.org/10.1038/s41467-023-44244-5

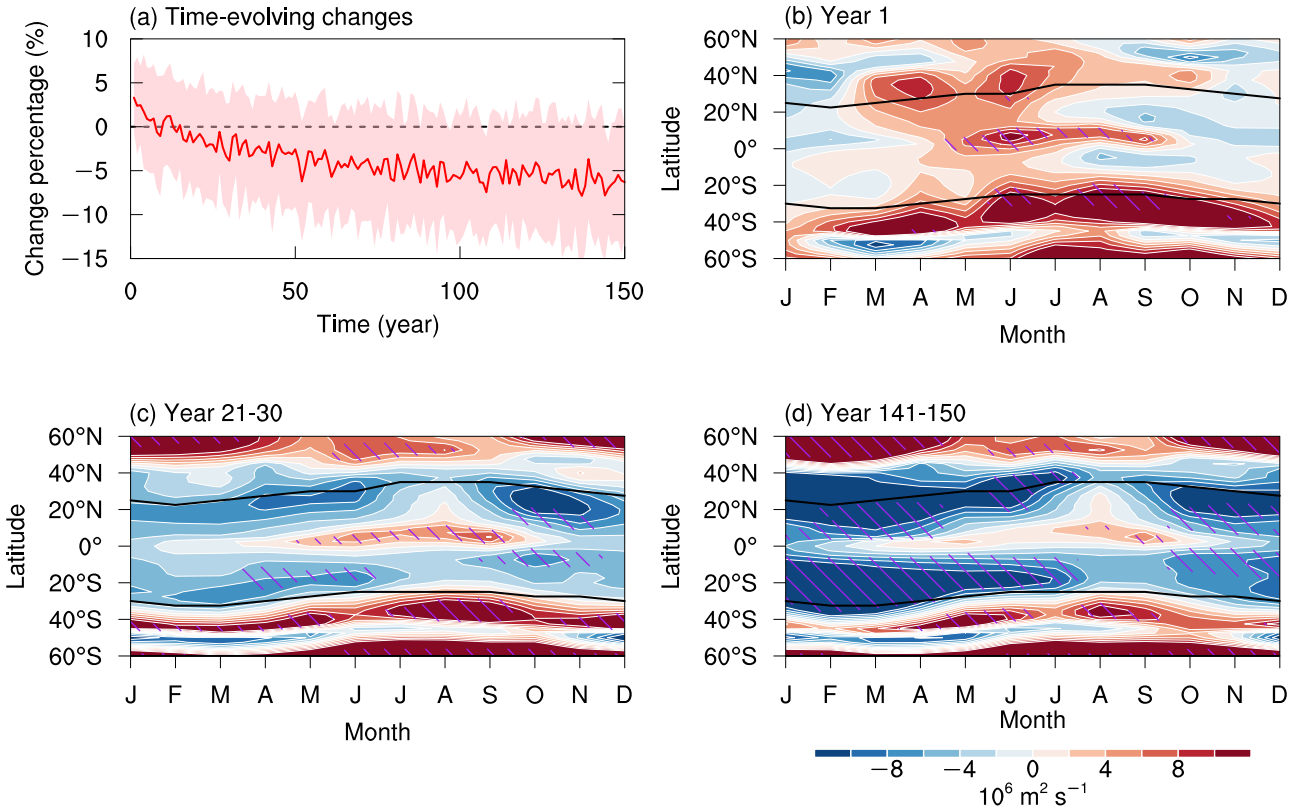

Fig. 6 | Time evolution of the changes in the global subtropical circulation. **a** Multi-model mean of the intensity change in the 850 hPa streamfunction (10°–45°S and 10°–45°N) and one inter-model standard deviation range (shading) in the abrupt-4×CO2 experiment relative to the piControl experiment. **b**–**d** Seasonal and latitudinal intensity changes in the 850 hPa streamfunction during **b** year 1, **c** years 21–30, and **d** years 141–150 in the abrupt-4×CO2 experiment relative to the climatology of second 100 years in piControl experiment. The black curves in **b**–**d** indicate the center of the subtropical circulation in each hemisphere. Hatching indicates that the change is robust (see the "Methods" section for the details of the criteria).

regions, especially in the Northern Hemisphere. This implication seemingly contradicts the prior conclusion of a broader range of monsoon rainfall linked to increased moisture due to global warming[54,55]. The contradiction arises from the linkage of SC change to CO_2 emission trajectory and projection term, owing to the varied impact of processes across timescales. This matter is crucial for projecting climate change under undetermined CO_2 emission trajectories toward carbon neutrality[56–59]. While various CMIP6 models consistently project a significant decline in SC, the extent of this decline varies among models, possibly resulting from factors of uncertainty such as sensitivity to CO_2 concentration, circulation response to uniform warming, and land–sea contrast strength.

Although the global and seasonal variation in SC changes are evident, significant regional disparities still exist[27]. In addition to the intensity changes, shifts in the location of certain regional SC systems have also been identified[19,22], which receives limited discussion in this study. Some shifts occur in regions where multiple subsystems of SC are interconnected, making them difficult to interpret solely in terms of overall intensity change. Despite this, our method can efficiently isolate overall intensity changes in global SC or in a relatively large domain, aiding the focus on more specific changes in regional SC in future research. Furthermore, once the domain selection is established, this method can be employed to analyze regional SC changes for distinguishing the changes in intensity and in location.

Methods

CMIP6 simulations

The historical simulation and the SSP5-8.5 experiment from 34 CMIP6 models[60] are used to represent the present-day and future climates, respectively. The simulation skills of historical SC in these models are evaluated by comparing them with the European Centre for Medium-Range Weather Forecasts Reanalysis v5 (ERA5) reanalysis dataset[61]. As shown in Supplementary Fig. S17, the Taylor diagram[62] for the spatial correlation coefficients and standard deviations of the 850 hPa streamfunction from 60°S to 60°N illustrates that most models show a good performance on the simulation of SC. Thus, we do not further pick out models in the present analyses. The pre-industrial control simulation (piControl) and the simulation forced by an abrupt quadrupling of the pre-industrial CO_2 level (abrupt-4×CO2) from 32 CMIP6 models are also used to study the timescales of different processes.

A set of atmosphere-only experiments[45], including the amip, amip-p4K, amip-4×CO2, and amip-future4K from 10 CMIP6 models, are used to investigate the role of different processes. The amip experiment is a control run forced by the observed monthly mean SST and sea ice concentration, whereas the amip-p4K, amip-4×CO2, and amip-future4K experiments are further forced by uniform SST warming, quadrupling of the pre-industrial CO_2 level and patterned SST warming derived from the CMIP3 coupled models, respectively. The prescribed SST warming pattern for each month is shown in Supplementary Fig. S8. The present study employs the 30 years, 1979–2008, of all the amip experiments. The details for selected models in the different experiments are shown in Supplementary Table S1.

We only select the first simulation of the ensembles for each model. All the monthly model data are interpolated onto a 2.5° × 2.5° grid (90°S–90°N, 0°–357.5°E) before analysis. This study presents the results as the multi-model mean unless stated otherwise.

Single-model initial-condition large ensembles

To evaluate the role of internal variability, five single-model initial-condition large ensembles (SMILEs) are used in this study[43], which are

CESM1-CAM5, CanESM2, CSIRO-Mk3-6-0, GFDL-CM3, and MPI-ESM with 40, 50, 30, 20, and 100 members, respectively. The historical and representative concentration pathway 8.5 (RCP8.5) simulations are used.

Database for policy decision making for future climate change

The large ensemble simulation named 'Database for Policy Decision Making for Future Climate Change' (d4PDF) is used to study the role of uncertainty in future SST warming patterns[44]. The Meteorological Research Institute AGCM, version 3.2 (MRI-AGCM3.2) used here includes the simulations for a present climate (1951–2010) with 100 members (HPB) and a future climate for 60-year integration with 90 members. In this model, the global-mean surface air temperature of the future climate is about 3.6 K warmer than that of the present climate, corresponding to the condition around the end of the 21st century under the RCP8.5 scenario[44]. These simulations consist of six experiments, each using a distinct SST change pattern from CMIP5 models (HFB_4K_CC, HFB_4K_GF, HFB_4K_HA, HFB_4K_MI, HFB_4K_MP, HFB_4K_MR; Supplementary Fig. S5) to capture the impacts of SST warming pattern diversity. For each experiment, 15 members for a 60-year future warming climate are conducted using different initial conditions and different small perturbations of SST. The first 15 ensemble members from 1979 to 2008 in historical simulation are used to represent the historical climate in this study. Different from the future patterned-SST forced experiments such as amip-p4K and amip-future4K from the CFMIP-3 in CMIP6, the greenhouse gases are set to the same value as the end of the RCP8.5 scenario in the global warming simulation from the d4PDF[44]. Thus, the intensity changes of global SC in the 4-K future climate simulations in d4PDF are lower than that in the amip-p4K and amip-future4K experiments and are close to the results in the SSP5-8.5 scenario.

Definition of the SC

In this study, we focus on the dominant rotational component of SC at the low level[63], represented by the 850 hPa streamfunction. The meridional center of SC for each month is defined as the maximum of the climatological zonal-mean 850 hPa streamfunction in the Northern Hemisphere (20°–40°N) and the minimum of the climatological zonal-mean 850 hPa streamfunction in the Southern Hemisphere (20°–40°S) in the historical, amip and piControl experiments. The SC center and the climatological 850 hPa streamfunction in the historical experiment are shown in Supplementary Fig. S6.

Intensity change

The overall intensity change in global SC is defined by the projection of the changes in global SC (10°–45°S and 10°–45°N) onto its 12-month climatology calculated as:

$$A = \frac{\sum_{k=1}^{n}\sum_{j=1}^{n}\sum_{i=1}^{n}\left(X_{ijk}Y_{ijk}\right)}{\sum_{k=1}^{n}\sum_{j=1}^{n}\sum_{i=1}^{n}\left(Y_{ijk}Y_{ijk}\right)} \quad (1)$$

where A represents the intensity change (unit: %); X and Y represent the change and climatology of a circulation system, respectively; i, j, and k represent the latitude, longitude, and month dimensions, respectively. This definition is independent of the domain and the seasonal evolution of SC. We also test other latitudinal ranges, including 45°S–45°N, 10°–40°S, and 10°–40°N and 10°–50°S and 10°–50°N, which do not influence the conclusions (Supplementary Fig. S18). The projection method defining the percentage intensity change prevents unreasonable large values in cases where the climatological SC is close to 0, unlike the conventional method that divides changes by climatology.

Considering SC is seasonally and latitudinally varying, we also project the SC change on the climatological SC latitude-by-latitude and month-by-month calculated as:

$$A_{ik} = \frac{\sum_{j=1}^{n}X_{ijk}Y_{ijk}}{\sqrt{\sum_{j=1}^{n}Y_{ijk}Y_{ijk}}} \quad (2)$$

Test of robustness

A change is considered robust if it meets two criteria: the ratio of multi-model mean to inter-model standard deviation of the change is >1 and at least 66% of the models show a change greater than the internal-variability threshold γ. This test of robustness considers both the uncertainty across the models and internal variability, which is similar to the approach used in the IPCC AR6 WG1 report[64]. The ratio test is stricter than the sign agreement test often used in previous studies to evaluate the inter-model robustness. The internal-variability threshold is defined as $\gamma = \sqrt{2} \cdot 1.645 \cdot \sigma_{30yr}$, where σ_{30yr} is the standard deviation of 30-year climatology of thirteen periods separated from 500-year simulation in the piControl in which the first 100 years are ignored[64].

Linear baroclinic model

We use a simple dry model, Linear baroclinic model (LBM)[65], to investigate the atmospheric response to prescribed heating[66]. The LBM applied here consists of primitive equations linearized concerning a climatological state of June–September, with a horizontal resolution of T42 (roughly equivalent to 2.8°) and 20 vertical sigma levels. The spatial patterns of prescribed heating and cooling maximum at 0.45 level are shown in Supplementary Fig. S14. The vertical profile of diabatic heating forcing the LBM is shown in Supplementary Fig. S15, with a maximum (minimum) at sigma = 0.45 level. The LBM is run up to 30 days, and the 850 hPa streamfunction in the 21–30 days is used to represent the steady response shown in Supplementary Fig. S16.

Data availability

The CMIP6 data is available at https://esgf-node.llnl.gov/projects/esgf-llnl/. The SMILEs data is available at https://www.cesm.ucar.edu/projects/community-projects/MMLEA/. The ERA5 reanalysis dataset is available at https://www.ecmwf.int/en/forecasts/datasets/reanalysis-datasets/era5. The d4PDF is available at http://search.diasjp.net/search?lang=en&k=d4PDF.

Code availability

The data in this study are analyzed with NCAR Command Language. The code used in this study is available on request from the corresponding author.

References

1. Rodwell, M. J. & Hoskins, B. J. Subtropical anticyclones and summer monsoons. *J. Clim.* **14**, 3192–3211 (2001).
2. Lindzen, R. S. & Hou, A. V. Hadley circulations for zonally averaged heating centered off the equator. *J. Atmos. Sci.* **45**, 2416–2427 (1988).
3. Wu, G. & Liu, Y. Summertime quadruplet heating pattern in the subtropics and the associated atmospheric circulation. *Geophys. Res. Lett.* **30**, 1201 (2003).
4. Seager, R. et al. Air–sea interaction and the seasonal cycle of the subtropical anticyclones. *J. Clim.* **16**, 1948–1966 (2003).
5. Nakamura, H. & Miyasaka, T. Structure and formation mechanisms of the Northern Hemisphere summertime subtropical highs. *J. Clim.* **18**, 5046–5065 (2005).
6. Wang, B. et al. Northern Hemisphere summer monsoon intensified by mega-El Niño/southern oscillation and Atlantic multidecadal oscillation. *Proc. Natl Acad. Sci. USA* **110**, 5347–5352 (2013).
7. Chan, S. C., Behera, S. K. & Yamagata, T. Indian Ocean Dipole influence on south American rainfall. *Geophys. Res. Lett.* **35**, L14S12 (2008).

8. Li, L., Li, W. & Kushnir, Y. Variation of the North Atlantic subtropical high western ridge and its implication to southeastern US summer precipitation. *Clim. Dyn.* **39**, 1401–1412 (2012).
9. Sun, X., Cook, K. H. & Vizy, E. K. The south Atlantic subtropical high: Climatology and interannual variability. *J. Clim.* **30**, 3279–3296 (2017).
10. Wang, B., Xiang, B. & Lee, J. Y. Subtropical high predictability establishes a promising way for monsoon and tropical storm predictions. *Proc. Natl Acad. Sci. USA* **110**, 2718–2722 (2013).
11. Kosaka, Y., Chowdary, J. S., Xie, S.-P., Min, Y.-M. & Lee, J.-Y. Limitations of seasonal predictability for summer climate over East Asia and the northwestern Pacific. *J. Clim.* **25**, 7574–7589 (2012).
12. Li, W., Li, L., Fu, R., Deng, Y. & Wang, H. Changes to the North Atlantic subtropical high and its role in the intensification of summer rainfall variability in the southeastern United States. *J. Clim.* **24**, 1499–1506 (2011).
13. Richter, I., Mechoso, C. R. & Robertson, A. W. What determines the position and intensity of the south Atlantic anticyclone in austral winter?—An AGCM study. *J. Clim.* **21**, 214–229 (2008).
14. Zhou, S., Huang, G. & Huang, P. Changes in the East Asian summer monsoon rainfall under global warming: Moisture budget decompositions and the sources of uncertainty. *Clim. Dyn.* **51**, 1363–1373 (2018).
15. Zhang, L. & Zhou, T. Drought over East Asia: A review. *J. Clim.* **28**, 3375–3399 (2015).
16. Chen, X. & Zhou, T. Relative contributions of external SST forcing and internal atmospheric variability to July–August heat waves over the Yangtze River valley. *Clim. Dyn.* **51**, 4403–4419 (2017).
17. Jin, C., Wang, B. & Liu, J. Future changes and controlling factors of the eight regional monsoons projected by CMIP6 models. *J. Clim.* **33**, 9307–9326 (2020).
18. Fahad, A. A., Burls, N. J. & Strasberg, Z. How will southern hemisphere subtropical anticyclones respond to global warming? Mechanisms and seasonality in CMIP5 and CMIP6 model projections. *Clim. Dyn.* **55**, 703–718 (2020).
19. He, C., Wu, B., Zou, L. & Zhou, T. Responses of the summertime subtropical anticyclones to global warming. *J. Clim.* **30**, 6465–6479 (2017).
20. Li, W., Li, L., Ting, M. & Liu, Y. Intensification of Northern Hemisphere subtropical highs in a warming climate. *Nat. Geosci.* **5**, 830–834 (2012).
21. Song, F., Leung, L. R., Lu, J. & Dong, L. Seasonally dependent responses of subtropical highs and tropical rainfall to anthropogenic warming. *Nat. Clim. Change* **8**, 787–792 (2018).
22. Shaw, T. A. & Voigt, A. Tug of war on summertime circulation between radiative forcing and sea surface warming. *Nat. Geosci.* **8**, 560–566 (2015).
23. Vecchi, G. A. & Soden, B. J. Global warming and the weakening of the tropical circulation. *J. Clim.* **20**, 4316–4340 (2007).
24. Held, I. M. & Soden, B. J. Robust responses of the hydrological cycle to global warming. *J. Clim.* **19**, 5686–5699 (2006).
25. Tanaka, H. L., Ishizaki, N. & Kitoh, A. Trend and interannual variability of Walker, monsoon and Hadley circulations defined by velocity potential in the upper troposphere. *Tellus Ser. A* **56**, 250–269 (2004).
26. Ueda, H., Iwai, A., Kuwako, K. & Hori, M. E. Impact of anthropogenic forcing on the Asian summer monsoon as simulated by eight GCMs. *Geophys. Res. Lett.* **33**, L06703 (2006).
27. Cherchi, A. et al. The response of subtropical highs to climate change. *Curr. Clim. Change Rep.* **4**, 371–382 (2018).
28. He, C. & Zhou, T. J. Distinct responses of North Pacific and North Atlantic summertime subtropical anticyclones to global warming. *J. Clim.* **35**, 4517–4532 (2022).
29. Li, W. et al. Intensification of the Southern Hemisphere summertime subtropical anticyclones in a warming climate. *Geophys. Res. Lett.* **40**, 5959–5964 (2013).
30. Li, T. et al. Distinctive south and East Asian monsoon circulation responses to global warming. *Sci. Bull.* **67**, 762–770 (2022).
31. Kamae, Y., Watanabe, M., Kimoto, M. & Shiogama, H. Summertime land–sea thermal contrast and atmospheric circulation over East Asia in a warming climate—Part I: Past changes and future projections. *Clim. Dyn.* **43**, 2553–2568 (2014).
32. Kamae, Y., Watanabe, M., Kimoto, M. & Shiogama, H. Summertime land–sea thermal contrast and atmospheric circulation over East Asia in a warming climate—Part II: Importance of CO_2-induced continental warming. *Clim. Dyn.* **43**, 2569–2583 (2014).
33. Fahad, A. A. & Burls, N. J. The influence of direct radiative forcing versus indirect sea surface temperature warming on southern hemisphere subtropical anticyclones under global warming. *Clim. Dyn.* **58**, 2333–2350 (2021).
34. Bony, S. et al. Robust direct effect of carbon dioxide on tropical circulation and regional precipitation. *Nat. Geosci.* **6**, 447–451 (2013).
35. Chadwick, R., Good, P., Andrews, T. & Martin, G. Surface warming patterns drive tropical rainfall pattern responses to CO_2 forcing on all timescales. *Geophys. Res. Lett.* **41**, 610–615 (2014).
36. Vecchi, G. A. et al. Weakening of tropical Pacific atmospheric circulation due to anthropogenic forcing. *Nature* **441**, 73–76 (2006).
37. Hu, K., Huang, G., Huang, P., Kosaka, Y. & Xie, S.-P. Intensification of El Niño-induced atmospheric anomalies under greenhouse warming. *Nat. Geosci.* **14**, 377–382 (2021).
38. Huang, P., Zheng, X. T., Li, X., Hu, K. & Zhou, Z. Q. More complex interactions: Continuing progress in understanding the dynamics of regional climate change under a warming climate. *Innovation* **4**, 100398 (2023).
39. Huang, P., Xie, S.-P., Hu, K., Huang, G. & Huang, R. Patterns of the seasonal response of tropical rainfall to global warming. *Nat. Geosci.* **6**, 357–361 (2013).
40. Chadwick, R., Boutle, I. & Martin, G. Spatial patterns of precipitation change in CMIP5: Why the rich do not get richer in the tropics. *J. Clim.* **26**, 3803–3822 (2013).
41. Wilcox, P. S. et al. A Walker switch mechanism driving millennial-scale climate variability. *Innov. Geosci.* **1**, 100026 (2023).
42. Pascale, S. et al. Weakening of the North American monsoon with global warming. *Nat. Clim. Change* **7**, 806–812 (2017).
43. Deser, C. et al. Insights from Earth system model initial-condition large ensembles and future prospects. *Nat. Clim. Change* **10**, 277–286 (2020).
44. Ryo, M. et al. Over 5,000 years of ensemble future climate simulations by 60-km global and 20-km regional atmospheric models. *Bull. Am. Meteorol. Soc.* **98**, 1383–1398 (2017).
45. Webb, M. J. et al. The cloud feedback model intercomparison project (CFMIP) contribution to CMIP6. *Geosci. Model Dev.* **10**, 359–384 (2017).
46. Ceppi, P., Zappa, G., Shepherd, T. G. & Gregory, J. M. Fast and slow components of the extratropical atmospheric circulation response to CO_2 forcing. *J. Clim.* **31**, 1091–1105 (2018).
47. O'Neill, B. C. et al. The scenario model intercomparison project (ScenarioMIP) for CMIP6. *Geosci. Model Dev.* **9**, 3461–3482 (2016).
48. Xie, S.-P. et al. Global warming pattern formation: Sea surface temperature and rainfall. *J. Clim.* **23**, 966–986 (2010).
49. Grise, K. M. & Polvani, L. M. The response of midlatitude jets to increased CO_2: Distinguishing the roles of sea surface temperature and direct radiative forcing. *Geophys. Res. Lett.* **41**, 6863–6871 (2014).
50. Lu, J., Vecchi, G. A. & Reichler, T. Expansion of the Hadley cell under global warming. *Geophys. Res. Lett.* **34**, L06805 (2007).
51. Lee, S.-K., Mechoso, C. R., Wang, C. & Neelin, J. D. Interhemispheric influence of the northern summer monsoons on southern subtropical anticyclones. *J. Clim.* **26**, 10193–10204 (2013).

52. Fahad, A. A., Burls, N. J., Swenson, E. T. & Straus, D. M. The influence of south Pacific convergence zone heating on the south Pacific subtropical anticyclone. *J. Clim.* **34**, 3787–3798 (2021).
53. Gill, A. E. Some simple solutions for heat-induced tropical circulation. *Q. J. R. Meteorol. Soc.* **106**, 447–462 (1980).
54. Wang, B. et al. Monsoons climate change assessment. *Bull. Am. Meteorol. Soc.* **102**, E1–E19 (2021).
55. Kitoh, A. et al. Monsoons in a changing world: A regional perspective in a global context. *J. Geophys. Res.: Atmos.* **118**, 3053–3065 (2013).
56. Wang, F. et al. Technologies and perspectives for achieving carbon neutrality. *Innovation* **2**, 100180 (2021).
57. Huang, G. et al. Critical climate issues toward carbon neutrality targets. *Fund. Res.* **2**, 396–400 (2022).
58. Zhou, S., Huang, P., Xie, S.-P., Huang, G. & Wang, L. Varying contributions of fast and slow responses cause asymmetric tropical rainfall change between CO_2 ramp-up and ramp-down. *Sci. Bull.* **67**, 1702–1711 (2022).
59. Wang, F. et al. Climate change: Strategies for mitigation and adaptation. *Innov. Geosci.* **1**, 100015 (2023).
60. Eyring, V. et al. Overview of the coupled model intercomparison project phase 6 (CMIP6) experimental design and organization. *Geosci. Model Dev.* **9**, 1937–1958 (2016).
61. Hersbach, H. et al. The ERA5 global reanalysis. *Q. J. R. Meteorol. Soc.* **146**, 1999–2049 (2020).
62. Taylor, K. E. Summarizing multiple aspects of model performance in a single diagram. *J. Geophys. Res.: Atmos.* **106**, 7183–7192 (2001).
63. Trenberth, K. E., Stepaniak, D. P. & Caron, J. M. The global monsoon as seen through the divergent atmospheric circulation. *J. Clim.* **13**, 3969–3993 (2000).
64. IPCC. *Climate Change 2021: The Physical Science Basis* (Cambridge University Press, 2021).
65. Watanabe, M. & Kimoto, M. Atmosphere–ocean thermal coupling in the North Atlantic: A positive feedback. *Q. J. R. Meteorol. Soc.* **126**, 3343–3369 (2000).
66. Hu, P. et al. The leading mode and factors for coherent variations among the subsystems of tropical Asian summer monsoon onset. *J. Clim.* **35**, 1597–1612 (2022).

Acknowledgements

This work was supported by the National Key Research and Development Program of China (2019YFA0606703), the National Natural Science Foundation of China (42105027 and 41975116), the China Postdoctoral Science Foundation (BX20200329 and 2020M680646) and the Youth Innovation Promotion Association of CAS (Y202025). This work was also supported by the National Key Scientific and Technological Infrastructure project "Earth System Numerical Simulation Facility" (EarthLab). We acknowledge the World Climate Research Programme's Working Group on Coupled Modeling, which is responsible for CMIP6, and the climate modeling groups for producing and making available their model output.

Author contributions

S.Z. and P. Huang conceived the study, performed the analyses, and wrote the paper. L.W., K.H., and G.H. helped with interpretation and feedback. P. Hu helped run the LBM experiments. All authors approved the final manuscript.

Competing interests

The authors declare no competing interests.

Additional information

Supplementary information The online version contains supplementary material available at https://doi.org/10.1038/s41467-023-44244-5.

Correspondence and requests for materials should be addressed to Ping Huang or Lin Wang.

Peer review information *Nature Communications* thanks Abdullah Al Fahad and the other, anonymous, reviewers for their contribution to the peer review of this work. A peer review file is available.

Reprints and permissions information is available at http://www.nature.com/reprints

Publisher's note Springer Nature remains neutral with regard to jurisdictional claims in published maps and institutional affiliations.

Open Access This article is licensed under a Creative Commons Attribution 4.0 International License, which permits use, sharing, adaptation, distribution and reproduction in any medium or format, as long as you give appropriate credit to the original author(s) and the source, provide a link to the Creative Commons licence, and indicate if changes were made. The images or other third party material in this article are included in the article's Creative Commons licence, unless indicated otherwise in a credit line to the material. If material is not included in the article's Creative Commons licence and your intended use is not permitted by statutory regulation or exceeds the permitted use, you will need to obtain permission directly from the copyright holder. To view a copy of this licence, visit http://creativecommons.org/licenses/by/4.0/.

© The Author(s) 2024

nature COMMUNICATIONS

ARTICLE

https://doi.org/10.1038/s41467-022-31108-7 OPEN

Tropical volcanism enhanced the East Asian summer monsoon during the last millennium

Fei Liu[1], Chaochao Gao[2✉], Jing Chai[3,4], Alan Robock[5], Bin Wang[6,7✉], Jinbao Li[8], Xu Zhang[9], Gang Huang[4] & Wenjie Dong[1]

Extreme East Asian summer monsoon (EASM) rainfall frequently induces floods that threaten millions of people, and has been generally attributed to internal climate variability. In contrast to the hydrological weakening theory of volcanic eruptions, here we present convergent empirical and modeling evidence for significant intensification of EASM rainfall in response to strong tropical volcanic eruptions. Our multi-proxy analyses show a significantly increased EASM in the first summer after tropical eruptions from 1470 AD to the present, and the more frequent occurrence of El Niños in the first boreal winter after eruptions is necessary for the enhanced EASM. Model simulation ensembles show that a volcano-induced El Niño and the associated stronger than non-volcanic El Niño warm pool air-sea interaction intensify EASM precipitation, overwhelming volcanic-induced moisture deficiency. This work sheds light on the intertwined relationship between external forcing and internal climate variability and potential flood disasters resulting from tropical volcanic eruptions.

[1] School of Atmospheric Sciences Sun Yat-Sen University, Key Laboratory of Tropical Atmosphere-Ocean System Ministry of Education, and Southern Marine Science and Engineering Guangdong Laboratory, Zhuhai 519082, China. [2] College of Environmental and Resource Sciences, Zhejiang University, Hangzhou 310058, China. [3] Plateau Atmosphere and Environment Key Laboratory of Sichuan Province, School of Atmospheric Sciences, Chengdu University of Information Technology, Chengdu 610225, China. [4] State Key Laboratory of Numerical Modeling for Atmospheric Sciences and Geophysical Fluid Dynamics, Institute of Atmospheric Physics, Chinese Academy of Sciences, Beijing 100029, China. [5] Department of Environmental Sciences, Rutgers University, New Brunswick, NJ 08901, USA. [6] Department of Atmospheric Sciences and International Pacific Research Center, University of Hawaii at Manoa, Honolulu, HI 96822, USA. [7] Earth System Modeling Center and Climate Dynamics Research Center, Nanjing University of Information Science & Technology, Nanjing 210044, China. [8] Department of Geography, University of Hong Kong, Hong Kong SAR, China. [9] Alpine Paleoecology and Human Adaptation Group (ALPHA), State Key Laboratory of Tibetan Plateau Earth System, Resources and Environment (TPESRE), Institute of Tibetan Plateau Research, Chinese Academy of Sciences, Beijing, China. ✉email: gaocc@zju.edu.cn; wangbin@hawaii.edu

The record-breaking EASM rainfall in 2020 caused a humanitarian disaster, affecting 45.4 million people in China and resulting in over 142 human casualties and more than 16 billion US dollars in economic loss[1]. EASM rainfall is usually enhanced by moisture advection and convergence due to southwesterly anomaly of an enhanced western North Pacific subtropical high, following an El Niño peak in the previous winter[2–6]. A recent study also proposed that El-Niño-related tropical tropospheric warming could shift the midlatitude westerlies southward, which would impinge on the Tibetan Plateau and induce northerlies downstream of the plateau to intensify the East Asian early summer rainband[7].

Large volcanic eruptions are one of the major natural external forcings of Earth's climate variability from interannual to centennial time scales[8,9]. The EASM is found to be suppressed after volcanic eruptions in model simulations[10–12] due to the reduction of surface shortwave radiation and the associated slowdown of the global hydrological cycle[13–16]. Volcanic eruptions have been suggested as the cause of some historical drought events[17–19]. However, no significant drought was recorded in the Chinese chronicles following the large 1815 Tambora eruption[20], nor in observations following the 1982 El Chichón and 1991 Pinatubo eruptions[21]. These case studies raise a question about the perception of EASM suppression by volcanic perturbations.

Previous studies of the effects of volcanic eruptions on EASM commonly overlook the role of El Niño, although it has been suggested by a number of proxy-reconstructed El Niño/Southern Oscillation (ENSO) indices that the likelihood of an El Niño increases after tropical eruptions[22–28]. Two main mechanisms have been proposed using state-of-the-art model simulations to explain this connection: the ocean dynamic thermostat mechanism[29–31] and the land-sea thermal contrast mechanism[32–34].

This work investigates the response of the EASM-tropical Pacific system to tropical volcanism to understand the interaction and relative roles of internal climate feedback and external forcing. We analyze long-term multi-proxy data and multi-model simulations and find that a volcano-induced El Niño and the associated warm pool air-sea interaction can intensify the EASM precipitation, overshadowing the hydrological weakening by volcanic eruptions.

Results

Proxy evidence of enhanced EASM rainfall following eruptions. We first examine the EASM-tropical Pacific response to 22 precisely dated tropical large volcanic eruptions[35] for the period from 1470 to 1999 AD using the gridded precipitation proxy data[36] and the ensemble mean of 11 sets of ENSO paleoclimate reconstructions (see "Methods").

The composite results of East Asian rainfall reconstruction in the first post-eruption summer show significant (at the 90% confidence level) positive precipitation anomalies centered around the Yangtze River basin, northeast China, and Kyushu of Japan, accompanied by negative, albeit not significant, anomalies over the Indo-China Peninsula and the Philippines (Fig. 1a). This meridional dipole precipitation anomaly pattern resembles the enhanced EASM-Pacific High response in the first post-El Niño summer, which is well observed with instrumental observations[2,4,5]. Enhanced EASM precipitation in the first post-eruption summer is also observed in two other well-known precipitation reconstructions over China[37] and over all of Asia[38] (Supplementary Fig. 1). Significant positive EASM (25°–34°N, 106°–122°E) precipitation anomalies (at the 95% confidence level), mainly over the middle-lower reach of Yangtze River, are only observed in the first boreal summer after the eruption (Fig. 1b).

Strengthened El Niño-EASM relationship. The ensemble mean of 11 available ENSO reconstructions indicates a significant post-eruption precipitation increase following an El Niño (Fig. 2a), in contrast to the normal EASM precipitation anomalies after an eruption without a preceding El Niño (Fig. 2b). Significantly negative anomalies, on the other hand, are observed over the Indo-China Peninsula, Taiwan, and the Philippines, demonstrating compelling evidence for an El Niño-enhanced Pacific High and its role in modulating the volcanic-induced EASM response. For the non-volcanic El Niño (Fig. 2c), the EASM precipitation increase is much weaker than that after a volcano-induced El Niño. Our multi-proxy analysis results thus demonstrate that explosive tropical eruptions tend to strengthen the El Niño-EASM relationship and increase EASM rainfall in the first subsequent boreal summer, suggesting seasonal monsoon-ocean feedback after large tropical eruptions.

Multi-model evidence of enhanced EASM following eruptions. Next, we investigate the last-millennium climate simulation results of 13 different models from the Paleoclimate Modeling Intercomparison Project phases 3 and 4 (PMIP3 & PMIP4) to interpret the monsoon-ocean response to tropical large volcanic eruptions in the context of the current state-of-the-art models. Based on the actual volcanic forcing used in each model, the 13 simulations amount to 92 eruption events for the common pre-industrial period from 1470 to 1849 AD, and they are used to construct a superposed epoch analysis (see "Methods"). The average of these 92 eruption simulations shows a relative El Niño signal, i.e., a reduced zonal gradient of Pacific equatorial sea surface temperature (SST), in the first post-eruption boreal winter (Supplementary Fig. 2a). In the first post-eruption summer, Indo-Pacific oceanic cooling and Asian drying are simulated, and maximum drying is found over the western Indo-China peninsula (Fig. 3a). Positive precipitation anomalies are simulated over the middle-lower reach of Yangtze River but are significant only in a small area. The associated EASM circulation index, defined by the lower-tropospheric zonal wind shear vorticity of the enhanced Pacific High (see "Methods"), exhibits a significantly negative anomaly, demonstrating an enhanced EASM circulation in the multi-model ensemble mean results (Fig. 3a).

The responses of EASM precipitation to the direct volcanic forcing and to an El Niño can be differentiated by comparing two sets of composites with or without the preceding El Niño among the 92 events (Supplementary Fig. 2). In the first post-eruption summer (Fig. 3b), the composite for 65 out of the 92 events without a preceding El Niño mainly exhibits a direct cooling and drying volcanic effect over most parts of the globe. A relative El Niño signal is simulated and the reduced zonal SST gradient across the Pacific weakly enhances the Pacific High, represented by an anticyclonic anomaly mainly over the South China Sea. Studies have established that SST gradients across the tropical Pacific strongly influence global rainfall[39]. Thus, an El Niño-like response in non-El Niño events tends to offset the cooling-induced dry monsoon over East Asia, resulting in an insignificant decrease in the EASM rainfall, consistent with reconstructions (Fig. 2b). In the presence of a preceding El Niño, the model results show increased post-eruption summer precipitation in the EASM region, and the most significant enhancement is located over the middle-lower reach of the Yangtze River, driven by the convergence and moisture advection of southwesterly wind anomalies of the enhanced Pacific High and extratropical northerly anomalies, albeit not significant, downstream of the Tibetan Plateau (Fig. 3c). Thus, the post-eruption El Niño cases can overwhelm the no-post-eruption El Niño cases, resulting in an overall increase in the EASM rainfall.

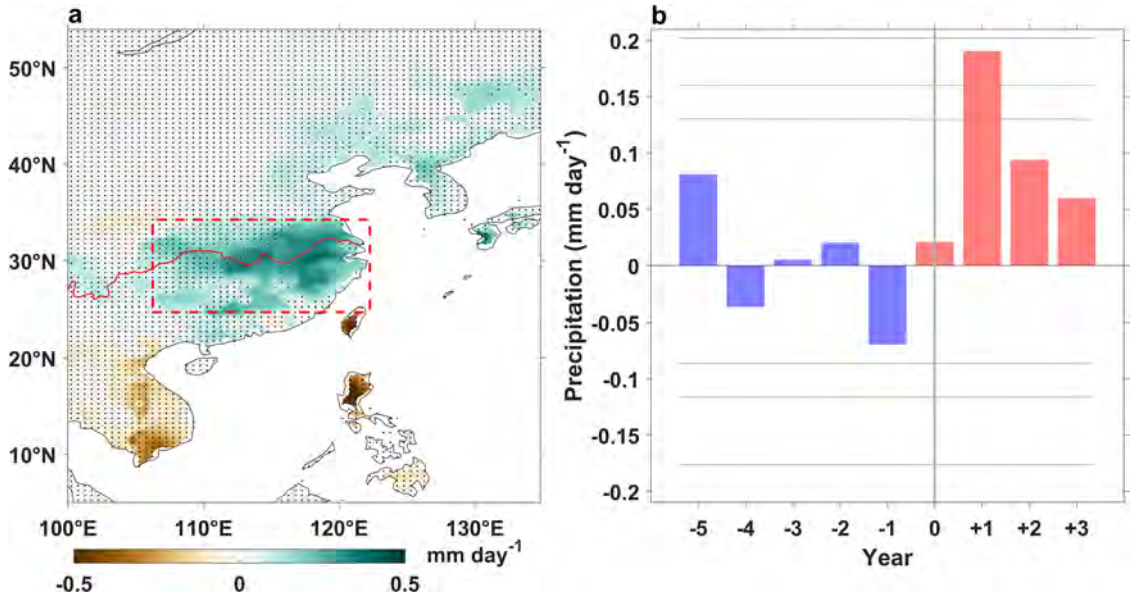

Fig. 1 East Asian summer monsoon (EASM) response to tropical eruptions based on reconstructions. a Superposed epoch analysis results of East Asian precipitation anomalies (shading) in the first boreal summer after 22 tropical eruptions from 1470 to 1999 AD. Stippling indicates precipitation anomalies not significant at the 90% confidence level. The red curve is the Yangtze River, and the red box indicates the EASM region (25°–34°N, 106°–122°E). **b** Composite EASM-averaged precipitation anomaly for 22 tropical eruptions. Confidence limits (90, 95, and 99%) are marked by horizontal lines. Red and blue colors mark the post-eruption and pre-eruption composites, respectively. Year 0 denotes the eruption year. This figure was created using MATLAB 2020a (http://www.mathworks.com).

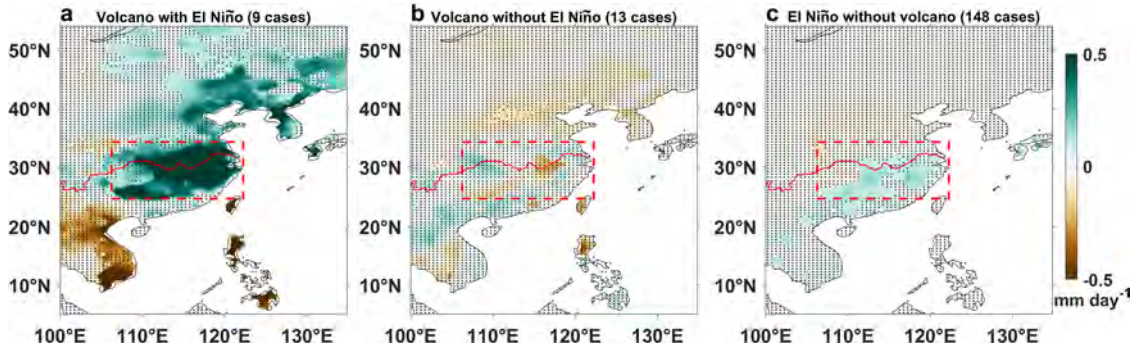

Fig. 2 Role of El Niño in post-eruption EASM change based on reconstructions. Superposed epoch analysis results of East Asian precipitation anomalies (shading) in the first boreal summer after **a** 9 tropical eruptions with and **b** 13 eruptions without an El Niño in the first winter after the eruption, and after **c** 148 non-volcanic El Niños during the period of 1470–1999 AD. An El Niño event is defined by the average of the 11 reconstructions of the ENSO index (see "Methods"). Stippling indicates precipitation anomalies not significant at the 90% confidence level. The red curve is the Yangtze River, and the red box indicates the EASM region. This figure was created using MATLAB 2020a (http://www.mathworks.com).

This El Niño-increased EASM precipitation after volcanic eruptions is also simulated when considering all 228 eruption events during the last millennium covering 850–1849 AD in all 13 PMIP models (Supplementary Fig. 3). Ten Community Earth System Model (CESM) last-millennium ensemble simulations from 1470 to 1999 AD also confirm the critical role of El Niño after volcanic eruptions in increasing EASM precipitation (Supplementary Fig. 4).

Volcanic-induced Pacific air-sea interaction. Eruption-induced radiative cooling leads to an El Niño in the post-eruption winter or an El Niño-like response in the following summer when the El Niño is not fully developed. The responses are determined by the coupled atmosphere-land-ocean dynamics. The decrease in SST gradient, i.e., relative warmer eastern Pacific, can be initiated by eruption-induced global cooling through the ocean dynamic thermostat mechanism[29,40] and land-sea thermal contrast[32,33]. This decreased SST gradient gives rise to a weakened pressure gradient and hence weaker easterly winds and Walker circulation (Supplementary Fig. 2a), which may, in turn, reduce the SST gradient, a mechanism known as "the Bjerknes feedback"[33,41].

Among the 92 eruption events, the post-eruption EASM precipitation change is significantly correlated with the preceding El Niño (0.19, at the 90% confidence level) two seasons before, and the correlation is higher for the EASM circulation (−0.44, at the 99% confidence level) than for the precipitation. This is because the EASM circulation index, i.e., the Pacific High, is better captured by numerical models than precipitation[42]. These significant relations indicate that a stronger El Niño tends to induce a larger EASM increase, consistent with the instrumental observations[43].

After a volcano-induced El Niño, strong negative precipitation anomalies are simulated over South Asia, consistent with previous studies demonstrating the drying effect of large volcanic eruptions on the South Asian monsoon[44,45]. The enhanced Pacific High is

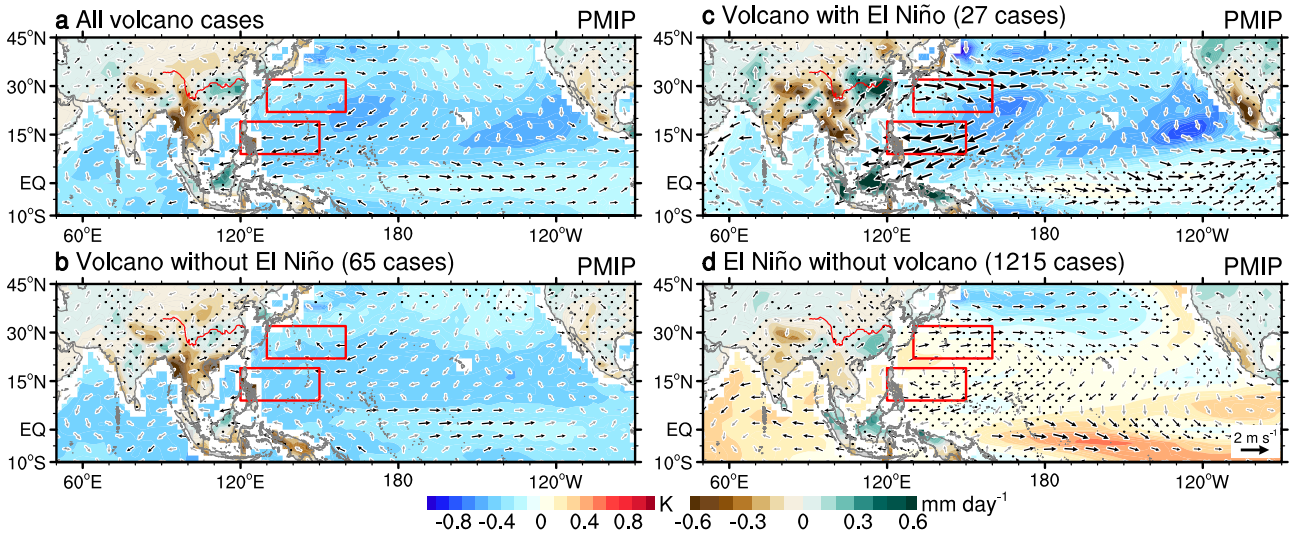

Fig. 3 Simulated EASM-ocean responses to tropical eruptions. Composite SST anomalies (shading over ocean), precipitation anomalies (shading over land), and 850 hPa wind anomalies (vectors) in the first boreal summer after **a** all 92 simulated tropical eruptions, **b** 65 eruptions without, and **c** 27 eruptions with an El Niño response in the first boreal winter after the eruption, as well as **d** composites for 1215 non-volcanic El Niños in 13 PMIP last millennium simulations from 1470 to 1849 AD. Stippling and gray vectors indicate precipitation and temperature anomalies and wind anomalies not significant at the 90% confidence level, respectively. The red curve is the Yangtze River. The red rectangles denote the locations where the EASM circulation index is defined: the 850 hPa zonal wind averaged in the southern box minus that in the northern box (see "Methods"). A negative value of this index represents enhanced Pacific high and associated East Asian subtropical rainfall. Maps created with The NCAR Command Language (Version 6.6.2) [Software]. (2019). Boulder, Colorado: UCAR/NCAR/CISL/TDD. https://doi.org/10.5065/D6WD3XH5.

tied to the SST cooling to its southeast (Fig. 3c), explained by the wind-evaporation SST feedback after an El Niño[4]. Easterly wind anomalies over the North Indian Ocean, which were also suggested to increase the Pacific High[5], are only significant over the Arabian Sea. Volcanic eruptions act to enhance this post-El Niño western North Pacific SST cooling and intensify the Pacific High (Fig. 3d), as found by previous simulations[26,46]. The resulted EASM enhancement is much larger than a non-volcanic El Niño would induce, confirming the proxy-finding of volcanic strengthened El Niño-EASM relationship.

The change of monsoon precipitation can be divided into dynamic and thermodynamic causes[47], which are related to the changes in circulation and moisture availability, respectively (see "Methods"). After a volcanic eruption, dynamic-related precipitation is increased while the thermodynamic-related precipitation is decreased, demonstrating the volcanic-induced cooling and drying (Fig. 4). The decreased thermodynamic-induced precipitation counteracts the increased dynamic-induced precipitation, resulting in a weak change in total precipitation. The presence of an El Niño tends to enhance the dynamic-related precipitation, while keeping the thermodynamic-related precipitation almost intact (Fig. 4). Results from these last-millennium experiments confirm the critical role of a preceding El Niño in enhancing the EASM, against the well-known cooling and hydrological weakening effect of volcanic eruptions[13–16].

Discussion

The fraction of El Niños occurring after volcanic eruptions in reconstructions is 41% for the study period from 1470 to 1999 AD (Fig. 2), or 44% if we expand the period to cover the last millennium from 901 to 1999 AD, which are both larger than the expected percentage (27%) for El Niño events without a volcanic effect. Despite the small sample sizes, i.e., 22 or 39 eruptions in the two periods, respectively, the results consistently suggest that tropical eruptions do increase the likelihood of an El Niño. This explains why the composite EASM rainfall after all eruptions is increased in reconstructions. In the models, this count fraction is only 29% for PMIPs (Fig. 3), resulting in a feeble EASM rainfall increase in the all-eruption case. This less frequent occurrence of El Niño, against a robust equatorial Pacific westerly response to tropical volcanic eruptions, was argued to be caused by weak coupling between central Pacific precipitation and westerly anomalies in the PMIP3 and CESM models[48].

Although our ensemble analysis shows that a tropical eruption can increase the likelihood of an El Niño, individual paleoclimate reconstructions exhibit divergent responses[22,28,49,50]. We use the ensemble mean to maximize the signals, but the results might be affected by the proxy overlap among the 11 available ENSO indices. The divergent ENSO[26,27] and hydrology[47,51–54] responses, plus the time-dependent shifts of the Intertropical Convergence Zone (ITCZ)[55] to volcanic eruptions with asymmetric hemispheric distributions further complicate the volcano-EASM relationship quantification. Future study expanding to Northern or Southern Hemispheric eruptions should correct for SST variations associated with such ITCZ shifts.

To conclude, this work finds an east-west asymmetric monsoonal-ocean response to the zonally symmetric volcanic forcing, highlighting the delayed oceanic responses to volcanic eruptions in exciting EASM precipitation changes. A precipitation increase due to wind convergence induced by the enhanced western North Pacific high overwrites the precipitation reduction due to the thermodynamically induced moisture deficiency. The tropical Pacific plays a critical role in modulating the climate system response to external volcanic forcing, i.e., increasing the likelihood of an El Niño and enhanced post-El Niño warm pool air-sea interaction. Similar cases are found in the Nuclear Niño[34] or the northern Eurasia winter warming responses to stratospheric soot and sulfate aerosols injections during volcanic scenarios[56]. Results obtained from this work demonstrate the important role and complexity of the coupled atmosphere-ocean dynamics in Pacific, and shed light on the potential impact of volcanic eruptions on EASM hydroclimate.

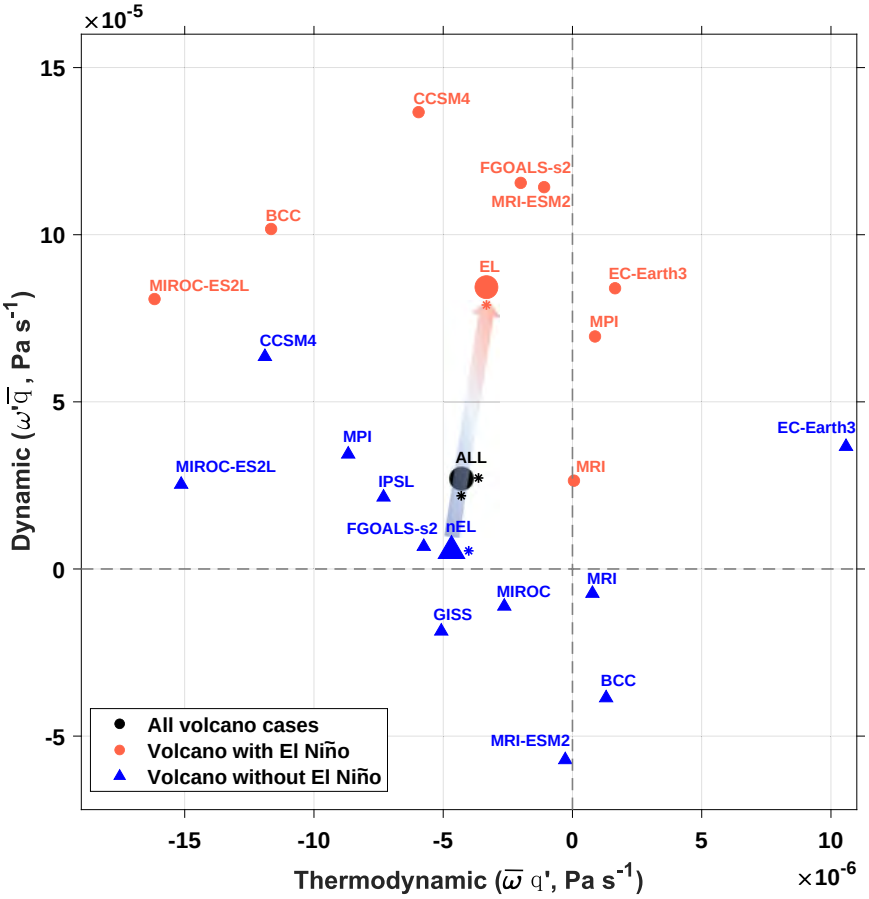

Fig. 4 Simulated dynamic and thermodynamic responses of EASM to tropical eruptions modulated by El Niño. Plotted are the composite dynamic part ($\omega'\bar{q}$) versus thermodynamic part ($\bar{\omega}q'$) of post-eruption EASM precipitation changes after all 78 eruptions in 11 PMIP last millennium simulations from 1470 to 1849 AD (All, dark dot), as well as those of the 21 eruptions with (EL, orange dot) and 57 eruptions without (nEL, blue triangle) El Niño responses in the first boreal winter after eruptions. CSIRO and HadCM last millennium simulations are not included due to the lack of vertical velocity. Asterisks to the right and bottom of the symbols denote the thermodynamic and dynamic anomalies significant at the 90% confidence level, respectively. The arrow indicates a change from the ensemble mean for eruptions without El Niño responses to those with El Niño responses. Results for each model are also shown by the small dots and triangles. Significant tests have not been performed for single models due to the small sample size of El Niño events. This figure was created using MATLAB 2020a (http://www.mathworks.com).

Methods

Proxy data. The proxy data we analyzed mainly include a long-term reconstruction of Asian summer precipitation[36] and 11 reconstructed ENSO indices (Supplementary Table 1). The Feng et al.[36] data are a gridded (0.5° × 0.5°) reconstruction of annual May–September precipitation from 1470 to 1999 AD over the whole Asian continent and are mainly based on 500-year historical documentary records, tree-ring data, ice-core records, and a few long-term instrumental data series. A regional empirical orthogonal function method is utilized to increase the signal-to-noise ratio. Two other gridded reconstructions of precipitation based on point-by-point regression methods are also analyzed in parallel, serving as confirmation of the results: a 530-yr multi-proxy May–September precipitation reconstruction over China (0.5° × 0.5°) based on the tree-ring chronologies and drought/flood indices from 1470 to 2000 AD[37], and an annual June-August rainfall reconstruction over the Asian land region (2° × 2°) generated by merging 453 tree-ring width chronologies and 71 historical documentary records from 1470 to 2013[38].

To test the potential role of a preceding El Niño on volcanic-induced EASM rainfall change, the ensemble mean of 11 available ENSO indices is reconstructed and applied, following the method used before[26] except adding one new proxy[49]. All of the 11 ENSO indices first go through a 9-yr Lanczos high-pass filter[57] to isolate the ENSO signal, and then are normalized according to their own standard deviations. The ensemble mean is utilized to remove proxy uncertainty. Since these 11 indices cover different periods, with the longest extending from 900 to 2002 AD and the shortest from 1706 to 1997 AD, the ensemble mean for each year from 1470 to 1999 AD is calculated as the average of available indices. The ensemble mean with any individual index removed is still highly correlated (above the 99% confidence level), with a minimum correlation coefficient of 0.95, to the ensemble mean of all 11 indices. The resulting ensemble mean has a high correlation with the instrumental December–February Niño3.4 index of 0.83 (at the 99% confidence level) for the period of 1871–1999, based on the averaged (5°N–5°S, 120°–170°W) SST anomaly from Hadley Centre Ice and SST version 1 (HadISST1)[58].

All 22 tropical eruptions from the Sigl et al.[35] volcanic reconstructions during the period of 1470–1999 AD, when Asian precipitation proxies are available, are used for the composite analysis. We define the peak aerosol loading year as the eruption year 0 (Supplementary Table 2).

Last-millennium simulations. All of the 10 last-millennium climate simulations in the PMIP3 and three simulations in the PMIP4 are analyzed to understand the underlying mechanisms of observed EASM response to large volcanic eruptions (Supplementary Table 3). Additional outputs from CESM's 10 last-millennium all-forcing simulations are also investigated, due to CESM's good performance in simulating ENSO seasonality, amplitude, frequency, and teleconnection[59]. Since different volcanic forcing reconstructions are used in the last-millennium simulations from PMIP models and CESM (Supplementary Table 3), the accuracy of the eruption date and strength in each last-millennium simulation is determined according to the volcanic forcing used, and year 0 denotes the year with maximum annual-mean stratospheric sulfate aerosol injection for each eruption, consistent with the using of peak aerosol loading year in reconstruction analysis[35]. A tropical eruption is defined when it has an aerosol density or aerosol optical depth in both hemispheres, following the ice core-based forcing reconstructions[60,61]. Thus, tropical eruptions have their maximum aerosol density or optical depth in the tropics (20°S–20°N)[47]. Since the PMIP simulations only cover the pre-industrial period before 1850, we have 92 eruption events in the 13 PMIP model simulations for a period of 1470–1849 AD and 228 events for the whole last millennium of 850–1849 AD, listed in Supplementary Table 4. In the 10 full forcing ensembles of CESM we have 90 eruption events for the period of 1470–1999 AD when the Asian precipitation reconstructions are available.

Composite and significance. A superposed epoch analysis[22] is used to evaluate the influence of explosive tropical volcanoes on global cooling and related EASM-ocean interaction. To isolate the climate responses to an eruption from the background noise, we obtain the anomaly by removing the climatology of the five years preceding the eruption. We apply the superposed epoch analysis to the reconstructed EASM precipitation and Niño3.4 indices based on the 22 reconstructed tropical eruptions, and internal variability is expected to be filtered out. A superposed epoch analysis is also performed on multi-model simulations from PMIP3 and PMIP4 and on multi-ensemble simulations from CESM. The significance of the superposed epoch analysis results for the 11-year window of five years before and six years after each eruption is calculated by the bootstrapped resampling method with 10,000 random draws from the full 500-year (i.e., 1470–1990 AD) study period[22].

Climate indices and variability. The Niño3.4 index is defined as the area-averaged SST anomaly over the area (5°N–5°S, 120°–170°W). To use the same standard for selecting an El Niño event list among reconstructions with different scales, an El Niño event is defined when the boreal winter Niño3.4 index is >0.5 standard deviations in both reconstructions and simulations. A non-volcanic El Niño is defined as when it occurs in a normal year without an eruption. Using different thresholds to select El Niño events does not change our results qualitatively. Boreal summer is defined as May–September, and boreal winter, as December–February, consistent with those used for reconstructions. The EASM region is defined as the region over (25°–34°N, 106°–122°E) in both reconstructions and simulations. Based on the simulated western North Pacific subtropical high, the EASM circulation index is defined as the 850-hPa zonal wind difference between the northern (22°–32°N, 130°–160°E) and southern (9°–19°N, 120°–150°E) regions, a little different from the original index between northern (22.5°–32.5°N, 110°–140°E) and southern (5°–15°N, 90°–130°E) regions from instrumental observations[62].

The monsoon precipitation index P can be represented by moisture convergence[47,63]:

$$P' = -(\bar{q}\omega' + q'\bar{\omega} + q'\omega') \quad (1)$$

where q denotes surface specific humidity and ω is the pressure velocity at 500 hPa. The overbar denotes the mean state before the eruption, while the prime, the anomaly after the eruption. $\bar{q}\omega'$ and $q'\bar{\omega}$ denote the dynamic and thermodynamic-related precipitation changes, respectively. $q'\omega'$represents the nonlinear feedback and is usually much smaller than the dynamic or thermodynamic counterparts.

Data availability

All data used in this study were obtained from publicly available sources. The PMIP model outputs are distributed by the Earth System Grid Federation (ESGF) at https://esgf-node.llnl.gov/projects/esgf-llnl/ (see Supplementary Table 3 for model details and references). Output from the CESM Last Millennium Ensemble (CESM-LME) can be downloaded at https://www.earthsystemgrid.org/dataset/ucar.cgd.ccsm4.cesmLME.html. Proxy reconstruction datasets are available at the National Centers of Environmental Information via https://www.ncdc.noaa.gov/data-access/paleoclimatology-data/datasets/climate-reconstruction.

Code availability

The code used to create Figs. 1–4 in this study is available on https://zenodo.org/record/6503745. Other analytical scripts are available from the authors upon request. All of the figures are created by the authors using MATLAB 2020a (http://www.mathworks.com/) or NCAR Command Language (NCL; http://www.ncl.ucar.edu/). The atlas imbedded in the figures are the by-default atlas from MATLAB or NCL.

Received: 21 November 2021; Accepted: 20 May 2022;
Published online: 14 June 2022

References

1. Wei, K. et al. Reflections on the Catastrophic 2020 Yangtze River Basin Flooding in Southern China. *Innovation* **1**, https://doi.org/10.1016/j.xinn.2020.100038 (2020).
2. Zhang, R., Sumi, A. & Kimoto, M. A diagnostic study of the impact of El Niño on the precipitation in China. *Adv. Atmos. Sci.* **16**, 229–241 (1999).
3. Chang, C.-P., Zhang, Y. & Li, T. Interannual and interdecadal variations of the East Asian summer monsoon and tropical Pacific SSTs. Part II: Meridional structure of the monsoon. *J. Clim.* **13**, 4326–4340 (2000).
4. Wang, B., Wu, R. & Fu, X. Pacific-East Asian teleconnection: how does ENSO affect East Asian climate? *J. Clim.* **13**, 1517–1536 (2000).
5. Xie, S.-P. et al. Indian Ocean capacitor effect on Indo-Western Pacific climate during the summer following El Niño. *J. Clim.* **22**, 730–747 (2009).
6. Takaya, Y., Kosaka, Y., Watanabe, M. & Maeda, S. Skilful predictions of the Asian summer monsoon one year ahead. *Nat. Commun.* **12**, 2094 (2021).
7. Kong, W. & Chiang, J. C. H. Southward shift of westerlies intensifies the East Asian early summer rainband following El Niño. *Geophys. Res. Lett.* **47**, e2020GL088631 (2020).
8. Robock, A. Volcanic eruptions and climate. *Rev. Geophys.* **38**, 191–219 (2000).
9. Mann, M. E., Steinman, B. A., Brouillette, D. J. & Miller, S. K. Multidecadal climate oscillations during the past millennium driven by volcanic forcing. *Science* **371**, 1014–1019 (2021).
10. Man, W., Zhou, T. & Jungclaus, J. H. Effects of large volcanic eruptions on global summer climate and East Asian monsoon changes during the last millennium: analysis of MPI-ESM simulations. *J. Clim.* **27**, 7394–7409 (2014).
11. Wegmann, M. et al. Volcanic influence on European summer precipitation through monsoons: possible cause for "years without summer". *J. Clim.* **27**, 3683–3691 (2014).
12. Peng, Y., Cheng, H., Chen, K. & Huang, S. Modeling study of severe persistent drought events over Eastern China during the last millennium. *Quat. Sci.* **39**, 282–293 (2019).
13. Trenberth, K. E. & Dai, A. Effects of Mount Pinatubo volcanic eruption on the hydrological cycle as an analog of geoengineering. *Geophys. Res. Lett.* **34**, https://doi.org/10.1029/2007GL030524 (2007).
14. Schneider, D. P., Ammann, C. M., Otto-Bliesner, B. L. & Kaufman, D. S. Climate response to large, high-latitude and low-latitude volcanic eruptions in the community climate system model. *J. Geophys. Res.: Atmos.* **114**, https://doi.org/10.1029/2008JD011222 (2009).
15. Joseph, R. & Zeng, N. Seasonally modulated tropical drought induced by volcanic aerosol. *J. Clim.* **24**, 2045–2060 (2011).
16. Iles, C. E., Hegerl, G. C., Schurer, A. P. & Zhang, X. The effect of volcanic eruptions on global precipitation. *J. Geophys. Res.: Atmos.* **118**, 8770–8786 (2013).
17. Shen, C., Wang, W.-C., Hao, Z. & Gong, W. Exceptional drought events over eastern China during the last five centuries. *Clim. Change* **85**, 453–471 (2007).
18. Shen, C., Wang, W.-C., Hao, Z. & Gong, W. Characteristics of anomalous precipitation events over eastern China during the past five centuries. *Clim. Dyn.* **31**, 463–476 (2008).
19. Chen, K. et al. Nonlinear responses of droughts over China to volcanic eruptions at different drought phases. *Geophys. Res. Lett.* **49**, e2021GL096454 (2022).
20. Gao, C., Gao, Y., Zhang, Q. & Shi, C. Climatic aftermath of the 1815 Tambora eruption in China. *J. Meteorol. Res.* **31**, 28–38 (2017).
21. Liu, Y., Li, Y. & Jia, P. A comparative analysis of effect of volcanic eruptions at low and mid-high latitudes on drought/flood in China. *Meteorol. Monthly* **19**, 3–7 (1993).
22. Adams, J. B., Mann, M. E. & Ammann, C. M. Proxy evidence for an El Nio-like response to volcanic forcing. *Nature* **426**, 274–278 (2003).
23. D'Arrigo, R., Wilson, R. & Tudhope, A. The impact of volcanic forcing on tropical temperatures during the past four centuries. *Nat. Geosci.* **2**, 51–56 (2009).
24. McGregor, S., Timmermann, A. & Timm, O. A unified proxy for ENSO and PDO variability since 1650. *Climate* **6**, 1–17 (2010).
25. Wilson, R. et al. Reconstructing ENSO: the influence of method, proxy data, climate forcing and teleconnections. *J. Quat. Sci.* **25**, 62–78 (2010).
26. Liu, F. et al. Divergent El Niño responses to volcanic eruptions at different latitudes over the past millennium. *Clim. Dyn.* **50**, 3799–3812 (2018).
27. McGregor, S. et al. The effect of strong volcanic eruptions on ENSO. *El Niño Southern Oscillation in a Changing Climate*, 267–287 (2020).
28. Robock, A. Comment on "No consistent ENSO response to volcanic forcing over the last millennium". *Science* **369**, https://doi.org/10.1126/science.abc0502 (2020).
29. Mann, M. E., Cane, M. A., Zebiak, S. E. & Clement, A. Volcanic and solar forcing of the tropical Pacific over the past 1000 years. *J. Clim.* **18**, 447–456 (2005).
30. Maher, N., McGregor, S., England, M. H. & Gupta, A. S. Effects of volcanism on tropical variability. *Geophys. Res. Lett.* **42**, 6024–6033 (2015).
31. Predybaylo, E., Stenchikov, G. L., Wittenberg, A. T. & Zeng, F. Impacts of a Pinatubo-size volcanic eruption on ENSO. *J. Geophys. Res.: Atmos.* **122**, 925–947 (2017).
32. Ohba, M., Shiogama, H., Yokohata, T. & Watanabe, M. Impact of strong tropical volcanic eruptions on ENSO simulated in a coupled GCM. *J. Clim.* **26**, 5169–5182 (2013).
33. Khodri, M. et al. Tropical explosive volcanic eruptions can trigger El Niño by cooling tropical Africa. *Nat. Commun.* **8**, 778 (2017).
34. Coupe, J. et al. Nuclear Niño response observed in simulations of nuclear war scenarios. *Commun. Earth Environ.* **2**, 18 (2021).
35. Sigl, M. et al. Timing and climate forcing of volcanic eruptions for the past 2,500 years. *Nature* **523**, 543–549 (2015).

36. Feng, S., Hu, Q., Wu, Q. & Mann, M. E. A gridded reconstruction of warm season precipitation for Asia spanning the past half millennium. *J. Clim.* **26**, 2192–2204 (2013).
37. Shi, F., Zhao, S., Guo, Z., Goosse, H. & Yin, Q. Multi-proxy reconstructions of May–September precipitation field in China over the past 500 years. *Climate* **13**, 1919–1938 (2017).
38. Shi, H., Wang, B., Cook, E. R., Liu, J. & Liu, F. Asian summer precipitation over the past 544 years reconstructed by merging tree rings and historical documentary records. *J. Clim.* **31**, 7845–7861 (2018).
39. Ropelewski, C. F. & Halpert, M. S. Global and regional scale precipitation patterns associated with the El Niño/southern oscillation. *Monthly Weather Rev.* **115**, 1606–1626 (1987).
40. Clement, A. C., Seager, R., Cane, M. A. & Zebiak, S. E. An ocean dynamical thermostat. *J. Clim.* **9**, 2190–2196 (1996).
41. Bjerknes, J. Atmospheric teleconnections from the equatorial Pacific. *Monthly Weather Rev.* **97**, 163–172 (1969).
42. Wang, B., Xiang, B. & Lee, J.-Y. Subtropical high predictability establishes a promising way for monsoon and tropical storm predictions. *Proc. Natl Acad. Sci. USA* **110**, 2718–2722 (2013).
43. Wang, B., Li, J. & He, Q. Variable and robust East Asian monsoon rainfall response to El Niño over the past 60 years (1957–2016). *Adv. Atmos. Sci.* **34**, 1235–1248 (2017).
44. Singh, M. et al. Fingerprint of volcanic forcing on the ENSO–Indian monsoon coupling. *Sci. Adv.* **6**, eaba8164 (2020).
45. Paik, S., Min, S.-K., Iles, C. E., Fischer, E. M. & Schurer, A. P. Volcanic-induced global monsoon drying modulated by diverse El Niño responses. *Sci. Adv.* **6**, eaba1212 (2020).
46. Sun, W. et al. A "La Niña-like" state occurring in the second year after large tropical volcanic eruptions during the past 1500 years. *Clim. Dyn.* **52**, 7495–7509 (2019).
47. Liu, F. et al. Global monsoon precipitation responses to large volcanic eruptions. *Sci. Rep.* **6**, 1–11 (2016).
48. Chai, J. et al. A robust equatorial Pacific westerly response to tropical volcanism in multiple models. *Clim. Dyn.* **55**, 3413–3429 (2020).
49. Dee, S. G. et al. No consistent ENSO response to volcanic forcing over the last millennium. *Science* **367**, 1477–1481 (2020).
50. Zhu, F. et al. A re-appraisal of the ENSO response to volcanism with paleoclimate data assimilation. *Nat. Commun.* **13**, 747 (2022).
51. Colose, C., LeGrande, A. & Vuille, M. The influence of volcanic eruptions on the climate of tropical South America during the last millennium in an isotope-enabled general circulation model. *Climate* **12**, 961–979 (2016).
52. Stevenson, S., Otto-Bliesner, B., Fasullo, J. & Brady, E. "El Niño like" hydroclimate responses to last millennium volcanic eruptions. *J. Clim.* **29**, 2907–2921 (2016).
53. Zuo, M., Zhou, T. & Man, W. Hydroclimate responses over global monsoon regions following volcanic eruptions at different latitudes. *J. Clim.* **32**, 4367–4385 (2019).
54. Gao, C.-C., Yang, L.-S. & Liu, F. Hydroclimatic anomalies in China during the post-Laki years and the role of concurring El Niño. *Adv. Clim. Change Res.* **12**, 187–198 (2021).
55. Erez, M. & Adam, O. Energetic constraints on the time-dependent response of the ITCZ to volcanic eruptions. *J. Clim.* **34**, 9989–10006 (2021).
56. Coupe, J. & Robock, A. The influence of stratospheric soot and sulfate aerosols on the northern hemisphere wintertime atmospheric circulation. *J. Geophys. Res.: Atmos.* **126**, e2020JD034513 (2021).
57. Duchon, C. E. Lanczos filtering in one and two dimensions. *J. Appl. Meteorol. Climatol.* **18**, 1016–1022 (1979).
58. Rayner, N. A. et al. Global analyses of sea surface temperature, sea ice, and night marine air temperature since the late nineteenth century. *J. Geophys. Res.: Atmos.* **108**, https://doi.org/10.1029/2002JD002670 (2003).
59. Bellenger, H., Guilyardi, E., Leloup, J., Lengaigne, M. & Vialard, J. ENSO representation in climate models: from CMIP3 to CMIP5. *Clim. Dyn.* **42**, 1999–2018 (2014).
60. Gao, C., Robock, A. & Ammann, C. Volcanic forcing of climate over the past 1500 years: an improved ice core-based index for climate models. *J. Geophys. Res.: Atmos.* **113**, https://doi.org/10.1029/2008JD010239 (2008).
61. Crowley, T. J. et al. Volcanism and the little ice age. *PAGES N.* **16**, 22–23 (2008).
62. Wang, B. & Fan, Z. Choice of South Asian summer monsoon indices. *Bull. Am. Meteorol. Soc.* **80**, 629–638 (1999).
63. Hsu, P.-C. et al. Increase of global monsoon area and precipitation under global warming: a robust signal? *Geophys. Res. Lett.* **39**, https://doi.org/10.1029/2012GL051037 (2012).

Acknowledgements

F.L. is supported by the National Natural Science Foundation of China (Grant 41975107). C.G. is supported by the National Natural Science Foundation of China (Grant 41875092). A.R. is supported by the U.S. National Science Foundation grant AGS-2017113. B.W. acknowledges support from U.S. National Science Foundation grant 2025057. G.H. is supported by the National Natural Science Foundation of China (Grant 41721004, 41831175).

Author contributions

F.L., C.G., and B.W. conceptualized and led the work. F.L., C.G., and J.C. contributed to data analysis including validation and interpretation of the results. F.L., C.G., A.R., and B.W. wrote the manuscript, J.L., X.Z., G.H., and W.D. reviewed and edited the manuscript.

Competing interests

The authors declare no competing interests.

Additional information

Supplementary information The online version contains supplementary material available at https://doi.org/10.1038/s41467-022-31108-7.

Correspondence and requests for materials should be addressed to Chaochao Gao or Bin Wang.

Peer review information *Nature Communications* thanks Ori Adam and the other, anonymous, reviewer(s) for their contribution to the peer review of this work. Peer reviewer reports are available.

Reprints and permission information is available at http://www.nature.com/reprints

Publisher's note Springer Nature remains neutral with regard to jurisdictional claims in published maps and institutional affiliations.

Open Access This article is licensed under a Creative Commons Attribution 4.0 International License, which permits use, sharing, adaptation, distribution and reproduction in any medium or format, as long as you give appropriate credit to the original author(s) and the source, provide a link to the Creative Commons license, and indicate if changes were made. The images or other third party material in this article are included in the article's Creative Commons license, unless indicated otherwise in a credit line to the material. If material is not included in the article's Creative Commons license and your intended use is not permitted by statutory regulation or exceeds the permitted use, you will need to obtain permission directly from the copyright holder. To view a copy of this license, visit http://creativecommons.org/licenses/by/4.0/.

© The Author(s) 2022

OCEANOGRAPHY

Greenhouse warming intensifies north tropical Atlantic climate variability

Yun Yang[1,2]*, Lixin Wu[3], Ying Guo[1], Bolan Gan[3], Wenju Cai[3,4], Gang Huang[2,5,6], Xichen Li[7], Tao Geng[3], Zhao Jing[3], Shujun Li[3], Xi Liang[8], Shang-Ping Xie[9]

Copyright © 2021 The Authors, some rights reserved; exclusive licensee American Association for the Advancement of Science. No claim to original U.S. Government Works. Distributed under a Creative Commons Attribution NonCommercial License 4.0 (CC BY-NC).

Variability of North Tropical Atlantic (NTA) sea surface temperature (SST), characterized by a near-uniform warming at its positive phase, is a consequential mode of climate variability. Modulated by El Niño–Southern Oscillation (ENSO) and the North Atlantic Oscillation, NTA warm anomalies tend to induce La Niña events, droughts in Northeast Brazil, increased frequency of extreme hurricanes, and phytoplankton blooms in the Guinea Dome. Future changes of NTA variability could have profound socioeconomic impacts yet remain unknown. Here, we reveal a robust intensification of NTA variability under greenhouse warming. This intensification mainly arises from strengthening of ENSO-forced Pacific-North American pattern and tropospheric temperature anomalies, as a consequence of an eastward shift of ENSO-induced equatorial Pacific convection and of increased ENSO variability, which enhances ENSO influence by reinforcing the associated wind and moist convection anomalies. The intensification of NTA SST variability suggests increased occurrences of extreme NTA events, with far-reaching ramifications.

INTRODUCTION

Variability of North Tropical Atlantic (NTA) sea surface temperature (SST) (hereafter the NTA) typically peaks in boreal spring (March, April, and May, MAM1, where "1" refers to the current year) and is characterized by basin-wide SST warming at its positive phase (*1*, *2*). Coupled with a latitudinal movement of the intertropical convergence zone, the NTA profoundly influences precipitation in Northeast Brazil and Sahel (*3*–*6*). An anomalous NTA warming during 1979 to 1981 induced severe drought in Northeast Brazil, leading to a more than 70% reduction in production of rice, beans, and cotton (*7*). An intense NTA warming contributed to the 2012 to 2016 drought in Northeast Brazil, affecting 33.4 million people and resulting in losses of U.S. $30 billion (*8*). By modulating the intensity, number, and track pattern of Atlantic tropical cyclones, an NTA warm event increases the number of major hurricanes and their landfall frequency along the U.S. East Coast (*9*–*12*). Moreover, the NTA has a prominent influence on the Guinea Dome (*13*), chlorophyll-α concentration, and ecosystems (*14*, *15*). In addition to regional influences, the NTA exerts its climatic impacts over the globe, including El Niño–Southern Oscillation (ENSO) in the Pacific (*16*), sea ice distribution in the Antarctic (*17*), and anomalous global mean temperature (*18*). Because of these severe effects, determining the response of NTA to greenhouse warming is an issue of great importance.

The NTA mainly arises from latent heat flux anomalies associated with anomalous northeasterly trades (*19*–*21*). Specifically, the wind-evaporation-SST feedback (*22*), mainly confined to the deep tropics, contributes to the development of anomalous SST (*23*, *24*), but forcings outside of the tropical Atlantic are required to reinforce the NTA temperature anomaly (*2*, *25*, *26*). The North Atlantic Oscillation (NAO) is one such forcing (*27*, *28*). During a negative NAO event, the northeasterly trades weaken in response to a slackened Subtropical High, reducing surface latent heat flux and leading to an anomalous NTA warming. Another important forcing comes from ENSO (*29*, *30*), which exerts its influence in several pathways. During El Niño, tropospheric temperature over the central and eastern equatorial Pacific increases and propagates eastward in the form of equatorial Kelvin waves, which reduces moist convection over the northern tropical Atlantic and gives rise to warm SST anomalies, a process referred to as "tropospheric temperature" mechanism (*20*, *31*). Furthermore, convective anomalies associated with increased precipitation in the western and central equatorial Pacific excite the Pacific–North American (PNA) pattern (*32*), a Rossby wave train with a ridge over the western North America and troughs over the Aleutians and the southeastern United States. In response, the northeasterly trades weaken over the northern tropical Atlantic, reducing evaporation and generating warm SST anomalies. In addition, El Niño induces a negative diabatic heating over the Amazon basin, which, in turn, generates an anomalous Atlantic Hadley circulation (*33*) and a Gill-type response (*34*), contributing to the weakened northeasterly trades.

Despite the advances described above, how the NTA may respond to greenhouse warming remains unknown. Below, we show that most of the Coupled Model Intercomparison Project Phase 6 (CMIP6) models simulate an increase in NTA variability.

RESULTS

Observed NTA SST variability

To identify the observed NTA, we applied empirical orthogonal function (EOF) analysis to quadratically detrended SST anomalies (see the "EOF analysis" section in Materials and Methods) averaged

[1]College of Global Change and Earth System Science, Beijing Normal University, Beijing, China. [2]State Key Laboratory of Numerical Modeling for Atmospheric Sciences and Geophysical Fluid Dynamics, Institute of Atmospheric Physics, Chinese Academy of Sciences, Beijing, China. [3]Key Laboratory of Physical Oceanography/Institute for Advanced Ocean Studies, Ocean University of China and Qingdao National Laboratory for Marine Science and Technology, Qingdao, China. [4]Centre for Southern Hemisphere Oceans Research (CSHOR), CSIRO Oceans and Atmosphere, Hobart, Tasmania, Australia. [5]Laboratory for Regional Oceanography and Numerical Modeling, Qingdao National Laboratory for Marine Science and Technology, Qingdao, China. [6]University of Chinese Academy of Sciences, Beijing, China. [7]Institute of Atmospheric Physics, Chinese Academy of Sciences, Beijing, China. [8]Key Laboratory of Research on Marine Hazards Forecasting, National Marine Environmental Forecasting Center, Beijing, China. [9]Scripps Institution of Oceanography, University of California, San Diego, La Jolla, CA 92037, USA.
*Corresponding author. Email: yunyang@bnu.edu.cn

Downloaded from http://advances.sciencemag.org/ on August 25, 2021

over boreal spring when the NTA reaches its peak. Here, we take the normalized principal component (PC) time series as the NTA index. Given that ENSO can trigger NAO events (*35*, *36*), a partial regression (partial correlation) is conducted to extract the "pure" NAO influence on (connection with) the NTA (see the "Partial regression" and "Partial correlation" sections in Materials and Methods).

As the leading mode in boreal spring, the observed NTA accounts for 64% of the total SST variance (fig. S1). It is tightly related with ENSO and the NAO in previous winter (December, January, and February, D0JF1, where "0" refers to the previous year), due to their influence on northeasterly trades and latent heat flux (Fig. 1, A and B). The (partial) correlation coefficient between MAM1 NTA and D0JF1 ENSO (NAO) reaches 0.59 (−0.5) over the period of 1951 to 2014 (red star, Fig. 1C).

Model selection

We conducted similar EOF analysis using outputs from 23 CMIP6 models that are forced with historical forcing during the same period (1951 to 2014) as in observations. EOF analysis is useful in extracting the pattern of NTA variability, allowing models to have different spatial patterns. The NTA emerges as the first EOF mode in each model, consistent with the observations. However, several models underestimate the NTA connections with ENSO or the NAO (Fig. 1C). Among them, 16 models produce reasonable connections, with both correlation coefficients exceeding 50% in amplitude of the observed values. These models reproduce reasonably well the observed influences from ENSO and the NAO (Fig. 1, A and B versus D and E), with maximum wind and SST anomalies located over the NTA center (box in Fig. 1), although in most models, the influence is underestimated for both ENSO and the NAO. By comparison, the remaining seven models, featuring a westward (northward) shift of anomalous trades, generate weaker SST and wind responses to ENSO (the NAO) forcing (Fig. 1, A and B versus F and G). These wind shifts are related to a westward-displaced ENSO center (*37*, *38*) and an underestimated magnitude of NAO variability simulated in models (*2*, *39*). Nevertheless, the selected models reasonably simulate the amplitude of observed NTA variability (0.40°C, defined by SST SD averaged over the NTA center), with a range from 0.30° to 0.46°C and an ensemble mean of 0.35°C. Therefore, we use the 16 models that realistically simulate the connections with ENSO and the NAO to study the response of the NTA to greenhouse warming.

Increased NTA variability in the future climate

We performed EOF analysis to quadratically detrended MAM1 SST anomalies over the period of 1900 to 2099 in the 16 selected models. These models are forced with historical forcing until 2014 and with Shared Socioeconomic Pathways (SSP) 2-4.5 emission scenario from 2015 onward. We compared the SD of NTA variability between the present (1900 to 1999) and future (2000 to 2099) climate. A total of 12 of the 16, or 75%, selected models simulate increased NTA variability (Fig. 2A). The ensemble mean increase is 8.3%, significant above the 95% confidence level according to a bootstrap test (see the "Bootstrap test" section in Materials and Methods) (fig. S2A). This increase is underpinned by a robust (15 of the 16 selected models) enhancement of SST variability averaged over the NTA center (fig. S3A), with a significant ensemble mean increase of 10% (fig. S3B).

In association, occurrences of extreme NTA events, defined as |PC| greater than 1.75 SD, become more frequent under greenhouse warming (Fig. 2B). Aggregated over the 16 models, the frequency increases by 38%, from 1 event every 14.7 years (109 events in 1600 years) in the present period to 1 event every 10.7 years (150 events in 1600 years) in the future period. This increase in frequency enjoys a strong intermodel consensus (Fig. 2B) and an ensemble mean increase significant above the 95% confidence level (fig. S2B). In addition, the frequency of extreme events increases by 21 or 57%, when using threshold values of 1.5 or 2.0 SD, respectively, further supporting our result.

A sensitivity test further reveals that the increase in NTA variability is not sensitive to model selection. Even when all the 23 models are considered, the intermodel consensus on the increased NTA variability is still significant, with 16 of the 23 models (70%) producing an increase (fig. S4A). Identically, the increased frequency of extreme NTA events is still robust when considering all the 23 models (fig. S4B).

Enhancement in ENSO influence under greenhouse warming

An ensemble mean of the NTA response to NAO forcing barely changes in the future climate, indicating a minor role of the NAO in driving increased NTA variability (fig. S5). Instead, a change in ENSO teleconnection and in ENSO variability under greenhouse warming is the key driver of the increase in variability of the NTA.

To describe ENSO, we use Niño3.4 index normalized by the SD over the full 200 years to enhance intermodel comparability. Total response of the NTA to ENSO forcing in each period is calculated by regressing the NTA onto the Niño3.4 index and then multiplying the regression coefficient by 1 SD value of the Niño3.4 index. A comparison of the total response shows a substantial enhancement in a warming climate (Fig. 3A) (see the "Regression analysis" section in Materials and Methods). The enhanced response to ENSO is found consistently in all the 16 models except one (94% of the models), with an ensemble mean enhancement of 20% (from 0.56 in the present climate to 0.67 in the future climate) statistically significant according to a bootstrap test (Fig. 3B). In association, ENSO influence strengthens (Fig. 3, C and D), contributing to the increase in NTA variability. Specifically, models with a greater enhancement of NTA response to ENSO forcing produce a larger increase in NTA variability, and the intermodel correlation between changes in NTA response to ENSO and in NTA variability reaches 0.83 (Fig. 3E). Moreover, the enhanced NTA response to ENSO forcing is related to more frequent extreme NTA events, while that to the NAO forcing barely contributes (fig. S6).

An eastward intensification of ENSO teleconnection

The enhanced NTA response to ENSO forcing is, in part, induced by an eastward shift of ENSO-induced response in convection (Fig. 4A). In the present climate, precipitation response to ENSO is centered over the western equatorial Pacific (fig. S7A). Under greenhouse warming, these anomalies intensify in the central to eastern equatorial Pacific (black box, fig. S7B), suggesting an eastward shift of convective anomalies (*40*–*44*). This shift in convection strengthens the sensitivity of PNA teleconnection to ENSO forcing (*40*), especially over the lobe of southeast United States, as seen in sensitivity of 200-hPa geopotential height anomalies to the Niño3.4 index (fig. S8). Specifically, 14 of 16 (88%) models produce a deepening of low-pressure anomalies, with an ensemble mean increase of 39%.

Increased ENSO variability

In addition, ENSO variability increases in a warming climate, enhancing its remote forcing on NTA variability (Fig. 4B). A total of

Downloaded from http://advances.sciencemag.org/ on August 25, 2021

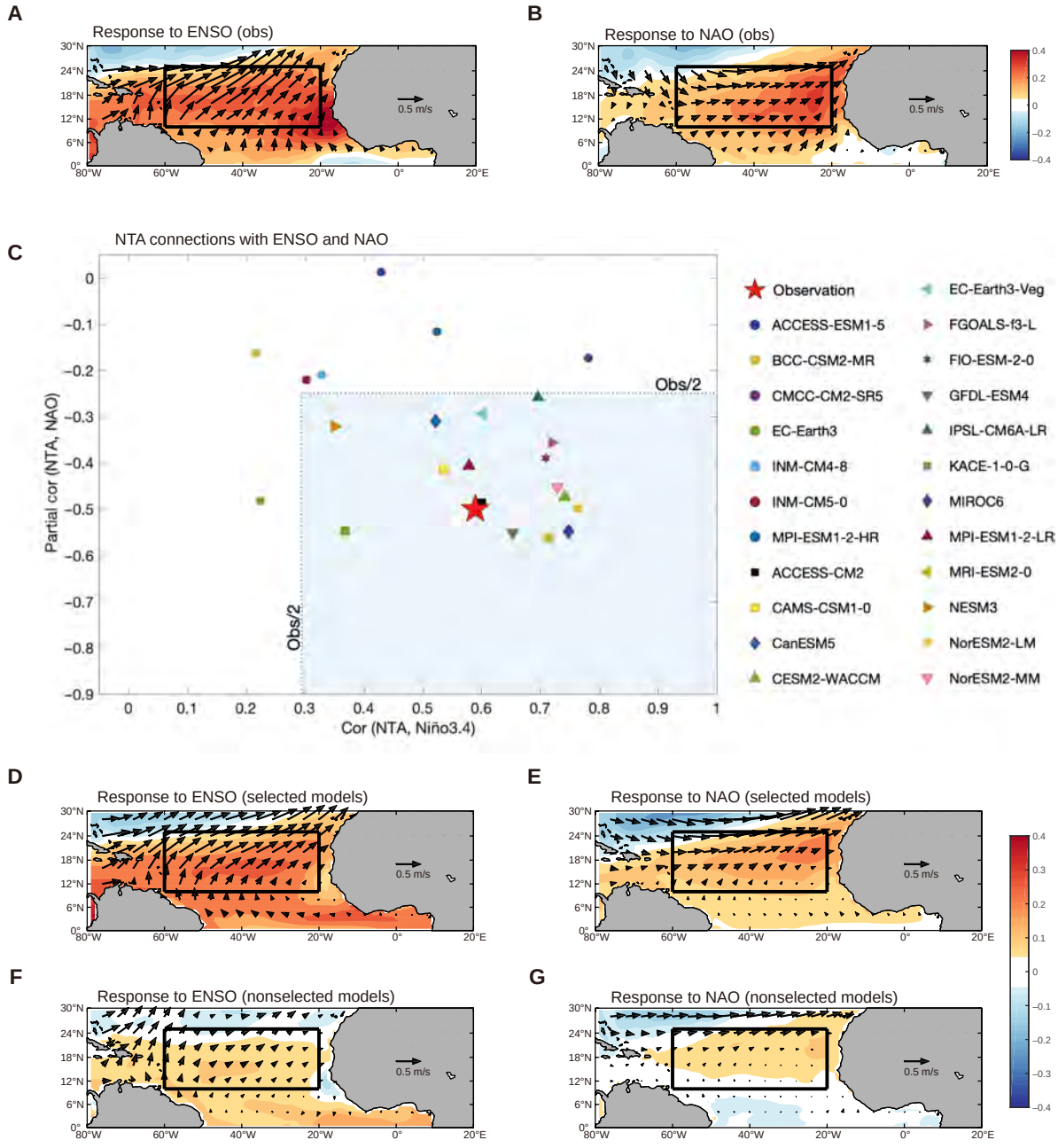

Fig. 1. NTA connections with ENSO and the NAO in observation and CMIP6 models. (**A**) Response of MAM1 SST (°C, color shading) and FMA1 wind (meters per second, vector) to observed Niño3.4 over the period of 1951 to 2014, calculated by regressing SST and wind anomalies onto Niño3.4 index and then multiplying the regression coefficients by 1 SD value of Niño3.4 index. (**B**) Same as (A) except for partial regression against an NAO index (reversed sign) by removing variability associated with Niño3.4 index (see the "Partial regression" and "EOF analysis" sections in Materials and Methods for NTA, NAO, and Niño3.4 indices). (**C**) Correlation coefficients between the NTA and Niño3.4 (*x* axis) and partial correlation coefficients between the NTA and the NAO (*y* axis; see the "Partial correlation" section in Materials and Methods). The large red-filled star indicates the observed value. In seven models, marked by circles, two generate an NTA-ENSO correlation and six produce an NTA-NAO correlation that are smaller than 50% in amplitude of the observations. These are referred as nonselected models. The remaining 16 models in blue quadrant are selected models. The dashed lines represent 50% of the observed values. (**D** and **E**) Same as (A) and (B) but for an ensemble mean of 16 selected models. (**F** and **G**) Same as (A) and (B) but for an average of the two models that produce a too-weak connection between the NTA and ENSO (correlation coefficients lower than 50% of the observed) (F) and for an ensemble mean of the six models that fail to generate the connection with the NAO (G). The boxes represent the NTA center (10°N to 25°N and 60°W to 20°W).

12 of the 16 (75%) models produce increased Niño3.4 variability, with an ensemble mean increase of 11% (fig. S9). When all 23 models are considered, an increase in variability is simulated by 16 of the 23 (70%) models (fig. S4C), consistent with previous findings of enhanced variability in both eastern Pacific and central Pacific El Niño (*45*). The enhancement in ENSO variability further strengthens the ENSO-forced response in PNA teleconnection. Here, we examine the total change in the PNA teleconnection that includes change in PNA

Downloaded from http://advances.sciencemag.org/ on August 25, 2021

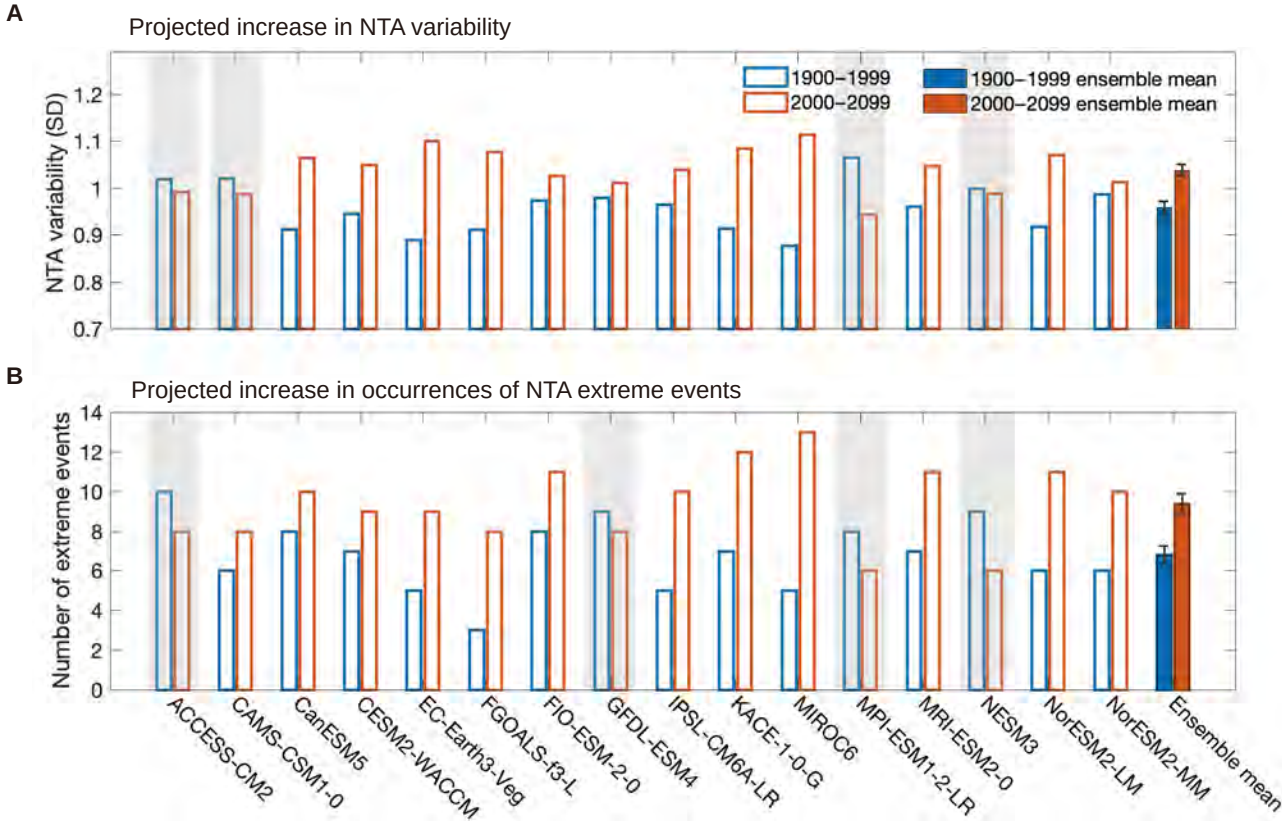

Fig. 2. Projected increase in NTA variability and occurrences of extreme NTA events. (**A**) Comparison of the NTA SD over the present (1900 to 1999, blue-edged bars) and future (2000 to 2099, red-edged bars) periods in the 16 selected models. (**B**) Same as (A), but for the number of extreme events (|PC| > 1.75 SD). The multimodel ensemble means over the present and future periods are shown in blue-filled and red-filled bars, respectively; error bars are calculated as 1 SD of a total of 10,000 interrealizations of a bootstrap method (see the "Bootstrap test" section in Materials and Methods); models that simulate a reduction are grayed out. Variability of the NTA and the frequency of extreme NTA events are projected to increase under greenhouse warming.

sensitivity to ENSO and change in ENSO variability itself. Hence, for each individual period, we regress geopotential height anomalies onto the Niño3.4 index and then multiply the regression coefficients by 1 SD value of the Niño3.4 index. In this case, a deepening of the low-pressure anomalies over the southeast United States is simulated by 15 of the 16 models (94%), with an ensemble increase reaching 53% (Fig. 4, C to E). The strengthening of PNA teleconnection is also seen in sea level pressure anomalies (fig. S10).

Consequence of enhanced ENSO teleconnections

As a result of the intensification of the PNA pattern, ENSO-forced response in wind is enhanced over the northern tropical Atlantic (Fig. 3, C and D), with a maximum increase north of 15°N. The enhanced wind speed response, with an ensemble mean increase of 21%, significantly contributes to the increase in the NTA response to ENSO forcing (Fig. 5A). The intermodel correlation between changes in the wind response and in the NTA response reaches −0.83.

In addition, SST of the NTA center becomes more sensitive to wind forcing, as seen in MAM1 SST anomalies regressed onto unnormalized February, March, April (FMA1) wind speed anomalies (fig. S11A), which measures the sensitivity of SST to 1 m/s of wind speed change. In a warming climate, the ocean mixed layer depth shoals over the northern tropical Atlantic, a robust feature among all models (using all models with available outputs; fig. S11B). This shoaling arises from an intensification of oceanic stratification (*46*–*48*) and from a weakening of climatological northeasterly trades (using all models with available outputs; fig. S11, C and D). As a result of the shallower mixed layer, SST response to a given wind forcing increases in most of the models. However, its contribution to the NTA response to ENSO forcing is not statistically significant and therefore plays a minor role (fig. S11E).

Furthermore, under greenhouse warming, tropospheric temperature anomalies are intensified due to increased ENSO variability (fig. S12) and an amplified vapor response to ENSO (*49*), contributing to the enhanced NTA response to ENSO forcing (Fig. 5B). An intermodel correlation between changes in ENSO-forced response of tropospheric temperature and changes in the NTA response to ENSO forcing ($R = 0.63$), although not as high as that between changes in ENSO-forced response of wind speed and changes in the NTA response to ENSO forcing ($R = -0.83$; Fig. 5A), indicates a substantial contribution from the tropospheric temperature mechanism.

DISCUSSION

ENSO-forced responses in PNA teleconnection and tropospheric temperature are important mechanisms in driving the variability of NTA (Fig. 6A). Both of these mechanisms enhance under greenhouse warming, due to an eastward shift of ENSO-induced response in equatorial Pacific convection and an enhancement of ENSO

Downloaded from http://advances.sciencemag.org/ on August 25, 2021

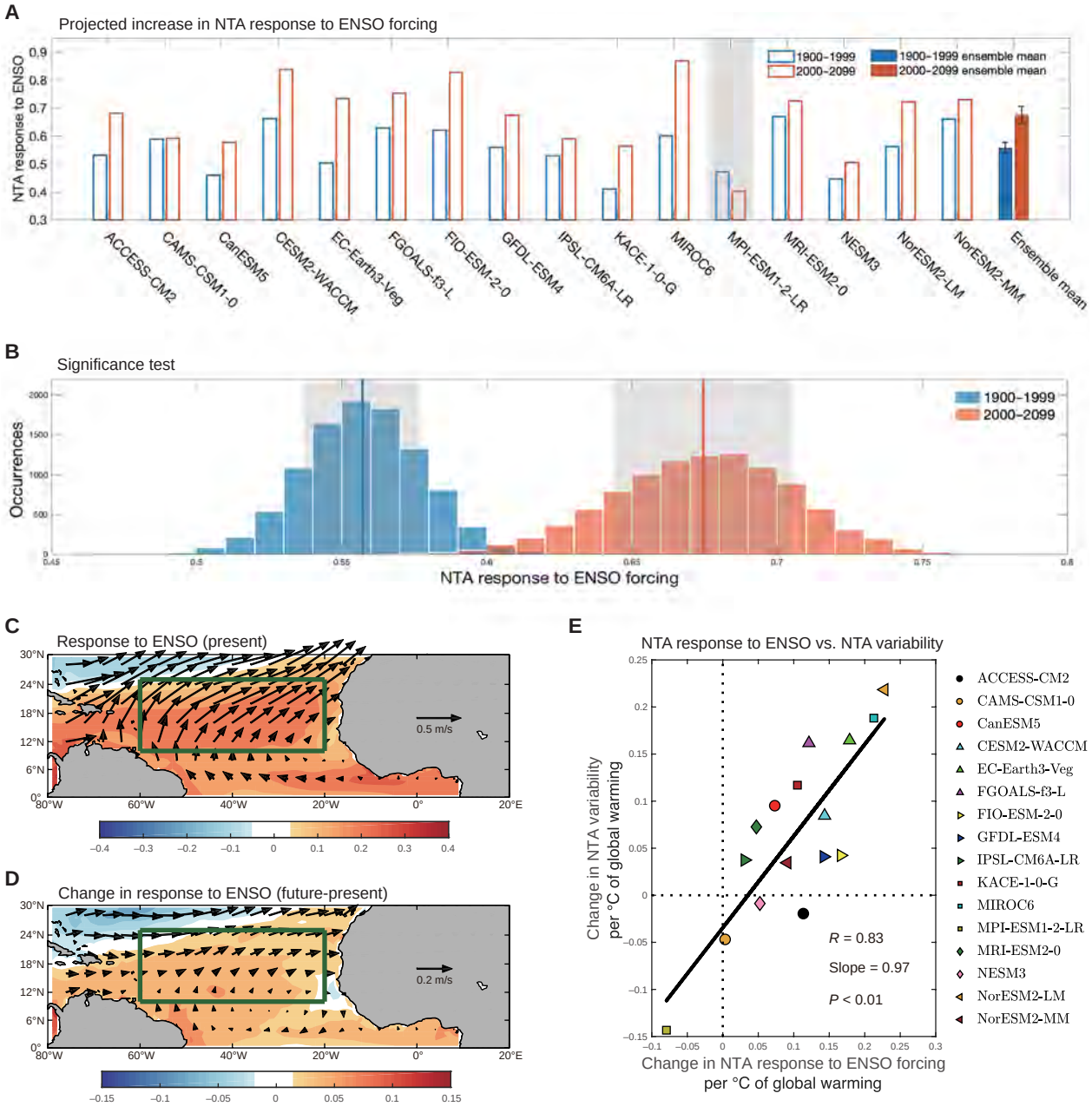

Fig. 3. Change in NTA response to ENSO forcing and the projected increase in NTA variability. (**A**) Comparison of NTA response to ENSO forcing (SD) over the present (1900 to 1999, blue-edged bars) and future (2000 to 2099, red-edged bars) periods in the 16 selected models. The multimodel ensemble means over the present and future periods are shown in blue-filled and red-filled bars, respectively; error bars are calculated as 1 SD of a total of 10,000 inter-realizations of a bootstrap method (see the "Bootstrap test" section in Materials and Methods); models that simulate a reduction are grayed out. (**B**) Histograms of 10,000 realizations of a bootstrap method for NTA response to ENSO forcing in the present (1900 to 1999, blue) and future (2000 to 2099, red) climate. The blue and red lines indicate the mean values of the 10,000 realizations for the present and future periods, respectively. The gray shaded areas refer to the respective 1 SD of the 10,000 realizations. (**C** and **D**) Response of MAM1 SST (°C, color shading) and FMA1 surface winds to ENSO (meters per second, vector), in the present climate (C) and their projected changes (future minus present) (D). Green boxes (10°N to 25°N, 60°W to 20°W) represent the NTA center. (**E**) Intermodel relationship between the change in NTA response to ENSO (SD) and in NTA variability (SD). To enhance intermodel comparability, we scale the changes by an increase in global mean SST of each model. Linear fit (black solid line) is shown together with the correlation coefficient *R*, slope, and *P* value from the regression. The NTA response to ENSO forcing is projected to increase, contributing to enhanced NTA variability.

variability. In association, ENSO-forced responses in wind speed and tropospheric temperature strengthen under greenhouse warming (Fig. 6B), leading to the increase in the amplitude of NTA SST variability and the frequency of extreme NTA events.

We note that most of the models simulate an overly weak relationship between NTA and NAO variability. Although the weak relationship might represent a source of uncertainty, there is no intermodel consensus on a simulated increase in NAO variability

Downloaded from http://advances.sciencemag.org/ on August 25, 2021

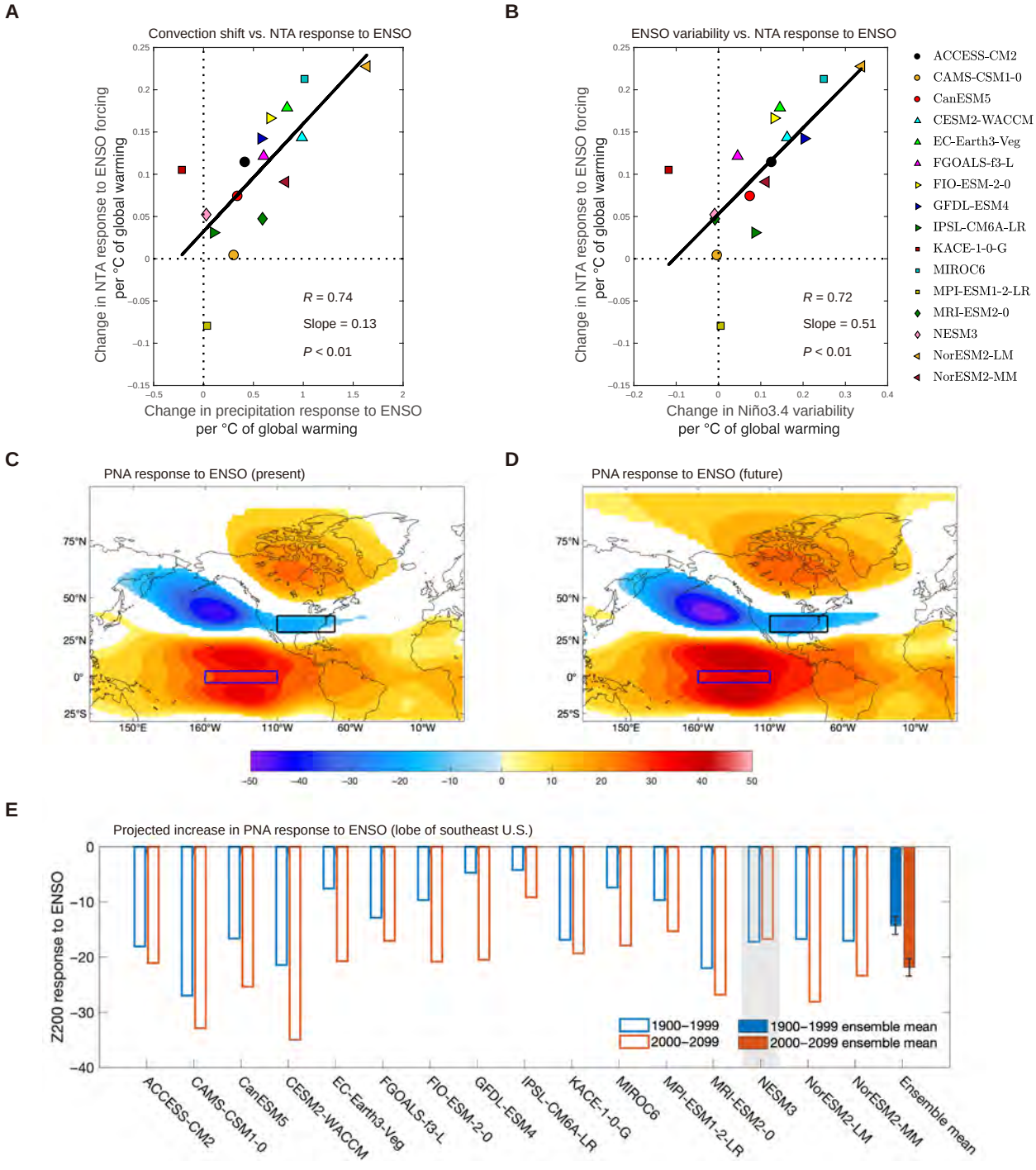

Fig. 4. Strengthening of PNA teleconnection. (**A** and **B**) Intermodel relationships between change in NTA response to ENSO (SD) and in FMA1 precipitation response to ENSO (millimeters per day) averaged over the central to eastern equatorial Pacific [blue boxes in (C) and (D)] (A) and in Niño3.4 variability (SD) (B). To enhance intermodel comparability, we scale the changes by an increase in global mean SST of each model. Linear fits (black solid line) are shown together with the correlation coefficients *R*, slopes, and *P* values from the regression. (**C** and **D**) Multimodel ensemble mean of the D0JF1 200-hPa geopotential height response to ENSO (meters), in the present (1900 to 1999) (C) and future (2000 to 2099) (D) climate. Only values exceeding 1 SD of intermodel spread are shown in color shading. Black and blue boxes represent the PNA center over the southeast United States (30°N to 40°N, 110°W to 70°W) and the central to eastern equatorial Pacific (4°S to 4°N, 160°W to 110°W), respectively. (**E**) Comparison of the D0JF1 200-hPa geopotential height response to ENSO (meters), averaged over the southeast United States [black boxes in (C) and (D)], in the present (1900 to 1999, blue-edged bars) and future (2000 to 2099, red-edged bars) periods in the 16 selected models. The multimodel ensemble means over the present and future periods are shown in blue-filled and red-filled bars, respectively; error bars are calculated as 1 SD of a total of 10,000 inter-realizations of a bootstrap method (see the "Bootstrap test" section in Materials and Methods); models that simulate a reduction are grayed out. The ENSO-induced PNA teleconnection is projected to increase, due to an increase in ENSO variability and an eastward shift of ENSO-induced equatorial Pacific convection.

Downloaded from http://advances.sciencemag.org/ on August 25, 2021

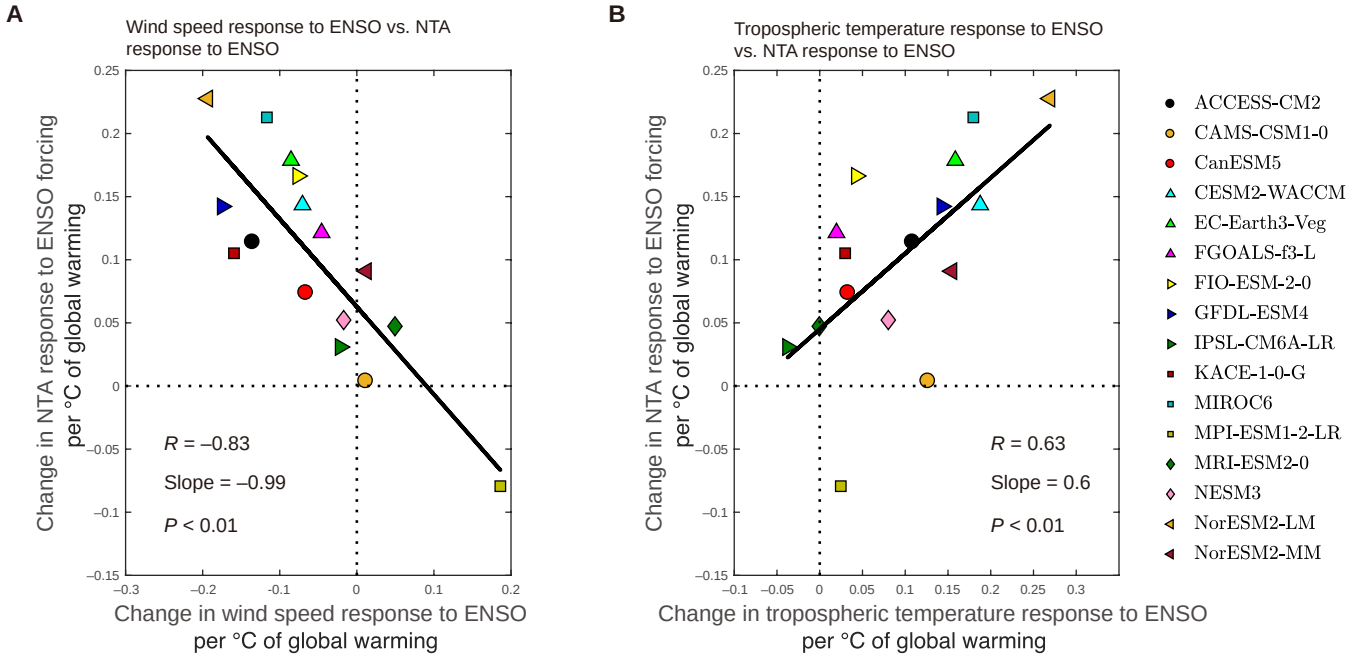

Fig. 5. Mechanism for the projected increase in NTA response to ENSO forcing. Intermodel relationships between change in NTA response to ENSO (SD) and in FMA1 wind speed response to ENSO (meters per second) averaged over the NTA center (**A**) and in tropospheric temperature response to ENSO (°C) averaged over the NTA center (**B**). To enhance intermodel comparability, we scale the changes by an increase in global mean SST of each model. Linear fits (black solid line) are shown together with the correlation coefficients *R*, slopes, and *P* values from the regression. The projected increase in NTA response to ENSO is primarily due to increased ENSO-induced wind speed variability and considerably due to increased ENSO-induced tropospheric temperature variability.

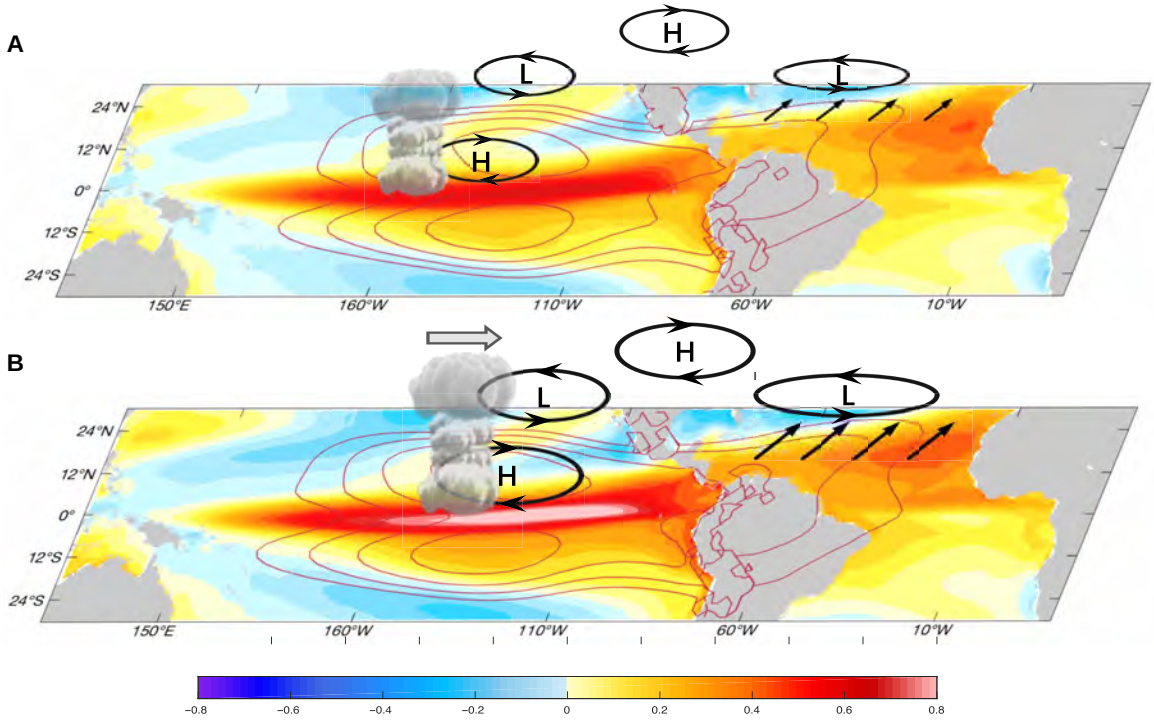

Fig. 6. Schematic diagram of the physical mechanisms responsible for increased NTA variability. ENSO-induced MAM1 SST (color shading), wind (vectors), tropospheric temperature (red contour), convection (cloud) anomalies, and the associated PNA (high/low-pressure anomalies) teleconnection seen in the present-day climate (**A**) intensify and undergo an eastward shift (marked by the gray arrow) as greenhouse warming proceeds into the future climate (**B**), leading to increased NTA variability in the future climate. H, high; L, low.

Downloaded from http://advances.sciencemag.org/ on August 25, 2021

(*39*), indicating an inconsequential impact from NAO variability on the increase in NTA variability. This result could change if there is a forced NAO signal that is currently underestimated (*50*). Other biases are found over the tropical Atlantic and the Pacific, for example, a bias of a double intertropical convergence zone over the Atlantic and a weaker-than-observed influence of the tropical Atlantic on ENSO (*51*–*53*). Hence, interactions between NTA variability and ENSO, and ENSO properties, may be affected by model biases. However, the nature of impacts from tropical biases on the change of tropical Atlantic SST variability is not clear, and there is no evidence that these biases may affect the strengthening of ENSO-forced responses in PNA teleconnection and tropospheric temperature, the main factors that force the increase in NTA variability.

Thus, the consequence of an increase in ENSO variability and its teleconnections under greenhouse warming is more severe than previously thought, as the increase can energize dominant modes of climate variability remote from the Pacific, such as the NTA. Given the profound climatic impacts of the NTA in inducing droughts, floods, and extreme Atlantic hurricanes in affected regions, which are projected to increase (*54*, *55*), our results add to the urgency of reducing emissions of greenhouse gases.

MATERIALS AND METHODS

Observed and CMIP6 data

To characterize the NTA connection with ENSO and with the NAO, we use monthly SST reanalysis from Hadley Centre Sea Ice and Sea Surface Temperature dataset version 1.1 (HadISST v1.1) (*56*) during 1951 to 2014 and monthly 200- and 500-hPa geopotential height from the National Centers for Environmental Prediction and the National Center for Atmospheric Research global reanalysis (*57*) for the period of 1951 to 2014. Also, we analyze outputs from 23 CMIP6 models, with historical and ssp2-4.5 emission scenario forcings over the period of 1900 to 2014 and 2015 to 2099, respectively (table S1) (*58*).

EOF analysis

To capture observed and model-simulated NTA variability, EOF analysis (*59*) is performed on quadratically detrended MAM1 SST anomalies over the northern tropical Atlantic (0°N to 30°N and 80°W to 20°E). The NTA index is referred to as the normalized PC time series. To identify the NAO variability, the same approach was applied to quadratically detrended 500-hPa geopotential height over the North Atlantic (20°N to 70°N and 60°W to 0°E) in D0JF1. ENSO is represented by the normalized Niño3.4 index (SST anomalies averaged over 5°S to 5°N and 170°W to 120°W) after quadratically detrended in D0JF1. All data have been quadratically detrended before analysis.

Regression analysis

Regression analysis is conducted to study the influence of B on A. When regressing index A onto index B, we are interested in the sensitivity of A to B. When regressing A onto B and multiplying the slope by the SD of B, we are interested in the total response of A to B, resulting from the sensitivity of A to B and SD of B.

Bootstrap test

Bootstrap test (*60*) is conducted to examine whether a change is statistically significant. A total of 10,000 realizations are conducted to obtain the mean from the 16 selected models. Each realization is averaged over 16 samples that are independently and randomly resampled from the 16 selected models. In this resampling process, any model is allowed to be selected more than once. The SD of the 10,000 realizations is calculated for each period. If the mean value difference between the future and present periods is greater than the sum of the two separate 10,000-realization SD values, then the change is statistically significant above 95% confidence level.

Partial correlation

To exclude ENSO influence and achieve the "pure" relationship between the NAO and NTA, a partial correlation analysis is applied

$$R_{Y(B|A)} = \frac{R_{YB} - R_{YA} * R_{AB}}{\sqrt{1 - R_{YA}{}^2} * \sqrt{1 - R_{AB}{}^2}} \quad (1)$$

where Y, B, and A represent the variables (such as the NTA), the NAO index, and Niño3.4 index, respectively. R denotes the correlation coefficient, and $R_{Y(B|A)}$ for partial correlation coefficient between the variable Y and NAO index (B), after the influence of ENSO (A) is removed from NAO (B).

Partial regression

To obtain the "pure" influence of NAO, a partial regression analysis is applied to exclude the ENSO influence. The partial regression coefficient is as

$$C_{Y(B|A)} = \frac{R_{YB} - R_{YA} * R_{AB}}{\sqrt{1 - R_{AB}{}^2}} * \frac{S_Y}{S_{B|A}} \quad (2)$$

where $C_{Y(B|A)}$ is the partial regression coefficient between the target variable Y and NAO index (B), after the influence of ENSO (A) is removed from NAO (B). S_Y and $S_{B|A}$ represent the SD of variable Y and NAO (B) after removing the factor Niño3.4 (A).

SUPPLEMENTARY MATERIALS

Supplementary material for this article is available at http://advances.sciencemag.org/cgi/content/full/7/35/eabg9690/DC1

REFERENCES AND NOTES

1. B. Huang, P. S. Schopf, J. Shukla, Coupled ocean–atmosphere variability in the tropical Atlantic Ocean, in *CLIVAR Exchanges*, Vol. 7, No. 3/4 (International CLIVAR Project Office, Southampton, United Kingdom, 2002), pp. 24–27.
2. Y. Yang, S.-P. Xie, L. Wu, Y. Kosaka, J. Li, ENSO forced and local variability of North Tropical Atlantic SST: Model simulations and biases. *Climate Dynam.* **51**, 4511–4524 (2018).
3. S.-P. Xie, J. A. Carton, Tropical Atlantic variability: Patterns, mechanisms, and Impacts, in *Earth's climate* (American Geophysical Union, 2004).
4. S. Hastenrath, Exploring the climate problems of Brazil's Nordeste: A review. *Clim. Change* **112**, 243–251 (2012).
5. A. Giannini, R. Saravanan, P. Chang, Oceanic forcing of Sahel rainfall on interannual to interdecadal time scales. *Science* **302**, 1027–1030 (2003).
6. W. Cai, M. J. McPhaden, A. M. Grimm, R. R. Rodrigues, A. S. Taschetto, R. D. Garreaud, B. Dewitte, G. Poveda, Y.-G. Ham, A. Santoso, B. Ng, W. Anderson, G. Wang, T. Geng, H.-S. Jo, J. A. Marengo, L. M. Alves, M. Osman, S. Li, L. Wu, C. Karamperidou, K. Takahashi, C. Vera, Climate impacts of the El Niño–Southern Oscillation on South America. *Nat. Rev. Earth Environ.* **1**, 215–231 (2020).
7. J. A. Marengo, R. R. Torres, L. M. Alves, Drought in Northeast Brazil—Past, present, and future. *Theor. Appl. Climatol.* **129**, 1189–1200 (2017).
8. J. A. Marengo, L. M. Alves, R. C. S. Alvala, A. P. Cunha, S. Brito, O. L. L. Moraes, Climatic characteristics of the 2010-2016 drought in the semiarid Northeast Brazil region. *An. Acad. Bras. Cienc.* **90**, 1973–1985 (2018).
9. L. Xie, T. Yan, L. J. Pietrafesa, J. M. Morrison, T. Karl, Climatology and interannual variability of North Atlantic hurricane tracks. *J. Climate* **18**, 5370–5381 (2005).

Downloaded from http://advances.sciencemag.org/ on August 25, 2021

10. D. J. Vimont, J. P. Kossin, The Atlantic meridional mode and hurricane activity. *Geophys. Res. Lett.* **34**, L07709 (2007).
11. G. A. Vecchi, B. J. Soden, Effect of remote sea surface temperature change on tropical cyclone potential intensity. *Nature* **450**, 1066–1070 (2007).
12. H. Murakami, E. Levin, T. L. Delworth, R. Gudgel, P.-C. Hsu, Dominant effect of relative tropical Atlantic warming on major hurricane occurrence. *Science* **362**, 794–799 (2018).
13. T. Doi, T. Tozuka, T. Yamagata, Interannual variability of the Guinea Dome and its possible link with the Atlantic Meridional Mode. *Climate Dynam.* **33**, 985–998 (2009).
14. S. R. Signorini, R. G. Murtugudde, C. R. McClain, J. R. Christian, J. Picaut, A. J. Busalacchi, Biological and physical signatures in the tropical and subtropical Atlantic. *J. Geophys. Res.* **104**, 18367–18382 (1999).
15. Y. Pradhan, S. J. Lavender, N. J. Hardman-Mountford, J. Aiken, Seasonal and inter-annual variability of chlorophyll-*a* concentration in the Mauritanian upwelling: Observation of an anomalous event during 1998–1999. *Deep Sea Res. Part II Top Stud. Oceanogr.* **53**, 1548–1559 (2006).
16. Y. G. Ham, J. S. Kug, J. Y. Park, F.-F. Jin, Sea surface temperature in the North Tropical Atlantic as a trigger for El Niño/Southern Oscillation events. *Nat. Geosci.* **6**, 112–116 (2013).
17. X. Li, D. M. Holland, E. P. Gerber, C. Yoo, Impacts of the north and tropical Atlantic Ocean on the Antarctic Peninsula and sea ice. *Nature* **505**, 538–542 (2014).
18. X. Li, S.-P. Xie, S. T. Gille, C. Yoo, Atlantic-induced pan-tropical climate change over the past three decades. *Nat. Clim. Change* **6**, 275–279 (2016).
19. G. R. Foltz, M. J. McPhaden, R. Lumpkin, A strong Atlantic Meridional Mode event in 2009: The role of mixed layer dynamics. *J. Climate* **25**, 363–380 (2012).
20. L. Jiang, T. Li, Relative roles of El Niño-induced extratropical and tropical forcing in generating Tropical North Atlantic (TNA) SST anomaly. *Climate Dynam.* **53**, 3791–3804 (2019).
21. J.-H. Park, T. Li, Interdecadal modulation of El Niño–tropical North Atlantic teleconnection by the Atlantic multi-decadal oscillation. *Climate Dynam.* **52**, 5345–5360 (2019).
22. S.-P. Xie, S. G. H. Philander, A coupled ocean–atmosphere model of relevance to the ITCZ in the eastern Pacific. *Tellus* **46**, 340–350 (1994).
23. P. Chang, L. Ji, H. Li, A decadal climate variation in the tropical Atlantic Ocean from thermodynamic air–sea interactions. *Nature* **385**, 516–518 (1997).
24. L. Wu, Q. Zhang, Z. Liu, Toward understanding tropical Atlantic variability using coupled modeling surgery, in *Earth Climate: The Ocean–Atmosphere Interaction*, vol. 147 (Geophysical monograph series, American Geophysical Union, 2004), pp. 157–170.
25. J. C. H. Chiang, Y. Kushnir, A. Giannini, Deconstructing Atlantic Intertropical Convergence Zone variability: Influence of the local cross-equatorial sea surface temperature gradient, and remote forcing from the eastern equatorial Pacific. *J. Geophys. Res.* **107**, 4004 (2002).
26. D. J. Amaya, M. J. DeFlorio, A. J. Miller, S.-P. Xie, WES feedback and the Atlantic Meridional Mode: Observations and CMIP5 comparisons. *Climate Dynam.* **49**, 1665–1679 (2017).
27. A. Czaja, P. van der Vaart, J. Marshall, A diagnostic study of the role of remote forcing in tropical Atlantic variability. *J. Climate* **15**, 3280–3290 (2002).
28. M. Visbeck, E. P. Chassignet, R. G. Curry, T. Delworth, G. Krahmann, The ocean's response to North Atlantic Oscillation variability, in *The North Atlantic Oscillation: Climate Significance and Environmental Impact*, J. W. Hurrell, Y. Kushnir, G. Ottersen, M. Visbeck, Eds. (Amer. Geophys. Union, 2003), pp. 113–146.
29. R. Saravanan, P. Chang, Interaction between tropical Atlantic variability and El Niño-Southern oscillation. *J. Climate* **13**, 2177–2194 (2000).
30. A. S. Taschetto, R. R. Rodrigues, G. A. Meehl, S. McGregor, M. H. England, How sensitive are the Pacific–tropical North Atlantic teleconnections to the position and intensity of El Niño-related warming? *Climate Dynam.* **46**, 1841–1860 (2016).
31. P. Chang, Y. Fang, R. Saravanan, L. Ji, H. Seidel, The cause of the fragile relationship between the Pacific El Niño and the Atlantic Niño. *Nature* **443**, 324–328 (2006).
32. D. B. Enfield, D. A. Mayer, Tropical Atlantic sea surface temperature variability and its relation to El Niño-Southern Oscillation. *J. Geophys. Res.* **102**, 929–945 (1997).
33. C. Wang, ENSO, Atlantic climate variability, and the Walker and Hadley circulations, in *The Hadley Circulation: Present, Past and Future* (Springer, 2004), pp. 173–202.
34. J. García-Serrano, C. Cassou, H. Douville, A. Giannini, F. J. Doblas-Feyes, Revisiting the ENSO teleconnection to the tropical North Atlantic. *J. Climate* **30**, 6945–6957 (2017).
35. C. Cassou, L. Terray, Dual influence of Atlantic and Pacific SST anomalies on the North Atlantic/Europe winter climate. *Geophys. Res. Lett.* **28**, 3195–3198 (2001).
36. D. R. Fereday, R. Chadwick, J. R. Knight, A. A. Scaife, Tropical rainfall linked to stronger future ENSO-NAO teleconnection in CMIP5 models. *Geophys. Res. Lett.* **47**, e2020GL088664 (2020).
37. N.-C. Lau, M. J. Nath, Impact of ENSO on the variability of the Asian–Australian monsoons as simulated in GCM experiments. *J. Climate* **13**, 4287–4309 (2000).
38. N.-C. Lau, M. J. Nath, Atmosphere–ocean variations in the Indo-Pacific sector during ENSO episodes. *J. Climate* **16**, 3–20 (2003).
39. L. Ning, R. S. Bradley, NAO and PNA influences on winter temperature and precipitation over the eastern United States in CMIP5 GCMs. *Climate Dynam.* **46**, 1257–1276 (2016).
40. Z. Q. Zhou, S.-P. Xie, X. T. Zheng, Q. Liu, H. Wang, Global warming–induced changes in El Niño teleconnections over the North Pacific and North America. *J. Climate* **27**, 9050–9064 (2014).
41. P. Huang, S. P. Xie, Mechanisms of change in ENSO-induced tropical Pacific rainfall variability in a warming climate. *Nat. Geosci.* **8**, 922–926 (2015).
42. W. Cai, S. Borlace, M. Lengaigne, P. Van Rensch, M. Collins, G. Vecchi, A. Timmermann, A. Santoso, M. J. McPhaden, L. Wu, M. H. England, G. Wang, E. Guilyardi, F.-F. Jin, Increasing frequency of extreme El Niño events due to greenhouse warming. *Nat. Clim. Change* **4**, 111–116 (2014).
43. S. B. Power, F. Delage, C. T. Chung, G. Kociuba, K. Keay, Robust twenty-first century projections of El Nino and related precipitation variability. *Nature* **502**, 541–547 (2014).
44. Z. Yan, B. Wu, T. Li, M. Collins, R. Clark, T. Zhou, J. Murphy, G. Tan, Eastward shift and extension of ENSO-induced tropical precipitation anomalies under global warming. *Sci. Adv.* **6**, eaax4177 (2019).
45. W. Cai, G. Wang, B. Dewitte, L. Wu, A. Santoso, K. Takahashi, Y. Yang, A. Carreric, M. McPhaden, Increased variability of Eastern Pacific El Niño under greenhouse warming. *Nature* **564**, 201–206 (2018).
46. Y. Yang, L. Wu, C. Fang, Will global warming suppress North Atlantic Tripole decadal variability? *J. Climate* **25**, 2040–2055 (2012).
47. T. Geng, Y. Yang, L. Wu, On the mechanisms of Pacific Decadal Oscillation Modulation in a warming climate. *J. Climate* **32**, 1443–1459 (2019).
48. S. Li, L. Wu, Y. Yang, T. Geng, W. Cai, B. Gan, Z. Chen, Z. Jing, G. Wang, X. Ma, The Pacific Decadal Oscillation less predictable under greenhouse warming. *Nat. Clim. Change* **10**, 30–34 (2020).
49. K. Hu, G. Huang, P. Huang, Y. Kosaka, S.-P. Xie, Intensification of El Niño-induced atmospheric anomalies under greenhouse warming. *Nat. Geosci.* **14**, 377–382 (2021).
50. D. M. Smith, A. A. Scaife, R. Eade, P. Athanasiadis, A. Bellucci, I. Bethke, R. Bilbao, L. F. Borchert, L.-P. Caron, F. Counillon, G. Danabasoglu, T. Delworth, F. J. Doblas-Reyes, N. J. Dunstone, V. Estella-Perez, S. Flavoni, L. Hermanson, N. Keenlyside, V. Kharin, M. Kimoto, W. J. Merryfield, J. Mignot, T. Mochizuki, K. Modali, P.-A. Monerie, W. A. Müller, D. Nicolí, P. Ortega, K. Pankatz, H. Pohlmann, J. Robson, P. Ruggieri, R. Sospedra-Alfonso, D. Swingedouw, Y. Wang, S. Wild, S. Yeager, X. Yang, L. Zhang, North Atlantic climate far more predictable than models imply. *Nature* **583**, 796–800 (2020).
51. Y. Yang, S.-P. Xie, L. Wu, Y. Kosaka, J. Li, Causes of enhanced SST variability over the equatorial Atlantic and its relationship to the Atlantic zonal mode in CMIP5. *J. Climate* **30**, 6171–6182 (2017).
52. I. Richter, S.-P. Xie, S. K. Behera, T. Doi, Y. Masumoto, Equatorial Atlantic variability and its relation to mean state biases in CMIP5. *Climate Dyn.* **42**, 171–188 (2014).
53. F. Jia, W. Cai, L. Wu, B. Gan, G. Wang, F. Kucharski, P. Chang, N. Keenlyside, Weakening Atlantic Niño–Pacific connection under greenhouse warming. *Sci. Adv.* **5**, eaax4111 (2019).
54. M. A. Bender, T. R. Knutson, R. E. Tuleya, J. J. Sirutis, G. A. Vecchi, S. T. Garner, I. M. Held, Modeled impact of anthropogenic warming on the frequency of intense Atlantic hurricanes. *Science* **327**, 454–458 (2010).
55. J. A. Marengo, A. P. Cunha, W. R. Soares, R. R. Torres, L. M. Alves, S. S. B. Brito, L. A. Cuartas, K. Leal, N. G. Ribeiro, R. C. S. Alvalá, A. R. Magalhaes, Increase risk of drought in the semiarid lands of Northeast Brazil due to regional warming above 4 °C, in *Climate Change Risks in Brazil*, C. A. Nobre, J. A. Marengo, W. R. Soares, Eds. (Springer, 2019), pp. 181–200.
56. N. A. Rayner, D. E. Parker, E. B. Horton, C. K. Folland, L. V. Alexander, D. P. Rowell, E. C. Kent, A. Kaplan, Global analyses of sea surface temperature, sea ice, and night marine air temperature since the late nineteenth century. *J. Geophys. Res.* **108**, 4407 (2003).
57. E. Kalnay, M. Kanamitsu, R. Kistler, W. Collins, D. Deaven, L. Gandin, M. Iredell, S. Saha, G. White, J. Woollen, Y. Zhu, M. Chelliah, W. Ebisuzaki, W. Higgins, J. Janowiak, K. C. Mo, C. Ropelewski, J. Wang, A. Leetmaa, R. Reynolds, R. Jenne, D. Joseph, The NCEP/NCAR 40-year reanalysis project. *Bull. Am. Meteorol. Soc.* **77**, 437–472 (1996).
58. V. Eyring, S. Bony, G. A. Meehl, C. A. Senior, B. Stevens, R. J. Stouffer, K. E. Taylor, Overview of the Coupled Model Intercomparison Project Phase 6 (CMIP6) experimental design and organization. *Geosci. Model Dev.* **9**, 1937–1958 (2016).
59. E. N. Lorenz, Empirical Orthogonal Functions and Statistical Weather Prediction, in *Statistical Forecast Project Report 1* (MIT Department of Meteorology, 1956).
60. P. C. Austin, J. V. Tu, Bootstrap methods for developing predictive models. *Am. Stat.* **58**, 131–137 (2004).

Acknowledgments

Funding: This work is supported by the National Key R&D Program of China (grant no. 2016YFA0601803), Strategic Priority Research Program of Chinese Academy of Sciences (XDB40000000), National Natural Science Foundation of China (NSFC) project (grant nos. 41976005, 41676190, 41976193, 41831175, 41922039, and 91858102), and Chinese Academy of Science (COMS2019Q03). W.C. is supported by the Centre for Southern Hemisphere Oceans Research, a joint research center between QNLM and CSIRO. S.-P.X. is supported by the NSF

Downloaded from http://advances.sciencemag.org/ on August 25, 2021

(AGS 1637450). Computation is supported by the Center for High Performance Computing and System Simulation, Pilot National Laboratory for Marine Science and Technology (Qingdao). **Author contributions:** Y.Y. conceived and wrote the initial manuscript in discussion with L.W. and W.C. Y.Y. and Y.G. conducted the analysis. S.-P.X., G.H., and X. Li contributed to interpreting results. All authors contributed to improving the manuscript. **Competing interests:** The authors declare that they have no competing interests. **Data and materials availability:** All data needed to evaluate the conclusions in the paper are present in the paper and/or the Supplementary Materials.

Submitted 8 February 2021
Accepted 6 July 2021
Published 25 August 2021
10.1126/sciadv.abg9690

Citation: Y. Yang, L. Wu, Y. Guo, B. Gan, W. Cai, G. Huang, X. Li, T. Geng, Z. Jing, S. Li, X. Liang, S.-P. Xie, Greenhouse warming intensifies north tropical Atlantic climate variability. *Sci. Adv.* **7**, eabg9690 (2021).

Downloaded from http://advances.sciencemag.org/ on August 25, 2021

nature climate change

ARTICLES

https://doi.org/10.1038/s41558-020-00943-1

Check for updates

Opposite response of strong and moderate positive Indian Ocean Dipole to global warming

Wenju Cai[1,2]✉, Kai Yang[3], Lixin Wu[1]✉, Gang Huang[3,4], Agus Santoso[2,5], Benjamin Ng[2], Guojian Wang[1,2] and Toshio Yamagata[6]

A strong positive Indian Ocean Dipole (pIOD) induces weather extremes such as the 2019 Australian bushfires and African floods. The impact is influenced by sea surface temperature (SST), yet models disagree on how pIOD SST may respond to greenhouse warming. Here we find increased SST variability of strong pIOD events, with strong equatorial eastern Indian Ocean cool anomalies, but decreased variability of moderate pIOD events, dominated by western warm anomalies. This opposite response is detected in the Coupled Model Inter-comparison Project (CMIP5 and CMIP6) climate models that simulate the two pIOD regimes. Under greenhouse warming, the lower troposphere warms faster than the surface, limiting Ekman pumping that drives the moderate pIOD warm anomalies; however, faster surface warming in the equatorial western region favours atmospheric convection in the west, strengthening equatorial nonlinear advection that forces the strong pIOD cool anomalies. Climate extremes seen in 2019 are therefore likely to occur more frequently under greenhouse warming.

A positive Indian Ocean Dipole (pIOD) refers to a sea surface temperature (SST) pattern that features warm anomalies in the equatorial western Indian Ocean and cold anomalies in the east, described by a positive dipole mode index (DMI)[1]. A pIOD event usually peaks in austral spring (September, October, November; SON) but starts to develop in austral winter, with an initial cooling off Sumatra–Java suppressing the local atmospheric convection there and generating anomalous southeasterly winds. The anomalous winds promote upwelling and lift the thermocline that in turn reinforces the initial cooling[1,2], a process referred to as local Bjerknes feedback. During a strong pIOD, the growth of cool anomalies causes a northwestward shift of atmospheric convection and a westward extension of the southeasterly trades that usually flow over the southern tropical Indian Ocean in austral winter and spring. The anomalous easterlies extend across the equatorial Indian Ocean, where weak westerlies normally prevail[3] (Extended Data Fig. 1). The anomalous easterly winds promote warm SST anomalies, convergence, and rainfall in the equatorial western Indian Ocean[1–3].

The altered ocean–atmosphere circulations induce weather extremes in Indian Ocean-rim countries[1–9], such as droughts, heatwaves and bushfires in Indonesia and Australia[4–7], floods and malaria outbreaks in East Africa[9,10], and coral reef death across western Sumatra[11]. During the 1997 strong pIOD event[2] (Extended Data Fig. 1), floods in the African countries led to several thousand deaths and hundreds of thousands of people displaced, whereas wildfires in the eastern Indian Ocean regions affected the lives of tens of millions[3] and the global carbon budget[12]. Similar severe impacts also occurred during the 2019 strong pIOD event[13], and Australia experienced a devastating bushfire season, referred to as the Black Summer, with a burnt area of more than 170,000 km^2, 30 people killed and 3,000 buildings destroyed[14].

Determining how pIOD SST may change under greenhouse warming is one of the most important issues in climate science; however, for several climate model generations, there has been either a lack of intermodel consensus or no statistically significant change using the conventional DMI (refs. [15–17]).

Long-standing uncertainty in projected pIOD SST change

Uncertainty in projected pIOD SST change is despite a strong intermodel consensus on a mean state change in the tropical Indian Ocean, which features equatorial easterly wind trends and a faster warming rate in the northwest than in the southeast of the tropical Indian Ocean, a shallowing equatorial thermocline[15–19], and some changes in characteristics of strong pIOD[20,21]. First, the faster warming in the west equatorial Indian Ocean facilitates an increased frequency of a westward-shifted atmospheric convergence zone from the east and hence there are more events with extreme impacts, even if SST variability does not change[20]. Second, the enhanced north-minus-south SST gradient inhibits the seasonal southward shift of the tropical Indian Ocean Intertropical Convergence Zone[21], leading to an anomalously weak convergence in the eastern Indian Ocean, particularly during a strong pIOD (Extended Data Figs. 1 and 2d–f). Third, although a projected thermocline shallowing in the eastern Indian Ocean increases the role of the relatively cold subsurface water through an increased thermocline response to winds, this is offset by a weakened response of equatorial winds to SST anomalies. The weaker wind response occurs because the lower atmosphere becomes more stable, as the low troposphere warms faster than the surface under greenhouse warming[16].

Palaeoclimate proxies show that pIOD was more intense during the past warmer period of the middle Holocene than in the twentieth century[7], and there is already an increase in the frequency and strength of pIOD events during the second half of

[1]Key Laboratory of Physical Oceanography–Institute for Advanced Ocean Studies, Ocean University of China and Qingdao National Laboratory for Marine Science and Technology, Qingdao, China. [2]Center for Southern Hemisphere Oceans Research (CSHOR), CSIRO Oceans and Atmosphere, Hobart, Tasmania, Australia. [3]State Key Laboratory of Numerical Modeling for Atmospheric Sciences and Geophysical Fluid Dynamics, Institute of Atmospheric Physics, Chinese Academy of Sciences, Beijing, China. [4]Laboratory for Regional Oceanography and Numerical Modeling, Qingdao National Laboratory for Marine Science and Technology, Qingdao, China. [5]Australian Research Council (ARC) Centre of Excellence for Climate Extremes, The University of New South Wales, Sydney, New South Wales, Australia. [6]Application Laboratory, JAMSTEC, Yokohama, Japan. ✉e-mail: wenju.cai@csiro.au; lxwu@ouc.edu.cn

the twentieth century[8]; however, climate model projections of the response of pIOD SST variability to greenhouse warming remain uncertain[15]. Using the DMI determined from the observed poles assumes that the pIOD possesses little pattern diversity and that the simulated location of pIOD SST anomaly centres across models is the same as the observed. Here we show that there are two pIOD regimes—thus requiring at least two separate indices—and that their associated anomaly patterns differ vastly from one model to another. Furthermore, there is a robust pIOD SST change if we focus on SST variability patterns and centres unique to each individual model.

Dynamics of the two distinct pIOD regimes in observations

Previous studies have shown that pIOD events display different flavours[20,22–25]. During a strong pIOD, the anomalous cooling off Java–Sumatra expands northward and then westward along the equator[20], inhibiting the seasonal southward shift of the intertropical convergence zone towards the equatorial eastern Indian Ocean and inducing a westward shift of the equatorial eastern Indian Ocean convergence zone[21], generating strong easterlies along the equator (Extended Data Fig. 1d–f). These winds in turn enhance the equatorial west-minus-east SST gradient through a positive nonlinear zonal and vertical feedback, dramatically increasing the anomalous cooling in the equatorial eastern Indian Ocean[20].

During moderate pIOD events such as in 1982, Bjerknes feedback drives moderate cooling off Sumatra–Java (Extended Data Fig. 2a–c); to the west, the dominant forcing of the broad area of warming includes an anomalous Ekman pumping that arises from westward propagation of off-equatorial downwelling Rossby waves that are generated by equatorial anomalous easterlies in the eastern Indian Ocean during the development phase, and their subsequent reflection at the western boundary as downwelling Kelvin waves[26]. Heat budget analysis shows that Ekman pumping is the dominant forcing of the warm anomalies (Extended Data Fig. 3, see also the 'Heat budget analysis' section in the Methods).

Depiction of the two distinct pIOD regimes

The large difference in the spatial pattern and the dynamics between the strong and moderate pIOD indicates that at least two indices are needed to distinguish them[13,20,27]. To construct the indices, we use the first two principal modes of an empirical orthogonal function (EOF) analysis of SON-averaged SST anomalies that cover the 1982–2015 period, each described by a principal spatial pattern and a principal component (PC) time-series that is scaled to have a variance of unity (see the 'Data, models and EOF analysis' section in the Methods). At their positive phase, EOF1 shows a cold-anomaly centre off Sumatra–Java, which is accompanied by warming in much of the tropical Indian Ocean basin, analogous to that associated with the DMI (correlation of 0.90); this is accompanied by a shoaled equatorial thermocline in the east but a deepened equatorial thermocline to the west (Fig. 1a). EOF2 exhibits a cold-anomaly maximum in the eastern equatorial region, which tends to be equatorially symmetric and extends westward (Fig. 1b). This reflects the impact of equatorial nonlinear advection[13,20,27].

The two PC time-series display a nonlinear relationship (Fig. 1c). A pIOD event can be constructed by a combination of the two EOFs to realize event diversity. Strong pIOD events appear in the quadrant in which both PCs are positive, that is, with the equatorially symmetric cold anomalies of EOF2 superimposed onto the cold anomalies off Sumatra–Java of EOF1 such that these events are dominated by cold anomalies, as occured in 1997 and 2019 (refs. [20,27]). Strong pIOD events can therefore be described by a strong pIOD index, defined as $S=(\mathrm{PC1}+\mathrm{PC2})/\sqrt{2}$. By contrast, moderate pIOD events appear in the quadrant in which PC1 is positive but PC2 is negative, such that cold anomalies in the east are weak and warm anomalies to the west dominate, as occured in 1982. Moderate pIOD events can thus be described as $M=(\mathrm{PC1}-\mathrm{PC2})/\sqrt{2}$. The two indices separate the observed pIOD events identified by the DMI into two groups: strong events such as 1994, 1997, 2006 and 2019 in the S-index (red curve); and moderate events such as the prominent 1982, 1987 and 2015 events in the M-index (green curve) (Fig. 1c,d). Our approach is similar to a previous analysis on rainfall[20], but we instead use SST, which allows depiction of both strong and moderate pIOD events using SST anomalies. This is the simplest objective description of pIOD diversity compared with other attempts[22,24].

Sea surface temperature anomaly patterns for the two types of pIOD constructed using PC1 and PC2 reproduce the salient features in raw data (Extended Data Figs. 1 and 2), in terms of dominance of the strong cold anomalies in strong pIOD events and by broad-scaled warm anomalies in moderate pIOD events, respectively (Fig. 1e,f). Dynamics that govern the ability to generate the two patterns in part depend on whether the cold anomalies grow northwest towards—and then westward along—the equator, triggering the equatorial nonlinear advective feedbacks that lead to the enhanced cooling represented by PC2, that is, PC2 is a nonlinear function of PC1, which is expressed as $\mathrm{PC2}(t)=\alpha[\mathrm{PC1}(t)]^2+\beta\mathrm{PC1}(t)+\gamma$, similar to that used for describing ENSO diversity[28,29], in which α, β and γ are the nonlinear coefficient, linear coefficient and constant of the quadratic function, respectively. For the observed, obtained from multireanalysis products (see Methods section 'Nonlinear dynamics and model selection'), the mean value of α is 0.42 (Fig. 1c). A large value of α represents strong nonlinearity that distinguishes moderate and strong pIOD events.

Simulation of the two pIOD regimes in climate models

We analyse outputs from 35 available CMIP5 (ref. [30]) and 19 CMIP6 (ref. [31]) models by applying the same EOF analysis on SON-averaged SST anomalies from the mean of the first 100 years, quadratically detrended over the full 1900–2099 period (see the 'Data, models and EOF analysis' section in the Methods). These models were forced with historical anthropogenic and natural forcings up to 2005 for CMIP5 or 2014 for CMIP6, and thereafter under a future greenhouse gas emission scenario of representative concentration pathway 8.5 (RCP8.5) for CMIP5 and the equivalent updated

Fig. 1 | Identification of observed strong and moderate pIOD events. a, SON SST and tropical vertical potential temperature anomalies (°C, colour) and wind stress anomalies (N m^{-2}, vectors) regressed onto the first principal component (PC1) of EOF of SON SST anomalies over the tropical Indian Ocean (5° S to 5° N and 40° E to 100° E) for the 1982–2015 period average across four reanalysis products (see the 'Data, models and EOF analysis' section in the Methods). Subsurface potential temperature and wind stress data are from ORA-S5. The vertical temperature anomalies are calculated as the average over 2.5° S to 2.5° N. **b**, Same as **a**, but for PC2. **c**, The nonlinear relationship between the normalized PC1 and PC2. Red dots indicate strong pIOD years (PC1 > 1 s.d. and PC2 > 0.5 s.d.); green dots denote moderate pIOD years (PC1 > 1 s.d. and PC2 < 0.5 s.d.); the black dot marks the 2019 pIOD, obtained by regressing the SST anomaly pattern over the tropical Indian Ocean in 2019 from the GODAS dataset onto the EOF1 and EOF2 patterns; and the purple curve shows a nonlinear fit $\mathrm{PC2}(t)=\alpha[\mathrm{PC1}(t)]^2+\beta\mathrm{PC1}(t)+\gamma$. **d**, The time-series of a DMI (upper panel) can be split into (red) strong ($S=(\mathrm{PC1}+\mathrm{PC2})/\sqrt{2}$) and (green) moderate pIOD ($M=(\mathrm{PC1}-\mathrm{PC2})/\sqrt{2}$) indices (lower panel) to capture the strong and moderate pIOD events in Fig. 1c. The black dashed line in upper half shows 0.75 s.d. of the DMI, whereas the red and green dashed lines in the lower half show 1.5 s.d. and 1.25 s.d. of the S- and M-index, respectively. **e**, Reconstruction of temperature anomalies (°C, colour shading) and wind stress anomalies (N m^{-2}, vectors) of strong pIOD using the two EOFs. The green boxes indicate areas used for calculating the DMI. **f**, Same as **e**, but for moderate pIOD.

scenario for CMIP6, that is, shared socioeconomic pathway 5–8.5 (SSP5–8.5) (refs. [30,31]). The simulated anomaly pattern of either the S- or M-index differs vastly from one model to another (Fig. 2a,b). In contrast to the use of the DMI, our approach accounts for diversity in patterns and thus facilitates assessment of the response of the pIOD SST variability as simulated by each individual model.

Most models examined here simulate a value of α that is lower than the observed and a total of 20 models produce a value of α that is greater than 50% of the observed (Fig. 2c). These 20 models simulate a reasonable nonlinear PC1 and PC2 relationship and the contrast in the cold- and warm-anomaly dominance between the strong and moderate pIOD events (Extended Data Fig. 4 for samples).

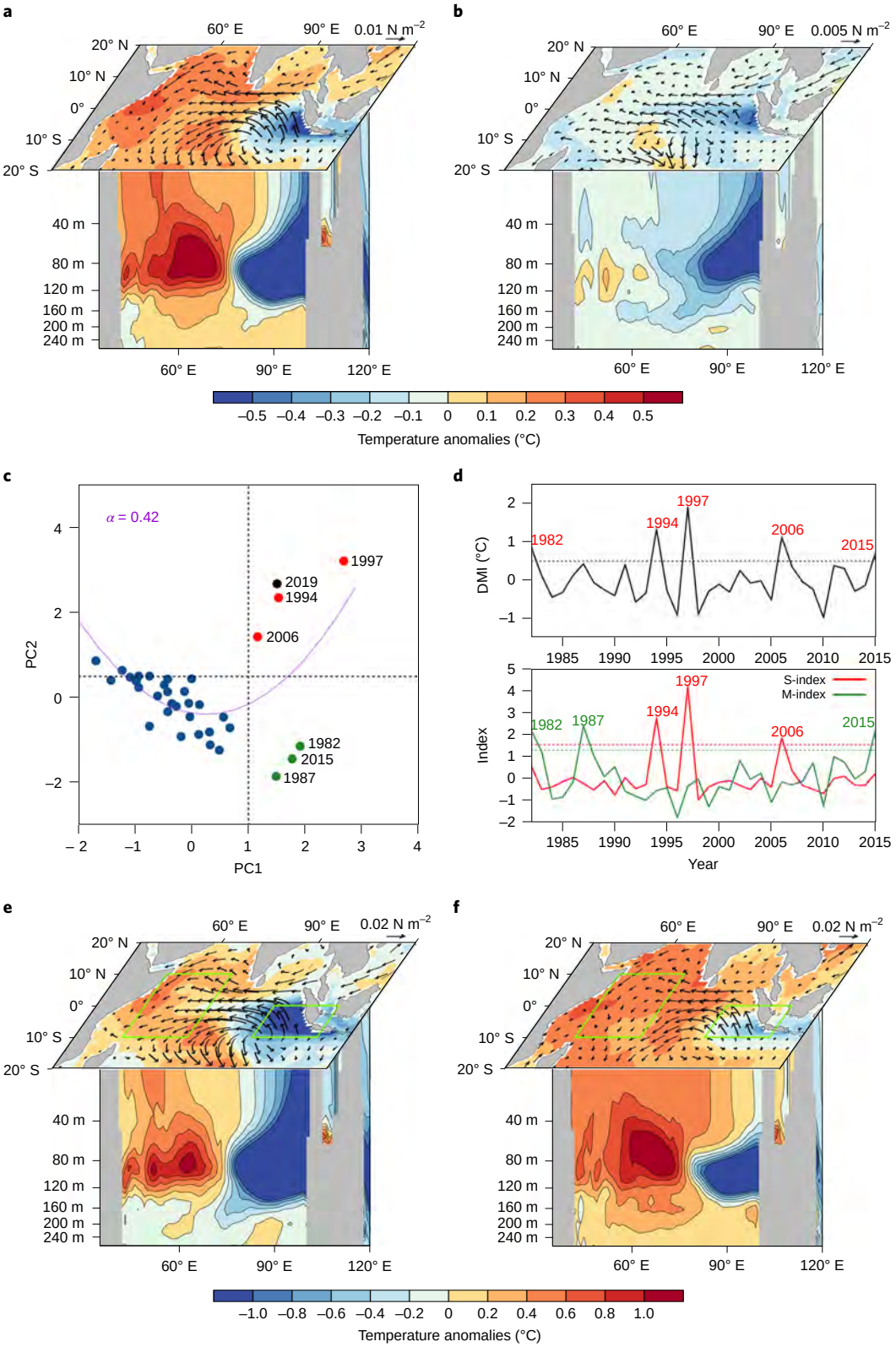

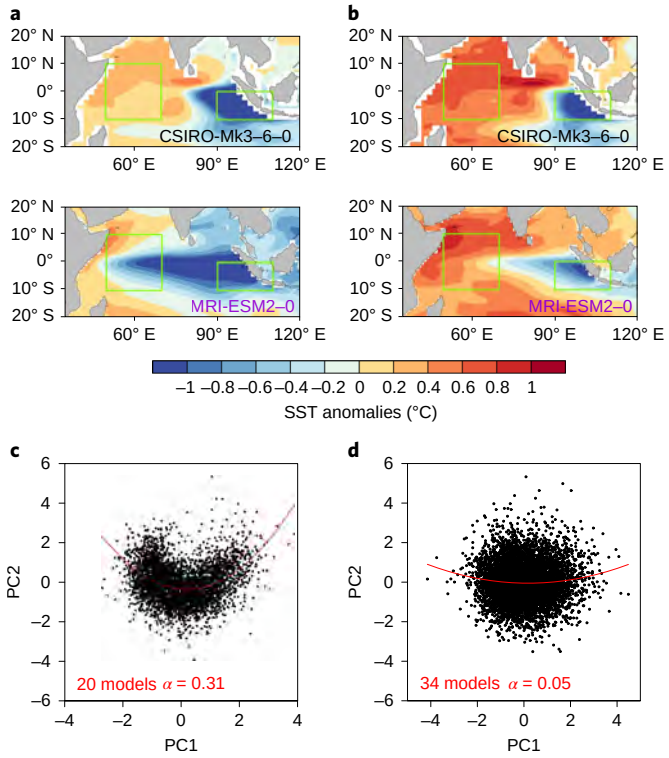

Fig. 2 | Selection of models based on pIOD nonlinearity. a, A composite of SST anomalies (in °C) for strong pIOD events (defined as S-index > 1.5 s.d.) in two models, showing vastly different pIOD patterns that cannot be fully represented by the DMI alone. The green boxes indicate areas for calculating the DMI as in ref. [1]. Strong and moderate pIOD indices (represented by the S- and M-index, respectively) are calculated from PCs of the EOF of SON SST anomalies over the tropical Indian Ocean for the period of 1900–2099 for each model. **b**, Same as **a**, but for the composite of moderate pIOD (defined as M-index > 1.25 s.d.) in the two shown models. **c**, A total of 20 models (including the two models shown in Fig. 2a,b) produce a nonlinear relationship between PC1 and PC2 with $\alpha \geqq 0.21$; that is, 50% of the observed value (Fig. 1c), and are thus selected for further analysis. A quadratic fit using PC1 and PC2 time-series from the aggregate of the 20 models produces a value of α of 0.31. **d**, Same as **c**, but for the discarded 34 models with $\alpha < 0.21$.

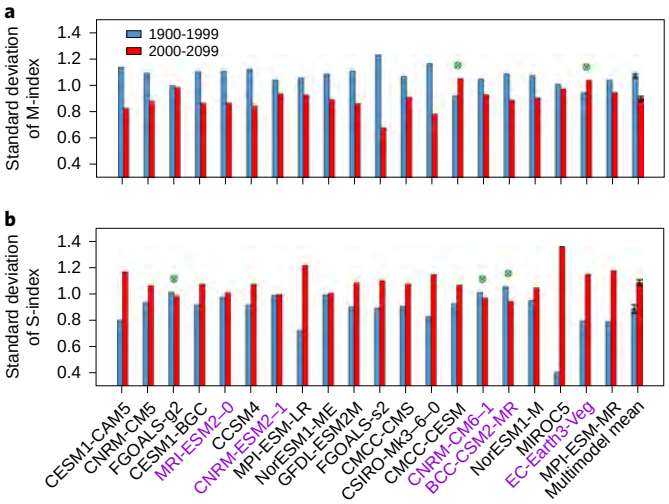

Fig. 3 | Projected opposite response of moderate and strong pIOD SST. The result shows a decrease in moderate pIOD variability but an increase in strong pIOD variability. **a**, A total of 18 out of the 20 selected models (90%) generate a reduction in moderate pIOD variability depicted by the M-index from the present-day (1900–1999, blue bars) to future (2000–2099, red bars) climate, with the exception of two models generating an increase (indicated by green circles). The multimodel mean reduction of 16% is statistically significant above the 95% confidence level according to a bootstrap test. The error bars in the multimodel mean represent the 95% confidence level determined by a bootstrap test. **b**, A total of 17 out of the 20 models (85%) simulate an increase in variability of strong pIOD described by the S-index from the present-day to the future climate, with the exception of three models generating a decrease (indicated by green circles). The multimodel mean increase of 22% is statistically significant above the 95% confidence level according to a bootstrap test. Models from CMIP6 are indicated in purple.

We examine this group of models for assessment of possible change in strong and moderate pIOD events under greenhouse warming. The remaining 34 models produce a far weaker nonlinear PC1 – PC2 relationship (Fig. 2d) and are not used.

Opposite response of the two pIOD regimes to global warming

We compare the standard deviation (s.d.) of the S- and M-index in the present-day (1900–1999) and future (2000–2099) periods. There is an opposite response: a total of 18 out of 20 (that is, 90%) models simulate decreased variability of the M-index (Fig. 3a), whereas a total 17 out of 20 models generate increased variability of the S-index in the future period (red bars, Fig. 3a,b). The ensemble-mean is a decrease of 16% for moderate, but an increase of 22% for strong pIOD variability, each statistically significant above the 95% confidence according to a bootstrap test (see the 'Statistical test' section in the Methods). This is in sharp contrast to the result using the DMI, which shows no statistically significant change in the multimodel mean change (Extended Data Fig. 5).

The decrease in M-index variability translates to a 52% reduction in occurrences of moderate pIOD events with an M-index > 1.25 s.d., as supported by 85% of the selected models (Extended Data Fig. 6a); however, the increase in S-index variability translates to a 66% increase in occurrences of strong pIOD events with an S-index > 1.5 s.d. (Extended Data Fig. 6b)—from one event every 13.3 years in the present-day climate to one event every eight years in the future climate, as supported by 80% of the selected models. The opposite response is despite a lack of frequency change in strong and moderate pIOD events combined (Extended Data Fig. 6a,b), in contrast to a tendency of increased pIOD frequency using DMI (ref. [32]). These results hold using other threshold values (Extended Data Fig. 6c,d). Climate extremes associated with strong pIOD events are thus likely to occur more frequently under greenhouse warming. The 2019 strong pIOD happened to occur in conjunction with a moderate Pacific warm condition[33], leading to more extreme impacts.

Using 30 models simulating a value of α that is at least 33% of the observed value, the intermodel consensus on the change of the two indices is still strong. A total of 27 out of 30 models (90%) simulate a decrease in moderate pIOD variability and a total of 23 out of 30 models (77%) produce an increase in strong pIOD variability, and their ensemble-mean changes are statistically significant (Extended Data Fig. 7). Sensitivity to emission scenarios shows that under RCP4.5, 13 out of 15 (87%) CMIP5 models that simulate a value of α greater than 50% of the observed value generate an increase in S-index variability, and 93% of the models produce a reduction in M-index variability (Extended Data Fig. 8).

Associated mechanisms arising from mean state changes

There is no intermodel relationship between changes in variability or frequency of a strong pIOD event and changes in El Niño

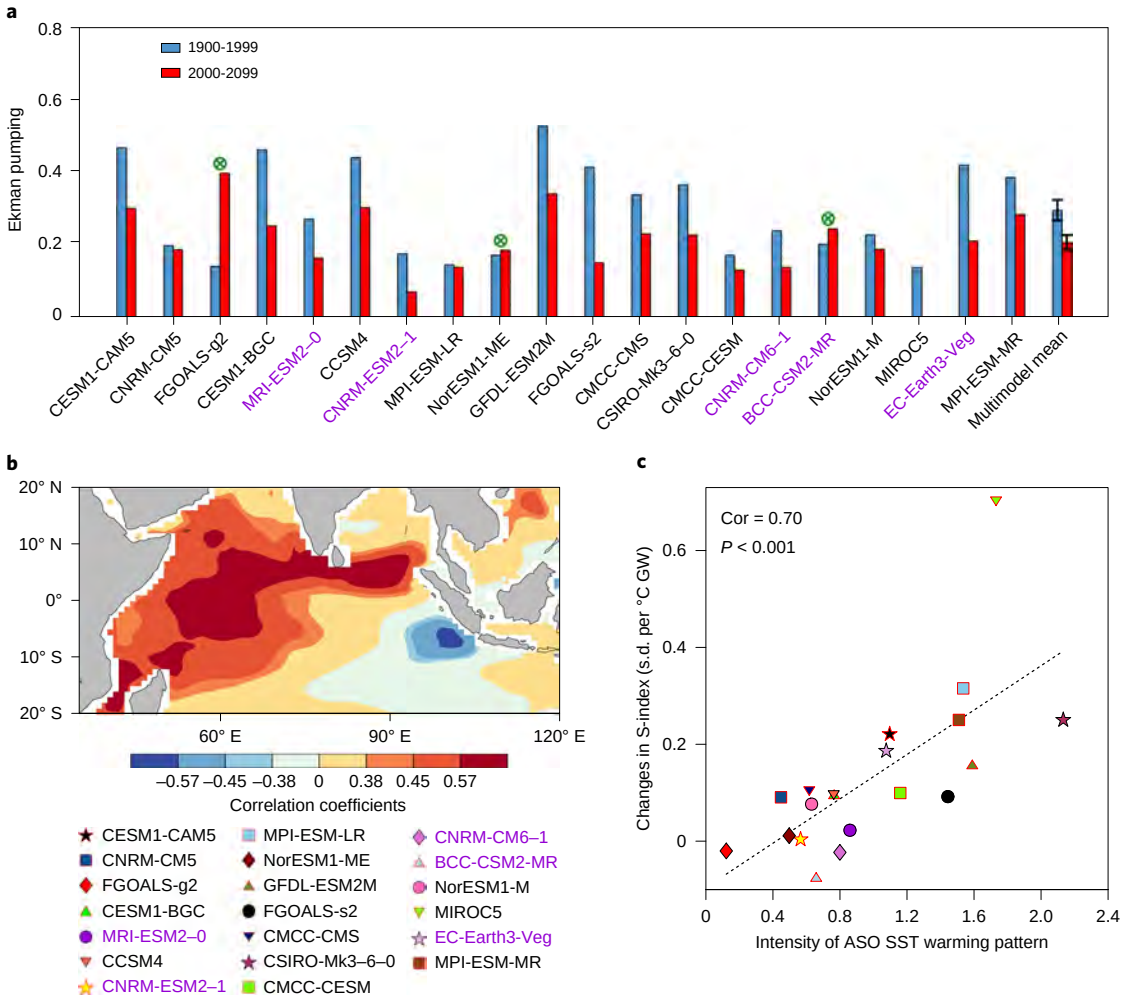

Fig. 4 | Mechanisms for the projected opposite change in moderate and strong pIOD. a, Ekman pumping term during the development phase (August, September, October (ASO)) averaged over the southwestern tropical Indian Ocean (10° S to 0° and 50° E to 80° E) regressed onto the M-index over the present-day (1900–1999, blue bars) and future (2000–2099, red bars) climate in the 20 selected models. A total of 17 out of the 20 selected models (85%) simulate decreased Ekman pumping during future moderate pIOD events. Models that simulate an increase are indicated by green circles. The associated multimodel mean decrease of 30% is statistically significant above the 95% confidence level according to a bootstrap test. Models from CMIP6 are indicated in purple. A time-series of the Ekman pumping term is normalized before regression. The error bar in the multimodel mean represents the 95% confidence level determined by a bootstrap test. **b**, A map of the intermodel correlation coefficients between the ASO warming pattern and the change in the S-index variability. The warming pattern is defined as the change in SST between the future and present-day. The S-index variability change and warming pattern have been scaled by the corresponding increase in global mean SST in each model. Correlation coefficients of ±0.38, ±0.45 and ±0.57 are significant at the 90%, 95% and 99% confidence levels, respectively. **c**, The statistically significant relationship between the intensity of ASO SST warming pattern and the change in s.d. of the S-index is shown, with the correlation (Cor) and its *P*-value indicated. The intensity of the SST warming pattern over 20° S to 20° N and 40° E to 100° E in each model is obtained by regressing onto the multimodel mean SST warming pattern in the same domain; the S-index variability change and warming pattern have been scaled by the corresponding increase in global mean SST in each model, taken as the intensity of global warming (GW).

variability or frequency (Extended Data Fig. 9a,c), which suggests that the changes of strong pIOD are not due to changes in the El Niño. There is a relationship between changes in variability or frequency of a moderate pIOD with changes in El Niño, but the fact that in the majority of models there is an increase in El Niño variability and El Niño frequency in contrast to a decrease in moderate pIOD (Extended Data Fig. 9b,d) rules out changes in the El Niño as the cause.

Instead, the opposite response arises from the mean state changes, featuring faster warming in the western and northern than the eastern and southern tropical Indian Ocean, supported by a trend of equatorial southeasterlies[15–19] and enhanced evaporation in the west (Extended Data Fig. 10). Under greenhouse warming, the lower troposphere warms faster than the surface, such that the response of equatorial easterlies to SST anomalies weakens[16]. Ekman pumping, which is the main forcing for warm anomalies in the tropical western Indian Ocean for moderate pIOD events (Extended Data Fig. 3), weakens in the future climate (Fig. 4a), causing decreased M-index variability. For cold-anomaly-dominated pIOD events (that is, strong pIOD events), the faster mean warming west and northwest of the tropical Indian Ocean[18,19] is conducive to anomalous atmosphere convection there, facilitating anomalous easterlies that extend to the equatorial central and western Indian Ocean, leading to a shallowing thermocline, enhanced equatorial nonlinear zonal and vertical advection, which is in turn conducive to cold anomalies[13,20,27]. Intermodel relationships between warming

trends and changes in S-index variability show that a greater intensity of the warming pattern leads to a great increase in S-index variability (Fig. 4b,c).

Conclusions

Our finding of an opposite response to greenhouse warming—with increased SST variability of strong pIOD events but decreased SST variability of moderate pIOD events—is in stark contrast with previous findings of no consensus using the DMI. Our robust result arises from a separation of the two types of pIOD events that are governed by different dynamics, which provides a physical basis for selecting models used in our pIOD future projections. This projected change of a reduced frequency of moderate pIOD but with more occurrences of stronger pIOD events has far-reaching implications for climate and weather extremes over regions influenced by the pIOD. For example, severe floods in eastern African regions and devastating bushfires in Australia, as seen in 2019, are likely to occur more frequently.

Online content

Any methods, additional references, Nature Research reporting summaries, source data, extended data, supplementary information, acknowledgements, peer review information; details of author contributions and competing interests; and statements of data and code availability are available at https://doi.org/10.1038/s41558-020-00943-1.

Received: 18 March 2020; Accepted: 29 September 2020;
Published online: 30 November 2020

References

1. Saji, N. H., Goswami, B. N., Vinayachandran, P. N. & Yamagata, T. A dipole mode in the tropical Indian Ocean. *Nature* **401**, 360–363 (1999).
2. Webster, P. J., Moore, A. M., Loschnigg, J. P. & Leben, R. R. Coupled ocean–atmosphere dynamics in the Indian Ocean during 1997–98. *Nature* **401**, 356–360 (1999).
3. Schott, F. A., Xie, S.-P. & McCreary Jr, J. P. Indian Ocean circulation and climate variability. *Rev. Geophys.* https://doi.org/10.1029/2007RG000245 (2009).
4. Ummenhofer, C. C. et al. What causes southeast Australia's worst droughts? *Geophys. Res. Lett.* https://doi.org/10.1029/2008GL036801 (2009).
5. Ashok, K., Guan, Z. & Yamagata, T. Influence of the Indian Ocean Dipole on the Australian winter rainfall. *Geophys. Res. Lett.* https://doi.org/10.1029/2003GL017926 (2003).
6. Cai, W., Cowan, T. & Raupach, M. Positive Indian Ocean Dipole events precondition southeast Australia bushfires. *Geophys. Res. Lett.* https://doi.org/10.1029/2009GL039902 (2009).
7. Abram, N. J. et al. Seasonal characteristics of the Indian Ocean Dipole during the Holocene epoch. *Nature* **445**, 299–302 (2007).
8. Abram, N. J., Gagan, M. K., Cole, J. E., Hantoro, W. S. & Mudelsee, M. Recent intensification of tropical climate variability in the Indian Ocean. *Nat. Geosci.* **1**, 849–853 (2008).
9. Behera, S. K. et al. Paramount impact of the Indian Ocean Dipole on the East African short rains: A CGCM study. *J. Clim.* **18**, 4514–4530 (2005).
10. Hashizume, M., Chaves, L. F. & Minakawa, N. Indian Ocean Dipole drives malaria resurgence in East African highlands. *Sci. Rep.* **2**, 269 (2012).
11. Abram, N. J., Gagan, M. K., McCulloch, M. T., Chappell, J. & Hantoro, W. S. Coral Reef Death during the 1997 Indian Ocean Dipole Linked to Indonesian Wildfires. *Science* **301**, 952–955 (2003).
12. Page, S. E. et al. The amount of carbon released from peat and forest fires in Indonesia during 1997. *Nature* **420**, 61–65 (2002).
13. Wang, G., Cai, W., Yang, K., Santoso, A. & Yamagata, T. A unique feature of the 2019 extreme positive Indian Ocean Dipole event. *Geophys. Res. Lett.* https://doi.org/10.1029/2020GL088615 (2020).
14. Richards, L. Brew, N. & Smith, L. *2019–20 Australian Bushfires—Frequently Asked Questions: a Quick Guide* (Parliament of Australia, 2020); https://www.aph.gov.au/About_Parliament/Parliamentary_Departments/Parliamentary_Library/pubs/rp/rp1920/Quick_Guides/AustralianBushfires
15. Cai, W. et al. Projected response of the Indian Ocean Dipole to greenhouse warming. *Nat. Geosci.* **6**, 999–1007 (2013).
16. Zheng, X.-T. et al. Indian Ocean dipole response to global warming in the CMIP5 multimodel ensemble. *J. Clim.* **26**, 6067–6080 (2013).
17. Hui, C. & Zheng, X.-T. Uncertainty in Indian Ocean Dipole response to global warming: the role of internal variability. *Clim. Dyn.* **51**, 3597–3611 (2018).
18. Vecchi, G. A. & Soden, B. J. Global warming and the weakening of the tropical circulation. *J. Clim.* **20**, 4316–4340 (2007).
19. Xie, S.-P. et al. Global warming pattern formation: sea surface temperature and rainfall. *J. Clim.* **23**, 966–986 (2010).
20. Cai, W. et al. Increased frequency of extreme Indian Ocean Dipole events due to greenhouse warming. *Nature* **510**, 254–258 (2014).
21. Weller, E. et al. More-frequent extreme northward shifts of eastern Indian Ocean tropical convergence under greenhouse warming. *Sci. Rep.* **4**, 6087 (2014).
22. Du, Y., Cai, W. & Wu, Y. A new type of the Indian Ocean Dipole since the mid-1970s. *J. Clim.* **26**, 959–972 (2013).
23. Anil, N., Kumar, R., R., M., Sajeev, R. & Saji, P. K. Role of distinct flavours of IOD events on Indian summer monsoon. *Nat. Hazards* **82**, 1317–1326 (2016).
24. Verdon-Kidd, D. C. On the classification of different flavours of Indian Ocean Dipole events. *Int. J. Climatol.* **38**, 4924–4937 (2018).
25. Endo, S. & Tozuka, T. Two flavors of the Indian Ocean Dipole. *Clim. Dyn.* **46**, 3371–3385 (2016).
26. Du, Y., Xie, S.-P., Huang, G. & Hu, K. Role of air–sea interaction in the long persistence of El Niño–induced north Indian Ocean warming. *J. Clim.* **22**, 2023–2038 (2009).
27. Yang, K. et al. Oceanic processes in ocean temperature products key to a realistic presentation of positive Indian Ocean Dipole nonlinearity. *Geophys. Res. Lett.* **46**, e2020GL089396 (2020).
28. Karamperidou, C., Jin, F.-F. & Conroy, J. L. The importance of ENSO nonlinearities in tropical pacific response to external forcing. *Clim. Dyn.* **49**, 2695–2704 (2017).
29. Cai, W. et al. Increased variability of eastern Pacific El Niño under greenhouse warming. *Nature* **564**, 201–206 (2018).
30. Taylor, K. E., Stouffer, R. J. & Meehl, G. A. An overview of CMIP5 and the experiment design. *Bull. Am. Meteorol. Soc.* **93**, 485–498 (2012).
31. Eyring, V. et al. Overview of the coupled model intercomparison project phase 6 (CMIP6) experimental design and organization. *Geosci. Model Dev.* **9**, 1937–1958 (2016).
32. Abram, N. J. et al. Palaeoclimate perspectives on the Indian Ocean Dipole. *Quat. Sci. Rev.* **237**, 106302 (2020).
33. Doi, T., Behera, S. K. & Yamagata, T. Predictability of the super IOD Event in 2019 and its link with El Niño Modoki. *Geophys. Res. Lett.* **47**, e2019GL086713 (2020).

Publisher's note Springer Nature remains neutral with regard to jurisdictional claims in published maps and institutional affiliations.

© The Author(s), under exclusive licence to Springer Nature Limited 2020

Methods

Data, models and EOF analysis. We use four SST reanalysis products to construct pIOD patterns, covering a common period from 1982 to 2015. Most of these products are produced in a system that specifically considers the impact of subsurface ocean temperature on SST, which is essential for the nonlinear oceanic feedback responsible for the pIOD dominated by cold SST anomalies, that is, strong pIOD episodes. The only exception is OISST, which although not derived from a system explicitly with a subsurface ocean, assimilates weekly observations from different platforms including satellites, ships and buoys. For each of these four data, anomalies are constructed with reference to the mean of the full period, and then detrended. A multiproduct average of the anomalies is then calculated. These products are:

- GODAS (NCEP Global Ocean Data Assimilation System from 1980 to 2019) (ref. [34]);
- ORA-S5 (ECMWF Ocean Reanalysis System 5 from 1979 to 2018) (ref. [35]);
- OISST v2 (NOAA Optimum Interpolation SST version 2 from 1982 to 2019) (ref. [36]);
- SODA3.3.1 (Simple Ocean Data Assimilation version 3.3.1 from 1980 to 2015) (ref. [37]).

To assess the impact of greenhouse warming on pIOD changes, we take outputs from 35 CMIP5 (ref. [30]) and 19 CMIP6 (ref. [31]) coupled global climate models forced with historical anthropogenic and natural forcings, and future greenhouse gases under RCP8.5 for CMIP5 and SSP5–8.5 for CMIP6, covering a 200-year period of 1900–2099 (refs. [30,31]). Monthly anomalies referenced to the climatology of 1900–1999 were constructed and quadratically detrended.

We apply EOF analysis[38] to the SON average of SST anomalies in an equatorial Indian Ocean domain (5° S to 5° N, 40° E to 100° E), which yield the two dominant modes, each with a principal pattern and a PC scaled to unity. The two PC time-series display a nonlinear relationship. A combination of the two EOFs is used to describe the two types of pIOD. Indices of moderate and strong pIOD are described by the M-index $((\mathrm{PC1}-\mathrm{PC2})/\sqrt{2})$ and the S-index $((\mathrm{PC1}+\mathrm{PC2})/\sqrt{2})$, respectively. The two indices separate the pIOD events identified by the DMI into two groups: strong events such as 1994, 1997 and 2006 in the S-index (red curve), and moderate events such as 1982, 1987 and 2015 events (green curve) in the M-index (Fig. 1d). Using these ocean-model-based products identifies the 2006 event as a strong pIOD, as opposed to a moderate one using non-oceanic-based products[20]. Data for the 2019 pIOD event are available in GODAS (ref. [34]), and a pattern regression onto EOF1 and EOF2 shows it to be a strong pIOD, second only to the 1997 event (Fig. 1c).

Heat budget analysis. We examine the surface heat balance of the tropical Indian Ocean, which is expressed as:

$$\partial T^a/\partial t = -\begin{bmatrix} \left(u^a \partial T^a/\partial x + \overline{u}\partial T^a/\partial x + u^a \partial \overline{T}/\partial x\right) \\ +\left(v^a \partial T^a/\partial y + \overline{v}\partial T^a/\partial y + v^a \partial \overline{T}/\partial y\right) \\ +\left(w^a \partial T^a/\partial z + \overline{w}\partial T^a/\partial z + w^a \partial \overline{T}/\partial z\right) \end{bmatrix} + Q + \text{residual} \qquad (1)$$

The variables T, u, v and w are the potential temperature and the zonal, meridional and vertical ocean current velocities, respectively, averaged over the top 50 m (vertical motion over the top 50 m is represented by w at 50 m). The vertical gradient of climatological temperature $(d\overline{T}/dz)$ is taken as the difference between the average over the top 50 m and temperature at 60 m depth. Differential operators, x, y, z, and t represent zonal, meridional and vertical directions, and time, respectively. All variables are from the ECMWF ORA-S5 dataset[35] at a horizontal resolution of 1° latitude by 1° longitude for the period of 1979 to 2018. The rate of change of the mixed-layer temperature $(d\overline{T}/dt)$ is calculated using a centred-difference approximation. The superscript a and overbar denote anomalous and long-term averaged quantities, respectively. The tendency of the surface temperature is balanced by zonal advection of heat by the zonal currents (first bracketed terms on the right-hand side), meridional advection (second bracketed terms), vertical advection (third bracketed terms), the net surface air–sea heat flux (Q) and all other factors not explicitly expressed (residual), such as mixing and diffusion. We examine the heat budget terms averaged over the developing period of IOD events (August to October), which contributes most to the mature SST anomalies. All variables in (1) are linearly detrended.

We first examine the heat budget for the observations in an area average over the equatorial region (10° S to 10° N and 40° E to 100 °E). For strong pIOD events, nonlinear zonal and vertical advection terms are particularly important for generating cold anomalies in the equatorial eastern Indian Ocean[20], and Ekman pumping plays a key role in the generation of warm anomalies (Extended Data Fig. 3a). For moderate pIOD events, Ekman pumping dominates warming (Extended Data Fig. 3a). Inspection of $d\overline{T}/dt$ finds that the region where maximum warming tendency occurs is in the southwestern tropical Indian Ocean (10° S to 0°, 50° E to 80° E, green box of Extended Data Fig. 3b,c). Propagation into the region of downwelling Rossby waves driven by equatorial easterly anomalies associated with a developing pIOD, and their subsequent reflection at the western boundary as downwelling equatorial Kelvin waves induce the broad surface warming[26]. That Ekman pumping in the southwestern tropical Indian Ocean is an important term in the total tendency, and is driven by equatorial easterly anomalies, is reaffirmed by a simple analysis (Extended Data Fig. 3d–f).

We then examine the heat budget for climate models. Data from all models have been interpolated to a horizontal grid of 1°×1° (bilinear interpolation) and a vertical grid with 5 m intervals (linear interpolation). The vertical velocity w at 50 m is used to represent the vertical motion over the upper 50 m layer. Monthly anomalies of w and zonal wind stress are calculated with reference to the 1900–1999 climatology and quadratically detrended. As in observations, nonlinear equatorial zonal and vertical advection are dominant in forcing strong pIOD events, and these terms increase under greenhouse warming[20].

For the present-day and future model climate, we take the climatological mean temperature $(\overline{T})$ as the average over the 1900–1999 and 2000–2099 periods, respectively. There is a general decrease in the response of zonal wind stress to SST in the equatorial eastern Indian Ocean, as a consequence of a more stable atmosphere that results from a faster warming in the lower troposphere than at the surface under greenhouse warming[16]. The associated decrease in variability of zonal wind stress anomalies, which drive Ekman pumping that dominates moderate pIOD events, leads to decreased variability of moderate pIOD in the future climate. In the 20 selected models, 19 models generate a future decrease of w variability in the development phase over the southwestern tropical Indian Ocean (green box, Extended Data Fig. 3b). A bootstrap test finds that the multimodel mean decrease of 21% is statistically significant. By contrast, for strong pIOD events, equatorial nonlinear zonal and vertical advection occurs more frequently as a consequence of faster warming in the northwestern equatorial Indian Ocean under greenhouse warming[20].

Nonlinear dynamics and model selection. During strong pIOD events, the initial cooling grows such that it extends northward first and then westward along the equator, triggering the equatorial nonlinear ocean–atmosphere feedback: an equatorial west-minus-east zonal SST gradient drives easterly anomalies, leading to nonlinear vertical and nonlinear zonal advection extending the cold anomalies along the equatorial eastern Indian Ocean[13,20,27], as represented by PC2. The dynamics that govern PC2 and the associated pattern depends nonlinearly on cold anomalies presented in PC1 that first grow northwest towards and then westward along the equator, such that $\mathrm{PC2}(t)=\alpha[\mathrm{PC1}(t)]^2+\beta\mathrm{PC1}(t)+\gamma$. For the observed, the value of α is 0.42 (Fig. 1c); a greater value of α means a clearer separation of the two types of the pIOD events.

Not all models produce the nonlinear dynamics that separate the strong and moderate pIOD events, and most models produce a weaker nonlinearity than seen in the observed. We select 20 CMIP5 and CMIP6 models that simulate an α, calculated over the 200 years, greater than half of the observed value. The 20 selected models together yield a mean α amplitude of 0.31 (Fig. 2c). A total of 30 models simulate an α greater than 33% of the observed value and we use this group to test the sensitivity of our results.

Statistical significance test. A bootstrap method[39] is used to examine whether the increased S-index variance and decreased M-index variance are statistically significant. The 20 s.d. values of the S- and M-index in the present-day climate (1900–1999) from the 20 selected models are resampled randomly to construct 10,000 realizations of the mean standard deviation. In this random resampling process, a model is allowed to be selected again. The s.d. of the 10,000 interrealizations of mean s.d. in the present-day climate is 0.0312 for the S-index (0.0157 for the M-index). The same test is carried out for the future climate (2000–2099) and the s.d. of the interrealization is 0.0212 for the S-index (0.0185 for the M-index). The increased s.d. for the S-index (or decreased s.d. for the M-index) in the future period is greater than the sum of the two s.d. values, indicating statistical significance above the 95% confidence level.

Data availability

Data relevant to the paper can be downloaded from websites listed below:
OISST v2 at https://www.esrl.noaa.gov/psd/data/gridded/data.noaa.oisst.v2.html;
ORA-S5 at https://icdc.cen.uni-hamburg.de/daten/reanalysis-ocean/easy-init-ocean/ecmwf-oras5.html;
SODA3.3.1 at https://www2.atmos.umd.edu/~ocean/index_files/soda3.3.1_mn_download.htm;
GODAS at https://www.esrl.noaa.gov/psd/data/gridded/data.godas.html;
CMIP5 database at http://www.ipcc-data.org/sim/gcm_monthly/AR5/;
CMIP6 database at https://esgf-node.llnl.gov/projects/cmip6/;
19 CMIP6 models are used in this study, including: MRI-ESM2–0 (refs. [40,41]); CNRM-ESM2–1 (refs. [42,43]); CNRM-CM6–1 (refs. [44,45]); BCC-CSM2-MR (refs. [46,47]); EC-Earth3-Veg (refs. [48,49]); NorESM2-LM (refs. [50,51]); MIROC6 (refs. [52,53]); CESM2 (refs. [54,55]); CAMS-CSM1-0 (refs. [56,57]); CESM2-WACCM (refs. [58,59]); MIROC-ES2L (refs. [60,61]); IPSL-CM6A-LR (refs. [62,63]); INM-CM4-8 (refs. [64,65]); INM-CM5-0 (refs. [66,67]); CanESM5 (refs. [68,69]); MPI-ESM1-2-LR (refs. [70,71]); UKESM1-0-LL (refs. [72,73]); MCM-UA-1-0 (refs. [74,75]); GFDL-CM4 (refs. [76,77]).

Code availability

Codes for calculating EOF, the parameter $|\alpha|$ can be downloaded from https://drive.google.com/open?id=1d2R8wKpFNW-vMIfoJsbqIGPIBd9Z_8rj.

References

34. Behringer, D. & Xue, Y. Evaluation of the global ocean data assimilation system at NCEP: the Pacific Ocean. In *Eighth Symposium on Integrated Observing and Assimilation Systems for Atmosphere, Oceans, and Land Surface* (Americal Meteorological Society, 2004).
35. Zuo, H., Balmaseda, M. A., Tietsche, S., Mogensen, K. & Mayer, M. The ECMWF operational ensemble reanalysis–analysis system for ocean and sea ice: a description of the system and assessment. *Ocean Sci.* **15**, 779–808 (2019).
36. Reynolds, R. W., Rayner, N. A., Smith, T. M., Stokes, D. C. & Wang, W. An improved in situ and satellite SST analysis for climate. *J. Clim.* **15**, 1609–1625 (2002).
37. Carton, J. A., Chepurin, G. A. & Chen, L. SODA3: A new ocean climate reanalysis. *J. Clim.* **31**, 6967–6983 (2018).
38. Lorenz, E. N. *Empirical Orthogonal Functions and Statistical Weather Prediction* Statistical Forecast Project Report 1 (Department of Meteorology, Massachusetts Institute of Technology, 1956).
39. Austin, P. C. & Tu, J. V. Bootstrap methods for developing predictive models. *The American Statistician* **58**, 131–137 (2004).
40. Yukimoto, S. et al. *MRI MRI-ESM2.0 Model Output Prepared for CMIP6 CMIP Historical* Version 20200102 (Earth System Grid Federation, 2019); https://doi.org/10.22033/ESGF/CMIP6.6842
41. Yukimoto, S. et al. *MRI MRI-ESM2.0 Model Output Prepared for CMIP6 ScenarioMIP ssp585* Version 20200102 (Earth System Grid Federation, 2019); https://doi.org/10.22033/ESGF/CMIP6.6929
42. Seferian, R. *CNRM-CERFACS CNRM-ESM2-1 Model Output Prepared for CMIP6 CMIP Historical* Version 20200102 (Earth System Grid Federation, 2018); https://doi.org/10.22033/ESGF/CMIP6.4068
43. Voldoire, A. *CNRM-CERFACS CNRM-ESM2-1 Model Output Prepared for CMIP6 ScenarioMIP ssp585* Version 20200102 (Earth System Grid Federation, 2019); https://doi.org/10.22033/ESGF/CMIP6.4226
44. Voldoire, A. *CMIP6 Simulations of the CNRM-CERFACS Based on CNRM-CM6-1 Model for CMIP Experiment Historical* Version 20200102 (Earth System Grid Federation, 2018); https://doi.org/10.22033/ESGF/CMIP6.4066
45. Voldoire, A. *CNRM-CERFACS CNRM-CM6-1 Model Output Prepared for CMIP6 ScenarioMIP ssp585* Version 20200102 (Earth System Grid Federation, 2019); https://doi.org/10.22033/ESGF/CMIP6.4224
46. Wu, T. et al. *BCC BCC-CSM2MR Model Output Prepared for CMIP6 CMIP Historical* Version 20200102 (Earth System Grid Federation, 2018); https://doi.org/10.22033/ESGF/CMIP6.2948
47. Xin, X. et al. *BCC BCC-CSM2MR Model Output Prepared for CMIP6 ScenarioMIP ssp585* Version 20200102 (Earth System Grid Federation, 2019); https://doi.org/10.22033/ESGF/CMIP6.3050
48. EC-Earth Consortium (EC-Earth) *EC-Earth-Consortium EC-Earth3-Veg Model Output Prepared for CMIP6 CMIP Historical* Version 20200102 (Earth System Grid Federation, 2019); https://doi.org/10.22033/ESGF/CMIP6.4706
49. EC-Earth Consortium (EC-Earth) *EC-Earth-Consortium EC-Earth3-Veg Model Output Prepared for CMIP6 ScenarioMIP ssp585* Version 20200102 (Earth System Grid Federation, 2019); https://doi.org/10.22033/ESGF/CMIP6.4914
50. Seland, Ø. et al. *NCC NorESM2-LM Model Output Prepared for CMIP6 CMIP Historical* Version 20200102 (Earth System Grid Federation, 2019); https://doi.org/10.22033/ESGF/CMIP6.8036
51. Seland, Ø. et al. *NCC NorESM2-LM Model Output Prepared for CMIP6 ScenarioMIP ssp585* Version 20200102 (Earth System Grid Federation, 2019); https://doi.org/10.22033/ESGF/CMIP6.8319
52. Tatebe, H. & Watanabe, M. *MIROC MIROC6 Model Output Prepared for CMIP6 CMIP Historical* Version 20200102 (Earth System Grid Federation, 2018); https://doi.org/10.22033/ESGF/CMIP6.5603
53. Shiogama, H., Abe, M. & Tatebe, H. *MIROC MIROC6 Model Output Prepared for CMIP6 ScenarioMIP ssp585* Version 20200102 (Earth System Grid Federation, 2019); https://doi.org/10.22033/ESGF/CMIP6.5771
54. Danabasoglu, G. *NCAR CESM2 Model Output Prepared for CMIP6 CMIP Historical* Version 20200102 (Earth System Grid Federation, 2019); https://doi.org/10.22033/ESGF/CMIP6.7627
55. Danabasoglu, G. *NCAR CESM2 Model Output Prepared for CMIP6 ScenarioMIP ssp585* Version 20200102 (Earth System Grid Federation, 2019); https://doi.org/10.22033/ESGF/CMIP6.7768
56. Rong, X. C. A. M. S. CAMS_CSM1.0 *Model Output Prepared for CMIP6 CMIP Historical* Version 20200102 (Earth System Grid Federation, 2019); https://doi.org/10.22033/ESGF/CMIP6.9754
57. Rong, X. *CAMS CAMS-CSM1.0 Model Output Prepared for CMIP6 ScenarioMIP ssp585* Version 20200102 (Earth System Grid Federation, 2019); https://doi.org/10.22033/ESGF/CMIP6.11052
58. Danabasoglu, G. *NCAR CESM2-WACCM Model Output Prepared for CMIP6 CMIP Historical* Version 20200102 (Earth System Grid Federation, 2019); https://doi.org/10.22033/ESGF/CMIP6.10071
59. Danabasoglu, G. *NCAR CESM2-WACCM Model Output Prepared for CMIP6 ScenarioMIP ssp585* Version 20200102 (Earth System Grid Federation, 2019); https://doi.org/10.22033/ESGF/CMIP6.10115
60. Hajima, T. et al. *MIROC MIROC-ES2L Model Output Prepared for CMIP6 CMIP Historical* Version 20200102 (Earth System Grid Federation, 2019); https://doi.org/10.22033/ESGF/CMIP6.5602
61. Tachiiri, K. et al. *MIROC MIROC-ES2L Model Output Prepared for CMIP6 ScenarioMIP ssp585* Version 20200102 (Earth System Grid Federation, 2019); https://doi.org/10.22033/ESGF/CMIP6.5770
62. Boucher, O. et al. *IPSL IPSL-CM6A-LR Model Output Prepared for CMIP6 CMIP Historical* Version 20200102 (Earth System Grid Federation, 2018); https://doi.org/10.22033/ESGF/CMIP6.5195
63. Boucher, O. et al. *IPSL IPSL-CM6A-LR Model Output Prepared for CMIP6 ScenarioMIP ssp585* Version 20200102 (Earth System Grid Federation, 2019); https://doi.org/10.22033/ESGF/CMIP6.5271
64. Volodin, E. et al. *INM INM-CM4-8 Model Output Prepared for CMIP6 CMIP Historical Version 20200102* (Earth System Grid Federation, 2019); https://doi.org/10.22033/ESGF/CMIP6.5069
65. Volodin, E. et al. *INd INM-CM4-8 Model Output Prepared for CMIP6 ScenarioMIP ssp585* Version 20200102 (Earth System Grid Federation, 2019); https://doi.org/10.22033/ESGF/CMIP6.12337
66. Volodin, E. et al. *INM INM-CM5-0 Model Output Prepared for CMIP6 CMIP Historical* Version 20200102 (Earth System Grid Federation, 2019); https://doi.org/10.22033/ESGF/CMIP6.5070
67. Volodin, E. et al. *INM INM-CM5-0 Model Output Prepared for CMIP6 ScenarioMIP ssp585* Version 20200102 (Earth System Grid Federation, 2019); https://doi.org/10.22033/ESGF/CMIP6.12338
68. Swart, N. C. et al. *CCCma CanESM5 Model Output Prepared for CMIP6 CMIP Historical* Version 20200102 (Earth System Grid Federation, 2019); https://doi.org/10.22033/ESGF/CMIP6.3610
69. Swart, N. C. et al. *CCCma CanESM5 Model Output Prepared for CMIP6 ScenarioMIP ssp585* Version 20200102 (Earth System Grid Federation, 2019); https://doi.org/10.22033/ESGF/CMIP6.3696
70. Wieners, K.-H. et al. *MPI-M MPI-ESM1.2-LR Model Output Prepared for CMIP6 CMIP Historical* Version 20200102 (Earth System Grid Federation, 2019); https://doi.org/10.22033/ESGF/CMIP6.6595
71. Wieners, K.-H. et al. *MPI-M MPI-ESM1.2-LR Model Output Prepared for CMIP6 ScenarioMIP ssp585* Version 20200102 (Earth System Grid Federation, 2019); https://doi.org/10.22033/ESGF/CMIP6.6705
72. Tang, Y. et al. *MOHC UKESM1.0-LL Model Output Prepared for CMIP6 CMIP Historical* Version 20200102 (Earth System Grid Federation, 2019); https://doi.org/10.22033/ESGF/CMIP6.6113
73. Good, P. et al. *MOHC UKESM1.0-LL Model Output Prepared for CMIP6 ScenarioMIP ssp585* Version 20200102 (Earth System Grid Federation, 2019); https://doi.org/10.22033/ESGF/CMIP6.6405
74. Stouffer, R. *UA MCM-UA-1-0 Model Output Prepared for CMIP6 CMIP Historical* Version 20200102 (Earth System Grid Federation, 2019); https://doi.org/10.22033/ESGF/CMIP6.8888
75. Stouffer, R. *UA MCM-UA-1-0 Model Output Prepared for CMIP6 ScenarioMIP ssp585* Version 20200102 (Earth System Grid Federation, 2019); https://doi.org/10.22033/ESGF/CMIP6.13901
76. Guo, H. et al. *NOAA-GFDL GFDL-CM4 Model Output* Version 20200102 (Earth System Grid Federation, 2018); https://doi.org/10.22033/ESGF/CMIP6.1402
77. Guo, H. et al. *NOAA-GFDL GFDL-CM4 Model Output Prepared for CMIP6 ScenarioMIP* Version 20200102 (Earth System Grid Federation, 2018); https://doi.org/10.22033/ESGF/CMIP6.9242

Acknowledgements

This work is supported by National Key R&D Program of China (grant no. 2018YFA0605700). L.W. is supported by the National Natural Science Foundation of China (NSFC) projects (grant nos. 41490643, 41490640, U1606402 and 41521091). W.C., G.W., A.S. and B.N. are supported by CSHOR and the Earth System and Climate Change Hub of the Australian Government's National Environment Science Program. CSHOR is a joint research Center for Southern Hemisphere Oceans Research between QNLM and CSIRO. G.H. is supported by NSFC (grant nos. 41831175 and 91937302), CAS XDA20060501 and COMS2019Q03. K.Y. is supported by China Postdoctoral Science Foundation (grant no. 2018M640168) and a scholarship from China Scholarship Council. We acknowledge the World Climate Research Programme's Working Group on Coupled Modelling, which is responsible for CMIP, and we thank the climate modeling groups for producing and making available their model output. For CMIP, the US Department of Energy's Program for Climate Model Diagnosis and Intercomparison provides coordinating support and led development of software infrastructure in partnership with the Global Organization for Earth System Science Portals. We are grateful to the reanalysis groups for making the datasets publicly available.

Author contributions

W.C. conceived the study and wrote the initial manuscript in discussion with K.Y. K.Y. performed all analysis and generated final figures. All authors contributed to interpreting results, discussion of the associated dynamics and improvement of this paper.

Competing interests

The authors declare no competing interests.

Additional information

Extended data is available for this paper at https://doi.org/10.1038/s41558-020-00943-1.

Correspondence and requests for materials should be addressed to W.C. or L.W.

Peer review information *Nature Climate Change* thanks Jasti Chowdary and the other, anonymous, reviewer(s) for their contribution to the peer review of this work.

Reprints and permissions information is available at www.nature.com/reprints.

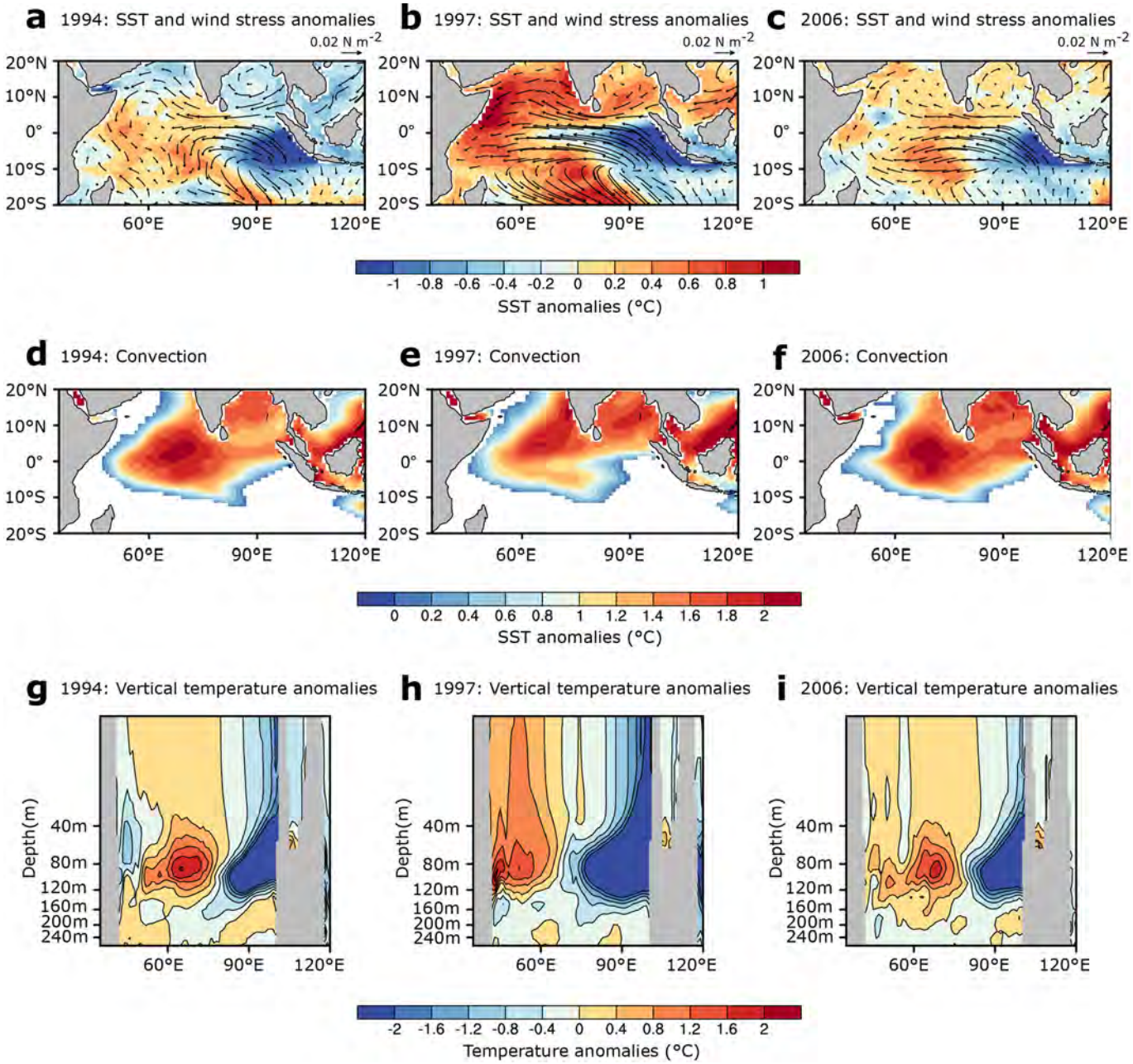

Extended Data Fig. 1 | Characteristics of strong pIOD events. a–c, SON SST anomalies (°C, color shading) and wind stress anomalies (N m^{-2}, vectors) for the 1994, 1997, and 2006 strong pIOD event, respectively. The pattern is dominated by strong cooling in the equatorial eastern Indian Ocean. Strong equatorial easterly anomalies extend to the central-western Indian Ocean. The anomalies are referenced to the average over the 1982–2015 period. **d–f**, SON SST anomalies (in °C) relative to the SST threshold for tropical convection, defined as the SON SST average over 20°S to 20°N, for the 1994, 1997, and 2006 strong pIOD event, respectively. Areas with SST lower than the convection threshold have been masked; there is a large area of suppressed convection in the equatorial eastern Indian Ocean. **g–i**, Equatorial vertical potential temperature anomalies (in °C) over SON of 1994, 1997, and 2006, respectively. The equatorial vertical potential temperature is calculated as the average between 2.5°S to 2.5°N. Strong equatorial cooling is seen in the eastern Indian Ocean. Vertical potential temperature and wind stress data are from ORA-S5.

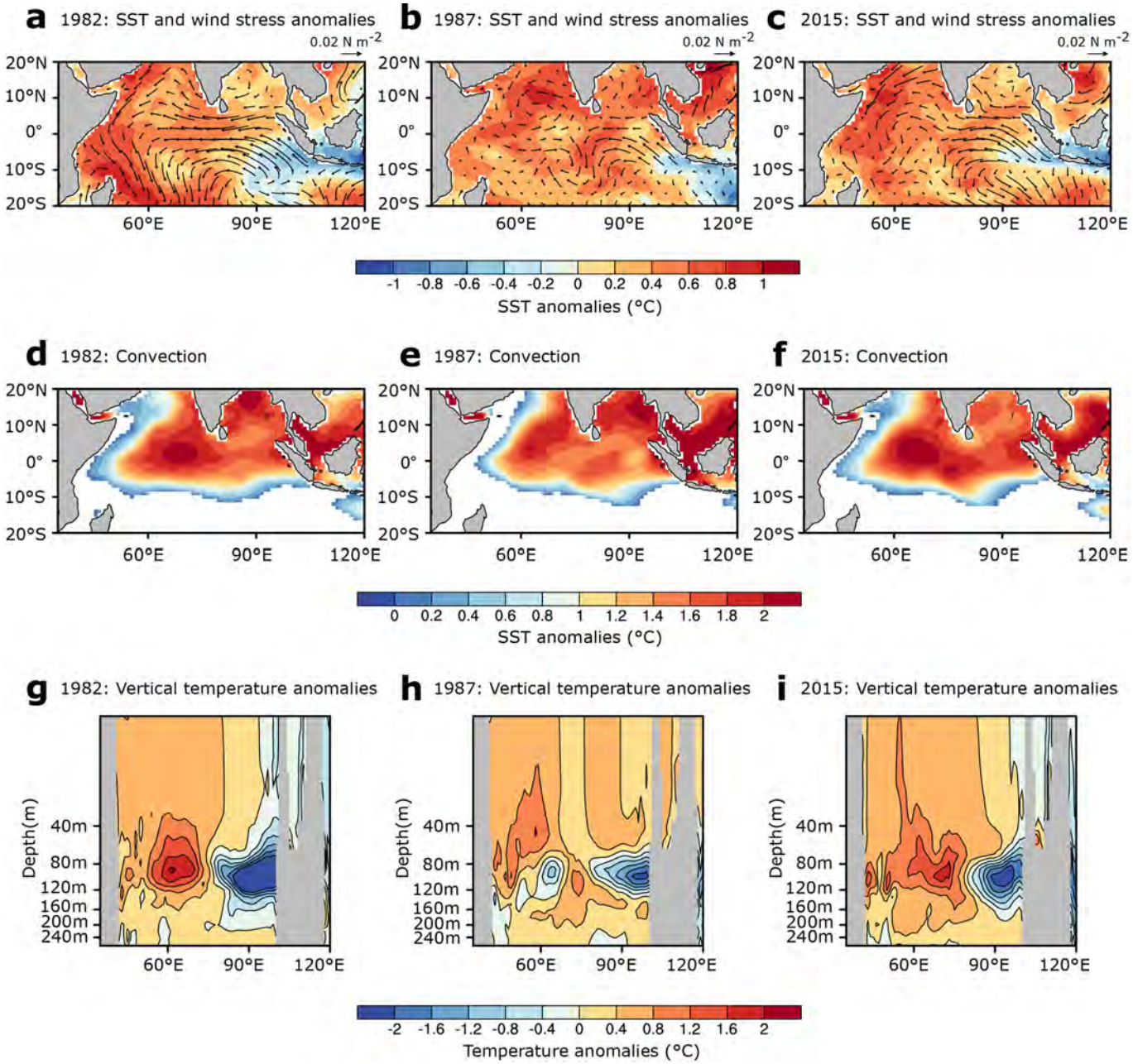

Extended Data Fig. 2 | Characteristics of moderate pIOD events. a–c, SON SST anomalies (°C, color shading) and wind stress anomalies (N m^{-2}, vectors) for the 1982, 1987, and 2015 moderate pIOD event, respectively. The pattern is dominated by a broad-scale warming over the western Indian Ocean. Easterly anomalies are confined to the equatorial central-eastern Indian Ocean. The anomalies are referenced to the average over the 1982–2015 period. **d–f**, SON SST anomalies (in °C) relative to SST threshold for tropical convection, defined as SON SST average over 20°S to 20°N for 1982, 1987, and 2015 moderate pIOD event, respectively. Areas with SST lower than the convection threshold have been masked; there is a small area of suppressed convection in the equatorial southeastern Indian Ocean. **g–i**, Equatorial vertical potential temperature anomalies (in °C) over SON of 1982, 1987, and 2015, respectively. The equatorial vertical potential temperature is calculated as the average between 2.5°S to 2.5°N. There is a general lack of cooling in the equatorial eastern Indian Ocean as cooling occurs only off Sumatra-Java. Vertical potential temperature and wind stress data are from ORA-S5.

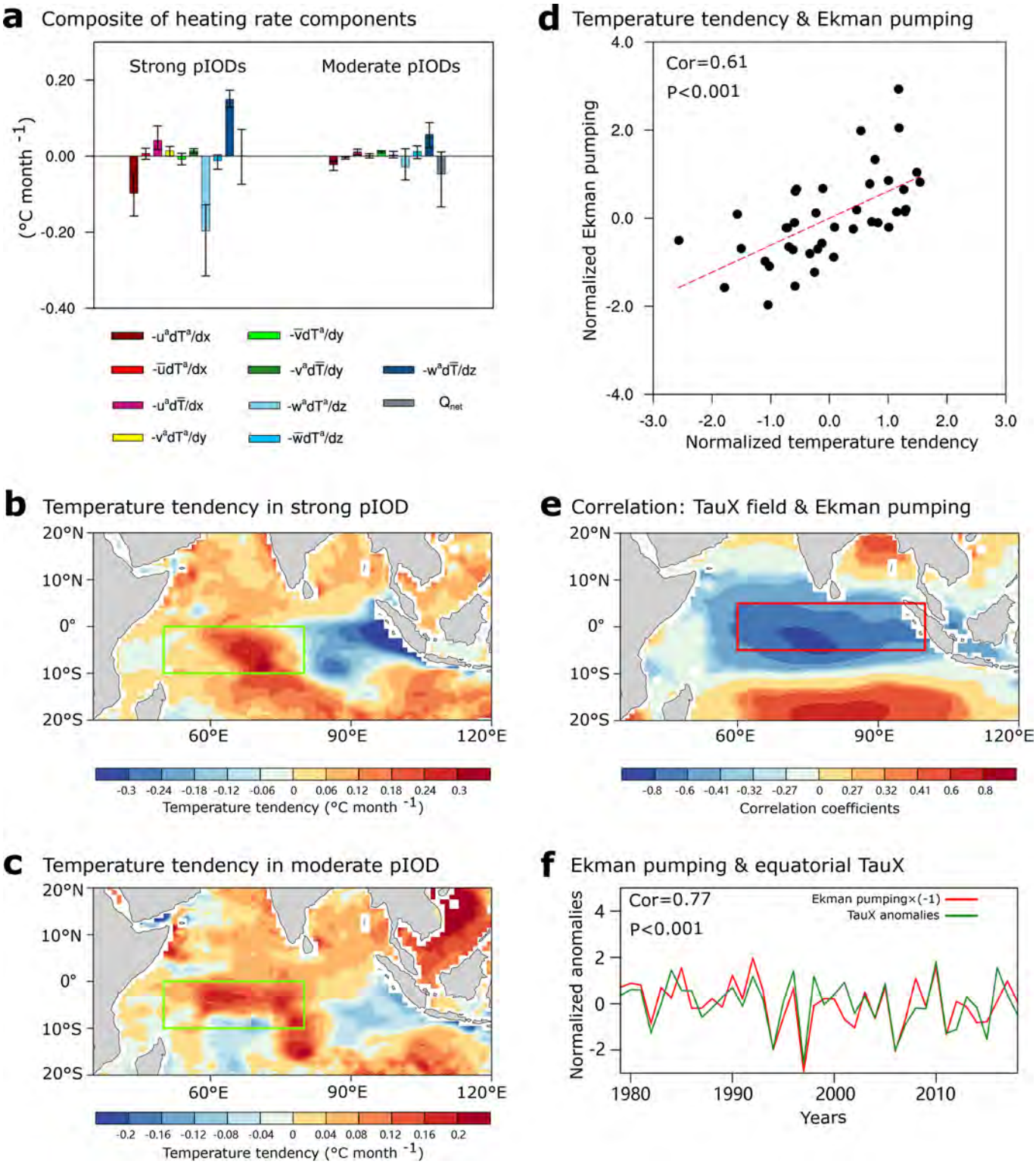

Extended Data Fig. 3 | Heat budget analysis based on observations. a, Composite of heat budget terms over the equatorial Indian Ocean (10°S–10°N, 40°E–100°E) in August-September-October (ASO). The uncertainty bar on each composite represents the range over the three strong or three moderate pIOD events. **b**, **c**, Composite of ASO temperature tendency during strong and moderate pIOD events. The green box marks the area where the main warm temperature tendency is located over the southwestern Indian Ocean (10°S–0°, 50°E–80°E). **d**, Relationship between normalized temperature tendency and the Ekman pumping term in ASO averaged over the main warming area in the southwestern Indian ocean (10°S–0°, 50°E–80°E, green box in c), with statistical properties shown. **e**, Map of ASO correlation coefficients between the Ekman pumping term averaged over 10°S–0°, 50°E–80°E and zonal wind stress (TauX) anomalies. Correlation coefficients of ±0.27, ±0.32, ±0.41 are statistically significant at the 90%, 95%, and 99% confidence levels, respectively. The area indicated by the red box is used to calculate the average zonal wind stress anomalies. **f**, Time series of normalized ASO Ekman pumping term averaged over the western Indian Ocean (10°S–0°, 50°E–80°E) (red curve) and zonal wind stress (TauX) anomalies averaged over the equatorial Indian Ocean (5°S–5°N, 60°E–100°E, red box in e) (green curve). The Ekman pumping term has been multiplied by −1 for plotting. The data used in this figure are from ORA-S5 for the period of 1979–2018.

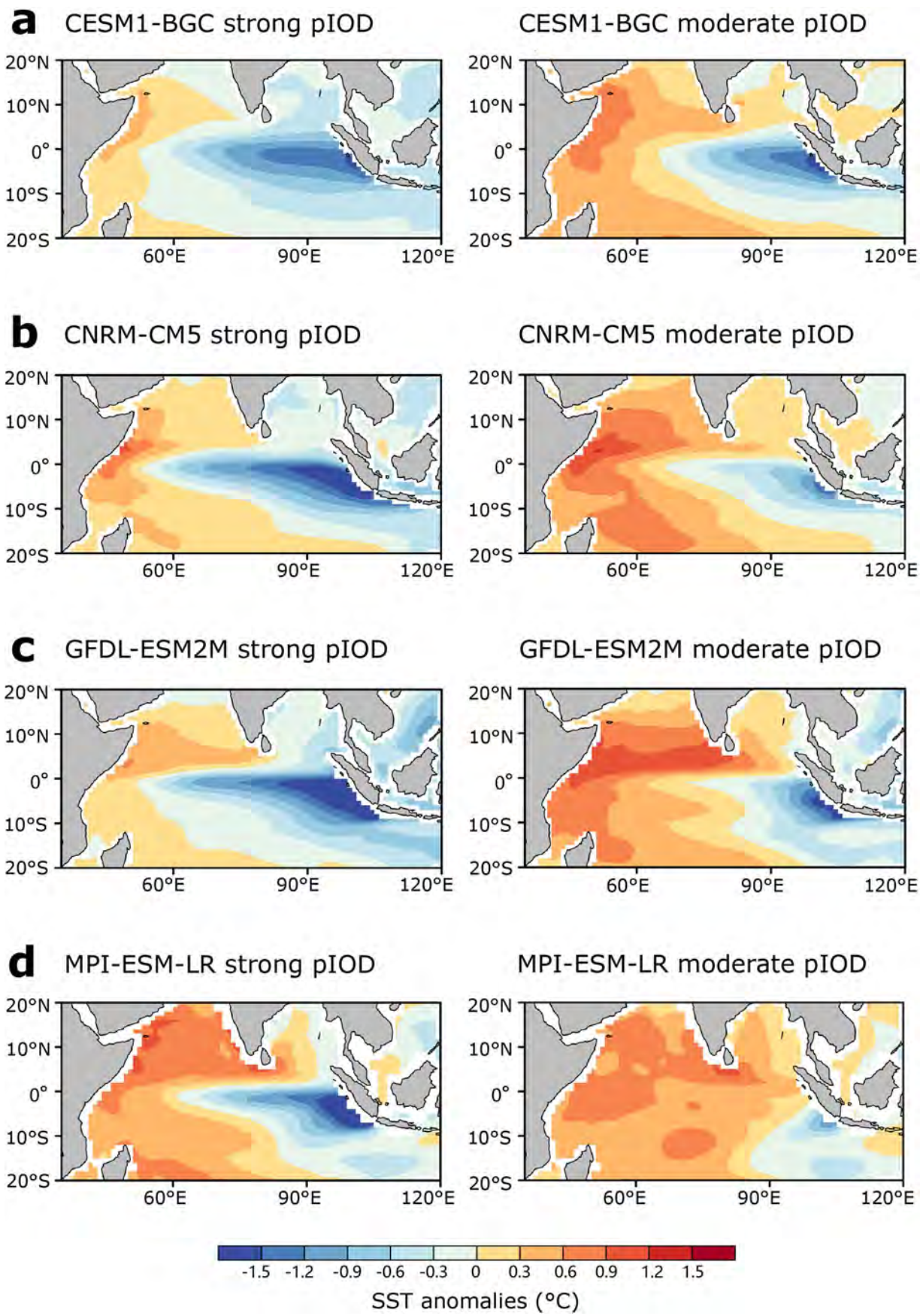

Extended Data Fig. 4 | Anomaly patterns of strong and moderate pIOD in some selected models. A composite of SON SST anomalies (°C) for strong pIOD with an S-index>1.5 s.d. and moderate pIOD with an M-index>1.25 s.d. in **a** CESM1-BGC, **b** CNRM-CM5, **c** GFDL-ESM2M, **d** MPI-ESM-LR. Left panels show strong pIOD and right panels show moderate pIOD. These show that anomaly patterns can be rather different from one model to another.

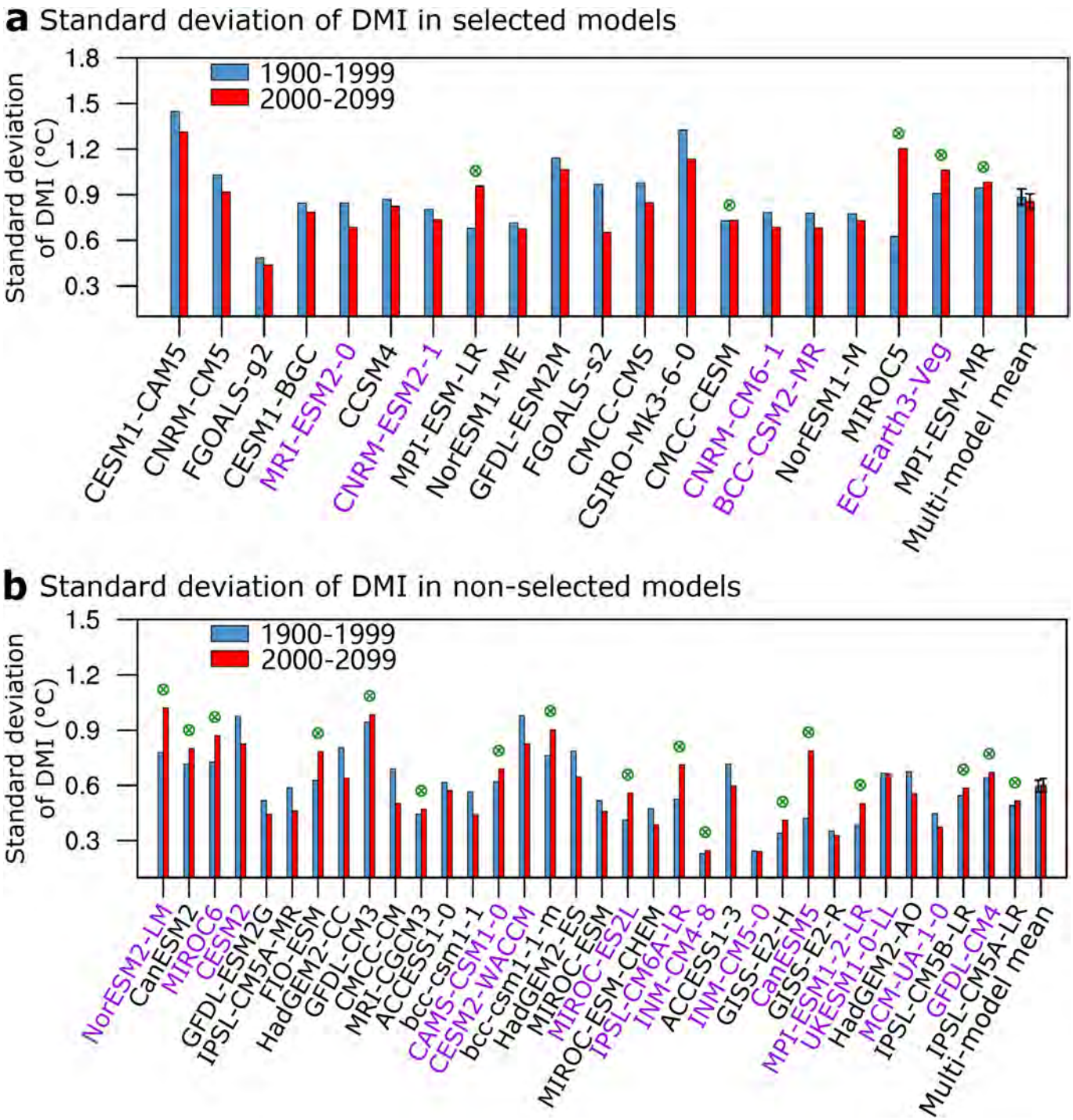

Extended Data Fig. 5 | Uncertainty in projected pIOD SST using the DMI. a, Comparison of the standard deviation of the DMI in the present-day (1900–1999) and future (2000–2099) climate in 20 models that simulate a nonlinear coefficient α greater than 50% of the observed in the quadratic fit between the first two principal components (PC1 and PC2) from EOF analysis on SON SST anomalies, $PC2(t) = \alpha\,[PC1(t)]^2 + \beta\,PC1(t) + \gamma$. Although a total of 15 out of the 20 selected models simulate lower DMI variability in the future period (red bars) than in the present-day climate (blue bars), the multi-model mean decrease is not statistically significant. The error bar represents the 95% confidence level. Models that simulate an increase in variability are indicated by green circles. Models from CMIP6 are shown in purple. **b**, Same as **a**, but for 34 models that simulate an α smaller than 50% of the observed value. A total of 17 out of the 34 models (50%) simulate smaller variability in the DMI in the future period than in the present-day period. There is no inter-model consensus, and the multi-model mean change is not statistically significant.

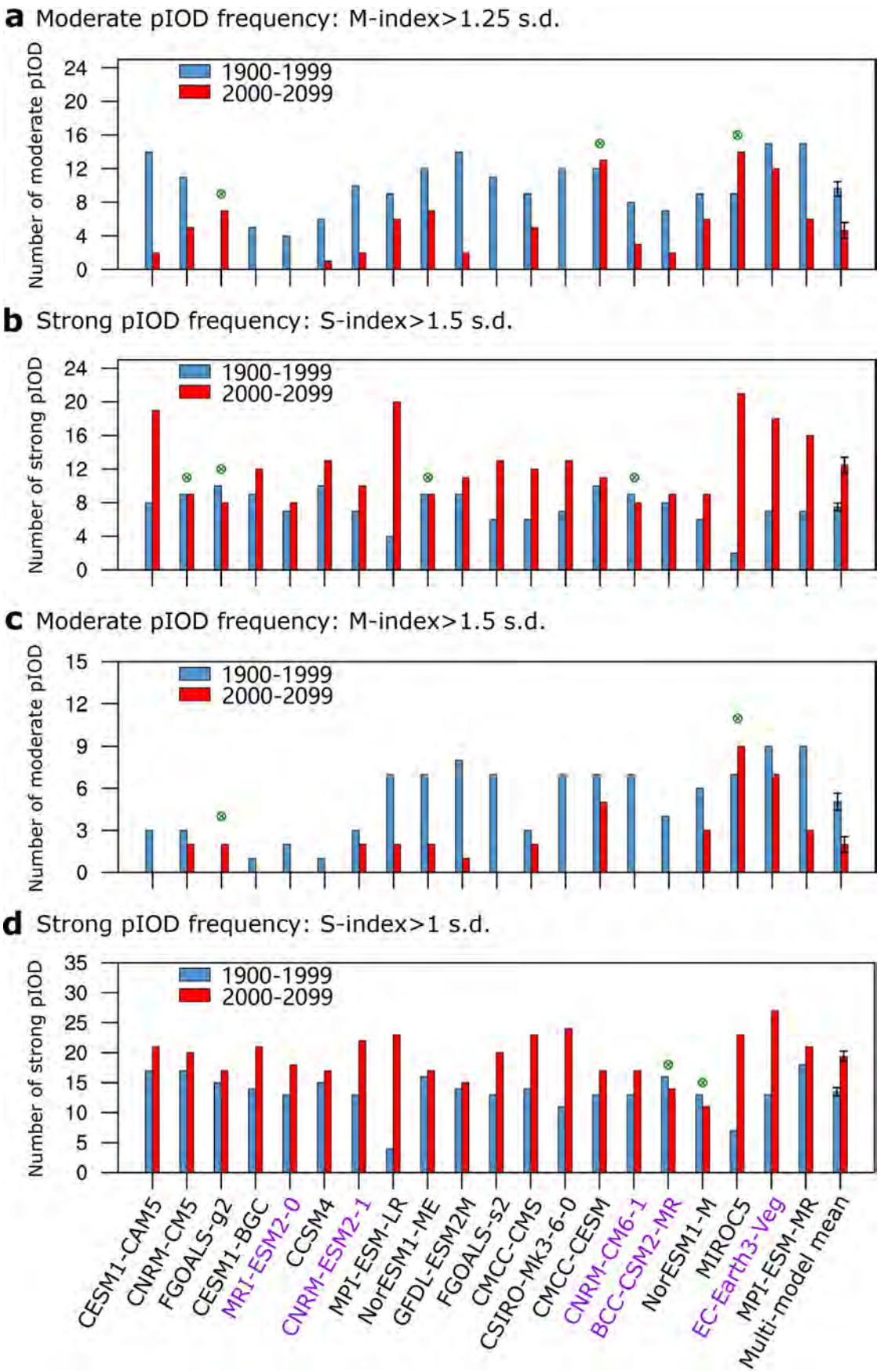

Extended Data Fig. 6 | See next page for caption.

Extended Data Fig. 6 | Projected change in pIOD frequency. a, Moderate and **b**, strong pIOD using a threshold of M-index>1.25 s.d. and S-index>1.5 s.d., respectively. Shown is the comparison of frequency (events per 100 years) in the present-day (1900–1999) and future (2000–2099) climate in the 20 selected models, that is, with an α greater than 50% of the observed value. A total of 17 out of the 20 models (85%) simulate a decreased frequency in moderate pIOD events, with a statistically significant decrease of 52% in the multi-model mean, from 9.60 events per 100 years in the present-day (blue bars) to 4.65 events per 100 years (red bars) in the future climate. By contrast, a total of 16 out of the 20 models (80%) simulate an increased frequency in strong pIOD events, with a statistically significant increase of 66% in the multi-model average, from 7.5 events per 100 years in the present-day (blue bars) to 12.45 events per 100 years (red bars) in the future climate. Models that simulate an opposite change to the multi-model mean are indicated by green circles. **c**, Same as **a**, but using a threshold of M-index>1.5 s.d. A total of 18 out of the 20 selected models (90%) simulate a decreased frequency in moderate pIOD events, with a statistically significant decrease of 60% in the multi-model ensemble mean. **d**, Same as **b**, but using a threshold of S-index>1 s.d. A total of 18 out of the 20 models (90%) simulate an increased frequency in strong pIOD, with a statistically significant increase of 44% in the multi-model ensemble mean. Models from CMIP6 are indicated in purple.

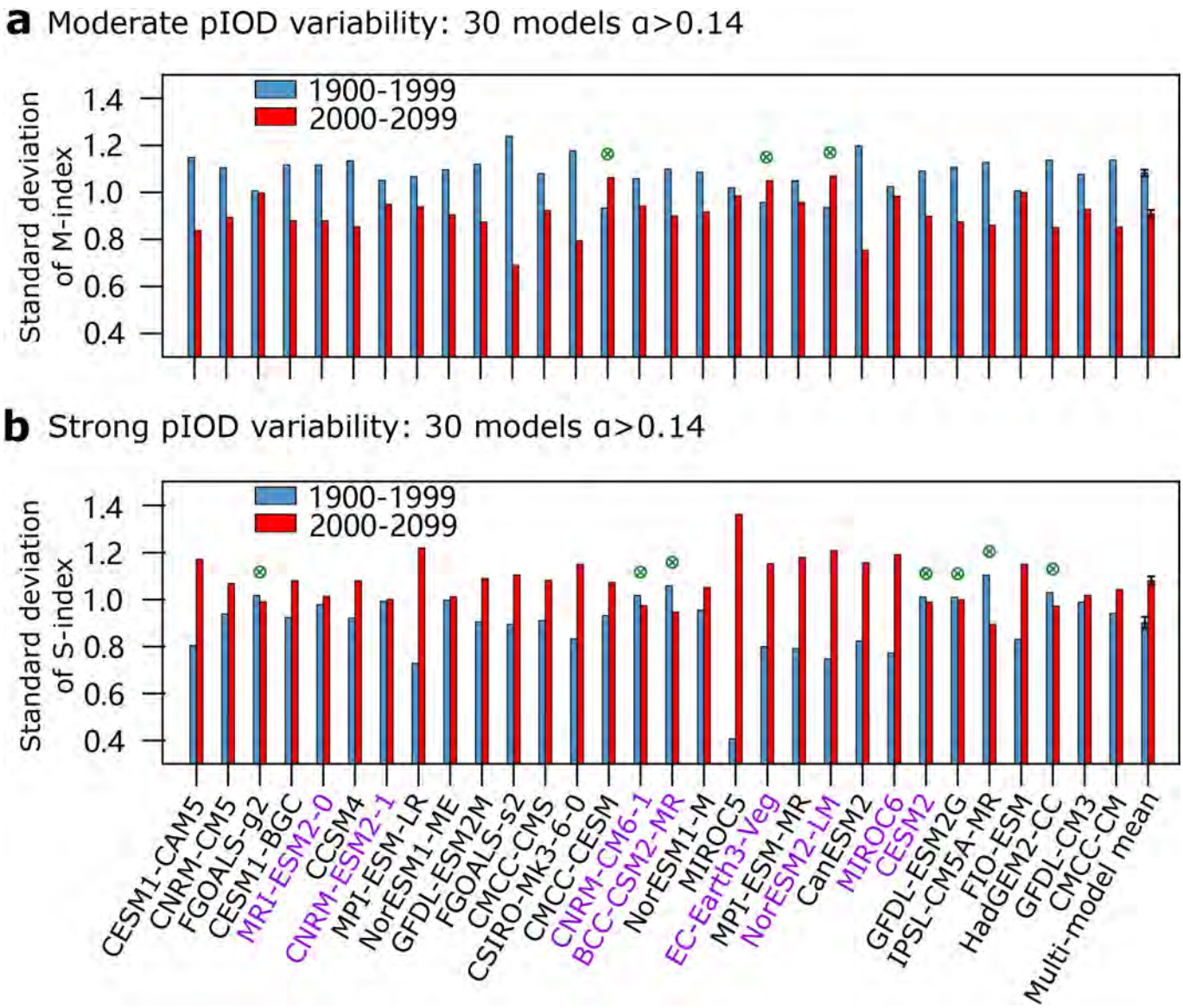

Extended Data Fig. 7 | Sensitivity of projected changes in pIOD variability to model selections. a, **b**, Comparison of variability of the moderate pIOD (M-index) and strong pIOD (S-index), respectively, in the present-day (1900–1999) and future (2000–2099) climate in 30 models that simulate a nonlinear coefficient α greater than 33.3% of the observed value. In **a**, a total of 27 out of the 30 models (90%) simulate a decrease in M-index variability in the future period (red bars) from that in the present-day period (blue bars). This leads to a multi-model mean decrease of 17%, statistically significant above the 95% confidence level, as indicated by the error bars. In **b**, a total of 23 out of the 30 selected models (77%) simulate an increase in S-index variability in the future climate, with a multi-model mean increase of 19%, statistically significant above the 95% confidence level. Models from CMIP6 are indicated in purple. Models that simulate an opposite change to the multi-model mean are indicated by green circles.

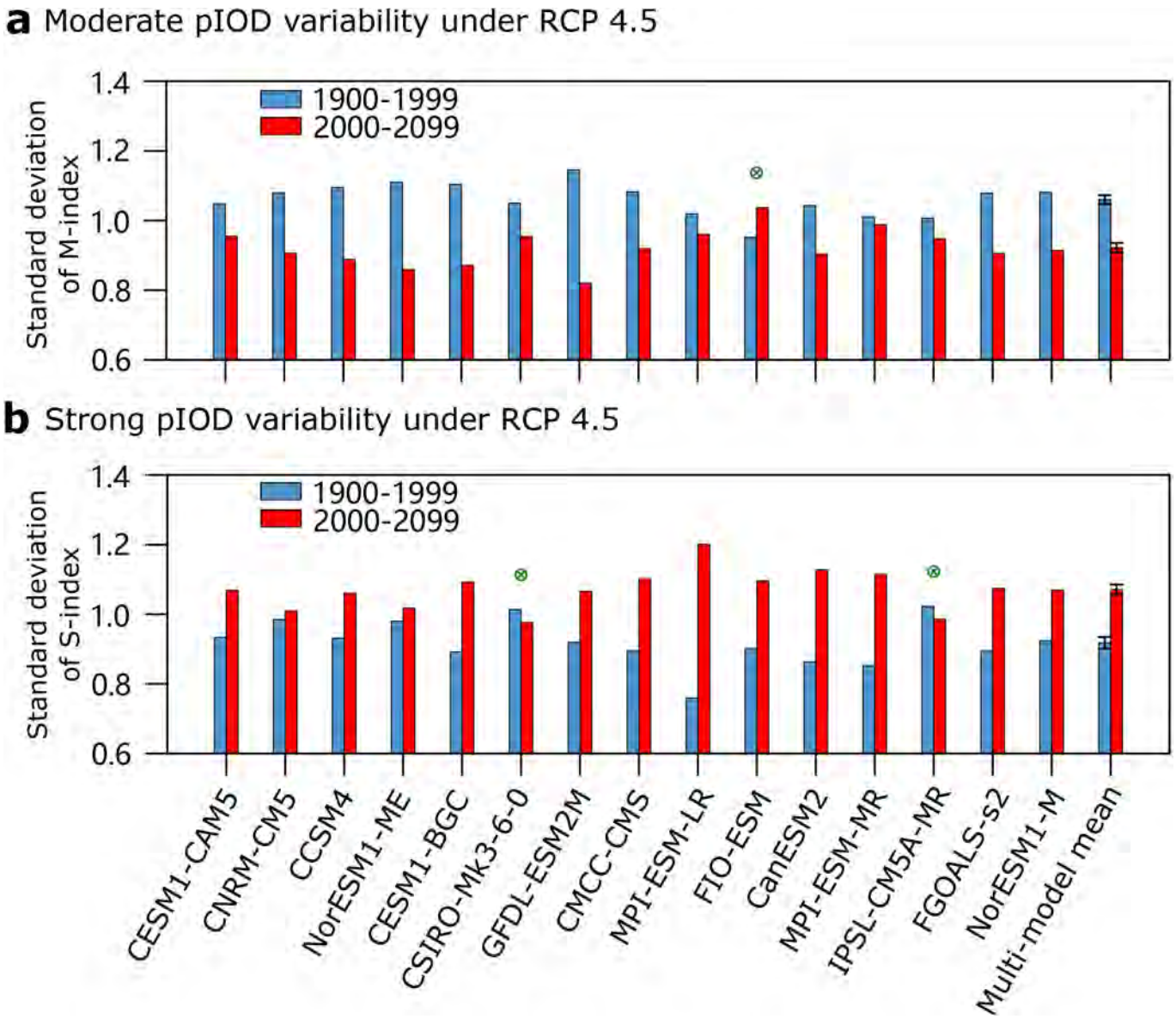

Extended Data Fig. 8 | Sensitivity of projected changes in pIOD variability to emission scenario. Shown are results for emission scenario RCP 4.5. **a**, **b**, Comparison of variability of the moderate pIOD (M-index) and strong pIOD (S-index), respectively, in the present-day (1900–1999) and future (2000–2099) climate in 15 out of 33 CMIP5 models that simulate a nonlinear coefficient α greater than 50% of the observed value. In **a**, a total of 14 out of the 15 models (93%) simulate a decrease in M-index variability in the future period (red bars) from that in the present-day period (blue bars). This leads to a multi-model mean decrease of 13%, statistically significant above the 95% confidence level, as indicated by the error bars. In **b**, a total of 13 out of the 15 selected models (87%) simulate an increase in S-index variability in the future climate, with a multi-model mean increase of 16%, statistically significant above the 95% confidence level. Models that simulate an opposite change to the multi-model mean are indicated by green circles. A total of 33 CMIP5 models are used here as outputs from CMCC-CESM and FGOALS-g2 are unavailable.

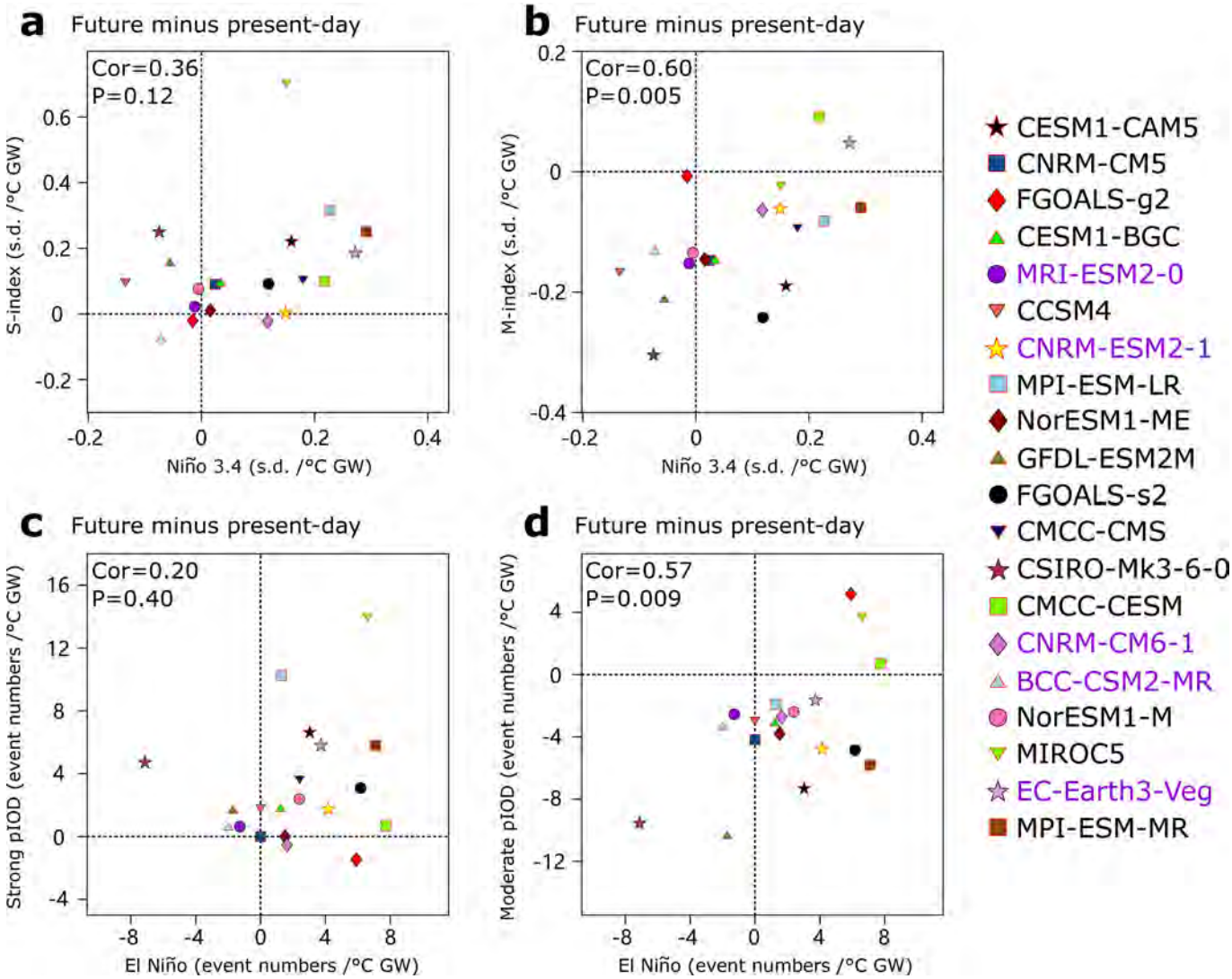

Extended Data Fig. 9 | Relationship between projected changes in ENSO and in pIOD. a, Scatter plot of changes in September, October, and November (SON) S-index variability versus changes in SON Niño3.4 index variability. The change is defined as the difference between the present-day (1900–1999) and future (2000–2099) period scaled by the corresponding increase in global mean SST in each model. **b**, Same as **a**, but between changes in SON M-index variability and in SON Niño3.4 index variability. **c, d**, Same as **a, b**, but for changes in strong pIOD (S-index>1.5 s.d.) or moderate pIOD (M-index>1.25 s.d.) frequency (events per 100 years) vs frequency of El Niño (Niño3.4>1.0 s.d.). The associated correlation coefficient and *P*-value are plotted. There is no relationship between changes in El Niño and S-index in **a** and **c**. Although there is a positive correlation in **b** and **d**, the changes in M-index and in El Niño are in the opposite direction, contravening the relationship between El Niño and M-index.

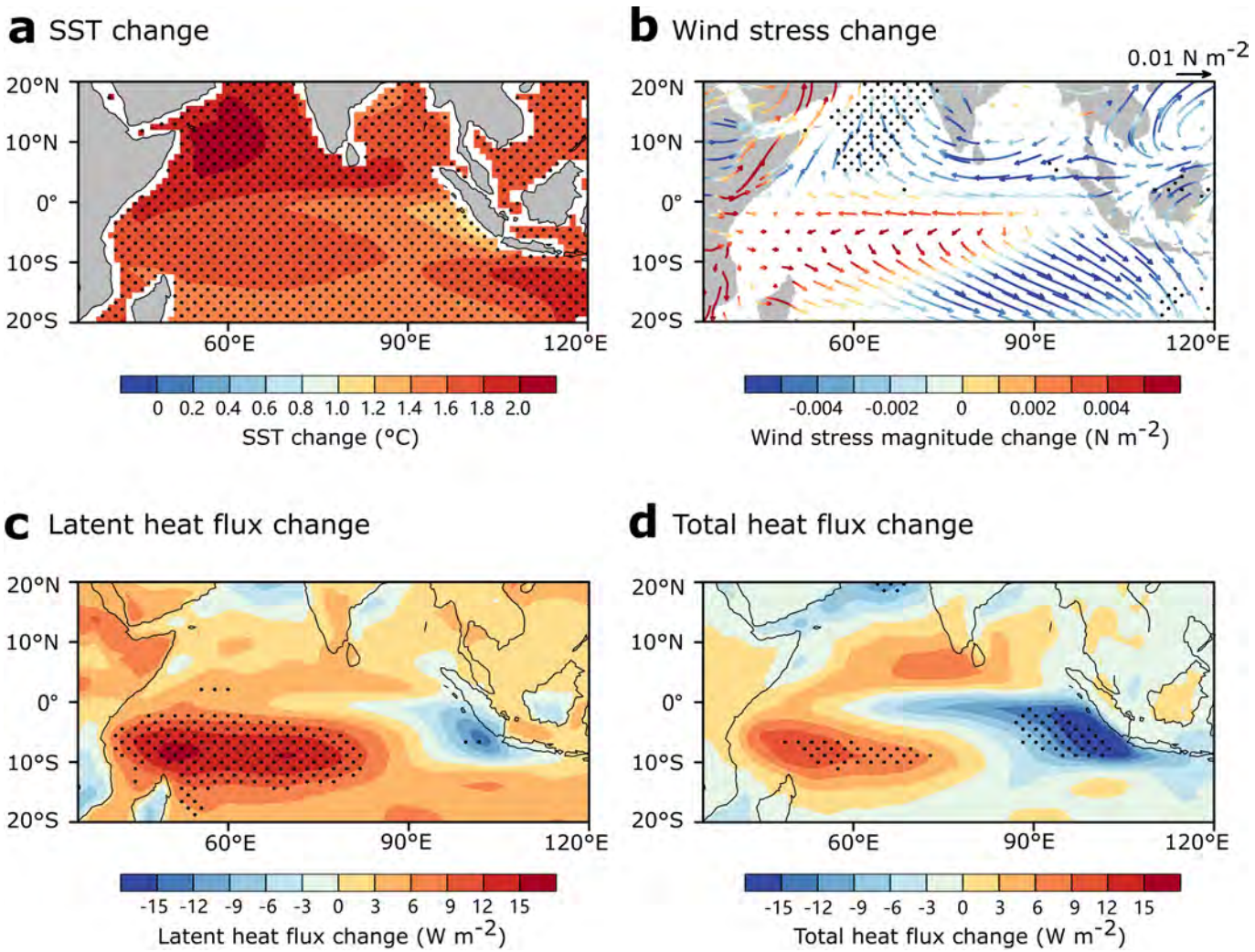

Extended Data Fig. 10 | Projected mean state change in the tropical Indian Ocean. Shown are averages over the 20 models that simulate a nonlinear coefficient α greater than 50% of the observed value. **a**, Multi-model ensemble averaged mean state changes of SON SST (in °C) between the future (2000–2099) and the present-day (1900–1999) climate. **b**, Same as **a**, but for the mean state change in surface wind stress (in N m^{-2}); changes in wind stress magnitude (in N m^{-2}) are indicated by colors. **c**, Same as **a**, but for the mean state change in latent heat flux (in W m^{-2}). **d**, Same as **a**, but for the mean state change in total heat flux (in W m^{-2}); positive values indicate an upward transfer of energy. Stippled areas indicate where changes are statistically significant above the 95% confidence level according to a two-tailed Student's *t*-tests.

ANNUAL REVIEWS

Annual Review of Earth and Planetary Sciences

Responses of the Tropical Atmospheric Circulation to Climate Change and Connection to the Hydrological Cycle

Jian Ma,[1] Robin Chadwick,[2] Kyong-Hwan Seo,[3] Changming Dong,[4,5] Gang Huang,[6,7,8,9] Gregory R. Foltz,[10] and Jonathan H. Jiang[11]

[1]College of Marine Sciences, Shanghai Ocean University, 201306 Shanghai, China; email: majian@shou.edu.cn

[2]Met Office Hadley Centre, Exeter, EX1 3PB, United Kingdom; email: robin.chadwick@metoffice.gov.uk

[3]Department of Atmospheric Sciences, Pusan National University, Busan, 46279, South Korea; email: khseo@pusan.ac.kr

[4]School of Marine Sciences, Nanjing University of Information Science and Technology, 210044 Nanjing, China

[5]Department of Atmospheric and Oceanic Sciences, University of California, Los Angeles, California 90095, USA; email: cdong@atmos.ucla.edu

[6]State Key Laboratory of Numerical Modeling for Atmospheric Sciences and Geophysical Fluid Dynamics, Institute of Atmospheric Physics, Chinese Academy of Sciences, 100029 Beijing, China; email: hg@mail.iap.ac.cn

[7]Qingdao National Laboratory for Marine Science and Technology, 266237 Qingdao, China

[8]Joint Center for Global Change Studies, 100875 Beijing, China

[9]University of Chinese Academy of Sciences, 100049 Beijing, China

[10]Atlantic Oceanographic and Meteorological Laboratory, National Oceanic and Atmospheric Administration, Miami, Florida 33149, USA; email: gregory.foltz@noaa.gov

[11]Jet Propulsion Laboratory, California Institute of Technology, Pasadena, California 91109, USA; email: jonathan.h.jiang@jpl.nasa.gov

Annu. Rev. Earth Planet. Sci. 2018.46:549-580. Downloaded from www.annualreviews.org
Access provided by 210.73.15.3 on 06/09/18. For personal use only.

ANNUAL REVIEWS **Further**

Click here to view this article's online features:

- Download figures as PPT slides
- Navigate linked references
- Download citations
- Explore related articles
- Search keywords

Annu. Rev. Earth Planet. Sci. 2018. 46:549–80

First published as a Review in Advance on March 26, 2018

The *Annual Review of Earth and Planetary Sciences* is online at earth.annualreviews.org

https://doi.org/10.1146/annurev-earth-082517-010102

Copyright © 2018 by Annual Reviews.
All rights reserved

Keywords

climate change, tropical atmospheric circulation, ocean precipitation, sea surface temperature, land rainfall, Hadley circulation

Abstract

This review describes the climate change–induced responses of the tropical atmospheric circulation and their impacts on the hydrological cycle. We depict the theoretically predicted changes and diagnose physical mechanisms

for observational and model-projected trends in large-scale and regional climate. The tropical circulation slows down with moisture and stratification changes, connecting to a poleward expansion of the Hadley cells and a shift of the intertropical convergence zone. Redistributions of regional precipitation consist of thermodynamic and dynamical components, including a strong offset between moisture increase and circulation weakening throughout the tropics. This allows other dynamical processes to dominate local circulation changes, such as a surface warming pattern effect over oceans and multiple mechanisms over land. To improve reliability in climate projections, more fundamental understandings of pattern formation, circulation change, and the balance of various processes redistributing land rainfall are suggested to be important.

Annu. Rev. Earth Planet. Sci. 2018.46:549-580. Downloaded from www.annualreviews.org
Access provided by 210.73.15.3 on 06/09/18. For personal use only.

1. INTRODUCTION

Global warming is likely to alter the distribution of water resources (Held et al. 2005, Seager et al. 2007, Zhang et al. 2007, Hegerl et al. 2015), and this redistribution will create socioeconomic, environmental, and security challenges. This is particularly true in the tropics, where almost half of the world's population and more than 80% of terrestrial biodiversity reside, and where societies are often extremely vulnerable to rainfall variability and change. Changes in the hydrological cycle at regional scales are closely related to the tropospheric circulation, which is primarily generated by the uneven distribution of diabatic heating and cooling (e.g., latent heating in convergence zones and radiative cooling in subsidence zones), and partly affected by synoptic eddy–induced heat and moisture transports (Pierrehumbert & Roca 1998, Schneider et al. 2010). Anthropogenic climate change modifies the stratification and diabatic forcing, and the large-scale circulation has to adjust accordingly to restore thermodynamic balance (e.g., Rodwell & Hoskins 1996). In this review, we examine how these adjustments occur and their likely impacts on the hydrological cycle.

Previous research focused on the effects of the global-mean increase of sea surface temperature (SST) as the zero-order problem, in order to define constraints for climate projections. The most important large-scale response of the circulation is a weakening in the tropical troposphere. Radiative and thermodynamic relations were proposed to diagnostically explain this slowdown (Knutson & Manabe 1995, Allen & Ingram 2002, Stephens & Ellis 2008), and the mean advection of stratification change (MASC) was more recently suggested (Ma et al. 2012) to explain how the atmospheric warming dynamically weakens the tropical circulation. Changes in the lapse rate have also been found to be responsible for the robust poleward expansion of the subsiding branches of the Hadley circulation in observations (Hu & Fu 2007) and general circulation model simulations (Frierson et al. 2007, Lu et al. 2007, Johanson & Fu 2009). However, these arguments are insufficient to explain why the intensity change of the Hadley cells is not as robust as that of the Walker cell (Vecchi & Soden 2007b).

On very large averaged spatial scales, regional precipitation change has been interpreted as a wet-get-wetter, dry-get-drier pattern, with rainfall increases at the core of existing rainy regions and decreases in current dry areas (Held & Soden 2006) and at the convective margins (Neelin et al. 2003, Chou & Neelin 2004, Chou et al. 2009). However, the dry-get-drier argument has been questioned (Scheff & Frierson 2012), because reduced precipitation appears along the outer flanks of the subtropics due to the poleward expansion of the subtropical dry zones. Nor does the wet-get-wetter interpretation hold at the smaller country-level scales relevant to climate change impacts (Chadwick et al. 2013, Greve et al. 2014, Roderick et al. 2014), where rainfall changes are strongly associated with circulation change. At regional scales, the dominant changes are often shifts in the

Sea surface temperature (SST): the water temperature close to the ocean's surface, often measured at 1 m depth

Hadley circulation: a large-scale tropical circulation, with air rising near the equator and descending in the subtropics and flowing equatorward near the surface and poleward near the tropopause

positions of convective regions, with associated changes in rainfall and water availability. These shifts are associated with a number of mechanisms that differ between land and ocean.

The wet-get-wetter, dry-get-drier hypothesis implicitly assumes a spatially uniform SST increase (SUSI); however, spatial variations in surface ocean warming are of considerable magnitude (Xie et al. 2010), with coherent seasonal variability (Sobel & Camargo 2011). Substantial research attention has therefore been downscaled to regional climate change (Xie et al. 2015) as the first-order problem. A warmer-get-wetter paradigm has been recognized as essential for the tropical ocean, casting SST patterns—i.e., deviations from the tropical-mean SST increase—as an important parameter for the adjustment in atmospheric circulation, not only shifting regional precipitation (Xie et al. 2010, Sobel & Camargo 2011, Su et al. 2017) and the Hadley cells but also altering tropical cyclone activity (Vecchi & Soden 2007a, Knutson et al. 2008, Vecchi et al. 2008, Zhao & Held 2012).

The most recent comprehensive review of circulation change under warming is that by Schneider et al. (2010); it emphasizes theoretical analyses of water vapor latent heat release and the Hadley circulation, constrained by energetic, hydrological, and angular momentum balances, with idealized experiments between cold and warm extremes. The current review uses theories for atmospheric circulation to guide the diagnostic understandings of the changes that occur in observations and complex climate models, such as those in the Coupled Model Intercomparison Project (CMIP) phases 3 (Meehl et al. 2007) and 5 (Taylor et al. 2012).

The review covers existing and proposed theories; diagnosed mechanisms framed with spatial scales of the changes (e.g., global and regional, ocean and land); and future research directions. In Section 2, we summarize the theories for precipitation and the Walker and Hadley circulations and address their predictions. In Section 3, we first introduce the diagnostic slowdown of the tropical circulation and related physical mechanisms, then discuss regional precipitation change throughout the tropics. We review the unique mechanism that dominates precipitation change over oceans and influences the structure of the Hadley circulation in Section 4. In Section 5, we summarize the complicated change of land rainfall and introduce the direct radiative effect of CO_2. We discuss potential future research directions in Section 6 and follow with a summary in Section 7.

Spatially uniform SST increase (SUSI): an experiment with an atmosphere-only model forced by the same SST warming everywhere (usually 2 or 4 K)

Coupled Model Intercomparison Project (CMIP): a community-based standard experimental protocol for climate (change) model diagnosis, validation, intercomparison, documentation, and data access

Intertropical convergence zone (ITCZ): an area encircling Earth where the northeast and southeast trade winds converge within approximately ±20° of the equator

Moist static energy (MSE): combination of an air parcel's internal energy and energy for expansion, potential energy, and latent energy

Geopotential: magnitude of gravitational potential energy per unit mass, after removing the effects of rotation (e.g., centrifugal acceleration)

2. THEORETICAL FUNDAMENTALS AND PREDICTIONS

In the rising branches of the atmospheric circulation, air expands and cools, condensing water vapor, and the droplets grow, causing rainfall. The highly coupled climate system organizes the precipitation into zonally oriented bands. The tropical rain bands include the intertropical convergence zone (ITCZ), with precipitation that peaks near but to the north of the equator. Dry zones exist in the equatorial cold tongue and subtropical regions, with the exception of heavy monsoon rainfall over South and East Asia during summer.

Precipitation releases huge amounts of latent heat, which concentrates along these narrow rain bands in the tropics but also interacts strongly with the global atmospheric circulation. This can be explained with moist static energy (MSE), h, which is defined as $h = Lq + C_pT + \Phi$, where q is specific humidity, L is the latent heat of condensation per unit mass, T is temperature, C_p is the heat capacity of air at constant pressure, and Φ is the geopotential. Circulation is directly linked to gross moist stability, which can be interpreted as the MSE export from a tropospheric column by the mean circulation per unit of mean upward mass flux (Back & Bretherton 2006).

Regions with larger gross moist stability require smaller vertical circulation strength to export a given amount of MSE than do regions of smaller gross moist stability and therefore can be thought of as being more stable in a large-scale sense. Conversely, lower gross moist stability translates to

Annu. Rev. Earth Planet. Sci. 2018.46:549-580. Downloaded from www.annualreviews.org
Access provided by 210.73.15.3 on 06/09/18. For personal use only.

larger upward velocities, and hence less stability, for a given export of MSE. Strong surface/low-level wind and moisture convergence over warm waters provides sufficient instability and latent heating to drive intense convection, so that the tropical precipitation bands are associated with SST of at least 26.5–27°C. The thermodynamic coupling between SST and deep convection also plays an important role in shaping rainfall change in global warming.

Walker circulation: a thermally driven equatorial zonal and vertical circulation, e.g., rising above the western Pacific, near the maritime Asian continent, and sinking over the eastern Pacific

2.1. Theories for Tropical Tropospheric Overturning Circulations

The tropical atmosphere is dominated by thermally driven overturning cells and monsoon circulations. As the monsoons have been systematically reviewed in the literature (An et al. 2015, Véspoli de Carvalho & Jones 2016), this section only discusses mechanisms driving and shaping the Walker and Hadley circulations.

2.1.1. Walker circulation and Bjerknes feedback. The equatorial Pacific Ocean features strong zonal asymmetry, characterized by the warm pool in the west and cold tongue in the east. The equatorial Atlantic Ocean has a similar thermal distribution, though the variations are weaker. The westward SST gradient confines deep convection mainly to the west warm pool, favoring an eastward gradient in sea surface pressure. As the Coriolis force is weak near the equator, the pressure gradient force drives prevailing easterly winds, generating oceanic equatorial upwelling via horizontal divergence induced by poleward Ekman currents. The westward wind forcing also tilts the sea surface to generate a balancing eastward pressure gradient force in the ocean, which shoals the eastern thermocline and allows cold water to be upwelled into the mixed layer and maintain the cold tongue. Such easterly winds at the surface, convection in the west, subsidence in the east, and westerly counterflow in the upper atmosphere compose the Walker circulation. This circular argument and interdependence between the ocean and atmosphere constitute the Bjerknes feedback (Bjerknes 1969) and are essential for explaining the slowdown of the Walker circulation in response to both El Niño and global warming (see the sidebar titled Bjerknes and Wind-Evaporation-SST Feedback).

2.1.2. Hadley circulation and northward-displaced intertropical convergence zone. On average, the tropics receive more solar radiation than the extratropics, and this energy imbalance is equilibrated by the heat transport via oceanic and atmospheric motion. The Hadley circulation is an important agent for poleward dry energy transport by the tropical atmosphere. This zonal-mean cell is located in both hemispheres and features ascent near the equator and subsidence in the

BJERKNES AND WIND-EVAPORATION-SST FEEDBACK

The Bjerknes feedback is an ocean-atmosphere positive feedback shaping equatorial climate variability and change. For example, in the equatorial Pacific, relaxation of the easterly trade winds causes a flattening of sea level and thermocline, and hence a reduced upwelling-induced cooling of the eastern Pacific. This local warming effect decreases the westward SST gradients and hence further weakens the winds.

The wind-evaporation-SST feedback is an ocean-atmosphere interaction process shifting the intertropical convergence zone northward from the equator. A disturbance of SST to be warmer north of the equator causes cross-equatorial southerly winds. The Coriolis force then deflects the winds, decelerating the trade winds north of the equator and accelerating winds to the south. The evaporation of the northern tropics is weakened, thereby warming the local SST, and vice versa to the south. This positive feedback amplifies the initial disturbance.

Annu. Rev. Earth Planet. Sci. 2018.46:549-580. Downloaded from www.annualreviews.org
Access provided by 210.73.15.3 on 06/09/18. For personal use only.

subtropics. The poleward flow in the upper troposphere is turned by the Coriolis force, forming strong westerly subtropical jets at the poleward edges of the Hadley cells, with the help of eddy momentum fluxes. In contrast, the air moves equatorward at the surface, and the Coriolis force results in easterly trade winds.

However, the rising branch of the Hadley circulation, known as the ITCZ, is not on the equator but to the north, despite the strongest solar insolation occurring at the equator. A wind-evaporation-SST feedback (Xie & Philander 1994) was suggested to explain this displacement (see the sidebar titled Bjerknes and Wind-Evaporation-SST Feedback). Assuming an SST perturbation, with positive anomalies to the north and negative to the south of the equator, the induced atmospheric pressure anomalies would drive a southerly cross-equatorial wind. The Coriolis would force wind anomalies to be easterly to the south and westerly to the north of the equator, increasing and decreasing the local easterly trade wind speed, and hence intensifying and reducing the corresponding evaporative cooling, respectively. This warms the SST to the north and vice versa, amplifying the initial perturbation. Thus, a positive wind-evaporation-SST feedback is formed to break the equatorial symmetry set by the annual-mean solar radiation, yet it does not favor either hemisphere. The following processes have been demonstrated to initiate the climatic asymmetry: asymmetric land-sea distribution, westward-propagating asymmetric Rossby waves, and SST-stratus feedback over the broad subtropical subsidence regions.

2.1.3. Latitudinal boundary of the Hadley cell. The Hadley circulation is thought to be caused by thermal gradients extending from the equator to the poles; however, the cells cease at around 30°N/S. Held & Hou (1980) explained this lateral restriction with simplified dry thermodynamics, by considering an axisymmetric flow and assuming the atmosphere is semifree of friction. First, the angular momentum conservation is used at the tropopause with the assumption of negligible vertical motion and friction, equivalent to a simplified zonal momentum equation. From this simplified momentum balance, the upper-level zonal wind can be determined as a function of latitude. The upper-level winds also define the average vertical wind shear, because the surface zonal wind is negligible due to surface friction. Then the meridional geostrophic balance, or the equivalent thermal wind balance, can be used to derive the meridional profile of tropospheric-mean potential temperature as a function of latitude and tropopause height.

The latitudinal integration of the tropospheric-mean potential temperature minus its radiative equilibrium value should be zero from the equator to the poleward boundary of the Hadley cell because the energy of the circulating air is conserved. At the poleward boundary, the actual and equilibrium potential temperatures should also be equal because of the below-discussed nature of radiative transfer. When an air parcel moves from the equator to the pole, it is cooler than it would be in radiative equilibrium. It is therefore warmed at first, and after it exceeds the equilibrium temperature, it starts to lose heat. After it reaches the equilibrium temperature again, there is no such energy source to heat it again, so the motion has to cease. This determines the latitudinal boundary of the Hadley circulation, which is proportional to the square root of the tropopause height and related to the shape of the equilibrium temperature.

Taking typical values observed from the current climate as input, the Hadley cell is constrained to terminate at 20–30°N/S and cannot extend all the way to the poles. The Hadley circulation flattens the meridional temperature profile by transporting heat poleward: High potential temperature is transported poleward in the upper troposphere, and cold air returns equatorward near the surface. This cools temperature at the equator and raises temperature at the poleward terminus of the circulation, compared to the radiative-convective equilibrium. Midlatitude eddies with traveling lows and highs also transport both sensible and latent heat poleward, helping to terminate the Hadley circulation in the subtropics.

Annu. Rev. Earth Planet. Sci. 2018.46:549-580. Downloaded from www.annualreviews.org
Access provided by 210.73.15.3 on 06/09/18. For personal use only.

2.2. Future Changes Predicted by the Theories

The meridional Hadley circulation acts with the Walker circulation to regulate atmospheric temperature, humidity, cloudiness, and rainfall in the tropics and subtropics, with important implications for the hydrological cycle over ocean and land. In order to predict the changes in both circulations, it is necessary to extend the above theories to a warming climate. This section discusses a poleward expansion of the subsidence branch of the Hadley circulation, an energy constraint for slowdown of the tropical circulation, and a hypothetical pattern of future rainfall change.

Greenhouse gas (GHG): a gas in the atmosphere absorbing and emitting infrared radiation and warming Earth; examples include H_2O, CO_2, CH_4, N_2O, O_3

Thermal wind relation: vertical wind shear (variation of geostrophic wind with pressure) in proportion to horizontal temperature gradient with a direction paralleling the isotherms

2.2.1. Poleward expansion of the tropics. Although the inviscid theory of Held & Hou (1980) omitted two important dynamical factors, upper-level friction and moisture effect of latent heating, their simplified framework still predicts a poleward expansion of the Hadley cell. Increases in greenhouse gas (GHG) concentrations warm the troposphere and cool the stratosphere, resulting in a rise of the tropopause. This allows the circulating air of the Hadley cell to travel further, as tropopause height was shown to be important for its poleward limit. The connection between tropopause height and Hadley cell can be explained in the context of the thermal wind relation. An upward extension of the troposphere reduces vertical wind shear since the momentum conservation is hardly influenced. As a consequence of the thermal wind balance, the meridional gradient of potential temperature is reduced, extending poleward the latitude at which the potential temperature matches the equilibrium temperature. This is consistent with the slowdown of the tropical circulation associated with a flattened temperature gradient suggested by MASC (Ma et al. 2012).

More realistic theories that include the effects of midlatitude eddies give similar predictions with three dynamical mechanisms to explain global warming–induced expansion of the tropics more than Held & Hou (1980) would suggest. Lu et al. (2007) suggested that an increase in static stability and an associated reduction in baroclinicity in the subtropics (baroclinicity describes the misalignment between pressure and density gradients) cause eddy activity to retreat to higher latitudes and the Hadley cell to expand poleward. Changes in vertical wind shear could also contribute to the expansion.

The second mechanism involves upper-tropospheric baroclinic waves. With the rising tropopause in the subtropics, the phase speed of waves increases, weakening the waves' equatorward penetration and resulting in a poleward shift of the eddy momentum flux convergence and the position of the eddy-driven jet (Chen & Held 2007, Lorenz & DeWeaver 2007, Chen et al. 2008). For the third mechanism, Kidston et al. (2015) explained the tropical expansion from the standpoint of the stratosphere. They suggested that the stratospheric circumpolar westerly jet forming in winter has a coupled influence on tropospheric dynamics. Global warming induces a strengthening of the circumpolar jet, causing a poleward shift in the storm tracks and tropospheric jet stream.

Model diagnostics also suggest that radiative changes associated with clouds and water vapor affect the extent of the tropical boundaries. For example, Voigt & Shaw (2015) found that changes in tropical ice clouds contribute to an expansion of the tropics, while increased water vapor reduces the expansion, with significant intermodel uncertainty in the magnitude of these effects. Using a global model simulation, Wang et al. (2015) found a reduced meridional stream function and zonal winds over the tropics, as well as a poleward shift of the jet stream. They attributed the weakened and expanded tropical circulation to global redistribution of aerosol emissions from traditional industrialized countries to fast-developing Asia, which has caused a weakening of the meridional temperature gradient.

There is accumulating observational evidence confirming the theoretical prediction that the subsidence boundaries of the tropics in both hemispheres are expanding poleward. In a critical

Annu. Rev. Earth Planet. Sci. 2018.46:549-580. Downloaded from www.annualreviews.org
Access provided by 210.73.15.3 on 06/09/18. For personal use only.

assessment, Lucas et al. (2014) identified five methodologies used to define the tropical expansion: tropopause-, satellite-, stream function–, jet stream–, and surface-based methods.

In summary, observations, model diagnostics, and theoretical predictions agree that the tropics should have expanded poleward, though there is uncertainty in the rate of the expansion, and there are multiple ways to understand it. The poleward extension of the subtropical dry zone with the poleward expansion of the tropics may bring drought conditions to certain regions that currently enjoy temperate weather (Seidel et al. 2008). Fu et al. (2006) demonstrated that the poleward shift leads to midlatitude warming and contributes to an increased frequency of drought in both hemispheres, including in many heavily populated regions. Therefore, reducing uncertainties in estimates and providing robust information for the expansion and its interpretation are important goals of future research.

Annu. Rev. Earth Planet. Sci. 2018.46:549-580. Downloaded from www.annualreviews.org
Access provided by 210.73.15.3 on 06/09/18. For personal use only.

2.2.2. Moist static energy constraint for tropical circulation. A series of studies (Chou & Neelin 2004; Chou et al. 2009, 2013b; Chou & Chen 2010) used conservation of the aforementioned MSE to examine projected changes in the tropical circulation. MSE is imported into ascent regions through low-level moisture convergence and exported at upper levels through the horizontal divergence of high-MSE air. As there is a net flux of MSE into ascent regions from surface and radiative fluxes within those regions, this must be balanced by MSE export at upper levels. A number of mechanisms for circulation change were proposed under this framework, two of which (the dynamical rich-get-richer and upped-ante hypotheses) are described in Section 2.2.3.

A third mechanism predicts that the tropical circulation should weaken in global warming, with the effect of increasing depth of convection on the efficiency of net MSE export from tropical ascent regions (i.e., the gross moist stability). Under global warming, low-level temperature, moisture, and MSE import increase, which, therefore, has to be balanced by an increase of the MSE being exported at upper levels (assuming no large compensating changes in surface or radiative fluxes in ascent regions). This is achieved both by the enhanced warming of air at upper levels (discussed in Section 3.1.3) and by an increase in the height of convective outflow (as MSE increases with height in the upper troposphere).

In order for the tropical circulation to weaken, this increase in MSE at the level of convective outflow must not only balance the increase in low-level MSE but also overcompensate, so that the efficiency of net MSE export is increased and the same amount of MSE can be exported by a weaker circulation (increased gross moist stability). Chou et al. (2013b) showed that warming at upper levels alone is not enough to produce a sufficient increase in MSE export for the circulation to weaken, and that the height of convective outflow (depth of convection) must also increase for this to occur. Therefore, the weakening tropical circulation appears to be closely linked to the increased depth of convection, which is itself strongly related to changes in radiative emission by water vapor at upper levels (Hartmann & Larson 2002, Ingram 2010, Zelinka & Hartmann 2011).

2.2.3. The rich-get-richer theory for regional rainfall change. The wet-get-wetter concept was raised to describe how the patterns of evaporation (E) and precipitation (P) would change under global warming, including two related but slightly different hypotheses. The most commonly used version (Held & Soden 2006) proposed that in the (hypothetical) absence of circulation change, increased atmospheric water vapor implies an increased moisture transport from dry to wet regions, and hence an increased gradient of $P–E$. This leads to greater $P–E$ in wet regions and greater $E–P$ in dry regions, which appears to have been confirmed on very large averaged spatial scales by both observational (Allan et al. 2010, Durack et al. 2012) and modeling (Allan 2011) studies and

WET-GET-WETTER AND WARMER-GET-WETTER

In the (hypothetical) absence of circulation change, increased atmospheric water vapor implies an increased moisture transport from dry to wet regions, and hence an increased precipitation gradient; i.e., rainfall increases in the core of existing rainy regions and decreases in current dry areas and at convective margins.

A general warming of the tropical troposphere raises the SST threshold for tropical convection, so that convective precipitation increases where SST warming exceeds the tropical mean and decreases where relatively weak warming exists. This SST pattern effect is achieved by adjusting the atmospheric circulation and corresponding surface divergence field, including two outstanding modes: an equatorial peak anchoring a local precipitation increase, and a meridional dipole with increased rainfall and weakened trade winds over the warmer hemisphere.

Annu. Rev. Earth Planet. Sci. 2018.46:549-580. Downloaded from www.annualreviews.org
Access provided by 210.73.15.3 on 06/09/18. For personal use only.

is often described as the thermodynamic component of water cycle change (see the sidebar titled Wet-Get-Wetter and Warmer-Get-Wetter).

The alternative version is a dynamical feedback on this increased atmospheric moisture (Neelin et al. 2003, Chou & Neelin 2004), described as the rich-get-richer or anomalous gross moist stability mechanism. Originally based on experiments with a coupled ocean-atmosphere-land model of intermediate complexity (Neelin & Zeng 2000, Zeng et al. 2000), this mechanism was also examined in the CMIP3 projections (Chou et al. 2009). Under global warming, the moistened boundary layer (i.e., the lowest part of the atmosphere, which is sensitive to the presence of Earth's surface) reduces gross moist stability and consequently enhances convection and precipitation in convective regions. If it applied throughout the tropics, a consequence of this dynamical feedback would be enhanced convergence into ascent regions, and hence a strengthened tropical circulation. As overall the circulation actually weakens (see Section 3.1), this dynamical rich-get-richer mechanism cannot be the dominant controller of tropical circulation change in response to warming, though it could be important locally.

To explain the shift of the maximum rainfall increase from the core rainy regions (see Section 3.2.1), Chou & Neelin (2004) raised the additional upped-ante hypothesis, arguing that a warmer troposphere increases the boundary-layer moisture threshold (the ante) for convection. This could result in reduced rainfall in the margins of convective regions, if the increase in moisture advection into these regions is insufficient to meet the raised convective threshold. However, rainfall does not reduce in all convective margins, meaning that the upped-ante applies selectively in some regions but not others (Chadwick et al. 2013). Indeed, this convective threshold-raising theory is part of the warmer-get-wetter view (Ma & Xie 2013; discussed in Section 4.1.1), and is applicable only on the margins where the SST increase is lower than the tropical mean. Otherwise the ante needed to start convection remains roughly the same.

Boundary layer: the lowest part of the atmosphere, directly influenced by the surface, with turbulent wind, temperature, and moisture and strong vertical mixing

3. LARGE-SCALE CIRCULATION AND REGIONAL PRECIPITATION CHANGES ACROSS THE TROPICS

Here we extend Section 2.2.2 by introducing diagnostic evidence and mechanisms raised to explain the large-scale slowdown of the tropical circulation. We then compare the spatial pattern of the weakening with the precipitation gradient increase theoretically hypothesized in Section 2.2.3. As the universal dynamical and thermodynamic components of regional rainfall change across the tropics, they are found to significantly offset each other.

3.1. Weakening of the Large-Scale Atmospheric Circulation

A weakening of the tropical circulation and an associated increase in the average atmospheric residence time of water vapor are robust projections of all climate models. This section discusses observational evidence for the circulation slowdown and physical mechanisms to explain it.

3.1.1. Observed and simulated weakening of tropical circulation. Since the mid-nineteenth century there has been a weakening trend in the Indo-Pacific zonal sea level pressure gradient, which was suggested by Clarke & Lebedev (1996) as evidence of a weakening Walker circulation. Vecchi et al. (2006) demonstrated that model simulations could accurately reproduce the observed trend in sea level pressure gradient, but only when they included anthropogenic forcing, indicating that the weakening Walker circulation was primarily due to human activities. Recent work has raised more uncertainty about the weakening of the surface winds, with observed global and tropical increases in wind speed during 1987–2006 (Wentz et al. 2007, Ma et al. 2016) and a positive trend in the global evaporation since the late 1970s (Yu 2007). A new data set, which uses wave height to compensate for errors due to a changing level of wind observations (Tokinaga & Xie 2011), suggests that there has indeed been a Walker circulation slowdown over the past 60 years (Tokinaga et al. 2012), though overall twentieth-century trends of surface temperature and pressure in the Pacific remain uncertain across different data sets (Solomon & Newman 2012).

This observational evidence supports model projections of further weakening of the tropical atmospheric circulation during the twenty-first century (Tanaka et al. 2004). Held & Soden (2006) found a reduction in the amount of convection in CMIP3 models, which is also present in the more recent CMIP5 projections (Chadwick et al. 2013, Su et al. 2014). Vecchi & Soden (2007b) further reported a reduction in the frequency of strong updrafts and an increase in the frequency of weak updrafts.

Several complementary hypotheses have been proposed to explain the slowing of the tropical tropospheric circulation, and these are outlined here. This large-scale circulation response to general SST warming can be viewed from a variety of different perspectives, such as the differing rates of change in water vapor, lapse rate, precipitation, and radiative cooling (see the sidebar titled Thermodynamic, Radiative, and Dynamical Hypotheses for Tropical Circulation Weakening). In fact, these diagnostic results are likely to all be part of the same overall mechanism, with unsolved questions remaining besides the convective depth–related constraint (Section 2.2.2).

THERMODYNAMIC, RADIATIVE, AND DYNAMICAL HYPOTHESES FOR TROPICAL CIRCULATION WEAKENING

The global-mean water vapor and vertical gradient of air temperature increase at ~7% K^{-1} of surface warming, but the fractional changes in global-mean precipitation and net longwave radiative cooling are only 1–2% K^{-1} based on model projections. This contrast indicates a weakening of the circulation at a rate of ~5% K^{-1} in both convective and subsidence regions.

Mean advection of stratification change (MASC) is a dynamical mechanism proposed to explain the weakening of the tropospheric circulation throughout the tropics in climate change. Following moist adiabats, tropics-wide warming increases with height and stabilizes the atmosphere. This leads to relative cooling of the air column in ascending regions due to anomalous cold advection of low-level air, and relative warming in subsidence regions due to warm advection. This reduces air temperature and pressure gradients between ascent and descent regions, opposes the climatological circulation, and slows it down as an adiabatic forcing.

Annu. Rev. Earth Planet. Sci. 2018.46:549-580. Downloaded from www.annualreviews.org
Access provided by 210.73.15.3 on 06/09/18. For personal use only.

Clausius-Clapeyron equation: a relation giving the slope of the pressure-temperature coexistence curve of a phase transition in terms of entropy and volume changes across the transition

Moist adiabatic lapse rate: the rate at which atmospheric temperature decreases with an increase in altitude, including latent heating by condensation of water vapor

Annu. Rev. Earth Planet. Sci. 2018.46:549-580. Downloaded from www.annualreviews.org
Access provided by 210.73.15.3 on 06/09/18. For personal use only.

3.1.2. Thermodynamic relation on convective mass-flux change. Held & Soden (2006) combined the Clausius-Clapeyron equation for the saturation vapor pressure with an approximate equation for precipitation,

$$P = Mq, \qquad 1.$$

to diagnose how the tropical circulation should change under warming. Here P is precipitation, M is the vertical convective mass flux, and q is a typical boundary-layer specific humidity. This can be understood simply as "what goes up must come down," and it shows that any increase in boundary-layer moisture (q) must result in increased precipitation unless it is balanced by a decrease in convective mass flux (M).

For CMIP3 A1B simulations, the global-mean water vapor increase was diagnosed to be $\sim$7% K^{-1}, in close agreement with the expected increase in saturation vapor pressure from Clausius-Clapeyron. The fractional change in global-mean precipitation, however, is only 1–2% K^{-1} based on projections from coupled climate models. This contrast indicates that the circulation in the convective regions has to slow down at a rate of $\sim$5% K^{-1} of the global ocean surface warming. This reduction in time-mean convective mass flux appears to manifest itself in a decrease in the frequency and/or duration of convective events (Sun et al. 2007), which is robustly seen in climate model and high-resolution cloud resolving model simulations (Singh & O'Gorman 2013), rather than a reduction in the updraft intensity of individual storms.

Yet the relation itself is only part of the explanation of the slowdown, with the dynamical mechanism that constrains the interaction between precipitation and radiation to have a muted response still lacking.

3.1.3. Radiative relation on subsidence change. A time-mean reduction of upward motion over the entire rising branch of the Walker circulation was reported by Knutson & Manabe (1995), accompanied by a similar weakening of the easterly trade winds throughout the tropical Pacific. This result seemed surprising at the time, given increased condensation and enhanced precipitation over the western Pacific warm pool region, which is now known to result from the ability of the atmosphere to hold more moisture. They attributed the weakening of the circulation to an imbalance in the subsidence regions important for regulating the overall distribution of the tropical greenhouse effect (Pierrehumbert 1995, Williams et al. 2009): Net radiative cooling of the troposphere in these regions does not increase as quickly as the vertical gradient of air temperature, as discussed in more detail below.

Temperature follows an approximately moist adiabatic lapse rate almost uniformly throughout the tropics, a quasi-uniformity known as the weak temperature gradient approximation (e.g., Bretherton & Sobel 2002). In ascent regions convection causes the atmospheric temperature profile to be moist adiabatic, and this vertical profile is then propagated to the rest of the tropics by fast equatorial waves. A global SST increase shifts the temperature profile throughout the whole atmospheric column, with air warming increasing with height according to the curvature feature of the moist adiabats. Recent work (O'Gorman & Singh 2013) suggests that the change in the atmospheric temperature profile in response to surface warming may be more accurately represented by a transformation involving an upward shift. Nevertheless, both descriptions result in enhanced warming at upper levels.

In the energy budget for subsidence regions, radiative cooling is mainly balanced by adiabatic warming via large-scale descent. Therefore, any change in radiative cooling must be balanced by some combination of change in lapse rate and change in circulation strength, which together determine the magnitude of the change in adiabatic warming. As models predict that the lapse rate

decreases more than the relatively weak enhancement in radiative cooling, the vertical motion in descent regions has to weaken to maintain the balance.

The thermodynamic and radiative relations use similar formulations between the convective and subsidence regions, respectively. This can be explained by an energy balance argument that latent heating of the troposphere (i.e., precipitation) increases as fast as net tropospheric longwave radiative cooling (1–2% K^{-1}), as the two are diagnosed to approximately balance (Allen & Ingram 2002). However, the amount of latent heat release demanded by the surface energy budget (Pierrehumbert 2010) can be achieved through many different atmospheric adjustments rather than radiative cooling (Pierrehumbert 1999). As a result, the latent heating and radiative cooling may be only weakly coupled, unless there exists a more subtle collective behavior involving the interaction of large-scale dynamics with radiation and convection. The solar energy absorbed at the surface (Le Hir et al. 2009) can be used as a constraint for evaporation to limit precipitation, but at the current climate status this constraint is insufficient to achieve the muted responses, since at least a 5% K^{-1} increase can be yielded in a column radiative-convective model (Pierrehumbert 2002). Thus, the mechanisms that constrain the increase in radiative cooling have still not been convincingly explained.

3.1.4. A dynamical mechanism associated with lapse-rate change. Also related to lapse-rate change is the MASC mechanism of Ma et al. (2012). As discussed in Section 3.1.3, global SST warming leads to a tropics-wide warming that increases with height in the atmosphere. This stabilization results in a further effect on total column temperature through vertical advection of the change in lapse rate by the mean circulation. In contrast to the thermodynamic and radiative relations, which apply respectively to convective and subsidence regions, MASC is applicable throughout the tropics.

Upper-level air warms more than lower-level air, so this leads to relative cooling of the air column in ascending regions due to upward advection of cooler low-level air and relative warming of the column in subsidence regions due to downward advection of warmer upper-level air. This MASC advective effect distorts isotherms of air warming, and the effect is similar with or without spatial variation of the SST increase. In this way, vertical advection tends to reduce air temperature and pressure gradients between ascent and descent regions. This can be viewed as an adiabatic forcing opposing the climatological circulation, with the effect of slowing it down.

The MASC effect has an analytical expression and can be diagnosed from general circulation models and applied to a linear baroclinic model to examine the effect of such geographically uneven heating on atmospheric circulation (Watanabe & Kimoto 2000). The individual effect of MASC significantly weakens tropical thermal-driven circulations, including the Walker and Hadley cells and monsoon winds (Ma & Yu 2014b, Qu & Huang 2016), and reduces the meridional air temperature gradient and hence the tropical wind shear through thermal wind relation. As a purely dry effect, MASC is able to offset the enhanced latent heating due to moisture increase, because vertical temperature advection nearly balances diabatic heating in the long-term-mean large-scale tropical atmospheric dynamics. In addition, global warming features a pronounced tropical-mean SST warming four times larger than the spatial patterns, resulting in significant atmospheric stabilization and hence the MASC effect. In order for the linear baroclinic model to properly reproduce circulation change in a fully coupled model under GHG forcing, this effect has to be explicitly assigned, since it is not included by default. In contrast, for internal variability, such as El Niño, spatial variations in SST anomalies are 40% greater than the mean warming, so that stratification is less affected and latent heating can be used to drive the linear model effectively without MASC.

Annu. Rev. Earth Planet. Sci. 2018.46:549-580. Downloaded from www.annualreviews.org
Access provided by 210.73.15.3 on 06/09/18. For personal use only.

Furthermore, since the climatological circulation is relatively similar between models and scenarios, as are the tropical-mean moist adiabats, the magnitude of MASC is also fairly independent of model physics and forcing scenarios. **Figure 1** provides evidence for this argument in the form of an empirical orthogonal function analysis of the MASC forcing among 76 simulations under three scenarios, including CMIP3 A1B and CMIP5 Representative Concentration Pathways (RCPs) 6.0 and 8.5, corresponding to medium and high GHG emission scenarios. Dominating 68.3% of the total variance, the first leading mode (**Figure 1*a***) shows significant spatial dependence on climatological pressure velocity, which indicates that the intermodel/interscenario variability is primarily in the magnitude of the circulation change as a whole, rather than in local differences due to model details and radiative forcing. A high correlation of 0.92 between the first principal component against tropical-mean (40°S–40°N) SST increase suggests that the strength of the MASC effect is mainly dependent on the magnitude of spatially uniform warming in each model (**Figure 1*b***).

Representative Concentration Pathways (RCPs): four GHG concentration (not emissions) trajectories adopted by the Intergovernmental Panel on Climate Change for its *Fifth Assessment Report* in 2014

3.2. Tropics-Wide Changes in Regional Precipitation

In addition to the global-mean warming effects, regional climate change is very important from a practical standpoint, and robust information is urgently needed (Xie et al. 2015). This section describes the observed regional circulation and rainfall changes in response to increased GHG concentrations, then discusses the offsetting mechanisms of change in the whole tropics. In addition to GHG forcing, the effects of which we examine here, changes in aerosol concentrations have been linked to large regional changes in circulation and the hydrological cycle. These aerosol-circulation interactions are not discussed, as they are reviewed by Lee et al. (2014).

3.2.1. What do the observations tell? Lau & Wu (2007) analyzed global precipitation products and found a positive trend along the equatorial oceans (5°S–5°N), but negative trends over the Indo-Pacific warm pool and central Africa. Zhou et al. (2011) found similar patterns, with the maximum rainfall increase occurring at 5°N, and interpreted the result as a strengthening of the ITCZ, consistent with the wet-get-wetter view. Allan et al. (2010) also examined trends during 1988–2008 (earlier data were considered less reliable), averaged separately over all ascending and all descending areas of the tropics. They found an increasing trend in wet ascent regions and a decreasing trend in dry descent regions, also consistent with a large-scale wet-get-wetter, dry-get-drier thermodynamic view of rainfall change. However, the maximum rainfall increase is actually shifted equatorward from the ITCZ's core, suggesting the importance of dynamical processes. In situ sea surface salinity observations (Curry et al. 2003, Durack & Wijffels 2010) also show trends consistent with an apparent acceleration of the hydrological cycle (enhanced rainfall in the tropics and enhanced evaporation in the subtropics), with patterns similar to large-scale CMIP5 predictions (Durack et al. 2012), though the magnitude is higher in the observations.

At very large averaged scales over land, there is evidence of wet seasons getting wetter and dry seasons drier (Chou et al. 2013a). However, at impacts-relevant regional scales over land, observed rainfall trends do not support a wet-get-wetter, dry-get-drier paradigm (Greve et al. 2014, Roderick et al. 2014). Hegerl et al. (2015) summarized these observed hydrological cycle changes in the context of the existing theories and predictions, e.g., wet-get-wetter, muted precipitation response, and intensified weather extremes. However, they suggested that although observations show robust evidence for theoretically derived and numerically predicted changes, uncertainties from the small signal-to-noise ratio of natural variability and limitations of short, discontinuous, and inhomogeneous observational data sets pose serious difficulties for determining the anthropogenic contributions.

Annu. Rev. Earth Planet. Sci. 2018.46:549-580. Downloaded from www.annualreviews.org
Access provided by 210.73.15.3 on 06/09/18. For personal use only.

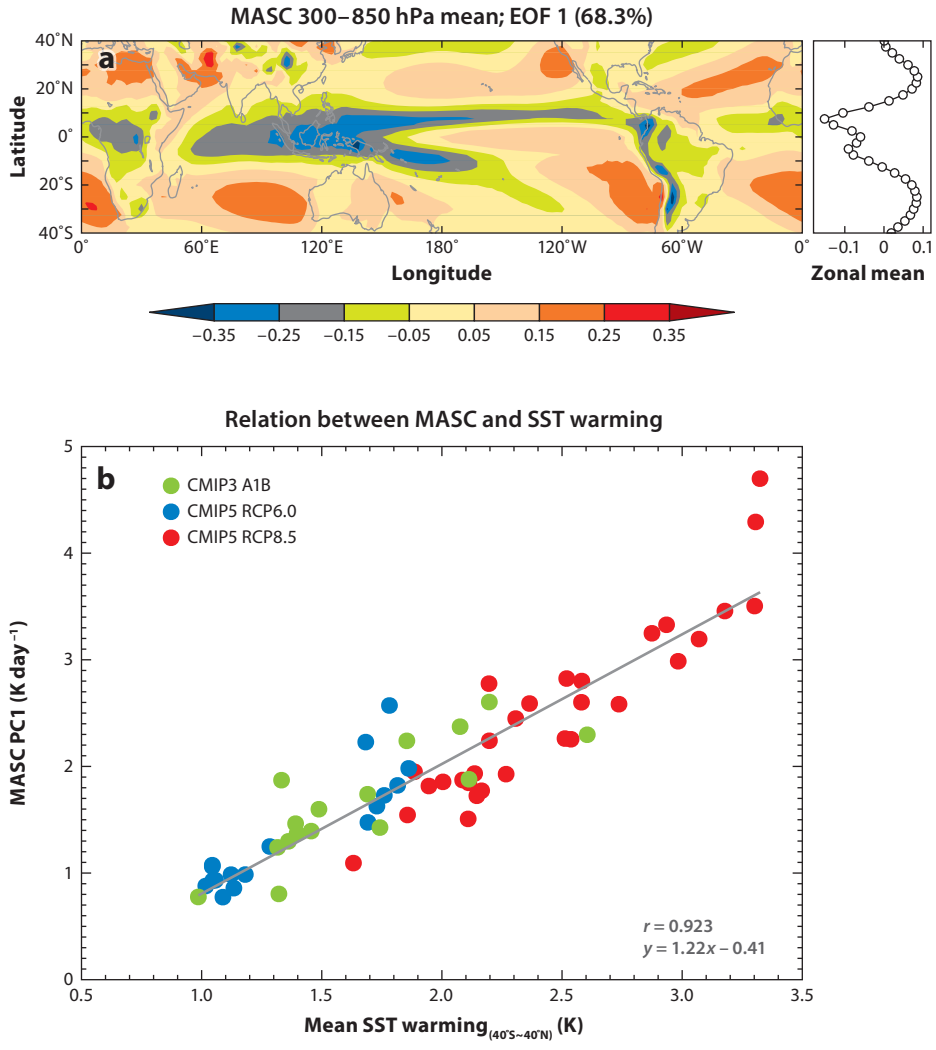

Figure 1

First leading mode of the intermodel empirical orthogonal function (EOF) analysis for the vertical-averaged mean advection of stratification change (MASC) forcing calculated with 76 simulations for three scenarios: the Special Report on Emissions Scenarios A1B (22) of Coupled Model Intercomparison Project (CMIP) phase 3 and the Representative Concentration Pathways (RCPs) 6.0 (23) and 8.5 (30) of CMIP5. Spatial mode 1 (panel *a*) shows its pattern (nondimensional) dependence only on climatological vertical velocity, and a scatter between tropical-mean sea surface temperature (SST) warming and the first principal component (PC) (panel *b*) indicates its magnitude dependence only on the general warming extent.

3.2.2. Decomposition of precipitation change mechanisms. A number of studies have used moisture and energy budgets to examine the regional response of circulation and precipitation change to GHG forcing and to decompose the total response into components associated with various mechanisms. Often the total precipitation change is partitioned into changes associated with thermodynamic (atmospheric moisture increases in response to warming) and dynamical

Annu. Rev. Earth Planet. Sci. 2018.46:549-580. Downloaded from www.annualreviews.org
Access provided by 210.73.15.3 on 06/09/18. For personal use only.

(circulation) processes. Dynamical and thermodynamic changes interact to produce the total pattern of rainfall change, where the thermodynamic component usually represents a rich-get-richer term due to moisture increases.

The first such decomposition (Chou & Neelin 2004) used the MSE and moisture budgets to analyze regional rainfall change and proposed a number of mechanisms that could drive regional rainfall change. These are the dynamical rich-get-richer hypothesis (see Section 2.2.3), which could lead to increased rainfall in ascent regions; the increased depth of convection (Section 2.2.2), which could weaken the circulation and decrease rainfall; and the upped-ante mechanism (Section 2.2.3), which could cause rainfall decreases on certain margins of ascent regions.

More recent decompositions have used moisture (Seager et al. 2010, Bony et al. 2013, Chadwick et al. 2013) or dry static energy (Muller & O'Gorman 2011, Richardson et al. 2016) budgets to understand rainfall and circulation change. These studies found that at regional scales, the pattern of rainfall change is determined more by dynamical circulation changes than by thermodynamic moisture increases, e.g., subtropical rainfall reduction due to poleward shifts of the storm tracks (Scheff & Frierson 2012). In fact, the spatial correlation between the patterns of present-day rainfall and future change is low across future CMIP5 projections (Chadwick et al. 2013), which would not be the case if these changes were dominated by a rich-get-richer response to moisture increases. This can be explained by dynamical precipitation decreases, associated with the weakening circulation, tending to oppose the rich-get-richer pattern (Seager et al. 2010).

3.2.3. Wet-get-wetter versus the regional weakening of circulation. On the tropical-mean spatial scale, the circulation is diagnosed to weaken, and this must also be reflected in local circulation changes. Of the mechanisms described in Section 3.1, only MASC (Ma et al. 2012) provides a prediction of how this overall weakening manifests itself on a regional scale. Chadwick et al. (2013) used this to explicitly separate dynamical rainfall changes into a component corresponding to the weakening circulation and a residual associated with spatial shifts in convection. Under this formulation, the pattern of thermodynamic rainfall increases is strongly anticorrelated with rainfall decreases caused by the weakening circulation, resulting in a strong cancellation between the two terms.

Because MASC involves the mean vertical motion acting on the changes in spatially averaged stratification, its pattern is negatively proportional to the climatological circulation. **Figure 1*a*** shows anomalous cooling in the convective regions over the Indo-Pacific warm pool and ITCZ, and warming in the subtropical subsidence centers. **Figure 2** presents the effect of this forcing pattern in a linear baroclinic model, producing a fractionally uniform decrease in upper-level divergence over the warm pool. This represents a weakening of the Walker circulation, which in the mean is characterized by strong upper-level divergence (and lower-level convergence) over the warm pool. The uniformity in the decrease is stronger at upper rather than lower levels, possibly due to the physical effects of friction and orography or artifacts in the velocity potential calculation due to interference from orography.

Therefore, the prediction of MASC is that regions of strongest present-day vertical motion will experience the greatest future weakening, i.e., a wet-get-drier effect on regional precipitation. As part of the dynamical effect, this would oppose and mitigate the wet-get-wetter mechanism, increasing the relative importance of other dynamical processes. Indeed, the overall pattern of rainfall change is dominated by the pattern of shifts in convective regions (Chadwick et al. 2013), which could be driven by any mechanism that affects the locations where convection preferentially occurs. The balance of these processes differs between ocean and land: Certain dynamical mechanisms are more important over the former, while others dominate over the latter, so we now consider such details separately in the following two sections.

Annu. Rev. Earth Planet. Sci. 2018.46:549-580. Downloaded from www.annualreviews.org
Access provided by 210.73.15.3 on 06/09/18. For personal use only.

Annu. Rev. Earth Planet. Sci. 2018.46:549-580. Downloaded from www.annualreviews.org
Access provided by 210.73.15.3 on 06/09/18. For personal use only.

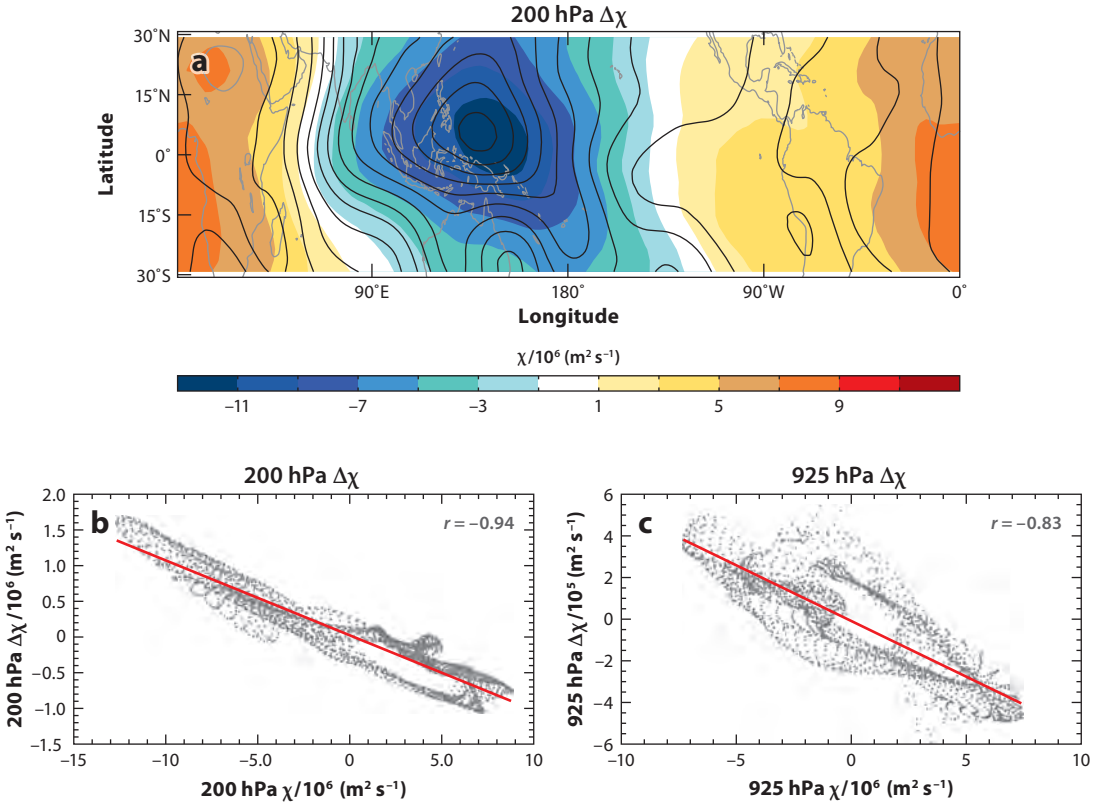

Figure 2

Local weakening of circulation induced by mean advection of stratification change forcing (**Figure 1*a***) in a linear baroclinic model. Represented with velocity potential (χ), panel *a* shows the horizontal distribution of change (*contours*) over climatology (*color*) at the 200-hPa level, and scatterplots indicate their negative linear relationship at (*b*) 200 hPa and (*c*) 925 hPa.

4. CHANGES RELATED TO SEA SURFACE TEMPERATURE PATTERNS

As mentioned in Section 2, SST is a predominant driver shaping atmospheric circulation and precipitation. Here we show that dynamical mechanisms associated with SST patterns are important for changes in oceanic rainfall and the Hadley circulation.

4.1. Circulation and Precipitation Changes over the Oceans

An equatorial peak of precipitation change was frequently illustrated in previous studies. Because the global zonal-mean view makes it difficult to distinguish the rainfall patterns from the purely thermodynamic prediction, it was considered wet-get-wetter. However, both the full two-dimensional pattern and the zonal mean of the projected rainfall change are correlated weakly with climatological rainfall in the tropics (Ma & Xie 2013), showing the importance of mechanisms other than the wet-get-wetter.

4.1.1. The warmer-get-wetter paradigm. The SST and tropospheric temperature anomalies seem to lack spatial variations in comparison with the mean warming across the tropics (e.g.,

Neelin et al. 2003); however, the warmer-get-wetter mechanism suggests that such SST pattern change is influential in regional rainfall and circulation change, with increased convection and ascent over regions where SSTs warm the most (see the sidebar titled Wet-Get-Wetter and Warmer-Get-Wetter). It was first proposed from a gross moist instability estimation by Xie et al. (2010), in which the instability was defined as the difference in MSE between the ocean surface and upper troposphere. In the tropics, the upper-tropospheric temperature increase varies spatially by <0.3 K, with its gradients flattened by fast equatorial wave adjustments (Sobel et al. 2001, Bretherton & Sobel 2002). Consequently, a general warming of the tropical troposphere raises the SST threshold for tropical convection (Johnson & Xie 2010), and moist instability and thus convective precipitation increase where the SST warming exceeds the tropical mean and decrease where relatively weak warming exists. The upped-ante theory (Chou & Neelin 2004) is the moisture alternative of this threshold-raising effect in the convective margins where the SST increase is weak.

Xie et al. (2010) decomposed SST warming into a tropical mean and spatial deviations, and Ma & Xie (2013) examined the warmer-get-wetter effect induced by the SST patterns with large CMIP3 and CMIP5 ensembles. Two SST patterns stand out: an equatorial peak (Liu et al. 2005) anchoring a local precipitation increase, and a meridional dipole mode with increased rainfall and weakened trade winds over the warmer hemisphere. These SST patterns were found to be important for explaining both the ensemble mean distribution and intermodel variability of rainfall change over the tropical oceans (Ma & Xie 2013, Ma & Yu 2014a). As commonly seen in the tropics (e.g., Back & Bretherton 2006), this effect is shown by a moisture budget analysis to involve strong positive feedback between atmospheric circulation and convection.

4.1.2. Combined mechanism for tropical oceanic rainfall change. The warmer-get-wetter mechanism is not the only mechanism controlling the regional oceanic rainfall response, but it is a very strong mechanism for spatially shifting convection over the oceans (Section 3.2). Chadwick et al. (2013) and Ma & Xie (2013) suggested that the regional oceanic rainfall change is given by the following approximate expression, derived from Equation 1 (P, M, and q are precipitation, vertical convective mass flux, and boundary-layer specific humidity, respectively):

$$\begin{aligned} \delta P/P &= \delta M_{\text{shift}}/M + (\delta M_{\text{weak}}/M + \delta q/q) \\ &= \alpha\, T^* + \beta\, \overline{T} \end{aligned}, \qquad 2.$$

where $\bar{T}$ is tropical-mean SST warming, T^* denotes SST patterns, α and β are parameters describing the corresponding strength of the response, and the subscripts "weak" and "shift" refer to the circulation slowdown and spatial shift of precipitation, respectively. In percentage form, this approximates the full mechanism controlling the regional precipitation response over the tropical oceans.

The global SST warming contains a uniform increase and spatial patterns. If T^* is zero, Equation 2 represents the rainfall response in the SUSI. As mentioned in Section 2.2.3, the general warming moistens the atmosphere to cause wet-get-wetter ($\delta q/q$), and at the same time reduces the tropical circulation ($\delta M_{\text{weak}}/M$) to mitigate the moisture effect. This results in a muted precipitation response ($\beta \bar{T}$). However, even if T^* is moderate in comparison to $\bar{T}$, it can dominate circulation and precipitation change over the SUSI effect in the coupled climate system, since the factor $\alpha = 44\%\ \text{K}^{-1}$ is much larger than $\beta = 2\%\ \text{K}^{-1}$, according to a linear fit of spatial distribution between T^* and $\delta P/P$ in the CMIP3 ensemble mean (Ma & Xie 2013). The SST patterns shift the atmospheric circulation ($\delta M_{\text{shift}}/M$), causing a warmer-get-wetter ($\alpha\, T^*$) rainfall response.

As moisture budget analyses (Seager et al. 2010, Chadwick et al. 2013) show, wet-get-wetter is the thermodynamic component of regional precipitation change, and circulation slowdown and the

Annu. Rev. Earth Planet. Sci. 2018.46:549-580. Downloaded from www.annualreviews.org
Access provided by 210.73.15.3 on 06/09/18. For personal use only.

SST pattern effects are the dynamical components. Because the circulation weakening contributes a wet-get-drier effect, counteracting the wet-get-wetter effect, the atmospheric circulation change associated with SST patterns (warmer-get-wetter) dominates the total rainfall redistribution over the tropical oceans.

4.2. Structural Changes of the Hadley Circulation

Besides a poleward expansion, more complicated changes occur to the circulation structure within the Hadley cells. They include a plausible shift of the ITCZ and an inhomogeneous intensity change reflecting a competition between circulation weakening and the SST pattern effect.

4.2.1. Interhemispheric energy balance and the intertropical convergence zone shift. Constituting the upward branch of the Hadley cell, the ITCZ is the strongest convection belt in the tropics. A growing body of research has examined the link between the interhemispheric energy balance and the position of the zonal-mean ITCZ, including its response to forcing. These studies have often used idealized models to examine the underlying processes more clearly, and the extent to which the same effects determine the response of more complex fully coupled models to forcing is an open question.

Kang et al. (2009) used a comprehensive atmosphere model coupled to a slab mixed layer ocean (i.e., ocean dynamics were suppressed) to study the effects of the extratropics on the position of the ITCZ. They imposed a cross-equatorial heat flux beneath the ocean's surface mixed layer to cool the northern extratropics and warm the southern extratropics, and this induced a southward shift in the ITCZ. This displacement can be understood as a compensation by the atmospheric energy transport in response to the imposed oceanic heat flux in the tropics: In response to the southward shift of heat in the ocean, the ITCZ shifts southward and the northern Hadley cell strengthens, resulting in an increase in the northward atmospheric heat transport. The magnitude of the ITCZ shift was found to be sensitive to cloud feedback.

Using fundamental energy constraints to analyze the responses of nine CMIP3 slab ocean model simulations to a doubling of CO_2, Frierson & Hwang (2012) found that differences in extratropical clouds control the diversity of ITCZ responses. Positive feedbacks involving water vapor and high clouds in the tropics were shown to reinforce the initial ITCZ responses. Seo et al. (2014a) found that high-latitude forcing causes a larger shift in the ITCZ than forcing in the tropics. Equivalent simulations without cloud and water vapor feedbacks, however, showed a weaker ITCZ shift when the forcing was farther from the equator, emphasizing the importance of radiative feedbacks in their experiments. Related to this, Fučkar et al. (2013) suggested that the ocean's meridional overturning circulation causes the ITCZ to be located in the Northern Hemisphere, where deep water is produced, since the Southern Hemisphere circumpolar flow forces northward oceanic heat transport.

4.2.2. Inhomogeneous change of the Hadley cell intensity. Section 3.1 discussed the slowdown of the tropical tropospheric circulation; however, robust observational evidence of this slowdown is found only for the Walker cell. In contrast, strengthening trends in the Hadley cell over the past few decades are reported based on prevailing reanalysis data sets, though this could be internal multidecadal variability rather than a forced trend (Quan et al. 2004; Tanaka et al. 2004; Mitas & Clement 2005, 2006). Future climate model projections suggest stronger future weakening of the Walker than the Hadley circulation (Gastineau et al. 2009, Ma & Xie 2013). Current theories on large-scale circulation change are insufficient to explain these different responses, so that regional effects have to be accounted for (Xie et al. 2015). Equation 2 suggests that the SST

Annu. Rev. Earth Planet. Sci. 2018.46:549-580. Downloaded from www.annualreviews.org
Access provided by 210.73.15.3 on 06/09/18. For personal use only.

pattern effect turns out to be important for the oceanic rainfall change, with the partial offset between an increase in humidity and a decrease in circulation. For circulation change, humidity is irrelevant, so that the circulation weakening is as important as the SST pattern effect. Together, they are the dominant dynamical components of circulation change (Section 4.1.2) over the ocean.

Ma & Xie (2013) found that while the weakening circulation acts to slow down both the Hadley and Walker circulations, as shown in SUSI experiments, their different responses in the coupled models could be explained by the influence of SST pattern change. Weakening of the Walker cell is well established because the influence of the SST pattern effect is either weak (because of zonal symmetry in CMIP3) or acting to enhance the slowdown (due to the eastern Pacific peak in SST warming in CMIP5). However, the impact of the weakening circulation on the Hadley cell is more influenced by the SST patterns. They are additive in some geographical regions and opposing in others, resulting in robust weakening north of the equator but weak and highly uncertain changes near and south of the equator. This is due to the latitudinal dependence of the SST patterns, representing a combination of the equatorial peak and meridional asymmetry. However, the seasonal changes in the Hadley circulation (Seo et al. 2014b) are dominated by changes in the latitudinal potential temperature gradient across the subtropics, including the robust (slight) weakening of the Hadley cell during boreal winter (summer).

Outside of the tropics, the pattern of future SST change appears to have overall little impact on the response of the atmospheric circulation and, in turn, on the resulting changes in precipitation. This is due to the insensitivity of Rossby wave generation to the changes in near-equatorial upper-level divergence (He et al. 2014).

5. DIRECT CO_2 EFFECT AND LAND RAINFALL CHANGE

Extra absorption of upwelling longwave radiation by increased GHG concentrations enables the troposphere to be moderately warmed even without SST increases. This warming (with a maximum at about 700 hPa) can reduce the radiative cooling of the troposphere and thus the convective mass flux, slowing the tropical circulation and weakening global- and tropical-mean precipitation (Allen & Ingram 2002, Sugi & Yoshimura 2003, Yang et al. 2003, Lambert & Webb 2008, Dong et al. 2009, Andrews et al. 2010, Bala et al. 2010, Cao et al. 2012, O'Gorman et al. 2012, Kamae et al. 2015). This is known as the direct radiative effect of CO_2 on precipitation change, and it could also strengthen and shift poleward the midlatitude westerly winds (Deser & Phillips 2009). In addition, the land surface is free to warm in response to the increased downwelling longwave radiation from the extra CO_2, and this can destabilize the atmosphere (Giannini et al. 2013); increase flow from ocean to land; and enhance convection, rainfall, and evaporation over land but suppress precipitation over ocean. This section first evaluates the former, then discusses the latter along with other mechanisms of land rainfall change.

5.1. The Direct CO_2 Radiative Effect

The direct CO_2 effect is commonly diagnosed from atmosphere model experiments where CO_2 concentrations are increased but SSTs held constant. This causes problems of interpretation, because keeping SST fixed provides an infinite energy source/sink, voiding energetic consistency.

Bony et al. (2013) found that by the end of the twenty-first century, under a high GHG forcing scenario, approximately one-quarter to one-third of the projected mean tropical circulation change is independent of global-mean surface warming and can thus be attributed to the direct CO_2 effect. Because aqua-planet experiments (all land removed and replaced with ocean) show tropical-mean results that are consistent with simulations that include land, they rejected a major contribution

Annu. Rev. Earth Planet. Sci. 2018.46:549-580. Downloaded from www.annualreviews.org
Access provided by 210.73.15.3 on 06/09/18. For personal use only.

from land warming toward these regional circulation changes. Chadwick et al. (2014) followed up this work and confirmed that the tropical-mean circulation change is substantially affected by the direct radiative effect and is therefore to some extent independent of global-mean temperature change. However, regional patterns of rainfall change are dominated by surface warming patterns, including both SST pattern change and land-sea temperature contrast change. They suggested that future regional rainfall changes should be studied primarily with coupled models.

He et al. (2014) and He & Soden (2015) examined these mechanisms in more detail and confirmed that mean SST warming, the direct CO_2 effect (including land warming), and SST pattern change all play roles in regional circulation change, though the effects of SST pattern change are mainly limited to the tropics. Deser & Phillips (2009) investigated the relative importance of direct atmospheric radiative and observed SST forcing on observed global atmospheric circulation trends during December through February of 1950–2000. They suggested that both drive distinct responses that contribute about equally to the full circulation pattern trend and are approximately additive and partially offsetting. Direct radiative effects drive the strengthening and poleward shift of the midlatitude westerly winds in the Southern Hemisphere (and to a lesser extent over the Atlantic-Eurasian sector in the Northern Hemisphere), while SST trends (especially in the tropics) act to intensify the Aleutian low and weaken the Walker circulation.

Model simulations show differences between global precipitation changes during the twentieth and twenty-first centuries (Thorpe & Andrews 2014), which can be attributed to the changing balance between the influence of SST warming and direct atmospheric absorption. The historical precipitation changes little despite increasing SSTs, because large direct effects from CO_2 and black carbon oppose the surface warming–induced precipitation increase, while in future scenarios the importance of these direct effects declines and the SST increase dominates in both ensemble mean and uncertainty and in both global mean and spatial patterns.

5.2. Circulation and Precipitation Changes over Land

Circulation changes over tropical land are generally less well understood than those over the oceans, and they have often been analyzed on a region-by-region basis. There is a large body of research describing circulation changes in monsoon regions (An et al. 2015, Véspoli de Carvalho & Jones 2016), and we do not attempt to describe monsoon or other region-specific mechanisms here in as much detail. We instead discuss a number of mechanisms proposed to drive circulation and rainfall changes across the tropical land.

5.2.1. Amplified land warming and effect on the circulation. Surface temperatures warm more over land than over the oceans in response to GHG forcing, and this is associated with pressure, circulation, and rainfall changes (Bayr & Dommenget 2013). This enhanced land warming is true even at equilibrium (Joshi et al. 2008), so while the smaller heat capacity and faster warming response of the land surface compared to the oceans play a role in the land amplification in transient warming scenarios, the heat capacity is not the main cause of the effect.

The land surface is warmed by increased net downwelling radiation due to the direct response of the atmosphere to CO_2 forcing, but also by the response of the atmosphere and land surface fluxes to remote SST warming (Giannini 2010), and in fact, the remote response is larger (Chadwick 2016). Compo & Sardeshmukh (2009) attributed the recent worldwide land warming to the SST warming rather than the direct GHG effect. Atmospheric model simulations of the past half-century successfully reproduced most of the land warming when prescribed with observed SST, but without GHG changes. Hydrodynamic-radiative teleconnections were suggested to be the primary mechanism for warming the land, mainly through moistening and warming the air over

Annu. Rev. Earth Planet. Sci. 2018.46:549-580. Downloaded from www.annualreviews.org
Access provided by 210.73.15.3 on 06/09/18. For personal use only.

HYDRODYNAMIC-RADIATIVE TELECONNECTIONS AND THE BOWEN RATIO

Hydrodynamic-radiative teleconnections are a thermodynamic process in climate change enabling the oceans warmed by a greenhouse gas increase to influence land warming. Horizontal advection, diffusivity, and/or wave actions from the ocean can increase moisture and temperature of the air over land, both of which enhance the downward longwave radiation at the surface. This may account for most of the land warming.

The Bowen ratio is the ratio of surface-to-atmosphere sensible heat divided by latent heat. The surface sensible heat is generated by the difference between surface temperature and near-surface air temperature; the surface latent heat is generated by the difference of saturation mixing ratio at surface temperature and the actual specific humidity of near-surface air. The Bowen ratio is an indicator of the type of surface (<1 over surfaces with abundant water supplies), e.g., tropical oceans (<0.1), rainforests (0.1–0.3), temperate forests and grasslands (0.4–0.8), semiarid landscapes (2.0–6.0), and deserts (>10.0).

Annu. Rev. Earth Planet. Sci. 2018.46:549-580. Downloaded from www.annualreviews.org
Access provided by 210.73.15.3 on 06/09/18. For personal use only.

land by the ocean and increasing the downward longwave radiation at the land surface (see the sidebar titled Hydrodynamic-Radiative Teleconnections and the Bowen Ratio).

As described in Section 3.1.3, SST warming leads to a quasi-moist-diabatic response of the vertical temperature profile (diabatic, the opposite of adiabatic, refers to a thermodynamic change with exchange of heat into or out of the system). In the free troposphere this warming is homogenized across the tropics by equatorial waves (e.g., Bretherton & Sobel 2002), leading to an almost uniform horizontal temperature distribution at mid- and upper levels. Over land, the vertical temperature profile in the boundary layer and at the surface must adjust so as to maintain a smooth vertical temperature profile (Joshi et al. 2008). As moisture supply is limited over land but not over the oceans, the present-day balance between latent and sensible surface heat fluxes (the Bowen ratio; see the sidebar titled Hydrodynamic-Radiative Teleconnections and the Bowen Ratio) varies between the two, with a larger proportion of sensible heating over land. Equivalently, land has less water to evaporate than the oceans, so that more energy goes into warming the surface (Sutton et al. 2007). So in general the mean lower-tropospheric lapse rate over land is larger (more dry-adiabatic and less moist-adiabatic) than over the oceans. For a given temperature in the midtroposphere, the surface temperature over land would therefore be higher than the equivalent surface temperature over the oceans. In a similar way, the response of land surface temperatures to SST-driven free-tropospheric warming is larger than the SST warming itself, as sensible heating increases more relative to latent heating over land than it does over the oceans (Joshi et al. 2008, Lambert et al. 2011).

Free troposphere: atmosphere above the boundary layer, where winds are approximately geostrophic (parallel to isobars), and usually nonturbulent or only intermittently turbulent

Equivalent potential temperature: the temperature an air parcel would reach if brought adiabatically to sea level, with all its water vapor condensed

Relative humidity (RH): the ratio of the partial pressure of water vapor to the equilibrium vapor pressure at a given temperature

This argument can be formulated in an alternative way as a requirement that the change in equivalent potential temperature is uniform over both land and ocean (Byrne & O'Gorman 2013). As atmospheric moisture increases less over land than over the oceans, this leads to the requirement that land warming must be greater than ocean warming. In this framework the enhanced land warming is due to a combination of the lower relative humidity (RH) over land than over ocean in the present-day warming, and further decreases in future land RH.

Clearly this land temperature adjustment is coupled to evaporation and humidity change, and it is also closely related to circulation change. Enhanced warming over land extends from the surface through the lower troposphere, and this leads to pressure anomalies and circulation changes (Bayr & Dommenget 2013). Additionally, SST-driven general warming in the free troposphere has the effect of stabilizing the atmosphere over land and suppressing convection (Joshi et al. 2008, Giannini et al. 2013), which reduces rainfall and couples with evaporation changes. These two

effects may be in competition with each other, as the surface warming should drive a sea breeze–type anomalous circulation, bringing air from the oceans to land, whereas suppression of convection and convective heating over land would tend to reduce the flow from ocean to land. It is possible that different circulation changes are seen at different vertical levels. Overall, the net effect of tropical-mean SST warming is to reduce convection and rainfall over land (Bony et al. 2013, Giannini et al. 2013, Chadwick et al. 2014, He et al. 2014).

5.2.2. The direct CO_2 effect–associated land warming. Land heating in response to increased downwelling longwave radiation also drives a circulation response. This can be relatively simply interpreted as being due to destabilization of the atmosphere over land (Giannini et al. 2013), with increased flow from ocean to land and increased convection, rainfall, and evaporation over land (Dong et al. 2009, Cao et al. 2012, Biasutti 2013, Bony et al. 2013). In this case, pressure changes from land warming and increased convective heating would combine to drive increased sea-land flow. Ackerley & Dommenget (2016) examined the effects of increasing land surface temperatures while keeping SSTs and CO_2 concentrations constant and found that the pattern of circulation and rainfall change is very similar to that of experiments where CO_2 is increased but SSTs fixed. This suggests that the main influence of direct CO_2 heating on regional circulation change is via land heating, rather than atmospheric stabilization.

The competing effects of direct local CO_2 warming and remote uniform SST warming on circulation and rainfall change (Giannini et al. 2013) can be examined in idealized atmosphere-only model experiments, where one aspect is fixed and the other increased (Bony et al. 2013, Chadwick et al. 2014, He & Soden 2015, Richardson et al. 2016). As expected, the two effects generally oppose each other, and in many regions the total response is a relatively small residual of the two larger terms.

5.2.3. Relative humidity decreases over land. Over the oceans, surface RH is predicted to remain approximately constant under warming (Held & Soden 2000, Schneider et al. 2010), with only small RH increases projected to inhibit latent heat increase (Richter & Xie 2008). Over land, however, substantial future decreases in RH are projected in many regions (O'Gorman & Muller 2010, Byrne & O'Gorman 2015). As on long timescales almost all moisture over land originates from the oceans, it has been suggested that this RH drying over land is due to amplified land warming, as advection of moisture from the relatively less-warmed oceans is unable to keep up with the increased moisture-holding capacity of the warmer air over land (Rowell & Jones 2006, Simmons et al. 2010, O'Gorman & Muller 2010).

RH decreases can be driven by circulation, precipitation, and evaporation changes, but they are also themselves a driver of circulation and water cycle change. This is most obvious in the relationship between RH and boundary-layer moisture, which controls the thermodynamic change in future precipitation through local moisture availability (Chou et al. 2009, Seager et al. 2010, Chadwick et al. 2013) and potentially also via advection of humidity gradients by the circulation (Byrne & O'Gorman 2015).

There is also a possible dynamical influence of RH decreases on circulation change, due to the influence of RH on cloud-base height (Fasullo 2012). Lower RH could lead to higher cloud-base heights, potentially suppressing convection, and intermodel correlations are seen in many regions between the magnitude of RH changes and shifts in the regions of convection (Chadwick 2016), though this does not necessarily imply causality.

The coupling between humidity, water cycle, and circulation change makes the chain of causality difficult to entangle, and targeted idealized modeling experiments may be the best way to gain a better understanding of these mechanisms. Overall, the circulation and water cycle response over

Annu. Rev. Earth Planet. Sci. 2018.46:549-580. Downloaded from www.annualreviews.org
Access provided by 210.73.15.3 on 06/09/18. For personal use only.

tropical land is likely to consist of a combination of responses to the various mechanisms listed here, with different balances of change emerging in different regions. If these mechanisms can be better understood, it should be possible to reduce the currently substantial intermodel uncertainty in future simulations by evaluating the most important physical processes for any given region between models and observations. Other mechanisms may also be important in some regions, but their description is underdeveloped; they are discussed in Section 6.3.

6. DIRECTIONS FOR FUTURE RESEARCH

This section identifies promising fields for future research, in order to constrain uncertainties and provide more reliable climate projections. We suggest that fundamental understandings are needed on the mechanisms shaping the changes in SST, the ITCZ, atmospheric circulation, tropical cyclone activity, and land rainfall.

6.1. Combining Sea Surface Temperature Pattern Change and Intertropical Convergence Zone Shifts

It is noteworthy that the extratropical forcing of the ITCZ shift associated with oceanic energy transport has been studied mostly with idealized models (see Section 4.2.1). However, it is also important to investigate the projections by comprehensive coupled models for which ITCZ shifts have to be consistent with SST pattern changes and tropical air-sea interactions. As mentioned in Section 4.1.1, one major feature of the SST warming is the interhemispheric asymmetry, with stronger warming to the north contributing to weakening of the Hadley circulation there. Indeed, Friedman et al. (2013) showed an increasing trend of the south-to-north gradient in the observed SST (<0.8 K) since 1980 and inferred a northward shift of the ITCZ. They showed that this SST gradient trend is simulated by the CMIP5 models and is projected to continue increasing significantly in the twenty-first century.

Figure 3 uses SST and rainfall as indicators to show the projected change in position of the tropical Pacific ITCZ in the twenty-first century. Simulated by 19 CMIP5 RCP4.5 models, the SST maximum not only shifts northward but also expands toward the equator, and the southward expansion is more significant than the northward expansion. This translates to an ITCZ widening at ~0.5° latitude per century toward both hemispheres, consistent with maximum SST warming on the equator and in the northern subtropics. The precipitation change supports this interpretation, showing equatorward expansion, consistent with more climatological precipitation toward the equator and the abovementioned energy theories.

As previous studies suggested, in addition to the impact of the atmosphere and ocean energy transport on the ITCZ position, local dynamical and thermodynamic ocean-atmosphere interactions associated with the SST patterns may also be important. For instance, the northward ITCZ expansion may be attributed to a wind-evaporation-SST feedback (Ma & Xie 2013), and the equatorward expansion to the reduced damping rate with lower mean surface evaporative cooling of the colder SST (Xie et al. 2010, Lu & Zhao 2012), enhanced by the Bjerknes feedback. Moreover, linking SST patterns to the ITCZ change may provide an alternative view of the tropical climate change dynamics. At least in the Northern Hemisphere, the widening of the ITCZ can be a part of the tropical expansion. The MASC effect also acts to reduce the surface air temperature gradients and may influence the SST through evaporation adjustment. Combined, these mechanisms can put the atmospheric circulation change in a new perspective and link the uncertainties in climate projection to the biases in simulating the climatology.

The current consensus considers the ITCZ shift and SST patterns separately, though they are likely to be two sides of the same coin. Long et al. (2016) attempted to link the interhemispheric

Annu. Rev. Earth Planet. Sci. 2018.46:549-580. Downloaded from www.annualreviews.org
Access provided by 210.73.15.3 on 06/09/18. For personal use only.

Annu. Rev. Earth Planet. Sci. 2018.46:549-580. Downloaded from www.annualreviews.org
Access provided by 210.73.15.3 on 06/09/18. For personal use only.

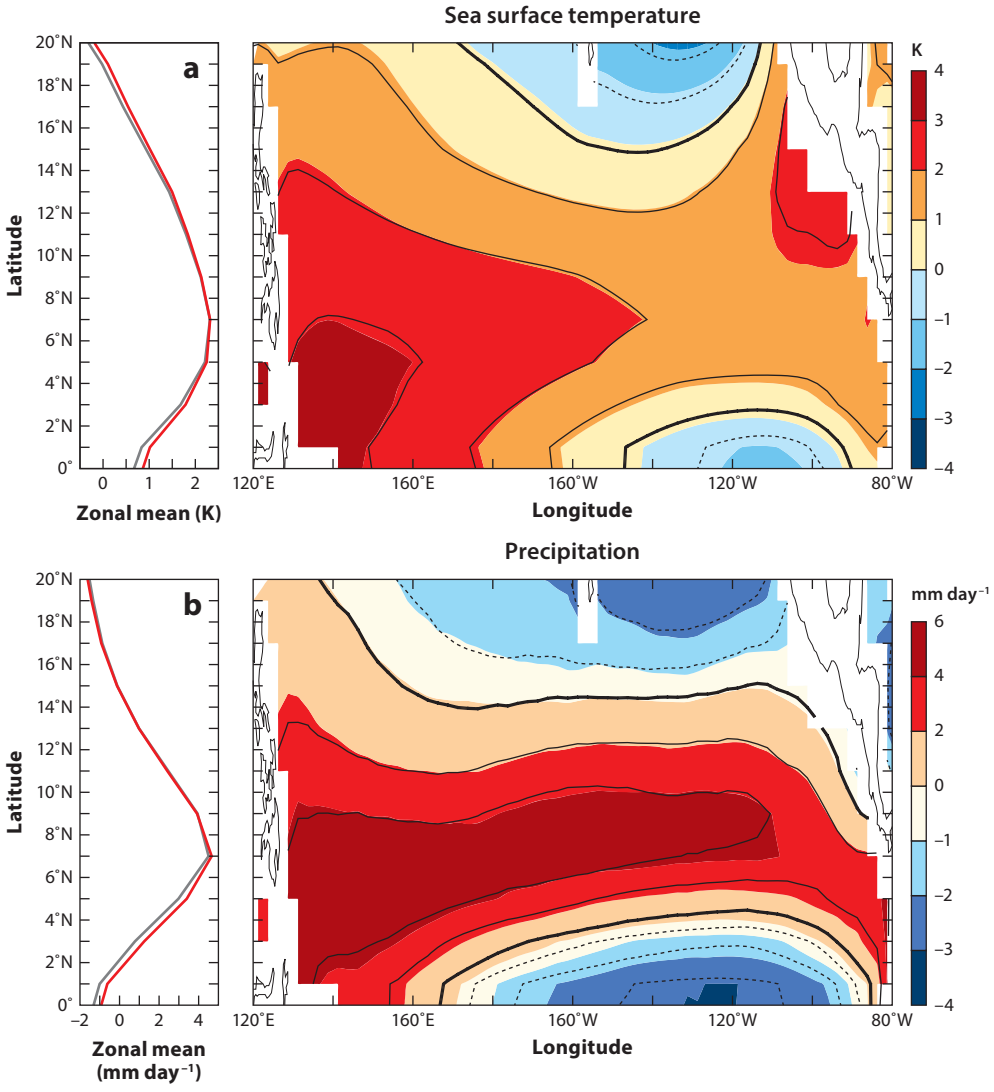

Figure 3

Ensemble and time mean of (*a*) sea surface temperature (K) and (*b*) precipitation (mm day^{-1}) illustrating change of the Pacific intertropical convergence zone in the twenty-first century as simulated by 19 Coupled Model Intercomparison Project phase 5 (CMIP5) models along Representative Concentration Pathway 4.5. The current climate is calculated as the average during 2006–2015 (*contour*; *black* for zonal mean) and the future climate as the average during 2089–2098 (*color*; *red* for zonal mean). The patterns show the deviations from the tropical Pacific (30°S–30°N, 120°E–80°W) mean.

energy balance that drives the ITCZ change to the SST patterns; however, more work is needed to fundamentally understand how the SST patterns emerge. We suggest a synthesized budget analysis combining both sides—surface fluxes and ocean transport. Besides short- and longwave radiation, surface latent and sensible heat fluxes are worth examining, since they involve the influence from winds, RH, and air-sea instability.

6.2. Impact of Circulation Change on Tropical Cyclones

Tropical cyclones constitute a significant part of seasonal rainfall in the tropics, and environmental conditions influence their genesis and development, primarily through vertical wind shear and SST (DeMaria 1996). As global warming weakens the tropical circulation, wind shear should lessen, increasing intense tropical cyclone activity and intensity (Knutson et al. 2008, Bender et al. 2010). Nevertheless, Vecchi & Soden (2007c) reported enhanced shear in the main hurricane development regions in the tropical Atlantic and East Pacific, supported by past observations (Wang & Lee 2008, Wang et al. 2008). This enhancement was shown to be caused by SST patterns (weaker warming in the north relative to the equator) and would not suggest a strong anthropogenic increase in hurricane activity. In addition, the relative SST change was reported to be important (Vecchi et al. 2008, Wang & Lee 2008) to provide static energy and moisture to penetrate the increased threshold for convection.

We have illustrated that the reduction of vertical wind shear associated with MASC is nearly model and scenario independent (**Figure 1**), and that much of the uncertainty in hurricane responses should come from the SST patterns (Zhao & Held 2012). We suggest an intermodel analysis comparing the influence of large-scale slowdown and SST pattern mechanisms on hurricane change for both the past and the future as an important direction for future study. Two key measures should be investigated: maximum potential intensity for development (Emanuel 1999), which is primarily controlled by SST patterns, and genesis potential index (Camargo et al. 2007) or the recently developed cyclone genesis index (Bruyère et al. 2012) for genesis, which considers both SSTs and wind shear.

6.3. Balance of Processes Driving Circulation Change over Land

As described in Section 5.2, there are several processes that could potentially lead to circulation changes over land, and the balance of these differs among regions. Understanding more about these processes is crucial for narrowing the large uncertainty in climate model projections of future regional circulation and water cycle change.

A new set of atmosphere-only time-slice experiments (the piSST experiments based on the preindustrial control coupled simulation and a4SST experiments on the run with abruptly quadrupling CO_2) will be included in the contribution of the Cloud Feedbacks Model Intercomparison Project phase 3 to CMIP6 (Webb et al. 2017), designed to analyze the processes that drive regional climate change. These numerical experiments will isolate the individual responses of climate models to direct CO_2 forcing, uniform SST warming, pattern SST warming, the plant physiological effect, and sea ice change and should provide a much greater understanding of the processes that drive change and uncertainty across coupled climate models for any given land region, as is done for the ocean (Section 4.1.2).

7. SUMMARY

This article reviews the past ~20 years of progress in understanding tropical atmospheric circulation change cause by global warming and its impacts on the hydrological cycle. We summarize the theories of atmospheric circulation and their predictions, present the diagnosed physical mechanisms underlying large-scale and regional changes in observations and climate models, and suggest a few promising future directions for improved climate projections. We decompose the global-mean warming effects from the tropics-wide regional climate change, considering both thermodynamic and dynamical components that drive circulation and precipitation changes. Various mechanisms for precipitation change are discussed separately over oceans and land, with related changes in the Hadley circulation and the direct CO_2 radiative effect, respectively.

Annu. Rev. Earth Planet. Sci. 2018.46:549-580. Downloaded from www.annualreviews.org
Access provided by 210.73.15.3 on 06/09/18. For personal use only.

Theoretical predictions of the atmospheric circulation change, and its effects on the hydrological cycle, have been identified, including a poleward expansion of the Hadley cell, the slowdown of the tropical circulation, and a wet-get-wetter pattern for precipitation. Diagnostic results then suggest that the latter two significantly offset each other, giving rise to an SST pattern dominance of regional precipitation change over the oceans. As a result, robust weakening is found only for the Walker circulation and the Hadley circulation in the northern subtropics, with great uncertainty for the latter near and to the south of the equator. These changes are also related to shifts of storm tracks and the ITCZ.

Dynamical mechanisms such as the MASC effect and the warmer-get-wetter paradigm were proposed for these equilibrium changes. More complicated mechanisms are likely to be important over land, and this is an important area of ongoing research effort. Many other challenges also remain for future research, including the tropical cyclone environment and ITCZ shifts. In general, a more fundamental understanding of the pattern formation of SST, circulation, and rainfall will be crucial to narrowing uncertainty in future climate projections.

Annu. Rev. Earth Planet. Sci. 2018.46:549-580. Downloaded from www.annualreviews.org
Access provided by 210.73.15.3 on 06/09/18. For personal use only.

SUMMARY POINTS

1. Significant progress has been made in understanding the climate change–induced responses of the tropical atmospheric circulation and hydrological cycle.
2. These changes can be separated into large-scale responses and regional changes, showing connections between sea surface temperatures, winds, precipitation, and energy transport.
3. Theoretical predictions include a poleward expansion of the Hadley cell, the slowdown of the tropical circulation, and a wet-get-wetter trend for precipitation.
4. The large-scale weakening of the tropical circulation exerts a regional dynamical impact on precipitation change, by partially offsetting the thermodynamic wet-get-wetter effect.
5. This allows local dynamical processes to dominate regional circulation and precipitation changes, e.g., the warmer-get-wetter effect over ocean and the land surface warming and CO_2 effects over land.
6. Impacts of circulation weakening and sea surface temperature patterns are comparable for the Hadley cell change and competitive near and south of the equator, which may be related to a shift of the intertropical convergence zone.

FUTURE ISSUES

1. A combined understanding of changes in the sea surface temperature patterns and the intertropical convergence zone may provide an alternative view for global warming pattern formation, so that uncertainties in climate projections can be traced back to the biases in current climate simulations.
2. Uncertainty in environmental change of tropical cyclones needs to be better understood.
3. A budget analysis for land rainfall change is needed to examine the balance of multiple processes for various land regions.

DISCLOSURE STATEMENT

The authors are not aware of any affiliations, memberships, funding, or financial holdings that might be perceived as affecting the objectivity of this review.

ACKNOWLEDGMENTS

We acknowledge various modeling groups for producing and providing their output, the Program for Climate Model Diagnosis and Intercomparison for collecting and archiving the CMIP3 and CMIP5 multimodel data, the World Climate Research Programme's Working Group on Coupled Modelling for organizing the analysis activity, and the Office of Science, US Department of Energy, for supporting these data sets in partnership with the Global Organization for Earth System Science Portals. We thank all excellent scientists for their previous studies as material necessary to compose this comprehensive article. The Atlantic Oceanographic and Meteorological Laboratory (AOML) internal reviewer, C. Wang, is gratefully appreciated for helpful suggestions. We thank the Co-Editors, R. Jeanloz and K.H. Freeman, and signed reviewer, R.T. Pierrehumbert, for their careful and constructive comments. The Ferret program was used for analysis and graphics. This work was funded by the National Natural Science Foundation of China (NSFC) (41675070), Shanghai Eastern Scholar Program (TP2015049), and Expert Development Fund (2017033). R.C. was supported by the Joint UK Department of Energy and Climate Change/Defra Met Office Hadley Centre Climate Programme (GA01101). K.H.S. was supported by the National Research Foundation of Korea (NRF-2015R1A2A2A01006663) and Korea Meteorological Administration Research and Development Program (KMIPA 2015-2113). C.D. appreciates support from the National Programme on Global Change and Air-Sea Interaction (GASI-03-IPOVAI-05), the National Key Research Program of China (2016YFA0601803), the NSFC (41476022, 41490643), and the Program for Innovation Research and Entrepreneurship Team in Jiangsu, China. G.H. gratefully acknowledges support from the NSFC (41425019, 41721004, 41661144016) and the Public Science and Technology Research Funds Projects of Ocean (201505013). G.R.F. was supported by the National Oceanic and Atmospheric Administration (NOAA)/Climate Program Office's Climate Observations and Monitoring Program and base funds to NOAA/AOML. J.H.J. was supported by the Jet Propulsion Laboratory, California Institute of Technology, sponsored by NASA. Requests for obtaining the data used to produce the results of this article should be addressed to J.M.

LITERATURE CITED

Ackerley D, Dommenget D. 2016. Atmosphere-only GCM (ACCESS1.0) simulations with prescribed land surface temperatures. *Geosci. Model Dev.* 9:2077–98

Allan RP. 2011. Regime dependent changes in global precipitation. *Clim. Dyn.* 39:827–40

Allan RP, Soden BJ, John VO, Ingram W, Good P. 2010. Current changes in tropical precipitation. *Environ. Res. Lett.* 5:025205

Allen MR, Ingram WJ. 2002. Constraints on future changes in the hydrological cycle. *Nature* 419:224–28

An Z, Wu G, Li J, Sun Y, Liu Y, et al. 2015. Global monsoon dynamics and climate change. *Annu. Rev. Earth Planet. Sci.* 43:29–77

Andrews T, Forster PM, Boucher O, Bellouin N, Jones A. 2010. Precipitation, radiative forcing and global temperature change. *Geophys. Res. Lett.* 37:L14701

Back LE, Bretherton CS. 2006. Geographic variability in the export of moist static energy and vertical motion profiles in the tropical Pacific. *Geophys. Res. Lett.* 33:L17810

Bala G, Caldeira K, Nemani R. 2010. Fast versus slow response in climate change: implications for the global hydrological cycle. *Clim. Dyn.* 35:423–34

Annu. Rev. Earth Planet. Sci. 2018.46:549-580. Downloaded from www.annualreviews.org
Access provided by 210.73.15.3 on 06/09/18. For personal use only.

Annu. Rev. Earth Planet. Sci. 2018.46:549-580. Downloaded from www.annualreviews.org
Access provided by 210.73.15.3 on 06/09/18. For personal use only.

Bayr T, Dommenget D. 2013. The tropospheric land-sea warming contrast as the driver of tropical sea level pressure changes. *J. Clim.* 26:1387–402

Bender MA, Knutson TR, Tuleya RE, Sirutis JJ, Vecchi GA, et al. 2010. Modeled impact of anthropogenic warming on the frequency of intense Atlantic hurricanes. *Science* 327:454–58

Biasutti M. 2013. Forced Sahel rainfall trends in the CMIP5 archive. *J. Geophys. Res.* 118:1613–23

Bjerknes J. 1969. Atmospheric teleconnection from the equatorial Pacific. *Mon. Weather Rev.* 97:163–72

Bony S, Bellon G, Klocke D, Sherwood S, Fermepin S, et al. 2013. Robust direct effect of carbon dioxide on tropical circulation and regional precipitation. *Nat. Geosci.* 6:447–51

Bretherton CS, Sobel AH. 2002. A simple model of a convectively-coupled Walker circulation using the weak temperature gradient approximation. *J. Clim.* 15:2907–20

Bruyère CL, Holland GJ, Towler E. 2012. Investigating the use of a genesis potential index for tropical cyclones in the North Atlantic basin. *J. Clim.* 25:8611–26

Byrne MP, O'Gorman PA. 2013. Link between land-ocean warming contrast and surface relative humidities in simulations with coupled climate models. *Geophys. Res. Lett.* 40:5223–27

Byrne MP, O'Gorman PA. 2015. The response of precipitation minus evapotranspiration to climate warming: why the "wet-get-wetter, dry-get-drier" scaling does not hold over land. *J. Clim.* 28:8078–92

Camargo SJ, Emanuel KA, Sobel AH. 2007. Use of a genesis potential index to diagnose ENSO effects on tropical cyclone genesis. *J. Clim.* 20:4819–34

Cao L, Bala G, Caldeira K. 2012. Climate response to changes in atmospheric carbon dioxide and solar irradiance on the time scale of days to weeks. *Environ. Res. Lett.* 7:034015

Chadwick R. 2016. Which aspects of CO_2 forcing and SST warming cause most uncertainty in projections of tropical rainfall change over land and ocean? *J. Clim.* 29:2493–509

Chadwick R, Boutle I, Martin G. 2013. Spatial patterns of precipitation change in CMIP5: Why the rich do not get richer in the tropics. *J. Clim.* 26:3803–22

Chadwick R, Good P, Andrews T, Martin G. 2014. Surface warming patterns drive tropical rainfall pattern responses to CO_2 forcing on all timescales. *Geophys. Res. Lett.* 41:610–15

Chen G, Held IM. 2007. Phase speed spectra and the recent poleward shift of Southern Hemisphere surface westerlies. *Geophys. Res. Lett.* 34:L21805

Chen G, Lu J, Frierson DMW. 2008. Phase speed spectra and the latitude of surface westerlies: interannual variability and the global warming trend. *J. Clim.* 21:5942–59

Chou C, Chen CA. 2010. Depth of convection and the weakening of the tropical circulation in global warming. *J. Clim.* 23:3019–30

Chou C, Chiang JCH, Lan CW, Chung CH, Liao YC, Lee CJ. 2013a. Increase in the range between wet and dry season precipitation. *Nat. Geosci.* 6:263–67

Chou C, Neelin JD. 2004. Mechanisms of global warming impacts on regional tropical precipitation. *J. Clim.* 17:2688–701

Chou C, Neelin JD, Chen CA, Tu JY. 2009. Evaluating the "rich-get-richer" mechanism in tropical precipitation change under global warming. *J. Clim.* 22:1982–2005

Chou C, Wu TC, Tan PH. 2013b. Changes in gross moist stability in the tropics under global warming. *Clim. Dyn.* 41:2481–96

Clarke AJ, Lebedev A. 1996. Long-term change in the equatorial Pacific trade winds. *J. Clim.* 9:1020–29

Compo GP, Sardeshmukh PD. 2009. Oceanic influences on recent continental warming. *Clim. Dyn.* 32:333–42

Curry R, Dickson B, Yashayaev I. 2003. A change in the fresh-water balance of the Atlantic Ocean over the past four decades. *Nature* 426:826–29

DeMaria M. 1996. The effect of vertical shear on tropical cyclone intensity change. *J. Atmos. Sci.* 53:2076–87

Deser C, Phillips AS. 2009. Atmospheric circulation trends, 1950–2000: the relative roles of sea surface temperature forcing and direct atmospheric radiative forcing. *J. Clim.* 22:396–413

Dong B, Gregory JM, Sutton RT. 2009. Understanding land-sea warming contrast in response to increasing greenhouse gases. Part I. Transient adjustment. *J. Clim.* 22:3079–97

Durack PJ, Wijffels SE. 2010. Fifty-year trends in global ocean salinities and their relationship to broad-scale warming. *J. Clim.* 23:4342–62

Durack PJ, Wijffels SE, Matear RJ. 2012. Ocean salinities reveal strong global water cycle intensification during 1950 to 2000. *Science* 336:455–58

Emanuel KA. 1999. Thermodynamic control of hurricane intensity. *Nature* 401:665–69
Fasullo J. 2012. A mechanism for land-ocean contrasts in global monsoon trends in a warming climate. *Clim. Dyn.* 39:1137–47
Friedman AR, Hwang YT, Chiang JCH, Frierson DMW. 2013. Interhemispheric temperature asymmetry over the twentieth century and in future projections. *J. Clim.* 26:5419–33
Frierson DMW, Hwang YT. 2012. Extratropical influence on ITCZ shifts in slab ocean simulations of global warming. *J. Clim.* 25:720–33
Frierson DMW, Lu J, Chen G. 2007. Width of the Hadley cell in simple and comprehensive general circulation models. *Geophys. Res. Lett.* 34:L18804
Fu Q, Johanson CM, Wallace JM, Reichler T. 2006. Enhanced mid-latitude tropospheric warming in satellite measurements. *Science* 312:1179
Fučkar NS, Xie SP, Farneti R, Maroon EA, Frierson DMW. 2013. Influence of the extratropical ocean circulation on the intertropical convergence zone in an idealized coupled general circulation model. *J. Clim.* 26:4612–29
Gastineau G, Li L, Le Treut H. 2009. The Hadley and Walker circulation changes in global warming conditions described by idealized atmospheric simulations. *J. Clim.* 22:3993–4013
Giannini A. 2010. Mechanisms of climate change in the semiarid African Sahel: the local view. *J. Clim.* 23:743–56
Giannini A, Salack S, Lodoun T, Ali A, Gaye AT, Ndiaye O. 2013. A unifying view of climate change in the Sahel linking intra-seasonal, interannual and longer time scales. *Environ. Res. Lett.* 8:024010
Greve P, Orlowsky B, Mueller B, Sheffield J, Reichstein M, et al. 2014. Global assessment of trends in wetting and drying over land. *Nat. Geosci.* 7:716–21
Hartmann DL, Larson K. 2002. An important constraint on tropical cloud - climate feedback. *Geophys. Res. Lett.* 29:1951
He J, Soden BJ. 2015. Anthropogenic weakening of the tropical circulation: the relative roles of direct CO_2 forcing and sea surface temperature change. *J. Clim.* 28:8728–42
He J, Soden BJ, Kirtman B. 2014. The robustness of the atmospheric circulation and precipitation response to future anthropogenic surface warming. *Geophys. Res. Lett.* 41:2614–22
Hegerl GC, Black E, Allan RP, Ingram WJ, Polson D, et al. 2015. Challenges in quantifying changes in the global water cycle. *Bull. Am. Meteorol. Soc.* 96:1097–115
Held IM, Delworth TL, Lu J, Findell KL, Knutson TR. 2005. Simulation of Sahel drought in the 20th and 21st centuries. *PNAS* 102:17891–96
Held IM, Hou AY. 1980. Nonlinear axially symmetric circulations in a nearly inviscid atmosphere. *J. Atmos. Sci.* 37:515–33
Held IM, Soden BJ. 2000. Water vapor feedback and global warming. *Annu. Rev. Energy Environ.* 25:441–75
Held IM, Soden BJ. 2006. Robust responses of the hydrological cycle to global warming. *J. Clim.* 19:5686–99
Hu Y, Fu Q. 2007. Observed poleward expansion of the Hadley circulation since 1979. *Atmos. Chem. Phys.* 7:5229–36
Ingram W. 2010. A very simple model for the water vapour feedback on climate change. *Q. J. R. Meteorol. Soc.* 136:30–40
Johanson CM, Fu Q. 2009. Hadley cell widening: model simulations versus observations. *J. Clim.* 22:2713–25
Johnson NC, Xie SP. 2010. Changes in the sea surface temperature threshold for tropical convection. *Nat. Geosci.* 3:842–45
Joshi MM, Gregory JM, Webb MJ, Sexton DMH, Johns TC. 2008. Mechanisms for the land/sea warming contrast exhibited by simulations of climate change. *Clim. Dyn.* 30:455–65
Kamae Y, Watanabe M, Ogura T, Yoshimori M, Shiogama H. 2015. Rapid adjustments of cloud and hydrological cycle to increasing CO_2: a review. *Curr. Clim. Change Rep.* 1:103–13
Kang SM, Frierson DMW, Held IM. 2009. The tropical response to extratropical thermal forcing in an idealized GCM: the importance of radiative feedbacks and convective parameterization. *J. Atmos. Sci.* 66:2812–27
Kidston J, et al. 2015. Stratospheric influence on tropospheric jet streams, storm tracks and surface weather. *Nat. Geosci.* 8:433–40

Annu. Rev. Earth Planet. Sci. 2018.46:549-580. Downloaded from www.annualreviews.org
Access provided by 210.73.15.3 on 06/09/18. For personal use only.

Knutson TR, Manabe S. 1995. Time-mean response over the tropical Pacific to increased CO_2 in a coupled ocean-atmosphere model. *J. Clim.* 8:2181–99
Knutson TR, Sirutis JJ, Garner ST, Vecchi GA, Held IM. 2008. Simulated reduction in Atlantic hurricane frequency under twenty-first-century warming conditions. *Nat. Geosci.* 1:359–64
Lambert FH, Webb MJ. 2008. Dependency of global mean precipitation on surface temperature. *Geophys. Res. Lett.* 35:L16706
Lambert FH, Webb MJ, Joshi MM. 2011. The relationship between land-ocean surface temperature contrast and radiative forcing. *J. Clim.* 24:3239–56
Lau KM, Wu HT. 2007. Detecting trends in tropical rainfall characteristics, 1979–2003. *Int. J. Climatol.* 27:979–88
Le Hir G, Donnadieu Y, Goddéris Y, Pierrehumbert RT, Halverson GP, et al. 2009. The Snowball Earth aftermath: exploring the limits of continental weathering processes. *Earth Planet. Sci. Lett.* 277:453–63
Lee SS, Tao WK, Jung CH. 2014. Aerosol effects on instability, circulations, clouds, and precipitation. *Adv. Meteorol.* 2014:683950
Liu Z, Vavrus S, He F, Wen N, Zhong Y. 2005. Rethinking tropical ocean response to global warming: the enhanced equatorial warming. *J. Clim.* 18:4684–700
Long SM, Xie SP, Liu W. 2016. Uncertainty in tropical rainfall projections: atmospheric circulation effect and the ocean coupling. *J. Clim.* 29:2671–87
Lorenz DJ, DeWeaver ET. 2007. Tropopause height and zonal wind response to global warming in the IPCC scenario integrations. *J. Geophys. Res.* 112:D10119
Lu J, Vecchi GA, Reichler T. 2007. Expansion of the Hadley cell under global warming. *Geophys. Res. Lett.* 34:L06805
Lu J, Zhao B. 2012. The role of oceanic feedback in the climate response to doubling CO_2. *J. Clim.* 25:7544–63
Lucas C, Timbal B, Nguyen H. 2014. The expanding tropics: a critical assessment of the observational and modeling studies. *WIREs Clim. Change* 5:89–112
Ma J, Foltz GR, Soden BJ, Huang G, He J, Dong C. 2016. Will surface winds weaken in response to global warming? *Environ. Res. Lett.* 11:124012
Ma J, Xie SP. 2013. Regional patterns of sea surface temperature change: a source of uncertainty in future projections of precipitation and atmospheric circulation. *J. Clim.* 26:2482–501
Ma J, Xie SP, Kosaka Y. 2012. Mechanisms for tropical tropospheric circulation change in response to global warming. *J. Clim.* 25:2979–94
Ma J, Yu JY. 2014a. Linking centennial surface warming patterns in the equatorial Pacific to the relative strengths of the Walker and Hadley circulations. *J. Atmos. Sci.* 71:3454–64
Ma J, Yu JY. 2014b. Paradox in South Asian summer monsoon circulation change: lower tropospheric strengthening and upper tropospheric weakening. *Geophys. Res. Lett.* 41:2934–40
Meehl GA, Covey C, Taylor KE, Delworth T, Stouffer RJ, et al. 2007. The WCRP CMIP3 multimodel dataset: a new era in climate change research. *Bull. Am. Meteorol. Soc.* 88:1383–94
Mitas CM, Clement A. 2005. Has the Hadley cell been strengthening in recent decades? *Geophys. Res. Lett.* 32:L03809
Mitas CM, Clement A. 2006. Recent behavior of the Hadley cell and tropical thermodynamics in climate models and reanalyses. *Geophys. Res. Lett.* 33:L01810
Muller CJ, O'Gorman PA. 2011. An energetic perspective on the regional response of precipitation to climate change. *Nat. Clim. Change* 1:266–71
Neelin JD, Chou C, Su H. 2003. Tropical drought regions in global warming and El Niño teleconnections. *Geophys. Res. Lett.* 30:2275
Neelin JD, Zeng N. 2000. A quasi-equilibrium tropical circulation model—formulation. *J. Atmos. Sci.* 57:1741–66
O'Gorman PA, Allan RP, Byrne MP, Previdi M. 2012. Energetic constraints on precipitation under climate change. *Surv. Geophys.* 33:585–608
O'Gorman PA, Muller C. 2010. How closely do changes in surface and column water vapor follow Clausius-Clapeyron scaling in climate change simulations? *Environ. Res. Lett.* 5:025207
O'Gorman PA, Singh MS. 2013. Vertical structure of warming consistent with an upward shift in the middle and upper troposphere. *Geophys. Res. Lett.* 40:1838–42

Annu. Rev. Earth Planet. Sci. 2018.46:549-580. Downloaded from www.annualreviews.org
Access provided by 210.73.15.3 on 06/09/18. For personal use only.

Pierrehumbert RT. 1995. Thermostats, radiator fins, and the local runaway greenhouse. *J. Atmos. Sci.* 52:1784–806
Pierrehumbert RT. 1999. Subtropical water vapor as a mediator of rapid global climate change. In *Mechanisms of Global Change at Millennial Time Scales*, ed. PU Clark, RS Webb, LD Keigwin. Geophys. Monogr. Ser. 112. Washington, DC: Am. Geophys. Union
Pierrehumbert RT. 2002. The hydrologic cycle in deep time climate problems. *Nature* 419:191–98
Pierrehumbert RT. 2010. The surface energy balance. In *Principles of Planetary Climate*, pp. 386–431. Cambridge, UK: Cambridge Univ. Press
Pierrehumbert RT, Roca R. 1998. Evidence for control of Atlantic subtropical humidity by large scale advection. *Geophys. Res. Lett.* 25:4537–40
Qu X, Huang G. 2016. The global warming–induced South Asian high change and its uncertainty. *J. Clim.* 29:2259–73
Quan XW, Diaz HF, Hoerling MP. 2004. Change in the tropical Hadley cell since 1950. In *The Hadley Circulation: Past, Present, and Future*, ed. HF Diaz, RS Bradley. New York: Cambridge Univ. Press
Richardson T, Forster P, Andrews T, Parker D. 2016. Understanding the rapid precipitation response to CO_2 and aerosol forcing on a regional scale. *J. Clim.* 29:583–88
Richter I, Xie SP. 2008. The muted precipitation increase in global warming simulations: a surface evaporation perspective. *J. Geophys. Res.* 113:D24118
Roderick ML, Sun F, Lim WH, Farquhar GD. 2014. A general framework for understanding the response of the water cycle to global warming over land and ocean. *Hydrol. Earth Syst. Sci.* 18:1575–89
Rodwell MJ, Hoskins BJ. 1996. Monsoons and the dynamics of deserts. *Q. J. R. Meteorol. Soc.* 122:1385–404
Rowell D, Jones R. 2006. Causes and uncertainty of future summer drying over Europe. *Clim. Dyn.* 27:281–99
Scheff J, Frierson D. 2012. Twenty-first-century multimodel subtropical precipitation declines are mostly midlatitude shifts. *J. Clim.* 25:4330–47
Schneider T, O'Gorman PA, Levine XJ. 2010. Water vapor and the dynamics of climate changes. *Rev. Geophys.* 48:RG3001
Seager R, Naik N, Vecchi GA. 2010. Thermodynamic and dynamic mechanisms for large-scale changes in the hydrological cycle in response to global warming. *J. Clim.* 23:4651–68
Seager R, Ting M, Held I, Kushnir Y, Lu J, et al. 2007. Model projections of an imminent transition to a more arid climate in southwestern North America. *Science* 316:1181–84
Seidel DJ, Fu Q, Randel WJ, Reichler TJ. 2008. Widening of the tropical belt in a changing climate. *Nat. Geosci.* 1:21–24
Seo J, Kang SM, Frierson DMW. 2014a. Sensitivity of intertropical convergence zone movement to the latitudinal position of thermal forcing. *J. Clim.* 27:3035–42
Seo KH, Frierson DMW, Son JH. 2014b. A mechanism for future changes in Hadley circulation strength in CMIP5 climate change simulations. *Geophys. Res. Lett.* 40:5251–58
Simmons A, Willett K, Jones P, Thorne P, Dee D. 2010. Low-frequency variations in surface atmospheric humidity, temperature and precipitation: inferences from reanalyses and monthly gridded observational datasets. *J. Geophys. Res.* 115:D01110
Singh MS, O'Gorman PA. 2013. Influence of entrainment on the thermal stratification in simulations of radiative-convective equilibrium. *Geophys. Res. Lett.* 40:4398–403
Sobel AH, Camargo SJ. 2011. Projected future changes in tropical summer climate. *J. Clim.* 24:473–87
Sobel AH, Nilsson J, Polvani LM. 2001. The weak temperature gradient approximation and balanced tropical moisture waves. *J. Atmos. Sci.* 58:3650–65
Solomon A, Newman M. 2012. Reconciling disparate twentieth-century Indo-Pacific ocean temperature trends in the instrumental record. *Nat. Clim. Change* 2:691–99
Stephens GL, Ellis TD. 2008. Controls of global-mean precipitation increases in global warming GCM experiments. *J. Clim.* 21:6141–55
Su H, Jiang JH, Neelin JD, Shen TJ, Zhai C, et al. 2017. Tightening of tropical ascent and high clouds key to precipitation change in a warmer climate. *Nat. Commun.* 8:15771
Su H, Jiang JH, Zhai C, Shen TJ, Neelin JD, et al. 2014. Weakening and strengthening structures in the Hadley circulation change under global warming and implications for cloud response and climate sensitivity. *J. Geophys. Res.* 119:5787–805

Annu. Rev. Earth Planet. Sci. 2018.46:549-580. Downloaded from www.annualreviews.org
Access provided by 210.73.15.3 on 06/09/18. For personal use only.

Sugi M, Yoshimura J. 2003. A mechanism of tropical precipitation change due to CO_2 increase. *J. Clim.* 17:238–43
Sun Y, Solomon S, Dai A, Portmann RW. 2007. How often will it rain? *J. Clim.* 20:4081–818
Sutton RT, Dong B, Gregory JM. 2007. Land/sea warming ratio in response to climate change: IPCC AR4 model results and comparison with observations. *Geophys. Res. Lett.* 34:L02701
Tanaka HL, Ishizaki N, Kitoh A. 2004. Trend and interannual variability of Walker, monsoon and Hadley circulations defined by velocity potential in the upper troposphere. *Tellus* 56A:250–69
Taylor KE, Stouffer RJ, Meehl GA. 2012. An overview of CMIP5 and the experiment design. *Bull. Am. Meteorol. Soc.* 93:485–98
Thorpe L, Andrews T. 2014. The physical drivers of historical and 21st century global precipitation changes. *Environ. Res. Lett.* 9:064024
Tokinaga H, Xie SP. 2011. Weakening of the equatorial Atlantic cold tongue over the past six decades. *Nat. Geosci.* 4:222–26
Tokinaga H, Xie SP, Timmermann A, McGregor S, Ogata T, et al. 2012. Regional patterns of tropical Indo-Pacific climate change: evidence of the Walker circulation weakening. *J. Clim.* 25:1689–710
Vecchi GA, Soden BJ. 2007a. Effect of remote sea surface temperature change on tropical cyclone potential intensity. *Nature* 450:1066–70
Vecchi GA, Soden BJ. 2007b. Global warming and the weakening of the tropical circulation. *J. Clim.* 20:4316–40
Vecchi GA, Soden BJ. 2007c. Increased tropical Atlantic wind shear in model projections of global warming. *Geophys. Res. Lett.* 34:L08702
Vecchi GA, Soden BJ, Wittenberg AT, Held IM, Leetmaa A, Harrison MJ. 2006. Weakening of tropical Pacific atmospheric circulation due to anthropogenic forcing. *Nature* 441:73–76
Vecchi GA, Swanson KL, Soden BJ. 2008. Whither hurricane activity? *Science* 322:687–89
Véspoli de Carvalho LM, Jones C, eds. 2016. *The Monsoons and Climate Change*. New York: Springer
Voigt A, Shaw TA. 2015. Circulation response to warming shaped by radiative changes of clouds and water vapor. *Nat. Geosci.* 8:102–6
Wang C, Lee SK. 2008. Global warming and United States landfalling hurricanes. *Geophys. Res. Lett.* 35:L02708
Wang C, Lee SK, Enfield DB. 2008. Atlantic warm pool acting as a link between Atlantic multidecadal oscillation and Atlantic tropical cyclone activity. *Geochem. Geophys. Geosyst.* 9:Q05V03
Wang Y, Jiang JH, Su H. 2015. Atmospheric responses to the redistribution of anthropogenic aerosols. *J. Geophys. Res.* 120:9625–41
Watanabe M, Kimoto M. 2000. Atmosphere-ocean thermal coupling in the North Atlantic: a positive feedback. *Q. J. R. Meteorol. Soc.* 126:3343–69. Corrigendum. *Q. J. R. Meteorol. Soc.* 127:733–34
Webb MJ, Andrews T, Bodas-Salcedo A, Bony S, Bretherton CS, et al. 2017. The Cloud Feedback Model Intercomparison Project (CFMIP) contribution to CMIP6. *Geosci. Model Dev.* 10:359–84
Wentz FJ, Ricciardulli L, Hilburn K, Mears C. 2007. How much more rain will global warming bring? *Science* 317:233–35
Williams IN, Pierrehumbert RT, Huber M. 2009. Global warming, convective threshold and false thermostats. *Geophys. Res. Lett.* 36:272–77
Xie SP, Deser C, Vecchi GA, Collins M, Delworth TL, et al. 2015. Towards predictive understanding of regional climate change. *Nat. Clim. Change* 5:921–30
Xie SP, Deser C, Vecchi GA, Ma J, Teng H, Wittenberg AT. 2010. Global warming pattern formation: sea surface temperature and rainfall. *J. Clim.* 23:966–86
Xie SP, Philander SGH. 1994. A coupled ocean-atmosphere model of relevance to the ITCZ in the eastern Pacific. *Tellus* 46A:340–50
Yang F, Kumar A, Schlesinger ME, Wang W. 2003. Intensity of hydrological cycles in warmer climates. *J. Clim.* 16:2419–23
Yu L. 2007. Global variations in oceanic evaporation (1958–2005): the role of the changing wind speed. *J. Clim.* 20:5376–90
Zelinka MD, Hartmann DL. 2011. The observed sensitivity of high clouds to mean surface temperature anomalies in the tropics. *J. Geophys. Res.* 116:D23103

Annu. Rev. Earth Planet. Sci. 2018.46:549-580. Downloaded from www.annualreviews.org
Access provided by 210.73.15.3 on 06/09/18. For personal use only.

Zeng N, Neelin JD, Chou C. 2000. A quasi-equilibrium tropical circulation model—implementation and simulation. *J. Atmos. Sci.* 57:1767–96

Zhang X, et al. 2007. Detection of human influence on twentieth-century precipitation trends. *Nature* 448:461–65

Zhao M, Held IM. 2012. TC-permitting GCM simulations of hurricane frequency response to sea surface temperature anomalies projected for the late 21st century. *J. Clim.* 25:2995–3009

Zhou YP, Xu KM, Sud YC, Betts AK. 2011. Recent trends of the tropical hydrological cycle inferred from Global Precipitation Climatology Project and International Satellite Cloud Climatology Project data. *J. Geophys. Res.* 116:D09101

Annu. Rev. Earth Planet. Sci. 2018.46:549-580. Downloaded from www.annualreviews.org
Access provided by 210.73.15.3 on 06/09/18. For personal use only.

nature geoscience

LETTERS

PUBLISHED ONLINE: 14 APRIL 2013 | DOI: 10.1038/NGEO1792

Patterns of the seasonal response of tropical rainfall to global warming

Ping Huang[1]*, Shang-Ping Xie[2,3,4]*, Kaiming Hu[1], Gang Huang[5] and Ronghui Huang[1]

Tropical convection is an important factor in regional climate variability and change around the globe[1,2]. The response of regional precipitation to global warming is spatially variable, and state-of-the-art model projections suffer large uncertainties in the geographic distribution of precipitation changes[3–5]. Two views exist regarding tropical rainfall change: one predicts increased rainfall in presently rainy regions (wet-get-wetter)[6–8], and the other suggests increased rainfall where the rise in sea surface temperature exceeds the mean surface warming in the tropics (warmer-get-wetter)[9–12]. Here we analyse simulations with 18 models from the Coupled Model Intercomparison Project (CMIP5), and present a unifying view for seasonal rainfall change. We find that the pattern of ocean warming induces ascending atmospheric flow at the Equator and subsidence on the flanks, anchoring a band of annual mean rainfall increase near the Equator that reflects the warmer-get-wetter view. However, this climatological ascending motion marches back and forth across the Equator with the Sun, pumping moisture upwards from the boundary layer and causing seasonal rainfall anomalies to follow a wet-get-wetter pattern. The seasonal mean rainfall, which is the sum of the annual mean and seasonal anomalies, thus combines the wet-get-wetter and warmer-get-wetter trends. Given that precipitation climatology is well observed whereas the pattern of ocean surface warming is poorly constrained[13,14], our results suggest that projections of tropical seasonal mean rainfall are more reliable than the annual mean.

The increase in atmospheric water vapour is a robust change under global warming as relative humidity remains relatively unchanged. The resultant intensification of the vertical moisture gradient, advected by the mean vertical motion, causes rainfall to increase where net water flux at the surface (P–E) is positive, and vice versa (wet-get-wetter)[7]. The enhanced lateral advection calls for reduced precipitation on the margins of a climatological rain band (upped-ante)[6,8]. The wet-get-wetter and upped-ante mechanisms do not emphasize the spatial variations in sea surface temperature (SST) warming. In Coupled Model Intercomparison Project (CMIP) models, the spatial distribution of tropical rainfall response is highly correlated with the overlooked SST pattern[5]. As tropospheric temperature is flattened by fast equatorial waves and set by the tropical mean SST (refs 10,15), local change in convective instability and hence rainfall is determined by relative SST defined as the deviation from the tropical mean (warmer-get-wetter, WaGW)[9,15]. We show that both the WaGW and wet-get-wetter (WeGW) mechanisms are important for tropical rainfall change, dominating the annual mean and seasonal anomalies, respectively. The result has implications for constraining rainfall projection.

The historical simulation and the representative concentration pathway 4.5 (RCP 4.5) experiment from 18 CMIP5 models (see Methods) are used to represent the present and future climates, respectively[16]. Figure 1 shows multi-model ensemble (MME) and zonal mean change in precipitation (P) and SST. The WeGW effect is obvious as ΔP moves back and forth across the Equator following the seasonal cycle of $\bar{P}$ (refs 17,18). (The overbar and Δ denote the present climatology and change in future climate, respectively.) The ocean warming (ΔSST) peaks on the Equator and shows a weak seasonal cycle[9,19]. (Seasonal variations of ΔSST are only 6% of the annual-mean, spatial variations.) On close inspection, the deviations from the WeGW pattern are apparent: precipitation increase (ΔP) exhibits smaller meridional excursions than $\bar{P}$, with the maximum displaced on the equatorward flank of the climatological rain band. The peak rainfall is larger in March than September for ΔP but the opposite is true for $\bar{P}$. We will show that these deviations from WeGW are ΔSST effects. (The upped-ante mechanism calls for rainfall reduction on both margins of the mean convergence zone, and does not explain the consistent equatorward displacement of ΔP relative to $\bar{P}$.)

To isolate the ΔSST effect, we also analyse a pair of additional atmospheric experiments in CMIP5, forced respectively by a spatially uniform SST increase (SUSI) of 4 K and by the spatially patterned SST increase (SPSI) derived from MME CMIP3 quadruple CO_2 (1%to4×) simulations[16,20,21]. The observed SST climatology is used for both runs. The SST warming pattern used in the SPSI run is very similar to ΔSST in RCP 4.5, both with an equatorial peak and a weak seasonal cycle (Supplementary Fig. S1). The SPSI results are scaled by its tropical mean SST increase, so the SPSI minus SUSI difference represents the SST pattern effect under the assumption that the nonlinear dependency on ΔSST amplitude is small.

A band of increased precipitation in SUSI marches across the Equator following $\bar{P}$, and the peak of ΔP coincides with that of $\bar{P}$ (Fig. 2a). This validates the WeGW mechanism. Precipitation change in SPSI is similar to that in RCP 4.5 runs (Figs 2b and 1a) but deviates markedly from SUSI runs. Compared with SUSI, the anomalous rain band in SPSI features small meridional swings and rainfall increase is enhanced near the Equator. The SPSI minus SUSI difference shows only a weak seasonal cycle and is tightly trapped on the Equator, consistent with the ΔSST structure. The ΔSST effect is stronger in the first than in the second half of

[1]Center for Monsoon System Research, Institute of Atmospheric Physics, Chinese Academy of Sciences, Beijing 100190, China, [2]Scripps Institution of Oceanography, University of California at San Diego, La Jolla, California 92093, USA, [3]Physical Oceanography Laboratory, Ocean University of China, Qingdao 266003, China, [4]International Pacific Research Center, University of Hawaii at Manoa, Honolulu, Hawaii 96822, USA, [5]Key Laboratory of Regional Climate-Environment Research for Temperate East Asia, Institute of Atmospheric Physics, Chinese Academy of Sciences, Beijing 100190, China. *e-mail: huangping@mail.iap.ac.cn; sxie@ucsd.edu.

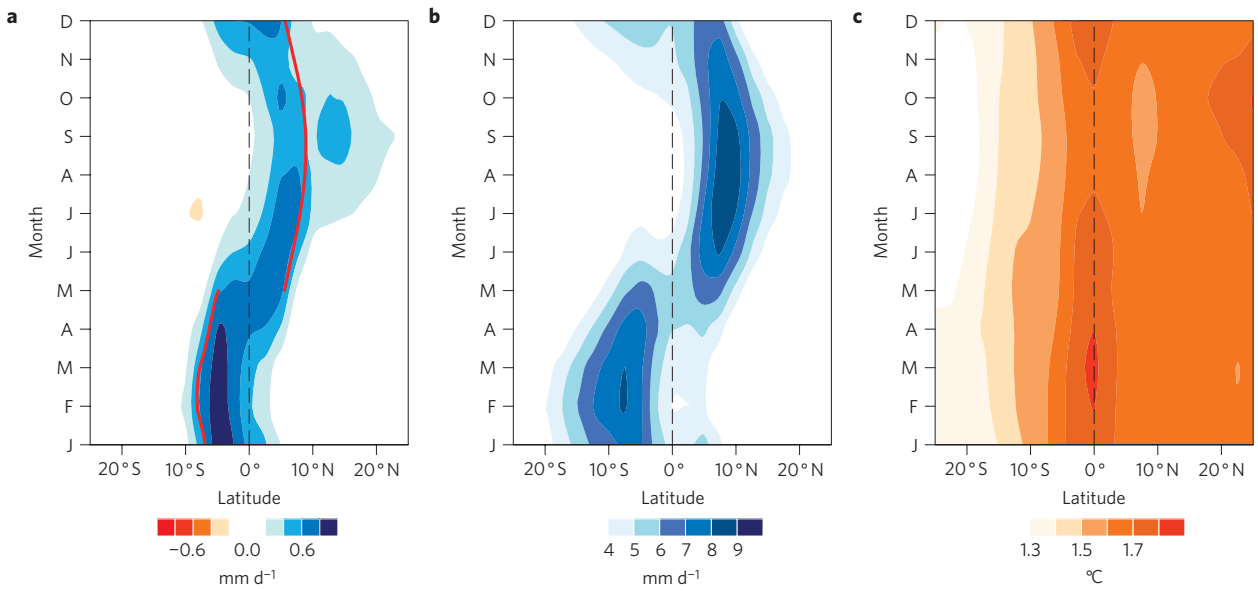

Figure 1 | Seasonal cycle of precipitation and SST change. a–c, Precipitation change (**a**), the precipitation climatology (**b**) and SST change (**c**) in RCP 4.5, all in zonal and MME mean. In **a**, the red curve marks the latitude of the maximum in mean precipitation.

the year because the seasonal development of equatorial upwelling suppresses the SST warming[9].

Vertical velocity change ($\Delta\omega$), overlooked in the WeGW hypothesis, proves important for rainfall change. In SUSI, $\Delta\omega$ broadly represents a weakening of tropical circulation (Fig. 2d) as required by a muted response of global precipitation[8,14]. In SPSI, $\Delta\omega$ is greatly enhanced near the Equator owing largely to the SST effect (Fig. 2e). The SST-induced change in $\Delta\omega$ closely resembles that in ΔP (Fig. 2f,c). The ΔSST peak anchors the anomalous rising motion near the Equator and compensating subsidence on the flanks. Even the weak seasonal cycle is mutually consistent among ΔSST, $\Delta\omega$ and ΔP, modulated to some degree by convective feedback[22]. The time–latitude evolution of $\Delta\omega$ is similar between SPSI and RCP 4.5 runs (Figs 2e and 3a). The ΔSST effect on $\Delta\omega$ can alternatively be understood from a moist instability argument[9]. ΔSST and surface Δq dominate the regional distribution of convective instability change because of the flattened upper tropospheric temperature change[9,10]. Specifically on the Equator where ΔSST peaks, the enhanced convective instability anchors a maximum in precipitation increase and anomalous upward motion.

The water vapour budget can decompose tropical rainfall change into

$$\Delta P \sim \Delta\omega \cdot \bar{q} + \bar{\omega} \cdot \Delta q \qquad (1)$$

where q denotes surface specific humidity, ω is the pressure velocity at 500 hPa, and lateral advection has been neglected, a good approximation for the tropics[7]. Figure 3 shows the decomposition results for RCP 4.5 runs. Equation (1) reproduces ΔP well from full models (Figs 1a and 3d). (The calculation using the full vertical-integrated budget yields nearly identical results.) As both $\bar{q}$ and Δq have broad structures that peak in the climatological rain band (Supplementary Fig. S2), both terms in equation (1) are dominated by vertical velocity in meridional structure (Fig. 3), although the poleward moisture decrease reduces the effect of vertical motion on precipitation away from the deep tropics. The thermodynamic component $\bar{\omega} \cdot \Delta q$ represents the WeGW effect, with the upward motion in the climatological rain band pumping up the moisture increase near the surface. The dynamic component $\Delta\omega \cdot \bar{q}$ causes rainfall to increase (decrease) near (off) the Equator, consistent with the vertical circulation change induced by the equatorial peak in SST warming. We have repeated the decomposition for SUSI and SPSI runs (Supplementary Fig. S3). The results confirm that the dynamic component is due to the SST effect following the WaGW pattern. Remarkably, the thermodynamic component is nearly identical between SUSI and SPSI runs, illustrating that the seasonal cycle in precipitation change is dominated by the WeGW mechanism.

Monthly mean ΔP is significantly correlated with both $\bar{P}$ and ΔSST at 0.67 and 0.60, respectively (Fig. 4), indicating that the WeGW and WaGW mechanisms are both important. The correlation is taken for the seasonal cycle within 10° S–10° N, a latitudinal band that pronounced precipitation change is confined to (Fig. 1a). To illustrate the combined WeGW–WaGW effect, we construct a multi-variant regression

$$\Delta P = a\bar{P} + b(\Delta\mathrm{SST} - c) \qquad (2)$$

for latitude–seasonal variations of zonal and MME means within 10° S and 10° N for 12 months. With $a = 0.11$, $b = 2.23$ and $c = 1.76$, the regression correlates with ΔP from CMIP5 models at 0.89, significantly higher than the correlation with either $\bar{P}$ or ΔSST for the MME analysis. A similar multi-variant regression analysis is performed for each model. The coefficient $a \approx \beta \cdot \langle\Delta\mathrm{SST}\rangle$, where the angle brackets denote the tropical mean and $\beta = 0.07\,\mathrm{K}^{-1}$ is the Clausius–Clapeyron coefficient, represents the thermodynamic effect on ΔP, whereas the coefficient $c \approx \langle\Delta\mathrm{SST}\rangle$ relates the change in the SST threshold for atmospheric convection to the tropical mean SST warming[10] (Supplementary Fig. S4). We use a non-dimensional ratio $\alpha = (b \cdot \sigma(\Delta\mathrm{SST} - c)/a \cdot \sigma(\bar{P}))$ to measure the relative importance of the WaGW to WeGW effect, where σ denotes the standard deviation. For MME, $\alpha = 0.9$, indicating that the WeGW and WaGW effects contribute nearly equally to ΔP. MME average generally underestimates the SST pattern and its effect on rainfall. Indeed the same regression analysis for individual models yields $\alpha > 0.9$ for 13 out of 18 models (Fig. 4d). (Results are not shown for FGOALS-s2 and MIROC5, in which the ΔSST pattern effect is so strong that ΔP is negatively correlated with $\bar{P}$.) The ratio α is significantly correlated with the standard deviation of SST pattern at 0.55 among models, indicating that the stronger the SST pattern is, the greater its relative importance for precipitation change.

In summary, we show that the seasonal precipitation response to global warming is a hybrid of WeGW and WaGW effects (WeWa).

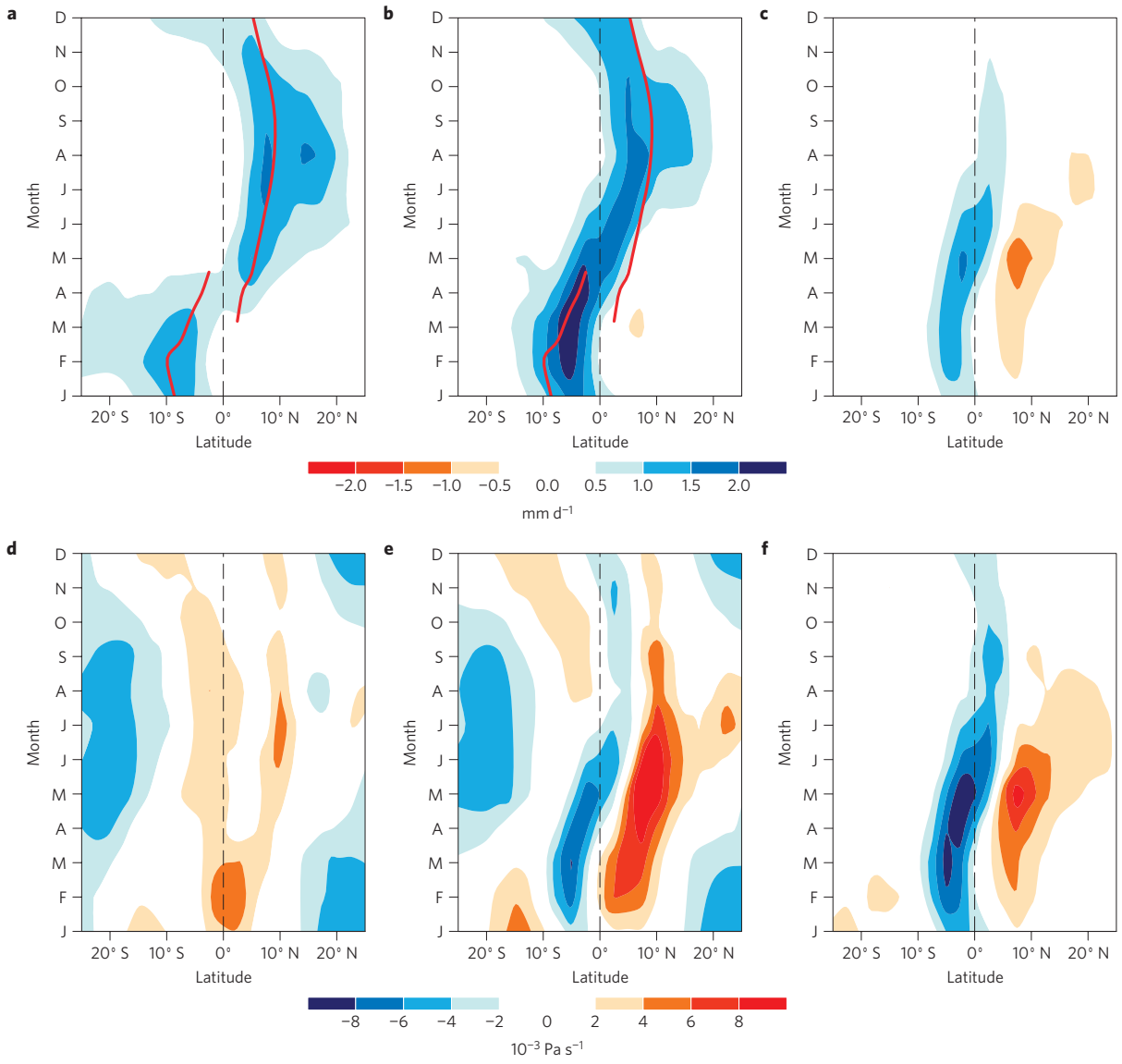

Figure 2 | Seasonal cycle of precipitation and circulation changes in SUSI and SPSI runs. a–c, ΔP in SUSI (**a**) and SPSI (**b**) runs, and their difference (**c**). **d–f**, The same as in **a–c** but for pressure velocity $\Delta\omega$ at 500 hPa. The solid red lines in **a**,**b** mark the latitude of the climatological precipitation maximum in the control. The SPSI results are scaled by the 20° S–20° N mean ΔSST to match SUSI.

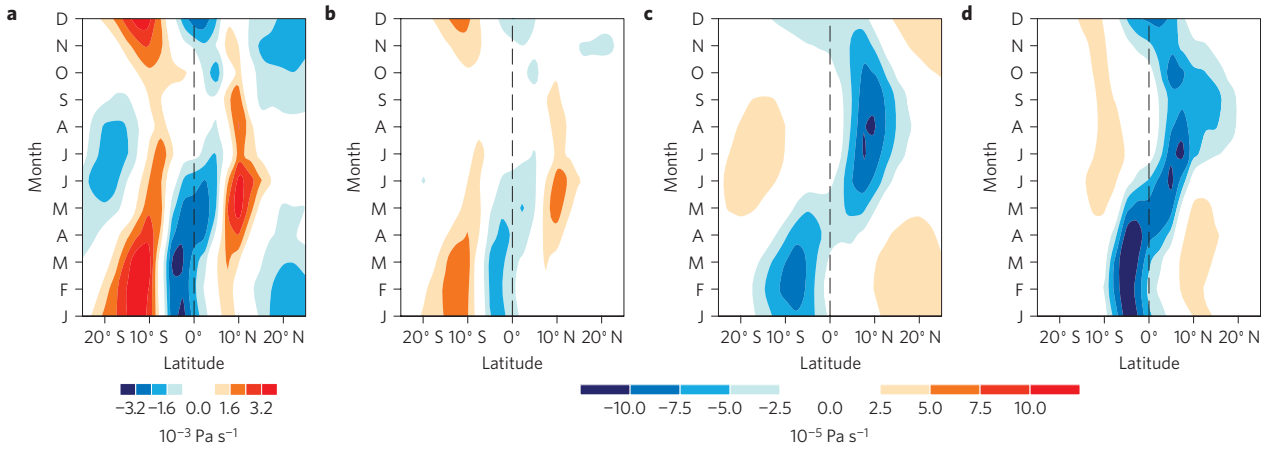

Figure 3 | Circulation change and decomposition of precipitation change. a–d, $\Delta\omega$ at 500 hPa (**a**); dynamic ($\Delta\omega \cdot \bar{q}$) (**b**) and thermodynamic ($\bar{\omega} \cdot \Delta q$) (**c**) components of rainfall change and their sum (**d**).

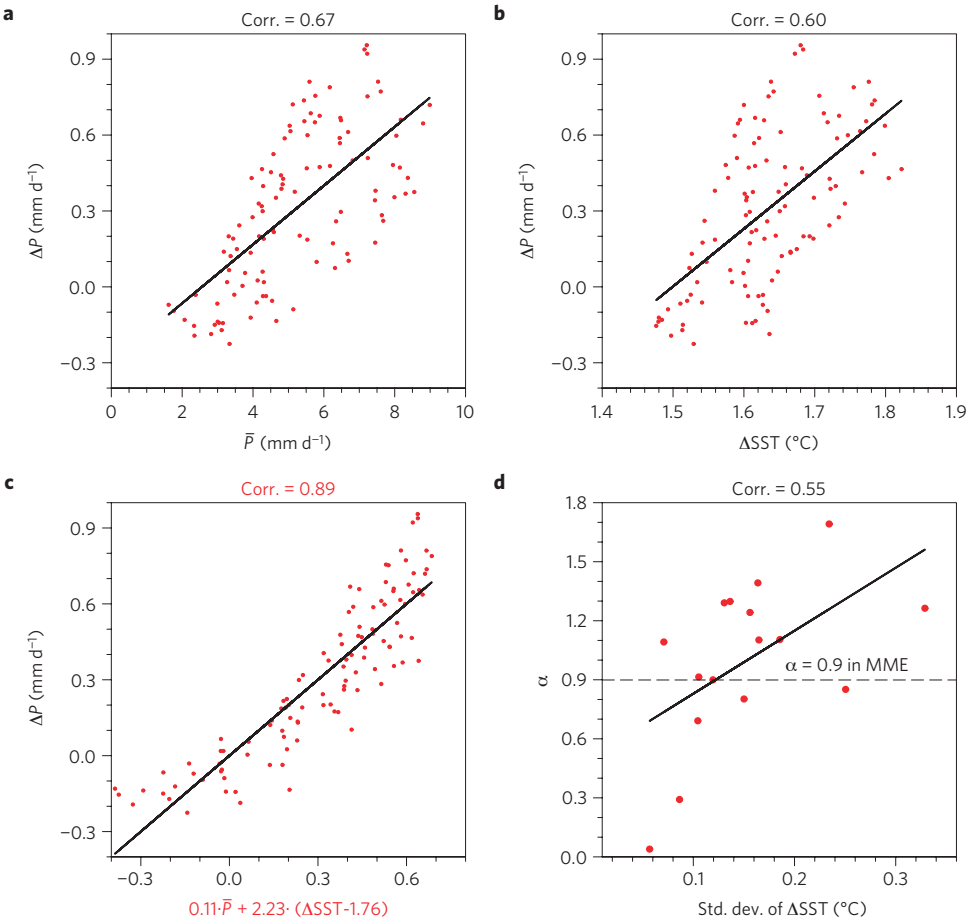

Figure 4 | Relationship of precipitation change to mean precipitation, SST change pattern and their linear combination. a–c, Scatter plots of MME precipitation change with mean precipitation (**a**), SST change (**b**) and their linear combination (equation (2); **c**) in 10° S–10° N through the seasonal cycle. The solid line indicates the linear fit, with the correlation coefficient shown at the top. **d**, The multi-variant regression analysis is also performed for each model, and the ratio α is shown in relation to the spatial standard deviation of ΔSST.

The two effects are not mutually exclusive but complementary, and the combined WeWa view best explains the seasonal precipitation change in the tropics (Fig. 4c). The anomalous rain band moves back and forth across the Equator but is consistently displaced on the equatorward flank of the climatological rain band. The displacement is due to the SST pattern effect. Specifically, the peak of SST warming anchors a band of anomalous ascent and rainfall increase near the Equator. Superimposed on this annual mean pattern, the upward motion in the climatological convergence zone sucks up the moisture increase from the boundary layer like a vacuum cleaner, dragging the band of rainfall increase back and forth across the Equator. We have repeated the linear regression analysis for the annual mean, and two seasons when the climatological rain band is farthest away from the Equator (February–April and August–October). The ratio of the WaGW to WeGW effect α is 1.35, 0.71 and 0.63, respectively (Supplementary Fig. S5). Thus, the WaGW effect is more obvious in the annual mean rainfall change whereas the WeGW effect is more dominant for the seasonal mean.

Regional precipitation projection is important for adaptation but subject to inherent uncertainty much greater than temperature[23,24]. The WeGW and WaGW effects are distinct in the nature of uncertainty regarding regional projection. If the WeGW mechanism dominates, the well-observed climatology can be used to constrain rainfall projection[25]. If the WaGW mechanism were to dominate, on the other hand, the uncertainty would be much greater because the SST warming pattern varies among models[5,26] and is poorly constrained by observations[13,14,27]. In light of the fact that the WeGW effect contributes more to the seasonal than the annual mean rainfall, we suggest that model projection is more reliable for the seasonal than annual mean rainfall in the tropics. This explains why the global monsoon rainfall increases consistently across models[28,29], a change that our results suggest probably takes place, with great environmental and socio-economic impacts.

Methods

CMIP5 models. We use the historical and RCP 4.5 experiments from 18 coupled general circulation models contributing to CMIP5 at http://pcmdi9.llnl.gov/ (ref. 16). They are BCC-CSM1.1, CanESM2, CCSM4, CNRM-CM5, CSIRO-Mk3.6.0, FGOALS-s2, GFDL-CM3, GFDL-ESM2G, GISS-E2-R, HadGEM2-ES, INM-CM4, IPSL-CM5A-LR, IPSL-CM5A-MR, MIROC5, MIROC-ESM, MIROC-ESM-CHEM, MRI-CGCM3 and NorESM1. See http://cmip-pcmdi.llnl.gov/cmip5/availability.html for details. The 1981–2000 mean defines the present climatology, the 2081–2100 mean in RCP 4.5 runs the future climatology, and their difference represents the change under global warming. The MME is defined as the simple average of 18 models.

Output from six atmospheric models (CanAM4, CNRM-CM5, HadGEM2-A, IPSL-CM5A-LR, MIROC5 and MRI-CGCM3) is available for a set of control, SUSI, and SPSI runs, called amip, amip4K and amipFuture in CMIP5, respectively[16,21]. In SUSI, a spatially uniform SST increase of 4 K (constant in time) is superimposed on the observed SST whereas SPSI uses the spatially patterned SST increase derived from the MME CMIP3 quadruple CO_2 (1%to4×) simulation. The SST pattern in SPSI is similar to that in CMIP5 RCP 4.5 runs, both with a peak on the Equator and a weak seasonal cycle (Supplementary Fig. S1 and Fig. 1c). The climate change

is defined as the 20-year monthly climatology for 1981–2000 in SUSI and SPSI runs minus that in the control runs. We scaled the SPSI results so that the tropical mean SST increase is the same as SUSI.

Received 30 October 2012; accepted 6 March 2013; published online 14 April 2013

References

1. Alexander, M. A. *et al.* The atmospheric bridge: The influence of ENSO teleconnections on air–sea interaction over the global oceans. *J. Clim.* **15,** 2205–2231 (2002).
2. Shin, S-I. & Sardeshmukh, P. D. Critical influence of the pattern of Tropical Ocean warming on remote climate trends. *Clim. Dyn.* **36,** 1577–1591 (2011).
3. Meehl, G. A. *et al.* in *Climate Change 2007: The Physical Science Basis* (eds Solomon, S. *et al.*) Ch. 10, 747–845 (Global Climate Projections, Cambridge Univ. Press, 2007).
4. Zhang, X. *et al.* Detection of human influence on twentieth-century precipitation trends. *Nature* **448,** 461–465 (2007).
5. Ma, J. & Xie, S-P. Regional patterns of sea surface temperature change: A source of uncertainty in future projections of precipitation and atmospheric circulation. *J. Clim.* http://dx.doi.org/10.1175/JCLI-D-1112-00283.00281 (in the press, 2013).
6. Neelin, J., Chou, C. & Su, H. Tropical drought regions in global warming and El Nino teleconnections. *Geophys. Res. Lett.* **30,** 2275 (2003).
7. Held, I. M. & Soden, B. J. Robust responses of the hydrological cycle to global warming. *J. Clim.* **19,** 5686–5699 (2006).
8. Chou, C., Neelin, J., Chen, C. & Tu, J. Evaluating the 'rich-get-richer' mechanism in tropical precipitation change under global warming. *J. Clim.* **22,** 1982–2005 (2009).
9. Xie, S-P. *et al.* Global warming pattern formation: Sea surface temperature and rainfall. *J. Clim.* **23,** 966–986 (2010).
10. Johnson, N. C. & Xie, S-P. Changes in the sea surface temperature threshold for tropical convection. *Nature Geosci.* **3,** 842–845 (2010).
11. Sobel, A. H. & Camargo, S. J. Projected future seasonal changes in tropical summer climate. *J. Clim.* **24,** 473–487 (2011).
12. Chadwick, R., Boutle, I. & Martin, G. Spatial patterns of precipitation change in CMIP5: Why the rich don't get richer in the tropics. *J. Clim.* http://dx.doi.org/10.1175/JCLI-D-1112-00543.00541 (in the press, 2013).
13. Tokinaga, H., Xie, S. P., Deser, C., Kosaka, Y. & Okumura, Y. M. Slowdown of the Walker circulation driven by tropical Indo-Pacific warming. *Nature* **491,** 439–443 (2012).
14. Vecchi, G. & Soden, B. Global warming and the weakening of the tropical circulation. *J. Clim.* **20,** 4316–4340 (2007).
15. Vecchi, G. A. & Soden, B. J. Effect of remote sea surface temperature change on tropical cyclone potential intensity. *Nature* **450,** 1066–1070 (2007).
16. Taylor, K. E., Stouffer, R. J. & Meehl, G. A. An overview of CMIP5 and the experiment design. *Bull. Am. Meteorol. Soc.* **93,** 485–498 (2012).
17. Chou, C. & Tu, J. Y. Hemispherical asymmetry of tropical precipitation in ECHAM5/MPI-OM during El Niño and under global warming. *J. Clim.* **21,** 1309–1332 (2008).
18. Tan, P-H., Chou, C. & Tu, J-Y. Mechanisms of global warming impacts on robustness of tropical precipitation asymmetry. *J. Clim.* **21,** 5585–5602 (2008).
19. Liu, Z., Vavrus, S., He, F., Wen, N. & Zhong, Y. Rethinking tropical ocean response to global warming: The enhanced equatorial warming. *J. Clim.* **18,** 4684–4700 (2005).
20. Cess, R. D. *et al.* Intercomparison and interpretation of climate feedback processes in 19 atmospheric general circulation models. *J. Geophys. Res.* **95,** 601216 (1990).
21. Bony, S. *et al.* CFMIP: Towards a better evaluation and understanding of clouds and cloud feedbacks in CMIP5 models. *CLIVAR Exchanges* **56,** 20–24 (2011).
22. Watanabe, M. & Jin, F. F. A moist linear baroclinic model: Coupled dynamical-convective response to El Nino. *J. Clim.* **16,** 1121–1139 (2003).
23. Lau, K. M. & Wu, H. T. Detecting trends in tropical rainfall characteristics, 1979–2003. *Int. J. Climatol.* **27,** 979–988 (2007).
24. Wentz, F. J., Ricciardulli, L., Hilburn, K. & Mears, C. How much more rain will global warming bring? *Science* **317,** 233–235 (2007).
25. Allan, R. P., Soden, B. J., John, V. O., Ingram, W. & Good, P. Current changes in tropical precipitation. *Environ. Res. Lett.* **5,** 025205 (2010).
26. Lu, J. & Zhao, B. The role of oceanic feedback in the climate response to doubling CO_2. *J. Clim.* **25,** 7544–7563 (2012).
27. Deser, C., Phillips, A. & Alexander, M. Twentieth century tropical sea surface temperature trends revisited. *Geophys. Res. Lett.* **37,** L10701 (2010).
28. Hsu, P. C. *et al.* Increase of global monsoon area and precipitation under global warming: A robust signal? *Geophys. Res. Lett.* **39,** L06701 (2012).
29. Kitoh, A. *et al.* Monsoons in a changing world: a regional perspective in a global context. *J. Geophys. Res.* http://dx.doi.org/10.1002/jgrd.50258 (2013).

Acknowledgements

The work was supported by the National Basic Research Program of China (2012CB955604 and 2010CB950403), the Natural Science Foundation of China (41105047 and 41275083) and the US National Science Foundation. We wish to thank C. Chou for helpful discussions, and X. Qu for data processing. We acknowledge the World Climate Research Programme's Working Group on Coupled Modelling, which is responsible for CMIP5, and we thank the climate modeling groups (listed in the Methods of this paper) for producing and making available their model output.

Author contributions

P.H. designed and performed the analysis. S-P.X. contributed to improving the analysis and interpretation. K.H. and G.H. prepared part of the data. P.H. and S-P.X. wrote the paper. All authors discussed and commented on the paper.

Additional information

Supplementary information is available in the online version of the paper. Reprints and permissions information is available online at www.nature.com/reprints. Correspondence and requests for materials should be addressed to P.H. or S-P.X.

Competing financial interests

The authors declare no competing financial interests.

LETTERS
PUBLISHED ONLINE: 6 MAY 2011 | DOI: 10.1038/NCLIMATE1086
nature climate change

Interdecadal modulation of El Niño amplitude during the past millennium

Jinbao Li[1,2]*, Shang-Ping Xie[1,3,4], Edward R. Cook[2], Gang Huang[5], Rosanne D'Arrigo[2], Fei Liu[1], Jian Ma[3] and Xiao-Tong Zheng[4]

The El Niño/Southern Oscillation (ENSO) is the dominant mode of interannual climate variability on Earth, alternating between anomalously warm (El Niño) and cold (La Niña) conditions in the tropical Pacific at intervals of 2–8 years[1,2]. The amplitude of ENSO variability affects the occurrence and predictability of climate extremes around the world[3,4], but our ability to detect and predict changes in ENSO amplitude is limited by the fact that the instrumental record is too short to characterize its natural variability[5–8]. Here we use the North American Drought Atlas[9,10]—a database of drought reconstructions based on tree-ring records—to produce a continuous, annually resolved record of ENSO variability over the past 1,100 years. Our record is in broad agreement with independent, ENSO-sensitive proxy records in the Pacific and surrounding regions. Together, these records indicate that ENSO amplitude exhibits a quasi-regular cycle of 50–90 years that is closely coupled to the tropical Pacific mean state. Anomalously warm conditions in the eastern Pacific are associated with enhanced ENSO variability, consistent with model simulations[11]. The quasi-periodic ENSO amplitude modulation reported here offers a key observational constraint for improving models and their prediction of ENSO behaviour linked to global warming.

Despite great efforts to understand the El Niño/Southern Oscillation (ENSO) phenomenon, there is still much uncertainty in changes in ENSO amplitude. Instrumental records indicate marked variations in ENSO amplitude, large around the 1890s–1900s and 1970s–1990s, but small between these periods and before 1890 (Supplementary Fig. S1). Existing proxy records suggest significant variability in ENSO amplitude in the past[2,12,13], but they cover only the past few centuries or noncontinuous periods of the past millennium. Current general circulation models (GCMs) give different projections of future ENSO-related change, with some showing an increase and others no change or even a decrease in ENSO amplitude[6,7]. Therefore, it is crucial to develop long, continuous, high-resolution proxy records to determine the characteristics of natural ENSO variability, and to provide observational constraints for improving the models[7,8].

Proxy records from the equatorial Pacific are valuable for studying past ENSO behaviour[12–14], yet very few such records exist. This situation has impeded the study of long-term ENSO amplitude modulation. By contrast, thousands of tree-ring records without these deficiencies are available for North America, a region where hydroclimate is sensitive to tropical Pacific climate anomalies on various timescales[15,16]. Such tree-ring records have been used to develop the gridded North America Drought Atlas[9,10] (NADA) (see Methods and Supplementary Information). Here we demonstrate the fidelity of NADA in recording long-term ENSO variability, particularly variations in ENSO amplitude on interdecadal to centennial timescales.

The leading empirical orthogonal function (EOF) of NADA, which accounts for 23.5% of the total variance, shows a distinct moisture pattern heavily loaded over southwest North America (Methods and Fig. 1a), a region strongly affected by ENSO variability[15,16]. The explained variance of the first EOF for the southwest North America domain rises to 49.5% (Supplementary Fig. S3), and its principal component (PC) has a correlation of 0.99 with that for the whole of North America over the past 1,100 years. This confirms that NADA PC1 dominates variability in southwest North America.

The fidelity of NADA PC1 in representing ENSO variability is demonstrated in five ways: (1) NADA PC1 is significantly correlated with equatorial Pacific sea surface temperatures[17] (SSTs) during the instrumental period (Fig. 1c). For example, its correlation with the January–March (JFM) ENSO Niño3 index for 1870–2002 is 0.51 ($P < 0.001$) (Supplementary Fig. S4). (2) NADA PC1 is significantly correlated with a modern coral record from Palmyra Island in the central tropical Pacific[13], at $r = -0.58$ for the common period 1891–1994 ($P < 0.001$) (Supplementary Fig. S5). After adjusting relict coral U/Th dates within the analytical error windows[13], we found possible correlations between North American drought and tropical corals that persisted throughout the past millennium (Methods and Fig. 1d). Considering the independent nature of these proxy records, this agreement is remarkable, strongly indicative of a coherent relationship between ENSO and North American drought over the past millennium. (3) NADA PC1 is highly correlated with, but is significantly longer than, the existing ENSO reconstructions (Supplementary Table S1). Most of these reconstructions are largely, although not entirely, independent, as they only share a few common tree-ring data from southwest North America. This suggests that NADA PC1 represents reasonable estimates of ENSO variability over the past millennium. (4) Separate composite analysis of NADA for periods of large and small PC variability over the past millennium shows nearly identical patterns (Supplementary Fig. S6). This pattern stability suggests that the westerly waveguide is stable in tropical forced stationary waves, and that NADA PC1 represents the modulation of ENSO itself. (5) Separate EOF analysis shows that the first EOF of NADA is heavily loaded over southwest North America both before and after the 1976/1977 climate regime shift[18,19], and the PC is highly correlated with tropical eastern Pacific SSTs for both periods

[1]International Pacific Research Center, University of Hawaii at Manoa, Honolulu, Hawaii 96815, USA, [2]Lamont-Doherty Earth Observatory, Columbia University, Palisades, New York 10964, USA, [3]Department of Meteorology, University of Hawaii at Manoa, Honolulu, Hawaii 96815, USA, [4]Physical Oceanography Laboratory and Ocean–Atmosphere Interaction and Climate Laboratory, Ocean University of China, Qingdao 266100, China, [5]Institute of Atmospheric Physics, Chinese Academy of Sciences, Beijing 100029, China. *e-mail: jinbao@hawaii.edu.

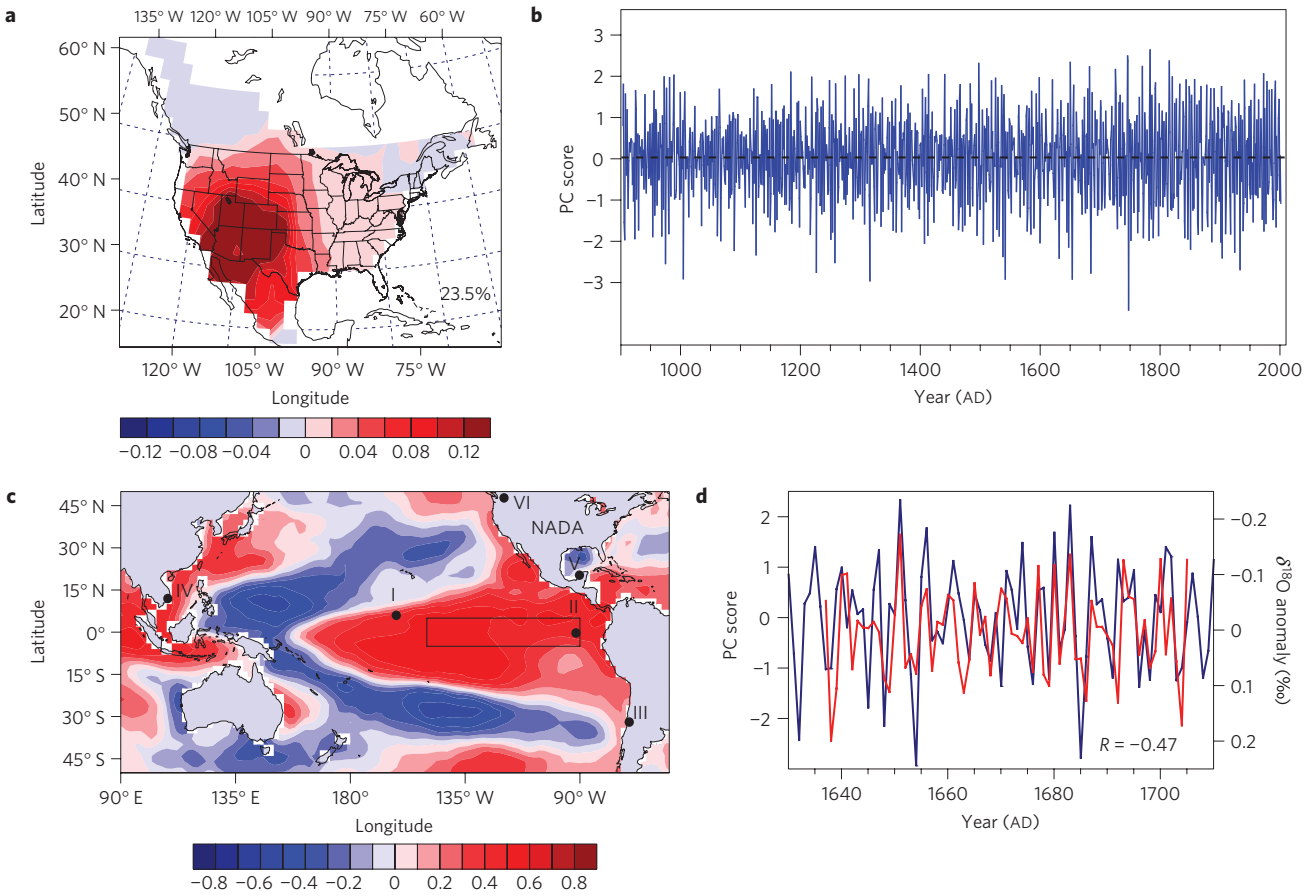

Figure 1 | The leading EOF pattern of NADA, its PC series and correlation of the PC series with tropical records. a, Spatial pattern of the leading EOF over North America, and **b**, its PC time series. The percentage variance accounted for by the leading EOF is labelled in **a**. **c**, Spatial correlation of NADA PC1 with global JFM SSTs (ref. 17) during 1870–2002. The SSTs were processed using a 9-yr Lanczos high-pass filter[30] to isolate interannual variability. The box denotes the Niño3 region, and the dots indicate the site locations mentioned in the text (I: Palmyra corals[13], II: Galápagos coral[12], III: Chile tree rings[23], IV: Vietnam tree rings[24], V: Mexico sediment[26], VI: Washington sediment[27]). **d**, Comparison of NADA PC1 (blue) with the dating-error corrected Palmyra relict coral δ^{18}O series[13] (red) over 1637–1705.

(Supplementary Fig. S7). Although there exist some differences in the EOF pattern and correlation with tropical SSTs between the two periods, these results indicate that moisture variability in southwest North America has been sensitive to ENSO variability both before and after the 1976/1977 climate regime shift. The relationship to ENSO is further confirmed by the SST correlation pattern for 1870–2002 (Fig. 1c). Therefore, teleconnections of canonical eastern Pacific ENSO (hereafter simply ENSO) are probably stable over southwest North America. On the basis of these validations, we consider that NADA PC1 represents a continuous record of interannual ENSO variability during the past millennium.

As inferred from NADA PC1, ENSO amplitude has been highly variable during the past millennium, with many El Niño/La Niña events of larger amplitude than observed in the instrumental period (Fig. 1b). Here we calculated a 21-yr running biweight variance[20] to measure changes in ENSO amplitude. This technique highlights the interdecadal amplitude modulation of a time series while reducing bias that might be introduced by extreme outliers in a 21-yr window. As shown in Fig. 2a, superimposed on a general rising trend are large fluctuations in ENSO variance on interdecadal to centennial timescales. ENSO variance was reduced in the Medieval Climate Anomaly (MCA) period, with the eleventh-century variance being the lowest of the past millennium. Following this, the variance showed an increasing trend in the Little Ice Age (LIA), and maintained a high level from the eighteenth century to the Current Warm Period (CWP). On average, the eighteenth-century ENSO variance was the strongest of the past millennium.

A multi-taper method[21] (MTM) spectral analysis reveals two significant quasi-regular periodicities at 50–60-yr and 82–90-yr bands, respectively (Fig. 3a), confirming the visual impression of interdecadal modulation of ENSO amplitude. A time-space wavelet transform[22] exhibits a marked shift in the dominant periodicity, concomitant with the transition from the MCA into the LIA, from a 82–90-yr cycle during AD 900–1300 to a 50–60-yr cycle thereafter (Fig. 3b). Meanwhile, a 30-yr cycle is present during AD 1500–1800 and in the MTM analysis. The shifts in ENSO periodicity, together with a general increase in variance (Fig. 2a), may reflect major reorganizations within the tropical ocean–atmosphere system, or alternatively significant ENSO teleconnection changes from the MCA to LIA.

We found evidence for such interdecadal fluctuations in ENSO variance elsewhere, especially in the equatorial Pacific and regions under strong ENSO teleconnections. Variance modulation in North American tree rings is consistent with that observed in the Niño3 SST, and the two variance series are correlated at 0.64 ($P < 0.001$) during their common period 1880–1992 (Fig. 2a). A coral annual average oxygen isotopic (δ^{18}O) record from the Galápagos Islands in the eastern equatorial Pacific[12] exhibits quasi-periodic variance modulation similar to that in North American tree rings during the past four centuries (Fig. 2b). The coral δ^{18}O records from Palmyra Island in the central tropical Pacific[13], although not continuous,

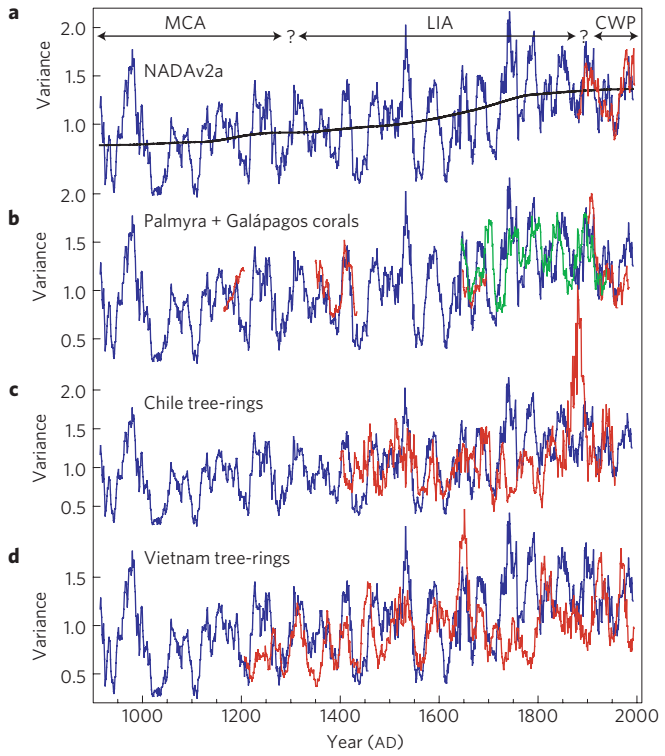

Figure 2 | Comparison of records of ENSO variance. NADA-derived ENSO variance (blue) along with those derived from: **a**, the observed Niño3 SST (ref. 17; red) over 1880–1995; **b**, coral records from both the Galápagos Islands in the eastern equatorial Pacific[12] (green) and Palmyra Island in the central tropical Pacific[13] (red); **c**, tree-ring record from an ENSO-sensitive site in El Asiento, Chile[23] (red); **d**, tree-ring record from the Bidoup Nui Ba National Park in southern Vietnam[24] (red). All records were processed using a 9-yr Lanczos high-pass filter[30] before calculating a 21-yr running biweight variance. The black bold line in **a** denotes a 400-year low-pass filter to indicate the long-term trend.

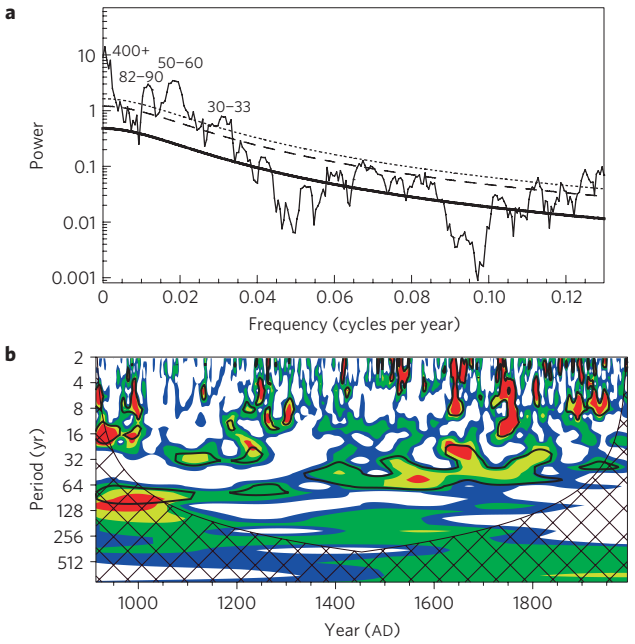

Figure 3 | Spectral property of the NADA-derived ENSO variance series. **a**, MTM (ref. 21) spectral density of the ENSO variance series. The bold line indicates the null hypothesis, and the dash (dotted) line indicates the 95% (99%) significance level, using a red-noise background spectrum. Periodicities of significant peaks are labelled above the spectral density line. **b**, The wavelet power spectrum[22]. The power has been scaled by the global wavelet spectrum. The cross-hatched region is the cone of influence, where zero padding has reduced the variance. Black contour is the 90% significance level, using a red-noise background spectrum.

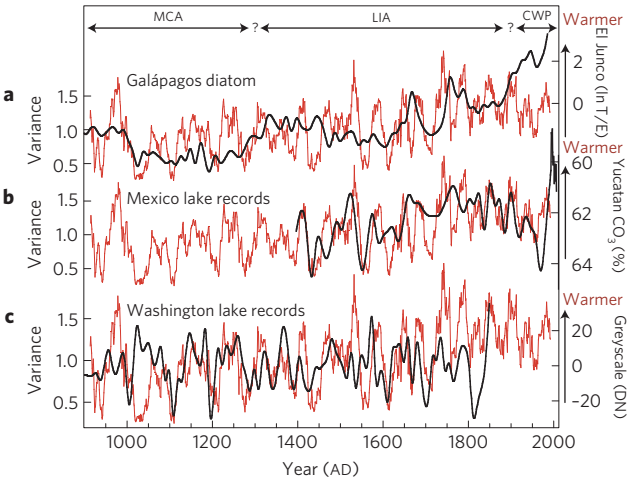

Figure 4 | Comparison of the NADA-derived ENSO variance series with records of the tropical Pacific mean state. NADA-derived ENSO variance (red) along with: **a**, a diatom record from El Junco Lake, Galápagos, in the eastern equatorial Pacific[14] (black). **b**, A carbonate ion (CO_3^{2-}) record from Aguada X'caamal Lake in northwest Yucatan, Mexico[26] (black). **c**, A greyscale record from Castor Lake in Washington state, USA (ref. 27) (black). All lake records were smoothed using a 9-yr low-pass filter. Upward swings in black curves represent a warm state of the tropical Pacific.

show broadly consistent changes in variance during the past nine centuries (Fig. 2b). Tree-ring records from an ENSO-sensitive site in El Asiento, Chile, in the Southern Hemisphere[23], exhibit similar interdecadal fluctuations in variance over most of the past six centuries, except during the late nineteenth century, when there is an out-of-phase relationship (Fig. 2c). Recent tree-ring records from the highlands of Bidoup Nui Ba National Park in southern Vietnam[24], a tropical region strongly influenced by ENSO teleconnections, also show in-phase fluctuations in variance with North American tree-rings during the thirteenth to seventeenth and most of the twentieth centuries, although this relationship was out-of-phase during the eighteenth to nineteenth centuries (Fig. 2d). We note two caveats of the above proxy comparisons. First, unlike the NADA, which is based on nearly two-thousand tree-ring chronologies across North America, other proxy data often consist of only a single series for a given site, and are prone to chaotic noise and regional variability. Second, the long-term stability of ENSO influence in other teleconnection regions needs further investigation, unlike North America where we have validated a persistent relationship to ENSO during the past millennium. Overall these records from the tropics and mid-latitudes in both the Northern and Southern Hemispheres are mutually consistent. Together they show quasi-periodic amplitude modulation, and suggest that such modulation is fundamental to ENSO physics.

How ENSO amplitude modulation is related to changes in the tropical Pacific mean state is a key question for ENSO physics[6,11,25]. Here we examine this relationship during the past millennium by comparing the NADA-derived ENSO variance series with three proxy records for the tropical Pacific mean state. The first is a diatom record from El Junco Lake, Galápagos, an indicator of SSTs in the eastern equatorial Pacific[14] (Fig. 4a). The second is a carbonate ion (CO_3^{2-}) record from Aguada X'caamal Lake in

northwest Yucatan, Mexico (Fig. 4b) that indicates SST changes in the surrounding ocean[26]. The third is a greyscale record from a sediment core from Castor Lake in the Pacific Northwest, whose low-frequency variations are interpreted as changes in the tropical and extratropical Pacific mean state[27] (Fig. 4c).

Despite discrepancies that may reflect either data uncertainties or changes in SST spatial structure, these three records indicate that the eastern tropical Pacific was in a cooler state at the peak of the MCA (~AD 1000–1200), and that there was a persistent positive temperature trend in the LIA and CWP (Fig. 4). ENSO variance was thus greatly reduced during most of the MCA, increased persistently in the LIA, and maintained a high level in the CWP. Moreover, interdecadal fluctuations in ENSO variance seem closely related to anomalies in the Pacific mean state during the past millennium. The Castor Lake data, in particular, suggest that a warm (cool) eastern tropical Pacific is associated with increased (reduced) ENSO variance over most of the 1,000-year record (Fig. 4c). These observations suggest that ENSO variability during the past millennium is closely coupled to changes in the background mean state, a finding that is supported by recent model simulations[6,11].

The quasi-regular nature of ENSO amplitude modulation, and the co-variations with the equatorial Pacific mean state, support the emerging idea that there is a positive feedback between the mean state and ENSO variance[11]. An increase in ENSO amplitude causes the eastern equatorial Pacific to warm, a mean-state change that amplifies ENSO variability. If fully tested in observations and process-oriented model studies, this idea can be exploited for decadal prediction of ENSO amplitude.

In summary, using data on North American tree rings, we have produced a continuous, annually resolved record of ENSO variability for the past millennium. This record is in broad agreement with independent proxy records in and surrounding the Pacific over most of their common periods, revealing a marked quasi-regular interdecadal modulation of ENSO amplitude throughout the past millennium. The amplitude modulation is closely associated with changes in the tropical Pacific mean state, suggesting an interactive relationship. This observation alone implies that the continued increase in eastern-central tropical Pacific SSTs in a future warmer climate[5,7] will lead to enhanced ENSO variability and more extreme climate conditions around the globe. The diverse response of a host of ocean–atmospheric feedbacks complicates such a prediction of ENSO amplitude change[5,7]. Regardless, the quasi-periodic modulation of ENSO amplitude provides a crucial observational constraint that can be used to guide model improvement towards reduced uncertainties in predicting future ENSO behaviour. Finally, the further study of the mechanisms responsible for such ENSO amplitude modulation (for example, stochastic atmospheric noise[28] and external forcing[29]) will help shed light on ENSO dynamics.

Methods

The updated North America Drought Atlas (NADA). The NADA (ref. 9) consists of annually resolved summer (June–August) Palmer Drought Severity Index (PDSI) reconstructions derived from tree rings, available on a 2.5° × 2.5° grid over most of North America (Supplementary Information). Compared with the initial release of the NADA, the updated version (NADAv2a) used more tree-ring chronologies (1845 in total) to improve the PDSI reconstructions, but the grid spacing, series length, and statistical methods remain unchanged[10]. Here we analyse the updated NADA for AD 900–2006, a period when reconstructed values are available at more than 60% of all grid points (Supplementary Fig. S2). Time series at each grid point were processed using a 9-yr Lanczos high-pass filter[30] to preserve variability in the classical ENSO band of 2–8 years[1,2]. Empirical orthogonal function (EOF) analysis was used to objectively define the dominant mode of summer drought over NA, and the associated principal component (PC) series was used to indicate its variability over time.

Relict coral dating error corrections. By splicing together relict coral oxygen isotopic (δ^{18}O) records from Palmyra Island in the central tropical Pacific, Cobb *et al.*[13] provided 30-150-yr windows of tropical Pacific climate variability over the past 1,100 years. Their modern coral samples were exactly dated, whereas relict corals were dated using the U/Th method, which contains a general dating error of ± 5–10-yr. Therefore, if there were a coherent relationship between ENSO and North American drought over the past millennium, then, by adjusting the relict coral sequences within the range of their U/Th-dating errors, a firm match could be achieved between the coral δ^{18}O sequences and NADA PC1.

We first examined the modern coral record. As NADA PC1 represents seasonally averaged moisture variability that has its highest correlation with winter (January–March) tropical Pacific SSTs, we herein used the January–March mean coral δ^{18}O records to make them directly comparable. All series were processed using a 9-yr Lanczos high-pass filter[30] to highlight interannual variability. The highest correlation of the modern coral δ^{18}O record with NADA PC1 over their common period 1891–1994 is −0.58, which is close to its correlation with the Niño3 index (−0.61) in the same period. The highest correlation was achieved at lag zero, confirming that there is no dating error for modern coral. This good match between modern coral and NADA PC1 corroborates the dating error correction method.

The seventeenth-century sequence was spliced from three relict coral δ^{18}O records (SB3, SB13, and SB8), and was correlated at −0.06 with NADA PC1 before dating errors were corrected. Dating error for each of the three individual series was corrected by adjusting years within the range of U/Th-dating errors. A firm match with NADA PC1 was achieved for each series after dating adjustments, with correlations improved from 0.17 to −0.41 for SB3, −0.20 to −0.62 for SB13, and −0.27 to −0.51 for SB8. After correcting the dating errors and re-splicing the three sequences together, a good match between relict corals and NADA PC1 was achieved, with a correlation of −0.47 over their common period 1637–1705 (Supplementary Fig. S4). Similarly, dating errors were corrected for the fourteenth–fifteenth-century sequence, and its correlation with NADA PC1 improved from −0.14 to −0.35 over the common period 1339–1443.

The tenth- and twelfth-century sequences are both single relict coral δ^{18}O records. The best match between the tenth-century sequence and NADA PC1 was achieved after adjusting the start year of the relict coral sequence from AD 933 to AD 931, and their correlation over the common period 931–954 improved from 0.08 to −0.43. The correlation of the twelfth-century sequence with NADA PC1 over their common period 1154–1215 is −0.19, and there is no significant improvement when its dating was adjusted within the range of its U/Th-dating error. Therefore, we did not make a dating error correction for this sequence.

Received 21 December 2010; accepted 25 March 2011; published online 6 May 2011

References

1. Deser, C., Alexander, M. A., Xie, S-P. & Phillips, A. S. Sea surface temperature variability: Patterns and mechanisms. *Annu. Rev. Mar. Sci.* **2,** 115–143 (2010).
2. D'Arrigo, R., Cook, E. R., Wilson, R. J., Allan, R. & Mann, M. E. On the variability of ENSO over the past six centuries. *Geophys. Res. Lett.* **32,** L03711 (2005).
3. McPhaden, M. J., Zebiak, S. E. & Glantz, M. H. ENSO as an integrating concept in Earth science. *Science* **314,** 1740–1745 (2006).
4. Tang, Y., Deng, Z., Zhou, X., Cheng, Y. & Chen, D. Interdecadal variation of ENSO predictability in multiple models. *J. Clim.* **21,** 4811–4833 (2008).
5. Collins, M. *et al.* The impact of global warming on the tropical Pacific Ocean and El Niño. *Nature Geosci.* **3,** 391–397 (2010).
6. Yeh, S. W. & Kirtman, B. P. ENSO amplitude changes due to climate change projections in different coupled models. *J. Clim.* **20,** 203–217 (2007).
7. Guilyardi, E. *et al.* Understanding El Niño in ocean–atmosphere general circulation Models: Progress and challenges. *Bull. Am. Meteorol. Soc.* **90,** 325–340 (2009).
8. Wittenberg, A. T. Are historical records sufficient to constrain ENSO simulations? *Geophys. Res. Lett.* **36,** L12702 (2009).
9. Cook, E. R., Woodhouse, C., Eakin, C. M., Meko, D. M. & Stahle, D. W. Long-term aridity changes in the western United States. *Science* **306,** 1015–1018 (2004).
10. Cook, E. R. *et al. North American Summer PDSI Reconstructions, Version 2a.* IGBP PAGES/World Data Center for Paleoclimatology Data Contribution Series # 2008-046 (NOAA, NGDC Paleoclimatology Program, 2008).
11. Choi, J., An, S-I., DeWitte, B. & Hsieh, W.W. Interactive feedback between the tropical Pacific Decadal Oscillation and ENSO in a coupled general circulation model. *J. Clim.* **22,** 6597–6611 (2009).
12. Dunbar, R. B., Wellington, G. M., Colgan, M. W. & Glymn, P. W. Eastern Pacific sea surface temperature since 1600 AD: The δ^{18}O record of climate variability in Galápagos coral. *Paleoceanography* **9,** 291–315 (1994).
13. Cobb, K. M., Charles, C. D., Cheng, H. & Edwards, R. L. El Niño/Southern Oscillation and tropical Pacific climate during the last millennium. *Nature* **424,** 271–276 (2003).
14. Conroy, J. L. *et al.* Unprecedented recent warming of surface temperatures in the eastern tropical Pacific Ocean. *Nature Geosci.* **2,** 46–50 (2009).
15. Seager, R., Kushnir, Y., Herweijer, C., Naik, N. & Velez, J. Modelling of tropical forcing of persistent droughts and pluvials over western North America: 1856–2000. *J. Clim.* **18,** 4068–4091 (2005).

16. Cook, E. R., Seager, R., Cane, M. A. & Stahle, D. W. North American droughts: Reconstructions, causes and consequences. *Earth Sci. Rev.* **81,** 93–134 (2007).
17. Smith, T. M., Reynolds, R. W., Peterson, T. C. & Lawrimore, J. Improvements to NOAA's historical merged land–ocean surface temperature analysis (1880–2006). *J. Clim.* **21,** 2283–2296 (2008).
18. Mantua, N. J., Hare, S. R., Zhang, Y., Wallace, J. M. & Francis, R. C. A Pacific interdecadal climate oscillation with impacts on salmon production. *Bull. Am. Meteorol. Soc.* **78,** 1069–1079 (1997).
19. Zhang, Y., Wallace, J. & Battisti, D. ENSO-like decade-to-century scale variability: 1900–93. *J. Clim.* **10,** 1004–1020 (1997).
20. Lanzante, J. R. Resistant, robust & non-parametric techniques for the analysis of climate data: Theory and examples, including applications to historical radiosonde station data. *Int. J. Climatol.* **16,** 1197–1226 (1996).
21. Mann, M. E. & Lees, J. Robust estimation of background noise and signal detection in climatic time series. *Clim. Change* **33,** 409–445 (1996).
22. Torrence, C. & Compo, G. P. A practical guide to wavelet analysis. *Bull. Am. Meteorol. Soc.* **79,** 61–78 (1998).
23. LaMarche, V. C. Jr., Holmes, R. L., Dunwiddie, P. W. & Drew, L. G. Tree-ring chronologies of the southern hemisphere: Chile. *Lab. Tree-Ring Res. Chronol. Ser.* **2,** 1–43 (1979).
24. Buckley, B. M. *et al*. Climate as a contributing factor in the demise of Angkor, Cambodia. *Proc. Natl Acad. Sci. USA* **107,** 6748–6752 (2010).
25. Fedorov, A. V. & Philander, S. G. A stability analysis of the tropical ocean–atmosphere interactions: Bridging measurements and theory for El Niño. *J. Clim.* **14,** 3086–3101 (2001).
26. Hodell, D. A. *et al*. Climate change on the Yucatan Peninsula during the Little Ice Age. *Quat. Res.* **63,** 109–121 (2005).
27. Nelson, D. B. *et al*. Drought variability in the Pacific Northwest from a 6,000-yr lake sediment record. *Proc. Natl Acad. Sci. USA* doi:10.1073/pnas.1009194108 (2011).
28. Burgman, R. J., Schopf, P. & Kirtman, B. P. Decadal modulation of ENSO in a hybrid coupled model. *J. Clim.* **21,** 5482–5500 (2008).
29. Mann, M. E., Cane, M. A., Zebiak, S. E. & Clement, A. Volcanic and solar forcing of the tropical Pacific over the past 1,000 years. *J. Clim.* **18,** 447–456 (2005).
30. Duchon, C. E. Lanczos filtering in one and two dimensions. *J. Appl. Meteorol.* **18,** 1016–1022 (1979).

Acknowledgements

We gratefully acknowledge the researchers who have contributed their tree-ring data for NADA development. This research was funded by the National Science Foundation, the National Oceanic and Atmospheric Administration, the Japan Agency for Marine-Earth Science and Technology, the National Basic Research Program of China (2011CB309704), and the National Science Foundation of China (No.40890155). This is a International Pacific Research Center/School of Ocean and Earth Science and Technology Contribution (774/8128) and a Lamont–Doherty Earth Observatory Contribution (7462).

Author contributions

J.L., S-P.X. and E.R.C. contributed to data analysis. J.L., S-P.X., E.R.C., G.H., and R.D. contributed to writing the paper. All authors discussed the results and commented on the manuscript.

Additional information

The authors declare no competing financial interests. Supplementary information accompanies this paper on www.nature.com/natureclimatechange. Reprints and permissions information is available online at http://npg.nature.com/reprintsandpermissions. Correspondence and requests for materials should be addressed to J.L.

LETTERS
PUBLISHED ONLINE: 6 MAY 2011 | DOI: 10.1038/NCLIMATE1086
nature climate change

Interdecadal modulation of El Niño amplitude during the past millennium

Jinbao Li[1,2]*, Shang-Ping Xie[1,3,4], Edward R. Cook[2], Gang Huang[5], Rosanne D'Arrigo[2], Fei Liu[1], Jian Ma[3] and Xiao-Tong Zheng[4]

The El Niño/Southern Oscillation (ENSO) is the dominant mode of interannual climate variability on Earth, alternating between anomalously warm (El Niño) and cold (La Niña) conditions in the tropical Pacific at intervals of 2–8 years[1,2]. The amplitude of ENSO variability affects the occurrence and predictability of climate extremes around the world[3,4], but our ability to detect and predict changes in ENSO amplitude is limited by the fact that the instrumental record is too short to characterize its natural variability[5–8]. Here we use the North American Drought Atlas[9,10]—a database of drought reconstructions based on tree-ring records—to produce a continuous, annually resolved record of ENSO variability over the past 1,100 years. Our record is in broad agreement with independent, ENSO-sensitive proxy records in the Pacific and surrounding regions. Together, these records indicate that ENSO amplitude exhibits a quasi-regular cycle of 50–90 years that is closely coupled to the tropical Pacific mean state. Anomalously warm conditions in the eastern Pacific are associated with enhanced ENSO variability, consistent with model simulations[11]. The quasi-periodic ENSO amplitude modulation reported here offers a key observational constraint for improving models and their prediction of ENSO behaviour linked to global warming.

Despite great efforts to understand the El Niño/Southern Oscillation (ENSO) phenomenon, there is still much uncertainty in changes in ENSO amplitude. Instrumental records indicate marked variations in ENSO amplitude, large around the 1890s–1900s and 1970s–1990s, but small between these periods and before 1890 (Supplementary Fig. S1). Existing proxy records suggest significant variability in ENSO amplitude in the past[2,12,13], but they cover only the past few centuries or noncontinuous periods of the past millennium. Current general circulation models (GCMs) give different projections of future ENSO-related change, with some showing an increase and others no change or even a decrease in ENSO amplitude[6,7]. Therefore, it is crucial to develop long, continuous, high-resolution proxy records to determine the characteristics of natural ENSO variability, and to provide observational constraints for improving the models[7,8].

Proxy records from the equatorial Pacific are valuable for studying past ENSO behaviour[12–14], yet very few such records exist. This situation has impeded the study of long-term ENSO amplitude modulation. By contrast, thousands of tree-ring records without these deficiencies are available for North America, a region where hydroclimate is sensitive to tropical Pacific climate anomalies on various timescales[15,16]. Such tree-ring records have been used to develop the gridded North America Drought Atlas[9,10] (NADA) (see Methods and Supplementary Information). Here we demonstrate the fidelity of NADA in recording long-term ENSO variability, particularly variations in ENSO amplitude on interdecadal to centennial timescales.

The leading empirical orthogonal function (EOF) of NADA, which accounts for 23.5% of the total variance, shows a distinct moisture pattern heavily loaded over southwest North America (Methods and Fig. 1a), a region strongly affected by ENSO variability[15,16]. The explained variance of the first EOF for the southwest North America domain rises to 49.5% (Supplementary Fig. S3), and its principal component (PC) has a correlation of 0.99 with that for the whole of North America over the past 1,100 years. This confirms that NADA PC1 dominates variability in southwest North America.

The fidelity of NADA PC1 in representing ENSO variability is demonstrated in five ways: (1) NADA PC1 is significantly correlated with equatorial Pacific sea surface temperatures[17] (SSTs) during the instrumental period (Fig. 1c). For example, its correlation with the January–March (JFM) ENSO Niño3 index for 1870–2002 is 0.51 ($P < 0.001$) (Supplementary Fig. S4). (2) NADA PC1 is significantly correlated with a modern coral record from Palmyra Island in the central tropical Pacific[13], at $r = -0.58$ for the common period 1891–1994 ($P < 0.001$) (Supplementary Fig. S5). After adjusting relict coral U/Th dates within the analytical error windows[13], we found possible correlations between North American drought and tropical corals that persisted throughout the past millennium (Methods and Fig. 1d). Considering the independent nature of these proxy records, this agreement is remarkable, strongly indicative of a coherent relationship between ENSO and North American drought over the past millennium. (3) NADA PC1 is highly correlated with, but is significantly longer than, the existing ENSO reconstructions (Supplementary Table S1). Most of these reconstructions are largely, although not entirely, independent, as they only share a few common tree-ring data from southwest North America. This suggests that NADA PC1 represents reasonable estimates of ENSO variability over the past millennium. (4) Separate composite analysis of NADA for periods of large and small PC variability over the past millennium shows nearly identical patterns (Supplementary Fig. S6). This pattern stability suggests that the westerly waveguide is stable in tropical forced stationary waves, and that NADA PC1 represents the modulation of ENSO itself. (5) Separate EOF analysis shows that the first EOF of NADA is heavily loaded over southwest North America both before and after the 1976/1977 climate regime shift[18,19], and the PC is highly correlated with tropical eastern Pacific SSTs for both periods

[1]International Pacific Research Center, University of Hawaii at Manoa, Honolulu, Hawaii 96815, USA, [2]Lamont-Doherty Earth Observatory, Columbia University, Palisades, New York 10964, USA, [3]Department of Meteorology, University of Hawaii at Manoa, Honolulu, Hawaii 96815, USA, [4]Physical Oceanography Laboratory and Ocean–Atmosphere Interaction and Climate Laboratory, Ocean University of China, Qingdao 266100, China, [5]Institute of Atmospheric Physics, Chinese Academy of Sciences, Beijing 100029, China. *e-mail: jinbao@hawaii.edu.

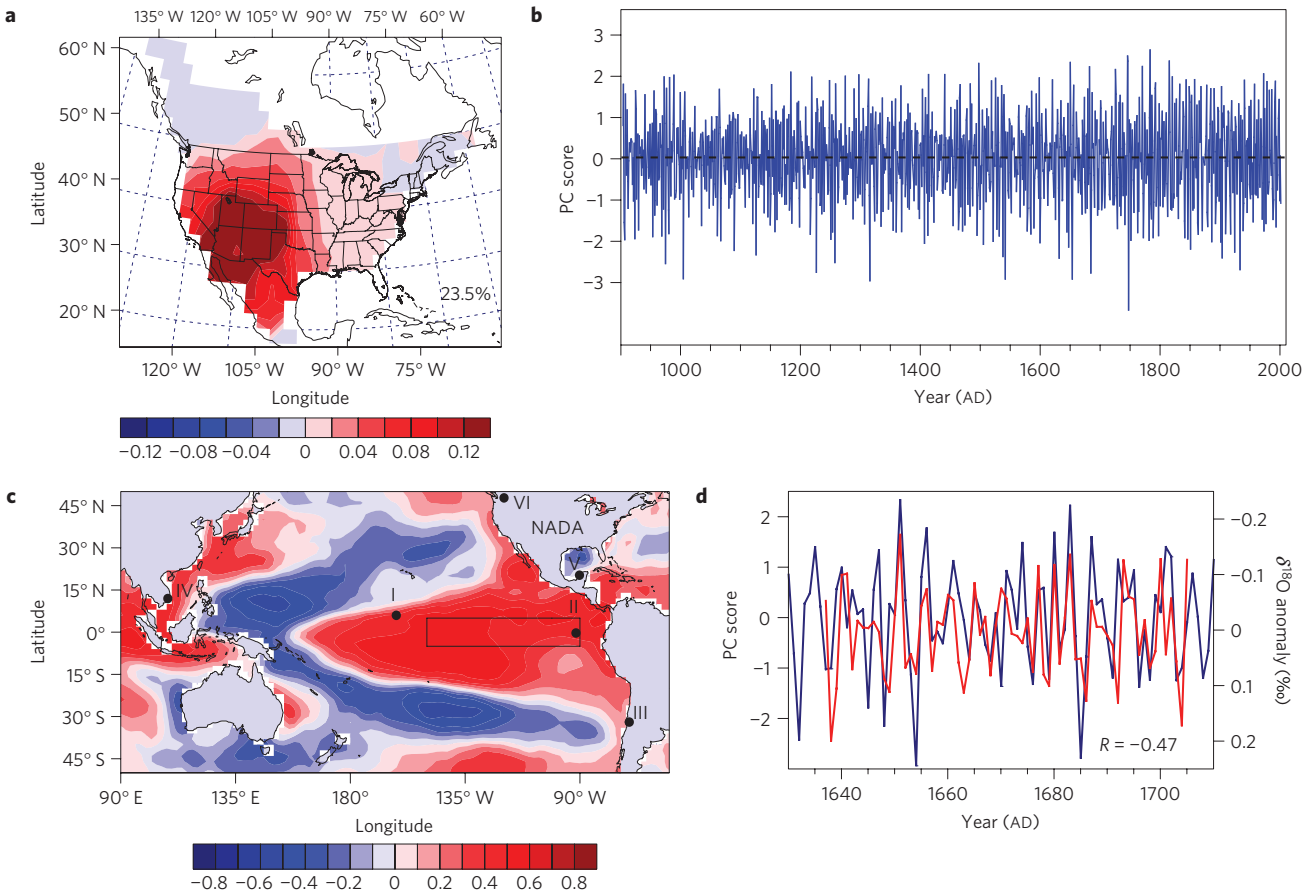

Figure 1 | The leading EOF pattern of NADA, its PC series and correlation of the PC series with tropical records. a, Spatial pattern of the leading EOF over North America, and **b**, its PC time series. The percentage variance accounted for by the leading EOF is labelled in **a**. **c**, Spatial correlation of NADA PC1 with global JFM SSTs (ref. 17) during 1870–2002. The SSTs were processed using a 9-yr Lanczos high-pass filter[30] to isolate interannual variability. The box denotes the Niño3 region, and the dots indicate the site locations mentioned in the text (I: Palmyra corals[13], II: Galápagos coral[12], III: Chile tree rings[23], IV: Vietnam tree rings[24], V: Mexico sediment[26], VI: Washington sediment[27]). **d**, Comparison of NADA PC1 (blue) with the dating-error corrected Palmyra relict coral δ^{18}O series[13] (red) over 1637–1705.

(Supplementary Fig. S7). Although there exist some differences in the EOF pattern and correlation with tropical SSTs between the two periods, these results indicate that moisture variability in southwest North America has been sensitive to ENSO variability both before and after the 1976/1977 climate regime shift. The relationship to ENSO is further confirmed by the SST correlation pattern for 1870–2002 (Fig. 1c). Therefore, teleconnections of canonical eastern Pacific ENSO (hereafter simply ENSO) are probably stable over southwest North America. On the basis of these validations, we consider that NADA PC1 represents a continuous record of interannual ENSO variability during the past millennium.

As inferred from NADA PC1, ENSO amplitude has been highly variable during the past millennium, with many El Niño/La Niña events of larger amplitude than observed in the instrumental period (Fig. 1b). Here we calculated a 21-yr running biweight variance[20] to measure changes in ENSO amplitude. This technique highlights the interdecadal amplitude modulation of a time series while reducing bias that might be introduced by extreme outliers in a 21-yr window. As shown in Fig. 2a, superimposed on a general rising trend are large fluctuations in ENSO variance on interdecadal to centennial timescales. ENSO variance was reduced in the Medieval Climate Anomaly (MCA) period, with the eleventh-century variance being the lowest of the past millennium. Following this, the variance showed an increasing trend in the Little Ice Age (LIA), and maintained a high level from the eighteenth century to the Current Warm Period (CWP). On average, the eighteenth-century ENSO variance was the strongest of the past millennium.

A multi-taper method[21] (MTM) spectral analysis reveals two significant quasi-regular periodicities at 50–60-yr and 82–90-yr bands, respectively (Fig. 3a), confirming the visual impression of interdecadal modulation of ENSO amplitude. A time-space wavelet transform[22] exhibits a marked shift in the dominant periodicity, concomitant with the transition from the MCA into the LIA, from a 82–90-yr cycle during AD 900–1300 to a 50–60-yr cycle thereafter (Fig. 3b). Meanwhile, a 30-yr cycle is present during AD 1500–1800 and in the MTM analysis. The shifts in ENSO periodicity, together with a general increase in variance (Fig. 2a), may reflect major reorganizations within the tropical ocean–atmosphere system, or alternatively significant ENSO teleconnection changes from the MCA to LIA.

We found evidence for such interdecadal fluctuations in ENSO variance elsewhere, especially in the equatorial Pacific and regions under strong ENSO teleconnections. Variance modulation in North American tree rings is consistent with that observed in the Niño3 SST, and the two variance series are correlated at 0.64 ($P < 0.001$) during their common period 1880–1992 (Fig. 2a). A coral annual average oxygen isotopic (δ^{18}O) record from the Galápagos Islands in the eastern equatorial Pacific[12] exhibits quasi-periodic variance modulation similar to that in North American tree rings during the past four centuries (Fig. 2b). The coral δ^{18}O records from Palmyra Island in the central tropical Pacific[13], although not continuous,

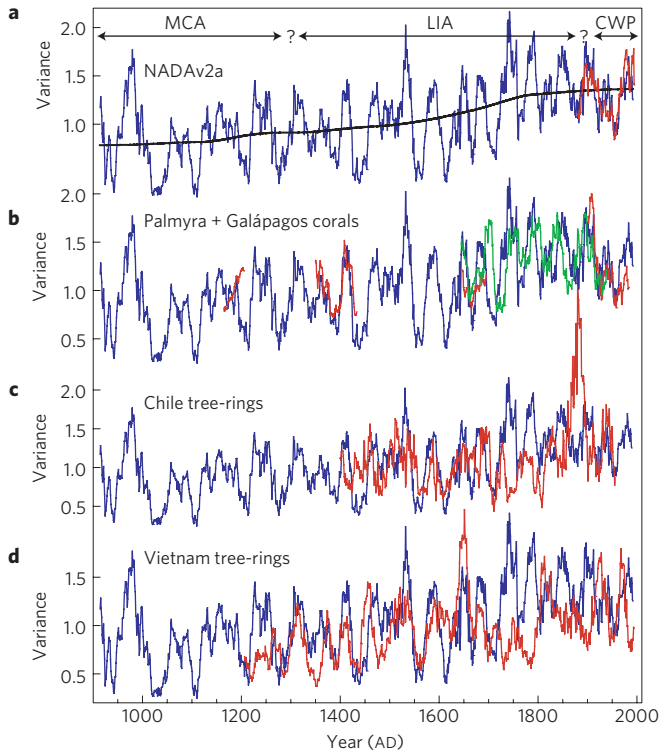

Figure 2 | Comparison of records of ENSO variance. NADA-derived ENSO variance (blue) along with those derived from: **a**, the observed Niño3 SST (ref. 17; red) over 1880–1995; **b**, coral records from both the Galápagos Islands in the eastern equatorial Pacific[12] (green) and Palmyra Island in the central tropical Pacific[13] (red); **c**, tree-ring record from an ENSO-sensitive site in El Asiento, Chile[23] (red); **d**, tree-ring record from the Bidoup Nui Ba National Park in southern Vietnam[24] (red). All records were processed using a 9-yr Lanczos high-pass filter[30] before calculating a 21-yr running biweight variance. The black bold line in **a** denotes a 400-year low-pass filter to indicate the long-term trend.

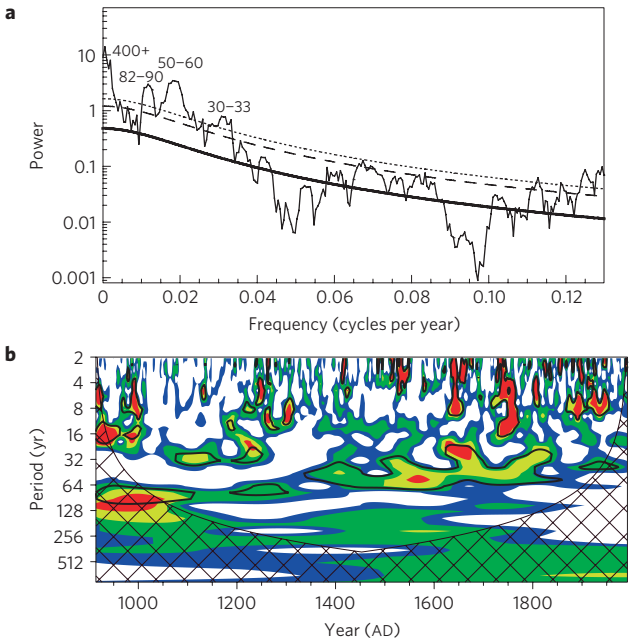

Figure 3 | Spectral property of the NADA-derived ENSO variance series. **a**, MTM (ref. 21) spectral density of the ENSO variance series. The bold line indicates the null hypothesis, and the dash (dotted) line indicates the 95% (99%) significance level, using a red-noise background spectrum. Periodicities of significant peaks are labelled above the spectral density line. **b**, The wavelet power spectrum[22]. The power has been scaled by the global wavelet spectrum. The cross-hatched region is the cone of influence, where zero padding has reduced the variance. Black contour is the 90% significance level, using a red-noise background spectrum.

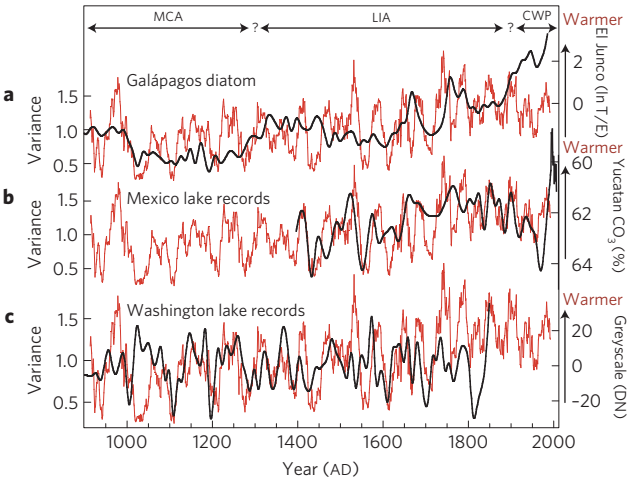

Figure 4 | Comparison of the NADA-derived ENSO variance series with records of the tropical Pacific mean state. NADA-derived ENSO variance (red) along with: **a**, a diatom record from El Junco Lake, Galápagos, in the eastern equatorial Pacific[14] (black). **b**, A carbonate ion (CO_3^{2-}) record from Aguada X'caamal Lake in northwest Yucatan, Mexico[26] (black). **c**, A greyscale record from Castor Lake in Washington state, USA (ref. 27) (black). All lake records were smoothed using a 9-yr low-pass filter. Upward swings in black curves represent a warm state of the tropical Pacific.

show broadly consistent changes in variance during the past nine centuries (Fig. 2b). Tree-ring records from an ENSO-sensitive site in El Asiento, Chile, in the Southern Hemisphere[23], exhibit similar interdecadal fluctuations in variance over most of the past six centuries, except during the late nineteenth century, when there is an out-of-phase relationship (Fig. 2c). Recent tree-ring records from the highlands of Bidoup Nui Ba National Park in southern Vietnam[24], a tropical region strongly influenced by ENSO teleconnections, also show in-phase fluctuations in variance with North American tree-rings during the thirteenth to seventeenth and most of the twentieth centuries, although this relationship was out-of-phase during the eighteenth to nineteenth centuries (Fig. 2d). We note two caveats of the above proxy comparisons. First, unlike the NADA, which is based on nearly two-thousand tree-ring chronologies across North America, other proxy data often consist of only a single series for a given site, and are prone to chaotic noise and regional variability. Second, the long-term stability of ENSO influence in other teleconnection regions needs further investigation, unlike North America where we have validated a persistent relationship to ENSO during the past millennium. Overall these records from the tropics and mid-latitudes in both the Northern and Southern Hemispheres are mutually consistent. Together they show quasi-periodic amplitude modulation, and suggest that such modulation is fundamental to ENSO physics.

How ENSO amplitude modulation is related to changes in the tropical Pacific mean state is a key question for ENSO physics[6,11,25]. Here we examine this relationship during the past millennium by comparing the NADA-derived ENSO variance series with three proxy records for the tropical Pacific mean state. The first is a diatom record from El Junco Lake, Galápagos, an indicator of SSTs in the eastern equatorial Pacific[14] (Fig. 4a). The second is a carbonate ion (CO_3^{2-}) record from Aguada X'caamal Lake in

northwest Yucatan, Mexico (Fig. 4b) that indicates SST changes in the surrounding ocean[26]. The third is a greyscale record from a sediment core from Castor Lake in the Pacific Northwest, whose low-frequency variations are interpreted as changes in the tropical and extratropical Pacific mean state[27] (Fig. 4c).

Despite discrepancies that may reflect either data uncertainties or changes in SST spatial structure, these three records indicate that the eastern tropical Pacific was in a cooler state at the peak of the MCA (~AD 1000–1200), and that there was a persistent positive temperature trend in the LIA and CWP (Fig. 4). ENSO variance was thus greatly reduced during most of the MCA, increased persistently in the LIA, and maintained a high level in the CWP. Moreover, interdecadal fluctuations in ENSO variance seem closely related to anomalies in the Pacific mean state during the past millennium. The Castor Lake data, in particular, suggest that a warm (cool) eastern tropical Pacific is associated with increased (reduced) ENSO variance over most of the 1,000-year record (Fig. 4c). These observations suggest that ENSO variability during the past millennium is closely coupled to changes in the background mean state, a finding that is supported by recent model simulations[6,11].

The quasi-regular nature of ENSO amplitude modulation, and the co-variations with the equatorial Pacific mean state, support the emerging idea that there is a positive feedback between the mean state and ENSO variance[11]. An increase in ENSO amplitude causes the eastern equatorial Pacific to warm, a mean-state change that amplifies ENSO variability. If fully tested in observations and process-oriented model studies, this idea can be exploited for decadal prediction of ENSO amplitude.

In summary, using data on North American tree rings, we have produced a continuous, annually resolved record of ENSO variability for the past millennium. This record is in broad agreement with independent proxy records in and surrounding the Pacific over most of their common periods, revealing a marked quasi-regular interdecadal modulation of ENSO amplitude throughout the past millennium. The amplitude modulation is closely associated with changes in the tropical Pacific mean state, suggesting an interactive relationship. This observation alone implies that the continued increase in eastern-central tropical Pacific SSTs in a future warmer climate[5,7] will lead to enhanced ENSO variability and more extreme climate conditions around the globe. The diverse response of a host of ocean–atmospheric feedbacks complicates such a prediction of ENSO amplitude change[5,7]. Regardless, the quasi-periodic modulation of ENSO amplitude provides a crucial observational constraint that can be used to guide model improvement towards reduced uncertainties in predicting future ENSO behaviour. Finally, the further study of the mechanisms responsible for such ENSO amplitude modulation (for example, stochastic atmospheric noise[28] and external forcing[29]) will help shed light on ENSO dynamics.

Methods

The updated North America Drought Atlas (NADA). The NADA (ref. 9) consists of annually resolved summer (June–August) Palmer Drought Severity Index (PDSI) reconstructions derived from tree rings, available on a 2.5° × 2.5° grid over most of North America (Supplementary Information). Compared with the initial release of the NADA, the updated version (NADAv2a) used more tree-ring chronologies (1845 in total) to improve the PDSI reconstructions, but the grid spacing, series length, and statistical methods remain unchanged[10]. Here we analyse the updated NADA for AD 900–2006, a period when reconstructed values are available at more than 60% of all grid points (Supplementary Fig. S2). Time series at each grid point were processed using a 9-yr Lanczos high-pass filter[30] to preserve variability in the classical ENSO band of 2–8 years[1,2]. Empirical orthogonal function (EOF) analysis was used to objectively define the dominant mode of summer drought over NA, and the associated principal component (PC) series was used to indicate its variability over time.

Relict coral dating error corrections. By splicing together relict coral oxygen isotopic (δ^{18}O) records from Palmyra Island in the central tropical Pacific, Cobb *et al.*[13] provided 30-150-yr windows of tropical Pacific climate variability over the past 1,100 years. Their modern coral samples were exactly dated, whereas relict corals were dated using the U/Th method, which contains a general dating error of ± 5–10-yr. Therefore, if there were a coherent relationship between ENSO and North American drought over the past millennium, then, by adjusting the relict coral sequences within the range of their U/Th-dating errors, a firm match could be achieved between the coral δ^{18}O sequences and NADA PC1.

We first examined the modern coral record. As NADA PC1 represents seasonally averaged moisture variability that has its highest correlation with winter (January–March) tropical Pacific SSTs, we herein used the January–March mean coral δ^{18}O records to make them directly comparable. All series were processed using a 9-yr Lanczos high-pass filter[30] to highlight interannual variability. The highest correlation of the modern coral δ^{18}O record with NADA PC1 over their common period 1891–1994 is −0.58, which is close to its correlation with the Niño3 index (−0.61) in the same period. The highest correlation was achieved at lag zero, confirming that there is no dating error for modern coral. This good match between modern coral and NADA PC1 corroborates the dating error correction method.

The seventeenth-century sequence was spliced from three relict coral δ^{18}O records (SB3, SB13, and SB8), and was correlated at −0.06 with NADA PC1 before dating errors were corrected. Dating error for each of the three individual series was corrected by adjusting years within the range of U/Th-dating errors. A firm match with NADA PC1 was achieved for each series after dating adjustments, with correlations improved from 0.17 to −0.41 for SB3, −0.20 to −0.62 for SB13, and −0.27 to −0.51 for SB8. After correcting the dating errors and re-splicing the three sequences together, a good match between relict corals and NADA PC1 was achieved, with a correlation of −0.47 over their common period 1637–1705 (Supplementary Fig. S4). Similarly, dating errors were corrected for the fourteenth–fifteenth-century sequence, and its correlation with NADA PC1 improved from −0.14 to −0.35 over the common period 1339–1443.

The tenth- and twelfth-century sequences are both single relict coral δ^{18}O records. The best match between the tenth-century sequence and NADA PC1 was achieved after adjusting the start year of the relict coral sequence from AD 933 to AD 931, and their correlation over the common period 931–954 improved from 0.08 to −0.43. The correlation of the twelfth-century sequence with NADA PC1 over their common period 1154–1215 is −0.19, and there is no significant improvement when its dating was adjusted within the range of its U/Th-dating error. Therefore, we did not make a dating error correction for this sequence.

Received 21 December 2010; accepted 25 March 2011; published online 6 May 2011

References

1. Deser, C., Alexander, M. A., Xie, S-P. & Phillips, A. S. Sea surface temperature variability: Patterns and mechanisms. *Annu. Rev. Mar. Sci.* **2,** 115–143 (2010).
2. D'Arrigo, R., Cook, E. R., Wilson, R. J., Allan, R. & Mann, M. E. On the variability of ENSO over the past six centuries. *Geophys. Res. Lett.* **32,** L03711 (2005).
3. McPhaden, M. J., Zebiak, S. E. & Glantz, M. H. ENSO as an integrating concept in Earth science. *Science* **314,** 1740–1745 (2006).
4. Tang, Y., Deng, Z., Zhou, X., Cheng, Y. & Chen, D. Interdecadal variation of ENSO predictability in multiple models. *J. Clim.* **21,** 4811–4833 (2008).
5. Collins, M. *et al.* The impact of global warming on the tropical Pacific Ocean and El Niño. *Nature Geosci.* **3,** 391–397 (2010).
6. Yeh, S. W. & Kirtman, B. P. ENSO amplitude changes due to climate change projections in different coupled models. *J. Clim.* **20,** 203–217 (2007).
7. Guilyardi, E. *et al.* Understanding El Niño in ocean–atmosphere general circulation Models: Progress and challenges. *Bull. Am. Meteorol. Soc.* **90,** 325–340 (2009).
8. Wittenberg, A. T. Are historical records sufficient to constrain ENSO simulations? *Geophys. Res. Lett.* **36,** L12702 (2009).
9. Cook, E. R., Woodhouse, C., Eakin, C. M., Meko, D. M. & Stahle, D. W. Long-term aridity changes in the western United States. *Science* **306,** 1015–1018 (2004).
10. Cook, E. R. *et al. North American Summer PDSI Reconstructions, Version 2a.* IGBP PAGES/World Data Center for Paleoclimatology Data Contribution Series # 2008-046 (NOAA, NGDC Paleoclimatology Program, 2008).
11. Choi, J., An, S-I., DeWitte, B. & Hsieh, W.W. Interactive feedback between the tropical Pacific Decadal Oscillation and ENSO in a coupled general circulation model. *J. Clim.* **22,** 6597–6611 (2009).
12. Dunbar, R. B., Wellington, G. M., Colgan, M. W. & Glymn, P. W. Eastern Pacific sea surface temperature since 1600 AD: The δ^{18}O record of climate variability in Galápagos coral. *Paleoceanography* **9,** 291–315 (1994).
13. Cobb, K. M., Charles, C. D., Cheng, H. & Edwards, R. L. El Niño/Southern Oscillation and tropical Pacific climate during the last millennium. *Nature* **424,** 271–276 (2003).
14. Conroy, J. L. *et al.* Unprecedented recent warming of surface temperatures in the eastern tropical Pacific Ocean. *Nature Geosci.* **2,** 46–50 (2009).
15. Seager, R., Kushnir, Y., Herweijer, C., Naik, N. & Velez, J. Modelling of tropical forcing of persistent droughts and pluvials over western North America: 1856–2000. *J. Clim.* **18,** 4068–4091 (2005).

16. Cook, E. R., Seager, R., Cane, M. A. & Stahle, D. W. North American droughts: Reconstructions, causes and consequences. *Earth Sci. Rev.* **81,** 93–134 (2007).
17. Smith, T. M., Reynolds, R. W., Peterson, T. C. & Lawrimore, J. Improvements to NOAA's historical merged land–ocean surface temperature analysis (1880–2006). *J. Clim.* **21,** 2283–2296 (2008).
18. Mantua, N. J., Hare, S. R., Zhang, Y., Wallace, J. M. & Francis, R. C. A Pacific interdecadal climate oscillation with impacts on salmon production. *Bull. Am. Meteorol. Soc.* **78,** 1069–1079 (1997).
19. Zhang, Y., Wallace, J. & Battisti, D. ENSO-like decade-to-century scale variability: 1900–93. *J. Clim.* **10,** 1004–1020 (1997).
20. Lanzante, J. R. Resistant, robust & non-parametric techniques for the analysis of climate data: Theory and examples, including applications to historical radiosonde station data. *Int. J. Climatol.* **16,** 1197–1226 (1996).
21. Mann, M. E. & Lees, J. Robust estimation of background noise and signal detection in climatic time series. *Clim. Change* **33,** 409–445 (1996).
22. Torrence, C. & Compo, G. P. A practical guide to wavelet analysis. *Bull. Am. Meteorol. Soc.* **79,** 61–78 (1998).
23. LaMarche, V. C. Jr., Holmes, R. L., Dunwiddie, P. W. & Drew, L. G. Tree-ring chronologies of the southern hemisphere: Chile. *Lab. Tree-Ring Res. Chronol. Ser.* **2,** 1–43 (1979).
24. Buckley, B. M. *et al*. Climate as a contributing factor in the demise of Angkor, Cambodia. *Proc. Natl Acad. Sci. USA* **107,** 6748–6752 (2010).
25. Fedorov, A. V. & Philander, S. G. A stability analysis of the tropical ocean–atmosphere interactions: Bridging measurements and theory for El Niño. *J. Clim.* **14,** 3086–3101 (2001).
26. Hodell, D. A. *et al*. Climate change on the Yucatan Peninsula during the Little Ice Age. *Quat. Res.* **63,** 109–121 (2005).
27. Nelson, D. B. *et al*. Drought variability in the Pacific Northwest from a 6,000-yr lake sediment record. *Proc. Natl Acad. Sci. USA* doi:10.1073/pnas.1009194108 (2011).
28. Burgman, R. J., Schopf, P. & Kirtman, B. P. Decadal modulation of ENSO in a hybrid coupled model. *J. Clim.* **21,** 5482–5500 (2008).
29. Mann, M. E., Cane, M. A., Zebiak, S. E. & Clement, A. Volcanic and solar forcing of the tropical Pacific over the past 1,000 years. *J. Clim.* **18,** 447–456 (2005).
30. Duchon, C. E. Lanczos filtering in one and two dimensions. *J. Appl. Meteorol.* **18,** 1016–1022 (1979).

Acknowledgements

We gratefully acknowledge the researchers who have contributed their tree-ring data for NADA development. This research was funded by the National Science Foundation, the National Oceanic and Atmospheric Administration, the Japan Agency for Marine-Earth Science and Technology, the National Basic Research Program of China (2011CB309704), and the National Science Foundation of China (No.40890155). This is a International Pacific Research Center/School of Ocean and Earth Science and Technology Contribution (774/8128) and a Lamont–Doherty Earth Observatory Contribution (7462).

Author contributions

J.L., S-P.X. and E.R.C. contributed to data analysis. J.L., S-P.X., E.R.C., G.H., and R.D. contributed to writing the paper. All authors discussed the results and commented on the manuscript.

Additional information

The authors declare no competing financial interests. Supplementary information accompanies this paper on www.nature.com/natureclimatechange. Reprints and permissions information is available online at http://npg.nature.com/reprintsandpermissions. Correspondence and requests for materials should be addressed to J.L.

Indian Ocean Capacitor Effect on Indo–Western Pacific Climate during the Summer following El Niño

SHANG-PING XIE,*,+ KAIMING HU,# JAN HAFNER,* HIROKI TOKINAGA,* YAN DU,*,@ GANG HUANG,# AND TAKEAKI SAMPE*

* *International Pacific Research Center, University of Hawaii at Manoa, Honolulu, Hawaii*
+ *Department of Meteorology, University of Hawaii at Manoa, Honolulu, Hawaii*
# *Institute of Atmospheric Physics, Chinese Academy of Sciences, Beijing, China*
@ *South China Sea Institute of Oceanology, Chinese Academy of Sciences, Guangzhou, China*

(Manuscript received 24 March 2008, in final form 7 July 2008)

ABSTRACT

Significant climate anomalies persist through the summer (June–August) after El Niño dissipates in spring over the equatorial Pacific. They include the tropical Indian Ocean (TIO) sea surface temperature (SST) warming, increased tropical tropospheric temperature, an anomalous anticyclone over the subtropical northwest Pacific, and increased mei-yu–baiu rainfall over East Asia. The cause of these lingering El Niño effects during summer is investigated using observations and an atmospheric general circulation model (GCM). The results herein indicate that the TIO warming acts like a capacitor anchoring atmospheric anomalies over the Indo–western Pacific Oceans. It causes tropospheric temperature to increase by a moist-adiabatic adjustment in deep convection, emanating a baroclinic Kelvin wave into the Pacific. In the northwest Pacific, this equatorial Kelvin wave induces northeasterly surface wind anomalies, and the resultant divergence in the subtropics triggers suppressed convection and the anomalous anticyclone. The GCM results support this Kelvin wave–induced Ekman divergence mechanism. In response to a prescribed SST increase over the TIO, the model simulates the Kelvin wave with low pressure on the equator as well as suppressed convection and the anomalous anticyclone over the subtropical northwest Pacific. An additional experiment further indicates that the north Indian Ocean warming is most important for the Kelvin wave and northwest Pacific anticyclone, a result corroborated by observations.

These results have important implications for the predictability of Indo–western Pacific summer climate: the spatial distribution and magnitude of the TIO warming, rather than simply whether there is an El Niño in the preceding winter, affect summer climate anomalies over the Indo–western Pacific and East Asia.

1. Introduction

El Niño–Southern Oscillation (ENSO) is the dominant mode of climate variability on instrumental records. Typically, El Niño develops during boreal summer, peaks during early winter, and decays the following spring (Fig. 1). Hereafter, seasons refer to those for the Northern Hemisphere. We denote the ENSO-developing year as year 0 and the following year as year 1. Thus, the summer [June–August (JJA)] of the ENSO-developing year is symbolized as JJA(0), while the summer of the following year as JJA(1). By JJA(1), eastern Pacific sea surface temperature (SST) returns either to or slightly below normal. By shifting tropical convection, El Niño excites atmospheric teleconnection into other tropical oceans and the extratropical Pacific–North America (PNA) sector. The so-called atmospheric bridge effect in the tropics is manifested in the delayed spring warming of the Indian (Klein et al. 1999) and North Atlantic (Enfield and Mayer 1997) Oceans. Because of large SST anomalies in the tropics and an effective tropics-to-midlatitude waveguide, the PNA teleconnection is most pronounced during the peak phase of El Niño, providing winter climate predictability for North America (Trenberth et al. 1998; Alexander et al. 2002).

Pronounced ENSO-related anomalies linger mysteriously during JJA(1) after eastern Pacific SST anomalies have dissipated. Chinese researchers have long suggested that during the summer, following El Niño,

Corresponding author address: Shang-Ping Xie, IPRC, SOEST, University of Hawaii at Manoa, Honolulu, HI 96822.
E-mail: xie@hawaii.edu

DOI: 10.1175/2008JCLI2544.1

© 2009 American Meteorological Society

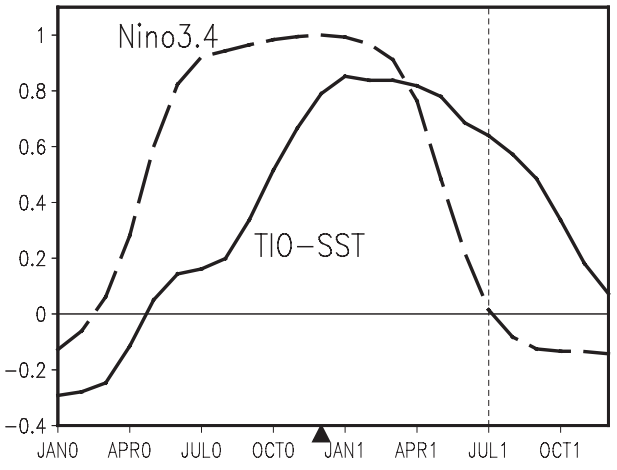

FIG. 1. Correlation of tropical Indian Ocean (20°S–20°N, 40°–100°E) SST (solid) with the Niño-3.4 (5°S–5°N, 170°–120°W) SST index for November(0)–December(0)–January(1). Numerals in parentheses denote years relative to El Niño: 0 for its developing and 1 for decay year. The dashed curve is the Niño-3.4 SST autocorrelation as a function of lag. The black triangle denotes December(0), the peak phase of ENSO.

pronounced precipitation anomalies tend to take place near the Yangtze River (Fu and Teng 1988; Huang and Wu 1989; Huang et al. 2004), causing major floods there as in 1954 and 1998 summers. Over the northwest (NW) Pacific, climatic anomalies can be even larger and more robust during the summer following than preceding the El Niño peak, despite much weaker SST anomalies in the eastern Pacific.

Figure 2 illustrates some of the mysterious JJA(1) anomalies based on surface observations over the NW Pacific, as represented by correlation with the Niño-3.4 (5°S–5°N, 120°–170°W) SST index at its peak phase [November–December (ND)(0)–January(J)(1), hereafter NDJ(0)]. At Guam (13.5°N, 145°E), precipitation is not significantly correlated with ENSO during its developing phase. A negative correlation begins to develop around December–February (DJF)(1), peaks during February–March(1), and persists through JJA(1) (Fig. 2a, solid) when the eastern Pacific SST index already turns slightly negative. Consistent with the rainfall correlation, sea level pressure (SLP) in the broad subtropical NW Pacific begins to develop strong positive correlation with El Niño at NDJ(0), which peaks during the spring (Wang et al. 2003). This correlation decays thereafter but remains significant at the 95% level through JJA(1) (Fig. 2b). The South China Sea (SCS) is the third example, displaying pronounced warming twice at the peak phase of El Niño (Liu et al. 2004) and July–September (JAS)(1) (Xie et al. 2003; Wang et al. 2006), respectively (Fig. 2c). The summer warming is associated with a reduction in the southwest monsoon and ocean upwelling it induces. The delayed ENSO effects extend to the midlatitude atmosphere. Precipitation at Hachijo Island (33.1°N, 139.8°E) south of Tokyo, Japan, displays two peaks in correlation with ENSO (Fig. 2a, dashed): one in DJF(1) and one in JJA(1), both of which are well above the 95% significance level. The summer correlation at Hachijo is of the opposite sign to that at Guam, linked by a meridional teleconnection pattern (Nitta 1987). Our last example is Ishigaki Island (24.3°N, 124.2°E), Japan, where sea level shows a significant positive correlation at a very long lag, during November–December(1) (Fig. 2d). Such prolonged ENSO effects during JJA(1) are the focus of the present study.

Over the subtropical NW Pacific, an anomalous high pressure system with an anticyclonic surface circulation begins to appear at the ENSO mature phase (winter) and develops into maximum intensity during spring (Harrison and Larkin 1996; Wang et al. 2000, 2003), broadly consistent with Fig. 2b. At its peak phase (spring), this surface high is roughly collocated with negative SST anomalies, suggestive of a local ocean–atmosphere interaction (Wang et al. 2000; Lau and Nath 2003). Wang et al. (2000) propose that SST-induced anticyclonic circulation, superimposed on the spring northeast trades, acts to reinforce the initial SST anomalies via surface evaporation and wind stirring. Their mechanism is a variant of wind–evaporation–SST (WES) feedback that emphasizes the role of meridional wind instead of zonal wind in the previous literature (Xie 2004). The anticyclonic anomaly persists into JJA(1) as corroborated by in situ observations (Fig. 2), but the local SST feedback does not seem to persist through summer. A local feedback requires positive correlation between SST and precipitation but observations indicate that this correlation is weak or even negative during summer (Wang et al. 2005). Results from the present study show that atmospheric anomalies during JJA(1) over the NW Pacific are forced not by local SST, but remotely by Indian Ocean SST.

The tropical Indian Ocean (TIO) warms up following the El Niño peak because of the downwelling ocean Rossby waves in the southwestern basin (Xie et al. 2002; Huang and Kinter 2002) and heat flux changes elsewhere (Klein et al. 1999; Tokinaga and Tanimoto 2004). See Schott et al. (2008) for a recent review of the TIO response to ENSO. During the El Niño mature phase, precipitation decreases over the TIO despite this basin-wide warming, leading to a notion that the TIO warming is largely a passive response to ENSO teleconnection without much climatic influences. Countering this notion, however, recent modeling studies suggest that the TIO warming is partially responsible for the formation of the

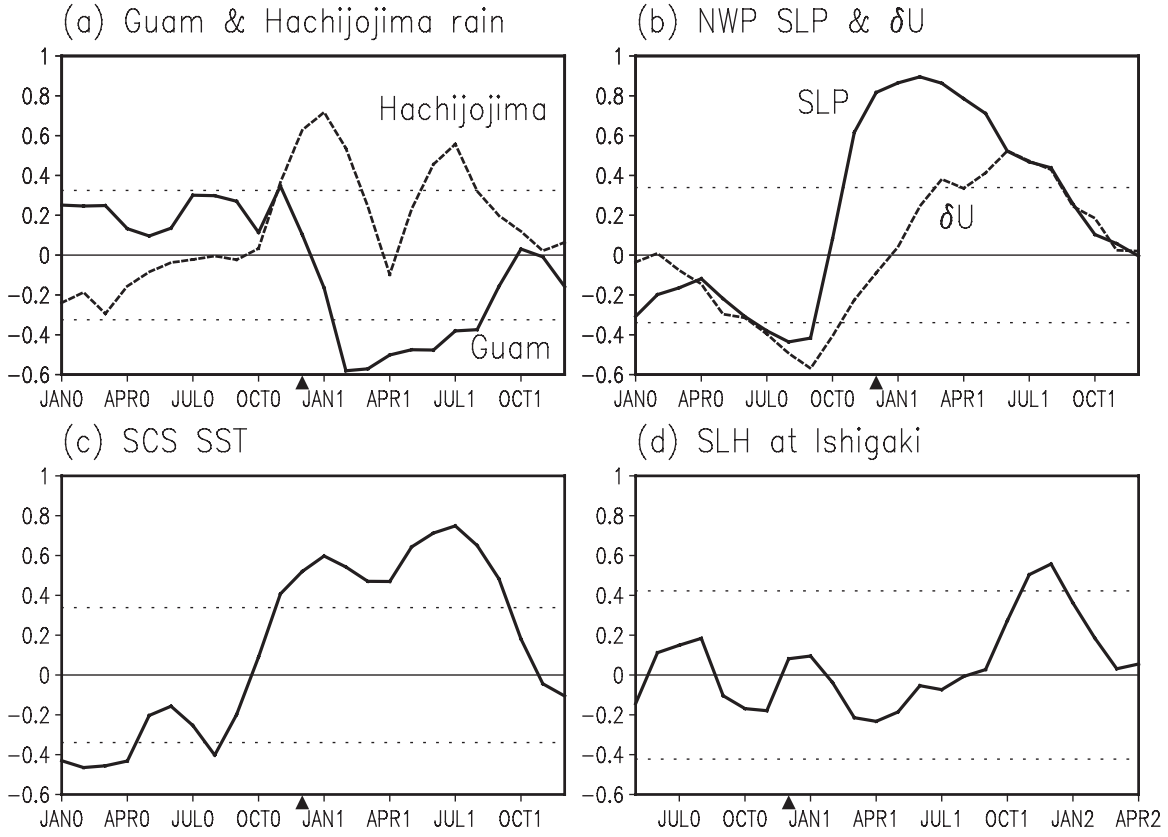

FIG. 2. Correlation with the NDJ(0) Niño-3.4 SST index: (a) rainfall at Guam and Hachijo Islands; (b) subtropical NW Pacific SLP (10°–25°N, 130°–170°E), and surface wind vorticity defined as (27°–33°N) minus (11°–15°N) zonal wind difference averaged in 120°–150°E; (c) SCS SST (5°–15°N, 110°–125°E); and (d) sea level height at Ishigaki Island. (b) and (c) Based on ICOADS. Dotted lines indicate the 95% significance level, which varies with the data record length. (In (a), the significance level is 0.44 for the shorter Hachijo record.) The black triangle denotes December(0), the peak phase of ENSO.

NW Pacific anticyclone anomaly from winter to spring (Watanabe and Jin 2003; Annamalai et al. 2005), and its persistence into JJA(1) (Yang et al. 2007). These results form the following capacitor hypothesis (Yang et al. 2007): El Niño teleconnection causes TIO SST to increase like a battery charging a capacitor; the TIO warming persists through the summer [JJA(1)], and exerts its climatic influences on surrounding regions after the El Niño decay, like a discharging capacitor. Early studies based on correlation (Wu et al. 1995) and idealized general circulation model (GCM) experiments (Wu and Liu 1995) have hinted at TIO SST effects on East Asian-western Pacific climate in summer. More recently, Yoo et al. (2006) note that spring TIO SST is a good predictor for the summer NW Pacific anticyclone. While they do not clarify what maintains this relationship between spring SST and summer atmospheric anomalies, Fig. 1 shows that the TIO SST persistence is the likely cause. Ohba and Ueda (2006) suggest that SST gradients between the North Indian and NW Pacific Oceans are important for June precipitation variability east of the Philippines. While the persistence of the NW Pacific anticyclone through summer may indeed be due to the TIO capacitor effect, the mechanism by which TIO SST affects the subtropical NW Pacific remains unclear.

The TIO capacitor effect may go beyond the subtropical NW Pacific surface circulation. Tropospheric temperature is known to increase over the tropics following El Niño (Yulaeva and Wallace 1994; Sobel et al. 2002), and the tropospheric warming lasts much longer than El Niño itself. Atmospheric GCM experiments show that much of the persistence in zonal-mean tropospheric temperature increase is not due to eastern Pacific SST, but to the SST warming over the tropical Indian and Atlantic Oceans (Kumar and Hoerling 2003; Lau et al. 2005). It is unclear whether and how the lingering tropospheric warming is related to surface anomalies, such as the subtropical NW Pacific anticyclone.

The present study examines robust, ENSO-induced climatic anomalies during JJA(1) when SST anomalies have mostly vanished over the equatorial Pacific. They include the TIO warming, NW Pacific anticyclone,

and tropospheric warming. As reviewed briefly above, these anomalies have previously been studied somewhat in isolation. We note that most literature on the NW Pacific anticyclone deal with its formation and development from winter to spring (Wang et al. 2000, 2003; Watanabe and Jin 2003; Annamalai et al. 2005), but few focus on its maintenance for JJA(1) (Yang et al. 2007). Summer is the rainy season for East Asia when precipitation variability has huge socioeconomic impacts. The present study attempts a synthesis to reveal relationships among and mechanisms for these anomalies by tracking ENSO correlation into JJA(1). Specific questions of interest include the following: What maintains the robust precipitation and circulation anomalies over the NW Pacific? Is there evidence for remote influences of the TIO on the NW Pacific; what about local SST effect? Is the long-lasting tropospheric warming in any way related to surface anticyclone over the NW Pacific? Observational diagnostics are the main approach but numerical modeling is also used as necessary to test hypotheses.

In the following, section 2 describes the datasets and atmospheric GCM. Section 3 presents observational diagnosis, discusses the ENSO-induced anomalies during JJA(1) in the global tropics and over the Indo–western Pacific region, and tests the local SST and TIO capacitor hypotheses. Section 4 examines atmospheric anomalies in response to the TIO warming in models. Section 5 is a summary and discusses broad implications.

2. Methods

a. Observational data

We use the Hadley Centre Global Sea Surface Temperature (HadSST) dataset (Rayner et al. 2006), the Center for Climate Prediction (CPC) Merged Analysis of Precipitation (CMAP; Xie and Arkin 1996), and the National Centers for Environmental Prediction–National Center for Atmospheric Research (NCEP–NCAR) atmospheric reanalysis (Kalnay et al. 1996), originally on 1°, 2.5°, and 2.5° grids, respectively. We have regridded these datasets onto a common 2.5° latitude × 10° longitude grid for a 29-yr period from 1979 to 2007 (limited by CMAP's satellite rainfall estimates). All of the features to be discussed have large zonal scales, and the coarse zonal grid spacing is to help suppress small-scale variability.

We complement the above data-assimilated/statistically interpolated datasets with ship observations in the International Comprehensive Ocean–Atmospheric Data Set (ICOADS; Worley et al. 2005), originally on a 2° grid. Grid points without at least one observation for a given month are flagged as missing. No additional interpolation is made. We regrid ICOADS onto the same 2.5° latitude × 10° longitude grid, and limit our analysis to after 1950, when observations are relatively abundant.

To extend the precipitation record back beyond the CMAP period, monthly observations at Guam are used to track rainfall over the subtropical and midlatitude NW Pacific, respectively. We average data at five stations to form an island-mean precipitation series, which runs nearly continuously from 1945. A different method by normalizing data at each station with its standard deviation yields a similar island-mean series. Observations at Hachijo Island for a shorter period (1980–2007) are used to monitor rainfall in the midlatitude NW Pacific. Monthly-mean sea level height data (1969–2007) at Ishigaki Island are obtained from the University of Hawaii Sea Level Center.

The present study focuses on interannual variability associated with ENSO. To reduce the effect of pronounced intraseasonal variability over the Indo–western Pacific Oceans, we perform a 3-month running average. A 9-yr running mean is then applied (separately for each calendar month) to remove decadal and longer variations, which are significant over the tropical Indo-Pacific Oceans (Deser et al. 2004; Du and Xie 2008). We use SST averaged over the eastern equatorial Pacific (Niño-3.4: 5°S–5°N, 120°–170°W) to track ENSO, which is referred to as the ENSO index. Typical decorrelation time for such bandpass-filtered time series is slightly more than half a year (Fig. 1). We estimate the total degree of freedom as (analysis period in years)/1.5. For a 29-yr time series, a correlation of 0.43 reaches the 95% significance level based on t test.

b. GCM

The atmospheric GCM used is the ECHAM5, the latest Hamburg version of the European Centre for Medium-Range Weather Forecasts (ECMWF) model. A detail description of ECHAM5 is given by Roeckner et al. (2003). ECHAM5 employs a spectral dynamic core. We use a version with triangular truncation at zonal wavenumber 63 (T63; equivalent to 1.9° horizontal resolution) and 19 sigma levels in the vertical.

The model is forced with the observed monthly climatology of SST and sea ice. We analyze a 20-yr period of the control (CTL) simulation. We carry out two additional experiments. In the TIO run, we add 1°C SST over the TIO (20°S–20°N, 40°–110°E). In the other experiment, the same SST anomalies are imposed on the South Indian Ocean (SIO; 20°S–0°, 40°–110°E). Experiments with a more realistic 0.5°C SST anomaly yield similar results. In both TIO and SIO runs, the SST

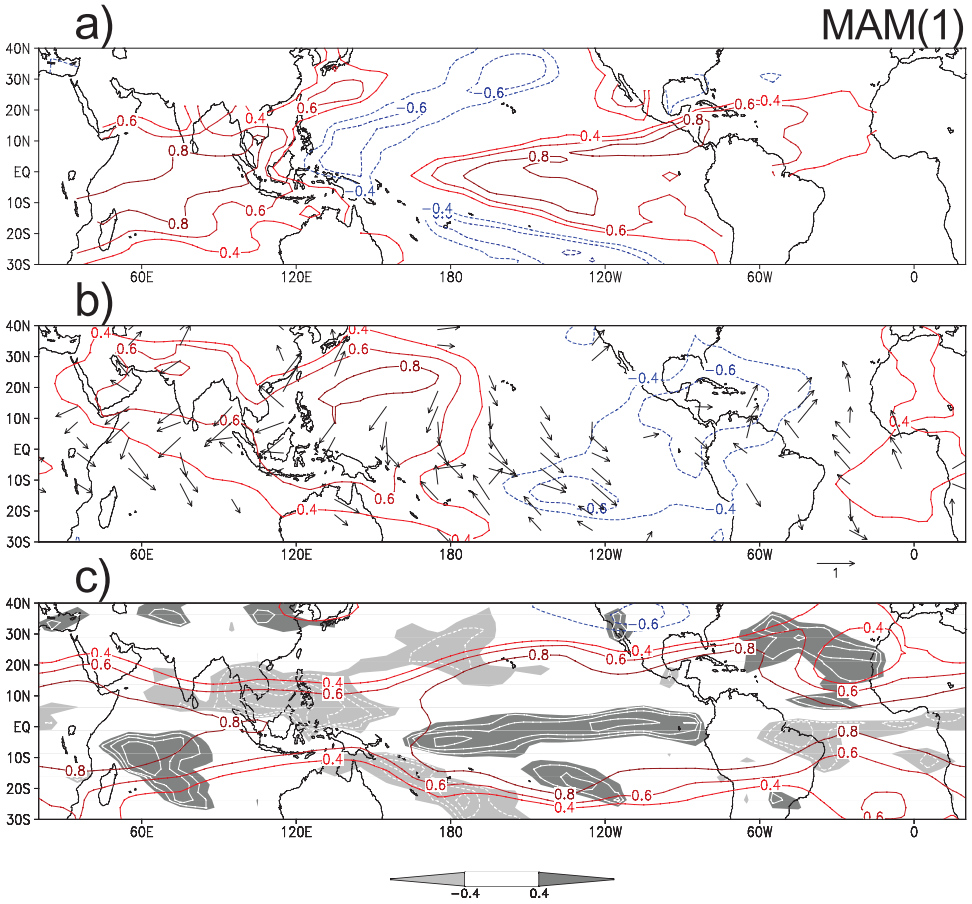

FIG. 3. MAM(1) correlation with the NDJ(0) Niño-3.4 SST index: (a) SST, (b) SLP (contours) and surface wind velocity, and (c) precipitation (gray shade and white contours at intervals of 0.1) and tropospheric temperature (contours).

anomalies are kept constant in time and the model is integrated for 20 yr. Thus, the experiments are equivalent to 20-member ensemble runs.

3. Observational analysis

This section examines spatiotemporal variations in ENSO correlation to infer the mechanisms for atmospheric anomalies.

a. MAM(1)

During March–May (MAM)(1), El Niño begins to decay but large positive anomalies of SST and precipitation remain in the eastern equatorial Pacific (Fig. 3). The westerly wind anomalies near the international date line are displaced south of the equator, rendering them ineffective to sustain the Bjerknes feedback and El Niño (Vecchi and Harrison 2006; Lengaigne et al. 2006). Precipitation decreases over the off-equatorial western Pacific, with a broad high pressure anomaly over the NW Pacific. The anomalous winds there intensify the prevailing northeast trades, contributing to the SST cooling (Wang et al. 2000). The upwelling Rossby waves in the ocean may also be a factor for the surface cooling (Wang et al. 1999).

Positive SST anomalies cover the entire TIO, with the maximum (>0.8) over the tropical southwest Indian Ocean (SWIO), a signature of the downwelling Rossby waves over the shallow thermocline dome (Murtugudde and Busalacchi 1999; Behera et al. 2000; Xie et al. 2002; Huang and Kinter 2002). While the SST anomalies are more or less symmetrical, precipitation anomalies are nearly antisymmetric about the equator, positive over the SWIO, and negative over the eastern north Indian Ocean (NIO). Surface winds show a C-shaped pattern typical of the response to antisymmetric heating, northeasterly north and northwesterly south of the equator. Kawamura et al. (2001) and Wu et al. (2008) suggest that this antisymmetric atmospheric pattern is due to be the WES feedback

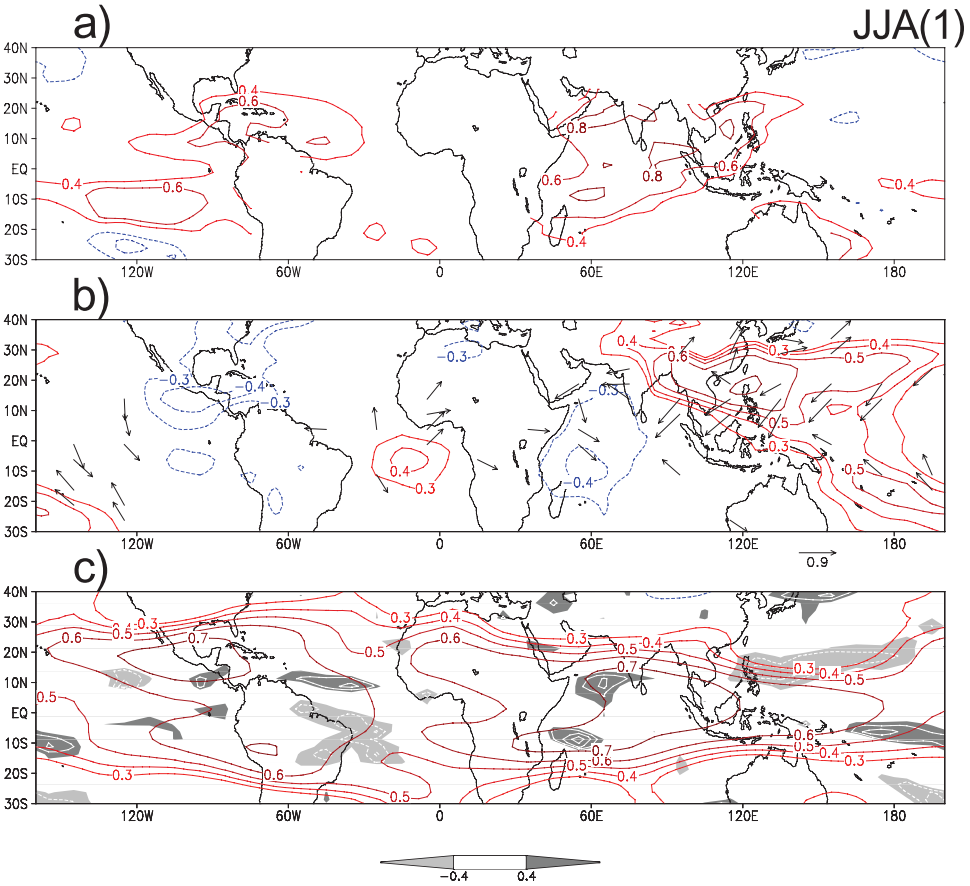

FIG. 4. Same for Fig. 3, except for JJA(1).

within the TIO. The northeasterly anomalies, in particular, help sustain the NIO warming through summer after the onset of the southwest monsoon in May (Du et al. 2009).

The free troposphere warms up along the entire equatorial belt, with tropospheric temperature correlation above 0.8 everywhere except over the western Pacific (minimum ~0.5° at 160°E). The correlation features an off-equatorial maximum on either side of the equator over the central/eastern Pacific and an equatorial maximum to the east, reminiscent of the Matsuno–Gill pattern (Matsuno 1966; Gill 1980) anchored by the eastern Pacific warming. This tropical-wide tropospheric warming takes place despite the tropical-mean precipitation anomaly being nearly zero, supporting the idea that deep convection adjusts tropospheric temperature to a moist-adiabatic profile over the warming eastern Pacific, spreading the tropospheric warming throughout the tropics via fast equatorial waves (Su et al. 2001; Chiang and Sobel 2002). El Niño–induced tropospheric warming has been proposed to cause SST to increase over other tropical oceans that support deep convection (Chiang and Sobel 2002; Chiang and Lintner 2005).

b. JJA(1)

Figure 4 shows JJA(1) correlations with the NDJ(0) ENSO index. SST anomalies vanish along the equator across the Pacific while SST correlation remains strong and exceeds 0.6 over much of the TIO. In contrast to MAM(1), when the decaying El Niño remains the major forcing for atmospheric anomalies, strong atmospheric correlations with coherent large-scale structure shift to the TIO and neighboring NW Pacific. The strongest atmospheric anomalies at the surface are located over the NW Pacific, including decreased rainfall and increased SLP. An anomalous anticyclone develops there, with northeasterly anomalies from the Bay of Bengal to the international date line. This summer anticyclone has been noted in previous studies (e.g., Wang et al. 2003) and the resultant weakening of the southwesterly monsoon wind causes a pronounced warming over the SCS (Xie et al. 2003; Wang et al. 2006). SST correlation is weakly negative but statistically marginal over the

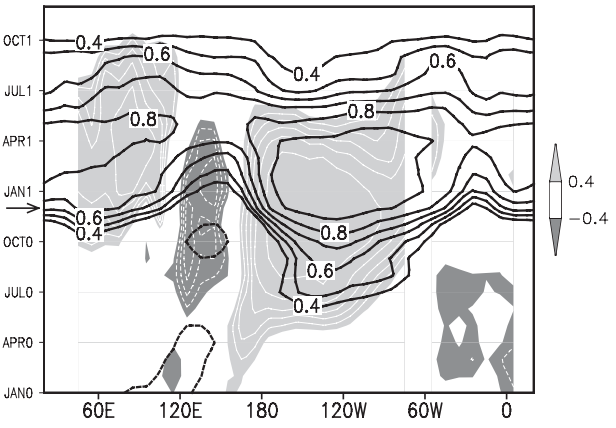

FIG. 5. Longitude–time section of correlation with the NDJ(0) Niño-3.4 index: SST (light shade > 0.4; dark < -0.4; white contours at intervals of 0.1), and tropospheric temperature (black contours) on the equator. The black arrow denotes December(0), the peak phase of ENSO.

eastern half of the NW Pacific anticyclone (maximum correlation $r_{\max} \sim -0.4$), suggesting that local SST is not the main anchor for the decreased precipitation and increased SLP there. (More analysis of the SST correlation will be presented in section 3c.) This anticyclone is the most significant surface atmospheric anomaly during JJA(1) ($r_{\max} \sim 0.7$) that originates from ENSO, while the TIO warming is the most significant major SST anomaly ($r_{\max} \sim 0.8$), implying that the latter is the cause of the former. An empirical orthogonal function (EOF) analysis confirms this conclusion (see the appendix).

Tropospheric temperature displays a Matsuno–Gill pattern that is consistent with a localized heating in the TIO, with a Kelvin wave–like wedge penetrating into the western Pacific on the equator and Rossby wave–like, off-equatorial maxima over the western Indian Ocean to Africa. Tropical convection adjusts tropospheric temperature close to a moist-adiabatic profile, consistent with the equivalent potential temperature (θe) in the planetary boundary layer (Emanuel et al. 1997). Thus, an SST increase over a convective region acts to warm the tropospheric column. The spatial pattern of tropospheric temperature anomalies (Figs. 3c, 4c) appears to support this moist-adiabatic adjustment to ocean warming. Figure 5 shows tropospheric temperature correlation with the NDJ(0) ENSO index in the tropical Pacific and TIO, along with the SST correlation. Over the tropical Pacific, the troposphere begins to warm up soon after the development of El Niño. The tropospheric warming there reaches the maximum about a season after the El Niño peak and decays rapidly after April(1), falling below the 95% significance level by July(1). Over the TIO, on the other hand, tropospheric warming commences quite late, developing rapidly in November(0) and reaching the peak in April(1). It persists at high correlation until August(1), and then decays rapidly with the TIO SST warming.

SST correlation falls to near zero on the equator (as the thermocline begins to shoal), but significant SST warming remains on either side of the equator in the eastern Pacific during JJA(1) (Fig. 4a). The southern SST warming does not have much of a signature in SLP because the mean SST is too cold for deep convection (Figs. 4b,c). North of the equator, by contrast, the SST warming over the far eastern Pacific warm pool and Caribbean Sea induces weak negative SLP anomalies and appears to reinvigorate the off-equatorial tropospheric warming. Because of the great geographical distance, it is unlikely that the lingering eastern Pacific SST anomalies north of the equator are the main cause of the NW Pacific anticyclone.

c. *Kelvin wave–induced divergence off the equator*

Precipitation correlation is weakly positive over the warm TIO, but not well organized in space. Restoring tropospheric temperature toward a moist-adiabatic profile, Su and Neelin (2003) show that their model simulates tropospheric temperature and precipitation anomalies during the developing and mature phases of El Niño. They report that the precipitation response is rather complicated and not necessarily correlated with local SST.

Given weak local SST correlation, the robust NW Pacific anticyclone at the surface is mysterious. We propose a mechanism for the TIO to force this surface anticyclone remotely. The moist-adiabatic adjustment provides a mechanism that couples SST and tropospheric temperature over the warm TIO (Emanuel et al. 1997; Neelin and Su 2005). Via this coupling, the TIO warming forces a warm equatorial Kelvin wave to the east. Figure 6 superimposes tropospheric temperature and surface wind correlations with the NDJ(0) ENSO index. Surface friction drives northeasterly winds onto the equatorial low pressure in the baroclinic Kelvin wave, inducing surface divergence and suppressing deep convection in the subtropical NW Pacific.

The circulation–convection feedback is important to amplify this Kelvin wave–induced Ekman divergence (WIED). While the Kelvin wave in the free troposphere is nearly symmetric about the equator, the response of convective and surface anomalies clearly favors the summer hemisphere (Fig. 6), where convective feedback is strong with high SST and precipitation in the mean. The negative rainfall anomalies

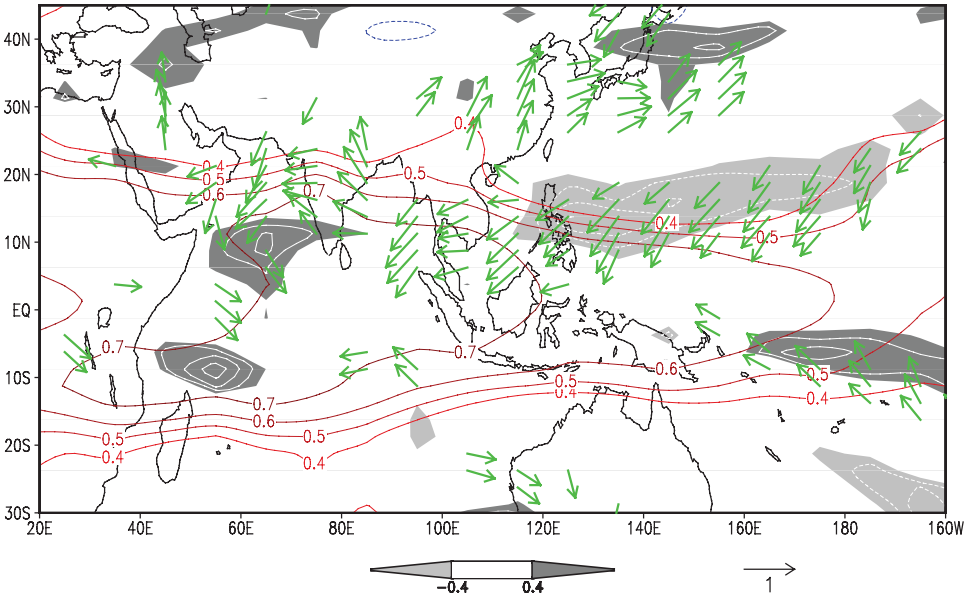

FIG. 6. JJA(1) correlation with the NDJ(0) Niño-3.4 SST index: tropospheric (850–250 hPa) temperature (contours), precipitation (white contours at intervals of 0.1; dark shade > 0.4; light < −0.4), and surface wind velocity (vectors).

over the NW Pacific excite an equatorial Kelvin wave of an opposite sign, weakening the warm Kelvin wave wedge emanating from the TIO. Indeed, the warm Kelvin wave wedge is much shorter in zonal extension than the off-equatorial Rossby waves to the west (Fig. 4c), opposite to the Matsuno–Gill model prediction.[1] In the warm Kelvin wave wedge near the equator, precipitation anomalies are not very coherent as the deep subsidence of the wave in the free troposphere opposes the surface convergence in creating precipitation changes. Section 4 tests this hypothesis further with an atmospheric GCM.

Modeling studies suggest a TIO contribution to the NW Pacific anticyclone anomaly during MAM(1) (Su et al. 2001; Watanabe and Jin 2003; Annamalai et al. 2005). We note that from the NIO to NW Pacific during MAM(1), northeasterly wind anomalies and the negative precipitation band are located on the northern edge of the warm Kelvin wave wedge (Fig. 3c). This collocation of surface anomalies with the Kelvin wave's northern flank is consistent with our Kelvin WIED mechanism.

d. Northwest Pacific precipitation

The NW Pacific warm pool reaches far north during summer, with the 27°C SST contour expanding north of 30°N (Fig. 7). In addition to the basin-scale intertropical convergence zone (ITCZ) anchored by an off-equatorial warm SST band, a subtropical rainband develops during late summer and early fall (July–September) in the NW Pacific, riding on the expanding warm pool. This subtropical rainband appears as a local meridional maximum in precipitation (15°–25°N), and it is a key element of the NW Pacific monsoon (Murakami and Matsumoto 1994; Wang and LinHo 2002). The late-July onset of this subtropical NW Pacific convection weakens and displaces the mei-yu–baiu rainband northward that covers east China and Japan during June to mid-July (Ueda et al. 1995, 2009).

Interestingly, summer precipitation variance is much stronger in the subtropical rainband than in the ITCZ over the NW Pacific despite the mean precipitation being much larger in the latter (Fig. 7). Figure 8a shows the time–latitude section of local correlation between monthly SST and precipitation over the western Pacific. In the subtropical NW Pacific, the subtropical rainfall variance intensifies during July–September but is not correlated with the local SST. Our analysis of ENSO correlation indicates that much of the subtropical NW Pacific rainfall variability is instead remotely forced, by the TIO warming in particular. This TIO capacitor effect is pronounced during JJA(1), possibly corresponding to interannual variability in the onset and early development period of subtropical NW Pacific convection. The cause of high variance from August onward needs further investigation.

[1] Factors such as the mean flow and its shear as well as heating latitude also influence the apparent zonal extent of these waves.

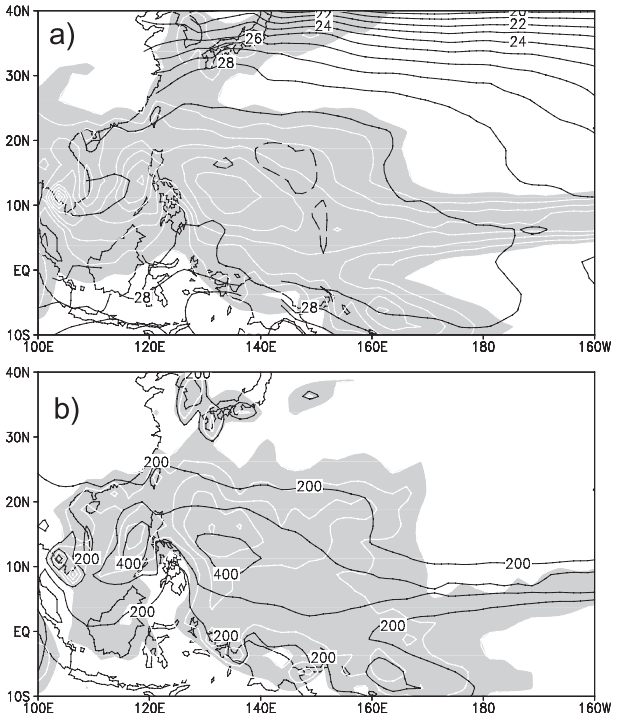

FIG. 7. (a) July–September climatology of SST (black contours with 29.5°C dashed) and precipitation (shade > 150 mm month^{-1}; white contours at 50 mm month^{-1} intervals). (b) Standard deviation of precipitation for July–September (shade > 75 mm month^{-1}; white contours at 25 mm month^{-1} intervals), along with the precipitation climatology (black contours).

The anticyclone anomaly over the subtropical NW Pacific begins to develop during the El Niño winter. Figure 9 shows the ENSO correlations of precipitation (shade), SST (color contours), and surface wind velocity in the NW Pacific. In Fig. 9, the onset of the El Niño–induced anticyclone in December(0) is manifested as the sudden appearance of the anomalous northerlies and SST cooling in 0°–10°N. Wang et al. (2000) suggest that the rapid onset of the anticyclone and SST cooling is due to their mutual interaction as follows. The SST cooling north of the equator reduces precipitation, exciting a westward-propagating Rossby wave. The resulting northerly wind anomalies intensify the mean northeast trades and amplify the initial SST cooling via evaporation and wind stirring. Hereafter we call this the WES-V feedback to emphasize the importance of meridional wind perturbations, where the traditional WES feedback considers the zonal wind effect on evaporation (Xie and Philander 1994). Mean northerly winds (V) are a necessary condition for this WES-V feedback, which is indeed met during December–April (Fig. 8b). (One may use $V = 2$ m s^{-1} as a threshold for the WES-V feedback to operate given that weather-related variance is high in the ITCZ.) The mean northerlies weaken from February on, and the WES-V mechanism is unlikely to be important from April into the summer, as corroborated by the rapid transition of the local SST–precipitation correlation from positive to negative in 0°–10°N during April–July (Fig. 8a). Here we have used the SST–precipitation correlation as a test for the ocean-to-atmospheric feedback.

Figure 9 shows that ENSO correlations also display a rapid transition from May(1) to July(1). The center of negative rainfall correlation is confined to 0°–10°N up to May(1), and jumps to 10°–20°N in June(1). The northward shift is also seen in the center of the anticyclonic vorticity (as measured by the meridional shear). The northward shift in the anticyclonic center suggests that different mechanisms are at work before May(1) and during JJA(1), consistent with our inference that Pacific and TIO SST anomalies are important for the respective periods. The northward shift of precipitation correlation is also consistent with the evolution of precipitation variance, whose maximum shifts from the ITCZ during winter and spring to the subtropical rainband during summer. The El Niño–induced negative SST anomalies in the ITCZ decay rapidly from April(1). At 145°E, the negative JJA(1) precipitation anomalies at 15°N are not associated with significant SST correlation (Fig. 9), indicating the importance of remote forcing for the maintenance of the subtropical anticyclone during JJA(1).

e. Further teleconnections

Atmospheric anomalies in the subtropical NW Pacific during JJA(1) excite additional teleconnections in both the ocean and atmosphere. In the ocean, the anticyclonic wind curl anomalies force downwelling Rossby waves that propagate westward (results not shown from an ocean reanalysis), leading to a rise in sea level at Ishigaki Island that peaks in the following December (Fig. 2d), almost a year after the mature phase of El Niño. In the atmosphere, the southwesterly anomalies on the western flank of this anomalous anticyclone transport moisture from the SCS, increasing summer rainfall over the mid-/lower reaches of the Yangtze River of China. Suppressed convection over the subtropical NW Pacific, through upper-tropospheric convergence, excites the Pacific–Japan (PJ) teleconnection (Nitta 1987), with a low pressure centered east of Japan (Fig. 6). Developing under the vertically sheared climatological meridional flow, the PJ vorticity anomalies exhibit an apparent poleward phase tilt with height (Kosaka and Nakamura 2006). The surface low around Japan is associated with an anomalous increase in local precipitation near Japan as observed at Hachijo Island (Fig. 2a).

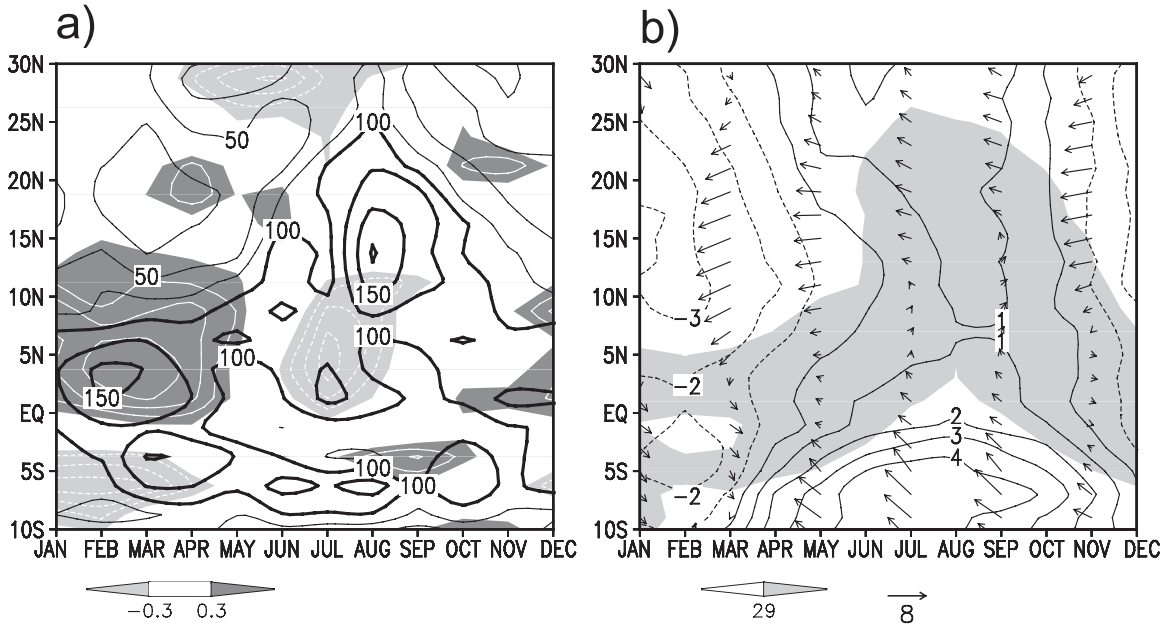

FIG. 8. (a) Monthly precipitation standard deviation (black contours, mm month^{-1}) and SST–precipitation correlation (dark shade > 0.3; light < -0.3; white contours at 0.1 intervals) at 145°E as a function of time and latitude. (b) ICOADS climatology of surface wind velocity (vectors, m s^{-1}), its meridional component (contours), and regions with SST > 29°C (shade) as a function of time and latitude over the western Pacific (145°E).

4. Model results

This section uses atmospheric GCM experiments to test the hypothesis that the TIO warming affects NW Pacific climate during summer. In the GCM, the imposed TIO warming[2] causes precipitation to increase over much of the basin (Fig. 10a). Over the equatorial Indian Ocean, precipitation somehow decreases despite the SST increase. Precipitation decreases and a surface anticyclone forms over the subtropical NW Pacific, with a cyclonic circulation to the northeast of Japan. In 0°–20°N from the NIO to western Pacific, the southwest monsoonal winds weaken, helping sustain the SST warming there in observations (Xie et al. 2003; Du et al. 2009). The model response is qualitatively consistent with observations (Figs. 4 and A1), but the NW Pacific anomalies are too weak while TIO precipitation anomalies too large. This result is consistent with a multimodel study of Li et al. (2008).

TIO-induced tropospheric warming forms a spatial pattern reminiscent of the Matsuno–Gill pattern, with the Kelvin wave response extending eastward and covering the entire equatorial Pacific (Fig. 10b). Compared with JJA(1) observations (Fig. 4), the eastward extension of the baroclinic Kelvin wave response is too large, resulting in unrealistic, strong surface easterly anomalies over the equatorial Pacific. This too-strong Kelvin wave response is related to too weak a precipitation reduction over the NW Pacific, which would otherwise excite a baroclinic Kelvin wave of the opposite sign and leaves little net anomalies in the equatorial Pacific. Thus, TIO warming indeed forces a baroclinic Kelvin wave with low SLP centered on the equator, triggering a precipitation reduction and surface anticyclone to the north. The model result of too weak a NW Pacific response suggests that the feedback between local convection and circulation is important for their anomalies to amplify and reach the observed magnitude. A comparison with the observed JJA climatology indicates that model precipitation is weaker by a factor of 2 over the subtropical NW Pacific, limiting the convection–circulation feedback. The poor simulations of subtropical NW Pacific summer rainfall have been flagged as a major problem for atmospheric GCMs (Kang et al. 2002).

The Japan pole of the PJ pattern is too weak and shifted northward compared to observations. Such deficiencies may be due to too-weak convective anomalies

[2] Care needs to be taken in designing SST-forced, atmospheric GCM experiments because SST changes may be a response to a remote forcing as happens over the TIO during the developing and mature phases of ENSO (Kumar and Hoerling 1998; Wu et al. 2006; Deser and Phillips 2006; Copsey et al. 2006). Our prescription of TIO SST as forcing here is justified by the facts that it is the most robust SST anomalies of the global ocean during JJA(1) and that tropospheric temperature anomalies are consistent with a Matsuno–Gill pattern forced by a heat source over the TIO (Fig. 4).

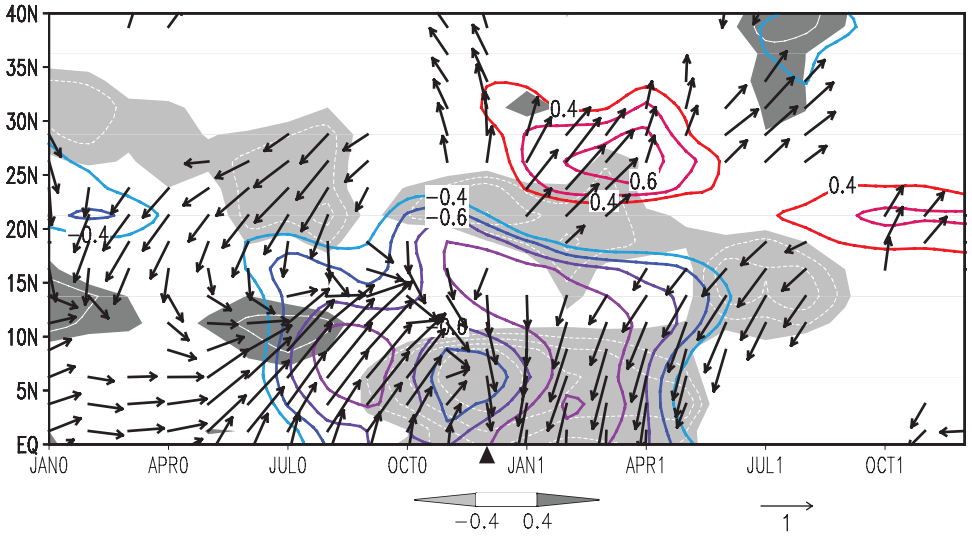

FIG. 9. Time–latitude section of correlation at 145°E with the NDJ(0) Niño-3.4 index: SST (color contours), precipitation (dark shade > 0.4; light shade < −0.4; white contours at 0.1 intervals), and surface wind velocity (vectors). The black triangle denotes December(0), the peak phase of ENSO.

in the subtropical NW Pacific and/or errors in simulating mean precipitation and mean flow, from which the PJ mode draws energy (Kosaka and Nakamura 2006).

a. Linear baroclinic model

To illustrate the importance of the convection–circulation feedback, we turn to a primitive-equation model linearized around the observed JJA mean state

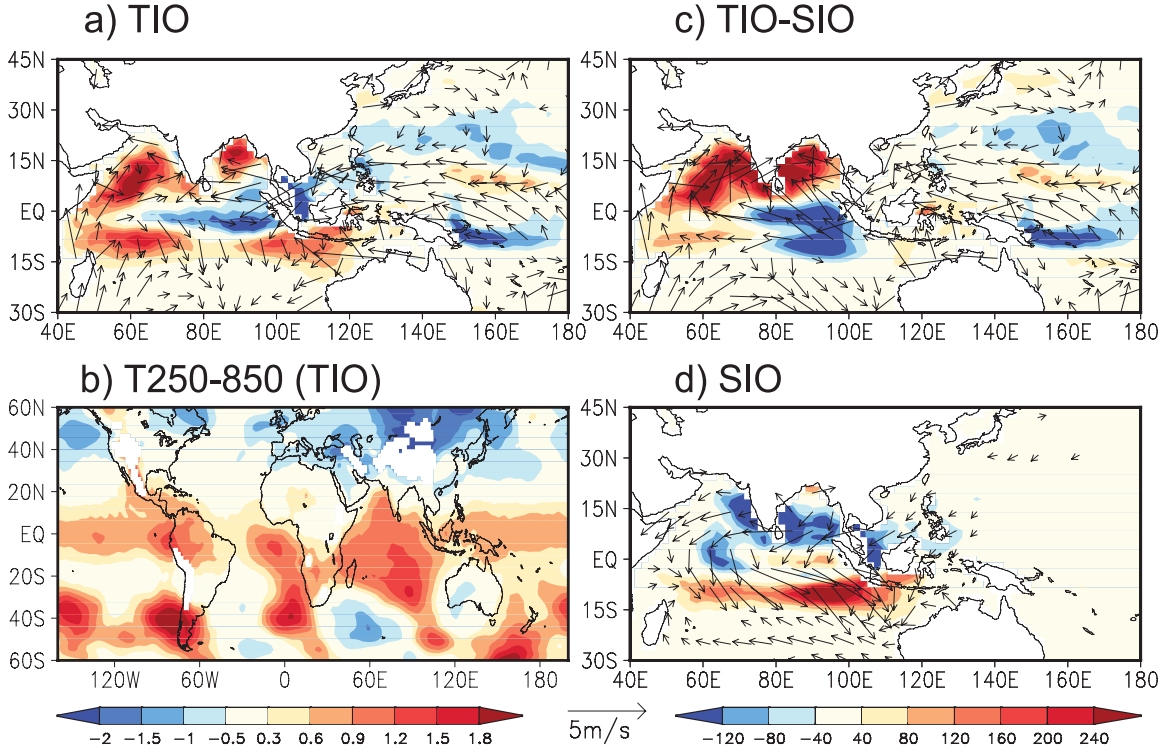

FIG. 10. Anomalies of precipitation (color, mm month^{-1}; right color bar) and surface wind velocity (m s^{-1}; wind speed smaller than 0.5 m s^{-1} has been masked out) in (a) the TIO and (d) SIO atmospheric GCM runs, and (c) TIO–SIO difference. (b) Anomalies of tropospheric temperature (°C; left color bar) in the 250–850-hPa layer in the TIO run.

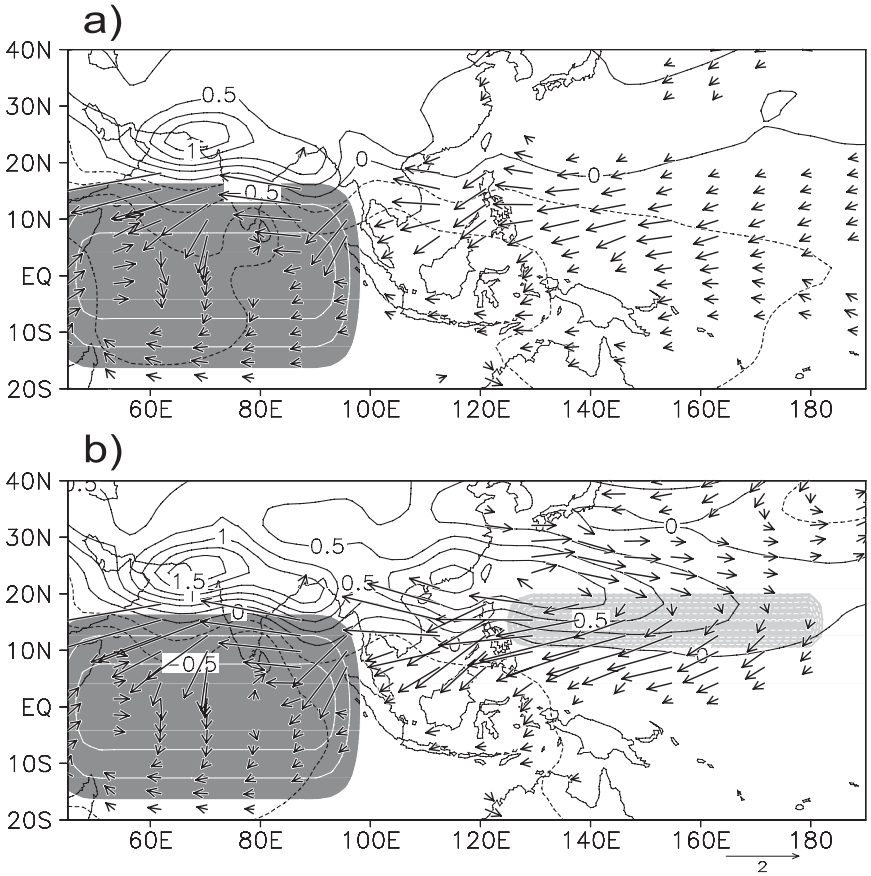

FIG. 11. The linear atmospheric model response to the TIO heating (a) with and (b) without interactive heating over the subtropical NW Pacific: sea level pressure (black contours, hPa), wind velocity (m s^{-1}) at 1000 hPa, and diabatic heating rate at 500 hPa (dark shade > 0.25; light < -0.25 K day^{-1}; white contours at 0.25 K day^{-1} intervals).

as represented by the NCEP–NCAR reanalysis. The detailed description of the linear baroclinic model (LBM) may be found in Watanabe and Kimoto (2000). We use a version with T42 resolution in the horizontal and 20 sigma levels in the vertical. The model is forced by prescribed diabatic heating. In the vertical, the heating is confined between 900 and 100 hPa, with a peak at 500 hPa to mimic condensational heat release in deep convection. The heating (Q) is confined in the horizontal, following a half-cosine function in latitude (y),

$$Q = Q_0 \cos \pi\left[(y - y_s)/(y_n - y_s) - 1/2\right], \text{ for } y_s < y < y_n. \quad (1)$$

Within a longitudinal band $x_w < x < x_e$, it is zonally uniform except in a 5° zone on east and west sides where it ramps off to zero.

Figure 11a shows the LBM surface response near the steady state to a broad heating over the TIO: $x_w = 40°\text{E}$, $x_e = 100°\text{E}$; $y_s = 20°\text{S}$, $y_n = 20°\text{N}$. The maximum heating rate is set at 1 K day^{-1}. Because of the strong monsoon circulation in the JJA mean state, the low-level circulation anomalies are rather asymmetric, with a stronger response north than south of the equator. Equatorial symmetry strengthens at upper levels and near the international date line near the surface. The Kelvin wave response is visible in the sea level pressure field. On the northern flank of the Kelvin wave, surface friction turns the winds northeasterly, causing surface divergence there.

To test whether this Kelvin wave–induced divergence would lead to a strong anticyclone with the help of convection–circulation feedback, we conduct the following experiment with interactive heating over the NW Pacific. For simplicity, the horizontal and vertical structure of the interactive heating follows Eq. (1), with $x_w = 120°\text{E}$, $x_e = 180°$; $y_s = 10°\text{N}$, $y_n = 20°\text{N}$, a NW Pacific region chosen based on observations (Fig. 4). The magnitude of convective heating is parameterized as a linear function of surface convergence $Q_0 = -\alpha\nabla \bullet u_s$,

where $\mathbf{u}_s$ is the perturbation surface wind velocity averaged in the same NW Pacific region, and the coefficient α controls the strength of the convection–circulation feedback. Although crude, the empirically based parameterization is intended to illustrate the effect of this feedback on the development of NW Pacific anomalies in response to the TIO heating. The LBM is forced by the same broad TIO heating as before, but with an additional, interactive heat source over the NW Pacific. Convective feedback coefficient α is chosen so that the maximum heating rate is 1.8 K day^{-1} in the steady state. The results are qualitatively insensitive to the choice of α.

Figure 11b shows the LBM response on day 30 when it is in a nearly steady state. The model response is now dominated by a strong anticyclone from the SCS to NW Pacific, where the convection–circulation feedback amplifies the Kelvin wave–induced Ekman divergence and maintains a strong diabatic cooling. The model response resembles observed anomalies during JJA(1) from the north Indian Ocean to the NW Pacific (Figs. 4 and A1), including anomalous easterlies in 10°–20°N from the Arabian Sea to the international date line. The importance of reduced convection over the NW Pacific for the anticyclonic circulation is consistent with Terao and Kubota's (2005) linear model study using prescribed heating. The LBM with interactive NW Pacific heating even simulates a weak cyclonic circulation east of Japan, consistent with observations and with Kosaka and Nakamura's (2006) suggestion that the PJ pattern is a dynamical mode of the atmosphere shaped by the summer mean flow. The general agreement between the LBM experiment and observations supports our hypothesis that the Kelvin wave forced by the TIO warming triggers the suppression of convection and the development of a surface anticyclone over the NW Pacific.

b. North Indian Ocean effect

An additional GCM experiment has been carried out to narrow down the TIO subdomain that is most important for the formation of the NW Pacific anticyclone. In the SIO run where the SST increase is limited to the tropical South Indian Ocean (SIO), precipitation increases south and decreases north of the equator, with a C-shaped, antisymmetric wind pattern (Fig. 10d), similar to observations over the western TIO (Fig. 6). The positive and negative anomalies of this precipitation dipole in the meridional direction are nearly equal in magnitude, rendering a small basin mean. As a result, anomalies over the Pacific are negligible. Figure 10c shows the TIO–SIO difference, which may be taken as the response to an NIO warming. The rainfall increase over the NIO is much larger than the reduction south of the equator. The net increase in the basin-mean precipitation forces a Kelvin wave response with low pressure and easterly wind anomalies over the equatorial Pacific, triggering a reduction in precipitation and the formation of a surface anticyclone over the subtropical NW Pacific. These model results indicate that SST anomalies over the NIO are more important for NW Pacific summer anomalies than those over the SIO. The preference for the NIO is likely due to higher mean SST, and hence stronger SST forcing of the atmosphere than over the SIO.

Figure 12 shows the observed SST correlation with a summer NW Pacific anticyclone index defined as the (27.5°–32.5°N) minus (10°–15°N) difference in surface zonal wind averaged in 130°–160°E. The correlation is low with local SST but strong over the NIO and SCS, corroborating the GCM results. SST correlation is also high over the equatorial southeast Indian Ocean, where negative IOD events sometimes develop during JJA(1), as in 1998. GCM results show that during summer of 1998, the east equatorial Indian Ocean warming is important in reducing precipitation anomalies in East Asian and the NW Pacific (Shen et al. 2001). There is a tendency for NW Pacific precipitation to correlate negatively with that over the TIO, the middle reach of the Yangtze River, and near Japan, broadly consistent with the GCM.

5. Summary and discussion

We have investigated ENSO-induced anomalies during the summer [JJA(1)] following its peak phase using observations and atmospheric models. The anticyclone centered in the subtropical NW Pacific emerges as the dominant anomaly pattern in the lower troposphere from our correlation and EOF analyses. This anomalous anticyclonic circulation explains many regional JJA(1) climate anomalies related to ENSO in Fig. 2. The weakened southwest monsoon causes the SCS to warm up; precipitation decreases at Guam and SLP increases in the anticyclone; the negative wind curls force downwelling ocean Rossby waves detected as a sea level rise at Ishigaki Island a few months later; and the PJ teleconnection from the subtropics intensifies baiu rainfall over Japan as observed at Hachijo Island.

Such summer atmospheric anomalies must be anchored by SST anomalies somewhere even though eastern Pacific SST anomalies have dissipated by JJA(1). The SST increase over the TIO and SCS is the most robust ocean anomaly pattern during JJA(1), making it a likely cause of persistent atmospheric anomalies (block arrow in Fig. 13). The tropospheric temperature anomaly pattern resembles the Matsuno–Gill response to a localized heat source over the TIO, offering additional support for the capacitor mechanism in which the El Niño–induced TIO warming

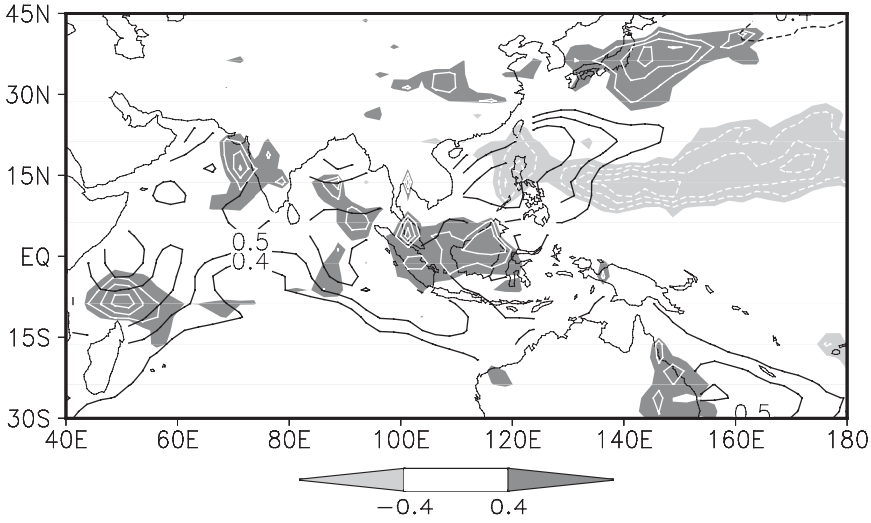

FIG. 12. Precipitation (gray shade and white contours) and SST (black contours) correlation during JJA with a NW Pacific anticyclone index, defined as (27.5°–32.5°N) minus (10°–15°N) zonal wind difference averaged in 120°–150°E. Only correlation above ±0.4 is shown, and contour intervals are 0.1.

persists through the summer and sustains atmospheric anomalies after El Niño itself is gone. Observed precipitation anomalies are weak over the TIO, suggesting the moist-adiabatic adjustment as the mechanism for the SST forcing of tropospheric temperature.

Atmospheric GCM experiments show that the long persistence of positive SST anomalies outside the tropical Pacific maintains the delayed tropospheric warming during and after the decay of El Niño (Kumar and Hoerling 2003; Lau et al. 2005). Our results suggest that this tropospheric warming triggers the suppression of NW Pacific convection. To our knowledge, our study is the first that relates these two robust atmospheric anomaly patterns that outlast El Niño. The JJA(1) tropospheric warming displays a Kelvin wave wedge extending into the western Pacific, acting to lower SLP near the equator and induce northeasterly winds and divergence north of the equator. The Ekman divergence initiates the suppression of deep convection over the NW Pacific (Fig. 6). The linear atmospheric model results support the Kelvin WIED mechanism and illustrate the importance of circulation–convection feedback for amplifying the surface high over the NW Pacific: surface divergence in the high pressure suppresses convection while the reduced latent heating intensifies the high and anticyclonic circulation.

We have conducted an atmospheric GCM experiment by increasing SST over the TIO. The model reproduces the baroclinic Kelvin wave over the equatorial Pacific and the anticyclone anomaly in the NW Pacific, in support of the above Kelvin wave–induced Ekman divergence mechanism. The NW Pacific anticyclone is too weak compared to observations because the model underestimates the summer precipitation climatology in the subtropical rainband, and hence the local circulation–convection feedback. An additional experiment with the SST warming confined to the south of the equator indicates that the NIO SST warming is the most important forcing of the Pacific response both on and north of the equator. This model result is consistent

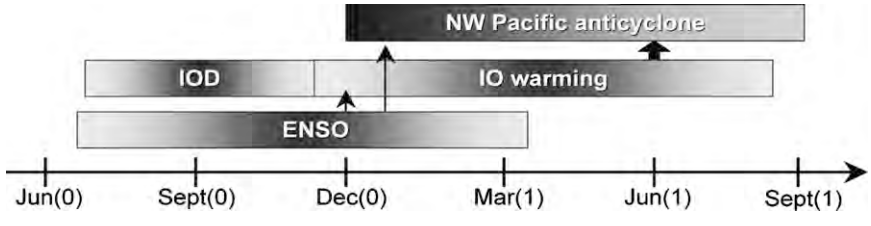

FIG. 13. Seasonality of major modes of Indo–western Pacific climate variability. Vertical arrows indicate causality, and the block arrow emphasizes the TIO capacitor effect, the major finding of the present study.

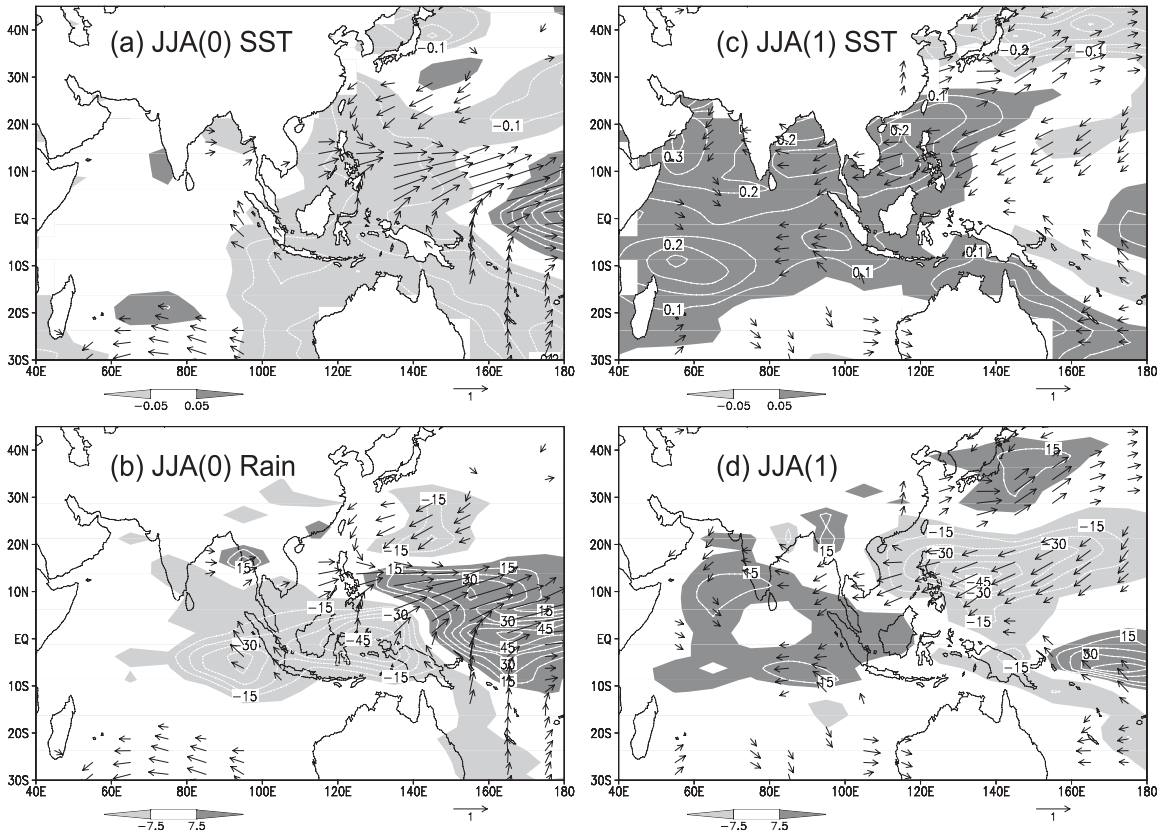

FIG. A1. Regression upon the NDJ(0) Niño-3.4 index for (left) JJA(0) and (right) JJA(1): (top) SST (°C) and (bottom) precipitation (mm month^{-1}).

with the observational analysis that NW Pacific anticyclone is most highly correlated with NIO SST.

The NW Pacific anticyclone anomaly begins to develop at the peak of El Niño and persists through the following summer (Harrison and Larkin 1996; Wang et al. 2003). The center of this anticyclone, as well as the center of negative precipitation anomalies, displays a northward shift from 5°–10°N during winter to 15°N during summer (Fig. 9). This meridional shift reflects a change in mechanism for maintaining the anticyclone. During winter, the precipitation decrease is collocated with negative SST anomalies, with the latter possibly being induced by the intensified northeasterly trades through the WES-V mechanism (Wang et al. 2000) with contributions from the TIO warming via the Kelvin WIED mechanism. During JJA(1), the precipitation decrease is most highly correlated with NIO SST, reflecting the remote influence from there, likely via the baroclinic Kelvin wave. Local JJA(1) SST anomalies are rather complicated, varying from positive in the western to marginally negative in the central and eastern parts of the NW Pacific anticyclone (Fig. 4).

The schematic in Fig. 13 summarizes the results. El Niño develops during the summer of year 0, peaks in winter, and decays in the spring of year 1. It induces the basin-wide warming over the TIO that persists through JJA(1). During the summer following El Niño, the TIO warming is the main culprit for the anomalous anticyclone and suppressed rainfall over the subtropical NW Pacific.

The following important question still remains: how is the TIO warming maintained through JJA(1)? A companion paper (Du et al. 2009) suggests that ocean–atmosphere interaction within the TIO is important.

TABLE A1. Statistics of summer (JJA) EOF modes over the Indo-western Pacific: explained variance (row 2), and season relative to the peak of El Niño (row 3) inferred from correlation (r) with the NDJ(0) ENSO index (row 4). For comparison, row 5 lists the simultaneous correlation with the JJA ENSO index. The PC pairs of (SST-2, Rain-1) and (SST-1, Rain-2) are correlated at 0.78 and 0.74, respectively.

EOF	SST-2	Rain-1	SST-1	Rain-2
Variance (%)	16	21	29	17
Season inferred	JJA(0)	JJA(0)	JJA(1)	JJA(1)
r-Niño NDJ(0)	0.71	0.76	0.69	0.75
r-Niño JJA	0.66	0.72	0.33	0.05

Specifically, the downwelling ocean Rossby wave anchors the warming, not only over the SWIO thermocline dome but also over the NIO by inducing northeasterly wind anomalies, which relax the southwest monsoon during early summer and reduce latent heat flux from the ocean.

Acknowledgments. We wish to thank R.-H. Huang, Q. Liu, W. Chen, J. Yang, and H. Annamalai for helpful discussion, M. Watanabe for making the LBM available, G. Wu and T. Terao for pointing us to earlier modeling work on TIO effects, and H. Nakamura and an anonymous reviewer for their useful comments. This work is supported by the U.S. National Science Foundation, Japan Agency for Marine-Earth Science and Technology, Natural Science Foundation of China (NSFC), and Chinese Academy of Sciences (CAS). IPRC/SOEST Publication 541/7584.

APPENDIX

JJA(0) and JJA(1) Comparison

A typical El Niño event affects the Indo–western Pacific climate during summers of both its developing and decay years. Figure A1 compares ENSO-induced anomalies between JJA(0) and JJA(1) based on a regression analysis referenced to the NDJ(0) ENSO index. During JJA(0), El Niño warming already takes shape over the equatorial Pacific, increasing rainfall and inducing westerly wind anomalies there to sustain the Bjerknes feedback. South of the equator from the Maritime Continent to the eastern Indian Ocean, SST decreases, suppressing atmospheric convection there. Over the eastern Indian Ocean, the SST cooling is coupled with the southeasterly wind anomalies, and the couplet often develops into an Indian Ocean dipole (IOD) mode, growing on the Bjerknes feedback (Saji et al. 1999; Webster et al. 1999; Schott et al. 2008). In the subtropical NW Pacific (15°–20°N), a surface cyclonic anomaly develops as part of the baroclinic Rossby wave forced by the Pacific warming.

While the centers of action for SST, precipitation, and surface winds are in the tropical Pacific during JJA(0), they shift to the Indo–western Pacific during JJA(1), anchored by the TIO warming (Figs. 4 and A1c,d). Decreased precipitation and the anticyclonic circulation over the subtropical NW Pacific are the most pronounced anomalies of the atmosphere during JJA(1). From the NIO to the NW Pacific, anomalies of precipitation and surface winds tend to have opposite signs during JJA(0) and JJA(1). This biennial tendency of the Indo–western Pacific response to ENSO, previously noted (e.g., Wang et al. 2003; Alexander et al. 2004), is due to the difference in forcing mechanism: the JJA(0) anomalies are largely forced directly by eastern Pacific SST while the JJA(1) anomalies are largely forced by TIO SST.

We have performed EOF analyses separately for precipitation and SST over the Indo–western Pacific Oceans (20°S–40°N, 40°E–180°) for the JJA season. The dominant modes are similar to the regression patterns in Fig. A1 (Table A1). Specifically, the second SST and first precipitation modes resemble the JJA(0) regressions, explaining 16% and 21% of the total variance, respectively. Their principal components (PCs) correlate highly with the NDJ(0) ENSO index. The first SST and second precipitation EOF modes resemble the JJA(1) regressions, explaining 29% and 17% of the total variance, respectively. Their PCs correlate highly with the ENSO index 6 months before [NDJ(0)], but not simultaneously [JJA(1)], which is indicative of the TIO capacitor effect.

REFERENCES

Alexander, M. A., I. Bladé, M. Newman, J. R. Lanzante, N.-C. Lau, and J. D. Scott, 2002: The atmospheric bridge: The influence of ENSO teleconnections on air–sea interaction over the global oceans. *J. Climate,* **15,** 2205–2231.

——, N.-C. Lau, and J. D. Scott, 2004: Broadening the atmospheric bridge paradigm: ENSO teleconnections to the tropical West Pacific-Indian Oceans over the seasonal cycle and to the North Pacific in summer. *Earth Climate: The Ocean-Atmosphere Interaction, Geophys. Monogr.,* Vol. 147, Amer. Geophys. Union, 85–103.

Annamalai, H., P. Liu, and S.-P. Xie, 2005: Southwest Indian Ocean SST variability: Its local effect and remote influence on Asian monsoons. *J. Climate,* **18,** 4150–4167.

Behera, S. K., P. S. Salvekar, and T. Yamagata, 2000: Simulation of interannual SST variability in the tropical Indian Ocean. *J. Climate,* **13,** 3487–3499.

Chiang, J. C. H., and A. H. Sobel, 2002: Tropical tropospheric temperature variations caused by ENSO and their influence on the remote tropical climate. *J. Climate,* **15,** 2616–2631.

——, and B. R. Lintner, 2005: Mechanisms of remote tropical surface warming during El Niño. *J. Climate,* **18,** 4130–4149.

Copsey, D., R. Sutton, and J. R. Knight, 2006: Recent trends in sea level pressure in the Indian Ocean region. *Geophys. Res. Lett.,* **33,** L19712, doi:10.1029/2006GL027175.

Deser, C., and A. S. Phillips, 2006: Simulation of the 1976/77 climate transition over the North Pacific: Sensitivity to tropical forcing. *J. Climate,* **19,** 6170–6180.

——, ——, and J. W. Hurrell, 2004: Pacific interdecadal climate variability: Linkages between the tropics and the North Pacific during boreal winter since 1900. *J. Climate,* **17,** 3109–3124.

Du, Y., and S.-P. Xie, 2008: Role of atmospheric adjustments in the tropical Indian Ocean warming during the 20th century in climate models. *Geophys. Res. Lett.,* **35,** L08712, doi:10.1029/2008GL033631.

——, ——, G. Huang, and K.-M. Hu, 2009: Role of air–sea interaction in the long persistence of El Niño–induced North Indian Ocean warming. *J. Climate,* in press.

Emanuel, K. A., J. D. Neelin, and C. S. Bretherton, 1997: Reply to comments by Bjorn Stevens, David A. Randall, Xin Lin and Michael T. Montgomery on 'On large-scale circulations in convecting atmospheres.' *Quart. J. Roy. Meteor. Soc.,* **123,** 1779–1782.

Enfield, D. B., and D. A. Mayer, 1997: Tropical Atlantic SST variability and its relation to El Niño–Southern Oscillation. *J. Geophys. Res.,* **102,** 929–945.

Fu, C., and X. Teng, 1988: The relationship between ENSO and climate anomaly in China during the summer time. *Sci. Atmos. Sin.,* **12,** 133–141.

Gill, A. E., 1980: Some simple solutions for heat-induced tropical circulation. *Quart. J. Roy. Meteor. Soc.,* **106,** 447–462.

Harrison, D., and N. K. Larkin, 1996: The COADS sea level pressure signal: A near-global El Niño composite and time series view, 1946–93. *J. Climate,* **9,** 3025–3055.

Huang, B., and J. L. Kinter III, 2002: Interannual variability in the tropical Indian Ocean. *J. Geophys. Res.,* **107,** 3199, doi:10.1029/2001JC001278.

Huang, R., and Y. Wu, 1989: The influence of ENSO on the summer climate change in China and its mechanism. *Adv. Atmos. Sci.,* **6,** 21–32.

——, W. Chen, B. Yang, and R. Zhang, 2004: Recent advances in studies of the interaction between the East Asian winter and summer monsoons and ENSO cycle. *Adv. Atmos. Sci.,* **21,** 407–424.

Kalnay, E., and Coauthors, 1996: The NCEP/NCAR 40-Year Reanalysis Project. *Bull. Amer. Meteor. Soc.,* **77,** 437–471.

Kang, I.-S., and Coauthors, 2002: Intercomparison of the climatological variations of Asian summer monsoon precipitation simulated by 10 GCMs. *Climate Dyn.,* **19,** 383–395.

Kawamura, R., T. Matsumura, and S. Iizuka, 2001: Role of equatorially asymmetric sea surface temperature anomalies in the Indian Ocean in the Asian summer monsoon and El Niño–Southern Oscillation coupling. *J. Geophys. Res.,* **106,** 4681–4693.

Klein, S. A., B. J. Soden, and N.-C. Lau, 1999: Remote sea surface temperature variations during ENSO: Evidence for a tropical atmospheric bridge. *J. Climate,* **12,** 917–932.

Kosaka, Y., and H. Nakamura, 2006: Structure and dynamics of the summertime Pacific-Japan teleconnection pattern. *Quart. J. Roy. Meteor. Soc.,* **132,** 2009–2030.

Kumar, A., and M. P. Hoerling, 1998: Specification of regional sea surface temperatures in atmospheric general circulation model simulations. *J. Geophys. Res.,* **103,** 8901–8907.

——, and ——, 2003: The nature and causes for the delayed atmospheric response to El Niño. *J. Climate,* **16,** 1391–1403.

Lau, N.-C., and M. J. Nath, 2003: Atmosphere–ocean variations in the Indo-Pacific sector during ENSO episodes. *J. Climate,* **16,** 3–20.

——, A. Leetmaa, M. J. Nath, and H. L. Wang, 2005: Influences of ENSO-induced Indo–western Pacific SST anomalies on extratropical atmospheric variability during the boreal summer. *J. Climate,* **18,** 2922–2942.

Lengaigne, M., J. P. Boulanger, C. Menkes, and H. Spencer, 2006: Influence of the seasonal cycle on the termination of El Niño events in a coupled general circulation model. *J. Climate,* **19,** 1850–1868.

Li, S., J. Lu, G. Huang, and K. Hu, 2008: Tropical Indian Ocean basin warming and East Asian summer monsoon: A multiple AGCM study. *J. Climate,* **21,** 6080–6088.

Liu, Q., X. Jiang, S.-P. Xie, and W. T. Liu, 2004: A gap in the Indo-Pacific warm pool over the South China Sea in boreal winter: Seasonal development and interannual variability. *J. Geophys. Res.,* **109,** C07012, doi:10.1029/2003JC002179.

Matsuno, T., 1966: Quasi-geostrophic motions in the equatorial area. *J. Meteor. Soc. Japan,* **44,** 25–43.

Murakami, T., and J. Matsumoto, 1994: Summer monsoon over the Asian continent and western North Pacific. *J. Meteor. Soc. Japan,* **72,** 719–745.

Murtugudde, R., and A. J. Busalacchi, 1999: Interannual variability of the dynamics and thermodynamics, and mixed layer processes in the Indian Ocean. *J. Climate,* **12,** 2300–2326.

Neelin, J. D., and H. Su, 2005: Moist teleconnection mechanisms for the tropical South American and Atlantic sector. *J. Climate,* **18,** 3928–3950.

Nitta, T., 1987: Convective activities in the tropical western Pacific and their impact on the Northern Hemisphere summer circulation. *J. Meteor. Soc. Japan,* **65,** 373–390.

Ohba, M., and H. Ueda, 2006: A role of zonal gradient of SST between the Indian Ocean and the western Pacific in localized convection around the Philippines. *SOLA,* **2,** 176–179.

Rayner, N. A., P. Brohan, D. E. Parker, C. K. Folland, J. J. Kennedy, M. Vanicek, T. Ansell, and S. F. B. Tett, 2006: Improved analyses of changes and uncertainties in sea surface temperature measured in situ since the mid-nineteenth century: The HadSST2 dataset. *J. Climate,* **19,** 446–469.

Roeckner, E., and Coauthors, 2003: Atmospheric general circulation model ECHAM5: Part I. Max-Planck-Institut für Meteorlogie Rep. 349, 140 pp.

Saji, N. H., B. N. Goswami, P. N. Vinayachandran, and T. Yamagata, 1999: A dipole mode in the tropical Indian Ocean. *Nature,* **401,** 360–363.

Schott, F. A., S.-P. Xie, and J. P. McCreary, 2008: Indian Ocean circulation and climate variability. *Rev. Geophys.,* in press.

Shen, X., M. Kimoto, A. Sumi, A. Numaguti, and J. Matsumoto, 2001: Simulation of the 1998 East Asian summer monsoon by the CCSR/NIES AGCM. *J. Meteor. Soc. Japan,* **79,** 741–757.

Sobel, A. H., I. M. Held, and C. S. Bretherton, 2002: The ENSO signal in tropical tropospheric temperature. *J. Climate,* **15,** 2702–2706.

Su, H., and J. D. Neelin, 2003: The scatter in tropical average precipitation anomalies. *J. Climate,* **16,** 3966–3977.

——, ——, and C. Chou, 2001: Tropical teleconnection and local response to SST anomalies during the 1997–98 El Niño. *J. Geophys. Res.,* **106,** 20 025–20 043.

Terao, T., and T. Kubota, 2005: East-west SST contrast over the tropical oceans and the post E1 Niño western North Pacific summer monsoon. *Geophys. Res. Lett.,* **32,** L15706, doi:10.1029/2005GL023010.

Tokinaga, H., and Y. Tanimoto, 2004: Seasonal transition of SST anomalies in the tropical Indian Ocean during El Niño and Indian Ocean dipole years. *J. Meteor. Soc. Japan,* **82,** 1007–1018.

Trenberth, K. E., G. W. Branstator, D. Karoly, A. Kumar, N.-C. Lau, and C. Ropelewski, 1998: Progress during TOGA in understanding and modeling global teleconnections associated with tropical sea surface temperatures. *J. Geophys. Res.,* **103,** 14 291–14 324.

Ueda, H., T. Yasunari, and R. Kawamura, 1995: Abrupt seasonal change of large-scale convective activity over the western Pacific in the northern summer. *J. Meteor. Soc. Japan,* **73,** 795–809.

——, M. Ohba, and S.-P. Xie, 2009: Important factors for the development of the Asian–northwest Pacific summer monsoon. *J. Climate,* in press.

Vecchi, G. A., and D. E. Harrison, 2006: The termination of the 1997–98 El Niño. Part I: Mechanisms of oceanic change. *J. Climate,* **19,** 2633–2646.

Wang, B., and LinHo, 2002: Rainy season of the Asian-Pacific summer monsoon. *J. Climate,* **15,** 386–398.

——, R. Wu, and X. Fu, 2000: Pacific–East Asia teleconnection: How does ENSO affect East Asian climate? *J. Climate,* **13,** 1517–1536.

——, ——, and T. Li, 2003: Atmosphere–warm ocean interaction and its impact on Asian–Australian monsoon variability. *J. Climate,* **16,** 1195–1211.

——, Q. Ding, X. Fu, I.-S. Kang, K. Jin, J. Shukla, and F. Doblas-Reyes, 2005: Fundamental challenge in simulation and prediction of summer monsoon rainfall. *Geophys. Res. Lett.,* **32,** L15711, doi:10.1029/2005GL022734.

Wang, C., R. H. Weisberg, and J. I. Virmani, 1999: Western Pacific interannual variability associated with the El Niño–Southern Oscillation. *J. Geophys. Res.,* **104,** 5131–5149.

——, W. Wang, D. Wang, and Q. Wang, 2006: Interannual variability of the South China Sea associated with El Niño. *J. Geophys. Res.,* **111,** C03023, doi:10.1029/2005JC003333.

Watanabe, M., and M. Kimoto, 2000: Atmosphere-ocean thermal coupling in the North Atlantic: A positive feedback. *Quart. J. Roy. Meteor. Soc.,* **126,** 3343–3369.

——, and F. F. Jin, 2003: A moist linear baroclinic model: Coupled dynamical–convective response to El Niño. *J. Climate,* **16,** 1121–1139.

Webster, P. J., A. M. Moore, J. P. Loschnigg, and R. R. Leben, 1999: Coupled oceanic-atmospheric dynamics in the Indian Ocean during 1997-98. *Nature,* **401,** 356–360.

Worley, S. J., S. D. Woodruff, R. W. Reynolds, S. J. Lubker, and N. Lott, 2005: ICOADS release 2.1 data and products. *Int. J. Climatol.,* **25,** 823–842.

Wu, G. X., and H. Liu, 1995: Neighborhood response of rainfall to tropical sea surface temperature anomalies. Part I: Numerical experiment. *Chinese J. Atmos. Sci.,* **19,** 422–434.

——, F. Sun, J. Wang, and X. Wang, 1995: Neighborhood response of rainfall to tropical sea surface temperature anomalies. Part II: Data analysis. *Chinese J. Atmos. Sci.,* **19,** 663–676.

Wu, R., B. P. Kirtman, and K. Pegion, 2006: Local air–sea relationship in observations and model simulations. *J. Climate,* **19,** 4914–4932.

——, ——, and V. Krishnamurthy, 2008: An asymmetric mode of tropical Indian Ocean rainfall variability in boreal spring. *J. Geophys. Res.,* **113,** D05104, doi:10.1029/2007JD009316.

Xie, P., and P. A. Arkin, 1996: Analyses of global monthly precipitation using gauge observations, satellite estimates, and numerical model predictions. *J. Climate,* **9,** 840–858.

Xie, S.-P., 2004: The shape of continents, air-sea interaction, and the rising branch of the Hadley circulation. *The Hadley Circulation: Past, Present and Future,* H. F. Diaz and R. S. Bradley, Eds., Kluwer Academic, 121–152.

——, and S. G. H. Philander, 1994: A coupled ocean-atmosphere model of relevance to the ITCZ in the eastern Pacific. *Tellus,* **46A,** 340–350.

——, H. Annamalai, F. A. Schott, and J. P. McCreary, 2002: Structure and mechanisms of South Indian Ocean climate variability. *J. Climate,* **15,** 864–878.

——, Q. Xie, D. Wang, and W. T. Liu, 2003: Summer upwelling in the South China Sea and its role in regional climate variations. *J. Geophys. Res.,* **108,** 3261, doi:10.1029/2003JC001867.

Yang, J., Q. Liu, S.-P. Xie, Z. Liu, and L. Wu, 2007: Impact of the Indian Ocean SST basin mode on the Asian summer monsoon. *Geophys. Res. Lett.,* **34,** L02708, doi:10.1029/2006GL028571.

Yoo, S.-H., S. Yang, and C.-H. Ho, 2006: Variability of the Indian Ocean sea surface temperature and its impacts on Asian-Australian monsoon climate. *J. Geophys. Res.,* **111,** D03108, doi:10.1029/2005JD006001.

Yulaeva, E., and J. M. Wallace, 1994: The signature of ENSO in global temperature and precipitation fields derived from the microwave sounding unit. *J. Climate,* **7,** 1719–1736.